

5th SCACR 2011
International Short Conference on
Applied Coastal Research



Honouring Prof. Robert A. Dalrymple

6th to 9th June, 2011

RWTH Aachen University, Germany

PROCEEDINGS

edited by

Holger Schüttrumpf and Giuseppe Roberto Tomasicchio

Table of Contents

Lectures

Jentsje van der Meer

Design aspects of breakwaters and sea defences 3

Panayotis Prinos

Integrated management of risk of coastal flooding and the European Directive 2007/60/EC for the assessment and management of risk 35

Pham Thanh Nam, Magnus Larson and Hans Hanson

Mathematical modeling of coastal sediment transport and beach evolution with special emphasis on coastal structures 60

Technical Session 1: Coastal Structures

Sevket Cokgor, Ozgur Durmus, Kaan Koca, Baris Ozen and Senol Dundar

Modeling of turbulence fields in front of the rubble mound breakwater..... 87

Peyman Aghtouman, Fatemeh Aliyari and Zeinab Aghtouman

Effect of berm width on reshaped profile of berm breakwaters..... 97

Anja Brüning, Hans Fabricius Hansen, Flemming Schlütter and Ulrich Vierfuß

A hybrid modelling approach for floating breakwater dimensioning..... 105

Antonino Viviano, Carlo Lo Re, Luca Cavallaro and Enrico Foti

Run-up over variable slope bottom. Validation for a fully nonlinear Boussinesq-type of model..... 113

Antje Bornschein, Stefanie Lorke and Reinhard Pohl

Influence of current and wind on wave run-up on slopes 121

Giuseppe Barbaro, Giandomenico Foti and Giovanni Malara

A probabilistic approach for run-up estimation 129

Hiroaki Kashima and Katsuy Hirayama

Effects of surf beat caused by long period swell on wave overtopping rate on complex bathymetry..... 136

Corrado Altomare, Leonardi Damiani and Xavier Gironella

Overtopping formula for vertical tiers-headed breakwaters 144

Technical Session 2: Coastal Processes

Luminita-Elena Boblea and Michael Hartnett

A development of an estuarine hydrodynamic model in cylindrical coordinates	155
--	------------

Peter Mewis

A 2D morphodynamic-numerical model of the surf zone “Strand”	163
---	------------

Paolo Blondeaux, Giovanna Vittori, Antonello Bruschi, Francesco Lalli and Valeria Pesarino

Steady streaming and sediment transport generated by propagating sea waves.....	171
--	------------

Alejandro López-Ruiz, Miguel Ortega-Sánchez, Asunción Baquerizo and Miguel Á. Losada

Short-term simulation of the evolution of a curvilinear coast.....	179
---	------------

Technical Session 3: Coastal Risk / Risk Management

Giovanna Vittori and Paolo Blondeaux

Turbulent boundary layer and sediment transport under a solitary wave: a RANS model	189
--	------------

Vincent Gruwez, Annelies Bolle, Toon Verwaest and Wael Hassan

Numerical and physical modelling of wave penetration in Oostende harbour during severe storm conditions	198
--	------------

Philippe Larroudé and Olivier Brivois

Numerical simulation for indicator of vulnerability to climate change on four French beaches.....	206
--	------------

Hartmut Hein, Stephan Mai and Ulrich Barjenbruch

Coastal long term processes, tidal characteristics and climate change.....	214
---	------------

Dörte Salecker, Angelika Gruhn, Christian Schlamkow and Peter Fröhle

Parameterization of storm surges as a basis for assessment of risks of failure for coastal protection measures	222
---	------------

Andreas Kortenhaus, Andreas Burzel, Marie Naulin, Dilani Dassanayake, Hocine Oumeraci, Jürgen Jensen, Thomas Wahl, Christoph Mudersbach, Gabriele Gönner, Birgit Gerkenmeier, Sigrid Thumm and Gehad Ujeyl

Integrated risk analysis for extreme storm surges (XtremRisk).....	230
---	------------

Frank Thorenz and Holger Blum

Implementing coastal defence strategies for sandy coasts – reinforcement of the Norderney dune revetment	238
---	------------

Technical Session 4: Coastal and Port Environments

Macarena Rodrigo, Francisco Vila, Antonio Ruiz-Mateo, Ana Álvarez, Ana Lloret and Manuel Antequera

Physical modelling of brine discharges from a cliff..... 247

Janina Sothmann, Dagmar Schuster, Jens Kappenberg and Nino Ohle

Efficiency of artificial sandbanks in the mouth of the Elbe Estuary for damping the incoming tidal energy 255

Theoharris Koftis and Panayotis Prinos

Estimation of wave attenuation over Posidonia Oceanica 264

Maike Paul and Tjeerd Bouma

The effect of organism traits and tidal currents on wave attenuation by submerged vegetation 272

Kubilay Cihan, Yalçın Yüksel and Seda Cora

Dynamic analysis of gravity quay walls under seismic forces 280

Koen Van Doorslaer, Julien De Rouck, Leen Baelus and Stefaan Gysens

(Architectural) measures to control wave overtopping inside the harbour of Oostende..... 289

Technical Session 5: Coastal Developments

Hanz D. Niemeyer, Cordula Berkenbrink, Marco Miani, Anne Ritzmann, Pushpa Dissanayake, Heiko Knaak, Andreas Wurpts and Ralf Kaiser

Coastal protection of lowlands: Are alternative strategies a match to effects of climate change 299

Kai Wirtz and Friedhelm Schroeder

Product orientation in COSYNA: integrating coastal observation and models . 308

Giorgio Manno, Carlo Lo Re and Giuseppe Ciraolo

Shoreline detection in a gentle slope Mediterranean beach 316

Andrew Brown and Jon Kemp

Re-examining the Dean Profile for designing artificial beaches in Dubai..... 324

Giuseppe Roberto Tomasicchio, Felice D'Alessandro and Gianluca Tundo

On wave transmission coefficient at low-crested structures 332

Maria Gabriella Gaeta and Alberto Lamberti

A numerical study for the stability analysis of articulated concrete mattress for submarine pipeline protection..... 340

Markus Wilke and Hartmut Hangen

**Geosynthetic tubes as construction element for coastal protection works –
Fundamental design aspects; Application possibilities and practical
experience** 348

Le Hai Trung, Henk Jan Verhagen and Jentsje van der Meer

Wave overtopping resistance of grassed slopes in Viet Nam..... 356

Technical Session 6: Modelling, Management

Sönke Dangendorf and Jürgen Jensen

**Methods to detect change points in water level time series –
Application to the German Bight**..... 367

Elke M. I. Meyer, Ralf Weisse, Janina Sothmann, Heinz Günther, Ulrich Callies, Hans von
Storch, Frauke Feser, Katja Woth and Iris Grabemann

The coastDat data set and its potential for coastal and offshore applications .. 375

Nor Aida Zuraimi Md-Noar and Martin Greenhow

Wave impact on a seawall with a deck and on a baffle in front of seawall 380

Dimitris Stagonas, Gerald Müller, William Batten and Davide Magagna

**Mapping the temporal and spatial distribution of experimental impact induced
pressures at vertical seawalls: a novel method** 388

Fabian Gier, Jens Mönnich, Hillel Rubin, Holger Schüttrumpf and Jentsje van der Meer

Experimental study on the stability of interlocking block placed revetments ... 395

Poster Presentations

Hany Ahmed and Andreas Schlenkhoff

**Investigation of the effect of permeability on wave interaction with a barrier by
application of PIV**..... 405

Corrado Altomare and Girolamo Mauro Gentile

**Monitoring phases of the re-naturalization process of the Torre del Porto
Beach** 414

Susumu Araki, Saki Fujii and Ichiro Deguchi

Numerical simulation on the motion of cubic armour block..... 422

Elvira Armenio, Felice D'Alessandro, Giuseppe Roberto Tomasicchio and Francesco
Aristodemo

**Estimation and verification of long-shore sediment transport (LST) at
Lecce coastline** 430

Arne Arns, Doris Blutner, Hilmar von Eynatten, Roger Häußling, Frerk Jensen, Volker Karius, Christoph Mudersbach, Dirk van Riesen, Malte Schindler, Holger Schüttrumpf, Henrike Strack, Theide Wöffler and Jürgen Jensen

Developing sustainable coastal protection- and management strategies for Schleswig-Holstein's Halligen considering climate changes (ZukunftHallig) 437

Marcus Behrendt

Artificial surfing reefs – An option for the German Baltic Sea coast? 445

Duccio Bertoni, Giovanni Sarti, Giuliano Benelli and Alessandro Pozzebon

Abrasion rates of coarse sediments on two artificial pebble beaches at Marina di Pisa (Italy) 451

Holger Blum, Frank Thorenz and Hans-Jörg Lambrecht

The risk assessment for North Sea coastal lowlands 459

Sandro Carniel, Mauro Sclavo and Renata Archetti

The use of integrated wave-current-sediment numerical tools to model coastal dynamics: an applications in the North Adriatic Sea 466

Carla Faraci, Enrico Foti and Rosaria E. Musumeci

Estimate of cross-shore coastal erosion induced by extreme waves and by effects of sea level rise through ETS model 474

Christian Grimm, Daniel Bachmann and Holger Schüttrumpf

Risk management in coastal engineering – A case study in northern Germany 482

Angelika Gruhn, Peter Fröhle, Dörte Salecker and Christian Schlamkow

On the failure mechanism and failure probabilities of flood protection dunes at the German Baltic Sea Coast – first results of a research project – 490

Bahare Majdi, Freydoon Vafai, S. Mohammad Hossein Jazayeri Shoushtari and Alireza Kebriaee

Opportunities and threats along Iranian coastlines 498

Christos Makris, Constantine Memos and Yannis Krestenitis

Modelling of breaking wave dynamics, surf zone turbulence and wave-induced mean flows with the SPH numerical method 507

Samir Medhioub, Abir Baklouti and Chokri Yaich

Impact of the dredging process on the granulometry of a shelly sand. Case study of TAPARURA project, Sfax, Tunisia 515

Diogo R. C. B. Neves, Luiz A. M. Endres, Conceição J. E. M. Fortes, Takashi Okamoto

Physical modelling of wave propagation and wave breaking in a wave channel 526

Paulo Duarte Raposeiro, Maria Teresa Reis, Diogo Neves, Conceição Juana Fortes, João Alfredo Santos, Adriana Vieira, Javier Ramalheira, Anabela Simões, Eduardo Brito de Azevedo and M. Conceição Rodrigues

Methodology for overtopping risk assessment in port areas. Application to the Port of Praia da Vitória (Azores, Portugal) 536

Renata Archetti, Sandro Carniel, Claudia Romagnoli and Mauro Sclavo

Rapid evolution of shoreline after a beach nourishment downdrift of a groin and at an embayed beach: theory vs. observation 544

Felice D'Alessandro and Giuseppe Roberto Tomasicchio

Dune erosion regimes observed in large-scale experiments 552

Björn R. Rübke, Holger Schüttrumpf, Theide Wöffler, Hanna Hadler, Timo Willershäuser and Andreas Vött

Tsunamis in the Gulf of Kyparissia (western Peloponnese, Greece) – risk assessment based on numeric simulation and field evidence 560

Fenneke Sterlini, Thaiënne A. G. P. van Dijk, Steven IJzer and Suzanne J. M. H. Hulscher

Seasonal changing sand waves and the effect of surface waves 570

Pietro Danilo Tomaselli, Carlo Lo Re and Giovanni Battista Ferreri

Analysis of tide measurements in a Sicilian harbour 579

Valentina Vannucchi and Lorenzo Cappietti

Estimation of wave energy potential of the northern Mediterranean Sea 587

Adriana S. Vieira, Conceição J. E. M. Fortes, Geraldo de Freitas Maciel and Carlos Roberto Minussi

Comparative analysis of wind generated waves on the Ilha Solteira lake, by using numerical models OndisaCAD and SWAN 594

Lectures

Design aspects of breakwaters and sea defences

Jentsje van der Meer¹

Abstract

As a keynote lecture this paper does not focus on one subject, but treats four main aspects to some depth, including new not yet published items. The first item is on definition of design wave climate and parameters. The design method for rock slopes, the Van der Meer formulae, have been related to the version in the new Rock Manual. A method has been given to calculate cumulative damage in an easy way. A new proposed classification of berm breakwaters has been given with new design information on berm breakwaters. Berm breakwaters can be divided in hardly, partly and fully reshaping berm breakwater. Finally, the Wave Overtopping Simulator has been described with its main results and conclusions on strength of grass covered landward slopes of dikes. Moreover, the Simulator has also been used to test vertical storm walls. The most recent innovation is the wave run-up simulation.

Keywords: rock slope, berm breakwater, overtopping, run-up, stability, grass slope

1 Design wave climate, definitions and parameters

For breakwater design in this paper it is assumed that physical site conditions and data collection have been established and are available. These are mainly the bathymetry, the hydraulic boundary conditions and geotechnical investigations and data. Required design conditions are mainly on wave heights, wave periods, water depths, water levels and tidal variation for various return periods.

The conditions have to be described at the toe of the structure as these are the waves that will attack the structure and by using these conditions, the design methods will give a fair prediction of behaviour. In case the conditions change quickly in the last wave length before reaching the breakwater, it may be a good design decision to take the conditions half a wave length or more in front of the structure, instead at the toe. Such a decision will give a design with more safety, but will actually give a less accurate description of the behaviour of the structure.

The wave height to be used is the incident significant wave height H_s at the toe of the structure. Often the spectral wave height, $H_{m0} = 4(m_0)^{0.5}$ is taken as this wave height comes from wave climate studies. Another definition of significant wave height is the average of the highest third of the waves, $H_{1/3}$. This wave height is, in principle, the wave height that should be used in the Van der Meer formulae (Van der Meer (1988-1)). In deep water both definitions produce almost the same value, but situations in shallow water can lead to differences of 10-15%. In shallow water conditions one may also consider the use of the $H_{2\%}$, especially if stability formulae are used.

In many cases, a foreshore is present on which waves can break and by which the significant wave height is reduced. There are models that in a relatively simple way can predict the reduction in energy from breaking of waves and thereby the accompanying wave height at the toe of the structure. The wave height must be calculated over the total spectrum including any long-wave energy present.

Based on the spectral significant wave height, it is reasonably simple to calculate a wave height distribution and accompanying significant wave height $H_{1/3}$ using the method of Battjes and Groenendijk (2000).

Various wave periods can be defined for a wave spectrum or wave record. Conventional wave periods are the peak period T_p (the period that gives the peak of the spectrum) and the average period T_m (calculated from the wave record). The relationship T_p/T_m usually lies between 1.1 and 1.25. A wave period that is used more often in recent years, certainly in wave run-up and

¹ Van der Meer Consulting BV. P.O. Box 423, 8440 AK, Heerenveen, the Netherlands. jm@vandermeerconsulting.nl

overtopping formulae, is the spectral period $T_{m-1,0}$ ($= m_{-1}/m_0$). This period gives more weight to the longer periods in the spectrum than an average period and, independent of the type of spectrum, gives similar wave run-up or overtopping for the same values of $T_{m-1,0}$ and the same wave heights. In this way, wave run-up and overtopping can be easily determined for double-peaked and "flattened" spectra, without the need for other difficult procedures. It is a wave period that has not been used a lot in breakwater design, yet. For a single peaked spectrum the ratio $T_p/T_{m-1,0}$ is close to 1.1. Any formulae can actually be rewritten by the use of this ratio and, in case of bi-modal or flattened spectra, the use of $T_{m-1,0}$ will then give a more accurate prediction.

Wave steepness is defined as the ratio of wave height to wave length, $s_o = H_s/L_o$. Here L_o is the deep water wave length $L_o = 2\pi H_s/(gT^2)$. With use of T_p the steepness becomes s_{op} , with the mean period T_m it becomes s_{om} and finally, with the period $T_{m-1,0}$ it becomes $s_{om-1,0}$. The wave steepness tells something about the wave's history and characteristics. Generally a steepness of $s_{om} = 0.01$ indicates a typical swell sea and a steepness of $s_{om} = 0.04$ to 0.06 a typical wind sea. Swell seas will often be associated with long period waves. But also wind seas may become seas with low wave steepness if the waves break on a gentle foreshore. By wave breaking the wave period does not change much, but the wave height decreases. This leads to a lower wave steepness. A low wave steepness on relatively deep water means swell waves, but for depth limited locations it often means broken waves on a (gentle) foreshore.

Stability formulae include often the stability number $H_s/\Delta D_{n50}$. Here Δ is the relative buoyant density, $\Delta = (\rho_r - \rho_w)/\rho_w$, with ρ_r is the mass density of the rock and ρ_w the mass density of the water. The nominal diameter $D_{n50} = (M_{50}/\rho_r)^{1/3}$, where M_{50} is the average mass of the stone class. Actually, D_{n50} is the "cubical" size of the rock with the average mass, regardless of the actual shape of the rock.

Dynamically stable structures like rock, gravel and shingle beaches, can be described by a dynamically stable profile, see Van der Meer (1988-1). Such profiles change with the wave and water level conditions. The wave period has similar effects on the profile as the wave height, meaning that a longer wave period as well as a larger wave height would result in a "longer" profile. It is for this reason that Van der Meer (1988-1) introduced the dimensionless wave height - wave period parameter H_oT_o , which can be described by:

$$H_oT_o = H_s/\Delta D_{n50} T(g/D_{n50})^{0.5} \quad (1)$$

With a mean period T_m the parameter becomes H_oT_{om} and with the peak period H_oT_{op} . It is this parameter that also has been used in the past, like in PIANC (2003) to describe the recession of berm breakwaters.

Dynamically stable structures show some stability for a certain wave condition if a certain profile has been formed and this profile does not change as long as the wave conditions do not change. During every wave action (wave breaking, wave run-up and wave run-down) it is possible that individual stones move up and down, but this does not affect the profile. This is of course not a good situation for a breakwater. Dynamically stable for a berm breakwater means that under severe wave conditions and after reshaping still some stones move up and down the slope during individual wave action. This is different from the movement of rock during reshaping as in that situation rock move to a more stable position and then remain there.

Statically stable structures are stable under severe wave attack and only then may show a little movement of rock, called damage. Such damage, S_d , is related to the eroded area, A_e , around the water level, see Figure 1. This graph shows the original definition as given in Van der Meer (1988-1) with S as damage and A as erosion area. The definition of damage is:

$$S_d = A_e/D_{n50}^2 \quad (2)$$

Dynamically stable structures can be given by a profile, statically stable structures by the damage S_d . But what about berm breakwaters? In many cases the berm is not as stable as a statically stable structure and will reshape to some extent. PIANC (2003) used the recession, Rec , of the berm as a parameter to describe the behaviour of berm breakwaters. Figure 2 gives the principle idea of the recession parameter.

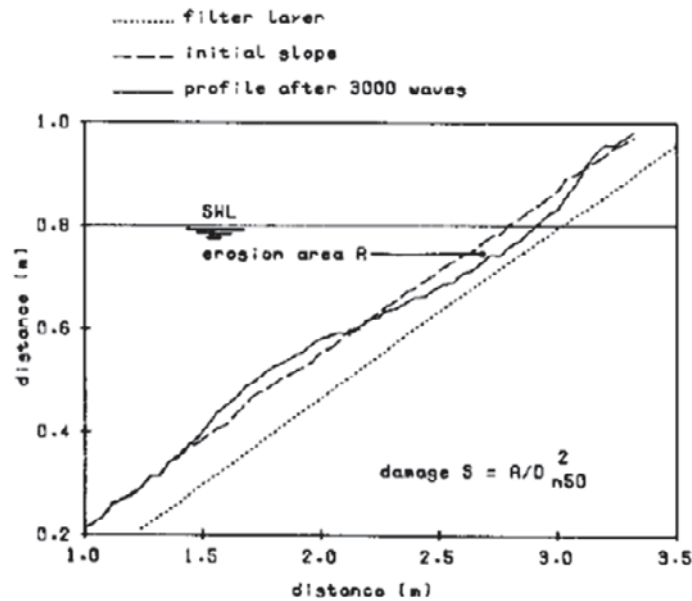


Figure 1: Definition of damage for a statically stable structure, Van der Meer (1988-1).

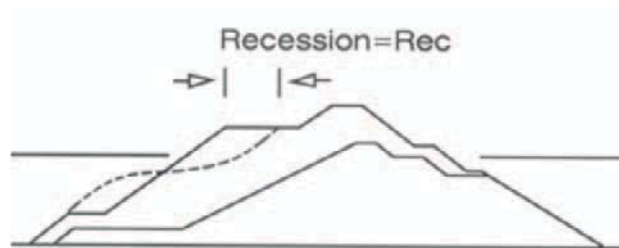


Figure 2: Principle idea of recession to describe the behaviour of a berm breakwater.

2 Rock slope stability

2.1 Van der Meer formulae

The original Van der Meer formulae for statically stable rock slopes were published in Van der Meer (1988-1), but also in journal papers Van der Meer (1987) and Van der Meer (1988-2). These formulae were also described in the first Rock Manual, 1992. The new Rock Manual, 2007, however, treats a rewritten version of the original Van der Meer formulae, and added the so-called modified Van der Meer formulae for shallow water. It should be noted that these latter formulae were not modified by Van der Meer, but were based on the limited and confidential work of Van Gent et al. (2004).

Different from the Rock Manual (2007), only the original Van der Meer formulae will be applied here. The formulae can be applied to shallow water conditions where the significant wave height on the foreshore has reduced to a minimum of 50% of its original value on deep water.

The original formulae are given by:

For plunging waves:

$$H_s/\Delta D_{n50} = 6.2P^{0.18}(S_d/\sqrt{N_w})^{0.2}\xi_m^{-0.5} \quad (3)$$

and for surging waves:

$$H_s/\Delta D_{n50} = 1.0P^{-0.13}(S_d/\sqrt{N_w})^{0.2}\sqrt{\cot\alpha}\xi_m^P \quad (4)$$

The transition of plunging (breaking) waves to surging (non-breaking) waves is given for:

$$\xi_{cr} = [6.2P^{0.31}\sqrt{\tan\alpha}]^{\frac{1}{P+0.5}} \quad (5)$$

- with: H_s = significant wave height at the toe of the structure (actually $H_{1/3}$)
 Δ = relative buoyant density: $\Delta = (\rho_r - \rho_w)/\rho_w$
 ρ_r = mass density of rock
 ρ_w = mass density of water
 D_{n50} = nominal diameter: $D_{n50} = (M_{50}/\rho_r)^{1/3}$
 M_{50} = average mass of the rock class
 P = notional permeability factor
 $P = 0.1$: impermeable core beneath the armour layer
 $P = 0.5$: permeable core beneath the armour layer
 $P = 0.6$: homogeneous structure (only one rock class)
 S_d = damage level
 N_w = number of waves in the considered sea state
 ξ_m = breaker parameter: $\xi_m = \tan\alpha/(2\pi H_s/(gT_m^2))^{0.5}$
 g = acceleration of gravity
 T_m = mean period from time domain analysis
 α = slope angle

For $\xi_{cr} < \xi_m$ Equation 3 applies and for $\xi_{cr} > \xi_m$ this is Equation 4.

For detailed description of the notional permeability factor P , short sea states with $N_w < 1000$ and long sea states with $N_w > 7500$, as well as the reliability of the formulae, one is referred to Van der Meer (1988-1, 1988-2, 1987-1) or the Rock Manuals (1992 and 2007). The easiest way to apply the formulae is to use the program Breakwat (commercial software from Deltares) as limitations with respect to the formulae are embedded in this program.

The classification of the damage level S_d for a two-diameter thick rock slope is given in Table 1. The initial damage (some settlement, first rocks moving) is given as $S_d = 2$ or 3 , depending on the slope angle. Failure of the rock layer is defined as under layer visible. In average about a layer of one diameter thickness will then be removed, with at certain locations a little more, showing the under layer. Intermediate damage is in between initial damage and failure. Table 1 has to be used in designing rock slopes on stability.

Table 1: Classification of the damage level S_d .

slope	initial damage	intermediate damage	failure (under layer visible)
1:1.5	2	3-5	8
1:2	2	4-6	8
1:3	2	6-9	12
1:4	3	8-12	17
1:6	3	8-12	17

The original Van der Meer formulae were modified in the Rock Manual (2007), based on the work of Van Gent et al. (2004 - confidential data). They applied a bulk analysis on their data, using the original Van der Meer formulae, but adopting different coefficients. Their work showed less stability in (very) shallow conditions and explanations for this were not given. For very shallow conditions it may well be that the trends in the Van der Meer formulae are no longer valid, like the relationship between damage and storm duration or number of waves, N : $S_d \equiv \sqrt{N}$; or the relationship between damage and wave height: $S_d \equiv H_s^5$. This was not considered in the analysis by Van Gent et al. (2004). The effect in the Rock Manual (2007) is that for rock slopes in shallow water one ends up with a (much) larger rock size than with the original Van der Meer formulae.

Another question is to what conditions of "shallow water" the original Van der Meer formulae would be correct. It is true that most of the tests of Van der Meer (1988-1) were performed for relatively deep water. One of the implications is then that the formulae are valid for Rayleigh-distributed wave heights. A limited number of tests in Van der Meer (1988-1) were performed on a 1:30 foreshore with breaking wave conditions. These tests showed that in more shallow conditions the distribution of wave heights is no longer according to a Rayleigh distribution and that less large wave heights occur. It means that in shallow water the stability *increases* if the

same significant wave height is present as in deep water. This is logical as less high wave heights are present in the shallow water case. For this reason it has been proposed in Van der Meer (1988-1) to use the $H_{2\%}$ instead of the significant wave height (and adjust the coefficient in the formulae). The important trend in shallow water is that stability increases if waves start to break. Using the $H_{2\%}$ -value in the Van der Meer formulae instead of the H_s leads for shallow water to a smaller required rock mass.

In very shallow water, however, other effects may play a role. If the original significant wave height reduces by breaking to 30% of its original value or even less, the wave steepness becomes very long and the shape of the waves may be very different from less shallow water situations. Short waves or high wave steepnesses do not longer exist for these conditions. It were mainly these kind of conditions that were the subject of the research of Van Gent et al. (2004). In their research, however, they never mentioned that the stability increases for first breaking of waves and they do not distinguish between first breaking and very large breaking.

2.2 Design method for rock slopes

The design of a breakwater or rock slope is often concentrated around extreme conditions close to or exceeding the estimated design life of the structure. But that is only a part of the whole picture. The full extreme distribution of wave conditions: wave heights, wave periods and water levels, should be considered. A picture like Figure 3 gives insight in possible wave climates and is a reproduction from PIANC (1992). It shows the (deep water) significant wave height versus the return period, from 1 - 1000 years

The curves show the different levels for the 100-years condition, which give an estimation of the severity of the wave climate. Another feature in Figure 3, however, is the steepness of the curves. A flat curve means that wave heights close to a 100-years condition occur fairly frequently, but this condition will never significantly be exceeded. On the other hand, a steep curve means that yearly wave heights may be quite low, but really extreme conditions significantly exceed a 100 years condition.

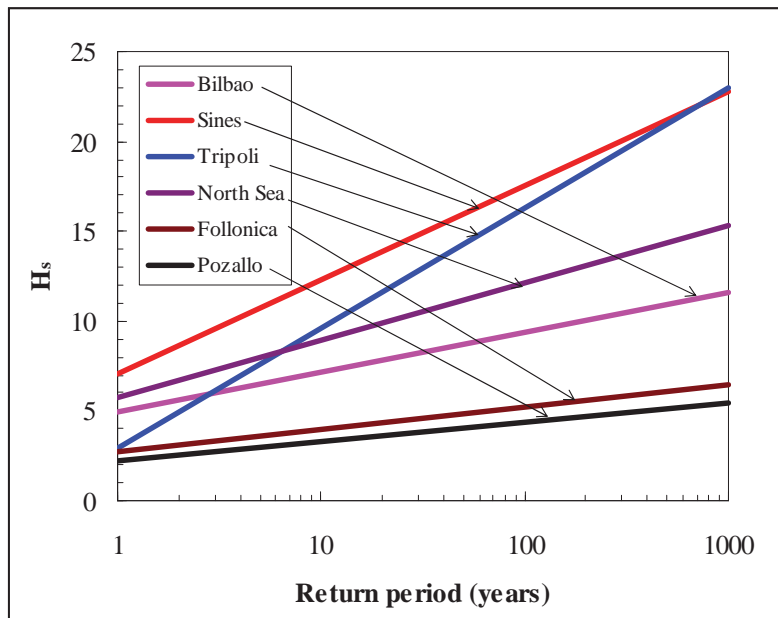


Figure 3: Deep water wave climates (from PIANC (1992)).

A good way to consider the whole wave climate for design of a rock slope is to consider a few practical return periods and define associated allowable damage levels. For instance, a small return period should not give any damage, however, for a very extreme return period damage is acceptable, but failure of the slope is not. An example is shown in Table 2, but it should be noted that this is an example and could be adjusted according to the client's desire for a more or less conservative structure.

Table 2: Example of allowable damage, depending on return period.

Return period	Allowable damage	
	Rock slopes	Concrete units
10 y	$S_d = 2$	$N_{od} = 0.2$
50-100 y	$S_d = 3-5$	$N_{od} = 0.5$
300-500 y	$S_d = 8-12$	$N_{od} = 1.0$ (depending on slope)

Equations 3 and 4 (or the program Breakwat) can then be used to calculate the damages or required rock weights for each return period. It depends then on the actual wave climate which condition will be determining for design. In general, for flat curves like the Pozallo curve in Figure 3, the 10-years condition will govern the design. For steep curves, like Bilbao, it will be the very extreme conditions.

2.3 Cumulative damage

The Van der Meer formulae are based on one test condition per test. After each test of 3000 waves the slope was reconstructed for the next test. In this way test results were not influenced by earlier test conditions. But in reality a structure will experience many storms with different attitude. Also testing of breakwaters for design is often performed with a series of increasing sea states. The Van der Meer formulae can be applied to such situations by the cumulative damage method, which has been described in Van der Meer (1985-discussion) and which has also been implemented in Breakwat.

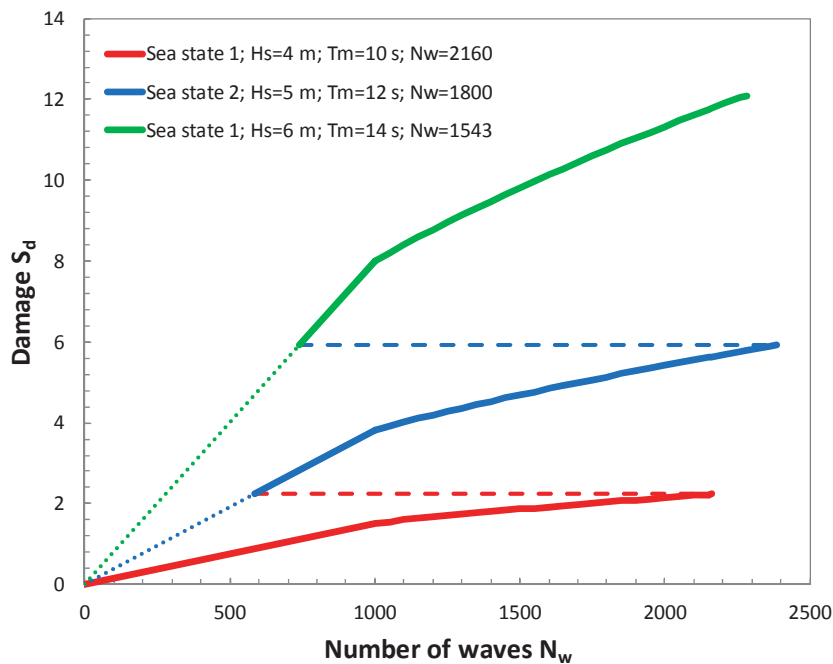


Figure 4: Cumulative method to calculate damage for various consecutive sea states.

In fact the method is fairly easy. A first sea state, given by the significant wave height H_{s1} , or by $H_{2\%1}$, mean period T_{m1} and number of waves N_{w1} , gives a calculated damage level S_{d1} . A second sea state would be defined by H_{s2} , (or $H_{2\%2}$), T_{m2} and N_{w2} . The next calculation is to determine the number of waves N_{w12} that is required for the second sea state to create the damage S_{d1} that was caused by the first sea state. Then the damage S_{d2} for the second sea state can be calculated, but now by applying $N_{w12} + N_{w2}$ as the number of waves. A third sea state would be calculated by repeating the same procedure.

Figure 4 gives an example calculation. The structure has a slope with $\cot\alpha = 1.5$, a notional permeability of $P = 0.55$ and a rock class with average mass $M_{50} = 10$ t and density $\rho_r = 2700$

kg/m³. The mass density of the water is $\rho_w = 1025 \text{ kg/m}^3$. Three consecutive sea states have been defined. each lasting for six hours:

- Sea state 1; $H_s=4 \text{ m}$; $T_m=10 \text{ s}$; $N_w=2160$
- Sea state 2; $H_s=5 \text{ m}$; $T_m=12 \text{ s}$; $N_w=1800$
- Sea state 1; $H_s=6 \text{ m}$; $T_m=14 \text{ s}$; $N_w=1543$

For each of the sea states the $S_d - N_w$ curve can be calculated using Equations 3 and 4. The damage development is a straight line for the first 1000 waves and then continues as a square root function $S_d \equiv \sqrt{N}$. The damage after the first sea state can directly be calculated: $S_d = 2.24$. This damage is reached for the second sea state for 585 waves. The damage for the second sea state is then calculated for $N_w = 1800 + 585 = 2385$ and amounts to $S_d = 5.92$. This damage is reached with 738 waves for the third sea state and the final damage is then calculated with $N_w = 1543 + 738 = 2281$ and amounts to $S_d = 12.01$. The damage for sea state 3 only would be $S_d = 9.96$, so the two first seas states increased the final damage by about 20%.

3 Berm breakwaters

3.1 Classification

The principle design of reshaping berm breakwaters, as described by Baird and Hall (1984), has been developed further into less reshaping and more stable berm breakwaters with more rock classes compared to only a small and a large class, core and rock. PIANC (2003) gave a classification of berm breakwaters as shown in Table 3.

Table 3: Classification of berm breakwaters by PIANC, 2003.

Type of breakwater	$H_s/\Delta D_{n50}$	$H_o T_{om}$
Statically stable non-reshaped. In this condition few stones are allowed to move, similar to the condition for a conventional rubble mound breakwater.	< 1.5-2	< 20-40
Statically stable reshaped. In this condition the profile is allowed to reshape into a profile, which is stable and where the individual stones are also stable.	1.5-2.7	40-70
Dynamically stable reshaped. In this condition the profile is reshaped into a stable profile, but the individual stones may move up and down the front slope.	>2.7	>70

The classification uses both the stability number $H_s/\Delta D_{n50}$ as well as the dimensionless wave height - wave period parameter $H_o T_{om}$. There is a large difference between the parameters as the stability number does not include any wave period effect and the $H_o T_{om}$ parameter gives similar effect to wave height and wave period. PIANC (2003) does not conclude on which parameter should be decisive for berm breakwaters, although formulae on recession of the berm have been given as function of $H_o T_{om}$.

The classes of statically non-reshaped and reshaped berm breakwaters overlap the range of $H_s/\Delta D_{n50} = 1.5 - 2$, although a different range in $H_o T_{om}$ is given. This might suggest that a longer wave period results in more reshaping and a less stable profile. Proof of this, however, is not given.

Dynamically stable means that rock will move continuously under (severe) wave attack, which may lead to breaking of the rock and to longshore transport. Significant longshore transport, affecting the stability of the structure, should be avoided at all times. This is different from reshaping, where it is expected that displacement of rock will result in a more stable profile. One may actually conclude that dynamically stable (berm) breakwaters are not acceptable, as breakwaters during their life time should be statically stable.

PIANC (2003) has given a classification of berm breakwaters that shows that there are different types of berm breakwaters with different structural behaviour. In that sense the classification in

Table 3 is very useful. But given the remarks above and developing insight in the stability of berm breakwaters, the classification can be updated.

The reshaping (mass armoured) berm breakwater has a large berm with mainly one rock class. The berm may be long and just above design water level, but may also be quite high - even similar to the crest height - and then with a narrower berm. As the berm will reshape it is mainly the volume or cross-section of the berm that determines the design, not the width of the berm only. The seaward slope of the berm is often quite steep, up to the angle of repose of rock. The structure will be unstable as constructed, but statically stable after reshaping. The behaviour is best described by the profile of the structure and only partly by recession. The construction should be easy without significant requirements and only a few rock classes have to be made, without very large sizes. A reshaping berm breakwater will be stable for overload conditions, but then not much resiliency (reserve capacity) will be left. Experience shows that this kind of berm breakwater may need some maintenance (adding berm rock) during the life time of the structure.

A hardly reshaping Icelandic-type berm breakwater will have a high berm and the total cross-section or volume will be less compared to a reshaping berm breakwater. The high berm has also a function as it will absorb the energy of large and long waves overtopping the berm. The hardly-reshaping Icelandic-type of berm breakwaters need fairly large rock, but in small quantities. Getting large rock, using the right experience, shows that this in many cases will not significantly increase the cost of the structure. In many cases the largest class of rock above the water line will be placed according to specifications that enhance stability. In fact these stones can be placed in such a way that rocks on the outer layer are in contact with each other and loose rocks do hardly exist.

The mass armoured as well as the Icelandic-type berm breakwater may show only partly recession when designed for it. In this case it is advised to have the berm level of the mass armoured berm breakwater at the same level as the Icelandic-type. The ability to absorb wave energy with a relatively high berm is also good for the partly reshaping mass armoured berm breakwater, as partly reshaping means that quite some part of the berm is left in place. There are, however, no placement specifications for the mass armoured berm breakwater and the seaward slope still may be quite steep. If this is indeed the case, the first reshaping may be earlier than for an Icelandic-type berm breakwater, but after some reshaping they will show similar reshaping or stability.

Hardly reshaping berm breakwaters may be described by conventional damage levels S_d as well as start of recession. For partly reshaping berm breakwaters there will be more damage as well as recession. The fully reshaping berm breakwater only considers recession or actually reshaping. Based on these types of structures a new classification for berm breakwaters, including indicative values for the stability number, the damage and the recession, is shown in Table 4. These values are given for a 100-years wave condition. For wave conditions with smaller return periods the values will be smaller and consequently, for more severe wave conditions, like overload tests, the values may be larger.

Table 4: Proposed classification of berm breakwaters.

<i>Breakwater</i>	$H_s/\Delta D_{n50}$	S_d	Rec/D_{n50}
Hardly reshaping berm breakwater (Icelandic-type)	1.7 - 2.0	2 - 8	0.5 - 2
Partly reshaping Icelandic-type berm breakwater	2.0 - 2.5	10 - 20	2 - 5
Partly reshaping mass armoured berm breakwater	2.0 - 2.5	10 - 20	2 - 5
Reshaping berm breakwater (mass armoured)	2.5 - 3.0	--	5 - 12

3.2 PIANC (2003) recession data for berm breakwaters

PIANC (2003) presented recession data of many research projects, mainly with traditional reshaping berm breakwaters as well as partly Icelandic-type berm breakwaters, see Figure 5. Most of the data represent a recession larger than $5 \cdot D_{n50}$ and a stability parameter $H_0 T_{om}$ larger than 70. A large scatter is present due to various influences. Some of them would be the definition of wave height (at the toe or more at deep water), placement of rock (dumped or carefully placed), way of measuring recession, seaward slope angle, etc.

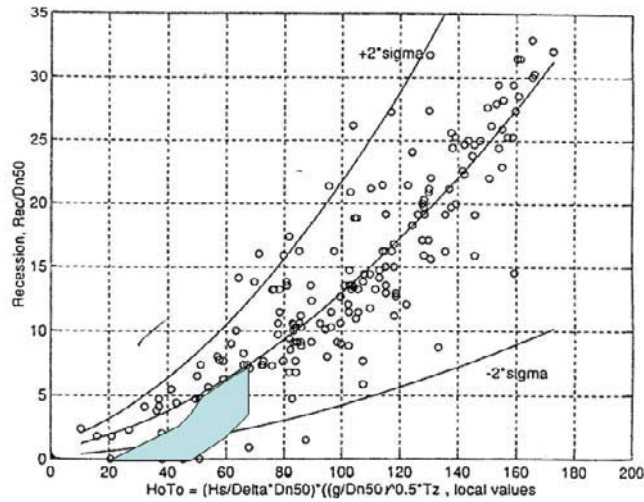


Figure 5: Recession data from PIANC (2003), including the data in Sigurdarson et al. (2008) on stable Icelandic-type berm breakwaters.

As stated above most of the PIANC (2003) data represented large recession and high stability numbers, H_oT_{om} . Focusing only on Icelandic-type berm breakwaters changes the area of interest. With the limits of $H_oT_{om} < 70$ and not more than 7-8 stones removed across the berm ($Rec/D_{n50} < 8$) leaves only the data of the lower left corner of Figure 5. In this region there are data points which do not show any recession for $H_oT_{om} = 40-50$ and others that show recession to be 7 or 8 stone wide. Also, there are data points showing recession of 2 stone wide for H_oT_{om} values of only 10. The only conclusion is that the data given in PIANC (2003) are not able to give any reliable design guideline for the Icelandic-type berm breakwater. More well-defined data are required to give such guidelines.

Sigurdarson et al. (2008 and 2011) defined requirements for reliable data representing the Icelandic-type berm breakwater and identified three data sets which fulfilled these requirements: MAST II (1996 and 1997), Myhra (2005) and Sveinbjörnsson (2008). The recession data cover the area shown in Fig. 5 and is really focussed around small recession. They found that the best fit for the recession data was obtained using the parameter H_oT_{op} , which includes the peak period, T_p , instead of the mean period, T_m . But the difference with using only the stability number $H_o = H_s/\Delta D_{n50}$, so not considering the wave period, was not large. Based on that data Sigurdarson et al. (2008) derived the following formula that provided a reasonable fit to the data shown in Figure 6:

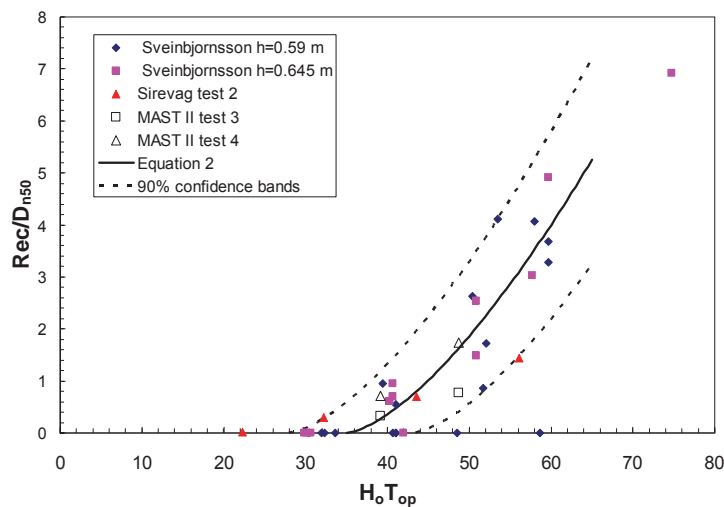


Figure 6: Recession data for an Icelandic-type berm breakwater, using the peak period T_p and showing the recession formula (6) with 90% confidence band as presented by Sigurdarson et al. (2008).

$$\text{Rec}/D_{n50} = 0.032 (H_o T_{op} - Sc)^{1.5}$$

with: $\text{Rec}/D_{n50} = 0$ for $H_o T_{op} < Sc$

(6)

and: $\mu(Sc) = 35$ and $\sigma(Sc) = 5$ and $H_o T_{op} < 70$

3.3 New and accurate data set including analysis

3.3.1 Optimized definition of recession

A statically stable design of an Icelandic-type berm breakwater has been tested in a wave flume at HR Wallingford, where the behaviour from the start of moving of the first stones, up to a few times an overload condition, was measured very precisely.

At the start of damage the recession of the berm profile varies considerably along the profile. But when the damage gets larger and the berm really reshapes into the well-know S-profile, the recession becomes more. In that case it is sufficient to measure only a few profiles, average them and measure the recession, the horizontal retreat of the berm, given in nominal diameter of the armour stone protecting the berm, D_{n50} . This has often been done in berm breakwater research, also for the less reshaping Icelandic-type berm breakwater.

In the research at HR Wallingford a very accurate laser profiler has been used and according to the method in Van der Meer (1988-1) ten profiles have been averaged to give a good description of the behaviour of the structure. Figure 7 shows an example of damage development of the averaged 10 profiles from the pre-test condition, through the full sequence of testing. Some profile or damage development starts, ending in a little reshaping at the end of the test series. Figure 8 shows on the other hand the individual ten profiles after two times the design condition. It is clear that the scatter between the different profiles is considerably larger than the average profile development over the full test sequence.

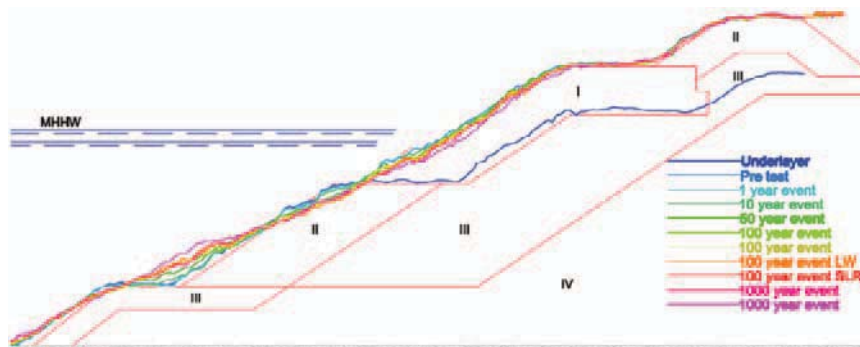


Figure 7: Development of profiles of an Icelandic-type berm breakwater under increasing wave conditions, measured with a laser profiler; each profile is the average of 10 individual profiles.

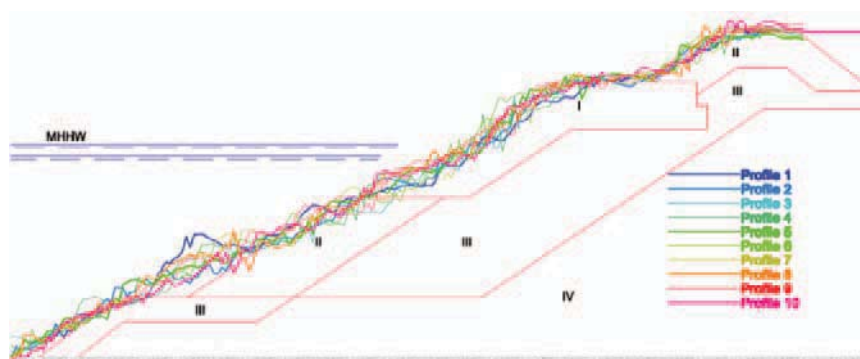


Figure 8: Ten individual profiles of the same Icelandic-type berm breakwater measured with a laser profiler after two times the design event, showing the large scatter of individual profiles.

The recession of a berm breakwater is usually defined as shown in Figure 2, that is the horizontal recession on top of the berm. This may be alright for structures that experience considerable recession but not so good for structures experiencing less recession. The damage or displacement of stones usually starts at around the still water level and then proceeds upward. For limited damage, as for the Icelandic-type berm breakwater, the damage might not have proceeded up to the top of the berm where the recession usually is measured. Another practical issue is that the recession on top the berm is not easy to define. The front slope and top of the berm of the Icelandic-type berm breakwater is covered with large stones and when these are profiled, the profile rarely shows a sharp intersection between the front slope and top of berm.

Therefore, it was necessary to modify the definition of recession to take note of profile development on the full slope from top of the berm down to low water level, not only on top of the berm. The recession is taken as the horizontal difference between the as-built profile of the Class I armour and the profile recorded after the test, see Fig. 9. Two recession parameters have been proposed. The maximum recession distance, Rec_{max} , is the greatest recession measured on any individual profile, and the average recession distance, Rec_{av} , is the recession of the average profile averaged between low water level and top of the berm.

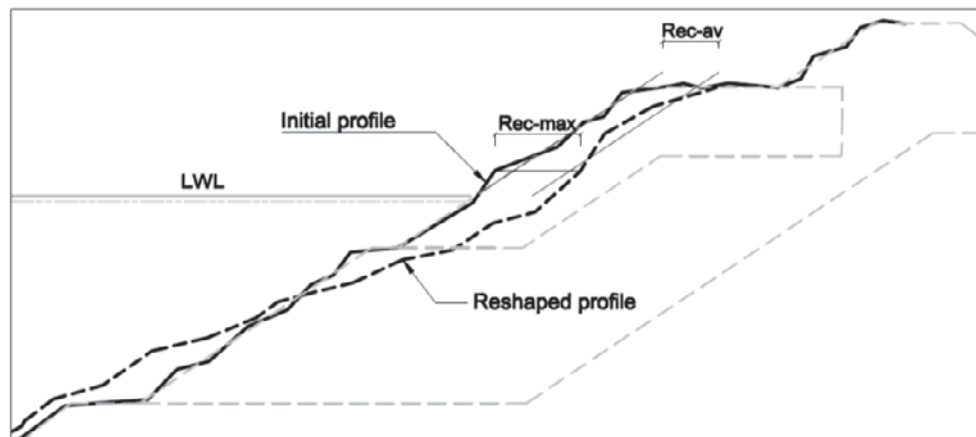


Figure 9: The modified definition of a berm recession.

3.3.2 The dataset

The seaward slope of the berm had a slope of 1:1.5. The berm itself is very porous with large rock in the whole berm. According to Van der Meer (1988-1) this would give a notional permeability factor of around $P = 0.55 - 0.6$. The erosion area A_e can also be found from the profile, which results in the damage parameter $S_d = A_e/D_{n50}^2$. It is, therefore, interesting to make a comparison between damage measured for the Icelandic-type berm breakwater and damage calculated by stability formulae for rock slopes.

Details of wave conditions, damage and recession for the three tests are given in Table 5. Design conditions for about 100-years return period are reached for stability numbers of $H_s/\Delta D_{n50} = 1.5-1.7$. Overload conditions are reached for $H_s/\Delta D_{n50} = 2.0 - 2.4$. Note that in many tests the wave steepness was quite low and therefore the wave period fairly long. This results in fairly large $H_o T_{om}$ and $H_o T_{op}$ values. Maximum recessions in Tests 1 and 2 amount to about $Rec_{av}/D_{n50} = 5$ with damage up to $S_d = 9-12$. This is well in the range of rock slope stability, see Van der Meer (1988-1). In Test 2 the rock below swl was placed a little more randomly, resulting in a slightly more damage and recession compared to Test 1. The rock used in Test 3 was slightly larger and more elongated and placed with good interlocking above swl. This resulted in hardly increase in damage and recession for the overload situations.

Table 5: Recession and damage results of 3 tests on Icelandic-type berm breakwater.

	$H_s/\Delta D_{n50}$	s_{op}	$H_o T_{om}$	$H_o T_{op}$	S_d	Rec_{av}	S_d Breakwat
Test 1	0.95	0.011	24.6	28.0	0.00	0.20	
	1.50	0.013	45.7	51.0	1.39	0.29	
	1.67	0.012	53.3	62.0	2.81	0.82	
	1.79	0.031	47.1	43.5	4.87	1.54	
	1.75	0.015	55.6	61.1	5.73	1.69	
	1.99	0.015	66.2	73.8	7.18	2.44	
	2.40	0.039	55.0	60.4	8.94	3.92	
Test 2	0.95	0.011	24.8	28.2	0.00	0.29	0.08
	1.49	0.013	45.4	50.7	2.45	0.86	0.84
	1.68	0.012	48.9	63.6	5.13	2.10	2.33
	1.65	0.019	43.6	48.8	5.80	2.31	2.96
	1.69	0.013	51.2	62.5	6.26	2.55	3.54
	1.94	0.014	64.5	71.9	9.15	4.10	4.90
	2.36	0.038	53.9	59.2	11.56	5.20	7.16
	1.66	0.014	52.9	58.1	11.62	5.19	7.16
Test 3	0.88	0.010	22.5	25.8	0.00	0.15	0.05
	1.38	0.012	41.5	46.4	0.71	0.25	0.54
	1.50	0.013	45.0	52.0	1.37	0.20	1.07
	1.56	0.013	44.9	54.9	1.56	0.36	1.71
	1.71	0.031	44.2	40.4	1.90	0.50	2.61
	1.60	0.013	50.1	56.1	2.31	0.51	2.64
	1.54	0.013	46.0	54.2	2.01	0.56	2.64
	1.85	0.014	60.5	68.3	2.40	0.56	3.67
	2.30	0.037	51.9	58.0	2.43	1.21	5.86

3.3.3 Description and comparison of damage S_d

The stability formulae of Van der Meer (1988-1) include the significant wave height, mean wave period, slope angle and notional permeability. It is also possible to calculate cumulative damage (mainly through BREAKWAT), which makes it possible to simulate the whole test sequence in a test. In the test sequence (see Table 5) sometimes the wave height was kept the same or even lowered, while the wave period was changed. The stability formulae suggest that stability would increase with increasing wave period, as surging or non-breaking waves are present for a steep slope and with a large notional permeability.

Figure 10 shows the measured damage as a function of the stability number. Damage increases as long as the wave height is increased and the increase in damage is small if tests with similar wave heights have been performed. As explained before, only the overload situation in Test 3 ($H_s/\Delta D_{n50} = 2.3$) showed remarkable stability, due to specific placement of the larger rock.

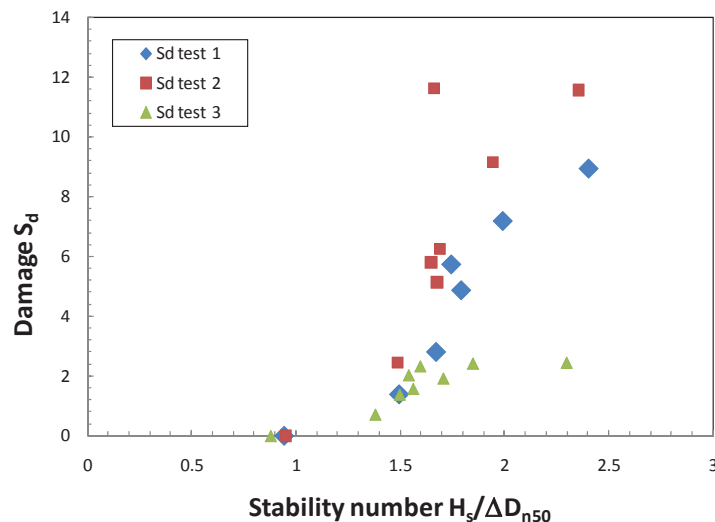


Figure 10: Damage versus stability number, as measured.

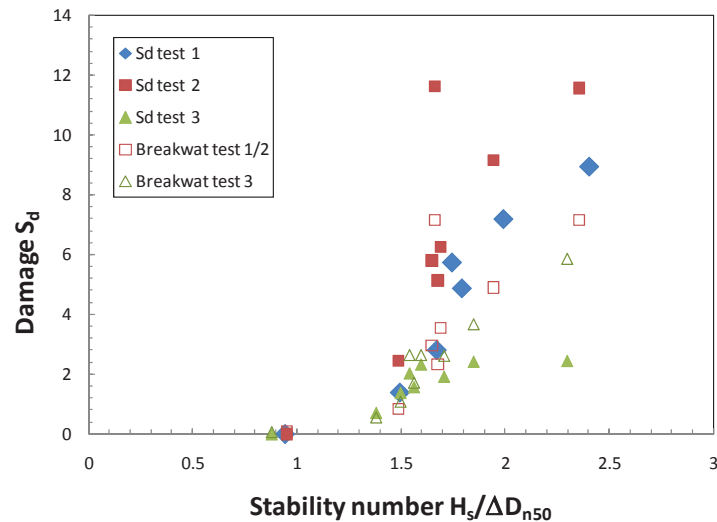


Figure 11: Damage versus stability number, measured and calculated.

For Test 2 Figure 10 shows a similar damage of $S_d = 11.6$ for $H_s/\Delta D_{n50} = 2.36$ and 1.66. Actually, in the last test the wave height was lowered (and the wave period increased), but this did not lead to larger damage.

Figure 11 is similar to Figure 10, but now the results of the damage calculations have been included. The cumulative damage was calculated for Test 2 (open squares), which has actually similar conditions as Test 1, and also for Test 3 with different rock size and test conditions (open triangles). Results of calculations depend on the input. The original Van der Meer equations were used through Breakwat and cumulative damage was calculated. The berm is very permeable, but the structure is not completely a homogeneous structure. For this reason a notional permeability factor of $P = 0.55$ was used. The seaward slope of the berm breakwater is 1:1.5. But it would not give a correct comparison if this slope was used in the calculations. The berm breakwater has a horizontal berm and also some horizontal parts below water level (between rock classes I and II and at the toe). The *average* slope from toe to the crest level was close to 1:2 and therefore this slope angle was used for calculations.

Calculated damages are slightly lower for Test 3 than for Tests 1 and 2, which is according to the measurements. It is clear, however, that the berm breakwater in Test 3 showed very good behaviour for the final wave height, better than the prediction of the stability formulae.

Note also that the calculations give similar damage for the last two test series in Test 2, where the wave height was lowered (with an increase in wave period). This is completely according to the measurements, although the damage in average was a little larger in the tests than predicted by the stability formulae.

It can be concluded that the stability formulae for rock slopes in average give a fairly good prediction of the damage at the seaward side of a statically stable Icelandic-type of berm breakwater. The measurements also confirm the stability formulae in the sense that a larger wave period does not really increase damage. Wave height seems to be more important than wave period.

3.4 Detailed analysis of recession Rec

Figures 12 and 13 show the development of the average recession, as defined in Figure 9, for the three tests. In Figure 12 the recession is given versus $H_o T_{op}$, which is comparable with Figure 6. Figure 13 uses $H_s/\Delta D_{n50}$ instead of $H_o T_{op}$, and is more comparable with Figure 10.

The data points have been connected by lines as this shows better the sequence of the test series in the test. Figure 12 clearly shows where sometimes the $H_o T_{op}$ condition was lowered (similar or even larger wave height, but with smaller wave period). If the use of $H_o T_{op}$ would be correct, then a significantly lower $H_o T_{op}$ value should *not* lead to significant increase of

recession. All tests, however, show that recession increases, even with a much lower H_oT_{op} value.

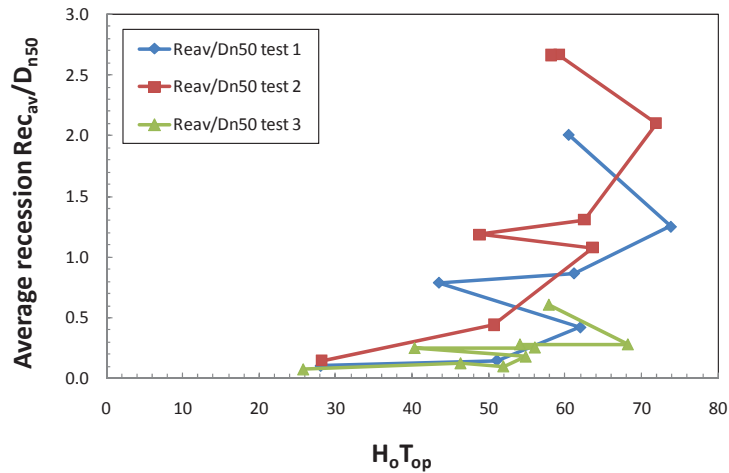


Figure 12: Average recession Rec_{av} versus H_oT_{op} .

That is different in Figure 13, where damage increases if $H_s/\Delta D_{n50}$ increases and where damage remains the same if the wave height is reduced. Figure 13 shows a similar behaviour as for the damage in Figure 10. Again it must be concluded that the wave period has hardly any effect on recession and that the wave height is the governing parameter.

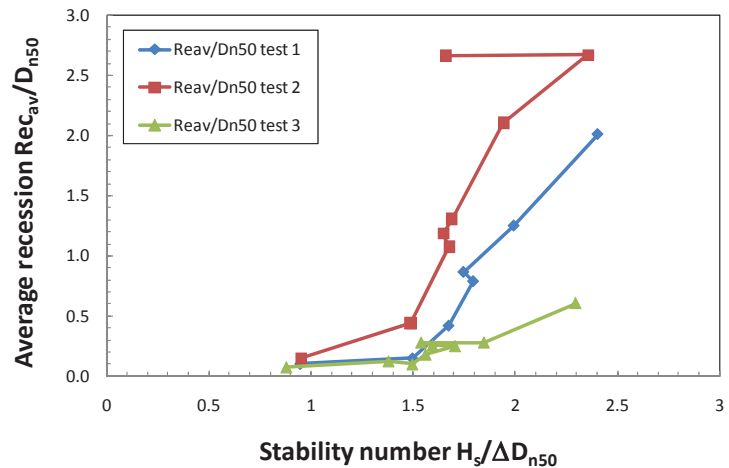


Figure 13: Average recession Rec_{av} versus $H_s/\Delta D_{n50}$.

It does not mean that the parameter H_oT_{op} is not a good parameter to describe recession or reshaping. The parameter was developed for dynamically stable structures like gravel and cobble beaches, see Van der Meer (1988-1), and also performs well for really reshaping berm breakwaters with $H_s/\Delta D_{n50}$ around 3. But start of damage or recession describes more statically stable rock slopes (specifically almost homogeneous structures) and here stability and recession are not really influenced by the wave period.

Figure 6, taken from Sigurdarson et al. (2008), shows three data sets with Equation 6 as prediction formula. Figure 14 shows the same data, but now with the data of the new tests. As in many test series long wave periods were applied, most of the tests are on the right side of the prediction curve and far outside the 90% confidence band. As concluded above, it is not a good way to include the wave period for start of recession, comparable to statically stable rock slopes.

Figure 15 shows the average recession versus the stability number $H_s/\Delta D_{n50}$. The results of Test 2 fall exactly within the earlier data, Test 1 shows a little more reshaping and Test 3, for the final wave height, a little lower. The points of Sveinbjornsson (2008) with $Rec = 0$ are mainly due to inaccuracy as only one profile was measured, not ten as in the latest tests.

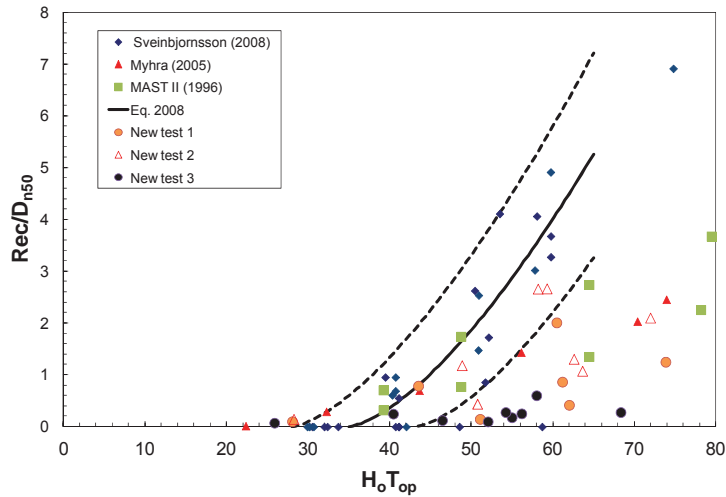


Figure 14: Average recession versus $H_o T_{op}$ and data of Sigurdarson et al. (2008).

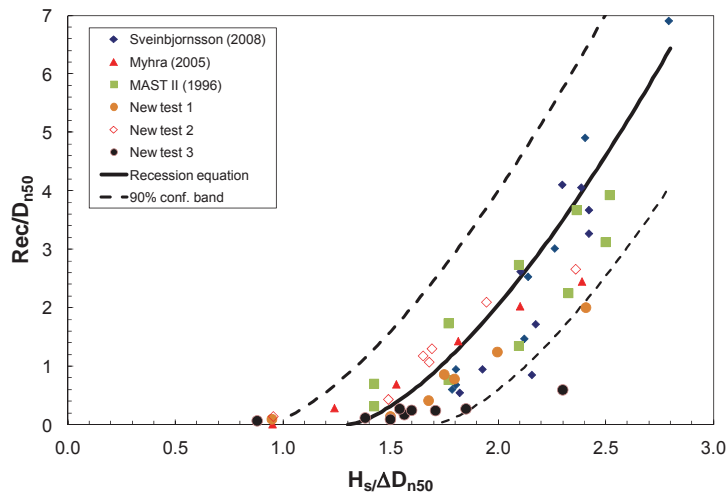


Figure 15: Average recession Rec_{av} versus $H_s / \Delta D_{n50}$, with data from Sigurdarson et al. (2008) and with a new prediction formula.

A formula that fits closely to the majority of the data points in Figure 15 is given by:

$$Rec_{av}/D_{n50} = 3.5 (H_s/\Delta D_{n50} - Sc)^{1.5} \quad (7)$$

with: $Rec_{av}/D_{n50} = 0$ for $H_s/\Delta D_{n50} < Sc$

and: $\mu(Sc) = 1.3$ and $\sigma(Sc) = 0.2$ and $H_s/\Delta D_{n50} < 2.8$

The formula shows that for a statically stable Icelandic-type berm breakwater with a design value of $H_s/\Delta D_{n50} = 1.5$ the expected recession is not more than about half a stone diameter. For $H_s/\Delta D_{n50} = 2.0$ this may increase to 1.5 to 3 stone diameters, depending on how accurate the rock above swl has been placed.

4 Wave overtopping and run-up simulation and destructive tests at grassed slope of dikes and boulevards

4.1 The Wave Overtopping Simulator

The Wave Overtopping Simulator was developed in 2006 and destructive tests have been performed in February and March of 2007 - 2011 and in November and December 2010. The tests show the behaviour of various landward slopes of dikes, embankments or levees under simulation of wave overtopping, up to a mean overtopping discharge of 125 l/s per m.

All research performed was commissioned by the Dutch Rijkswaterstaat, Centre for Water Management. The research was performed by a consortium of partners and was led by Deltares. Consortium partners were Deltares (project leader, geotechnical issues, model descriptions, hydraulic measurements), Infram (logistic operation of testing), Alterra (grass issues), Royal Haskoning (consulting) and Van der Meer Consulting (performance of Wave Overtopping Simulator and hydraulic measurements).

The process of wave overtopping on a dike, levee, seawall or embankment is well known, see the Overtopping Manual (2007). In contrast, the erosive impact of wave overtopping on these structures is not known well, mainly due to the fact that research on this topic cannot be performed on a small scale, as it is practically impossible to scale clay and grass down properly. Only some tests have been performed in large wave flumes, like the Delta flume in the Netherlands and the GWK in Germany, see Smith (1994) and Oumeraci et al. (2000). But these tests are costly and the dike can only partly be modelled. Therefore, the Wave Overtopping Simulator has been developed, see Van der Meer et al. (2006, 2007 and 2008) for more details.

The Simulator consists of a high-level mobile box to store water. The maximum capacity is 5.5 m^3 per m width (22 m^3 for a 4 m wide Simulator). This box is continuously filled with a predefined discharge and emptied at specific times through a butter-fly valve and a guidance to the crest, in such a way that it simulates the overtopping tongue of a wave at the crest and inner slope of a dike. The discharge of water is released in such a way that for each overtopping volume of water the flow velocity and thickness of the water tongue at the crest corresponds with the characteristics that can be expected. See Figure 16 for the principle of the Wave Overtopping Simulator. Various overtopping volumes are released randomly in time, see Figure 17.

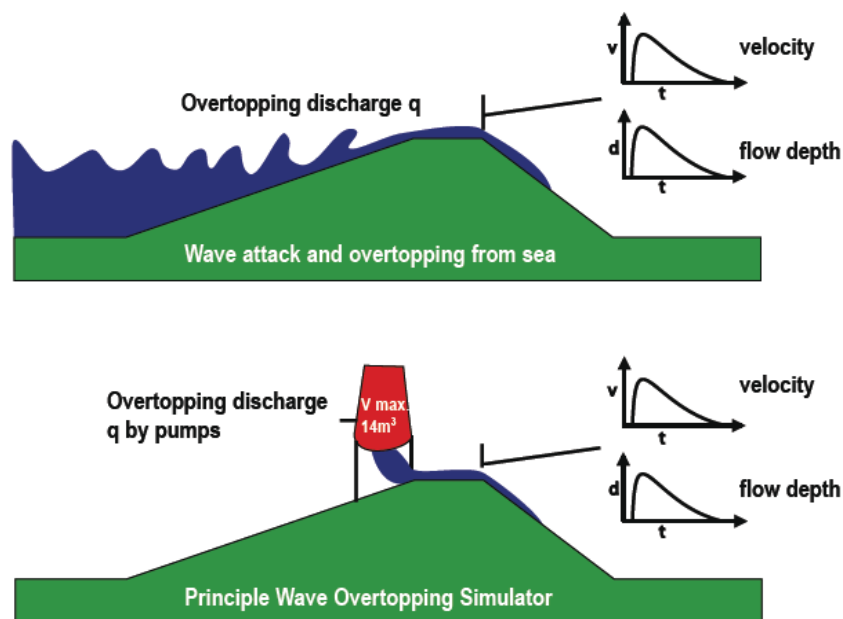


Figure 16: Principle of Wave Overtopping Simulator.

Field tests on real dikes have been carried out from 2007 - 2011, all at the end of the winter and one in November/December, when grass roots are in worst condition. Figure 18 shows the set-up of the simulator at the crest and seaward side of a dike and very close to a highway. The design and calibration of the Wave Overtopping Simulator has been described by Van der Meer (2007) and the test results of the first tested dike have been described by Akkerman et al. (2007-1 and 2007-2). Part of the tests in 2008 have been described by Steendam et al. (2008). A summary report on all the testing in 2007 and 2008 has been described by Van der Meer (2008). Tests and results of 2009 - 2010 have been described in Steendam et al. (2010, 2011) and Van der Meer et al. (2009, 2010, 2011).



Figure 17: Release of a wave.



Figure 18: Set-up of Wave Overtopping Simulator close to a highway (February 2009).

Most test conditions were given by a mean discharge and lasted for 6 hours. Test conditions increased from 0,1 l/s per m to 1; 10; 30; 50 and 75 l/s per m. A full test on a dike section took about one week and often more than 14,000,000 litres of water flowed over the inner slope of 4 m width. Each test condition consisted of simulation of the required distribution of overtopping volumes (see the Overtopping Manual (2007)). Such a distribution depends on expected conditions at sea: a larger significant wave height (as at sea dikes) will show fewer overtopping waves, but the volume in the overtopping waves will be bigger than for a smaller wave height (as for example at river dikes). All tests until now have assumed a significant wave height of 1, 2 or 3 m with a wave steepness of 0.04 (using the peak period). Distributions of overtopping volumes for a condition with 2 m wave height and for various mean discharges are given in Figure 19.

Figure 19 clearly shows that for each mean discharge there are only a small number of waves that give large overtopping volumes. The general behaviour of wave overtopping can be described by a large number of fairly small overtopping waves and a few which are much bigger. These few but bigger waves often cause the damage to the inner slope.

In the first years of testing it appeared to be very difficult to measure any hydraulic parameter on the inner slope, like flow velocity or flow depth. The velocities can approach 8 m/s and the water is very turbulent with a lot of air entrainment, see also Figure 17. Laboratory instruments have not been designed for this kind of conditions. In 2009 a lot of attention was focussed on improving the measurements. Amongst them a floating device to measure the flow depth and front velocities of an overtopping wave. The floating device is a curved board which has been hinged about 1 m above the slope and which floats on top of the flowing water. The rotation at

the hinge is measured and gives the flow depth. Figure 20 shows the record of this floating device for three consecutive overtopping volumes of 3.0 m^3 per m width each. Recording started exactly when the signal was given to open the valve. The overtopping volumes and the records of flow depth reproduce very nicely. The maximum flow depth was about 0.25 m.

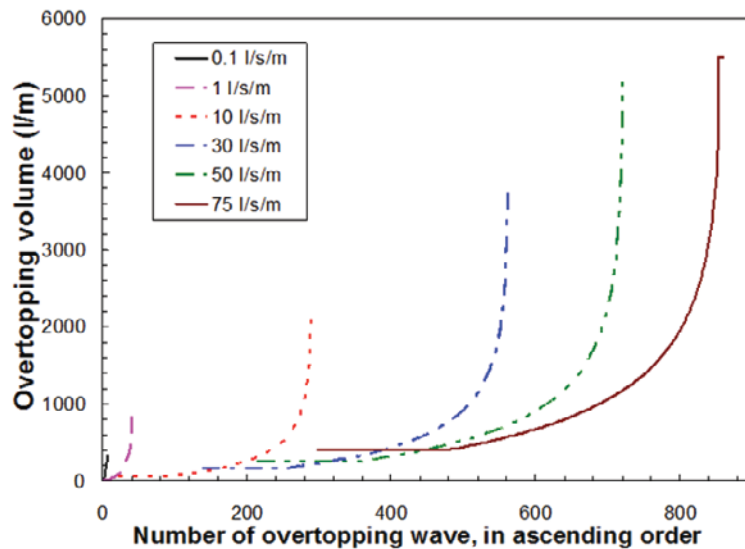


Figure 19: Distribution of overtopping volumes of waves for sea dikes and various mean overtopping discharges, as simulated by the Wave Overtopping Simulator.

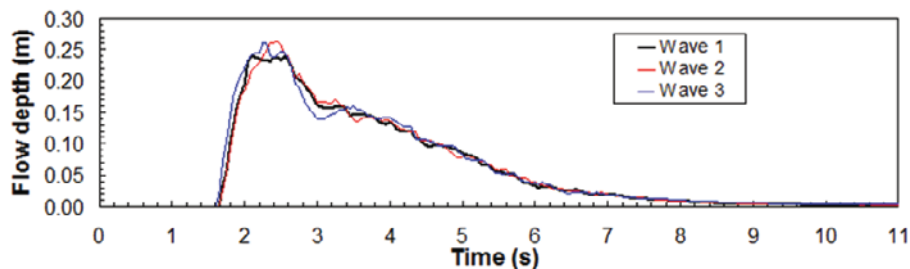


Figure 20: Record of flow depth with floating device for 3 overtopping waves of $3 \text{ m}^3/\text{m}$.

4.2 Destructive field tests

4.2.1 Failure mechanisms

Wave overtopping may lead to failure of the crest and landward slope of a dike. In principle there are two different failure mechanisms. Fast overtopping water may damage the surface of the crest and landward slope and, if initial damage or erosion has occurred, this may continue to the layer underneath the grass cover and may lead to an initial breach. This is actually the process which is simulated by the Wave Overtopping Simulator: erosion of the slope.

A major failure mechanism on steep landward faces (typically 1:1.5 and 1:2) in the past was slip failure of the landward slope. Such slip failures may lead directly to a breach. For this reason most dike designs in the Netherlands in the past fifty years have used a 1:3 landward slope, where it is unlikely that slip failures will occur due to overtopping. This mechanism might however occur for landward slopes steeper than 1:3 and should then be taken into account in safety analysis. This failure mechanism is NOT simulated by the overtopping tests, as a slip failure needs more width to develop than the 4 m wide test section. Another test method should be used to investigate this failure mechanism, which is not described in this paper.

4.2.2 Locations of tests

In total eight locations, seven in the Netherlands and one in Belgium were tested on wave overtopping, see Figure 21. Various tests were performed at each location, in total 27 tests on grassed or reinforced slopes, with or without objects like trees and stair cases.



Figure 21: Locations of testing in the Netherlands and Belgium.

4.2.3 Some observations

The easiest way to describe observations of the testing is by photographs. This section gives an some examples of observed damages for each tested location. Each photograph has a legend describing the observation. For a complete overall view one is referred to the given references above.

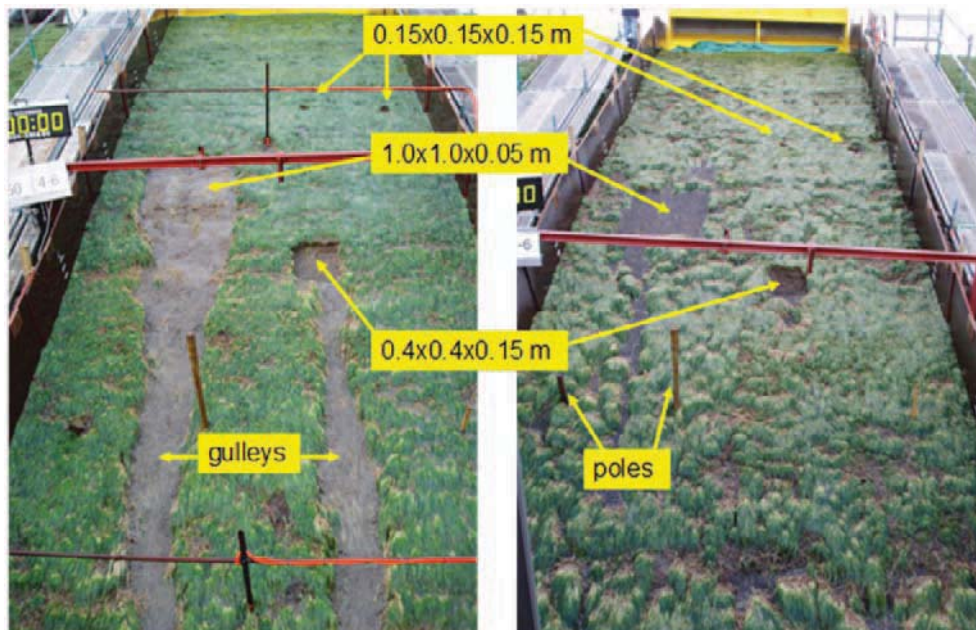


Figure 22: Final result Delfzijl, Groningen, sections 1 and 2. No damage after 50 l/s per m. Left: test section 1 of the present dike after manual initiation of damage (four holes in the slope: 1x1x0.05 m; 0.4x0.4x0.15 m; in the upper part two holes 0.15x0.15x0.15 m) and after 6 hours with 50 l/s per m. Gully development for the two largest holes, none for the smaller. Right: a reinforced section 2 with geotextile, again after manual initiation of damage, where no gulleys were developed.



Figure 23: Delfzijl, Groningen, section 3. Bare clay (0.2 m grass cover was removed). Mean discharges of 1; 5; and 10 l/s per m, each during 6 hours. Ongoing erosion during each condition, which resulted in head cut erosion: a horizontal part with a vertical slope; the vertical slope erodes by lumps of clay from the vertical front and the hole increases upwards.



Figure 24: Final result Boonweg, Friesland, sections 1 and 2. No damage after 75 l/s per m. In the last hour of 75 l/s per m damage to the toe (hidden path of brick stone, see photo right).



Figure 25: Final result Boonweg, Friesland; section 4. After 5 hours and 51 minutes with 75 l/s per m. The sand core has been eroded to at least 1 m depth and the right side wall is about to collapse. Final result about 45 minutes after first damage was observed.



Figure 26: Final result St Philipsland, Zeeland. Damage to the rear side at the maintenance road, which started at 30 l/s per m. Removal of the whole maintenance road. Picture taken half way the 75 l/s per m test. The hole became at the end 15 m wide and about 1 m deep.



Figure 27: Kattendijke, Zeeland, section 1. Damage to the rear side at the maintenance road, which started at 30 l/s per m. Removal of the whole maintenance road. Picture taken half way the 75 l/s per m test. The hole became at the end 15 m wide and about 1 m deep.



Figure 28: Afsluitdijk. Grass toe, section 1. Grass ripped off on many locations on the slope and completely at the horizontal part, where a section of 4x4 m² was created without grass. The good clay (still with roots) showed hardly any erosion and resisted without problems 75 l/s per m. Erosion holes near toe about 0.4 m deep.



Figure 29: Afsluitdijk. Staircase with fence, before and after testing, section 3. Left: before testing and right: after 2 hours of 75 l/s per m. The concrete staircase is near failure. Grass ripped off the slope, but gully development occurred only along the staircase where concentration of flow was observed. Hardly damage to the clay layer. The brick path to the staircase was completely destroyed, as well as the fence gate. Two erosion holes developed at the toe, due to the concentrated flow along the staircase. Holes about 1 m deep, but not reaching the sand core (cover by 0.4 m clay and 1 m boulder clay). Situation after 2 hours of 75 l/s per m.

A tested landward slope of a dike, covered with a good grass cover on clay, never failed by erosion due to overtopping for a mean overtopping discharge of 30 l/s per m or less. Only one section failed at 50 l/s per m; some at 75 l/s per m, but part of the sections did not fail, even not for 75 l/s per m. More recent tests at Tholen and near Antwerp with a very bad grass cover, however, showed early failure, even up to 1 l/s per m. The grass cover is very essential for the strength of the slope.

It seems that the large erosion resistance of the landward slope of a dike is determined by the *combination* of good grass cover and clay. The grass cover or mattress seems stronger if it grows on a sandy clay. Such a grass cover may resist even up to 75 l/s per m, but if significant damage occurs, the clay layer is not very erosion resistant (Figure 25). On the other hand, a good quality clay does not produce a very strong grass cover (it is difficult for roots to penetrate into the clay) and the grass may rip off for overtopping discharges around 30 l/s per m

(Figure 28). But in that case the remaining good quality clay layer, still reinforced with some roots, has a large erosion resistance against overtopping waves.

This leads to the conclusion that a good grass cover on a sandy clay and a worse grass cover on good clay show different failure mechanisms, but they show more or less similar strength against wave overtopping. The variability of the grass sod may, therefore, have less influence on the total strength than previously anticipated, except that there should be a fairly well closed grassed cover layer. This could lead to the conclusion that the way of maintenance of the grass has only minor effect on the strength of the landward slope as long as closed grass cover is present. The test at St Philipsland may show that the bad grass coverage (small open areas without grass) on sandy clay may show less resistance (Figure 26).

Transitions from slope to horizontal are probably the most critical locations for initial and increasing damage (Figures 24, 26 - 28). During the tests this was often the transition from the landward slope to the toe of the dike, with or without a maintenance road. The tests in 2009 were focused on these kind of transitions. Damage was initiated by a mean discharge of 10 l/s per m or more. As the damage occurred at the lowest part of the landward slope it will take time for damage to extend to the crest level and subsequently cause a dike breach. Transitions higher on the landward slope (cycle paths, stability or piping berms with or without maintenance road, tracks of tractors, roads crossing the dike), which have not yet been investigated, might be more critical. Further investigation may give more confirmative conclusions.

A hole in the layer of clay, which reaches the under laying sand core and created at a large mean overtopping discharge of 50 l/s per m or more, will give a very quick ongoing erosion. This has not been observed for smaller overtopping discharges, for the simple reason that these smaller discharges never created significant damage to the landward slope. But a test on a parking place of bricks showed that sand erosion with 30 l/s per m, and even with 10 l/s per m, goes fairly quickly. It must be noted that although the test was stopped for 30 l/s per m due to fast ongoing damage to the parking area, the dike itself was not in danger at all.

Small obstacles like poles did not show any erosion. Small holes from mice and moles did not initiate damage to the grass cover layer. Also a fence and a little bigger pole (0.15 m by 0.15 m) showed no initiation of erosion. The grass around a fence at the toe of the dike had some influence on initiation of erosion, probably due to larger forces in this area. An obstacle like a concrete staircase on the landward slope was totally destroyed at a stage with 75 l/s per m overtopping (Figure 29). It should be noted, however, that also here the dike itself was not in danger, due to the large erosion resistance of the clay. Still, further research may give more final conclusions on other large obstacles.

4.3 Erosional indices

The first three years of testing in the Netherlands with the Wave Overtopping Simulator was done for an assumed wave condition of $H_s = 2$ m and $T_p = 5.7$ s, being an average wave condition for the Dutch dikes. But estuaries, rivers and small lakes may have design conditions which are smaller, whereas dikes directly facing the North Sea may have larger conditions. It is the crest freeboard that governs the actual overtopping discharge, but the wave conditions determine how overtopping occurs. Larger waves give larger overtopping volumes, but less overtopping waves. From that point of view the overtopping discharge does not describe the full story of wave overtopping.

The objective of tests with the Wave Overtopping Simulator is to test the erosional strength of the crest and landward slope against wave overtopping. But do different wave conditions indeed give different moments for damage or failure of the grass? Tests performed in February and March 2010 at the Vechtdijk near Zwolle were performed with different wave conditions, in order to establish the influence of wave climate on erosional resistance. The tests have been described by Steendam et al. (2010). The wave conditions are given in Table 6 and can be characterized by wave heights of 1 m, 2 m and 3 m. A wave height of 1 m gives almost two times more incident waves in 6 hours than a wave height of 3 m.

Table 6: Wave conditions simulated at the Vechtdijk, Zwolle.

Seaward slope 1:4 Test duration 6 hours	Wave height H_s		
	1 m	2 m	3 m
Peak period T_p (s)	4.0	5.7	6.9
Mean period T_m (s)	3.3	4.7	5.8
Number of waves N_w	6545	4596	3724
Run-up, $Ru_{2\%}$ (m)	1.99	3.98	5.94

The three wave conditions give different overtopping parameters, like the crest freeboard, percentage of overtopping waves, number of overtopping waves and largest overtopping wave volume, all related to a certain overtopping discharge. All these values have been given in Table 7. A wave height of 1 m, for example, gives for an overtopping discharge of 10 l/s per m 2336 overtopping waves in 6 hours. For a 3 m wave height this reduces to 456 overtopping waves, which is only 20% of the number for 1 m waves, but the overtopping discharge is the same. It is clear that the larger wave height will then give larger overtopping volumes, which in this example is 4.5 m³/m as largest volume for a 3 m wave height and only 1.2 m³/m for a 1 m wave height.

Table 7: Wave overtopping for three wave heights.

		Mean overtopping discharge q (l/s per m)					
		0.1	1	5	10	30	50
$H_s = 1$ m	Crest freeboard R_c (m)	2.24	1.63	1.2	1.02	0.73	0.6
	Percentage overtopping waves P_{ov}	0.7	7.2	24	35.7	59	70
	Number overtopping waves N_{ow}	45	471	1573	2336	3861	4583
	Maximum overtopping volume V_{max} (l/m)	256	440	831	1197	2359	3401
$H_s = 2$ m	Crest freeboard R_c (m)	5.06	3.84	2.98	2.61	2.03	1.76
	Percentage overtopping waves P_{ov}	0.2	2.7	11.4	18.9	36.6	47
	Number overtopping waves N_{ow}	9	126	525	867	1683	2160
	Maximum overtopping volume V_{max} (l/m)	769	1222	2018	2697	4707	6387
$H_s = 3$ m	Crest freeboard R_c (m)	7.98	6.16	4.89	4.35	3.48	3.08
	Percentage overtopping waves P_{ov}	0.085	1.49	7.05	12.3	26.1	34.9
	Number overtopping waves N_{ow}	3	55	262	456	972	1300
	Maximum overtopping volume V_{max} (l/m)	1424	2254	3478	4509	7375	9709

The Vechtdijk was a 100% sandy dike, strengthened with only a good grass cover. It was expected that failure of the grass would certainly be achieved for each of the wave conditions and probably for different overtopping discharges. This was, however, not always the case due to early failure of a tree in the slope and a particular transition (see Steendam et al. (2010)) and it was not always possible to reach failure of the grassed slope itself.

It became also clear that it is not so easy to decide when a grassed slope has start of damage, developing damage or failure. Failure is the most easy definition: the sand core underneath the soil layer becomes free and damage develops fast. Start of damage would actually be the first small hole in the grass cover and this is not a consistent parameter as it may depend on the existence or non-existence of one weak spot on a fairly large surface. A more consistent definition would be "various damaged locations", meaning that it does not depend solely on one

weak spot. In the case the grassed slope did not fail the condition "no failure" became also a criterion.

In summary the following damage criteria were used:

- First damage (Figure 30);
- Various damaged locations (Figure 31);
- Failure (Figure 32);
- Non-failure after testing (Figure 33).



Figure 30: First damage.



Figure 31: Various damaged locations.



Figure 32: Failure.



Figure 33: Non-failure after testing.

The theory of shear stress with a threshold was taken as a basis for development, see also Hoffmans et al. (2008). The development, however, took place at the same time when Dean et al. (2010) worked on their erosional equivalence, but it was not yet published at that time. Dean et al. (2010) considered three possible developments, which in essence can be described as follows:

$$\text{Erosion due to excess velocity: } E = K \Sigma((u - u_c) t) \quad [\text{m/s}] \quad (8)$$

$$\text{Erosion due to excess shear stress: } E = K \Sigma((u^2 - u_c^2) t) \quad [\text{m}^2/\text{s}] \quad (9)$$

$$\text{Erosion due to excess of work: } E = K \Sigma((u^3 - u_c^3) t) \quad [\text{m}^3/\text{s}] \quad (10)$$

In all cases the velocity of the overtopping wave plays a role and a critical velocity, which should be exceeded before erosion will take place. In the equations also the time that the critical velocity is exceeded, is important.

The analysis of the Vechtdijk results had as basis Equation 9 (Hoffmans et al. (2008)). The testing showed indeed that only waves of a certain volume (or velocity) damaged the slope. Smaller volumes did not contribute to the development of damage. This confirms the use of a threshold like u_c . But one main modification was made, based on observed behaviour during testing. In Equations 8 - 10 the time that u_c is exceeded is taken into account. The origin of this comes from tests with continuous overflow, where indeed time, or the duration that the flow is present, is important.

But (severe) wave overtopping is different from continuous overflow. First of all, velocities in an overtopping wave are much larger than velocities in continuous overflow, for the same discharge. Secondly, the duration that u_c is exceeded in an overtopping wave is quite short, in the order of 1-3 s, and this duration is fairly constant and in total much shorter than for continuous overflow.

The observation of overtopping waves has taught us that a wave front rushes over the slope with large velocity. Within tenths of seconds (see Figure 20) the maximum velocity is reached. The grass feels this as a kind of "impact" and it is this impact that causes initiation or further development of damage. It is believed that this impact is more important than the duration of the overtopping wave above a certain threshold. For this reason Equation 9 was rewritten to an erosional index called "cumulative overload", where the actual time or duration for an overtopping wave was omitted:

$$\text{Cumulative overload: } \Sigma(u^2 - u_c^2) \quad [\text{m}^2/\text{s}^2] \quad (11)$$

With known distributions of overtopping wave volumes and known velocities per overtopping wave volume it is possible to calculate the cumulative overload for each wave overtopping condition, or a number of tests, to a certain moment when a damage criterion is reached. And the cumulative overload depends of course on the critical velocity u_c that is taken.

The main question is then: what is the critical velocity, u_c , that brings the damage observed for different hydraulic regimes, together?

The four damage criteria, see Figures 30-33, were taken for all tests and the results were compared for critical velocities of 0; 3.1; 4.0; 5.0 and 6.3 m/s, which are in accordance with overtopping wave volumes of 0; 0.25; 0.5; 1 and 2 m³/m.

The following conclusions could be made for the Vechtdijk:

- A critical velocity should be used of $u_c = 4$ m/s ($V_c = 0.5$ m³/m)
- Start of damage: $\Sigma(u^2 - u_c^2) = 500$ m²/s²
- Various damaged locations: $\Sigma(u^2 - u_c^2) = 1000$ m²/s²
- Failure (by mole holes): $\Sigma(u^2 - u_c^2) = 3500$ m²/s²
- Non-failure for normal slope: $\Sigma(u^2 - u_c^2) < 6000$ m²/s²

A confirmation of above analysis and conclusions could be established by looking at the damage on the slope after hydraulic measurements. Here only about 40 overtopping waves rushed down the slope instead of many hours like for normal testing, but many large volumes were present. The hypothesis of cumulative overload should work for many hours of testing, but also for the "artificial" distribution of a small number, but mainly very large overtopping waves.

The observation of the slope after the hydraulic measurements could best be described as "various damaged locations". A number of small holes were observed and one location with a little larger damaged area.

The cumulative overload for these 40 waves, using $u_c = 4$ m/s, amounted to 946 m²/s². This is very well comparable with the 1000 m²/s² that was given for this damage criterion. It can be concluded that this very short session of large waves can very well be compared with many hours of testing of real wave overtopping. The analysis confirmed the hypothesis of cumulative overload.

In future also the method of "excess of work" (Equation 10), which was preferred by Dean et al. (2010), should be elaborated, maybe with ongoing work in the US with a new Wave Overtopping Simulator (see Van der Meer et al. (2011) and Thornton et al. (2011)). The reason for Dean et al., however, to choose for excess of work instead of excess of shear stress was that excess of work fitted better to known stability curves for continuous overflow, not wave overtopping. Dean et al. (2010) did not possess the results of simulation of wave overtopping at real dikes as in the Netherlands.

Another difference between the two methods is the value of the critical velocity u_c . Based on continuous overflow critical velocities are in the range of 1-2 m/s. But the very "weak" Vechtdijk (sand with a good grass cover) needs a critical velocity of 4 m/s and this can be considered as a lower boundary. Other dike sections tested need probably a critical velocity in the range of 5-7 m/s. It is, therefore, still an open question which method would work best with real wave overtopping at dikes

4.4 Forces on vertical walls

The Belgium Integrated Master Plan for Coastal Safety has been developed to protect the coast sufficiently against severe storm events. Weak spots have been determined, and safety measures were proposed, based on an intense campaign of numerical and experimental research. One of these measures are storm walls located at 10 to 15 m behind the crest of a dike or boulevard (along the coastline) or quay wall (in harbours). These walls are designed to withstand wave impacts and are therefore subject to very high forces. The magnitude of these forces and force-over-time signal will determine the foundation, rebar and dimensions of the walls. But also a lot of buildings exist on top of the sea wall and overtopping waves could hit walls of such buildings.



Figure 34: Impression of wave force measurements.

Up till now, there are no theoretical formulae which allow design engineers to estimate these wave forces on a storm wall due to overtopping waves. The Wave Overtopping Simulator was therefore used to simulate an overtopping wave which impacts a storm wall located at 10 m behind the crest (Figure 34). Two aluminium plates acted as storm walls: one vertical (1.7 m high x 0.5 m wide) and one horizontal (0.5 m high x 1.7 m wide). Each plate was equipped with 4 force sensors, one in every corner of the plate. The force records of the 4 sensors in the vertical plate are shown in Figure 35.

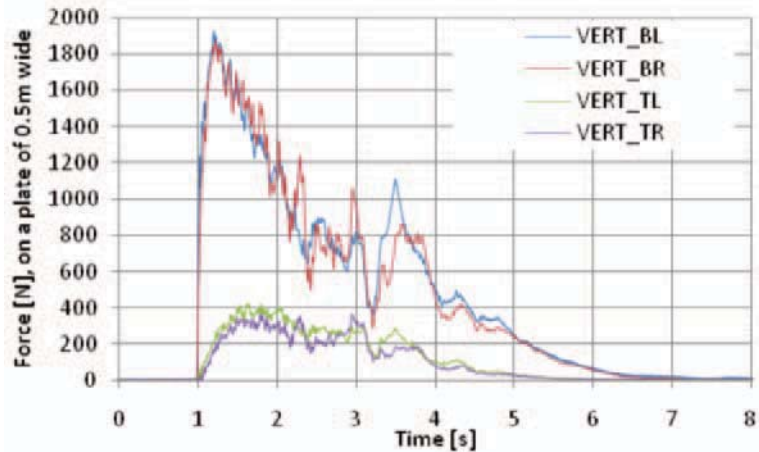


Figure 35: Force record over time on a vertical plate, for a wave of 3500 l/m.

The force record of a bottom sensors (red/blue - upper records) shows a very steep rise over time, and reach much higher values than the top sensors (purple/green - lowest records). The flow depth, located near the bottom sensor, is a governing parameter for the force distribution over height.

In Figure 36 the maximum forces per meter width on the horizontal plate (0.5 m high) and the vertical plate (1.7 m high) have been plotted versus the overtopping wave volume. There is a very clear trend between both

Horizontal plate: $F = 2.24 V$ (11)

Vertical plate: $F = 0.13V^2 + 2.22V$ (12)

with: $F =$ force per meter width (KN/m)

$V =$ overtopping wave volume (m^3/m)

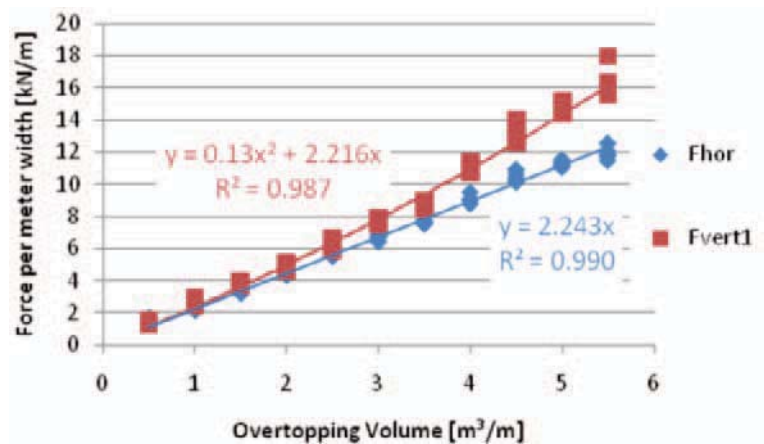


Figure 36: Force as a function of volume. Horizontal plate blue, vertical red.

The difference between horizontal and vertical plate is rather small, despite the vertical plate being 3 times higher. The flow depth is a governing parameter for the force distribution over height.

As first analysis it can be concluded that:

- the wave forces rise very fast, but no impulse peak is visible;
- wave forces on a wall oriented 45 degrees to the wave direction result in a force that is a factor 2 smaller than perpendicular wave attack;
- the wave force above the flow depth is negligible.

4.5 Wave run-up simulation

The idea of the Wave Run-up Simulator is based on the experiences with the Wave Overtopping Simulator, see the previous sections. It is possible to simulate wave tongues overtopping a dike crest in reality. It must also be possible to simulate waves in the run-up and run-down zone of the seaward slope. This is the zone after waves have broken and when they rush-up the slope.

This section describes shortly this new idea of the Wave Run-up Simulator, why it is useful to develop the machine, to perform research with it and to develop a prediction method for slope strength. In fact, a prediction method can already be developed from the Cumulative Overload Method, which was developed on the basis of results with the Wave Overtopping Simulator, see Section 4.3. It also means that tests on the seaward slope will be done for validation purposes only. Not a lot of research has been performed to describe the wave run-up process in detail, physically nor statistically.

The first question is whether it is useful to develop and construct a Wave Run-up Simulator to look at strength of seaward slopes with grass coverage. The majority of Dutch seadikes, however, have a run-up zone at the seaward side, above a protected berm at storm surge level, which is covered with grass. Right now no validated safety assessment method exists for these kind of slopes above the wave impact zone.

Flow velocities, run-up levels and flow depths must be known over the full run-up zone in order to make a good simulation. Some research has been performed, but never with the objective to design a Wave Run-up Simulator. For this reason a detailed analysis has been performed on what is known in literature and on analysis of existing data from tests. One method is to look at the records of wave run-up gauges. The derivative of the location of the up-rushing wave front gives the front velocity over the full run-up zone, not only at a fixed position. It appears that the velocity along the slope does not linearly decrease with the run-up level. Almost from the start of run-up to about three quarters of the maximum run-up level the flow velocity is high and close to the maximum velocity. The velocity decreases suddenly in the last quarter of the run-up.

This conclusion returns in the final description of flow velocities in the run-up zone, see Fig. 37. An average trend exists that flow velocity increases with increasing maximum run-up level, but a large range of flow velocities exist for similar run-up levels. This is more or less similar to waves: various wave periods exist for similar individual wave heights. Wave height as well as wave periods have both a certain distribution and are not directly correlated by an equation. The simulation of up-rushing waves in the run-up zone must exist of the simulation of different flow velocities, whilst a similar maximum run-up has to be reached. This can only be realized if the opening of the valve of the Simulator is part of the steering for the run-up. This method has already been developed for the Wave Overtopping Simulator in the US (Van der Meer et al., 2011).

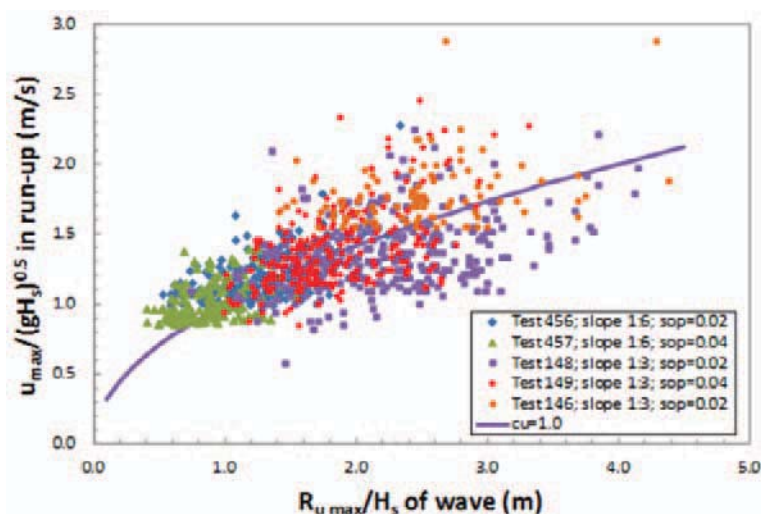


Figure 37: Relative maximum velocity versus relative run-up on the slope.

The maximum velocity on a slope during an individual wave run-up can be calculated by:

$$u_{\max}/(gH_s)^{0.5} = c_u (Ru_{\max}/H_s)^{0.5} \quad (13)$$

with c_u as stochastic variable with $\mu(c_u) = 1.0$ and a normal distribution with $V = 0.25$.

A first pilot test with the actual Wave Overtopping Simulator has been performed in March 2011, without any modifications to the Simulator. The Simulator was placed on the seaward slope and berm at storm surge level (asphalt) and run-up simulation started at this almost horizontal berm. The upper grass slope had a 1:3 slope and the Simulator was able to create run-up as well as wave overtopping at the dike crest, see Fig. 38. The maximum run-up was 3.5 m (measured vertically). After up-rush the water comes back in the run-down and in order to release this water the Simulator was placed 0.2 m above the slope. Measurements were performed on up-rush as well as down-rush, on velocities and flow depths.

Five test conditions were conducted, starting with a low 2%-run-up level. This run-up level was increased with each following test. Damage was developed at the transition from berm to upper slope, see Fig. 39. The theoretical and practical test procedure will be described elsewhere.



Figure 38: Pilot test on wave run-up simulation



Figure 39: Damage after 5 tests with various $Ru_{2\%}$ -levels

5 Acknowledgments

Although a keynote lecture is given by one person only, the work described in this paper has become available through cooperation with many colleagues from various companies, universities or institutes. Acknowledged is Sigurdur Sigurdarson of IceBreak Consulting Engineers for his excellent cooperation on berm breakwaters. Furthermore, the SBW-project group on "Strength of grass covered dikes due to wave overtopping" is acknowledged for many years of cooperation: André van Hoven (Deltares), Henk Verheij (Deltares), Gijs Hoffmans (Deltares), Gosse Jan Steendam (Infram), Maurice Paulissen (Alterra) and Gert-Jan Akkerman (Royal Haskoning).

6 References

- Akkerman, G.J., P. Bernardini, J.W. van der Meer, H. Verheij and A. van Hoven, (2007-1). Field tests on sea defences subject to wave overtopping. Proc. of Coastal Structures Conference. Venice.
- Akkerman, G.J., K.A.J. van Gerven, H.A. Schaap and J.W. van der Meer, (2007-2): Wave overtopping erosion tests at Groningen sea dyke. ComCoast, Workpackage 3: Development of Alternative Overtopping-Resistant Sea Defences, phase 3. See www.comcoast.org.
- Baird, W.F. and K.R. Hall, (1984): The design of breakwaters using quarried stones. ASCE, Proc. ICCE, Houston, 2580-2591.
- Battjes, J.A. and H.W. Groenendijk, (2000): Wave height distributions on shallow foreshores. Journal of Coastal Engineering 40 (2000) 161-182.
- Dean, R.G., J.D. Rosati, T.L. Walton and B.L. Edge, (2010): Erosional equivalences of levees: Steady and intermittent wave overtopping. Journal of Ocean Engineering 37 (2010) 104-113.
- EurOtop Manual, (2007). Wave Overtopping of Sea Defences and Related Structures – Assessment Manual. UK: N.W.H. Allsop, T. Pullen, T. Bruce. NL: J.W. van der Meer. DE: H. Schüttrumpf, A. Kortenhaus. www.overtopping-manual.com.
- Hoffmans, G., G.J. Akkerman, H. Verheij, A. van Hoven and J.W. van der Meer, (2008): The erodibility of grassed inner dike slopes against wave overtopping. ASCE, Proc. ICCE 2008, Hamburg, p. 3224-3236.
- MAST II, (1996): Influence of Permeability and Stone Gradation. MAST II – Berm breakwater structures. Contract MAS2-CT94-0087.
- Myhra, H., (2005): Berm breakwaters. Influence of construction method and storm duration on stability. Ice ride-up. MSc-thesis NTNU, Norway.
- Oumeraci, H., H. Schüttrumpf, J. Möller and M. Kudella, (2000): Large scale model tests on wave overtopping with natural sea states. LWI-Bericht Nr. 852.
- Overtopping Manual, (2007). EurOtop. Wave Overtopping of Sea Defences and Related Structures – Assessment Manual. UK: N.W.H. Allsop, T. Pullen, T. Bruce. NL: J.W. van der Meer. DE: H. Schüttrumpf, A. Kortenhaus. www.overtopping-manual.com.
- PIANC, (2003): State-of-the-Art of designing and constructing berm breakwaters. MarCom Report of WG 40.
- PIANC, (1992): Analysis of rubble mound breakwaters. Report on Working Group 12.
- Rock Manual, (2007): The use of rock in hydraulic engineering. CIRIA, CUR, CETMEF. C683, CIRIA, London.
- Rock Manual, (1992): Manual on the use of rock in coastal and shoreline engineering. CIRIA Special Publication 83. CUR Report 154.
- Sigurdarson, S. and J.W. van der Meer, (2011): Front slope stability of the icelandic-type berm breakwater. ASCE, Proc. Coastal Structures 2011, Yokohama, Japan.

- Sigurdarson, S., J.W. van der Meer, A. Tørum and R. Tomasicchio, (2008): Berm recession of the Icelandic-type berm breakwater. ASCE, Proc. ICCE 2008, Hamburg, 3311-3323.
- Smith, G.M., (1994): Grasdijken (Dutch). Grass dikes. Delft Hydraulics report H1565, Delft
- Sveinbjörnsson, P.I., (2008): Stability of Icelandic type Berm Breakwaters. MSc-thesis TU Delft.
- Steendam, G.J., P. Peeters, J.W. van der Meer, K. VanDoorslaer and K. Trouw, (2011): Destructive wave overtopping tests on Flemish dikes. ASCE, Proc. Coastal Structures 2011, Yokohama, Japan.
- Steendam, G.J., J.W. van der Meer, B. Hardeman and A. van Hoven (2010). Destructive wave overtopping tests on grass covered landward slopes of dikes and transitions to berms. ASCE, Proc. ICCE 2010, Shanghai, China.
- Steendam, G.J., J.W. van der Meer, G. de Raat, W. de Vries and J.Y. Frissel, (2008). Influence of Management and Maintenance on erosive impact of wave overtopping on grass covered slopes of dikes. International Symposium on Floodrisk. Oxford.
- Thornton, C., J.W. van der Meer, B. Scholl, S.A. Hughes and S. Abt, (2011): Testing levee slope resiliency at the new Colorado State University Wave Overtopping Test Facility. Proc. Coastal Structures 2011, Japan.
- Van der Meer, J.W., C. Thornton and S. Hughes (2011): Design and operation of the US Wave Overtopping Simulator. ASCE, Proc. Coastal Structures 2011, Yokohama, Japan.
- Van der Meer, J.W., B. Hardeman, G.J. Steendam, H. Schüttrumpf and H. Verheij (2010): Flow depths and velocities at crest and inner slope of a dike, in theory and with the Wave Overtopping Simulator. ASCE, Proc. ICCE 2010, Shanghai, China.
- Van der Meer, J.W., R. Schrijver, B. Hardeman, A. van Hoven, H. Verheij and G.J. Steendam (2009): Guidance on erosion resistance of inner slopes of dikes from three years of testing with the Wave Overtopping Simulator. Proc. ICE, Coasts, Marine Structures and Breakwaters 2009, Edinburgh, UK.
- Van der Meer, J.W., (2008): Erosion strength of inner slopes of dikes against wave overtopping. Preliminary conclusions after two years of testing with the Wave Overtopping Simulator. Summary Report.
- Van der Meer, J.W., G.J. Steendam, G. de Raat and P. Bernardini. 2008: Further developments on the wave overtopping simulator. ASCE, proc. ICCE 2008, Hamburg.
- Van der Meer, J.W., P. Bernardini, G.J. Akkerman and G.J.C.M. Hoffmans, 2007: The wave overtopping simulator in action. ASCE, proc Coastal Structures, Venice, Italy, p. 645-656.
- Van der Meer, J.W., W. Snijders and E. Regeling, 2006: The wave overtopping simulator. ASCE, proc. ICCE 2006, San Diego, p. 4654-4666.
- Van der Meer, J.W., (1987): Stability of breakwater armour layers - Design formulae. Journal of Coastal Engineering, 11, pp. 219-239.
- Van der Meer, J.W., (1988-1): Rock slopes and gravel beaches under wave attack. Doctoral thesis, Delft University of Technology. Also Delft Hydraulics Publication no. 396.
- Van der Meer, J.W., (1988-2): Deterministic and probabilistic design of breakwater armour layers. Proc. ASCE, Journal of WPC and OE, Vol. 114, No. 1.
- Van der Meer, J.W., (1985): Stability of rubble mound revetments and breakwaters. Proc. ICE, Developments in Breakwaters. Discussion pp 191 -202.
- Van Gent, M.R.A., A.J. Smale and C. Kuiper, (2003): Stability of rock slopes with shallow foreshores. ASCE, Proc. Coastal Structures, Portland, USA.

Integrated management of risk of coastal flooding and the European Directive 2007/60/EC for the assessment and management of risk

Panayotis Prinos¹

Abstract

In this work the basic concepts of coastal flooding risk management are presented in relation with the requirements of the European Directive 2007/60/EC for the assessment and management of risk. The key terms are defined and the conceptual framework is presented based on the Source-Pathway-Receptor model. Characteristic examples of flood hazard and flood risk maps are given. Such maps are the basic elements for the integrated management of risk and the development of management plans according to the Directive. The data needed and the methods of calculation for risk sources, pathway and receptor are described.

Keywords: Risk, Coastal Flooding, European Directive, Integrated Management

1 Basic Concepts for Risk Management and Coastal Flooding

The definitions of key terms and concepts presented in this section take into account a number of existing official glossary definitions (ISO 2009; IPCC 2007a; IPCC 2007b; UNISDR, 2009) but also reflect the fact that concepts and definitions evolve as knowledge, needs and contexts vary. Various dynamic fields, like risk management and climate change adaptation, continue to exhibit an evolution in concepts and definitions of key notions. Key concepts involved in disaster risk management and climate change adaptation, and the interaction of these with sustainable development have been under discussion in the upcoming IPCC report (IPCC 2011).

Disaster risk is defined as the potential for loss or damage to lives, livelihoods, health status, economic and cultural assets, services (including environmental) and infrastructure, which could occur in a community or society due to the effect of particular physical events occurring within some specified future time period.

Disaster risk cannot exist without the potential occurrence of damaging physical events. But such events are not in and of themselves sufficient to explain disaster risk or project its potential magnitude. When physical events, such as floods, droughts and landslides among others, can affect exposed elements of human systems in a negative manner, they assume the characteristic of **hazard**. Hazard is the potential occurrence of a natural or human-induced physical event that can contribute to negative effects such as loss of life, injury or other health impacts, as well as damage and loss to assets, infrastructure, livelihoods, service provision and environmental resources.

Exposure refers to the presence of people, livelihoods, environmental services and resources, economic, social and cultural assets, and infrastructure in areas subject to the occurrence of potentially damaging physical events and which, thereby, are subject to potential future loss and damage. Quantification of such loss depends, among other things, on the magnitude of an event in a given location. The definition of exposure subsumes physical and biological systems under the concept of "environmental services and resources", accepting that these are fundamental for human welfare and security (Gasper, 2010).

Under exposed conditions, future loss and damage will be the result of a physical event interacting with socially constructed conditions denoted as **vulnerability**. Vulnerability, when used with reference to human systems, is defined here as the susceptibility or predisposition for

¹ Professor, Hydraulics Laboratory, Department of Civil Engineering, Aristotle University of Thessaloniki, 54124, Thessaloniki, Greece, prinosp@civil.auth.gr

loss and damage to human beings and their livelihoods, as well as their physical, social and economic support systems, when affected by physical events. This includes the characteristics of a person or group and their situation that influences their capacity to anticipate, cope with, resist and recover from the impact of a physical event (Wisner *et al.*, 2004). Vulnerability may be evaluated according to a variety of quantitative and qualitative metrics (Schneider *et al.*, 2007; Cardona, 2010).

Vulnerability is a function of diverse historical, social, economic, political, cultural, institutional, natural resource, and environmental conditions and processes. The concept has been developed as a theme in disaster work since the 1970s (Wisner *et al.*, 1977, Gaillard, 2010) and modified in different fields and applications. Four approaches to understand vulnerability and its causes can be distinguished between those that are rooted in: political economy, social-ecology, vulnerability and disaster risk assessment from a holistic view, and climate change systems science.

a) Pressure and release (PAR) model (Blaikie *et al.* 1994, Wisner *et al.* 2004) is common to social science related vulnerability research and makes emphasis on the social conditions of exposure and the root causes that generate unsafe conditions. This approach links vulnerability to unsafe conditions in a continuum of vulnerability that connects local vulnerability to wider national and global shifts in the political economy of resources and political power.

b) The social-ecology perspective emphasizes the need to focus on coupled human-environmental systems (Hewitt and Burton, 1971). This perspective stresses transformative qualities of society for nature and also the effects of changes in the environment for social and economic systems. It argues that the exposure and susceptibility of a system can only be adequately understood if these coupling processes and interactions are addressed.

c) Holistic perspectives from vulnerability have tried to extend from technical modelling to embrace a wider and comprehensive explanation of vulnerability. These approaches differentiate as causes or factors of vulnerability the fact to be exposed, susceptibility and societal response capacities (Cardona 2010, Birkmann 2006, Birkmann and Fernando 2008). A core element of these approaches is the feedback-loop that underline that vulnerability is dynamic and is the main driver and determinant of current or future risk.

d) In the context of climate change adaptation vulnerability is understood as a function of exposure, sensitivity and adaptive capacities (IPCC 2007a, O'Brien *et al.* 2008a, b). These approaches differ from the understanding of vulnerability in the disaster risk management perspectives as the rate and magnitude of climate change is considered. The concept of vulnerability here includes external environmental factors of shock or stress. Therefore, in this view, the magnitude and frequency of potentially hazard events is to be considered in the vulnerability to climate change. This view also differs in its focus upon long-term trends and stresses rather than on current shock forecasting, something not explicitly excluded but rather rarely considered within the disaster risk management approaches.

Taking into account that the measurement of vulnerability is a challenge and using the more compatible approaches of the above mentioned frameworks the MOVE project (Methods for Improvement of Vulnerability Assessment in Europe, www.move.eu) addresses vulnerability and disaster risk to natural and socio-natural hazards, emphasizing the association of risk assessment, risk reduction, adaptation and decision making. It provides a summary of the causal and intervention aspects associated with this holistic vision of risk and vulnerability including adaptation as a key component of disaster risk management (Birkmann *et al.* 2011).

Disaster risk management is defined as the systematic process of using administrative directives, organizations and operational skills, abilities and capacities to implement policies, strategies and specific mechanisms which promote increased or improved risk awareness and evaluation, tangible means to reduce disaster risks, disaster response, increased coping capacities and recovery practices, and lessen the potential or actual adverse impacts of physical events on society.

Probabilistic Risk Analysis (PRA, Bedford and Cooke, 2001) provides an important set of quantitative concepts used to estimate various risks and to evaluate alternative options for reducing and managing them. The disaster risk management and climate change literatures use

this framework for the risk analysis stage of risk governance. In many contexts, other, qualitative approaches are preferable to PRA, while in some situations resources and capabilities to implement PRA are simply unavailable. Nonetheless, PRA provides widely applicable methods and an important conceptual foundation for much of disaster risk management and climate change adaptation. In its simplest form, PRA defines risk as the product of the probability that some event will occur and the adverse consequences of that event ($\text{Risk} = \text{Probability} \times \text{Consequence}$).

Alternative, more complex formulations express risk as a product of hazard, exposure, and vulnerability. All three factors contribute to "consequences". Hazard and vulnerability can both contribute to the "probability": the former the likelihood of the physical event (coastal flooding) and the latter the likelihood of the consequence resulting from the event (casualties and economic disruption).

While simple in concept the equation for risk is often difficult to implement in practice. Estimates of the likelihood of consequences arising from some physical event require judgments about a community's ability to resist damage and to recover from any damage inflicted. The valuation of consequences can be determined via a variety of metrics and may vary greatly from person to person, depending on factors such as their values and interests, their previous experience with such consequences, and the extent to which they feel they have any control over the consequences.

The PRA framework supports risk management by providing information that can help in the evaluation and choice of options for managing, reducing, and transferring risk, and potentially, contribute to standardizing and integrating information and informing decisions across various levels of administration. Where one can quantify the costs of such actions in the same units as the consequences, one can compare those costs to their resulting reductions of risk and evaluate which combinations of actions provide the greatest expected gains in welfare. For instance, insurance companies will estimate their expected losses by using simulation models to project the frequency and intensity of future events (hazards model) and the damage and its distribution caused by such events (vulnerability models). Firms combine this information with estimates of the fraction of damage property covered by insurance to help set their prices for such insurance (SwissRe, 2010). The framework, in conjunction with tools like spatial modeling, also supports administrative judgments of where risk does and does not exist, for instance flood risk maps which use estimates of threshold probabilities to categorize particular regions as at risk for floods. In this way, it can inform resource allocation decisions. Where quantification proves more difficult, the conceptual framework of PRA may nevertheless provide general guidance for decisions. The overall risk governance framework put forward by Renn includes five steps: pre-assessment, appraisal, characterization/evaluation, management, and communications (Renn, 2008). PRA contributes most significantly to the characterization/evaluation stage.

The analytical basis for the determination of the coastal flooding impacts is the Source-Pathway-Receptor-Consequence (SPRC) model with a systems approach which identifies links between system components to give a comprehensive definition of the flood system (Figure 1).

The SPRC model is a simple linear conceptual model which describes current understanding and integrates both the natural and human elements and functioning of the flood system. It therefore captures these complex relationships in a form that can be used for further analysis, planning, restoration, and management. Essentially, the flood system is defined by identifying known route(s) for floodwaters (**Pathway(s)**) between their origin (**Source**) and impacts (**Receptor**). In the SPRC model, potential consequences are inherent to the nature of the source and, although there may be a number of Sources, areas affected (Receptors), type and nature of impacts, and linking Pathways, there must be at least one Pathway in order for a Receptor, Consequence, and ultimately risk, to exist. Use of this conceptual model encourages clarification of the underlying or implicit assumptions and local knowledge which provides significant benefit, particularly concerning the assessment of mitigation options (e.g., whether the greatest benefit for management techniques should be focussed on reducing the probability of the event at either the source or pathway stage, and/or altering the magnitude of exposure to the event by managing the Receptors).

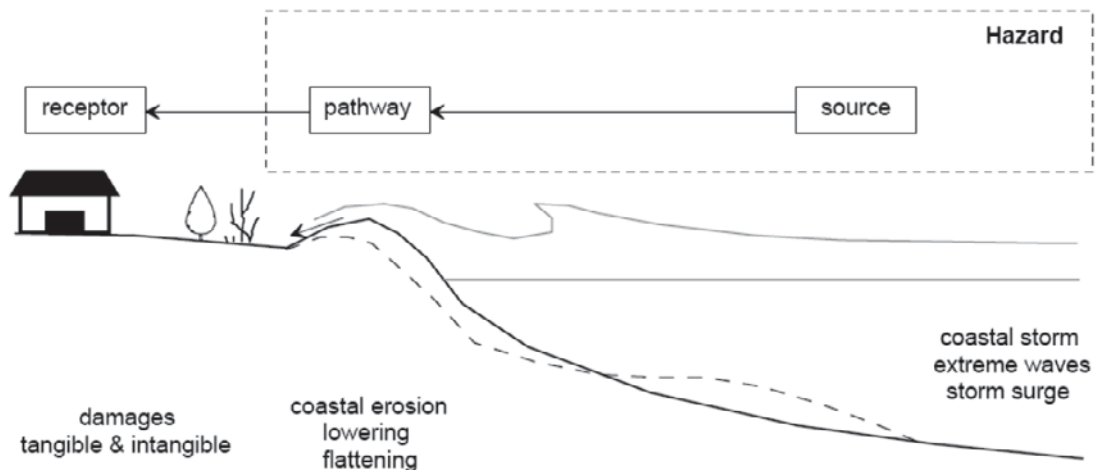


Figure 1: The Concept of Source-Pathway- Receptor for coastal flooding

Essential to the successful application of this model is the identification of the SPR components. This produces a classification of current land use (including current flood management and identification of habitats and potential sources of pollution during flood events) and the collection of information which will help to evaluate the Consequences of flooding, leading ultimately to assessments of risk.

The following definitions are applied:

Flood Event: Temporary covering of land by water which is outside its normal confines.

Flood System: The physical and human systems that cause, or are influenced by, flooding.

Driver: A process external to the flooding system which changes its state.

Sources (S): The Source is divided into primary and secondary sources:

Primary: The *primary* Source of a flood event is either the sea or a river i.e. where the flood waters originate.

Secondary: *secondary* sources are the physical aspects of the *primary* source which may change in response to Driver processes, in this case climate and weather-related phenomena (e.g. storms), directly generate potential flood waters.

Pathway (P): The Pathway is the link between the Receptor and the Source of the flood waters. The Pathway for an individual Receptor can be composed of other land-uses, relevant management infrastructure/regime and geomorphological response. A Pathway must exist for a Consequence to exist.

Receptor (R): Receptors are what is located on the land that is flooded. This includes people, residential and non-residential properties, existing coastal management, local infrastructure and natural habitats.

The SPRC concept has been applied to various European projects (FLOODsite, 2008, THESEUS 2010) for the assessment and management of flood risk (riverine and coastal). Figures 2 and 3 show the respective concepts for the two projects. Mapping of flood hazard and risk is an issue which is also included in the EU Directive 2007/60 for the assessment and management of risk. Flood hazard maps are detailed flood plain maps complemented with: type of flood, the flood extent; water depths or water level, flow velocity or the relevant water flow direction. Flood risk maps indicate potential adverse consequences associated with floods with several probabilities, expressed in terms of: the indicative number of inhabitants potentially affected, type of economic activity of the area potentially affected, installation which might cause accidental pollution in case of flooding. The most simple flood hazard map should be one just showing the extension of the area to be flooded during an event of a given probability or return period (Figure 4). A further developed hazard map is one that includes not only the extension of the area to be flooded but also the expected water depth (Figure 5). The Flood Hazard Map can also include the information of the different flood-related variables to derive a hazard scale. An example of such an approach is the development of flood hazard maps for events affecting people (Figure 6). In coastal sedimentary environments where the coastal fringe is capable of

responding to the impact of an event (a storm associated to a given probability), the hazard map can also include an indication of the areas prone to be eroded (Figure 7).

Coastal morphodynamic feedback influences the extension of flooding. Figure 8 shows that the selection of a given initial beach profile, from an existing dataset to characterize the coastal fringe, can result in variations of the duration of overtopping events of about 300 % (Alvarado-Aguilar and Jimenez, 2008).

2 The European Directive 2007/60

The purpose of this Directive is to establish a framework for the assessment and management of flood risks (Chapter I). Chapters III and IV deal with flood hazard, flood risk maps and flood risk management plans respectively. The main articles of these chapters are presented below.

Chapter I

GENERAL PROVISIONS

Article 1

The purpose of this Directive is to establish a framework for the assessment and management of flood risks, aiming at the reduction of the adverse consequences for human health, the environment, cultural heritage and economic activity associated with floods in the Community.

Article 2

For the purpose of this Directive, in addition to the definitions of 'river', 'river basin', 'sub-basin' and 'river basin district' as set out in Article 2 of Directive 2000/60/EC, the following definitions shall apply:

- 1) 'flood' means the temporary covering by water of land not normally covered by water. This shall include floods from rivers, mountain torrents, Mediterranean ephemeral water courses, and floods from the sea in coastal areas, and may exclude floods from sewerage systems;
- 2) 'flood risk' means the combination of the probability of a flood event and of the potential adverse consequences for human health, the environment, cultural heritage and economic activity associated with a flood event.

CHAPTER III

FLOOD HAZARD MAPS AND FLOOD RISK MAPS

Article 6

1. Member States shall, at the level of the river basin district or unit of management referred to in Article 3(2)(b), prepare flood hazard maps and flood risk maps, at the most appropriate scale for the areas identified under Article 5(1).
2. The preparation of flood hazard maps and flood risk maps for areas identified under Article 5 which are shared with other Member States shall be subject to prior exchange of information between the Member States concerned.

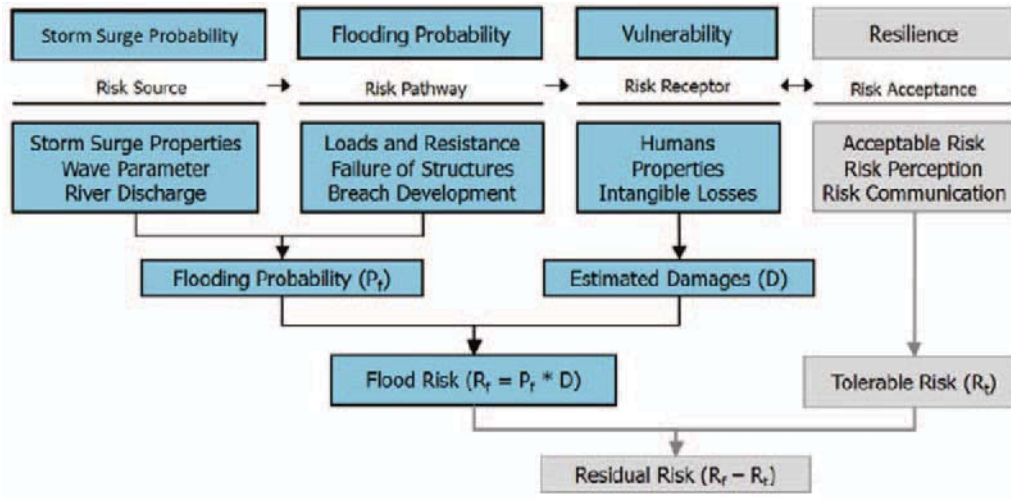


Figure 2: Integrated flood risk analysis flow chart (FLOODsite, 2008)

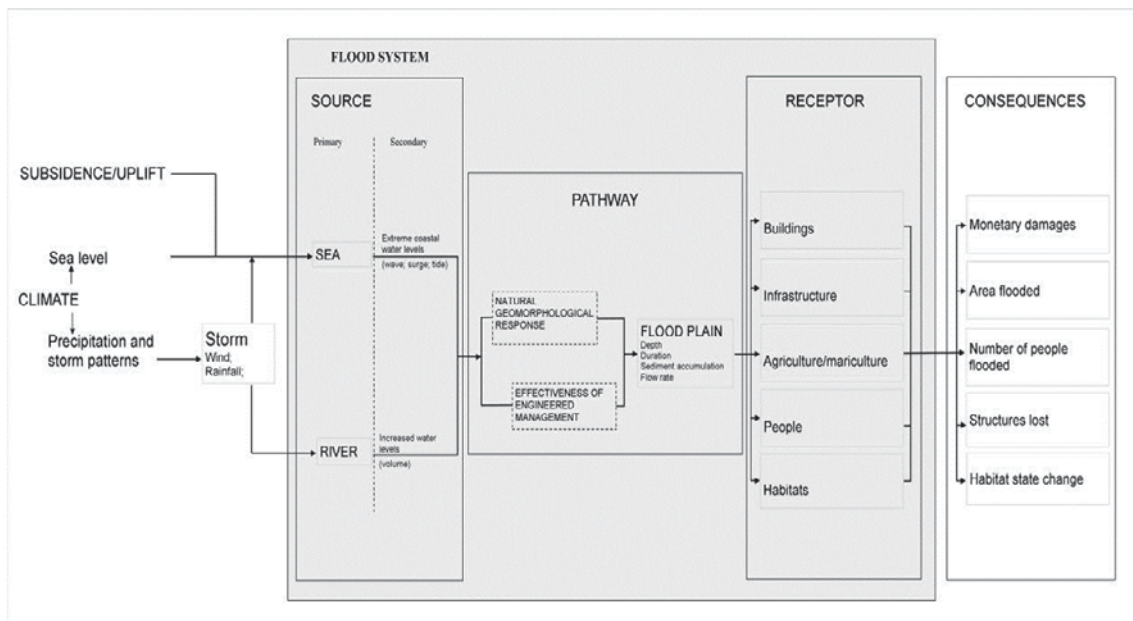


Figure 3: The Source-Pathway-Receptor Concept (THESEUS, 2010)

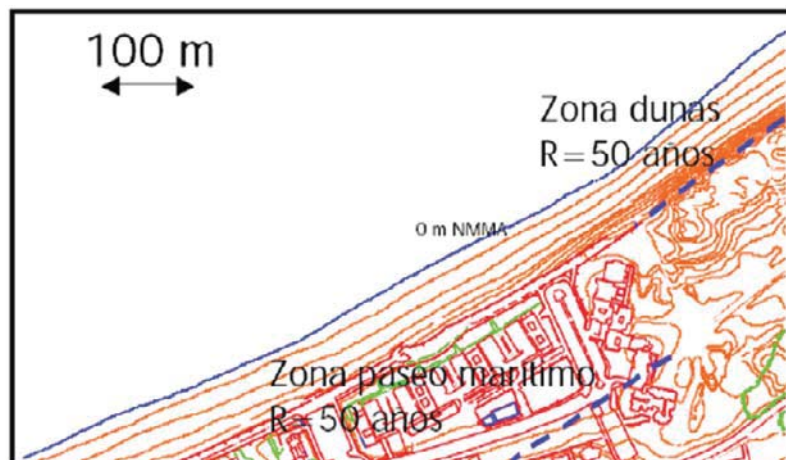


Figure 4: Delineation of flood hazard areas to a water level associated to a 50 years return period (dashed blue lines, GIOCC 1998).



Figure 5: Example of maximum flood inundation depth caused by sea flooding in the Netherlands (EXCIMAP, 2007a).

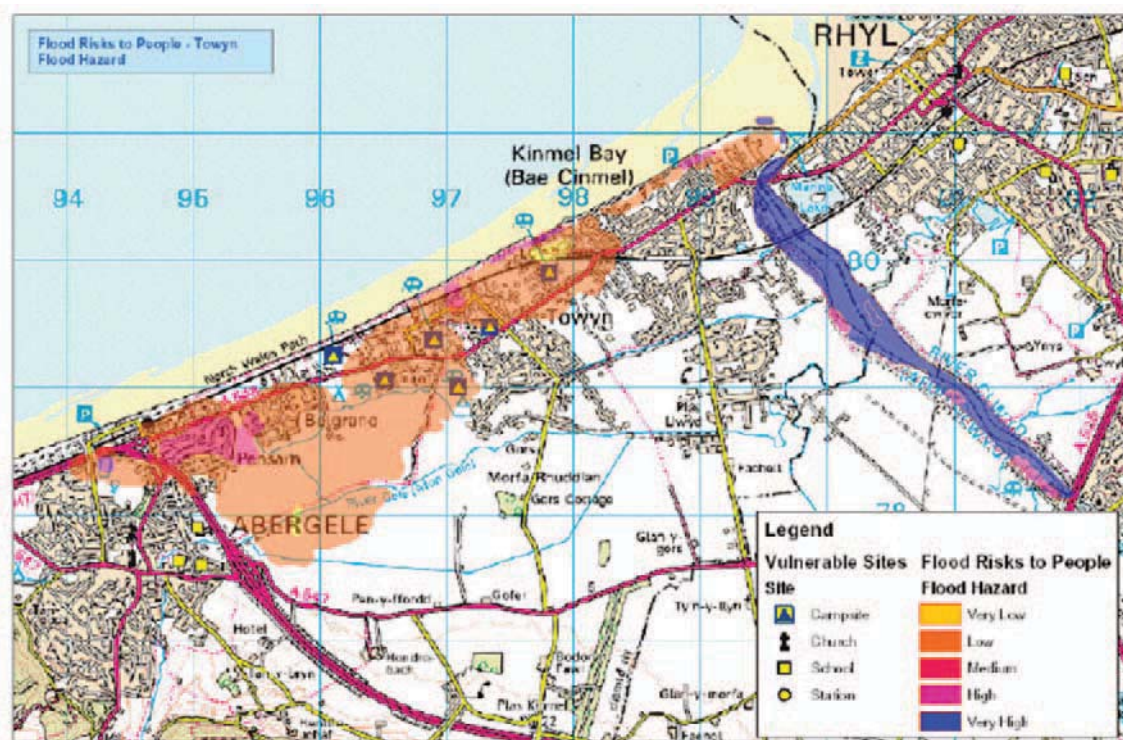


Figure 6: Example of Flood Hazard Map with a hazard scale in the UK (DEFRA, 2006).

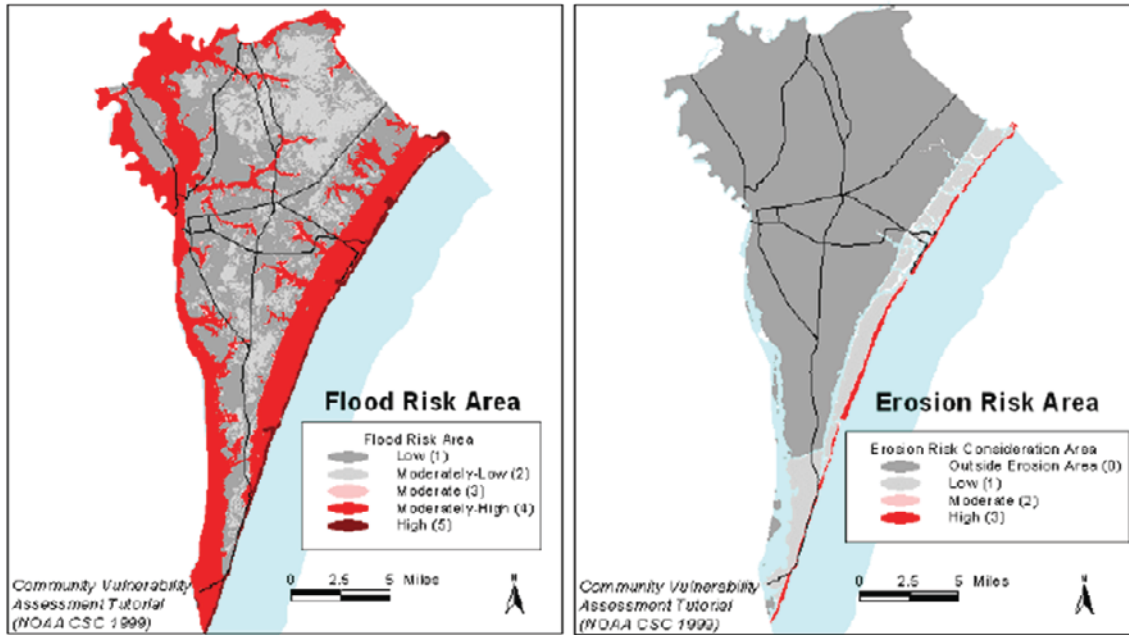


Figure 7: Example of Flood and Erosion Risk Maps in USA (NOAA, 2008).

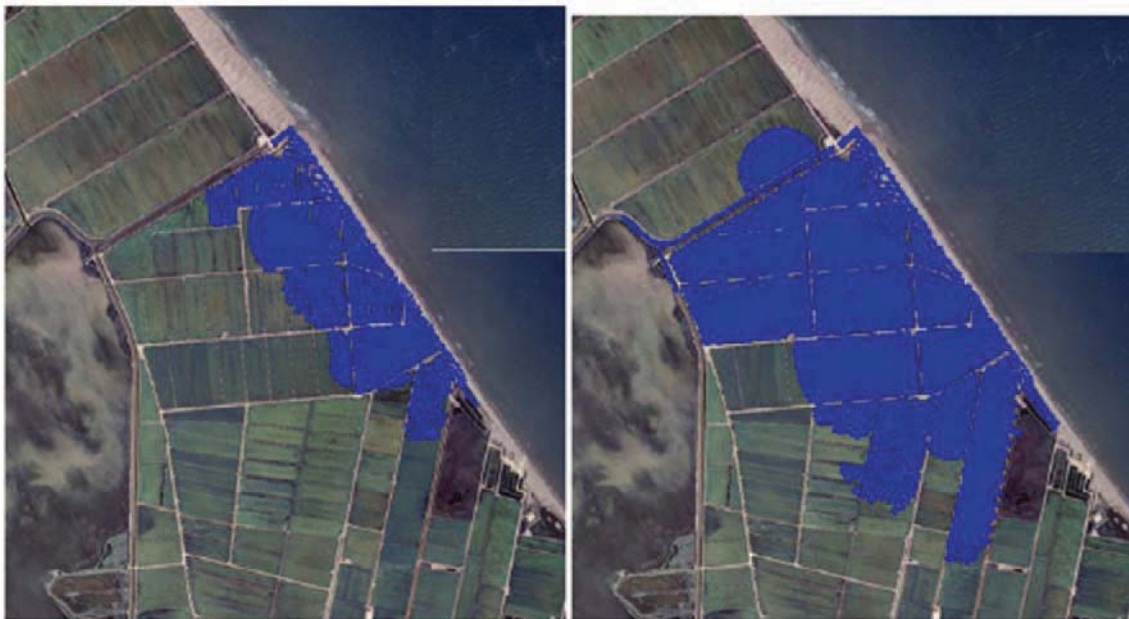


Figure 8: Changes in Flood hazard maps (extension of the flood) in the Ebro delta for a 100 year return period storm as a function of the initial beach morphology (Alvarado-Aguilar and Jimenez 2008).

3. Flood hazard maps shall cover the geographical areas which could be flooded according to the following scenarios:

- (a) floods with a low probability, or extreme events scenarios;
- (b) floods with a medium probability (likely return period ≥ 100 years);
- (c) floods with a high probability, where appropriate.

4. For each scenario referred to in paragraph 3 the following elements shall be shown:

- (a) the flood extent;
- (b) water depths or water level, as appropriate;
- (c) where appropriate, the flow velocity or the relevant water flow.

5. Flood risk maps shall show the potential adverse consequences associated with flood scenarios referred to in paragraph 3 and expressed in terms of the following:

- (a) the indicative number of inhabitants potentially affected;
- (b) type of economic activity of the area potentially affected;
- (c) installations as referred to in Annex I to Council Directive 96/61/EC of 24 September 1996 concerning integrated pollution prevention and control (1) which might cause accidental pollution in case of flooding and potentially affected protected areas identified in Annex IV(1) (i), (iii) and (v) to Directive 2000/60/EC;
- (d) other information which the Member State considers useful such as the indication of areas where floods with a high content of transported sediments and debris floods can occur.

CHAPTER IV

FLOOD RISK MANAGEMENT PLANS

Article 7

1. On the basis of the maps referred to in Article 6, Member States shall establish flood risk management plans coordinated at the level of the river basin district or unit of management referred to in Article 3(2)(b) for the areas identified under Article 5(1) and the areas covered by Article 13(1)(b) in accordance with paragraphs 2 and 3 of this Article.

2. Member States shall establish appropriate objectives for the management of flood risks for the areas identified under Article 5(1) and the areas covered by Article 13(1)(b), focusing on the reduction of potential adverse consequences of flooding for human health, the environment, cultural heritage and economic activity, and, if considered appropriate, on non-structural initiatives and/or on the reduction of the likelihood of flooding.

3. Flood risk management plans shall include measures that aim at achieving the objectives established in accordance with paragraph 2 and shall include the components set out in Part A of the Annex.

Flood risk management plans shall take into account relevant aspects such as costs and benefits, flood extent and flood conveyance routes and areas which have the potential to retain flood water, the environmental objectives of Article 4 of Directive 2000/60/EC, soil and water management, spatial planning, land use, nature conservation, navigation and port infrastructure.

Flood risk management plans shall address all aspects of flood risk management focusing on prevention, protection, preparedness, including flood forecasts and early warning systems and taking into account the characteristics of the particular river basin or sub-basin. Flood risk management plans may also include the controlled flooding of certain areas in the case of a flood event.

3 Data and Methodology

A critical issue in flood hazard and risk analysis and management is the collection of necessary data on the different aspects involved in the process. According to the SPRC methodology this implies to acquire data to properly describe the risk-sources, risk-pathways and risk-receptor. A general guide and recommendations for data collection is presented in the following sections for each type of data. In all the cases and as a general rule, the recommendations are given in terms of the best possible option. Also the methodology for calculating the various aspect of risk is presented.

3.1 Risk Sources

3.1.1 Data

The main input data for calculating flooding of a coastal area and creating coastal flood hazard and risk maps is the occurrence probability of the total water level at the shoreline. The total water level, ζ_t , can be expressed as

$$\zeta_t = \zeta_{as} + \zeta_{ss} + Ru + \zeta_{LF} + \zeta_{LT}$$

in which ζ_{as} =astronomical tide level, ζ_{ss} =storm surge (meteorological tide), Ru = wave induced run-up (which also includes the wave set-up at the shoreline), ζ_{LF} =component accounting for the contribution of low frequency forcing such as seiches and, ζ_{LT} = long-term component representing eustatic and/or local land-elevation (isostatic and/or subsidence) changes.

This last component, ζ_{LT} , is usually given as a magnitude associated to a climate scenario based on projections of climate change (Solomon et al., 2007) together with a local component accounting for the relative vertical movement of the land due to processes such as subsidence. This component should be included in any long-term flood hazard analysis. A recent example of how to deal with this component in coastal flood risk analysis from a probabilistic standpoint can be found in Purvis et al (2008).

The astronomical tidal level, ζ_{as} , is a deterministic process that can be easily estimated with available water level data. This data consists of water level data recorded by tide gauges that are usually located in major harbours and waterways worldwide. Detailed descriptions of tidal data analysis can be found in Pugh (1987).

The meteorological tide or storm surge, ζ_{ss} , is also obtained from recorded water levels by tide gages and it is the residual water level after subtracting the astronomical tide from the recorded water level (Pugh, 1987). This component integrates all the meteorological effects except the waves (i.e. atmospheric pressure and wind set-up). If there are no water level data for estimating this component directly, a storm-surge model can be used which, fed by wind data, simulates the generation and propagation of storm surge for any coastal domain. An example of the use of this kind of models (including a wave generation model) can be seen in Cheung et al (2003).

The long-frequency component, ζ_{LT} , can be obtained from recorded water levels by retaining the component associated to a range of frequencies longer than the ones associated to waves (25 sec) and shorter than the astronomical frequencies (Pugh, 1987).

The wave-induced runup, Ru , is usually not a measured variable but a calculated one. Wave data and beach profile characteristics are required for calculating it. With regard to wave data, most of the existing runup formulas require simultaneous information of wave height and period. This information is usually obtained from wave records acquired by using coastal buoys. To calculate runup the required information of the beach morphology is the beach slope, although in extreme dissipative beaches, the runup is usually considered to be independent of the slope. This information should be obtained from topographic and bathymetric data acquired in the coastal fringe. One of the most important aspects to be considered is the duration of the period covered by these data sets. As they are going to be used to define water levels associated to long return periods, very long time series are required. Various aspects on quality and length of time series required to make a reliable estimation of extremes are reviewed by Sánchez-Arcilla et al (2008). If a long time series of this information is not available elsewhere, it can be replaced by simulated data. This data consists of time series of water level and wave conditions generated by wave and surge generation models fed by meteorological time series (wind and atmospheric pressure fields). For the European coast there exist different data sets of hindcasted conditions for periods longer than 40 years, which is significantly longer than most of the existing recorded data sets. Examples of these hindcasts are the obtained data sets within the WASA and the HIPOCAS projects (WASA, 1998, Guedes Soares et al., 2002).

3.1.2 Calculation Methods

For the risk sources the estimation of the occurrence probability of a given water level is necessary. There are two main ways to calculate the probability distribution of the total water

level for coastal flooding analysis: (a) to directly estimate it from existing time series of water levels and (b) to estimate it by analysing the integrated contribution of each component.

In the first case, the procedure to follow is to analyse existing water level time series to obtain its extreme distribution and, to define the probabilities (or return periods) for the water levels required. How extreme distributions can be used in fitting water levels can be seen in Sobey (2005), Pirazzoli and Tomasin (2007) and a review by Sánchez-Arcilla et al (2008). The main problem with this approach is that water level records usually do not include wave-induced contributions. Thus, its use should only quantify the water level components associated to astronomical and meteorological tides.

In the second case, the contribution of each component has to be estimated and the joint probability has to be calculated. Here two main approaches exist: (i) response and (ii) event approaches (FEMA, 2005, Divoky and McDougal, 2006, Garrity et al, 2006). The event approach is a deterministic approach. It uses one or more combinations of water level and wave conditions (events) associated to a given probability and it computes the resulting flood level (response). The response method is based directly on measured or simulated water levels and waves as they occurred in nature and, the water level of interest (associated to a given probability or return period) is directly calculated from a probability distribution of total water levels. It is especially recommended when the variables (events) determining the flood level (response) are partially or poorly correlated, i.e. when surge and large waves are uncoupled and, for areas in which wave height and periods during storms (both will determine the wave run-up) are poorly correlated. At present, this approach is recommended by FEMA guidelines for flooding studies (Divoky and McDougal, 2006).

When the analysis is performed at a coast able to dynamically react to the impact of the storm, i.e. to be eroded, the most straightforward approach should be the *event* one. For this purpose, joint probability distributions of wave and water level conditions should be used to define the event assigned to a given probability or return period, which will be used to calculate the risk pathways. This is due to the fact that erosion and inundation are not necessarily correlated and, in consequence, hydrodynamic conditions resulting in a water level of a given probability and an erosion of the same probability should be different.

If the analysis is applied to a coast where one of the two processes (erosion and/or inundation) clearly dominates, the recommended approach should be the *response* one. For this purpose, joint probability distributions of wave and water level conditions should be used to build a probability distribution of the target variable (e.g. total water level by estimating the contribution of the different components), from which the value associated to a given return period is directly obtained. This should be the usual approach for static flooding analysis, i.e. when the coastal response is not included.

3.2 Risk Pathways

3.2.1 Data

Data required for risk pathways make reference to those used to characterize the intensity of the processes taking place (coastal erosion, overtopping and flooding). Data required for defining risk receptors make reference to those used to characterise the consequences of the inundation. To define both risk pathways and receptor, three main types of data are required: (a) topographic, (b) bathymetric and (c) land-use data.

Topographic data of the coastal zone will cover all the data to be gathered for the analysis. Due to the strong spatial gradients in dynamic conditions across the coastal zone, they can be separated in two major domains: (i) the floodplain and the (ii) coastal fringe (figure 9).

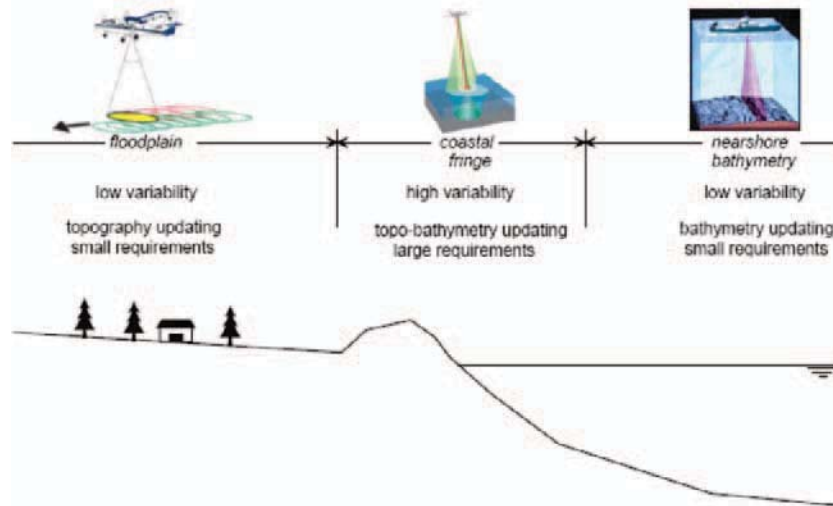


Figure 9: Domains for data acquisition.

Topographic data of the floodplain are needed to define the relief of the land to be inundated. The accuracy of these data will control the extension of the flood prone area for a given water level scenario and, in this sense, they should control the accuracy of the flood hazard map.

The general way to provide these data is through a Digital Terrain Model (DTM) or Digital Elevation Model (DEM) which is a mathematical 3D representation built from a data set composed by a collection of points of known elevation and spatial co-ordinates.

The presently most common way to obtain these topographic data in an efficient manner, in terms of accuracy and cost, is the LIDAR (Light Detection and Ranging). Essentially it is a remote sensing technology that derives the elevation of the terrain by measuring the time delay between the transmission of a laser pulse and the detection of the reflected signal from a plane. This technology permits to obtain a high density of points per scanned surface, although it has to be considered that “not always more is better”. Thus, point spacing (distance between points) and density (coverage of points within the area) are critical considerations in LIDAR mapping. Their optimum selections depend on the desired vertical accuracy, and type of terrain (slope) and land cover. Their number will control the cost and time of acquisition time and data processing (Anderson et al., 2005). Once these data are obtained, they have to be filtered in order to remove all the noise in the signal which is not corresponding to the real terrain topography. The whole process can efficiently be done by the service (LIDAR) supplier but it is important to know all about the process involved and, also to be sure about the accuracy obtained.

With the so measured data, a DTM or DEM has to be derived. The accuracy of this DEM will determine the accuracy of the flood mapping. The required DEM resolution to assure proper map accuracy will depend on the type of terrain to be analyzed. However, a reasonable DEM resolution should be of the order of 5 m cell (for raster DEMs). Because the size of cells will also determine the (computational) costs of inundation models, they can be later re-sampled to larger cells provided the relief is simple enough to do not soften the real topography nor mask existing canal networks.

In any case, before selecting the definitive cell size to be used in the analysis, it is recommended to test different options with the selected inundation model and to analyze the differences. Because this domain is usually of very low intensity dynamics, its updating needs are relatively small. Thus, it is not expected to significantly change in its relief unless a high energetic event should take place (e.g. a flood) or, the human influence should produce a major footprint such as building of infrastructures or artificial changes of the topography that should affect floodwaters' paths in the area. Once an accurate DEM is available, it is recommended to update the information, and later the DEM, of only those areas subjected to any change of any origin. Depending on the scale of these modifications, the proper acquisition method should be chosen (conventional surveying techniques such as total stations, DGPS or LIDAR). The new

data should be used to update the DEM in the corresponding area whereas the rest can remain as it was.

Topographic data of the coastal fringe are needed to characterize the morphology of the border between the sea and the land. This relatively narrow zone includes a subaerial (topography) part and a subaqueous one (bathymetry). It will act on the one hand as a barrier for the flooding, i.e. the main element of protection for the hinterland and, on the other hand, it will control the intensity of the flood by modifying wave and surge propagation. In addition to this, the flooding intensity can be affected by the changes in the morphology of the beach (run-up modification due to changes in beach slope, overtopping variation due to changes in dune and beach crest changes, etc.). Topographic data in this domain can be easily acquired when the topography of the floodplain is being gathered and, then, the same methodology as recommended before should be used. Moreover, due to the characteristics of this zone in which the terrain is usually free of obstacles masking the signal (forests, buildings, etc.), this measuring system is very efficient in this area and, the application of filters to the recorded signal is not required as frequent as in the previous case.

One of the main problems in coastal flooding analysis is to have a reliable coastal fringe morphology to represent the pre-storm conditions available. Thus the coastal fringe morphology is continuously updated at a "reasonable frequency". This "reasonable frequency" depends on the intensity of the local littoral dynamics, but assuming that most of sedimentary coasts will show a seasonal behaviour we can fit the "ideal" update scheme in two configurations per year. For those coastal environments protected by rigid structures such as dikes or seawalls or for rocky coasts, the floodplain update requirements should be applicable, i.e. data updating when significant changes are detected. This information update can be done by using the same methodology (LIDAR) or alternative techniques that provide enough resolution. This depends on the extension of the area to be covered and the type of morphology (dunes, low gradient beaches, etc.). An alternative technique to LIDAR to efficiently monitor coastal fringe topography in large areas is real time kinematic GPS (RTK-GPS) which allows sampling of the surface along a given path with the selected density and a 15cm vertical accuracy (Morton et al., 1999).

Bathymetric data of the coastal fringe are needed to characterize the underwater morphology of the border between the sea and the land. This is required to describe the coastal processes taking place in this area and it will affect the magnitude of the flooding. The characterisation of the bathymetry of this area is of relatively small use if it is not conveniently (frequently) updated. And unless an efficient system (in terms of cost and time) is available, this will not be the usual case. The "ideal situation" should be an area of analysis formed by relatively clear water. Under these conditions, the gathering of bathymetric data can be combined with topographic data by using the SHOALS (Scanning Hydrographic Operational Airborne Lidar Survey) system. This version of LIDAR is able to measure the bathymetry in shallow waters with accuracies up to ± 15 cm (Guenther et al. 2000). However, in areas with turbid waters the maximum surveyable depth could be very small and, even worse, the obtained accuracy should be unacceptable. Maximum surveyable depths range from around 50 meters in very clean offshore waters to less than 10 meters in murky near-shore waters. For extremely turbid conditions, surveying may not be possible (Guenther et al, 2000). Under ideal conditions, these bathymetric data should be collected simultaneously with the topographic ones and at the same frequency. In those cases where SHOALS cannot be used, an alternative technique should be employed. The traditional way is to make bathymetric surveys with echo-sounders as in the nearshore zone although with the additional problem of the existence of very shallow areas where ships cannot easily operate. Due to this and, to keep costs within reasonable limits, representative transects along the study area could be selected. These transects should be monitored at a frequency reflecting the natural seasonal variability as it was the case of the topographic data in this domain. Thus, a six-month frequency should be a reasonable choice.

Bathymetric data of the nearshore zone are needed to characterize the underwater morphology of this area where waves and surge propagate towards the coast. The presently most commonly used technology is the Multi-Beam Echosounder Surveying (MBES), which has demonstrated high quality with respect to meeting the IHO standards on depth accuracy (IHO, 1998). Because the bottom evolution in this zone (significant enough to modify wave and surge

propagation) is, usually, very slow, the requirements for data updating are low. Thus, once the bathymetry of the nearshore area is available, it is not expected to require major updates in periods shorter than decades. This will also depend on the intensity of the processes taking place in the area. Thus major changes due to human influence such as dredging will affect wave propagation and, in consequence, will make these updates necessary.

3.2.2 Calculation Methods

In this section, different methods to calculate the different variables required to characterize the risk pathways in a coastal flooding analysis are presented. They cover variables related to the quantification of the two main coastal processes taking place during the impact of a storm in the coast, inundation and erosion.

(a) Runup estimation

The wave induced runup can be simply defined as the height with respect to the still water level reached by the uprush of wave action. As it was previously mentioned this is a variable that it is usually calculated from wave data and, consequently, its accuracy will be strongly dependent on the model used.

There exist numerous models for estimating wave runup depending on the characteristics of the coastal fringe on which the waves impact. For runup estimations for coastal structures, a detailed review of existing formulas for the main coastal structures typologies together their range of application can be seen in Burcharth and Hughes (2003). For analysis of areas protected by coastal structures, the formula recommended for the corresponding structure typology should be used.

For wave runup estimations for beaches, there also exist different options in the literature. The use of the recently proposed by Stockdon et al. (2006) is recommended. This recommendation is due to the fact that this formula has been derived from reanalysis of run-up data obtained in field experiments and large scale laboratories.

(b) Wave overtopping discharge

Wave overtopping will occur when the beach/dune crest height is lower than the calculated potential run-up. Under these conditions, waves will reach and pass over the crest of the beach/dune and will flow into the hinterland. Thus, wave overtopping can be defined as the mean discharge of water per linear meter of width of the beach flowing landwards.

One of the problems when calculating overtopping discharges in beaches is that most of the existing formulas have been derived for coastal structures such as dikes and seawalls (EUROTOP, 2007), so their application to beaches can only be used as a approximation of the potential floodwater discharges occurring during a given event since these formulas are usually empirically derived. FEMA (2003) proposes a method to estimate wave overtopping discharges for coastal flood analysis.

(c) Coastal response

Once the storm impacts on the coast, two situations can occur: (i) the coast is rigid (e.g. protected by coastal structures) and will be inundated if total water level exceeds the crest of the structure or the structure fails and (ii) the coast is dynamic and reacts to the impact of the coast by being eroded. In the second case the inundation will not only be controlled by the initial beach/dune height but by its evolution during the event. Due to this, risk pathways in the case of coastal flooding analysis must include not only the inundation but the induced coastal changes.

The impact of extreme storms on sedimentary coast causes different morphodynamic processes and responses that can significantly affect coastal flooding. Their intensity correlates with the intensity of the storm. As an example, Figure 10 shows a qualitative hazard scale of coastal changes during storm impacts on barriers (applicable to any low-lying coast). It serves to illustrate the different regimes of functioning as a function of the water level. These regimes have been formalized in a conceptual model by Sallenger (2000) in: swash, collision-dune erosion, overwash and inundation regimes.

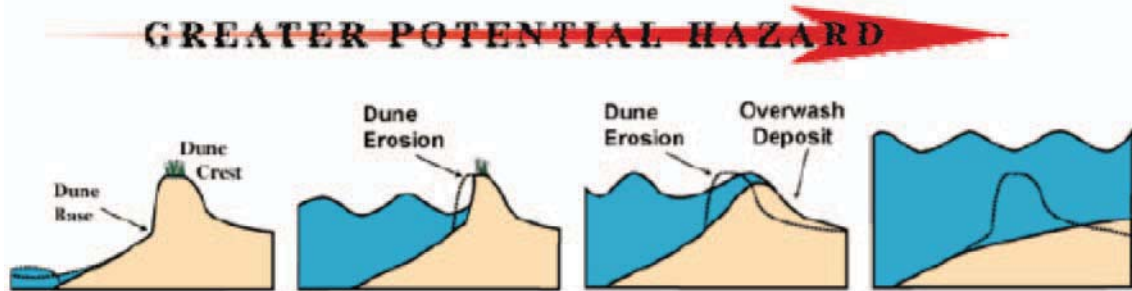


Figure 10: Qualitative hazard scale of coastal changes during storms as a function of water level (USGS, 2001).

The prediction of the evolution of the coastal fringe under the impact of the storm is a question far from trivial and, there is not a single morphodynamic model capable of simulating all the possible conditions at any coast. A discussion on different options for models to be used for coastal flood forecasting is given by HR Wallingford (2003). Although they are not specifically for morphodynamic modelling the given recommendations cover most of the aspects to be considered.

There exist different models to simulate the response of beaches and dunes to the impact of extreme storms. Generally speaking, the best model is that model that has been calibrated and/or developed for a specific coastal stretch. In this sense, the most general recommendation regarding this aspect is to work with calibrated and validated morphodynamic models. The most complicated model is not necessarily the best. In many cases they are difficult to calibrate and/or validate, although they give insight into the processes taking place during the storm,

One of the most common analytical models for the estimation of the erosion induced by the impact of a storm on a beach profile is that introduced by Vellinga (1986). The model has been widely used even in sites with completely different characteristics (in terms of coastal morphology and wave and water level climate) to the ones of the Dutch coast where this empirical model was developed.

Another simple geometric model to predict the erosion (retreat) of beach foredunes induced by wave runup during extreme storm events has been developed by Komar et al (1999, 2001). The model is similar to the Bruun's rule but applied to a shorter time scale in which the total water level during the storm is the driving force. As in the previous case, this model is an "equilibrium model" in the sense that it should predict the maximum erosion induced by a given event without taking into account its duration (storm of unlimited duration). When this type of models is used, the information to be obtained is the final dune/profile configuration after the impact of the storm. Under these conditions no intermediate updates on floodwaters can be obtained. The only possibility is to calculate run-up and overtopping discharges for the initial and final configurations and to estimate their range of variation due to beach evolution. This problem is common to any model providing the final configuration without information of the evolution of the process.

Recently, Larson et al. (2004) presented an analytical model to simulate the impacts of storms on dunes. The model quantifies the erosion in terms of recession distance and eroded volume. It uses a transport relationship based on the wave impact theory, where dune erosion is induced by individual swash waves impacting the dune face. The model was validated using different datasets obtained in the laboratory and the field. They conclude that the model produce reliable quantitative estimates of storm-induced dune erosion (retreat and volume loss), provided that the forcing conditions are known and that the geometry of the dune configuration is similar to the one assumed in the model (plane-sloping foreshore backed by a vertical dune). Finally, authors recommended applying the model using a range of transport coefficient values (calibration parameter) to include some uncertainty estimate in the calculated variables.

Numerical beach/dune erosion models are more versatile than analytical ones because there are no limitations to describing the initial beach profile and, in most of the cases, are able to include most of the variables characterising the forcing in a realistic manner. The major limitation will be the reliability of the sediment transport model included to simulate the process

(see e.g. Schoones and Theron, 1995) and, as it was mentioned before, they need to be calibrated/validated for the area of application.

Among the existing beach erosion models, the *Sbeach* model (Larson and Kraus, 1989, Wise et al. 1994) is the most common. It is an empirically based model that was originally developed using a large data set of cross-shore sand transport rates and geomorphic change obtained in large wave tanks.

It includes a module for wave propagation across the beach profile which is used to estimate the cross-shore transport rates in different zones from outside the surf zone to the swash zone. These transport rates are included in the conservation equation to estimate beach profile changes. The model requires an initial beach profile and the sediment grain size to characterize the receptor and, the wave height, period furthermore it requires the direction time series and the water level time series to characterize the forcing. The model has been largely validated via field cases and now it can be considered as a "standard" for beach/dune erosion calculations. In fact, it has been used to start beach erosion by overwash to be subsequently complemented with more sophisticated models such as Delft3D (Cañizares and Irish, 2008).

Due to its simplicity and its robustness, this model is recommendable for estimating the evolution of the beach during the impact of storms. It has to be noted that although coefficients to be used in the model have been calibrated in numerous applications and, default values have been recommended, results of its application without an ad-hoc calibration must be interpreted as an order of magnitude of the expected coastal response.

As storm magnitude increases, the dune and the beach are more frequently overtopped and overwash transport begins to be important. However, there are few models capable of dealing with overwash processes in a realistic manner. One of the last attempts to include the transport in a beach profile model has been made by Larson et al (2004) with the before mentioned analytical model for dune erosion. It also has to be mentioned that the last version of *Sbeach* simulates the effect of overwash transport on the beach profile evolution. However, this is a subject under development and a realistic model is still required (e.g. Donnelly, 2008).

During very intense storms, the final coastal response, especially in low-lying areas, is breaching. A breach is a new opening in a narrow landmass such as a barrier beach that allows water to flow from the sea to the area behind the barrier -a water body or a low-lying area- (Kraus and Wamsley, 2003). They usually occur during extreme events and, in consequence, they are associated to the inundation stage in the scale of Sallenger (2000). In spite of the potential importance of this process, the number of existing models able to simulate breaching is quite limited (Basco and Shin, 1999, Tuan et al, 2006, 2008). In spite of all of these attempts, there is not yet a morphodynamic model able to accurately simulate the dynamic response of low-lying coast to the impact of extreme events. Due to this, the USACE-ERDC has launched a program to develop an open-source program to simulate effects of hurricanes on low-lying sandy coasts. The aim of this program, XBeach (Roelvink et al., 2007), is to simulate the different phases taking place during the impact of extreme storms in low-lying coasts, i.e. dune erosion, overwashing and breaching. An overview of different morphodynamic models to predict changes in river, coasts and estuaries useful for flood hazard analysis can be seen in Reeve (2007).

3.3 Risk Receptor

3.3.1 Data

Finally, to fulfil the requirements of the EC Directive, it is necessary to obtain data for determining the inundation, flood damages and risk in the receptor. For this purpose, the main type of information to be included is the **land-use** of the floodplain. This will include all the relevant categories for economic and environmental damage analysis. In addition to this, information on the spatial distribution of the population or, in its absence, urbanization types should also be compiled. This data will also be relevant to gain information on the expected flood intensity such as roughness and permeability of the land. Moreover major infrastructures must be localized and, any obstacle to flood propagation should be identified to be included in the DEM.

The main source of information are data gathered by field surveys, data obtained from remote sensing techniques such as aerial photographs, satellite and/or airborne mounted multi-spectral sensors as well as pre-existing data sources such as the Corine Land Cover (although only valid for large scale analysis). A detailed review on land use data required for flood hazard and risk analysis can be seen in Messner et al (2007).

3.3.2 Calculation Methods

- Inundation

Once the design water level, the associated overtopping discharge and related probabilities of exceedance have been determined, the next step is to determine the extent of the area to be affected by inundation.

In some cases, depending on the estimated water level, the coastal area can be subjected to a full inundation with reformed broken waves able to propagate overland. On these occasions, it should be preferable to estimate the wave propagation to correctly delineate the inland extension of the inundation. For these situations, a wave propagation model capable of simulating the wave breaking and reforming in very shallow waters with artificial roughness (due to vegetation, buildings, etc.) should be used. Examples of such models are the simple approximation followed by FEMA (2003) with the Whafis model or, more process-oriented ones, such as the one by Möller et al (1999). Again the selection of the proper model will depend on the characteristics of the study area and on the importance of the hazard analysis.

However, before estimating any wave propagation overland, the first estimation to be done is the determination of the surface to be flooded. For this purpose, flood inundation models combined with Digital Terrain Models are used to describe the processes taking place in the flood plain.

As in the previous calculation methods, there exist different options to estimate the magnitudes of the inundation.

The simplest option is the use of the so called empirical models, which are often described as pure mapping. No physical laws are involved in the simulations performed. They are rather simple methods and of low cost, but they provide only poor estimates of flood hazard in large low lying or extensive areas where flows through a breach may be critical in determining the flood extent. They are usually applied to assess flood extents and flood depths on a broad scale. In essence they are just GIS routines to delineate areas to be inundated applied to a DTM. This can be done in different ways: (a) determining the extension of the coastal domain and its height below the target water level or (b) distributing the estimated water volume entering the hinterland depending on the internal topography.

The first case should be equivalent to assuming a situation in which the target water level is maintained for a certain time period long enough to supply the required water volume to "fill" the entire area. This option should be acceptable when analyzing the flooding associated with the relative sea level rise (RSLR)-induced water level scenarios and/or when the shoreward extension of the area to be inundated is relatively small.

The second case should be applicable in situations when the beach topography is not as simple and the event involves the overtopping of the beach/dune crest with a flow of water entering to a domain with a lower elevation than the beach crest. The application of the before mentioned method could result in projected inundated areas with a very unrealistic dimension landwards. In this case, the approach should be to estimate the total volume of water overtopping the beach along the coast and, to distribute it in the floodplain according to the existing topography.

However, in this second situation, i.e. time varying water levels pumping water towards the hinterland, the best way to determine the flood extension should be the use of inundation models. As in all the cases involving a model selection, there is no general rule for accepting the advantage of the use of one specific model over a different one other than an ad-hoc analysis of the case study. The best model appears to be one including the processes and conditions of the specific case, for which the required data is available and which has been calibrated / validated. Different available inundation models are presented by Woodhead (2007) together their range of validity.

- Damages

Damages are classified into tangible and intangible damages depending on whether or not the losses can directly be assessed in monetary values (Smith and Ward 1998). Tangible damages include damages to buildings and infrastructure, agricultural and industrial losses, costs related to evacuation, rescue operations and reconstruction, among others. Intangible damages include loss of life and health impacts, cultural losses, damages to the environment, and others. Furthermore, intangible damages are mainly categorized into two groups: social and environmental damages. Social damages are experienced by individuals, groups and the overall society, and mainly include loss of life, physical injuries and mental health impacts. Moreover, cultural damages are also considered under this category. Environmental damages are damages to ecosystems (Dassanayake et al. 2010).

Tangible damages can be classified in two types: direct damages or indirect damages. Direct damages are those caused by physical contact of floodwater, such as damages to buildings, general infrastructure, vehicles, transportation and communication features, agriculture, and others. Indirect flood damages refer to the economic impact caused through interruption or disruption of economic and social activities. Direct flood damages are normally estimated from systematically applied survey procedures, but can also be derived from the analysis of insurance claims data, historical flood data analysis, or any combination of these approaches. The results from these analyses are primarily expressed as depth-damage functions, or curves. One of the most significant problems regarding traditional methodologies is that there are no uniform guidelines for the collection of flood damage data. And, similarly, the methods used to evaluate the compiled data and to report these results greatly vary depending of the evaluating agency or institution. Therefore, as discussed by Downton et al. (2005), the records of historical flood damage data are often inadequate for scientific assessment.

Depth-damage curves recount the damage extent for a specific region based on the inundation depth. In some cases where the damage progresses as a function of time, the duration of the inundations might be considered. In the case of buildings, depth damage curves represent the average building damage that occurs at different inundation depths. These curves also consider building characteristics, including primary construction material (wood frame, steel frame, concrete-block bearing walls, or masonry bearing walls) and location (e.g., riverine A-zone, coastal A-zone, or coastal V-zone). Once developed, depth-damage curves are often used for future events or applied to similar regions since their use require less time, effort, and resources. Depth-damage curves are typically developed isolating the contents damage from the building/structural damage. Individual curves are then made available for each category.

The flood damage estimates provided by depth-damage curves can be highly uncertain due to the fact that these curves represent the aggregated damage caused by several different flood actions, but the damage is expressed just in terms of floodwater depth. As noted by FEMA (2005), the use of depth-damage curves is not recommended “whenever high velocity flows, ice or debris induced damage, erosion and soil/foundation failure, or unusually long-duration flooding are likely.”

One of the few exceptions where floodwater velocity was considered as part of the development of damage curves is the USACE Portland District’s velocity-based building collapse curves (USACE, 1985). These collapse curves correlate the floodwater depth and floodwater velocity with the collapse potential of building based on their material class: (1) wood frame, (2) masonry and concrete bearing walls and (3) steel frame. However, the only information provided by these curves is if the buildings could potentially collapse or not. Therefore, the information presented by these curves is very limited and does not provide any guidelines concerning the quantification of flood damage, such as the percentage of building damage, or even failure risk.

Studies proposing either alternative or complementary methods to assess flood damage are rather scarce. A study by Kelman (2002) focused on evaluating the physical vulnerability of residences to flood disasters in coastal eastern England. In addition to the typical evaluation of hydrostatic actions, Kelman examined the effects of: (1) hydrostatic forces resulting from floodwater depth differentials between the inside and outside of external walls and (2) floodwater velocity. Kelman’s study represents an excellent attempt at providing new knowledge and methods to evaluate the risks from coastal flooding scenarios. However, the actions

generated due to waves, debris impacts, or local soil scour, were not modeled. In addition, the study only evaluated the vulnerability of masonry walls and glass windows. The vulnerability of other structural components, such as columns or frames, was not assessed. Another recent flood damage study was performed by Delft Cluster in the Netherlands (Roos, 2003). The study evaluated the vulnerability of masonry and concrete buildings due to several loading cases, including: (1) hydrostatic forces due to floodwater level differentials, (2) floodwater velocity, (3) wave action and (4) pounding debris. The damage model compares the floodwater loads to the strength of the walls. However, the results from the Delft Cluster study were of qualitative nature. As discussed by Roos (2003), in the final analysis it was assumed that when a load-bearing wall fails, buildings could either collapse partially or totally. Then, "it is supposed that 70% of the partial collapsed buildings will totally collapse."

Flood damage models have been developed to perform a physically based assessment of direct losses on the built environment. For example, the software tools FloReTo (Manojlovic and Pasche, 2010) and the FEMA's HAZUS_HM flood model (Scawthorn et al, 2006a and b).

The HAZUS-MH (HAZards U.S. Multi-Hazard) is a nationally standardized methodology and risk assessment software program that comprises three models for estimating potential losses from natural disasters (i.e., earthquakes, hurricane winds, floods). HAZUS-MH flood model was released by FEMA in 2004. It currently comprises methods for the assessment of damages in riverine and coastal settings. These damages include buildings, transportation and utility lifelines, crops, vehicles, among others (Schneider and Schauer, 2006). The Federal Insurance Administration's and the USACE are the sources for most of the HAZUS-MH flood model depth-damage curves (Scawthorn et al. 2006b, Ding et al. 2008). The detailed methodology for this flood model is discussed by Scawthorn et al. (2006a, b). Some of the shortcomings of using HAZUS-MH are that: (1) the flood damage data and damage curves highest resolution is census block level and that (2) currently, there are very few velocity-damage curves. Although HAZUS-MH flood model is said to account for floodwater velocity (Schneider and Schauer 2006), this is actually done by indirect methods such as the application of adjustment factors. As discussed by Scawthorn et al. (2006a,b), in theory, the HAZUS's library of damage curves can be applied to individual buildings. However, since most damage estimates are computed at census block levels, damage predictions are more reliable for large groups of buildings. Regarding the limited availability of velocity-damage curves, the building collapse curves developed by the USACE Portland District are still the only functions included in the current version of the model that accounts for floodwater velocity. Therefore the direct effects of floodwaters or hydrodynamic forces are not actually considered by the model. The limitation is crucial since floods with significant velocity can generate more damage than inundation alone.

The estimation of social and ecological losses is based on methods considering flood depth, flow velocity as well as flood warning parameters, e.g. as the estimation of fatalities and injuries. The estimation of fatalities and injuries can be based on the methodology by Penning-Rowsell et al. (2005). It has been found that social and ecological aspects of flood related vulnerabilities are usually neglected though they may represent a considerable contribution to the total losses (Green and Penning-Rowsell, 1989). Evaluation methods for the intangible losses have been critically reviewed and analysed (Dassanayake et al. 2010).

A methodology for the consideration of tangible and intangible damages within an integrated risk analysis has to be developed. The aim is to perform an analysis considering both, tangible and intangible damages in order to calculate the overall risk and to develop optimal mitigation strategies for different scenarios. Several approaches have been reviewed in order to find an optimal strategy for the integration of tangible and intangible damages within an integrated risk analysis (Dassanayake et al., 2010).

As a first possibility, the presentation of damages and losses within damage categories, further termed as categorisation, has been examined. For this purpose, similar damages such as societal losses are grouped as one category. The main advantage is that optimal mitigation measures for each damage category can be specified. However, this approach is not a real integration, even though a full flood risk analysis is performed. Tangible and intangible losses are considered, but not expressed in the same terms within one risk analysis, since every risk is calculated separately and in different units. Furthermore, mitigation strategies for one damage

category influence other categories as well. These aspects cannot be considered properly by using the categorisation approach.

The second approach which has been examined is the Multi-Attribute-Utility (MAUT) approach.

This approach was tested and proposed for integrated risk analysis in the European Research Project FLOODsite (Meyer et al. 2007). The MAUT approach is based on the ranking between different options by the consideration of their utility functions. Utility functions are favoured as they express the economic behaviour of individuals or the society. Utility functions enable the weighting, balancing, and ranking of different options, such as mitigation strategies, within an integrated risk analysis. The aim is to maximise the sum of the utilities of all options. The following steps are required for the analysis within the MAUT approach (Meyer et al. 2007):

1. Standardise the criteria scores to values (or utilities) between 0 and 1.
2. Calculate weighted values for each criterion by multiplying the standardised value with its weight.
3. Calculate the overall value (utility) for each alternative by summing the weighted values (utilities) of each criterion.
4. Rank alternatives according to their aggregate value (utility).

The main advantage of the MAUT approach is the possibility to merge all weighted utilities into one mathematical model. As a result, an optimisation of all utilities will be performed while different strategies and preferences of prospective end-users can be considered. Finally, an optimal mitigation strategy can be identified. On the other hand, the estimation of utility functions might need an intensive economic analysis and survey. However, utility cannot be measured or observed directly. Instead, from the behaviour of individuals or the society, a utility must be derived under the assumption of a perfect economic market (Hanley and Spash 2003).

As a third approach, the monetary assessment of tangible and intangible losses has been examined. In this approach, all losses are considered within a cost-benefit analysis. Therefore, intangible losses, which are usually not expressed in monetary terms, have to be estimated by using socio-economic evaluation methods such as Contingent Valuation or Hedonic Price Method, among others. An advantage of this approach is the possibility to calculate the risk Rf for each damage category separately. Furthermore, cost-benefit ratios can be calculated for several mitigation strategies. However, the monetary assessment of intangible goods, such as human beings and the environment, is often opposed due to ethical constraints. Moreover, intangible losses are not adequately reflected in a cost-benefit analysis related to their importance. Hence, weighting factors for intangible goods must be implemented (RPA 2004).

4 References

- Alvarado-Aguilar D. and Jimenez J.A. (2008): Flood Hazard Mapping for Coastal Storms in the Delta Ebro. Proc. Of FLOODrisk 2008 Conference, Oxford, UK (available in CD Rom).
- Anderson, E. S., Thompson, J.A. and Austin, R.E. (2005): LiDAR density and linear interpolator effects on elevation estimates, *International Journal of Remote Sensing*, 26, 3889-3900.
- Basco, D.R., and Shin, C.S. (1999): A One-Dimensional Numerical Model for Storm-Breaching of Barrier Islands. *Journal of Coastal Research*, 15, 241-260.
- Bedford, T.J. and Cooke, R.M. (2001): *Probabilistic Risk Analysis: Foundations and Methods* New York & Cambridge: Cambridge University Press.
- Birkmann, J. (2006): Measuring vulnerability to promote disaster-resilient societies: conceptual frameworks and definitions. In Birkmann J (ed), *Measuring Vulnerability to Natural Hazards: Towards Disaster Resilient Societies*. United Nations University Press, Tokyo, Japan, pp. 9-54.
- Birkmann, J. and N. Fernando, (2008): Measuring revealed and emergent vulnerabilities of coastal communities to tsunami in Sri Lanka. *Disasters*, 32(1), 82-104.

- Birkmann J., O.D. Cardona, M.L. Carreño, A.H. Barbat, M. Pelling, S. Schneiderbauer, S. Kienberger, M. Keiler, P. Zeil, T. Welle, (2011): Framing vulnerability, risk and societal responses: the MOVE framework, *Global Environmental Change* (in press).
- Blaikie, P., T. Cannon, I. Davis, and B. Wisner, (1994): *At Risk: natural hazards, people's vulnerability and disasters*. Routledge. 1st edition.
- Burcharth, H.F. and Hughes, S.A. (2003): *Fundamentals of Design (Part VI)*. In: *Coastal Engineering Manual*, US Army Corps of Engineers.
- Callaghan, D.P., Nielsen, P., Short, A. and Ranasinghe, R. (2008): Statistical simulation of wave climate and extreme beach erosion. *Coastal Engineering*, 55, 375-390.
- Canizares, R. and Irish, J.L. (2008): Simulation of storm-induced barrier island morphodynamics and flooding. *Coastal Engineering*.
- Cardona, O.D., (2010): *Disaster Risk and Vulnerability: Notions and Measurement of Human and Environmental Insecurity*. In *Coping with Global Environmental Change, Disasters and Security - Threats, Challenges, Vulnerabilities and Risks*, Editors: H.G. Brauch, U. Oswald Spring, C. Mesjasz, J. Grin, P. Kameri-Mbote, B. Chourou, P. Dunay, J. Birkmann: Hexagon Series on Human and Environmental Security and Peace, vol. 5. Springer Verlag, Heidelberg, Berlin and New York.
- Cardona, O.D., (2004): *The Need for Rethinking the Concepts of Vulnerability and Risk from a Holistic Perspective: A Necessary Review and Criticism for Effective Risk Management*, In: *Mapping Vulnerability: Disasters, Development and People*, [Greg Bankoff, Georg Frerks, Dorothea Hilhorst, (eds.)]. London: Earthscan Publishers, 37-51.
- Cardona, O.D., A. Lavell, M. Hermelin, J.C. Bertoni, and T. Gibbs: (2009): *Understanding and Managing Risk Associated with Natural Hazards: An Integrated Scientific Approach in Latin America and the Caribbean*. International Council for Science Regional Office for Latin America and Caribbean.
- Cheung, K.F., Phadke, A.C., Wei, Y., Rojas, A.R., Douyere, Y.J.-M., Martino, C.D., Houston, S.H., Liu, P.L-F, Lynett, P.J., Dodd, N., Liao, D.S. and Nakazaki, E. (2003): Modeling of storm-induced coastal flooding for emergency management. *Ocean Engineering*, 30, 1353-1386.
- Dassanayake, D.R., Burzel A., Kortenhaus A., and Oumeraci H., (2010): *Framework and Methods for the Evaluation of Intangible Losses and their Integration in Coastal Flood Risk Analysis*. *Xtrem-RisK Progress Report*. Leichtweiß-Institute for Hydraulic Engineering and Water Resources, Technische Universität Braunschweig.
- DEFRA (2001): *National Appraisal of Assets at Risk from Flooding and Coastal Erosion, including the potential impact of climate change*. Final Report. Flood Management Division. Department for Environment, Food and Rural Affairs, London, UK.
- DEFRA (2006): *Flood Risk to the People*. FD2321/TR2 Guidance Document. Department for Environment, Food and Rural Affairs, London, UK.
- DELFT HYDRAULICS (1983): *Wave Runup and Overtopping at Dunes During Extreme Storm Surge*. Report M1819, Part II. Delft.
- DIRECTIVE 2007/60/EC OF THE EUROPEAN PARLIAMENT AND OF THE COUNCIL on the assessment and management of flood risks, 23/10/2007, Official Journal of the European Union, L 288/27 - L288/34
- Divoky, D. and McDougal, W.G. (2006): Response-based coastal flood analysis. Proc. 30th ICCE, ASCE, 5291-5301.
- Donnelly, C. (2008): *Coastal overwash: processes and modelling*. Ph D Thesis, University of Lund.
- Downton, M. W., Miller, J. Z. B., and Pielke, R. A., Jr. (2005): Reanalysis of U.S. National Weather Service flood loss database. *Nat. Hazards Rev.*, 6 (1), 13-22.

- EXCIMAP (2007a): Handbook on good practices for flood mapping in Europe. 57 pp.
- EXCIMAP (2007b): Atlas of Flood Maps. 197 pp.
- EUROTOP. (2007): Wave Overtopping of Sea Defences and Related Structures: Assessment Manual. Environment Agency (EA), Expertise Network Waterkeren (ENW), Kuratorium für Forschung im Küsteningenieurwesen (KFKI), www.overtopping-manual.com.
- FEMA. (2003): Guidelines and specifications for Flood Hazard Mapping Partners. Appendix D: Guidance for Coastal Flooding Analyses and Mapping.
- FEMA (2005): Wave runup and overtopping. FEMA Coastal Flood Hazard Analysis and Mapping Guidelines Focused Study Report, 51 pp.
- FEMA. (2005): Full data riverine BCA module. *Mitigation benefit-cost analysis toolkit*, FEMA, Washington, D.C.
- Gaillard, J.C., (2010): Vulnerability, Capacity, and Resilience: Perspectives for climate and development policy, *Journal of International Development*. 22, 218-232
- Garrity, N.J., Battalio, R., Hawkes, P.J. and Roupe, D. (2006): Evaluation of the event and response approaches to estimate the 100-year coastal flood for Pacific coast sheltered waters. *Proc. 30th ICCE, ASCE*, 1651-1663.
- Gasper, D., (2010): The Idea of Human Security, in *Climate Change, Ethics and Human Security*, K. O'Brien, A. L. St. Clair, B. Kristoffersen (eds.), Cambridge: Cambridge Univ. Press, 23-46.
- GIOC (1998): Atlas de inundación del litoral peninsular. Dirección General de Costas, Ministerio de Medio Ambiente.
- Green, C.H., and Penning-Rowsell E.C. (1989): Flooding and the Quantification of 'Intangibles'. *IWEM: Annual Symposium Paper No. 8*. pp 27-30.
- Guedes-Soares, C., Weisse, R., Carretero, J.C. and Alvarez, E. (2002): A 40 years hindcast of wind, sea level, and waves in European waters. 21st Int. Conf. OMAE, Oslo, 1-7.
- Guenther, G.C., Cunningham, A.G., Larocque, P.E. and Reid, D.J. (2000): Meeting the accuracy challenge in airborne lidar bathymetry. *Proceedings of EARSeL Symposium, Workshop Lidar, Dresden*.
- Hanley, N., and Spash C.L. (2003): *Cost-Benefit analysis and the environment*. Edward Elgar Publishing Ltd., Cheltenham.
- Hewitt, K. and I. Burton, (1971): *The Hazardousness of a Place: A Regional Ecology of Damaging Events*. Toronto, University of Toronto.
- HR WALLINGFORD. (2003): Guide to Best Practice in Coastal Flood Forecasting. R&D Technical Report FD2206/TR2, DEFRA
- IHO. (1998): IHO Standard for Hydrographic Surveys, IHB Sp Pub 44, 4th Ed, International Hydrographic Bureau, Monaco, 23pp.
- IPCC (2007a): *Climate Change 2007: Synthesis Report. Contribution of Working Groups I, II and III to the Fourth Assessment Report of the Intergovernmental Panel on Climate Change* [Core Writing Team, Pachauri, R.K and Reisinger, A.(eds.)]. IPCC, Geneva, Switzerland, 104 pp.
- IPCC (2007b): Appendix I: Glossary in *Climate Change 2007: Impacts, Adaptation and Vulnerability. Contribution of Working Group II to the Fourth Assessment Report of the Intergovernmental Panel on Climate Change* (M.L. Parry et al., Eds.). Print version: Cambridge University Press, Cambridge, U.K., and New York, N.Y., U.S.A.
- ISO 31000 (2009): *Risk management – Principles and guidelines*, International Organization for Standardization.

- Kelman, I. (2002): Physical flood vulnerability of residential properties in coastal, eastern England. Ph.D. dissertation, Univ. of Cambridge, Cambridge, U.K.
- Komar, P.D., McDougal, W.M., Marra, J.J. and Ruggiero, P. (1999) :. The Rational Analysis of Setback Distances: Applications to the Oregon Coast. *Shore & Beach* 67, 41-49.
- Komar, P.D., McDougal, W.M., MARRA, J.J. and Ruggiero, P. (2001): The rational analysis of setback distances: Applications to the Oregon Coast. *Journal of Coastal Research* 17, 407-419.
- Kraus, N. C. and Wamsley, T. V. (2003): Coastal barrier breaching, Part 1: Overview of breaching processes, ERDC/CHL CHETN IV-56, US Army Engineer Research and Development Center, Vicksburg.
- Larson M. and Kraus N.C. (1989): SBEACH: Numerical Model for Simulating Storm- Induced Beach Change, CERC-89-9, US Army Corps of Engineers, Vicksburg.
- Larson, M., Erikson, L. and Hanson, H. (2004): An analytical model to predict dune erosion due to wave impact. *Coastal Engineering* 51, 675- 696.
- Manojlovic N., and Pasche E. (2010): Theory and Technology to Improve Stakeholder Participation in the Development of Flood Resilient Cities, *Proc. Int. 21st IAPS Conference on Vulnerability, Risk and Complexity: Impacts of Global Change on Human Habitats*, Leipzig, Germany.
- MEA, (2005): *Ecosystems and Human Well-being, A framework for assessment*. Millenium Ecosystem Assessment Series, Island Press, Washington D.C.
- Meyer, V., Haase D., and Scheuer S. (2007): GIS-based Multicriteria Analysis as Decision Support in Flood Risk Management, *FLOODsite Project Report*, HR Wallingford, UK.
- Messner, F., Penning-Rowsell, E., Green, C., Meyer, V., Tunstall, S. and Van Der Veen, A. (Eds) (2007): Evaluating flood damage: guidance and recommendations on principles and methods. *FLOODsite report T09-06-01*.
- Messner, F. and Meyer V. (2005): Flood damage, vulnerability and risk perception - challenges for flood damage research. *UFZ Discussion Papers*. Department of Economics, Leipzig.
- Moller, I., Spencer, T., French, J.R., Leggett, D. and Dixon, M. (1999): Wave transformation over salt marshes: a field and numerical modelling study from North Norfolk, England. *Estuar. Coast. Shelf Sci.*, 49, 411-426.
- Morton, R.A., Leach, M.P., Paine, J.G. and Cardoza, M.A. (1999): Monitoring beach changes using GPS surveying techniques. *Journal of Coastal Research*, 9, 702-720.
- NOAA.(2008): HazardAnalysis. <http://www.csc.noaa.gov/products/nchaz/html/case2.htm>
- O'Brien, K., Sygna, L., Leinchenko, R., Adger, W.N., Barnett, J., Mitchell, T., Schipper, L., Tanner, T., Vogel, C.,Mortreux, C. (2008): Disaster Risk Reduction, Climate Change Adaptation and Human Security, GECHS Report47 2008:3.
- O'Brien, K., O'Keefe P., Meena H., Rose J. and Wilson L. (2008): Climate adaptation from a poverty perspective.*Climate Policy*, 8 (2), 194-201.
- Penning-Rowsell, E., Floyd P., Ramsbottom D., and Surendran S., (2005): Estimating Injury and Loss of Life in Floods: A Deterministic Framework. *Natural Hazards* (36) pp 43-64.
- Pirazzoli, P.A. and Tomasin, A. (2007): Estimation of return periods for extreme sea levels: a simplified empirical correction of the joint probabilities method with examples from the French Atlantic coast and three ports in the southwest of the UK. *Ocean Dynamics*, 57, 91-107.
- Pugh, D.T. (1987): *Tides, Surges, and Mean Sea-level*. Wiley, New York.
- Purvis, M.J., Bates, P.D. and Hayes, C.M. (2008): A probabilistic methodology to estimate future coastal flood risk due to sea level rise. *Coastal Engineering*, doi: 10.1016/j.coastaleng.2008.04.08.

- Reeve, D. (Ed.) (2007): Predicting morphological changes in rivers, estuaries and coasts. FLOODsite report T05-07-02.
- Renn, O., (2008): Risk Governance – Coping with Uncertainty in a Complex World. London, Earthscan.
- Roelvink, J.A., Reniers, A. Van Dongeren, A., De Vries, J.V.T., Lescinski, J. and Walstra, D.J. (2007): Modeling hurricane impacts on beaches, dunes and barrier islands. Proc. 10th workshop on Waves and Coastal Hazards, North Shore, Oahu
- Roos, W. (2003): Damage to buildings. *Rep. No. DC1-233-9*, TNO Built Environment and Geosciences—Delft Cluster, The Netherlands.
- RPA - Risk and Policy Analysts Ltd, (2004): Evaluating a multi-criteria analysis (MCA) methodology for application to flood management and coastal defence appraisals. *R&D Project Record FD2013/PR1*, DEFRA, UK
- Sallenger, A. (2000): Storm impact scale for barrier islands. *Journal of Coastal Research*, 16, 890-895.
- Sanchez-Arcilla, A., Gonzalez-Marco D., Doorn N. and Kortenhaus A. (2008): Extreme Values for coastal, estuarine and riverine environments. *Journal of Hydraulic Res.*, vol. 46, Extra Issue 2, 183-190.
- Scawthorn C., Blais N., Seligson H., Tate E., Mifflin E., Thomas W., Murphy J., and Jones J. (2006a): HAZUS-MH flood loss estimation methodology. I: Overview and flood hazard characterization. *Nat. Hazards Rev.*, 7(2), 60–71.
- Scawthorn C., Flores P., Blais N., Seligson H., Tate E., Chang S., Mifflin E., Thomas W., Murphy J., Jones C., and Lawrence M. (2006b): HAZUS-MH flood loss estimation methodology. II: Damage and loss assessment. *Nat. Hazards Rev.*, 7(2), 72–81.
- Schneider, P. J., and Schauer, B. A. (2006): HAZUS—Its development and its future. *Nat. Hazards Rev.*, 7(2), 40–44.
- Schneider, S.H., S. Semenov, A. Patwardhan, I. Burton, C.H.D. Magadza, M. Oppenheimer, A.B. Pittock, A. Rahman, J.B. Smith, A. Suarez and F. Yamin, (2007): Assessing key vulnerabilities and the risk from climate change. *Climate Change 2007: Impacts, Adaptation and Vulnerability. Contribution of Working Group II to the Fourth Assessment Report of the Intergovernmental Panel on Climate Change*, [M.L. Parry, O.F. Canziani, J.P. Palutikof, P.J. van der Linden and C.E. Hanson, (eds.)], Cambridge University Press, Cambridge, UK, 779-810.
- Sobey, R.J. (2005): Extreme low and high water levels. *Coastal Engineering*, 52, 63-77.
- Schoonees J. S. and Theron A. K. (1995): Evaluation of 10 cross-shore sediment transport/morphological models. *Coastal Engineering*, 25, 1-41.
- Solomon, S., D. Qin, M. Manning, Z. Chen, M. Marquis, K.B. Averyt, M. Tignor and H.L. Miller (Eds) (2007): *Climate Change 2007: The Physical Science Basis. Fourth Assessment Report of the Intergovernmental Panel on Climate Change*. Cambridge University Press, Cambridge.
- Stockdon, H.F., Holman, R.A., Howd, P.A. and SALLENGER, J.A.H. (2006): Empirical parameterization of setup, swash, and runup, *Coastal Engineering*, 53, 573–588.
- SwissRe, (2010): http://media.swissre.com/documents/Nat_Cat_reins_en.pdf
- Tuan, T.Q., Verhagen, H.J., Visser, P. and Stive, M.J.F. (2006): Numerical modelling of wave overwash on low-crested sand barriers. *Proc. 30th ICCE, ASCE*, 2831-2843.
- Tuan, T.Q., Stive, M.J.F., Verhagen, H.J. and Visser, P.J. (2008): Process-based modeling of the overflow-induced growth of erosional channels. *Coastal Engineering*, 55, 468-483.
- UNISDR (2009): Terminology: basic terms of disaster risk reduction, <http://www.unisdr.org/eng/library/lib-terminology-eng%20home.htm>.

- USACE (1985): Business depth damage analysis procedures. *Research Rep. 85-R-5*, USACE, Engineering Institute for Water Resources, Alexandria, Va.
- USGS. (2001): Mapping Coastal Change Hazards. Coastal Change Hazard Scale. <http://coastal.er.usgs.gov/hurricanes/mappingchange/scale.html>
- Vellinga, P., (1986): Beach and dune erosion during storm surges. PhD thesis, Delft Hydraulics Communications No. 372, Delft Hydraulics Laboratory, Delft, The Netherlands.
- WASA group (1998): Changing waves and storms in the Northeast Atlantic? *Bull. Amer. Met. Soc.* 79, 741-760.
- Wise, R.S., Smith, S.J. and Larson, M. (1994): SBEACH: Numerical model for simulating storm-induced beach change, CERC, US Army Corps of Engineers, Vicksburg.
- Wisner, B., P. O'Keefe, and K Westgate, (1977): Global systems and local disasters: the untapped power of peoples' science, *Disasters*, 1(1), 47-57.
- Wisner, B., P. Blaikie, et al., (2004): *At risk: Natural Hazards, People's Vulnerability, and Disasters*, 2nd ed. London, Routledge.
- Woodhead, S. (Ed.) (2007): Evaluation of inundation models. FLOODsite report T08-07-01.

Mathematical modeling of coastal sediment transport and beach evolution with special emphasis on coastal structures

Pham Thanh Nam¹, Magnus Larson², and Hans Hanson³

Abstract

A mathematical model of beach topography evolution was developed. The model includes five sub-models: random wave model, surface roller model, wave-induced current model, sediment transport model, and morphological model. The model was validated with unique high-quality data sets obtained from experiments on the morphological impact of a detached breakwater and a T-head groin in the basin of the Large-scale Sediment Transport Facility (LSTF) of the Coastal and Hydraulics Laboratory in Vicksburg, United States. The computations showed that the model could reproduce the wave conditions, wave-induced currents, and morphological evolution in the vicinity of the structures well.

Keywords: waves, current, beach evolution, coastal structures, mathematical modelling

1 Introduction

The nearshore zone is a highly dynamic area and the sediment is in constant motion due to forces such as wind, tide, waves, and currents. Gradients in the transport rate cause deposition or erosion of sediment, affecting the local topography. Such gradients in the nearshore transport may occur for natural reasons, for example, when there are changes in the wave and/or wind conditions. Currents induced by waves and wind may change, affecting the sediment transport rates and the resulting evolution of the local beach topography. However, gradients in the transport rate can also be induced by man-made structures and activities, for example, groins, detached breakwaters, sea walls, dredging, and beach nourishment. At many locations around the world, human activities, such as protection of the shoreline against erosion, construction of harbors, and implementation of navigation channels, have markedly changed the beach topography. Thus, the study of beach evolution is needed in order to gain knowledge for application in coastal engineering projects.

During the latest decades, numerical models of beach evolution have been useful tools in engineering projects. The first advantage of numerical models is that they are often less expensive than physical models. With numerical models, one can easily simulate the beach topography evolution under various scenarios of wave and current conditions that are difficult to carry out in the laboratory because of the high costs required. Furthermore, advanced and robust algorithms, as well as the capabilities of computers, are being developed and enhanced very quickly, enabling the improvement of numerical models for efficiently predicting the beach topography evolution.

A number of numerical models have been developed though the years for simulating beach topography evolution. These models can be classified into six groups as: (i) conceptual models, (ii) shoreline evolution models, (iii) profile evolution models, (iv) 2D horizontal morphological evolutions models, (v) fully 3D morphological models, and (vi) quasi-3D morphological models. The conceptual models (e.g., Gravens, 1996; Kana *et al.*, 1999; Kraus, 2000; Ruessink and Terwindt, 2000), which are often based on empirical formulations obtained from experiences and observations, are effective for qualitative assessment of beach evolution. Shoreline evolution models (e.g., Hanson and Kraus, 1989; Steetzel *et al.*, 2000) describe changes in the shoreline evolution due to gradients in the longshore transport. These models typically simulate shoreline evolution over decades with limited resolution of the response on the intra-annual

¹ Water Resources Engineering, Lund University, Box 118, Lund, Sweden (Thanh_Nam.Pham@tvrl.lth.se)

² Ditto (Magnus.Larson@tvrl.lth.se)

³ Ditto (Hans.Hanson@tvrl.lth.se)

scale. Profile evolution models compute changes in the profile shape due to cross-shore transport only (Larson and Kraus, 1989; Nairn and Southgate, 1993). Such models have traditionally been used to estimate the impact of storms, implying a characteristic scale of the processes on the order of days. The 2D horizontal morphological models employ the depth-averaged wave and current equations, neglecting the vertical variations of waves and current (Latteux, 1980; Watanabe, 1987; Johnson *et al.*, 1994; Nicholson *et al.*, 1997). These models can simulate the morphological evolution over a coastal area with a rather wide range of spatial scales and over time scales from individual storms to seasonal variations.

Fully 3D morphological model includes both the horizontal and vertical variations of waves and currents (*e.g.*, Roelvink and Banning, 1994; Lesser *et al.*, 2004). These models include various hydrodynamic processes, such as wind shear, wave forces, tidal forces, density-driven flows and stratification due to salinity and/or temperature gradients, atmospheric pressure changes, and drying and flooding of intertidal flats. However, the applications of these models for practical problems are still limited because long computational times. Quasi-3D models (*e.g.* Zyserman and Johnson, 2002; Drønen and Deigaard, 2007) enhance the 2D horizontal models by including the vertical current velocity at given locations, determined by the local forcing and the depth-integrated flow. The computational effort required by quasi-3D models is similar to that by 2D horizontal models. Therefore, presently, they are expected to be a feasible tool for simulating the long-term beach topographical evolution in large-scale coastal engineering projects.

The overall objective of this study is to develop a robust and reliable mathematical model to simulate beach morphological evolution under waves and currents with the emphasis on the evolution due to the impact of coastal structures, such as detached breakwaters and T-head groins. First, a theoretical description is given of the different sub-models employed to simulate wave, currents, sediment transport, and morphological change. Then, a short summary is given of the experimental data used for model development and validation. Finally, comparisons are shown between calculated and measured model quantities.

2 Mathematical Model Description

2.1 Random wave transformation model

The random wave transformation model in the present study was originally developed by Mase (2001) based on the Energy Balance Equation with a Diffraction term and an energy dissipation term (EBED). The governing equation, for steady state, is expressed as follows (Nam *et al.*, 2009; Nam and Larson, 2010),

$$\begin{aligned} \frac{\partial(v_x S)}{\partial x} + \frac{\partial(v_y S)}{\partial y} + \frac{\partial(v_\theta S)}{\partial \theta} \\ = \frac{\kappa}{2\omega} \left\{ (CC_g \cos^2 \theta S_y)_y - \frac{1}{2} CC_g \cos^2 \theta S_{yy} \right\} - \varepsilon_b S \end{aligned} \quad (1)$$

where S = angular-frequency spectrum density; (x,y) = horizontal coordinates; θ = angle measured counterclockwise from x axis; v_x , v_y , and v_θ = propagation velocities in their respective coordinate direction; ω = angular frequency; C = phase speed; C_g = group speed; κ = free parameter that can be optimized to change the influence of the diffraction effects; and ε_b = energy dissipation coefficient.

The propagation velocities are given as,

$$\{v_x, v_y, v_\theta\} = \left\{ C_g \cos \theta, C_g \sin \theta, \frac{C_g}{C} \left(\sin \theta \frac{\partial C}{\partial x} - \cos \theta \frac{\partial C}{\partial y} \right) \right\} \quad (2)$$

The first term on right hand of Eq. (1) was introduced by Mase (2001) in order to represent the diffraction effects. The second term represents the energy dissipation due to wave breaking.

The output of the random wave transformation model includes three main wave parameters: significant wave height H_s , significant wave period T_s , and mean wave direction $\bar{\theta}$.

The original EBED model is stable and can be applied to a complex beach topography in the coastal zone containing structures. However, it often overpredicts the wave conditions in the surf zone compared to measurements. The overestimation is mainly due to the algorithm describing wave energy dissipation caused by wave breaking. In the EBED model, the energy dissipation coefficient was determined by the Takayama *et al.* (1991) model. The calculation of this coefficient is rather complex and the coefficient does not easily lend itself to calibration.

In this study, the energy dissipation term was modified based on the Dally *et al.* (1985) model in order to improve the predictive capability of the wave model in the surf zone. The model is referred to as Modified-EBED model hereafter. The modified energy balance equation proposed is as follows (Nam *et al.*, 2009),

$$\begin{aligned} \frac{\partial(v_x S)}{\partial x} + \frac{\partial(v_y S)}{\partial y} + \frac{\partial(v_\theta S)}{\partial \theta} \\ = \frac{\kappa}{2\omega} \left\{ (CC_g \cos^2 \theta S_y)_y - \frac{1}{2} CC_g \cos^2 \theta S_{yy} \right\} - \frac{K}{h} C_g (S - S_{stab}) \end{aligned} \quad (3)$$

where h = still-water depth; K = dimensionless decay coefficient; and S_{stab} = stable wave spectrum density, which is determined based upon the stable wave height $H_{stab} (= \Gamma h)$, with Γ being a dimensionless empirical coefficient.

Assuming that the spectrum density S and the stable spectrum density S_{stab} are functions of H_s^2 and H_{stab}^2 , respectively, Eq. (3) can be rewritten as:

$$\begin{aligned} \frac{\partial(v_x S)}{\partial x} + \frac{\partial(v_y S)}{\partial y} + \frac{\partial(v_\theta S)}{\partial \theta} \\ = \frac{\kappa}{2\omega} \left\{ (CC_g \cos^2 \theta S_y)_y - \frac{1}{2} CC_g \cos^2 \theta S_{yy} \right\} - \frac{K}{h} C_g S \left\{ 1 - \left(\frac{\Gamma h}{H_s} \right)^2 \right\} \end{aligned} \quad (4)$$

Several previous studies have dealt with the empirical coefficients K and Γ . The values of these coefficients can be given by constants, e.g., $\Gamma = 0.4$, and $K = 0.15$ (Dally *et al.*, 1985), or empirical expressions containing the bottom slope (see Goda, 2006). In the Modified-EBED model, a good description was obtained of the wave conditions in the surf zone for the LSTF data by modifying the expressions for the coefficients proposed by Goda (2006),

$$\begin{cases} \Gamma = 0.45, K = \frac{3}{8}(0.3 - 19.2m) & : m < 0 \\ \Gamma = 0.45 + 1.5m, K = \frac{3}{8}(0.3 - 0.5m) & : 0 \leq m \leq 0.6 \end{cases} \quad (5)$$

where m = bottom slope.

The wave radiation-driven stresses were determined by the output from the wave transformation model as,

$$S_{xx} = \frac{E}{2} \left[2n(1 + \cos^2 \bar{\theta}) - 1 \right] \quad (6)$$

$$S_{yy} = \frac{E}{2} \left[2n(1 + \sin^2 \bar{\theta}) - 1 \right] \quad (7)$$

$$S_{yy} = \frac{E}{2} \left[2n \left(1 + \sin^2 \bar{\theta} \right) - 1 \right] \quad (8)$$

where $E = \rho_w g H_{rms}^2 / 8$ = wave energy per unit area, with ρ_w = density of water, g = acceleration due to gravity; and $n = C_g / C$ = the wave index.

2.2 Surface roller model

The wave energy balance equation for the surface roller in two dimensions is expressed as (Dally and Brown, 1995; Larson and Kraus, 2002),

$$\frac{\partial(MC_r)}{\partial t} + \frac{\partial}{\partial x} \left(\frac{1}{2} MC_r^2 \cos^2 \bar{\theta} \right) + \frac{\partial}{\partial y} \left(\frac{1}{2} MC_r^2 \sin^2 \bar{\theta} \right) = g \beta_D M - P_D \quad (9)$$

where P_D = wave energy dissipation; M = wave-period-averaged mass flux; C_r = roller speed; and β_D = roller dissipation coefficient.

The wave energy dissipation is determined as (Nam *et al.*, 2009),

$$P_D = \frac{KC_g \rho_w g}{8h} \left[H_{rms}^2 - (\Gamma h)^2 \right] \quad (10)$$

where H_{rms} = root-mean-square wave height, which can be derived from the output of the random wave transformation model.

The stresses due to the rollers are determined as follows:

$$R_{xx} = MC_r \cos^2 \bar{\theta} \quad (11)$$

$$R_{yy} = MC_r \sin^2 \bar{\theta} \quad (12)$$

$$R_{xy} = R_{yx} = MC_r \sin 2\bar{\theta} \quad (13)$$

2.3 Nearshore current model

The governing equations for the nearshore currents are written as (Militello *et al.*, 2004; Nam *et al.*, 2009; Nam and Larson, 2010),

$$\frac{\partial(h+\eta)}{\partial t} + \frac{\partial q_x}{\partial x} + \frac{\partial q_y}{\partial y} = 0 \quad (14)$$

$$\frac{\partial q_x}{\partial t} + \frac{\partial u q_x}{\partial x} + \frac{\partial v q_x}{\partial y} + g(h+\eta) \frac{\partial \eta}{\partial x} = \frac{\partial}{\partial x} D_x \frac{\partial q_x}{\partial x} + \frac{\partial}{\partial y} D_y \frac{\partial q_x}{\partial y} + f q_y - \tau_{bx} + \tau_{sx} \quad (15)$$

$$\frac{\partial q_y}{\partial t} + \frac{\partial u q_y}{\partial x} + \frac{\partial v q_y}{\partial y} + g(h+\eta) \frac{\partial \eta}{\partial y} = \frac{\partial}{\partial x} D_x \frac{\partial q_y}{\partial x} + \frac{\partial}{\partial y} D_y \frac{\partial q_y}{\partial y} - f q_x - \tau_{by} + \tau_{sy} \quad (16)$$

where η = water elevation; t = time; q_x and q_y = flow per unit width parallel to the x and y axes, respectively; u and v = depth-averaged velocity components in the x and y directions,

respectively; f = Coriolis parameter; D_x and D_y = eddy viscosity coefficients; τ_{bx} and τ_{by} = the bottom stresses; and τ_{Sx} , τ_{Sy} = wave stresses (the latter variables are all in the x - and y -directions, respectively).

Outside the surf zone, the depth-averaged horizontal eddy viscosity coefficient can be calculated as a function of the total water depth, current speed, and bottom roughness according to Falconer (1980),

$$D_0 = 1.154g(h+\eta)\frac{\sqrt{u^2+v^2}}{C_z^2} \quad (17)$$

where C_z = Chezy roughness coefficient.

In the surf zone, the eddy viscosity was taken to be a function of the wave properties following Kraus and Larson (1991) as,

$$D_1 = \Lambda U_w H_{rms} \quad (18)$$

where Λ = empirical coefficient; and $U_w = \pi H_{rms} / (T_s \sinh(kd))$ = wave orbital velocity at the bottom, in which $d = (h + \eta)$ = total depth, and k = wave number.

In the transition zone, the eddy viscosity is calculated as,

$$D_2 = (1 - \alpha)D_0 + \alpha D_1 \quad (19)$$

where $\alpha = (H_{rms} / d)^3$ = weighting parameter (see Militello *et al.*, 2004).

The bottom stresses under combined current and waves are determined following (Nishimura, 1988),

$$\tau_{bx} = C_b \left[\left(U_{wc} + \frac{\omega_b^2}{U_{wc}} \cos^2 \bar{\theta} \right) u + \left(\frac{\omega_b^2}{U_{wc}} \cos \bar{\theta} \sin \bar{\theta} \right) v \right] \quad (20)$$

$$\tau_{by} = C_b \left[\left(U_{wc} + \frac{\omega_b^2}{U_{wc}} \sin^2 \bar{\theta} \right) v + \left(\frac{\omega_b^2}{U_{wc}} \cos \bar{\theta} \sin \bar{\theta} \right) u \right] \quad (21)$$

in which C_b = bottom friction coefficient,

$$U_{wc} = \frac{1}{2} \left\{ \sqrt{u^2 + v^2 + \omega_b^2 + 2(u \cos \bar{\theta} + v \sin \bar{\theta}) \omega_b} + \sqrt{u^2 + v^2 + \omega_b^2 - 2(u \cos \bar{\theta} + v \sin \bar{\theta}) \omega_b} \right\} \quad (22)$$

$$\omega_b = \frac{\sigma H_{rms}}{\pi \sinh(kd)} \quad (23)$$

where σ = peak wave frequency.

The wave stresses are derived from the wave transformation model and the surface roller model. They are expressed by the following formulas:

$$\tau_{Sx} = -\frac{1}{\rho_w} \left[\frac{\partial}{\partial x} (S_{xx} + R_{xx}) + \frac{\partial}{\partial y} (S_{xy} + R_{xy}) \right] \quad (24)$$

$$\tau_{Sy} = -\frac{1}{\rho_w} \left[\frac{\partial}{\partial x} (S_{xy} + R_{xy}) + \frac{\partial}{\partial y} (S_{yy} + R_{yy}) \right] \quad (25)$$

In the present study, the Coriolis force due to rotation of the earth is neglected. Thus, the value of Coriolis parameter f is set to 0.

2.4 Sediment transport model

2.4.1 Swash zone transport

The net transport rates in the cross-shore and longshore directions can be calculated based on the study of Larson and Wamsley (2007) as (see also Larson *et al.*, 2011),

$$q_{bc,net} = K_c \frac{\tan \phi_m}{\tan^2 \phi_m - (dh/dx)^2} \frac{u_0^3}{g} \left(\frac{dh}{dx} - \tan \beta_e \right) \frac{t_0}{T} \quad (26)$$

$$q_{bl,net} = K_l \frac{\tan \phi_m}{\tan^2 \phi_m - (dh/dx)^2} \frac{u_0^2 v_0}{g} \frac{t_0}{T} \quad (27)$$

where $q_{bc,net}$, $q_{bl,net}$ = net transport in the cross-shore and longshore directions, respectively; K_c and K_l = empirical coefficients, ϕ_m = friction angle for a moving grain (≈ 30 deg.); β_e = foreshore equilibrium slope; u_0, v_0 and t_0 = scaling velocities and time, respectively; and T = swash duration (assumed that T is equal to the incident wave period).

Based on the ballistics theory, and assuming that the friction on the foreshore is zero, Larson and Wamsley (2007) derived the hydrodynamics in the swash zone as,

$$x_0 = x_s - \frac{1}{2} g t^2 \sin \beta + u_s t \quad (28)$$

$$u_0 = u_s - g t \sin \beta \quad (29)$$

$$y_0 = y_s + v_s t \quad (30)$$

$$v_0 = v_s \quad (31)$$

where x_0 = position of the wave front that travels along foreshore; y_0 = longshore direction of the front; u_s, v_s = wave front speeds at the start of the uprush; x_s, y_s = location at the start of the swash zone, $x_s = 0$ at the still-water shoreline; β = foreshore slope set to a constant.

The maximum uprush is attained at the time when the velocity is zero, as given by $t_{max} = u_s / (g \sin \beta)$ and the corresponding location is $x_{max} = u_s^2 / (2g \sin \beta)$. Based on the geometry, one can derive the runup height $R = x_{max} / \sin \beta = u_s^2 / (2g)$. The value of u_s might be difficult to determine, so the runup height can be used in calculations instead of this velocity. The runup height can be obtained by using various empirical formulas (e.g., Hunt, 1959; Mase, 1988; Mayer and Kriebel, 1994). In this study, the Hunt (1959) formula was employed for calculating the runup height.

The duration (t_0) at any location on the foreshore can be related to the swash duration and runup height (Larson and Wamsley, 2007) as,

$$\frac{t_0}{T} = \sqrt{1 - \frac{z_0}{R}} \quad (32)$$

where z_0 = vertical distance from the reference level to x_0 .

2.4.2. Nearshore and offshore transport

Camenen and Larson (2005, 2007, and 2008) developed a unified transport formulation for bed load and suspended load under combined waves and currents. It can be used for both sinusoidal and asymmetric waves, and is referred to as Lund-CIRP formula hereafter. To simplify calculations, the waves are assumed to be sinusoidal, having no asymmetry. Therefore, the contribution to the transporting velocity from waves is negligible, implying that only current moves the material. In such case, the bed load can be expressed as (Larson *et al.*, 2011; Nam *et al.*, 2011),

$$\frac{q_{bc}}{\sqrt{(s-1)gd_{50}^3}} = a_c \sqrt{\theta_c} \theta_{cw,m} \exp\left(-b_c \frac{\theta_{cr}}{\theta_{cw}}\right) \quad (33)$$

where q_{bc} = transport obtained in the direction of the current, the transport normal to current is zero; s = relative density between sediment and water ($= \rho_s / \rho_w$), in which ρ_s = density of sediment; d_{50} = median grain size; a_c , and b_c = empirical parameters; θ_{cr} = critical Shields parameter for initiation of motion; $\theta_{cw,m}$ and θ_{cw} = mean and maximum Shields parameters due to wave-current interaction, respectively.

The critical Shields parameter is calculated based on the formula proposed by Soulsby and Whitehouse (1997) as,

$$\theta_{cr} = \frac{0.24}{d_*} + 0.055 [1 - \exp(-0.02 d_*)] \quad (34)$$

where $d_* = \sqrt[3]{g(s-1)/\nu^2} d_{50}$ = dimensionless grain size, with ν = kinematic viscosity of water.

The mean and maximum Shields parameters due to wave-current interaction is calculated by vector addition as,

$$\theta_{cw,m} = \left(\theta_c^2 + \theta_{w,m}^2 + 2\theta_{w,m}\theta_c \cos\varphi\right)^{1/2} \quad (35)$$

$$\theta_{cw} = \left(\theta_c^2 + \theta_w^2 + 2\theta_w\theta_c \cos\varphi\right)^{1/2} \quad (36)$$

where θ_c and θ_w = Shields parameters due to current and wave, respectively; $\theta_{w,m}$ = mean wave Shields parameter, $\theta_{w,m} = \theta_w / 2$ for a sinusoidal wave profile; and φ = angle between the wave and the current direction.

The Shields parameters for current and wave is determined as follows,

$$\theta_c = \frac{\tau_c}{\rho_w(s-1)d_{50}} \quad (37)$$

$$\theta_w = \frac{\tau_w}{\rho_w(s-1)d_{50}} \quad (38)$$

where τ_c and τ_w = shear stresses due to current and wave, respectively. These stresses are given by,

$$\tau_c = \frac{1}{2} \rho_w f_c U_c^2 \quad (39)$$

$$\tau_w = \frac{1}{2} \rho_w f_w U_w^2 \quad (40)$$

in which f_c and f_w = friction factors due to current and wave, respectively; $U_c = \sqrt{u^2 + v^2}$ = magnitude of current vector.

Based on the roughness calculations, the friction factors due to current and waves are calculated after Soulsby (1997), and Swart (1974), respectively as,

$$f_c = 2 \left(\frac{0.4}{1 + (k_s / 30d)} \right)^2 \quad (41)$$

$$f_w = \begin{cases} \exp(5.21r^{-0.19} - 6.0) & r > 1.57 \\ 0.3 & r \leq 1.57 \end{cases} \quad (42)$$

where k_s = total roughness; $r = A_w / k_s$ = relative roughness, with $A_w = U_w T_s / 2\pi$ = semi-orbital excursion.

The total roughness is assumed to include three components: grain-related roughness k_{sd} , form-drag roughness k_{sf} , and sediment-related roughness k_{ss} (Soulsby, 1997). The total roughness is calculated by the linear sum of these components as,

$$k_s = k_{sd} + k_{sf} + k_{ss} \quad (43)$$

The grain related roughness is determined based on the median grain size as:

$$k_{sd} = 2.5d_{50} \quad (44)$$

The form-drag roughness can be related to the height Δ_r and wavelength λ_r of the ripples (Soulsby, 1997) as:

$$k_{sf} = 7.5 \frac{\Delta_r^2}{\lambda_r} \quad (45)$$

For current, the wavelength and height of the ripples can be calculated based on the median grain size by the following formulas (Soulsby, 1997):

$$\lambda_r = 1000 d_{50} \quad (46)$$

$$\Delta_r = \frac{\lambda_r}{7} \quad (47)$$

For waves, the ripple height and ripple length can be determined based on the following formulas (Van Rijn, 1993),

$$\left\{ \begin{array}{ll} \left[\begin{array}{l} \Delta_r = 0.22 A_w \\ \lambda_r = 1.25 A_w \end{array} \right. & \Psi \leq 10 \\ \left[\begin{array}{l} \Delta_r = 2.8 \times 10^{-13} (250 - \Psi)^5 A_w \\ \lambda_r = 1.4 \times 10^{-6} (250 - \Psi)^{2.5} A_w \end{array} \right. & 10 < \Psi \leq 250 \\ \left[\begin{array}{l} \Delta_r = 0 \\ \lambda_r = 0 \end{array} \right. & \Psi \geq 250 \end{array} \right. \quad (48)$$

where $\Psi = U_w^2 / ((s-1)d_{50}) =$ particle mobility parameter.

The sediment-related roughness is determined based on the formula proposed by Wilson (1989) as,

$$k_{ss} = 5d_{50}\theta_i \quad (49)$$

where $\theta_i =$ Shields parameter for current or wave ($i=c, w$, respectively, for current and wave).

Eq. (49) is of implicit type and therefore, an iterative method needs to be employed to solve the equation. In this study, the Newton-Raphson method was employed for solving the non-linear equation for sediment-related roughness.

Assuming that the suspended concentration is in equilibrium and current velocity is constant over the water column, Camenen and Larson (2007, 2008) derived the Lund-CIRP formula for suspended load as,

$$q_s = U_c c_R \frac{\varepsilon}{w_s} \left[1 - \exp\left(-\frac{w_s d}{\varepsilon}\right) \right] \quad (50)$$

where $c_R =$ reference concentration at the bottom; $w_s =$ sediment fall velocity; $\varepsilon =$ sediment diffusivity.

The bed reference concentration is obtained from,

$$c_R = A_{cR} \theta_{cw,m} \exp\left(-4.5 \frac{\theta_{cr}}{\theta_{cw}}\right) \quad (51)$$

where the coefficient A_{cR} is written as:

$$A_{cR} = 3.5 \times 10^{-3} \exp(-0.3d_*) \quad (52)$$

The sediment fall velocity is calculated from Soulsby (1997) as:

$$w_s = \frac{v}{d_{50}} \left[\left(10.36^2 + 1.049d_*^3 \right)^{1/2} - 10.36 \right] \quad (53)$$

The sediment diffusivity is related to the energy dissipation as (Camenen and Larson, 2008),

$$\varepsilon = \left(\frac{k_b^3 D_b + k_c^3 D_c + k_w^3 D_w}{\rho} \right)^{1/3} d \quad (54)$$

where $k_b, k_c,$ and $k_w =$ empirical coefficients; $D_b =$ energy dissipation due to wave breaking ($= P_D$); $D_c,$ and $D_w =$ energy dissipations from bottom friction due to current and waves, respectively, expressed as,

$$D_c = \tau_c u_{c*} \quad (55)$$

$$D_w = \tau_w u_{w*} \quad (56)$$

in which u_{c*} , and u_{w*} = shear velocities due to current and waves, respectively.

The empirical coefficient k_b is set to 0.017. The coefficients k_w , and k_c are calculated based on the Schmidt number,

$$k_i = 0.067 \sigma_i \quad (57)$$

where σ_i = Schmidt number; $i=c, w$ denotes current and wave, respectively.

The Schmidt number is determined by the following empirical formulas (Camenen and Larson, 2007),

$$\sigma_i = \begin{cases} A_{i1} + A_{i2} \sin^{2.5} \left(\frac{\pi w_s}{2 u_{i*}} \right) & \frac{w_s}{u_{i*}} \leq 1 \\ 1 + (A_{i1} + A_{i2} - 1) \sin^{2.5} \left(\frac{\pi w_s}{2 u_{i*}} \right) & \frac{w_s}{u_{i*}} > 1 \end{cases} \quad (58)$$

where i = subscript equal to c or w , $A_{c1} = 0.7$, $A_{c2} = 0.36$, $A_{w1} = 0.09$, and $A_{w2} = 1.4$.

Alternatively, the suspended load can be obtained by solving the AD equation. The two-dimensional time- and depth-averaged AD equation is expressed as (Larson *et al.*, 2011; Nam *et al.*, 2011),

$$\frac{\partial(\bar{C}d)}{\partial t} + \frac{\partial(\bar{C}q_x)}{\partial x} + \frac{\partial(\bar{C}q_y)}{\partial y} = \frac{\partial}{\partial x} \left(K_x \frac{\partial \bar{C}q_x}{\partial x} \right) + \frac{\partial}{\partial y} \left(K_y \frac{\partial \bar{C}q_y}{\partial y} \right) + P - D \quad (59)$$

where \bar{C} = depth-averaged sediment concentration; K_x , and K_y = sediment diffusion coefficients in x and y directions, respectively; P = sediment pick-up rate, and D = sediment deposition rate.

The sediment diffusion coefficient can be calculated from Elder (1959) as:

$$K_x = K_y = 5.93 u_{c*} d \quad (60)$$

The sediment pick-up and deposition rates are given by,

$$P = c_R w_s \quad (61)$$

$$D = \frac{\bar{C}}{\beta_d} w_s \quad (62)$$

where β_d = coefficient calculated based on Camenen and Larson (2008) as:

$$\beta_d = \frac{\varepsilon}{w_s d} \left[1 - \exp \left(- \frac{w_s d}{\varepsilon} \right) \right] \quad (63)$$

The concentration \bar{C} is calculated in the AD equation after steady-state condition is attained. The sediment transport rates in the x and y direction can be calculated from,

$$q_{sx} = \bar{C}q_x - K_x d \frac{\partial \bar{C}}{\partial x} \quad (64)$$

$$q_{sy} = \bar{C}q_y - K_y d \frac{\partial \bar{C}}{\partial y} \quad (65)$$

The sediment transport rate is often large near the shoreline due to the swash uprush and backwash processes. The observations from LSTF showed a peak in the sediment transport rate close to shoreline that was larger than the transport rate in the inner surf zone. The sediment transport rates in the swash zone can be well reproduced by the swash zone computation; the calculated transport rates increase in the seaward direction along the foreshore to the still-water shoreline. However, in the inner surf zone, the calculated sediment transport rates obtained by the currently available formulas often tend to decrease from offshore towards the still-water shoreline. Therefore, there is a significant difference between the calculated and measured sediment transport rates near the still-water shoreline, since the interaction between the swash and inner surf zones is not well described in most models.

In this study, the sediment transport rate at the still-water shoreline obtained from the swash zone computation is employed to determine the suspended sediment concentration at the boundary when solving the AD equation. The pick-up and deposition rate, described in the Eqs. (61) and (62), respectively, were also modified as follows,

$$\bar{P} = P \left[1 + \mathcal{G} \frac{\bar{V}}{v_0} \exp\left(-\mu \frac{d}{R}\right) \right] \quad (66)$$

$$\bar{D} = \frac{D}{\left[1 + \mathcal{G} \frac{\bar{V}}{v_0} \exp\left(-\mu \frac{d}{R}\right) \right]} \quad (67)$$

where \mathcal{G} and μ = free non-negative coefficients, \bar{V} = mean velocity across the profile. The velocity \bar{V} is determined as the average longshore current across the surf zone, v_0 is obtained from swash zone computation, and R is calculated by the Hunt (1959) formula.

The total load, which combines the bed load from the Lund-CIRP formula and the suspended load from the AD equation with the above modifications, is referred to as Lund-CIRP-AD hereafter. Calibration showed that $\mathcal{G} = 9.3$ and $\mu = 2.4$ were the most suitable values for all experimental cases studied (Nam *et al.*, 2010; Nam *et al.*, 2011). Although the modifications are somewhat *ad hoc*, the model reproduced the sediment transport rates near the still-water shoreline well.

2.5 Morphological evolution model

The morphological evolution is based on the sediment volume conservation equation,

$$\frac{\partial h}{\partial t} = \frac{1}{1-n_p} \left(\frac{\partial q_{tot,x}}{\partial x} + \frac{\partial q_{tot,y}}{\partial y} \right) \quad (68)$$

where n_p = porosity parameter; and $q_{tot,x}, q_{tot,y}$ = total load in x and y directions, respectively.

In the offshore and surf zone, the total load is the sum of bed load and suspended load, which are calculated based on Eqs. (33) and (59). In the swash zone, it is based on the net transport rates obtained from Eqs. (26) and (27).

Figure 1 presents a flowchart for the calculation of beach topography evolution, including the feedback loops. Based on the input data (offshore wave conditions), the Modified-EBED model is employed to calculate the wave field in the nearshore zone. The mass flux due to the roller is determined through the roller model. Thus, the wave stresses is calculated based on the random wave transformation model and the roller model. After that, the wave-induced current field at steady state is determined from the nearshore current model. The output from the wave and current models is used to compute the Shields parameters that are employed for determining the bed load in the offshore and surf zone. The coupling between the sediment transport in the swash and inner surf zone is included. When solving the advection-diffusion equation for the offshore and surf zone, the suspended sediment concentration at the still-water shoreline (boundary between swash and surf zone) is calculated based on the sediment transport rates obtained by the swash zone computations. The beach morphological change is determined from the volume conservation equation. In order to save time in the computations, the wave, current, and sediment transport fields are only re-calculated every n -th morphological time step ($n=5$ in the present study). The bed level is smoothed at an interval corresponding to 15 times the morphological time step, and the smoothing coefficient is 0.25 (Johnson and Zyserman, 2002).

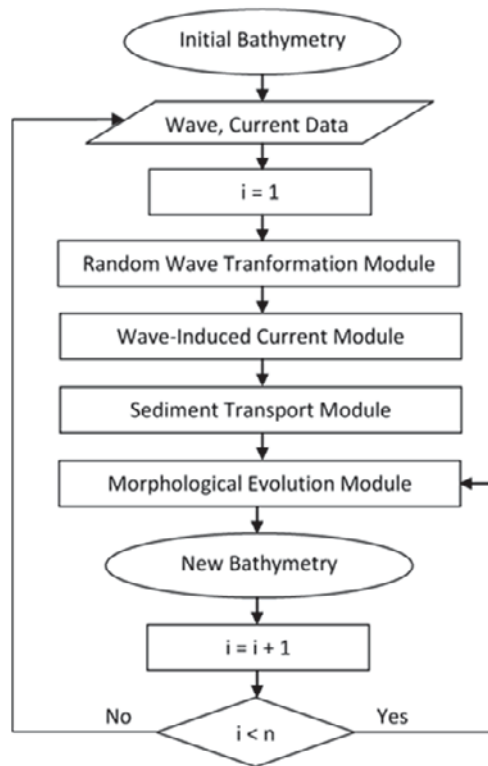


Figure 1: Calculation procedure in the morphological evolution model

2.6 Boundary conditions

The wave energy at the offshore boundary is based on theoretical spectrums such as JONSWAP or TMA. At the lateral boundaries, the wave energy gradient in alongshore direction is set to zero (*Neumann boundary condition*), whereas at the solid boundary (structures, land) the wave energy is set to zero (*Dirichlet boundary condition*).

At the offshore and solid boundaries, the mass flux due to the roller is assumed to be zero (*Dirichlet boundary condition*). The alongshore mass flux gradient is given as zero at the lateral boundaries (*Neumann boundary condition*).

The radiation boundary condition is employed to determine the currents at the offshore boundary (Reid and Bodine, 1968). At the lateral boundaries, the water fluxes were specified based on the measurement data of nearshore currents (*Dirichlet boundary condition*, applied for

this study). Alternatively, the alongshore water level gradient or gradient of cross-shore and longshore currents in the alongshore direction is set to zero at the lateral boundaries (*Neumann boundary condition*). No flow is assumed at solid boundaries.

The gradient of suspended concentration in alongshore direction is assumed to be zero at the offshore and lateral boundaries (*Neumann boundary condition*). At the boundary between the swash zone and inner surf zone, the suspended concentration is calculated based on the swash zone computation (*Dirichlet boundary condition*). The suspended concentration is given as zero at the location where the structures are placed (*Dirichlet boundary condition*), whereas the alongshore bed level gradient is given as zero at the offshore and lateral boundary (*Neumann boundary condition*).

2.7 Numerical implementation

A first-order upwind scheme and Gauss-Seidel method are employed to solve the energy balance equation (for details, see Mase, 2001). The mass flux due to the roller is calculated explicitly based using the FTCS (forward in time, center in space) scheme (Hoffman, 2001). The nearshore current is calculated based on the explicit scheme of Koutitas (1988). The Newton-Raphson method is used to solve the non-linear equation for the sediment-related roughness. The suspended sediment concentration is obtained by solving the AD equation using the Crank-Nicolson scheme (Hoffman, 2001). Finally, the explicit first-order upwind scheme FTBS (forward in time, backward in space) is employed to solve the sediment volume conservation equation (Long *et al.*, 2008).

3 Data Employed

Five series of physical model experiments were undertaken in the basin of the LSTF (Gravens and Wang, 2007; Wang *et al.*, 2002a, b). The main aim of these experiments was to obtain high-quality data sets for validating formulas for sediment transport, as well as to investigate the beach evolution in the vicinity of coastal structures. The first series of experiments, referred to as “Base Case”, consisted of four runs approximately 160 min each that were performed on a natural beach without structures. The second and third series of experiments, referred to as “Test 1” and “Test 2”, respectively, were carried out with a detached breakwater in the basin that was located between profile Y22 and Y26, at four meter distance from the initial still water shoreline (see Figure 2). The currents in Test 1 were generated by waves only, whereas in Test 2 the currents were a combination of wave-induced currents and external currents. Both Test 1 and Test 2 included eight runs approximately 190 min each. The fourth series, referred to as “Test 3”, included six runs 180 min each, performed on the natural beach with a T-head groin. The last series of experiments, referred to as “Test 4”, were conducted in the basin with a detached breakwater, but its length was shorter and its location was closer to the shoreline than those in Test 1 and Test 2.

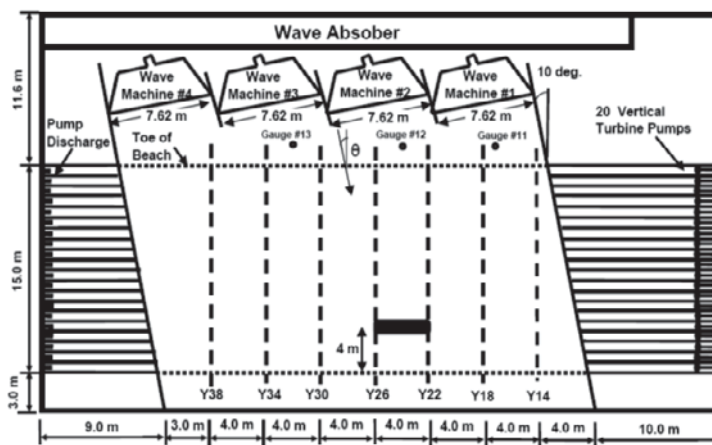


Figure 2: Detached breakwater layout in the LSTF for Test 1 and 2 (Gravens and Wang, 2007)

In all experimental runs, spilling breaking waves were generated by four wave-makers and the water was re-circulated by the pumping systems located up- and downstream of the basin (see Figure 3). Wave gages and acoustic doppler velocimeters were co-located at ten cross-shore positions on the instrument bridge (see Figure 4). The bridge instrument moved in the alongshore direction, thus the wave conditions and currents could be observed at specific cross-shore profiles. Three wave gages were located at three alongshore positions to measure the wave conditions seaward of the toe of the movable beach. A rod and acoustic survey techniques were employed to measure the beach profiles after each experimental run. The beach in the basin consisted of well-sorted sand with a median grain size of 0.15 mm.



Figure 3: Wave-maker layout in LSTF basin



Figure 4: Instrumental bridge and downstream sediment traps

In this paper, the data sets from Base Case, Test 1, and Test 3 were employed to validate the predictive capability of the numerical model. The parameters were used for validation consist of significant wave height, longshore current, cross-shore current, wave setup, longshore sediment flux, and bed level. The detail model validations against LSTF data were presented in Nam *et al.* (2009), Nam and Larson (2010), and Nam *et al.* (2011).

4 Selected Results

4.1 Nearshore wave

The calculation of the nearshore wave field was compared against the measurements obtained from the series of experiments in the LSTF basin. The simulations showed that the wave conditions predicted by the Modified-EBED model significantly improved compared to those obtained by the original EBED model. Nam *et al.* (2009) presented comparisons between measurements and calculations of significant wave height for three selected test cases without

structure: BC1, BC2, and BC4. As can be seen in Figure 5, the calculated significant wave height obtained by EBED model for BC1 overpredicted in the surf zone, whereas the one obtained by Modified-EBED model agreed well with measurements.

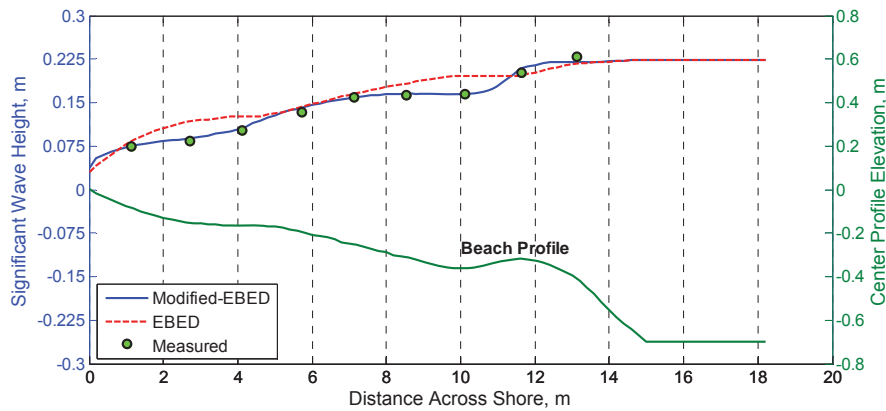


Figure 5: Calculated and measured significant wave height for Case BC1 (Nam *et al.*, 2009)

Nam and Larson (2010) and Nam *et al.* (2011) presented the detailed comparisons between calculated and measured significant wave height in the vicinity of the breakwater and T-head groin. Figure 6 illustrates the comparison of calculated significant wave height and measurement around the detached breakwater for T1C4. The model validation for T3C4 concerning the significant wave height is shown in Figure 7. As for BC1, the calculations of significant wave height obtained by Modified-EBED model were also better than those from the original EBED model. The Modified-EBED model reproduced well the wave conditions in the surf zone as well as in the lee of the detached breakwater and T-head groin.

Quantitative assessment of the EBED and Modified-EBED models using root-mean-square (rms) error clearly showed that the modified model produced better agreement with measurements. For example, the rms error in significant wave height by Modified-EBED model for BC1 was only 3.64 %, whereas it was 12.96 % by the original EBED model. For T1C4, the rms errors in significant wave height were 8.39% and 11.75 % for the Modified-EBED and original EBED models, respectively.

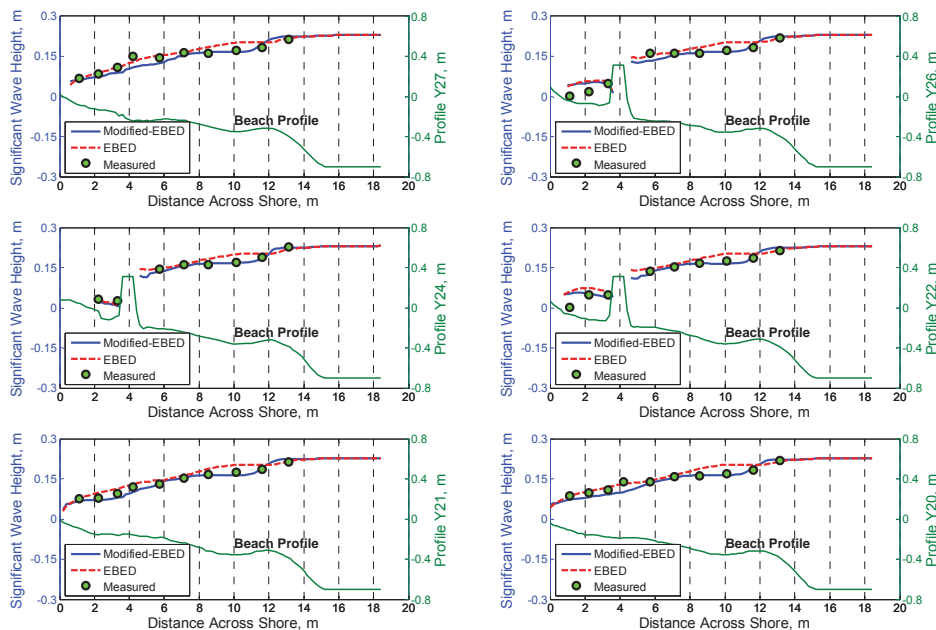


Figure 6: Calculated and measured significant wave height for Case T1C4 (Nam and Larson, 2010)

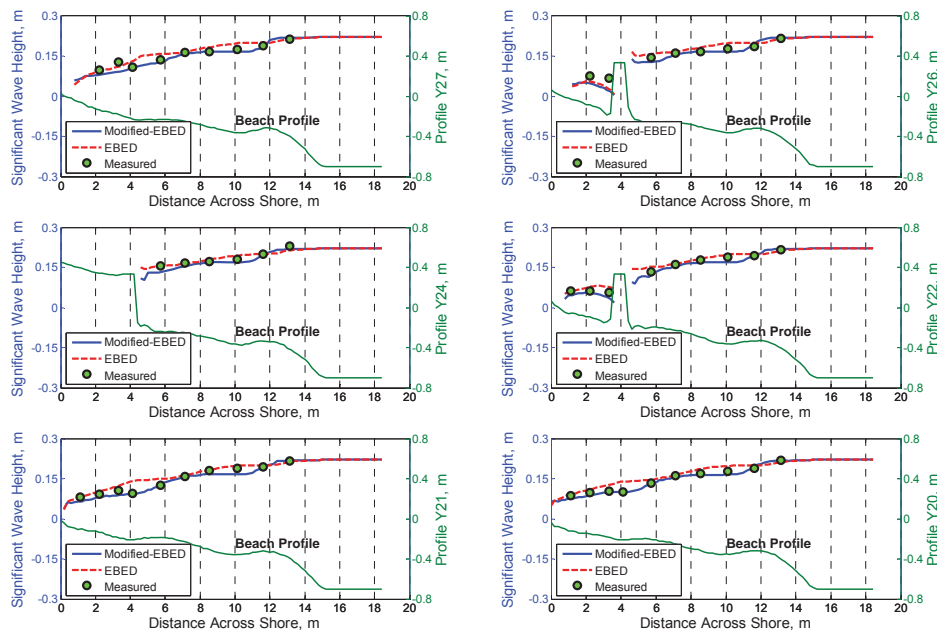


Figure 7: Calculated and measured significant wave height for Case T3C4 (Nam *et al.*, 2011)

The wave field simulation is the crucial first step in modeling beach morphological evolution. The accuracy of the current and sediment transport fields is strongly dependent on the output from the wave model. The diffraction term was included in the wave model so it can describe the diffraction effects in the lee of detached breakwater and T-head groin. The simulations showed that the calculated significant wave height in the lee of these structures agreed well with measurements, implying that the diffraction effect was well modeled in the random wave transformation model. In addition, the energy dissipation due to wave breaking plays a key role in calculating the wave conditions in the surf zone. In this study, the modification of the energy dissipation was based on Dally *et al.* (1985) model in which the decay and stable parameters were determined by Eq. (5), producing a significant improvement in calculating the wave conditions in the surf zone.

4.2 Nearshore currents and wave setup

The calculations of nearshore wave-induced currents and wave setup were compared against the measurements from the LSTF. Nam *et al.* (2009) presented comparisons between calculated longshore current and wave setup and observations for BC1, BC2, and BC4. The current was only generated by waves in test case BC1, whereas an external current was also given in BC2 and BC4. As can be seen in Figure 8, including the roller effects, the peak of the calculated longshore current for BC1 was shifted toward the shoreline and the magnitude of the current also increased in the surf zone, producing better agreement with measurements. The calculated wave setup for BC1 and the corresponding measurements are shown in Figure 9. In general, both calculations of wave setup with and without roller were in good agreement with observations.

Nam and Larson (2010) validated the model against three data sets of LSTF regarding the wave and current fields around a detached breakwater. A detailed comparisons between the calculated longshore current, cross-shore current, and wave setup, and the measurements along 12 cross-shore profile lines were carried out. Figures 10 and 11 show the comparisons of calculated and measured longshore current and cross-shore current for T1C4. In general, the longshore current was in good agreement with the measurements, whereas the cross-shore current somewhat underestimated the measurements. The eddy simulated downstream the breakwater caused a significant difference between calculated and measured cross-shore current at profile Y21 and Y20 (see Figures 11e and 11f). In this study, the undertow was not included in the model, which is probably the main reason for these discrepancies. However, the agreement between the calculations and observations was quite good in the lee of the detached

breakwater. Although the calculated wave setup was overpredicted compared to the measurements, the absolute errors between calculations and measurements were relatively small (for details, see Larson and Nam, 2010).

Nam *et al.* (2011) also validated the wave-induced currents for three test cases with a T-head groin. As for the test cases with detached breakwater, the obtained results on the longshore current agreed well with measurements, and the cross-shore current was also underestimated compared to the measurements.

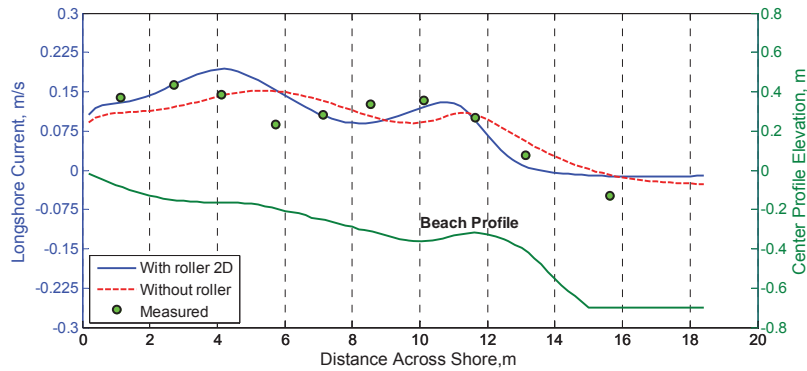


Figure 8: Calculated and measured longshore current for Case BC1 (Nam *et al.* , 2009)

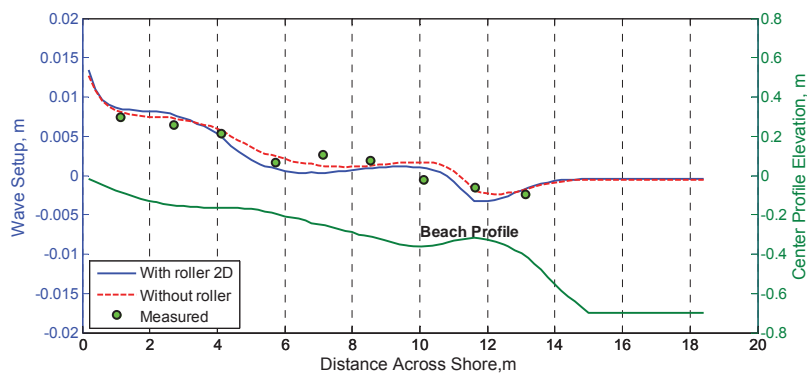


Figure 9: Calculated and measured wave setup for Case BC1 (Nam *et al.*, 2009)

4.3 Sediment Transport

Nam *et al.* 2009 and Larson *et al.* (2011) described the comparison of calculated longshore sediment flux and corresponding measurements. Figures 12 and 13 show the comparison between the calculated and measured longshore sediment flux for BC1 and BC4, respectively. As can be seen, the calculations obtained based on the Lund-CIRP formula agreed fairly well with measurements at offshore and outer surf zone. However, the discrepancies between the calculations and measurements near the shoreline were significant. Using the AD-Lund-CIRP formula with the modifications of the pick-up and deposition rates, the obtained results were in good agreement with measurements from the swash zone to the offshore.

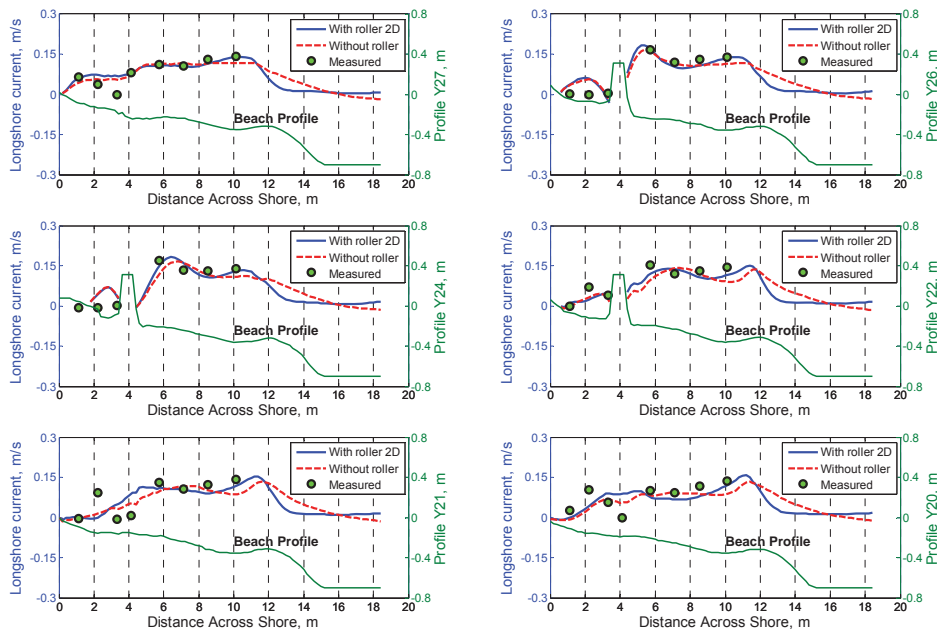


Figure 10: Calculated and measured longshore current for Case T1C4 (Nam and Larson, 2010)

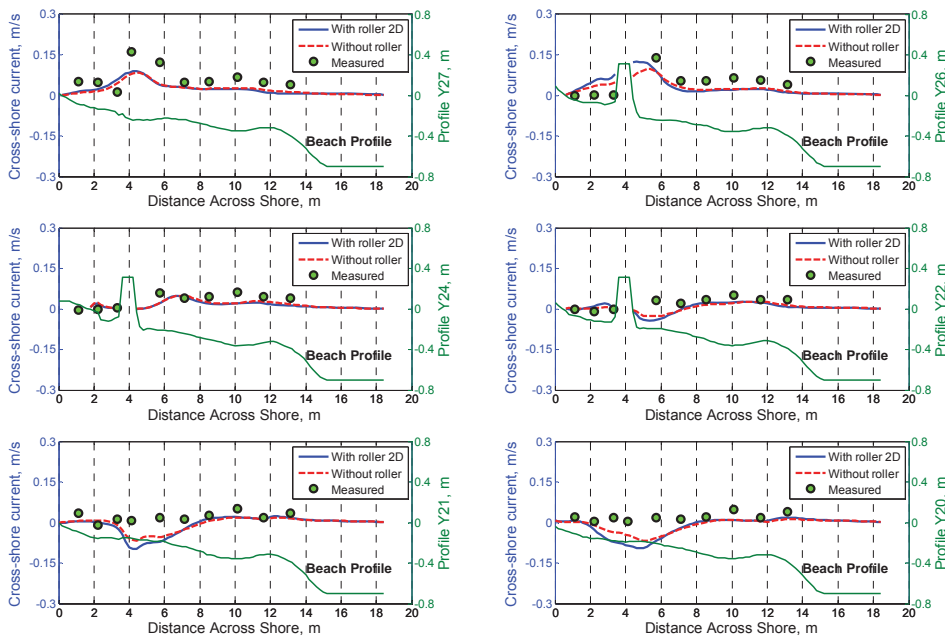


Figure 11: Calculated and measured cross-shore current for Case T1C4 (Nam and Larson, 2010)

Modifications of the pick-up and deposition rates are necessary to accurately simulate the sediment transport rates in both the swash and inner surf zones. Without these modifications, the results from the AD-Lund-CIRP formula decrease too quickly seaward from the still-water shoreline and results similar to the Lund-CIRP formula is obtained in the inner surf zone and offshore zone. Thus, the introduced modifications make the simulated sediment transport rates more reasonable and improve the agreement with the observations from LSTF basin.

The bottom roughness is one of the parameters in calculations of sediment transport that the model is most sensitive to. Using total roughness, including grain-related roughness, form-drag roughness, and sediment-related roughness will produce shear stresses that may be used to calculate the sediment transport rate with some confidence. However, the formula for sediment-

related roughness, given by Wilson (1989), is of implicit type and therefore an iterative method needs to be employed for solving the non-linear equation of sediment-related roughness. In this study, the Newton-Raphson method was used for solving this equation, yielding rapid convergence.

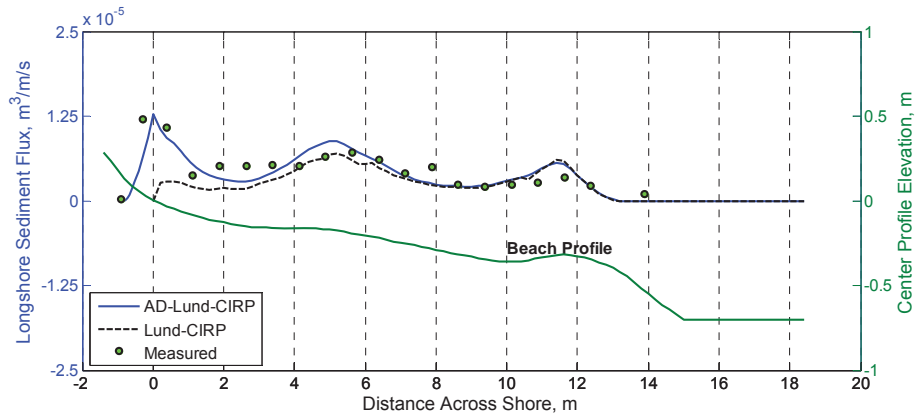


Figure 12: Calculated and measured longshore sediment flux for Case BC1 (Nam *et al.*, 2009)

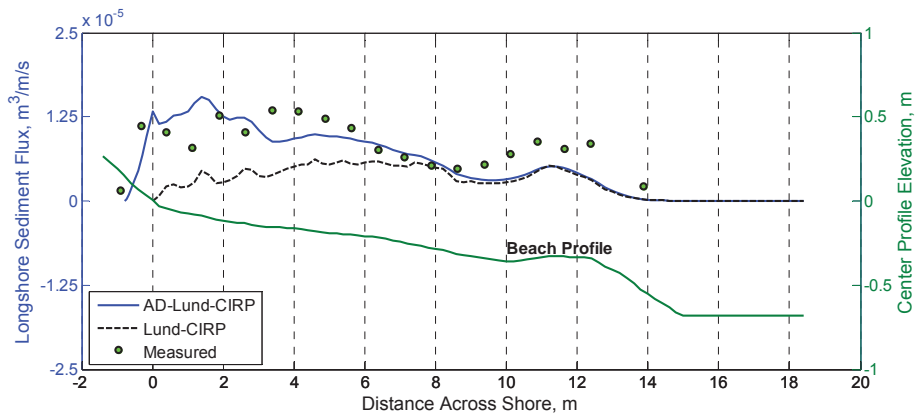


Figure 13: Calculated and measured longshore sediment flux for Case BC4 (Nam *et al.*, 2009)

4.4 Morphological evolution

The model validation of morphological evolution in the vicinity of detached breakwater and T-head groin based on the LSTF data sets are presented in Nam *et al.* (2011). Figure 14 illustrates a comparison between the calculated and measured bed levels after 190 min for T1C4. The solid line represents the calculated bed level, whereas the dotted line shows the measurements. As can be seen, the simulated beach morphological evolution in the vicinity of the detached breakwater agreed rather well with the measurements, especially regarding the salient development in the lee of the breakwater.

Figure 15 shows the comparison between the calculated bed levels after 180 min and the measurements for T3C4. The computations showed that the beach evolution was fairly well predicted; especially the shoreline change was in good agreement with the observations. However, the calculated sand accumulation downdrift the T-head groin exceeded what was observed in the data.

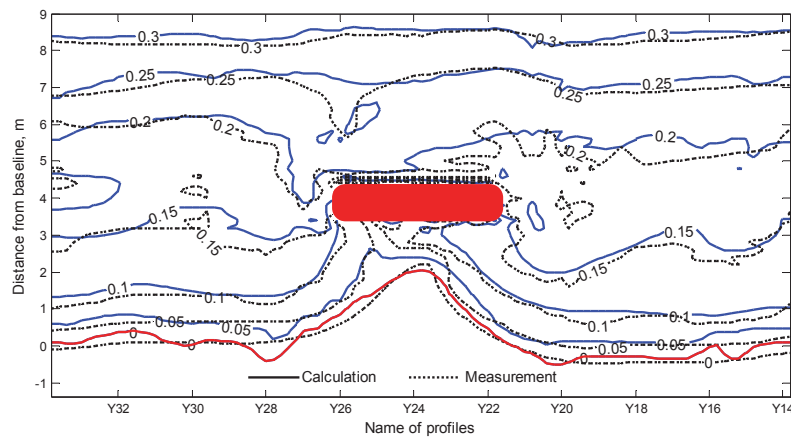


Figure 14: Calculated and measured bed level after 190 min for Case T1C4 (Nam *et al.*, 2011)

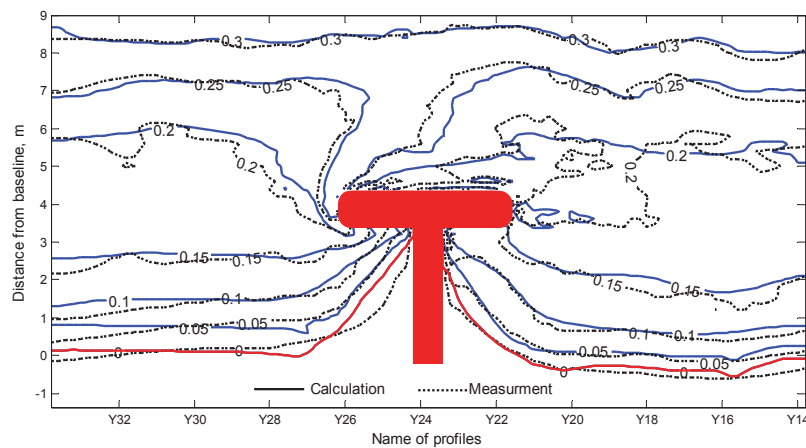


Figure 15: Calculated and measured bed level after 180 min for Case T3C4 (Nam *et al.*, 2011)

The prediction of beach morphological change strongly depends on not only the output of the models for waves, nearshore currents, and sediment transport, but also on the numerical method for solving the sediment volume conservation equation. Eq. (68) is a highly non-linear equation, and it is not easy to obtain a highly accurate solution. For example, many numerical models have employed the Lax-Wendroff scheme for solving this equation. However, this scheme suffers from the generation of nonphysical numerical oscillations (Long *et al.*, 2008). When this scheme is implemented, the bed celerity or bed form phase speed (Johnson and Zyserman, 2002; Long *et al.*, 2008) need to be determined, which may cause large errors in the calculations if the gradient of the bed form is relatively small. Johnson and Zyserman (2002) recommended smoothing and filtering techniques to overcome the dispersion problem associated with the Lax-Wendroff scheme. Recently, several high-order schemes were introduced by Long *et al.* (2008) that can be applied to solve the continuity equation without resorting to smoothing or filtering techniques and that enable high accuracy in the solution. However, when calculating the value of the bed level at one cell, a number of values on the bed levels in nearby cells need to be included. Therefore, ghost cells must be employed at open and solid boundaries, which can cause significant errors if the coastal area is complex and coastal structures are present. In this study, the first-order upwind scheme FTBS (forward in time, backward in space) was employed to solve the sediment conservation equation.

5 Conclusions

The main conclusions of this study can be summarized as follows:

- A unified numerical model of beach morphological evolution due to waves and currents was developed. It includes five sub-models, including nearshore random wave transformation, surface roller, wave-induced current, sediment transport, and morphological change models. Each sub-model has been validated carefully against the high-quality data sets obtained from the LSTF basin. The model can be applied to simulate the beach evolution in the vicinity of coastal structures in a non-tidal environment under wave and current action.
- The predictions of wave conditions in the surf zone were significantly improved after the energy dissipation term due to wave breaking was modified, providing reasonable and accurate wave conditions for the nearshore wave-induced current and sediment transport models.
- The importance of roller effects in calculation of wave-induced current was also investigated. The roller not only causes a shift in the peak of the longshore current towards the shoreline but it also increases the magnitude of the longshore current in the surf zone. By using a 2D surface roller model, energy conservation was expressed more accurately than for the 1D model.
- The predictions of longshore current were in good agreement with observations. However, the calculated cross-shore current was often underestimated compared to the measurements. The undertow current was not included in the model, which is probably the main cause of the discrepancy between calculations and measurements of the cross-shore current. The simulated wave setup somewhat overestimates the measured data, however, the absolute differences between calculations and measurements were relatively small.
- The computation of sediment transport in the swash zone needs to be included in models of beach morphological evolution. The sediment exchange between land and sea directly affects both the sub-aerial and sub-aqueous evolution of the beach. In the swash zone, the frequent uprush and backwash result in high transport rates in both the cross-shore and alongshore directions. Therefore, it is necessary to compute the transport rates in the swash zone, and couple those to the transport in the inner surf zone in order to realistically simulate the beach topography evolution. Prior to this work, studies on the swash zone transport were often undertaken separately from the inner surf zone, or not included at all in the modeling beach morphological evolution.
- Understanding the impacts of coastal structures on beach morphological evolution plays a key role in engineering projects for constructing harbors or preventing the beach erosion. Thus, accurate predictions of hydrodynamics and morphological evolution in the vicinity of coastal structures are necessary and important. In this study, the developed model reproduced the beach evolution in the vicinity of the detached breakwater and the T-head groin rather well compared with the measurements from the LSTF data.

6 Acknowledgements

This work was partly funded by Sida/SAREC in the framework of the Project VS/RDE/03 "The evolution and sustainable management in the coastal areas of Vietnam", partly by Lars Erik Lundberg Scholarship Foundation, partly by the Inlet Modeling System Work Unit of the Coastal Inlets Research Program, U.S. Army Corps of Engineers, and partly by ÅForsk. Dr. Hajime Mase at Kyoto University kindly provided the source code for the EBED model. Dr. Ping Wang at University of South Florida and Mr. Mark Gravens at CHL provided the experimental data from LSTF, which is greatly appreciated. The authors would also like to thank Dr. Nguyen Manh Hung and the late Prof. Pham Van Ninh for their great contributions to the Project VS/RDE/03.

7 References

- Camenen, B., Larson, M., 2005. A general formula for non-cohesive bed load sediment transport. *Estuarine, Coastal and Shelf Science* 63, 249-260.
- Camenen, B., Larson, M., 2007. A unified sediment transport formulation for coastal inlet application. Technical report ERDC/CHL CR-07-1, US Army Engineer Research and Development Center, Vicksburg, MS.
- Camenen, B., Larson, M., 2008. A general formula for noncohesive suspended sediment transport. *Journal of Coastal Research* 24(3), 615-627.
- Dally, W. R., Brown, C. A., 1995. A modeling investigation of the breaking wave roller with application to cross-shore currents. *Journal of Geophysical Research* 100(C12), 24873-24883.
- Dally, W. R., Dean, R. G., Dalrymple, R. A., 1985. Wave height variation across beaches of arbitrary profile. *Journal of Geophysical Research* 90(C6), 11917-11927.
- Drønen, N., Deigaard, R., 2007. Quasi-three-dimensional modelling of the morphology of longshore bars. *Coastal Engineering* 54, 197-215.
- Elder, J.W., 1959. The dispersion of marked fluid in turbulent shear flow. *Journal of Fluid Mechanics* 5, 544-560.
- Falconer, R. A., 1980. Modelling of planform influence on circulation in harbors. *Proceedings 17th International Conference on Coastal Engineering, ASCE, Sydney*, pp. 2726-2744.
- Goda, Y., 2006. Examination of the influence of several factors on longshore current computation with random waves. *Coastal Engineering* 53, 157-170.
- Gravens, M.B., 1996. Approach to modeling inlet and beach evolution. *Proceedings of the 25th International Conference on Coastal Engineering, ASCE, Orlando*, pp. 4477-4490.
- Gravens, M.B., Wang, P., 2007. Data report: Laboratory testing of longshore sand transport by waves and currents; morphology change behind headland structures. Technical Report, ERDC/CHL TR-07-8, Coastal and Hydraulics Laboratory, US Army Engineer Research and Development Center, Vicksburg, MS.
- Hanson, H., Kraus, N. C. 1989. GENESIS: Generalized model for simulating shoreline change, Report 1: Technical Reference. Technical Report CERC-89-19, U.S. Army Engineer Waterways Experiment Station, Coastal Engineering Research Center, Vicksburg, MS.
- Hoffman, J.D., 2001. Numerical methods for engineers and scientists (2nd edition). Marcel Dekker, Inc., USA, 823 pp.
- Hunt, I.A., 1959. Design of seawalls and breakwaters. *Journal of Waterways and Harbors Division* 85, 123-152.
- Johnson, H. K., Brøker, I. and Zyserman, J. A. 1994. Identification of some relevant processes in coastal morphological modeling. *Proceeding of the 24th International Conference on Coastal Engineering, ASCE, Kobe, Japan*, pp. 2871-2885.
- Jonhson, H.K., Zyserman, J.A., 2002. Controlling spatial oscillations in bed level update schemes. *Coastal Engineering* 46, 109-126.
- Kana, T.W., Hayter, E.J., Work, P.A., 1999. Mesoscale sediment transport at southeastern US tidal inlets: conceptual model applicable to mixed energy settings. *Journal of Coastal Research* 15 (2), 303-313.
- Koutitas, C.G., 1988. *Mathematical models in coastal engineering*. Pentech Press, London, England, 156 pp.
- Kraus, N.C., 2000. Reservoir model of ebb-tidal shoal evolution and sand bypassing. *Journal of Waterway, Port, Coastal, and Ocean Engineering* 126 (6), 305-313.

- Kraus, N. C., Larson, M., 1991. NMLONG: Numerical model for simulating the longshore current; Report 1: Model development and tests. Technical Report DRP-91-1, U.S. Army Engineer Waterways Experiment Station, Vicksburg, MS.
- Larson, M., Kraus, N.C., 1989. SBEACH: Numerical Model for Simulating Storm-Induced Beach Change; Report 1 - Empirical Foundation and Model Development. Technical Report CERC-TR-89-9-RPT-1, U.S. Army Engineer Waterways Experiment Station, Coastal Engineering Research Center, Vicksburg, MS.
- Larson, M., Kraus, N.C., 2002. NMLONG: Numerical model for simulating longshore current; Report 2: Wave-current interaction, roller modeling, and validation of model enhancements. Technical Report ERDC/CHL TR-02-22, US Army Engineer Research and Development Center, Vicksburg, MS.
- Larson, M., Wamsley, T.V., 2007. A formula for longshore sediment transport in the swash. Proceedings Coastal Sediments '07, ASCE, New Orleans, pp. 1924-1937.
- Latteux, B., 1980. Harbour design including sedimentological problems using mainly numerical techniques. Proceeding of the 17th International Conference on Coastal Engineering, ASCE, Sydney, pp. 2213-2229.
- Lesser, G.R., Roelvink, J.A, van Kester, J.A.T.M., Stelling, G.S., 2004. Development and validation of a three-dimensional morphological model. Coastal Engineering 51, 883-915.
- Long, W., Kirby, J.T., Shao, Z., 2008. A numerical scheme for morphological bed level calculations. Coastal Engineering 55, 167-180.
- Mase, H., 1988. Spectral characteristics of random wave run-up, Coastal Engineering 12, 175-189.
- Mase, H., 2001. Multi-directional random wave transformation model based on energy balance equation. Coastal Engineering Journal 43(4), 317-337.
- Mayer, R.H., Kribel, D.L., 1994. Wave runup on composite-slope and concave beaches. Proceedings 24th International Conference of Coastal Engineering, ASCE, 2325-2339.
- Militello, A., Reed, C.W., Zundel, A.K., Kraus, N.C., 2004. Two-dimensional depth-averaged circulation model M2D: version 2.0, Report 1, Technical document and User's Guide. Technical Report ERDC/CHL TR-04-2, Coastal and Hydraulics Laboratory, US Army Engineer Research and Development Center, Vicksburg, MS.
- Nairn, R.B., Southgate, H.N., 1993. Deterministic profile modelling of nearshore processes. Part 2. Sediment transport and beach profile development. Coastal Engineering 19(1-2), 57-96.
- Nam, P.T., Larson, M., Hanson, H., Hoan, L.X., 2009. A numerical model of nearshore waves, currents, and sediment transport. Coastal Engineering 56, 1084-1096.
- Nam, P.T., Larson, M., 2010. Model of nearshore waves and wave-induced currents around a detached breakwater. Journal of Waterway, Port, Coastal and Ocean Engineering 136 (3), 156-176.
- Nam, P.T., Larson, M., Hanson, H., Hoan, L.X., 2011. A numerical model of beach morphological evolution due to waves and currents in the vicinity of coastal structures. Coastal Engineering, 58(9), 863-876.
- Nicholson, J., Broker, I., Roelvink, J.A., Price, D., Tanguy, J.M., Moreno, L., 1997. Intercomparison of coastal area morphodynamic models. Coastal Engineering 31, 97-123.
- Nishimura, H., 1988. Computation of nearshore current. In: Horikawa, K. (Ed), Nearshore dynamics and coastal processes. University of Tokyo Press, Tokyo, Japan, pp. 271-291.
- Reid, R.O., Bodine, B.R., 1968. Numerical model for storm surges in Galveston Bay. Journal of Waterways and Harbors Division 94 (WWI), 33-57.

- Roelvink, J.A., Banning, G.K.F.M.v., 1994. Design and development of DELFT3D and application to coastal morphodynamics. In: Verwey, Minns, Babovic, Maksimovic (Eds.), *Proceeding of Hydroinformatics '94 Conference*. Balkema, Rotterdam, pp. 451–455.
- Ruessink, B.G., Terwindt, J.H.J., 2000. The behaviour of nearshore bars on the time scale of years: a conceptual model. *Marine Geology* 163, 289–302.
- Soulsby, D. H., 1997. *Dynamics of marine sands. A manual for practical applications*. Thomas Telford Publications, London, England, 249 pp.
- Soulsby, R.L., Whitehouse, R.J.S.W., 1997. Threshold of sediment motion in coastal environments. *Proceedings of Pacific Coasts and Ports '97 Conference*, Christchurch, Vol. 1, pp. 149-154.
- Steetzel, H.J., de Vroeg, H., van Rijn, L.C., Stam, J.-M., 2000. Long-term modelling of the Holland coast using a multi-layer model. *Proceeding of the 27th International Conference on Coastal Engineering*. ASCE, Sydney, Australia, pp. 2942–2955.
- Swart, D. H., 1974. *Offshore sediment transport and equilibrium beachprofiles*. Delft Hydraulics Laboratory Publications 131, Delft, The Netherlands, 302 pp.
- Takayama, T., Ikeda, N., Hiraishi, T., 1991. Wave transformation calculation considering wave breaking and reflection. *Rept. Port Harbor Res. Inst.* 30 (1), 21–67.
- Van Rijn, L., 1993. *Principles of sediment transport in rivers, estuaries, and coastal seas*. Aqua Publications, Amsterdam, The Netherlands.
- Wang, P., Ebersole, B.A., Smith, E.R., Johnson, B.D., 2002a. Temporal and spatial variations of surf-zone currents and suspended sediment concentration. *Coastal Engineering* 46, 175-211.
- Wang, P., Smith, E.R., Ebersole, B.A., 2002b. Large-scale laboratory measurements of longshore sediment transport under spilling and plunging breakers. *Journal of Coastal Research*, 18(1), 118-135.
- Watanabe, A., 1987. 3-Dimensional Numerical Model of Beach Evolution. *Proceeding of the Conference on Coastal Sediments '87*, ASCE, pp. 802-817.
- Wilson, K.C., 1989. Friction of wave-induced sheet flow. *Coastal Engineering* 12, 371–379..
- Zyserman, J.A., Johnson, H.K., 2002. Modelling morphological processes in the vicinity of shore-parallel breakwaters. *Coastal Engineering* 45, 261-284.

Technical Session 1: Coastal Structures

Chairman: Dr.-Ing. Rainer Lehfeldt

Modeling of turbulence fields in front of the rubble mound breakwater

Sevket Cokgor¹, Ozgur Durmus², Kaan Koca³, Baris Ozen⁴ and Senol Dundar⁵

Abstract

Laboratory data of velocity fields in front of a rubble-mound breakwater are presented and discussed for non-breaking wave condition. Velocity measurements were conducted near the breakwater by an acoustic Doppler velocimeter (Nortek Vectrino) under regular waves. The raw data were analyzed by using a numerical-filtering scheme so that turbulent fluctuations are separated from the phase-dependent wave motions. Root mean square (RMS) values of the turbulent fluctuations in the vertical and wave directions were obtained. The spatial variations of the turbulent shear stress and of the turbulent kinetic energy (TKE) in front of the breakwater were determined. The comparative analysis of two different wave conditions were performed. The results indicate that turbulent intensities take larger values when the wave contracts over the breakwater. On the other hand, maximum turbulent shear stress values were observed near the breakwater surface, as a consequence of the rough surface effect. The results also indicated that the long period wave has higher motional values than the shorter one.

Keywords: Turbulence intensity, Turbulence Shear Stress, Turbulence Kinetic Energy

1 Introduction

Breaking waves play significant roles in almost all coastal engineering problems. During last decades, the information gathered on the characteristics of these waves has been improved due to the advances in measuring capabilities and results of experimental studies focused on the velocity and turbulence intensities in breaking waves have been reported by many researchers (e.g., Stive, 1980; Stive and Wind, 1982; Nadaoka and Kondoh, 1982; Hattori and Aono, 1985; Mizuguchi, 1986; Nadaoka et al., 1989; Ting and Kirby, 1994, 1995, 1996; Sakakiyama and Liu, 2001; Losada et al., 1995). Measurements carried out within the context of these latter studies have been based on techniques using either a hot-film anemometer or a Doppler velocimeter. The Particle Image Velocimetry technique has been also applied frequently in the analysis of the instantaneous spatial velocity distributions under breaking waves and of the turbulence kinetic energy distribution (e.g., Lin and Rockwell, 1994, 1995; Skyner, 1996; Chang and Liu, 1998, 1999).

The interaction with waves must be taken into account in order to have an adequate design for coastal structures. Motions of the waves are changed due to the presence of the coastal structures and, due to the separation of the flow, the turbulence intensity is amplified in the vicinity of these latter ones. This enhanced turbulence, in turn, may have considerable effects on the wave force, on the scouring phenomenon at the toe of coastal structures, and on other mixing processes.

Studies carried out on the interaction between the waves and coastal structures have been mainly focused on the estimates of the wave reflection and transmission. Although these latter estimates provide the necessary information for the effectiveness of coastal structures to be determined, velocity measurements are crucial for the comprehension of the involved physical

¹Istanbul Teknik Üniversitesi, Hidrolik Laboratuvarı, 34469, İstanbul, cokgor@itu.edu.tr

²Istanbul Teknik Üniversitesi, Hidrolik Laboratuvarı, 34469, İstanbul, durmusoz@itu.edu.tr

³Istanbul Teknik Üniversitesi, Hidrolik Laboratuvarı, 34469, İstanbul, kkaan.koca@itu.edu.tr

⁴Istanbul Teknik Üniversitesi, Hidrolik Laboratuvarı, 34469, İstanbul, ozenb@itu.edu.tr

⁵Istanbul Teknik Üniversitesi, Hidrolik Laboratuvarı, 34469, İstanbul, s.dundar@itu.edu.tr

processes and for the justification of any mathematical and/or numerical model to be applied in the design of these structures.

In the present study, results from an experimental investigation of the turbulence characteristics near a rubble-mound breakwater are presented. This type of structure has been frequently applied all around the world for ages in order to resolve various coastal engineering problems. Main reasons that account for the analysis of the flow and associated velocities near these rubble-mound breakwaters are the structure functionality, structure stability, and their implications on the morphodynamics of nearby areas.

Important hydraulic processes which should be taken into account while analyzing the interaction between waves and rubble-mound breakwaters are the wave reflection, wave dissipation, and wave transmission. The modeling of the dissipation mechanisms due to wave breaking, turbulence, and generation of eddies in the fluid region as well as turbulence and friction within the porous material is not well established. The stability of the armor layers has also been studied intensively, and several formulations can be found in many articles. Most of these latter are based on experimental studies carried for both regular and irregular waves and require the evaluation of the velocity profile over the structure. This velocity is generally computed using linear wave theory or other nonlinear wave theories. However, and due to different reasons, most of the calculated velocities are seen to differ from experimental measurements. Moreover, the stone stability is also affected by the wave-induced flow within the porous media, since the pore pressure and the seepage velocity may reduce the effective stone weight. In general, the effects of the porous flow on the fluid velocities are

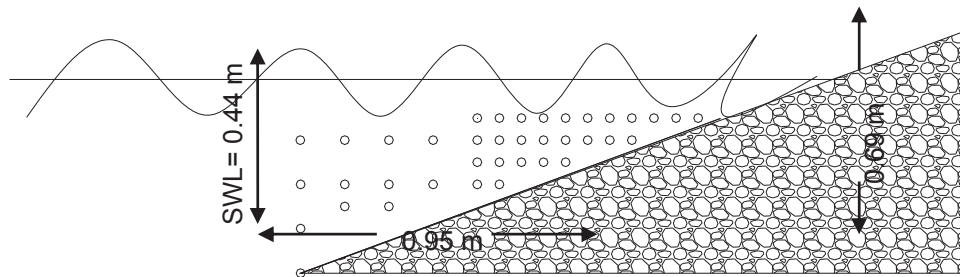


Figure 1: Measurement points in front of the structure

not considered. Moreover, the modeling studies assessing morphodynamic evolution in the presence of a rubble-mound breakwater require an appropriate modeling of the velocity field incident wave parameters, structure geometry, and permeable material characteristics.

2 Experimental setup

Experiments were carried out in a laboratory flume which has a length of 26 m, a width of 6 m, and a height of 1.4 m. Regular waves were generated with a palette of flap type. One of the waves has a period of $T=1.5$ s and 0.18 m height and the other one has 1.8 s period and 0.17 m height. The bottom of the flume was inclined in the offshore direction of the breakwater with a slope value of 1/25. Still water depth, d , was kept as constant with a value of 0.40 m at the front of the breakwater. The breakwater surface was covered by two layers of crushed stones having a mean height, D , of 5.3 cm and a standard deviation of 0.85 cm; an impermeable layer was underlying these crushed stones placed with a slope of 1/2.5. The crest of the breakwater (crown wall's top level) was 25 cm higher than the water level. Consequently, the waves were not able to pass over the breakwater except some splashes.

Two kinds of measurements were undertaken during the experiments: wave measurements by using a resistant type wave probe and velocity measurements by using a 16 MHz NORTEK Acoustic Doppler anemometer (ADV-VECTRINO). Measurements focused on the determination of wave characteristics (e.g., wave height, period) were conducted at three different points in front of the breakwater. These latter points were at a distance of 1 m, 2 m, and 5 m, respectively, to the breakwater. On the other hand, velocity measurements were made at points

which are shown in Figure 1. Turbulence characteristics were determined by using the data collected over periods of two minutes.

3 Results and Discussions

The time averaged values of variables play an important role in engineering designs. The turbulence intensity of a variable represents the turbulence level deviating from the mean value. With respect to incipient motion of the bed elements, the fluctuating forces superimposed on their averaged values make the bed elements to start moving. For the same time-averaged forces, it holds that the stronger turbulence intensities of the motions, the more easily the bed elements start moving (Xingkui, 1988). The time varying velocity data obtained during the above mentioned experiments were analyzed by decomposing the

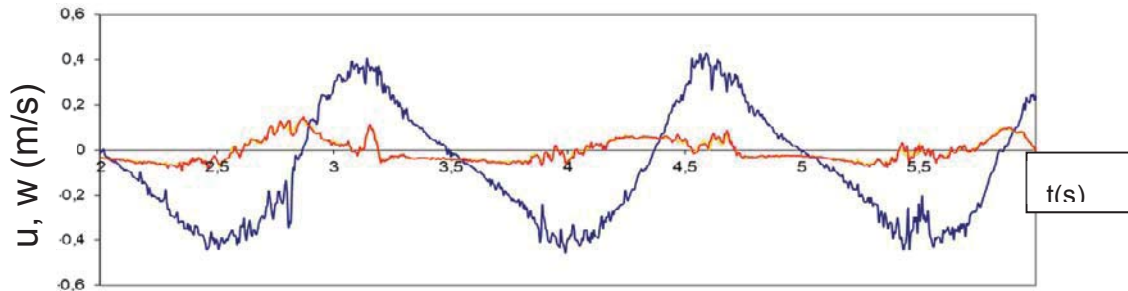


Figure 2: Time series of the velocity components, u and w, z=-0.08 m, x=-0.55 m

instantaneous velocity values into time-averaged mean values and fluctuation components. In the case of velocity measurements in steady flows, the time averaged mean velocity, \bar{u} , can be obtained easily by taking the average of the instantaneous velocity, because u is not a function of time. On the other hand, accurate definitions of both the mean value and the fluctuating component of the signal of measured quantities is one of the most challenging aspects of unsteady flows (Ting, 2001). In this case, there are several methods to be used in order to analyze the time-averaged mean velocity from the velocity records, including the moving average, ensemble averaging, phase averaging, Fast Fourier Transform, and digital filtering. Each signal analysis technique has its own advantages and disadvantages. The phase-averaging method is frequently applied in the previous studies on breaking waves over a uniform slope beach (Sakakiyama and Liu, 2001). However, in this paper, the smoothing algorithm is used to separate the mean velocity and the turbulence due to its simplicity. Smoothing algorithm takes the mean value of the n previous data to obtain the value of $(n+1)$ th value.

Velocity fluctuations were evaluated for both horizontal and vertical velocity components. The fluctuation components of the velocity data were derived by using the equations (1) and (2).

$$u = \bar{u} + u' \quad (\text{m/s}) \quad (1)$$

$$w = \bar{w} + w' \quad (\text{m/s}) \quad (2)$$

where u is the instantaneous velocity, \bar{u} is the time averaged mean velocity and u' is the fluctuating component. As it is inappropriate to present the measurements here, only raw velocity data and filtered velocity data components are shown in Figure 2 for the same measurement points.

In order to investigate the characteristics of the turbulence, power spectra of the velocity components u and w were calculated. The power spectra of the horizontal velocity component measured at two different locations, but at a same elevation ($z=-0.23$ m) are shown in Figure 3.

It is clear from Figure 3 that the turbulence is stronger at $x=-0.85$ m.

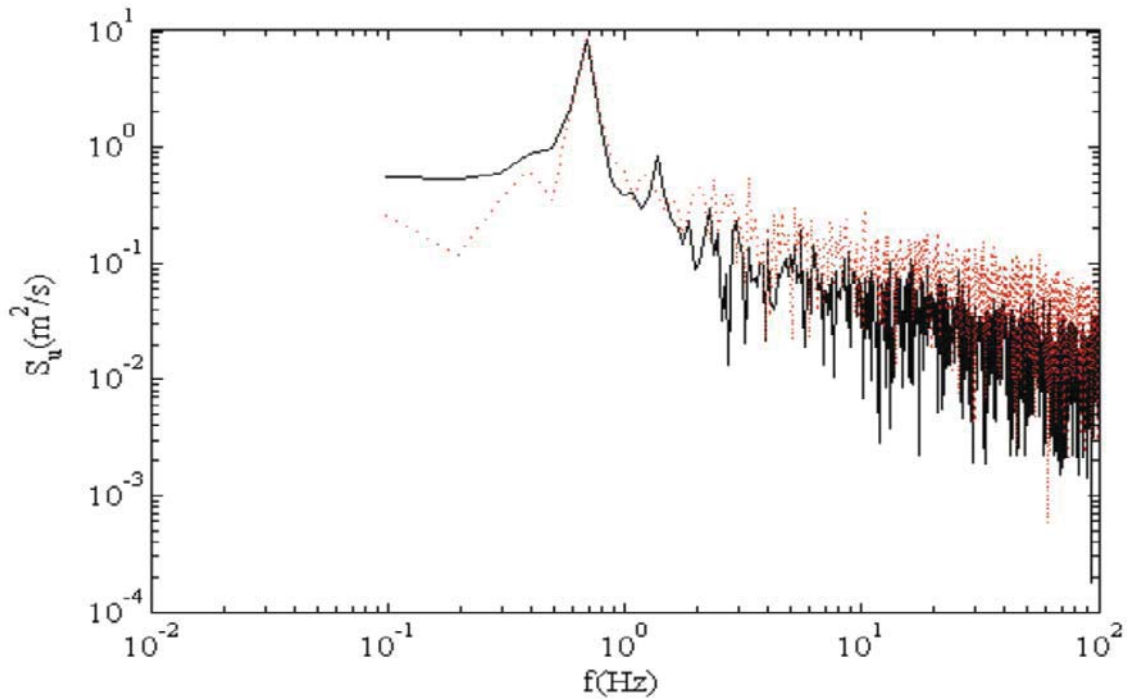


Figure 3: Power spectrum of the horizontal velocity component u at two different locations having the same elevation: $x=-0.75$ m (black line) and $x=-0.85$ m (red dotted line); $z: -0.23$ m.

Once the fluctuating components were determined, in order to investigate the turbulence flow distribution in front of the breakwater, we plotted the turbulence intensity maps. Figure 4 and 5 show the distribution of the horizontal and vertical components of the time-averaged turbulence intensity respectively. The turbulence intensities were calculated by root mean square (RMS) parameter. This parameter is defined as

$$u'_{\text{rms}} = \sqrt{u'^2} \text{ (m/s)} \quad (3)$$

Figure 4a) shows that between $z/D=0.6$ and $z/D=0.8$ levels and $x=[-0.6;-0.45]$ and $x=[-0.4;-0.2]$ the horizontal component of the turbulence intensity was stronger than that for the offshore. This can mainly be due to the wave breaking near the surface. In this region, one must draw attention to the fluctuation component of the velocity. Away from the offshore side and near to the breakwater surface and up to the crest the horizontal component of turbulence velocity was observe to have has its largest value in two adjacent zones for 1.9 s period wave. Approaching to the offshore zone and also to the toe of the breakwater, the horizontal component of 1.9 s period wave first decreases and then again increases. Figure 4b also shows that 1.5 s period wave also has its large values near the breakwater surface. By a comparative analysis of the two waves it can be observed that the long period wave has a wider amplitude motion than the shorter one.

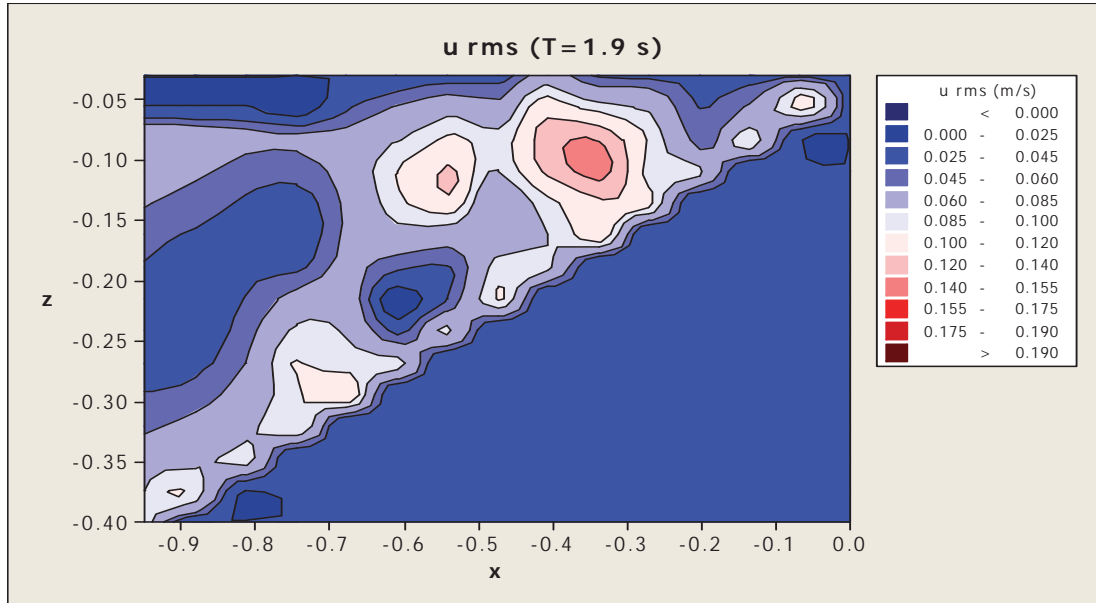


Figure 4.a): u' rms (Horizontal component of turbulence intensity T=1.9 s wave period)

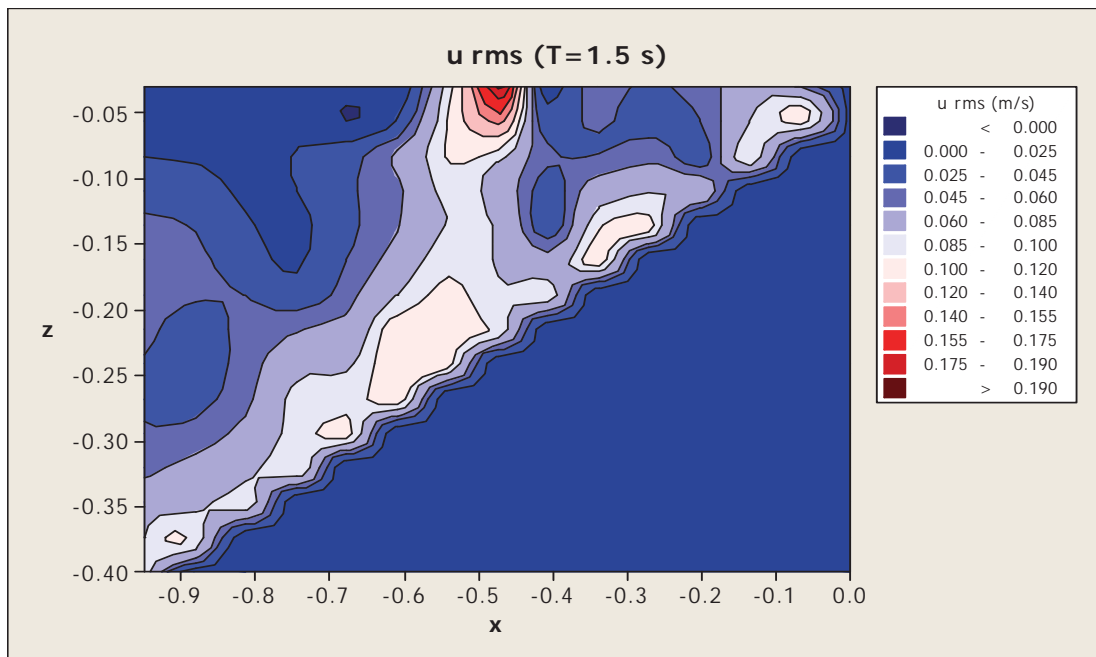


Figure 4.b): u' rms (Horizontal component of turbulence intensity T=1.5 s wave period)

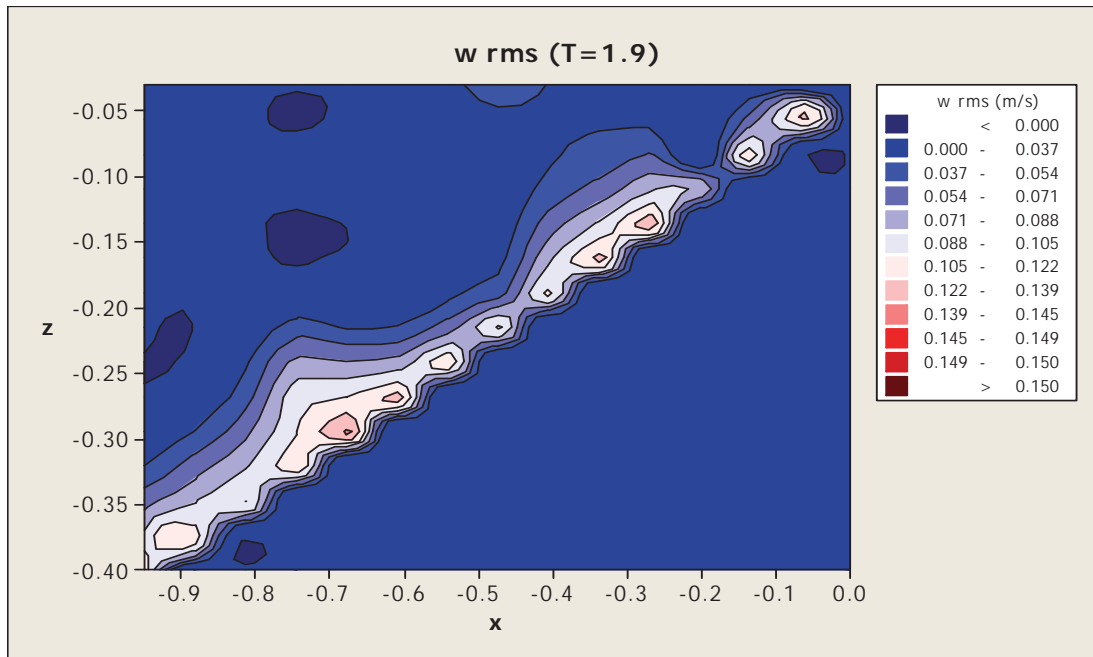


Figure 5.a): w' rms (vertical component of turbulence intensity $T=1.9$ s wave period)

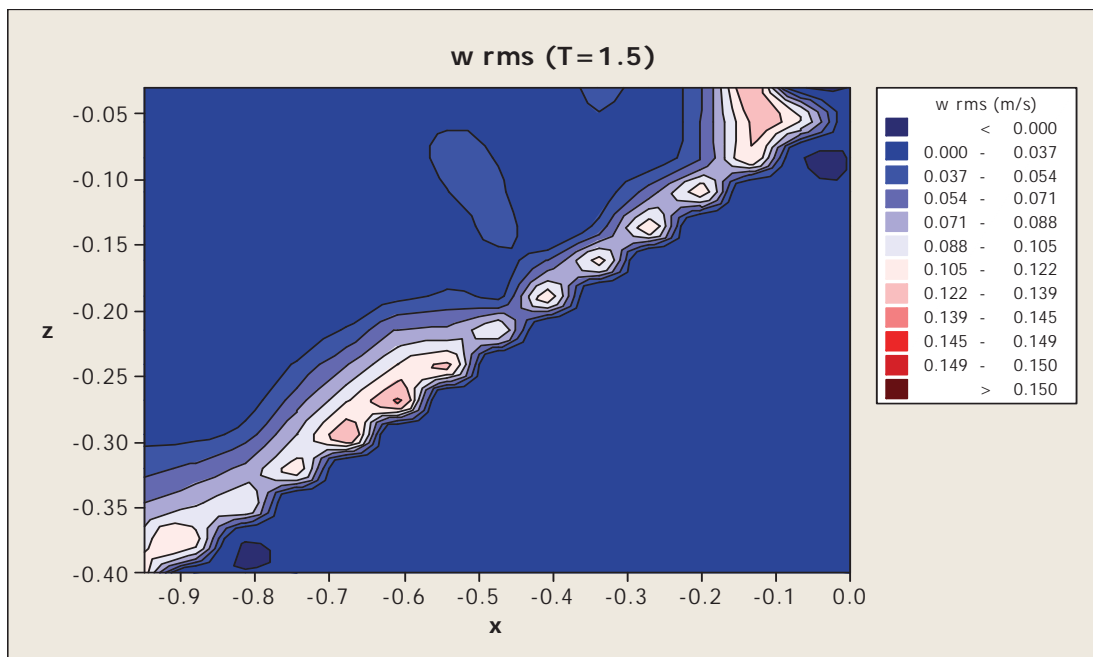


Figure 5.b): w' rms (vertical component of turbulence intensity $T=1.5$ s wave period)

The turbulence effects on the breakwater surface is obviously seen in the vertical component graphics. Figure 5a indicates that along the surface but particularly below the $z/D=0.5$ level the turbulence intensity is stronger. It is also observed in Figure 5b.

The knowledge of the shear stress and the kinetic energy distribution is an important factor for the stability of the structure. Figure 6 shows the turbulence shear stress map, which was obtained by using the following relation for the turbulence shear stress.

$$\tau_{xz} = -\rho \overline{u'w'} \tag{4}$$

Turbulence shear stress values were divided by the bottom shear stress which was defined by Fredsøe and Deigaard(1992) to make the values dimensionless.

Such maps provide the necessary information on the potential vulnerability of different zones around the structure.

As can be seen in Figure 6, for both of the waves the turbulence shear stresses have their largest values near the breakwater surface as expected. Particularly below $z/D=0.5$ level towards the toe a converging between the two stress values can be observed. On the contrary above the $z/D=0.5$ level the two waves stress values tend to differ from each other. This difference caused by the difference between the higher value locations of the two waves.

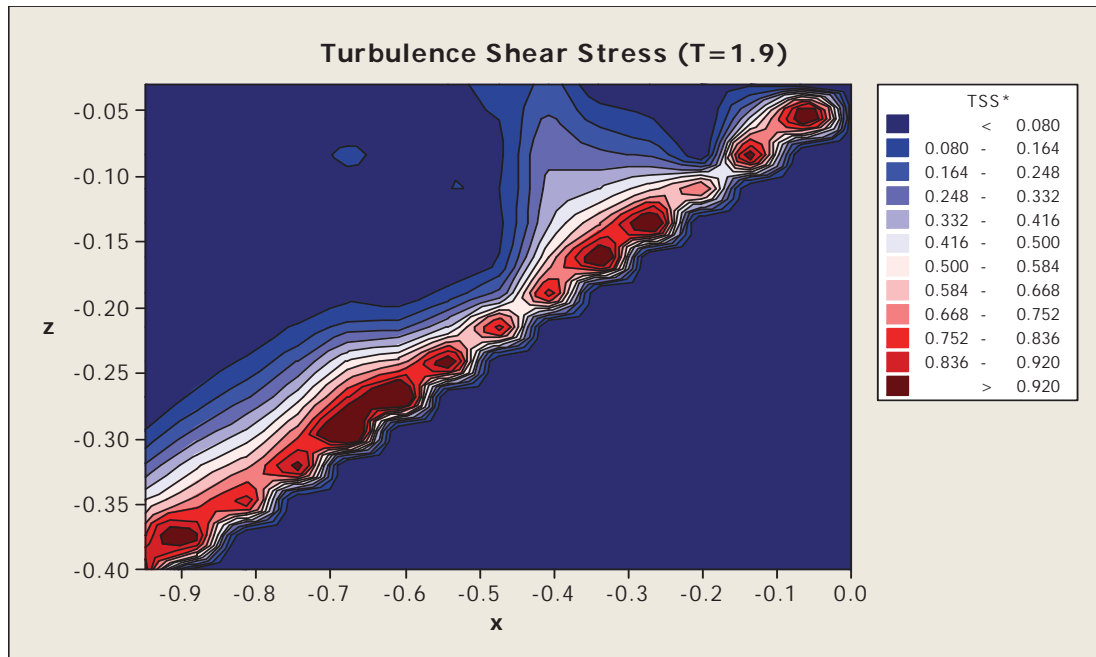


Figure 6.a): Turbulence shear stress map around the structure (T=1.9 s wave period)

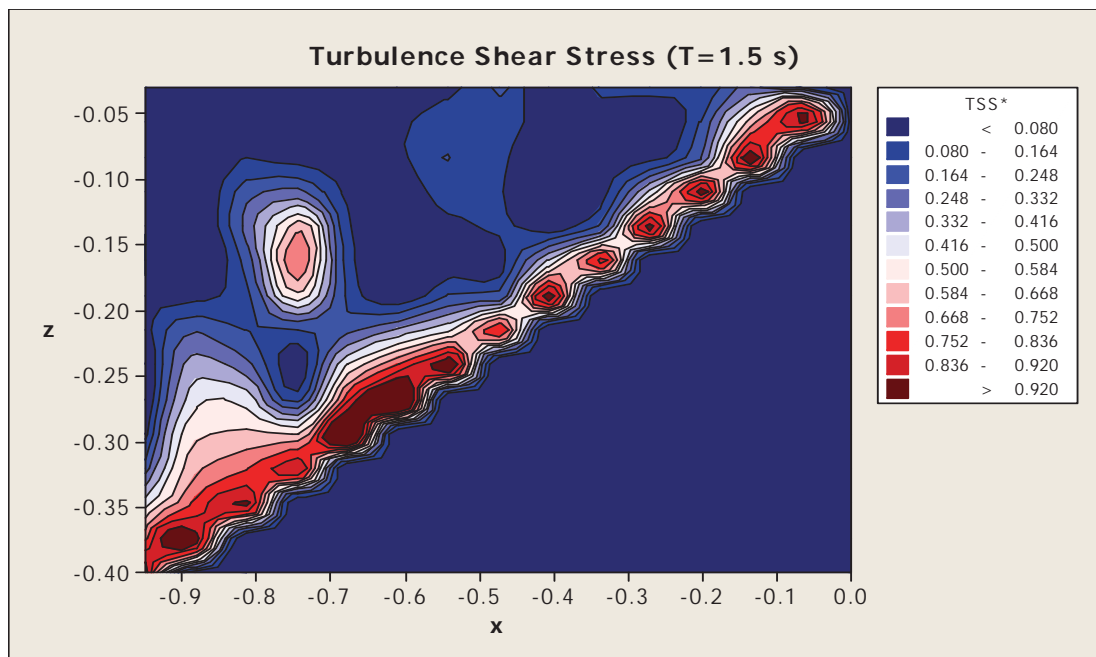


Figure 6.b): Turbulence shear stress map around the structure (T=1.5 s wave period)

The turbulence kinetic energy (TKE) is an estimation of the velocity increase due to the turbulence fluctuations. In order to investigate the horizontal structure of the turbulence flow, the depth averaged TKE values were determined by using Equation 5.

$$TKE = \frac{1}{2}(u^2_{rms} + w^2_{rms}) \text{ (m}^2/\text{s}^2) \quad (5)$$

Figure 7 shows the TKE map which suggests that the TKE was produced by the shear flow and the friction at the structure. The TKE presents larger values above $z/d=0.40$, and, as expected, it is easily identified at the crest of the structure. Figure 7a shows that for $T=1.9$ s period wave the highest kinetic energy values can be seen between $z/D=0.55$ and $z/D=0.85$ and $x=[-0.5;-0.2]$ locations. In Figure 7b apart from the offshore and along the surface of the breakwater towards the crest kinetic energy values are relatively higher.

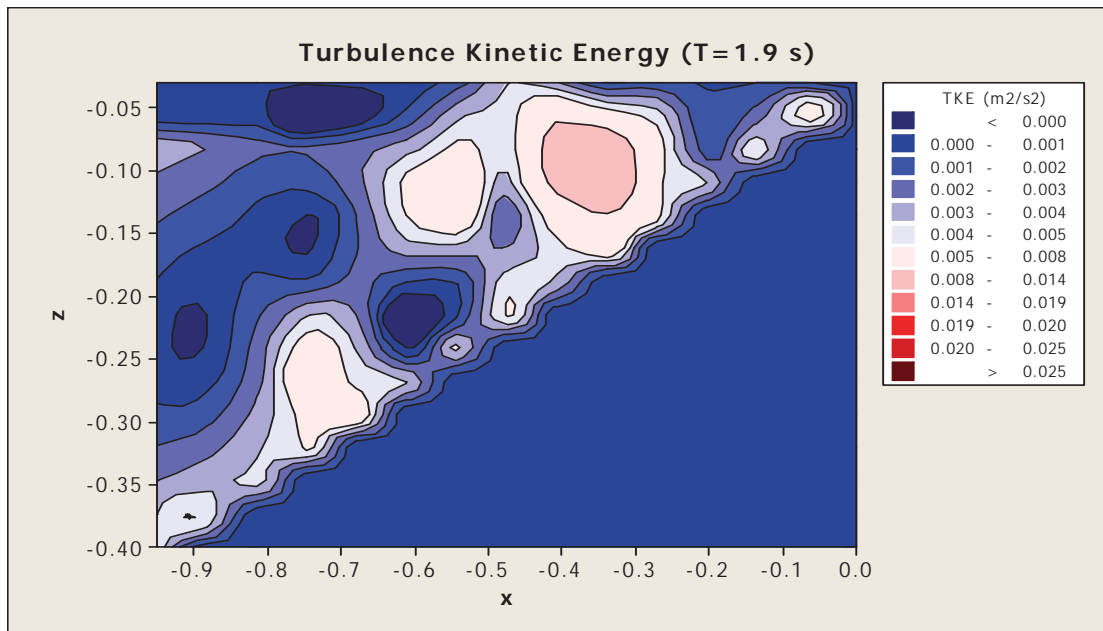


Figure 7.a): Turbulence kinetic energy (TKE) distribution around the structure. (T=1.9 s wave period)

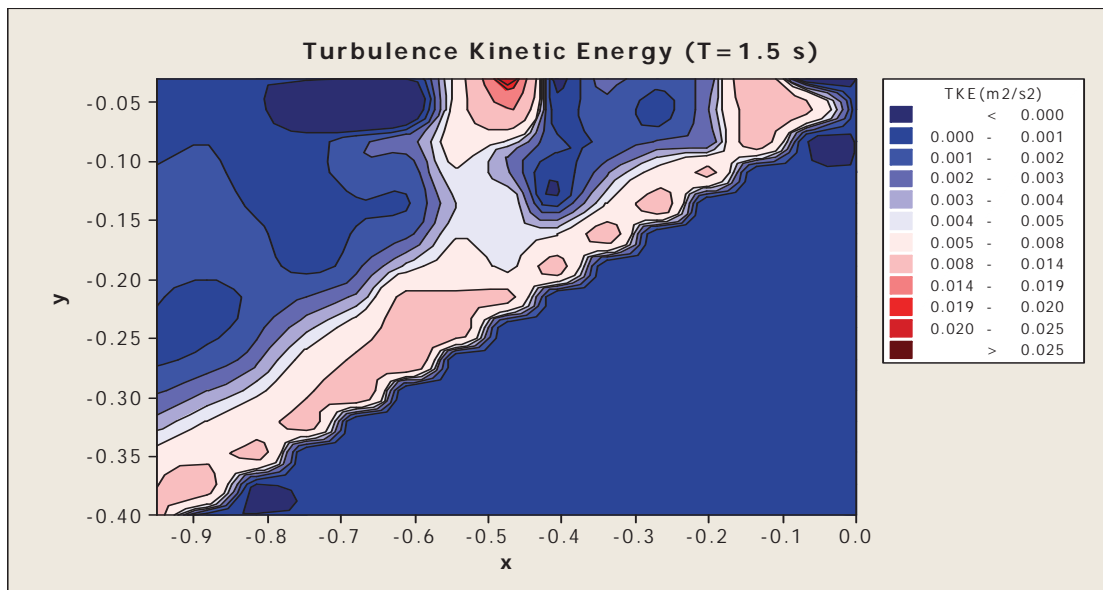


Figure 7.b): Turbulence kinetic energy (TKE) distribution around the structure. (T=1.5 s wave period)

The experiments which were undertaken within the context of the present study allowed the velocity field near the rubble-mound breakwaters to be investigated; the results obtained may be summarized as follows:

4 Conclusions

The experiments which were undertaken within the context of the present study allowed the velocity field near the rubble-mound breakwaters to be investigated; the results obtained may be summarized as follows:

1. Due to the contraction of waves over the breakwater, turbulence intensities (u', w') are observed to take larger values in a region ranging from 0.60 d to still water level (see Figures 4 and 5).
2. Reynolds shear stress is observed to take larger values over the surface of the rubble-mound breakwater. However, the maxima of this latter are observed in a zone ranging from 0.75d to 0.375d (see Figure 6).
3. The distribution of TKE is observed to be similar to the one observed for the horizontal component of the turbulent intensity (see Figure 7).
4. The Reynolds shear stress observed at toe of the breakwater is relatively significant; this is thought to be a consequence of the local scouring at this lower zone.
5. The results also indicated that the long period wave has higher motional values particularly on the horizontal plane than the short period wave.

The paper is presenting the results of the experiments in order to spread the knowledge regarding the turbulence generation and transport through the armor layer near the rubble-mound breakwater.

5 References

- Chang, K.-A. and Liu, P.L.-F., 1998. Velocity, acceleration and vorticity under a breaking wave. *Physics of Fluids*, 10, 327-329.
- Chang, K.-A. And Liu, P.L.-F., 1999. Experimental investigation of turbulence generated by breaking waves in water of intermediate depth. *Physics of Fluids*, 11, 3390-3400.
- Cokgor, S., Dundar, S., Koca, K., Ozen, B., 2011. Laboratory experiments for turbulence characteristics near the rubble mound breakwater. *Journal of Coastal Research*, (Proceedings of the 11th International Coastal Symposium), 488-491. Szczecin, Poland.
- Fredsoe, J., Deigaard, R., 1992. *Mechanics of coastal sediment transport*. Advanced Series on Ocean Engineering, 3, 24-26, Singapore.
- Hattori, M. and Aono, T., 1985. Experimental study on turbulence structure under spilling breakers. In: Toba, Y., Mitsuyasu, H.(Eds.), *The Ocean Surface* (Reidel, Boston, USA), pp. 419-424.
- Lin, J.-C. and Rockwell, D., 1994. Instantaneous structure of a breaking wave. *Physics of Fluids*, 6, 2877-2879.
- Lin, J.C. and Rockwell, D., 1995. Evolution of a quasi-steady breaking wave. *Journal of Fluid Mechanics*, 302, 29-44.
- Losada, J.J.; Losada, M.A., and Martin, F.L., 1995. Experimental study of wave-induced flow in a porous structure. *Coastal Engineering*, 26, 77-98.
- Mizuguchi, M., 1986. Experimental study on kinematics and dynamics of wave breaking. *Proceedings of the 20th International Conference on Coastal Engineering* (Reston VA, USA, ASCE), pp. 589- 603.
- Nadaoka, K. and Kondoh, T., 1982. Laboratory measurements of velocity field structure in the surf zone by LDV. *Coastal Engineering*. 25, 125-146.

- Nadaoka, K.; Hino, M., and Koyano, Y., 1989. Structure of the turbulent flow field under breaking waves in the surf zone. *Journal of Fluid Mechanics*, 204, 359-387.
- Sakakiyama, T. and Liu, P.L.-F., 2001. Laboratory Experiments for wave motions and turbulence flows in front of a breakwater. *Coastal Engineering*, 44, 117-139.
- Skyner, D., 1996. A comparison of numerical predictions and experimental measurements of the internal kinematics of a deepwater plunging wave. *Journal of Fluid Mechanics*, 315, 51-64.
- Stive, M.J.F., 1980. Velocity and pressure field of spilling breaker. *Proceedings of the 17th International Conference on Coastal Engineering (Reston VA, USA, ASCE)*. pp. 547-566.
- Stive, M.J.F. and Wind, H.G., 1982. A study of radiation stress and setup in the nearshore region. *Coastal Engineering*, 6, 1-25.
- Ting, F.C.K. and Kirby, J.T., 1994. Observation of undertow and turbulence in a laboratory surf zone. *Coastal Engineering*, 24, 51-80.
- Ting, F.C.K. and Kirby, J.T., 1995. Dynamics of surf-zone turbulence in a strong plunging breaker. *Coastal Engineering*, 24, 177- 204.
- Ting, F.C.K. and Kirby, J.T., 1996. Dynamics of surf-zone turbulence in a spilling breaker. *Coastal Engineering*, 27, 131- 160.
- Ting, F.C.K., 2001. Laboratory study of wave and turbulence velocities in a broad-banded irregular wave surf zone. *Coastal Engineering*, 43, 183-208.
- Xingkui, W., 1988. Dynamics forces on a bed element in Open Channel Flow with a Backward-facing step. *Delft University of Technology. Report No:9*, 56p.

Effect of berm width on reshaped profile of berm breakwaters

Peyman Aghtouman¹, Fatemeh Aliyari², Zeinab Aghtouman³

Abstract

Berm breakwater is a rubble mound structure and contains a wide range of armour stones. This kind of structures will reshape under wave attack and final stable profile is main design criterion. Apart from determining weight and grading of armour stones, a designer shall design the geometry of the structure including berm width. This research is an experimental study on the effect of berm width on reshaped profile of a berm breakwater. This enables us to find out an optimum width to obtain better performance.

Keywords: berm breakwater, berm width, reshaped profile, recession, physical modeling

1 Introduction

The berm breakwater reshapes under wave attacks and the final S-shaped profile is more stable after reshaping (Van der Meer, 1991). This is considered as an advantage to berm breakwaters in comparison with conventional ones.

Berm breakwaters are classified based on the non-dimensional parameter, H_o :

$$H_o = \frac{H_{m0}}{\Delta \cdot D_{n50}} \quad (1)$$

With H_{m0} Significant wave height

D Nominal diameter

Δ Is defined as: $\Delta = \frac{\rho_a}{\rho} - 1$

ρ & ρ_a Density of water and armour stone, respectively

But due to the importance of wave period which is missed in this parameter, Van der Meer (1988) recommended a non-dimensional parameter, $H_o T_o$, as below equation, he then presented his research results as a software called BREAKWAT:

$$H_o T_o = \frac{H_s}{\Delta D_{n50}} \times T_m \times \left(\frac{g}{D_{n50}} \right)^{\frac{1}{2}} \quad (2)$$

Where T_o Wave period non-dimensional parameter and is defined as:

$$T_o = T_m \times \left(\frac{g}{D_{n50}} \right)^{\frac{1}{2}} \quad (3)$$

With T_m Mean wave period

g Gravitational acceleration

According to this equation PIANC (2003) classified the berm breakwaters as follows:

¹ SCWMRI, Shafie st., Asheri st., Karaj Special Road, Tehran, P.O Box 13445-1136 I.R.Iran, payman_7@yahoo.com

² EIED(Energy Industries Engineering and Design), No.4, Second Koohestan st., Passdaran Ave., Nobonyad sq., Tehran 1958843811 I.R.Iran, aliyari-f@eied.com

³ Darya Negar Pars (DNP) Consulting Engineers, No. 41, 1st Towhid, Khovardin Blvd., Shahrake Gharb, Tehran, Postal code: 1466994853, zeinab.aghtouman@yahoo.com

Table 1: Types of berm breakwaters

Type of Breakwater	H_0	H_0T_0
Statically stable non-reshaped berm breakwater	<1.5-2	<20-40
Statically stable reshaped berm breakwater	1.5-2.7	40-70
Dynamically stable reshaped berm breakwater	>2.7	>70

For the first two types, the profile reshaping is limited and the erosion area of the berm, or the so-called recession width (Rec) is a significant parameter in designing a berm breakwater, so that, the structure would fail as soon as Rec exceeded the berm width, thus, employing a proper method in calculating berm width after erosion is essential. This area is investigated by several researchers.

Hall and Kao (1991) assessed the effect of gradation of armour stones and the amount of rounded stones in the armour on dynamically stable breakwaters. They measured the profiles of the structure during the various stages of reshaping. The results indicated that the toe width formed as a result of reshaping and the area of stones required for reshaping were dependent on the gradation of the armour stones and they presented following formula:

$$\frac{Rec}{D_{50}} = (-10.4 + 0.51.H_o^{2.5}) + 7.52\left(\frac{D_{85}}{D_{15}}\right) - 1.07\left(\frac{D_{85}}{D_{15}}\right)^2 + 6.12P_R \quad (4)$$

With D_{15} & D_{85} Sieve diameter exceeded by 85% & 15% of a sample respectively.

P_R Fraction of rounded stones in a sample

Torum (1998& 1999) presented a polynomial formula to calculate the berm recession as a function of H_0T_0 . Later in 2003, he modified the formula as follows:

$$\frac{Rec}{D_{50}} = 0.0000027(H_oT_o)^3 + 0.000009(H_oT_o)^2 + 0.11(H_oT_o) - 0.8 \quad (5)$$

Where f_g (Gradation Factor) = D_{n85}/D_{n15}

For all the experiments the parameter f_g has been considered about 1.7 and the formula is valid in range of $H_0T_0 > 20-30$.

To include stone gradation and water depth, Menze and others (2000) advanced the formula to the equation (6):

$$\frac{Rec}{D_{50}} = 0.0000027(H_oT_o)^3 + 0.000009(H_oT_o)^2 + 0.11(H_oT_o) - (9.9f_g^2 + 23.9f_g - 10.5) - f_d \quad (6)$$

With f_d Factor accounting for the influence of depth

Depth factor is analysed for two different non-dimensional depth as $d/D_{n50} = 12.5$ & 25 and could be estimated from following equation:

$$f_d = -0.16\left(\frac{d}{D_{n50}}\right) + 4.0 \quad (7)$$

This equation is valid in range of $1.3 < D_{n85}/D_{n15} < 1.8$

Andersen (2006) did several investigation on front side stability of berm breakwaters. his suggested recession formula is based on some theoretical considerations on the influence of front slope, water depth and berm elevation.

$$\frac{Rec}{D_{n,50}} = \frac{(1 + c_1).h - c_1.h_s}{h - h_B} . f_N . f_\beta . f_{H_0} . f_{grading} + \frac{\cot(\alpha_d) - 1.05}{2.D_{n,50}} . (h_B - h) \quad (8)$$

With	C_1	Constant equal to approximately 1.2
	h	Water depth
	h_B	Water depth above berm (negative if berm is elevated above SWL)
	h_S	Water depth above step
	α_d	Lower front slope (below berm)

To include wave direction, number of waves, armour gradation and stability number, Anderson used following equations:

$$\begin{cases} f_N = (N/3000)^{-0.046.H_o+0.3} & \text{for } H_o < 5 \\ f_N = (N/3000)^{0.07} & \text{for } H_o \geq 5 \end{cases} \quad (9)$$

$$f_\beta = \cos(\beta) \quad (10)$$

$$\begin{cases} f_{grading} = 1 & \text{for } f_g \leq 1.5 \\ f_{grading} = 0.43.f_g + 0.355 & \text{for } 1.5 < f_g \leq 2.5 \\ f_{grading} = 1.43 & \text{for } f_g > 2.5 \end{cases} \quad (11)$$

$$\begin{cases} f_{H_o} = 19.8 \cdot \exp\left(-\frac{7.08}{H_o}\right) \cdot s_{om}^{-0.5} & \text{for } T_o \geq T_o^* \\ f_{H_o} = 0.05 \cdot H_o T_o + 10.5 & \text{for } T_o < T_o^* \\ T_o^* = \frac{19.8 \cdot \exp\left(-\frac{7.08}{H_o}\right) \cdot s_{om}^{-0.5} - 10.5}{0.05 \cdot H_o} \end{cases} \quad (12)$$

Several other researches are done by other researchers in this area such as VanGent (1995), Sayo (2000), Aghtouman (2005), Rao (2004) Lissev& Daskalov (2007) & Moghim(2009).

Previous researches performed by Aghtouman (2005) on armour layer thickness of simple slope (mass armoured) reshaping breakwaters was the main Idea for finding out the berm width effect on reshaped profiles. In this research, effect of berm width on reshaped profile of a berm breakwater to obtain optimum width for better performance is investigated.

2 Test set up

The physical modelling tests have been carried out in the wave flume of SCWMRI (Soil Conservation and Watershed Management Research Institute). It's equipped with a vertical piston-type paddle and related irregular wave generation system, made by DHI. In this study irregular waves with JONSWAP spectrum were generated. Plan view of the wave flume, model and wave gage locations are presented in Figure 1.

Using Mansard(1980) method, three wave guages were located between the structure and the paddle to record the reflected waves. Another wave guage was installed at seaward side of the model to measure the incident wave height.

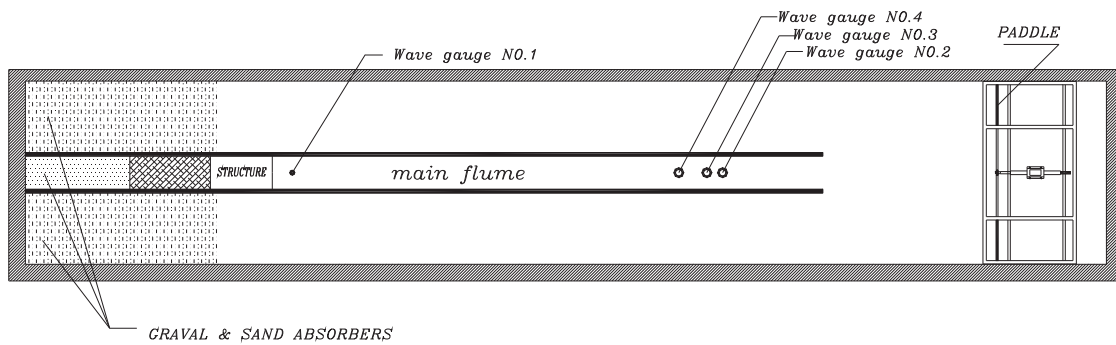


Figure 1: Wave flume plan and setup of wave height meters

Based on mass conservation law as a main assumption, traditional simple slope reshaping breakwater section has been changed to a berm breakwater. An upper part (U) of the armour layer has been cut out and added to the lower part (D). Therefore a berm breakwater section is formed by a geometric change of the traditional simple slope reshaping breakwater. Figure 2, illustrates the berm breakwater model and the design assumptions.

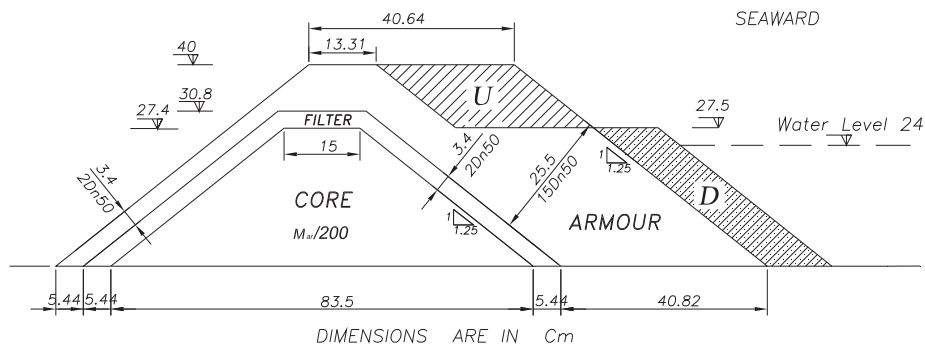


Figure 2: Section of Berm breakwater model in comparison with previous simple slope section

To investigate the effect of berm width on reshaped profile, four different relative berm widths, $B/D_{n50} = 17.6, 20.6, 23.6$ and 26.6 and four relative wave heights, $H/D_n = 4.0, 5.1, 6.2$ and 6.3 for each width were employed. For wave parameters effect on reshaping profile consideration, three different wave lengths, $d/L_{op} = 0.095, 0.051$ and 0.039 and constant water depth of $d/D_n = 14.1$ were used. Applied stone characteristics are tabulated in table 2:

Table 2: Stone characteristic

	Armour layer	Filter layer	Core
Nominal diameter (m)	0.017	0.008	0.003
Weight (kg)	0.013	0.0013	-
Density (kg/m^3)	2600	2600	1700

3 Data analysis and conclusion

Comparison between reshaped profiles of the four berm width of $B/D_{n50} = 17.6, 20.6, 23.6$ and 26.6 under the same wave condition are illustrated in Figures 3 to 7.

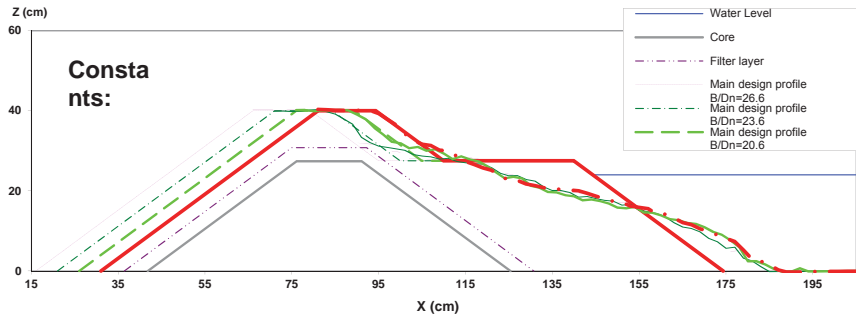


Figure 3: Comparison between reshaped profiles under the same wave condition of $H/D_n=4.0$ and $d/L_{op}=0.039$ for the different berm widths.

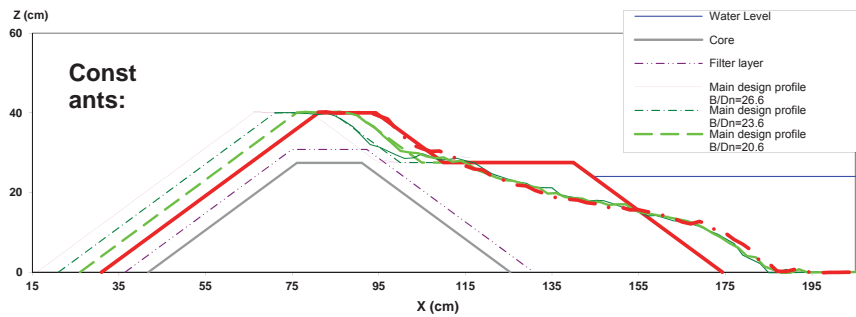


Figure 4: Comparison between reshaped profiles under the same wave condition of $H/D_n=5.1$ and $d/L_{op}=0.095$ for the different berm widths.

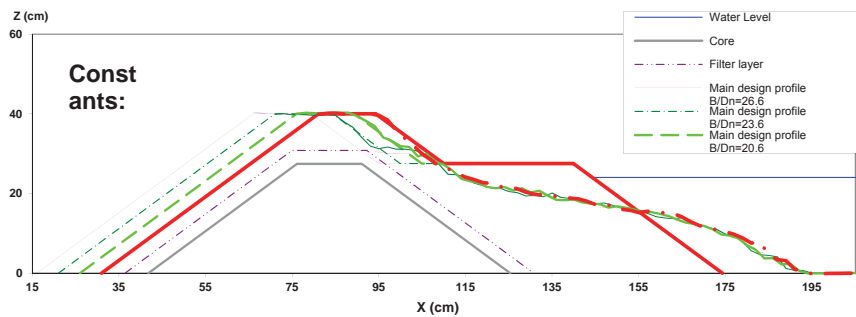


Figure 5: Comparison between reshaped profiles under the same wave condition of $H/D_n=6.2$ and $d/L_{op}=0.095$ for the different berm widths.

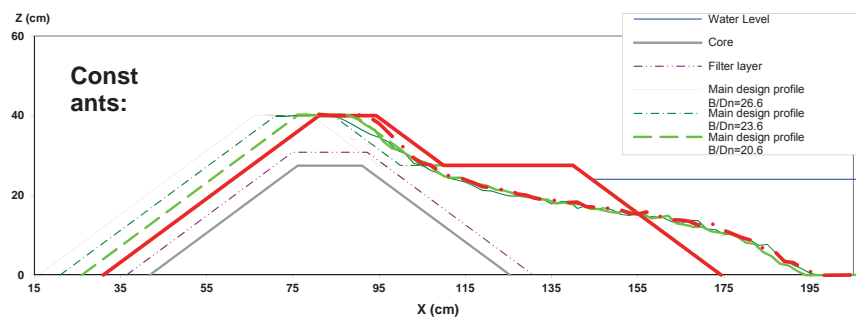


Figure 6: Comparison between reshaped profiles under the same wave condition of $H/D_n=6.3$ and $d/L_{op}=0.058$ for the different berm widths.

Tests results based on these comparisons show that the berm width has not significant effect on final reshaped profiles of the reshaping berm breakwaters. Also, author presented similar results for the different armour layer thickness of the mass armoured reshaping breakwaters on 2005 (Figure 7 and see the References).

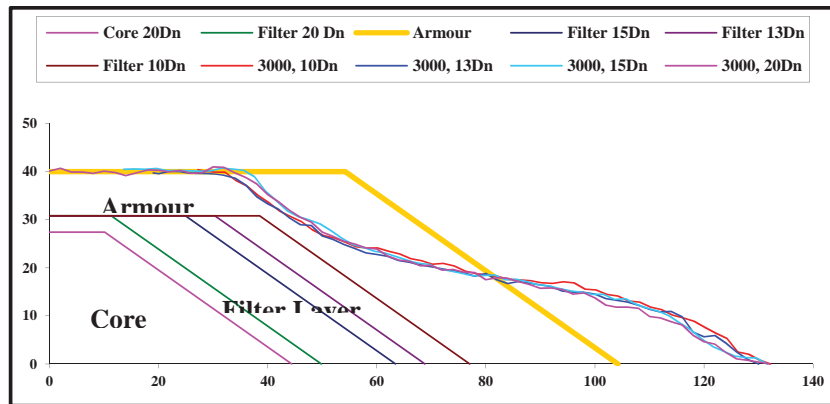


Figure 7: Comparison between reshaped profiles of the mass armoured reshaping breakwater under the same wave condition for the different armour layer thicknesses.

For more detail, comparison between the experimental results of this research has been performed with the BREAKWAT software outputs. These comparisons are presented in Figures 8 to 11.

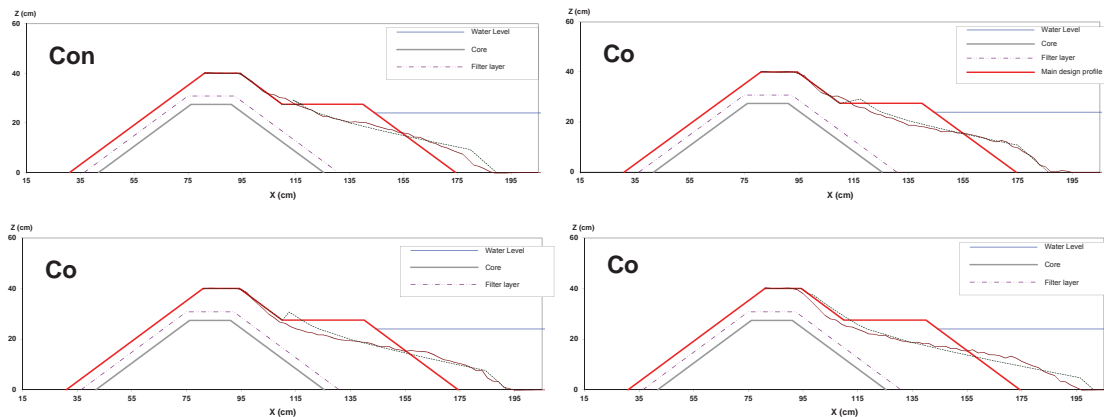


Figure 8: Comparison between reshaped profile of the present study with BREAKWAT output ($B/D_n=17.6$).

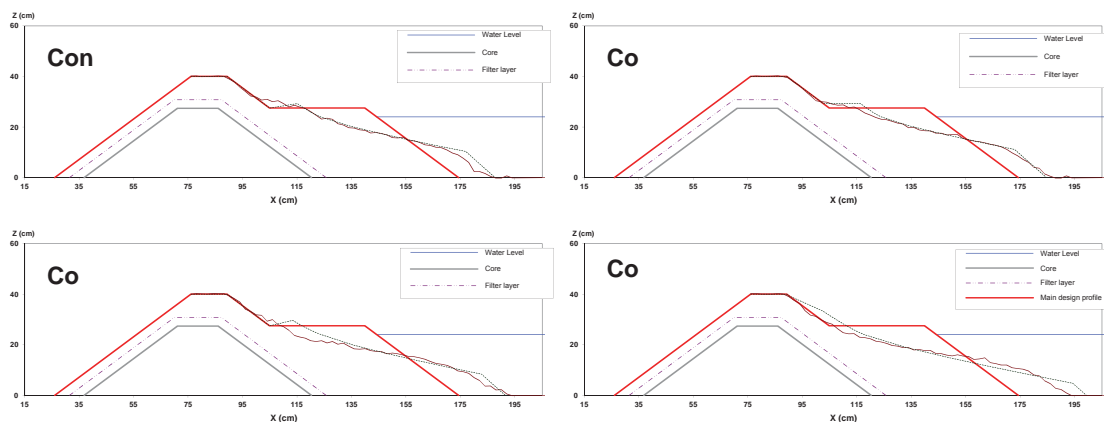


Figure 9: Comparison between reshaped profile of the present study with BREAKWAT output ($B/D_n=20.6$).

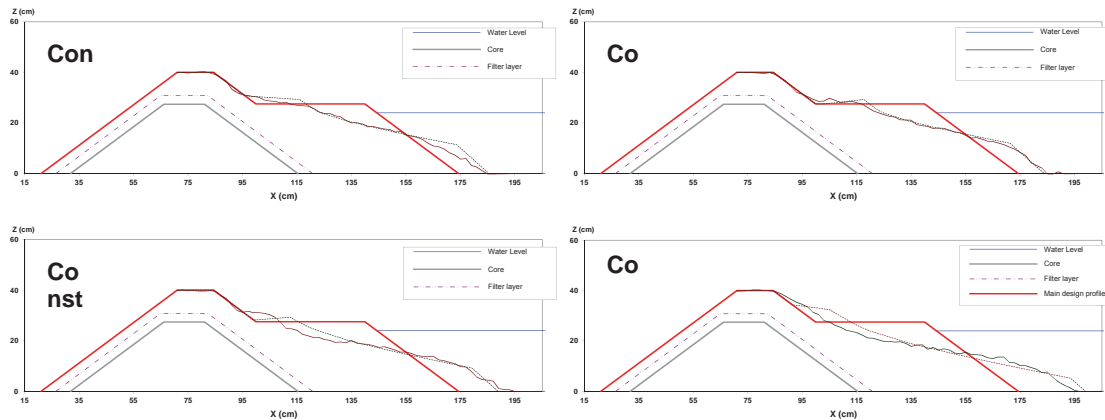


Figure 10: Comparison between reshaped profile of the present study with BREAKWAT output ($B/D_n=23.6$).

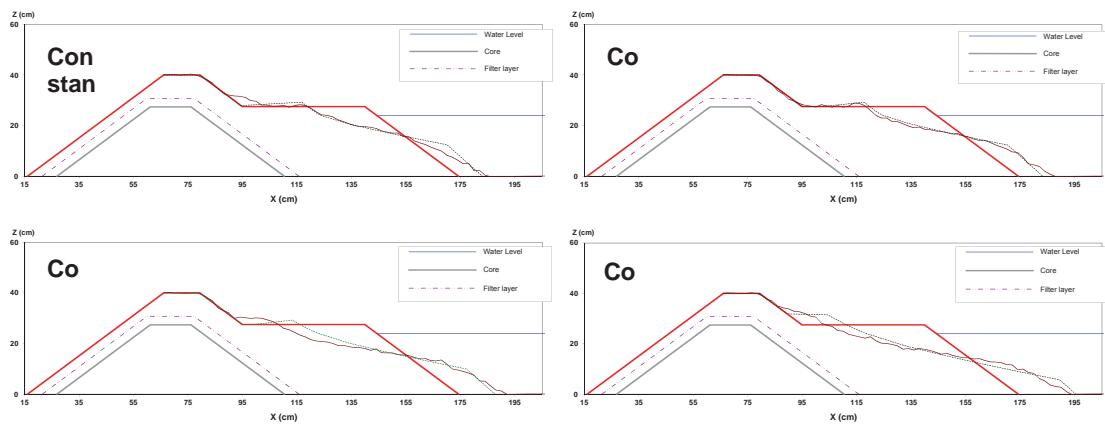


Figure 11: Comparison between reshaped profile of the present study with BREAKWAT output ($B/D_n=26.6$).

Similarly, four graphs have been plotted for the prediction of the BREAKWAT for the four different berm widths that are experimented. The results are illustrated in Figure 12.

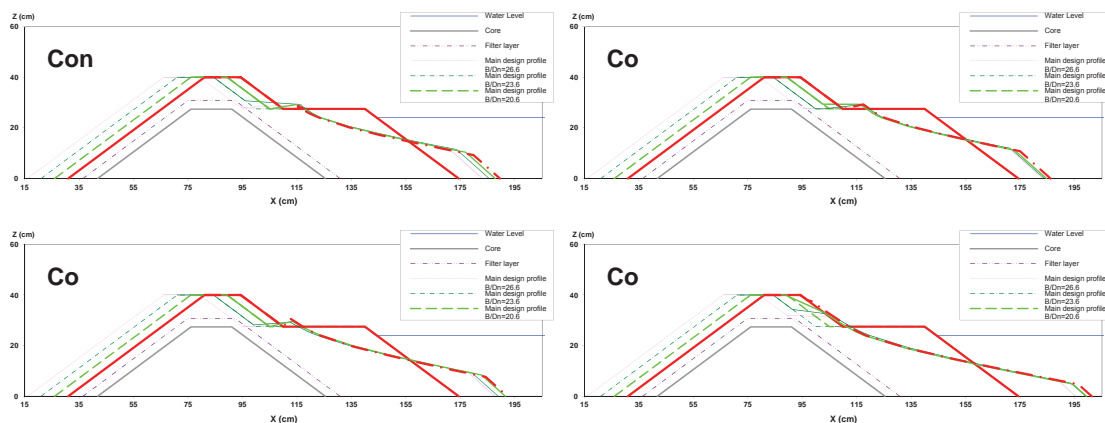


Figure 12: Comparison between reshaped profiles under the same wave condition of $H/D_n=6.3$ and $d/L_{op}=0.058$ for the different berm widths.

These figures show the recorded reshaping profiles in this research have both similarities and some differences with the BREAKWAT outputs. Final slope of the reshaped profiles are mostly similar but BREAKWAT predicts a little steeper above water level. Most of reshaped profiles that BREAKWAT predicts show less reshaping above the water level (at end of the berm) rather

than the recorded profiles in this research. It means that the eroded area predicted by BREAKWAT is less than that measured in this research. Moreover, accumulated materials at the toe of the structure which are predicted by BREAKWAT are more than that measured in this research most of the time. These differences increase when the wave conditions (wave height and period) increase. Figure 12 is showing that BREAKWAT predicts a progress in profile at accumulation zone but this research shows this part of profiles are approximately similar (see Figures 3 to 6).

4 References

- Andersen, T.L. (2006): Hydraulic Response of Rubble Mound Breakwaters (Scale Effects-Berm Breakwaters), Doctoral Thesis, University of Aalborg, Denmark, Under Supervision of Burcharth, H. F.
- Aghtouman, P., Chegini, V., Shirian N., Hejazi M., (2005): Design of reshaping breakwater's Armour layer thickness, 2nd International Coastal Symposium (ICS 2005), Hofn, Iceland.
- Baird, W.F. and Hall, K.R. (1984): The Design of Breakwaters Using Quarried Stone, 19th International Conference On Coastal Engineering, Houston, pp. 1024-103.
- Hall, K. and Kao, S. (1991): A Study of the Stability of Dynamically Stable Breakwaters, Canadian Journal of Civil Engineering, Vol. 18, pp.916-925.
- Menze, A. (2000): Stability of Multilayer Berm Breakwater, Diploma Thesis, University of Braunschweig, Germany, Carried out at SINTEF/NTNU, Trondheim, Norway, Under Supervision of Alf Torum.
- Kao, J. S. and Hall, K. R., (1990): Trends in stability of dynamically stable breakwaters. ASCE. Proc. 22nd ICCE, Delft, the Netherlands, Ch. 129
- Mansard, E.P.D. and Funke, E.R. (1980): The measurement of Incident And Reflected Spectral Using a Least Squares Method, Proc. 17th Coastal Engineering Conf., Sydney, Australia, pp. 154-172.
- Moghim M.N., Shafieefar M., Chegini V., Aghtouman P. (2009): Effects of irregular wave parameters on berm recession of reshaping berm breakwaters: Journal of Marine Engineering, Vol. 5, No. 9, pp. 35-51; ISSN 0733-950X
- PIANC MarCom WG 40. (2003): State of the art of the design and construction of berm breakwaters, PIANC, Brussels.
- Rao, S. and Pramod, Rao, B. (2003): Stability of Berm Breakwater with Reduced Armour Stone Weight, Ocean Engineering 31, pp. 1577-1589.
- Sayao, O.J. (2000): On the Profile Reshaping of Berm Breakwaters, Coastal Structures 99, Losada (ed.) Balkema, Rotterdam, Netherlands.
- Sigurdarson, S., Juhl, J., Sloth, P., Smarason, O.B. and Viggosson, G. (1998): Advances in Berm Breakwaters, Coastlines, Structures and Breakwaters Conference, London.
- Torum, A., Kuhnen, F. and Menze, A. (2003): On Berm Breakwaters. Stability, Scour, Overtopping, Elsevier, Journal of Coastal Engineering 49, Amsterdam, September Issue, pp. 209-238.
- Van der Meer, J.W. (1988): Rock slopes and gravel beaches under wave attack, Doctoral Thesis, Delft University of Technology, Also: Delft Hydraulics Communication No. 396.
- Van der Meer, J.W. and Koster, M.J. (1988): Application of Computational Model on Dynamic Stability, Proc. Breakwaters' 88, Eastaburne, Thomas Telford.
- Van Gent, Marcel M.A. (1995): wave Interaction with Berm Breakwaters, ASCE, J. of WPC. and OE., Vol. 121, No. 5, Sep / Oct 1995.

A hybrid modelling approach for floating breakwater dimensioning

Anja Brüning¹, Hans Fabricius Hansen² Flemming Schlütter³ and Ulrich Vierfuß⁴

Abstract

To fulfil the current requirements for a safe and unimpeded operation of the pilot ships at the Elbe River near Brunsbüttel, Germany, different alternatives were checked. One of the options is a new pier for pilot ships at the northern bank of the Elbe River close to the Kiel-Canal (NOK). Due to the large water depths and a desire to minimise influence on the sediment transport, a floating breakwater was chosen as a possible wave protection system for the new pier.

BAW, who was commissioned by the local water- and shipping administry (WSA Hamburg) for the conceptual planning, requested DHI to undertake numerical simulations and physical model tests in order to estimate the required dimensions and associated wave attenuation of the floating breakwater.

Design conditions at this particular location would result in significant wave heights up to 1.7 m during storm events with winds from WSW and wind speeds of 25 m/s. Ship induced waves were considered as well. Here only the secondary ship waves can be considered as primary waves are too long to be absorbed by the breakwater. The maximum acceptable significant wave height at the pier was $H_{m0,max}=0.95$ m.

This required a protective structure that is able to reflect some of the incoming wave energy in order to reduce the waves at the moored pilot ships to the acceptable level. Numerical models were used to estimate wave reflection and transmission for different layouts and wave conditions. Subsequently the most suitable dimensions of the floating breakwater were determined.



Figure 1: First and final layout of floating breakwater and pier from the conceptual planning (WSA Hamburg)

Keywords: floating breakwater, wave, current, numerical modelling, physical modelling

1 General Conditions, Challenges and Methods

As specific challenge, the initial conditions can be accentuated: The water depths are large and wave periods are relatively long. Knowledge of the dimensioning and construction of floating breakwaters is available (see PIANC 1994), but rarely for oblique wave attack and long wave

¹ DHI-WASY GmbH, Branch Office Syke, Max-Planck-Str. 6,28857 Syke, Germany, abu@dhigroup.com

² DHI, Agern Allé 5, 2970 Hørsholm, Denmark, hfh@dhigroup.com

³ DHI, Agern Allé 5, 2970 Hørsholm, Denmark, fls@dhigroup.com

⁴ Federal Waterways Engineering and Research Institute (BAW), Dienststelle Hamburg, Wedeler Landstrasse 157, 22559 Hamburg, Germany, Ulrich.Vierfuss@BAW.de

periods. Furthermore the oblique wave attack counteracts the damping effect, because wave energy partially reaches the berth from the side.

In cooperation with BAW, DHI chose a hybrid approach to determine a suitable solution by undertaking the following tasks:

1. First, the predefined design conditions were modelled for the area of interest in frequency domain using MIKE 21 SW wave modelling technology. From a study performed by BAW a wind generated design wave of $H_s = 1.8$ m, $T_{m01} = 4.0$ s ($T_p = 5.3$ s) was defined as boundary condition, coming from 250° (WSW). The applied water level is MSL+6.1 m.
2. From a starting layout a suitable floating structure was found by using the diffraction/radiation code WAMIT® to analyse the response in waves of the floating structures in order to obtain its ability to reduce wave heights for sheltered conditions.
3. After identifying the layout and dimensions of the floating breakwater physical model tests in DHI laboratories were used to verify the effectiveness of the floating breakwater. Additionally movements of the pontoons and forces on the structure were determined.
4. With the help of reflection and transmission properties and the forces found using the physical model tests, the WAMIT®-model was calibrated.

As the wind waves were the predominant influencing factor the paper will focus on this design parameter and the wave attenuation of the breakwater for numerical and physical modelling.

The schemes in Figure 2 indicate the above mentioned tasks. As first step the optimization of the breakwater layout is shown (left side). Afterwards the validation of the numerical Model against physical model tests is visualised (right).

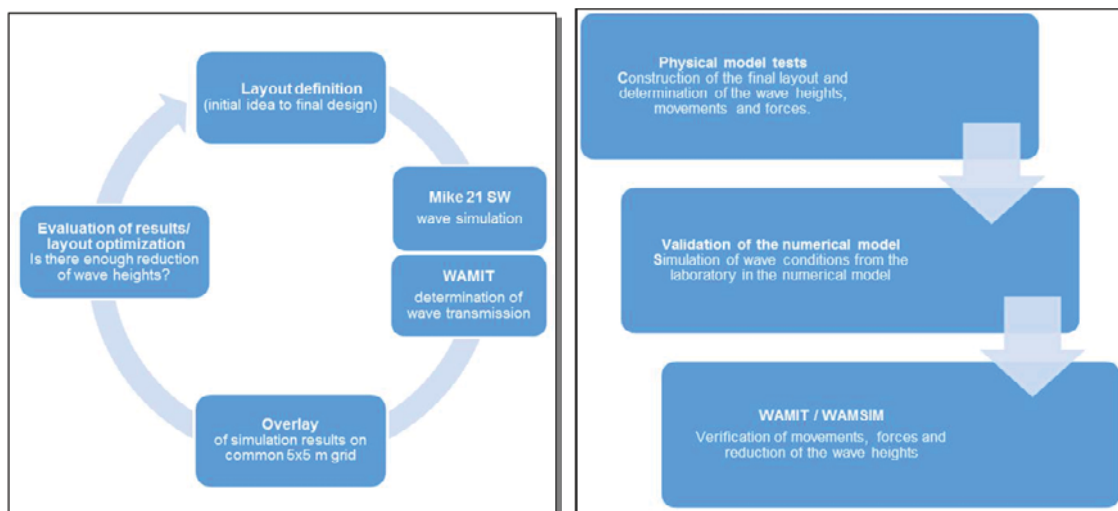


Figure 2: Scheme of Layout optimization (left) and validation of numerical model against physical model test (right)

1.1 Applied Software Products

MIKE 21 SW, a modern spectral wave model was used to determine the in situ wave field. The model simulates the growth, decay and transformation of wind-generated waves and swells in offshore and coastal areas. Model set up included a fully spectral formulation in quasi-stationary mode as the predefined conditions are a time independent design case.

Spectral discretization is of high importance due to the resolution of the wave input parameters and the coupling with WAMIT.

WAMIT, a linear radiation/diffraction panel method code, was used for the numerical model. It solves the interaction of surface waves and offshore structures using the panel method. The part of the structure below mean water level is discretised by quadrilateral panels. Please refer to MIT (2006) for a general description of WAMIT.

The multi-body option in WAMIT was used to evaluate the response of the breakwater, made up of a number of separate pontoons. The possibility to calculate the surface elevation resulting from the combination of incident, scattered and radiated waves was applied to evaluate the ability of the floating breakwater to reflect waves and thereby reduce wave heights behind the breakwater.

2 Optimization of breakwater layout

The floating breakwater was made up of a number of box-shaped pontoons each with a length of 25 m. All single pontoons were held in place by vertical piles (see e.g. Figure 3) and a mooring arrangement that allowed the pontoons to slide up and down the piles. The mooring arrangement was assumed to reduce the horizontal motions (surge, sway and yaw) of the pontoons to almost zero, while it posed no restrictions to the vertical motions (heave, roll and pitch). Resulting from this setup parameters such as width and draft were varied to optimize the layout.

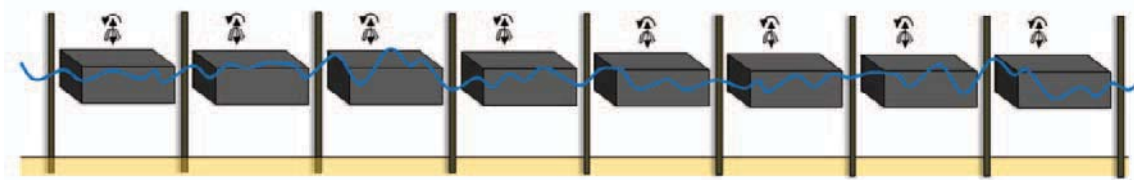


Figure 3: Layout of the final breakwater design: Movement in horizontal direction is fixed.

For the optimization of the breakwater layout a hybrid model was set up. WAMIT was combined with the MIKE 21 Spectral Wave (SW) model to estimate the resulting wave heights for different layouts of the breakwater. Both models work in the frequency domain and the combination was therefore straightforward. The following steps were involved in calculating the wave field around the breakwater:

1. The incident wave field was calculated using MIKE 21 SW in fully spectral, stationary mode. In this mode the incident wave energy was resolved in a number of discrete directions and frequencies. A directional discretization of 10° , resulting in 36 discrete directions, was considered adequate. The relevant wave frequency range was resolved by 22 discrete frequencies. The wave model includes relevant reflection from shore and all fixed structures but not the floating breakwater. The wave model results were stored as 36×22 matrices of wave energy on a 5×5 m grid around the position of the floating breakwater.
2. A multi-body WAMIT model with a given pontoon size and number was set up. The WAMIT model was executed for exactly the same number of discrete directions and frequencies as the wave model described above, i.e. a total of $36 \times 22 = 792$ solutions to the radiation/diffraction problem was obtained. The surface elevation was evaluated for each solution on the same 5×5 m grid for which wave model results were extracted.
3. The resulting energy density S_{res} in a given grid point at the discrete frequency, f_j , was then obtained by:

$$S_{res}(f_j) = \sum_{i=1}^{36} S_{inc}(f_j, \theta_i) \cdot \eta_{i,j}^2 \quad (1)$$

with $S_{inc}(f_j, \theta_i)$ incident wave energy density calculated at discrete frequency, f_j , and direction, θ_i , using MIKE 21 SW

$\eta_{i,j}$ surface elevation evaluated by WAMIT for the discrete frequency, f_j , and direction, θ_i

Integral spectral parameters such as the zero'th order moment wave height, H_{m0} (often referred to as the significant wave height) were obtained by proper integration over the discrete frequencies, i.e.:

$$H_{m0} = 4\sqrt{\int_0^{\infty} S_{res}(f) f^0 df} \quad (2)$$

Significant wave height plots of both incident and resulting waves were produced by solving eq. (2) in all grid points.

Evaluating a different breakwater layout involves repeating steps 2 and 3.

Five runs with different sizes and number of pontoons were simulated to optimize the effectiveness of the floating breakwater. Initially, the breakwater was planned to protect a boat landing located some distance behind the breakwater, as shown in Figure 1. However, during the project execution, it was decided to use the breakwater itself for mooring the pilot boats. At the same time the breakwater was moved closer to the river embankments. The final position can be seen in Figure 4.

Table 1: Results of breakwater layout optimization

Layout [-]	Dimensions [m×m×m]	Number of pontoons	Water depth [m]	Sign. Wave height at the pier H_{m0} [m]
#1	25×10×2,0	11	16.0	1.6
#2	25×10×4,0	11	16.0	1.4
#3	25×25×2,5	13	16.0	1.3
#4	25×25×5,0	13	22.1	1.0
#5	25×25×5,0	8	18.6	1.0

The starting layout (#1) was a simply sheltering structure consisting of 11 pontoons (25 m x 10 m x 2.0 m) that was finally replaced by a structure of 8 pontoons combining the breakwater and pier (#5).

Figure 4 shows the incident and resultant significant wave heights, H_{m0} , around the location of the floating breakwater for layout # 5 exposed to wind waves. The incident waves were directionally spread. The resulting wave heights in front of the breakwater increased relative to the incident wave heights due to wave reflection at the breakwater.

The coordinates in all wave height plots refer to a local coordinate system with x-axis parallel to the breakwater orientation and origin in the centre of the boat landing pier shown in Figure 1. The same origin is maintained also for the revised layout #5.

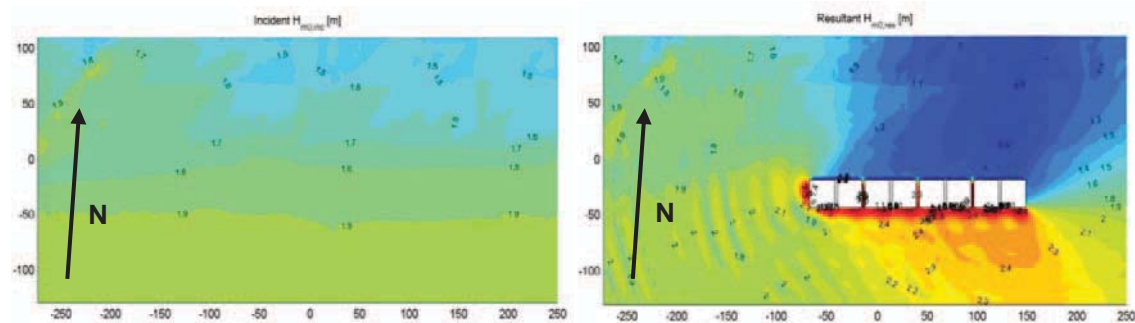


Figure 4: Incident wave field (left, $H_{m0} = 1.8$ m, $T_p = 5.3$ s, $MWD = 250^\circ N$) and resulting wave field (right) – 8 pontoons of 25x25x5 m. Simulation # 5.

3 Physical Model tests

After definition of the final layout of the floating Breakwater (see chapter 2) this arrangement was tested within DHI laboratory in Hørsholm, Denmark.

The important physical properties related to the present model study are inertia and gravitational forces. Therefore, Froude's model law was applied to convert between model measures and prototype measures. The length scale (horizontally and vertically) of the model was selected at 1:35. The choice of scale was made based on the requirements for the tests in question: water depth, wave height, pontoon sizes, etc.

The model consisted of eight pontoons and nine piles as seen in Figure 3. The 3D seabed bathymetry of the river in the model location was not reproduced. This was considered acceptable as the short wind-waves were only influenced slightly by the seabed due to the relative large water depths. Along the edges of the model, a spending beach was established in order to minimise wave reflection from the boundaries of the model (see Figure 5). The spending beach in the laboratory was reflecting about 5-20% of the incident wave energy.

The pontoons had the following dimensions: Width: 25m, length: 25m, height: 7.4m (2.4m freeboard). All pontoons were ballasted to a draft of 5m and 2.5m respectively during the testing. The ballast was placed evenly in the bottom part of the pontoons and consisted of concrete slabs and small lead weights to ensure that each pontoon rested horizontally in the water with the correct draft.

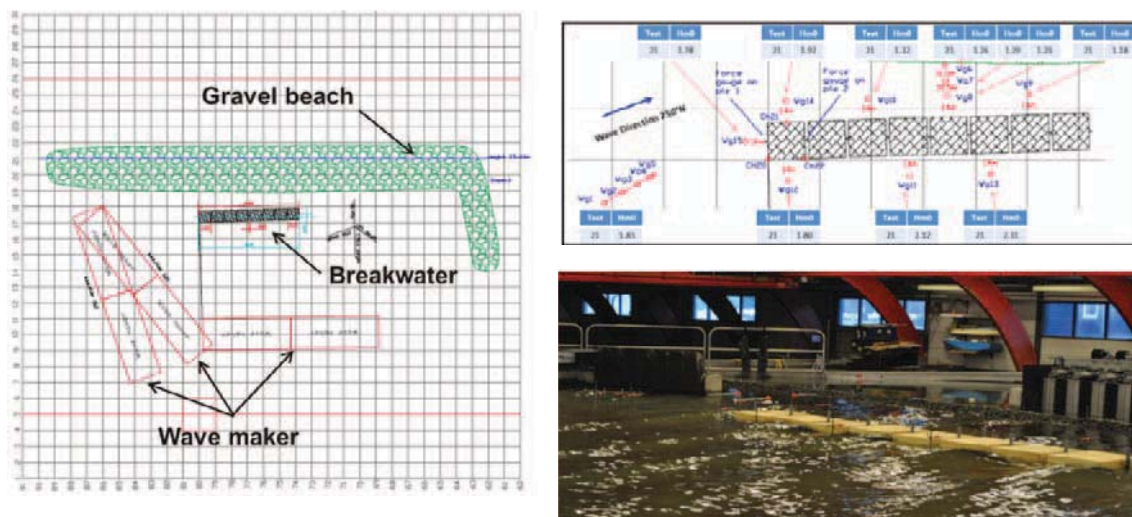


Figure 5: Layout of floating breakwater model in the model basin (plan view, close up and photo)

In order to develop a good test matrix for this study further parameters were varied in this model test:

- Water Level: 11.5 m; 15.75 m
- Pile Stiffness: soft; stiff
- Pontoon Draft: 2.5 m; 5 m
- MWD: WSW 250°; ESE 125°
- JONSWAP spectra; regular waves

A total number of 19 tests were carried out, including one test without breakwater.

Wave heights were measured at a number of locations such that the attenuation effect of the breakwater could be assessed. For the Initial Case with incident waves of $H_s = 1.8$ m, the waves were approximately dampened by the breakwater to 1.3 m at the sheltered locations of WG6 to 10 on the lee side of the breakwater, i.e. a reduction of the incident wave height by approximately 25%.

Tests with a reduced draft (2.5m) resulted generally in larger movements of the pontoons and less attenuation of the waves.

4 Results and Comparison

Comparing the wave heights of the initial numerical approach with the results from the physical tests, wave attenuation from the physical model was smaller. During the test, in which the floating breakwater was removed, it was observed that - in spite of an absorbing surface of the surrounding rubble berms - wave reflection off the basin's fringes was not negligible. Whereas in the original numerical simulation no reflection occurred due to the more slightly decreasing water depths. For more exact comparison of both models an updated spectral wave model was set up in which the reflection coefficient of the berm boundary was increased until similar wave heights were obtained in the numerical model as observed in the physical model. The resulting wave field and a comparison with measured wave heights in the physical model are shown in Figure 6. The variation between simulated and measured wave heights as initial Wave field was in the order of $\pm 5\%$ except for WG 13 where the difference yielded at 10%.

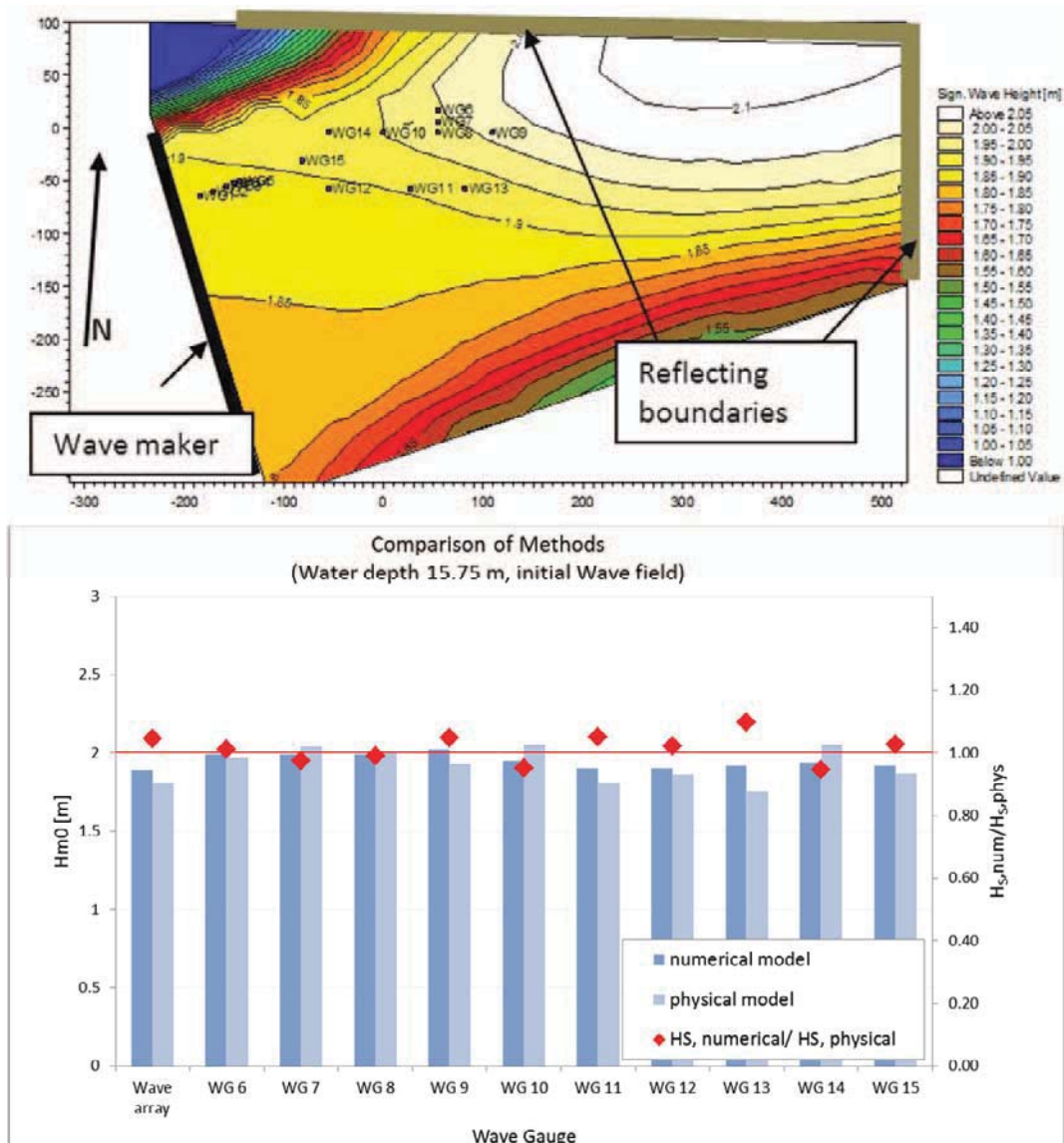


Figure 6: Wave heights from physical model tests for wind waves with reflecting north and east boundaries. Reflection coefficient = 0.4 (top); comparison of wave heights for numerical/ physical model (bottom)

Seven additional runs with different conditions (Table 2) were tested in the numerical model applying the incident wave field shown in Figure 6.

Table 2: Test runs of breakwater layout optimization

Run (Layout 5) [-]	Draft [m]	Water Depth [m]	Free horiz.Motion [-]
6	5.0	18.6	no
7	5.0	18.6	yes
8	2.5	18.6	no
9	2.5	18.6	yes
10	5.0	11.5	no
11	5.0	15.75	yes
12	2.5	15.75	yes

The physical model allowed for small horizontal motions of the pontoons, mainly because the lines connecting the mooring ring and pontoon had a little slack, but also, especially in the case of soft piles, due to pile deflection. In order to investigate the importance of the horizontal motions, some of the numerical simulations were carried out allowing no horizontal motions (surge, sway and yaw), while others were carried out without restrictions on the horizontal motions.

The calculated wave heights with the adjusted wave field are compared to the wave heights measured in the laboratory (see Figure 7).

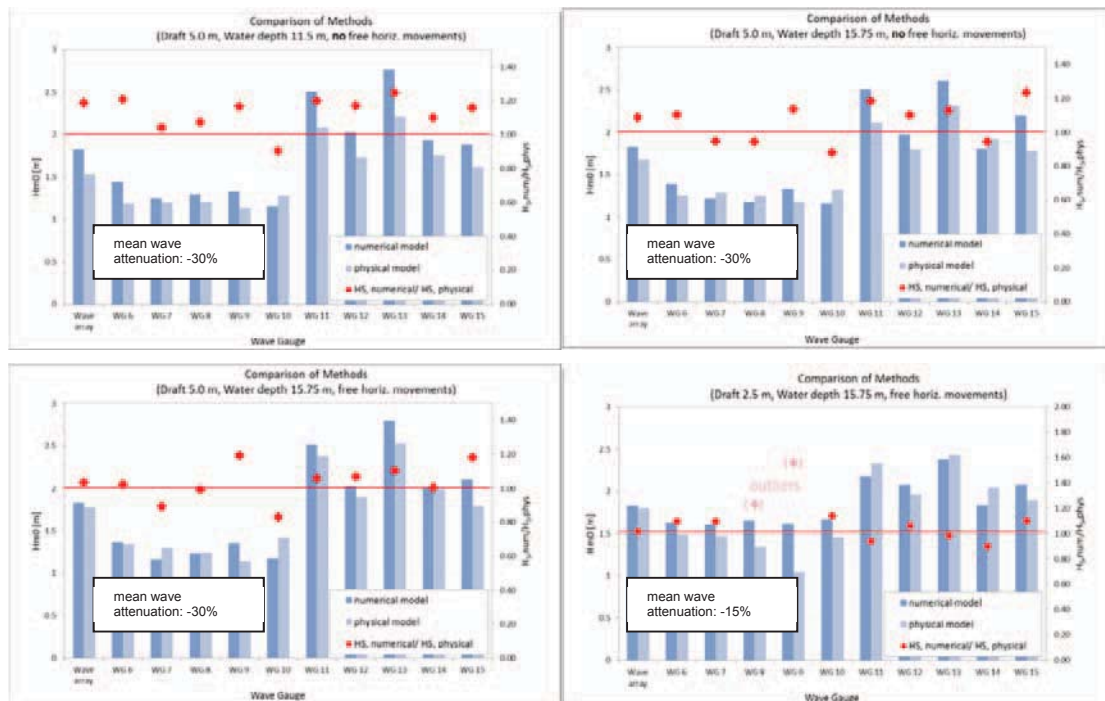


Figure 7: Resulting wave heights for comparable output points

It was difficult to verify the results of numerical and physical models in a quantitative way. The quality of test results was significantly influenced, i.e. wave reflections within the basin (formation of nodes and antinodes), reflections from the floating wave breaker itself (increasing with draft) and difficulties to model the correct pile stiffness.

The feasibility of exact the same conditions and mooring connection in numerical and physical models was limited, therefore significant differences between simulated and measured wave

heights could be found. Nevertheless the ratio between $H_{S,num}/H_{S,phys}$ showed, that the numerical results slightly overestimate the measured wave heights (less than 20%) and therefore provides a rather conservative “image”.

Within the given scope the following tendencies can be drawn as they reflect in the results of numerical and physical model tests:

- small or no dependence on different water depths (deep water conditions)
- reflection from the floating wave breaker caused a standing wave in front of it and therefore higher wave heights at locations of WG 11, 12, 13, 15
- the overall wave attenuation was in the order of 15 - 40%
- wave attenuation depends significantly on the pontoon draft

5 Summary and Conclusion

Originally, benchmarking the numerical model against physical model tests showed that in general the wave attenuation was smaller in the physical model compared to the numerical model. It was found that some of the wave energy behind the breakwater in the physical model resulted from wave reflections from the physical model boundary, and not necessarily wave energy transmitted directly through the breakwater. An attempt was made to compensate for this wave reflection in the numerical model by calibrating the wave reflection in the numerical model with laboratory measurements from a wave run without floating breakwater. The wave heights from numerical simulations with this calibrated wave field agreed well with the physical model test results (see Figure 6).

The fact that the waves were unidirectional led to large local differences in the resultant wave field as the diffracted and reflected waves mixed with the incident waves and created standing waves. The large local differences also added to the uncertainty, as a small offset in the positioning of wave gauges or small differences between targeted and achieved wave periods might have affected the results significantly.

The required wave conditions behind the breakwater could be reached, but only barely. A reduction of wave heights of about 40% was possible. In spite of all optimizations the dimensions of the floating breakwater would result in a large and uneconomic structure for the given initial conditions and requirements. So as a consequence the exposed position of the harbour was discarded.

Additional work that was not reported in this paper was carried out on wave induced movements and forces (using the “moored ship” simulation package WAMSIM), as well as on ship wake influencing the design case.

It is concluded that the calibrated numerical models were capable of providing good estimates of the wave transmission properties of the floating breakwater. Detailed modelling of an actual design using time domain simulations is likely to support the structural design of the device and its mooring piles.

6 References

- DHI (2011) Floating Breakwater Brunsbüttel, 3D Physical Model Tests, 20 January 2011, DHI Ref. 14800466-2
- DHI (2009a) “MIKE 21 SW: Spectral Waves FM Module, Scientific Documentation”, Hørsholm, Denmark.
- DHI (2009b) “MIKE 21 SW: Spectral Wave Module, User Guide”, Horsholm, Denmark.
- MIT (2006) User Manual. www.wamit.com
- PIANC (1994) Report of Working Group no. 13 - PTC II - Supplement to Bulletin N° 85 Floating Breakwaters – A practical guide for design and construction.

Run-up over variable slope bottom. Validation for a fully nonlinear Boussinesq-type of model.

Antonino Viviano¹, Carlo Lo Re², Luca Cavallaro³ and Enrico Foti⁴

Abstract

The cross-shore profile usually presents different slopes also because of infrastructures and coastal protection works. Such kind of a bottom profile has been first studied by means of a physical model considering monochromatic incident waves and two consecutive slopes of 10 and 30 degrees with respect to the horizontal plane. The main outcomes of such a model are the wave heights at the toe of the beach and the corresponding maximum run-up. The same wave conditions have been then studied numerically in order to validate the code in presence of both variable and high slope bottom case. In particular, the adopted Boussinesq-type of model manages the breaking by the roller concept and the shoreline motion is estimated by the solution of the Lagrangian shoreline equations together with a linear extrapolation of variables in the dry region. The comparison of the experimental and numerical maximum run-up shows a fairly good agreement, except for the case corresponding to very steep wave conditions.

Keywords: wave, variable bottom, physical modelling, numerical modelling, run-up, shoreline motion

1 Introduction

The interaction of waves with the coast produces a great number of effects which influence at a large extent the human activities near the sea. The main problems are caused by the erosion of beaches and the inundation of the land behind the coastline. As a matter of fact, these two effects are correlated; indeed the beach represents the first line of defence against extreme waves, therefore the erosion enhances coastal flooding with more and more frequencies also due to the climate changes. For such a reason, the eroded coasts are usually object of coastal protection works, i.e. construction of structures, and/or of sand nourishment. In both cases the cross-shore profile of the coast is strongly modified and typically presents several ranges with variable slopes which make the studies of run-up and overtopping and, in turn, of the coastal risk mapping difficult to be performed.

Several authors have studied the run-up and overtopping of coastal structures and beaches. Pullen et al. (2007), for example, collected a wide series of experiments and provided several formulae for the maximum run-up covering also the case of variable sloping bottom. The same authors have also inserted all their experimental data in a neural network code which can be used for the cases falling out the limit of applicability of the proposed formulae. However, the use of such a formulation represents an empirical approach to the problem and it is not correlated to the physical phenomenon of the wave approaching a slope.

In this framework, the present contribution aims at validating the physically based Boussinesq-type of model of Lo Re et al. (2011) for the variable slope bottom case. More in details, an analysis of the mentioned code has been performed when complex bathymetries characterized by high slopes are present. To this aim a comparison with the experimental results obtained by Cavallaro et al. (2001) about wave run-up over variable bottom slopes has been carried out.

¹ Department of Civil and Environmental Engineering, University of Catania, Viale Doria 6, 95125 Catania, Italy, nino.viviano@gmail.com

² Department of Hydraulic Engineering and Environmental. Application, University of Palermo, Viale delle scienze ed.8, 90128 Palermo, Italy, lore@idra.unipa.it

³ Department of Civil Engineering, University of Messina, Contrada di Dio, 98166 Messina, Italy, lcavallaro@ingegneria.unime.it

⁴ Department of Civil and Environmental Engineering, University of Catania, Viale Doria 6, 95125 Catania, Italy, efoti@dica.unict.it

2 Experimental set-up

The experiments have been carried out at the Hydraulics Laboratory of the Department of Civil and Environmental Engineering of the University of Catania. The wave flume, shown in Figure 1, is 18.0 m long, 3.6 m wide and 1.2 m high. It has lateral glass walls. Regular and irregular waves are obtained by means of a flap-type wavemaker which is located to the end of the wave flume and driven by a pneumatic system (electronically controlled).

On the opposite side of the flume an aluminium beach profile was built. The first stretch of the beach profile was characterized by a slope 1:5.76 for the first 1.44 m, followed by a stretch with a slope 1:1.7 and 0.17 m length, and then by a sub-horizontal stretch with a slope 1:32.

In order to detect the wave transformation along the beach profile, three resistive wave gauges have been placed along the profile itself, respectively located at 8 cm, 40 cm and 80 cm from the beginning of the beach profile. The wave run-up was detected with a measuring strip glued at the bottom and a video camera.

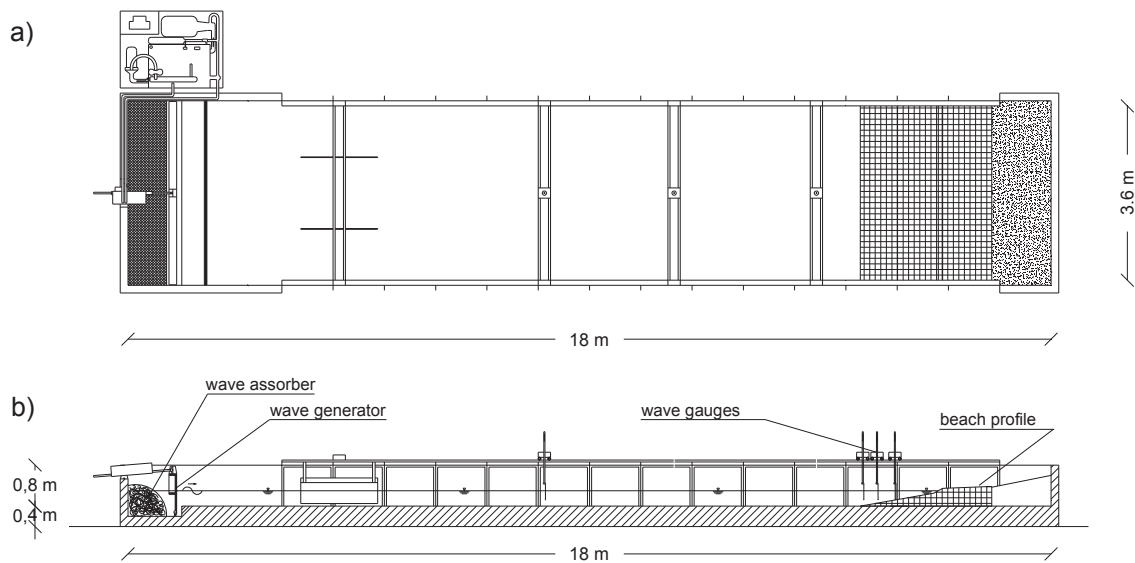


Figure 1: Experimental set-up: plane view (a), section (b).

3 The numerical model

3.1 Main characteristics

The governing equations of the proposed Boussinesq-type of model are solved in the $\zeta - \bar{u}$ form, where ζ is the free surface elevation and \bar{u} is the depth-averaged horizontal velocity. The values of the variables ζ and \bar{u} are determined within the entire wet domain, while at the shoreline the Lagrangian horizontal velocity of the shoreline itself u_s and the horizontal coordinate of the shoreline position ξ are evaluated by solving the equations which describe the shoreline motion, as will be discussed below. The flow within the surf zone is faced by means of the roller concept; in particular by adopting the hydraulic similarity of breaking waves and low Froude number hydraulic jumps. The continuity and the momentum equations are not reported, the reader is referred to the work of Musumeci et al. (2005) for the analytical details of the derivation.

It is worth pointing out that the momentum equation contains the so called 'breaking terms', since they make it possible to account for the excess of momentum flux induced by the presence of the breaking waves. In particular, such terms are functions of the breaking generated vorticity, which is assumed to be injected within the domain by the presence of the surface roller.

Finally, the fully nonlinearity of the equations makes it possible to obtain better shoaling properties. This characteristic is crucial for a proper prediction of the breaking point and an accurate modelling of both the transition and the inner surf zones, as it has been better specified by Musumeci et al. (2005).

The governing equations do not take into account the energy and the momentum dissipation due to the turbulence generated at the seabed. Indeed the model was derived specifically to solve wave propagation within the surf zone, where, in energetic terms, this dissipation is smaller than that generated by the breaking process. However, bottom friction is expected to have a major influence into the swash zone, and its influence should increase near the shoreline. Therefore the classical quadratic turbulent definition of bottom friction was implemented (Lo Re et al., 2011).

3.2 The shoreline model

The treatment of the shoreline motion is a critical issue in Boussinesq models since the numerical algorithm has to discriminate between the wet part of the computational domain, where calculations of the governing equations are required, and dry points more onshore, where no wave motion is defined. Although widely used, porous beach approaches are very far from simulating the interesting physics of the swash zone hydrodynamics, since the governing continuity and momentum equations cannot be rigorously satisfied.

In the present paper the approach by Lo Re et al. (2011), which tries to describe the physics of the swash zone hydrodynamics by solving the Lagrangian equations of the shoreline motion, is used. More in details, at the shoreline, where the water depth goes to zero, the volume fluxes also become zero, but the velocity of the fluid particles, which can be calculated by dividing the fluxes by the total water depth, are in general different from zero. However, such a velocity cannot be calculated by using the depth-integrated Eulerian equations of motion as the water depth is zero at the shoreline.

Therefore Lo Re et al. (2011) used specific physically based equations to calculate the velocity of the shoreline and the shoreline position, which can be solved once the velocities in the remaining (wet) domain are known. In particular, the kinematic condition at the shoreline states that the fluid particles at the shoreline remains at the shoreline. For the one-dimensional case, by following a Lagrangian approach, the x-coordinate of the shoreline is only function of time, i.e. $\xi = \xi(t)$. This implies that the material derivative of ξ must be equal to the shoreline velocity. In formulas:

$$\frac{d\xi}{dt} = u_s \quad (1)$$

In order to close the problem, the momentum equation at the shoreline must be also considered. Such an equation can be derived by assuming a ballistic approach, i.e. the acceleration of the shoreline is forced by the effect of gravity on the wave moving on the beach slope and is dumped by the friction forces F^{fric} , particularly at the bottom. In dimensional form the shoreline equation reads

$$\frac{du_s}{dt} = -g \left. \frac{\partial \zeta}{\partial x} \right|_s + F^{fric} \quad (2)$$

where $\left. \frac{\partial \zeta}{\partial x} \right|_s$ is the derivative of the surface elevation evaluated at the shoreline. It must be specified that the eqs. (1)-(2) are solved in such a way that the moving shoreline is not bounded to the numerical grid and it can continuously change its position on the beach. In this way, the position of the onshore boundary of the wet domain, where the continuity and the momentum equations of the Boussinesq model are solved, is determined based on the new position of the shoreline. Moreover, the numerical integration scheme used for the solution of both Boussinesq governing equations and eqs. (1)-(2) requires the knowledge of the values of the surface elevation ζ and of the depth-averaged horizontal velocity u not only within the wet domain but also in the dry domain, onshore of the shoreline itself. Such a value cannot be physically defined. In particular, in the model here used, the extrapolation is performed by considering the

velocity u_s and the surface elevation ζ_s calculated at the shoreline along with the last two wet points on the numerical grid. The approach is similar to the one used also by Lynett et al. (2002), although in the present case the variables at the shoreline are determined by means of the shore line equations (1)-(2), whereas in Lynett et al.'s work, the shoreline is bounded on the uniform fixed numerical grid and its position is determined simply through a minimum water depth criterion. It is worth mentioning that a special attention has been devoted in the used model to the treatment of the friction term within the swash zone, close to the shoreline, the friction term at the wet points of the domain is schematized at both stages of swash motion. However, when the value of F^{fric} becomes too large, due to the small value of the total water depth, a threshold is used.

3.3 Simulated conditions

The above Boussinesq-type of model has been applied for the estimation of shoreline position and velocity in a case in which the bottom is constituted by two flat parts with different slopes. The geometry follows the experimental setup described before in which the highest slope part is placed in the emerged beach and the slope change is located near the mean water level position.

The incident waves are monochromatic, as they are in the corresponding experimental model. In particular, in order to avoid the overtopping of the high slope part (see Figure 2), only a portion of the available experimental cases have been considered, as it is summarized in Table 1. The reason of such a choice is related to the will of analyze the effect of one slope change rather than more contemporaneous effects.

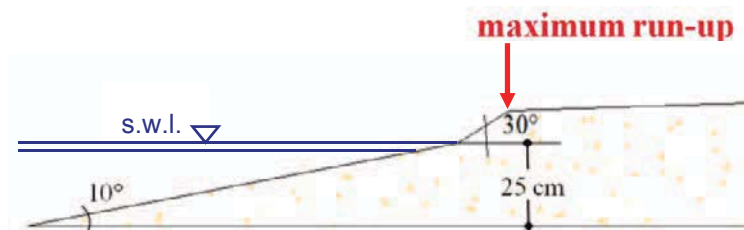


Figure 2: Sketch of the bottom profile with indication of the slope angles and of the maximum run-up position for all the numerical cases.

Table 1: Selected experimental cases adopted for the validation of the numerical code: h_0 is the still water depth, T and H are the wave period and height respectively.

Exp #	h_0 [cm]	T [s]	H [cm]
3	25	0.91	2.57
4	25	0.77	3.88
5	25	0.67	5.52
14	22	0.67	7.70
15	22	0.71	7.06
16	22	1.00	8.60

The experimental cases chosen for the numerical simulations have the maximum still water depth equal to 22 cm or 25 cm, the wave period of the monochromatic waves are in the range 0.67-1.00 s and the wave height are between 2.57 cm and 8.60 cm.

It is worth pointing out that for each numerical simulation the wave height has been extracted in the point at which the probe was located in the corresponding experiment. Therefore a comparison between physical and numerical modeling is available in such point and the input wave for the numerical code can be obtained after some iterations.

4 Results

4.1 Maximum run-up comparison

The applied numerical code represents a combination of a Boussinesq-type of model with a shoreline model. In particular, the first model gives the input condition for the solution of the shoreline equations. In the present application the results of the Boussinesq model along the domain have been used for ensuring the same wave conditions of the experimental data, since the high slope of the bottom causes the presence of reflection effects. On the other hand, indication about maximum run-up can be extracted from the obtained shoreline motion, in such a way this numerical result can be compared with the corresponding experimental data.

The validation of the applied model, by the comparison with the measured maximum run-up, has been carried out for the six experiments selected before having variable still water depth at the toe of the beach and variable wave characteristics, in terms of height and period. In order to match together such geometrical and wave characteristics, the wave slope H/L has been calculated for each experiment, where H is the previous analyzed wave height and L is the wave length at the water depth h_0 , estimated by the linear dispersion relation.

The results of the validation for the numerical model are summarized in Table 2 and Figure 3 in which the relative error is also present. Such error has been estimated by considering the difference between measured and estimated maximum run-up, called respectively R_{num} and R_{exp} , and then by dividing such a value by the measured run-up.

The presented results show a great variability in the error of the estimated maximum run-up, ranging between 0 to 21.8 %. In particular, it has been obtained that the error increases with the wave slope. Indeed such error is almost zero for wave slope equals to 0.02 while it increases dramatically for H/L greater than 0.1, i.e. for very steep waves. In the analyzed cases only one time the error is greater than 10 % (Experiment number 14), for all the other cases there is a fairly good match between numerical and experimental data. In particular, half of the analyzed cases have wave slope less or equal to 0.07 and relative error less than 2.2 %.

Table 2: Comparison of the maximum run-up between experimental data, R_{exp} , and numerical model results, R_{num} ; for each case the wave slope H/L and the relative error are also present.

Exp. #	H/L [-]	R_{exp} [cm]	R_{num} [cm]	err [%]
3	0.02	5.24	5.24	-
4	0.04	5.43	5.33	1.8
5	0.08	6.42	6.97	8.6
14	0.11	8.58	6.71	21.8
15	0.09	7.18	7.86	9.5
16	0.07	8.00	8.17	2.1

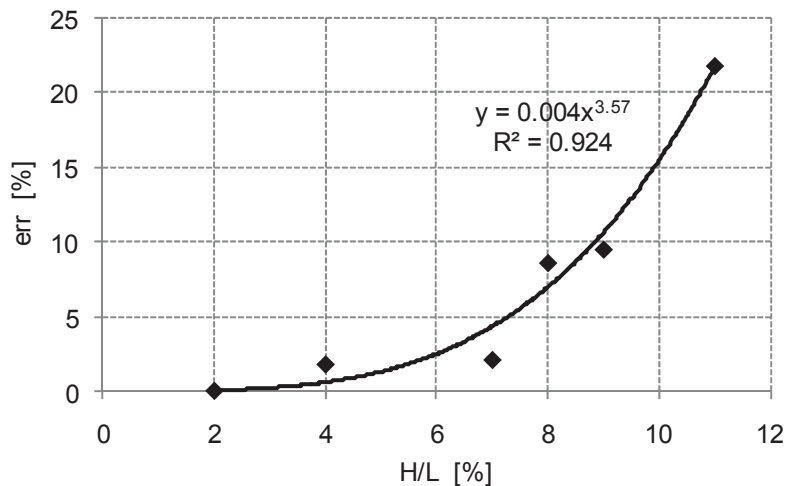


Figure 3: Relation between the wave slope (H/L) and the relative error (err) of the numerical code: the diamonds represent the simulated cases, the black curve is the obtained trend line. The corresponding formula and the coefficient of determination (R^2) are also showed.

4.2 Shoreline position and velocity

Since the maximum run-up has been estimated quite well by the applied numerical model, it is possible to assume that such model simulates in a correct way the actual phenomena related to the wave propagation over a bottom profile having parts with different slopes, included the shoreline motion. This assumption is supported by the results of Lo Re et al. (2011) for monochromatic waves approaching a single slope bottom. In particular, they obtained a fairly good matching of the shoreline position and velocity behaviour in time in comparison to other numerical and analytical formulations.

For the reasons discussed above, here the shoreline position and velocity have been analyzed in time for the variable slope bottom case in order to extract information about the behaviour of shoreline motion both in swash and back swash phases. In particular, in Figure 4 the results for the case number 3 have been showed, together with indication of swash and back swash phases, maximum run-up and minimum run-down.

The analysis of such results shows that the horizontal position of shoreline (ξ) is quite symmetrical for swash and back swash phase, with a behaviour that appears similar to the single slope case. The horizontal velocity of the shoreline (u_s) shows a different behaviour between the two phases of shoreline motion. In particular, in the back swash phase a relative maximum of velocity is present which is surrounded by two minima. Such maximum of velocity appears when the shoreline position passes through the still water level, where the slope change is located, so underlining a possible correlation.

In such a framework it is more difficult to understand why the velocity in the swash phase seems to be not affected by the presence of slope change. A possible explanation is related to the fact that the higher slope part is placed immediately after the still water level. For such a reason, the shoreline motion is similar to the single slope case during the swash, instead during the back swash part of the water is accumulated near the slope change so decreasing the absolute value of velocity. Such an effect corresponds to a relative maximum during the back swash phase (see Figure 4.b) because the velocity is considered negative if it is directed seaward.

The results showed for the case number 3 of the experiments provide a similar behaviour to those of the case number 4, for which the wave slope is less than 0.05; instead for the other cases no relative maximum is present during the back swash phase, probably because the more important presence of wave breaking than previous cases gives rise to a turbulent motion which nullifies the effects of the slope change.

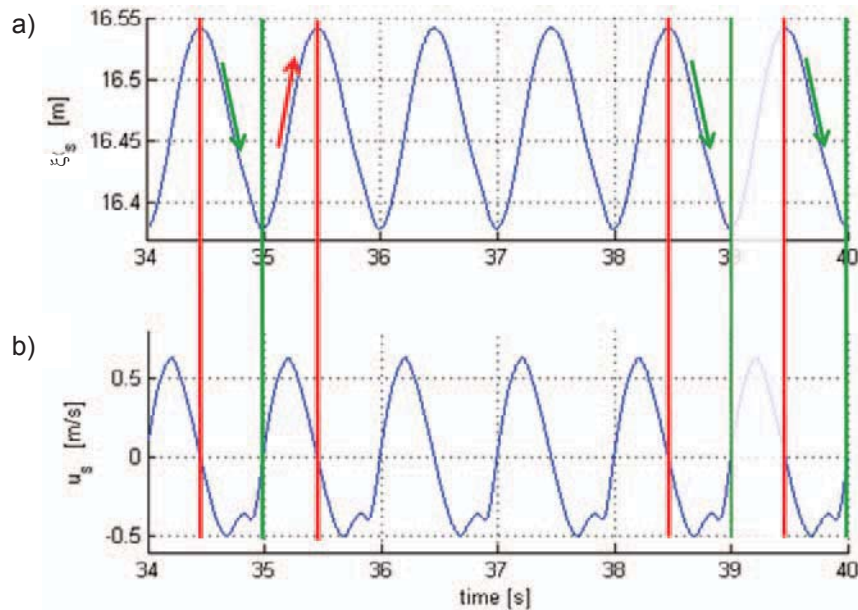


Figure 4: Shoreline position (a) and velocity (b) in time for the case number 3 of the experiments; the vertical lines indicate the maximum run-up and the minimum run-down, alternately; the upward arrow indicates the swash phase while the downward one the back swash phase.

5 Conclusions

In the present work the validation of a Boussinesq-type of model has been carried out by means of comparison with laboratory experimental data. In particular, the validation has been considered in presence of a very complex bottom bathymetry in order to analyze advantages and limits of the numerical code.

The applied Boussinesq-type of model considers rotational motion under breaking waves. Such model presents also the shoreline Lagrangian equations which are solved along with a linear extrapolation of variables out of the wet region. Due to the presence of high reflective bottom, the incident waves for the numerical model have been found iteratively by considering the same wave height of the experiments at the toe of the slope.

The incident waves are monochromatic with wave slope that ranges between the values 0.02 and 0.11. The comparison between physical and numerical model shows a fairly good agreement in terms of the maximum run-up, excepted that for very steep waves ($H/L=0.11$). In particular, the differences between computed and measured run-up increase with wave slope. However, for typical sea waves, i.e. for $H/L < 0.08$, there is a maximum error of about 2%.

Going to the analysis of shoreline motion in time, the cases no. 3 and 4 have been studied because the wave slope is less than 0.05 and then the relative error of the maximum run-up is minimum. In such cases the shoreline velocity shows a relative maximum during back swash, such an effect is related to the presence of the higher slope part immediately after the still water level. This last outcome is probably due to the fact that during back swash part of the water is accumulated in the groove over the point of slope change. However such peculiar behaviour should be deeply investigated in future works.

6 Acknowledgements

This work has been partly founded by the Project PRIN 2008, titled: "Operative instruments for the estimate of coastal vulnerability in the presence of sandy beaches also in the presence of coastal structures", founded by the Italian Ministry of education, University and Research.

7 References

- Cavallaro, L., Faraci, C., Foti, E., Giarrusso, C., Pugliese Caratelli, E. (2001): Il run-up su spiagge e su strutture ad alta pendenza con l'algoritmo McCormack-TVD. *L'Acqua*, 3, 2002, ISSN 1125-1255.
- Lo Re, C., Musumeci, R.E., Foti, E., (2011): A shoreline boundary condition for a highly nonlinear Boussinesq model for breaking waves, *Coastal Engineering*, In Press, ISSN 0378-3839, DOI: 10.1016/j.coastaleng.2011.08.003.
- Lynett P.J., Wu T., Liu P.L., (2002): Modeling wave runup with depth-integrated equations, *Coastal Engineering*, Volume 46, Issue 2, July 2002, Pages 89-107, ISSN 0378-3839, DOI: 10.1016/S0378-3839(02)00043-1.
- Musumeci, R.E., Svendsen, I.A., Veeramony J., (2005): The flow in the surf zone: a fully nonlinear Boussinesq-type of approach, *Coastal Engineering*, Volume 52, Issue 7, July 2005, Pages 565-598, ISSN 0378-3839, DOI: 10.1016/j.coastaleng.2005.02.007.
- Pullen, T., Allsop, N.W.H, Bruce, T., Kortenhaus, A., Schüttrumpf, H., van der Meer, J.W. (2007): Eurotop. Wave Overtopping of Sea Defences and Related Structures: Assessment Manual. www.overtopping-manual.com. ISBN 978-3-8042-1064-6.

Influence of current and wind on wave run-up on slopes

Antje Bornschein¹, Stefanie Lorke² and Reinhard Pohl¹

Abstract

The freeboard design of levees and dams is important for the safety of the structures itself as well as of the land protected by them. The paper discusses new aspects which came up recently during the analysis of wave run-up tests with oblique wave attack under the influence of longshore current and onshore wind. These tests considered sea state according to a JONSWAP-spectrum. Results considering oblique wave attack confirm former empirical investigations. Outcomes regarding onshore wind influence differ from those obtained in tests with monochromatic waves. No significant effect on wave run-up in case of a dike parallel current and a perpendicular wave attack was obtained.

Keywords: wave run-up, wave-current interaction, onshore wind, oblique wave attack

1 Introduction

Data required for freeboard calculation are hydrological data (like design water level in a river, at a sea coast or in a reservoir as a result of a flood event or high storm tide), meteorological data (wind velocity, duration and direction) and structure related data (e.g. slope of the construction surface upstream or on the sea side). The computation routine includes the estimation of the height of incident waves and wind set-up, wave run-up calculation and the determination of freeboard height regarding additional safety aspects.

The Guideline 246/1997 of the German Association for Water, Wastewater and Waste (DWA) is widely used in freeboard design in Germany. The calculation procedure of the German Freeboard Design Guideline was established considering still water bodies like lakes or reservoirs. It has to be discussed if it is appropriate to use it for rivers with wide floodplains or estuary dikes with considerable dike parallel currents and onshore wind.

2 Wave-current interaction

If a harmonic wave travels in a water area with a current its frequency and amplitude may change. Due to the bodily transport of the wave by the current the energy transport is no longer normal to the wave crest. Some energy propagates parallel to the wave crest. According to the general calculation formula for the wave run-up height (Hunt 1959):

$$R = C \cdot \sqrt{H \cdot L} \cdot \tan \alpha \quad (1)$$

with R wave run-up height [m]
 C coefficient [-]
 H wave height [m]
 L wave length [m]
 $\tan \alpha$ dike slope [-]

there should be an impact on the wave run-up height too if the wave length and the wave height are transformed.

¹ Institute of Hydraulic Engineering and Applied Hydromechanics, Technische Universität Dresden, 01062 Dresden, Germany, antje.bornschein@tu-dresden.de

² Institute of Hydraulic Engineering and Water Resources Management, RWTH Aachen, Kreuzherrenstraße 7, 52056 Aachen, Germany, lorke@iww.rwth-aachen.de

The following ways of interaction between wave and current are possible and are stated here as hypotheses. They are focused on the change in wave height. On a first thought it seems that a current causes only a displacement of every single water drop parallel to the wave crest. Characteristic wave parameters like wave period and wave height would not change and no influence of longshore current on wave run-up would be detectable. But if one considers in a second thought that the current causes a deflection of every water particle moving in circular paths, than every particle would move along a helix and has to travel a longer distance which would cause an additional energy loss and a lower wave run-up. If we consider a sea state we can distinguish further between its bigger and smaller waves. Particles in a longer wave would have to move in a less stretched helix as particles in a smaller wave because the pitches of the two helices would be proportional to the current and its diameters are equal to $2 \cdot H$. The wave run-up analysis is focused on larger waves and the according value of $R_{u2\%}$ - the wave run-up height which would be only exceeded by 2 % of the incoming waves. These considerations together lead to a less significant effect on $R_{u2\%}$.

But it is also possible that the current provides additional energy and this increases the wave energy and affects a higher wave run-up. The maximum attainable wave run-up height is equal to the kinetic energy head of the current ($v^2/(2g)$). A component of the current in wave direction may also increase the wave run-up velocity and leads to a higher wave run-up.

The change of the angular frequency and the connected parameters as wave period and wave length can be calculated according to Holthuijsen (2007). Considering a constant current the linear wave theory is still valid and the following relationship between the relative and absolute angular frequency can be stated:

$$\omega_{abs} = \omega_{rel} + k_{rel} \cdot v_{\beta} \quad (2)$$

- with
- ω_{abs} absolute angular frequency [1/s]
 - ω_{rel} relative angular frequency [1/s]
 - k_{rel} relative wave number $k = 2\pi/L$ [1/m]
 - v_{β} component of the current normal to the wave crest [m/s]

The absolute angular frequency can be derived from measurement data of the wave period obtained by measurement devices fixed to a river bed, sea ground or a basin bottom in a hydraulic model set-up.

$$\omega = \frac{2\pi}{T} \quad (3)$$

- with T spectral wave period [s]

Assuming deep water wave conditions the related parameters are defined as:

$$\omega = \sqrt{g \cdot k \cdot \tanh(k \cdot d)} \quad (4)$$

$$L = g \cdot \frac{T^2}{2\pi} \quad (5)$$

- with
- g acceleration due to gravity [m/s²]
 - k wave number [1/m]
 - d water depth [m]
 - L wave length [m]

If there is a component of the current in the direction of wave propagation the wave length would increase which leads to a higher run-up according to equation (1) and vice versa. If the component of the current in wave direction is equal to zero (the wave propagates in a perpendicular direction relative to the current) there would be no change in wave length. But

there would be still a change in the direction of wave energy transport, because some energy would propagate parallel to the wave crest.

3 Wave run-up and onshore wind

The influence of onshore wind on wave run-up is a much younger research topic than current-wave-interaction. One reason might be that it is more complicated to transfer the results of physical model tests into prototype conditions because the scaling laws of Froude (wave propagation, wave run-up), Reynolds (shear forces) and Weber (interface between water and air) do not correspond and cannot be fulfilled in one model set-up. Nevertheless it is commonly assumed that onshore wind has an increasing effect on wave run-up. Single reasons for that are that onshore wind pushes the water up the slope and the velocity in the wave run-up tongue increases. In addition the effect of downwash on the subsequent wave might be reduced. Other changes can be distinguished in the breaking process. Wind induces an earlier breaking of the waves and a change of the breaking type as well as of the breaking point on the slope. These effects have been summarized but could only partly be quantified by González-Ecrivá (2006).

Different hydraulic model tests were conducted to investigate the influence of wind on wave run-up (e. g. Ward et al. 1996, Medina 1998). The chosen facilities were flumes and monochromatic waves were studied. Wind speed created by wind machines ranged between 6.5 and 16 m/s. Whereas Ward et al. (1996) studied single slope structures the investigation of Medina (1998) considered complex breakwater cross sections and the wave run-up was observed e.g. at a vertical wall on the crest. In general it was found that lower wind speeds ($w < 6$ m/s) have no significant effect on wave run-up whereas higher wind speeds increases the wave run-up height substantially. This effect can be observed on smooth as well as on rough slope surfaces. In the case of flatter slopes the increasing effect is less. Ward et al. (1996) stated a linear increase of the equivalent wave run-up height (maximum wave run-up adjusted for the increase in still water level due to onshore wind) with the incident wave height for wind speed > 12 m/s. But if the wind induces wave breaking before the waves reach the test structure the wave run-up decreases with increasing incident wave height.

The OPTICREST-project was focused on storm induced wave run-up and collected prototype measurement data as well as model test results (de Rouck et al. 2001). Two prototype locations the Zeebrugge Breakwater (Belgium) and the Petten Sea-Defense (Netherlands) were investigated. While the first structure is a rubble mound breakwater the measured wave run-up height is strongly influenced by the permeability and the roughness of the slope surface. The second structure is a dike with a smooth impermeable surface but a berm and a long shallow foreshore. Mainly the foreshore has a significant influence on the measured wave run-up height. Most of the model tests did not include a wind generation. Also the conformity between physical model and prototype was ensured by applying the wave spectra measured in the prototype. Altogether these measurement results are not appropriate for comparison with the FlowDike model tests.

González-Ecrivá (2006) found that wind increases the energy of the wave spectrum slightly but no differences in the spectral width could be distinguished.

4 Model tests and data processing

To investigate the influence of oblique wave attack, dike parallel currents and wind two model test series were conducted at the laboratory of the Danish Hydraulic Institute (DHI) at Hørsholm, Denmark in January and November 2009. Figure 1 gives an overview of the model set-up. Lorke et al. (2010) have presented the model set-up in more detail.

The model tests include a 1:3 sloped dike as well as a 1:6 sloped dike. The wave run-up was measured by a capacitive wave gauge fitted to a 2 m wide wave run-up board and recorded in addition by a digital video camera.

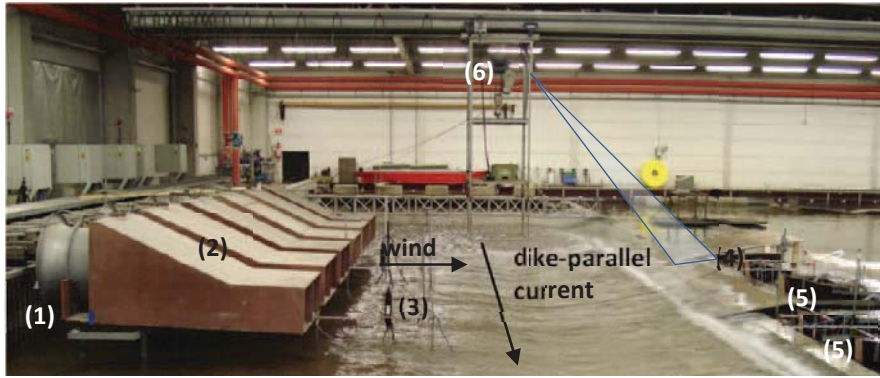


Figure 1: Model set-up in DHI laboratory in Denmark with wave maker (1), wind generator (2), wave gauges (3), run-up board with capacitive gauge (4), overtopping measurement units (5) and video camera (6).

The model set-ups were constructed to investigate different sea states (JONSWAP-spectra) with significant wave heights between 0.05 and 0.15 m and peak periods between 1.04 and 2.16 s. An oblique wave attack ($\beta = 15^\circ, 30^\circ, 45^\circ$) was considered in order to compare the measured data with former results. In addition the influence of an onshore wind perpendicular to the dike crest (1:3 sloped dike: $w = 5$ m/s and 10 m/s; 1:6 sloped dike: $w = 4$ m/s and 8 m/s) and a dike parallel current (1:3 sloped dike: $v = 0.15$ m/s, 0.3 m/s; 1:6 sloped dike: $v = 0.15$ m/s, 0.3 m/s, 0.4 m/s) were studied. Measurements included wind velocity, current velocity, wave parameter (wave height, wave period), wave overtopping and wave run-up.

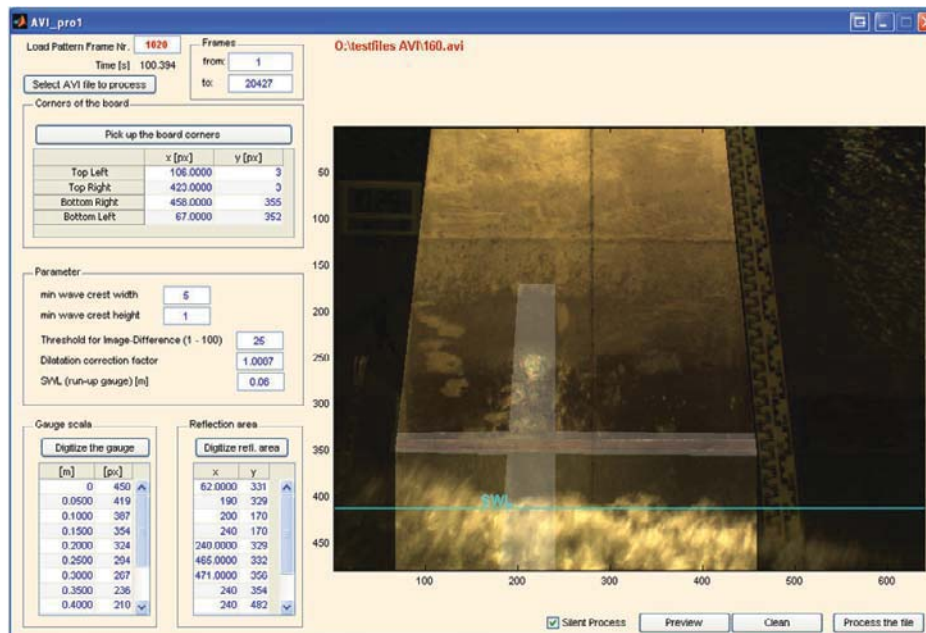


Figure 2: Video data analysis by means of a MATLAB-routine

To gain the wave run-up time series the data measured by the capacitive wave gauge needed only to be converted from Volts to meters by means of a calibration function according to the form

$$R[m] = a \cdot U[V] + b - SWL \quad (6)$$

with a, b constant values determined for each model set-up a [m/V], b [m]
 SWL still water level [m]
 U measured value [V]

The extraction of the wave run-up time series on the basis of video recordings was more sophisticated. Within a MATLAB-routine the brightness difference between two sequenced frames was determined. After that a new black/white frame was created. Pixels with a significant change in pixel brightness were defined as white pixels and all others as black pixels. In the next step the area of a certain width and height [pixel] was detected by a searching routine which was situated at the utmost position within the new frame. According to a scale at the right side of the wave run-up board (see figure 2) the wave run-up height [m] for each frame was thus determined and by assigning the record time of each frame to the wave run-up height the time series were created. To gain a considerable amount of results and data which are comparable to data obtained by the capacitive wave run-up gauge the video analysis was carried out for 10 vertical and separate stripes of the wave run-up board each 0.2 m wide.

After applying a crossing level analysis to each time series with a crossing level higher than zero the maximum wave run-up for each of the longer wave run-up events was extracted and put in descending order. At the end the value for $R_{u2\%}$ was determined as the wave run-up height which was only exceeded by 2 % of the incoming waves.

5 Results

To analyze the influence of oblique wave attack an influence factor γ_β was determined according to EurOtop (2007):

$$\frac{R_{u2\%}}{H_{m0}} = 1.65 \cdot \gamma_b \cdot \gamma_f \cdot \gamma_\beta \cdot \xi_{m-1,0} \quad (7)$$

with H_{m0} significant wave height [m/s²]

$\xi_{m-1,0}$ surf similarity parameter $\xi_{m-1,0} = \frac{\tan \alpha}{\sqrt{H_{m0} \cdot L}}$ [-]

γ_b factor representing the influence of a berm [-]

γ_f factor representing the influence of surface roughness [-]

γ_β factor representing the influence of oblique wave attack $\gamma_\beta = \frac{(R_{u2\%}/H_{m0})_\beta}{(R_{u2\%}/H_{m0})_{\beta=0}}$ [-]

The term $(R_{u2\%}/H_{m0})_\beta$ stands for the relative wave run-up height in a model test with oblique wave attack and $(R_{u2\%}/H_{m0})_{\beta=0}$ represents the relative wave run-up height in a test with perpendicular wave attack, the so called reference test. The influence of a berm or the surface roughness was not considered within the presented study. Analogue factors covering the influence of wind γ_w and of current velocity γ_c were defined as follow:

$$\gamma_w = \frac{(R_{u2\%}/H_{m0})_w}{(R_{u2\%}/H_{m0})_{w=0}} \quad (8)$$

$$\gamma_c = \frac{(R_{u2\%}/H_{m0})_c}{(R_{u2\%}/H_{m0})_{c=0}} \quad (9)$$

These factors should also be included in formula (7).

The following figures present the results for each influence factor (oblique wave attack, wind and current). The influence factor was calculated for each "measurement device" (capacitive gauge and video film analysis for 10 stripes of the run-up board) and each test. Mean values are the arithmetic average for each investigated value of an influence parameter (e.g. $\beta = 15^\circ$) considering all tests with this influence parameter and all measurement results of them.

Figure 3 shows the calculated results of the presented study covering the influence of oblique wave attack on wave run-up (tests without wind and without current). In addition some empirical relationships of former investigations are presented. The measured results show good agreement with these empirical functions. One data set (1:6 sloped dike, $\beta = 30^\circ$) was excluded from regression analysis due to dissimilarity with the other results. Two equations were fitted, each for one dike slope:

$$\gamma_{\beta} = 0.61 \cdot \cos^2 \beta + 0.39 \quad (1:3 \text{ sloped dike}) \quad (10)$$

$$\gamma_{\beta} = 0.49 \cdot \cos^2 \beta + 0.51 \quad (1:6 \text{ sloped dike}) \quad (11)$$

Further investigations for $\beta > 50^\circ$ are still needed to validate the formulae above for this co-domain.

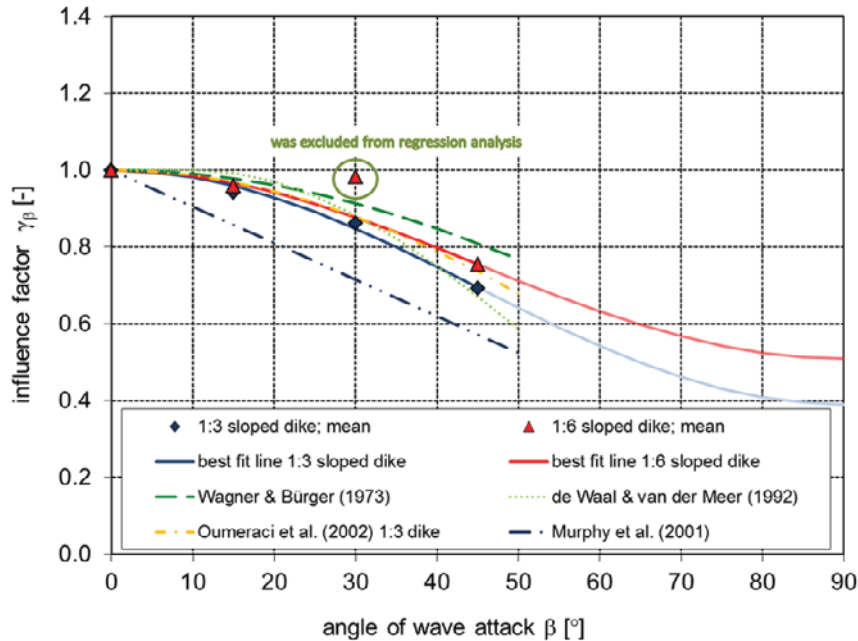


Figure 3: Factor γ_w covering the influence of oblique wave attack on wave run-up in dependence of the angle of wave attack

The calculated influence factors regarding wind (tests with onshore wind but without current and with perpendicular wave attack) are presented in figure 4. Different tests were excluded from further analysis because they showed inexplicable low values of γ_w which occurred mainly in video film analysis and here only for several stripes. These tests could be identified if the difference in the relative wave run-up between the different stripes and the capacitive gauge exceeded a predefined threshold. A possible reason for the differences within the results of some tests might be reflections of light on the run-up board which interfered with video analysis and wave run-up detection there.

The results indicate no noteworthy increasing effect of onshore wind on wave run-up as stated in the literature for wind speeds > 6 to 8 m/s. On the contrary there is a very slightly decreasing effect in case of the 1:6 sloped dike.

To estimate the corresponding prototype wind speed out of model wind speed the formula presented in González-Ecrivá (2006) might be useful but very few data were used to establish it:

$$w = \frac{w_p}{c} \quad (12)$$

with w_p prototype wind speed [m/s]

c constant factor $c = 1.2$ to 1.8 [-]

Figure 5 shows calculated values for the factor covering the influence of a dike parallel current together with a perpendicular wave attack and no wind. Green marked tests are characterized by significant differences between results from capacitive gauge and video analysis and were excluded from further analysis. There is no significant effect of a current on wave run-up considering current velocity up to 0.4 m/s.

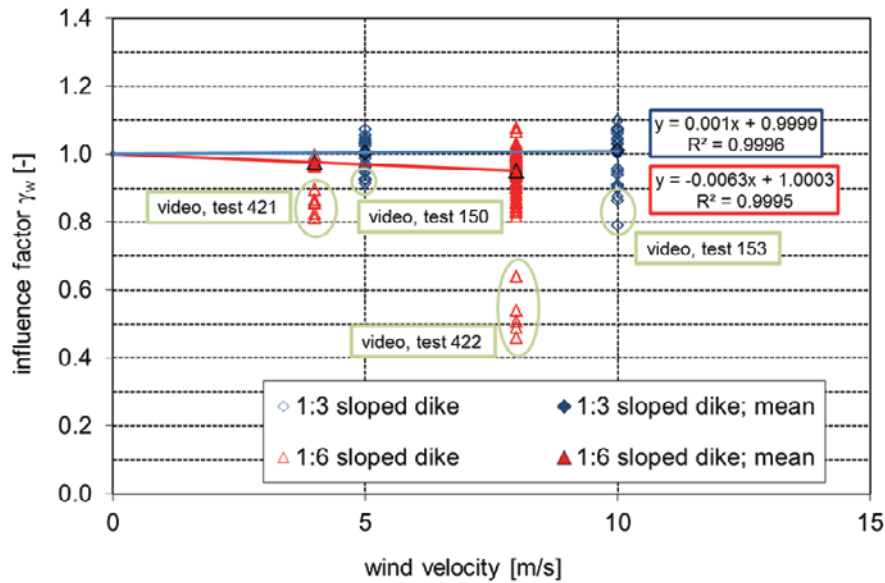


Figure 4: Factor γ_w covering the influence of onshore wind on wave run-up in dependence of wind velocity

It seems that in case of oblique wave attack and dike parallel current the different and in part opposing effects mentioned above together with refraction and shoaling results in a non-significant change of wave run-up height.

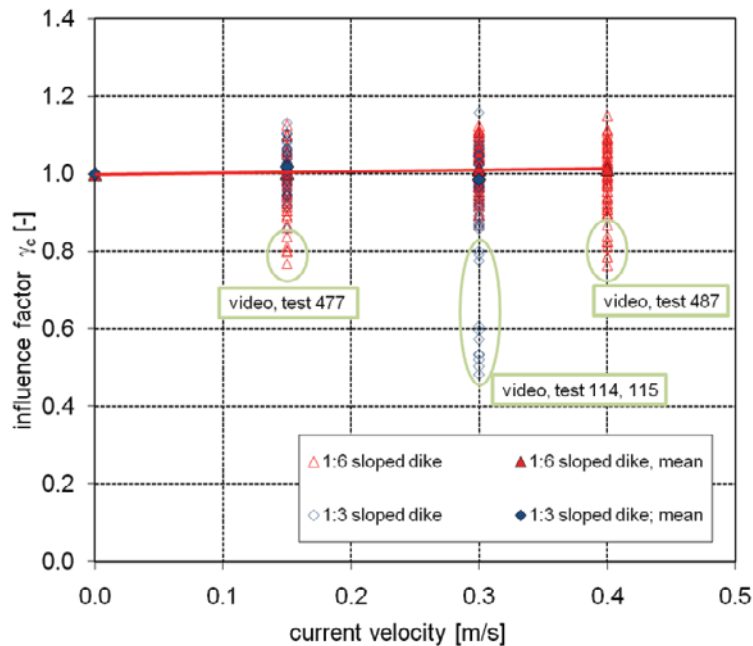


Figure 5: Factor γ_c covering the influence of current on run-up in dependence of current velocity

6 Summary

This paper presents results of a recent model investigation on wave run-up under the influence of oblique wave attack, current and wind. To quantify the influence of these parameters reduction factors were defined and calculated on basis of test results.

Results considering oblique wave attack confirm former empirical investigations. The increasing effect of onshore wind on wave run-up as described regarding former model tests with monochromatic waves could not be validated by the FlowDike test results. The investigated

onshore wind speed of < 10 m/s had no significant effect on the wave run-up in the model tests with the 1:3 sloped dike and a very slightly decreasing effect in the model tests with the 1:6 sloped dike. Furthermore no significant effect on wave run-up in case of a longshore current velocity < 0.4 m/s and a perpendicular wave attack was obtained.

Combined effects of these influence parameters were investigated too and will be presented later in a future paper.

7 Acknowledgements

The presented results are a part of a research project which was founded by German Ministry of Education and Research (BMBF) and the German Coastal Engineering Research Council (KFKI) (reference numbers: TU Dresden 03KIS076, RWTH Aachen 03KIS075). The model-tests at Hørsholm, Denmark were co-financed in the frame of HYDRALAB III program of the European Union (contract no. 022441). The authors wish to express their thanks for the financial support and for the research cooperation with VanderMeer Consulting B.V.

8 References

- De Rouck J., Boone C., van der Walle B. (2001): The optimization of crest level design of sloping coastal structures through prototype monitoring and modeling (OPTICREST). Final report, detailed scientific and technical report MAS03/1031, Ghent University, Zwijnaarde, Belgium
- de Waal J. P., van der Meer J.W. (1992): Wave run-up and overtopping on coastal structures, Proc. 23rd Internat. Conference on Coastal Engineering, Venice, Italy, pp. 1772-1784
- DVWK (1997): Freibordbemessung von Stauanlagen. DVWK-Merkblatt 246/1997
- EurOtop-Manual (2007): European Overtopping Manual. www.overtopping.manual.com
- Gonzales-Escriva (2006): The role of wind in wave run-up and wave overtopping of coastal structures. Proc. 30th Internat. Conference on Coastal Engineering, San Diego, California, USA, Vol. 5, pp. 4766-4778
- Holthuijsen L. (2007): Waves in Oceanic and Coastal Waters. Cambridge University Press, Cambridge, UK
- Hunt I. A. (1959): Design of seawalls and breakwaters. Journal of Waterway, Port, Coastal and Ocean Engineering, ASCE, New York, USA, pp. 123-152
- Lorke S., Brüning A., van der Meer J., Schüttrumpf H., Bornschein A., Gilli S., Pohl R., Spano M., Riha J., Werk S., Schlütter F. (2010): On the Effect of Current on Wave Run-up and Wave Overtopping, in: Proceedings of the 32nd International Conference on Coastal Engineering, Shanghai, China.
- Medina J.R. (1998): Wind effects on run-up and breakwater crest design. Proc. 26th Internat. Conference on Coastal Engineering, Copenhagen, Denmark pp. 1068-1081
- Oumeraci H., Möller J., Schüttrumpf H., Zimmermann C., Daemrich K.-F., Ohle N. (2002): Schräger Wellenauflauf an Seedeichen, Vol. LWI 881, FI 643/V, Braunschweig, Germany
- Wagner H. (1981) Seebau und Küstenschutz. Zentralstelle für Hochschulfernstudium, Dresden, Germany
- Wagner H, Bürger W (1973): Kennwerte zur Seedeichbemessung. Wasserwirtschaft Wassertechnik, Vol. 23, no 6, pp.204-207
- Ward D.L., Zhang J., Wibner C.G., Cinotto C.M. (1996): Wind effects on run-up and overtopping of coastal structures. Proc. 25th Internat. Conference on Coastal Engineering, Orlando, Florida, USA, pp. 2206-2215

A probabilistic approach for run-up estimation

Giuseppe Barbaro¹, Giandomenico Foti² and Giovanni Malara³

Abstract

This paper deals with run-up estimation. The run-up is the highest level where the water arrives on the beach. This parameter is essential for designing any coastal structure. It is a random variable related to the significant wave height of the sea state which occurs during a storm. In this paper, a probabilistic approach is proposed for run-up determination. It is based on the Equivalent Triangular Storm (ETS) model proposed by Boccotti in the eighties (see e.g. Boccotti 2000, Arena et al. 1999). This model is applied in conjunction with the empirical relation proposed by Stockdon et al. (2006). The model is used for determining the return period of a run-up level higher than a fixed threshold. Further, mean persistence of the run-up above this threshold is calculated. Application to practical situations is shown. The run-up is estimated from buoy data in Italian and in American locations. At this purpose, buoy data given by ISPRA (Istituto Superiore per la Protezione e la Ricerca Ambientale) and NDBC (National Data Buoy Center) are used.

1 Introduction

Wave run-up occurring in artificial and natural beaches is one of the topics of greater interest among the scientific community. It is a key factor for achieving a safe, but still cost-effective design of coastal structures. Wave run-up is often expressed in terms of a vertical excursion consisting of two components: a super elevation of the mean water level, wave setup, and fluctuations about that mean, swash. Waves approaching coasts dissipate the most of their energy by breaking across the surf zone. However, that energy is partially converted into potential energy as run-up on the foreshore of the beach (Hunt, 1959). In the context of random waves, Battjes (1974a) defined the principle of equivalency as the assumption that the run-up distribution of an irregular wave train can be found by assigning to each individual wave the run-up value of a periodic wave train of corresponding height and period. Massel & Pelinovsky (2001) considered the run-up of dispersive and breaking waves on a gentle beach slope. Recently, several approaches dealt with the estimation of run-up and of set-up have been formulated, consisting in empirical formulas for the estimation of maximum wave run-up, based on the statistics of data collected on a beach (Holman, 1986), or on run-up estimation on a flat seabed given the significant breaking wave height and the Iribarren Number (Battjes, 1974b; Van del Meer, 1992), or on numerical simulation of nonlinear wave run-up within a highly accurate Boussinesq-type model with a moving wet-dry boundary (Fuhrman & Madsen, 2008).

This paper discusses a probabilistic approach for run-up estimation. It is based on the ETS model introduced by Boccotti (see Boccotti 2000) in the eighties. This approach yields closed-form solutions for determination of statistical quantities of interest in the study of non-stationary processes. The ETS models is used in conjunction with the parameterization of run-up proposed by Stockdon et al. (2006). In this context, the return period of a run-up level higher than a fixed threshold is calculated. Further, mean persistence of run-up over a fixed threshold is calculated.

¹ "Mediterranea" University of Reggio Calabria, Via Graziella 1 - Loc. Feo di Vito - 89100 Reggio Calabria (Italy), giuseppe.barbaro@unirc.it

² "Mediterranea" University of Reggio Calabria, Via Graziella 1 - Loc. Feo di Vito - 89100 Reggio Calabria (Italy), giandomenico.foti@unirc.it

³ "Mediterranea" University of Reggio Calabria, Via Graziella 1 - Loc. Feo di Vito - 89100 Reggio Calabria (Italy), giovanni.malara@unirc.it

2 Background

A storm is defined as a sequence of sea states where the significant wave height is larger than a prescribed critical value and does not assume smaller values for a given time interval. In practical situations, the time interval is assumed 12 hours and the critical value of the significant wave height is 1.5 times the mean annual significant wave height.

The ETS model relates each storm to an equivalent triangular storm in which the height of the triangle is equal to the maximum significant wave height of the real storm and the base of the triangle, that is the duration of the equivalent triangular storm, is such that the maximum expected wave height of the equivalent triangular storm is equal to the maximum expected wave height of the actual storm.

In this context, equivalent sea can be defined as the sequence of the equivalent triangular storms. Thus, the equivalent sea consists of the same number of storms as the actual sea, each of them with the same maximum significant wave height.

As a consequence, the return period of a storm whose significant wave height exceeds a fixed threshold is the same in the actual sea and in the equivalent sea. Also, we can assume for the equivalent sea the same probability of exceedance of the maximum significant wave height of the actual sea. Thus, the equivalent sea rather than the actual sea can be assumed to greatly simplify the mathematical treatment.

The probabilistic approach shown in this paper uses the ETS model in conjunction with the empirical parameterization proposed by Stockdon et al. (2006) for run-up estimation. They proposed the following formula for run-up determination:

$$\frac{R_{u2\%}}{H_0} = K = 1.1 \left\{ 0.35 \beta_f \left(\frac{L_0}{H_0} \right)^{1/2} + \frac{1}{2} \left[\frac{L_0}{H_0} (0.563 \beta_f^2 + 0.004) \right]^{1/2} \right\}, \quad (1)$$

with $R_{u2\%}$ 2% exceedance value of run-up [m];

β_f beach slope;

H_0 wave height at deep water [m];

L_0 wave length at deep water [m].

Since random waves are under examination, H_0 and L_0 will be considered as significant wave height and dominant wavelength of a sea state.

3 Return period of a run-up level higher than a fixed threshold

Return period of a run-up level higher than a fixed threshold is determined as the ratio between a long time interval τ and the number $N(\tau)$ of run-up levels over the threshold during τ

$$R(R_{u2\%} > X) = \frac{\tau}{N(\tau)}. \quad (2)$$

Explicit determination of eq. (2) is achieved by relating $N(\tau)$ to the return period $R(H_s > h; \theta_i - \Delta\theta/2 < \theta < \theta_i + \Delta\theta/2)$ of a sea storm in which the significant wave height H_s exceeds a fixed threshold h and the dominant direction θ ranges from $\theta_i - \Delta\theta/2$ to $\theta_i + \Delta\theta/2$. This correspondence is based on the relation between wave height and run-up [eq. (1)]. It assures that run-up exceeds a fixed level when the wave height exceeds a certain threshold. $N(\tau)$ is related to $R(H_s > h; \theta_i - \Delta\theta/2 < \theta < \theta_i + \Delta\theta/2)$ by equation

$$N(\tau) = \sum_{i=1}^N \frac{\tau}{R(H_s > h; \theta_i - \Delta\theta/2 < \theta < \theta_i + \Delta\theta/2)}. \quad (3)$$

Eq. (3) is the ratio of a long time interval τ over the time in which significant wave height exceeds the fixed threshold during τ . It is derived by dividing wave direction in certain sectors. Then, the number of run-up levels over the threshold is given by the contribution from each sector. Substitution of eq. (3) in eq. (2) yields to the return period of a run-up level higher than a fixed threshold:

$$R(R_{u2\%} > X) = \left[\sum_{i=1}^N \frac{1}{R(H_s > h; \theta_i - \Delta\theta/2 < \theta < \theta_i + \Delta\theta/2)} \right]^{-1} \quad (4)$$

The return periods $R(H_s > h; \theta_i - \Delta\theta/2 < \theta < \theta_i + \Delta\theta/2)$ are explicitly calculated by the ETS model. Specifically, it is given by the equation (Arena & Barbaro, 1999)

$$R(H_s > h; \theta_i - \Delta\theta/2 < \theta < \theta_i + \Delta\theta/2) = \frac{\bar{b}(h; \theta_i - \Delta\theta/2 < \theta < \theta_i + \Delta\theta/2)}{\exp\left[-\left(\frac{h}{w_\alpha}\right)^u\right] \left[1 + u\left(\frac{h}{w_\alpha}\right)^u\right] - \exp\left[-\left(\frac{h}{w_\beta}\right)^u\right] \left[1 + u\left(\frac{h}{w_\beta}\right)^u\right]}, \quad (5)$$

being u, w_α, w_β parameters that depend on the location under examination,
 $\bar{b}(h; \theta_i - \Delta\theta/2 < \theta < \theta_i + \Delta\theta/2)$ a base – significant wave height regression of the sea states where the direction ranges from $\theta_i - \Delta\theta/2$ to $\theta_i + \Delta\theta/2$.

It is derived by assuming that directional probability of significant wave heights are interpreted according to the difference between two Weibull distributions. That is,

$$P(H_s > H_0; \theta_1 < \theta < \theta_2) = \exp\left[-\left(\frac{H_0}{w_\alpha}\right)^u\right] - \exp\left[-\left(\frac{H_0}{w_\beta}\right)^u\right]. \quad (6)$$

Arena & Barbaro (1999) have shown that the best fit regression depends on the location under examination and proposed the equations

$$\bar{b}(h) = b_{10} \left(1.12 - 0.12 \frac{h}{a_{10}} \right), \text{ for Italian waters,} \quad (7)$$

and

$$\bar{b}(h) = b_{10} C_1 \exp\left(-C_2 \frac{h}{a_{10}}\right), \text{ for ocean waves,} \quad (8)$$

with C_1, C_2, a_{10}, b_{10} parameters that depend on the location under examination,
 a_{10} average value of the heights of the $10n_{\text{years}}$ more sever storms recorded in n_{years} on the location under examination,
 b_{10} average value of the heights of the $10n_{\text{years}}$ more sever storms recorded in n_{years} on the location under examination,

Eq. (6) and eq. (7) are irrespective of the dominant direction, but they yield a conservative estimate of the return period (5), therefore they are used instead of $\bar{b}(h; \theta_i - \Delta\theta/2 < \theta < \theta_i + \Delta\theta/2)$.

For practical calculations, eq. (4) is determined by fixing a threshold X . Then, the significant wave height H_0 related to X is estimated by eq. (1). That is,

$$H_0 = \frac{X}{K}. \quad (9)$$

Finally, the return period (5) is calculated for each sector and $R(R_{u2\%}>X)$ is estimated. Note that, eq. (1) is irrespective of the direction of wave propagation. It is applied with the stipulation that oblique waves give run-up values smaller than waves orthogonal to the shoreline. In this context, the estimation yields to a conservative determination of K and, therefore, to a conservative value of $R(R_{u2\%}>X)$.

4 Mean persistence of the run-up above a fixed threshold

The mean persistence of the run-up above the fixed threshold X is determined, as well. It is given by the ratio of the time duration in which $R_{u2\%}>X$ (or, equivalently, $H_0>X/K$) in the long time interval τ , over the number of storms in which H_0 goes over the threshold X/K during τ . The first quantity is calculated as

$$P(H_0 > X/K) \cdot \tau, \quad (10)$$

being $P(H_0>X/K)$ the probability that significant wave height H_0 is larger than X/K in a given sea state. The second one is determined by equation

$$\tau / R(R_{u2\%} > X). \quad (11)$$

where $R(H_0>X/K)$ is the return period of a sea storm in which H_0 is larger than X/K . Eq. (9) and eq. (10) must consider the contribution due to sea states having different dominant directions. Consequently, time duration (10) and number of storms (11) are given by the summation of contributions relative to each sector of wave propagation. That is,

$$\bar{D}(X/K) = \frac{\sum_{i=1}^N P(H_0 > X/K; \theta_i - \Delta\theta/2 < \theta < \theta_i + \Delta\theta/2)}{\sum_{i=1}^N \frac{1}{R(H_0 > X/K; \theta_i - \Delta\theta/2 < \theta < \theta_i + \Delta\theta/2)}}. \quad (12)$$

Calculation of persistence (12) can be done by assuming the directional probability (6) and the return period (5).

5 Application

The return period of a storm in which run-up exceeds a fixed threshold and the mean persistence of run-up above that fixed threshold are estimated in Alghero (Italy) and in Kauai Island (Hawaii, USA) starting from buoy data given by, respectively, the ISPRA (Istituto Superiore per la Protezione e la Ricerca Ambientale) and NDBC (National Data Buoy Center). These locations (fig. 1-2) have been chosen for the availability of significant wave height and wave directional data.

Data processing requires determination of u , w_α and w_β parameters. They are calculated by best fit regression of directional probability (6) and of omnidirectional Weibull probability

$$P(H_s > h) = \exp\left[-\left(\frac{h}{w}\right)^u\right], \quad (13)$$

being w scaling factor [m].



Figure 1: Alghero, location of ISPRA buoy.



Figure 2: Kauai Island, location of NDBC buoy.

Details for estimation of all parameters are given in Arena & Barbaro (1999) and in Boccotti (2000). Results of calculation for the present application are shown in Table 1 and in Table 2 for the location of Alghero and for the location of Kauai Island, respectively. For the calculation, 16 wave propagation sectors are considered. Tables show only parameters relative to the sectors that give rise to run-up. That is, wave directions heading toward the location under examination. Indeed, opposite wave directions are excluded for the calculation, because they do not produce significant run-up values.

Table 1: Characteristics parameters of Alghero.

u	w [m]	a_{10} [m]	b_{10} [hours]					
1.116	1.289	5.6	84	Sector				
	1	2	3	4	5	6	7	8
w_{α} [m]	0.367	0.444	0.613	0.65	0.75	1.04	1.236	0.556
w_{β} [m]	0.311	0.404	0.557	0.565	0.699	0.905	0.942	0.534

Table 2: Characteristics parameters of Kauai Island.

u	w [m]	a ₁₀ [m]	b ₁₀ [hours]	C ₁	C ₂	Sector		
1.47	1.835	6.1	68	1.51	0.413			
						1	2	3
						4	5	6
						7	8	
w _α [m]	1.095	1.568	1.6	1.651	1.57	1.333	1.464	1.416
w _β [m]	1.077	1.423	1.298	1.56	1.431	1.18	1.362	1.319

Calculation of eq. (4) and eq. (12) is straightforward given parameters in table 1-2 and the threshold X. However, wave spectrum (for calculation of the dominant wave length) and beach slope must be specified for using eq. (1), as well. In the present application a mean JONSWAP spectrum has been considered and the same beach slopes have been considered in both locations ($\beta_f=0.015$).

Results are shown in figure 3 and in figure 4. The return period and the mean persistence are calculated as function of the threshold X. These representations are useful for design purposes. They show that there is a one-to-one relationship between return period and run-up. Therefore, they can be used for giving an immediate estimate of run-up levels for a given return period. Then, the mean persistence of run-up above the threshold is determined by figure 4.

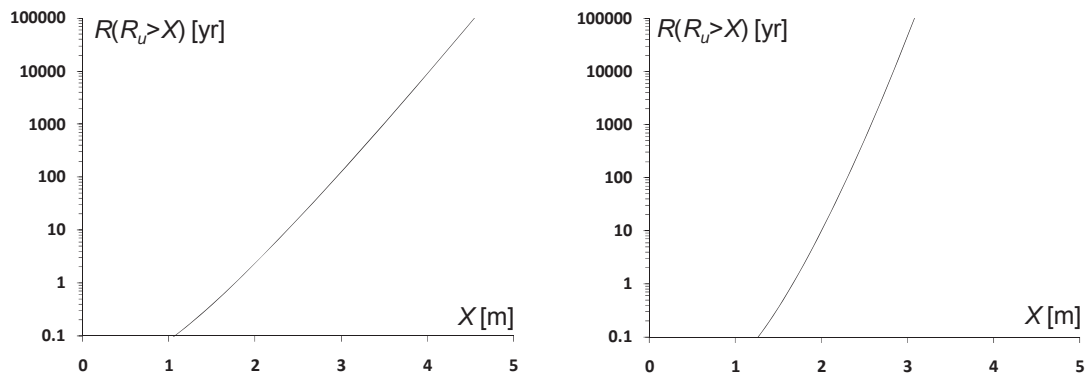


Figure 3: Return period of a storm in which run-up level exceeds a fixed threshold at the location of Alghero (left panel) and at Kauai Island (right panel).

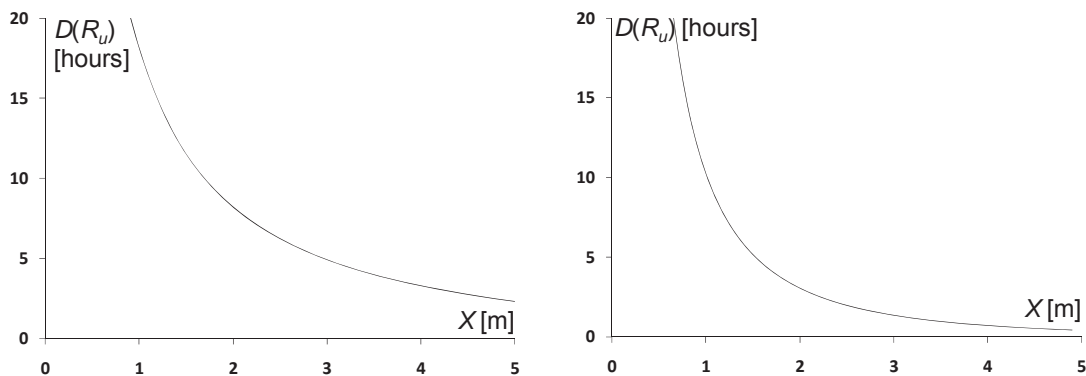


Figure 4: Mean persistence of run-up above the fixed threshold X at the location of Alghero (left panel) and at Kauai Island (right panel).

Consider the location of Alghero. If a return period of 10 years is assumed, figure 3 shows that the corresponding run-up value is 2.4m, and figure 4 shows that the mean persistence of run-up

above this value is 6.5 hours. The same line of reasoning can be followed for the location of Kauai Island. In this context, the threshold X relative to a return period $R(R_{u2\%}>X) = 10$ years is 2 m and the mean persistence is 3.4 hours.

6 Conclusions

This paper has described a probabilistic approach for estimating run-up levels. It is based on the Equivalent Triangular Storm (ETS) model proposed by Boccotti in the eighties (see Arena et al. 1999, Boccotti 2000) and has been applied in conjunction with the empirical relation proposed by Stockdon et al. (2006).

The probabilistic approach has been applied for estimating the return period of a storm in which run-up exceeds a fixed threshold. Further, the mean persistence of run-up above a fixed threshold has been calculated. This analysis has shown that characteristics of the waves and of the beach under examination are needed for a probabilistic estimation of the run-up.

The return period of a storm in which run-up exceeds a fixed threshold has been estimated at Alghero (Italy) and at Kauai Island (Hawaii, USA) starting from buoy data given by, respectively, ISPRA (Istituto Superiore per la Protezione e la Ricerca Ambientale) and NDBC (National Data Buoy Center). In both cases, directional and omnidirectional parameters have been estimated and the return period of a storm in which run-up exceeds a fixed threshold and the mean persistence of run-up above that fixed threshold have been calculated.

Application has shown that there is a one-to-one correspondence between return period and run-up threshold. This characteristic has allowed a straightforward determination of the run-up level given the return period $R(R_{2\%}>X)$. Further, it has been shown that, for a fixed threshold X , mean persistence is readily determined, as well.

7 References

- Arena, F., Barbaro, G. (1999): *Il rischio ondoso nei mari italiani* (in Italian). Ed. Bios Cosenza, Italy. ISBN 88-7740-276-8.
- Battjes, J. A. (1974a): Computation of set-up, longshore currents, run up and overtopping due to wind-generated waves. Department of Civil Engineering Delft University of Technology, Report 74.
- Battjes, J.A. (1974b): Surf similarity. In: Proceedings of the 14th Conference of Coastal Engineering, ASCE, pp. 466-480.
- Boccotti, P. (2000): *Wave Mechanics for Ocean Engineering*. Elsevier Science, Oxford. ISBN 0-444-50380-3.
- Fuhrman, D.R. and Madsen, P.A. (2008): Simulation of nonlinear wave run-up with a high-order Boussinesq model. In: *Coastal Engineering*, Vol. 55, pp. 139-154.
- Holman, R.A. (1986): Extreme value statistics for wave run-up on a natural beach. In: *Coastal Engineering*, Vol. 9, pp. 527-544.
- Holman, R.A. and Sallenger, A.H. Jr. (1985): Setup and swash on a natural beach. In: *Journal of Geophysical Research*, Vol. 90 (C1), pp. 945-953.
- Hunt, I.A. (1959): Design of seawalls and breakwaters. In: *Journal of Waterways and Harbours Division*, ASCE 85 (WW3), pp. 123-152.
- Massel, S.R. and Pelinovsky, E.N. (2001): Run-up of dispersive and breaking waves on beaches. In: *Oceanologia*, Vol. 43, pp. 61-97.
- Stockdon, H.F., Holman, R.A., Howd, P.A., Sallenger, A.H. Jr. (2006): Empirical parameterization of setup, swash, and runup. In: *Coastal Engineering*, Vol. 53, No. 7, pp. 573-588; ISSN 0378-3839.
- Van der Meer, J.W. (1992): Conceptual design of rubble-mound breakwaters. In: Proceedings of Short Course attached to the 23th International Conference of Coastal Engineering, pp. 447-510.

Effects of surf beat caused by long period swell on wave overtopping rate on complex bathymetry

Hiroaki Kashima¹ and Katsuya Hirayama²

Abstract

Recently, coastal disasters due to long period swell induced by heavy storms and catastrophic typhoons increase in the Japanese coasts and harbors. The long period swell is more susceptible to the bottom bathymetry of offshore deeper water and its wave height locally increases by the wave energy concentration under the effect of the complex bottom bathymetry in the relatively shallower water. In addition, the wave overtopping rate may become larger due to the surf beat in front of the seawall. In this study, the model experiments conducted in a large basin to investigate the characteristics of the surf beat in front of the seawall for influencing the heavy wave overtopping damages at the Shimonikawa Coast in 2008. The wave overtopping on the seawall shows quite similar spatial distribution of surf beat in front of the seawall, which depends on the slope of bathymetry and the existence of edge waves.

Keywords: long period swell, surf beat, wave overtopping, detached breakwater, submerged breakwater

1 Introduction

Recently, coastal disasters due to long period swell induced by heavy storms increase in the Japanese coasts and harbors. For example, the collapse of the seawalls and inundation behind the defending reclaimed area in Kuji Harbor were caused by wave overtopping due to 14.5s swell in 2006 (Hirayama et al., 2008). Moreover, the severe damages with properties and inhabitants in Ashizaki district of Nyuzen town at the Shimonikawa Coast were caused by long period swell with high wave height, which is called by local citizens as "Yorimawari-Nami", in 2008 (Kawasaki et al., 2008). These observed long period swells have a narrow-band spectra more than the one of wind wave and the grouping of high waves can be appeared in the time series of their wave profiles. Recent experimental studies have suggested that the wave overtopping volume on the seawall increases under the effect of the specific surf beat in front of the seawall for the unidirectional long period swell (Kashima and Hirayama, 2010). Therefore, it is important to consider not only the characteristics on the wave grouping but also the surf beat as a secondary nonlinear interaction wave in the discussion about wave overtopping for long period swell.

Some studies on the characteristics of long period swell transformation exist. Kashima and Hirayama (2009) calculated on the difference between the long period swell and wind wave transformations on the complex bathymetry. The long period swell is more susceptible to the bottom bathymetry of offshore deeper water than wind wave and its wave height locally increases by the wave energy concentration in the relatively shallower water. On the other hand, Fukase et al. (2009) and Tajima et al. (2009), analyzing observed data with focusing on the damage features, mentioned that the wave energy concentration to the damaged area is caused by the interactions among waves, bathymetry and near shore currents. In particular, the slowly varying wave-induced nearshore currents have one of significant impacts on local concentrations of waves around the sharply changing coastal bathymetries. However, these discussions are mainly focused on the wave energy concentration due to bottom bathymetry. The effects of the surf beat due to the long period swell on the wave overtopping are not well known owing to the lack of detail measurements. In addition, there are merely model experiments with considering the local topography including the sharply changing coastal bathymetry.

¹ Port and Airport Research Institute, 3-1-1 Nagase, Yokosuka, Kanagawa, 239-0826, Japan, kashima@pari.go.jp

² Port and Airport Research Institute, 3-1-1 Nagase, Yokosuka, Kanagawa, 239-0826, Japan, hirayama@pari.go.jp

The purpose of this study is to investigate the characteristics of the surf beat in front of the seawall for influencing the wave overtopping, using a wave basin installed with the complex bathymetry of the Shimonikawa Coast.

2 Wave overtopping experiments

2.1 Experimental setup

The model experiments were conducted in a large basin that is 48.0m times 25.0m long and 1.5m deep located in Port and Airport Research Institute in Japan. This basin has 100 wave paddles with active wave absorber in L-shape layout. A complex bathymetry model of the Shimonikawa Coast including the submerged and detached breakwaters located in front of seawall was installed. And the model was replaced by a mirror-image to prototype image because the layout of wave generator is unsuitable to generate damage wave. The experimental scale was 1/100 in Froude similarity rule. After that, the prototype value and image are used to show the experimental results. A detail of the experimental setup is shown in Fig.1. The horizontal (y) and vertical (x) axes are the distance from the ridge line ($y = 0$ km) and the wave generator ($x = 0$ km), respectively. The contour line indicates the water depth line drawn 2.0m apart. The circle and cross indicate the capacitance-type wave gauge and the electromagnetic velocity meter, respectively. The parenthesis number indicates the water catchment box number. The horizontal dotted line indicates the definition of measurement line which is used in following discussions.

49 capacitance-type wave gauges were installed in from offshore to onshore water to measure the distribution of wave height and 12 electromagnetic velocity meters were installed in the relatively shallower water to measure the distribution of wave-induced current and the direction of wave propagation. Moreover, 7 water catchment boxes were installed behind the seawall to measure the spatial distribution of wave overtopping volume.

2.2 Experimental condition

The model experiments were performed with the estimated wave from observed data. The significant wave height $H_{1/3}$ and wave period $T_{1/3}$ were estimated 5.97m and 13.9s in offshore. The frequency spectral shape was chosen as JONSWAP-type spectra with $\gamma = 4.0$ based on the case of Hirayama et al. (2009). The offshore water depth h was set at 90.21m in consideration of the sea level when the disaster wave was observed. The principal wave direction θ_p and the spreading parameter S_{max} were set at an angle rotated 15 degrees clockwise to the positive direction of x ($\theta_p = N18.5E$) and $S_{max} = 999$ by Kashima and Hirayama (2011).

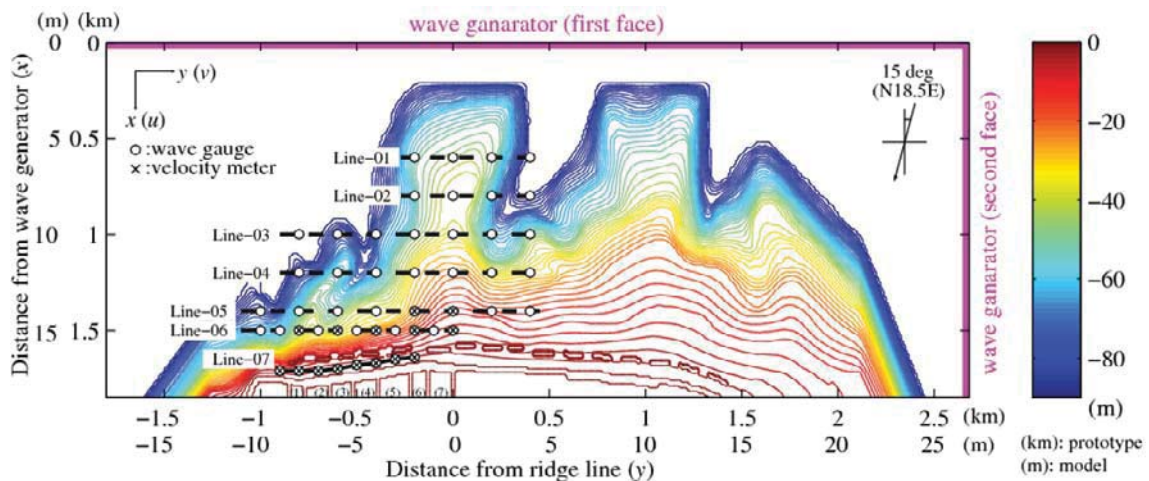


Figure 1: Illustration of experimental setup (contour line: water depth, circle: capacitive wave gauge, cross: electromagnetic velocity meter, circle with number: wave catchment box, dotted line: measurement line)

The data of the water surface elevation and the fluid velocity were recorded by 25Hz for maximally over 1000 waves by using the capacitance-type wave gauge and the electromagnetic velocity meter. The height of short wave of which period is less than 30s and surf beat of which period is from 30 to 300s in this study are defined as the significant wave height, respectively. The mean surface elevation increasing and the wave overtopping rate on the seawall are evaluated the time-averaged value of water surface elevation and wave overtopping volume in the water catchment box, respectively.

3 Results and discussions

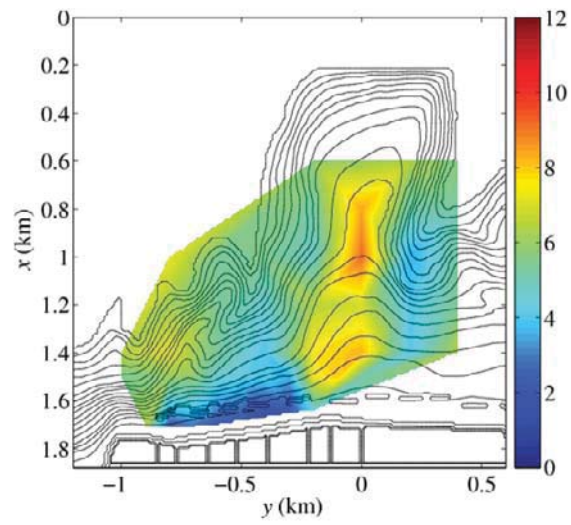
3.1 Spatial distributions of wave transformation and wave overtopping

Fig.2 shows the spatial distributions of the short wave height, surf beat height and the mean surface elevation increasing when the seawalls were damaged due to the long period swell. The contour indicates the value of each wave statistics. The short wave propagating from offshore concentrates on the ridge ($y = -0.3$ to 0 km) under the effects of the refraction and wave shoaling, and its height becomes larger than 7.0m. Moreover, the short wave height on the small ridge ($y = -0.7$ km and $x = 1.4$ km) increases locally. However, the short wave height behind the submerged and detached breakwaters on the steep slope side ($y = -0.8$ to -0.4 km) decreases by the wave breaking. On the other hand, as the water depth becomes shallower the surf beat height increases and reaches to 2.0m behind the submerged and detached breakwaters. Moreover, the mean surface elevation increasing also behaves in the similar tendency of the surf beat height distribution.

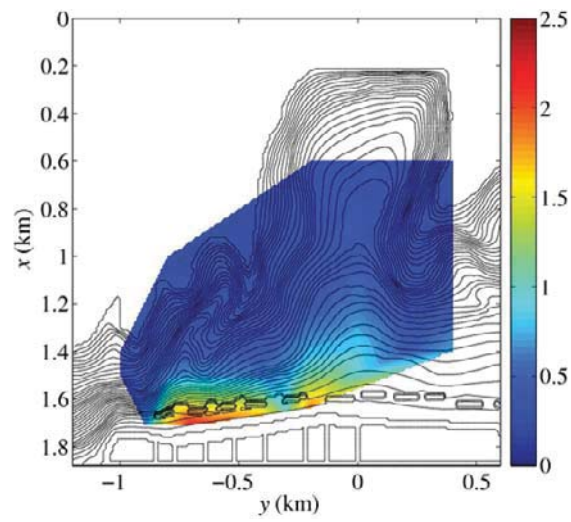
To discuss the characteristics of wave overtopping, Fig.3 shows the relationship between the wave statistics in front of the seawall and the wave overtopping rate on the seawall. The circle and cross indicate the data in front of (Line-06) and behind (Line-07) the submerged and detached breakwaters, respectively. As already shown in Fig.2, the short wave height becomes smaller and both the surf beat height and the mean surface elevation increasing become larger in front of the seawall. The wave overtopping rate on the seawall at $y = -0.8$ to -0.7 km, which is the heaviest damaged area, is the largest. Moreover, the distribution of wave overtopping rate is quite similar to the one of the surf beat height and is in a good agreement with the inundation area obtained by the field surveys on damage. According to the results of Kashima and Hirayama (2010), the wave overtopping rate becomes larger under the effects of the surf beat induced by wave grouping in front of the seawall. Therefore, these experimental results imply that the effects of surf beat in front of the seawall are important for the increase of the wave overtopping rate on the seawall. The detail of the surf beat characteristics in front of the seawall is discussed in next.

3.2 Surf beat characteristics in front of seawall

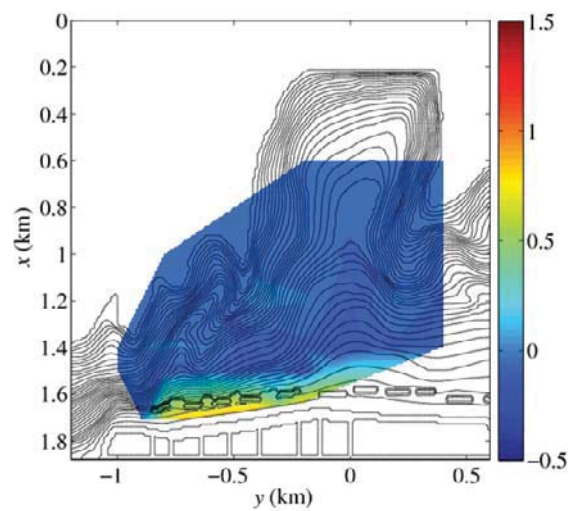
To investigate the behavior of the surf beat in front of the seawall, Fig.4 shows the spatial distributions of the cross-correlation coefficient between the surf beat and the enveloped wave from offshore to onshore. The enveloped wave is defined by List. (1992). Horizontal axis is time lag τ and the contour indicates the cross-correlation coefficient. The vertical dashed line is corresponding to $\tau = 0$ s and the horizontal dotted line in each figure from $y = -0.8$ to -0.2 km indicates the position of the submerged and detached breakwaters. The negative correlation can be observed from $x = 0.6$ km up to $x = 1.4$ km at zero time lag on the ridge ($y = 0.2$ to 0.4 km). On the other hand, in the range from $y = -0.8$ to -0.2 km, we can note that the correlation along $\tau = 0$ s is essentially inverted close to shoreline in comparison to the offshore situation. In offshore, the surf beat is negatively correlated with the enveloped wave at zero time lag, while in the near shore region the correlation at near-zero time lag is dominantly positive.



(a) Short wave height



(b) Surf beat height



(c) Mean surface elevation increasing

Figure 2: Spatial distributions of wave statistics when the seawall was damaged due to long period swell

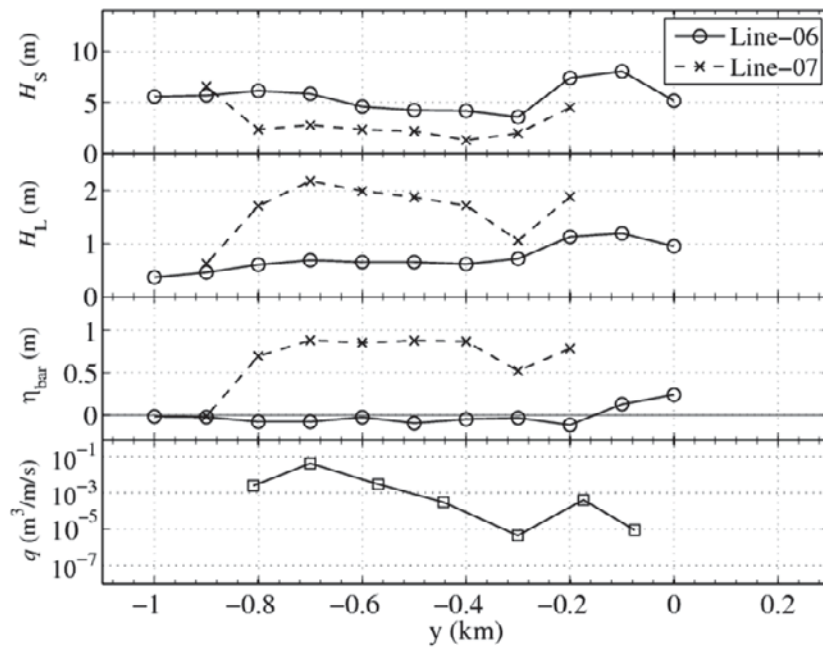
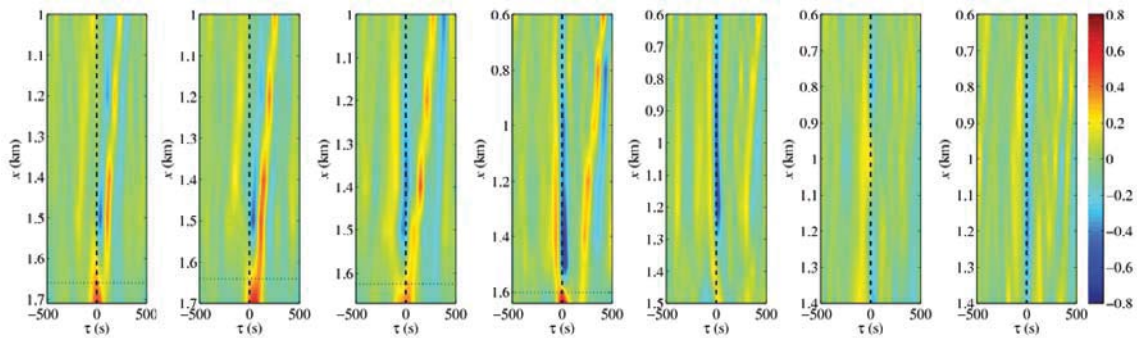


Figure 3: Relationship between wave statistics in front of the seawall and wave overtopping rate



(a) $y = -0.8\text{km}$ (b) $y = -0.6\text{km}$ (c) $y = -0.4\text{km}$ (d) $y = -0.2\text{km}$ (e) $y = 0\text{km}$ (f) $y = 0.2\text{km}$ (g) $y = 0.4\text{km}$

Figure 4: Spatial distributions of the cross-correlation coefficient between the surf beat and the enveloped wave (contour: cross-correlation coefficient, vertical dashed line: $\tau = 0\text{s}$, horizontal dotted line from $y = -0.8$ to -0.2km : position of the submerged and detached breakwaters)

Fig.5 shows the time series variation of water surface elevation of the surf beat (solid line) and the enveloped wave (dotted line) in front of the seawall. Horizontal axis is time and vertical axis is water surface elevation for two wave profiles. These figures show that the surf beat profile gives close agreement with the enveloped wave profile on the mild slope side ($y = -0.3$ to -0.2km). On the other hand, there is a small difference between the appeared time of crest amplitude of two wave profiles on the steep slope side ($y = -0.8$ to -0.4km). These results are corresponding to the results of List (1992) and Kashima and Hirayama (2010). That is, these experimental results indicate that the surf beat bound for short wave propagates from offshore to onshore and the surf beat is released from the incident bound waves due to the breaking of the short wave near the shoreline. However, a significant difference between the behavior of the surf beat on the mild and steep slope side is recognized from the standpoint of the difference of the appeared time of crest amplitude.

To check the behavior of the surf beat in front of the seawall, the spectra of water surface elevation and two-directional fluid velocities are shown in Fig.6. The vertical dashed line indicates the boundary period (30s) between short wave and surf beat. The along-shore fluid velocity spectra for the surf beat is $10^1 - 10^2$ times larger than the cross-shore spectra on the

mild slope side ($y = -0.3$ to -0.2 km). This implies that the free surf beat released due to breaking from wave grouping refracted on the ridge propagates along the seawall. On the other hand, the densities of cross-shore spectra is same as much as the one of the along-shore spectra on the steep slope side ($y = -0.8$ to -0.4 km). The surf beat in this area may include both the surf beat propagating from offshore and along the seawall. Therefore, it is supposed that the generation mechanism of surf beat on the mild and steep slope side is different.

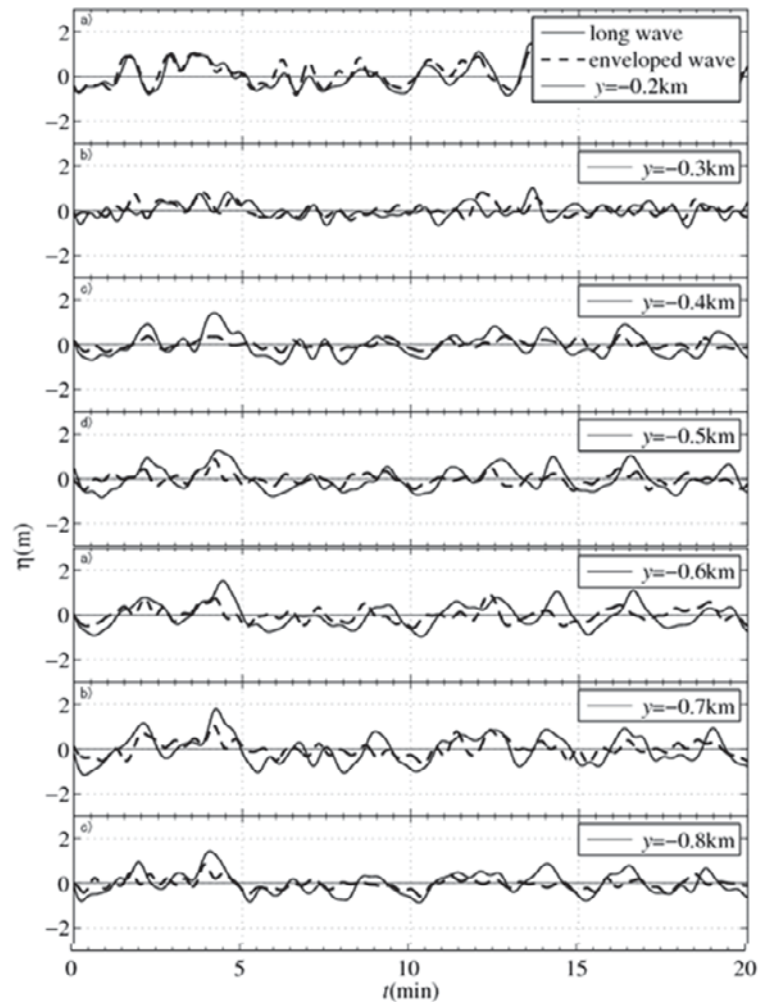
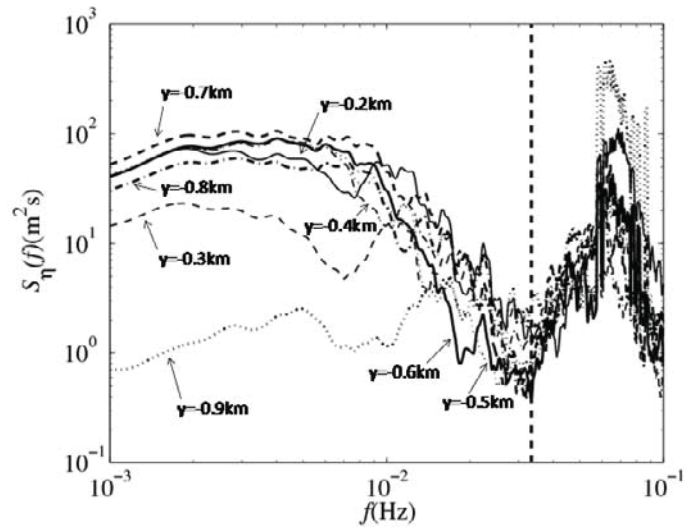


Figure 5: Time series variation of the surf beat and the enveloped wave in front of the seawall

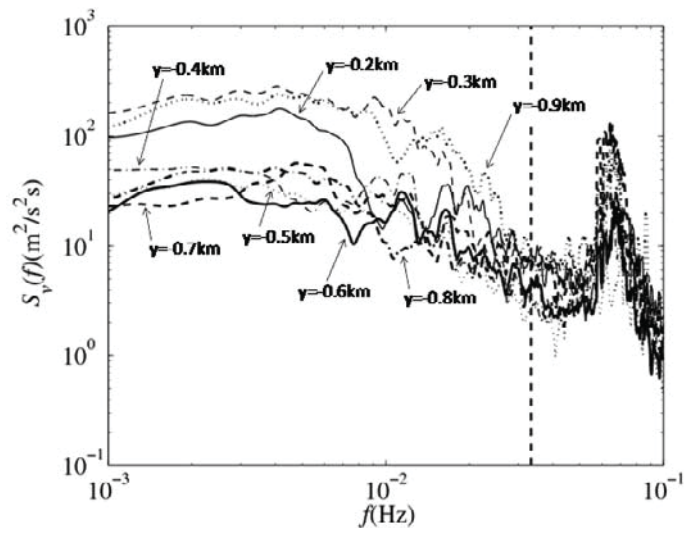
4 Conclusions

The model experiments were conducted in a large basin to investigate the effects of the surf beat induced by long period swell on wave overtopping. The wave overtopping on the seawall shows quite similar spatial distribution of surf beat in front of the seawall. On the mild slope side, surf beat released due to breaking from wave grouping refracted on the ridge propagates along the seawall. On the other hand, the sea level variation in front of seawall can be generated by the superposition of along-shore and cross-shore surf beat on the steep slope side.

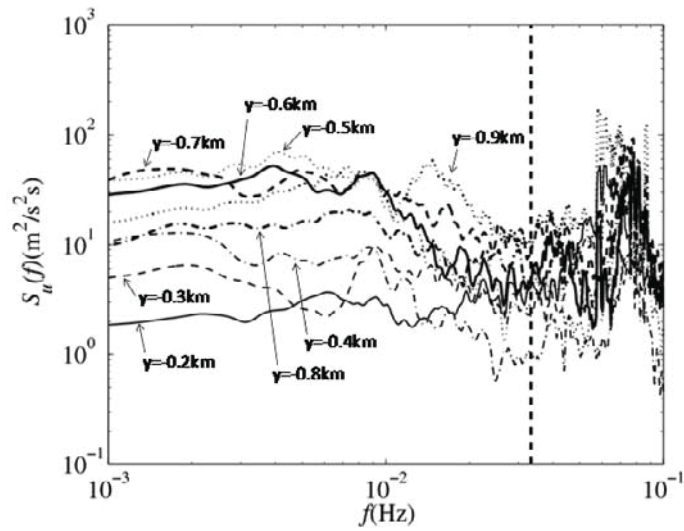
The detail experiments and analysis considering surf beat characteristics in front of seawall will be required to propose effective countermeasures for wave overtopping induced by long period swell.



(a) Water surface elevation



(b) Along-shore fluid velocity



(c) Cross-shore fluid velocity

Figure 6: Spectra of water surface elevation and fluid velocity in front of seawall

5 Acknowledgements

This research was partially supported by the Japan Railway Construction, Transport and Technology Agency.

6 References

- Fukase, Y., R. Suminda, Y. Tajima and S. Satoh (2009): Deformation of long-period giant waves on the Shimoniikawa coast, *Journal of JSCE, Ser. B2 (Coastal Engineering)*, Vol.65, pp.1411-1415 (in Japanese).
- Hirayama, K., H. Kashima and T. Hiraishi (2008): Examples of unexpected high waves in shallow water in Japan, *Proceedings of Rogue Waves 2008*.
- Hirayama, K., H. Kashima and K. Nakai (2009): A study on characteristics of long period swell spectrum and its grouping, *Annual Journal of Civil Engineering in the Ocean, JSCE*, Vol.25, pp635-640 (in Japanese).
- Kashima, H and K. Hirayama (2009): Effects of bottom topography characteristics on transformations of long period swell, in: *Proceedings of the 4th SCACR – International Short Conference on applied coastal Research*, pp.197-205. ISBN 978-3-00-030141-4. Barcelona, Spain.
- Kashima, H and K. Hirayama (2010): Experiments on wave overtopping rate and wave pressure on seawalls of long period swell, *Technical Note of The Port and Airport Research Institute*, No.1218, 26p (in Japanese).
- Kashima, H and K. Hirayama (2011): Experimental Study on Mechanism and Countermeasures for Wave Overtopping of Long-Period Swell in Shimoniikawa Coast, *Technical Report of The Port and Airport Research Institute* (in Japanese) (in press).
- Kawasaki, K., N. Mizutani, K. Iwata, T. Kobayashi, M. Yuhi, T. Saitoh, T. Kitano, H. Sumi, H. Mase and T. Yasuda (2008): Field survey of damage due to February 2008 high wave on east coast of Toyama Prefecture, *Annual Journal of Coastal Engineering, JSCE*, Vol.55, pp.151-155 (in Japanese).
- Tajima, Y., H. Ishizashi and S. Satoh (2009): Concentration of slowly-varying nearshore waves and currents around the edge of two different bottom slopes, *Journal of JSCE, Ser. B2 (Coastal Engineering)*, Vol.65, pp.211-215 (in Japanese).
- List, J.H. (1992): Wave groupiness variation in the nearshore, *Coastal Engineering*, Vol.15, pp.475-496.

Overtopping formula for vertical tiers-headed breakwaters

Corrado Altomare¹, Leonardo Damiani² and Xavier Gironella³

Abstract

The semi-empirical methods are useful tools to understand the wave overtopping phenomena, but uncertainty remains on their applicability. It's necessary to carry out campaign surveys or laboratory tests to support them. In this paper we apply the methods proposed in the European Overtopping Manual (2007) in order to assess the flows over a vertical breakwater, marking the need to calibrate those methodologies to take into account the peculiar geometry of the structural system. This was done by introducing appropriate correction factors. The results show an improved accuracy, among numerical results and physical ones.

Keywords: overtopping; empirical models; tandem breakwater.

1 Introduction

Coastal structures are commonly built to protect coastal zones against storm surges and large waves that may lead to several damages of the landward area, with hazards related to the security and human safety.

The wave overtopping is a phenomenon of wave - structure interaction that consists of waves passing over the crest of the coastal defense in the form of continuous sheet of water, plumes or splash, depending on the seaward geometry of the structure. The overtopping is complex and nonlinear, random in time and volume, set by different geometric – structural and hydrodynamic factors; it occurs for a given value of wave height and depends mainly on the freeboard of the structure as well as of the sea state.

The importance of this phenomenon is often undervalued by the final users, because of the sporadic occurrence of the event. In terms of risk the consequences can consist of different types: danger to pedestrian and vehicles, damage for seawalls, building, infrastructure and ships, internal residual agitation.

The available experimental data point out to the difficult description of the phenomenon in detail. Therefore the assessments of the mean overtopping discharge q and the total overtopped volume V are considered sufficient for the proper design of the coastal structures.

The analysis of the applicability of the predictive methods to vertical seawalls is described in the present paper. A peculiar seawall is studied: its complex configuration is set of its proper geometry and the coupling of the structure with a submerged breakwater.

The results of 2D model tests are shown: they suggested to adjust the methods in order to take into account that rare structural layout.

2 Wave overtopping assessment

The complexity in assessing the overtopping explains the huge development of multiple approaches leading to the estimate of the phenomenon: numerical models (SPH, 2006; VOF, 2007; etc.), empirical methods (Van der Meer et al. 1992, 2003, 2005, Franco 2005; etc.), neural networks (Medina 1999, Medina et al, 2002, EurOto Manual,2007) and physical model 2D and 3D experiments.

¹ PhD, Laboratori d'Enginyeria Marítima (LIM), Universitat Politècnica de Catalunya (UPC), Jordi Girona, 1-3, Edif. D1, Barcelona, 08034, Spain, corrado.altomare@upc.edu

² Professor, Water Engineering and Chemistry Department (DIAC), Technical University of Bari, via E. Orabona, Bari, 70125, ITALY, l.damiani@poliba.it

³ Professor, Laboratori d'Enginyeria Marítima (LIM), Universitat Politècnica de Catalunya (UPC), Jordi Girona, 1-3, Edif. D1, Barcelona, 08034, Spain, xavi.gironella@upc.edu

In the last years different European and International projects (VOWS 2000, OPTICREST 1998-2001, CLASH 2002-2005) led to the revisions or implementation of the mentioned above methodologies. These projects prove the growing interest in an holistic and more accurate assessment of the overtopping, leading to the creation of global databases of information. This would take to development of new models and methods (European Overtopping Manual 2007) supported by laboratory test results and measurements in situ, also considering the effects due to the model test scale and the complexity of the factors that affect the phenomenon in reality (wind, fluid viscosity, etc.).

2.1 The European Overtopping Manual (2007)

The European Overtopping Manual is perhaps today's most advanced tool for the assessment of the wave overtopping, as the formulations contained in it and the proposed tools (PC-overtopping and Neural Network) have been calibrated on data from over 10,000 tests performed worldwide and collected in the database of the European CLASH project (2002-2005).

Among the methods proposed in the manual, the empirical formulas and the Neural Network were analysed and applied to the analysed vertical seawall. The choice is derived from the geometric - structural configuration of the study case.

2.1.1 The empirical formulations

The empirical methods are simplified representations of the physics of the process, presented in a dimensionless equation, which relates the mean overtopping discharge to the main factors that characterize the phenomenon.

These methods are generally adjusted on the results of laboratory tests or prototype measurements. Several authors (Bradbury and Allsop 1988, Van der Meer 1992) quantified the mean overtopping discharge rate as a function of the principal geometrical and hydraulic parameters: the significant wave height H_s at the toe of the structure, the peak period T_p or mean spectral periods T_{0m} (in deep water) and $T_{0m-1,0}$ (in shallow water), the depth at the toe of the structure h_s , etc.

Some authors have also analyzed the effects due to: the roughness of the external layer of the seawall, the presence of a berm at the toe, the obliquity of the wave attack. The key relationships are of two types:

$$Q = aR e^{-bR} \text{ or } Q = aR^{-b} \quad (1)$$

where Q is the adimensional mean discharge per meter of crest length and R is the non-dimensional crest freeboard defined as the ratio between the geometrical crest freeboard and the incident significant wave height at the toe of the structure. The experimental coefficients a and b of the equation (1) depend on the configuration of the structure and of the sea conditions at the toe (fig. 1).

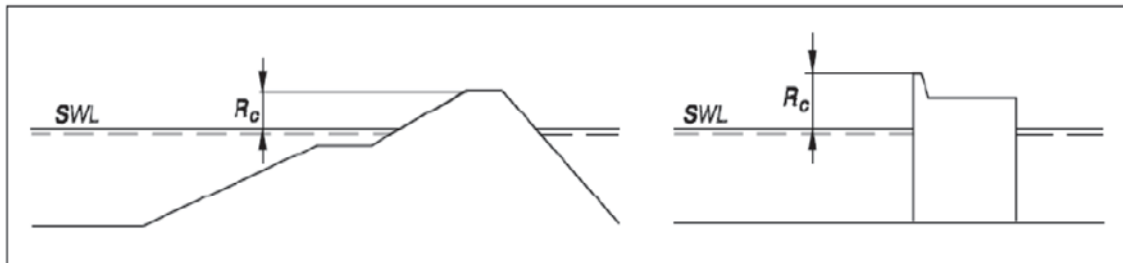


Figure 1: Reference scheme of the overtopping formulations

Referring to the vertical walls, in particular to the Vertical Composite Walls, as defined in the European Overtopping Manual, a fictitious depth value is introduced, taking into account the presence of a toe berm that induces changes on the characteristics of wave:

$$d^* = 1.35 (2d\pi h_s) / (H_{m0} T_{m-1,0}^2) \quad (2)$$

where H_{m0} e $T_{m-1,0}$ represent respectively the mean spectral wave height and period at the toe of the structure, h_s is the depth of the bottom close to the structure and d is the water depth in front of the toe berm.

The d^* parameter defines if the phenomenon conditions are impulsive or non-impulsive. The non-impulsive condition occurs when the waves are relatively small compared to the depth at the toe of the structure and have a low steepness. In contrast, the impulsive condition on the vertical walls occurs when the wave height is high compared to the depth, due, for example, to the shoaling bathymetry or structure toe, with waves breaking violently on the wall, creating very high pressures in small time intervals. Under these conditions, jets of water mixed with air are generated, that overtop the sea defences. In this paper we refer to non-impulsive conditions that characterized the carried out tests.

The expression between the mean overtopping discharge and the values of wave height and the crest freeboard in non-impulsive conditions ($d^* > 0.3$) is the following one:

$$q / \sqrt{(gH_{m0}^3)} = 0.04 \exp(-2.6 R_c / H_{m0}) \quad \text{valid for } 0.1 < R_c / H_{m0} < 3.5 \quad (3)$$

where R_c represent the crest freeboard.

2.1.2 The Neural Network for the overtopping assessment

The neural network (NN) is a non-linear structure of statistical data organized as a model tools, represented by the links among elements, called artificial neurons. In the past, NN has been successfully applied to the hydraulic engineering (Mase et al. 1995, Medina et al. 2002).

The Neural Network for overtopping assessment, proposed in the European Overtopping Manual has a three layered structured: the first layer contains 15 neurons, corresponding to the number of the input parameters (among these there are the spectral height and average period $H_{m0, toe}$ and $T_{0m-1,0}$ at the toe of the structure, surface roughness, berm width, water depth, obliquity of the wave attack, the seaward slope of the structure, etc.); the last layer contains only one neuron corresponding to the output value of mean overtopping discharge q . The middle one, finally, is the site of the synapses that connect input and output layers. The synapses were calibrated and weighted using the set of the reference data, collected in the database. The Figure 2 shows a scheme of the NN input parameters.

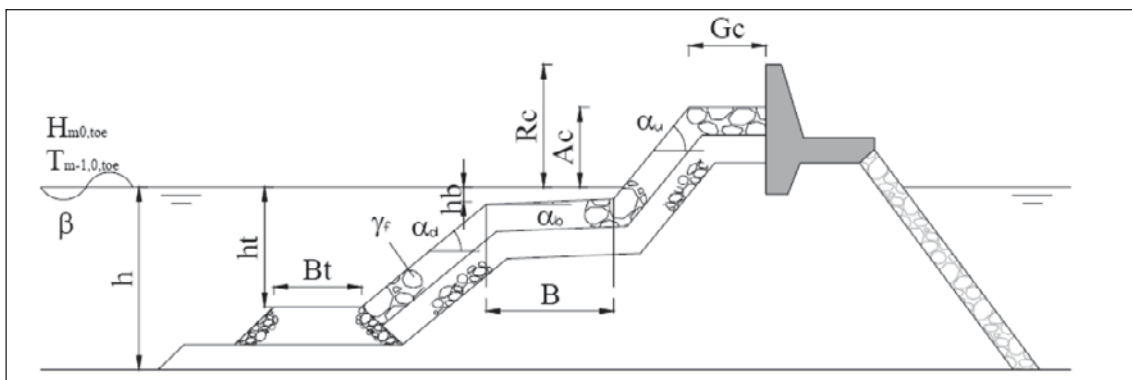


Figure 2: Scheme of the input parameters in the Neural Network for the overtopping assessment

3 The case of study

The main aim of the experimentation was to evaluate the mean overtopping discharge over a tandem breakwater composed by a vertical seawall coupled with a submerged breakwater. In the prototype scale the mean distance between the wall and the breakwater is about 60 m and

the submergence of the last one is 4 m. The tests were carried out at the Laboratory Maritime Engineering of the Technical University of Catalunya (CIIRC-LIM/UPC), in Barcelona, Spain.

Another special feature of the vertical structure is its crest, shaped as a flight of steps, with the maximum freeboard equal to 7:35 m above SWL. The lower part of the steps is 2.2 m above the SWL, in prototype scale (Fig. 3).

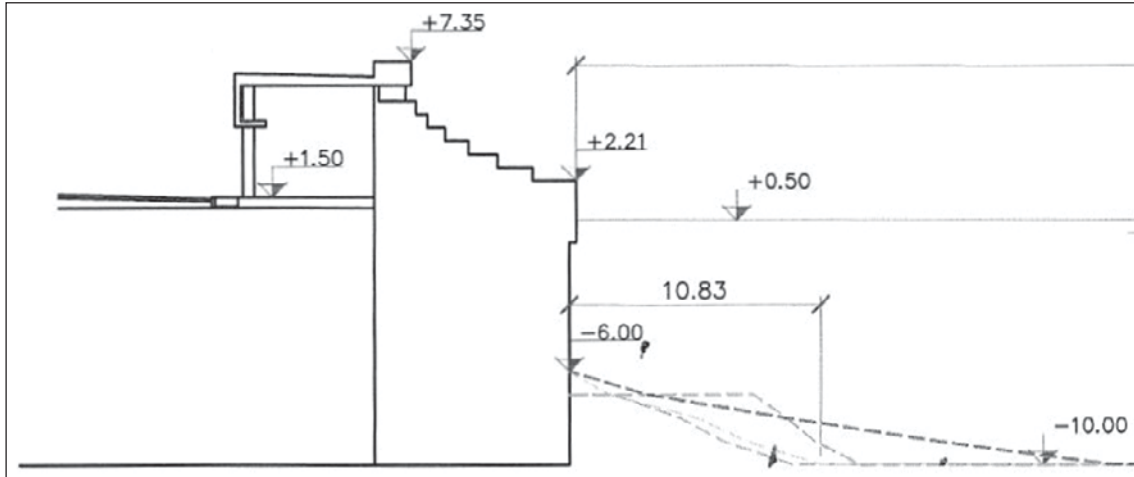


Figure 3: Vertical seawall in prototype scale

The water depth at the toe of the structure is approximately 10.00 m. The outer layer of the submerged breakwater is made of irregular blocks with a volume varying from 5 to 10 mc. This submerged breakwater has the task of dissipating the energy of the incident waves, reducing the possible erosion at the toe of the vertical wall.

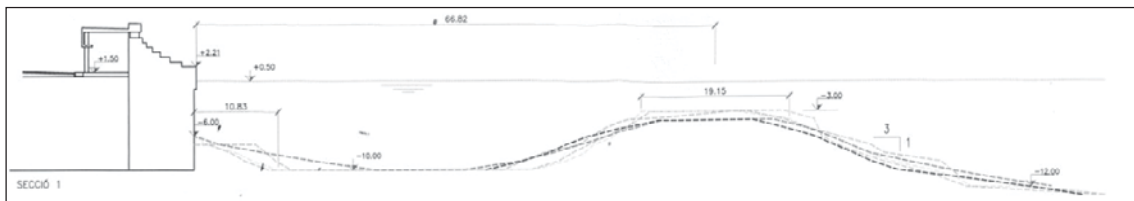


Figure 4: Layout of vertical seawall coupled with submerged breakwater (prototype scale)

The two-dimensional physical model tests were carried out in the small-scale flume, called CIEMito, in the CIIRC-LIM/UPC. The flume is 18 meters long and has a section of 38 cm wide and 50 cm high. The wave generator (piston type) allows the reproduction of irregular and regular wave trains with height up to 28 cm and maximum periods of 2 sec.

Storm surges have been reproduced with JONSWAP spectrum with a γ value of 3.0 and 300 waves for each train, considered as representative of a single storm.

The model scale is 1:50, according to Froude similarity. The model is built mainly in plywood; natural stones are used for the outer layer of the submerged breakwater. The significant wave height varies from 0.065 m to 0.102 m and the peak period from 0.98 s to 1.91 s, in model scale. The choice of the range for the wave characteristics depends on the will to analyze overtopping referring to extreme events with return periods of 1, 5 and 37 years.



Figure 5: View of the model during the experiments

The surface profile is measured by means of 8 resistive gauges, located along the flume. Analysing the wave signals it was possible to define the transmission due to the submerged breakwater and carry out the reflection analysis using the Mansard e Funke (1980) method. The mean wave overtopping rates were deduced by overtopped volumes collected in tanks, placed on the back of the main structure, and the duration of each test.

Due to the small scale of the tests, the measured discharges are corrected as well as indicated by De Rouck J. et al. (2005).

4 The application of the methods

The preliminary analysis of volumes and overtopping flows using empirical methods, has clashed with the inability to recognize the factors that could take into account the peculiar geometry of the vertical wall and its interaction with the submerged breakwater. The interest was therefore in finding a way that could describe the effects of this layout on the overtopping rate.

Previously it was necessary to analyze the wave surface profile, extracting the incident and reflected waves height from the total ones. Applying the methodology of Mansarde and Funke (1980), by means of the WaveLab software (<http://hydrosoft.civil.aau.dk/wavelab>), it was possible to reconstruct the effects of reflection due to the main breakwater and determine more precisely the spectral parameters of the incident wave at the toe. A set of tests, performed for the configuration without the submerged breakwater, made possible to assess its dissipative effects on the incident wave.

The main breakwater is similar to a composite vertical wall, as described into the EurOtop: therefore it was necessary to assess whether the wave conditions were non-impulsive or impulsive. The character of each test so calculated was verified also using a video analysis conducted for each experiment. Non-impulsive conditions were found in 77% of the cases. For them, representing the cases with higher probability of occurrence, the analysis, described in this paper, was carried out.

The application of the equation (3) led to high dispersion of results compared with experimental ones. This is because, with the formulations contained in the EurOtop, is not possible to introduce the effects of the studied particular layout on the overtopping flows. A correction factor was calculated by a linear regression analysis. This factor is a function of d^* . In particular:

$$\chi = \psi \sqrt{d^*} \quad (4)$$

for ψ between 1.68 and 1.89, where χ means a correction factor of the quantity R_c/H_{m0} appearing in the exponent of (3).

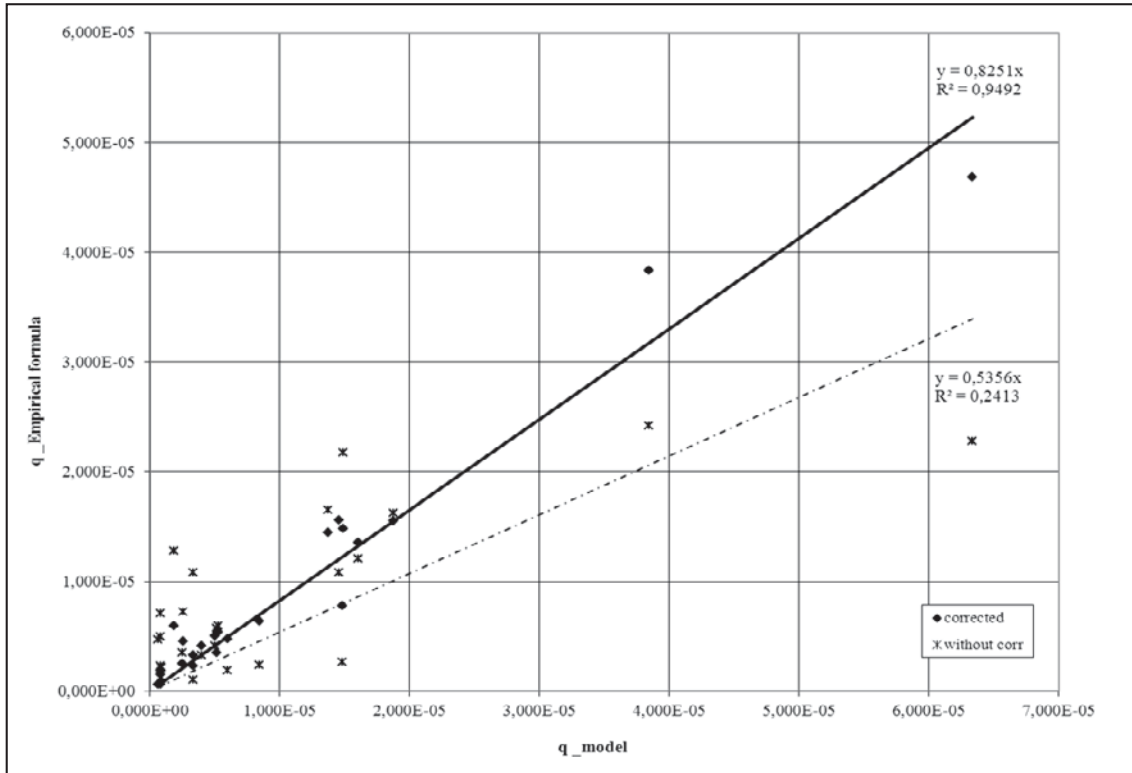


Figure 6: Results of the empirical formula compared with physical ones.

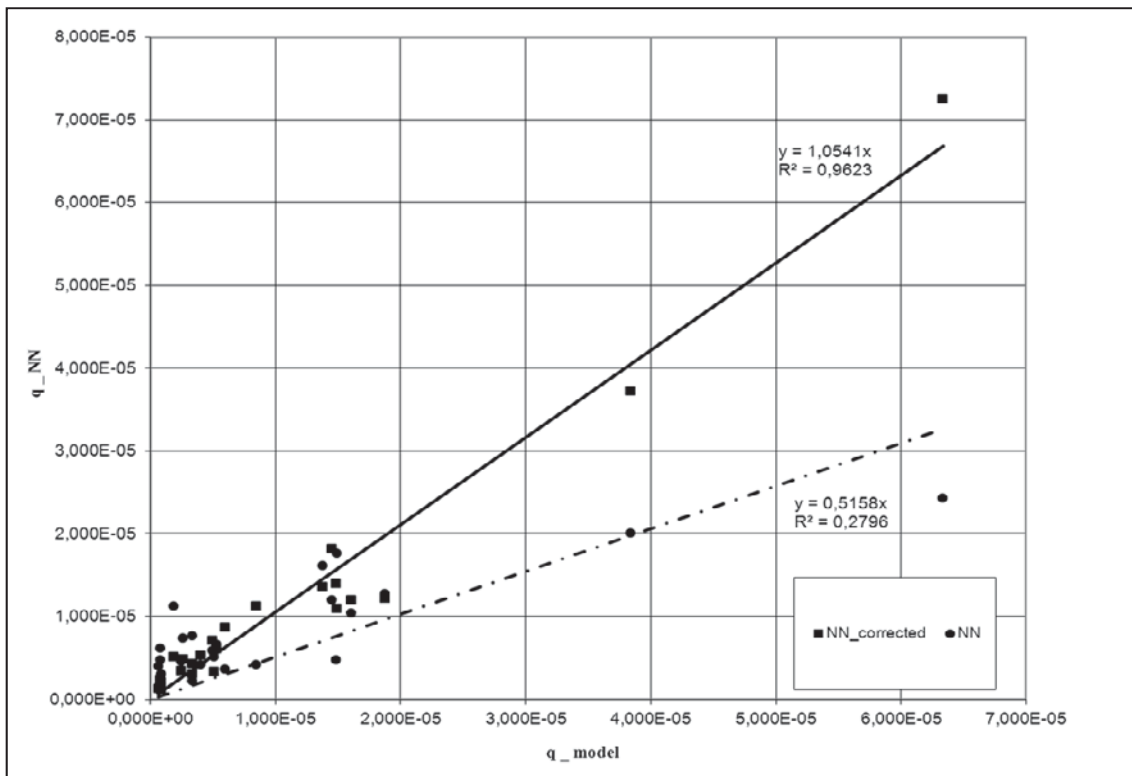


Figure 7: Results of the NN compared with physical ones.

The same analysis was carried out using the neural network for overtopping assessment, described in the European Overtopping Manual (2007). In the NN all the hydraulic and structural quantities were introduced, considering the input freeboard as the maximum freeboard of the

staircase. The results show dispersion, if compared with the physical ones. Therefore, because of both the formulas and the NN are calibrated using the same CLASH database, the same correction, found for the empirical formulations, was introduced in the neural network, as a fictitious value for the crest freeboard instead of the real one. In this way, a good accordance is obtained between calculated and measured overtopping discharges.

5 Conclusions and future developments

Nowadays the new planning environmental constrains and landscape demands require engineers to implement non-classical solutions, characterized by more complex structural configurations: the particular details and features of such new engineering choices lead to solutions that cannot be easily classified. This supposes to continually update the existing database in order to represent all the kind of structures.

In this paper we analyse the problems related to the assessment of overtopping discharge over coastal defences by means of predictive methods. In particular, it was checked the applicability of empirical formulas and neural network to a tandem system composed by a vertical seawall and a submerged breakwater.

The application of these methods, based on the CLASH database, highlighted the weaknesses of the models. These are mainly related to the inconsistency of the data set or the lack of data for certain kind of geometrical configurations. In this case it was necessary to introduce a correction factor that could take into account the effects generated by the particular shape of the vertical wall, with a crest shaped as a flight of steps and coupled with a submerged breakwater.

While the European Overtopping Manual remains at the time one of the most useful tools for understanding the overtopping phenomena, the experimental results show the necessity to adjust the proposed methods to the particular structure configurations. Therefore it is advisable to conduct further physical model tests or prototype measurements, by which to extend the applicability of these methods to a greater variety of real cases

6 Acknowledgements

To the staff of the LIM/CIIRC-UPC (Laboratory d'Enginyeria Marítima) of the Technical University of Catalunya for their contribution to the execution and analysis of physical model tests.

7 References

- W. Allsop, N.W.H., T. Pullen, J.W. van der Meer, H. Schüttrumpf and A. Kortenhaus. 2008. 'Improvements in wave overtopping analysis: the EurOtop overtopping manual and calculation tool', Proc. COPEDEC VII, Dubai, UAE.
- T. Pullen, W. Allsop, T. Bruce, A. Kortenhaus, H. Schüttrumpf, J.W. van der Meer. 2008. 'EurOtop – overtopping and methods for assessing discharge', Flood Risk Management: Research and Practice, Samuels et al. (eds.) ISBN 978-0-415-48507-4, pp 555-560.
- T. Pullen et al. 2008. 'Use of field measurements to improve probabilistic wave overtopping forecast', Proceedings of the 31TH International Conference of Coastal Engineering , Hamburg, Germany, pp. 3020-3031.
- EurOtop. 2007. 'Wave overtopping of sea defences and related structures: assessment manual', Die Küste, www.overtopping-manual.com.
- Losada I. et al. 2007. 'Numerical analysis of wave overtopping of rubble mound breakwaters', Journal of Coastal Engineering, Vol. 55, pp. 47-62.
- Shao S. et al. 2006. 'Simulation of wave overtopping by an incompressible SPH model', Journal of Coastal Engineering, Vol. 53, pp. 723-735.
- J. Van der Meer, M.R.A. van Gent, B. Pozueta, H. Verhaeghe, G.-J. Steendam, J.R. Medina. 2005. 'Applications of a neural network to predict wave overtopping at coastal structures', ICE, Coastlines, Structures and Breakwaters, London, pp. 259 – 268.

- De Rouck J. et al. 2005. 'New results on scale effects for wave overtopping at coastal structures', *Coastline, Structures and Berakwaters 2005*, Edited by N.W.H. Allsop, pp. 29-42.
- L. Franco. 2005. 'Nuove linee guida per la verifica delle dighe marittime nei riguardi della tracimazione ondosa', *Atti Giornate Italiane di Ingegneria Costiera VIII ediz.*, AIPCN, pp.51-57.
- G.J. Steendam, J.W. van der Meer, H. Verhaeghe, P. Besley, L. Franco, M.R.A. van Gent. 2004. 'The international database on wave overtopping', *ASCE, Proceedings ICCE 2004*, Lisbon, pp. 4301 – 4313.
- H. Verhaeghe, J.W. van der Meer, G.-J. Steendam, P. Besley, L. Franco and M.R.A. van Gent. 2003. 'Wave overtopping database as the starting point for a neural network prediction method', *ASCE, Proc. Coastal Structures 2003*, pp. 418 – 430.
- Medina, J.R, J.A. González-Escrivá, J. Garrido and J. De Rouck, 2002. 'Overtopping analysis using neural networks', *ASCE, Proc. ICCE 2002*.
- Medina, J.R. 1999. 'Neural network modelling of runup and overtopping', *ASCE, Proc. Coastal Structures, Santander, Vol. 1*, pp 421-429.
- Mase, H., M. Sakamoto and T. Sakai. 1995. 'Neural network for stability analysis of rubble-mound breakwaters', *J. of Waterway, Port, Coastal and Ocean Eng.*, ASCE, pp. 294-299
- Van der Meer, J.W. and Stam, C.J.M. 1992. 'Wave runup on smooth and rock slopes', *ASCE, Journal of WPC and OE, Vol. 188, No. 5*, pp. 534-550, New York. Also *Delft Hydraulics Publication No. 454*.
- Bradbury A.P. and Allsop N.W. 1988. 'Hydraulic effects of breakwater crown walls', *Proceedings of the Breakwaters'88 Conference*, Institution of Civil Engineers, Thomas Telford Publishing, London, UK, pp. 385-396.
- E.P.D. Mansard & E.R. Funke. 1980. 'The measurement of incident and reflected spectra using a least squares method', *Proc. 17th Coastal Eng. Conf.*, ASCE, Sidney, pp. 154–172.
- <http://hydrosoft.civil.aau.dk/wavelab/>, Aalborg University, WaveLab v.3 .

Technical Session 2: Coastal Processes

Chairman: Dr.-Ing. Stefan Schimmels

A development of an estuarine hydrodynamic model in cylindrical coordinates

Luminita-Elena Boblea¹ and Michael Hartnett²

1 Introduction

Estuaries and coastal areas have been the most populated regions around the world, with 60% of the world's population living in these regions. According to the US Bureau of the Census, worldwide the human population is doubling every 30-50 years; due to migration, along many coasts the population is doubling approximately every 20 years. Anthropogenic effects are adverse to these important systems due to discharging non point and point sources of waste. Although natural waters (rivers, lakes, oceans) have an ability of self-purification, impacts of pollutants in these waters have shown that legislation protecting them against polluters, improving or conserving their status has to exist. In Europe, Directives of the European Union, e.g. Water Framework Directive, regulate the water quality legislative framework. Also, coastal flooding due to tides, storm surges and waves needs to be mitigated against. Therefore, development of efficient hydrodynamic, solute transport and water quality models is necessary in order to help us better understand and forecast these complex phenomena.

In hydrodynamic modelling solution of the continuity and Navier-Stokes equations, also called governing equations, is sought. The Navier-Stokes equations describe water motion, whereas the continuity equation states that energy and mass are constant over the considered domain. The analytical solution of the governing equations cannot be obtained due to the complexity of the studied system. Hence, numerical methods are used for solving the complicated problems related to the hydrodynamic modelling of rivers, estuaries and oceans and they are applied to specific problems. There are two classes of numerical models commonly used: structured grid approaches (primarily finite difference algorithms) and unstructured grid approaches (including finite element and finite volume methods). The model grid results in a numerical method through the discretization of the domain. Discretization is the process of separating the continuous domain of the problem into numerous components, called elements. Structured grids are relatively straightforward and use efficient algorithms. Their main drawback is that they are limited as far as it concerns the flexibility in resolving the complex shorelines. These grids employ quadrilateral grid cells. Unstructured grid models use variable triangular and tetrahedral elements, but also elements of mixed type with irregular connectivity. The finite element methods present high sensitivity to numerical errors and they need longer running times [Lin and Chandler-Wilde (1996)]. Therefore, structured grids will be next considered. Factors such as problem size, problem complexity and the representation of reality converge to grid design. The choice of a suitable coordinate system considers the type of geometries describing the boundaries. Cartesian coordinates, handle the simple rectangular geometries with application to small geographical areas, whereas spherical coordinates are best used to describe large regions. Curvilinear coordinates are a natural choice for complex geometries. Curvilinear, boundary-fitted coordinates can be orthogonal or non-orthogonal. Orthogonal coordinates result in fewer computing operations, faster convergence and better stability and accuracy of the solution. Non-orthogonal coordinates are easier to generate and provide greater flexibility in the distribution of the grid points but show a reduced convergence rate, accuracy and stability. Most of the estuarine and coastal area models have been developed using rectangular [Falconer and Chen (1990), Burchard and Bolding (2002)], spherical [Muin and Spaulding (1996), (1997)], curvilinear orthogonal [Lin and Chandler-Wilde (1996), Nikitin (2006)] and non-orthogonal grids [Spaulding (1984), Sheng (1989), Klevanny et al. (1994), Andronosov et al. (1997), Ye et al. (1998), Barber and Scott (2000), Burchard and Bolding (2002), George (2007)].

¹ National University of Ireland, College of Engineering and Informatics, l.boblea1@nuigalway.ie

² National University of Ireland, College of Engineering and Informatics, michael.hartnett@nuigalway.ie

Details of development of a new two-dimensional estuarine hydrodynamic model in cylindrical polar coordinates are presented. The advantage of using this approach is that the coordinate system can be fitted to estuary's shape. This way a fine resolution is obtained in coastal area and a coarse resolution away from the coast provided that position of the pole is appropriately chosen. Moreover, the boundary error is reduced when compared to Cartesian coordinates. In the end, the model is aiming at obtaining more accurate results without increasing computational costs.

Section 2 describes mathematical modelling and methodology for obtaining the solution of the governing equations in two-dimensions, preliminary results are given in section 3, whereas section 4 presents conclusions of the present research.

2 Mathematical Modelling and Methodology

Water motion is described by the Navier-Stokes (NS) equations, which represent the basis of hydrodynamic modelling. They describe the changes in flow. The shallow water equations result from applying the specific properties of the estuary or coastal area to the momentum conservation (NS) equations. For a given domain, hydrodynamic modelling also implies the continuity principle, which states that mass and energy are constant. Due to the complexity of the studied system, the analytical solution of the continuity and momentum equations could not be obtained. Therefore numerical methods were employed. For a defined domain the Navier-Stokes and continuity equations were written in cylindrical coordinates in terms of instantaneous velocities and body force [equations (1)-(4)].

$$\begin{aligned} \frac{\partial \tilde{v}_r}{\partial t} + \frac{\partial \tilde{v}_r^2}{\partial r} + \frac{1}{r} \frac{\partial \tilde{v}_r \tilde{v}_\theta}{\partial \theta} + \frac{\partial \tilde{v}_r \tilde{v}_z}{\partial z} + \frac{\tilde{v}_r^2 - \tilde{v}_\theta^2}{r} = -\frac{1}{\rho} \frac{\partial \tilde{p}}{\partial r} + \frac{1}{\rho} \left(\frac{\partial \tilde{\tau}_{rr}}{\partial r} + \frac{1}{r} \frac{\partial \tilde{\tau}_{\theta r}}{\partial \theta} + \right. \\ \left. + \frac{\partial \tilde{\tau}_{zr}}{\partial z} + \frac{\tilde{\tau}_{rr}}{r} - \frac{\tilde{\tau}_{\theta\theta}}{r} \right) + \tilde{f}_r \end{aligned} \quad (1)$$

$$\begin{aligned} \frac{\partial \tilde{v}_\theta}{\partial t} + \frac{\partial \tilde{v}_r \tilde{v}_\theta}{\partial r} + \frac{1}{r} \frac{\partial \tilde{v}_\theta^2}{\partial \theta} + \frac{\partial \tilde{v}_z \tilde{v}_\theta}{\partial z} + 2 \frac{\tilde{v}_r \tilde{v}_\theta}{r} = \tilde{f}_\theta - \frac{1}{r} \frac{\partial \tilde{p}}{\partial \theta} + \\ + \frac{1}{\rho} \left(\frac{\partial \tilde{\tau}_{r\theta}}{\partial r} + \frac{1}{r} \frac{\partial \tilde{\tau}_{\theta\theta}}{\partial \theta} + \frac{\partial \tilde{\tau}_{z\theta}}{\partial z} + 2 \frac{\tilde{\tau}_{r\theta}}{r} \right) \end{aligned} \quad (2)$$

$$\begin{aligned} \frac{\partial \tilde{v}_z}{\partial t} + \frac{\partial \tilde{v}_r \tilde{v}_z}{\partial r} + \frac{1}{r} \frac{\partial \tilde{v}_\theta \tilde{v}_z}{\partial \theta} + \frac{\partial \tilde{v}_z^2}{\partial z} + \frac{\tilde{v}_r \tilde{v}_z}{r} = \\ = \tilde{f}_z - \frac{1}{\rho} \frac{\partial \tilde{p}}{\partial z} + \frac{1}{\rho} \left[\frac{\partial \tilde{\tau}_{zr}}{\partial r} + \frac{1}{r} \frac{\partial \tilde{\tau}_{z\theta}}{\partial \theta} + \frac{\partial \tilde{\tau}_{zz}}{\partial z} + \frac{\tilde{\tau}_{zr}}{r} \right] \end{aligned} \quad (3)$$

$$\frac{1}{r} \frac{\partial (r \tilde{v}_r)}{\partial r} + \frac{1}{r} \frac{\partial \tilde{v}_\theta}{\partial \theta} + \frac{\partial \tilde{v}_z}{\partial z} = 0 \quad (4)$$

with: $(\tilde{v}_r, \tilde{v}_\theta, \tilde{v}_z)$ instantaneous velocity components in the radial, angular and vertical directions [m/s]

$(\tilde{f}_r, \tilde{f}_\theta, \tilde{f}_z)$ body force terms in the three considered directions [N]

ρ density of sea water [kg/m^3] ($\rho = 1026 \text{ kg / m}^3$)

\tilde{p} instantaneous pressure [N/m^2]

$(\tilde{\tau}_{ij})$ instantaneous stress terms [N/m^2], ($i, j = r, \theta, z$)

Because the solution of the governing equations was sought for shallow water estuarine and coastal areas, the three-dimensional Navier-Stokes and continuity equations were depth integrated [equation (5)-(7)]. The shallow water assumption is that water depth is smaller than 20 times the length of the considered water body. Leibnitz integration rule and Boussinesq assumption were employed.

$$\begin{aligned} \frac{\partial V_r H}{\partial t} + \beta \left(\frac{\partial V_r V_r H}{\partial r} + \frac{1}{r} \frac{\partial V_r V_\theta H}{\partial \theta} + \frac{V_r^2 H - V_\theta^2 H}{r} \right) = \\ f_C V_\theta H - gH \frac{\partial \zeta}{\partial r} + \frac{\rho_a}{\rho} \gamma W_r W - g \frac{V_r V}{C^2} + \\ + \bar{E} H \left(\frac{\partial^2 V_r}{\partial r^2} + \frac{1}{r^2} \frac{\partial^2 V_r}{\partial \theta^2} + \frac{1}{r} \frac{\partial V_r}{\partial r} - \frac{2}{r^2} \frac{\partial V_\theta}{\partial \theta} - \frac{V_r}{r^2} \right) \end{aligned} \quad (5)$$

$$\begin{aligned} \frac{\partial V_\theta H}{\partial t} + \beta \left(\frac{\partial V_r V_\theta H}{\partial r} + \frac{1}{r} \frac{\partial V_\theta V_\theta H}{\partial \theta} + 2 \frac{V_r V_\theta H}{r} \right) = \\ - f_C V_r H - \frac{1}{r} gH \frac{\partial \zeta}{\partial \theta} + \frac{\rho_a}{\rho} \gamma W_\theta W - g \frac{V_\theta V}{C^2} + \\ + \bar{E} H \left(\frac{\partial^2 V_\theta}{\partial r^2} + \frac{1}{r^2} \frac{\partial^2 V_\theta}{\partial \theta^2} + \frac{1}{r} \frac{\partial V_\theta}{\partial r} + \frac{2}{r^2} \frac{\partial V_r}{\partial \theta} - \frac{V_\theta}{r^2} \right) \end{aligned} \quad (6)$$

$$\frac{\partial \zeta}{\partial t} + \frac{1}{r} \frac{\partial (r V_r H)}{\partial r} + \frac{1}{r} \frac{\partial (V_\theta H)}{\partial \theta} = 0 \quad (7)$$

with: (V_r, V_θ) depth-integrated velocity components in the radial and angular directions [m/s]

β correction factor for non-uniformity of vertical velocity profile [$\beta = 1.016$ for seventh power law velocity distribution]

H water depth [m]

f_C Coriolis acceleration term [rad/s]

ρ_a air density [kg/m^3] ($\rho_a = 1.25 \text{ kg/m}^3$)

(W_r, W_θ) wind speed components in the radial and angular directions [m/s]

C Chezy coefficient

Subsequently, the depth integrated equations were mapped onto a rectangular domain [equations (8), (9), (10)] using analytical relationships $\xi^r = \xi^r(r, \theta)$, $\xi^\theta = \xi^\theta(r, \theta)$, $r = r(\xi^r, \xi^\theta)$, $\theta = \theta(\xi^r, \xi^\theta)$ following Morinishi et al (2004). Figure 1 illustrates the physical and computational domain. Solution of the governing equations was obtained with a conservative finite difference. The finite difference methods present the advantages of being straightforward and easy to use unless the coefficients involved in the equations are discontinuous. Therefore, the transformed momentum and continuity equations were approximated using a finite difference scheme with an Arakawa C grid. Solutions of the governing equations were obtained with an Alternating Directions Implicit method. The ADI technique employed here assumes that the time step is split into two halves and at each time step the flux component in one direction and water elevation are computed at the upper time step, whereas all the other variables are written at the lower time step. Subsequently a tridiagonal system of equations resulted in each direction and solutions were got by means of Thomas algorithm.

$$\begin{aligned}
 & \frac{\partial q_{\xi^r}}{\partial t} + \beta \left\{ \frac{1}{J_{\xi}} \left[\frac{\partial}{\partial \xi^r} \left(\frac{J_{\xi}}{h_{\xi^r}} V_r q_r \right) + \frac{\partial}{\partial \xi^{\theta}} \left(\frac{J_{\xi}}{h_{\xi^{\theta}}} V_r q_{\theta} \right) \right] \right. \\
 & \left. + \frac{V_{\theta}}{J_{\xi}} \left(q_r \frac{\partial h_{\xi^r}}{\partial \xi^{\theta}} - q_{\theta} \frac{\partial h_{\xi^{\theta}}}{\partial \xi^r} \right) \right\} = \\
 & f_C V_{\theta} H - gH \frac{1}{h_{\xi^r}} \frac{\partial \zeta}{\partial \xi^r} + \frac{\rho_a}{\rho} \gamma W_r W - g \frac{V_r V}{C^2} \\
 & - \varepsilon H \left\{ \frac{1}{h_{\xi^r}} \frac{\partial}{\partial \xi^r} \left[\frac{1}{J_{\xi}} \frac{\partial (h_{\xi^{\theta}} V_r)}{\partial \xi^r} \right] + \frac{1}{h_{\xi^{\theta}}} \frac{\partial}{\partial \xi^{\theta}} \left[\frac{1}{J_{\xi}} \frac{\partial (h_{\xi^r} V_r)}{\partial \xi^{\theta}} \right] \right. \\
 & \left. + \frac{1}{h_{\xi^r}} \frac{\partial}{\partial \xi^r} \left[\frac{1}{J_{\xi}} \frac{\partial (h_{\xi^r} V_{\theta})}{\partial \xi^{\theta}} \right] - \frac{1}{h_{\xi^{\theta}}} \frac{\partial}{\partial \xi^{\theta}} \left[\frac{1}{J_{\xi}} \frac{\partial (h_{\xi^{\theta}} V_{\theta})}{\partial \xi^r} \right] \right\}
 \end{aligned} \tag{8}$$

$$\begin{aligned}
 & \frac{\partial q_{\theta}}{\partial t} + \beta \left\{ \frac{1}{J_{\xi}} \left[\frac{\partial}{\partial \xi^r} \left(\frac{J_{\xi}}{h_{\xi^r}} V_r q_{\theta} \right) + \frac{\partial}{\partial \xi^{\theta}} \left(\frac{J_{\xi}}{h_{\xi^{\theta}}} V_{\theta} q_{\theta} \right) \right] \right. \\
 & \left. + \frac{V_r}{J_{\xi}} \left(q_{\theta} \frac{\partial h_{\xi^{\theta}}}{\partial \xi^r} - q_r \frac{\partial h_{\xi^r}}{\partial \xi^{\theta}} \right) \right\} = \\
 & - f_C V_r H - gH \frac{1}{h_{\xi^{\theta}}} \frac{\partial \zeta}{\partial \xi^{\theta}} + \frac{\rho_a}{\rho} \gamma W_{\theta} W - g \frac{V_{\theta} V}{C^2} \\
 & - \varepsilon H \left\{ \frac{1}{h_{\xi^r}} \frac{\partial}{\partial \xi^r} \left[\frac{1}{J_{\xi}} \frac{\partial (h_{\xi^{\theta}} V_{\theta})}{\partial \xi^r} \right] + \frac{1}{h_{\xi^{\theta}}} \frac{\partial}{\partial \xi^{\theta}} \left[\frac{1}{J_{\xi}} \frac{\partial (h_{\xi^r} V_{\theta})}{\partial \xi^{\theta}} \right] \right. \\
 & \left. - \frac{1}{h_{\xi^r}} \frac{\partial}{\partial \xi^r} \left[\frac{1}{J_{\xi}} \frac{\partial (h_{\xi^r} V_r)}{\partial \xi^{\theta}} \right] + \frac{1}{h_{\xi^{\theta}}} \frac{\partial}{\partial \xi^{\theta}} \left[\frac{1}{J_{\xi}} \frac{\partial (h_{\xi^{\theta}} V_r)}{\partial \xi^r} \right] \right\}
 \end{aligned} \tag{9}$$

$$\frac{\partial \zeta}{\partial t} + \frac{1}{J_{\xi}} \frac{\partial}{\partial \xi^r} \left(\frac{J_{\xi}}{h_{\xi^r}} q_r \right) + \frac{1}{J_{\xi}} \frac{\partial}{\partial \xi^{\theta}} \left(\frac{J_{\xi}}{h_{\xi^{\theta}}} q_{\theta} \right) = 0 \tag{10}$$

with: $(h_{\xi^r}, h_{\xi^{\theta}})$ geometric scale factors of the transformation from cylindrical polar coordinates into rectangular coordinates [m]

J_{ξ} the Jacobian of the transformation from cylindrical into rectangular coordinates [$J_{\xi} = h_{\xi^r} h_{\xi^{\theta}}$]. It is called dilatation and represents the ratio of an elementary volume to its initial volume. A proper transformation requires that $0 < J_{\xi} < \infty$, i.e. the Jacobian has a finite positive value.

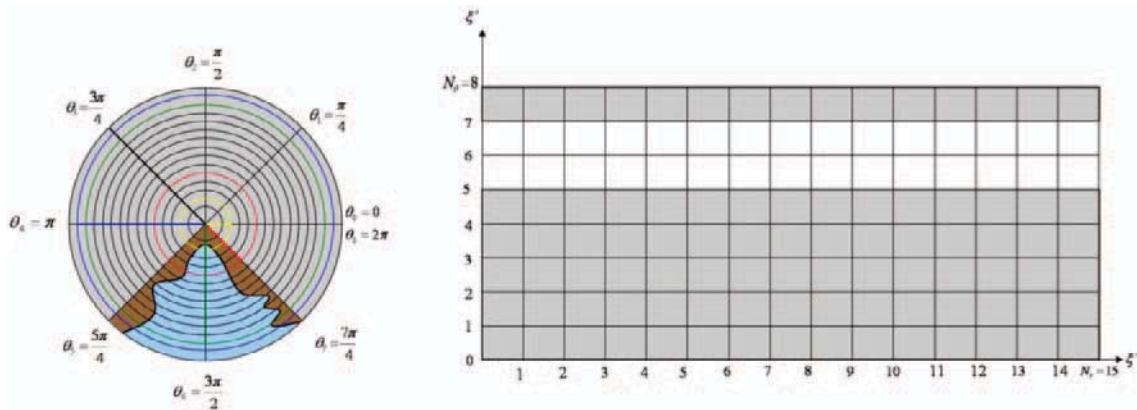


Figure 1: Simplified physical and computational plane for a hypothetical estuary [after Morinishi et al. (2004)]

The model simulated a 20km long harbour defined between two concentric circles ($r_1=7500\text{m}$, $r_2=27500\text{m}$) and two radii ($\theta_1=252^\circ$, $\theta_2=288^\circ$) making a 36° angle at the centre [figure 2]. A constant water depth of 10.0m and a uniform bed were considered. Tidal forcing was specified at the open boundary ($r_2=27500\text{m}$) by a sinusoidal wave with amplitude 2.077m and tidal forcing period 12.5 hours. Closed boundary condition assumed that normal velocity to the boundary is set to zero. New model included a weak temporal filter, namely the Robert-Asselin filter [Asselin (1972)], due to solution splitting at odd and even times. The value of the Asselin filter coefficient was chosen 0.1.

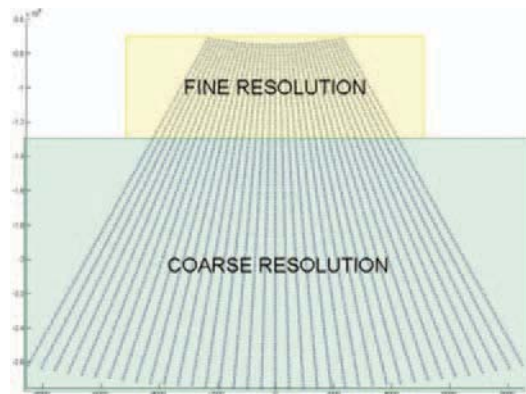


Figure 2: Considered domain

3 Preliminary Results

The Depth Integrated Velocities and Solute Transport model, a Cartesian coordinates model, was chosen for comparison of the results due to its extensive usage in industrial applications, i.e. Hartnett et al. (2010). Models set up and results obtained using both the rectangular model DIVAST and the new model for the same geometry were as follows:

- Boundaries of the considered harbour were represented by interpolation onto a rectangular grid for the rectangular model. Subsequently, a 60×52 grid was employed with grid spacing $\Delta x = \Delta y = 353\text{m}$. Simulation time was 144.00 hours, and time step was $\Delta t = 10.0\text{sec}$. Tidal forcing was specified within rectangular model on a straight line, due to the inability of specifying the forcing on a curved boundary.
- The new model was run for the same simulation time (144.00 hours), and $\Delta t = 10.0\text{sec}$. Computational grid dimensions were 42×38 with grid spacing $\Delta \xi^r = \Delta \xi^\theta = 1$. The geometrical scale factors were $h_{\xi^r} = 500\text{m}$, while h_{ξ^θ} varied from approx. 131m to 480m. Tidal forcing was specified with the same expression as within the rectangular model.

- Total velocities predicted by the new model were in agreement with those predicted by rectangular model. Also, a phase shift could be noticed in the new model predicted total velocities.
- Due to the geometry considered, with a larger width at $r_2=27500\text{m}$ and narrowing width until $r_1=7500\text{m}$, a slight increase in water level was expected. Both models predicted the increase, with new model results similar to those obtained from rectangular model. A phase shift was observed in the water levels obtained from new model.

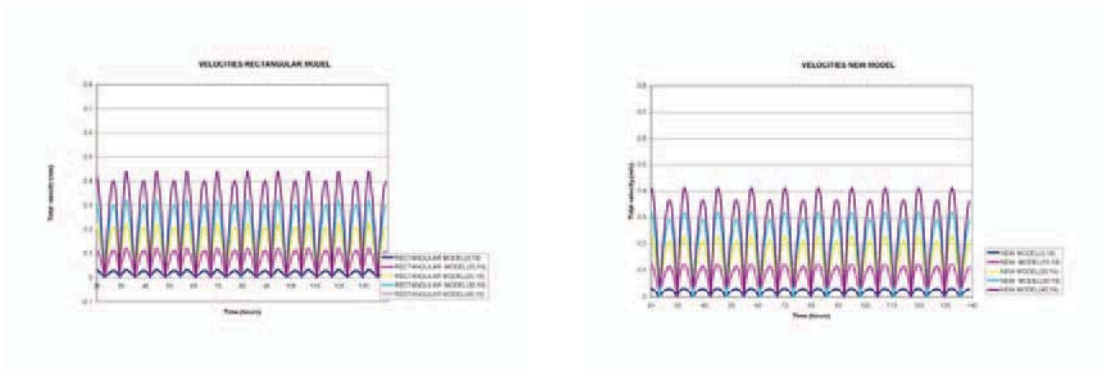


Figure 3: Total velocities comparison.

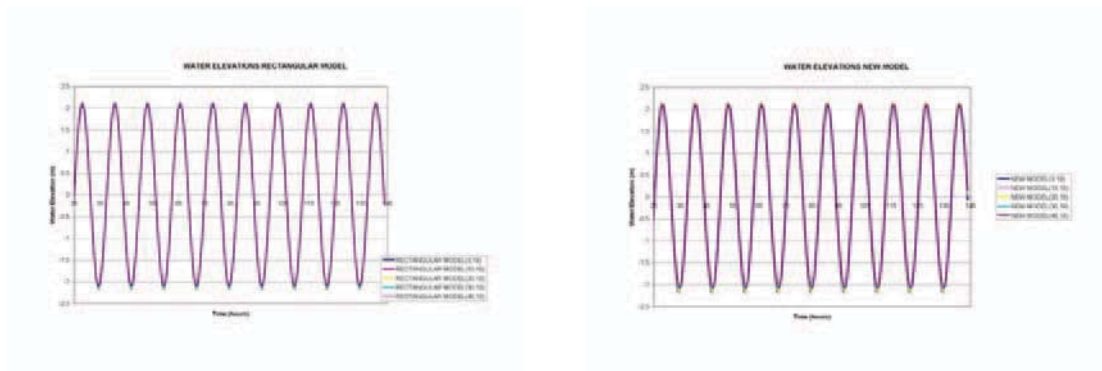


Figure 4: Water elevations comparison.

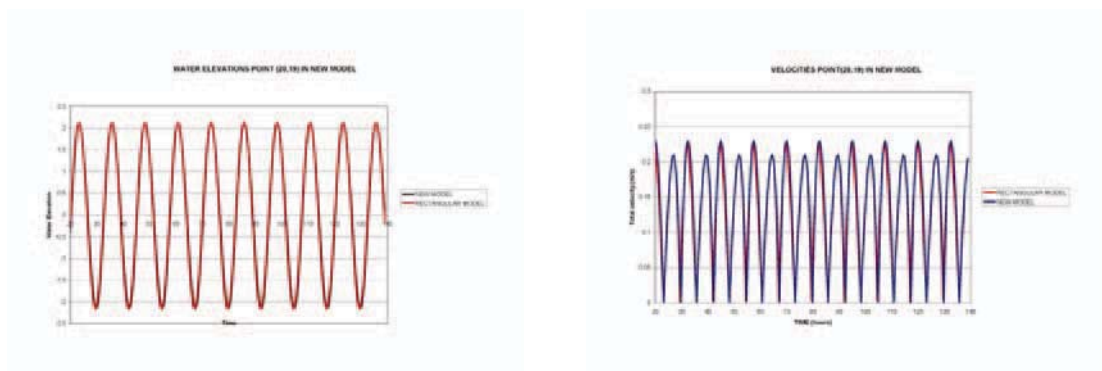


Figure 5: Water elevation and total velocities at $r=17000\text{m}$ in new model, corresponding to point C in rectangular model

Flow field for rectangular and new model is represented in figure 6.

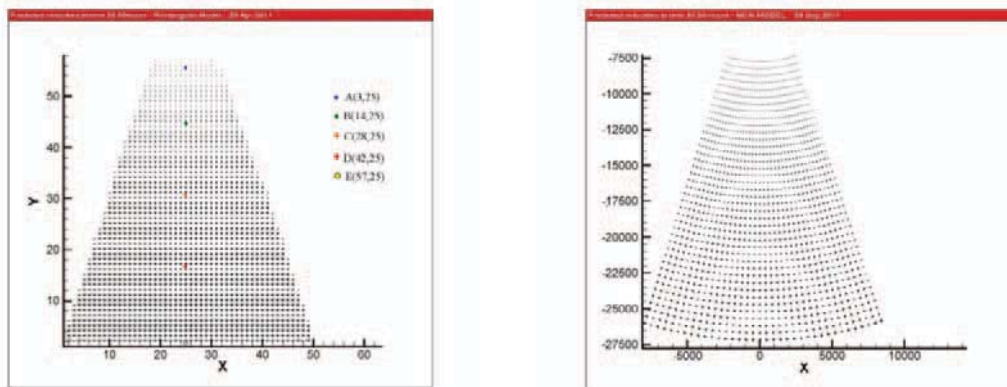


Figure 6: Flow field for rectangular model and new model. A, B, C, D, E were points where comparisons of water levels and total velocities with results from the new model were made

4 Conclusions

Development of a two-dimensional estuarine hydrodynamic model in cylindrical coordinates was described herein. The mathematical development including depth integration of the governing equations written in cylindrical coordinates and mapping transformations onto a rectangular grid was presented. The model was tested in a domain defined between two concentric circles and two radii. A uniform grid was employed in both directions with $\Delta x \neq \Delta y$ in the computational plane. The solution was obtained with an ADI technique combined with Thomas algorithm. Subsequently, the results were mapped back into the physical domain. A robust Cartesian coordinates model (DIVAST) with a uniform grid ($\Delta x = \Delta y$) was used for comparison of the results. A sinusoidal forcing was simulated at the outer radius with amplitude 2.077m and a period of 12.5 hours. The two models were run for a period of 144 hours. Comparisons between results obtained using both the new model and the rectangular model for the same geometry showed good agreement and further research is considered for evaluation and verification of the new model.

5 Acknowledgements

The research is funded by the IBM Smarter Cities Programme.

6 References

- Andronosov, A.A.; Vol'tzinger, N.E.; Liberman, Y.L. (1997): A two-dimensional model of the Barents Sea, *Oceanology*, Vol. 37, No., pp. 16–22, ISSN 00014370.
- Asselin, R. (1972): Frequency filter for time integrations, *Monthly Weather Review*, Vol. 100, No.6, pp.487-490, ISSN 1520-0493.
- Bao, X.W.; Yan, J.; Sun, W.X. (2000): A three-dimensional tidal model in boundary-fitted curvilinear grids, *Estuarine, Coastal and Shelf Science*, Vol. 50, No., pp. 775–788, ISSN 0272-7714.
- Barber, R.W.; Scott, L.J. (2000): Numerical modelling of tidal propagation in the Severn Estuary using a depth-adapted non-orthogonal grid, *Environmental and Coastal Regions III*, WIT Press, Vol. 5, pp. 127-136, ISBN 1-85312-827-9.
- Borthwick, A.G.L.; Kaar, E.T. (1993): A non-orthogonal curvilinear systems model of species transport in shallow flow domains, *Advances in Water Resources*, Vol.16, No. 6, pp. 331-350, ISSN 0309-1708.
- Burchard, H.; Bolding, K. (2002): GETM – a general estuarine transport model, Scientific documentation, Tech. Rep. EUR 20253 EN, European Commission, 157 pp.

- Falconer, R.A., Chen, Y. (1990): Modelling transport and water quality processes on tidal floodplains, in: *Floodplain Processes*, M.G. Anderson, D.E. Walling, P.D. Bates editors, John Wiley and Sons, Chichester, pp. 361-397, ISBN 0-471-96679-7, 658 S.
- George, K. (2007): A depth-averaged tidal numerical model using non-orthogonal curvilinear coordinates, *Ocean Dynamics*, Vol.57, No.4-5, pp. 363–374, ISSN 1616-7228.
- Hartnett, M.; Berry, A. (2010): Transport of lead in the Mersey Estuary: The development of a novel approach to deriving partition coefficients, *Advances in Engineering Software*, Vol. 41, No. 1, pp.84-91, ISSN 0965-9978.
- Klevanny, K.A.; Matveyev, G.V.; Voltzinger, N.E. (1994): An integrated modelling system for coastal area dynamics, *International Journal for Numerical Methods in Fluids*, Vol.19, No.3, pp.181-206, ISSN 1097-0363.
- Lin, B.; Chandler-Wilde, S.N. (1996): A depth integrated 2D coastal and estuarine model with conformal boundary fitted mesh generation, *International Journal for Numerical Methods in Fluids*, Vol. 23, No. 8, pp. 819–846, ISSN 1097-0363.
- Morinishi, Y.; Vasilyev, O.V.; Ogi, T. (2004): Fully conservative finite difference scheme in cylindrical coordinates for incompressible flow simulations. In: *Journal of Computational Physics*, Vol.197, No. 2, pp. 686-710, ISSN 0021-9991.
- Muin, M.; Spaulding, M. (1996): Two dimensional boundary-fitted circulation model in spherical coordinates, *Journal of Hydraulic Engineering*, Vol.122, No.9, pp. 512-521, ISSN 0733-9429.
- Muin, M.; Spaulding, M. (1997): Three dimensional boundary-fitted circulation model, *Journal of Hydraulic Engineering*, Vol. 123, No. 1, January 1997, pp. 2-12, ISSN 0733-9429.
- Nikitin, N. (2006:) Finite-difference method for incompressible Navier–Stokes equations in arbitrary orthogonal curvilinear coordinates, *Journal of Computational Physics*, Vol. 217, No. 2, pp. 759-781, ISSN: 0021-9991.
- Roy, G.D.; Humayun Kabir, A.B.M.; Mandal, M.M.; Haque, M.Z. (1999): Polar coordinates shallow water storm surge model for the coast of Bangladesh. In: *Dynamics of Atmospheres and Oceans*, Elsevier, Amsterdam, PAYS-BAS, INIST-CNRS, pp.397-413; ISSN 0377-0265.
- Sheng, Y.P. (1989): Evolution of a three-dimensional curvilinear-grid hydrodynamic model for estuaries, lakes and coastal waters:CH3D, in: *Estuarine and Coastal Modelling*, ASCE, Proceedings of the Estuarine and Coastal Circulation and Pollution Transport Model Data Comparison Specialty Conference, pp. 40-49, ISBN 9780872627581, Newport, Rhode Island, USA.
- Ye, J.; McCorquodale, J.A.; Barron, R.M. (1998): A three-dimensional hydrodynamic model in curvilinear coordinates with collocated grid, *International Journal for Numerical Methods in Fluids*, Vol.28, No.7, pp. 1109–1134, ISSN 1097-0363.

A 2D morphodynamic-numerical model of the surfzone

“Strand”

Peter Mewis¹

Abstract

“Strand” is a two-dimensional numerical model for the simulation of morphodynamic changes in the surf zone. It is based on unstructured triangular mesh. It simulates vertically integrated flow velocities and sediment fluxes and is coupled with the wave model SWAN. The important processes of surf zone development are implemented. Due to the process based approach it is well suitable for prognostic simulations.

Two-dimensional modeling of the near-shore bears the potential of computing the cross- and long-shore transport rates at the same time and in their direct interrelation. Coastal structures are resolved by the model mesh and their action can be investigated.

The model is capable of reproducing a concave beach profile, which is similar to the well known Bruun's profile. It is also capable of reproducing a breaker bar.

The application of the model is possible for the simulation of morphodynamic response around jetties, breakwaters, artificial reefs, permeable and impermeable groines and for the siltation of navigational channel. It can also be applied for the optimization of beach nourishment campaigns.

An example application is given for the depth development of a 5 km long part of the Baltic Sea coast, where a harbor has been build.

Keywords: morphodynamic modeling, sediment transport, coastline development, numerical modelling

1 Introduction

The sediment transport processes and the resulting morphodynamics of the nearshore coastal zone are quite complex. Self developing structures can be met, as there are longshore bars, crescentic bars, beach cusps and others. The intense near-shore coastal morphodynamic processes that make up the dynamics are not entirely understood today. New proposals like acceleration based transport are under consideration.

New formulas for net transport rates are still being developed. Beside field measurements the complex behaviour can be investigated with the help of numerical models. It is already a long time ago, that the model SBEACH has been developed. A rough division of the surf zone is made, for the application of specific formulas in the divisions. On the other hand the experience in the application of those models let the engineers trust the results of the computations within certain limits. In one-dimensional models the interaction of long-shore and cross-shore transport rates is not accounted for. Nevertheless in many applications it is unclear whether the cross-shore processes play a significant role or not. It would be of great advantage to have a two-dimensional model that describes all the different modes of transport in a natural process based manner. Because a large fraction of the sediment is transported along the bar, it is desirable to incorporate the bars in the simulation system. Unfortunately the dynamics of the bars is still difficult to be predicted.

Bagnold 1981 was the first who used the wave induced transport and the downslope transport to calculate the equilibrium beach profile on a process base.

The basic near-shore processes have been described by Roelvink and Stive 1989. An early attempt for 2D coastal modelling is described in de Vriend et al 1993. Even today highly

¹ Institute of Hydraulic Engineering and Water Resources Research, Technische Universität Darmstadt, Petersenstr. 13, 64286 Darmstadt, mewis@wb.tu-darmstadt.de

simplified formulas and models are applied, when the development of the coastline is to be calculated.

2 Parameterizations

Some of the relevant processes are acting down to a water depth of 10 m and more. The sediment is transported by a combination of the depth averaged velocity and other components like undertow, the mass transport velocity, asymmetry of the waves and the bed slope. The sediment diffusion and the downslope transport have been implemented in the transport formula for the moving sediment. The sediment transport is implemented as a single mode for both bedload and suspended load in a mass conservative way. For the entrainment of sediment the following formula is used:

$$E = a(bu_{bot}^2 + \bar{u}^2 - \bar{u}_{cr}^2)^{1.5} \quad (1)$$

with \bar{u}^2 mean current velocity [m^2/s^2]

u_{bot}^2 bottom orbital velocities [m^2/s^2]

u_{cr}^2 critical velocity for initiation of sediment transport including bed slope [m^2/s^2]

a, b calibration constants

The entrainment of sediment into the water column depends on flow velocity, wave orbital velocity and wave breaking. The breaker energy flux may also be incorporated in the entrainment function E . In the examples below it is however not switched on.

The model calculates the actual sediment transport rates as concentrations with a certain velocity. The transport velocity of the sediment is calculated by the following formula:

$$\vec{u}_{sed} = \vec{u} + \vec{w} \cdot (masstr + asymmetry - roller) \quad (2)$$

with \vec{w} is the energy mean propagation direction of the waves

\vec{u} is the mean vertical averaged current velocity computed by the flow model

$masstr$ is the classical formula for the mass transport velocity

$roller$ is the roller mass flux divided by the water depth

$asymmetry$ is a function of water depth, wave length and wave height, described by a set of values pre-computed from the stream function wave theory under the assumption of a horizontal bed. This function is strongly increasing with wave shoaling. Before wave breaking it is however slightly decreasing.

In the computations one mean grain size is used. The resulting cross shore bed profiles are in agreement with the measurements and also with the typical one found by Bruuns and Dean.

Because the breaker zone starts right at the seaward slope of the bar and depth induced breaking stops at the crest of the bar, an undertow proportional to the roller energy would prescribe the maximum seaward velocities at the crest of the bar. For a proper calculation the undertow cannot be the largest directly at the crest of the bar, as computed with this standard formulation. This is because the bar starts to move (seaward) in this case. It seems, that without a delay of the undertow, no stable bar will develop. In this case the bar is always propagating seaward. Otherwise, with an artificial shift of the wave energy to the shore, the bar becomes stable at a certain point, that depends on the parameters. For the shift simply a fixed distance of about 20 m was used.

3 Numerical scheme

The flow chart of "Strand" is given in figure 1.

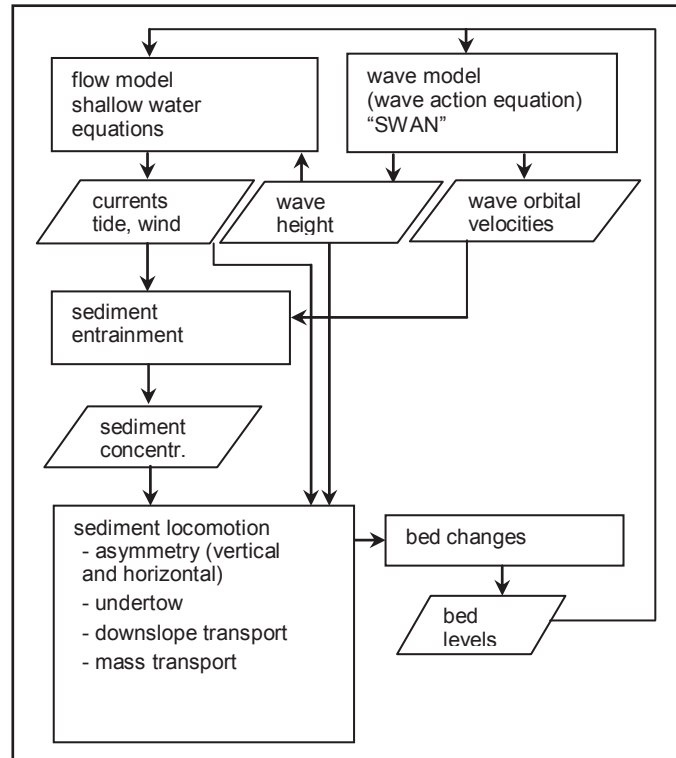


Figure 1: Flow chart of the computation in "Strand"

The morphodynamic model that has been applied in this study has been developed by the author. It comprises a flow solver based on the shallow water equations and a transport solver for sediment concentrations.

The model is based on the finite element method using triangular elements. This way unstructured grid can be used, that are very flexible in resolving hard structures. The model allows for wetting and drying. It is very stable und exactly mass conserving with respect to water and sediment.

One specific feature is the possibility to account for permeable groins. The elements, where the groins are located have an additional friction that depending on the permeability of the groin decelerates the current.

Wave propagation into shallow water is computed with SWAN. The roller concept of Svendsen 1984 is applied to calculate the radiation stress and undertow velocities. In SWAN the wave breaking is implemented according to Battjes and Janssen, that means the waves break when a certain relation between depth and wave height: $\gamma = H_{\max} / d = 0,73$ is reached. Wave Triad interactions are switched on. Radiation stresses are computed in Strand after Svendsen from wave height and roller energy gradient.

The model is a coupled morphodynamic model that calculates the waves, currents and the bed changes with instantaneous feed back. Coupling between SWAN and Strand is realized via the unix-pipe mechanism, that allows for a very fast transfer and a perfect timing of the runtime of the two computational processes.

Costal areas of 10-20 km length can be simulated for several days. With this kind of complex model it is not possible to compute the bed changes of a time series with a length of several years. Therefore a combination of the time-lapse or morphodynamic factor and a morphodynamic representative wind and wave load scenario has been chosen. The scenarios

with their forcing needs to be selected carefully for the purpose of long term simulations, as described by D. Roelvink earlier.

Because not each individual wave but only the wave energy is simulated, the swash zone cannot be described by this type of model. Nevertheless the surf beat phenomenon Thornton et al 1996 can in principle be modelled this way. For a depth range between 0.5 m below water level and twice the significant wave height above the water level a prescribed inclination of the bed in the swash zone has been implemented. This means that the sediment is redistributed in the swash zone to obtain a certain inclination of the bed in the direction of wave propagation. Using this approach sediment can be eroded from dry areas, thus allowing in principle for dune erosion.

Boundary conditions are equilibrium transport at the open boundaries. The bed-levels are fixed in small part all along the open boundaries. This way The appropriate wave, flow and sediment concentration patterns can establish.

4 Application of the model to the tide-less Baltic Sea coast

The study area is located at the coast of the Baltic Sea (see Fig. 2), that has nearly no tidal range. At several locations the coast is protected against erosion by permeable wood pile groins at the Baltic Sea coast. These groins can be taken into account in the model Strand.

Several years ago the marina of the town Kühlungsborn was constructed. To investigate the influence of a harbour jetty system on the long-shore sediment transport in combination with the cross-shore transport the model Strand is applied. The bed levels have been kindly provided by the State Department of Environment (LANU) of the German state Mecklenburg-Vorpommern.

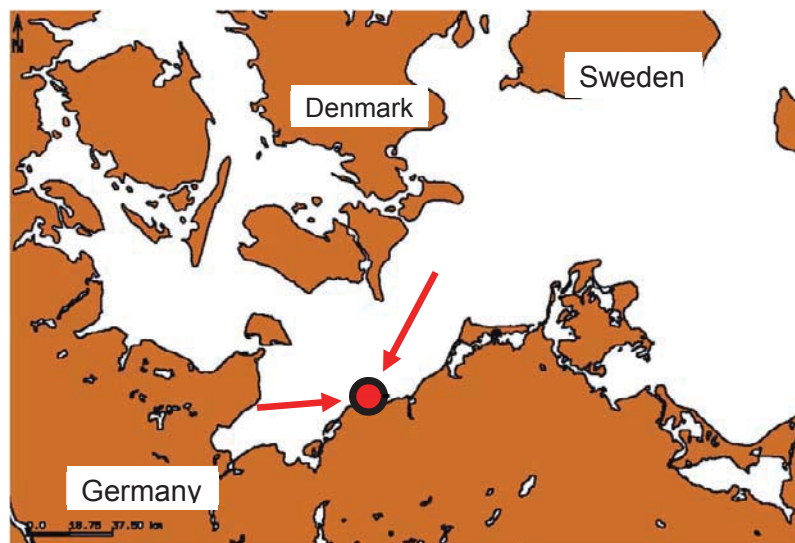


Figure 2: Location of the study area in the south west Baltic Sea.

The model is driven by the wind and wave boundary conditions. The orientation of the coastline is almost east-west. The wind is blowing mostly from west, sometimes from north-east. The wave propagation is fetch limited in this south-west part of the Baltic Sea. Two major wave directions prevail, one is from north-east the other is from west-south-west. An averaging with respect to the effect on the long-shore sediment transport rate is possible by using the weight $\cos(\alpha)\sin(\alpha)$, where α is the angle between the wave propagation direction and the orientation of the coastline. The transport direction is changing often within a year. For westerly wind directions the waves are running at a high angle to the shore. The main transport direction is from west to east.

A 5 km long and 2 km wide part of the coastline (fig. 3) has been simulated with the model. The grid is based on triangular elements. The grid consists of about 50000 nodes and 100000 elements. For the wave model a curvilinear grid consisting of 60000 nodes has been used (see fig. 4). In this part the coast of the Baltic Sea is characterised by longshore bars. A significant

fraction of the longshore transport takes place at the bars, what has a significant effect on the resulting bed level changes.

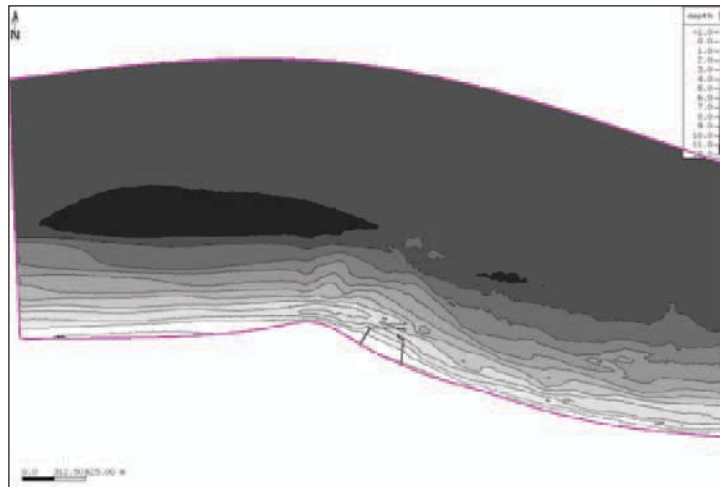


Figure 3: Depth contours of the entire model domain. The harbour jetties are very well reproduced with finite elements in depth distribution.

In the FEM model grid the harbour jetties are implemented in the depth distribution (see Figure 3). The mesh-nodes of the jetties are not erodible in the model, thus representing a hard structure. For the wave model the jetties are given by polygons. Due to interpolation between the curvilinear and the triangle-mesh problems have occurred close to the jetties when calculating the radiation stress. After careful adjustment of the FEM grid and of the polygons used in SWAN these difficulties have been overcome.

For the wave model SWAN a curvilinear grid shown in figure 4 had to be constructed, that covers almost the same area as the flow model.

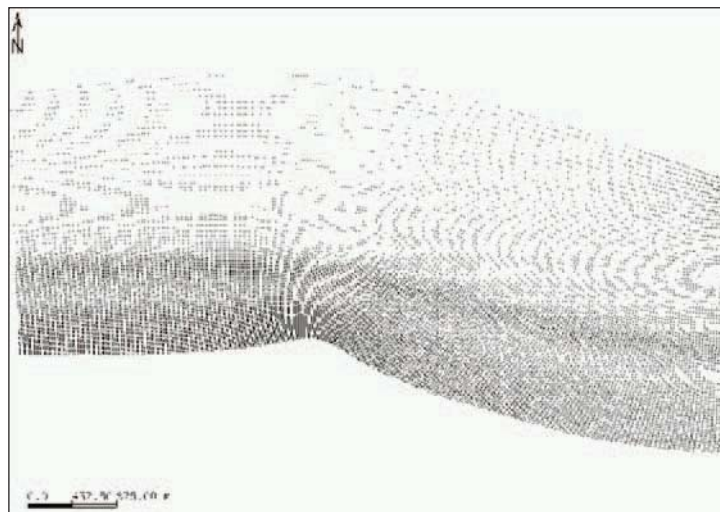


Figure 4: Computational grid for the SWAN model.

The model has been calibrated mainly to reproduce the appropriate suspended sediment concentrations and realistic long-shore current velocities. It is assumed, that the transport rates are also realistic if these two quantities are well estimated. Thus within the calibration the empirical factors for the entrainment function are adjusted. A very sensitive part is the adjustment of the values for the undertow. As mentioned above the shift of the wave energy is purely hypothetical and prescribed in the simulations. The weighting of the involved processes is therefore also vague and aims on the reproduction of the average inclination of the bed at this coast and on the long-shore bar geometry.

5 Simulation results

Two different wind directions 10° and 290° were calculated. The first one hits the coast almost perpendicular; the second induces intensive longshore currents. Here the results of the 290° simulations are shown.

Due to the jetty system the long-shore current is deflected into the deeper parts of the model domain. Behind the jetties a backwater or recirculation zone establishes in the flow field. The complex flow patterns shown in figure 5 arise from wave breaking over the shallow parts of the model domain. The wave field is reacting on this flow field. The currents carry sediment in a complex way along the coastline. Not in every case a straight longshore bar is forming. A typical plot of the resulting sediment transport pattern for 10° wind direction is shown in figure 5.

The initial topography of the model is constructed from measurements and can be seen in figure 6. At the time of measurement the harbor already existed for about one year. Therefore the influence of the jetties is at least partially already present in the depth distribution.

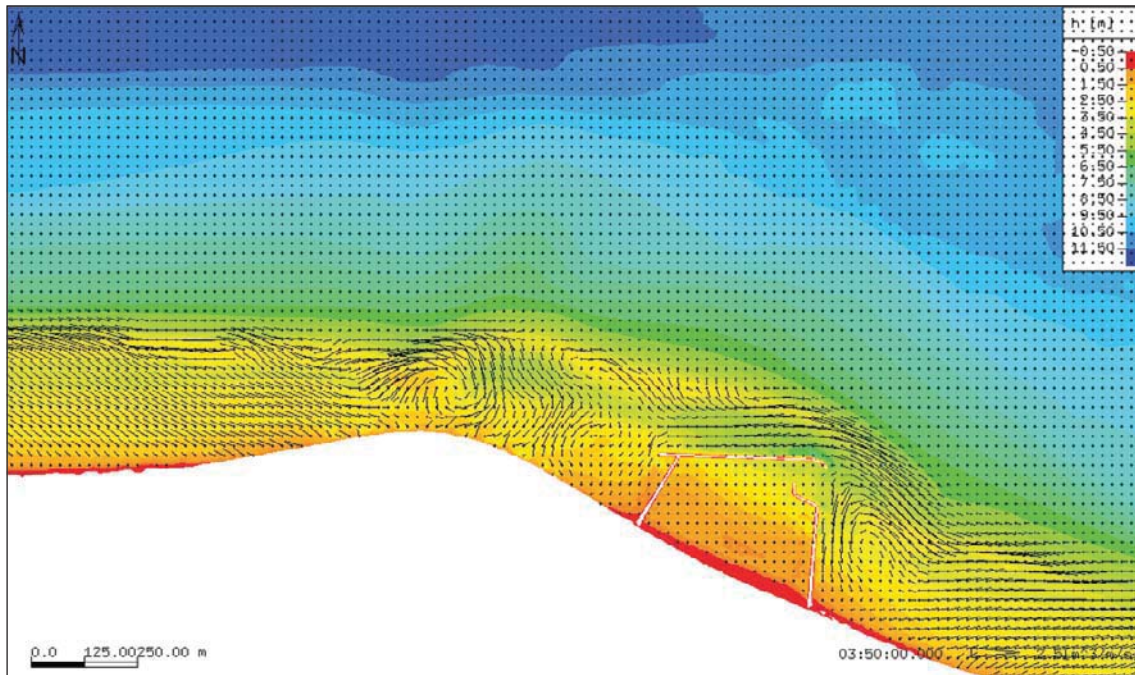


Figure 5: Vectors of the sediment transport rates at a certain time instant of the unsteady computation on depth contours. Wave direction is 10° .

Behind the structure the sediments are re-approaching the beach. The distance, at which the sediment is moving back to the beach is longer than expected, in other words the leeside erosion is very elongated and less severe than expected in advance. A similar result has been obtained by Roelvink and Walstra 2004.

In Figure 6 and 7 the initial and final depth distribution in the model domain is shown. The simulation was run for wind and waves from WNW 290° . The computation was a real time (no acceleration) storm event with a wind speed of 20 m/s that lasted constantly for 11,5 days. Depth changes are limited to the shallower near-shore parts of the model domain, where the wave induced currents are strong. In the figures the sediment accumulation in front of the cross-jetty can be seen. This bar like structure drains the sediment around the jetties. Thus the long-shore transport is moved a bit seaward.

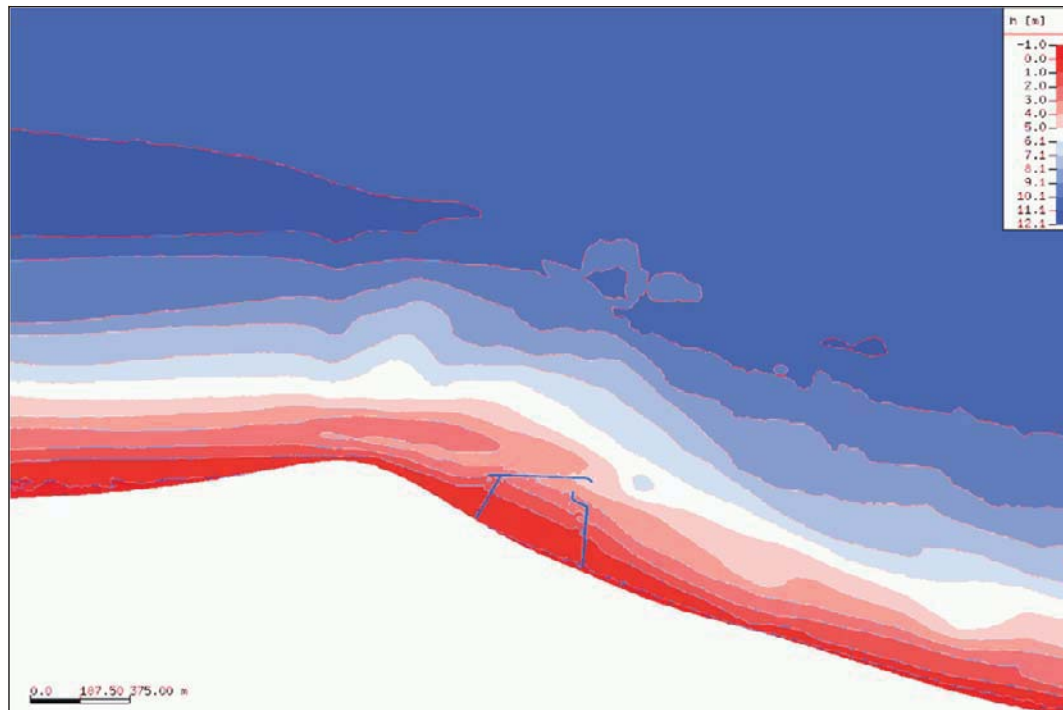


Figure 6: Depth distribution for the initial state of a computation. Red color indicates shallow.

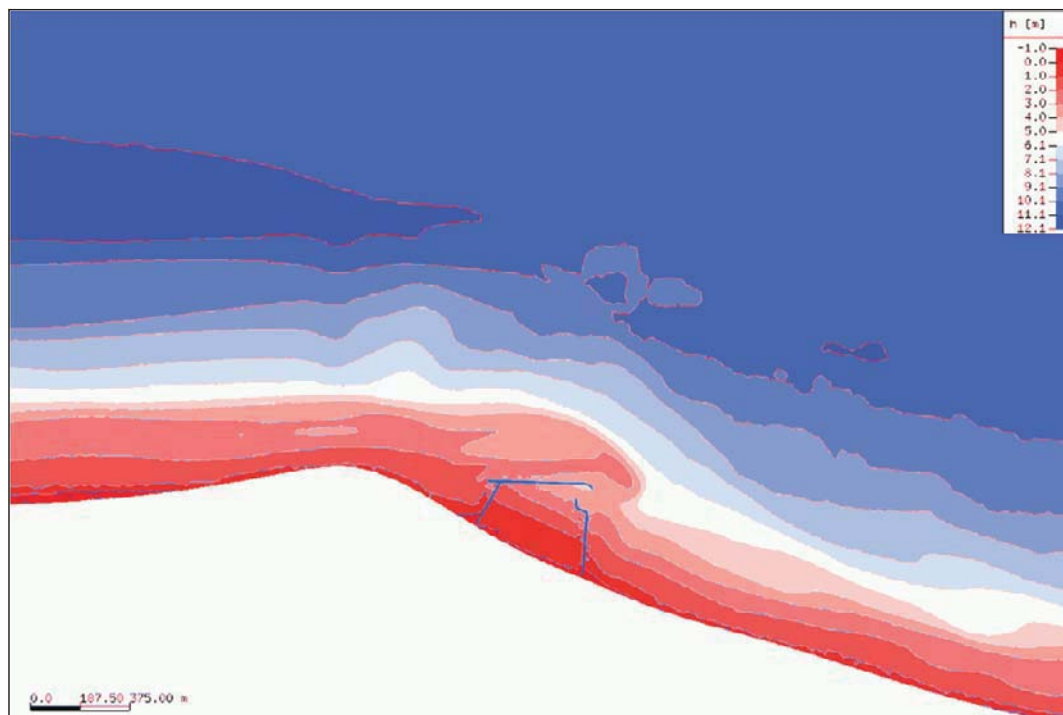


Figure 7: Depth distribution for the final state of a computation with wind and waves from 290°.

In the 10° simulation, not shown here, no intense long-shore transport is developing, but instead a bar is developing in the western part of the model domain.

6 Conclusion

The model Strand has been applied to the tideless Baltic Sea Coast at two locations. It is shown that the model is capable of reproducing a concave beach profile, which is similar to the well known Bruun's profile. Moreover it reproduces a long-shore breaker bar. This is a result of the opposing action of the onshore directed transport processes wave induced transport via asymmetry and mass transport velocity and offshore directed transport processes downslope transport and undertow.

In the example of a harbour in Kühlungsborn the sediment moves along a bar to the seaward end of a harbour jetty, thus establishing a transport route around it. The ability to simulate the beach development behind a breakwater producing a salient or tombolo has also been shown earlier.

The model can be applied for the simulation of morphodynamic response around jetties, breakwaters, artificial reefs, permeable and impermeable groines and for the siltation of navigational channel. It can also be applied for the optimization of beach nourishment campaigns.

7 References

- De Vriend, H.J., J. Zyserman, J. Nicholson, J.A. Roelvink, P. Pechon, and H.N. Southgate. 1993. Medium-term 2DH coastal area modeling, *Coastal Engineering*, 21, 193-224.
- Mewis, P. 2006. Nearshore morphodynamic-numerical computation of the influence of harbour jetties. *Proceeding of the 30th International Conference on Coastal Engineering 2006*, Vol. 4, 3835-3842.
- Roelvink, J.A. and M.J.F. Stive. 1989. Bar-generating cross-shore flow mechanisms on a beach. *Journal of Geophysical Research*, 94, 4785-4800.
- Roelvink D. and J.-D. Walstra. 2004. Keeping it simple by using complex models. *Proceedings of the 6th International Conference on Hydroscience and Engineering*, Brisbane, Australia.
- Svendsen, I.A. 1984. Wave heights and setup in a surf zone. *Coastal Engineering*, 8, 303-329.
- Thornton, E.B., R.T. Humiston and W. Birkemeier. 1996. Bar/trough generation on a natural beach. *Journal of Geophysical Research*, 101, 12097-12110.

Steady streaming and sediment transport generated by propagating sea waves

Paolo Blondeaux¹, Giovanna Vittori², Antonello Bruschi³, Francesco Lalli⁴, Valeria Pesarino⁵

Abstract

A numerical model for the simulation of flow and sediment transport in the bottom boundary layer generated by regular sea waves is presented. Both the velocity field and the sediment transport rate are determined up to the second order of approximation, thus evaluating the steady streaming and the net (wave averaged) flux of sediment induced by nonlinear effects. Turbulence closure is implemented by means of a two-equation eddy viscosity model (Saffman, 1970). The suspended sediment concentration is determined by solving an advection-diffusion equation, and then the suspended load is evaluated by computing the sediment flux. Empirical relationships are used to estimate the bed load.

Keywords: sea waves, boundary layer, sediment transport.

1 Introduction

In the present paper we tackle the theme of sediment transport due to waves propagating at the sea surface. At the first order of approximation in the wave steepness, a symmetric oscillatory flow is induced close to the bottom, and there is no net sediment motion. On the other hand, at the second order of approximation, nonlinear effects in the bottom boundary layer produce a steady streaming and a net sediment transport, which becomes significant for waves of large amplitude. Hence, to obtain reliable estimates of the sediment transport rate in coastal environments and to predict erosion and deposition processes, it is necessary to have a detailed knowledge of the flow within the bottom boundary layer generated by propagating surface waves and, in particular, to take into account nonlinear effects.

An oscillatory boundary layer with a uniform velocity in the flow direction is considered in many studies and experimental works as a prototype of the boundary layer at the bottom generated by propagating sea waves. In particular oscillating water tunnels are used to reproduce the hydrodynamics and sediment transport induced by sea waves close to the bottom (Van der Werf et al., 2009). However, as recently pointed out by Gonzalez-Rodriguez & Madsen (2011), the flow at the bottom of sea waves depends on the coordinate pointing in the direction of wave propagation and this spatial dependence induces a steady streaming, which is not reproduced in a symmetric oscillating flow. In particular, in the mentioned paper it is shown that the sediment transport is largely affected by the steady component of the velocity field.

The increasing power of actual computers would suggest to determine the turbulent flow at the bottom of gravity waves through direct numerical simulations (DNS) of continuity and Navier-Stokes equations. A simulation of the transition from the laminar to turbulent regime and an attempt to reproduce the elementary process which maintain the turbulence in oscillatory boundary layers was made by Vittori & Verzicco (1998) and by Costamagna et al. (2003).

¹ Department of Civil, Environmental and Architectural Engineering . University of Genoa, Via Montallegro 1, 16145 Genova, Italy, blx@dicat.unige.it

² Department of Civil, Environmental and Architectural Engineering . University of Genoa, Via Montallegro 1, 16145 Genova, Italy, vittori@dicat.unige.it

³ ISPRA – Italian Institute for Environmental Protection and Research, Via Vitaliano Brancati 48, 00144 Roma, Italy, antonello.bruschi@isprambiente.it

⁴ ISPRA – Italian Institute for Environmental Protection and Research, Via Vitaliano Brancati 48, 00144 Roma, Italy, francesco.lalli@isprambiente.it

⁵ ISPRA – Italian Institute for Environmental Protection and Research, Via Vitaliano Brancati 48, 00144 Roma, Italy, valeria.pesarino@isprambiente.it

Actually the more reliable models used to estimate sediment transport are based on intra-wave approaches, i.e. they are based on a full time-dependent simulation of sediment concentration during the wave cycle. Vittori (2003) evaluated sediment concentration under progressive sea waves, employing the flow field provided by direct numerical simulations and using a Lagrangian approach to determine sediment dynamics. However, field cases are often characterized by large values of the Reynolds number, hence for their simulation it is necessary to use Reynolds averaged Navier-Stokes (RANS) equations. Numerous works based on RANS equations have been devoted to determine the amount of sediment moved by propagating sea waves. An exhaustive review is not the aim of the present paper. Let us only point out that, to our knowledge, both the theoretical/numerical analyses and the laboratory experiments consider a streamwise uniform flow. For example, recently, Hassan & Ribberink (2010) have used a one dimensional RANS diffusion model to study sand transport processes in an oscillatory boundary layer and verified the results of their model by comparing the theoretical predictions with laboratory measurements performed in different wave tunnels.

In this paper we present the results of a detailed analysis of the streaming velocity and sediment dynamics in a fully developed turbulent boundary layer produced by a uniform train of progressive finite-amplitude surface waves. Turbulence characteristics are determined by means of the two-equation closure model of turbulence proposed by Saffman (1970). The unsteady turbulent boundary layer at the bottom of gravity waves is studied, taking into account second order effects in the wave steepness. Moreover, we estimate the sediment transport rate by evaluating the bed load by means of an empirical predictor and the suspended load as the sediment flux. The latter is computed after the evaluation of sediment concentration which is given by the solution of an appropriate advection-diffusion equation.

2 Mathematical formulation

In this paper we propose a model for simulating the flow field induced by a two-dimensional monochromatic surface gravity wave, propagating in waters of constant depth h_0^* [m], close to the bottom. In the following we use a $*$ to denote a dimensional quantity, while the same symbol without $*$ represents the dimensionless counterpart. The wave period and length are $T=2\pi/\omega^*$ [s] and $L^*=2\pi/k^*$ [m] respectively, where ω^* indicates the wave's angular frequency [s^{-1}] and k^* its wave number [m^{-1}]. Then, let us introduce a Cartesian coordinate system (x^*, y^*, z^*) , with the origin on the sea bottom, with x^* axis directed along the direction of the wave propagation and pointing off-shore, and the y^* axis directed upward. Hence, the free surface is described by:

$$y^* = h_0^* + \eta^*(x^*, t^*) = h_0^* + \frac{a^*(x^*)}{2} \left[e^{i(k^* x^* + \omega^* t^*)} + c.c. \right] + h.o.t. \quad (1)$$

with $a^*(x^*)$ wave amplitude [m]

c.c. complex conjugate

h.o.t. higher order terms

η^* free surface elevation [m].

The problem is formulated in terms of the following dimensionless variables:

$$(x, y) = \frac{(x^*, y^*)}{L^*}, \quad t = t^* \omega^*, \quad \eta = \frac{\eta^*}{a_0^*/S} \quad (2)$$

$$(u, v) = \frac{(u^*, v^*)}{a_0^* \omega^*/S}, \quad p = \frac{p^*}{\rho^* a_0^* (\omega^*)^2 L^*/S} \quad (3)$$

with u^* and v^* components of the velocity vector along the x and y axes respectively [m/s]

and

ρ^*	water density	[Kg/m ³]
p^*	pressure	[N/m ²]
S	factor equal to $\sinh(2\pi h_0^*/L^*)$.	

Hence, the velocity field can be obtained by solving the following equations:

$$\frac{\partial u}{\partial x} + \frac{\partial v}{\partial y} = 0 \quad (4)$$

$$\frac{\partial u}{\partial t} + \frac{a_0^*}{L^* S} \left(u \frac{\partial u}{\partial x} + v \frac{\partial u}{\partial y} \right) = \frac{\partial T_{xx}}{\partial x} + \frac{\partial T_{yx}}{\partial y} \quad (5)$$

$$\frac{\partial v}{\partial t} + \frac{a_0^*}{L^* S} \left(u \frac{\partial v}{\partial x} + v \frac{\partial v}{\partial y} \right) = \frac{\partial T_{xy}}{\partial x} + \frac{\partial T_{yy}}{\partial y} \quad (6)$$

In (5) and (6) T is the stress tensor, given by:

$$T_{xx} = -P + 2 \frac{\nu^*}{\omega^* (L^*)^2} (1 + \nu_T) \frac{\partial u}{\partial x}; \quad T_{yy} = -P + 2 \frac{\nu^*}{\omega^* (L^*)^2} (1 + \nu_T) \frac{\partial v}{\partial y}; \quad (7)$$

$$T_{xy} = T_{yx} = - \frac{\nu^*}{\omega^* (L^*)^2} (1 + \nu_T) \left(\frac{\partial u}{\partial y} + \frac{\partial v}{\partial x} \right) \quad (8)$$

where ν^* kinematic viscosity of the water [m²/s]

ν_T^* eddy viscosity ($\nu_T = \nu_T^*/\nu^*$) [m²/s]

and P is the dynamic pressure expressed by

$$P = p + \frac{g^* S}{a_0^* (\omega^*)^2} (y - h_0). \quad (9)$$

The problem is then closed by the no-slip boundary condition at the bottom and by the kinematic and dynamic conditions at the free surface. Furthermore, in order to describe the damping of the wave amplitude due to viscous effects, a new variable is introduced:

$$\chi = x \frac{\delta^*}{L^*} \quad (10)$$

with $\delta^* = \sqrt{2\nu^*/\omega^*}$ thickness of the bottom viscous boundary layer. [m]

It is also useful to introduce a set of coordinates to describe the flow in the bottom boundary layer and to incorporate the periodic variability in space and time:

$$(\tilde{x}, \tilde{y}) = \frac{(x, y)}{\delta}, \quad \tilde{t} = 2\pi x + t \quad (11)$$

A standard two-equation turbulence model (Saffman, 1970) is used to evaluate eddy viscosity ν_T^* . The eddy viscosity is assumed to be a function of turbulence local properties, namely a pseudo energy e^* and a pseudo-vorticity Ω^* (see relationship (12)), which are assumed to satisfy nonlinear diffusion equations and appropriate boundary conditions (Blondeaux, 1987). In particular, at the bottom, the pseudo vorticity is forced to assume a value which depends on the roughness size (Saffman, 1970) while the pseudo-vorticity vanishes.

$$v_T^* = \frac{e^*}{\Omega^*} \quad (12)$$

The resulting problem is characterized by the small parameter $\delta = \delta^*/\omega^*$, which turns out to be a small parameter. The solution is expanded in terms of δ :

$$(u, v, p, e, \Omega) = (u_0, v_0, p_0, e_0, \Omega_0) + \delta(u_1, v_1, p_1, e_1, \Omega_1) + O(\delta^2) \quad (13)$$

and the problems at the different orders of approximation, which are obtained by substituting (14) into the governing equations are solved in succession.

The sediment transport is split into two parts: suspended sediment transport (Q_s) and the bed load rate (Q_b). Once the hydrodynamic field is determined, the suspended sediment concentration c is obtained by solving the advection-diffusion equation:

$$\begin{aligned} \frac{\partial c}{\partial \tilde{t}} + \frac{R_s}{2} \left(u \frac{\partial c}{\partial \tilde{x}} + 2\pi\delta u \frac{\partial c}{\partial \tilde{t}} + (v - v_s) \frac{\partial c}{\partial \tilde{y}} \right) = \\ + \frac{1}{2} \left\{ \frac{\partial}{\partial \tilde{x}} \left[D_T \left(\frac{\partial c}{\partial \tilde{x}} + 2\pi\delta \frac{\partial c}{\partial \tilde{t}} \right) \right] + \right. \\ \left. + 2\pi\delta \frac{\partial}{\partial \tilde{t}} \left[D_T \frac{\partial c}{\partial \tilde{x}} \right] + 2\pi\delta \frac{\partial}{\partial \tilde{t}} \left[D_T 2\rho\delta \frac{\partial c}{\partial \tilde{t}} \right] + \frac{\partial}{\partial \tilde{y}} \left[D_T \frac{\partial c}{\partial \tilde{y}} \right] \right\} \end{aligned} \quad (14)$$

where $D_T = v_T^*/\nu^*$ and v_s is the dimensionless fall velocity of the sand particles ($v_s = v_s^*/U_0^*$), which is assumed to depend on the sediment Reynolds number R_p :

$$R_p = \frac{\sqrt{(\rho_s^*/\rho^* - 1)g^*(d^*)^3}}{\nu^*} \quad (15)$$

As for the hydrodynamic problem, the solution is expanded in terms of the small parameter δ :

$$c = c_0 + \delta c_1 \quad (16)$$

Then Q_s is evaluated by integrating c from a reference level close to the bottom, up to the free surface (17).

$$Q_s = \frac{\Psi_d}{d} \int_{\tilde{y}_{ref}}^{\infty} u c d\tilde{y}; \quad \text{where } \Psi_d = \frac{U_0^{*2}}{(\rho_s^*/\rho^* - 1)g^* d^*}; \quad d = \frac{d^*}{\delta^*} \quad (17)$$

The reference level and the bed load rate can be evaluated using several empirical formulations. In this paper we use those proposed by Garcia & Parker (1991) and by Zysermann & Fredsoe (1994).

The outlined continuous model is transformed in a discrete problem by means of finite difference approximations. Spatial derivatives are discretized by second order centred schemes, whereas time marching is performed by means of a second order Runge-Kutta scheme.

3 Results

In order to test the model, numerical results have been compared with laboratory experiments. Since most laboratory experiments have been performed in U-tubes, the present model has been adapted, by assuming uniform flow, to simulate this case too. However, as already pointed out, even if U-tubes are capable of reproducing an oscillating flow over a sandy bottom at first order, they can not reproduce the steady streaming component (which is $O(\delta)$). To show the difference between the two approximations in modelling the actual boundary layer, the results of the model for the case of the wave-induced flow are compared with those obtained for the U-tube. The two solutions do not differ at the leading order of approximation, hence in figure 1 only

the dimensionless value of the steady velocity component at the second order u_1 (multiplied by δ) is shown.

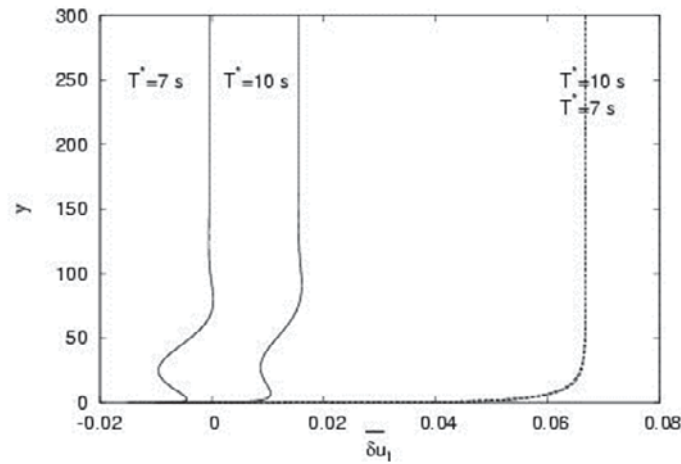


Figure : Steady velocity component generated by an oscillatory boundary layer in a U-tube (broken line) and at the bottom of sea waves (solid lines) for two different values of T^* ($U_{rms}^*=0.6$ m/s, $R=0.6$, $d=0.13$ mm).

Figure 1 shows, for values of the parameters similar to those of the experiment of Ribberink & Al-Salem (1994), the time-averaged velocity profiles both for the U-tube arrangement and under a sea wave. It is worth pointing out that $U_{rms}=0.6$ m/s, $R=0.6$ and $T=7$ s and $T=10$ s correspond to waves characterized by amplitudes of about 1.1 m, 1.3 m, wavelengths of about 47.9 m, 89.7 m, propagating in waters of constant depth equal to about 5.6 m and 9.3 m, respectively. Hereafter U_{rms} indicates the root mean square of the velocity outside the bottom boundary layer and R is the asymmetry index defined as $U_c/(U_c+U_t)$ (where U_c is the crest velocity and U_t is the trough one). It can be appreciated that even though the values of U_{rms} , T , R and d (sediment size, i.e. D_{50}) are the same for the U-tube and wave cases, the U-tube case leads to values of the steady streaming which are different from those found for an actual wave because of the x -dependence of the latter. Moreover, the former does not depend on the wave period T .

Figure 2 shows a comparison between the numerical predictions at the leading order of approximation and the experimental measurements carried out in a U-tube for the rough wall case by Jensen et al. (1989). The agreement is good and a similar agreement is obtained if a smooth wall is considered.

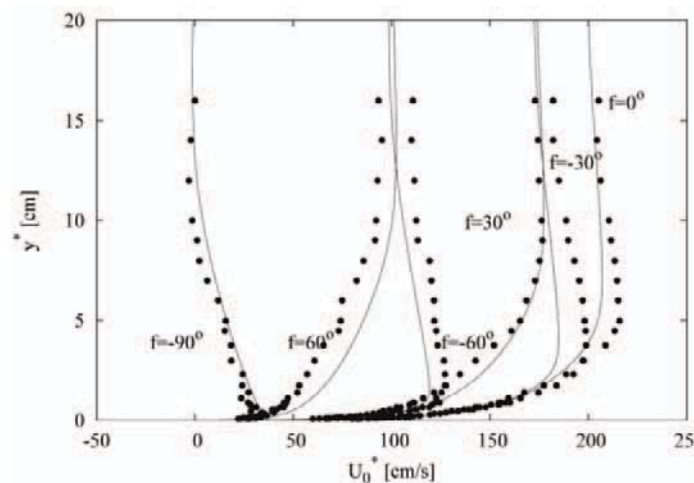


Figure 2: Dimensional velocity profiles for an oscillating flow over a rough wall. Labels are wave phases in degrees. For phase falling between -180° and -90° and between 90° and 180° , the flow is a mirror image of the one shown in the figure. The solid curves are calculated profiles and the dots are the data from test13 in Jensen et al. (1989).

Therefore present results as well as those described in Blondeaux (1987) support the numerical solution at the leading order. However, the main purpose of the present analysis is the investigation of the steady streaming generated by propagating sea waves, which appears at the second order of approximation. A comparison of the computed values of the streamwise steady velocity with the experimental results obtained by Van Doorn (1981) in a wave channel is shown in figure 3. Hereinafter, negative values of the steady velocity indicate currents in the direction of wave propagation. The parameters of the model are fixed considering a wave amplitude equal to 5.2 cm, a wave period equal to 2 s, a water depth of about 30 cm and a regular roughness characterized by a size equal to 2.1 cm. Van Doorn (1981) measured the velocity profile in two positions: above the crest and the trough of roughness elements. Close to the bottom, a fair agreement between the numerical results and the average of the measurements above the crests and troughs of the roughness elements is found and supports the present model. Far from the bottom, significant differences appear which might be induced by the finite length of the wave channel used in the experiments which induce a strong return flow.

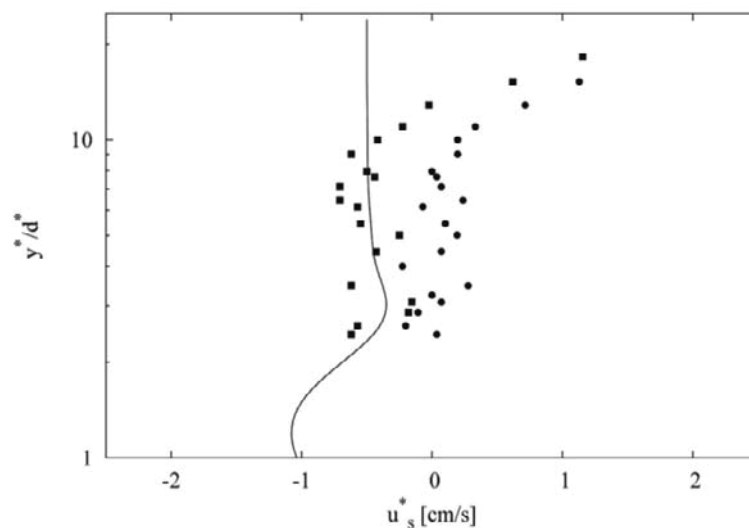


Figure 3: Comparison between the steady velocity profile and the experimental data of Van Doorn (1981). Black squares are the velocity measurements above the roughness crests and the dots are the velocity measurements above the roughness troughs.

Figure 4 shows a comparison between the sediment concentrations obtained by means of the present numerical model and the ones measured by Ribberink & Al-Salem (1994) in a U-tube, for $U_{rms}=0.51$ m/s and 0.56 m/s, $R=0.64$ and $R=0.62$, and two quite different values of T , namely 5 s and 12 s. Taking into account the empiricism of the bottom boundary condition for sediment concentration, the agreement between the model predictions and the laboratory measurements is satisfactory.

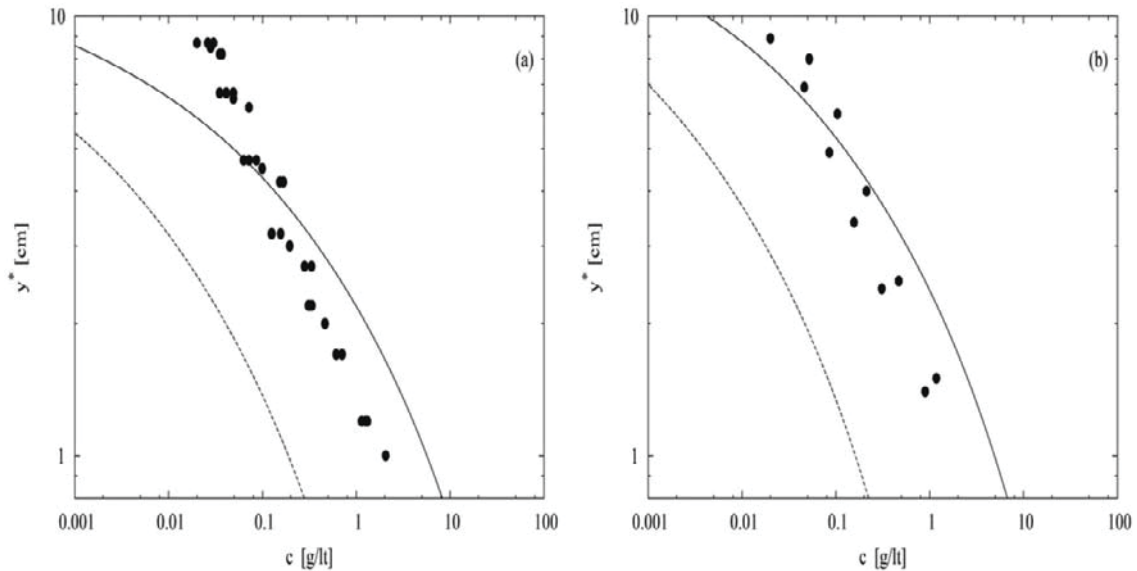


Figure 4: Suspended concentration profile in plane-bed and sheet flow conditions. The solid curves are the profiles calculated using the reference concentration of Zyserman & Fredsoe (1994), the broken curves are the profiles calculated using the reference concentration of Garcia & Parker (1991) and the dots are the data from Ribberink & Al-Salem (1994). The values of the parameters are $U_{rms}=0.51$ m/s and 0.56 m/s, $R=0.64$ and $R=0.62$, and two quite different values of T , namely 5 s (test B15 left) and 12 s (test B16 right).

4 Conclusions

In this work an analysis of the turbulent boundary layer induced by a sea surface wave is performed, by means of a in-house numerical model for the flow and sediment dynamics. Calculated and measured velocities are compared, showing a reasonable agreement. A comparison of the predictions of the sediment concentration and of the sediment transport rate with laboratory measurements further supports the model formulation. As a result, the proposed numerical model is capable to reproduce the pick-up of sediment and its concentration generated at the bottom of surface waves: such flow-particle interactions are significantly different from the ones induced in a wave tunnel by an oscillatory flow.

5 Acknowledgements

This study has been partially funded by the 'Ministero dell'Istruzione, dell'Università e della Ricerca' under the research project 2008YNPNT9-003 'Idrodinamica e morfodinamica nella regione dei frangenti'.

6 References

- Blondeaux, P. (1987): Turbulent boundary layer at the bottom of gravity waves. In: *J. Hydraulic Res.* 25 (4), 447-464.
- Costamagna, P., Vittori, G. & Blondeaux, P. (2003): Coherent structures in oscillatory boundary layers. In: *J. Fluid Mech.* 474, 1-33.
- Garcia, M.H. & Parker, G. (1991): Entrainment of bed sediment into suspension. In: *J. Hydraulic Eng.* 117 (4), 414-435.
- Gonzalez-Rodriguez, D. & Madsen, O.S. (2011): Boundary layer hydrodynamics and bed load sediment transport in oscillating water tunnels. In: *J. Fluid Mech.* 667, 48-84.
- Hassan, W.N. & Ribberink, J.S. (2005): Transport processes of uniform and mixed sands in oscillatory sheet flow. In: *Coastal Engineering*, 52, 745-770.

- Hassan, W.N.M. & Ribberink, J.S. (2010): Modelling of sand transport under wavegenerated sheet flows with a RANS diffusion model. In: Coastal Engineering 57 (1), 19-29.
- Jensen, B.L., Summer, B.M. & Fredsoe, J. (1989): Turbulent oscillatory boundary layers at high Reynolds numbers. In: J. Fluid Mech. 206, 265-297.
- Ribberink, J.S. & Al-Salem, A.A. (1994): Sediment transport in oscillatory boundary layers in cases of rippled beds and sheet flows. In: J. Geophys. Res. 99 (C6), 12707-12272.
- Ribberink, J.S. & Z. Chen (1993). Sediment transport of fine sand under asymmetric oscillatory flow. In: Delft Hydraulics data report H840.20, Part VII.
- Saffman, P.G. (1970): A model for inhomogeneous turbulent flow. In: Proc. Roy. Soc. London A 317, 417-433.
- Van der Werf, J.J., Schretlen, J.J.L.M., Ribberink, J.S. & O'Donoghue, T. (2009): Database of full-scale laboratory experiments on wave-driven sand transport processes. In: Coastal Eng. 56 (7), 726-732.
- Van Doorn, T. (1981): Experimental investigation of near-bottom velocities in water waves with and without a current. In: Rep. MI. 423 Delft Hydraulics Lab.
- Vittori, G. & Verzicco, R. (1998): Direct simulation of transition in an oscillatory boundary layer. In: J. Fluid Mech. 371, 207-232.
- Vittori, G. (2003): Sediment suspension due to waves. In: J. Geophys. Res. Oceans 108 (C6), 3173, 4-1/4-17.
- Zyserman, J.A. & Fredsoe, J. (1994): Data analysis of bed concentration of suspended sediment. In: Hydraul. Engineering 120 (9), 1021-1042.

Short-term simulation of the evolution of a curvilinear coast

Alejandro López-Ruiz¹, Miguel Ortega-Sánchez², Asunción Baquerizo³ and Miguel Á. Losada⁴

Abstract

This work explain the formation and evolution of shoreline undulations on the curvilinear coast of the Doñana Spit at the Guadalquivir estuary (Spain) using a one-line type model. The model takes into account the variation of the surf zone width due to the convergence and divergence of the waves propagating over a conical bathymetry with a small radius of curvature. The system was forced with a series of five-year wave climate simulations and the intrinsic uncertainty associated to the climatological agents was measured. A predictive analysis of the shoreline position after 5 years of climatic forcing is presented focusing on the wavelength and amplitude of the shoreline undulations developed.

Keywords: shoreline sand waves, curvilinear coasts, surf zone, alongshore sediment transport

1 Introduction

Coastal zone management requires the proper modeling of morphological changes that occur as a result of a complex multi-scale interaction between the climatic conditions and the topography. It also requires accounting for the intrinsic uncertainty associated to the stochastic character of the climatic forcing (Baquerizo and Losada, 2008). This is particularly important at littoral zones with a relevant environmental and socio-economic value, like the spits at the mouth of estuaries. One example of this mophology is the Doñana spit, located at the Guadalquivir River mouth (Southern Spain), study zone of this work (Figure 1).



Figure 1: Location and aerial photographs of Doñana spit taken in 1956 (left) and 2008 (right). The shoreline undulations (white dashed line) are present in both photographs. The wave rose of the zone is plotted in the right picture.

¹ Centro Andaluz de Medio Ambiente. Universidad de Granada. Avda. del Mediterráneo, s/n. 18006 Granada, Spain. alopezruiz@ugr.es

² miguelos@ugr.es

³ abaqueri@ugr.es

⁴ mlosada@ugr.es

One of the shoreline features associated to the spits are the medium to large scale shoreline undulations. They are slight undulations of the shoreline with wavelength of $\lambda \approx 10^1 - 10^3$ and amplitude $a \approx \lambda/10$ that can be ephemeral or permanent, and that generally appear where the coast become curvilinear. These features can also migrate changing their location as the wave conditions change. These shoreline morphologies can be observed in Doñana spit (Figure 1) but also in other spits around the world (Figure 2).



Figure 2: Examples of shoreline undulations observed in Sylt Island Spit, Germany; Cape Lookout Spit, North Carolina, USA; Arçay Spit, France; and Sandy Hook Spit, USA [Courtesy of Google Earth].

Although no conclusive explanation has been found in the literature for the formation of the shoreline undulations at the rounded edge of spits, there are some theories about the development of similar coastline features like sand waves, characterized by alongshore spatial scales larger than those of the surf zone. The wider extended theory for the formation of these sand waves is the *High Angle Wave Instability* (HAWI). It was originally proposed and developed by Ashton et al. (2001), and further completed by Falqués (2003) and Ashton and Murray (2006a,b). According to these studies, the predominance of offshore HAW can cause a shoreline to self-organize into regular, quasi-periodic shapes (sand waves) similar to those found along many natural coasts at different scales. The one-line type models developed from the HAWI are capable to reproduce alongshore sand waves on rectilinear coasts.

López-Ruiz et al. (2011) have shown that the formation, growth and decay of shoreline undulations at spits is strongly dependent not only on the wave climate severity and persistence but also on the alternance of storms with mild conditions. To study these morphologies they used in their work a one-line model that incorporates a sediment transport formulation that accounts for the effect of wave propagation at a conic-type bathymetry associated to a curvilinear coast.

Otherwise, for changes occurring over decadal scales, Baquerizo and Losada (2008) presented a methodology to predict the evolution of morphological features driven by climatological agents and the assessment of the associated intrinsic uncertainty. In this work we use their methodology with the model proposed by López-Ruiz et al. (2011) to analyse the uncertainty of the evolution of the shoreline undulations observed at the Doñana Spit, located at the Guadalquivir estuary (Spain). It will be shown that these shoreline undulations seem to be generated by the simultaneous effect of the local alongshore variation of energy (due to the morphology of the coastline) and the obliquity of incident waves. The model takes into account the variation in the surf zone width caused by the convergence or divergence of the waves propagating over a conical bathymetry of small radius of curvature. The longshore sediment

transport varies with the angle formed by the wave crests and coastline, and with the surf zone width. To complement previous experimental and numerical studies (Petersen et al., 2008), this model focuses on the physical processes. Despite simplifications, this model was found to adequately reproduce the length as well as the amplitude of the undulations observed.

2 Methodology

The methodology applied in this work has three steps: (1) wave climate simulation obtained from wave data near the study zone; (2) application of a one line model defined for curvilinear coasts; and (3) measurement of the intrinsic uncertainty associated to the climatological agents. These steps are described in the following sections.

2.1 Wave climate simulation

Wave climate conditions were simulated using the methodology developed by Solari and Losada (2011) for the wave height and a Vector Autoregressive (VAR) model for the wave peak period and the wave angle.

The methodology of Solari and Losada (2011) for wave height simulation depends on two steps: (1) the definition of a non-stationary probability distribution function that considers the seasonal and annual variations, and (2) the study of the temporal dependency by means of the copulas. A mixed parametric model with the Log-Normal (LN) distribution for the central area and two Generalized Pareto Distributions (GPD's) for the extremes were used for the non-stationary distribution function. The thresholds between each distribution are time dependent to take into account the seasonal variability of the wave climate. Using these functions, and imposing the continuity condition and that the lower limit of the minimum GPD is zero, the model has 5 parameters obtained with maximum likelihood and the Bayesian Information Criteria (BIC). It allows using the copulas method to deal with the time dependence. This time dependence is modelled with an asymmetric Gumbell-Hougaard copula for the first order Markov process and two Frechet-type copulas for the second and third order Markov process. Using this definition, every wave height value obtained depends on the previous four.

The application of the VAR model has three main stages: (1) estimation of the non-stationary distribution functions for both wave peak period and angle; (2) adjustment of the VAR model used to explain the time dependence and the dependence between the variables; and (3) simulation of the variables using the non-stationary distribution functions. For the wave period, a mixed model with two LN distributions was defined, while for the wave angle a mixed model with four stationary normal distributions truncated at 0 and 360° was used. The wave climate forcing was provided to the one line model presented in the next section as a series of three-hour sea states, the first of which started with the initial shoreline.

2.2 One line model for the evolution of a curvilinear coast

The one line model presented by López-Ruiz et al. (2011) is applied in this methodology. It takes into account that along curved stretches of coast with conic bathymetry of small radius of curvature the breaking wave height cannot be considered constant. The wave propagation over these contours produces a convergence of the rays on the coastal zone nearest to the direction of the incident waves and a divergence in the opposite direction (Pocinki, 1950). To properly characterize the wave energy variation along a schematic spit, the Ref-Dif model was used to generate different cases of wave propagation over an idealized conical bathymetry with a straight stretch of coastline followed by a curved stretch (Kirby and Dalrymple, 1983). The results show a progressive decay in the surf zone width towards the tip of the spit for a high-angle wave approach (Figure 3a). However, when waves arrive approximately normal to the rectilinear stretch, (i.e. with angles of incidence close to zero) or with negative values, an energy concentration is observed with a maximum in the surf zone width in the transition from a straight to a rounded coast (Figure 3b). The latest effect was already observed in the numerical and experimental study of Petersen et al. (2008).

Thus, for curvilinear coasts such as prograding spit fronts, the variation in the deep-water wave angle induces alongshore gradients in the surf zone width, and therefore in the alongshore energy. These gradients are expected to trigger the development of shoreline sand waves (López-Ruiz et al. 2011).

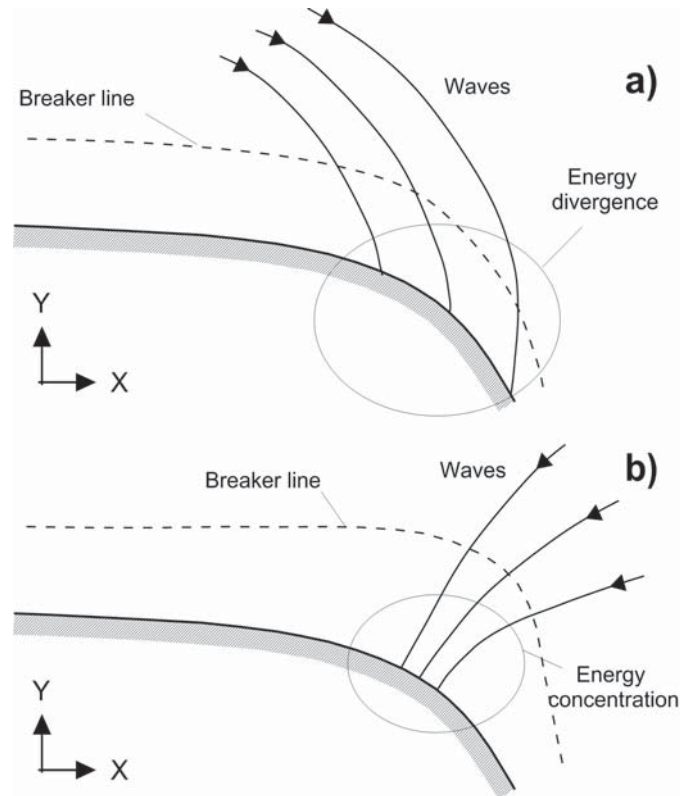


Figure 3: Wave energy pattern at the prograding front of a spit: a) energy divergence associated with high-angle wave approach; b) energy concentration associated with normal to negative wave angle values. The angles of incidence are measured counterclockwise from the positive Y axis.

To account for these longitudinal variability, López-Ruiz et. al (2011) solved the mass conservation equation in curvilinear coordinates using a sediment transport formula that integrates the Inman and Bagnold (1963) formulation along a section perpendicular to the shore. The reference frame was a curvilinear coordinate system (s,y) , with s parallel to the shoreline and y perpendicular to it (Figure 4).

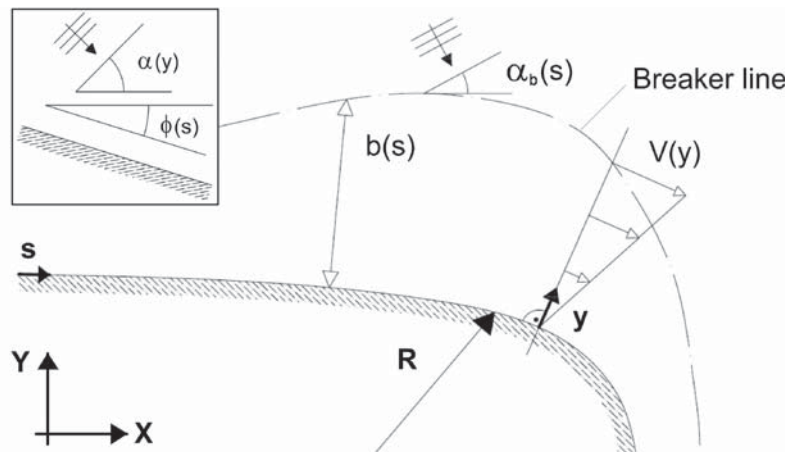


Figure 4: System of coordinates with s the curvilinear coordinate of the shoreline; y the normal coordinate; $V(y)$ the alongshore current; R the radius of the mean coastal alignment; $\alpha_b(s)$ the wave angle at breaking; $b(s)$ the surf zone width $\alpha(y)$ the wave angle; and $\phi(s)$ the angle of the coastline.

The hypotheses adopted for the analysis were the following: (1) since wave breaking is depth-limited and the surf zone is saturated, the wave height in the surf zone $H(y)$, the alongshore component of the radiation stress $S_{sy}(y)$, and the wave energy flux $E(y)c_g(y)$ are functions that decrease monotonically towards the coast and which are assumed to be continuous with continuous derivatives. Their values can be obtained with the Snell law and linear theory as exemplified in other works, such as Ashton and Murray (2006a), something usual in the definition of one-line type models; (2) sediment size monotonically varies cross shore along the beach according to Dean and Dalrymple (2001); (3) the turbulent diffusion is negligible. Consequently, and ignoring the slope effects, the alongshore current generated by the breaking waves and the associated alongshore transport are both parallel to the bathymetry.

Using these definitions and hypothesis, the one line model was defined using a modification of the Inman and Bagnold (1963) formula, in which the cross shore variation of the sediment size and the changes in the coastline orientation are included using the definition of angles given in Figure 4. The total sediment transport parallel to the coastline $Q(s)$ is obtained by averaging the modified Inman and Bagnold (1963) expression in the surf zone:

$$Q(s) = \frac{1}{b(s)} \int_0^{b(s)} S_{lst}(s, y) dy = P_1(b(s)) \cos(2\phi(s)) + P_2(b(s)) \sin(2\phi(s)) \quad (1)$$

with S_{lst} the modified Inman and Bagnold (1963) formula [m³/s]

In this expression P_1 and P_2 are polynomial functions that take into account the variation of the surf zone width and wave angle at breaking and the sinusoidal functions consider the variation of the angle of the coastline. If this expression is introduced in the sediment conservation equation, the following expression is obtained:

$$\frac{\partial \eta}{\partial t} = -\frac{1}{D} \frac{\partial Q}{\partial s} = -\frac{1}{D} \left[(P_2 \cos(2\phi) - P_1 \sin(2\phi)) \frac{\partial \phi}{\partial s} + \left(\frac{\partial P_1}{\partial b} \cos(2\phi) + \frac{\partial P_2}{\partial b} \sin(2\phi) \right) \frac{\partial b}{\partial s} \right] \quad (2)$$

with $\eta(s, t)$ the position of the shoreline [m]

D the closure depth [m]

The first part of the right hand side of the equation above considers the shoreline curvature while the second part takes into account the alongshore wave energy variation. The shoreline position for every time step during the morphological simulation is obtained with this equation, given the wave climate parameters obtained in the previous section.

2.3 Assessment of the associated intrinsic uncertainty

To analyze the uncertainty of the shoreline predictions obtained with the one line model, the following scheme was applied (Baquerizo and Losada, 2008). From the climatic data base we performed a number of N 5-years wave climate simulations. For these N experiments the shoreline evolution was simulated using the model described in the previous section, obtaining N different shorelines. With these shoreline solutions, the EOF analysis and statistical inference can be done to obtain a higher number of experiments and the probability distribution function of some of the geometric characteristics of the coastline. Given the main objectives of this work, the variables studied were the amplitude and the wavelength of the shoreline sand waves obtained.

3 Application to Doñana Spit (Spain)

For the application of the proposed methodology to the Doñana Spit, the definition of the geometric and sediment grain size characteristics of the study zone is necessary. The slope at Doñana spit is 0,004 (in average) with a medium grain size of 0,17mm. Regarding the geometric dimensions, the spit is about 1km width by 1.5 km long (the curved part).

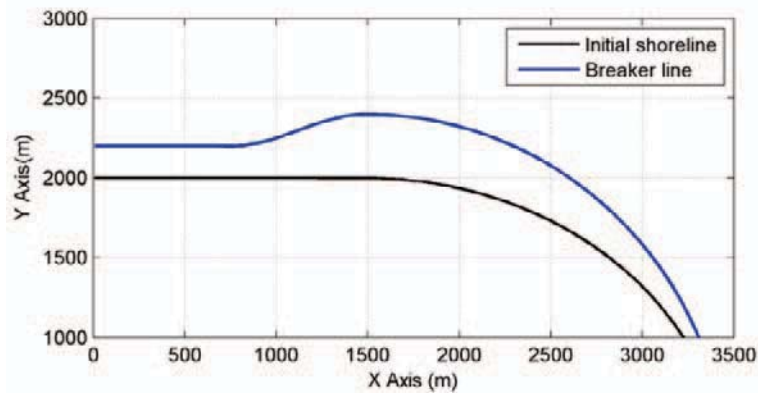


Figure 5: Geometric characteristics of the study zone modeled for the one line application to Doñana Spit.

For the wave climate simulations, we used the data obtained at hindcasting point WASA14718 (36.5° N, 7° W), provided by Puertos del Estado (Ministry of Public Works, Spain, WANA project) to obtain 100 series of five-year wave climate.

In the next step, during the five-year shoreline simulation, a different surf zone width was defined for each 3hr sea state. The breaker line shape showed in Figure 5 corresponds to the predominant wave incoming direction. However, the shape of this line evolves during the simulation depending on the wave incoming direction (following the patterns observed in the Ref-Dif propagations results, see Figure 3) and the deep-water wave height. In relation with the propagation during the process, H_b is calculated imposing the surf zone width (which is similar to using the breaking index), and α_b is calculated propagating with the Snell law. The 100 final shoreline obtained are showed in Figure 6a. In all the calculated shorelines, two shoreline undulations with a different geometry are observed. They have wavelengths similar to the ones we observed at Doñana. The observations at Doñana are derived from rectified aerial photographs of different years. These undulations are present in all the photographs that we have analyzed. Also, when comparing to the original shoreline position, a net advance of the spit is observed. It is also important to mention that the net spit advance may be exaggerated since river and tidal currents are not being considered.

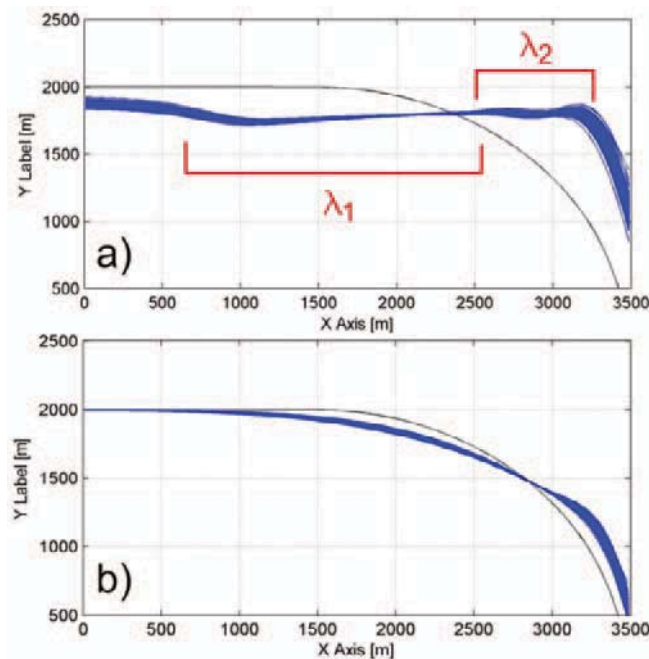


Figure 6: Geometric characteristics of the study zone modeled for the one line application to Doñana Spit.

Figure 6 also show the comparison of the previous results with the case of a spit where the surf zone width does not vary alongshore Figure 6b. It can be seen that some slight variation in the shape of the shoreline is produced as well as a net advance of the spit, although for constant b the shoreline undulations are not generated. Thus, it can be concluded that a combination of the curvature of the coastline and an alongshore variation of the wave energy are required to generate the shoreline undulations.

Once the 100 final shorelines were obtained, the EOF analysis was used to obtain the values of the undulations wavelength and amplitude after 500 experiments. With the available data, this analysis is capable to explain the 95% of the shoreline evolution variance considering only the first eigenfunction and more than 99% considering the first three (Baquerizo and Losada, 2008).

The analysis of the 500 amplitudes and wavelengths of the undulations shows that the value of the wavelength is a quasi-deterministic parameter with $\lambda_1 \approx 2000$ m and $\lambda_2 \approx 700$ m. However, the amplitude shows certain variability and their cumulative probability functions can be obtained using statistical inference (Figure 7).

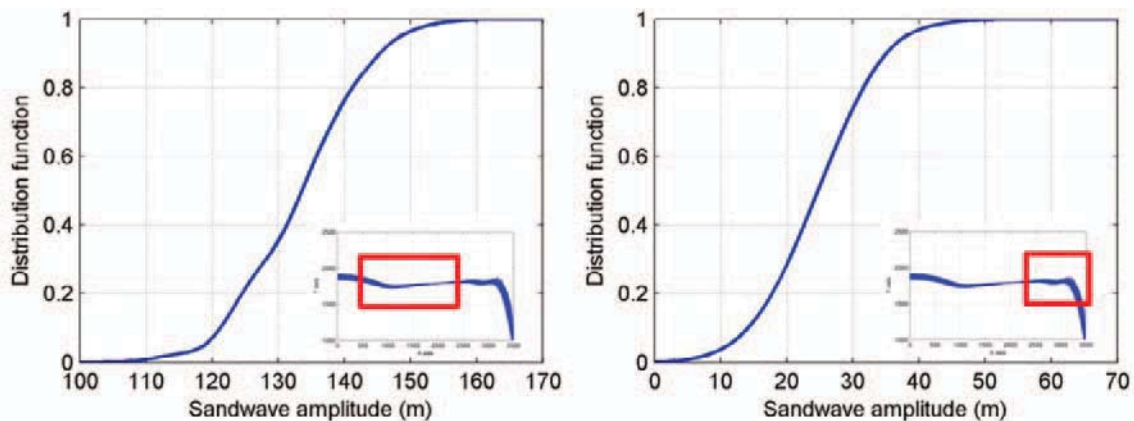


Figure 7: Geometric characteristics of the study zone modeled for the one line application to Doñana Spit.

4 Conclusions

This work applies a one line model specially defined for curvilinear coast and uncertainty assessment techniques to study the evolution and predict the geometry of the shoreline undulations observed in the curvilinear coast of the Doñana Spit, located at the mouth of the Guadalquivir River (Southern Spain). Special attention is focus on the variability of the wave energy along the coastline depending on the deep-water wave height and direction. After applying the proposed methodology, the following conclusion can be drawn:

1. The shoreline modelling of a curvilinear coast requires consideration of (1) coastline curvature; (2) alongshore gradient of the surf zone width induced by the wave propagation over a conical bathymetry; and (3) inclusion of both effects in the sediment transport formulation.
2. Results after 100 experiments of five-year shoreline simulation show that shoreline undulations with similar wavelength and amplitude to observations are always developed.
3. After the simulations, a net longitudinal growth of the spit is observed, although probably this effect is greater than reality because the effect of the river discharge and tidal currents was neglected.
4. The proposed mechanism for the shoreline undulations development can be complementary to others such as the instability mechanism of Ashton et al. (2001). Indeed, the variations in shoreline morphology induced by the instability mechanism can generate alongshore variations in surf zone width, which can initiate this process. On the other hand, the morphology obtained with our model can provide the obliquity necessary to activate the instability mechanism.

5 Acknowledgements

This work was funded in part by the Spanish Ministry of Science and Education (Project IMASDEi CTM2009-10520/MAR) and the Andalusian Regional Government (Project TEP-4630). The work of the first author was partially funded by the Ministry of Education (Spain), Research Grant AP2009-2984.

6 References

- Ashton, A.; Murray, A. B. (2006a): High angle wave instability and emergent shoreline shapes: 1. Modeling of sand waves, flying spits, and capes. In: *Journal of Geophysical Research*, Vol. 111, F04011, doi: 10.1029/2005JF000422
- Ashton, A.; Murray, A. B. (2006b): High angle wave instability and emergent shoreline shapes: 1. Wave climate analysis and comparisons to nature. In: *Journal of Geophysical Research*, Vol. 111, F04012, doi: 10.1029/2005JF000423.
- Ashton, A.; Murray, A. B.; Arnoult, O. (2001): Formation of coastline features by large-scale instabilities induced by high-angle waves. In: *Nature*, Vol. 414, pp 296-300.
- Baquerizo, A.; Losada, M. A. (2008): Human interaction with large scale coastal morphological evolution. An assessment of the uncertainty. In: *Coastal Engineering*, Vol. 55, pp 569-580.
- Falqués, A. (2003): On the diffusivity in coastline dynamics. In: *Geophysical Research Letters*, 30(21), 1-5. doi:10.1029/2003GL017760
- Dean, R. G.; Dalrymple, R. A. (2001): *Coastal processes with engineering applications*. Cambridge University Press, ISBN 978-0521602754.
- Inman, D. L.; Bagnold, R. A. (1963): Littoral processes. In: *The sea*. Volume 3. Wiley-Interscience, New York.
- Kirby, J.; Dalrymple, R. (1983): A parabolic equation for the combined refraction-diffraction of Stokes waves by mild varying topography. In: *Journal of Fluid Mechanics*, Vol. 136, pp 543-566.
- López-Ruiz, A; Ortega-Sánchez, M.; Baquerizo, A; Losada, M. (2011): Shoreline undulations on curvilinear coasts. Submitted to *Geomorphology*. Manuscript Number GEOMOR - 2984
- Petersen, D.; Deigaard, R.; Fredsøe, J. (2008): Modeling the morphology of sandy spits. In: *Coastal Engineering*, Vol. 55, pp 671-684.
- Pocinki, L. S. (1950): The application of conformal transformations to ocean wave refraction problems. In: *Trans. Am. Geophys. Union*, Vol. 31, pp 856-860.
- Solari, S.; Losada, M. A. (2011): Non-stationary wave height climate modelling and simulation. Accepted in: *Journal of Geophysical Research*, Manuscript Number 2011JC007101R.

Technical Session 3: Coastal Risk / Risk Management

Chairman: Prof. Ing. Giuseppe Roberto Tomasicchio

Turbulent boundary layer and sediment transport under a solitary wave: a RANS model

Giovanna Vittori¹ and Paolo Blondeaux¹

Abstract

The flow field in the boundary layer at the bottom of a solitary wave is determined when the flow regime is turbulent by solving Reynolds and continuity equations. The turbulent stresses are quantified using the two-equation turbulence model of Saffman (1970) and Saffman & Wilcox (1978) which appears to describe also the transition process. The results obtained for a smooth wall show a good agreement with the experimental measurements of Sumer et al. (2010) and with numerical simulations of Vittori & Blondeaux (2008, 2011). The model allows also a rough wall to be considered. Attention is focused on the estimation of the bottom shear stress and the evaluation of the sediment transport rate.

Keywords: solitary wave, boundary layer, turbulence, sediment transport

1 Introduction

To obtain accurate quantitative results on the flow field generated at the bottom of the sea by the propagation of solitary waves, numerical simulations (Vittori & Blondeaux 2008, 2011) and laboratory investigations (Sumer et al., 2010) have recently been made. These studies have shown that the flow regime is laminar throughout the wave cycle, if the amplitude of the wave is relatively small. Turbulence appears after the passage of the crest of the wave, if the ratio between its amplitude and the water depth is larger than a critical value which depends on the ratio between the thickness of the bottom boundary layer and the water depth. Close to the critical conditions, both numerical simulations and laboratory experiments have shown that the instability of the laminar flow leads to the appearance of regular two-dimensional vortices with their axis parallel to the bottom and orthogonal to the direction of wave propagation. These vortices are produced by the growth of two-dimensional perturbations, induced by the presence of a negative pressure gradient that causes flow reversal near the bottom and an inflectional point in the velocity profile. When the amplitude of the wave is only slightly larger than its critical value and the thickness of the boundary layer is not too small, the numerical simulations have shown that the vortices generated by the growth of two-dimensional Tollmien-Schlichting waves dissipate because of viscous effects and do not induce a turbulent flow. Therefore, even if the laminar regime is unstable, the motion can not be defined as turbulent and, following Sumer et al. (2010), we adopt the term "transitional". For larger values of the wave amplitude, the two-dimensional vortices described above are unstable, break and generate three-dimensional incoherent vortices and a turbulent flow.

Although the numerical simulations of Vittori & Blondeaux (2008, 2011) provide a detailed picture of the flow field even in the turbulent regime, existing computers do not allow the use of this approach for practical applications. In addition, current numerical techniques make it very difficult to integrate the flow equations for the case of a rough wall, which is the most relevant case from the engineering point of view. Indeed, the presence of ripples, triggered by an instability mechanism (Dodd et al., 2003; Foti & Blondeaux, 1995), makes the sea bed to behave like a rough bed since the vortices shed by the ripples (Blondeaux & Vittori, 1991a,b) are similar to the eddies shed by roughness elements. Liu (2006) studied the boundary layer, considering Reynolds averaged equations, introducing the Boussinesq assumption and assuming the turbulent viscosity to be a function of the distance from the bottom. Its analytical solution provide interesting results and in particular it allows to quantify the decay of the wave. However, the algebraic turbulence model used by Liu (2006) does not allow an accurate

¹ Department of Civil, Environmental and Architectural Engineering, University of Genoa, Via Montallegro 1, 16145 Genoa, Italy. blx@dicat.unige.it

description of turbulence. For example, for a fixed value of the shear velocity, the adopted model provides the same turbulence intensity, both during the accelerating phase and the decelerating one while it is well known that turbulence is more intense during the decelerating phase. A better description of the dynamics of turbulence in the boundary layer at the bottom of a solitary wave has been recently obtained by Suntoyo & Tanaka (2009) by means of the two-equation turbulence model of Menter (1994). Menter (1994) used the model of Wilcox (1988) in the region nearest to the bottom and the $k-\varepsilon$ model far from it. To achieve this goal, Menter (1994) transformed the $k-\varepsilon$ model using a formulation similar to the $k-\omega$ model and then multiplied it by a function F_1 and added it to the $k-\omega$ model multiplied by $(1-F_1)$. Of course the function F_1 was chosen equal to 1 in the region closer to the bottom and 0 far from it. In agreement with the experimental data, the results show that the turbulent kinetic energy during the decelerating phase is larger than that characterizing the accelerating phase (see figure 7 of Suntoyo & Tanaka's paper). However, the experimental measurements of Sumer et al. (2010) show a well-defined second peak of the wall shear stress that is not reproduced by the model used by Suntoyo & Tanaka (2009). In addition, the turbulence model used by Suntoyo & Tanaka (2009) provides a critical value of the Reynolds number for the onset of turbulence that is smaller than the value suggested by Sumer et al. (2010) on the basis of their laboratory experiments.

Recently, Blondeaux & Vittori (2011) have studied the boundary layer generated by the propagation of a solitary wave, using the two-equation turbulence model of Saffman (1970) (see also Saffman & Wilcox (1974)). As pointed out by Menter (1994) this model is superior to other models close to the bottom and it was applied with success to investigate the structure of turbulence in the boundary layer generated at the bottom of a progressive wave by Blondeaux (1987), who showed its capability to provide an accurate description of the differences between the turbulence structure during the accelerating and decelerating phases of the wave cycle and to describe the process of transition from the laminar to the turbulent regime. The Reynolds stress tensor is expressed in terms of an eddy viscosity and the rate of strain tensor. The eddy viscosity is assumed to depend on two local turbulence densities, named pseudo-energy e^* and pseudo-vorticity Ω^* , which satisfy nonlinear diffusion-convection equations. Since, the flow is also determined in the viscous sublayer, the model is able to describe the smooth wall case without introducing any damping function. Moreover, the use of an appropriate boundary condition for the pseudo-vorticity allows the rough wall case to be described. In the present paper, the model proposed by Blondeaux & Vittori (2011) is used to quantify the sediment transport induced by the propagation of a solitary wave. Both the bed load and the suspended load are taken into account. The former is quantified by means of an empirical formula and the latter is evaluated by computing sediment concentration as a function of space and time and integrating the sediment flux from the bottom up to distances from it such that the sediment concentration is negligible. The problem is formulated in the next section, where the details of the turbulence model are given along with the description of the approach used to quantify the sediment transport. In section 3, the numerical approach employed to determine the solution is summarized and the results are presented. The final section is devoted to the conclusions.

2 Formulation of the Problem

Let us consider a two-dimensional solitary wave of height H_0^* , which propagates along the direction X_1^* , in shallow waters of constant depth h_0^* (hereinafter an asterisk indicates a dimensional quantity). In natural environments, the Reynolds number of the phenomenon is large and viscous effects can be neglected. Hence, the flow field induced by wave propagation can be described by Grimshaw's (1970, 1971) solution which is based on an expansion of the flow field in terms of the small ratio ε between the wave height and local water depth ($\varepsilon=H_0^*/h_0^*$). At the bottom, the vertical velocity component V_2 vanishes, while the horizontal component V_1 turns out to be described by

$$V_1 = s^2 + \varepsilon \left[\frac{1}{4} s^2 - s^4 \right] + \varepsilon^2 \left[\frac{19}{40} s^2 + \frac{1}{5} s^4 - \frac{6}{5} s^6 \right] + O(\varepsilon^3) \quad (1)$$

where the variable s and the constants β, C are defined by

$$s = \operatorname{sech}[\beta(X_1 - Ct)]; \quad \beta = \sqrt{\frac{3\varepsilon}{4} \left[1 - \frac{5\varepsilon}{8} + \frac{71\varepsilon^2}{128} + O(\varepsilon^3) \right]}; \quad C = \sqrt{1 + \varepsilon - \frac{\varepsilon^2}{20} + O(\varepsilon^3)} \quad (2)$$

and the following dimensionless variables are introduced

$$t = \frac{t^* \sqrt{g^* h_0^*}}{h_0^*}; \quad (X_1, X_2) = \frac{(X_1^*, X_2^*)}{h_0^*}; \quad (V_1, V_2) = \frac{(V_1^*, V_2^*)}{\varepsilon \sqrt{g^* h_0^*}} \quad (3)$$

To determine the flow close to the bottom, it is necessary to introduce the new spatial coordinates

$$(x_1, x_2) = (X_1^*, X_2^*) / \delta^* = (X_1, X_2) / \delta \quad (4)$$

where the ratio $\delta = \delta^* / h_0^*$ between the viscous length $\delta^* = \sqrt{2\nu^* h_0^* / \sqrt{g^* h_0^*}}$ and the average water depth h_0^* is a parameter much smaller one. Moreover, let us denote by (v_1, v_2) the components of the velocity inside the bottom boundary layer. A simple analysis of orders of magnitude of the different terms that appear into continuity and momentum equations shows that, at the leading order of approximation, the vertical component of the velocity is negligible and the dynamic pressure remains constant along the vertical direction. If the turbulent Reynolds stresses are quantified by introducing Boussinesq hypothesis and an eddy viscosity, the problem is reduced to the determination of $v_1(x_2, t)$ which is provided by the solution of the component of the Reynolds equation along the x_1 -direction

$$\frac{\partial v_1}{\partial t} = -\frac{\varepsilon}{\delta} \frac{\partial p}{\partial x_1} + \frac{1}{2} \frac{\partial}{\partial x_2} \left[\left(1 + \frac{\nu_T^*}{\nu^*} \right) \frac{\partial v_1}{\partial x_2} \right] \quad (5)$$

where the dimensionless dynamic pressure $p = p^* / (\varepsilon^2 \rho^* g^* h_0^*)$ appears along with the dimensionless parameters ε and δ previously defined. Obviously, in (5), the velocity component v_1 and the pressure p are the averaged values of the instantaneous quantities. The motion described by (5) must be congruent with the irrotational flow far from the bottom and must satisfy the no-slip condition at the bottom. Far from the bottom, the equation of motion in the direction x_1 gives the value of $\partial p / \partial x_1$ which turns out to be

$$\frac{\partial p}{\partial x_1} = -\frac{\delta}{\varepsilon} \left(\frac{\partial V_1}{\partial t} \right)_{x_2=0} \quad (6)$$

where $(\partial V_1 / \partial t)_{x_2=0}$ is calculated by means of (1), although a rigorous approach would require to cancel the terms of $O(\varepsilon)$. To evaluate the eddy viscosity ν_T^* , the turbulence model of Saffman (1970) is employed. The model assumes that the eddy viscosity is a function of two local turbulence densities, namely the pseudo-energy e^* and the pseudo-vorticity Ω^* , which satisfy nonlinear convection-diffusion equation. With the above assumptions and by introducing the following dimensionless variables

$$e = \frac{e^*}{\varepsilon h_0^* \delta^*}; \quad \Omega = \frac{\Omega^* \delta^*}{\varepsilon \sqrt{g^* h_0^*}} \quad (7)$$

the following equations are obtained

$$\frac{\partial e}{\partial t} = \frac{\varepsilon}{\delta} e \left[\alpha_e \left| \frac{\partial v_1}{\partial x_2} \right| - \beta_e \Omega \right] + \frac{1}{2} \frac{\partial}{\partial x_2} \left[\left(1 + \sigma_e \frac{\nu_T^*}{\nu^*} \right) \frac{\partial e}{\partial x_2} \right] \quad (8)$$

$$\frac{\partial \Omega^2}{\partial t} = \frac{\varepsilon}{\delta} \Omega^2 \left[\alpha_\Omega \left| \frac{\partial v_1}{\partial x_2} \right| - \beta_\Omega \Omega \right] + \frac{1}{2} \frac{\partial}{\partial x_2} \left[\left(1 + \sigma_\Omega \frac{v_T^*}{v^*} \right) \frac{\partial \Omega^2}{\partial x_2} \right] \quad (9)$$

where α_e , α_Ω , β_e , β_Ω , σ_e , σ_Ω are universal constants. The values of the constants were determined by Saffman & Wilcox (1974) on the basis of theoretical arguments. In addition, by dimensional analysis it follows that

$$v_T^* = \frac{e^*}{\Omega^*}; \quad \frac{v_T^*}{v^*} = 2 \frac{e}{\Omega} \quad (10)$$

Equations (5) and (8)-(9) along with the relation (10) and appropriate boundary conditions give rise to a well-posed problem. For large values of x_2 , we force the matching of the flow field with the external irrotational velocity and the vanishing of e^* and Ω^* . At the bottom, the velocity satisfies the no-slip condition. In addition, Saffman (1970) assumed that the pseudo-vorticity depends on a dimensionless roughness $z_w = z_r^* u^* / v^*$ through a universal function $S(z_w)$, where

z_r^* and $u^* = \sqrt{\tau_w^* / \rho^*}$ represent the roughness of the bottom and the friction velocity and τ_w^* is

the shear stress at the bottom. It turns out that $\Omega^* = (\tau_w^* / (\rho^* v^* \alpha_e)) S(z_w)$. Later Saffman & Wilcox (1974) linked the function S with the logarithmic velocity profile but they did not provide an explicit relationship for the function S . Following a procedure similar to that used by Saffman & Wilcox (1974), Blondeaux & Colombini (1985) obtained an explicit relationship for S . This relationship can be used by noticing that at the wall

$$\Omega = (\tau_w / \alpha_e) S(z_r \sqrt{2\varepsilon \tau_w / \delta}) \quad (11)$$

where $\tau_w = \partial v_1 / \partial x_2 \big|_{x_2=0}$.

If vanishing values of e are used as initial conditions and e is set equal to zero at the wall, turbulence appearance is not triggered. To trigger the transition and to observe a turbulent flow, it is necessary to introduce a perturbation of e either at the beginning of the simulation or at the wall. While the first approach simulates the presence of an initial perturbation, the second simulates the effect of wall imperfections which, as discussed by Blondeaux & Vittori (1994), play a crucial role in triggering turbulence in oscillating boundary layers. For this reason, the second approach is currently preferred. As expected, the transition to turbulence depends on the value e_w of e imposed at the wall. The results described in the following sections are obtained by setting $e_w = 10^{-18}$, but further runs have been made with different values, to find what are the effects of different wall imperfections on the transition process. The sediment transport can be evaluated using an empirical formula to estimate the bed load and integrating the flux of sediment from the reference level, where the boundary condition for the sediment concentration is forced, up to the irrotational region where sediment concentration vanishes. The bed load is determined by means of the relationship

$$Q_b = \frac{Q_b^*}{\sqrt{(\rho_s^* / \rho^* - 1) g^* d^{*3}}} = \frac{30}{\pi} (|\theta| - \theta_c) \left(\sqrt{|\theta|} - 0.7 \sqrt{\theta_c} \right) \frac{\theta}{|\theta|} \quad (12)$$

where the Shields parameter θ is defined as

$$\theta = \frac{\tau_w^*}{(\rho_s^* - \rho^*) g^* d^*} \quad (13)$$

and θ_c is the critical value of the Shields parameter for the initiation of sediment transport. The dimensionless suspended sediment transport rate turns out to be

$$Q_s = \frac{Q_s^*}{\sqrt{(\rho_s^* / \rho^* - 1)g^* d^{*3}}} = \frac{\varepsilon \delta}{\sqrt{(s-1)(d^* / h_0^*)^3}} \int_{x_{ref}}^{\infty} v_1 c dx_2 \quad (14)$$

The use of (14) implies the knowledge of the sediment concentration c which is calculated with the equation of mass balance, assuming that the sediments are advected by the motion of the water and diffuse because of turbulence. Since sediment concentration decays rapidly away from the bottom and is significant only within the boundary layer, the sediment balance provides the following equation

$$\frac{\partial c}{\partial t} + (v_2 - v_s) \frac{\partial c}{\partial x_2} = \frac{1}{2} \frac{\partial}{\partial x_2} \left[\frac{v_T^*}{v^*} \frac{\partial v_1}{\partial x_2} \right] \quad (15)$$

where $v_s = v_s^* / U_0^*$ is the dimensionless sediment fall velocity which depends on the sediment Reynolds number

$$R_p = \frac{\sqrt{(\rho_s^* / \rho^* - 1)g^* d^{*3}}}{v^*} \quad (16)$$

and the sediment diffusivity can be assumed to be equal to the eddy viscosity. As already pointed out, it is assumed that c vanishes for x_2 tending to infinity, and c is set equal to c_{ref} for $x_2 = x_{ref}$, where c_{ref} is provided by an empirical relationship and x_{ref} is set equal to twice the size of the sediment. Several formulae can be used to quantify c_{ref} . In this present paper, we use the Zysermann & Fredsoe's formula (Zysermann & Fredsoe, 1994)

$$c_{ref} = 0.331 \frac{c_m (|\theta| - \theta_c)^{1.75}}{c_m + 0.331 (|\theta| - \theta_c)^{1.75}} \quad (17)$$

where the maximum value of c_m of concentration is assumed to be 0.32.

3 Results

Equation (5) together with equations (8) and (9), which describe turbulence dynamics, are integrated numerically. A logarithmic scale for the vertical coordinate x_2 is introduced, to have an accurate description of the velocity close to the bottom. The numerical approach uses a finite difference scheme of second order to describe the spatial derivatives while the integration over time is performed by a second order Runge-Kutta scheme. Numerical experiments were performed to choose the time step Δt , the size x_{2f} of the domain in the vertical direction and the number of points N of the numerical grid. Preliminary tests were conducted to ensure that the results described below are not affected by the chosen values t_i , Δt , x_{2f} and N . Moreover, the equation which provides the spatial and temporal distribution of sediment concentration, is solved by means of the same numerical approach.

The numerical simulations of Vittori & Blondeaux (2008, 2011) and the experimental measurements of Sumer et al. (2010) show that, for small values of ε , the flow regime in the bottom boundary layer remains laminar throughout the wave cycle. Using the present model, for small values of ε , the pseudo-energy e is negligible during the whole cycle of the wave, the eddy viscosity vanishes and the velocity does not differ from laminar solution. In this case, the roughness of the bottom, i.e. the value of $z_r = z_r^* / \delta^*$, does not affect the results. The present numerical results are in good agreement with the analytical solution of Liu et al. (2007), valid for the laminar regime, and support the accuracy and reliability of the numerical approach used to solve the problem. The results show that, after the passage of the wave crest, the fluid motion close to the bottom reverses its direction and negative velocities are generated. If the value of δ is fixed and increasing values of ε are considered, a critical value ε_c is encountered above which the value of e , which initially is zero, grows during the decelerating phase leading to the turbulent flow regime. If the value of ε is further increased, non-vanishing values of e appear earlier and e reaches higher values. The flow regimes (laminar/turbulent) are shown in figure 1.

Since the value of eddy viscosity, which is used to identify the flow regime, is a continuous function of the parameters, to obtain a quantitative criterion, the flow regime is defined laminar if the maximum value of the eddy viscosity during the wave cycle is smaller or equal to ν^* . If the maximum value of ν^*/ν^* is larger than than 10, the flow regime is defined to be turbulent while, when the maximum value falls between 1 and 10, the transitional regime takes place. The results of figure 1 show that the transition from the laminar to the turbulent regime takes place when the parameter ε is larger than a critical value ε_c that depends on δ .

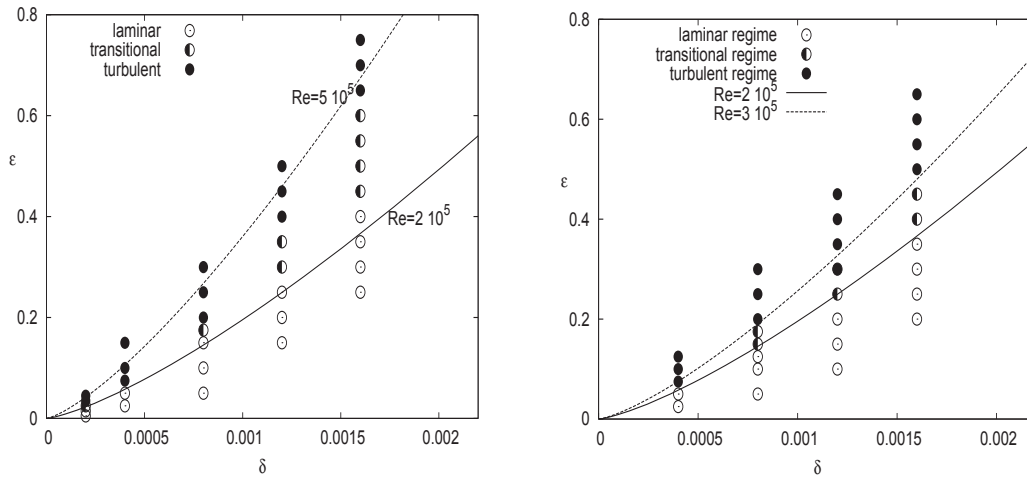


Figure 1: Flow regime in the (δ, ε) -plane for (a) $z_r=0.01$ (hydrodynamically smooth wall), (b) $z_r=1$ (rough wall). The white points represent the laminar regime, the black points represent the turbulent regime and the white/black points represent the transitional regime. In panel (a), the continuous curve describes the relationship $Re=2 \cdot 10^5$, which is the limit between the laminar and transitional regimes suggested by Sumer et al. (2010) while the broken line is the curve $Re=5 \cdot 10^5$ which is the limit suggested by Sumer et al. (2010) for the appearance of the turbulent regime.

Despite the transition to turbulence depends on both ε and δ , for practical purposes the conditions for transition can be determined in terms of a single parameter. Following Sumer et al. (2010), in analogy with oscillating boundary layers, we can introduce the Reynolds number $Re=U^{*2}/(\omega^*\nu^*)=4\varepsilon^{3/2}/(\sqrt{3}\delta^2)$ (where ω^* is $\sqrt{H_0^*g^*/h_0^{*2}}$) and determine the conditions for transition to turbulence by introducing a critical value Re_c of the Reynolds number so that for $Re>Re_c$ turbulence appears. Sumer et al. (2010) suggest a value of Re_c equal to $2 \cdot 10^5$ for the appearance of what they call the transitional regime, i.e. a regime characterized by the presence of "regular" vortices. The same authors observed a fully turbulent regime for values of Re larger than $5 \cdot 10^5$. These values, shown in Figure 1, allow a comparison between the criteria of Sumer et al. (2010) and the results of the present model. To assess the agreement between the numerical results and the experimental measurements, one must take into account that both in the numerical simulations and in the experiments, wall imperfections and/or other sources of significant disturbances (e.g. vibrations of the equipment) play an important role in the transition process, as it happens in the oscillatory boundary layer (Stokes layer) under monochromatic sea waves (Blondeaux & Vittori, 1994). The results shown in figure 1a are obtained for values of z_r that correspond to a hydrodynamically smooth wall. When the value of z_r is increased, the roughness affects the transition process from the transitional to the turbulent regime and an increase of z_r leads to a significant decrease of the critical wave amplitude, while the boundary between laminar regime and transitional regime is only slightly modified. Obviously, the roughness of the bottom affects significantly also the velocity field and the bottom shear stress. The results obtained for rough walls are discussed in Blondeaux & Vittori (2011).

As already pointed out by Sumer et al. (2010) and Vittori & Blondeaux (2008, 2011), in depth-averaged models, the bottom shear stress τ_w^* is usually evaluated by means of the Chezy law and assumed proportional to the square of the irrotational velocity evaluated close to the bottom $V_1|_{x_2=0}$ ($\tau_w^*=\rho^*c_fV_1^*|_{x_2=0}$, where c_f is a drag coefficient). The results, like those of Liu et al.

(2007) for the laminar regime and those obtained by Vittori & Blondeaux (2008, 2011) for the turbulent regime, show that the shear stress at the bottom assumes also negative values even though $V_1|_{x_2=0}$ is always positive and points in the direction of wave propagation. Hence, the relation $\tau_w^* = \rho^* c_f V_1^* |V_1|_{x_2=0}$ can not be used after the passage of the wave crest, when the shear stress reverses its direction. This result is supported by the proposed model, which shows a rapid growth of turbulence, which occurs during the decelerating phase of the wave cycle and leads not only to differences between the accelerating and decelerating phases of the wave cycle but also to a second positive peak of bottom shear stress. The presence of a second peak in the time development of the bottom shear stress is also shown by the experimental measurements of Sumer et al. (2010) and the numerical results obtained by Vittori & Blondeaux (2011). Figure 2 shows a comparison between the results of the model and some of the laboratory data obtained by Sumer et al. (2010) for a value of the Reynolds number equal to $2 \cdot 10^6$. As in Sumer et al. (2010), in figure 2 the shear stress is scaled with its first relative maximum, which takes place shortly before the passage of the wave crest. The dimensional value of the first maximum $\tau_{w,max1}^*/\rho^*$ computed by the present model is about $0.74 \cdot 10^{-3} \text{ m}^2/\text{s}^2$ while that measured by Sumer et al. (2010), estimated looking at their figure 15, turns out to fall between $0.7 \cdot 10^{-3}$ and $1.4 \cdot 10^{-3} \text{ m}^2/\text{s}^2$. The agreement can be considered good, taking into account the differences between the pressure gradient used in the experiments and the one used in the numerical simulations.

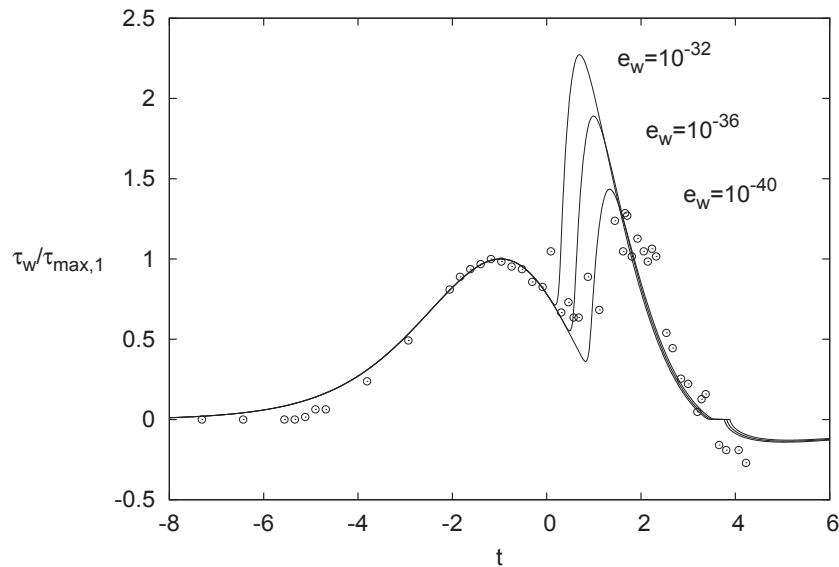


Figure 2: Bottom shear stress plotted versus time for $z_r=0.01$ and values of δ and ε such that $Re=2 \cdot 10^6$. The continuous lines are the result of the present model and the points are the experimental data of Sumer et al. (2010).

The various curves obtained by means of the present model and plotted in figure 2, are characterized by different values of e_w . We remind to the reader that e_w is related to wall imperfections, i.e. to the amplitude of the perturbations of the flow introduced by the wall waviness. In figure 3a the time development of the sediment transport rate is plotted versus time along with the contributions of the bed load (Q_b) and of the suspended load (Q_s) for $\varepsilon=0.5$, $\delta=0.00086$, $d=d^*/h^*=5.2 \cdot 10^{-4}$, $R_p=21.5$, $z_r=1 \cdot 10^{-3}$. The sediment transport rate is characterized by the presence of a first maximum that is the result of the passage of the wave crest, although it is slightly shifted. Then, a second relative maximum of the sediment transport rate is observed which is induced by turbulence which appears explosively during the decelerating phase. The onset of turbulence leads to a significant increase of the bottom shear stress and of mixing processes that have a large influence on the suspended load. Finally, during the latter stages, the sediment transport reverses its direction and is directed towards the offshore region because the motion in the proximity to the bottom reverses its direction. Similar results are obtained for different values of the parameters even if the variation of sediment characteristics gives rise to different values of the ratio between the bed load and the suspended load. For

example, figure 3b shows that, increasing the grain size, the suspended load decreases. Moreover, the shear stress under the wave crest is too weak to pick-up the sediment from the bottom and to carry it into suspension and the suspended sediment transport becomes significant only during the decelerating phase when turbulence appears and enhances transport processes.

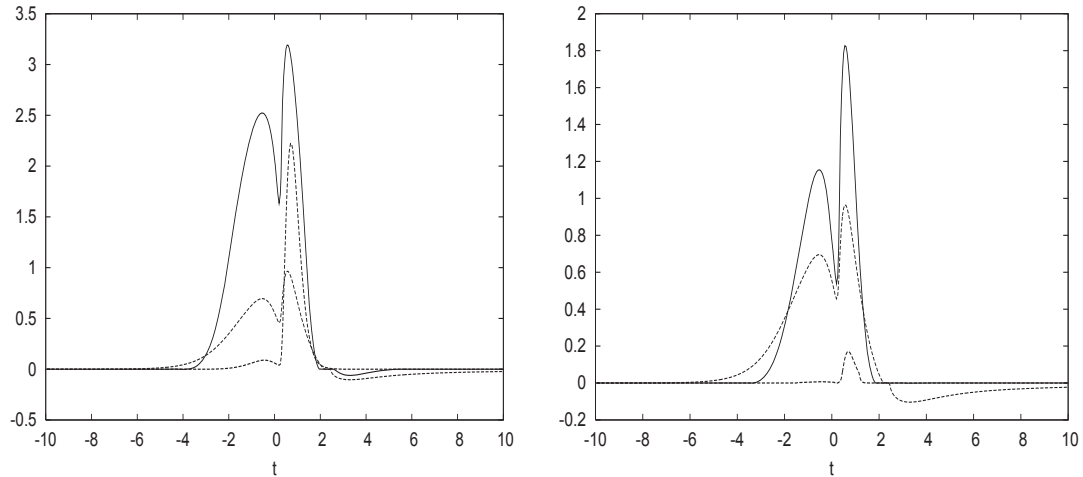


Figure 3: Bed load sediment transport (continuous line), suspended sediment transport (thick broken line) and Shields parameter (thin broken line) plotted versus time ($\delta=0.00086$, $\varepsilon=0.5$) a) $z_r=1 \cdot 10^{-3}$, $R_p=21.5$ and $d^*/h^*_0=0.00052$; b) $z_r=2 \cdot 10^{-3}$, $R_p=60.7$ and $d^*/h^*_0=0.001$.

4 Conclusions

The two-equation turbulence model of Saffman (1970) is used to study the boundary layer generated near the sea bottom by the propagation of a solitary wave. Both the smooth wall case and the rough wall case are considered. The results show that turbulence usually appears during the decelerating phase, when the height of the wave is larger than a critical value that depends on δ . In a wide range of the parameters, the bottom shear stress τ_w is characterized by the presence of two maxima: the first does not depend on δ but only on the ratio between the thickness of the boundary layer and local water depth, the second maximum and minimum shear stress depend both on δ and ε . The model finally allows the sediment transport rate, taking place both as bed load and suspended load, to be evaluated.

5 Acknowledgements

This study was partially funded by the Ministry of Education, of Univesity and Research through the research project 2008YNPNT9-003 'Hydrodynamics and morphodynamics in the surf region'.

6 References

- Blondeaux, P. (1987): Turbulent Boundary Layer at the Bottom of Gravity Waves. In: J. Hydraulic Res., Vol 25, no. 4, pp. 447-464.
- Blondeaux, P.; Colombini, M. (1985): Pulsatile Turbulent Pipe Flow. In: V Symposium on 'Turbulent Shear Flows, Ithaca (U.S.A.), 7-9 August 1985.
- Blondeaux, P.; Vittori, G. (1991a): Vorticity dynamics in an oscillatory flow over a rippled bed. In: J. Fluid Mech., Vol. 226, pp. 257-289.
- Blondeaux, P.; Vittori, G. (1991b): A route to chaos in an oscillatory flow: Feigenbaum scenario. In: Phys. Fluids, Vol. A3, pp. 2492-2495.
- Blondeaux, P.; Vittori, G. (1994): Wall imperfections as a triggering mechanism for Stokes layer transition. In: J. Fluid Mech., Vol. 264, pp. 107-135.

- Blondeaux, P.; Vittori, G. (1999): Boundary layer and sediment dynamics under sea waves. In: Adv. in Coastal and Ocean Engineering, Vol. 4, pp. 133-190.
- Blondeaux, P.; Vittori, G. (2011): RANS modelling of the turbulent boundary layer under a solitary wave. To appear in: Coastal Engineering.
- Dodd, N.; Blondeaux, P.; Calvete, D.; De Swart, H.; Falques, A.; Hulscher, S.J.M.H; Rozynsky, G.; Vittori, G. (2003): Understanding coastal morphodynamics using stability methods. Cont. Shelf Res., Vol. 19 (4), pp. 849-865.
- Foti, E.; Blondeaux, P. (1995): Sea ripple formation: the turbulent boundary layer case. In: Coastal Engineering, Vol. 25 (3-4), pp. 237-253.
- Grimshaw, R.H.J. (1970): The solitary wave in water of variable depth. In: J. Fluid Mech., Vol. 42, (3), pp. 639-656.
- Grimshaw, R.H.J. (1971): The solitary wave in water of variable depth Part 2. In: J. Fluid Mech., Vol. 46, (3), pp. 611 - 622.
- Liu, P.L.F. (2006): Turbulent boundary layer effects on transient wave propagation in shallow water. In: Proc. Roy. Soc. London, Vol. 462, (2075), pp. 3481-3491.
- Liu, P.L.F.; Park, Y.S.; Cowen, E.A. (2007): Boundary layer flow and bed shear stress under a solitary wave. In: J. Fluid Mech., Vol. 574, pp. 449 - 463.
- Menter, F.R. (1994): Two-equation eddy-viscosity turbulence models for engineering applications. In: AIAA J., Vol. 32, (8), pp. 1598-1605.
- Saffman, P.G. (1970): A model for inhomogeneous turbulent flow. In: Proc. R. Soc. London. Series A: Mathematical and Physical Sciences, Vol. 317, (1530), pp. 417-433.
- Saffman, P.G.; Wilcox, D.C. (1974): Turbulence-model predictions for turbulent boundary layers. In: AIAA J., Vol. 12, pp. 541-546.
- Sumer, B.M.; Jensen, P.M.; Soerensen, L.B.; Fredsoe, J.; Liu, P.L.F. (2010): Coherent structures in wave boundary layers. Part 2. Solitary motion. In: J. Fluid Mech., Vol. 646, pp. 207-231.
- Suntoyo; Tanaka, H. (2009): Numerical modeling of boundary layer flows for a solitary wave. In: J. Hydro-environment Res., Vol. 3, pp. 129-137.
- Vittori, G.; Blondeaux, P. (2008): Turbulent boundary layer under a solitary wave. In: J. Fluid Mech., Vol. 615, pp. 433-443.
- Vittori, G.; Blondeaux, P. (2011): Characteristics of the boundary layer at the bottom of a solitary wave. In: Coastal Eng., Vol. 58, (2), pp. 206-213.
- Wilcox, D.C. (1988): Reassessment of the scale-determining equation for advanced turbulence models. In: AIAA J., Vol. 26, (11), pp. 1299-1310.
- Zyserman, J.A.; Fredsoe, J. (1994): Data analysis of bed concentration of suspended sediment. In: Hydraul. Engineering, Vol. 120, (9), pp. 1021-1042.

Numerical and physical modelling of wave penetration in Oostende harbour during severe storm conditions

Vincent Gruwez¹, Annelies Bolle², Toon Verwaest³ and Wael Hassan⁴

Abstract

Hydrodynamic boundary conditions are needed for the design of new sea defence structures in the harbour of Oostende along all quays to defend the city centre and hinterland from flooding during a super storm. The wave climate in the harbour was decoupled to wave penetration and locally generated wind waves to allow separate modelling of both phenomena. The wave penetration was modelled with a physical wave model, a mild slope equations model MILDwave and a Boussinesq equations model Mike 21 BW. The locally wind generated waves were modelled with the spectral model SWAN. By using a thin sponge layer along the boundaries in the numerical wave penetration models to model partial reflection inside the harbour, very good correspondence is found between the numerical wave penetration models and the physical model. Finally, the wave penetration energy and locally generated wave energy were superposed to obtain the complete wave climate along all structures inside the harbour during severe storm conditions.

Keywords: wave penetration in harbour, physical modelling, numerical modelling, mild slope equations, Boussinesq equations, local wind generated waves

1 Introduction

1.1 Harbour of Oostende

The harbour of Oostende is located on the Belgian coast facing the North Sea. As a part of the master plan for coastal safety of the Belgian coast, safety against flooding and wave overtopping has to be assured during super storms. A minimum safety level is prescribed based on a super storm with a return period of 1000 years.

The still water level during such a storm at Oostende was determined to be +7.20m TAW, including a 0.30m sea level rise due to climate change expected until 2050. The crest level of the quay walls inside the harbour is approximately +6.90m TAW and the city centre is well below this level (+4.50m TAW). It is clear that during a 1000 year storm the quay walls are too low to prevent flooding of the city centre and hinterland. The flooding and overtopping danger is illustrated in Figure 1: even for a storm with return period of 5 years, water can already reach the quay crest level.

Therefore, new sea defence structures are needed to achieve this minimum safety level prescribed by the master plan (e.g. storm walls on the quays). The hydrodynamic boundary conditions along all the tide and wave afflicted constructions in the inner harbour are required for the design of these structures.

At the moment the configuration of the outer harbour is being changed dramatically as the old harbour dams are replaced by two new rubble-mound breakwaters (cf. Figure 2) and the access channel is broadened and deepened to improve maritime access. The wave modelling efforts in

¹ International Marine and Dredging Consultants (IMDC NV), Coveliersstraat 15, 2600 Berchem (Antwerp), Belgium, vgr@imdc.be

² International Marine and Dredging Consultants (IMDC NV), Coveliersstraat 15, 2600 Berchem (Antwerp), Belgium, abo@imdc.be

³ Flanders Hydraulics Research (Waterbouwkundig Laboratorium), Berchemlei 115, 2140 Antwerp, Belgium, Toon.Verwaest@mow.vlaanderen.be

⁴ Flanders Hydraulics Research (Waterbouwkundig Laboratorium), Berchemlei 115, 2140 Antwerp, Belgium, Wael.Hassan@mow.vlaanderen.be

this paper are only focussed on the future situation for which the new sea defence structures need to be designed.



Figure 1: Water reaches quay crest level during a 5-year storm in the harbour of Oostende.



Figure 2: Harbour of Oostende, original harbour dam layout (left), future breakwater layout (right)

Physical and numerical wave modelling was done to obtain the hydrodynamic boundary conditions. Boundary conditions such as the significant wave height H_s , the average wave period $T_{m-1,0}$ and wave direction are needed for the functional (wave overtopping) and structural (wave forces) design of the new sea defence structures. This paper will focus on the accurate determination of the significant wave height all around the harbour during severe storm conditions.

2 Physical wave modelling

The physical model of the future configuration of the harbour was built in the wave basin of Flanders Hydraulics Research (Hassan et al., 2011) on a scale of 1:100 (cf. Figure 3). A piston type wave paddle generates the waves in this basin and only long-crested wave generation is possible. All time series were based on a JONSWAP spectrum. Wave measurements were performed in the model at more than 40 locations with non-directional wave gauges. Some of these locations are shown in Figure 7.

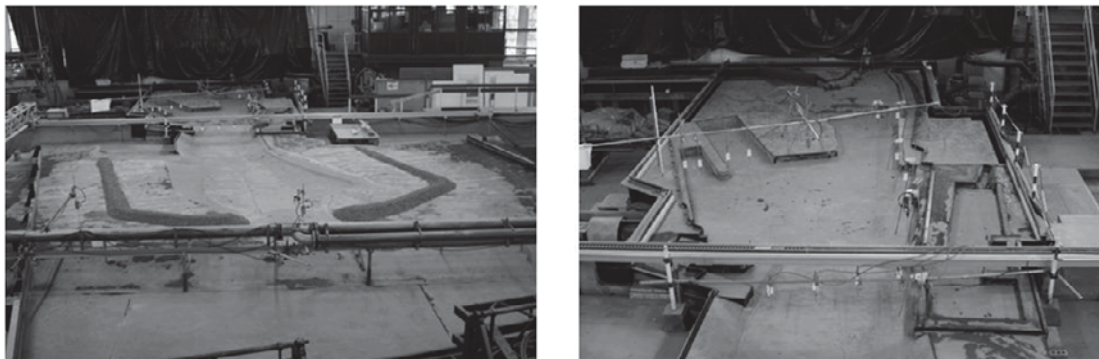


Figure 3: Physical model, outer harbour (left), inner harbour (right)

Storm conditions with a return period of 1000yrs are a water level of +7.20m TAW⁵, significant wave height of 5.20m and peak wave period of 12.0s. In addition, several other wave conditions were modelled corresponding to lower and higher water levels in order to deliver input for the flood risk modelling of Verwaest et al. (2008). All wave conditions are shown in Table 1. Three wave directions were simulated in the wave basin: NW, NNW and -37° which is the direction for which the most wave energy penetrates the harbour. In total more than 40 wave conditions were modelled.

Table 1: Hydrodynamic boundary conditions used in the physical model. The prototype values are given.

Still water level [m TAW]	Max. water depth [m]	Significant wave height H_s [m]	Peak wave period T_p [s]
6.00	14.90	4.60	12.0; 10.0
6.50	15.40	4.80	12.0; 10.0
6.80	15.70	5.00	12.0; 10.0
7.00	15.90	5.10	12.0; 10.0
7.20	16.10	5.20	12.0; 10.0; 8.0; 6.0
7.50	16.40	5.40	12.0; 10.0
8.00	16.90	5.70	12.0; 10.0

The physical model wave data provide calibration and validation data for the numerical models.

3 Numerical wave modelling

3.1 The numerical models

The most important physical processes in a harbour are diffraction, depth refraction/shoaling, (partial) reflection, transmission and non-linear wave-wave interactions (Battjes, 1994). Phase-resolving numerical models are used for the modelling of wave penetration because they can simultaneously account for diffraction and reflection (and standing waves) as opposed to phase-averaged wave models. Two phase-resolving models were used: MILDwave (Troch, 1998) and Mike 21 BW (DHI, 2009). MILDwave is a linear time dependant wave model based on the mild-slope equations of Radder and Dingemans (1985) and Mike 21 BW is a more complex non-linear time dependant wave model based on the enhanced Boussinesq equations of Madsen et al. (1991, 1992). By comparing both numerical models and validation with the physical model data, the applicability of each model is identified.

A severe storm is accompanied by extreme wind speeds (20m/s – 30m/s and higher), which cause local generation of very short waves with relatively high wave heights even for the relatively short fetch lengths in a harbour (van der Meer et al., 2002). Especially at the more landward areas of the harbour, these waves are substantial and cannot be ignored because of the low wave penetration energy in these parts. The spectral model SWAN (TUDelft, 2010) is a phase-averaged wave model, based on the action balance equation (Booij, 1999) and can model wave generation by wind. However, because it is phase-averaged, SWAN is not able to simulate diffraction⁶ and standing waves due to reflection and cannot therefore model the wave penetration into the harbour accurately. Due to the local nature of wave generation by wind, diffraction plays a minor role in the harbour for these waves. The use of the phase-averaged wave model SWAN in harbours is therefore expected to be acceptable for and is limited to the simulation of local wave generation by extreme wind speeds.

⁵ TAW or „Tweede Algemene Waterpassing“ is a reference level used in Belgium. A level of 0.00m TAW corresponds to the average low tide level at Oostende.

⁶ SWAN does have a limited capability to model diffraction, but not in combination with reflection (TUDelft, 2010)

The physical model and both phase-resolving models cannot on their part account for locally wind generated waves⁷. This is why the modelling of wave penetration and locally wind generated waves was decoupled as proposed by van der Meer et al. (2002).

3.2 Wave penetration modelling

3.2.1 Set-up of models

The bathymetry used for the numerical models is shown in Figure 4 and is similar to the bathymetry used in the physical modelling. The bathymetry of the outer harbour was based on plans of the future harbour entrance channel. The bottom levels in the inner harbour were based on the prescribed dredging depths, resulting in a bathymetry with the highest possible water depths, allowing the most wave penetration.

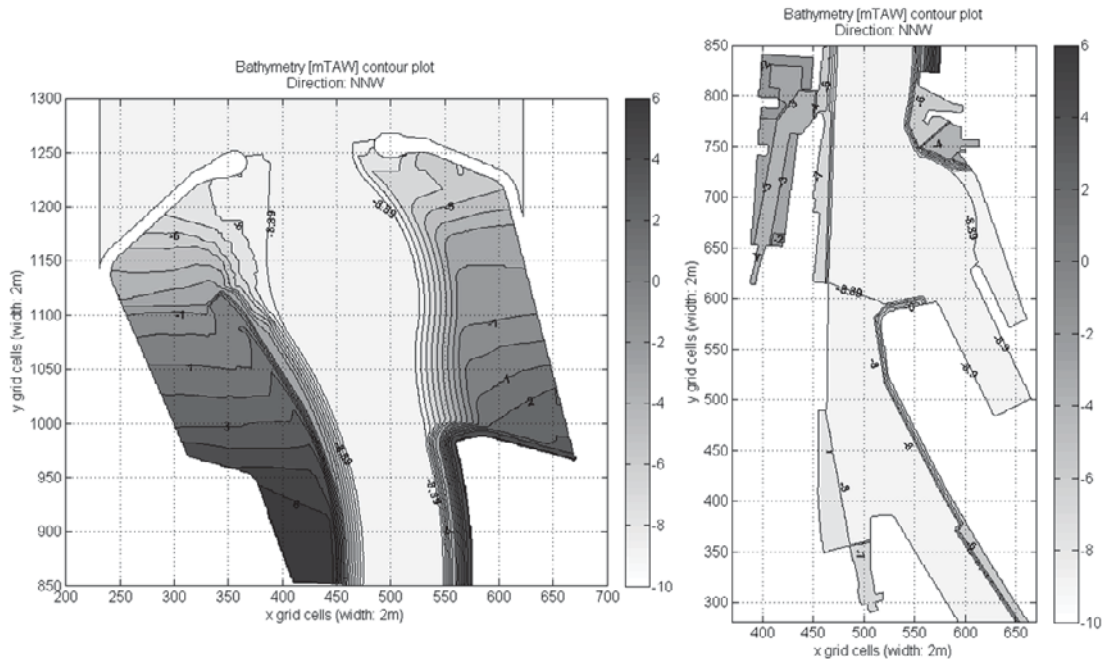


Figure 4: Bathymetry of outer (left) and inner harbour (right). Bottom levels are given in [m TAW].

The computational domain was restricted outside the harbour as much as possible to limit the calculation time by using artificial land (cf. Figure 5). Waves are generated in the phase resolving models by an internal wave generation line at a distance of two wave lengths from the harbour entrance. Seaward of the wave generation line, a sponge layer was added to absorb all outgoing wave energy.

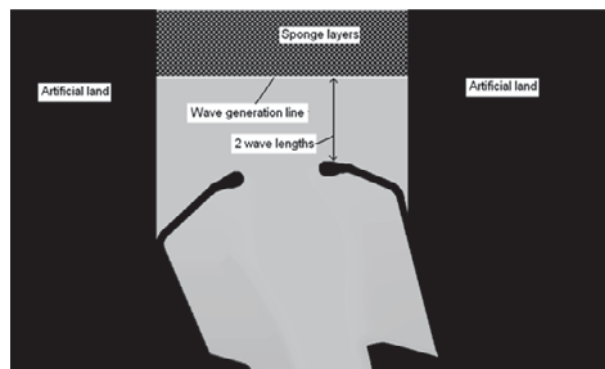


Figure 5: Computational domain at the outer harbour with indication of artificial land, internal wave generation line and sponge layers

⁷ Wind generation of waves is currently under development for MILDwave by the University of Ghent.

The grid spacing is 2.00m in both x and y direction and a time step of 0.05s was used. A minimum water depth was set to 2.00m to avoid having to include wave run-up. Wave breaking was included in both models because wave breaking on the shallow areas in the outer harbour could have an important effect on the wave climate in the inner harbour. Transmission of wave energy over the harbour dams was neglected, since this is not important for the inner harbour.

To model the partial reflection in the harbour, a different approach than use of porosity layers – as suggested by DHI (2009) – was used. This is because the necessary width of a porosity layer is $L_p/4$ (with L_p the wave length corresponding to the peak wave period T_p), which would take up too much space inside the harbour because of its small dimensions in relation to the wave length. Instead of using porosity layers, a thin sponge layer of one grid cell in front of each partially reflecting boundary was used. This was shown by Brorsen (2000) to be an effective and practical numerical partial reflection method for wave propagation models. The same approach has been used in the MILDwave model.

Appropriate reflection coefficients were determined for each structure in the harbour (e.g. (flooded) quay walls, dikes, rubble mounds,...). The corresponding sponge layer coefficients were calculated iteratively with a 1DH-model of a cross section of the considered structure and a reflection analysis, or where possible by calibration with the physical model results.

3.2.2 Results and comparative analysis

Most wave conditions from Table 1 were simulated with the wave penetration models. They were also based on a JONSWAP spectrum and only long-crested waves were generated. The results shown in this paper will only be limited to the 1000-year wave condition (cf. SWL = +7.20m TAW in Table 1) and for wave direction NNW, but the same conclusions count for all.

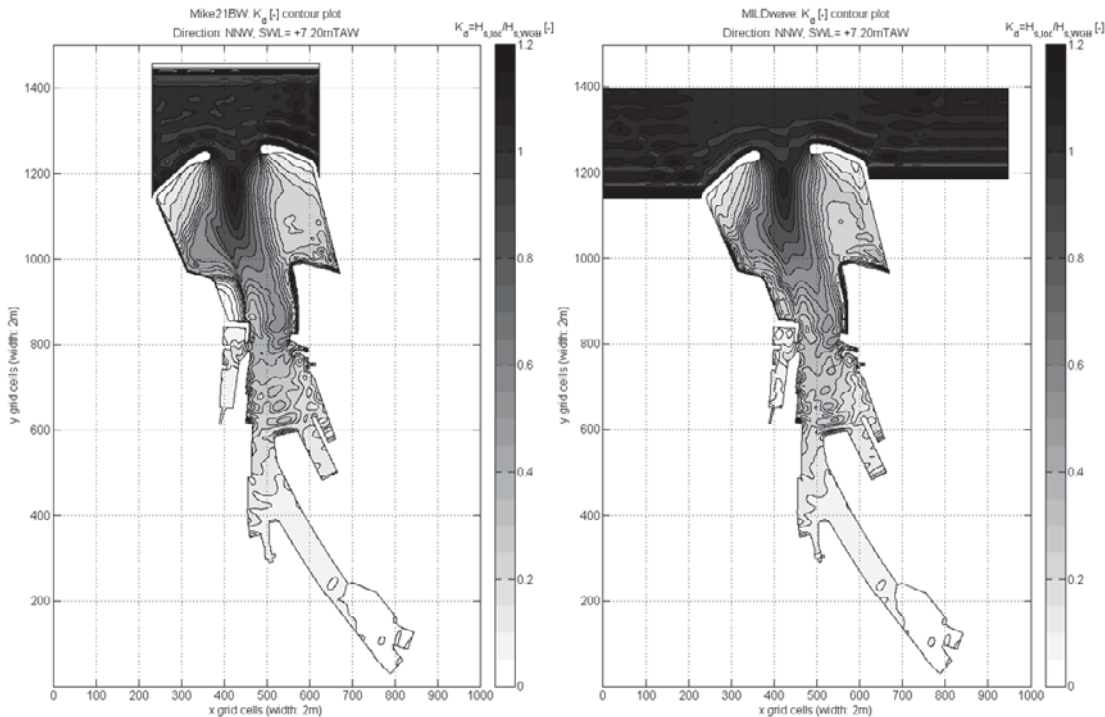


Figure 6: Comparison of Mike 21 BW (left) and MILDwave (right) wave disturbance result.

A very good correspondence of the wave disturbance coefficient $K_d (=H_{s,location}/H_{s,wave\ generation\ line})$ between both phase resolving models is found (cf. Figure 6). This is also shown in Figure 7 where the wave disturbance is compared at the exact locations of the wave gauges in the physical model. A very good correspondence is also found of both numerical models with the physical model wave disturbance results. Some exceptions (cf. G06_{left} and G14_{left} in Figure 7) are mainly due to the sensitive location of standing wave oscillations.

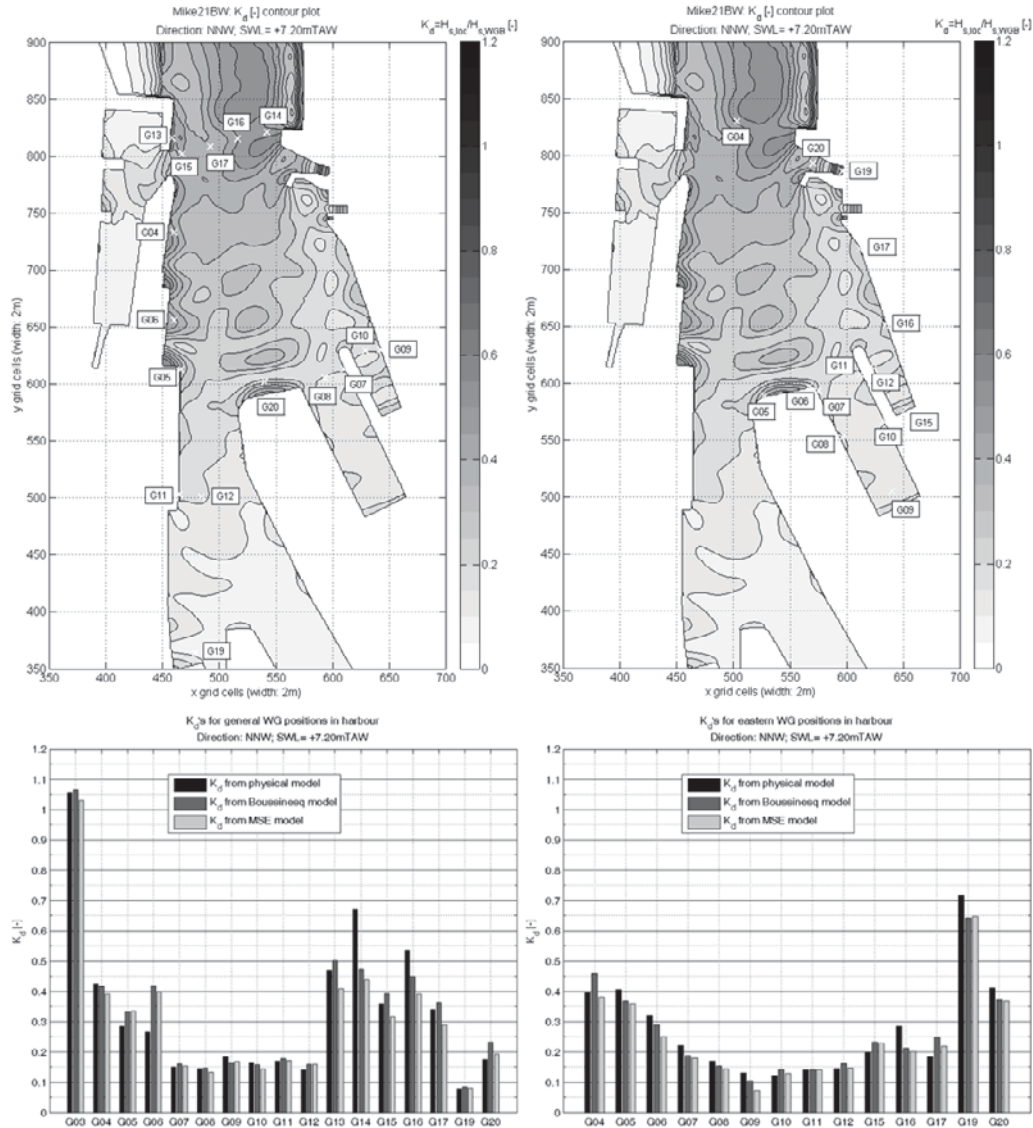


Figure 7: Comparison of the wave disturbance at the wave gauge locations of the physical model. Location of G03_{left} is at the harbour entrance.

The mild-slope model MILDwave seems to be just as capable as the Boussinesq model Mike 21 BW to model wave disturbance in harbours, and this with a lower calculation time.

3.3 Local wave generation by extreme wind speed

3.3.1 Set-up of model

The bathymetry of the SWAN model includes the most landward parts of the harbour as shown in Figure 8, which is a continuation of the inner harbour bathymetry from Figure 4. This part was not included in the wave penetration models because the wave penetration energy is negligible here as opposed to the locally generated wind waves.

The harbour entrance was closed and no waves were imposed at the boundaries. A uniform wind field was defined covering the complete calculation domain. All onshore wind directions and corresponding extreme wind speeds (~24 m/s at 10m height for RP = 1000yrs) were modelled to obtain the most disadvantageous conditions for each area in the harbour.

During a 1000-year storm, locally generated wind waves with significant wave height H_{m0} of up to 0.80m and an average wave period $T_{m-1,0}$ of 2.1s are generated for the available fetch length inside the harbour. These waves are not negligible, certainly not at the most landward areas of the harbour (cf. right in Figure 9) where almost no wave penetration energy is left (cf. Figure 6).

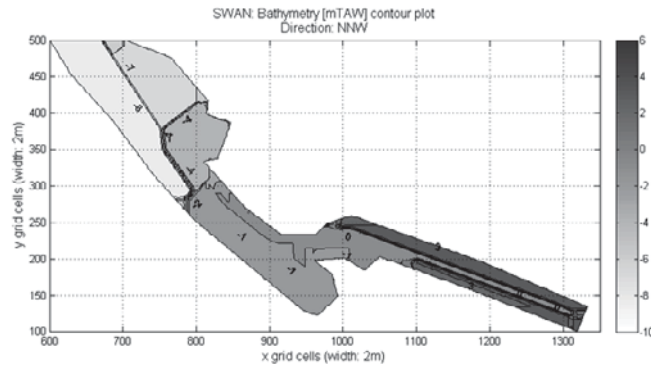


Figure 8: Bathymetry of the most landward part of the harbour. Bottom levels are given in [m TAW] (attention: different origin of axis than in Figure 4).

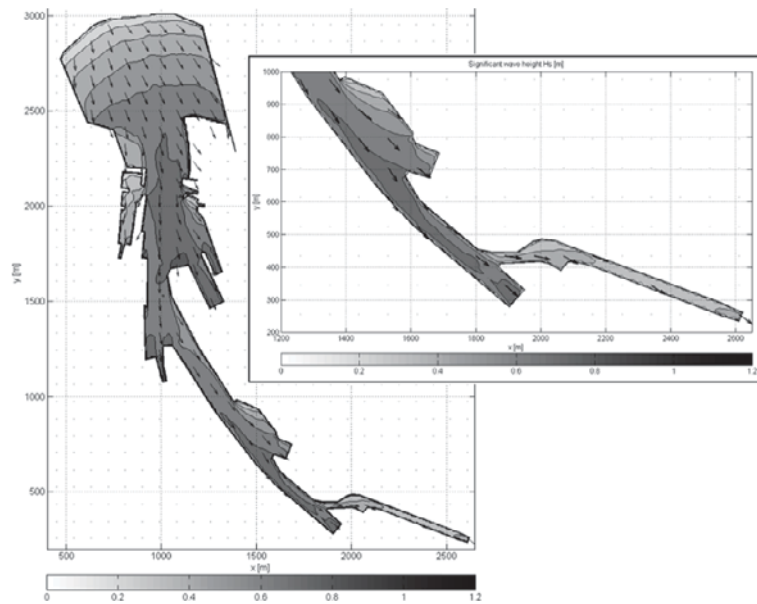


Figure 9: Significant wave height H_{m0} [m] and direction (arrows). Wind speed is 24m/s (from NW). Left: complete model domain, right: zoom to most landward areas of harbour.

3.4 Resulting boundary conditions in the inner harbour

The total wave climate on each location in the harbour is obtained by superposition of the wave penetration energy and the locally wind-generated wave energy according to equation (1) as proposed by van der Meer et al. (2002).

$$H_{m0} = \sqrt{H_{m0,1}^2 + H_{m0,2}^2} \quad (1)$$

with $H_{m0,1}$ significant wave height of the wave penetration [m]

$H_{m0,2}$ significant wave height of the locally wind generated waves [m]

Functional design of the new sea defence structures is based on a limitation of the overtopping discharge and associated flooding risks for people and properties. Formulas to calculate overtopping require the incoming significant wave height. All wave models deliver the total significant wave height which includes both the incoming and reflected wave energy. Because of the small dimensions of the harbour and the complexity of the reflected wave field, conventional reflection analysis in the harbour is very difficult if not impossible. An expert judgement is recommended to take reflection effects into account when interpreting the results of the wave penetration models. Otherwise, it is possible that too conservative significant wave heights are used for the functional design.

4 Conclusions

New sea defence structures are needed in the harbour of Oostende to assure safety against flooding and wave overtopping during severe storm conditions. Therefore accurate hydrodynamic boundary conditions are needed for the design of these structures. This paper provided an overview of how the significant wave height in the harbour of Oostende during these severe storm conditions was obtained.

Modelling of the wave climate was decoupled to wave penetration and locally wind generated waves by the extreme wind speed. The wave penetration was simulated with the phase-resolving models MILDwave and Mike 21 BW, the local wind generated waves by the phase-averaged model SWAN. Using a sponge layer of one grid cell to model partial reflection in the phase-resolving models proved to be a very good method as the validation with the physical model data showed. The linear wave model MILDwave and non-linear wave model Mike 21 BW showed comparable results for the wave disturbance inside the harbour. The results of the SWAN model showed that severe storm wind can generate substantial waves for the relatively short fetch lengths inside the harbour. These waves are particularly important for the most landward parts of the harbour where almost no wave penetration energy is left.

The wave penetration energy and local wind generated wave energy were finally superposed, providing the complete wave climate inside the harbour during severe storm conditions.

5 Acknowledgements

The Flemish government (Coastal Department) is acknowledged for funding this research.

6 References

- Battjes, J.A. (1994): Shallow water wave modelling, M. Isaacson and M. Quick (Eds.), Proc. Waves-Physical and Numerical Modelling, University of British Columbia, Vancouver.
- Booij, N.; Ris, R.C.; Holthuijsen, L.H. (1999): A third-generation wave model for coastal regions, Part I, Model description and validation. In: J. Geoph. Research, Vol. 104, pp.7649-7666
- Brorsen, M. (2000): Reflection of short-crested waves from thin sponge layers in numerical models. In: Proceedings of the Fourth International Conference on Hydrodynamics.
- DHI (2009): Mike 21 BW: Boussinesq Waves Module, Danish Hydraulic Institute.
- Hassan, W.; Willems, M.; Verwaest, T.; Mostaert, F. (2011): Extreme wave characteristics inside the harbour of Oostende: physical modelling with different storm directions (T2).
- Madsen, P.A.; Murray R.; Sørensen, O.R. (1991): A new form of the Boussinesq equations with improved dispersion characteristics. In: Coastal Engineering, Vol. 15, pp. 371-388.
- Madsen, P.A.; Sørensen, O.R. (1992): A new form of the Boussinesq equations with improved dispersion characteristics. Part 2. A slowly-varying bathymetry. In: Coastal Engineering, Vol. 18, pp. 183-204.
- Radder, A.C. and Dingemans, M.W. (1985): Canonical equations for almost periodic, weakly nonlinear gravity waves. In: Wave Motion, Vol. 7, pp. 473-485.
- Troch, P. (1998): MILDwave – A numerical model for propagation and transformation of linear water waves. In: Internal Report, Department of Civil Engineering, Ghent University.
- TU Delft (2010): SWAN (Simulating WAVes Nearshore); a third generation wave model Copyright © 1993-2011 Delft University of Technology.
- van der Meer, J.W.; Langenberg, J.W.; Breteler, M.K.; Hurdle, D.P.; den Heijer, F. (2002): Wave boundary conditions and overtopping in complex areas. In: Coastal Engineering, 2002, pp. 2092-2104.
- Verwaest, T.; Van der Biest, K.; Vanpoucke, P.; Reyns, J.; Vanderkimpen, P.; De Vos, L.; De Rouck, J.; Mertens, T. (2008): Coastal flooding risk calculations for the Belgian coast. In: Proc. of 31st Int. Conf. on Coastal Engineering, Hamburg, Germany.

Numerical simulation for indicator of vulnerability to climate change on four French beaches

Philippe Larroude¹ and Olivier Brivois²

Abstract

First, we established a procedure for binding three codes to simulate realistic or idealized climates. This procedure is validated in terms of hydrodynamics and morpho-dynamic evolution. These models have been used as part of a cycle of meteorological simulations describing the evolution of monthly events or hydrodynamic factors. Then, the vulnerability can be studied: the vulnerability of the coast will be defined and studied on the basis of in situ observations and model results will come from a set of simulations based on different scenarios (current and 2030). In a context of climate change, we will present the methodology of the modelling approach to analyze the sensitivity of several beaches of the French coast to forcing conditions changes. We will evaluate, for all four French sites, the parameter of vulnerability against this set of scenarios. All these studies have been done within the ANR research project called VULSACO. One of the aims is to set-up vulnerability indicators of sandy beaches against the climate change predictions for 2030.

Keywords: morphodynamic, indicator of vulnerability, numerical modelling

1 Introduction

The nearshore region frequently exhibits complicated motions. This complexity is perhaps particularly prominent in the changes that can take place in the morphology of many beaches.

On this nearshore region the climate change induced vulnerability is defined by the Intergovernmental Panel on Climate Change (IPCC) as the combination of sensitivity to climatic variations, probability of adverse climate change, and adaptive capacity. As stated by the IPCC (Watson et al., 1997), the “*coastal systems should be considered vulnerable to changes in climate*”. In these areas, amongst the most serious impacts of sea-level rise are erosion and marine inundation.

Within this context, the present paper will give a methodology for the modelling approach to analyse the vulnerability of several beaches on the French coast and, more particularly, on four beaches complementary in terms of hydrodynamic forcing. The coast of metropolitan France is composed of 30% sandy coasts and is potentially vulnerable. All these studies are involved in the VULSACO project (Idier et al, 2009).

The purpose of the exercise will be to assess, through mid-term bathymetric evolution simulation, at all the relevant parameters. Then, vulnerability can be studied: the vulnerability of coast/beach will be defined and studied based on in-situ observations and model results will be taken into account as a modulator of the physical vulnerability.

The understanding of these processes needs, at this time the in situ data but also the development of models, mathematics and numerical codes. Hence, following the work of De Vriend (1987) and De Vriend & Stive (1987), we try to improve the classic quasi-steady procedure. This methodology for morphodynamic evolution is also used more recently in Smit et al. 2008. The objectives of this work will be therefore to model and to simulate processes of sedimentary transport on sandy beaches with varied weather conditions in the medium term time scale (from a few days to a few months). The coastal morphology evolution cannot be represented with average climatic conditions but needs to simulate such extreme events as storms and therefore, in a long term approach, the morphological evolution is the result of the combination of storm events and calm periods.

¹ LEGI, BP 53 38041 Grenoble France, larroude@hmg.inpg.fr

We will present two simple indicator methods to analyze the vulnerability of the four beaches based on the results of simulations for different scenarios. The first method is based on the method described in Idier et al. (2006, 2010). In the present study, we calculate the maximum grain size potentially mobilized but with a simpler approach, based on analysis in different point on several cross shore profile. The second method which will be presented is the analysis of the temporal evolution of cross-shore profiles for each site for the same scenarios presented above. This study shows the possibility and the limitation of these two simple methods to extract indicator of vulnerability from numerical 2DH simulation.

2 Description of the beach

In this national research programme we are looking at the climate change influence on four different beaches in France. These beaches are representative of linear sandy beaches of the coastal region. The third of the French coastline is composed of sandy beaches. They are also representative of forcing and of various important factors.

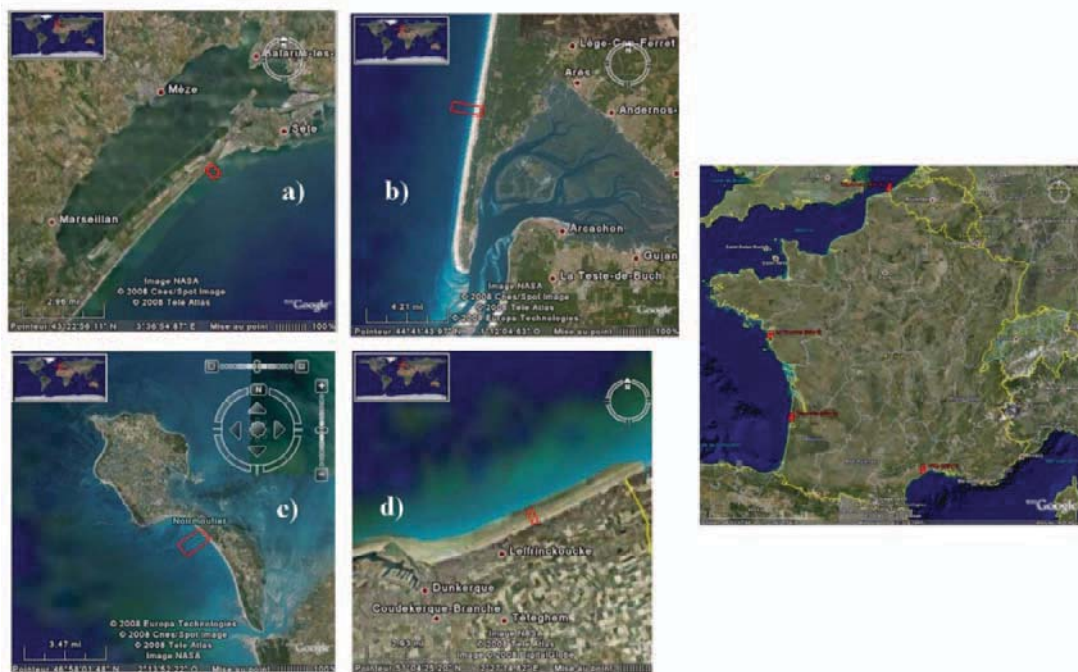


Figure 1: a) Lido de Sète, b) Truc Vert, c) Noirmoutier and d) Dunkirk (from Idier et al. 2007)

The four sites studied (see figure 1) were chosen to have complementarily hydrodynamic contexts (covering some of the possible hydrodynamic and wave conditions on the French metropolitan coast, Table I)

2.1 Sète

The site studied is located in the northern part of the Lido de Sète. The beach is a linear sandy beach with one or two offshore bars. The tourism of this area and the local fisheries are important factors to be taken into consideration. Several measurement surveys have already been carried out on this site (PNEC programme), as well as numerous development studies, Certain et Barusseau (2005).

2.2 Truc Vert

The site is characterized by its high exposure to waves from the Atlantic. There are rhythmic surf zone bars and their related morphodynamic self-organization. The system of bars/bâines in the intertidal zone has already been studied in Castelle, B. *et al.* (2006), Sénéchal et al (2009).


2.3 Noirmoutier

On the coast of the Noirmoutier (Vendée) peninsula, a succession of three barrier beaches demarcating zones liable to flooding in the west can be observed: two in the north supported on reef flats and one (the longest) able to move in the south, Fattal et al (2010).

2.4 Dunkirk

The site is located between Dunkirk and the Belgian border. Dunkirk is on the boundary of a sedimentary layer stretching up eastwards to the Belgian border. Data is available concerning the following fields of study: morphodynamic, hydrodynamic and aerodynamic conditions. The system is complex with the presence of banks in the open sea which attenuate the energy of waves and protect the coast, but which also reduce sedimentary provisions towards beaches (by diminishing the intensity of oscillatory currents onshore), Maspataud et al (2009) ; Ruz et al (2009).

Table I: Synthesis of the main hydrodynamic environments of the 4 sites studied

Site	Zone	Tide	Wave exposure	 Geographical positioning
1 - Sète	Mediterranean	Micro	High	
2 - Truc Vert	Atlantic coast (South)	Meso	High	
3 - Noirmoutier	Atlantic coast (North)	Macro	High	
4 - Dunkirk	Channel	Macro	Moderate	

3 Model and Methodology

Using the computer code 2DH Telemac, we set up a quasi-permanent binding calculations for the wave (wave modeling is done through the Artemis code that solves the equation of Berkhoff with process integration dissipation by wave breaking and bottom friction), for the calculation of the hydrodynamics and for the simulation of the sea bed evolution with a choice of sediment transport formulae (Camenen & Larroude, 2003 [2]) (Fig. 2). The calculation chain Telemac is a complete model using the finite element method and allows the realization of various sedimentary hydrodynamic calculations.

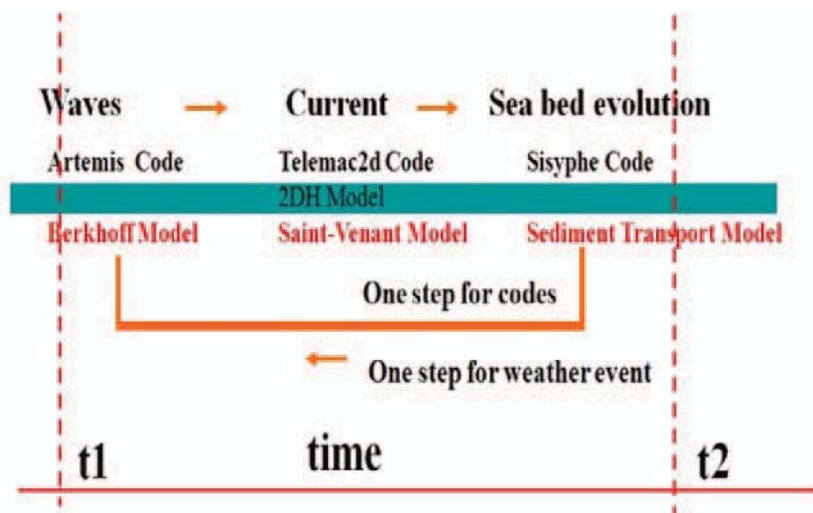


Figure 2: Technical drawing (Artemis-Telemac-Sisyph: ATS) loop on a time step weather event (between t1 and t2) used in our simulations. For the Noirmoutier and Dunkirk site we used (Tomawac-Telemac-Sisyph: TTS).

The equations of the three modules are detailed in Hervouet (2007) [6]. This modeling methodology morphodynamics of sandy beaches is already validated in terms of mesh, time step and convergence in Falquès et al. (2008) [5] and Larroudé (2008) [10].

All the comparisons with in-situ data are show for the Truc Vert in Idier et al. (2011) [9], for other sites see Maspataud et al. (2010) [11] and ANR-Vulsaco reports. The physical presentation of the sites is described in Vinchon et al, 2008 [14].

4 Results

We will present two ways of looking at possibly the vulnerability of beaches by analyzing the results of simulations of different scenarios.

The first method is based on the method described in Idier et al. (2006) [7]. We will initially look at the maximum grain size mobilized with a simpler approach. Indeed the calculation of the stress at the bottom will be estimated only from the velocity of the simulations after coupled waves-tides and/or waves only on each site. It also determines the critical Shields using the equation proposed by Soulsby and Whitehouse in Soulsby (1997, p105 [13]). In the Tables II to V, we show the results of the maximum size of grain mobilized by inverse method.

Table II: Results of the maximum diameter mobilized (m) with the inverse method of Sète site

Site 1 : Sète	Base scenario	Storm surge (Ss) +120%	Hs +10% Ss +120%	Incidence (-10°) Ss+120%
Point 1.1	0.00583	0.00584	0.00590	0.00580
Point 1.2	0.00580	0.00580	0.00580	0.00580
Point 1.3	0.00581	0.00581	0.00580	0.00580
	Case 1	Case 2	Case 3	Case 4

Table III: Results of the maximum diameter mobilized (m) with the inverse method of Truc Vert site

Site 2 : Truc Vert	Base scenario	Storm surge (Ss) +120%	Hs +10% Ss +120%	Incidence (-10°) Ss+120%
Point 2.1.1	0.04307	0.02389	0.024122	0.03466
Point 2.1.2	0.04776	0.05012	0.041834	0.04778
Point 2.1.3	0.00657	0.00708	0.006945	0.00742
Point 2.2.1	0.02329	0.02635	0.025837	0.05493
Point 2.2.2	0.00847	0.00874	0.008820	0.00785
Point 2.2.3	0.00713	0.00734	0.007563	0.00721

Table IV: Results of the maximum diameter mobilized (m) with the inverse method of Noirmoutier site

Site 3 : Noirmoutier	Base scenario	Storm surge (Ss) +120%	Hs +10% Ss +120%	Incidence (-10°) Ss+120%
Point 3.1	0.00585	0.00588	0.00588	0.00588
Point 3.2	0.00591	0.00597	0.00596	0.00596

Table V: Results of the maximum diameter mobilized (m) with the inverse method of Dunkirk site

Site 4 : Dunkirk	Base scenario	Storm surge (Ss) +120%	Hs +10% Ss +120%	Incidence (-10°) Ss+120%
Point 4.1	0.00893	0.00603	0.00605	0.006155
Point 4.2	0.00719	0.00682	0.00719	0.006610

In these tables the columns represent the four scenarios: the base scenario for each site is the scenario constructed from current data, for the second scenario the storm surge is increased by 120%, for the third scenario we change the height of significant waves with a 10% increase from the scenario case 2 off and the last one (case 4) we change the direction of the incident waves. We make calculations of maximum grain size mobilized within a few points along cross-shore profile at each site (see Figure 3).

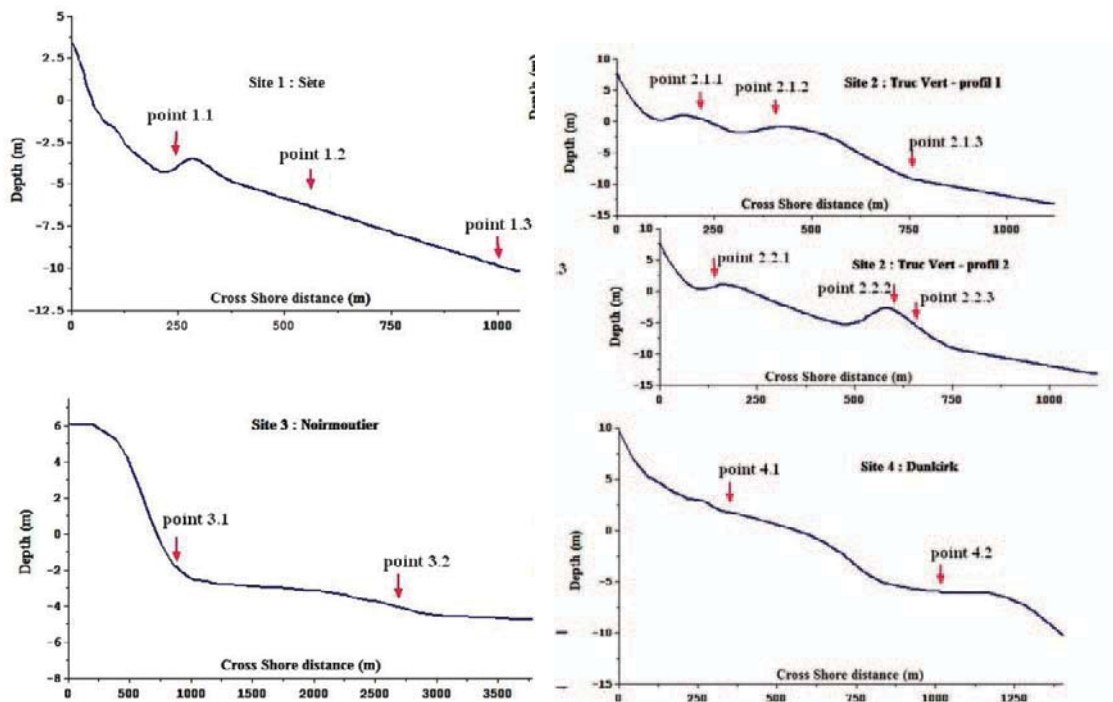


Figure 3: Cross-shore profiles of the four sites used for this study with the position of points used for calculations of maximum grain sizes.

This criterion is to be confirmed by the analysis of all the simulations, but it does not seem completely relevant to the vulnerability of the beach. What criteria of vulnerability of the beach can we extract from these results? If the maximum diameter mobilized decreases, it means that a greater amount of sand along the profile will be removed. In this case we can imagine that the risk of beach erosion increases, especially if the point used is closest to the beach. We find this configuration only in the case of Dunkirk (Table V). In some cases, this test works for some other site but not for all scenarios together (see Table III, point 2.1.1 and 2.2.2).

It can be completed by the second method in this paper: the analysis of the temporal evolution of cross-shore profiles for each site for the same scenarios presented above. This criterion is not convincing at sites where tidal currents are predominant (Noirmoutier and Dunkirk). For these sites where we are less convinced by the relevance of our results with our morphodynamic simulations TTS. Figure 4 shows that the study on these a bed evolution of cross-shore profile can be complementary to a vulnerability study by conventional indicators. Indeed we see the influence of the increase of the storm surge, the change in direction for the incident wave or the increase of the significant height of waves on the evolution of multiple profiles on the site of the Truc Vert. This influence could be important and we also analyze that

these sea bed evolution are very dependent of the choice we made on the sediment transport formula. These results have to be completed with further study.

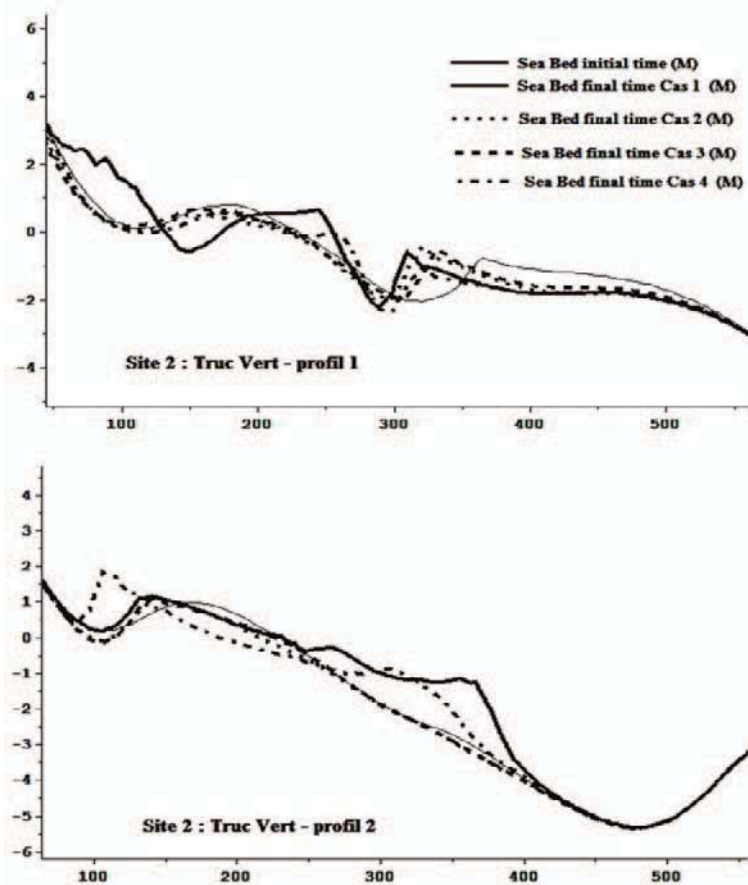


Figure 4: Profile cross shore of the Truc vert site for the four scenarios of the Table III.

5 Conclusions

This work allowed us to validate and improve our procedures for calculating the evolution of morpho-dynamic calculation chain Telemac. We show in this paper a simplified approach of first calculating the data as an indicator of vulnerability of sandy beaches. This approach shows the limits and must be complemented by a full analysis of simulations of different scenarios and a more classical approach of the evaluation indicators

6 Acknowledgements

This work has been supported by French Research National Agency (ANR) through the Vulnerability Milieu and Climate program (project VULSACO, n° ANR-06-VMC-009). We highly appreciate the constructive discussions with D. Idier, (BRGM, Orléans, France), Raphaël Certain and Nicolas Robin from the University of Perpignan. We also thank all the program partners Vulsaco for the data.

7 References

- Castelle, B., Bonneton, P., Butel, R., 2006. Modeling of crescentic pattern development of nearshore bars, Aquitanian Coast, France. *C.R. Geoscience*, 338(11), 795-801
- Castelle B, Bonneton P, Dupuis H, Sénéchal N. (2007) Double bar beach dynamics on the high-energy meso-macrotidal French Aquitanian Coast: A review. *Marine Geology* 245: 141–159.

- Camenen, B. and Larroudé, Ph., 2003, Comparison of sediment transport formulae for a coastal environment, *Journal of Coastal Engineering*, 48, pp. 111-132.
- Certain R. and Brusseau J.P. (2005) Conceptual modelling of sand bars morphodynamics for a microtidal beach (Sète, France), *Bull. Soc. géol. Fr.*, 176(4), pp. 343-354.
- De Vriend, H.J., 1987, 2DH Mathematical Modelling of Morphological Evolutions in Shallow Water, *Coastal Engineering*, 11, pages 1-27
- De Vriend, H.J. and Stive M.J.F., 1987, Quasi-3D Modelling of Nearshore Currents, *Coastal Engineering*, 11, pp. 565-601.
- Falques A., Dodd N., Garnier R., Ribas F., MacHardy L.C., Sancho F., Larroudé Ph. and Calvete D., 2008, Rhythmic surf zone bars and morphodynamic self-organization, *Coastal Engineering* 55, pp 622–641.
- Fattal P., Maanan M., Tillier I., Rollo N., Robin M., and Ottier P. (2010) Coastal vulnerability to oil spill pollution: the case of Noirmoutier island (France), *J. of coastal Res.*, 26(5), 879-887.
- Hervouet, J.M., *Hydrodynamics of Free Surface Flows: Modelling With the Finite Element Method*, 2007, John Wiley & Sons, 360p.
- Idier D., Pedreros R., Oliveros C., Sottolichio A., Chopin L. et Bertin X., (2006), Contributions respectives des courants et de la houle dans la mobilité sédimentaire d'une plateforme interne estuarienne. Exemple : le seuil interinsulaire, au large du Pertuis d'Antioche, France. *C.R. Geoscience*, Vol. 338, 718-726.
- Idier, D., Parisot J.P., Ruz M.H., Certain R., Bouchette F., Chateauminous E., Larroudé Ph., Robin M. and Poumadère M., *Vulnérabilité de systèmes côtiers sableux face aux changements climatiques et pressions anthropiques*, Congrès SHF-29Journées de l'hydraulique : «Variations climatiques et hydrologie», Lyon, 27-28 mars 2007
- Idier D., Falqués A., Mallet C., Castelle B., Parisot J.P., Le Cozannet G. and Delvallée E. (2009) Shoreline sandwaves along the Aquitanian Coast (France): influence of climate change, *Geophysical Research Abstracts*, Vol. 11, EGU General Assembly 2009.
- Idier D., Boulahya F., Brivois O., Castelle B., Larroudé P., Romieu E., Le Cozannet G., Delvallée E. and Thiébot J., 2011, Morphodynamic modeling : climate variability scenarios and sensitivity study. Application to the Truc Vert beach (France). *Coastal Sediments 2011*, Miami (USA), 2011.
- Larroudé Ph., 2008, Methodology of seasonal morphological modelisation for nourishment strategies on a Mediterranean beach, *Marine Pollution Bulletin* 57, pp 45-52.
- Maspataud, A., Ruz, M.H. and Héquette, A. (2009) Spatial variability in post-storm beach recovery along a macrotidal barred beach, southern North Sea. *Journal of Coastal Research*, SI 56: 88-92.
- Maspataud A., Idier D., Larroudé Ph., Sabatier F., Ruz M.H., Charles E., Levacheux S., Héquette A., L'apport de modèles numériques pour l'étude morphodynamique d'un système dune-plage macrotidal sous l'effet des tempêtes : plage de la dune Dewulf, Est de Dunkerque, France, (pp. 353-360), DOI:10.5150/jngcgc.2010.042-M
- Ruz, M-H., Héquette, A. and Maspataud, A. (2009) Identifying forcing conditions responsible for foredune erosion in the northern coast of France, *Journal of Coastal Research*, SI 56, p. 356-360.
- Sénéchal N; Gouriou T., Castelle B., Parisot J.P., Capo S., Bujan S. and Hova H. (2009) Morphodynamic response of a meso- to macro-tidal intermediate beach based on a long term data set, *Geomorphology*, 107(3-4), p. 263-274.
- Smit M.W.J., Reniers A.J.H.M., Ruessink B.G., Roelvink J.A., 2008, The morphological response of a nearshore double sandbar system to constant wave forcing, *Coastal Engineering* 55, pp. 761–770.

Soulsby R., Dynamics of marine sand, Thomas Telford. 245 pp.

Vinchon C., Idier D., Balouin Y., Capo S., Castelle B., Chateauminois E., Certain R., Crillon J., Fattal P., Hequette A., Maanan M., Mallet C., Maspataud A., Oliveros C., Parisot J.P., Robin M., Ruz M., Thiebot J. (2008) - Projet VULSACO. Vulnérabilité de plages sableuses face au changement climatique et aux pressions anthropiques. Module 1 : Caractérisation des sites. Rapport final, BRGM/RP-56618-FR, 114 p., 48 fig., 16 tabl., 7 ann.

Watson, R.; Zinyowera, M.; Moss, R.; Dokken, D. (1997) - The regional impacts of climate change: an assessment of vulnerability. Summary for policymakers. *Report of IPCC Working group II*. 16pp

Coastal long-term processes, tidal characteristics and climate change

Hartmut Hein¹, Stephan Mai¹ and Ulrich Barjenbruch¹

Abstract

Climate change will change coastal long-term processes. For the waterways in the southern North Sea we discuss these changes by the use of two different ways. At first we analyse the long-term changes of the sea level rise. Secondly, we go into the detail of a so called "model chain". The model chain is the synonym for the regionalisation from global climate models toward the coastline. To decompose the processes we use a multi-scale analysis by the means of a wavelet-transform. The recent water level is to understand as the superposition of several processes with different periods on (multi-)decadal scales. If we consider the superposition of the processes an acceleration of the sea level rise is not likely. The model chain reproduces several of the processes, which are observed. However, not all periods can be detected. So we conclude that the model chain must be used with care. The test of long-term coastal hydrodynamic model as the last step of the chain shows sufficient results. The artificial addition of the missing processes into the model chain must be discussed. It is an open question if the model chain can reproduce an increase of long-term variability sufficiently well.

Keywords: sea level rise, regional climate models, coastal hydrologic processes, multi-scale analysis

1 Background: Global Climate Change and regional impact

It is widely accepted, that climate-related sea level rise (SLR) influences the long-term coastal processes. In this context the term "climate mean" is defined as the characteristic frequency distribution of local conditions and processes for a sufficient period of time. This period reflects the probability density of states and processes of the typical conditions in the region. The Mean Sea Level (MSL) as climatologically value of the sea level is defined as "the average height of the surface of the sea at a tide station for all stages of the tide over a 19-year period" (IHO, 1994). For the presentation of the SLR (SLR) often the secular rise (100 years) is a common used period. An almost linear secular rise of about 1-2 mm per year (Wahl et al., 2010, Wahl et al., 2011, Hein et al. 2011) has already been observed in the southern German Bight (Figure 1). A future acceleration of global SLR is expected (IPCC, 2007). However, besides linear secular trends, nothing seems proven with the SLR, yet processes seem not to be understood. For several regions of the world the trend of the sea level shows no significant acceleration, even deceleration has been calculated (Houston and Dean, 2011). Other studies found evidence for acceleration on century time scales (Woodworth et al., 2009). So it is essential to provide detailed studies for each region to improve knowledge about future SLR and its impact. Sensitivity studies (e.g. Mai et al., 2004a, b) show a variation of tidal water levels, of significant wave heights and also the morphology at the North Sea coast as the result of climate change. One predominant process, influencing most other parameters is the change of tidal characteristics. Coastal long-term processes (CLP) superpose the climate signal (Woodworth et al., 2009). Their study shows acceleration on decadal periods and suggest connections to long-term changes of the atmosphere and ocean circulation changes.

It remains to be proven how these CLP influence the regional tidal characteristics. Our study investigates into these long-term processes by two approaches: The first method, to draw conclusions for the future changes of the tidal characteristics, is to examine historic gauging data, in order to derive the recent rise of sea level. However, an extrapolation of SLR is difficult, because of its non-linearity. The second method is the use of a so called "Model Chain" (MC), to transfer the results of global climate models into results for coastal areas. It is yet to

¹ Federal Institute of Hydrology, Am Mainzer Tor 1, 56068 Koblenz, hein@bafg.de

shown whether these MCs, which still base on very rough global climate models, are applicable for regionalization at all.

2 Methods and Data

To estimate the historic SLR, 8 tide gauges provided by the Waterways and Shipping Administration of the Federal Government of Germany (Emden Neue Seeschleuse, Norderney, Helgoland, Cuxhaven, Lt. Alte Weser, Wilhelmshaven, Bremerhaven and Husum), which are located in the southern German Bight (figure 1), are combined to one theoretical mean gauge. They are representative for the coastal region both due to their spatial extent and due to their distance to the coast-line. The data set is of a never before reached accuracy, because several new technical approaches for quality management and averaging are used to estimate the mean climatologically curve of SLR in this region. The data set is quality controlled and corrected for local datum shifts (Sudau and Weiß, 2010; Hein et al., 2010a). We use a fuzzy logic approach to extend the shorter time series of some gauges towards secular and even towards longer periods. The k-value approach by Lassen und Seifert (1991) and a low pass filtering with the Singular Spectrum Analysis is used to calculate the MSL. Moreover, land-subsidence is included by recognizing both, geodetic (Wanninger, 2009) and hydrologic data sets. One major uncertainty of the geodetic dataset is defined by the general bearing of the network, rather than by the point to point observation uncertainty of the geodetic methods. With this assumption it is possible to combine the sinking rates from long-term trends of the different tide gauge observations and the geodetic observations with a least squares fit. A more detailed description of the method is to be found in the study of Hein et al. (2011).

The modal chain used in the research program KLIWAS (Mai et al. 2009) of the German Federal Ministry of Transport, Building and Urban Development, by the Federal Institute of Hydrology together with several partners is given in Figure 2. The MC downscales the scenario towards long-term simulations of the German North Sea estuaries. The MC starts with different emission scenarios. These are used to run various global climate models, to derive atmospheric and oceanographic parameter on a global scale. Secondly, it is necessary to transform the results of global climate models with regional downscaling into results for the region. This is usually done with the uncoupled models of ocean and atmosphere. In KLIWAS we also test coupled models on the regional scale. The last step is to scale the regional climate models down towards the certain stretch of the coastline. So we applied numerical hydrological models for the estuaries. Because the whole MC is used to simulate climate-relevant periods, we used simple and fast models, which are still in the position to reproduce baroclinic frontal processes (Hein, 2007). Within the MC the lack of tidal information in most of the climate models is one challenge for the simulation of coastal the processes. We use additional global models of tides. It must be ensured for the sea-state, that the influence is considered, which is caused by the changing characteristics of future tides (Hein, 2010b). The MC is tested by hind-casting the recent climate and by comparing this results with the tide gauge measurements. Then the future long-term processes are compared with the recent conditions.

Two pathways of the model chain are tested. The first is the hind-cast which is based on the HAMSOM North Sea model published by Pohlmann (2006). The hind-cast covers the period of 1948 to 2007. The validation of the model by means of observed sea surface temperature data and of temperature data from a hydrographic transect demonstrates that the model is able to reproduce the observations of temperature reasonably well, nearer inspections of the sea level was not done. The second pathway based on the same HAMSOM North Sea model, but instead of the atmospheric hind-cast this model is driven by a regional climate model (REMO). The regional climate model was forced by ECHAM5 / MPIOM (figure 2).

To find the long-term processes which are present in both, observed and modeled data, we decompose the time series into the frequency space by the means of a wavelet transform (WT). The WT allows us to determine dominant modes of the fluctuation in the series as well as such modes which varies in time. For assistance of the reader we briefly introduce into the concept of wavelet transformation and refer to Torrence and Compo (1998) for those, who delve into the thematic.

The WT starts simply with ζ_t , which is a equidistant time varying water level and the following equation:

$$\psi_0(\eta) = \pi^{-0.25} e^{i\theta\eta} e^{-\eta^2/2} \quad (1)$$

This is the so called “Morlet-wavelet”, which depends on dimensionless time η and non-dimensional frequency θ . We use the typical Morlet-wavelet with $\theta = 6$, which results in about three oscillations inside the wavelet envelope and frequency = 1.03s, so the that Wavelet scale is approximately equal to the Fourier period. The wavelet transform itself is defined with the following equation:

$$W(\tau, s) = \sum_{n=0}^{N-1} \zeta_t \left[\psi_0 \left(\frac{(t - \tau)}{s} \right) \right]_{\tau, s}^* \quad (2)$$

N the length of the time-series, s is the position in the frequency space and τ the position in time. The star (*) indicates that the complex conjugate is used. This allows us to decompose the one-dimensional time-series of water levels into a two-dimensional time-series with respect to the time varying water level on different time scales.

3 Recent coastal long-term processes of the sea level rise

We start our investigations with the observed long-term variability of the SLR. Figure 3 shows the long-term fluctuation of the SLR, after the filtering process. The figure shows that the values shift periodically with time between approximately 0 cm a⁻¹ and 0.3 cm a⁻¹. In the last years the rise is strongest but not in an uncommon range. In the period between 1960 and 1980 the sea level decreased. The orange line shows the approximation with a sum of sine functions, which seems to reproduce the variations in the SLR. In general an acceleration is not to be found.

Figure 4 presents the wavelet spectra of the sea level. This allows us to detect long-term processes. First, greatest variability is to find on that scales, which are representative for typical atmospheric timescales of months to several years. We can conclude that sea level periods shorter than one year seem to be dominated by white noise processes, which may related to quasi random storm events. The SLR is positively correlated with the changes of the NAO on time-scales of 4 to 7 years ($\approx 40 - 80$ months). Variability on periods in the range of the Nodaltide (223 month) is indicated since 1930 and before 1900. Moreover periods of 30 to 40 years (≈ 400 months), are important and their amplitude increases with time. Theoretically, this is possible with the change of processes of self-oscillation of the basin; both North Sea or North Atlantic could have changed their characteristics. Self oscillation is related to the depth (sea level) of the basin, so the changes of the long-term processes related to the self-oscillation is likely. Additionally, periods of approximately 70 to 80 years (≈ 900 months) are present (however, not shown in figure 4). In general the scales of variability agree with actual studies of the North Atlantic, e.g. Medhaug and Furevik (2011) discuss this multi-decadal variability. Woodworth et al.(2010) presented, that on the regional scale we always must consider changes in the current system, because they can significantly influence the long-term trend.

4 Analysis of the model chain

The results of the WT of both, MC and observations are compared. However, instead of considering the known uncertainty of the MC we rather turn the question around and ask whether we found even useful, actionable information in the MC. The analysis of the MC shows that there is only small influence originating form the emissions scenarios on SLR. So we start with the output from the regional models, which provide important boundary information for coastal models. Figure 5 shows a) WT from historic observations in the period 1948 – 2007, which is the period of the North Sea model hind-cast (b). Generally, the hind-cast can reproduce the mayor variability of the observations. However, in detail there are some differences. The increase of variability, which is indicated on a scale of 100 month is not simulated by the model. The important scale of 400 month is also not well reproduced by the model. It is to discuss, if periods of hind-casts are to short to indicate climate change signals. However, the period of

approx 60 years is typical for hind-casts, which means that this seems a general problem of climate hind-casts.

Figure 5 c shows results from the regionalization of the climate model for the period of the hind-cast. Surprisingly, the variability itself is better represented by the climate model. But, the periods are shifted with time. For example, this means that we observed an increase of SLR in the last 10 years but the climate model reproduced a decrease. However, if we use the multi-scale analysis we can address this fact and may consider the shift in our analysis. Against the hind-cast results the increase of variability (100 month) is indicated, but not so strong as in the observations. Further analysis of the MC shows that global climate models provide realistic simulations only for a number of key aspects of natural internal variability, which we observed by measurements. We agree with several other studies (e.g. Chase et al. 2011, Hawkins and Sutton, 2009, Keenlyside, 2008) which analyze climate models for several different parameter: Climate-models are not useful for day-to-day or year-to-year predictions. For many, but not for all regions, the reproduction of the regional long-term climate is well done by the climate models. For many aspects this is true for the SLR in the southern German Bight. The modes of variability (eg. North Atlantic Oscillation) and the displacements of these modes, which have been shown by observations, are poorly represented in most climate models.

Figure 5c show what happens in the future – by the means of the model. In general, the variability remains in the same range. In the scale-range of 100 to 200 month the variability is increased in comparison to recent years. If we consider that the increase of variability during the reference period is below that of the observations we suggest an underestimation of these increase of variability. The wavelet analysis shows that the modes are represented in the regional climate models but they are shifted in time. However, this natural internal variability is the major factor of uncertainty in the observed SLR in the southern North Sea (Hein, 2010a). On the regional scale (North Sea), some tests of coupled regional models done by Schrum (2001) indicate that the results of global models as driver of regional models are inadequate to reproduce the regional sea level in a deterministic way – independent if the models are coupled or not. Future work of simulations of longer-terms with coupled models must be done.

Figure 6 shows first results from the last step of the model chain. The applicability of long-term simulation of coastal and estuarine regions is tested by the implementation of a coarse resolution HAMSOM model, which is optimized for coastal purposes. A short validation is done by Hein (2010b). The figure shows the year-to-year variability of four winter periods and indicate that the strength of the year-to-year variability lies in the range of the climate signal. It remains to optimize boundary conditions which originate from the MC. We must discuss bias-corrections as well as the additionally inclusion of processes, which are not adequately solved by climate models. However, the long-term coastal models provide a new insight into the impact of climate change as well as the impact of the long-term processes on the tidal characteristics.

5 Conclusion

We analyze long-term processes and their statistics from both observations and simulations. The rate of the SLR varies even on the long-term systematically with an amplitude, stronger than the signal of climate change. Against the calculations for the rate of global SLR (Church and White, 2006, Woodworth et al, 2009) a significant acceleration is not detectable, but a superposition of several processes. The results of our MC are therefore analyzed by the means of a multi-scale analysis. Our study shows that, due to the large uncertainties in the MC, it is necessary to extract exactly, what "information" still exist at the end of the MC. Additionally, it should be noted, that the description of several physical long-term processes in the MC suffers. Future investigation should test to add missing processes synthetically into the results of the climate models. Despite all uncertainties of climate models the increase of the strength of the long-term processes is indicated. This is not a really nice information, because the change of physical long-term processes causes non-stationary of the statistics. By the use of hydrodynamic models we show that the year-to-year variability is as strong as the climate signal. Future studies must investigate also in long-term simulations of the estuaries to analyze the impacts of the deduced increase of variability on the tidal characteristics.

6 Figures

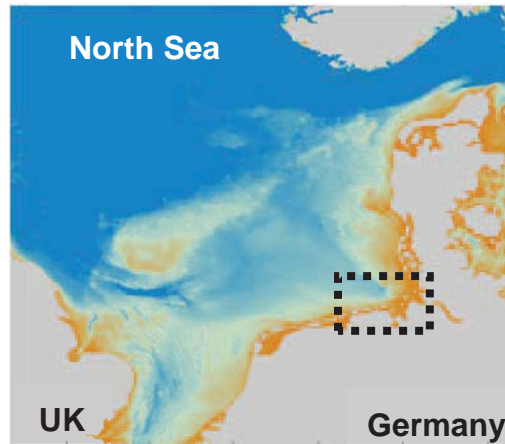


Figure 1: Map of the North Sea. The investigation area is located in the dashed box.

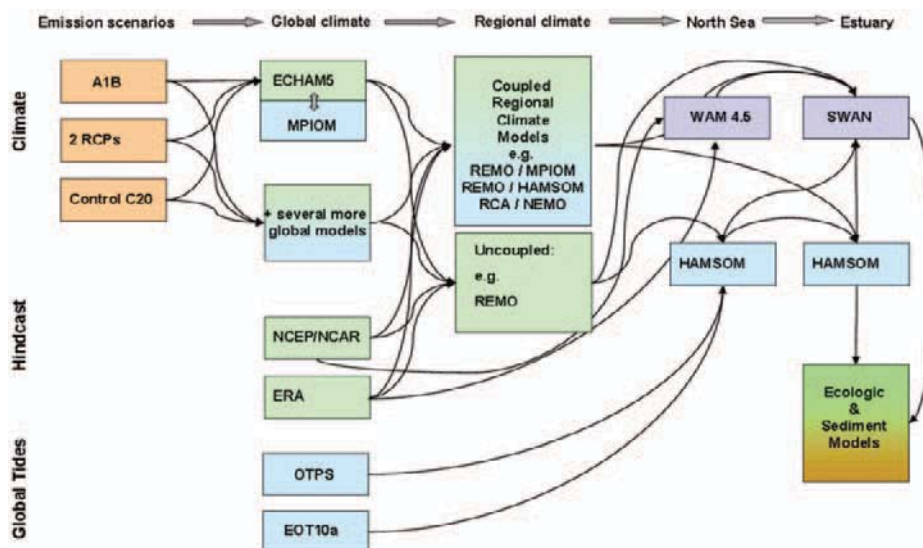


Figure 2: Model-chain from emission scenarios towards the coastal processes.

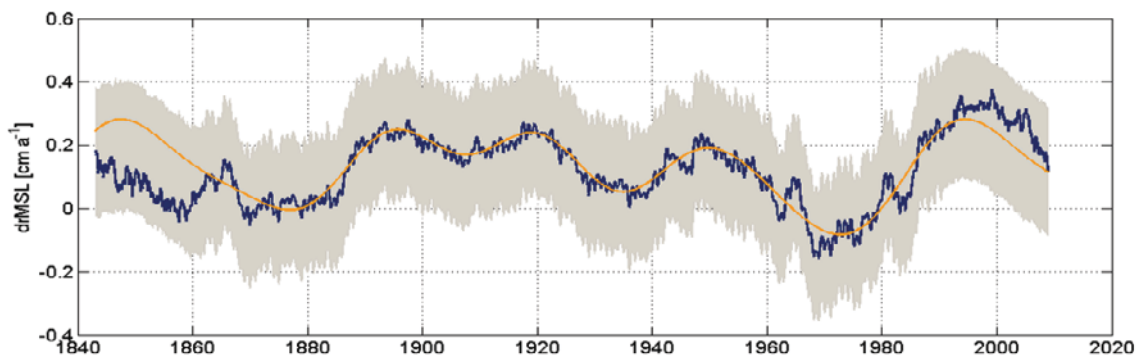


Figure 3: Rate of sea level rise in the southern German Bight.

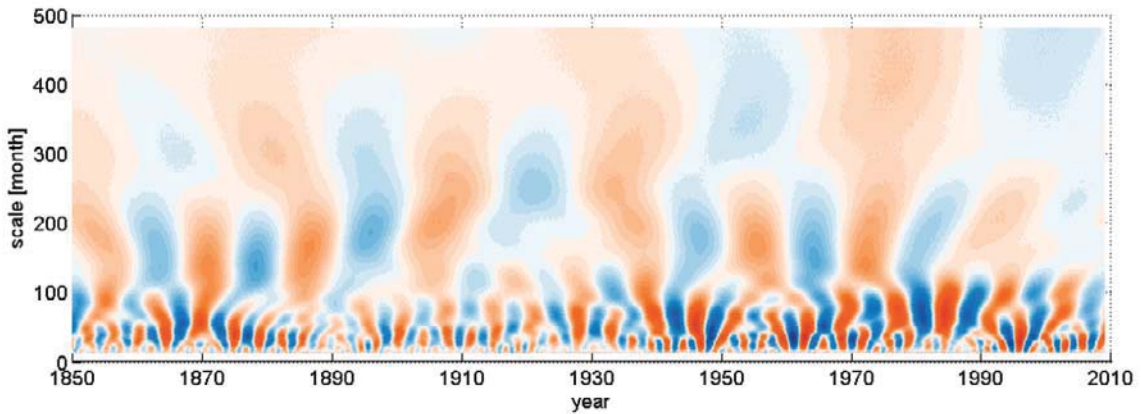


Figure 4: Wavelet transform of the rate of sea level variability. Blue areas indicate rise, red areas, fall of the sea level.

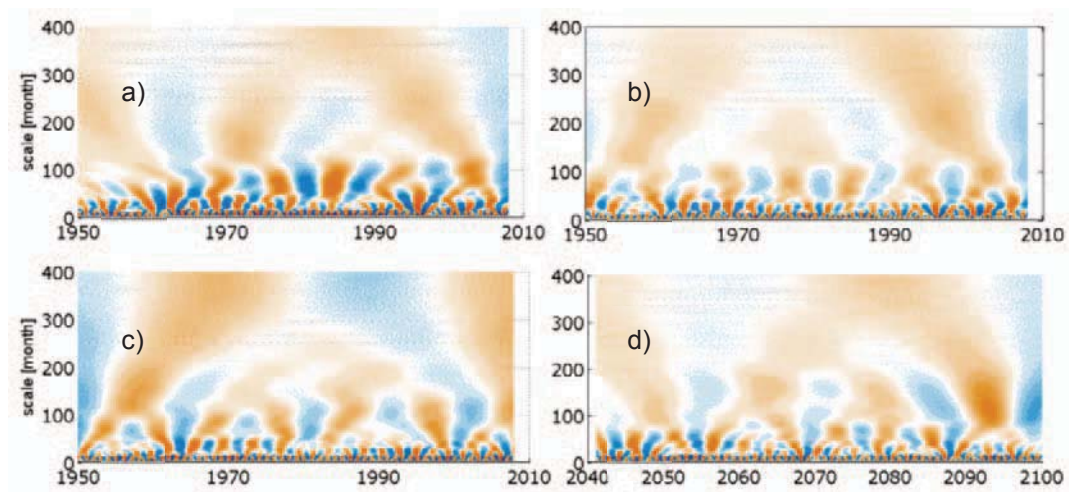


Figure 5: Wavelet transform of the rate of sea level variability. a) Observations, b) Hind-cast, c) climate model reference cast, d) climate model future.

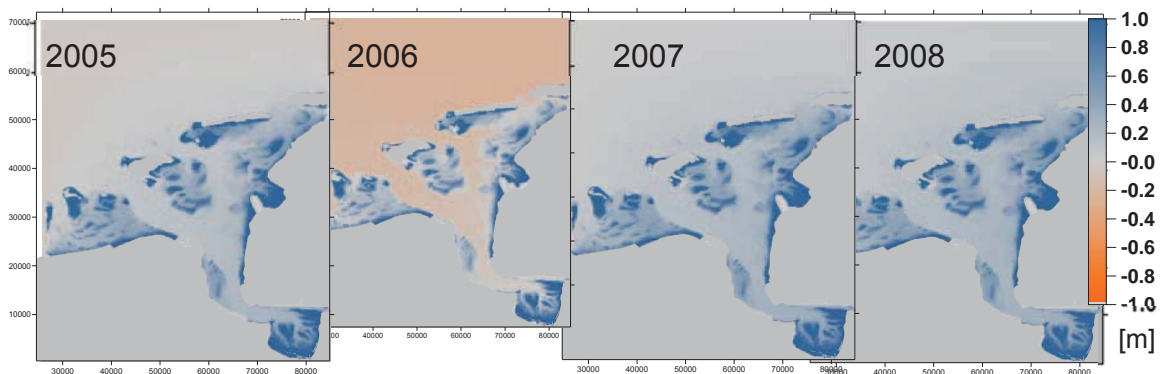


Figure 6: Example of the last step of the MC. Test-run of the coastal numerical model. The result of the mean winter sea level of four years are shown.

7 Acknowledgements

KLIWAS is funded by Federal Ministry of Transport, Building and Urban Development. Robert Weiss was responsible for the zero-point corrections of the gauges. Moritz Mathis simulated the climate run – thank you very much, that you provide your unpublished data for our analysis.

8 References

- Chase, T N.; Pielke, Roger Sr; and Castro, C. (2011): Are Present Day Climate Simulations Accurate Enough for Reliable Regional Downscaling?, *Journal of Contemporary Water Research and Education*: Vol. 124: Iss. 1, Article 5.
- Church, J. A., and N. J. White (2006): A 20th century acceleration in global sea-level rise, *Geophys. Res. Lett.*, 33, L01602, doi:10.1029/2005GL024826.
- Hawkins, E., and R. Sutton (2009): The potential to narrow uncertainty in regional climate predictions. *Bull. Amer. Meteor. Soc.*, 90, 1095–1107.
- Hein, H., Karfeld, B., Pohlmann, T. (2007): Mekong water dispersion: Measurements and consequences for the hydrodynamic modelling, *Journal of Water Resources and Environmental Engineering*, Special Issue, August 2007, 21 – 28.
- Hein, H., Weiss, R., Barjenbruch, U., Mai, S., (2010a): Uncertainties of Tide gauges and the estimation of SLR, *Proceedings of the Hydro2010*, Warnemünde.
- Hein, H., Mai, S., Barjenbruch, U., (2010b): Simulation of interactions between wind-waves and currents in estuaries with a focus on climate change. *Proc. of the 9th Int. Conf. on Hydro Science and Engineering ICHE*, Madras, Indien, 2010,
- Hein, H., Mai, S., Barjenbruch, U. (2011): What tide gauges reveal about the future sea level, *Aqua Alta*, Hamburg, Conference Proceedings.
- Houston, J.R. and Dean, R.G., (2011): Sea-level acceleration based on U.S. tide gauges and extensions of previous global-gauge analyses. *Journal of Coastal Research*, 27(3), 409–417. West Palm Beach (Florida), ISSN 0749-0208.
- IHO (1994): *International Hydrographic Organization Dictionary*, S-32, 5th Edition, 3156.
- IPCC (2007): *Climate change 2007: The physical sciences basis*, Working group I report, IPCC, Geneva.
- Keenlyside, N., M. Latif, J. Junclaus, L. Kornblueh, and E. Roeckner (2008): Advancing decadal climate scale prediction in the North Atlantic. *Nature*, 453, 84–88.
- Lassen, H. und Seifert (1991): Örtliche und zeitliche Variationen des Meeresspiegels in der südöstlichen Nordsee, *Die Küste*, 52, 85–136.
- Mai, S. (2004a): *Klimafolgenanalyse und Risiko einer Küstenzone am Beispiel der Jade-Weser-Region*. Von dem Fachbereich Bauingenieur- und Vermessungswesen der Universität Hannover genehmigte Dissertation, 391 S., Hannover, 2004 (auch in: *Mitteilungen des Franzius-Instituts*, H. 91, S. 1 - 275, Hannover, 2004).
- Mai, S., Stoschek, O., Geils, J., Matheja, A., (2004b): Numerical Simulations in Coastal Hydraulics & Sediment Transport. *Proc. of the NATO Advanced Research Workshop (ARW)*, S. 149 - 169, Varna, Bulgaria, 2004.
- Mai, S., Heinrich, H., Heyer, H., (2009): Das hydrologische System der Wasserstraßen im Küsten- und Ästuarbereich - KLIWAS-Vorhaben 2.Tagungsband des 1. KLIWAS-Statusseminars 17.03.2009, S. 36 - 41, Bonn.
- Medhaug I, and Furevik T (2011): North Atlantic 20th century multidecadal variability in coupled climate models: sea surface temperature and ocean overturning circulation. *Ocean Sci* 7:389–404. doi:10.5194/os-7-398-2011.
- Schrum. C. (2001): Regionalization of climate change for the North Sea and Baltic Sea. *Climate Research*, 18, 31-37.
- Sudau, A., Weiß, R (2010): Der Einfluss vertikaler Landbewegungen auf langwellige Wasserstandsänderungen, 40. IWASA, Internationales Wasserbau-Symposium Aachen, 08. Januar 2010.
- Pohlmann, T., (2006): A meso-scale model of the central and southern North Sea: consequences of an improved resolution. *Continental Shelf Research* 26, 2367 – 2385.

- Torrence C, Compo GP (1998): A practical guide to wavelet analysis. *Bull Am Meteorol Soc* 79:61–78.
- Wahl, T.; Jensen, J.; Frank, T., (2010): “On analysing sea level rise in the German Bight since 1844”, *Natural Hazards and Earth System Science*, Volume 10, Issue 2, pp.171-179.
- Wahl, T., Jensen, J., Frank, T., Haigh, I.D. (2011): Improved estimates of mean sea level changes in the German Bight over the last 166 years, *Ocean Dynamics*, online first: <http://dx.doi.org/10.1007/s10236-011-0383-x>.
- Wanninger , L., Rost, Ch., Sudau, A., Weiss, R., Niemeier, W., Tengen, D., Heinert, M., Jahn, C.-H., Horst, S., Schenk, A.(2009): Bestimmung von Höhenänderungen im Küstenbereich durch Kombination geodätischer Messtechniken. *Die Küste*, Heft 76/2009, S. 121–180.
- Woodworth PL, White NJ, Jevrejeva S, Holgate SJ, Church JA, Gehrels WR (2009a) Evidence for the accelerations of sea level on multi-decade and century timescales. *Int J Climatol* 29:777–789. doi: 10.1002/joc.1771.
- Woodworth PL, Pouvreau N, Woßpelmann G (2010) The gyre-scale circulation of the North Atlantic and sea level at Brest. *Ocean Sci* 6:185–190

Parameterization of storm surges as a basis for assessment of risks of failure for coastal protection measures

Dörte Salecker¹, Angelika Gruhn¹, Christian Schlamkow¹ and Peter Fröhle¹

Abstract

To assess risks of flooding in coastal areas, dimensions of flooded areas as well as the water depths are needed. Input information for these analyses are amongst others, storm surge hydrographs and corresponding probabilities. In order to create these hydrographs, recorded time series of water levels were investigated at four locations along the German Baltic Sea coast (Wismar, Rostock (Warnemünde), Stralsund and Greifswald). Annual peak water levels and maximum fullness of storm surge hydrographs were statistically classified, using univariate as well as bivariate models. Different techniques have been applied to derive dimensionless storm surge hydrograph shapes from the time series of water levels. By scaling these dimensionless hydrograph shapes, using random pairs of water levels and fullness with a given probability, an arbitrary number of storm surge hydrographs with that probability can be gained.

Keywords: Univariate statistics, Bivariate statistics, Copulas, Storm surge Hydrographs

1 Objective

Coastal structures protect large areas of the German North Sea and Baltic Sea Region. The failure of those structures would lead to the inundation of approximately 12.000 km² of low lying land and would therefore cause major damage along the coast line.

All member states of the European Union have to provide "Flood hazard maps", "Flood risk maps" as well as "Flood risk management plans" for all areas endangered by floods, in order to fulfil the requirements of the "Directive of the European parliament and the council on the assessment and management of flood risk" (2007/60/EC).

Against this background the HoRisK project is conducted. Within the project, methods for an application-orientated flood damage- and flood risk analyses are being developed. Those methods provide a basis for the creation of "Flood hazard maps", "Flood risk maps" and "Flood risk management plans" for local authorities.

Hydrodynamic forces that affect coastal structures and might cause their failure, may result from high water levels, local sea state, currents and at least temporarily from ice drift, also their combined occurrence has to be considered. Since currents and ice drift are of minor importance in the German Baltic Sea as well as the North Sea, in the course of the HoRisK project, the emphasis is put on analysing water levels as well as the sea state. In this paper the focus is on analyzing water level time series.

Past experiences have shown that the failure of coastal structures might occur even though water levels are moderately high, if the duration of the storm surge is long. Hence, it is obviously necessary to include durations of extreme events in the statistical analyses, especially when storm surge hydrographs are generated.

In order to detect sizes of potentially flooded areas as well as the water depth, numerical models are being used. Next to various input data, these models require storm surge hydrographs mentioned above with defined probabilities of occurrence.

¹ University of Rostock, Institute of Environmental Engineering, Coastal Engineering Group, Justus-von-Liebig-Weg 6, D18059 Rostock, Email: doerte.salecker@..., angelika.gruhn@..., christian.schlamkow@..., peter.froehle@uni-rostock.de

2 Methodology

2.1 Input Data and sampling

Water level time series at four locations along the Mecklenburg-Vorpommern Baltic Sea coast (Wismar, Rostock (Warnemünde), Stralsund and Greifswald) were statistically analyzed. Investigated were hourly measurements (dataset 1) as well as peak water levels of the highest storm surges recorded (dataset 2).

Lengths of available time series vary depending on the location. The longest complete time series of hourly measurements (dataset 1) is available for the location Rostock (Warnemünde) with 57 years of data, the shortest time series includes 45 years of measurements at the tide gauge Stralsund. Deriving from the time series of hourly measured water levels, the fullness of storm surge hydrographs was determined (see 2.4).

Information on annual peak water levels (dataset 2) is available for longer periods. Including minor gaps, data is available from 1848 for the location Wismar, from 1855 for the location Rostock (Warnemünde) and from 1873 for the locations Stralsund and Greifswald.

The latter dataset can already be treated as a sample of annual maximum water levels. Samples taken from dataset 1 as well as samples of measures that were derived from that time series were taken choosing annual maximum values, respectively.

2.2 Univariate Statistics

In the univariate case, extreme value distribution functions (Weibull distribution, Log-Normal distribution, Generalised Extreme Value distribution (GEV) and Gumbel distribution) were fitted to all samples examined. The parameters of each function were estimated using the maximum likelihood method.

Table 1: Cumulative distribution functions (cdf) $F(x)$ and logarithmized likelihood functions $\log L$ of some distributions (Johnsson et al. 1994, EAK 2002, Coles 2001)

$F(x)$	$\log L$
Weibull	
$1 - e^{-\left(\frac{x_i}{\beta}\right)^\alpha}$	$\beta^{-\alpha} \left(\beta^\alpha \left(n(\log \alpha - \alpha \log \beta) + (-1 + \alpha) \sum_{i=1}^n \log x_i \right) - \sum_{i=1}^n x_i^\alpha \right)$
Log-Normal	
$\frac{1}{2} \operatorname{Erfc} \left[\frac{\mu - \log x_i}{\sqrt{2}\sigma} \right]$	$-\frac{n(\mu^2 + \sigma^2 \log(2\pi)) + 2\sigma^2 \log \sigma + 2(-\mu + \sigma^2) \sum_{i=1}^n \log x_i + \sum_{i=1}^n \log x_i^2}{2\sigma^2}$
GEV	
$e^{-\left(1 + \frac{\xi(-\mu + x_i)}{\sigma}\right)^{-\frac{1}{\xi}}}$	$-\frac{(1 + \xi) \sum_{i=1}^n \log \left(1 + \frac{\xi(-\mu + x_i)}{\sigma} \right) + \xi \left(n \log \sigma + \sum_{i=1}^n \left(1 + \frac{\xi(-\mu + x_i)}{\sigma} \right)^{-\frac{1}{\xi}} \right)}{\xi}$
Gumbel	
$e^{-e^{-\frac{\alpha + x_i}{\beta}}}$	$\frac{-n(\alpha + \beta \log \beta) - \beta \sum_{i=1}^n e^{-\frac{\alpha + x_i}{\beta}} + \sum_{i=1}^n x_i}{\beta}$

The cumulative distribution functions ($F(x)$) as well as the logarithmized likelihood functions ($\log L$) of the four investigated univariate models are shown in table 1. Functions to estimate the parameters of each model can be generated by the derivative of the logarithmized likelihood functions with respect to the respective parameter, setting the equation equal to zero and solving the latter equation for the parameter.

Functions that were fitted to the samples were displayed in combination with the observed data, using the Hazen plotting position, in order to determine the model that describes the data best.

2.3 Bivariate Statistics

The correlation of two measured variables was described using the rank correlation coefficient Kendall's τ .

$$\tau = \frac{P_n - Q_n}{\binom{n}{2}} \quad (1)$$

P_n and Q_n are the numbers of concordant and discordant pairs, n is the number of observations.

The dependence of two measures was modeled using copula functions (Clayton, Gumbel, Frank and Joe). The dependence parameter Θ of each copula was estimated using the particular generator function $\varphi(t)$ shown in table 2.

When replacing $\varphi(t)$ by the generator function and it's first derivative, respectively the correlation coefficient τ can be expressed as a function of Θ (equation 2).

$$\tau = 1 + 4 \int_0^1 \frac{\varphi(t)}{\varphi'(t)} dt \quad (2)$$

By solving equation 2 the dependence parameter Θ can be estimated.

Table 2: Cumulative distribution functions (cdf) $C(u,v)$ and generator functions $\varphi(t)$ of some Copulas (Nelson 2006)

Copula	$C(u,v)$	$\varphi(t)$
Clayton	$(u^{-\theta} + v^{-\theta} - 1)^{-\frac{1}{\theta}}$	$\frac{t^{-\theta} - 1}{\theta}$
Gumbel	$e^{\left[-\left((-\log u)^{\theta} + (-\log v)^{\theta}\right)^{\frac{1}{\theta}}\right]}$	$ \log t ^{\theta}$
Frank	$-\frac{1}{\theta} \log \left[1 + \frac{(e^{-\theta u} - 1)(e^{-\theta v} - 1)}{e^{-\theta} - 1} \right]$	$-\log \frac{e^{-\theta t} - 1}{e^{-\theta} - 1}$
Joe	$1 - \left[(1-u)^{\theta} + (1-v)^{\theta} - (1-u)^{\theta}(1-v)^{\theta} \right]^{\frac{1}{\theta}}$	$-\log[-1(1-t)^{\theta}]$

An arbitrary number of uniform distributed pairs (u, u^*) on the interval $(0,1)$ can be simulated.

If an explicit formula exists the inverse function of the derivative of the copula with respect to u , can be used to model dependant data pairs (u,v) (equ. 4). (Genest & Favre, 2007)

$$Q_u(v) = \frac{\partial}{\partial u} C(u, v) \quad (3)$$

$$v = Q_u^{-1}(u^*) \quad (4)$$

The goodness of fit was evaluated visually by comparing the simulated data pairs (u,v) and the transformed ranks of the observations $(R_i/(n+1), S_j/(n+1))$. Probabilities of a conjoint occurrence of u and v were estimated using the copulas cumulative distribution functions $C(u,v)$.

The simulated data pairs (u,v) are being transformed into original units of measurement using the inverse of the best fitted functions in the univariate case.

$$(x, y) = (F_1^{-1}(u), F_2^{-1}(v)) \quad (5)$$

After transforming the data the goodness of fit was checked once again visually.

2.4 Storm surge hydrographs

For each location, shapes of storm surge hydrographs were derived from the time series of measured hourly water levels (dataset 1).

In a first step all water level progressions above 60 cm NHN were selected. From all these hydrographs and for each location the hydrograph containing the highest water level (shape: "max. water level") and the hydrograph with the highest fullness (shape: "max. fullness") were selected.

The measure fullness is the area between the threshold value of 60 cm NHN and the storm surge water level. The unit of the fullness is cmh. As the fullness is related to periods that are usually longer than one hour it was assigned to the date and time the highest water level occurred during the particular storm surge.

The detected hydrograph shapes were converted into dimensionless hydrographs so that the water level as well as the time ranges from 0 to 1.

In a next step heights and durations of hydrograph shapes were scaled using combinations of water levels and fullness. The combined probability of occurrence of both scaling parameters was calculated using copula models. (see 2.3)

3 Results

3.1 Water level

Because of the extent of the available data annual maximum water levels (dataset 2) have been analysed. Out of the four univariate models (table 1) and for all locations the Gumbel distribution could describe the annual maximum water levels best. For all locations, the location (α) and scale (β) parameters of the Gumbel distribution fitted to the data via maximum likelihood method are summarized in table 3.

Table 3: Location (α) and scale (β) parameters of the Gumbel distribution fitted to annual maximum water levels (dataset 2)

	Wismar	Rostock	Stralsund	Greifswald
Gumbel α	122,91	111,22	100,30	114,50
Gumbel β	27,72	22,54	20,30	22,53

3.2 Fullness

To calculate the fullness of hydrographs water level time series with a higher temporal resolution are needed. Therefore dataset 1 was utilised and the annual maximum fullness for all locations were analysed further.

No unitary model could be found to describe the fullness at all locations. For the locations Wismar und Rostock the Log-Normal distribution gave the best results. For the locations Stralsund and Greifswald the best fitting results were achieved using the Weibull distribution. The parameters of the fitted functions are shown in table 4.

3.3 Combined Probabilities

Next to univariate analyses of measured variables, combined probabilities of occurrence of high water levels and fullness were considered.

Table 4: Parameters of the best fitted univariate models fitted to annual maximum fullness (dataset 1)

	Wismar	Rostock	Stralsund	Greifswald
Weibull α			1,621	1,731
Weibull β			1022,234	1280,547
Log-Normal μ	6,923	6,696		
Log-Normal σ	0,568	0,640		

As the applied method to calculate combined probabilities requires pairs of water levels and fullness that occurred coevally, input data was selected from dataset 1. The dependence of both measures was described using Kendall's tau. The results are shown in table 5. It can be seen that high water levels and fullness are correlated. That means in general the fullness of a storm hydrograph tends to increase with higher water levels.

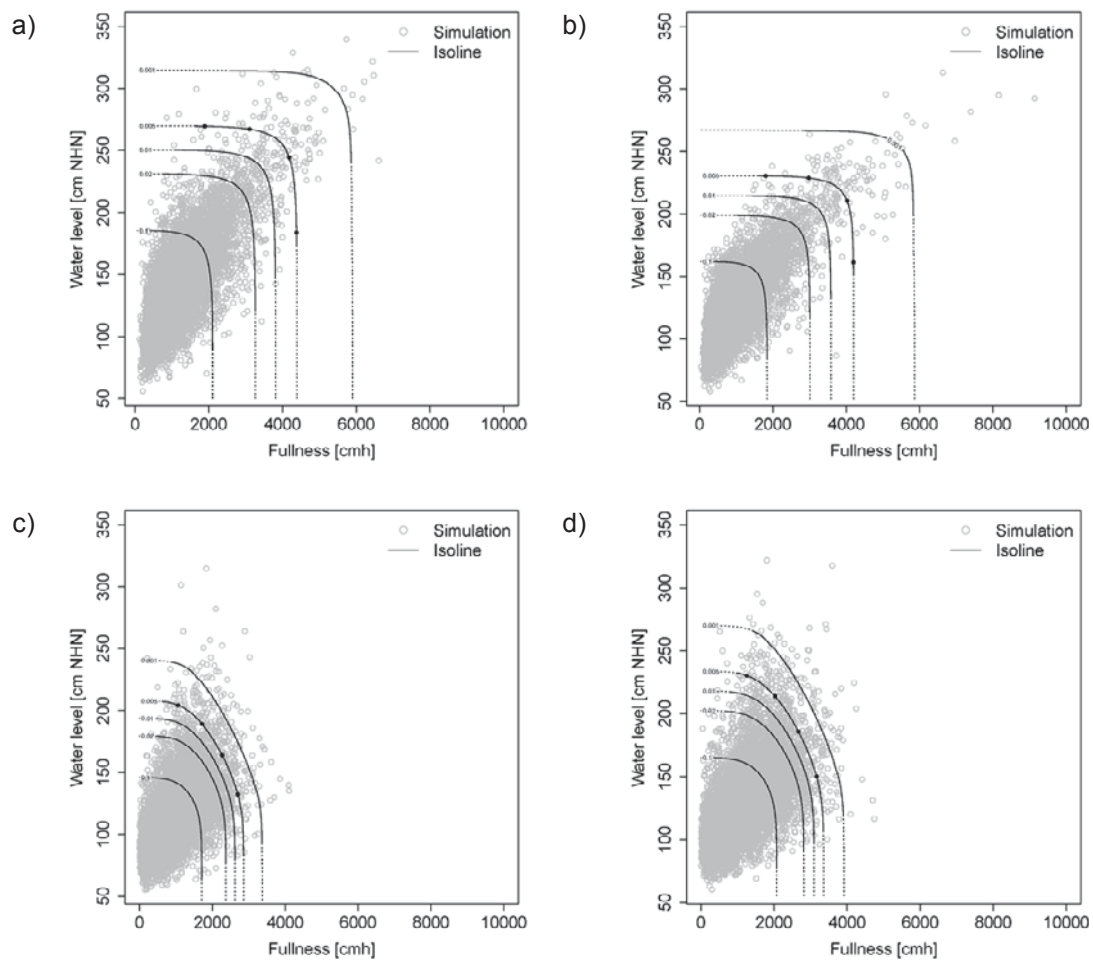


Figure 1: Simulated data pairs of water levels and fullness and isolines of equal probability at the locations: a) Wismar, b) Rostock (Warnemünde), c) Stralsund, d) Greifswald

The locations Wismar and Rostock (Warnemünde) show a stronger correlation between the two variables than the locations Stralsund and Greifswald.

Also different copula models were found to give the best fitting results for eastern and western locations. For the locations Wismar and Rostock (Warnemünde) the Gumbel Copula, for the

locations Stralsund and Greifswald the Frank Copula gave the best results. The dependence parameters of the best fitted models are summarized in table 5.

Table 5: Correlation coefficient Kendall's τ for annual maximum water levels and fullness and Dependence parameter Θ for the best fitted Copula model

	Wismar	Rostock	Stralsund	Greifswald
τ	0.518	0.553	0.473	0.453
Gumbel Θ	2.076	2.238		
Frank Θ			5.261	4.933

Although the dependence between water levels and fullness was analysed using samples taken from dataset 1, the transformation of the simulated data pairs (u,v) back to real units was performed using models that were fitted to the water level samples taken from dataset 2. It was thus assumed that the dependency structure is constant over the time.

In figure 1 the simulated data pairs after the back transformation is shown. Furthermore lines of equal probability are plotted (probabilities of 0.1, 0.02, 0.01, 0.005 and 0.001). Along these lines all combinations of water levels and fullness have the same probability of occurrence.

3.4 Storm surge hydrographs

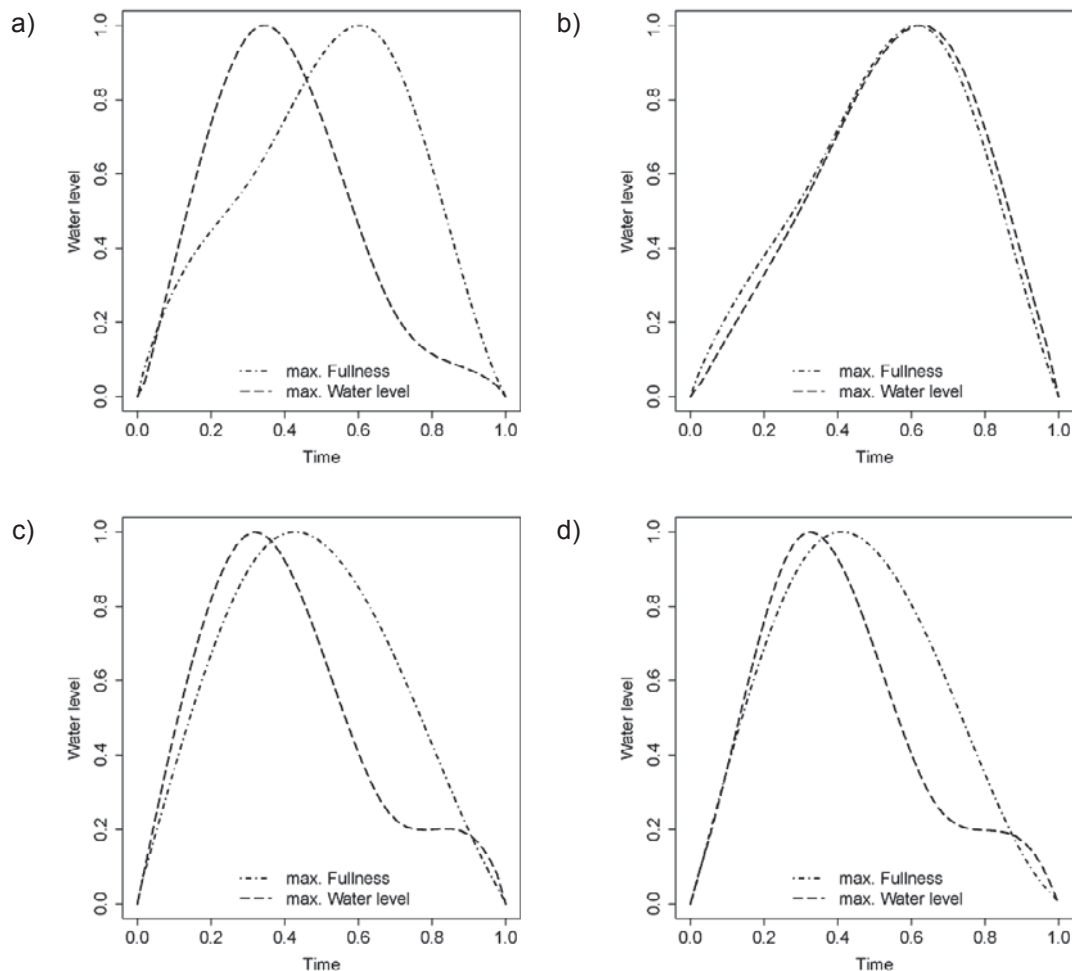


Figure 2: Dimensionless shapes of storm surge hydrographs for the locations: a) Wismar, b) Rostock (Warnemünde), c) Stralsund, d) Greifswald

In figure 2 two dimensionless storm surge hydrograph shapes for each location are shown. These shapes are being scaled in height and width by dint of combinations of water levels and fullness with a requested probability.

Exemplarily four pairs of water levels and fullness have been chosen on each 0.005 isoline. In figure 1 these pairs are marked as black dots.

In a first step the height of the storm surge hydrograph is being scaled by multiplying the desired peak water level. In a second step the storm surge hydrograph is scaled in width by multiplying the ratio of the desired to the actual fullness.

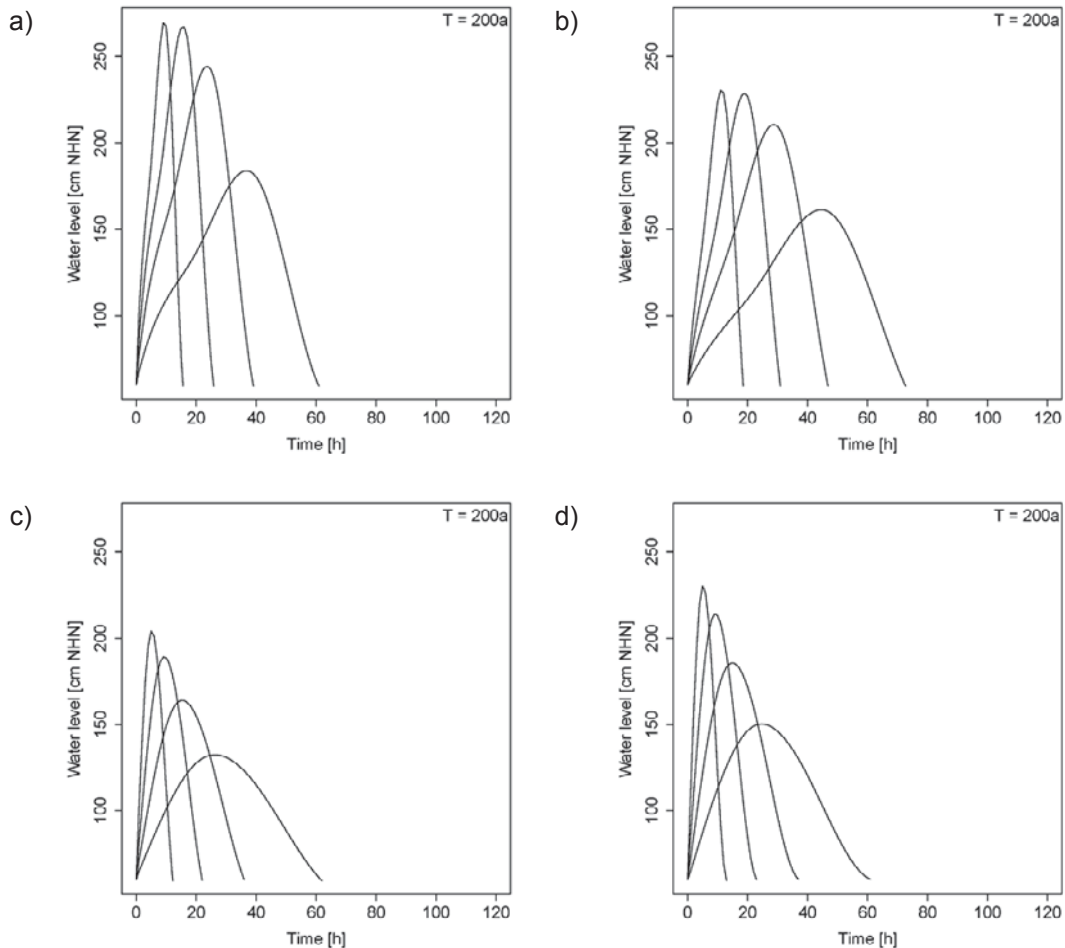


Figure 3: Scaled storm surge hydrographs with a return period of 200 years for the locations: a) Wismar, b) Rostock (Warnemünde), c) Stralsund, d) Greifswald

For each location a multitude of hydrographs can be simulated all with the same probability of occurrence. In figure 3 the hydrograph shape “max. fullness” was scaled exemplarily for all locations, using the combinations of water levels and fullness marked in figure 1. With respect to their peak water level and their fullness all scaled hydrographs shown have a probability of occurrence of 0.005. This equals a return period of 200 years.

4 Conclusion

The presented methods provide a basis to generate storm surge hydrographs for Baltic Sea regions that vary in terms of their peak water level as well as their duration. In this respect the real conditions can be simulated. This was proved by comparisons of generated storm surge hydrographs and actually measured storm surge hydrographs.

However the method is not appropriate to simulate more complex shapes like storm surge hydrographs with two or more peak water levels.

There is furthermore no definite prove for the assumption that the relation between peak water levels and fullness of storm surge hydrographs remains unchanged. At least the best fitted univariate distribution function is the Gumbel distribution for water level samples taken from both dataset 1 and dataset 2. However the water level samples taken from dataset 2 provide much information that should be considered when simulating storm surge hydrographs.

The presented results lead one to assume that the correlation between high water levels and fullness is depending on the region as water levels and fullness show a stronger correlation for western locations. A possible regional connection has to be analyzed further.

5 Acknowledgements

The HoRisk project is funded by the Federal Ministry for Education and Research and supported by KFKI (German Coastal Engineering Research Council).

6 References

- Brechmann E. (2010): Truncated and simplified regular vines and their applications. München, Germany: Technische Universität München, Diplomarbeit
- Coles S. (2001): An Introduction to statistical modelling of extreme values. Springer-Verlag London, Great Britain, ISBN 1-85233-459-2
- EAK (2002): Empfehlungen des Arbeitsausschusses Küstenschutzwerke. Die Küste. Heft 65 Westholsteinische Verlagsanstalt Boyens &Co. Germany: Heide i. Holstein. ISBN 3-8042-1056-2
- Genest, C and Favre, A-C. (2007): Everything You Always Wanted to Know about Copula Modeling but Were Afraid to Ask. In: Journal of Hydrologic Engineering, 12, pp. 347-368.
- Joe, H. (1997): Multivariate Models and Dependence Concepts. Chapman and Hall, London. ISBN 0-412-07331-5
- Johnsson, N.L., Kotz S. and Balakrishnan, N. (1994): Continuous Univariate Distributions Volume 1. 2nd Edition. John Wiley and Sons, New York. ISBN 0-471-58495-9
- Klein, B. (2009). Ermittlung von Ganglinien für die risikoorientierte Hochwasserbemessung von Talsperren. Schriftenreihe Hydrologie & Wasserwirtschaft Ruhr- Universität Bochum, Heft 25, Bochum, Germany: Ruhr-Universität Bochum, Ph.D. thesis.
- Nelson, R.B., 2006. An Introduction to Copulas. 2nd Edition. Springer New York, NY. ISBN 978-0-387-28659-4
- Sackl, B. (1987): Ermittlung von Hochwasser – Bemessungsganglinien in beobachteten und unbeobachteten Einzugsgebieten. Graz, Austria: Technische Universität Graz, Ph.D. thesis
- Salvadori, G., De Michele, C., Kottegoda, N. T. and Rosso, R. (2007): Extremes in Nature - An Approach Using Copulas. Springer-Verlag Dordrecht, Netherlands. ISBN 978 1 4020 4414 4.

Integrated risk analysis for extreme storm surges (XtremRisk)

Andreas Kortenhaus¹, Andreas Burzel¹, Marie Naulin¹, Dilani Dassanayake¹, Hocine Oumeraci¹, Jürgen Jensen², Thomas Wahl², Christoph Mudersbach², Gabriele Gönner³, Birgit Gerkenmeier³, Sigrid Thumm, and Gehad Ujeyl⁴

Abstract

Extreme storm surges have frequently led to major damages also along the German coastline. The joint research project 'XtremRisk' was initiated to improve the understanding of risk-related issues due to extreme storm surges and to quantify the flood risk for two pilot sites at the open coast and in an estuarine area under present and future climate scenarios. In this context, an integrated flood risk analysis is performed based on the source-pathway-receptor concept under consideration of possible tangible and intangible losses. This paper describes the structure of the project, the methodology of the subprojects, and first results. Moreover, integration approaches are discussed. The results of 'XtremRisk' will be used to propose flood risk mitigation measures for the prospective end-users.

Keywords: integrated flood risk analysis, source-pathway-receptor concept, storm surge, intangible flood damages

1 Introduction

In the past, storm surges have frequently led to major damages also along the German coastline. Responsible authorities accomplished considerable efforts in order to reduce and prevent flood damages. However, due to future climate change (IPCC 2007) and increasing frequencies of storm surges, it may be expected that storm surge hazards will significantly increase in the coming decades. Hence, it is urgently required to develop reliable assessment and mitigation tools and further improve mitigation measures under sustainability aspects.

Therefore, the joint research project 'XtremRisk' (Extreme Storm Surges at Open Coasts and Estuarine Areas – Risk Assessment and Mitigation under Climate Change Aspects) was initiated in 2008 (Burzel et al. 2010). XtremRisk aims to improve the understanding of extreme storm surges, including the joint probability of extreme water levels and sea states. It will also provide tools to exemplarily quantify the overall flood risk under present and future climate conditions for an open coast (pilot site Sylt Island) and a megacity in an estuarine area (pilot site Hamburg), respectively. Future conditions in 2100 under consideration of the impacts due to climate change are described and analysed by means of scenarios.

The XtremRisk project brings together scientists from different German universities (Braunschweig, Siegen, Hamburg) as well as from the Agency of Roads, Bridges and Waters in Hamburg. The end-users of the prospective results for Hamburg (Hamburg Port Authority, Agency of Roads, Bridges and Waters Hamburg) and Sylt Island (Government-Owned Company for Coastal Protection, National Parks and Ocean Protection, Schleswig-Holstein) are involved as cooperative partners. Moreover, there is a close cooperation with other related national and international research projects.

The paper provides an overview of the XtremRisk project and its background, describes the methodology, and discusses some of the results obtained. Finally, a summary with future prospects is provided.

¹ Technische Universität Braunschweig, Leichtweiß-Institute for Hydraulic Engineering and Water Resources, Department of Hydromechanics and Coastal Engineering, Beethovenstraße 51a, 38106 Braunschweig (Germany) contact author: a.kortenhaus@tu-braunschweig.de

² Research Institute for Water and Environment, University of Siegen, Siegen (Germany)

³ Agency of Roads, Bridges and Waters, Hamburg (Germany)

⁴ Department of River and Coastal Engineering, Hamburg University of Technology (TUHH), Hamburg (Germany)

2 Pilot Sites

As mentioned above, two pilot sites in Germany (Figure 1) were selected in order to exemplarily quantify the potential subsequent damages and the overall flood risk for a megacity in an estuarine area and an island at the open coast, respectively. In close collaboration with the responsible authorities, for both pilot sites flood risk mitigation measures will be proposed.

However, the methods to be developed in XtremRisk will be generic enough to be applied to other coastal and estuarine areas at risk. Worldwide, risk is permanently increasing in coastal zones and estuarine regions, which are increasingly favoured for settlement, economic development and amenity. Moreover, coastal areas are of highest ecological value, though these ecosystems are extremely endangered (MEA 2005):

- The expected climate change will lead to increased frequencies of storm surges (Woth 2005).
- Accelerated urbanisation in coastal zones and world population growth result in increased vulnerability (Schwartz 2005).
- Rising economic wealth will cause increased losses in coastal zones in the future.
- Significant degradation of coastal zones ecosystems, which are of highest value for flood defences, food supply and recreation (Oumeraci 2004).

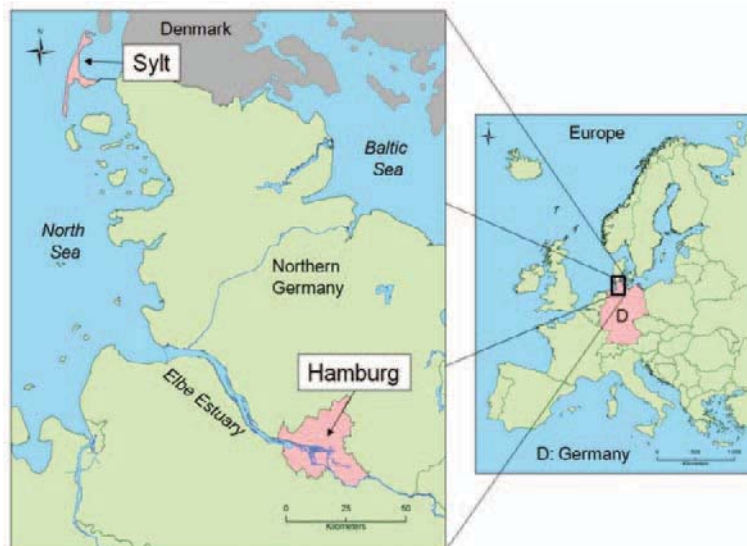


Figure 1: Location of pilot sites Hamburg and Sylt Island (Naulin et al. 2010)

The city of Hamburg is the second largest city in Germany with about 1.8 million inhabitants. Hamburg is a centre for trade, transportation and services and one of the most important industrial sites in Germany. In addition, the port of Hamburg is the largest seaport of Germany.

Hamburg is located 100 km upstream of the Elbe estuary. There is a strong influence of the tidal dynamics of the North Sea with a mean high tide in Hamburg of 2.1 m above Normal Null (NN, datum for water level in Germany) (see Naulin et al. 2010). In the past, Hamburg was affected by very high storm surges. In 1962, a storm surge caused 315 fatalities and considerable damages. Even though a more extreme storm surge with the highest observed water level in Hamburg of 6.45 m NN occurred in 1976, the storm surge caused no fatalities due to an improved flood defence system.

Furthermore, the Island of Sylt was selected as a pilot site at the open coast. Sylt Island is particularly known for tourism, recreation and its ecosystems. In contrast, sea state and storm surges, among other factors, permanently cause erosion of beaches and dunes. However, the analysis of flood risk on Sylt Island will not be discussed in this paper.

Within Hamburg, the quarter Hamburg-Wilhelmsburg is investigated in detail. In the following sections, the analysis and results with respect to this area will be described.

Hamburg-Wilhelmsburg is located on an Elbe River Island together with the districts Veddel, Kleiner Grasbrook and Steinwerder. The island is surrounded by the Northern and Southern Elbe River branches. The overall area of the Elbe River Island is 50 km². With an area of 35 km², Hamburg-Wilhelmsburg is the largest quarter of Hamburg (Burzel et al., 2010).

Most areas on the Elbe River Island have an elevation between 0 m NN and 3 m NN. Hamburg-Wilhelmsburg is protected by a flood defence ring of dikes and two flood protection walls with an overall length of 24 km and heights varying from 7.80 m NN to 8.35 m NN. Approximately 50,000 inhabitants are living here, i.e. 1,400 inhabitants per km² (Statistik Nord 2009). Most of the residential areas (about 15 km² in total) are located in flood prone areas.

3 Methodology

In XtremRisk, the flood risk R_f is defined as the combination of the probability of flooding P_f and the expected damages D . For the integrated risk analysis, a source-pathway-receptor concept is used (see Oumeraci 2004), which was successfully applied in the European research project FLOODsite.

The integrated risk analysis comprises the investigation of largest physically possible storm surges (risk sources), coastal defence failure probabilities and related flooding probabilities (risk pathways), the estimation of consequences due to flooding by inundation and damage modelling (risk receptors) and the integration of all results as shown in the flow chart in Figure 2.

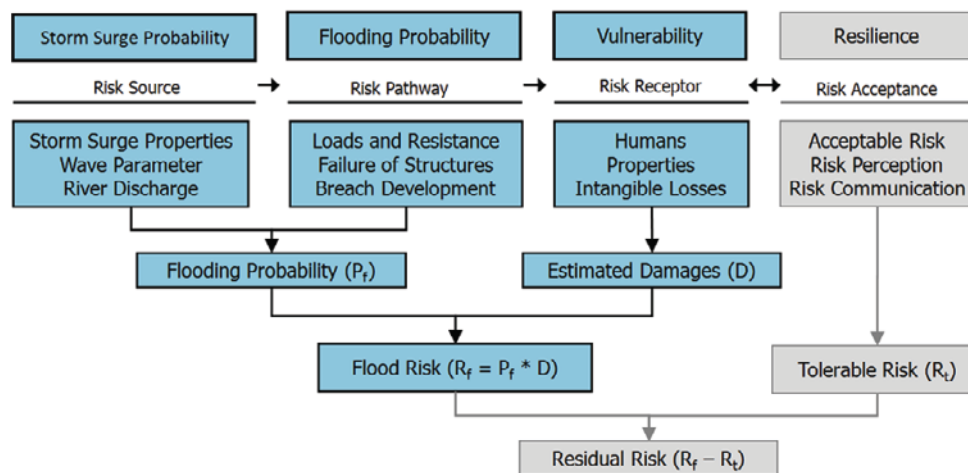


Figure 2: Integrated flood risk analysis flow chart (Burzel et al. 2010)

Based on the concept summarised in Figure 2, XtremRisk consists of four subprojects (SP):

- SP1: Extreme storm surges (risk sources),
- SP2: Loading, breaching and breach development of flood defence structures (risk pathways),
- SP3: Damage assessment and evaluation (risk receptors),
- SP4: Risk analysis, risk evaluation and recommendations for risk mitigation (integration).

Subproject 4 (SP4) aims at integrating the results achieved in SP1, SP2 and SP3 in order to determine the overall flood risk. Therefore, subproject 4 aims to perform a risk analysis, to evaluate the current level of risk and to propose and discuss risk mitigation measures.

Damages D are classified into tangible and intangible damages depending on whether or not the losses can directly be assessed in monetary values (Smith and Ward 1998). Tangible

losses include damages to buildings and infrastructure, agricultural and industrial losses, costs related to evacuation, rescue operations and reconstruction, among others. Intangible losses include loss of life and health impacts, cultural losses, damages to the environment, and others (Dassanayake et al. 2010).

Furthermore, intangible losses are mainly categorized into two groups: social and environmental losses. Social losses are experienced by individuals, groups and the overall society, and mainly include loss of life, physical injuries and mental health impacts. Moreover, cultural losses are also considered under this category (Dassanayake et al. 2010). Environmental losses are damages to ecosystems, which will not be further discussed in this paper.

The analysis will be performed on the basis of storm surge scenarios under current (2010) and future (2100) climate conditions. Tangible damages will be estimated by flood depth-damage curves. The estimation of social and ecological losses is based on methods considering flood depth, flow velocity as well as flood warning parameters, e.g. as the estimation of fatalities and injuries. A methodology for the consideration of tangible and intangible damages within an integrated risk analysis is under development.

4 First Results

For the evaluation of coastal flood risks, knowledge of the characteristics of extreme storm surges is essential. Therefore, the objective of subproject 1 is to investigate extreme values of storm surge components, which are physically possible under present and future climate change conditions (Gönnert and Sossidi 2011) including the joint probability of extreme water levels (Wahl et al. 2010).

With regard to this aim a method to assess extreme storm surge events is developed which includes physically meaningful combinations of these parameters leading to storm surge scenarios for which the investigated study areas may suffer significant damages. As a first step, storm surges since 1901 at the Cuxhaven Gauge in the Elbe Estuary and their constitutive components wind surge, astronomical tide and external surge have been analysed, such as the storm surge in 1976 (Figure 3).

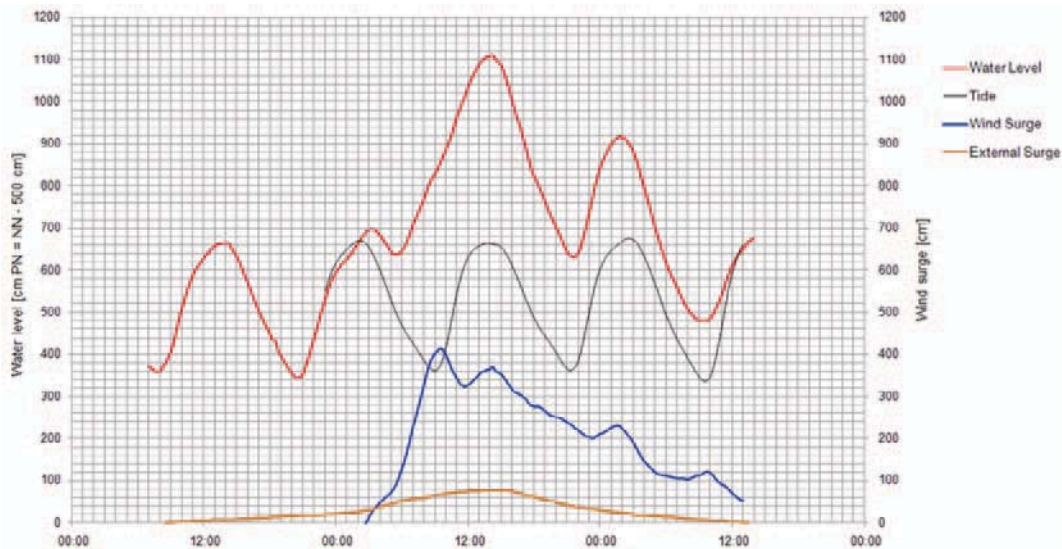


Figure 3: The extreme storm surge (water level=red line) and its components spring tide (black), wind surge (blue) and external surge (orange) at tidal gauge Cuxhaven. Due to non-linear interaction between these components, level and curve of external surge and astronomical tide are reduced.

The analysis has documented the nonlinear interaction of these components (Gönnert and Sossidi 2011). This result and further analysis with regard to the interaction between tide and surge as well as the interaction between surge and external surge will provide reliable storm surge curves and enables more precise prediction of maximum water levels for extreme storm surges. Moreover, this approach enables the generation of storm surge curves and not only

maximum water levels. The first extreme storm surge event HH_XR2010A under current climate conditions based on the 1976 event has been developed by the new approach performing a non-linear superposition of the highest of each of the components wind surge, spring tide and external surge. The development of the extreme storm surge scenario has been done at tidal Cuxhaven (Figure 3) whereupon the propagation of the surge upstream to Hamburg St. Pauli has been calculated numerically by the Federal Waterways Engineering and Research Institute. This storm surge would lead to a water level of approximately 8.0 m NN in Hamburg.

In addition to this analysis, a methodology based on multivariate statistics supported by the knowledge of the physics of the constitutive components and their possible superposition, as described above, has been developed in SP1. For this analysis, tide gauge observations from 1901 until today have been digitized and analysed. For every storm surge curve, 25 parameters are determined, and for each parameter, an extreme value distribution is assigned. With these results, Monte-Carlo simulations for 10,000,000 events were performed in order to generate a sample of extreme storm surges (Figure 4) (Wahl et al. 2011). As a result of SP1, the calculated joint probabilities of storm surge events will be used to determine failure probabilities of flood defence structures and the probability of flooding in subproject 2.

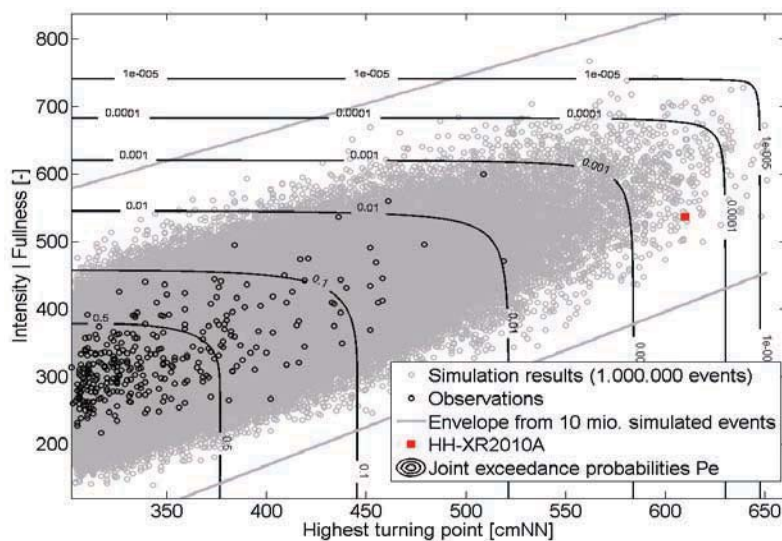


Figure 4: Synthetic storm surges by statistical simulations (grey) based on observed events (black dots) and the synthetic storm surge event HH_XR2010A (red) including the joint probability of each storm surge curve (black contour lines) (Wahl et al. 2010).

Subproject 2 uses the extreme storm surges developed in SP1 and determines the loading and the stability of all components of the flood defence system. The analysis of the failure of flood defence components requires a detailed appraisal of location, type and characteristics of defence structures.

For this purpose, an overview and detailed parameterisation of all flood defence structures were performed based on an intensive data collection in cooperation with the local flood defence authorities, in order to analyse and map the flood defence structures by using a GIS environment (Naulin et al. 2010). In addition, limit state equations for the failure modes of dikes, dunes and other types of structures developed in former research projects such as FLOODsite (Allsop et al. 2007) and ProDeich (Kortenhaus 2003), among others, have been used to calculate the failure probabilities of the flood defence structures. For these calculations, more than 80 limit state equations are available (Naulin et al. 2010). In order to calculate failure probabilities of the flood defences, sections along the defence line with similar properties such as outline, geometric parameters, sea state parameters, geotechnical parameters, among others, were defined. The ultimate result is the failure probability of the flood protection systems (and thus the flooding probability) as the first component of flood risk (Figure 5) (Naulin et al. 2010).

Additionally, the initial conditions of the flood wave propagation, starting from the breach of the flood defences, the breach growth duration, the final breach width and depth and an outflow

hydrograph at the breach location will be determined. The latter is needed by SP3 to simulate the flood inundation and related damages in the pilot site.

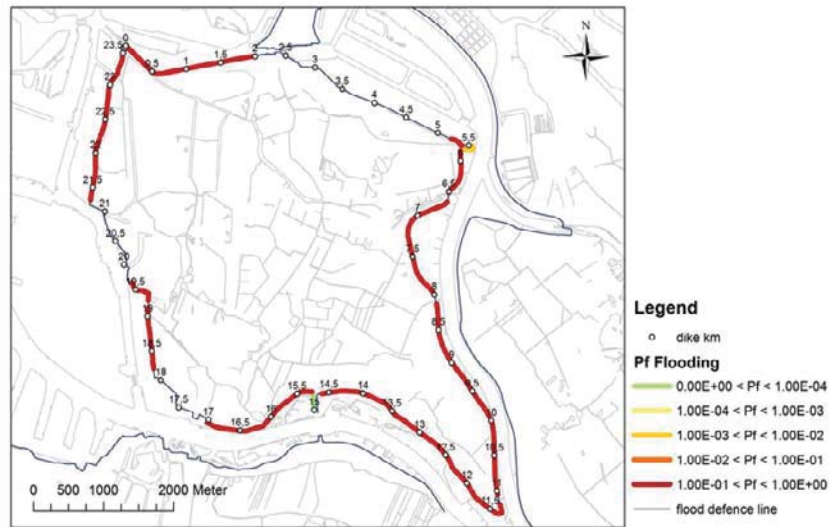


Figure 5: Sections of the flood defence line failure probabilities of the top event flooding for the synthetic storm surge HH_XR2010A with a maximum water level of 8.00 m (Naulin et al. 2010).

Within SP3, the expected direct and indirect economic losses (tangible losses) within the pilot site are assessed and evaluated. The analysis is performed by comprehensive means of scenario simulations. For this purpose, a sample-type approach is used for private households. Hereby, a micro scale analysis of damage costs for exemplary sample-type buildings is conducted. The buildings are distinguished based on criteria concerning the type of building, use of the ground floor and wall construction.

A flood damage model has been developed to perform a physically based assessment of direct losses on private households and enterprises. The assessment is carried out using generated damage curves for each sample-type building of the private households. Damages on the enterprises are aggregated to the level of economic sectors following the German sector classification system. The damages are calculated based on relative damage curves for economic sectors based on surveys and fixed assets based on the national accounts are applied by considering the number of employees for each enterprise. For the analysis, 2D numerical flood simulations were performed using MIKE21 by DHI to determine the flooding of the project area.

However, for the integrated flood risk analysis, intangible damages also have to be considered. Therefore, within subproject 4 (SP4) possible socio-economic (intangible) losses are analysed by using socio-economic evaluation methods in addition to the tangible losses in SP3. In Hamburg-Wilhelmsburg, the analysis encompasses fatalities, injuries and psychological impacts.

The state-of-the-art in flood damage analysis mainly focuses on the evaluation of economic flood consequences (Messner and Meyer 2005). It has been found that social and ecological aspects of flood-related vulnerabilities are neglected though they may represent a considerable contribution to the total losses (Green and Penning-Rowsell 1989). However, the integration of intangible and tangible damages is difficult since methods to assess these damages are not yet available or are very simplistic. Therefore, evaluation methods for the intangible losses have been critically reviewed and analysed (Dassanayake et al. 2010).

Eventually, tangible and intangible losses must be integrated into a risk analysis. The aim is to perform an analysis considering both, tangible and intangible damages in order to calculate the overall risk and to develop optimal mitigation strategies for different scenarios. Therefore, SP4 integrates all results from all subprojects and aims at performing a full flood risk analysis for the pilot sites based on the source-pathway-receptor concept as described above.

As a first approach, the presentation of damages and losses within specific damage categories, further termed as categorisation, are examined. For this purpose, similar damages such as societal losses are grouped as one category. The main advantage is that optimal mitigation measures for each damage category can be specified. However, this approach is not a real integration, even though a full flood risk analysis is performed. Tangible and intangible losses are not expressed in the same terms within one risk analysis, since every risk is calculated in different units. Furthermore, mitigation strategies for one damage category influence other categories as well. These aspects cannot be considered properly by using the categorisation approach.

The second approach which has been examined is the Multi-Attribute-Utility (MAUT) approach. This approach was tested and proposed for integrated risk analysis in the European Research Project FLOODsite (Meyer et al. 2007). The approach is based on the ranking between different options by the consideration of their utility functions. Utility functions are favoured as they express the economic behaviour of individuals or the society. Utility functions enable the weighting, balancing, and ranking of different options, such as mitigation strategies, within integrated risk analysis. The aim is to maximise the sum of the utilities of all options (Meyer et al. 2007).

As a third approach, the monetary assessment of tangible and intangible losses has been examined. In this approach, all losses are considered within a cost-benefit analysis. Therefore, intangible losses, which are usually not expressed in monetary terms, have to be estimated by using socio-economic evaluation methods such as Contingent Valuation or Hedonic Price Method, among others. An advantage of this approach is the possibility to calculate the risk R_f for each damage category separately. Furthermore, cost-benefit ratios can be calculated for several mitigation strategies. However, the monetary assessment of intangible goods, such as human beings and the environment, is often opposed due to ethical constraints. Moreover, intangible losses are not adequately reflected in a cost-benefit analysis related to their importance. Hence, weighting factors for intangible goods must be implemented (RPA 2004).

5 Concluding Remarks

As described above, the integrated risk analysis described in this paper is based on intermediate results only. Therefore, all results have to be verified and completed. The aforementioned approaches will be further tested. Later on, the risk analysis will be performed on the basis of scenarios under current and future climate conditions. All results will be compared to each other in order to find an optimal approach for the integration of tangible and intangible losses as well as for the full flood risk analysis. In addition, the approach must be suitable for decision making with respect to different mitigation strategies and multi-criteria optimisation.

Further information about the XtremRisk project, the ongoing research and intermediate results are also presented at the project website under www.xtremrisk.de.

6 Acknowledgements

This study within the joint research project XtremRisk is funded by the German Federal Ministry of Education and Research BMBF (Project. No. 03 F 0483 A).

Moreover, the collaboration and the provision of data by the Cooperative and Consulting Partners of the project such as LKN-SH (Schleswig-Holstein Agency for Coastal Defence, National Park und Marine Conservation), HPA Hamburg (Hamburg Port Authority) and LSBG Hamburg (Agency of Roads, Bridges and Waters, Hamburg) are gratefully acknowledged.

7 References

Allsop, N.W.H., F. Buijs, M.W. Morris, R. Hassan, M.J. Young, N. Doorn, J.W. Van der Meer, A. Kortenhaus, P.H.A.J.M. Van Gelder, M. Dyer, M. Redaelli, P.J. Visser, R. Bettess, and D. Lesniewska, 2007. Failure mechanisms for flood defence structures. FLOODsite Res.-Report, T04-05-01, Task 4, 150 p.

- Burzel, A.; Dassanayake, D.; Naulin, M.; Kortenhaus, A.; Oumeraci, H.; Wahl, T.; Mudersbach, C.; Jensen, J.; Gönnert, G.; Sossidi, K.; Ujeyl, G.; Pasche, E. (2010): Integrated flood risk analysis for extreme storm surges (XtremRisk). Proceedings 32nd International Conference Coastal Engineering (ICCE), ASCE, Shanghai, China, 13 p.
- Dassanayake, D.R., A. Burzel, A. Kortenhaus, and H. Oumeraci, 2010. Framework and Methods for the Evaluation of Intangible Losses and their Integration in Coastal Flood Risk Analysis. XtremRisk Progress Report. LWI, Technische Universität Braunschweig.
- Green, C.H., and E.C. Penning-Rowsell, 1989. Flooding and the Quantification of 'Intangibles'. IWEM: Annual Symposium Paper No. 8., pp 27-30.
- Gönnert, G., and K. Sossidi, 2011. A new approach to calculate extreme storm surges: Analyzing the interaction of storm surge components. In: Benassai, G., C.A. Brebbia and G.R. Rodriguez (Edit): Coastal Processes II. Southampton, P. 139-150
- IPCC, 2007. Climate change 2007: WG II: Impacts, Adaptation and Vulnerability, Chap. 6. Coastal systems and low lying areas. Intergovernmental Panel on Climate Change (IPCC), Cambridge University Press.
- Kortenhaus, A., 2003. Probabilistische Methoden für Nordseedeiche. Ph.D. thesis, Dissertation, LWI, Technische Universität Braunschweig, Braunschweig, 154 p.
- MEA, 2005. Ecosystems and Human Well-being, A framework for assessment. Millenium Ecosystem Assessment Series, Island Press, Washington D.C.
- Messner, F., and V. Meyer, 2005. Flood damage, vulnerability and risk perception - challenges for flood damage research. UFZ Discussion Papers. Department of Economics, Leipzig.
- Meyer, V., D. Haase, and S. Scheuer, 2007. GIS-based Multicriteria Analysis as Decision Support in Flood Risk Management, FLOODsite Project Report, HR Wallingford, UK.
- Naulin, M., A. Kortenhaus, and H. Oumeraci, 2010. Failure Probability of Flood Defence Structures/ Systems in Risk Analysis for Extreme Storm Surges. Proceedings 32nd International Conference Coastal Engineering (ICCE), Shanghai, China.
- Oumeraci, H., 2004. Sustainable coastal flood defences: scientific and modelling challenges towards an integrated risk-based design concept. Proc. First IMA International Conference on Flood Risk Assessment, Session 1, Bath, UK, pp. 9-24.
- RPA - Risk and Policy Analysts Ltd, 2004. Evaluating a multi-criteria analysis (MCA) methodology for application to flood management and coastal defence appraisals. R&D Project Record FD2013/PR1, DEFRA, UK.
- Schwartz, M., 2005. Encyclopedia of Coastal Science. Dordrecht, Springer
- Smith, K., R. and Ward, 1998. Floods: Physical processes and human impacts. John Wiley and Sons, Chichester, UK.
- Wahl, T., J. Jensen, and C. Mudersbach, 2010. A Multivariate Statistical Model for Advanced Storm Surge Analyses in the North Sea, Proceedings 32nd International Conference Coastal Engineering (ICCE), Shanghai, China.
- Wahl, T., C. Mudersbach, C. and J. Jensen, 2011: Assessing the hydrodynamic boundary conditions for risk analyses in coastal areas: a stochastic storm surge model, Nat. Hazards Earth Syst. Sci., 11, 2925-2939, doi:10.5194/nhess-11-2925-2011, 2011.
- Woth, K., 2005. Regionalization of global climate change scenarios: An ensemble study of possible changes in the North Sea storm surge statistics, PhD Thesis prepared within the International Max Planck Research School on Earth System Modelling, Hamburg.

Implementing coastal defence strategies for sandy coasts – reinforcement of the Norderney dune revetment

Frank Thorenz¹, Holger Blum²

Abstract

The sandy barrier island of Norderney is at its north-western side protected by a dune revetment and groins against erosion and flooding due to storm surges. Here also the city of Norderney is situated. Norderney represents one of the very important sea resorts along the German North Sea Coast with tourism as the main economic factor.

A check of design parameters and functionality of the dune revetment by a combination of hydro-numerical wave modelling and large scale hydraulic model tests was executed. Determined wave-overtopping volumes of more than 120 l/(s.m) and maximum surface pressures of 200 kPa showed the need for heightening and strengthening of a 2 km stretch of the construction, in order to guarantee an adequate protection level of the adjacent city against the hazard of flooding in case of storm surges. Due to unremovable buildings within one 300 m and one 100 m long section no space for areal extension of the construction was available. Hence, alternatives were investigated by hydraulic model tests aiming on reduction of wave run-up.

Innovative wall-elements situated in the upper section of the revetment and crest walls were found to be very effective measures, in order to limit wave run-up and wave overtopping for these sections with limited planning space. The design of the elements took demands of tourism and urban planning into account, leading to an integrated and harmonised planning for the important sea resort Norderney.

Besides its technical complexity, this construction also shows the need to reserve planning space for coastal defence measures in the long term. The capability to adapt coastal defence structures to the effects of sea level rise and climate change in order to achieve an adequate level of flood protection for flood prone areas demands a further integration of coastal defence and spatial planning.

Keywords: dune revetment, model tests, wave run-up, overtopping

1 Introduction

In front of the mainland coast of the German Federal State of Lower Saxony seven inhabited sandy barrier islands are located [Fig. 1]. These islands nowadays represent important sea resorts, whereas the island of Norderney is the most frequented one with more than 3 million overnight stays [NLWKN, 2010; Thorenz, 2006]. The city of Norderney is located at the western part of the island. Due to an ongoing negative sediment balance of the beaches, the western part of the island is protected by a system of a dune revetment and groins against erosion and flooding [Fig. 2]. Since 1950 additional beach nourishments are carried out on demand. Oldest sections of the revetment were built already in 1858. The Master Plan Coastal Defence for the District Weser-Ems [1997] stated the general necessity to strengthen and heighten significant parts of the revetment. The Lower Saxony Coastal Defence, Water Management and Nature Conservation Agency (NLWKN) investigated in detail the functionality of the revetment. Model tests showed the necessity to rebuild significant sections of the revetment due to loading and wave overtopping.

¹ Lower Saxony Water Management, Coastal Defence and Nature Conservation Agency (NLWKN), Jahnstr.1, D-26506 Norden, Germany, frank.thorenz@nlwkn-nor.niedersachsen.de

² Lower Saxony Water Management, Coastal Defence and Nature Conservation Agency (NLWKN), Jahnstr.1, D-26506 Norden, Germany, holger.blum@nlwkn-nor.niedersachsen.de



Figure 1: Overview – Location island of Norderney

The nearness of buildings limits at some stretches of the revetment available space for extension of the construction by a slope and crest heightening. Besides its function as a coastal defence structure, the berms integrated in the revetment have an important function as a well known promenade in an economical important, highly frequented sea resort. Therefore additionally touristic and urbanistic demands have to be considered in order to achieve an integrated planning.



Figure 2: Areal photo of the planning area

2 Initial state of the construction

The initial construction of the Norderney dune revetment was built 1857/58 in order to protect the expanding city against increasing erosion and flooding encompassing a total length of 900 m. Until the end of the 20th century several reinforcements and extensions of the construction as well in cross section as in length were executed as a consequence of damages and erosion of unprotected dunes in severe storm surges. In the recent past the severe storm surges of February 1962 and January 1976 lead to significant damages of the revetment and flooding of parts of the city of Norderney due to wave overtopping.

The resulting construction shows a total length of 4.9 km consisting of several sections. For a 2 km long section, stretching from the locations "Cafe Cornelius" over "Georgshöhe", "Milchbar"

to “Strandstraße” a primary need for reinforcement was determined [Fig. 2]. Here the typical cross section shows a width of 34 m for the revetment and a clay slope with a crest height of 8.5 m above NN (German datum level) and varying slope and length depending on the distance of adjacent buildings. Design water level is designated to 5.0 meter NN [Fig. 3].

A typical construction element of the revetment marks an s-shaped profile consisting of sandstone blocks, which is part of the initial revetment build in the 19th century. The upper section of the construction consist of a 16 cm thick concrete slab berm and a 1 : 3 sloped pavement of 30 x 30 x 20 cm non-interconnected concrete blocks.

In the locations “Georgshöhe” and “Milchbar” existing buildings with a right of continuance are located very close to or even within the revetment [Fig. 2].

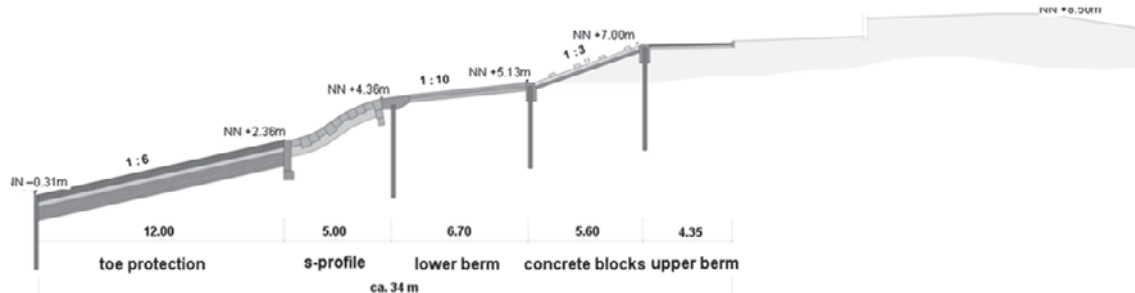


Figure 3: Typical cross section of the initial dune revetment at Norderney

3 Coastal defence strategy, legal and spatial boundary conditions

Legal basis of coastal defence for the Federal State of Lower Saxony is the Lower Saxony Dike Law [NDG, 2010]. The dike law defines legal coastal defence elements such as coastal defence dunes, erosion protection structures, main dikes, storm surge barriers and dike foreland. The Lower Saxony coastal defence strategy and legal boundary conditions are stated in the Master Plan Coastal Defence Eastfrisian Islands [NLWKN, 2010]. In case of structural eroding coasts and high vulnerability such as the western part of Norderney the strategy of preservation of the existing coastline and protection against flooding is implemented. The area seaward the existing buildings including the revetment is designated as a coastal defence dune by decree [Fig. 2].

4 Investigation of hydrodynamical loading

In order to determine design parameters for the existing construction, combined numerical and hydraulic model tests were performed. Hydronumerical calculation of the sea state conditions for design water level were conducted by the former Lower Saxony State Board of Ecology with the spectral wave model SWAN, taken JONSWAP spectra as well as natural spectra as boundary conditions into account.

Since the foreshore including the Norderney tidal inlet ebb delta is characterized by ongoing morphological changes, sea state simulations also considered different states of bathymetry. Design wave heights up to $H_s = 3.5$ m and wave periods up to $T_{m-1,0} = 10$ s in front of the construction were calculated [Niemeyer et. al., 2000].

In order to determine wave run-up, wave overtopping and loading for the initial construction as well as for planning alternatives, large scale model test were executed in the large wave flume of the coastal research centre in Hannover by the Technical University of Braunschweig – Leichtweiß-Institute. The model tests scaled 1 : 2.75 for the initial state of the construction yielded overtopping rates of more than 120 l/(s·m), maximum surface pressures of 200 kPa and also significant uplift pressures [Schüttrumpf et al., 2001]. These loadings were not tolerable concerning the stability of the upper part of the construction and the hazard of flooding of the city.

5 Results of planning

General planning objectives are a robust construction as well as limitation of wave run-up and overtopping in order to achieve a defined safety level against flooding. In two sections of the revetment at the more than 300 m long stretch “Georgshöhe” and the ca. 100 long stretch “Milchbar”, no sufficient space for an extension and heightening of the upper slope was available due to the nearness of buildings. Therefore, special technical alternatives to limit wave overtopping were investigated theoretically or by model tests. Most effective solutions were found by two lines of wall elements located in the upper part of the revetment adjoining the upper berm with a height of 1.3 m and length of 7.5 and 6.0 m as well as a crest wall with a height of 0.8 m. Gaps between the elements provide backflow of water overtopping the wall elements. Whereas the wall elements limit wave overtopping to 25 l/s m and the crest wall to 43 l/s m, a combination leads to an acceptable overtopping of 3 l/s m for the location “Georgshöhe” [Fig. 4a/b]. The design loading of the curved wall elements was determined to 185 kPa, for the straight elements to 137 kPa and for the crest wall to 15 kPa.

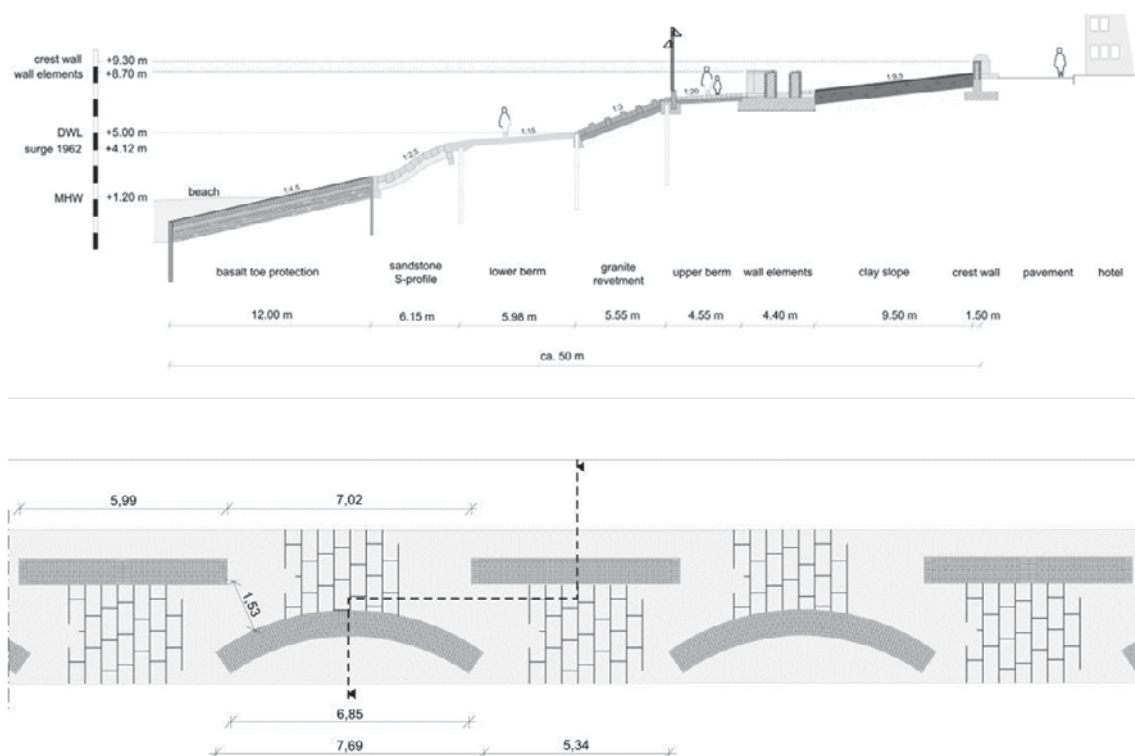


Figure 4a/b: Cross section and site plan location “Georgshöhe”

The construction height was chosen in order to integrate the demands of technical functionality as a coastal defence structure and demands of tourism in a prospering sea resort. The wall elements allow a walking adult to look over them, whereas the crest wall shows a typical balustrade height.

Technical the two lines of wall elements are constructed as a reinforced concrete core connected with a surface foundation of 4.6 m width and sections of ca. 25 m length. The sections are connected by steel tubes, in order to disseminate the horizontal forces induced by waves. In order to integrate urbanistic and touristic demands, a mantle of clinker bricks and a sandstone pavement as typical regional building materials are applied. In the summer season, benches can be placed in front of the elements, providing shelter against wind and offering an attractive view to the sea. The upper wall shows a similar construction.

At the location “Milchbar” a complex planning situation can be found. Here an important access from the city of Norderney to the promenade is situated as well as a restaurant and a hotel within or very close to the revetment.

Here also model test were executed in order to optimise the design of the revetment and yielded an integrated planning. Wall elements with a height of 80 cm located adjacent to the upper berm reduce wave run-up and limit overtopping over the vertical crest wall effectively. Within this, an opening consisting of three sections is integrated to enable a barrier free connection from the city to the promenade and locking devices with stop-locks in case of storm surges [Fig. 5a/b].

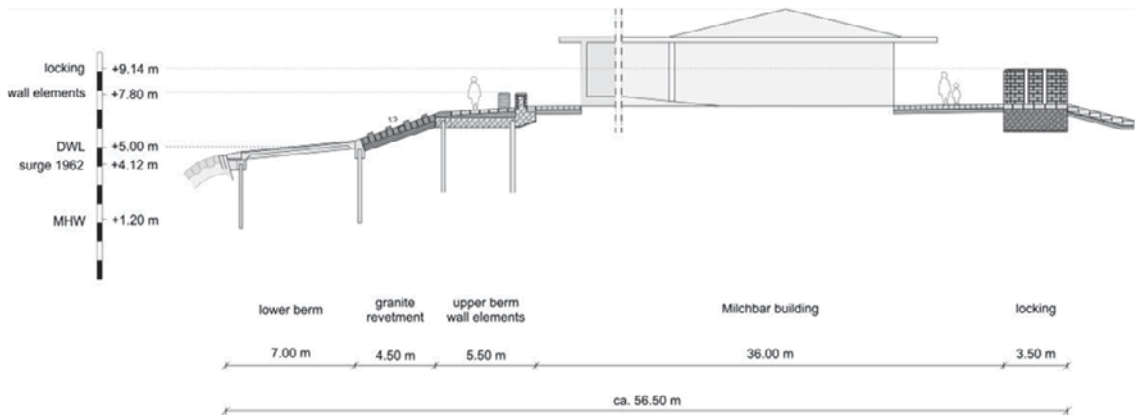


Figure 5a/b: Cross section and 3d animation location "Milchbar"

In order to reduce wave run-up, an impermeable granite block revetment sloped 1 :3 with a thickness of 33 cm and additional roughness elements forms the connection between the lower and the upper berm. Additionally, the historical s-profile was renovated by grouting of the subsoil and renovation of the joints. In 2011 a renovation of a 550 m long section of the lower berm is additionally executed.

The total construction costs amount to approximately 30 Mio. € financed by the European Union, the Federal Republic and the Federal State of Lower Saxony. The work has been carried out from 2001 to 2008 and in 2011.

6 Summary and Outlook

The island of Norderney is protected at its western side by groins and a dune revetment against storm surges and erosion. The revetment borders the city of Norderney, an important sea resort at the German North Sea Coast. In order to determine the loading and functionality of the construction under design storm surge conditions, a combination of numerical modelling of sea state conditions and hydraulic model tests for the construction were executed. Results of the model test showed the necessity to strengthen and heighten a 2 km long stretch of the revetment. Due to limited space resulting from adjacent buildings, in two cases wave run-up reduction wall elements were designed. These walls limit wave overtopping efficiently and meet

the needs of tourism for an important recreation locality [Fig. 6]. Similar constructions are currently under investigation for the dune revetment at the island of Baltrum located eastward Norderney [Liebisch et al. 2011].

The need for such a complex construction with vertical elements and in consequence high loading to protect a settlement against flooding shows on the other hand the need of planning space for future coastal defence measures in order to provide less complex mild sloped solutions. In the context of future sea level rise and consequences of climate change, the reservation of space for coastal defence works will be an issue of growing importance for spatial planning and the demand of integration of different public and private interests.



Figure 6: Dune revetment with wall elements - summertime and storm surge conditions

7 References

- Bezirksregierung Weser-Ems (1997): Generalplan Küstenschutz für den Regierungsbezirk Weser-Ems. Oldenburg, Germany.
- Liebisch, S.; Kortenhaus, A.; Oumeraci, H.; Thorenz, F.; Blum, H. (2011): Wellenüberlauf und welleninduzierte Belastung des Deckwerks auf der Insel Baltrum, in: Tagungsband 8. FZK-Kolloquium, pp. 69-74. ISSN 1610-5249. Hannover, Germany.
- NDG (2010): Niedersächsisches Deichgesetz i.d.F. vom 23. Februar 2004 (Nds. GVBl. S. 83) zuletzt geändert durch Artikel 2 des Gesetzes vom 19. Februar 2010 (Nds. GVBl. S. 64).
- Niemeyer, H. D., Kaiser, R., Weiler, B. (2000): Bemessungsseegang für die Deckwerke am Nordweststrand von Norderney, internal report.
- NLWKN (2010): Generalplan Küstenschutz Niedersachsen – Ostfriesische Inseln. Norden, Germany.
- Schüttrumpf, H.; Oumeraci, H.; Thorenz, F.; Möller, J. (2001): Reconstruction and rehabilitation of a historical seawall at Norderney, in: Proceedings ICE Int. Conference Breakwaters, coastal structures and coastlines, Thomas Telford, London, U.K., pp. 257-268.
- Thorenz, F. (2006): Coastal defence strategies as a building block for integrated coastal zone management. Proc. Third Chinese-German Joint Symposium on Coastal and Ocean Engineering, pp. 463-472. ISBN-13 957-986-00-7143-6. Tainan, Taiwan.

Technical Session 4: Coastal and Port Environments

Chairman: Dr. Gerald Müller

Physical modelling of brine discharges from a cliff

Macarena Rodrigo¹, Francisco Vila², Antonio Ruiz-Mateo³, Ana Álvarez⁴, Ana Lloret⁵,
Manuel Antequera⁶

Abstract

Physical models are useful tools to improve the desalination plants discharge conditions as well as to calibrate mathematical models since they allow the evaluation of the effectiveness of their discharge designs and to choose the most appropriate one. Depending on the chosen disposal system, the behaviour of the brine effluent, mixing and dilution with seawater are influenced in different ways. The case of study focuses on the discharges from a cliff to show some results. The conclusions obtained with the performed physical model will be presented in this communication since the brine discharge is a hypersaline effluent, with higher density than the medium, which spreads along the bottom and it can cause harmful effects on marine ecosystems.

Keywords: physical model, brine discharge, dilution, desalination

1 Introduction

1.1 Brine discharge

The sea water desalination process is a strong bet for developing regions, like the Spanish Mediterranean or the Canary Islands, to satisfy the increasing fresh water demand, being the desalination the most important artificial water resource.

The most recent plants in Spain use reverse osmosis (RO) technology to desalinate seawater, with conversion rates of about 40-50%. The plants generate a brine effluent waste product with approximately twice the salinity and with a higher density than that of seawater.

Table 1: Typical brine discharge in the Mediterranean Sea

Sea water	Salinity	37.5 psu
	Density (at 20 °C)	1027 kg / m ³
Brine discharge	Salinity	68.2
	Density (at 20 °C)	1050 kg / m ³

1.1.1 Brine behaviour

Brine discharge, which is denser than sea water, behaves as a negatively buoyant effluent, sinking to the bottom. To study the behaviour of brine discharge into sea water two regions can be separated: near field and far field. Near field is located near the discharge point and it is characterized by the initial mixing because of a competition between kinetic and potential energy is produced and it implies a high turbulence zone. For this region, brine behaviour depends on discharge device, brine effluent and ambient properties. Far field is the region located far away from the discharge point, where the turbulent is attenuated and the mixing ends forming a hyperdense layer that flows over the bottom, spreading out and tending to follow

¹ Centre for Studies Ports and Coast of CEDEX, Antonio López, 81, 28026, Madrid, Spain, macarena.rodrigo@cedex.es

² Centre for Studies Ports and Coast of CEDEX, Antonio López, 81, 28026, Madrid, Spain, francisco.vila@cedex.es

³ Centre for Studies Ports and Coast of CEDEX, Antonio López, 81, 28026, Madrid, Spain, antonio.ruiz@cedex.es

⁴ Centre for Studies Ports and Coast of CEDEX, Antonio López, 81, 28026, Madrid, Spain, ana.alvarez@cedex.es

⁵ Centre for Studies Ports and Coast of CEDEX, Antonio López, 81, 28026, Madrid, Spain, ana.lloret@cedex.es

⁶ Centre for Studies Ports and Coast of CEDEX, Antonio López, 81, 28026, Madrid, Spain, manuel.antequera@cedex.es

the direction of the maximum slope. In this case, brine behaviour depends on ambient conditions and the difference of density between hypersaline plume and receiving water (Palomar et al., 2010).

1.1.2 Brine impact

The discharge of the concentrated effluent into the sea may cause a negative impact in the sea water quality and its ecosystems. Particularly benthonic species, with low tolerance to salinity variations in the environment, are susceptible to be impacted. Regarding the sea grass meadows that cover the Mediterranean coast, it is important to consider the sea grass *Posidonia oceanic*⁷, or another species such as *Cymodocea nodosa* (Ruiz-Mateo et al., 2008).

Taking into account the regulation for such discharges, there is no legislation or recommendations to establish critical values of salinity leading to the protection of some valuable habitats. In this context, a number of experiments were conducted in order to limit the excess salt value, detailed in Sánchez Lizaso et al. (2008).

1.2 MEDVSA Project

In order to make the development of the desalination plants sustainable, the Spanish Ministry of the Environment and Rural and Marine Affairs agreed to invest in Experimental Development Projects within its National Plan for Scientist Research, Development and Technological Innovation. The project entitled “Development and implementation of a methodology to reduce the environmental impact of brine discharges from desalination plants” has been approved and supported as part of the Plan. This project is being carried out by the Environment Hydraulics Institute (IH) of the University of Cantabria and the Spanish Centre for Experimentation on Public Works (CEDEX) of the Ministry of Public Works.

The main objectives of the project are:

- To optimize the systems and to propose criteria for brine discharges into the sea generated in Spanish desalination plants.
- To develop a general methodology for studies of brine discharges into the sea of the rejection waters.
- To achieve criteria to decide the most advisable device for discharging in each case.
- To ensure the protection of the marine environment, particularly the benthic ecosystems.

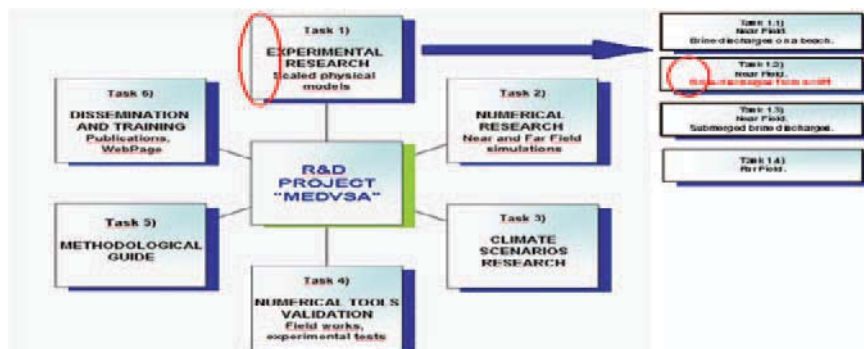


Figure 1: Tasks of the project (Palomar et al., 2010).

MEDVSA Project is divided in six different tasks, as it is shown in the sketch. This communication is focused on experimental research, which includes different discharge devices, but the discharge from a cliff is the case of study, one of the the most representative of desalination plants located in Spain.

⁷ The *Posidonia oceanic Meadows* are included in the Annex I (natural habitat types of community interest whose conservation requires the designation of special areas of conservation) of the Council Directive 92/43/EEC of 21 May 1992 on the conservation of natural habitats and of wild fauna and flora.

2 Physical model

2.1 Facilities

The experiments have been performing in the facilities of the Marine Experimental Laboratory of the Centre for Studies on Ports and Coasts of CEDEX. Tests were carried out in a flume with dimensions of 70 meters long, although only 22 meters long were used, 1 meter wide, 2 meters high and with a 2% fixed slope until the end of the model. The different simulations were chosen according to a fixed flow changing some variables such as the height of the cliff, the width of the overflow discharge and the depth of the column water.

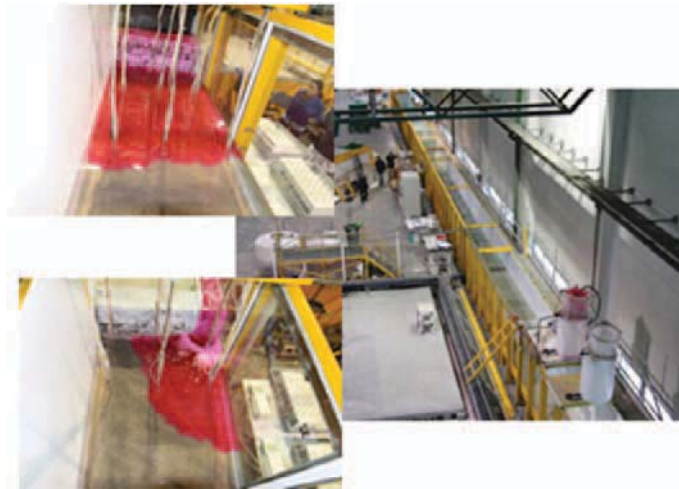


Figure 2: Flume of the physical model (right). The wall, simulating the cliff, and the width of the overflow discharge (left)

There are two types of tests, one of them uses all the width of the flume and the second type takes one wall of the flume as a vertical plane of symmetry therefore the results may be extended to twice the width of the discharge.

2.2 Effluent

In the case of physical model tests, the water of the receiving environment has much lower salinity than the one of sea water. Thus, the discharge which simulates the brine of the desalination plant, was modified in order to maintain the similarity of the Froude densimetric number⁸ of the prototype to the model. This implies that the relative density difference between the effluent and the receiving water were the same in the physical model and in the prototype.

Table 2: Relative density difference where ρ_0 is the effluent density and ρ_a is the environmental density

		BRINE	AMBIENT	$\Delta\rho/\rho_0$
PROTOTYPE	Salinity	68.2	37.5	$\frac{\rho_0 - \rho_a}{\rho_0} \approx 0.0224$
	Temperature	20	18	
	Density	1050.74	1027.18	
MODEL	Salinity	30.4	0.3	$\frac{\rho_0 - \rho_a}{\rho_0} \approx 0.0224$
	Temperature	10	10	
	Density	1021.75	998.83	

The discharge is stained with Rhodamine WT, which is used to keep track and provide some measurements during the experiment (Vila et al., 2010).

⁸ The Froude densimetric number is a dimensionless number relating the inertial to gravity forces acting on the fluid.

2.3 Instrumentation

The tests were performed using different instrumentation to measure, mainly, conductivity, temperature and velocity within the near field.

2.3.1 Discharge device

Discharge device consists of several brine tanks with a pump leading the brine can be discharged by overflow. Flow can be measured by a flow-meter and regulated with a flow control valve. The hydraulic system is shown in figure 3.



Figure 3: Tanks and hydraulic system (left and centre). Flow-meter and flow control valve (right)

2.3.2 Pipettes – Peristaltic pumps

Glass and copper pipettes, attached through silicone tubes with peristaltic pumps, were sucked up liquid sample to measure the conductivity and the temperature in the laboratory. Several pipettes were placed in the same vertical profile, at a given distance from the discharge point and for different cross-sections.



Figure 4: Vertical profile of pipettes (left). Peristaltic pumps and samples (centre). Laboratory conductivity meter (right)

2.3.3 Portable conductivity meter – Microconductivity meter

Portable conductivity meter is used during the test if necessary or to measure the effluent sample of the tank and the environmental sample of the flume.

The microconductivity meter provides 20 measurements per second. It is sampled at a point with a resolution of 3mm. Moreover it is placed next to a given pipette to compare both results.

2.3.4 Ultrasonic profiler velocity Doppler

It performs speed profiles with high resolution. It is positioned with a fixed angle from the horizontal to measure the velocity of the hyperdense layer at particular times. A good seeding of particles leads to reflect the ultrasonic beam.



Figure 5: Microconductivity meter next to copper pipettes (left). Ultrasonic profiler velocity Doppler positioned with a certain angle (centre). Portable conductivity meter (right)

3 Theoretical analysis

Flow rate (Q_0), momentum flux (M_0), buoyancy flux (G_0), longitudinal-variable (x), cross-variable (y), flow width at inlet (B_0), flume width (B_c), depth of the column water (h_a) and height of the cliff (h_0) are the variables considered at this study.

$$G_0 = g_0 \times Q_0 \quad (1)$$

with g_0 reduce gravitational acceleration [m/s]

Q_0 flow rate [m³/s]

There are two independent dimensions (length and time) because the mass is removed by considering only the g_0 as representative of the mass implied.

An asymptotic approach can be performed without making excessive errors for the cases of surface discharges. It is assumed that the initial momentum tends quickly to zero, so M_0 is neglected. Moreover, monomials are obtained with a single dimension (length) as follows:

$$L_{QG} = Q_0^{3/5} \times G_0^{-1/5} \quad (2)$$

The different simulations were chosen according to a fixed flow, (CEDEX, 2003 and CEDEX, 2009) then it is calculated the height of the cliff, the width of the overflow and the depth of the column water taking into account the following dimensionless monomials:

$$B = B_c / B_0 \quad (3)$$

$$H_a = h_a / L_{QG} \quad (4)$$

$$H_0 = (h_0 - h_a) / h_a \quad (5)$$

Table 3: Performed tests. The specific values are obtained from certain values of the dimensionless numbers ($B = 1 / 5$, $H_a = 2 / 6$, $H_0 = 0.5 / 1 / 2$)

$B_0 = 20$ cm (attached to the wall)			$B_0 = 1$ m		
$Q_0 = 30$ l/min			$Q_0 = 60$ l/min		
h_a (cm)	h_0 (cm)	Name of the test	h_a (cm)	h_0 (cm)	Name of the test
12.8	19.2	ECRPP2H _a 2H ₀ 0.5B5	16.9	25.4	ECRPP2H _a 2H ₀ 0.5B1
	25.7	ECRPP2H _a 2H ₀ 1B5		33.9	ECRPP2H _a 2H ₀ 1B1
	38.5	ECRPP2H _a 2H ₀ 2B5		50.8	ECRPP2H _a 2H ₀ 2B1
35.5	57.7	ECRPP2H _a 6H ₀ 0.5B5	50.8	76.2	ECRPP2H _a 6H ₀ 0.5B1
	77	ECRPP2H _a 6H ₀ 1B5		101.6	ECRPP2H _a 6H ₀ 1B1
	115.5	ECRPP2H _a 6H ₀ 2B5		152.4	ECRPP2H _a 6H ₀ 2B1

To analyze the discharge concentration it is used the magnitude of the dilution but for the treatment of the results it was found more intuitive to work with the Percentage Increase in Salinity, IS%, which is also called Percentage of the Remaining Discharge, because it has the advantage that its value is always between zero (water of the environment) and one hundred (undiluted effluent).

$$IS_{\%} = 100 \times \left(\frac{s - s_a}{s_0 - s_a} \right) \quad (6)$$

with s salinity of the sample [psu]
 s_a salinity of the environment [psu]
 s_0 salinity of the effluent [psu]

4 Results

The aim is to study the mixing processes that affect the hypersaline effluent in contact with the marine environment. For this reason, the main measurements to be taken into account refer to the characteristic positions for this type of discharge (next to the point of discharge and certain distances from it) as well as the characteristics of the hyperdense layer formed on the bottom. These measurements are obtained for each performed test and are compared each other and with the different instrumentation used.

The specific results performed for each test are the following:

4.1 Visual results

1. Location of the representative points to take different measurements such as the conductivity and temperature.

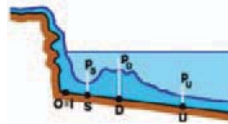


Figure 6: Sketch of the representative points for brine discharges from a cliff

2. Hyperdense layer thickness (it consists of homogeneous and interface layer thickness).
3. Overflow thickness to study laminar or turbulent flow regime.
4. Velocity of the hyperdense layer (tracking the head or using density marbles).
 Widening of brine discharge in the transversal axis (for B5 type tests).

4.2 Pipette results

Other results come from the dilution calculated through the samples obtained from the pipettes. They take profile measurements in different cross sections along the flume.

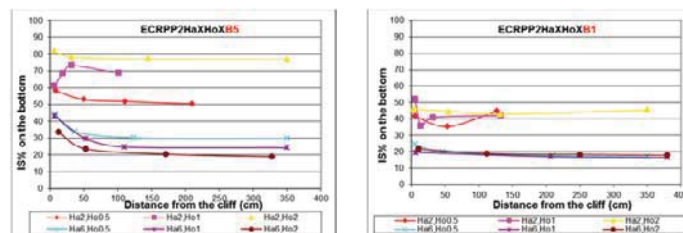


Figure 7: Bottom values obtained from the pipettes for each test at different points

4.3 Microconductivimeter results, MC

Usually, the MC was positioned next to a given pipette to compare both results but the difference is that the pipette provides an average of salinity during 2 or 3 minutes, while the MC gives statistical results, taking each measurement every 0.05sec., so it provides a powerful tool to observe the temporal variability.

The MC is located on the bottom of the physical model and for different characteristic zones.

4.4 Ultrasonic profiler velocity Doppler results, UPV

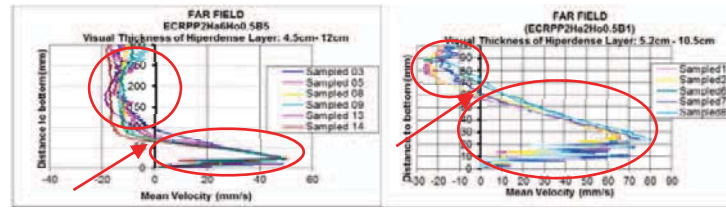


Figure 8: Several examples of the UPV results for two different test (B1 and B5)

The hyperdense layer velocity was measured with the UPV for certain moments within a test. In the graphs it is clear there are two different values. The positive velocities are placed on the bottom of the water column and they show the velocity of the density current meaning a forward movement of the hyperdense layer. The negative velocities are placed in the part of the water column above the hyperdense layer and they show the velocity of the entrainment meaning a reverse movement of the ambient. The velocity zero shows the interface between discharge and environment (Vila et al., 2010).

5 Conclusions

The conclusions try to explain the behaviour of the fluid and the hyperdense layer as well as the statistical and instantaneous values of the dilution to this particular type of brine discharge device. For this purpose the main variables that influence in this study, such as the height of the cliff and the depth of the column water, are specially considered.

- Behaviour.

The characteristic points have approximately the same position in each test except when the distance between the point of the discharge and the level of the seawater is the highest then these points are significantly more separated. On the other hand, brine discharge width across the transversal axis shows different behaviour. It gets wider before as the difference between the height of the cliff and the depth of the column water are getting higher.

- Dilution.

It is obtained better dilutions in the performed tests with high values of the depth of the receiving environment probably because of there is more turbulence so the brine fills the column. The dilution usually remains stable as we move along the longitudinal axis although in some cases it gets better values according to this direction.

- Statistical measurements.

Pipette dilution measurements usually are lower than microconductivimeter data because of it is compared values on the bottom and microconductivimeter sometimes is placed around one cm over it because its probe can be damaged.

It is observed more fluctuation for the statistical graphs taken from microconductivimeter measurements in the areas called I and D (see figure 6) because these are more turbulent zones.

- Hyperdense layer.

There are two different behaviours for the hyperdense layer thickness depending on the height of the water column. For low values, the hyperdense layer gets wider as the height of the cliff is lower but the effect is the opposite in the case of high values of the depth of the column water.

For the performed tests, in which the effects of the ambient conditions are not considered, dilution occurs very slowly due to a high density difference between the effluent and the

receiving environment. The project will be extend with new variables considering the effect of currents on the trajectory and dilution, taking into account one of the ambient condition with the highest influence on brine density current behaviour.

6 References

- Palomar, P.; Ruiz-Mateo, A.; Losada, I. J.; Lara, J. L.; Lloret, A.; Castanedo, S.; Álvarez, A.; Méndez, F.; Rodrigo, M.; Camus, P.; Vila, F.; Lomónaco, P.; Antequera, M. (2010): MEDVSA: a methodology for design of brine discharges into seawater. In: Desalination and Water Reuse, Vol. 20/1, pp. 21-25.
- Ruiz-Mateo, A.; Antequera, M.; González, J. (2008): Physical modelling of brine discharges to the sea, in Proceedings of the MWWD 2008 – 5th Internacional conferences on Marine Waste Water Discharges and Coastal Environment, Com 65. Cavtat, Croatia.
- Sánchez Lizaso, J.; Romero, J.; Ruiz, J.; García, E.; Buceta, J.; Invers, O.; Fernández, Y.; Mas, J.; Ruiz-Mateo, A.; Manzanera, M. (2008): Salinity tolerance of the Mediterranean seagrass *Posidonia oceanica*: recommendations to minimize the impact of brine discharges from desalination plants. In Desalination, Vol. 221, pp. 602-607.
- Vila, F.; Ruiz-Mateo, A.; Rodrigo, M.; Álvarez, A.; Antequera, M.; Lloret, A. (2010): 3D Physical Modelling in a wave flume of brine discharges on a beach, in Proceedings of the Euromed 2010 - Desalination for Clean Water and Energy, Com. 21. Tel Aviv, Israel.
- Centre for Studies on Ports and Coast (2003): Research on discharge into the sea of rejection water from desalination plants. Final report. CEDEX, Technical Report 23-500-7-005. In Spanish.
- Centre for Studies on Ports and Coast (2009): Behaviour of rejection water discharged into the sea from the desalination plant of Melilla. Final report. CEDEX, Technical Report 23-403-1-005. In Spanish.

Efficiency of artificial sandbanks in the mouth of the Elbe Estuary for damping the incoming tidal energy

Janina Sothmann¹, Dagmar Schuster², Jens Kappenberg³, Nino Ohle⁴

Abstract

The tidal system of the Elbe Estuary has changed significantly in the past. Due to anthropogenic interventions and natural changes flood plains were reduced and the friction of the Elbe Estuary decreased. As a result tidal range and sediment transport increased upstream. Furthermore the tidal wave propagates faster through the estuary and produces an increased tidal range in Hamburg. This leads to a heightening of the flooding risk along the Elbe Estuary. In the framework of the European Project THESEUS the efficiency of five different artificial sandbanks scenarios in the mouth of the Elbe Estuary for attenuating the incoming tidal energy by reflection itself or by increasing the friction is investigated by means of a hydrodynamical numerical model. The results show that the effect of sandbanks above mean sea level on the currents and water elevations is rather local, the sandbanks are only relevant during flood-tide, and will not change the hydrodynamics along the Estuary significantly. Another option, the introduction of underwater sandbanks in tidal creeks, seems to be more effective.

Keywords: coastal defence, artificial sandbanks, THESEUS, numerical modelling, damping tidal energy

1 Introduction

Coastal zones play a vital role in terms of settlement, industry, trade, agriculture and tourism to mention some key sectors. Even though they make up only a small part of the world's land area they are among the most densely populated zones. Since the concentration of people in coastal areas is expected to grow fast in the next decades and economies continue to develop the asset base of risk will increase. Furthermore global climate change will raise the likelihood of extreme events, as well as accelerate habitat decline. The combination of increasing economic and social values and the impacts of climate change will lead to a growing pressure on coastal systems (HORSTMAN ET AL. 2009).

The EU-Project THESEUS will investigate the applicability of innovative combined coastal mitigation and adaption technologies. Besides technical aspects, social, economic and environmental factors are included. The main aim is to deliver both a low-risk coast for human use and healthy habitats for evolving coastal zones subject to multiple change factors (THESEUS 2009). European Estuaries, like the Elbe Estuary, are under special investigation. The Elbe Estuary has undergone in the past several natural and anthropogenic changes. They led amongst others to a reduction of the friction of the Elbe Estuary and to an increase in tidal range. As a result the tidal wave enters the Estuary with more energy and the risk of flooding is heightened. In the framework of the THESEUS project the Helmholtz-Zentrum Geesthacht and the Hamburg Port Authority are investigating how artificial sandbanks in the mouth of the Elbe Estuary could be used to attenuate the tidal energy along the Elbe Estuary. In the following text the investigation area is introduced first and in a second step the simulated hydrodynamic measures and their effectiveness are presented.

¹ Helmholtz-Zentrum Geesthacht, Max-Planck-Strasse 1, 21502 Geesthacht, Janina.Sothmann@hzg.de

² Hamburg Port Authority AöR, Neuer Wandrahm 4, 20457 Hamburg, DagmarSchuster@hpa.hamburg.de

³ Helmholtz-Zentrum Geesthacht, Max-Planck-Strasse 1, 21502 Geesthacht, Jens.Kappenberg@hzg.de

⁴ Hamburg Port Authority AöR, Neuer Wandrahm 4, 20457 Hamburg, Nino.Ohle@hpa.hamburg.de

2 Area under investigation

2.1 Characteristics

The Elbe River reaches from the Giant Mountains in the Czech Republic to the German Bight, North Sea. With a length of about 1094 km and a catchment area of 148,268 km² the Elbe River is one of the important rivers of Europe. The tidally influenced part, the Elbe Estuary, extends from the tidal weir in Geesthacht to the North Sea and has a length of about 142 km (IKSE 2005).

The tidal system of the Elbe Estuary is influenced by the tidal wave entering the Elbe from the North Sea, the freshwater inflow from the catchment area of the Elbe and the characteristics of the Elbe River itself (BOEHLICH ET AL. 2008). The mean low water discharge of the Elbe River is about 145 m³s⁻¹, the mean fresh water run-off about 708 m³s⁻¹ and the mean high water discharge about 3620 m³s⁻¹ (DGM 2007). The tidal dynamic in the German Bight has a great influence on the hydrodynamic and morphodynamic processes in the Elbe Estuary. The tidal regime in the North Sea is characterized by a semidiurnal astronomical signal with two main constituents, the M2 and the S2 tide (SEISS ET AL. 2003). The amplitudes and phases of the tides are heavily modified by the basin bathymetry and already get deformed by the reflection in the German Bight. The tide in the Elbe Estuary has a mean period of 12 hours and 25 minutes and the tidal regime is characterized by a diurnal asymmetry. As the tidal wave is getting steeper during its way through the Estuary the duration of the flood is shorter than the duration of the ebb tide. The tidally influenced part of the Elbe River has an artificial border at the weir of Geesthacht. Except in the case of storm surges the tidal weir is closed and the tidal wave is reflected (FICKERT ET AL. 2007). The tidal wave is reflected at two further locations in the region of Hamburg, where the depth of the Elbe River decreases to -11.40 m below German datum and to -6.40 m below German datum, respectively (FICKERT ET AL. 2007).

2.2 Anthropogenic interventions

In the past the whole Elbe River has undergone a couple of anthropogenic changes. There have been several deepening events of the navigation channel. The outer and lower Elbe River was dredged between 1936 and 1950 up to -10 m and between 1957 and 1962 up to -11 m below Chart datum. Few years later, between 1964 and 1969, the channel was deepened up to -12 m and between 1974 and 1978 up to -13.50 m. Since 1999 the shipping channel reaches a maintained depth of -14.50 m below Chart datum (BOEHLICH ET AL. 2008). Further anthropogenic changes are the construction of the longitudinal dikes Kugelbake and Pagensand Nord, several extensions of the harbour of Hamburg, the building of underwater deposition areas or measures for flood protection (BOEHLICH ET AL. 2008).

Especially due to the construction of river barriers as flood protection measures, the foreshore areas of the tributaries are no longer available as flood plains. Although some measures within the mouth of the estuary helped to restrict storm surges, analyses by SIEFERT ET AL. (1988) showed that the total of the diking and poldering measures led to an increase of the maximum peak water level of almost half a meter in Hamburg during storm surges.

Moreover these anthropogenic interventions in combination with natural changes in hydrodynamics led to a reduction of the friction of the Elbe Estuary. As a result not only the storm surge levels, but also the tidal range, sediment transport and siltation rate increased upstream. The tidal range of the monitoring station St. Pauli for example augmented in the last century from 160 cm to 360 cm (FREITAG ET AL. 2008).

2.3 Model area

For the model simulations an area was chosen which is large enough to simulate the physical processes in the Elbe Estuary (Figure 1). The model area reaches from the weir of Geesthacht in the southeast to the German Bight in the northwest.

3 Scenario simulations

3.1 Positions and characteristics of the different sandbank scenarios

In the framework of this paper five different sandbank scenarios are simulated. Form and positions of the sandbank scenarios are shown in Figure 1. All sandbanks have a maximum height of 4 m above German datum and are placed in regions which are considered as morphological relatively stable. Sandbank scenario 1 consists of two sandbanks in the west and east of the Medemrinne. Together they have a volume of about 3.62 Mio m³. Sandbank scenario 2 is made up by one sandbank on the south coast of the Elbe River on the opposite of Brunsbüttel (volume of about 2.06 Mio m³) and scenario 3 by one sandbank in the opening mouth in the near Cuxhaven (volume of about 3.32 Mio m³). Sandbank scenario 4 combines all artificial sandbanks of scenario 1-3. This simulation is carried out to show whether there is a cumulative effect or not. The fifth scenario, a hypothetical one, is an extension of scenario 1 and has a volume of about 21.7 Mio m³.

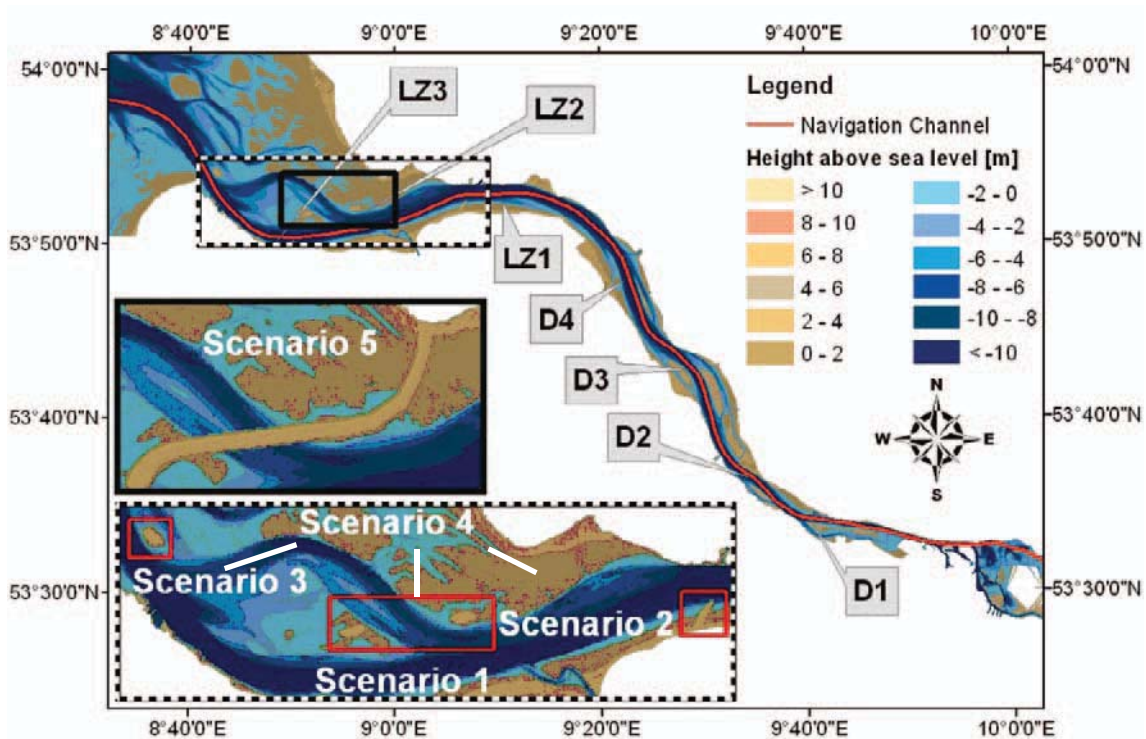


Figure 1: Form and position of the investigated artificial sandbanks. Monitoring stations D1-D4, LZ1-LZ3 (Reference: authors design).

3.2 Monitoring Stations

To investigate the effects of the different scenarios on water level and current velocity seven monitoring stations along the Elbe Estuary are considered (D1-D4 and LZ1-LZ3). Monitoring station D1 is situated close to the Port of Hamburg and LZ3 is placed in the outer Estuary (Figure 1). At the positions of the stations the modelled time-series of water level and current velocity are compared to the reference situation (no sandbanks) and the recorded current velocity data.

4 Numerical simulations

4.1 Hydrodynamic model TRIMNP

For numerical simulations an extension of the hydrodynamic model TRIM (Tidal, Residual, Intertidal Mudflat Model), called TRIMNP (Nested Parallel Processing), is applied. The depth-averaged 2-dimensional hydrodynamic model calculates the water level and current velocity on a rectangular horizontal grid. To solve the depth averaged shallow water equations a semi-

implicit, time-stepping, finite-difference method is used (CHENG ET AL. 1993). As most tidal hydrodynamic processes are convection dominated, the advection terms in the momentum equations are solved by an Eulerian–Lagrangian method (ELM). The model is also able to treat flooding and drying of computational cells. The governing equations include the conservation equations of mass, momentum, conservative scalar variables, and an equation of state (CHENG ET AL. 1993).

To allow the investigation of the effects of the artificial sandbanks on water level and currents in the inner estuary a spatial resolution of 50 m and a temporal resolution of 15 minutes is used. The time domain of the simulations is the year 2006. As CHENG ET AL. (1993) figured out the numerical method is “unconditionally stable” if the baroclinic forcing is ignored. For this reason and out of time restrictions the barotropic version was applied.

The model is driven on the north western open boundary by the model outputs water level and current velocity of the operational circulation model of the German Federal Maritime Office (BSH). This 3-dimensional model is daily run on two spherical grid nets. For this purpose the results of the grid including the German Bight and the western Baltic Sea are applied. The model calculates currents, water levels, water temperatures, salinity and ice cover. Grid spacing in the German Bight and the western Baltic Sea is 1.8 km. Model inputs are current meteorological conditions, tides and river runoff as well as external surges which enter the North Sea from the Atlantic.

Another forcing parameter is the freshwater inflow from upstream. These data are daily values measured 53 km upstream of the weir Geesthacht at the village Neu Darchau. A further boundary condition is the wind over the model area. Wind data are model outputs of the regional climate model REMO for the year 2006.

The bathymetry of the year 2006 serves as reference situation. This bathymetry is modified in the different sandbank scenarios and the results of the model runs are compared to the reference situation. No other parameters are changed, so variations in current velocities and water levels can be clearly referred to the hydraulic measures.

4.2 Model Validation

The validation of the original model TRIM has already been carried out for San Francisco Bay, California (CHENG ET AL. 1993). They found that the model is stable and computationally efficient. As an extended version of the original model TRIM is used, further model validations are implemented. Comparisons between the model outputs and measured values of the applied model for the Elbe Estuary have shown that there is a good agreement in current velocities between modelled and measured values. On the other hand, comparisons of modelled and measured water levels show that the low tide is underestimated. This is caused by the uncertainties of the water level boundary data. For this reason modifications of all input parameters are carried out and re-investigated. Validations resulting from modifications of the input parameters tidal amplitude and bottom friction are discussed in the following sections. Modifications of the wind will be done soon.

4.2.1 Modifications of the tidal amplitude

In a first step, model outputs of the tidal amplitude of the driving model are set 1.5-times higher and in a second step tidal amplitude is halved. Those two modifications are run for the reference scenario and the scenario 4, including four sandbanks. First model results of the reference scenario with the ‘normal’ amplitude are compared to the reference scenario with the 1.5-times higher amplitude. Results show that the 1.5-times higher amplitude leads to an increase of about 0.6 m in mean maximum high water level at the different monitoring stations (Table 1). Mean minimum low water level decreases on average about 0.39 m, mean maximum flood current velocity increases about 0.23 ms^{-1} and mean minimum ebb current velocity increases about 0.11 ms^{-1} at the different monitoring stations. The same results can be found for scenario 4.

Furthermore effects of scenario 4 with the modified amplitude (difference between scenario four and the reference scenario, in each case with increased amplitude of 1.5) on water level and

current velocity are considered. The differences are in the same order of magnitude like those of the scenario 4 with the 'normal' amplitude (Chapter 5.1).

Table 1: Differences between the modified and the original scenarios. Differences are means of the seven monitoring stations (Reference: authors design).

Scenario	Modification	Mean max. HW level (m)	Mean min. LW level (m)	Mean max. flood CV (ms ⁻¹)	Mean max. ebb CV (ms ⁻¹)
Reference	1.5 Amplitude	0,60	-0,39	0,23	0,11
Scenario 4	1.5 Amplitude	0,59	-0,39	0,22	0,10
Reference	Friction 10 ⁻⁶	0,12	-0,14	0,12	0,09
Scenario 4	Friction 10 ⁻⁶	0,12	-0,14	0,12	0,09
Reference	Friction 10 ⁻⁴	-0,14	0,13	-0,13	-0,10
Scenario 4	Friction 10 ⁻⁴	-0,13	0,13	-0,13	-0,10

4.2.2 Modifications of the bottom friction

The second part of the validation is made up by modifications of the bottom friction. In the reference situation the bottom friction is set in the whole investigation area to the roughness length 10⁻⁵ m. This constant is firstly modified to a roughness length of 10⁻⁶ m and secondly to a roughness length of 10⁻⁴ m. Both modifications are run for the reference situation and scenario 4. A reduction of the friction from 10⁻⁵ m to 10⁻⁶ m in the reference scenario leads to an increase in mean maximum high water level of about 0.12 m and a decrease in mean minimum low water level of about 0.14 m at all monitoring stations (Table 1). Maximum flood current velocity increases about 0.12 ms⁻¹ and minimum ebb current velocity increases about 0.09 ms⁻¹. For scenario 4 (with modified roughness length) the same values are found.

An increase of the bottom friction from 10⁻⁵ m to 10⁻⁴ m in the reference scenario leads to a decrease in mean maximum high water level of about 0.14 m and an increase in mean minimum low water level of about 0.13 m at all monitoring stations. Maximum flood current velocity decreases about 0.13 ms⁻¹ and minimum ebb current velocity also decreases about 0.10 ms⁻¹ (Table 1). For scenario 4 (with modified roughness length) similar values can be found.

Furthermore effects of scenario 4 with modified friction (difference between scenario 4 and the reference scenario, in each case with increased/decreased friction) on water level and current velocity are considered. Effects on water level as well as effects on current velocity remain in each case almost the same as in the model runs with the 'normal' friction (Chapter 5.1).

The results of the model runs with modified amplitude and bottom friction show that the model is sensitive to changes of input parameters. Furthermore it could be demonstrated that - even if some input parameters are changed - the differences between the reference scenario and scenario 4 remain almost the same as in the runs with the original parameters. As for the purpose of this study only differences between the reference situation and the sandbanks scenarios are considered it could be shown that simplified assumptions like treating the bottom friction as a constant have for this purpose no influence on the accuracy of the results.

5 Results

To investigate the efficiency of the different scenarios differences in water level and current velocity between the reference scenario and the sandbank scenarios are analyzed. As an indication for the effectiveness of the sandbanks scenarios the resulting maximum and minimum values are relevant and therefore discussed.

5.1 Efficiency of sandbank scenario 1-4

First the effects of sandbank scenarios 1-3 on maximum high water and minimum low water level at the different monitoring stations are investigated. Results show that on average none of these sandbank scenarios has a significant influence on maximum or minimum values. There is also no change in mean maximum high and mean minimum low water level when all sandbanks are simulated together (scenario 4).

In a second step effects of sandbank scenario 1-3 on current velocity are examined. Sandbank scenario 1 and 2 as well as scenario 3 has on average no significant influence on maximum flood current or ebb current velocity at the different monitoring stations. Scenario 4 also causes no significant change. Summarized even though all sandbanks have a relatively great volume none of them shows a significant influence on water level or current velocity at the different monitoring stations.

To explain this flood and ebb currents are considered. Figure 2 shows the differences in flood currents between the reference scenario and scenario 4 on October the 1st of the year 2006 at 3 AM. The differences in flood currents are in the whole investigation area relatively small (1 to 4 cm s^{-1}). Only in the vicinity of the sandbanks and in the north western part of the Elbe Estuary greater differences can be detected. During the ebb tide two of four sandbanks fall completely dry (sandbanks of scenario 1). Hence, the sandbanks have no influence on the hydrodynamic regime of the Elbe Estuary during the maximum ebb tide (Figure 3). The remaining two sandbanks lead to modifications of the ebb currents in the surrounding areas. Largest modifications can be detected in the Medemrinne.

This leads to the conclusion that the different sandbanks of sandbank scenario 1-4 cause changes in currents and water levels during the flood tide in the vicinity of the sandbanks in the mouth of the Estuary but show small effects in the further upstream parts of the study site. Hence an attenuation of the incoming tidal energy along the Elbe Estuary cannot be achieved.

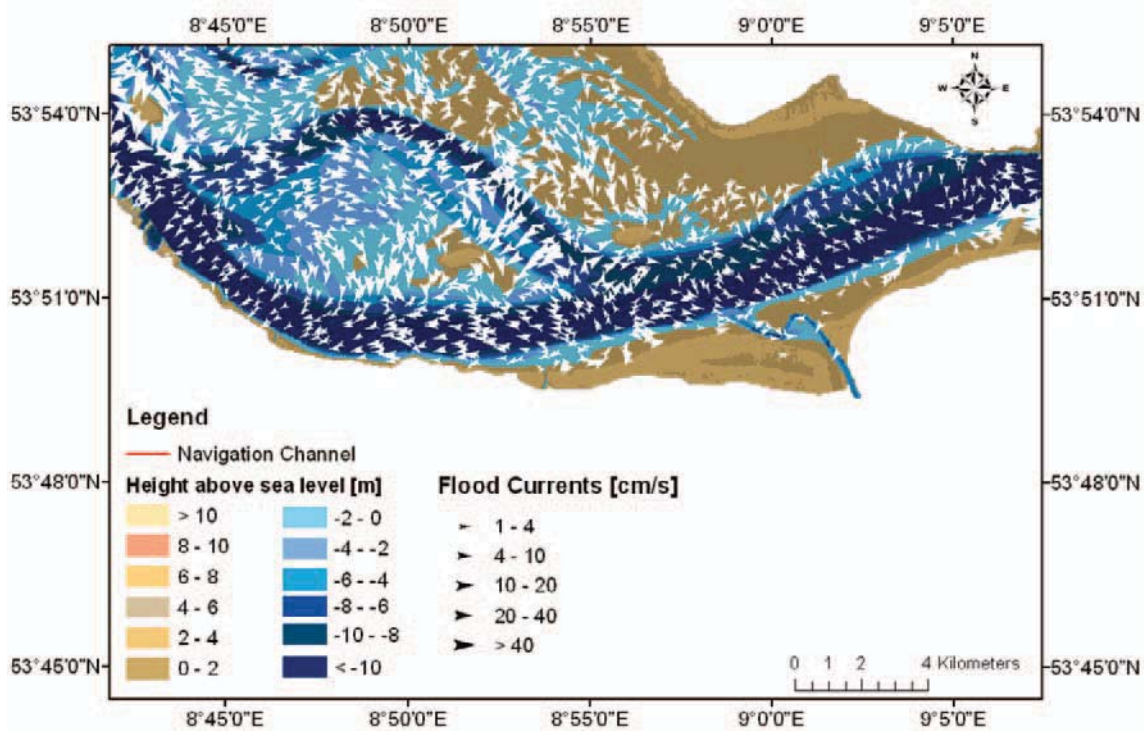


Figure 2: Differences in flood currents [cm/s] between the reference scenario and the scenario 4 on October the 1st in the year 2006 at 3 AM (Reference: Authors design).

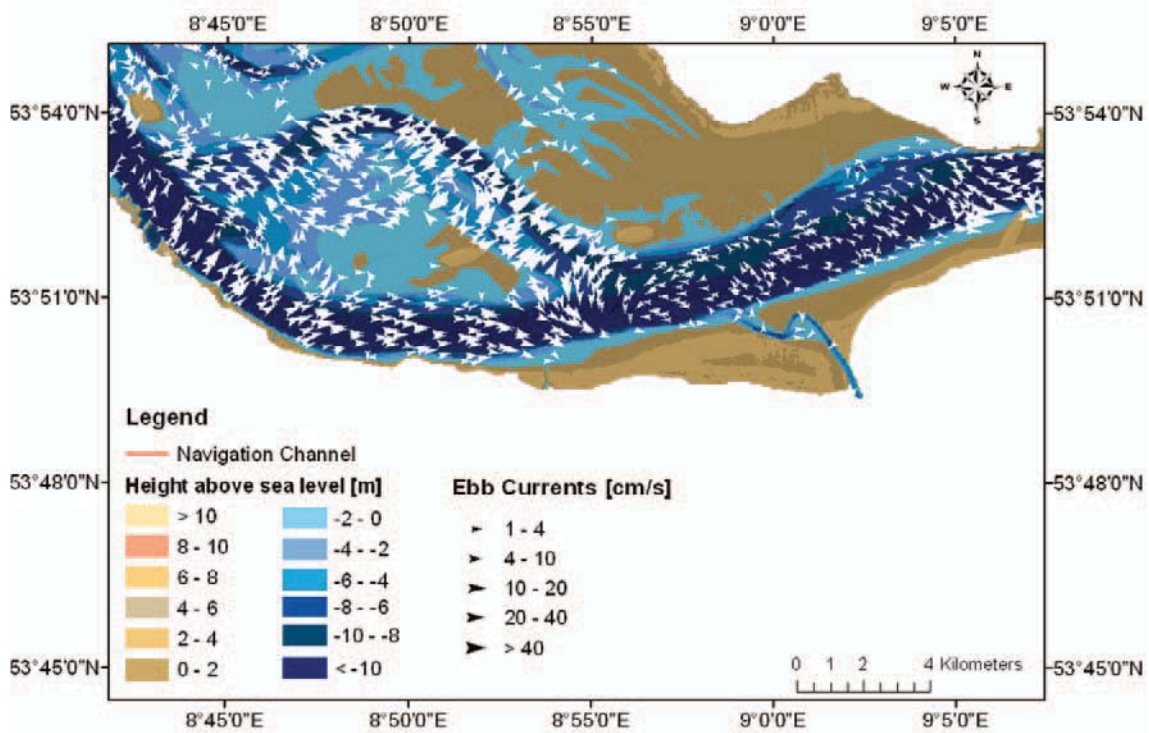


Figure 3: Differences in ebb currents [cm/s] between the reference scenario and the scenario 4 on October the 1st of the year 2006 at 10 AM (Reference: Authors design).

5.2 Efficiency of the hypothetical sandbank scenario 5

As the sandbank scenarios 1-4 show no significant influence on water level and current velocity at the seven monitoring stations a fifth sandbank scenario of larger extend is investigated. This scenario is a hypothetical enhancement of scenario 1 and leads from the northern margin of the Elbe River to the navigation channel (Figure 1). This scenario is classified as hypothetical as an implementation will be impossible due to nautical, nature conservation and legal feasibility reasons.

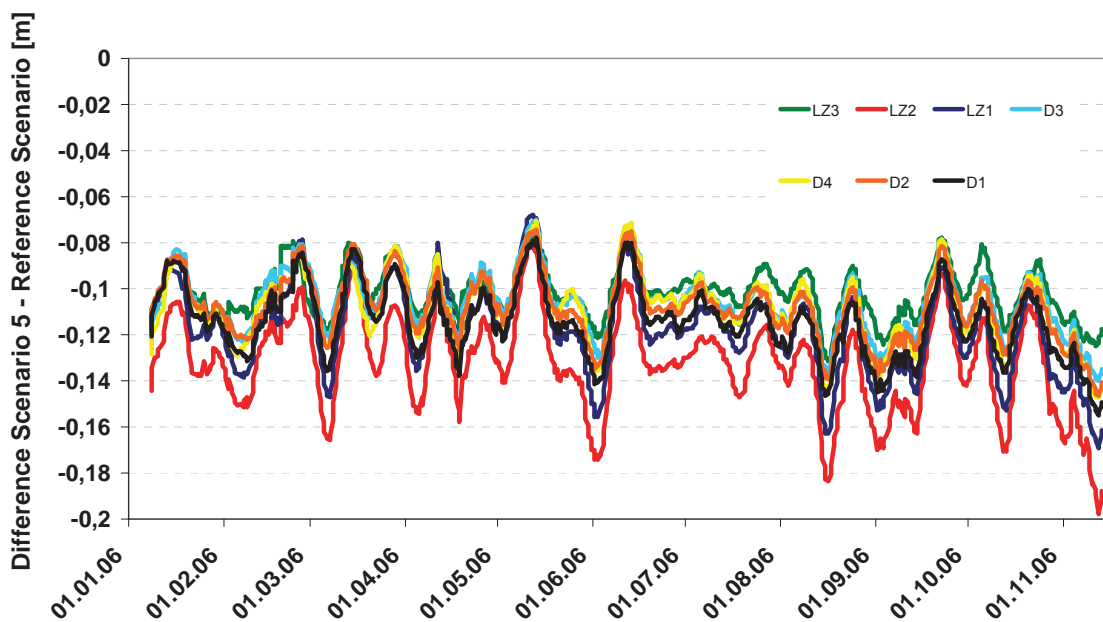


Figure 4: Differences between scenario 5 and the reference scenario: 7-Days moving average of maximum high water level [m] (Reference: Authors design).

Again, differences in water level and current velocity between the reference scenario and the scenario 5 are analyzed. Figure 4 shows that mean maximum high water level decreases at all monitoring stations about 12 cm. Mean minimum low water level increases at the different monitoring stations between 4 to 16 cm (Table 2). Differences in current velocities could be also found. Mean maximum flood current velocities decrease in the upper part of the Elbe Estuary (monitoring station LZ1, D1-D4) up to 6 cms^{-1} . In the lower part, at the monitoring station LZ3, an increase in mean maximum flood current velocity of about 33 cms^{-1} can be detected. Mean maximum ebb current velocity also increases at the monitoring station LZ3 but experiences in mean a decrease at the other monitoring stations (2 to 7 cms^{-1}).

Table 2: Differences in water level and current velocity between scenario 5 and the reference scenario at the different monitoring stations (Reference: Authors design).

Variable / Station	LZ3	LZ2	LZ1	D4	D3	D2	D1
Mean Maximum HW Level [m]	-0,10	-0,13	-0,12	-0,11	-0,11	-0,11	-0,11
Mean Minimum LW Level [m]	0,04	0,16	0,16	0,15	0,14	0,14	0,14
Flood Current Velocity [ms^{-1}]	0,33	0,01	-0,02	-0,02	-0,05	-0,06	-0,06
Ebb Current Velocity [ms^{-1}]	0,07	-0,07	-0,05	-0,02	-0,05	-0,05	-0,03

6 Discussion

In the past the tidal system of the Elbe Estuary has changed significantly. One possible opportunity to reduce this incoming energy is to reflect it in the mouth of the Estuary. One hydrodynamic measure is the construction of artificial sandbanks. Analysis of the simulations of the first four sandbank scenarios show that they cause modifications of water levels and current velocities in their surroundings in the mouth of the Elbe Estuary. In contrast further upstream those hydrodynamic measures have no significant influence on water level and current velocities. Analysis of ebb and flood currents suggests that the different sandbanks lead only to a small reflection of the incoming tidal energy but to a stronger redirection. In a second step a hypothetical fifth sandbank scenario is carried out. As investigations show this sandbank leads to modifications of the water level and the current velocities. As the fifth sandbank closes the Medemrinne, an important channel for the water body, the incoming tidal energy is partly reflected. In the southern part of the sandbank the water is redirected through the navigation channel. This leads to an increase in current velocities at the nearest located monitoring stations.

7 Conclusion and outlook

Five different sandbank scenarios in the mouth of the Elbe Estuary have been simulated in the framework of this paper. The aim was to investigate if they could be used to damp the tidal energy along the Elbe River in order to get safer coasts. As results show the first four sandbank scenarios only lead to a redirection of the incoming tidal energy. Water levels and current velocities are only modified in the vicinity of the sandbanks. In contrast the hypothetical sandbanks scenario 5 leads to modifications of the investigated variables at the different monitoring stations. As the important natural water way, the Medemrinne, only the southern part of the water body could be redirected through the navigation channel. As a result the incoming tidal energy could be partly reflected.

As the fifth scenario is only a hypothetical one, further investigations of various sandbank scenarios are necessary. Furthermore the efficiency of the sandbank scenarios under storm surge and climate change conditions will be analyzed.

8 Acknowledgements

The support of the European Commission through FP7.2009-1, Contract 244104 - THESEUS ("Innovative technologies for safer European coasts in a changing climate"), is gratefully acknowledged.

9 References

- Boehlich, M.J., Strotmann, T. (2008): The Elbe Estuary. In: Die Küste, Archive for Research and Technology on the North Sea and Baltic Coast, Heft 74, 288-306.
- Casulli, V., Walters, R.A. (2000): An unstructured grid, three-dimensional model based on the shallow water equations. In: International Journal for Numerical Methods in Fluids. Vol. 32, 331-348.
- Cheng, R.T., Casulli, V., Gartner, J.W. (1993): Tidal, Residual, Intertidal Mudflat (TRIM) Model and its Applications to San Francisco Bay, California. In: Estuarine, Coastal and Shelf Science. Vol. 36, 235-280.
- Fickert, M., Strotmann, T. (2007): Hydrodynamische Entwicklung der Tideelbe. In: Coastline Reports. Vol. 9, 59-68.
- Freitag, C., Ohle, N., Strotmann, T., Glindemann, H. (2008): Concept of a sustainable development of the Elbe Estuary. In: Proceedings of the 5th IAHR Symposium on River, Coastal and Estuarine Morphodynamics (RCEM 2007), Enschede, The Netherlands, 17.09.-21.09.2007, Vol. 2, 1085-1092.
- Horstmann, E.M., Wijnberg, K.M., Smale, A.J., Hulscher, S.J.M.H. (2009): On the consequences of a long-term perspective for coastal management. In: Ocean and Coastal Management. Vol. 52, 593-611.
- IKSE (2005): Die Elbe und ihr Einzugsgebiet. Ein geographisch-hydrologischer und wasserwirtschaftlicher Überblick. Magdeburg.
- Seiss, G., Pluess, A. (2003): Tideverhältnisse in der Deutschen Bucht. In: Mitteilungsblatt der Bundesanstalt für Wasserbau. Vol. 86, 61-64.
- Siefert, W., Havnoe, K. (1988): Einfluß von Baumaßnahmen in und an der Tideelbe auf die Höhe hoher Sturmfluten. In: Die Küste, Archive for Research and Technology on the North Sea and Baltic Coast, Heft 47, 51-101.
- THESEUS (2009): Protecting our coasts. <http://www.theseusproject.eu/>

Estimation of wave attenuation over *Posidonia Oceanica*

Theoharris Koftis¹ and Panayotis Prinos²

Abstract

Submerged vegetation, such as seagrasses has the following functions regarding hydrodynamic aspects; wave attenuation, protection of the hinterland from wave attack, stabilizing the seabed. The purpose of the present study is to quantify the effect of submerged vegetation and more specifically of *Posidonia oceanica* on wave attenuation. The data of large scale experiments, conducted in the CIEM flume of UPC for irregular water waves over artificial *P. oceanica* meadow, are analyzed. Results show that the wave height attenuation over the meadow, ranges from 10%-35%, depending on the plant characteristics, such as the submergence ratio $\alpha = h_s/h$ (h_s : meadow height, h : water depth) and plant density N (stems/m²) and the wave period. The effect of these parameters on the wave damping coefficient K_v is quantified. The drag coefficient C_d , characteristic for the *P. oceanica* is estimated, which can be used for the calculation of the wave attenuation in numerical studies.

1 Introduction

The importance of coastal vegetation, such as seagrasses and salt marshes, regarding biological and physical aspects has been well recognized (Borum et al. 2004). Due to their capacity to alter their environment, seagrasses have been referred to as "ecosystem engineers", because they partly create their own habitat: the leaves attenuate wave and current action increasing sedimentation and the seagrass roots and rhizomes stabilize the seabed.

The most common seagrass species in the Mediterranean Sea is *Posidonia Oceanica*, which can colonize soft substrates such as sand in wave-sheltered areas and also attach to rocks being exposed to relatively high wave energy wind driven currents (Koch et al, 2006). *P. oceanica* seagrass meadows are usually distributed in shallow areas from the surface to a depth of 30-40 m in clear conditions, while the plants density varies from sparse (<150 stems/m²) found in deeper waters to dense (>700 stems/m²) (Giraud (1977)). The plant has ribbon-like leaves, 1.0 cm wide and up to 1.0 m long. Regarding the ability to attenuate wave energy, it depends both on the seagrasses characteristics (the seagrass density, the canopy height, the stiffness of the plant and the bending of the shoots) and the wave parameters (wave height, period and direction)

Various studies on wave attenuation due to coastal vegetation have been performed. In Fonseca and Cahalan (1992) flume study of four species of seagrass, the wave attenuation was found 20% - 76% over 1 m length when the plants were occupying the entire water depth. In early theoretical and numerical studies the plants (particularly flexible ones) have been simulated as rigid cylinders with different values to the drag coefficient (Dalrymple et al 1984, Kobayashi et al 1993). Mendez and Losada (2004) developed an empirical model which includes wave damping and wave breaking over vegetation fields on variable depths. Suzuki and Dijkstra (2007) used a VOF model to simulate wave attenuation over strongly varying beds and vegetation fields, where among others they showed that the complex relationship between storm waves and seagrass-induced wave attenuation still needs to be verified. Recently Li and Zhang (2010) developed a 3D RANS model to investigate the hydrodynamics and mixing induced by random waves on vegetation, which is represented as an array of cylinders with the drag coefficient expressed with an empirical relation. Regarding the estimation of the plant's drag coefficient C_d , characteristic of the seagrass plant, an empirical relationship is given with

¹ Hydraulics Laboratory, Department of Civil Engineering, Aristotle University of Thessaloniki, 54124, Thessaloniki, Greece, thkoftis@civil.auth.gr

² Hydraulics Laboratory, Department of Civil Engineering, Aristotle University of Thessaloniki, 54124, Thessaloniki, Greece, prinosp@civil.auth.gr

the Reynolds number as in Mendez (1999) and Cavallaro et al. (2010) or the Keulegan-Carpenter number (Mendez and Losada, 2004)

In the present work, the data of large scale experiments, conducted in the CIEM flume for irregular waves over artificial *Posidonia oceanica* meadow, are analyzed. The study focuses on the effects of the submergence ratio $\alpha = h_s/h$ (h_s =height of seagrass, h =water depth) and the seagrass density N (stems/m²) on the wave height attenuation. The effect of these parameters on the wave height damping coefficient, which is often used in literature for wave-vegetation interactions is quantified. An empirical relationship for the drag coefficient C_d related to the Reynolds number, is obtained, characteristic for the plant of *P. oceanica*, which can be useful in numerical studies of wave-submerged vegetation interactions.

2 Experimental setup

The experiments were conducted in the CIEM large wave flume (Canal d'Investigació i Experimentació Marítima) at the Universitat Polytechnica de Catalunya, Barcelona. A series of experiments were performed for waves propagating over artificial *Posidonia Oceanica* patch in intermediate and shallow waters. The CIEM wave flume is 100 m long, 5 m deep and 3 m wide. A sandy slope beach of 1:15 was installed at the end of the flume for the elimination of wave reflection. A 20 m long horizontal and flat sandy area was created in the central part of the flume and the patch of artificial *P. oceanica*, with a total length $L=10.70$ m and height $h_s=0.55$ m, was placed above, as shown in Figure 1.

The artificial seagrass meadows were made of polypropylene strips and carefully designed to reproduce the flexibility and buoyancy properties typical of the natural *P. oceanica* plants. Figure 2 shows the dimensions and structure of the mimics. More details about the experimental setup and the artificial plant characteristics can be found in Stratigaki et al. (2010).

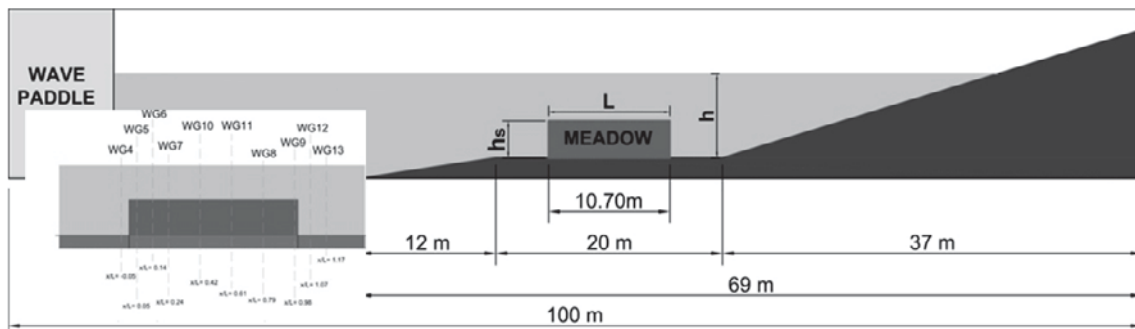


Figure 1: Sketch of the experimental setup of the CIEM flume

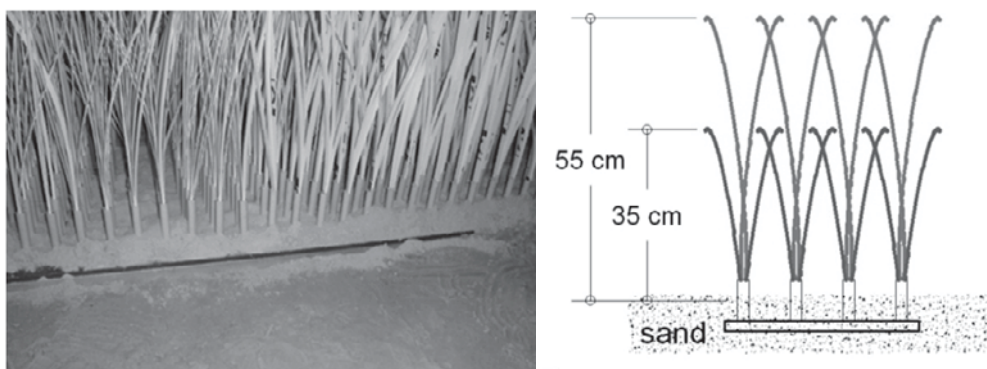


Figure 2: Detail and schematic detail of the artificial *Posidonia Oceanica*

Wave transformation was monitored by wave gauges distributed along the flume; the location of the wave gauges along the artificial meadow is shown in Figure 1. The experiments were performed for irregular waves over the artificial *P. oceanica* meadow, with four different submergence ratios ($\alpha=h_s/h$ equal to 0.32, 0.37, 0.42 and 0.50) and two seagrass densities

($N=180$ and 360 stems/ m^2). A summary of the wave and plant characteristics is shown in Table 1.

Table 1: Wave and plant characteristics

Water depth h (m)	Peak wave period T_p (s)	Wave height H_s (m)	Wave length L (m)	h/L	Plant density N (stems/ m^2)	Submergence ratio $\alpha=h_s/h$
1.10	2.0	0.28				0.32
1.30	3.0	0.30			180	0.37
1.50	3.5	0.35	5.36-17.34	0.09-0.29	360	0.42
1.70	4.0	0.40				0.50
	4.5					

3 Analysis of results

3.1 Wave height attenuation

An analytical expression for the wave height decay over submerged vegetation is given in equation (1), as presented in Dalrymple et al. (1984) and Mendez and Losada (2004):

$$H = K_v H_o \quad (1)$$

with H wave height [m]. For irregular waves is the root mean square wave height, H_{rms}

H_o incident wave height before meadow [m]. For irregular waves is $H_{rms,o}$

K_v damping coefficient, defined in equation (2)

$$K_v = \frac{H}{H_o} = \frac{1}{1 + \beta x} \quad (2)$$

with β parameter related to the plant and wave characteristics

x distance along meadow [m]

For irregular waves, the conservation of energy equation leads to the following expression for β (Mendez and Losada, 2004).

$$\beta = \frac{1}{3\sqrt{\pi}} C_d b_v N H_o k \left[\frac{\sinh^3 kah + 3 \sinh kah}{(\sinh 2kh + 2kh) \sinh kh} \right] \quad (3)$$

with C_d average drag coefficient of the meadow

b_v plant area per unit height of each vegetation stand normal to horizontal velocity [m]

k wave number [m^{-1}]

From the above parameters, the difficulty is to estimate the drag coefficient C_d , which is characteristic for each submerged plant's stiffness; work that is performed in paragraph 3.3. In the following figures (Figure 3, 4) the experimental results for the damping coefficient K_v ($=H/H_o$) are shown, together with the plot of equation (2). The details of each experimental test and the value of C_d as computed are also shown. It can be seen that the experimental wave height distribution along the meadow follows the proposed analytical equation given from theory. The wave damping varies and is related to the plant and wave characteristics as shown in the next paragraph 3.2.

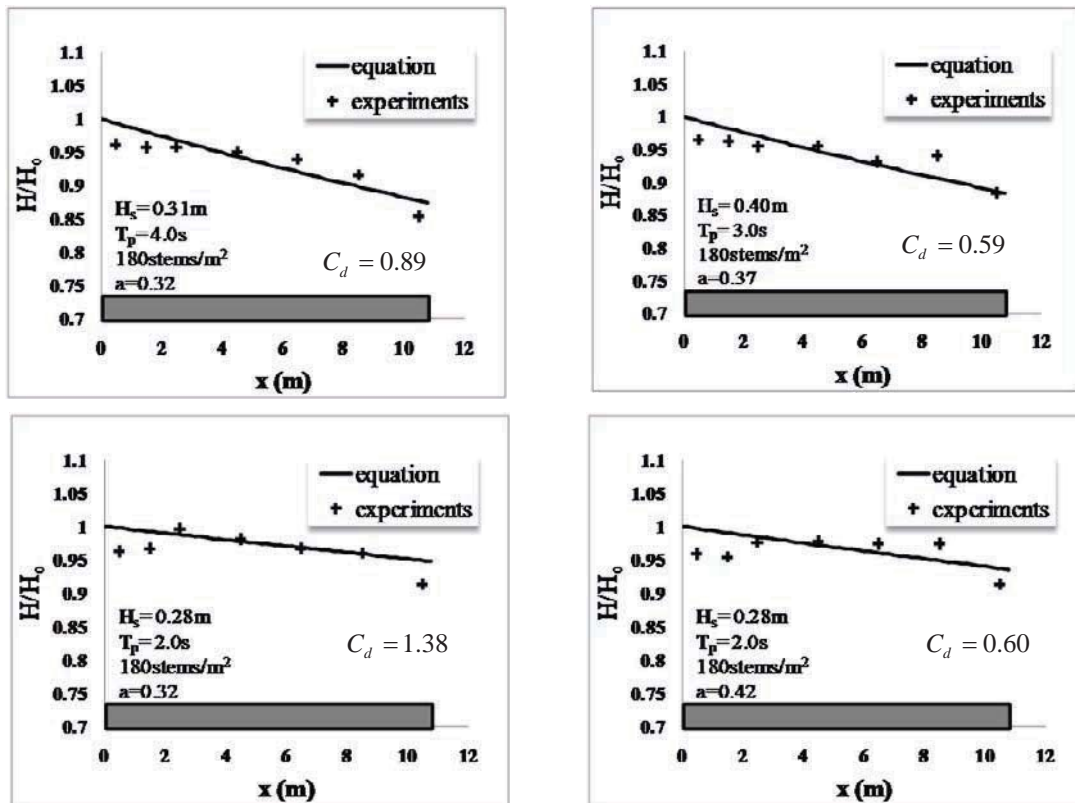


Figure 3: K_v variation over artificial *P. oceanica* meadow ($N=180$ stems/ m^2).

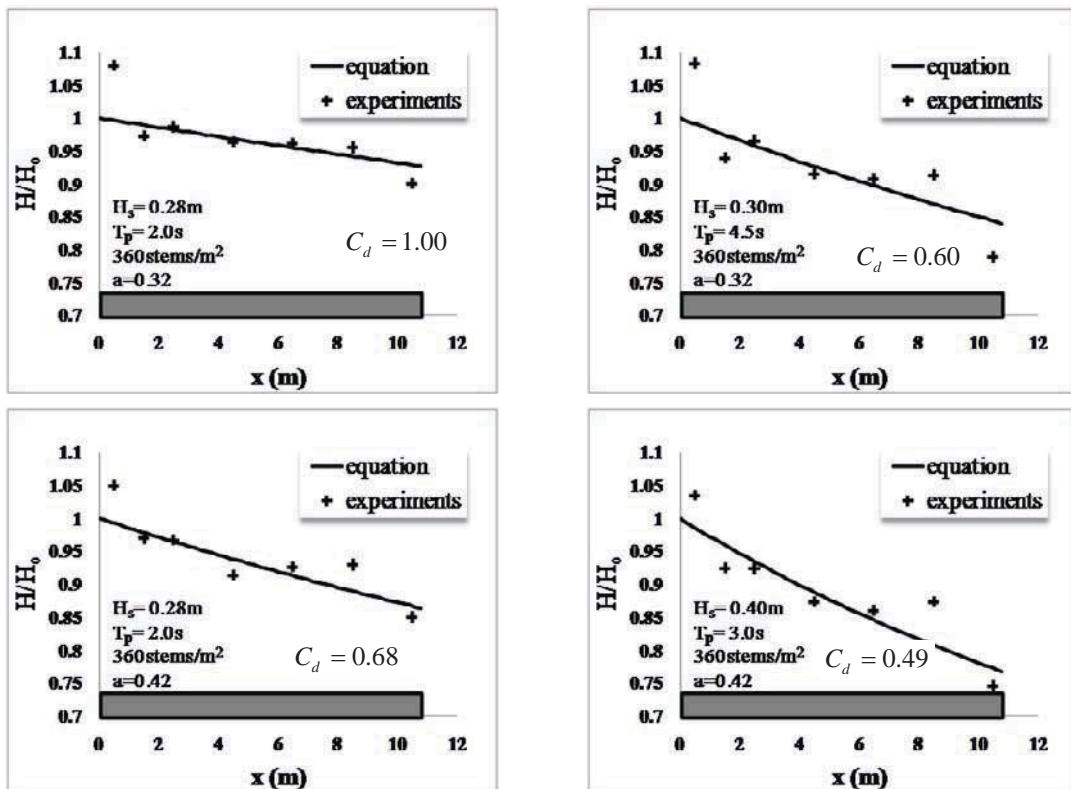


Figure 4: K_v variation over artificial *P. oceanica* meadow ($N=360$ stems/ m^2).

3.2 Effect of plant and wave characteristics on wave damping coefficient

3.2.1 Effect of submergence ratio h_s/h and plant density N

The effect of the submergence ratio on wave attenuation is shown in Figure 5 where K_v is plotted for same wave conditions ($H_s = 0.28$ m, $T_p = 2$ s) and density $N = 360$ stems/ m^2 and 180 stems/ m^2 respectively. For both densities the incident wave height (H_0 as measured in $x/L = -0.05$) is reduced by ~15-25%, with larger attenuation observed for the more dense meadow. It can also be noticed that due to the “plant resistance” to the flow, in the upward side of the meadow, part of the wave energy is reflected and the wave height increases ($x/L = 0.05$) for the more dense case (360 stems/ m^2). The effect of submergence ratio on wave attenuation is also evident.

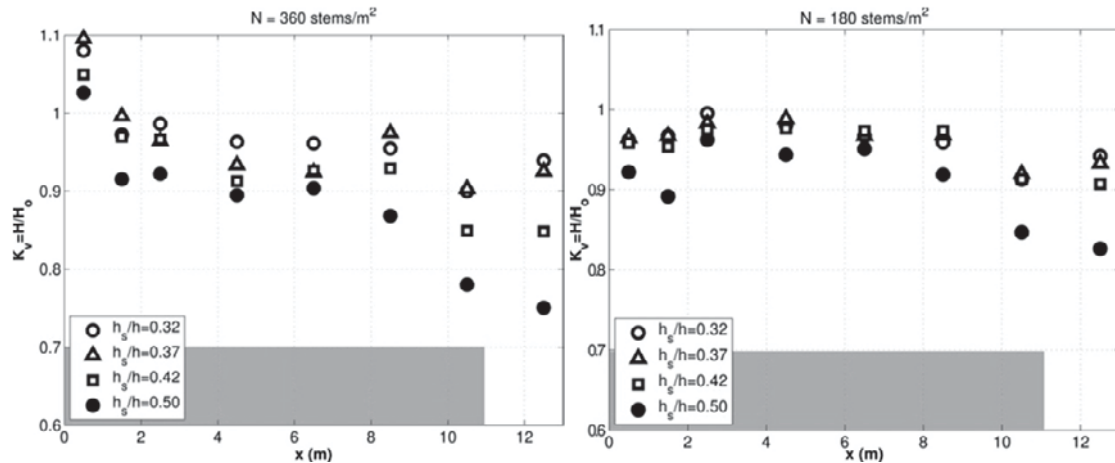


Figure 5: K_v variation over the meadow for various submergence ratios h_s/h . $N=360$ stems/ m^2 (left) and $N=180$ stems/ m^2 (right).

3.2.2 Effect of wave period T_p

The effect of the wave period T_p on wave attenuation is shown in Figure 6 where K_v is plotted for same plant configuration ($N=360$ stems/ m^2 and 180 stems/ m^2 respectively, $h_s/h=0.50$) and variable wave conditions. The longer waves are mostly attenuated from the artificial meadow with maximum wave attenuation up to 35% observed for $T_p=4$ s and the dense plant ($N=360$ stems/ m^2).

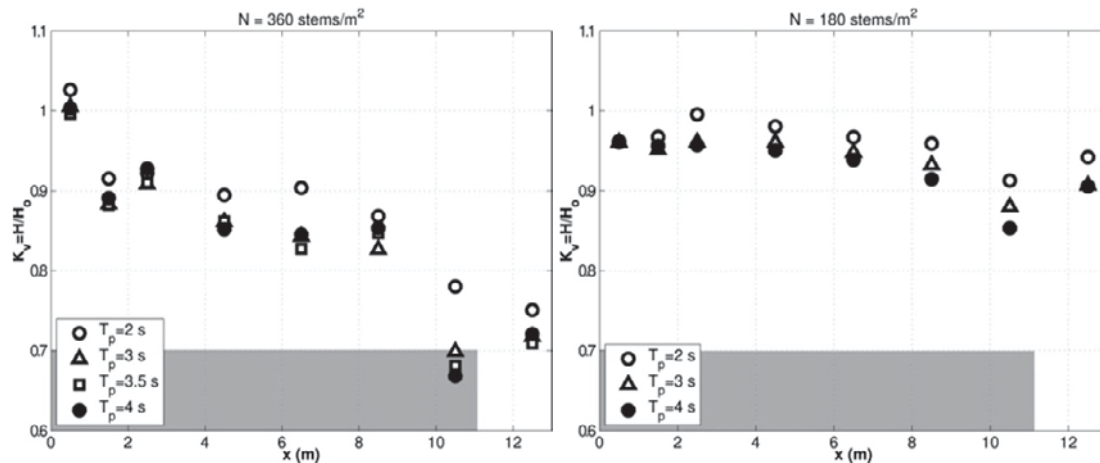


Figure 6: K_v variation over the meadow for various T_p . $N=360$ stems/ m^2 (left) and $N=180$ stems/ m^2 (right).

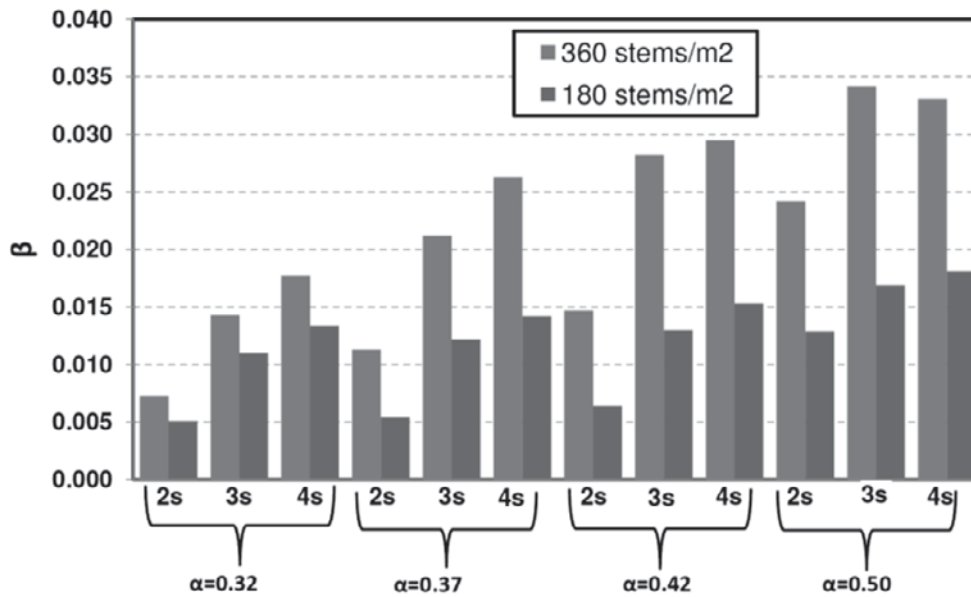


Figure 7: β parameter variation for various experimental configurations

The effect of the above characteristics on the β parameter which is used for the calculation of the damping coefficient K_v is shown in Figure 7, where values of β range from 0.005 to 0.035. It is shown that a 50% increase of the submergence ratio, α (from 0.32 to 0.50) results in average 117% increase of β . Also a 100% increase of the plant density, N (from 180 to 360) results in average 80% increase of β . The effect of the wave period is also significant since a 100% increase of T_p (from 2s to 4s) results in average 115% increase of β .

3.3 Estimation of C_d

As shown above, the average drag coefficient of the meadow, C_d , is the most important parameter for the calculation of the damping coefficient. C_d is usually related to the Reynolds number, Re , as in equation (4)

$$C_D = a + \left(\frac{\beta}{Re} \right)^\gamma \quad (4)$$

where the coefficients α, β, γ depend on the plant characteristics (shape of leaves, length and thickness of leaves, density, modulus of elasticity, stiffness) with values found in literature shown in Table 2, while the Reynolds number is given from equation (5)

$$Re = \frac{u \cdot b_v}{\nu} \quad (5)$$

with u characteristic velocity, taken as the maximum horizontal velocity at the meadow edge and calculated from linear wave theory, as shown in equation (6)

ν kinematic viscosity of water, $\nu = 10^{-6} \text{ m}^2/\text{s}$

$$u = \frac{\pi H \cosh(k \cdot h_s)}{T \sinh(kh)} \quad (6)$$

Table 2: Values of coefficients α, β, γ found in literature

Study	α	β	γ
Mendez et al (1999) – rigid plant	0.40	2200	2.2
Cavallaro et al (2010) – swaying plant	0	2100	1.7
Present study – swaying plant	0.10	2100	1.0

Figure 8 shows the measured C_d values against the Reynolds number, together with the plot of Eq. (4) for the coefficients α, β and γ taken from Mendez et al. (1999) study on rigid plants and Cavallaro et al. (2010) on *P. oceanica* artificial meadow. The Reynolds number considered in the present study varies from 1000-3200, while in the above mentioned studies it varies from 200-15500. In the experimental results a best fit curve is shown with the respective coefficients shown in Table 2. It should be noticed that the validity of such a relationship is subject to the efficient modeling of the mechanical properties of the artificial plant used. Results from other experimental studies on wave and submerged vegetation interaction (Augustin et al., 2009) show that such a correlation can be poor. This might be due to the fact that also other parameters affect the average C_d such as the submergence ratio (Mendez et al., 2004) and the stems density (Huang et al. 2011).

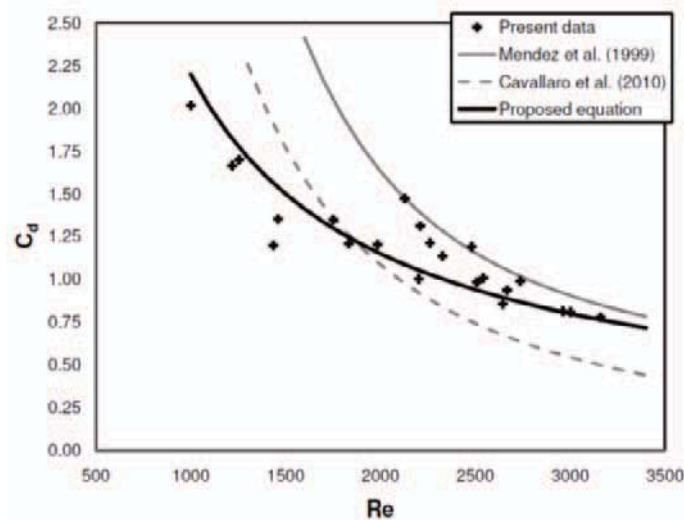


Figure 8: Variation of C_d with Reynolds number.

4 Conclusions

In the present work the effect of *Posidonia oceanica* meadow on wave height attenuation is studied, with the analysis of large scale experimental data. The main conclusions of this study are:

- The wave height is reduced between 10-35% over the artificial *P. oceanica* meadow depending strongly on the plant characteristics and the wave period. More specifically the wave height attenuation increases with increasing submergence ratio, plants density and wave period; longer waves are mostly attenuated from submerged vegetation.
- The wave height distribution over the meadow, expressed with the damping coefficient K_v , follows the proposed analytical formula found in literature, of the form $1/1+\beta x$, where the parameter β depends on the plant and wave characteristics.
- The plants stiffness is an important parameter for estimating the wave attenuation; its effect is included in the estimation of the drag coefficient C_d . Based on the results, an empirical relationship for the drag coefficient C_d related to the Reynolds number, is

obtained, representative of the plant of *P. oceanica*, which can be useful in numerical studies of wave-submerged vegetation interactions.

5 Acknowledgements

The authors acknowledge Vasiliki Stratigaki for providing the data from the experiments that were conducted within the frame of Hydralab III 022441 (RII3) EU project, under the supervision of the second author.

The support of the European Commission through FP7.2009-1, Contract 244104 - THESEUS ("Innovative technologies for safer European coasts in a changing climate"), is also acknowledged.

6 References

- Augustin L.N.; Irish J.L.; Lynett P. (2009): Laboratory and numerical studies of wave damping by emergent and near emergent wetland vegetation. In: Coastal Engineering, Vol. 56, No. 3, pp. 332-340.
- Cavallaro, L.; Lo Re, C.; Paratore, G.; Viviano, A.; Foti, E. (2010): Response of *Posidonia oceanica* to wave motion in shallow-waters - preliminary experimental results. In: Proceedings of the International Conference on Coastal Engineering, 1(32), Shanghai, China [Online], Jan 2011.
- Dalrymple R.A.; Kirby J.T.; Hwang P.A. (1984): Wave Diffraction Due to Areas of Energy Dissipation. In: Journal of Waterway Port Coastal and Ocean Engineering, Vol. 110, No. 1, pp. 67-79.
- Fonseca M.S.; Cahalan J.H. (1992): A preliminary evaluation of wave attenuation by four species of Seagrass. In: Estuarine, Coastal and Shelf Science, Vol. 35, Issue 6, pp. 565-576.
- Giraud G. (1977): Essai de classement des herbiers de *Posidonia oceanica* (L.) Delile. In: Botanica Marina, Vol. 20, pp. 487-491.
- Green E.P.; Short F.T. (2003): World Atlas of Seagrasses, UNEP-WCMC.
- Huang, Z.; Yao Y.; Sim S.Y.; Yao Y. (2011): Interaction of solitary waves with emergent, rigid vegetation. In: Ocean Engineering, Vol. 38, pp. 1080-1088.
- Kobayashi N.; Raichlen A.W.; Asano T. (1993): Wave Attenuation by Vegetation. In: Journal of Waterway Port Coastal and Ocean Engineering, Vol. 119, No. 1, pp. 30-48.
- Koch E.W.; Sanford L.P.; Chen S-N.; Shafer D.J.; Mckee Smith J. (2006): Waves in seagrass systems: Review and Technical recommendations. US Army Corps of Engineers®. Technical Report, ERDC TR-06-15.
- Li C.W.; Zhang M.L. (2010): 3D modelling of hydrodynamics and mixing in a vegetation field under waves. In: Computers & Fluids, Vol. 39, Issue 4, pp. 604-614.
- Mendez, F. J.; Losada I.J; Losada M. A. (1999): Hydrodynamics induced by wind waves in a vegetation field. In: Journal of Geophysical Research, Vol. 104, 18.383-18.396, doi:10.1029/1999JC900119
- Mendez F.J.; Losada I.J (2004): An empirical model to estimate the propagation of random breaking and nonbreaking waves over vegetation fields. In: Coastal Engineering, Vol. 51, No. 2, pp. 103-118.
- Stratigaki V.; Manca E.; Prinos P.; Losada I.; Lara J.; Sclavo M.; Caceres I.; Sanchez-Arcilla A. (2010): Large scale experiments on wave propagation over *Posidonia oceanica*. In: Journal of Hydraulic Research, IAHR, Special Issue of HYDRALAB III (accepted for publication).
- Suzuki T.; Dijkstra J. (2007): Wave propagation over strongly varying topography: cliffs & vegetation. In: Proceedings of 32nd IAHR Congress, Venice, Italy (CD-ROM).

The effect of organism traits and tidal currents on wave attenuation by submerged vegetation

Maike Paul¹ and Tjeerd Bouma²

Abstract

Accurate wave height prediction along the shore plays an important role in coastal protection and management. To account for the effect of submerged vegetation in wave attenuation models, it is important to understand how the interaction between vegetation characteristics and hydrodynamic forcing affects wave attenuation. To determine the effect of vegetation characteristics, we used sea grass mimics that varied in (1) blade stiffness, (2) shoot density and (3) leaf length; to investigate the effect of hydrodynamic forcing we studied wave attenuation in the absence and presence of a tidal current. Results show that wave attenuation is positively correlated with blade stiffness and for a given wave in shallow water; attenuation is dependent on a combination of shoot density and leaf length which can be described by the leaf area index. The presence of a tidal current strongly reduced the wave attenuating capacity of sea grass meadows and this reduction was most pronounced at high shoot densities. Thus, most studies that have been carried out under waves only, will structurally overestimate wave attenuation for tidal environments, emphasizing that tidal currents need to be taken into account in future studies on wave attenuation by vegetation.

Keywords: waves, currents, artificial sea grass, vegetation traits, wave attenuation

1 Introduction

The interaction of sea grass with hydrodynamics is widely recognized to affect ecological processes such as nutrient transport and pollen dispersal (Verduin et al. 2002), sediment dynamics and coastal erosion. One component of this effect is wave attenuation which has been addressed for a variety of sea grass species (Fonseca & Cahalan 1992, Verduin & Backhaus 2000) and studies have shown that submerged sea grass vegetation can have a significant impact on wave attenuation. To correctly account for the effect of sea grass on wave attenuation in coastal protection and management, it is important to understand which vegetation traits and hydrodynamic parameters drive wave attenuation by vegetation (Patil & Singh 2009).

In a laboratory study, Fonseca and Cahalan (1992) found a reduction in wave energy density of approx. 40% per meter sea grass meadow for four different sea grass species. A comparative study between sea grass and salt marsh species (Bouma et al. 2005) indicated that plant stiffness affects wave attenuation. The effect of stiffness on wave attenuation has also been described for large macro algae (Koehl 1996, Denny & Gaylord 2002 and references therein). However, when comparing wave attenuation over stiff *Spartina anglica* and flexible *Puccinellia maritima* marsh vegetation, Bouma et al. (2010) observed that differences disappear on a biomass basis, meaning that an increased shoot density can counteract the reduced wave attenuating capacity of flexible plants. While previous studies suggest that stiffness can play a role in wave attenuation by vegetation, most studies have been carried out on vegetation types other than sea grass (i.e. salt marsh or macro algae). Stiffness determines how much, and moreover in what way, a plant moves under the influence of waves. Depending on their stiffness, sea grasses move in a cantilever or a whip-like motion. A transition from the first to the latter takes place with increasing wave amplitude (Prinos et al. 2010) and the rate of this transition varies with stiffness. It is not yet clear what role this type of motion plays in wave attenuation by sea grass.

¹ Forschungszentrum Küste, Merkurstr. 11, 30419 Hannover, Germany, paul@fzk-nth.de

² Netherlands Institute of Ecology, Centre for Estuarine and Marine Ecology, P.O. Box 140, 4400 AC Yerseke, The Netherlands, T.Bouma@nioo.knaw.nl

The effect of shoot density on wave attenuation has been recognized in a number of studies (i.e. Bouma et al. 2005, Augustin et al. 2009, Prinós et al. 2010), but the number of used densities was generally low (2-3) and not sufficient to qualify its influence on wave attenuation. Augustin et al. (2009) observed that the influence of shoot density on wave attenuation increased with decreasing submergence ratio (defined as the ratio of water depth to vegetation height) for artificial salt marsh; this was recently confirmed for *Posidonia oceanica* mimics (Prinós et al. 2010). The effect of submergence ratio on wave attenuation has been previously addressed by changing the water depth over vegetation of constant height. This approach showed that wave attenuation is directly related to submergence ratio (Fonseca & Cahalan 1992, Bouma et al. 2005, Augustin et al. 2009, Prinós et al. 2010). However, a change in water depth resulted in a change in wave parameters such as wave height and/or period, making it unclear whether this change in hydrodynamics influenced the results. Hence there is a need to study this aspect by maintaining a constant water depth while varying the vegetation height.

In the past, laboratory studies have neglected the possible presence of a current. While this approach helps to understand the general processes of wave attenuation by vegetation, it is a simplification of the natural environment where most sea grass meadows are exposed to waves superimposed on a tidal flow. The effect of an underlying current on wave attenuation over unvegetated beds has been recognized (Madsen 1994) and a field study on kelp (Gaylord et al. 2003) investigated the effect of an alongshore current on wave forces. They observed that the current perpendicular to wave propagation reduced wave energy dissipation compared to rigid structures and the reduction increased with increasing flow velocity. To our knowledge Gaylord et al. (2003) are the only ones who considered the effect of combined waves and currents so far and the effect of a current on wave attenuation by sea grass has not yet been addressed.

Previous studies have identified submergence ratio, shoot stiffness and density as important factors in wave attenuation, but a more systematic analysis of their influence on wave attenuation is needed to understand the effect of submerged vegetation on wave height (Bouma et al. 2010) and to incorporate it in coastal design (Fonseca & Cahalan 1992). This study aims at investigating the impact of those three sea grass traits on wave attenuation. The effect of submergence ratio is addressed by changing the leaf length and conducting tests under identical wave conditions in constant water depth. Mimics with two different stiffnesses and bending behaviors are produced and a total of five densities are tested. Another objective for this study is to investigate how a tidal current affects wave attenuation by sea grass and the mimics will therefore be exposed to waves with and without an underlying steady current.

2 Materials and Methods

2.1 Sea grass mimics

This study focused on the sea grass species *Zostera noltii* which is native to the European Atlantic coast (Den Hartog 1970). In order to disentangle the impact of sea grass traits (1) vegetation density, (2) shoot flexibility and (3) leaf length on wave attenuation, while excluding effects of other morphological parameters, we used plant mimics based on *Z. noltii*, as this species has a simple and well described morphology (Den Hartog 1970). Single traits of the mimic can be changed while maintaining all other characteristics and therefore yielding information on the impact of single vegetation traits on hydrodynamics. Sea grass mimics have been successfully used in the laboratory (Bouma et al. 2005), and in field studies (Lee et al. 2001) and are widely accepted across disciplines.

The dimensions of the mimics were based on the natural size and density ranges of *Z. noltii*. Leaf width of all mimics was $2 \text{ mm} \pm 10\%$ which represents the upper limit of natural width of *Z. noltii* (Phillips & Meñez 1988). Mimics with two different flexibilities were developed and materials were chosen in a way that they showed a different bending behavior. The stiff mimic was similar to mimics that have been used to represent salt marsh vegetation (Bouma et al. 2005) and moved like a cantilever under wave motion. The flexible material was bending similar to *Z. noltii* plants in a whip like motion under waves. For both flexibilities, mimic meadows with a density of 1000 and 4000 shoots per m^2 were produced. For the flexible mimic additional meadows with densities of 500, 2000 and 8000 shoots per m^2 were generated. These densities

cover a wide range of natural densities of *Z. noltii* and yield a detailed investigation of the impact of shoot density on wave attenuation.

Leaf lengths under investigation covered the natural range for *Z. noltii*. The initial leaf length of the flexible meadows was 30 cm and during the course of the study it was reduced to 15 cm and then 10 cm to allow the investigation of wave attenuation under different submergence ratios, but with constant water depth. For the stiff meadows the initial leaf length was 15 cm which was reduced to 10 cm during the course of the experiments. The combination of the above flexibilities, densities and leaf lengths led to a total number of 19 different meadows. Each meadow was 3 m long and 0.6 m wide to cover the whole width of the flume (see below).

To create the meadow the mimics were tied to a canvas mesh with a mesh size of 0.8 cm. To achieve an evenly distributed and yet arbitrarily organized meadow that would be comparable to a natural distribution in the field, the canvas was segmented into squares of 3.4 x 3.4 cm. For the density of 1000 shoots per m² one strip was placed at a haphazard location within each square. For the other densities, the number of strips per square was reduced or increased accordingly. For each meadow, the canvas was then attached to a wooden board and the board was weighed down on the bottom of the flume for deployments.

2.2 Experimental setup

Experiments were carried out under controlled conditions in a racetrack wave flume (Figure 1a). The oval flume is 0.6 m wide and has a straight working section of 10.8 m. Water depth up to 0.4 m can be maintained. The flume is equipped with a conveyor belt system and a wave paddle. This combination allows generating unidirectional flow with velocities up to 0.45 ms⁻¹, waves of varying heights and periods or a combination of both. This feature provided us with the opportunity to investigate the influence of vegetation traits on waves only as well as on combinations of waves and steady currents. The latter represent more natural conditions where tidal currents act simultaneously with waves. However, only an incoming tide can be represented during the experiments as flow and waves could only be generated in the same direction. Additionally, the size of the flume enabled us to run the experiments on full scale and therefore eliminated possible errors that might occur during down-scaling of the mimics.

The water depth in the flume was set to 0.3 m which allowed a submergence ratio of 1:1, 2:1 and 3:1 for the respective leaf lengths. All of these ratios can be observed in the field (Koch 1994). Regular waves with a wave height of $H = 0.1$ m and a wave period of $T \approx 1$ s were generated by the wave paddle. The waves have been applied to all meadows once without and once with an underlying steady current of 0.1 ms⁻¹ which corresponds to low tidal currents typical for areas covered with sea grass in the field (Bouma et al. 2005). Additionally, runs were carried out in an empty flume under both hydrodynamic conditions as a control.

Wave height was measured with four conductivity gauges (from DHI) at a sampling rate of 25 Hz and recordings were taken for 600 s for each run (Figure 1b). Two of the gauges were placed 3.3 m in front of the meadow and spaced 21.5 cm apart to detect occurring reflection. One gauge was placed at the leading edge of the meadow and one at the end of meadow. Additionally, a video camera was used to record sea grass movement through the glass wall of the test section and an Acoustic Doppler Velocimeter (ADV) was used to monitor flow velocities. The filmed section was located 1.5 m into the meadow and film sequences were 300 s long for each run.

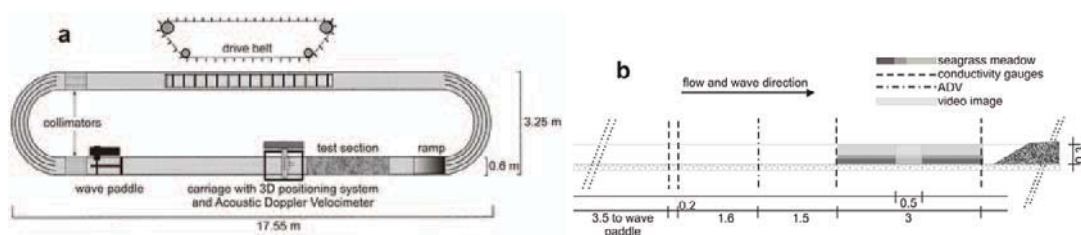


Figure 1: Schematic representation of (a) the flume (adapted from Bouma et al. 2005) and (b) the setup of instruments (all dimensions in m).

2.3 Data processing

Wave recordings were transformed into the frequency domain using Fast Fourier Transform. The data from the two upstream gauges were used to determine the reflection coefficient using the method developed by Baldock and Simmonds (1999). Data from the gauges at the beginning and end of the meadow were filtered for the determined reflection if the reflection coefficient exceeded 5%. Data were then transformed back into the time domain with an Inverse Fast Fourier Transform and zero-crossing was applied to obtain significant wave height at the beginning and end of the meadow. From these values the dissipated wave height ΔH per meter meadow was derived as:

$$\Delta H = (H_1 - H_2) / x \quad (1)$$

- with ΔH dissipated wave height [-]
 H_1 wave height at leading edge of meadow [m]
 H_2 wave height at end of meadow [m]
 x length of meadow [m]

This approach assumes linear wave dissipation along the meadow. Previous studies have shown that the relationship between wave dissipation and distance into a vegetated area is non-linear (Möller et al. 1999, Bouma et al. 2010). However, linearity is a valid simplification when studying flexible vegetations with relative small wave attenuating capacity over short distances (Fonseca & Cahalan 1992, Bouma et al. 2005).

As the meadows varied in leaf length as well as density, a parameter that includes both these values was required to compare all flume runs with each other. Therefore the leaf area index (LAI = leaf length * leaf width * density, $m^2 m^{-2}$) was calculated for each meadow and consequently used to compare the wave attenuating capacity of each meadow under investigation.

3 Results

For all sea grass meadows, the reduction of wave height exceeded the wave height reduction during the control runs with a bare bottom (Figures 2 and 3). Additionally, an effect of plant stiffness on wave attenuation was obvious when comparing the results from both materials used (Figure 2). Both stiffnesses yielded a clear linear relationship of wave dissipation with LAI. The attenuating effect of the stiff material was much higher for any given LAI compared to the flexible mimics, unless LAI was negligibly low.

Comparing wave attenuation in the absence or presence of an underlying current of 0.1 ms^{-1} revealed that if a current is present, both wave dissipation and the observed canopy height are reduced for any given vegetation length (Figure 3). The canopy height reduction by currents is

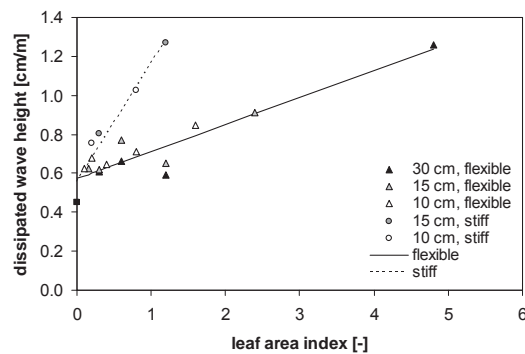


Figure 2: Dissipated wave height in cm/m as a function of leaf area index under waves only. The square indicates the value without any sea grass in the flume. Linear regression yields for the flexible material $\Delta H = 0.14 \cdot LAI + 0.57$ ($R^2 = 0.84$) and for the stiff material $\Delta H = 0.61 \cdot LAI + 0.56$ ($R^2 = 0.94$).

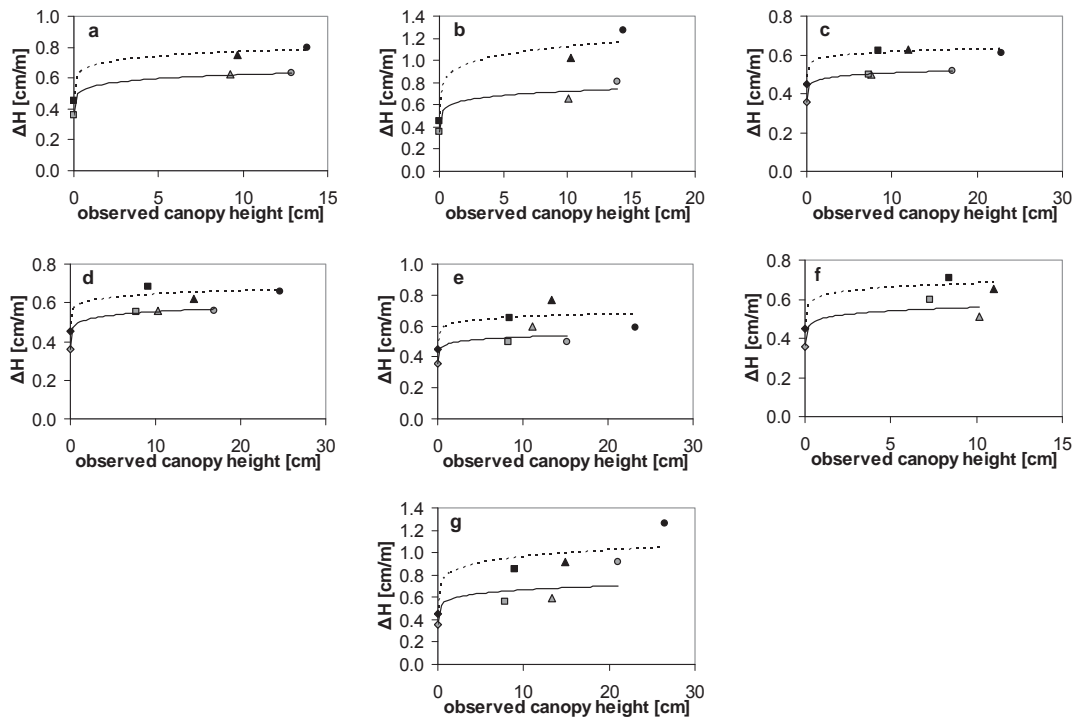


Figure 3: Examples of dissipated wave height ΔH as a function of canopy height for a) stiff mimics, 1000 shoots per m^2 , b) stiff mimics, 4000 shoots per m^2 , c) flexible mimics, 500 shoots per m^2 , d) flexible mimics, 1000 shoots per m^2 , e) flexible mimics, 2000 shoots per m^2 , f) flexible mimics, 4000 shoots per m^2 and g) flexible mimics, 8000 shoots per m^2 . Data for the wave only case are represented by black symbols and their best fit by dotted lines; data for the combined wave and current case are represented by grey symbols and their best fit by solid lines. The shapes of the symbols indicate leaf lengths: \circ = 30 cm, Δ = 15 cm, \square = 10 cm, \diamond = no sea grass.

up to 36% for the flexible material with the largest reduction for long flexible leaves compared to shorter ones (Figure 3c-g) and, not surprisingly, much smaller for the stiff material (up to 7%, Figure 3a-b). Leaf bending due to currents puts leaves lower in the water column where they are exposed to less orbital motion. However, even when comparing meadows with a similar actual canopy height (Figure 3), wave dissipation rates in the presence of a current are lower than in the absence of a current. This indicates that other processes than the position of the leaves in the water column causes the observed reduction in wave attenuation in the presence of a current. The constant offset between the regression lines with and without current suggest that the difference between ΔH_w (wave only) and ΔH_{wc} (combined waves and currents) remains constant with canopy height.

4 Discussion

The present study investigates the combined effect of vegetation characteristics (shoot stiffness, density and length) and the presence/absence of an underlying current on wave attenuation by submerged (mimic) vegetation. By using mimic meadows with different shoot densities and leaf lengths under constant hydrodynamic conditions, we found that for a given water depth, wave attenuation of shallow water waves depends on the leaf area index LAI. This observation applied to both stiffnesses used in this study; however, wave attenuation for a given LAI was much more pronounced for the stiff material. Additionally, tests with and without an underlying current revealed, to our knowledge for the first time, that the wave attenuating capacity of sea grass is significantly lower in the presence of a current.

4.1 Leaf area index

Previous studies (Ward et al. 1984, Fonseca & Cahalan 1992) showed that sea grass is the more effective in attenuating waves the more of the water column it occupies. This led to the

general understanding that wave attenuation depends on the submergence ratio. The present results extend these observations by showing that for a given small water depth, LAI as a combination of canopy height and shoot density, can be used as an integrating factor to predict wave attenuation.

In field studies (Ward et al. 1984, Koch et al. 2006) the sea grass canopy remained constant and water depth changed over the tidal cycle. As a result of changing water depth, wave height and period are likely to have changed. Paul and Amos (2011) showed that waves of different periods get attenuated differently by a *Zostera noltii* bed and it is possible that this response to differing wave periods is responsible for the difference in wave attenuation capacity with varying water depth. Fonseca and Cahalan (1992) varied water depth during their laboratory study on four different sea grass species. And although they applied waves with the same period, incident wave height varied between runs. Other laboratory studies adopted this approach and also changed the submergence ratio by adjusting water depth over vegetation with constant height (Augustin et al. 2009, Prinos et al. 2010).

During the present study, water depth and wave conditions remained constant and leaf length and shoot density were varied between runs. The results show a linear relationship of wave dissipation with LAI, which suggests that for a given wave in shallow water, a short but dense meadow has the same wave attenuating effect as a high but scarce meadow with the same leaf area index. This may be explained by the drag each unit leaf area poses on the water movement which in return loses momentum (Kobayashi et al. 1993). The sum of momentum loss generated by the whole leaf area leads to reduced wave energy and can be observed as wave height reduction. As a result it does not matter where in the water column the biomass is located and only the amount of biomass determines the rate of wave attenuation. However, we expect this to be only valid for cases where the waves are in shallow water and feel the bottom. In cases where the orbital wave motion does not reach the bottom, a higher meadow is likely to have a higher attenuating effect, because the wave would feel part of the long leaves while it may not feel a shorter meadow.

4.2 Stiffness

The materials chosen for the mimics strongly differed in stiffness which led to a different bending behavior under waves and resulted in different rates of wave attenuation. This agrees with a study carried out on real plants of contrasting stiffness (Bouma et al. 2005). A comparison between rigid and cantilever like structures, however, did not yield a significant difference in wave attenuation (Augustin et al. 2009). Hence, it is possible that the type of motion (cantilever vs. whip-like) is more important for wave attenuation than the material stiffness as such. A study on *Spartina anglica* and *Puccinellia maritima* (Bouma et al. 2010) found that the flexible plant (*P. maritima*) dissipated wave height at higher densities as effectively as the stiff one (*S. anglica*) at low densities. This observation was confirmed in the present study where the flexible material requires approx. four times the leaf area index of the stiff material to yield the same dissipated wave height.

4.3 Effect of current

In the presence of a current, wave attenuation shows the same systematic behavior than in the wave only case, but dissipated wave height is lower for a given canopy height when a current is present (Figure 3). To our knowledge no other study has addressed the influence of a current on wave attenuation by sea grass systematically so far, although its effect on wave attenuation has been recognized for unvegetated beds (Madsen 1994) and kelp (Gaylord et al. 2003). The presented results confirm that the same is true for sea grass beds and suggest that previous studies which neglected the effect of underlying currents overestimated the effect of sea grass on wave attenuation in tidal regions.

Wave attenuation by vegetation has three components. Plants (1) provide skin friction due to their surface structure, (2) pose form drag on the flow that depends on their shape and (3) they absorb wave energy by converting it into plant movement. Skin friction depends on the size of the wetted plant area and is therefore independent of flow velocities (Koehl 1996). The form drag of the plant's frontal area generates turbulence behind the plant which leads to energy dissipation (Nepf 1999). In the presence of a current, flexible plants change their shape by

bending which reduces the frontal area that poses drag on the flow (Boller & Carrington 2006). This streamlining allows flexible plants to reduce form drag under increased flows compared to rigid structures (Koehl 1996) which in return may contribute to the reduction in wave attenuation in the presence of a current.

Vegetation also reduces wave energy by transforming it into plant movement. This transformation results in less energy contained in the wave and can thus be observed in a reduced wave height, because the two parameters are related according to linear wave theory. In the wave-only case, sea grass can move freely within the limits of its stiffness and extract energy from the waves. An underlying current exerts an initial force on the plants which causes them to bend. This bending leads to a primary tension within the blades and the force required to bend the blade further increases with increasing bending angle. The same wave force would therefore generate a smaller plant movement, the higher the initial bent due to a steady current is. A study under unidirectional flow (Boller & Carrington 2006) showed that initially flexible macro algae were affected by flow velocities and behaved like rigid bodies once a critical velocity was exceeded. It could therefore be expected that the motion restrictive nature of the underlying current would increase with increasing flow velocity. Similar to macro algae (Boller & Carrington 2006) it may be possible that a critical velocity exists at which the sea grass blades are not able to move anymore and wave attenuation would remain constant when flow velocities increase above this threshold value. We hypothesize that the wave attenuation of plants that are exposed to currents above this threshold would still be higher than wave attenuation in the complete absence of plants due to skin friction and streamlined form drag.

5 Conclusions

Laboratory experiments with artificial sea grass were used to investigate the effect of leaf length, shoot density and stiffness on wave attenuation in the absence and presence of a tidal current. Results showed that stiffness and leaf area index determine wave attenuation. The leaf area index combines the effect of leaf length and shoot density and therefore indicates that density can compensate for lack of canopy height and vice versa with respect to wave attenuation. The presence of an underlying current led to a reduction in wave attenuation for all 19 meadows under investigation. While this phenomenon could not be fully explained with the data collected during this study, it clearly shows that experiments which are carried out under waves only, overestimate the wave attenuating capacity of sea grass compared to most natural environments where underlying currents are present in the form of tidal flow.

6 Acknowledgements

The authors kindly acknowledge the use of MatLab code for zero-crossing and wave reflection provided by Dr U. Neumeier and Dr T. Baldock, respectively. The lab experiments were possible thanks to a Peter Killworth Memorial Scholarship and the first author would like to thank Christel and Dieter from the Stiftung zur Förderung Paulscher Promotionen for uncounted hours of invaluable help during preparation and execution of the experiments.

7 References

- Augustin LN, Irish JL, Lynett P (2009) Laboratory and numerical studies of wave damping by emergent and near-emergent wetland vegetation. *Coastal Engineering* 56:332-340
- Baldock TE, Simmonds DJ (1999) Separation of incident and reflected waves over sloping bathymetry. *Coastal Engineering* 38:167-176
- Boller ML, Carrington E (2006) The hydrodynamic effects of shape and size change during reconfiguration of a flexible macroalga. *Journal of Experimental Biology* 209:1894-1903
- Bouma TJ, De Vries MB, Herman PMJ (2010) Comparing ecosystem engineering efficiency of 2 plant species with contrasting growth strategies. *Ecology* 91:2696-2704
- Bouma TJ, De Vries MB, Low E, Peralta G, Tánčzos IC, van de Koppel J, Herman PMJ (2005) Trade-offs related to ecosystem engineering: A case study on stiffness of emerging macrophytes. *Ecology* 86:2187-2199

- Den Hartog C (1970) *The sea-grasses of the world*, Vol. North Holland Publishing Company, Amsterdam
- Denny MW, Gaylord B (2002) The mechanics of wave-swept algae. *Journal of Experimental Biology* 205:1355-1362
- Fonseca MS, Cahalan JA (1992) A preliminary evaluation of wave attenuation by four species of seagrass. *Estuar Coast Shelf Sci* 35:565-576
- Gaylord B, Denny MW, Koehl MAR (2003) Modulation of wave forces on kelp canopies by alongshore currents. *Limnology and Oceanography* 48:860-871
- Kobayashi N, Raichle AW, Asano T (1993) Wave attenuation by vegetation. *J Waterw Port Coast, Oc Eng* 119:30-48
- Koch EW (1994) Hydrodynamics, diffusion-boundary layers and photosynthesis of the seagrasses *Thalassia-testudinum* and *Cymodocea-nodosa*. *Marine Biology* 118:767-776
- Koch EW, Ackerman JD, Verduin JJ, van Keulen M (2006) Fluid dynamics in seagrass ecology: From molecules to ecosystems. In: Larkum AWD, Orth RJ, Duarte CM (eds) *Seagrasses: Biology, ecology and conservation*. Springer, Berlin, p 193-225
- Koehl MAR (1996) When does morphology matter? *Annual Review of Ecology and Systematics* 27:501-542
- Lee SY, Fong CW, Wu RSS (2001) The effects of seagrass (*Zostera japonica*) canopy structure on associated fauna: A study using artificial seagrass units and sampling of natural beds. *Journal of Experimental Marine Biology and Ecology* 259:23-50
- Luhar M, Coutu S, Infantes E, Fox S, Nepf HM (2010) Wave-induced velocities inside a model seagrass bed. *Journal of Geophysical Research - Oceans* 115
- Möller I, Spencer T, French JR, Leggett DJ, Dixon M (1999) Wave transformation over salt marshes: A field and numerical modelling study from north Norfolk, England. *Estuar Coast Shelf Sci* 49:411-426
- Madsen OS (1994) Spectral wave-current bottom boundary layer flows. In: Edge BL (ed) 24 Conference of Coastal Engineering. Am. Soc. of Civil Eng., Kobe, Japan, p 384-398
- Nepf HM (1999) Drag, turbulence, and diffusion in flow through emergent vegetation. *Water Resources Research* 35:479-489
- Patil S, Singh VP (2009) Hydrodynamics of wave and current vegetation interaction. *J Hydrol Eng* 14:1320-1333
- Paul M, Amos CL (2011) Spatial and seasonal variation in wave attenuation over *Zostera noltii*. *J. Geophys. Res.*, 116, C08019, doi:10.1029/2010JC006797
- Phillips RC, Meñez EG (1988) *Seagrasses*. Smithsonian Contributions to the Marine Sciences 34
- Prinos P, Stratigaki V, Manca E, Losada IJ and others (2010) Wave propagation over *Posidonia oceanica*: Large scale experiments. In: Grüne J, Klein Breteler M (eds) *Hydralab III Joint Transnational Access User Meeting*, Hannover, p 57-60
- Verduin JJ, Backhaus JO (2000) Dynamics of plant-flow interactions for the seagrass *Amphibolis antarctica*: Field observations and model simulations. *Estuar Coast Shelf Sci* 50:185-204
- Verduin JJ, Backhaus JO, Walker DI (2002) Estimates of pollen dispersal and capture within *Amphibolis antarctica* (labill.) Sonder and Aschers. Ex Aschers. meadows. *Bulletin of Marine Science* 71:1269-1277
- Ward LG, Kemp WM, Boynton WE (1984) The influence of waves and seagrass communities on suspended particulates in an estuarine embayment. *Marine Geology* 59:85-103

Dynamic analysis of gravity quay walls under seismic forces

Kubilay Cihan¹, Yalçın Yüksel¹, Seda Cora¹

Abstract

Caissons are used effectively to protect shorelines and harbours by reflecting wave energy towards the open sea. The successful performance of caissons has been attributed to experience and continued research. The seismic design for caissons is important since the functional loss of ports may cause severe economic loss. It is necessary to conduct a seismic design in terms of functionality so that cargo handling facilities may continue to function even after severe earthquakes. Relative displacement is an important index when the functionality of crane rails on caisson-type quay walls is discussed. Recent design codes for caissons demand performance-based designs. These codes require that the seismic performance of the walls be evaluated based on the permanent wall displacement after an earthquake. The method of analysis for a port structure depends on structural type. The methods classified as (i) simplified analysis, (ii) simplified dynamic analysis, (iii) dynamic analysis. The seismic displacement of the caissons can be evaluated by dynamic analyses or simplified dynamic analyses based on the Newmark sliding block concept. Comprehensive results for the dynamic behaviour of soil and caissons can be obtained from dynamic analyses. In this study, the dynamic behaviour caissons were investigated by using FEM method, new Turkish design code for port structures based on performance-based approach and Newmark method and results were compared.

Keywords: caisson, quay wall, FEM, numerical analysis

1 Introduction

The stabilities of caisson quay walls against all forces act on their body are mostly provided by the friction existed at the bottom of the caisson. During earthquakes, the lateral earth pressure increases in the saturated backfill due to excess pore water pressures build up. This condition might cause liquefaction in the backfill soil. In the past earthquakes, some extensive damage such as sliding and tilting of caisson walls due to liquefaction has been observed. Yüksel et al., (2003), investigated the effects of the Eastern Marmara Earthquake occurred on 17 August 1999 on marine structures and coastal areas. Their experience reflected to a new design code which was based on performance design of marine structures (Aydinoglu et al., 2008)

The seismic displacement of the caissons can be evaluated by dynamic analyses or simplified dynamic analyses based on the Newmark sliding block concept. Comprehensive results for the dynamic behaviour of soil and caissons can be obtained from dynamic analyses. But various input parameters which are difficult to obtain are needed for dynamic analyses.

The simplified dynamic analyses based on the Newmark sliding block concept are widely used to obtain wall displacement due to earthquake effect. This method needs basic design parameters such as the weight of the wall, friction angle of backfill and friction coefficient between wall and foundation material. Richard and Elms (1979) and Whitman and Liao (1985) developed a simplified dynamic analyses method based on Newmark sliding block concept. According to their methods, there is only an acceleration value of wall defines yield acceleration that factor of safety of wall for sliding becomes 1 and wall displacement is assumed to begun when ground acceleration is higher than yield acceleration. However these analyses cannot take into account variation of wall thrust due to the development of excess pore pressure in the backfill.

To determine displacement of wall due to earthquake by using dynamics analyses with FEM or FDM or using simplified dynamic analyses is very difficult because stability of quay walls under seismic action is very complicated phenomenon. Several researchers carried on numerical and model studies to understand the seismic behavior of this type structures; Woodward and

¹ Yildiz Technical University, kcihan@yildiz.edu.tr

Griffiths (1996), Ghalandarzadeh et al. (1998), Zeng (1998), Yang et al (2001), Chen and Huang (2002), Hagiwara et al (2004), Kim et al. (2004, 2005), Hazarika et al (2006), Sadrekarimi et al. (2008), Moghadam et al (2009).

1.1 Performance-based design according to the RHA code

Recent design codes for caissons demand performance-based designs. These codes require that the seismic performance of the walls be evaluated based on the permanent wall displacement after an earthquake. The General Directorate for Construction of Railways, Harbours and Airports (RHA) of Ministry of Transportation of Turkish Republic has prepared a seismic code rest on a performance-based design philosophy. The RHA code for port structures includes the definition of the following performance-based design parameters:

1. Structural classes associated with the expected performance, usage and functional importance,
2. Seismic performance levels associated with expected damage levels,
3. Earthquake levels associated with frequent, rare and very rare earthquakes,
4. Seismic performance objectives under different earthquake levels.

In Table 1, performance-based design parameters according to the RHA code are shown.

Table 1: Minimum performance objectives for port structures (Aydinoğlu vd., 2008)

Structure Class	(E1) Earthq. Level	(E2) Earthq. Level	(E3) Earthq. Level
Special	-	MD	CD
Nominal	MD	CD	(ED)*
Simple	CD	(ED)*	-
Unimportant	(ED)*	(CS)*	-
*Implied objectives not requiring desing verication			

where,

MD is minimum damage performance level, CD is controlled damage level performance, ED is extensive damage performance level, CS is state collapse. E1 is earthquake level that the probability of exceedance of (E1) level earthquake in 50 years is 50%, which corresponds to a return period of 72 years. E2 is earthquake level that the probability of exceedance of (E2) level earthquake in 50 years is 10%, which corresponds to a return period of 475 years. E3 is earthquake level that the probability of exceedance of (E3) level earthquake in 50 years is 2%, which corresponds to a return period of 2475 years.

A caisson wall which has a height 15 m was chosen to determine its seismic behavior according to RHA code. Location of this caisson wall is 29.97° latitude, 40.76° longitude. It was assumed that structure was located on rock foundation defined A type soil in RHA code. Besides, seismic spectral acceleration of construction zone was obtained from RHA code. Structure class is nominal and considered earthquake level is E1.

1.2 Newmark sliding block method

The Newmark sliding block method defines the yield acceleration as the amplitude of the block acceleration when the factor of safety for sliding becomes 1.0, and evaluates the block displacement by double integration of the ground acceleration, which exceeds the yield acceleration. Several methods to calculate the block displacement by integration of the ground acceleration have been proposed. Among these, the integration method by Wilson and Keefer (1985) (Fig. 1) has been widely used. Fig. 1(a) shows the time history of the ground acceleration, which is compared to the yield acceleration, a_y . The wall displacement begins to occur at point X where the ground acceleration becomes larger than a_y (Fig. 1(c)). The

cumulative permanent displacement of the block is obtained by the double integration of the difference between the ground and yield accelerations until the velocity of the wall becomes zero (Fig. 1(c)) (Kim et al, 2005).

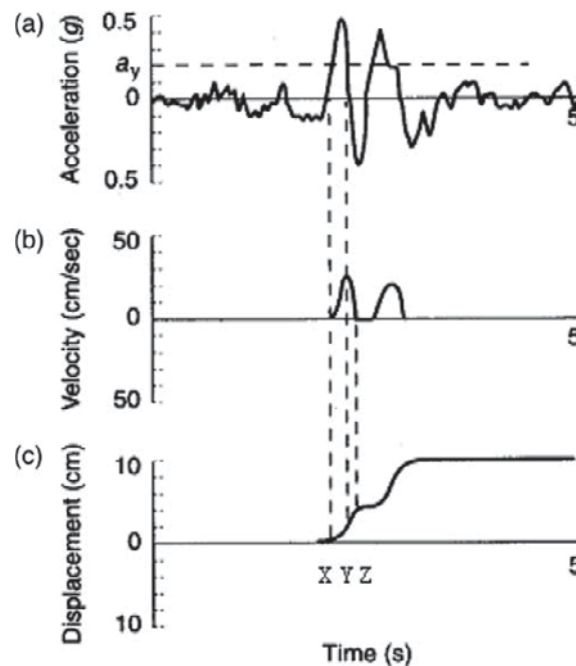


Figure 1: Development of displacement for actual earthquake ground motion (Wilson and Keefer, 1985)

Forces on caisson type quay wall during earthquake are shown in Fig. 2. In this study, Mononobe-Okabe equation was used to calculate static and dynamic earth thrust forces. And also hydrodynamic force was calculated by using Westergard's equation.

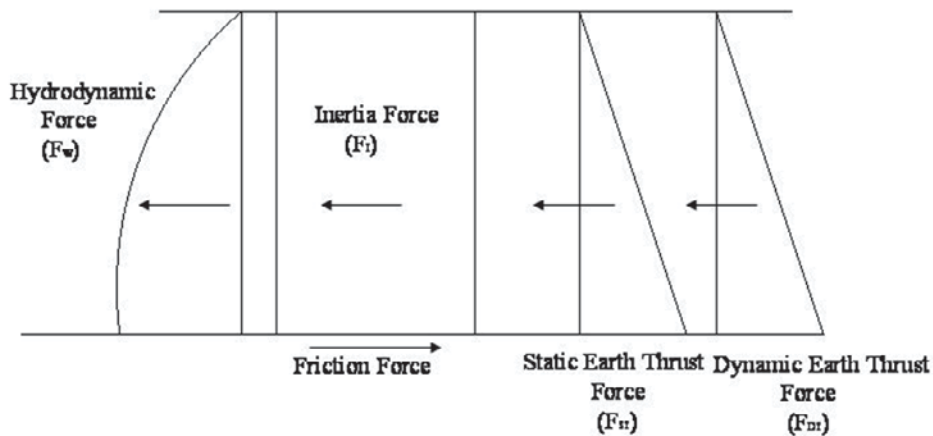


Figure 2: Forces on caisson type quay wall during earthquake

Equation 1 is obtained summing forces in the horizontal direction and imposing the requirements of equilibrium.

$$a_y = \left[\frac{(W\mu + (F_{ST} + F_{DT})\sin \delta) - (F_{ST} + F_{DT})\cos \delta - F_w}{W} \right] g \quad (1)$$

Hence the above equation cannot be solved explicitly since dynamic earth thrust force is a non-linear function of a_y . Iterative methods can be used to solve the equation.

1.3 Numerical analysis

Results of model shaking table test on seismic performance of caisson quay walls carried out by Hazarika et al (2006) were chosen to determine material properties for numerical analysis. A static analysis was performed for simulating the stress conditions before earthquakes.

Numerical analysis of dynamic response of caisson quay walls was carried out by using Plaxis V8.2 software that can calculate with FEM.

The numerical model used for caisson quay wall model carried out by Hazarika et al (2006) is illustrated in Figure 3.

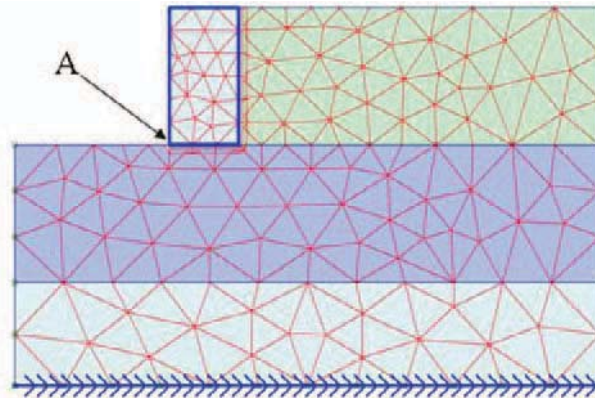


Figure 3: Numerical model in Plaxis

A sinusoidal loading was subjected to the soil-structure system for a period of 2 sec with 20 Hz of frequency. They were applied in several stages starting with 0.1g of acceleration and increasing up to 0.4g at an increment of 0.1g. Material properties, such as densities and relative densities, used in numerical model were chosen according to physical model's properties. Some material properties needed for FEM were used as recommended in Plaxis Manual. Material properties used in numerical model are shown in Table 2.

Table 2: Material properties in Plaxis

Symbol		Unit	Backfill	foundation	rubble	caisson
			Mohr-Coulomb	Mohr-Coulomb	Mohr-Coulomb	Linear-Elastic
γ_{unsat}	Unsaturated unit weight	kN/m ³	18	18	20	22
γ_{sat}	Saturated unit weight	kN/m ³	21	21	22	-
E_{50}^{ref}	Reference secant Young modulus	kN/m ²	40000	50000	60000	60000
c	Cohesion	kN/m ²	-	-	-	-
ϕ	Shear strength angle	°	35	40	45	45
ψ	Dilatancy angle	°	5	10	10	10
ν_{ur}	Poisson rate	-	0.2	0.2	0.2	0.2
p_{ref}	Reference stress	kN/m ²	100	100	100	100
m	Power for stress level dependency	-	0.5	0.5	0.5	0.5
$K_{0\text{nc}}$	Earth pressure coefficient at rest	-	0.357	0.331	0.309	0.309
R_f	Failure ratio	-	0.9	0.9	0.9	0.9

Permanent displacements obtained from FEM and measured experimentally are summarized in Table 3. From Table 3, it is seen that the numerical model simulates the physical model behavior successfully.

Table 3: Permanent displacements obtained from FEM, Newmark sliding block method, and measured experimentally

Amplitude of cyclic motion	Displacement (m) (Measured) $\times 10^{-3}$	Displacement (m) (FEM) $\times 10^{-3}$
0.1g	0.3	0.38
0.2g	0.5	0.68
0.3g	0.7	0.8
0.4g	0.8	0.92

After determination of materials (back-fill and caisson) properties, a numerical model for prototype shown in Figure 4 was composed. The foundation soil deformability was ignored to be able to compare displacements obtained from numerical model and from Newmark procedure.

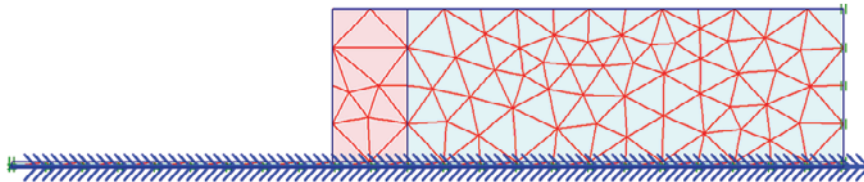


Figure 4: Numerical model in Plaxis for prototype caisson wall

Time history of acceleration used in numerical model is shown in Figure 5. It was recorded in Yarimca during the Eastern Marmara Earthquake occurred on 17 August 1999.

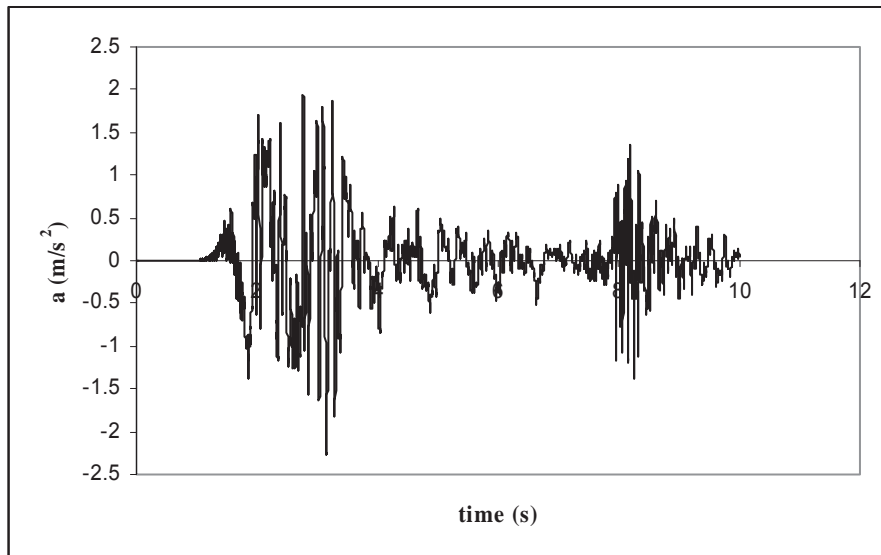


Figure 5: Time histories of acceleration used in numerical model

2 Results and Discussion

In present study, the dynamic behaviour caissons were investigated by using FEM method, new Turkish design code for port structures based on performance-based approach and Newmark method. Safety factors of caisson walls, which has same height (h) and different width (b), against sliding are shown in Figure 6. Considered structure is not safe against the sliding. It is

seen that safety factors against sliding increases with increasing b . Increasing of b supplies a rising of resistance force.

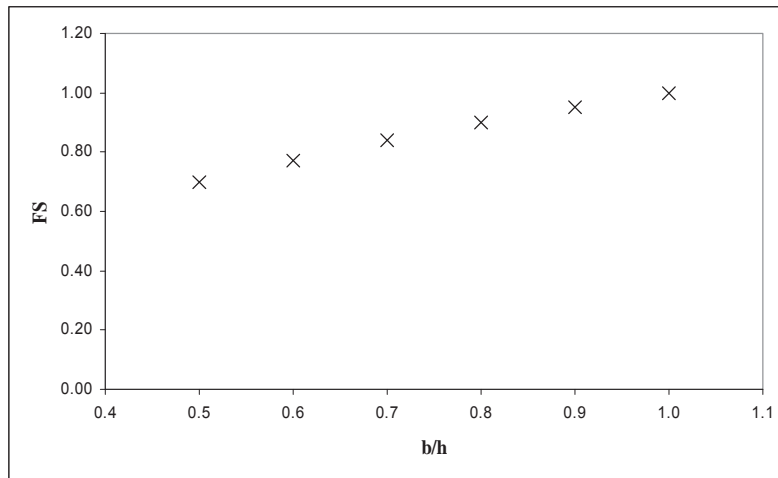


Figure 6: Safety factor against the sliding

Permanent displacements obtained from numerical analysis and Newmark sliding block method were compared. Friction coefficient, μ , between wall and foundation is so important parameter which is difficult to obtain, to determine yield acceleration. In this study, friction coefficient was 0.5. Permanent displacements obtained from FEM, Newmark sliding block method and yield acceleration values for different caisson walls are summarized in Table 4. In Figure 7, horizontal displacements at 10 s for caisson wall ($b/h=0.5$) are shown as vector quantity.

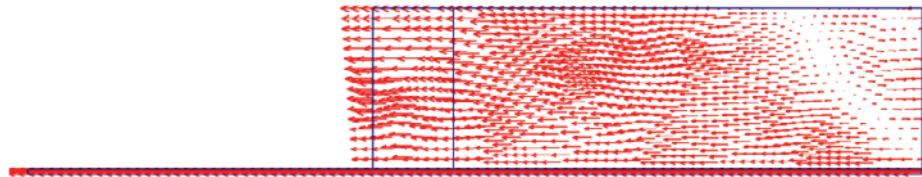


Figure 7: Horizontal displacements at 10 s for caisson wall ($b/h=0.5$)

Table 4: Permanent displacements obtained from FEM and Newmark sliding block method

b/h	Displacement (m) (Newmark) $\mu=0.5$	Displacement (m) (FEM) $\mu=0.5$	Yield acceleration $a_y(g)$
0.5	0.012	0.00257	0.08
0.6	0.008	0.00227	0.095
0.7	0.004	0.002	0.11
0.8	0.002	0.00192	0.125
0.9	0.0015	0.00185	0.13
1	0.001	0.0015	0.145

Variation of permanent displacements against b/h are shown in Figure 8 for FEM and Newmark sliding block method. Calculated displacements by using Newmark's method are bigger up to $b/h=0.8$. After this point, calculated displacement by using FEM are bigger. According to Newmark's method, the cumulative permanent displacement of the block is obtained by the double integration of the difference between the ground and yield accelerations until the velocity of the wall becomes zero. Displacements decreases with increasing yield acceleration. On the other hand, variation of calculated displacement using FEM is smoother than displacements of Newmark's method.

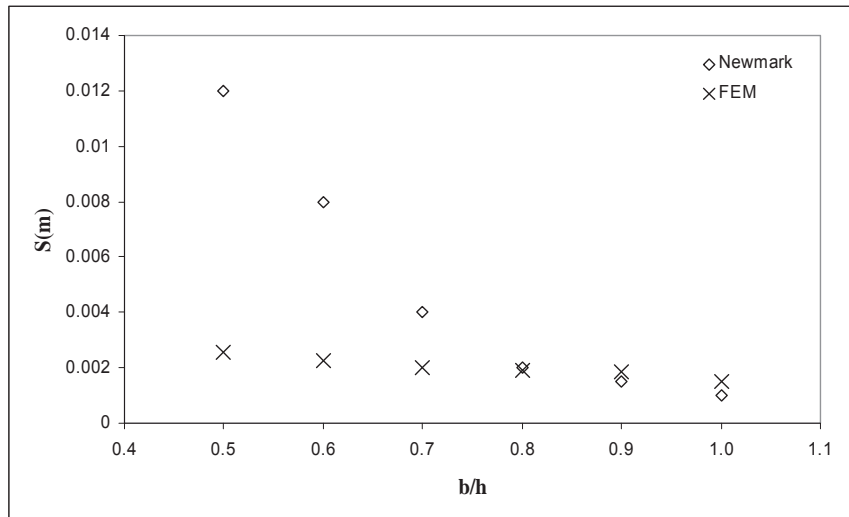


Figure 8: Variation of permanent displacements

Another numerical model was composed to investigate effect of friction layer on displacement. For this purpose, while b/h is increased from 0.5 up to 1, mass of structures are equal for all structures. Displacements calculated by numerical analysis are shown in Figure 9. It is seen that displacements decreases with increasing friction layer. And also there are differences of displacements calculated by numerical models, since inertia force increases with increasing b/h .

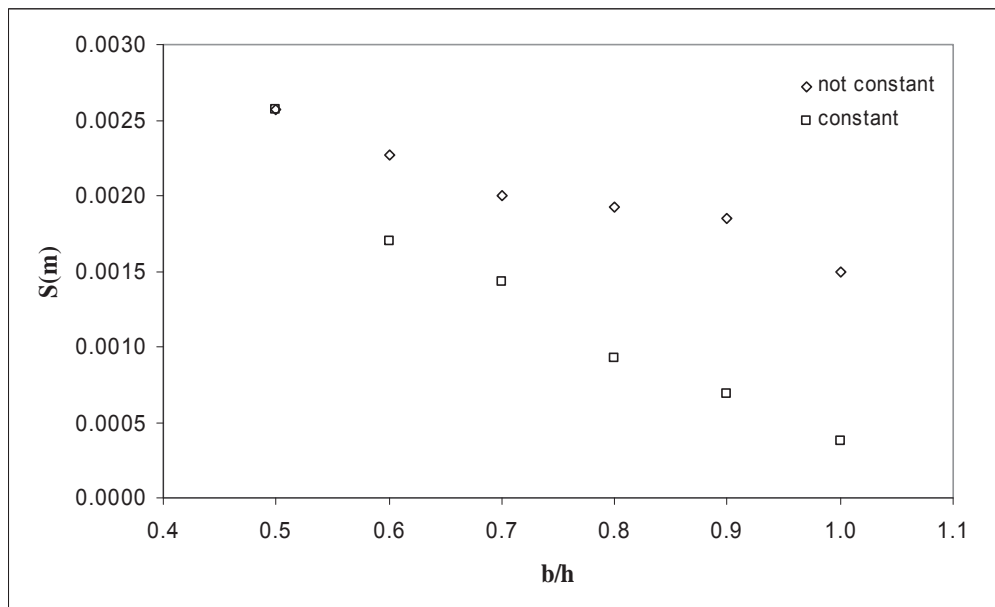


Figure 9: Displacements calculated by FEM

3 Conclusion

In present study, the dynamic behaviour caissons were investigated by using FEM method, new Turkish design code for port structures based on performance-based approach and Newmark method.

It is determined that displacements decreases with increasing b/h according to all analysis metod. Choosing material properties used numerical model is very important to simulate correctly. Results of Newmark's method is generally more conservative than results of numerical analysis. To enlarge friction surface decreases permanent displacements.

4 References

- Aydinoglu, N. M., Ergin, A., Guler, I., Yuksel, Y., Cevik, E. And alciner, A., (2008), New Turkish Seismic Design Code for Port Structures; A Performance-Based Approach", ICCE 2008 Ed. Lehfeldt, R. And Schuttrumpf, H., Hamburg.
- Chen, B.F., Huang, C.F., 2002. Hydrodynamic forces on concrete sea wall and breakwater during earthquakes: effects of bottom sediment layers and back-fill soil. *Ocean Engineering* 29, 783–814.
- Duncan, J. M., Chang, C.-Y., (1970), "Nonlinear Analysis of Stress and Strain in Soil", ASCE J. Of the Soil Mech. And Found. Div. Vol. 96, 1629-1653.
- Ghalandarzadeh, A., Orita, T., Towhata, I., Yun, F., 1998. Shaking table tests on seismic deformation of gravity quay walls. *Soils and Foundations* 38 (2), 115– 132 (Special Issue on Geotechnical Aspects of the January 17, 1995 Hyogoken- Nambu Earthquake
- Hagiwara, T., Yamazaki, H., Shiraishi, S., Fukumori, Y., Satoh, Y., Hirano, T., Yamada, H., Yamada, T., (2004), "Experimental study on stability of a caisson type quay wall by the artificial drain method using recycle material during earthquake", *Oceans '04. Mts/leee Techno-Ocean:2092-2097*, 9-12 November2004, Kobe.
- Hazarika,H., Sugano, T., Kikuchi, Y., Yasuhara,K., Murakami, S., Takeichi, H., Karmokar, K., Kishida, T., and Mitarai, Y.,(2006), Model Shaking Table Test on Seismic Performance of Caisson Quay Wall Reinforced with Protective Cushion, The Proceedings of The Sixteenth (2006) International Offshore And Polar Engineering Conference, Volumell, 309-316, San Francisco, California, USA,
- Kim, S.R., Kwon, O.S., Kim, M.M., 2004. Evaluation of force components acting on gravity type quay walls during earthquakes. *Soil Dynamics and Earthquake Engineering* 24, 853–866.
- Kim, S.R., Kwon, O.S., Kim, M.M., 2005. Evaluation of seismic displacements of quay walls. *Soil Dynamics and Earthquake Engineering* 25, 451–459.
- Kondner, R. L., (1963), "A Hyperbolic Stress Strain Formulation for Sands", 2. Pan. Am. ICOSFE Brazil, Vol. 1, 289-324
- Moghadam, M., Ghalandarzadeh, A., Towhata, I., Moradi, M., Ebrahimian, B.,and Hajjalikhani, P., (2009), Studying the effects of deformable panels on seismic displacement of gravity quay walls, *Ocean Engineering* Volume 36, Issues 15-16, November 2009, Pages 1129-1148
- Plaxis Manual, 2008.
- Richards R, Elms D. Seismic behavior of gravity retaining walls. *J Geotech Eng Div* 1979;105(4):449–64.
- Sadrekarami, A., Ghalandarzadeh, A. and Sadrekarami, J., (2008) "Static and Dynamic Behavior of Hunchbacked Gravity Quay Walls", *Soil and Earthquake Engineering*, 28:99-117.
- Schanz, T. (1998), "Zur Modellierung des Mechanischen Verhaltens von Reibungsmaterialien", Habilitation, Stuttgart Universitat.

- Whitman RV, Liao S. Seismic design of retaining walls. Miscellaneous paper GL-85-1, US Army engineer waterways experiment station, Vicksburg, MS 1985.
- Wilson RC, Keefer DK. Dynamic analysis of a slope failure from the 6 August 1979, Coyote Lake, CA, earthquake. *Bull Seismol Soc Am* 1983;73(3):863–77.
- Woodward, P.K., Griffiths, D.V., 1996. Comparison of the pseudo-static and dynamic behavior of gravity retaining walls. *Journal of Geotechnical and Geological Engineering* 14, 269–290.
- Yang, Z., Elgamal, A., Abdoun, T., Lee, C.J., 2001. A numerical study of lateral spreading behind a caisson-type quay wall. In: *Proceedings of the Fourth International Conference on Recent Advances in Geotechnical Earthquake Engineering and Soil Dynamics and Symposium in Honor of Professor WD Liam Finn*. San Diego, California, March 26–31.
- Yuksel, Y, Alpar, B, Yalciner, A,C, Cevik,E, Ozguven, O, Celikoglu, (2003), “ Effects of the Marmara Earthquake on the Marine Structures and Coastal Areas”, *ICE, Water and Maritime Eng. Journal*, 156:147-163.
- Zeng,X.,1998.Seismic response of gravity quay walls—I:centrifuge modeling. *Journal of Geotechnical and Geoenvironmental Engineering* 124(5), 406–417.

(Architectural) measures to control wave overtopping inside the harbor of Oostende

Koen Van Doorslaer¹, Julien De Rouck¹, Leen Baelus¹ and Stefaan Gysens²

Abstract

One of the weak zones in the safety of the coastal city Oostende, Belgium, are the quays in the inner harbour which are rather low. A storm wall is an easy and effective measure to reduce wave overtopping and prevent the city from flooding. The location of this storm wall (close by the quay wall (2m) versus further away from the quay wall (15m)), and architectural alternatives for better integration in the setting have been studied at Ghent University. This paper summarizes the results.

Keywords: wave overtopping, vertical wall, reduction, storm wall, berm.

1 Introduction

Oostende, a city located in the middle of the Belgian coastline, contains an important seaport. To make this harbor accessible for ships with a length of 200m, the access channel has been reoriented perpendicular on the coast line and is protected by two new breakwaters (Verhaeghe et al, 2010). Apart from its economic importance, tourism and culture are also attracting a lot of people to Oostende. About 70.000 people live in Oostende throughout the year, a number which can be quadrupled during summer. The safety level of Oostende needs to be guaranteed.



Figure 1: Artist impression of the new harbour entrance in Oostende, Belgium (works in progress).

According to the Belgian coastal safety plan, the coastline has to be protected against a storm with a return period of 1000 years. During this storm, waves of $H_s = 5.00\text{m}$ and $T_p = 12\text{s}$ can occur outside Oostende harbour, and the still water level inside the harbour is predicted at TAW + 7.20m, incl 0.30m sea level rise (TAW + 0.00m = average low low water spring + 0.388m). The city centre is located almost 3m below this water level (around mean high water level TAW + 4.50m), and is protected by the quaywalls of the harbor and the dikes along the coast line. Their height (average TAW + 7.00m for the quaywalls and TAW + 9.60m for dikes) is not sufficient when this design storm would occur. Flood risk calculations have been made to determine the critical locations, and scale model tests were carried out to define the necessary

¹ Ghent University, Civil Engineering Dept. Technologiepark 904, 9052 Zwijnaarde. koen.vandoorslaer@ugent.be, julien.derouck@ugent.be, leen.baelus@ugent.be

² Flemish Government, Coastal Division, Vrijhavenstraat 4, 8000 Oostende, stefaan.gysens@mow.vlaanderen.be

measures to control the situation and minimize the risk on flooding of the city center. The safety limit was set at an overtopping discharge of 1l/s/m during the 1000year storm.

As input for the scale model tests, a numerical diffraction model has been used to estimate the disturbance coefficients K_D inside the harbor. This coefficient needs to be applied to the incoming wave through the entrance between the new breakwaters. The wave conditions at the critical locations were determined.

All scale model tests have been carried out in the 2D wave flume of Ghent University. This flume is 30m long, 1m wide and 1.2m high. The geometric and hydraulic boundary conditions have been scaled down using a Froude scale model with scale factor of 20. The overtopping discharge was captured in a 20cm wide tray, positioned on the crest of the structure in the middle of the 1m wide flume. This tray led the water to a basin, which was weighed continuously on a balance to determine the weight (volume) of the overtopped water.

Since it's a 2D flume only long-crested perpendicular wave impacts can be tested, while in reality 3D short-crested and oblique waves occur along the quay walls in the harbor. This research project is to be used as input for the model tests in a 3D wave basin, to gain time and money: only final geometries deducted from the 2D research have to be tested in the 3D basin.

This paper treats wave overtopping over vertical walls (the harbor quay walls), and the reductive measures taken to control this situation. Not the specific results for the case of Oostende will be handled, but some remarkable and general conclusions from this project will be explained. In this research projects, only waves with very low wave steepness (low wave height, long wave period) are tested. Therefore, results might not be generally valid, but only within the tested range of parameters.

In the next paragraph 2, a simple storm wall is proposed as reductive measure. In the research project, this wall was positioned at 2m and 15m away from the quay. This paragraph handles about the reduction due to the distance away from the quay.

In paragraph 3 different architectural measures are proposed to come up with a reduction of the freeboard to guarantee the same safety level in the city behind the quay walls, or to reduce the overtopping discharges when the same freeboard is maintained.

Conclusions are made in the last paragraph.

2 Storm wall at different locations

2.1 Reference case

The hydraulic boundary conditions in front of the first critical location were estimated at $H_{m0} = 2m$, and $T_p = 10s$. This corresponds with waves of steepness s_0 of 1.3%. This wave steepness is kept constant during the test series in paragraph 2, while the wave height and wave period increase.

At first, a reference case has been tested: waves overtopping a simple vertical wall. Since the water level during the 1000 year storm (SWL = TAW + 7.20m, including 0.30m sea level rise) is higher than the original quay wall (crest level TAW + 7.00m), there was no use of testing this high water level for the original quay wall. The daily high water tide (TAW + 4.70m) and the storm level of the 100 year storm (TAW + 6.70m, including 0.30m sea level rise) have been tested instead.

Another geometry has been added to this "reference case", where the overtopping discharge is captured at 2m behind the crest. This geometry is called "berm 2m" (see Figure 2).

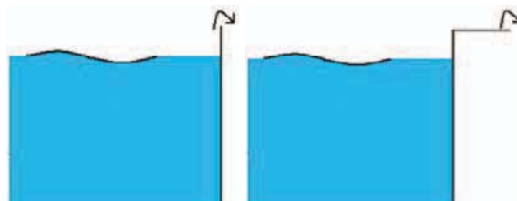


Figure 2: Berm 0m (left) and berm 2m (right): no difference in wave overtopping discharge.

No difference in overtopping discharge was distinguished, since all water coming over the quay wall is also captured 2m further (see Figure 3: no clear difference between red and blue symbols exists).

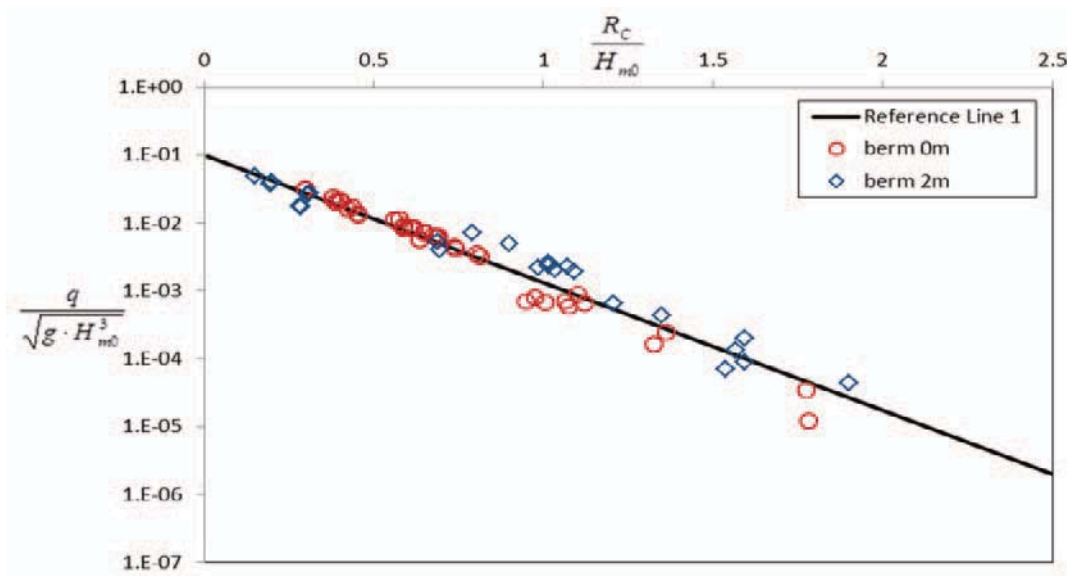


Figure 3: Dimensionless graph on overtopping discharge over a vertical wall (semi-logarithmic).

The data are presented in a typical semi logarithmic overtopping graph, where the dimensionless overtopping discharge is plotted on the Y-axis, the dimensionless freeboard on the X-axis. The black line is drawn as best fitting curve through the data from “berm 0m” and “berm 2m”. This line is now called Reference Line 1, to which all other tested geometries in this paragraph can be compared.

2.2 Storm wall at 2m behind the quay wall

The zone behind the quay wall is an open space, with possibility to build storm walls at certain distances behind the quay wall. A permanent or a mobile storm wall may be build. The latter can be constructed after a storm alert, for example by the fire department (see figure 4)



Figure 4: Firemen setting up the mobile storm wall.

To determine the necessary height and ideal location of these storm walls, model tests have been carried out. The tested water level now was TAW + 6.70m and TAW + 7.20m. A storm wall of different heights was built at 2m behind the quay wall, see Figure 5.

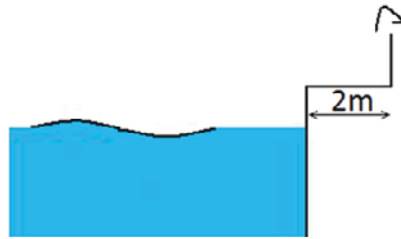


Figure 5: A storm wall at 2m behind the quay.

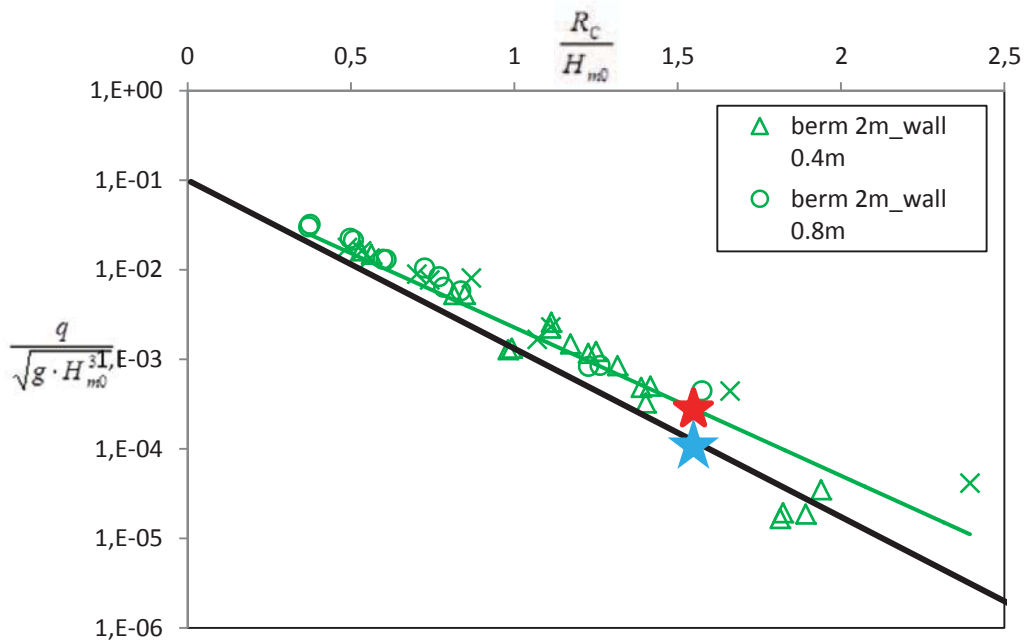


Figure 6: Dimensionless overtopping discharges over a storm wall located at 2m behind the quay.

Figure 6 clearly shows that nearly all data points are located above the Reference Line 1, deduced in Figure 3. This means that, for an equal freeboard R_c (see figure 7), a wave with height H_{m0} gives more overtopping when there is a storm wall at 2m distance from the quay wall (red star) than when the quay level is increased to the same level, without berm (blue star). The reason for this could be that when the berm is filled with water from a first wave, it helps the second incoming wave. It's like there is a triangular slope to "help" the next waves overtop the structure. Even though there is a berm, it has a negative influence!

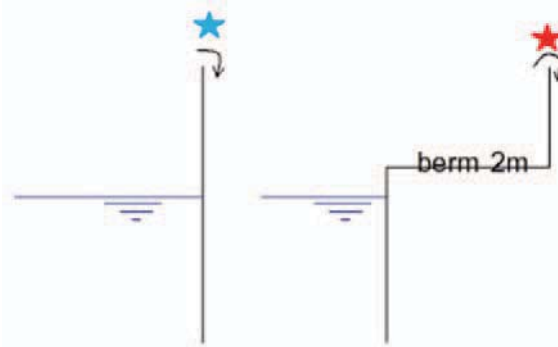


Figure 7: Two situations with the same freeboard R_c : left without storm wall but higher quay level, right with storm wall.

2.3 Storm wall at 15m behind the quay wall

Tests have been carried out with a storm wall further away from the quay: 15m (see Figure 8). The height of the tested storm walls and the wave conditions remained the same, for good comparison of the results.

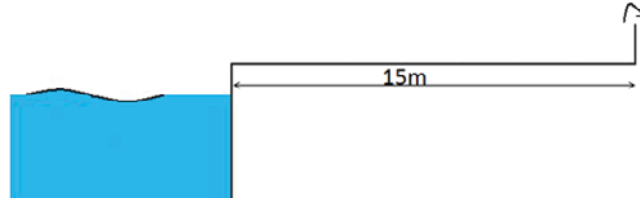


Figure 8: A storm wall at 15m behind the quay.

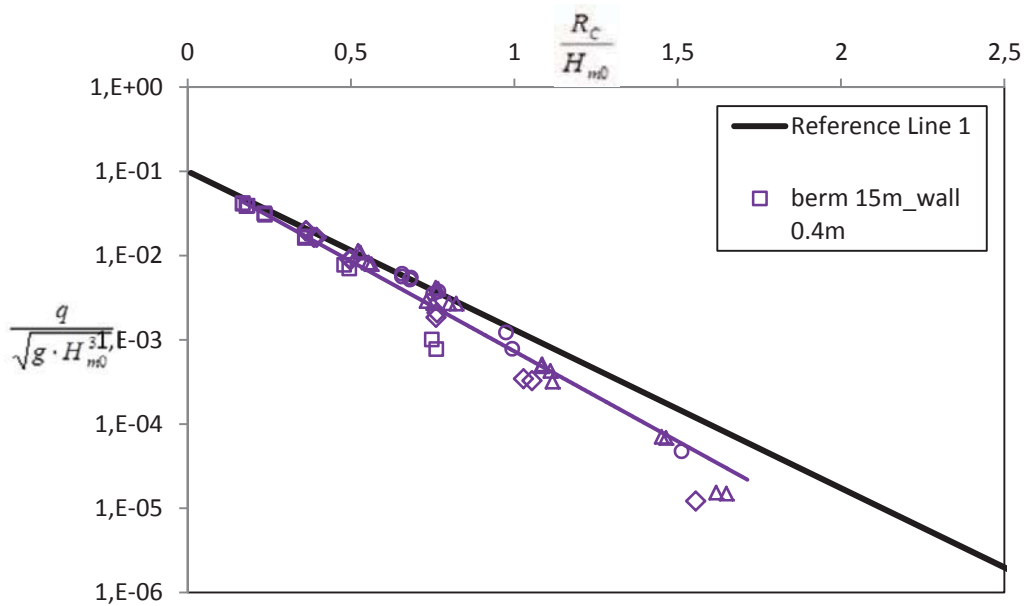


Figure 9: Dimensionless overtopping discharges over a storm wall located at 15m behind the quay wall.

For a longer berm (15m), this negative influence disappears: all purple data points are located below the reference line, see Figure 9. For the low steepness waves, the long berm (15m) reduces the wave overtopping while the short berm (2m) increases the wave overtopping, compared to a normal quay wall with the same freeboard.

3 Architectural measures

A second purpose of this research project was to study whether the implementation of architectural elements, without changing the crest level, could be used to reduce wave overtopping on critical locations. For a second critical location in the harbour, the wave conditions were estimated at $H_{m0} = 1.25\text{m}$, $T_P = 12\text{s}$ and $s_0 = 0.6\%$. The geometry of the second critical location is shown in Figure 10.

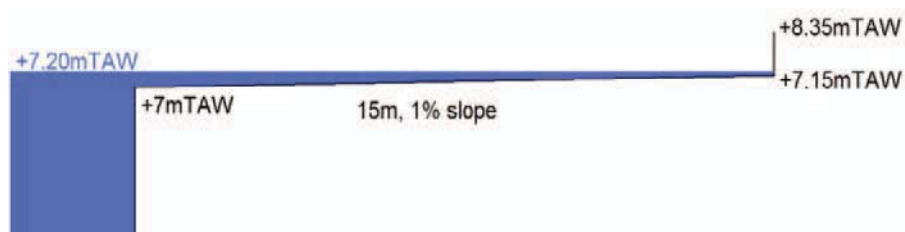


Figure 10: Geometry of the quay at a second critical location (Reference Line 2).

Tests have been carried out on the geometry of Figure 10 with $s_0 = 0.6\%$ kept constant during the whole test series. The geometrical variants which were tested are presented in Figure 11 to Figure 13: three wide steps of each 5m wide and 0.4m high (Figure 11), five short steps of each 20cm high and 30cm wide in the middle of the 15m wide platform (Figure 12), and three wide steps combined with open rows of storm walls (Figure 13).

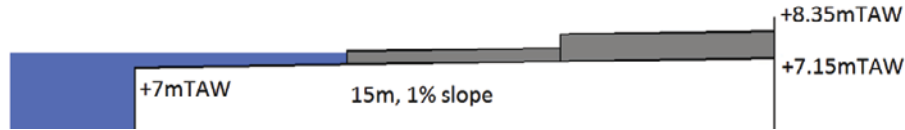


Figure 11: Three steps of each 5m wide.

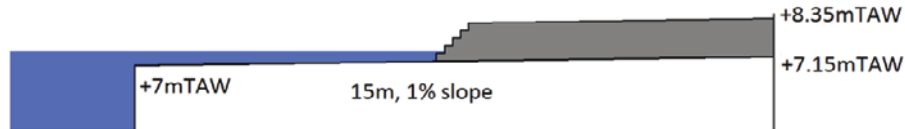


Figure 12: Short steps in the middle of the quay platform.

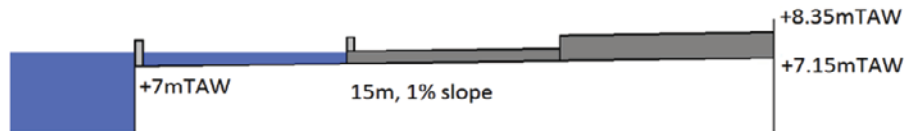


Figure 13: Wide steps with two open rows of walls. 1 open row walls at the seaside of 0.8m high, 1 open row on the first step of 0.4m high.

The data of the four proposed geometries (Figure 10 to Figure 13) are presented in a semi-logarithmic overtopping diagram, see Figure 14.

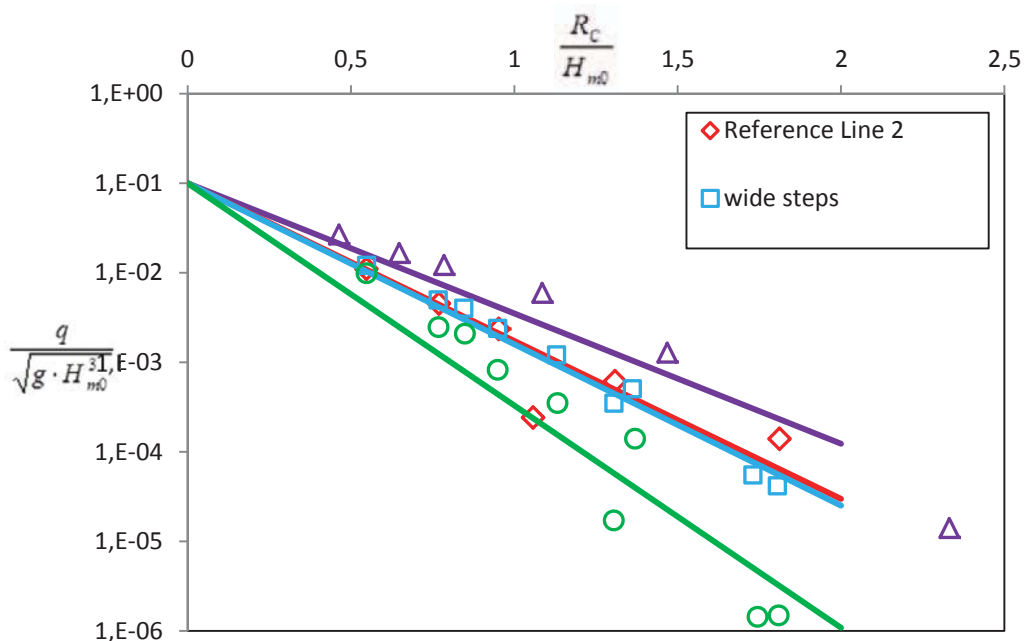


Figure 14: Dimensionless overtopping graph of all geometries related to the standard geometry (Reference Line 2).

The data of the standard geometry (Figure 10) are presented in red. The red line acts as Reference Line 2, to which the other three geometries can be compared. The same data can also be plotted in a non-dimensionless representation, see Figure 15.

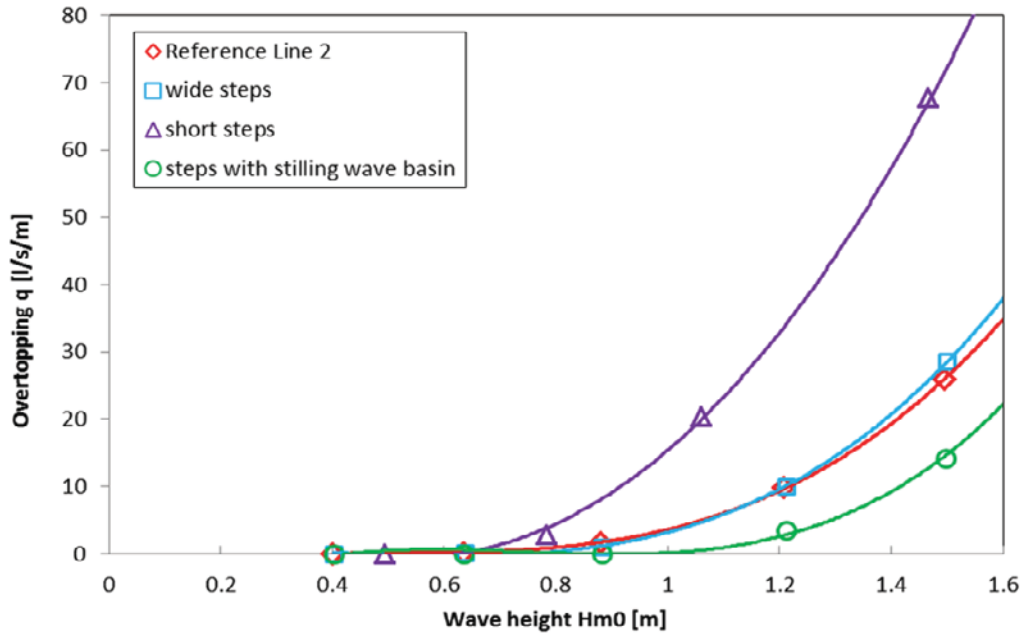


Figure 15: Non-dimensionless overtopping graph of all geometries related to Reference Line 2.

As can be seen from both Figure 14 and 15, the wide steps (blue data) have nearly no influence on the overtopping measured at the crest of the storm wall at TAW + 8.35m.

The short steps in the middle of the quay platform (purple data) have a (severe) negative influence. The steps act as a steep slope, which encourages the incoming wave to overtop this structure. More water is overtopping the landward crest of the storm wall at TAW + 8.35m.

The best reduction is, as expected, obtained by creating a kind of stilling wave basin (green data). The principle of this basin, first mentioned by Geeraerts et al (1996), is to allow waves to overtop the seaward wall. These waves “jump up against the wall and drop dead in a basin”, run back and forth between both rows of walls (which are open to let water evacuate, see Figure 18 top view) meanwhile losing their energy. They don’t have enough energy left to overtop the landward wall.

The open walls can easily be integrated in the (touristic) setting, for example by using benches. The reductive capacity can even be increased by changing the walls into parapets. This is done by adding a “nose” to the wall, creating a recurve wall (see figure 16 and 17 side view).



Figure 16: A parapet (recurve wall).

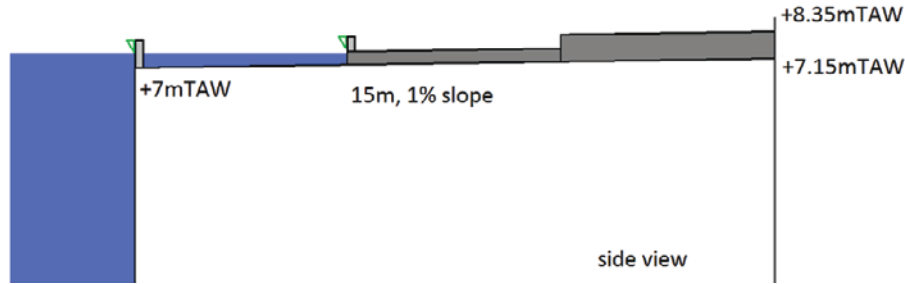


Figure 17: Reducing wave overtopping by changing the open row of walls by parapets, side view.



Figure 18: Top view of Figure 17, two open row of walls (with green parapet-nose) creating the stilling wave basin.

4 Conclusion

Traditionally in coastal engineering, one looks for the necessary freeboard, the height of the construction, to limit the overtopping discharge to a certain level (e.g. $q = 1\text{l/s/m}$). This research project has shown that the presence of steps, or a storm wall close by the quay wall can even increase the overtopping discharge (when comparing two geometries with the same freeboard!!).

- A storm wall at 2m away from the quay wall is more easily overtopped than a quay wall with the same height, while a storm wall at 15m away from the quay reduces the wave overtopping.
- Short steps on the quay platform act as a steep slope and stimulate wave overtopping.
- Two open rows of storm walls (Figure 17 and 18) work as a stilling wave basin, and reduce the wave overtopping drastically.

This paper proves that it is always strongly advised to carry out model tests, especially in case of non-typical layouts. Even small adaptations to the basic geometry, with preservation of the crest freeboard, can have severe negative influences on the overtopping discharge.

5 References

- Geeraerts, J., De Rouck, J., Beels, C., Gysens, S. and De Wolf, P. (2006) Reduction of wave overtopping at sea dikes: stilling wave basin (SWB). ASCE, Proc. ICCE 2006, San Diego, Volume 5 – pp. 4680-4691
- Verhaeghe, H., Van Damme, L., Goemaere, J., De Rouck, J., Van Alboom, W.(2010) Construction of two new breakwaters at Ostend leading to an improved harbor acces. Proc. ICCE 2010, Shanghai
- Van Doorslaer, K., De Rouck, J. (2010) Reduction of wave overtopping on a smooth dike by means of a parapet. Proc. ICCE 2010, Shanghai

Technical Session 5: Coastal Developments

Chairman: Dr.-Ing. Andreas Kortenhaus

Coastal protection of lowlands:

Are alternative strategies a match to effects of climate change

Hanz D. Niemeyer¹, Cordula Berkenbrink¹, Marco Miani¹, Anne Ritzmann¹, Pushpa Dissanayake¹, Heiko Knaack¹, Andreas Wurpts¹, Ralf Kaiser²

Abstract

Expected changes of global climate will create impacts being an unknown challenge for coastal protection: Accelerated sea-level rise and stronger storms create both higher storm surge levels and stronger waves. Moreover, the adaption of intertidal areas in the coastal areas might be delayed providing larger water depths in front of coastal structures allowing again the occurrence of stronger wave impacts on coastal structures. Therefore the future safety of coastal lowlands is of increasing importance. Alternative strategies to the presently exercised keeping the line of protection structures must be taken into consideration in order to provide appropriate solutions the safety of coastal lowlands in due time.

Keywords: Climate change, sea-level rise, coastal protection strategies

1 Introduction

Global climate changes and the consequently resulting acceleration of sea-level rise require a thorough reevaluation of coastal protection strategies in many parts of the world. This yields also for the lowlands at the southern North Sea coast in Europe which are protected by a line of dykes since about 1,000 years. The anticipation of an accelerated sea-level rise due to global warming has raised the question if this strategy of keeping the line will still be appropriate or if alternatives should be taken seriously into consideration. This yields the more since furthermore a number of secondary effects of climate change will lead to stronger loads on coastal protection structures: increasing intensity of storms and consequently higher set-ups of storm surges (Woth et al, 2005) create as well larger water depths in front of coastal structures as the delayed adaption of tidal flat levels to an accelerating sea-level rise (Müller et al, 2007). Since wave heights and periods on flats are strongly depth-controlled (Niemyer, 1983; Niemyer & Kaiser, 2001) any increase of local water depth is accompanied by corresponding higher wave loads on coastal structures.

Alternatives to line protection are well known from the past: retreat, accommodation and moving the protection line seaward (Figure 1). Their suitability is as well discussed as that of alternatives being introduced recently. Experience with alternative strategies in the past is considered.

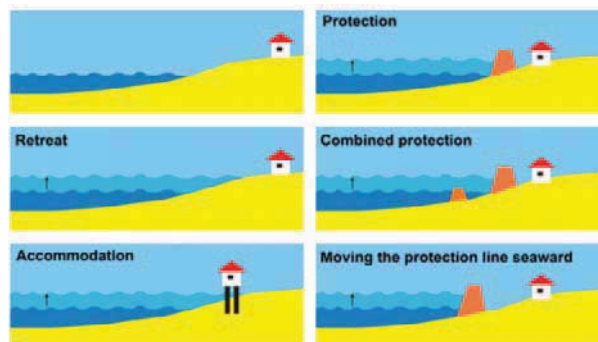


Figure 1: Basic strategic alternatives in response to sea-level rise (IPCC, 1990)

¹ Coastal Research Station - Lower Saxony Water Management, Coastal Defence and Nature Conservation Agency, 26548 Norderney, Germany

² Lower Saxon Ministry for Environment and Climate Protection, Germany

2 Coastal Protection Strategies in the Past

The post-glacial sea-level rise at the southern North Sea inundated large areas (Figure 2) leaving no alternatives to the coastal inhabitants than retreat, since there were on the one hand no tools available to defend land against the sea. On the other the high rates of sea-level rise occurring until 7,000 B.P. might even today pose an irresistible threat to coastal areas.

The later deceleration of sea-level rise and even periodical regression providing a rather stable coastline attracted settling in the fertile coastal lowlands. In order to get safe against temporary flooding of the marshlands the settlers in these coastal areas erected artificial dwelling mounds being sufficiently high to perform a safe haven during storm surges, called 'Warft' in Friesian language.

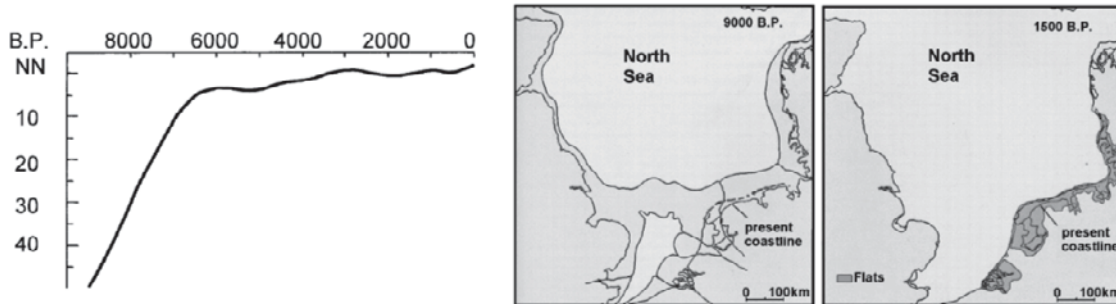


Figure 2: Sea-level rise at the coast of Schleswig-Holstein (Streif & Köster, 1978) between 9,000 B.P. and present and coastal retreat at the southern North Sea between 9,000 and 1,500 B.P. (Veenstra, 1976)

One of the first references about these settlements was given by the Roman historian Pliny who accompanied Roman naval forces to the coastal lowlands at the southern North Sea coast. These dwelling mounds have been enhanced more than once in the course of centuries in order to meet the sea-level rise (Figure 3, Left). The largest of these hills were populated by whole villages which are still well-known landmarks at the Friesian coast ranging from the Netherlands across Germany to Denmark (Figure 3 Right)

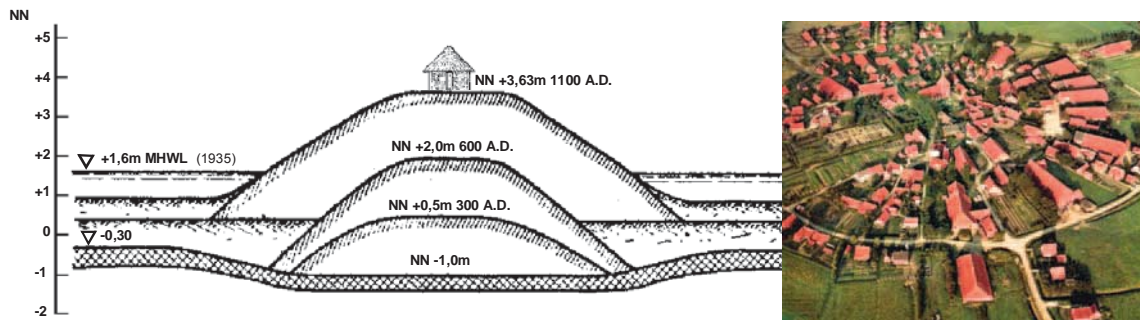


Figure 3: Left: Scheme of a dwelling mound with a single building and its adaptations to higher storm surge levels between 300 and 1,100 A.D.; adapted from Krüger (1938); Right: Aerial photograph of the village of Rysum in East Frisia. The ring road marks the border of the dwelling mound; the church at the top functioned as a safe haven as well during storm surges as against hostile invaders.

Early medieval storm surges inundated areas with extremely erodible soil like e. g. peat and created large bays being afterwards not in tune with hydrodynamics (Niemeyer, 1991). Consequently enormous silting-up took place which was supported by local coastal inhabitants with the aim of land reclamation. The siltation created a rise of the tidal flats significantly above mean high tide shaping supratidal salt marshes due to coincidental settlement of vegetation. From that stage of growth the height of the marshlands allowed enclosures by dykes with tools then available (Figure 4). The pride of the coastal inhabitants about their success against the sea created the saying: God made the sea, the Friesian the coastline.

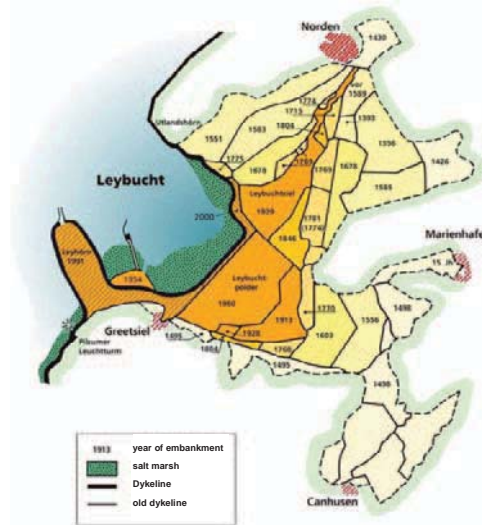


Figure 4: Embankments of supratidal salt marshes in the Ley Bay area in East Frisia since the 15th century (Homeier et al. 2010)

3 Research Concept

The currently existing knowledge allows in most cases only comparisons of the present and alternative coastal protection strategies for lowlands by verbal-argumentative assessment. With regard to the problems arising due to effects of climate change impacts and the necessarily high efforts for matching them successfully a more resilient and tangible basis for judging and planning is both strongly needed and will be highly cost effective. The Lower Saxon Ministry for Science and Culture has recently launched the research program KLIFF on impacts of climate change and appropriate adaptation as a call for bids. The proposal of the research project A-KÜST has been accepted by the jury and started in spring 2009.

Major aim of the project is the evaluation of impacts of climate change on a regional scale on the same technical and scientific level as that of real world design for coastal protection: storm intensity above the North Sea and adjacent Lower Saxon coast and the there occurring sea-level rise, storm surge water levels and waves, adaption of tidal flats, loads on coastal structures to be expected in 2030, 2070 and 2100 on the basis of the scenarios A1B and B1 of the IPCC (2007), the first one is more pessimistic with respect to future emission of greenhouse gases whereas the second one is more optimistic.

In a first step boundary conditions from the global climate model ECHAM5/MPIOM (resolution 200 km) are downscale to wind and pressure fields on a regional scale model COSMO-CLM for the North Sea area with a resolution of 20 km which provide in combination with an anticipated sea-level rise the necessary boundary condition for both tidal (TRIM) and wave (WAM) models for the North Atlantic and North Sea area. The resolution of the North Atlantic model is 50 km (WAM) and that of the North Sea model 10 km for tides (TRIM) and 5 km for waves (WAM) respectively. The North Atlantic model delivers the hydrodynamic boundary conditions for the North Sea model (Figure 5, Left).

In the coastal area a higher resolution is indispensable due to increasing variations of the bathymetry in order to get an appropriate reproduction of water levels, currents and waves. In the southern North Sea the German Bight model takes over the results from the North Sea model and provides approximately at the 30 m-depth contour the boundary conditions for the Ems-Dollard-estuary model (Figure 5, Right); tides and wave modeling is coupled using Delft-3D with SWAN and curved-linear grids with a resolution between 240 and 100 m. The water levels and waves at the coast are modeled in the Ems-Dollard-estuary model covering a smaller area (Figure 5, Right) with a higher resolution of the curved-linear grid between 210 and 60 m.

In a first step water levels and waves in front of the existing coastal structures are evaluated for the distinct climate scenarios using the described model chain for 2030, 2070 and 2100. Wave run-up and overtopping at coastal structures is modeled with OTT. For the pessimistic scenario

in 2100 and the highest water levels the before described alternative coastal protection strategies set-back, two lines, accommodation and retreat will be also evaluated. Flooding of the presently protected areas for the strategy accommodation will carried out by applying MIKE 21 and SWAN.

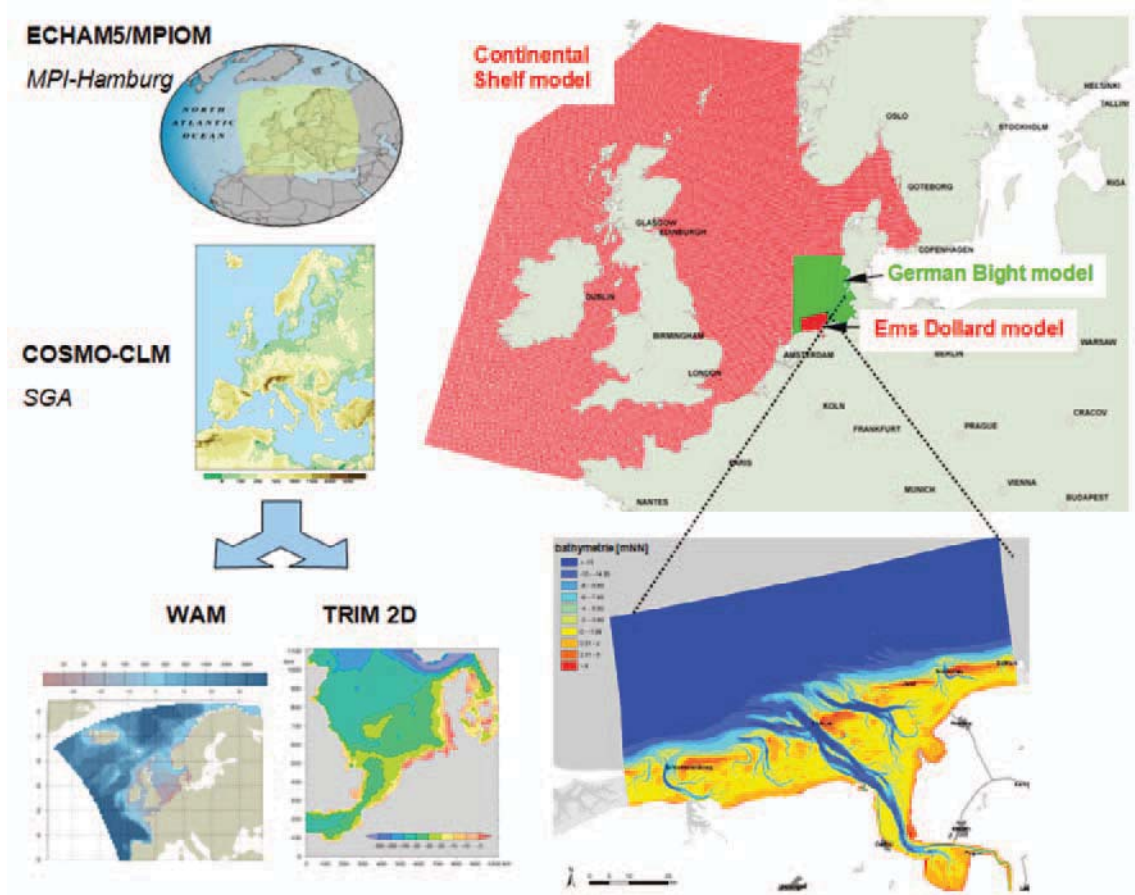


Figure 5: Left: Downscaling from the global climate model to the regional model COSMO-CLM and bathymetry of the North Atlantic- and North Sea model of the GKSS-Institute for Coastal Research; Right: Coupling of German Bight and Ems-Dollard-estuary model with model bathymetry of the Coastal Research Station

It is expected that the model results will deliver resilient quantitative foundation for the decision making on future coastal protection strategies enabling the coastal managers in the area for the first time to make proper cost estimates. This comparison will also include recently gained research results on increasing wave overtopping tolerance allowing higher design water levels for existing structures (Niemeyer et al, 2009, 2011). The research on the physical effects of climate change on the area of the Ems-Dollard estuary is accompanied by sociological research dealing with the position of the regional stakeholders.

4 Evaluation Alternatives

4.1 Retreat

A retreat from the inhabited coastal areas would enforce the loss of enormous assets. A resettlement of the coastal population in areas being safe from inundation due to storm surges without any requirement of protection against storm surges would furthermore create a large burden for both individuals and society. The extension of those areas becoming uninhabitable without protection against storm surges is enormous which is clearly demonstrated by those areas being nowadays designated by law as protected (Figure 6).

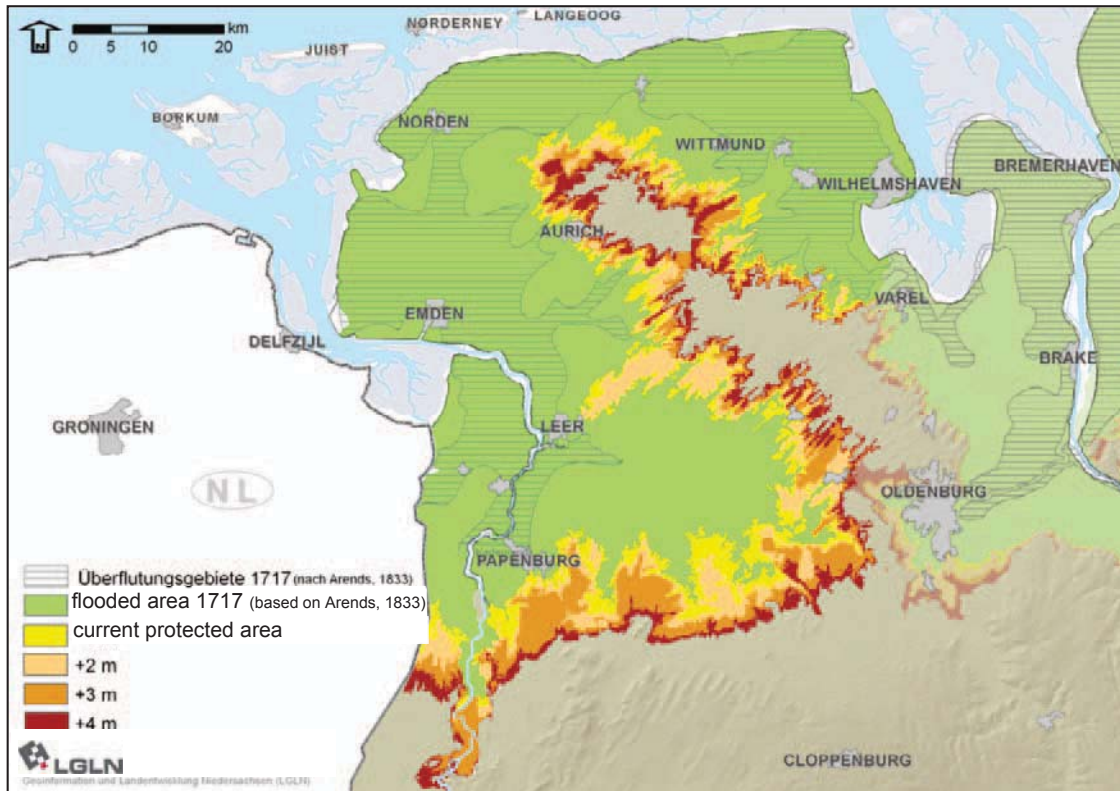


Figure 6: Coastal flood prone areas in Northwestern Lower Saxony as designated by Lower Saxon Dyke Act and flooded areas after Christmas storm surge in 1717

About 800,000 people living in the coastal lowlands of the State of Lower Saxony would lose their homes and economic basis and an almost equal number in neighboring states being indirectly dependent on the Lower Saxon coastal protection system. Furthermore an enormous part of the cultural heritage of the lowlands like e. g. the medieval churches or prehistoric stone graves would be lost forever. Comparing the cost saving aspects due to a total withdrawal from coastal protection with the implicit enormous economic and cultural losses this alternative is regarded as highly unfavorable. The effect of retreat in respect of corresponding losses is sufficiently highlighted by the coastal flood prone areas as designated by the Lower Saxon Dyke Act. The flooded areas after the Christmas surge of 1717 highlight dramatically the reliability of this design, particularly if taking into consideration that the peak of this storm surge would currently about 0,7 m higher due to sea-level rise since then. The impacts of future climate change can simply be evaluated by adding anticipated higher sea levels above present design water levels.

4.2 Accommodation

Accommodation in the lowlands requires numerous protected islands with settlements and industrial areas in the lowlands at the coast. The use of the former dwelling mounds (Figure 3, Left) is not purposeful: their surface is nowadays too low in respect of storm surges levels due to the sea-level rise which has taken place since their erection. A further heightening is only possible for a few ones without settlements and buildings since most of them are densely covered by buildings (Figure 3, Right). They prevent any rising of their surface without destruction of the developed infrastructure. Therefore the creation of well-chosen areas surrounded by dykes is regarded as more economic than the adaptation of most of the existing dwelling mound to present and future design conditions. Rough estimates of costs for this type of accommodation are expected to be at least as high as those for strengthening of the existing dykes at the coastline.

A schematic example for the western part of East Frisian highlights the enormous efforts being necessary to create those save havens against storm surges in coastal lowlands (Figure 7).

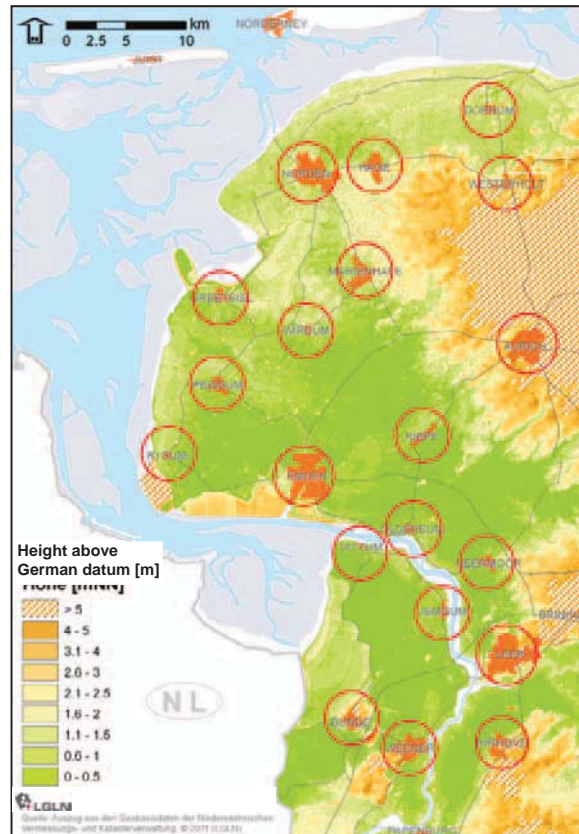


Figure 7: Scheme of save havens in western East Frisia

Furthermore infrastructure like e. g. roads or railways connecting those save havens are more vulnerable to the impact of storm surges and will require much higher maintenance costs than in protected areas. Already a rough comparison makes it evident that accommodation as an alternative coastal protection strategy for dealing with an accelerating sea-level rise will require high investments corresponding with enormous economic losses due to the abandonment of smaller settlements and agricultural revenues and maintenance of infrastructure after flooding due to storm surges. Nevertheless modeling of storm surge flooding and accompanying waves in these areas without the present dyke line for present and future design conditions will be carried out in order to put a figure on the efforts being necessary for creating save havens. This will provide a sound basis for a tangible comparison in respect of efficiency with the present strategy of line protection at the coast.

4.3 Set-back of dykes

Other options which are discussed as alternative strategies are modifications of keeping the line like the set-back of a dyke line by constructing a new dyke line in a larger distance from the coastline creating a belt of salt marshes with the aim to enforce a stronger attenuation of waves attacking the dyke (ComCoast 2007). But that concept neglects that no longer sedimentation could take place after earlier embankments of salt marshes. Whereas the salt marshes in front of the dykes could grow furthermore, the embanked ones remained at the level before their embankment. Therefore the gradient of the surface level is declining from the present coastline inland leading to lower surface levels the more away from the sea. After a set-back of a dyke line water depths in front of a dyke in a distance from the present coastline will increase. Consequently also wave loads on the dyke will there be higher than at the present coastline. An example of a set-back of 3.5 km at the Dollard Bay makes evident by wave modeling that for design conditions significant wave heights increase by approximately 15% and energy periods by approximately 8% (Figure 8) and resultantly to an increase of wave run-up of approximately 20%.

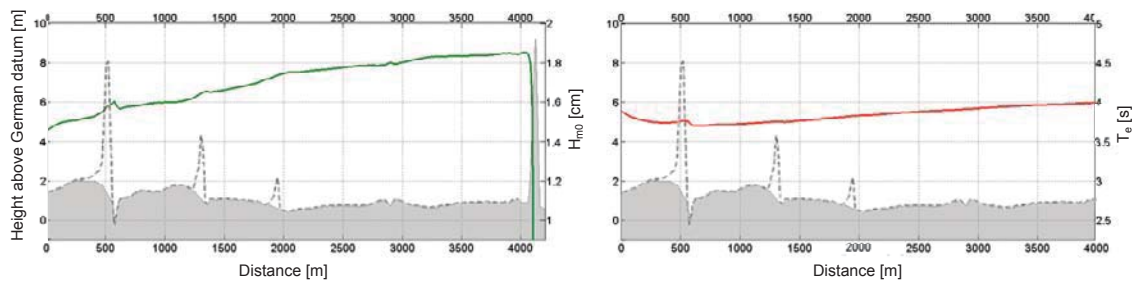


Figure 8: Increase of significant wave height (left) and energy period (right) at design water level after set-back of a dyke from position 500 to position 4.000

Already this simple example highlights that the set-back of a dyke line in coastal lowlands has no advantages: wave loads are higher and require a higher structure for protection against storm surges than at the present coastline. Furthermore that strategy would demand enormous efforts for the construction of a totally new dyke line landward of the existing one and the - according to existing law - necessary compensation of the private land owners. An unquestionable advantage being achieved by a set-back of a dyke line would be the creation of large areas of salt marshes which are regarded as highly valuable with respect to ecology. But in respect of coastal protection a set-back of dykes lines is unfavorable both in regard of safety and economically.

4.4 Combined Protection

Another alternative for protection of the hinterland is the two-line strategy with a combination of two structures for coastal protection (ComCoast, 2007): the most seaward one with the aim to act as a submerged breakwater and in a certain distance another one being sufficiently high to keep storm surges levels at bay but being attacked only -if even- only by very small waves. The latter will allow steeper slopes than with stronger wave action and therefore a smaller cross-section.

In order to create submerged breakwaters being even effective for an accelerating sea-level rise significantly high efforts would be required (Figure 9): Wave modeling at a combination of a breakwater and a secondary dyke in different distance from the breakwater highlights that there is only a quite small reduction of wave run-up in comparison to that at an conventional dyke (Figure 9): a breakwater with a crest width of 10 m will only reduce the wave run-up by less than 30% in the first position after the breakwater if the crest height is 0,15 m below still water-level and by less than 20% if its 0,40 m lower.

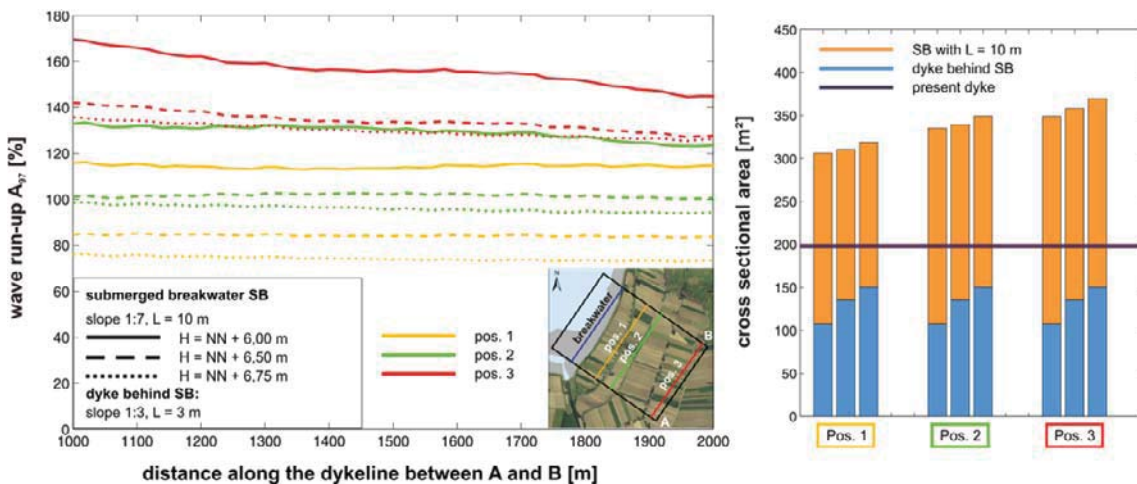


Figure 9: Left: Comparison of wave run-up at dykes behind a submerged breakwater subject to the distance to that and the present conventional dyke (100%); Right: Comparison of the required cross section areas for the different combined protections and the present conventional dyke

In all the cases no reduction of wave run-up is gained. Furthermore in all cases the joint crest-sectional area needed for combined protection is at least 50% larger than for a conventional dyke.

Investment costs will be very high since the construction must be strongly armored in order to avoid its destruction by overflow during a storm surge leading to strong wave attack on the second dyke which is highly vulnerable against wave attack would then endanger the whole protected hinterland.

5 Conclusions

The expected acceleration of sea-level rise due to global climate changes requires a reevaluation of coastal protection strategy. For 1000 years the lowlands at the southern North Sea coast have been protected by a chain of dykes. Alternatives to conventional coastal protection under discussion are on the one hand those strategies known from the past: retreat or accommodation. On the other hand modifications of the current strategy of protection by keeping the line are under discussion: set back of the protection line or splitting up into two lines.

Evaluations of these alternatives highlight up to now that there is no obvious evidence that one or some of them would outmatch the existing strategy by economic standards. A higher level of safety than provided by protection by holding the line could only be achieved by retreat from the areas endangered by storm surges accompanied by the total loss of these areas. Advantages evaluated by pure qualitative-phenomenological comparison have been proven as misleading when checked quantitatively by process-based mathematical modeling. For the anticipated rates of sea-level rise the protection of the lowlands at the southern North Sea coast by a chain of dykes is still an effective strategy with respect to both safety and economic efficiency; even if further unfavorable secondary effects of climate change are considered.

The risks for safety in coastal areas being expected in connection with climate change impacts require results providing decision makers with as well the necessary quantitative database as tangible process-based insights into the associated developments. This will enable them to evaluate technical and economical consequences of both continuing the current strategy and replacing it by alternatives. The research project A-KÜST will continue to deliver products aimed at this target.

6 Acknowledgments

The research on alternative coastal protection strategies is carried out jointly by the Coastal Research Station of the Lower Saxony Water Management, Coastal Defence and Nature Conservation Agency as lead partner with the following partner institutions in the framework of the project A-KÜST: HZG-Institute for Coastal Research, Coastal Research Laboratory / Kiel University, Institute for Communication on Environmental Problems / Lüneburg University. The project is part of the KLIFF-program (Research on Effects of Climate Change) being launched and sponsored by the Lower Saxon Ministry for Science and Culture.

7 References

- ComCoast (2007): The future of flood risk management. www.comcoast.org.
- Homeier, H.†; Stephan, H.J.; Niemeyer, H.D. (2010): Das Historische Kartenwerk Niedersächsische Küste der Forschungsstelle Küste (Maps of historical reconstructions of the Lower Saxon coast by Coastal Research Station). Berichte der Forschungsstelle Küste 43-2010, Norderney.
- IPCC (Intergovernmental Panel on Climate Change) (1990): Strategies for adaption to sea-level rise. Executive Summary of the Coastal Zone Management Subgroup. Intergovernmental Panel on Climate Change - Response Strategies Working Group. The Hague/The Netherlands.

- IPCC (Intergovernmental Panel on Climate Change) Solomon, S.; Qin, D.; Manning, M.; Chen, Z.; Marquis, M.; Averyt, K.B.; Tignor, M.; Miller, H.L. (eds) (2007): Summary for Policymakers. Climate Change 2007: The Physical Science Basis. Contribution of Working Group I to the Fourth Assessment Report of the IPCC. Cambridge University Press, United Kingdom and New York, NY, USA.
- Krüger, W. (1938): Die Küstensenkung an der Jade (Coastal decline at the Jade), in: Der Bauingenieur 19 (7/8), 91-99.
- Müller, J.-M.; Zitman, T.; Stive, M.; Niemeyer, H.D. (2007): Long-Term Morphological Evolution of the Tidal Inlet "Norderneyer Seegat". in: McKee Smith, J. (ed). Proc. 30th Int. Conf. Coast. Engg., San Diego, September 1-8, 2006, New World Scientific, New Jersey, 4035(11).
- Niemeyer, H.D. (1983): Über den Seegang an einer inselgeschützten Wattküste. (On the Wave Climate at an Island-sheltered Coast). BMFT-Forschungsber. MF 0203.
- Niemeyer, H.D. (1991): Case Study Ley Bay: An Alternative to Traditional Enclosure. Proc. 3rd Int. Conf. Coastal & Port Engg. in Devel. Countries. Mombasa/Kenya, September 16-20, 1991, pp. 43-58.
- Niemeyer, H.D. (2005): Coastal protection of Lowlands: Are alternative strategies purposeful for changing climate? Proc. 14th Biennial Coastal Zone Conference, New Orleans/La., July 17-21.
- Niemeyer, H.D.; Kaiser, R. (1998): Modeling of Effectiveness of Wave Damping Structures in Wadden Sea Areas. Proc. 5th Int. Workshop on Wave Hindcasting and Forecasting. Melbourne/FI., January 26-30, 1998, pp. 231-238.
- Niemeyer, H.D.; Kaiser, R. (2001): Hydrodynamische Wirksamkeit von Lahnungen, Hellern und Sommerdeichen (Hydrodynamical Effectiveness of Land Reclamation Structures, Salt Marshes and Summer Dykes). Die Küste, Vol. 64, pp. 16-58 (in German).
- Niemeyer, H.D.; Kaiser, R.; Berkenbrink, C. (2009): Increasing Dyke Overtopping Security as a Countermeasure to Accelerating Sea-level Rise. Proc. 33rd IAHR-Congress Vancouver/Canada, August 9-14, 2009, pp.6789-6796.
- Niemeyer, H.D., Kaiser, R.; Berkenbrink, C. (2011): Increased overtopping security of dykes: a potential for compensating future impacts of climate change. In: McKee Smith, J. (ed.): Proc. 32nd Int. Conf. Coast. Engg., Shanghai/China, June 30-July 5, 2010, New World Scientific, New Jersey.
- Streif, H.; Köster, R. (1978): Zur Geologie der deutschen Nordseeküste (On the geology of the German North Sea coast). Die Küste 32, pp. 30-49, Heide/Holstein.
- Veenstra, H. (1976): Struktur und Dynamik des Gezeitenraumes (Structure and dynamics of intertidal areas), in: Abrahamse, J., Joenje, W. and Leeuwen-Stelt, N. (eds.), Wattenmeer. Ein Naturraum der Niederlande, Deutschlands und Dänemarks, Wachholtz Verlag, Neumünster, pp. 19-45.
- Woth, K.; Weisse, R.; v. Storch, H. (2006): Climate Change and North Sea Storm Surge Extremes: Ensemble Study of Storm Surge Extremes Expected in a Changed Climate Projected by Four Different Regional Climate Models. Ocean Dynamics, Vol. 56, 3-15.

Product orientation in COSYNA: integrating coastal observation and models

Kai Wirtz¹ and Friedhelm Schroeder²

Abstract

Human interference with shelf and coastal seas creates various information needs. Given the strong variability and great complexity inherent in coastal systems, these needs can be best addressed using a synoptic approach. The Coastal Observation System for Northern and Arctic Seas (COSYNA) has the mission to generate a synopsis of a heavily used coastal sea, the German Bight. This short paper illustrates how the set-up of a large environmental observatory like COSYNA was guided by product orientation. At the start of COSYNA, information demands were collected and prioritized by stakeholder surveys. In order to generate time- and space-continuous products like maps for currents or suspended matter concentration, observational data are assimilated into state-of-the-art, high resolution models. This model-data approach ultimately relies on cost-effective and (space and time) extensive observational technologies which, in turn, lead to new challenges in data processing, quality assurance, data management, and in developing portals for end-users. Coastal observatories, insofar oriented towards specific products, join applied and fundamental coastal science and improve their efficacy.

Keywords: observatory, data-model integration, German Bight, platforms of opportunities, information products

1 Challenges for coastal and shelf sea research

1.1 Changing coasts under increasing pressures

Shelf and coastal seas are focal interfaces of the Earth System and intractably connected to the well-being of human societies. Coastal seas experience sudden and catastrophic events, or multi-scale shifts in key processes (Beaugrand 2004, Friedland & Hare 2007, Schlüter et al. 2008). Beside large natural fluctuations, they are also subject to direct or indirect anthropogenic forcing, such as climate change, eutrophication and oligotrophication, or substantially altered uses of sea space like offshore wind-energy conversion (Lozan et al, 2003). The sum of all these stresses shapes the physical state of coastal and shelf seas (e.g., changes in morphology, wave climate or water level) or the health of their ecosystems (water quality). Coastal ecosystems generate food resources (for birds, marine mammals or other higher trophic level organisms including humans), and mediate important matter fluxes (e.g. suspended organic material, lithogenic sediments, or CO₂). They provide various relevant services to human societies.

Societies living at or near coasts therefore have various information needs. Their stakeholders seek for specific forecasts or “what-if” decision help (scenarios) and ask for cost-effective but still reliable information. Questions may be related to system-wide or local phenomena. In most cases, they are difficult to address because of the interconnected processes involved. Coasts, by their complex topology, build the edge of most Earth System compartments. As interfaces between land and open ocean, between geosphere and atmosphere, sometimes also in connection to episodic or permanent ice, coastal systems respond to trans-boundary forces and strong variability. Multiple and interconnected process dependencies already emerge at the event scale. For example, whether a toxic oil spill reaches a vulnerable habitat or populated area is determined by complicated current patterns, superimposed wind-drifts, wave climate features, and by the occurrence and performance of oil-degrading (benthic or pelagic) bacteria.

¹ Institute of Coastal Research, Helmholtz Zentrum Geesthacht, D-21501 Geesthacht, Germany, kai.wirtz@hzg.de

² Institute of Coastal Research, Helmholtz Zentrum Geesthacht, D-21501 Geesthacht, Germany, friedhelm.schroeder@hzg.de

The mutual interconnectivity of driving processes even increases on longer (decadal) time-scales what is best seen in the multi-faceted type of past regime shifts (Schlüter et al.2008).

As a consequence, a basic prerequisite to meet relevant information demands is the capability to produce a coherent state description. This synoptic description needs a systematic integration of measurements and modelling. In light of the large uncertainties inherent to physical, geological, or biogeochemical models of coastal seas, such a description sets a benchmark for coastal observations which in the past have often been of fragmented nature.

1.2 Southern North Sea

Information demands arise along all coastlines and shelf seas worldwide. One long-lasting hotspot and therefore also relatively well researched area is the North Sea. This shelf sea is among the most actively used on our planet. Different types of utilisation, e.g., ship traffic, recreation, dredging, nature conservation, and offshore wind energy parks compete against each other and the political bodies need information for administrative decisions. Due to the counter-clockwise residual circulation in the North Sea, discharges of major western European rivers reach (and pass) the German Bight. At its southern and eastern boundary the German Bight hosts one of the most unique tidal ecosystems, the Wadden Sea. Relevant and recurrent management and research questions for the southern North Sea and the Wadden Sea are linked to decadal changes in water level and coastal morphology, sediment transport, safety of transportation, water quality, or ecological impacts of anthropogenic resource uses. Various scientific projects have generated a vast amount of data-sets for the German Bight in physical, geological, biological or chemical aspects. These, in general, were confined either in space (local) or in time (episodic) so that synoptic assessments are yet rather the exception.

1.3 Grand questions for COSYNA

1.3.1 Successive targets for a large coastal observatory

The systematic integration of measurements and modelling to cope with the information need at the regional scale requires a novel and necessarily multi-stage approach, with intermediate targets and milestones. Such an approach has recently been initiated with the Coastal Observation System for Northern and Arctic Seas (COSYNA). Similar shallow water observatories are underway off the coast of New Jersey (Schofield et al. 2002, Creed et al 2005), and for the Irish Sea Observatory in Liverpool Bay.

It is expected that COSYNA and similar initiatives are capable, within a few years, to produce coherent and reliable monitoring data which are effectively managed and integrated into operational coastal prediction systems. Setting-up, for the first time, a large integrated facility clearly defines in itself a goal for applied coastal research and engineering. COSYNA acknowledges the relevance of system development within its targets that ought to be addressed in a sequential way:

1. development in applied and operational oceanography (physical and biogeochemical)
2. generation –and communication– of specific information products
3. creating a synoptic view

1.3.2 Applied and operational research

There are only few existing technologies which allow for cost-effective and time- or space-continuous monitoring of oceanographic variables. Consequently, COSYNA has to trigger technological development in various fields of operational research (e.g. multi-sensor development, automated quality control, techniques for data assimilation and others). Given the extremely high costs of offshore platforms and ship operation, COSYNA seeks to make use of ships of opportunity and (semi)autonomous systems, e.g., gliders. In addition, the observatory aims to extend synergies with existing infrastructures in the German Bight, either provided by authorities or private companies. The usage of autonomous systems as well as platforms of opportunities, however, necessitates refined technical solutions for sensor maintenance and data handling. Employment of multiple sensor technologies, both *in situ* and remotely, also requires homogenization of data and advancing their quality, e.g., by ground-truthing. Near-time

transmission and processing of large data flows technically challenges hardware systems nowadays existing in operational coastal oceanography.

In a multi-component observatory, system integration is a central task. A grand software-engineering goal is to build a data management system, with common standards and with functionalities fitted to the needs of COSYNA operators and scientists as well as different external users. The data management system has to ensure near realtime processing of observations in order to constrain pre-operational models through data assimilation. Taken together, to generate cost-effective and region wide continuous monitoring data is ultimately meant to support coastal management and subsequently also fundamental environmental science, but at first place stimulates operational research.

1.3.3 Producing specific information

In order to make sure that information provided by an observatory can be effectively used as (decision) support for stakeholders, strong collaboration and interaction with end-users has to be secured starting already at the design stage. In the course of the COSYNA set-up, regular user workshops and participation of stakeholders (e.g., within steering committees) helped to define specific data and product needs. During the initial design phase (2009), two surveys were conducted, one among administrative or research representatives in countries adjacent to the Wadden Sea, the other among representatives of 60 German institutions related to the coastal issues. These surveys complemented the EuroGoos Marine Technology Survey from 1998 where the traditional physical oceanographic variables were at the top of the table, with an emphasis on waves and currents suspended sediments (Bosman et al 1998). The results from the COSYNA surveys revealed a first view on expectations for an integrated coastal monitoring and modeling system. In the national survey, most priorities were expressed towards wave climate and physical transport, but also information on ecological parameters was found important. It has to be noted, however, that expectations may and will change over time and – apart from a pure need- partly reflect experiences with predecessor model or monitoring data.

Table 1: Priorities for specific products or knowledge fields stated by different stakeholder groups in northern Germany (survey conducted in 2009 with 60 participants).

	Wave statistics	Ecosystem functions	Current fields	Sediment transport	other
Authorities	**			**	*
NGOs		**			*
Research & Consulting	**	*	**		*
Economy	**	*	**	**	

COSYNA aims at addressing those specified needs. Its envisaged products are continuous in space and time and, as a consequence, have to be generated by numerical models. These models should provide a now-cast and a two-day forecast for key state variables (e.g. current fields, temperature, salinity, wave height, phytoplankton or suspended matter concentration), while using measurements for correcting state estimates and constraining short-term forecasts.

2 Set-up of an integrated observatory

2.1 Large observatories require collaborative efforts

Given the extent of a large integrated observatory, collaborative efforts are clearly needed. This joined effort has been initiated for COSYNA by the Helmholtz Zentrum Geesthacht (HZG). During the first implementation stage, HZG organizes the cooperation with members of the German Marine Research Consortium (KDM), comprising most regional research institutes which conduct coastal research. Each member continues to use or newly employs operationally

working *in situ* measurement devices across the German Bight. The diversity of partner institutes, however, also creates the necessity of common standards in terms of observables, related sensors and protocols. A harmonisation of methods and data formats is carried out within the EU project JERICO. One COSYNA partner, the German Maritime and Hydrographic Agency (BSH), responsible for German Bight monitoring, currently co-develops standards with other European monitoring authorities (SEADATANET).

Coastal seas ignore territorial boundaries. Hence, on the long run, a large coastal observatory should ideally be an international one. For the German COSYNA initiative this means to link with parallel activities in other European member states. Active integration of COSYNA components or results into international projects and networks such as EMECO, GOOS, GMES, EMODNET, or GEOSS mark a first step.

2.2 *In situ* observation

2.2.1 Analysing the water column from platforms or moving along transects

The instrumental repertoire of COSYNA consists of a common package of state-of-the-art sensors at fixed and mobile platforms (Fig. 1).

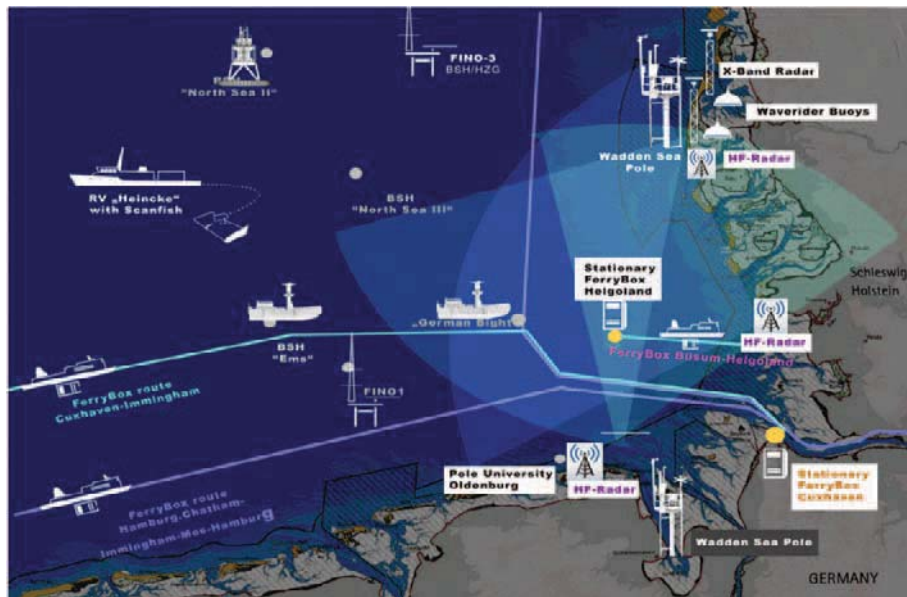


Figure 1: Observation modules of COSYNA within the German Bight

Automated FerryBox systems operate on ships of opportunity (Petersen et al. 2010) and on several piles in shallow water areas and at offshore platforms. Newly developed sensors enable the measurement of important chemical and biological parameters within the FerryBox systems (e.g., sensors for pCO₂, precision pH, alkalinity, genetic fingerprint of algal species, video observation of zooplankton).

High-resolution physical and biogeochemical measurements in 3D derive from regular ship transects using a towed undulating carrier (SCANFISH) and gliders. Gliders are remote-controlled applying current forecasts for route optimization. Despite the shallowness and strong currents in the southern North Sea they proved to be a valuable source for 3D information in areas without platforms or apart from regular ship routes.

2.2.2 Touching the ground: benthic lander systems and underwater stations

At selected sites, new sensors for measuring profiles and fluxes at the sediment-water, or for optical detection of biological key species are under development. A prerequisite for a reliable operation of such systems will be an underwater infrastructure (power supply and data telemetry). Regional underwater observatories up to now operated in deep water areas (NEPTUN Canada, VENUS, MARS, Barnes et al. 2010, Lintern et al. 2010). They, however, have to be newly developed for (cost effective) shallow water operations within COSYNA,

especially facilitating integration of different pelagic and benthic measurements systems (e.g., ADCPs, sensors for turbulence/eddy correlation, oxygen & turbidity, benthic chambers for automated measurement of nutrient fluxes across the sediment interface etc.). These sub-systems can be directly “plugged” into the underwater node, with high speed (glass fibre cable) data transmission and remote (home office) control of sensor devices.

2.3 Remote sensing

2.3.1 Radar

High Frequency (HF) and X-band radar systems provide 2D routine (20 min) measurements of waves, currents and near-coastal topography changes. Three antenna arrays of an “over-the-horizon” HF radar system (WERA) are located at Büsum and on the islands of Sylt and Wangerooge, covering nearly the entire German Bight. Near shore X-band observations of waves, currents and topographical changes, for example, allow to quantify the transport of sand during a storm in 2-3 km distance with an error of 25%.

2.3.2 Satellites and coastal algorithms

Hyperspectral satellite sensors, like the MERIS instrument on ENVISAT, accurately detect gradients in SST, suspended matter, or chlorophyll-a in open ocean surface waters. In coastal waters, however, due to optical disturbances by suspended matter and humic substances the quality of satellite data deteriorates, especially for chlorophyll. Therefore, satellite data for coastal waters need advanced algorithms (Doerffer 2007, COASTCOLOUR 2011, Ruddik et al. 2010). The COSYNA system serves as a ground-truthing system for developing these algorithms and for the correction of satellite errors (see also Fig.3).

2.4 Data assimilation into pre-operational models

A state-of-the-art high resolution 3D model can reproduce major hydrodynamic features of the German Bight already in a free run, if it is realistically forced (Staneva et al. 2009). Its accuracy yet can be much improved by near-time assimilation of continuous data using advanced Kalman Filter techniques (Barth et al. 2010). The study of Grayek et al. 2011 showed that availability of FerryBox data for sea surface salinity and temperature (SSS and SST) can enhance the reliability of the model (Fig. 2). This improvement, however, turns out to be in some cases confined to the area where observations are available (see SSS in Fig.2). Difficulties during the reconstruction point to possible weaknesses in the physical model and its set-up. They also underline the need for coherent, regional-scale data to improve coastal now- and forecasting. A pre-operational current velocity now-cast, the first COSYNA product, therefore uses WERA HF radar data for the inner German Bight (Stanev et al. 2011).

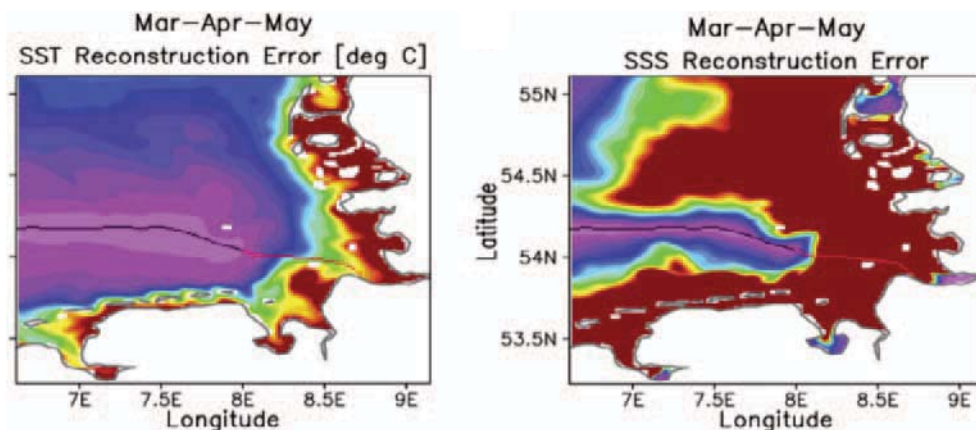


Figure 2: Residual simulation error after assimilating FerryBox temperature (left) and salinity (right) data taken along the ferry track (continuous line) into a hydrodynamic model (reprinted from Grayek et al, 2011, with kind permission).

2.5 Data management and communication

One of the most essential functionalities of a large observatory is data management. For the design of the COSYNA data system, product-orientation and common standards were first

guiding principles, alike for the observatory as a whole. The system thus comprises a modular user interface with an internet data portal as central element (Fig. 3). The newly developed portal allows for interactive search of information within meta-data and subsequent calls of web-services. These programs directly communicate with the core of the data-base which comprises observational data (at different processing stages) and model output. Web-services return informative graphs and maps, or files ready to download. In addition to the web based data portal, a virtual lab at the HZG facilitates user-friendly sharing or retrieving of data and products.

The modular structure of the COSYNA data management and the functionality provided by its embedded services allow effective usage by scientists with their often highly variable and specific data requests, as well as by non-scientific stakeholders who demand more standardized information.

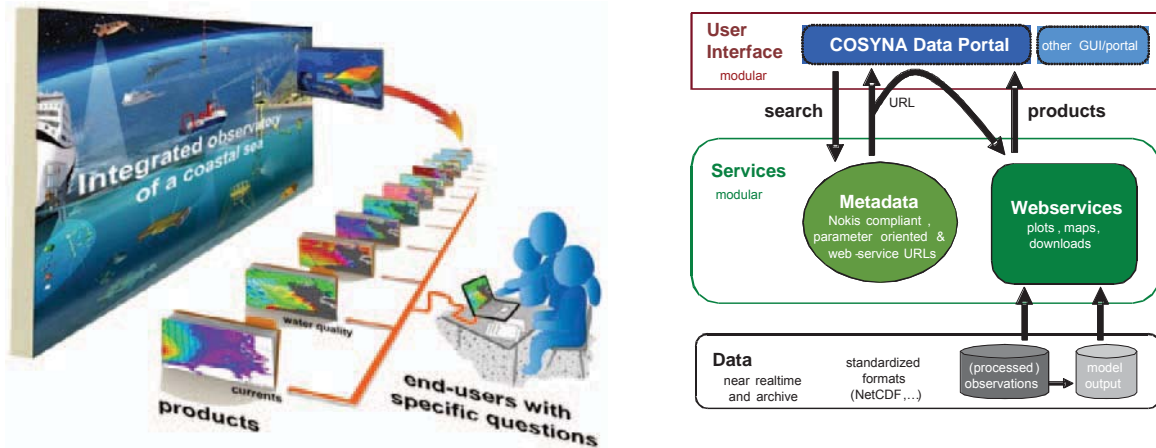


Figure 3: Left: Specific products mediate the information flows from a large coastal observatory to stake-holders. Right: Sketch of the COSYNA data management system. The data portal is a central element of the information flow to end-users.

3 Synergies and products

3.1 Ground-truthing and data quality

For achieving the coherent description demanded by pre-operational modeling, COSYNA generates time- and/or space-continuous data in a cost effective and thus often remote or automated way. This approach carries the risk of insecure or variable data quality (e.g., due to bio-fouling on sensors) and therefore triggered the development of quality assurance schemes. For example, near-realtime data needed for data assimilation schemes are subjected to automatic data quality flagging, i.e., computer driven plausibility checks that rely on a ten-year climatology compiled for different regions. This flagging is consistent with the norms in SEADATANET (SEADATANET 2011). It precedes but does yet not substitute a delayed manual examination.

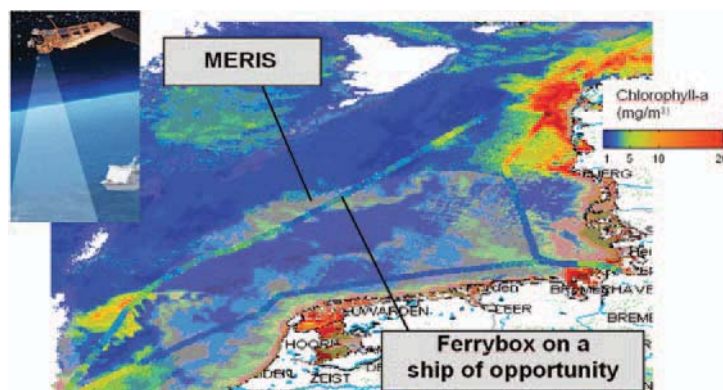


Figure 4: Chlorophyll-a distribution in the Southern North Sea. Satellite data (MERIS) are compared to optical in situ measurements of the FerryBox (polygonal tracks).

Owing to its multi-sensor approach, COSYNA can in addition tackle the data quality and ground-truthing problem by systematic comparison of different products like, e.g., fluorescence measured from the satellite and from the FerryBox (Fig. 4). Notwithstanding partial asynchronicity of measurements (between times of the satellite overflight and ship cruising), the example illustrates that regional differences in data quality (e.g., due to external disturbances) can lead to local differences in data products, and that their combined analysis can enhance reliability of each method.

3.2 Towards a synoptic view at the regional scale

To continuously monitor an Earth System hotspot at a regional scale and over longer time periods creates a unique data-set which may stimulate environmental research in different ways. The infrastructure of the coastal observatory will host or support independent (smaller) research projects. Single data products will allow further scientific analysis. Predecessor projects have expressed the relevance of accessing precise information at a regional scale (SYCON 2001, KDM 2007). In first research applications, indeed, the availability of contextual data has been proven highly valuable. For example, it much improved a mechanistic description of residual transport in tidal waters (Flöser et al. 2011), or complex biological response patterns to multi-scale atmospheric and hydrodynamic forcings (Tian et al. 2011).

Already two years after its onset, COSYNA has advanced our capability to (technologically) implement and (scientifically) use coastal and shelf sea observatories. With its integration of distributed observing systems and their model based processing it has defined a new infrastructure scale in environmental research. Most importantly, its strong orientation to provide reliable and specific information (for stake-holders incl. scientists) has stimulated a coherent development of instrumentation, monitoring strategies and data assimilation techniques.

3.3 New challenge: Offshore wind parks in the North Sea

Due to the rapid construction of offshore wind energy installations throughout the southern North Sea new information needs arise. Alone within the German Bight, the buildup of 6000-8000 installations raises questions about sustainable and safe operation, or physical and ecological impacts. COSYNA as a regional scale infrastructure can in particular help to assess cumulative effects of offshore wind parks.

4 Acknowledgements

We thank the many contributors to COSYNA and to ideas and figures presented here, especially Franciscus Colijn, Rolf Riethmüller, Roland Dörffer, Hans von Storch, Kay Emeis, Emil Stanev, Gisbert Breitbach, Beate Gardeike, and Christiane Eschenbach.

5 References

- Barnes, C. R.; Best, M.M.R; Johnson, F.R.; Pirene, B. (2010): Final installation and initial operation of the world's first regional cabled ocean observatory (NEPTUNE Canada). In: Canadian Meteorological and Oceanographic Society Bulletin, 38, pp. 89-96.
- Barth, A.; Alvera Azcarate, A.; Gurgel, K.; Staneva, J.; Beckers, J.; Port, A.; Stanev, E. (2010): Estimation of tidal boundary conditions and surface winds by assimilation of high-frequency radar surface currents in the German Bight. In: Ocean Sci., 6, pp. 161-178.
- Beaugrand, G. (2004): The North Sea regime shift: evidence, causes, mechanisms and consequences In: Progress in Oceanography, 60, pp. 245-262.
- Bosman, J.; Flemming, N C; Holden, N.; Taylor, K. (1998): The EuroGOOS Marine Technology Survey. In: EuroGOOS Publication No. 4, Southampton Oceanography Centre, Southampton. ISBN 0-904175-29-4.
- COASTCOLOUR: www.coastcolour.org
- Creed, E.L.; Glenn, S.; Schofield, O.M.; Barrier, H.; Petrecca, R.F.; Dobarro, J.A.; McLean, S.D.; Barnard, A.H.; Brown, K.M.; Adams, R.S.; Feener, S. (2005): LEO-15 Observatory - the next generation. OCEANS, 2005. Proceedings of MTS/IEEE. ISBN 0-933957-34-3

- Doerffer, R. and H. Schiller (2007): The MERIS Case 2 water algorithm. In: *Internat J. Remote Sensing*, 28, pp. 517-535.
- Flöser, G.; Burchard, H.; Riethmüller, R. (2011): Observational evidence for estuarine circulation in the German Wadden Sea. In: *Continental Shelf Research* 31, pp. 1633-1639.
- Friedland, K.; Hare, J. (2007): Long-term trends and regime shifts in sea surface temperature on the continental shelf of the northeast United States. In: *Continental Shelf Research* 27, pp. 2313-2328.
- Grayek, S.; Staneva, J.; Schulz-Stellenfleth, J.; Petersen, W.; Stanev, E. (2011): Use of FerryBox surface temperature and salinity measurements to improve model based state estimates for the German Bight. In: *Journal of Marine Systems*, 88, pp. 45-59.
- KDM (2007): Küstenmeere im Wandel. Forschungsbedarf der deutschen Küsten- und Randmeerforschung. Konsortium Deutsche Meeresforschung, Berlin. www.deutsche-meeresforschung.de
- Lintern, D. G.; Hill, P. R. (2010): An underwater laboratory at the Fraser River delta. In: *EOS AGU, Transactions*, 91: pp. 333-44.
- Lozan, J. L.; Rachor, E.; Reise, K.; Sündermann, J.; Westernhagen, H. v. (2003): Warnsignale aus Nordsee & Wattenmeer, Wissenschaftliche Auswertungen, Buchreihe, Hamburg.
- Petersen, W.; Schroeder, F. and Bockelmann, F.-D. (2010): FerryBox - Application of continuous water quality observations along transects in the North Sea. In: *Ocean Dynamics*. DOI: 10.1007/s10236-011-0445-0.
- Ruddick, K.; Brockmann, C.; Doerffer, R.; Leed, Z.; Brotas, V.; Fomferra, N.; Groomf, S.; Krasemann, H.; Martinez-Vicente, V.; Sa, C.; Santer, R.; Sathyendranath, S.; Stelzer, K.; Pinnock, S. (2010): The Coastcolour project regional algorithm round robin exercise. *Proc. of SPIE Vol. 7858* 785807-13
- Schlüter, M.; Merico, A.; Wiltshire, K.; Greve, W.; von Storch, H. (2008): A statistical analysis of climate variability and ecosystem response in the German Bight. In: *Ocean Dynamics*, 58, pp. 169-186
- Schofield, O.; Bergmann, T.; Bissett, P.; Grassle, J.F.; Haidvogel, D.B.; Kohut, J.; Moline, M.; Glenn, S.M. (2002): The Long-term Ecosystem Observatory: an integrated coastal observatory. In: *IEEE Journal of Oceanic Engineering*, Vol. 27. ISSN: 0364-9059.
- SEADATANET: Newsletters and working documents; online at www.seadatanet.org
- SYCON (2001): The Changing North Sea: Knowledge, Speculation and New Challenges. Synthesis and New Conception of North Sea Research (SYCON). *Berichte aus dem Zentrum für Meeres- und Klimaforschung; Reihe Z: Interdisziplinäre Zentrumsberichte*. Nr. 3-14. Eds.: Sündermann, J.; Beddig, S.; Kröncke, I.; Radach, G. and K. Heinke Schlunzen.
- Stanev, E.; Schulz-Stellenfleth, J.; Staneva, J.; Grayek, S.; Seemann, J. & Petersen, W. (2011) Coastal observing and forecasting system for the German Bight--estimates of hydrophysical states. In: *Ocean Sci.*, 7, pp. 1-15
- Staneva, J.; Stanev, E.; Wolff, J.; Badewien, T.; Reuter, R.; Flemming, B.; Bartholomä, A.; Bolding, K. (2009): Hydrodynamics and sediment dynamics in the German Bight. A focus on observations and numerical modelling in the East Frisian Wadden Sea. In: *Continental Shelf Research*, 29, pp. 302-319.
- Tian, T., Su, J., Wiltshire K., Flöser G.; Wirtz, K.W. (2011): Physical control of winter-spring algal community structure in the German Bight and its effect on bloom timing. In: *Continental Shelf Research*, 31, pp. 1140-1148.
- Weijerman, M.; Lindeboom, H.; Zuur, A. (2005): Regime shifts in marine ecosystems of the North Sea and Wadden Sea. In: *Marine Ecology Progress Series*, 298, pp. 21-39.

Shoreline detection in a gentle slope Mediterranean beach

Giorgio Manno¹, Carlo Lo Re¹ and Giuseppe Ciralo¹

Abstract

The paper presents a novel multidisciplinary method to estimate the shoreline position, using remotely sensed images and considering the effects of waves and tide. The shoreline position continually changes in time because of the dynamic nature of water levels at the coastal boundary. Traditionally, the shoreline is mapped by means of aerial images that are also used to detect past shoreline position. The shoreline position extracted from an aerial image is a wet/dry line that describes the instantaneous land-water boundary at the time of imaging rather than a "normal" or "average" condition. Each wave instantaneously influences the shoreline position and hence, to take into account shoreline oscillations due to wave motion, the use of an "ordinary" sea storm, defined as a one-year return period storm, is proposed.

Keywords: shoreline detection, beach, coast, waves, tides.

1 Introduction

Shoreline variability and erosion-accretion trends are essential for a broad range of investigations undertaken by coastal scientists, coastal engineers and coastal managers. Both coastal management and engineering design require information about the shoreline position in the past, in the present and in the future. For example, shoreline analysis is required in coastal protection design (e.g., Coastal Engineering Research Center, 1984), to calibrate and verify numerical models, to assess sea-level rise (Leatherman *et al.*, 2001), to develop hazard zones (Douglas *et al.*, 2001), to formulate policies, to regulate coastal development and to define legal properties boundary. To analyze shoreline variability and trends, a functional definition of the *shoreline* is required. Because of the dynamic nature of this boundary, the definition must consider the shoreline in both a temporal and a spatial sense and it must take into account the dependence of this variability on the time scale of the investigation. Traditionally, to identify the shoreline, an analysis of aerial images with a stereoscope is performed (Boak *et al.*, 2005). The line thus marked is an instantaneous shoreline since its position is the land-water interface at one instant time. Of course shoreline positioning depends on the consistency of the measurement techniques. This consistency is also dependent on the tidal level reference (MHW - Mean High Water). For example in the US the shoreline is legally defined as the boundary land-water corresponding to the average water level of all observed high tides. In the literature the boundary is often defined as the MHW (Mean High Water), neglecting the effect of waves and rising waves on the beach. However, Ruggiero *et al.*, (2003) demonstrate that the presence of the waves should be not ignored.

In this work we tried to join together different techniques, to create a multidisciplinary method. The application was performed on a Mediterranean beach. A beach of western Sicily in geomorphological equilibrium was chosen. The approach used for shoreline positioning was to perform both a topographic-geomorphological and a hydraulic study. Knowledge of the beach offshore, maritime climate (waves and tides) and beach morphological characteristics, allows a more accurate estimate of the shoreline position. In fact the dynamic nature of the shoreline suggests that this water-land boundary cannot be defined as a single line. The shoreline always fluctuates and for this reason its position can be defined within a strip. This beach area is regularly washed by the sea and it represents the seaward beach boundary.

¹ Dipartimento di Ingegneria Civile Ambientale e Aerospaziale (DICA), Area Ingegneria Idraulica e Ambientale. Università degli Studi di Palermo. Viale delle Scienze Ed 8, 90128 Palermo (Sicily - Italy).
e-mail: giorgiomanno@libero.it; lore@idra.unipa.it; giuseppe.ciralo@unipa.it

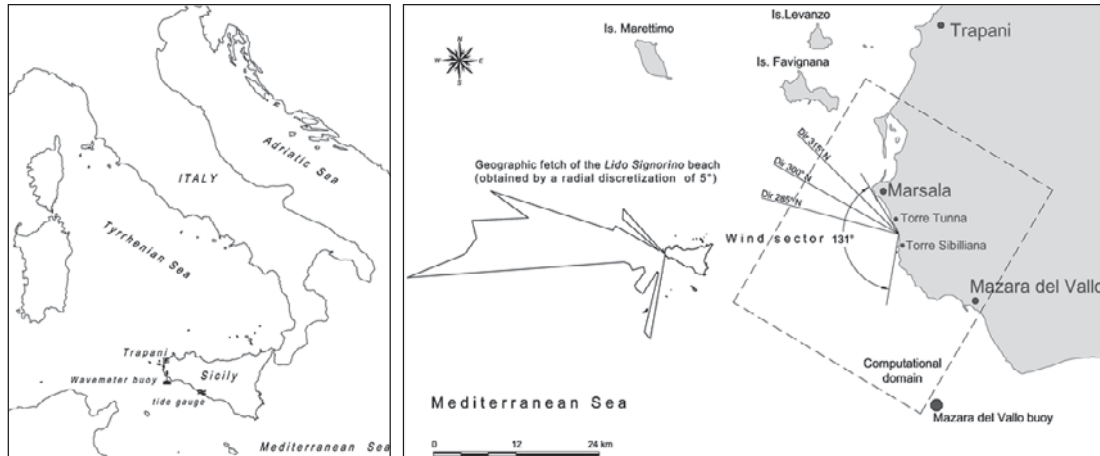


Figure 1: The left panel shows the wave-meter buoy and tide gauge locations. The right panel shows the *Lido Signorino* beach, the computational domain (dashed line), wind and critical wave directions and the geographic fetches.

2 Method

The proposed method aims to identify the shoreline position in a Mediterranean beach (figure 1). The application of this method involves different techniques from different disciplines integrated to aid shoreline positioning. Though the geological and the geomorphological survey were mainly descriptive, they are useful for the hydraulic study, aiming at quantifying the influence of the sea state in shoreline positioning. The geomorphological study made it possible to describe the beach physically, to underline the morphotypes of submerged and emerged beach, to identify the size and composition of sediments, to reconstruct profiles and to determine the average slope.

To perform a historical reconstruction of the shoreline positions all the available aerial images of the study area were analyzed. A time series analysis (from 1994 to 2006) was performed by means of high spatial resolution images. The images used were the following: *Volo Italia* 1994 (gray-scale image, characterized by a nominal spatial resolution of 1 m), *Volo Italia* 2000 (colour image with 1 m spatial resolution) and *Volo Italia* 2006 (colour image with 0.5 m spatial resolution). All images were georeferenced (UTM-WGS84-33N) and uploaded into a GIS (Geographic Information System). It should be noted that in order to compare images it is necessary to take into account accuracy of digitization (2 m), spatial resolution, georeferencing accuracy and tide and wave conditions at the time of the aerial acquisition.

To describe in detail the *Lido Signorino* beach morphology a survey was performed using a GPS (Global Position System) RTK (Real Time Kinematic). This technique is suitable applied to the studied beach, because there were no obstacles (trees, buildings, etc.) that could shield the receiver signal. The GPS-RTK allowed the acquisition of highly accurate and consistent data to reach centrimetric precision.

In the proposed method we considered only waves and tides neglecting sediment transport and currents. Wave and tidal data were collected using the wavemeter buoy of Mazara del Vallo and the Porto Empedocle tide-gauge both managed by ISPRA (*Istituto Superiore per la Protezione e la Ricerca Ambientale*). The wave-gauge (DATAWELL - directional wavec - Mk1) the vertical displacement within an interval of ± 20 m (resolution 0.10 m with an accuracy of 3%) and the direction within a range of 0° to 360° (resolution 1.5° with an accuracy from 0.5° to 2°).

Only significant wave heights (H_s [m]), peak and average wave periods (T_p and T_m [s]) and average direction (D_m [°N]) for an interval of time between July 1, 1989 and April 4, 2008 were used. The hydraulic study was divided into two sections: propagation of waves from offshore to nearshore and tide analysis.

To take into account the wave effects during one year we used the concept of "ordinary" sea storm, cited in the Italian juridical definition (*Corte di Cassazione, Sez., Un., 02/05/1962, n.849*):

as defined in Italian law the shoreline (*lido* in Italian), is the beach zone in contact with the sea and covered by water during an "ordinary" sea storm. A sea storm is a succession of sea states in which the significant wave height (H_s) is generally larger than a critical threshold (h_c), and does not fall below this threshold for a continuous time predetermined interval $\Delta_{t_{crit}}$. In the Mediterranean sea the values of h_c and $\Delta_{t_{crit}}$ are 1.5 m and 12 h respectively (Boccotti, 2000).

In this paper an ordinary storm was defined as a one-year return period storm. To make predictions on the significant wave height it is necessary to know its probability of exceedance $P(H_s > h)$. This is defined as ratio between the share of time in which the significant wave height keeps above any fixed threshold h and the total time of observation.

Wavemeter instrumental recordings obtained from the Mazara del Vallo buoy were not collected in front of the beach but on the southern side. For this reason it was necessary to transpose the buoy data, before they were treated according to a statistical analysis. In other words, it was necessary to "transfer" historical data from the measuring point to another "climate" similar but located far from the studied beach. After wave-meter data transposition a statistical analysis of extreme events was performed. This analysis was carried out using the concept of Equivalent Triangular Storm (ETS). The actual storms have some irregular histories generally different from one another. However, an equivalent triangular storm can be associated with each actual storm (Boccotti 2000). The equivalence between this triangular storm and the actual storm is full, since they have the same maximum value of the significant wave height and the same probability that the maximum wave height exceeds any fixed threshold H . Clearly, dealing with equivalent triangular storms rather than with actual storms simplifies the mathematical treatment (Boccotti, 2000).

To validate the results directional and omni-directional Weibull probability density functions were used. Both analyses gave as the result the significant wave height for each return period considered (i.e. $T_r=1$, $T_r=5$, $T_r=10$ [year]).

Once the significant wave heights and the associated return times for each wind sector (already transposed) were known, a propagation model (SWAN - Simulating Waves Nearshore) (Booij *et al.* 1999; Holthuijsen *et al.* 1993;) was used to calculate height and period changes of a wave from offshore to nearshore. To be able to use the model a special grid was built using a square mesh with a pitch of 250 m. Data obtained from the SWAN model were used to calculate the run-up. The run-up is defined as a local maximum or peak instantaneous elevation, η , near the shoreline. For this reason, the upper limit of the run-up is useful to identify the active portion of a beach profile. To calculate the run-up two different methods were used; 1) an empirical equation (Nielsen and Hanslow, 1991) and 2) a Boussinesq model with a shoreline boundary condition (Lo Re *et al.* 2011). In this paper a preliminary analysis of tide oscillations observed during the period 1999-2009 in a harbour located on the South coast of Sicily is reported.

3 Case study

To test the proposed method a sandy beach was chosen. The *Lido Signorino* beach belongs to Sicilian 14 PU (Physiographic Unit – a portion of the coast in which the displacement of sedimentary materials is confined within its boundaries). The beach is located in the southern area of the town of Marsala (Trapani). It is localized between two headlands in which there are two ancient towers (XVI sec.), the Tunna Tower (37° 45'32,26"N, 12° 27'40,00"E) and the Sibilliana Tower (37° 43'36,31"N, 12° 28'11,23"E) and it is about 3 km long. The beach belongs to the *Marsala - Mazara del Vallo* coastal plain. This plain is relatively flat with less than 20% slope (direction NE-SW) and elevations vary between a few meters a.s.l. along the coastline to approximately 250 m a.s.l., in the surrounding hills inland. A distinct series of marine terraces up to 170 m a.s.l. can easily be identified by the presence of a series of morphologic steps, leveled at the top by erosion.

Lido Signorino is a dissipative sandy beach. The beach sediments were originated from erosion of near coasts and from the sea floor. Geologically, these sediments fall within the *Calcarenites of Marsala* class (Pleistocene marine deposits).

During the past decades, the beach has been dramatically modified by human activity. Even so nowadays there are some distinctive morphotypes of the beach. In past years (1950-60) the

dunes were uniformly distributed and their height was about 5 m. Today they are unequally distributed on the beach and their heights are 2-3 m.

The wind sector has amplitude 131°; this amplitude is included between the directions 195° and 300° N, is shielded by Favignana island, (archipelago Egadi) in the 105° N direction. The characteristics of the wind sector shown in figure 2 were deduced from observations of the directions and wind speeds recorded at the Trapani meteorological station. The beach is formed by very fine sand from the Holocene age. The sediment size analysis performed on the swash zone and on the dune scarp samples showed sandy size and sub-rounded shape. Grains are composed by rocks and fossil shell fragments and their chemical composition is mainly calcium carbonate (CaCO₃).

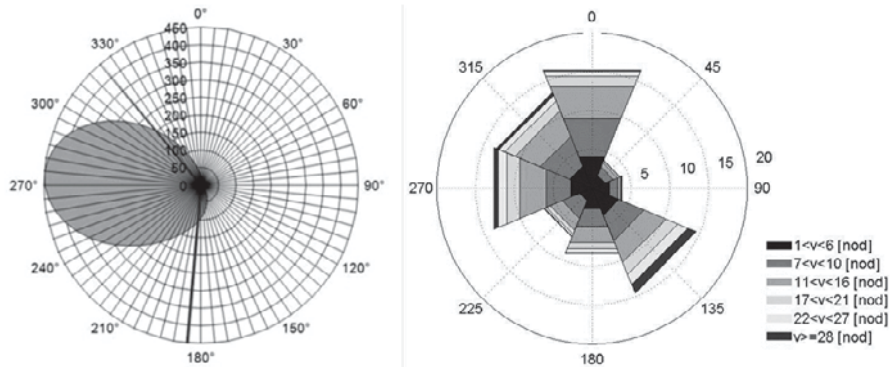


Figure 2: Left panel: effective fetch for Lido Signorino beach. Right panel: wind diagram for Trapani anemometric station

4 Results

The *Lido Signorino* beach is characterised by an average slope of 8.36%, (figure 3), corresponding to 4.77°. The submerged beach has a slope lower than the emerged one and its profile is well suited to the theoretical curves of the D_{50} (Dean, 1991) produced from samples of sand taken ($0.1 < D_{50} < 0.8$ mm). The gentle slope of the cross-sections of the beach and the presence of morphotypes such as bars and berms along the strip of submerged beach (as shown by bathymetric data), produce the dissipative characteristics. In this way the beach benefits from the attenuation effects of the incident wave.

The analysis of extreme events was performed on the 285°N direction because the latter is characterized by more frequent storms with higher peaks. For the proposed method and from the available data, 602 storms were recognized (figure 4).

In order to calculate H_s (R_p) for an assigned return period, we used equations (1), and (2).

$$R_p(H_s > h) = \frac{\bar{b}(h)}{1 + u \cdot \left(\frac{h}{w}\right)^u} \cdot \exp\left(\frac{h}{w}\right)^u \quad (1)$$

with R ($H_s > h$) return period [years]

h height threshold [m]

\bar{b} mean value of the equivalent triangular storm base (time). [hours]

u and w omnidirectional parameters

$$R(H_s > h, \theta_1 < \theta < \theta_2) = \frac{\bar{b}(h)}{\exp\left[-\left(\frac{h}{w_\alpha}\right)^u\right] \cdot \left[1 + u \cdot \left(\frac{h}{w_\alpha}\right)^u\right] - \exp\left[-\left(\frac{h}{w_\beta}\right)^u\right] \cdot \left[1 + u \cdot \left(\frac{h}{w_\beta}\right)^u\right]} \quad (2)$$

with $R(H_s > h, \theta_1 < \theta < \theta_2)$ return period [years]
 W_α and W_β directional parameters

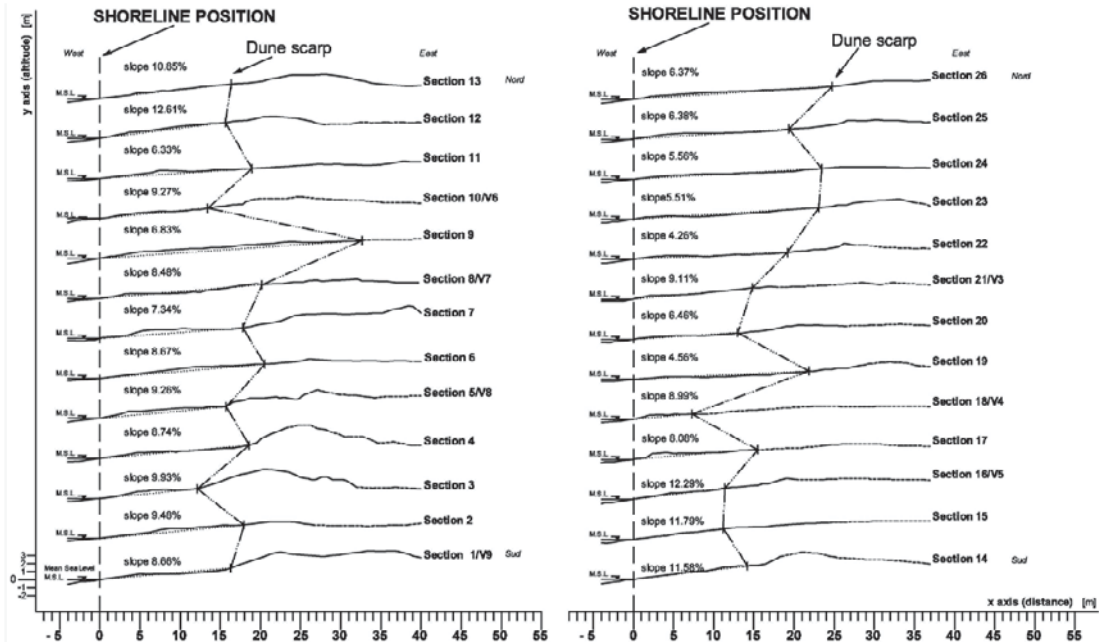


Figure 3: Vertical profiles from south (section number 1) to north (section number 26). The shoreline and dune scarp positions were shown.

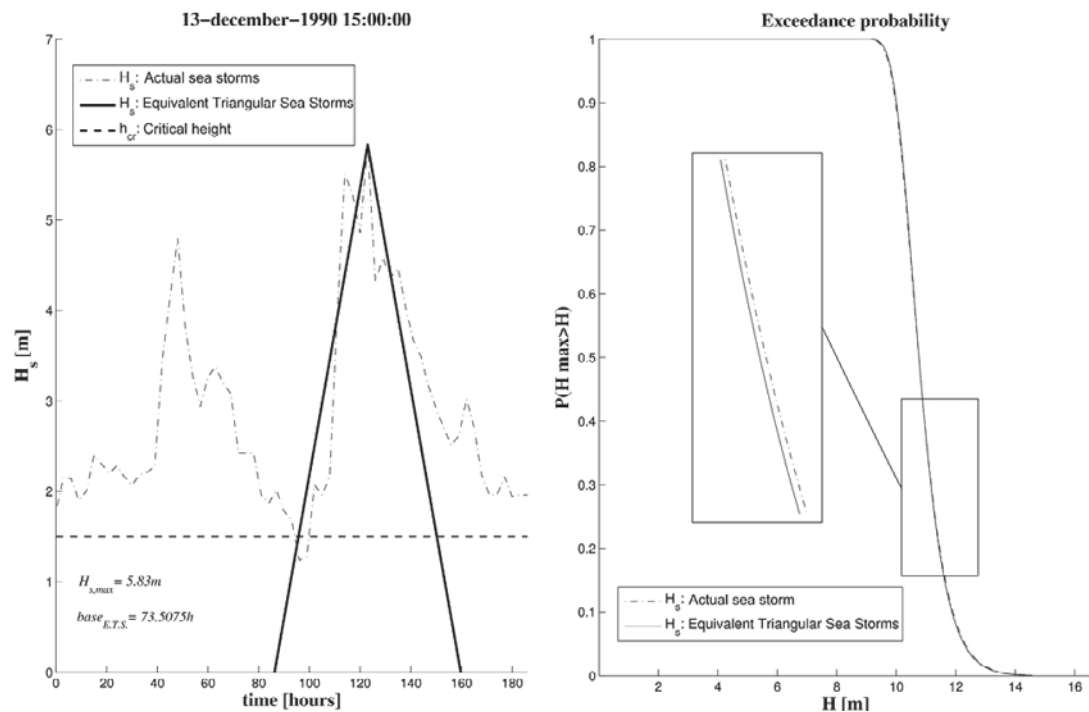


Figure 4: Left panel shows an actual storm recorded by the Mazara del Vallo wavemeter and its Triangular Equivalent Storm. The right panel shows the comparison between actual and Triangular Equivalent Storm exceedance cumulative probability.

In this study, the return period of peaks of the triangular sea-storm was calculated. This approach, according to a standard analysis of the extreme events, provided very accurate results.

In accordance with the definition of “ordinary storm” the return period of 1 year ($R_p = 1$) was taken into account. In particular for this period a significant wave height of 5.62 m was found. The peak period (T_p) was calculated according to equation (3) for a JONSWAP spectrum and its value was 10.11 s.

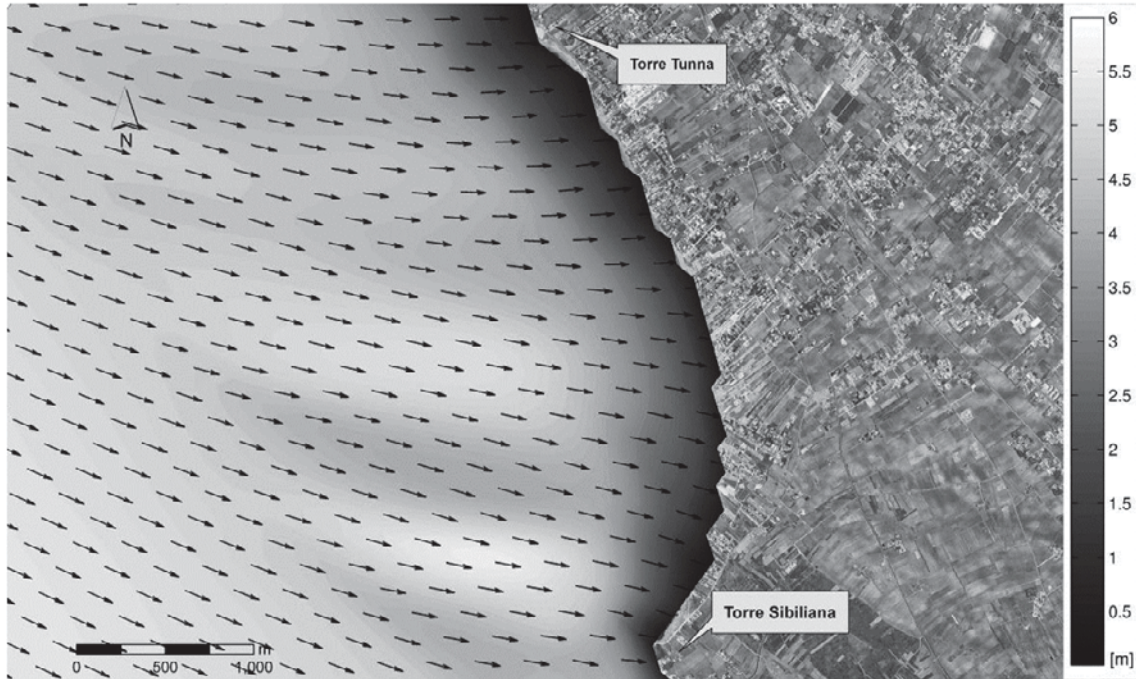


Figure 5: The spectral wave model outputs: arrows indicate the wave propagation direction superimposed on the significant wave heights [m] shown by a grey scale.

$$T_p = 8.5\pi \sqrt{\frac{H_s}{4g}} \quad (3)$$

with T_p peak period [s]

H_s significant high wave [m]

To propagate the waves from offshore to nearshore, the SWAN model was used. The graphical output of a generic simulation is shown in figure 5. Analyzing these data we computed the average of the significant wave height (H_s) and the peak period (T_p) (5.32 m and 7.79 s respectively) at a local depth of 60 m. These data were used to calculate the horizontal run-up, by means of the empirical formula proposed by Nielsen & Hanslow (1991). Furthermore, for each cross-section of the beach, a simulation was carried out using a Boussinesq type of model with a physically based boundary condition (Lo Re *et al.* 2011). To perform a simulation with the Boussinesq type of the model the offshore boundary condition was needed. Hence the $H_s = 2.91$ m and $T_m = 7.27$ s at a local depth of 5 m were extracted.

A cnoidal monochromatic wave train with wave height 2.91 m and period 7.27 s was taken into account. This wave corresponds to the peak of the “ordinary storm” and their values were used to simulate the run-up. The simulation was carried out for all cross-sections. The domain was discretized using $\Delta x = 1$ m and the integration time was $\Delta t = 0.0036$ s. The total running time was about 187 s corresponding to 120 waves. As an example the maximum run-up for profile number 8 was 10.26 m. In figure 6 the wave breaker on the beach is shown at 4 different time intervals: before breaking, incipient breaking, during breaking and when the maximum run-up was achieved. The mean run-up, calculated with the Boussinesq model, was 11.29 m.

Analyzing data collected from the tide gauge, the maximum tidal fluctuations (from 1998 to 2008) have excursions of about 0.4 m. Since the average slope of the beach is 8.36% the influence of the tide on the shoreline position change is ~ 10 m.

In this way both wave and tide effect generate a strip of about 21.29 m wide. Within this strip the shoreline position fluctuates (figure 7).

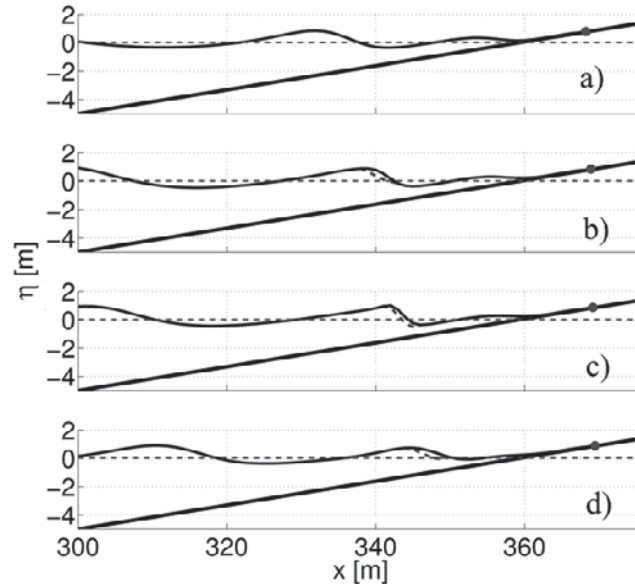


Figure 6: The run-up of the peak of an ordinary sea storm at profile no. 8 (slope beach 8.48%): a) the wave before breaking; b) the wave at incipient breaking; c) wave breaking; d) the wave maximum run-up. In the horizontal axis the distance from the numerical wavemaker. In the vertical axis the surface elevation. The gray dot is the shoreline position, the dashed horizontal line is the still water level, the dashed line under the wave crest is the breaking roller.



Figure 7: The shoreline strip linked to the ordinary storm (run-up and tide). The total width is about 21.29 m

5 Conclusion

Very often coastal scientists choose the shoreline as a marker of coast evolution. In the last few years to study beaches dynamic, coastal engineers have often performed a comparison of two or more aerial images (from different years). From this analysis, they would infer how the beach evolved. However, the shoreline position was extracted from the images not considering the effects of the sea state during the acquisition of aerial photography. Indeed the shoreline or land-water boundary is dynamic and its positioning requires the definition of a strip. The definition of this strip is influenced by sea effects as well as by the geomorphological characteristics of the beach. The proposed method evaluates tide and wave influence on shoreline positioning. Indeed, only an application at *Lido Signorino* beach was performed but the method could be standardized and be applied for other similar beaches. The beach strip, delimited using the "ordinary storm" concept, suggests that this area belongs statistically more to the sea than to the land. The shoreline positioning has many practical aspects of interest, mainly related to distinction between state owned areas and privately owned ones. From this point of view knowledge of the shoreline position can help engineers, geomorphologists and managers to discriminate the legitimacy of privately owned structures.

6 Acknowledgements

The authors would like to express their sincere acknowledgment to the *Istituto Idrografico della Marina* (Italian Navy Hydrographic Agency) for the bathymetric data.

7 References

- Boak, E.H.; Turner, I.L.; (2005): Shoreline definition and detection: a review. In: Journal of Coastal Research, Vol. 18, pp. 1-13. ISSN 0749-0208
- Boccotti, P. (2000): Wave mechanics for ocean engineering - Elsevier Oceanography Series. Amsterdam ISBN 0-444-50380-3.
- Booij, N.; Ris, R.C.; Holthuijsen, L.H.; (1999): A third generation wave model for coastal regions, part I: model description and validation. In: Journal of geophysical research, Vol. 104, pp. 7649-7666. ISBN 7649-7666
- Coastal Engineering Research Center; (1984): Shore Protection Manual. Volumes 1 and 2. Washington, DC: US Army Corps of Engineers, Waterways Experiment Station, Coastal Engineering Research Center.
- Dean, R.G.; (1991): Equilibrium beach profiles: characteristics and applications. In: Journal of Coastal Res., Vol. 7, pp. 53-84. ISSN 0749-0208
- Douglas, B.C.; Crowell, M.; (2000): Long-term shoreline position prediction and error propagation. In: Journal of Coastal Research Vol. 16, pp. 145-152. ISSN 0749-0208
- Holthuijsen, L.H.; Booij, N.; Ris, R.C.; (1993): A spectral wave model for the coastal zone, in 2nd International Symposium on Ocean Wave Measurements and Analysis. New Orleans, pp. 630-641. ISBN 978-0-87262-922-6
- Leatherman, S.P.; (2001): Sea Level Rise History and Consequences. Academic Press, San Diego, California pp. 232. ISBN 0-12-221345-9
- Lo Re, C.; Musumeci, R.E.; Foti, E.; (2011): A shoreline boundary condition for a highly nonlinear Boussinesq model for breaking waves, Coastal Engineering. In Press, ISSN 0378-3839, DOI 10.1016/j.coastaleng.2011.08.003
- Nielsen, P.; Hanslow, D.J.; (1991): Wave run-up distributions on natural beaches. In J. Coastal Res., Vol. 7, n. 4, pp. 1139-1152; ISSN 0749-0208
- Ruggiero, P.; List, J.H.; Haynes, D.M.; Eshleman, J.; (2006): Probabilistic Shoreline Change Modeling, in: Coastal Engineering Conference, Vol. 30, n.4, pp. 3417. ISBN: 978-981-270-636-2. San Diego California.

Re-examining the Dean Profile for designing artificial beaches in Dubai

Andrew Brown¹ and Jon Kemp²

Abstract

To aid in the design of artificial beaches, prediction of the equilibrium beach profile (EBP) is important. This paper presents a methodology for testing EBP predictors by comparing the mean profile of historical datasets with the predictor. A method for defining the EBP from beach crest to the closure depth in Dubai is put forward and a new Hybrid profile predictor following the simple form $h=Ax^{2/3}$ has been created.

Keywords: Equilibrium beach profile (EBP), Dean profile, Hybrid profile.

1 Introduction

When designing any artificial beach, it's desirable to avoid (or minimise) future maintenance commitments by arranging the initial beach profile so that it remains in dynamic equilibrium given the incident wave climate and provides protection to the hinterland. It is usual to provide a flat beach berm which will provide space for recreational usage and also dissipate wave energy in storm conditions, thus reducing overtopping. The beach berm height is usually the wave run-up height of the design wave and water level.

The complicated nature of the surf zone makes empirically describing a beach profile extremely difficult. Equilibrium beach profile theory was developed to provide a theoretical beach profile that can be used by engineers. It has proven useful as a reference plane for understanding complex transport and morphological processes, for determining the stability of beaches, for the design of artificial beaches and for determining fill amounts in re-nourishment projects.

The design beach slope has traditionally been estimated using Dean's Equilibrium Profile (Dean and Dalrymple, 2002). However, it has been observed at many beaches in Dubai where the upper beach is much steeper than that ascribed by Dean's profile predictor. Therefore, as a result of the continued development of artificial beaches in Dubai, there is a requirement for an equilibrium profile predictor for this region.

This paper therefore presents a new method for predicting the equilibrium beach profile (EBP), as well as the creation of a new Hybrid profile predictor. The new Hybrid profile predictor has been incorporated into a spreadsheet in order to streamline its application in the design of new stable beaches.

1.1 Aims and objectives

The aim of the research was to investigate the validity of the Dean profile for predicting equilibrium beach profiles, particularly when designing artificial beaches in Dubai. The objectives were to:

- Examine beach profile data from different beaches around the Gulf coast of Dubai. Calculate, from historical beach profiles, a mean profile assumed to reflect the equilibrium beach profile.

¹ HR Wallingford, Wallingford, Oxfordshire OX10 8BA, United Kingdom. a.brown@hrwallingford.com

² HR Wallingford, Wallingford, Oxfordshire OX10 8BA, United Kingdom. j.kemp@hrwallingford.com

- Determine the most appropriate water level to use as the shoreline datum for the Dean profile.
- Investigate and trial other EBP predictors.
- Propose a methodology for predicting EBP's in Dubai to aid in the design of artificial beach profiles and other coastal engineering applications.

2 Background

The EBP can be defined as the cross-shore profile of steady shape that is reached if exposed to constant forcing conditions for a sufficiently long time (Larson, 1991). A dynamic equilibrium exists where the profile does not undergo a net change even though particles are in motion.

Dean (1991) characterised equilibrium beach profile shape, explaining:

1. They usually concave upwards;
2. The smaller the sand diameter, the more gradual the slope;
3. The beach face is usually planar; and
4. Steeper waves result in more gradual slopes.

This general pattern has resulted in attempts to characterise the EBP using mathematical equations. A summary of the research related to EBP configuration is listed in Table 1. The Bruun/Dean equation has become the most commonly used due to its simplicity and is valid for the littoral zone i.e. out to the closure depth (Figure 1).

Table 1: Chronological summary of equilibrium beach profile studies

Author	Equation	Notes
Bruun (1954)	$h = Ax^{\frac{2}{3}}$	Uniform wave energy dissipation assumed, $n=2/3$
Dean (1977)	$h = Ax^n$	Uniform wave energy dissipation per unit volume assumed, $n=2/3$
Larson (1991)	$h = A \left(x + \frac{1}{\lambda} \left(\frac{D_o}{D_\infty} - 1 \right) (1 - e^{-\lambda x}) \right)^{\frac{2}{3}}$	Incorporates a varying grain size across-shore. Analysis of grain size variation is required.
Bodge (1992)	$h = B(1 - e^{-kx})$	Exponential for offshore grading of sediments. Can only be applied diagnostically.
Inman et al., (1993)	$h(1) = A(1).x(1)m(1), \dots, h(n) = A(n).x(n)m(n)$	Compound profile to describe bars and berms. Curve fitting approach that is subjective.
Komar and McDougal (1994)	$h = \frac{m_o}{k} (1 - e^{-kx})$	Beach face slope shows concavity and tidal effect is considered. Similar form to Bodge (1992). Can only be applied diagnostically.
Lee (1994)	$h = b \ln(1 + x/x_o)$	Airy's wave theory is considered

Bernabeu (1999)	<p>Surf profile:</p> $h = \left(\frac{x}{A}\right)^{\frac{3}{2}} + \frac{B}{A^2} x^3 \quad 0 \leq h \leq x_r$ <p>Shoaling profile:</p> $H = \left(\frac{x}{C}\right)^{\frac{3}{2}} + \frac{D}{C^2} x^3 \quad x_r \leq h \leq x_a$	Beach profile is split into two segments, surf and shoaling. Accounts for reflection and tidal variation. Where no reflection occurs in the surf zone the equation produces a profile very similar to that of the Dean profile.
Romanczyk et al., (2005)	$h = -A(x + x_s)^n$	Beach profile is considered in two sections. Extends the profile.
Dai et al., (2007)	$h = Ae^{Bx} + c$	Beach profile is divided into three different zones. Very complex methodology.

Note: (*h* and *H* the depth of water, *x* horizontal distance to the shoreline, *A B C D* shape parameters, *n* experience coefficients fitted to measured profiles, *b* depth which is asymptotically reached offshore, *k* profile curvature defined as distance, *m₀* measured slope of the beach face, *x_s* horizontal distance, *c* coefficient of mean slope, *x_r* the horizontal distance between the beginning of the surf profile and the virtual origin of the shoaling profile).

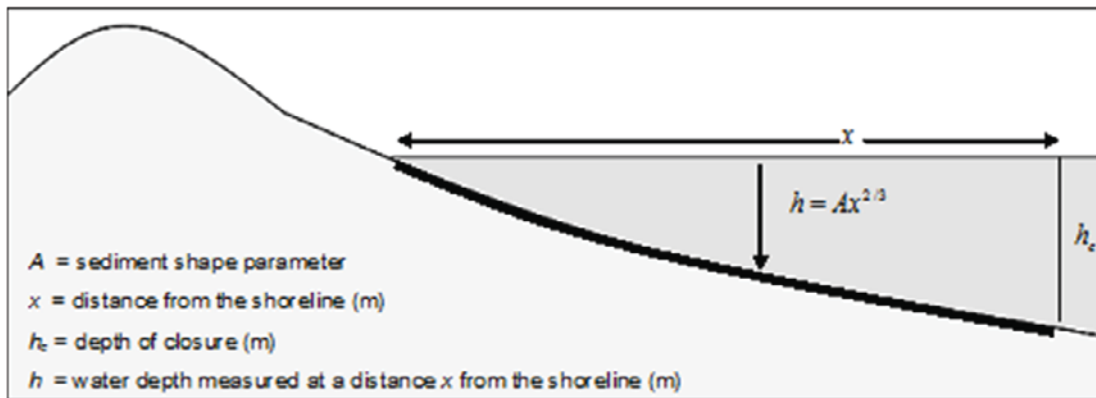


Figure 1: The Bruun/Dean model for predicting EBP

With coastal engineering being mainly located in the nearshore zone, definition of the entire beach profile is often required. Not defined by Bruun or Dean is the beach level at which the equilibrium profile should be taken from e.g. HAT or MHW (Figure 2). Simply taking MSL or still water level, as suggested by some authors, can give large discrepancies especially for beaches with a large tidal range. There is no definitive answer and as such best estimates are used. One of the aims of the research was to investigate the most appropriate shoreline datum for use in the Dean profile for Dubai.

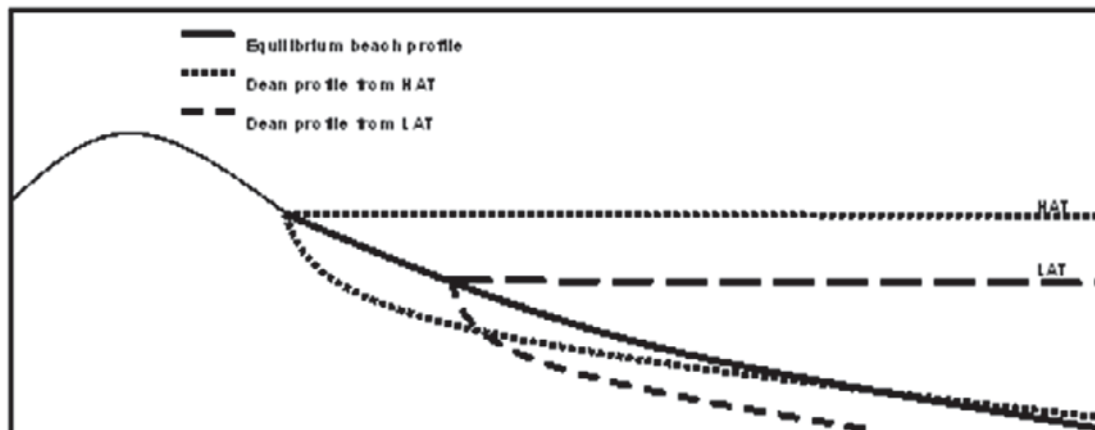


Figure 2: Variation of Dean profile when shoreline datum changes i.e. water level

3 Methodology

Using historical beach survey data collected and supplied by Dubai Municipality from along the Gulf coast of Dubai, the mean profiles for each of the beach profiles collected were calculated using HR Wallingford's Beach Data Analysis System (BDAS). A total of 16 profiles were examined from 5 sites along the Gulf coast of Dubai. Figure 3 shows the study site locations.

To determine the most suitable datum for use of the Dean profile in Dubai, the Dean profile was plotted at various water levels on the beach, from Highest Astronomical Tide (HAT) down to the Mean Lower Low Water (MLLW), as shown in Figure 4. It was found that the beaches along the Gulf coast of Dubai typically exhibit a steep upper beach slope (around a 1:8 slope) and a gently sloping lower beach (around a 1:45 slope); with a hinge point around the MHLW contour (Figures 4 and 5). With no sediment analysis at the time of the research study the sediment size was assumed constant for all profiles with a D50 of 0.2mm.

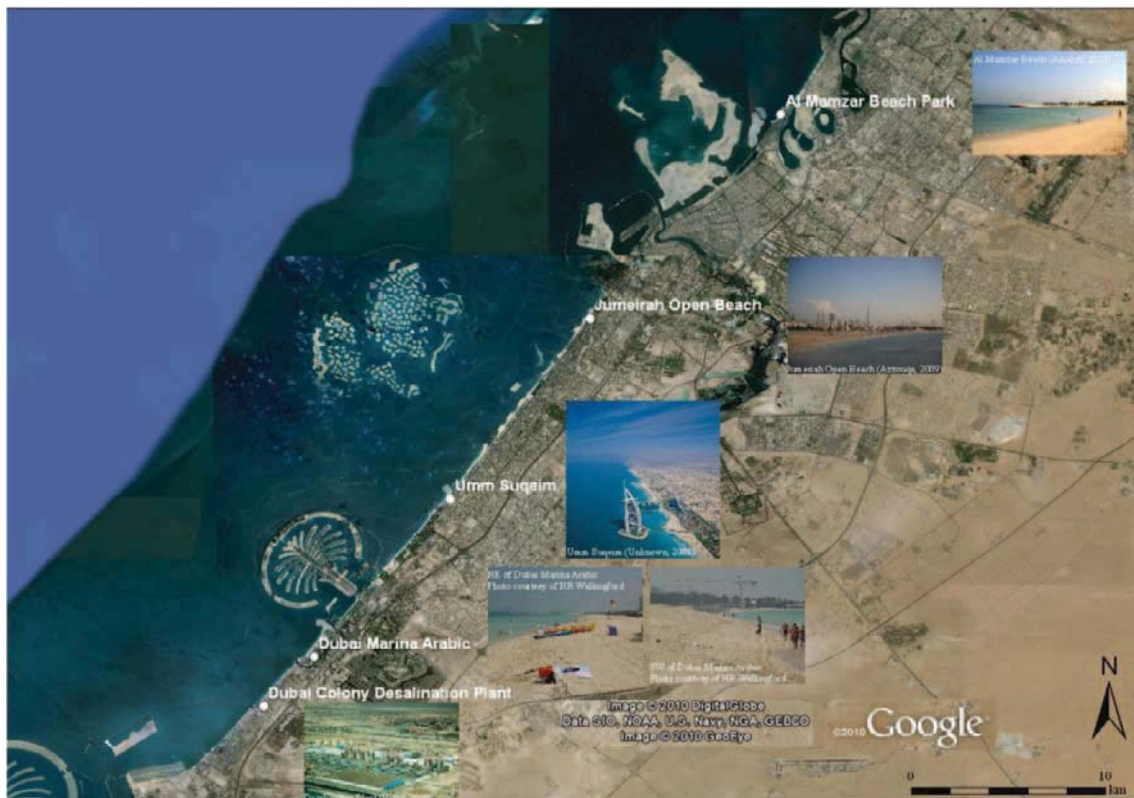


Figure 3: Dubai study sites

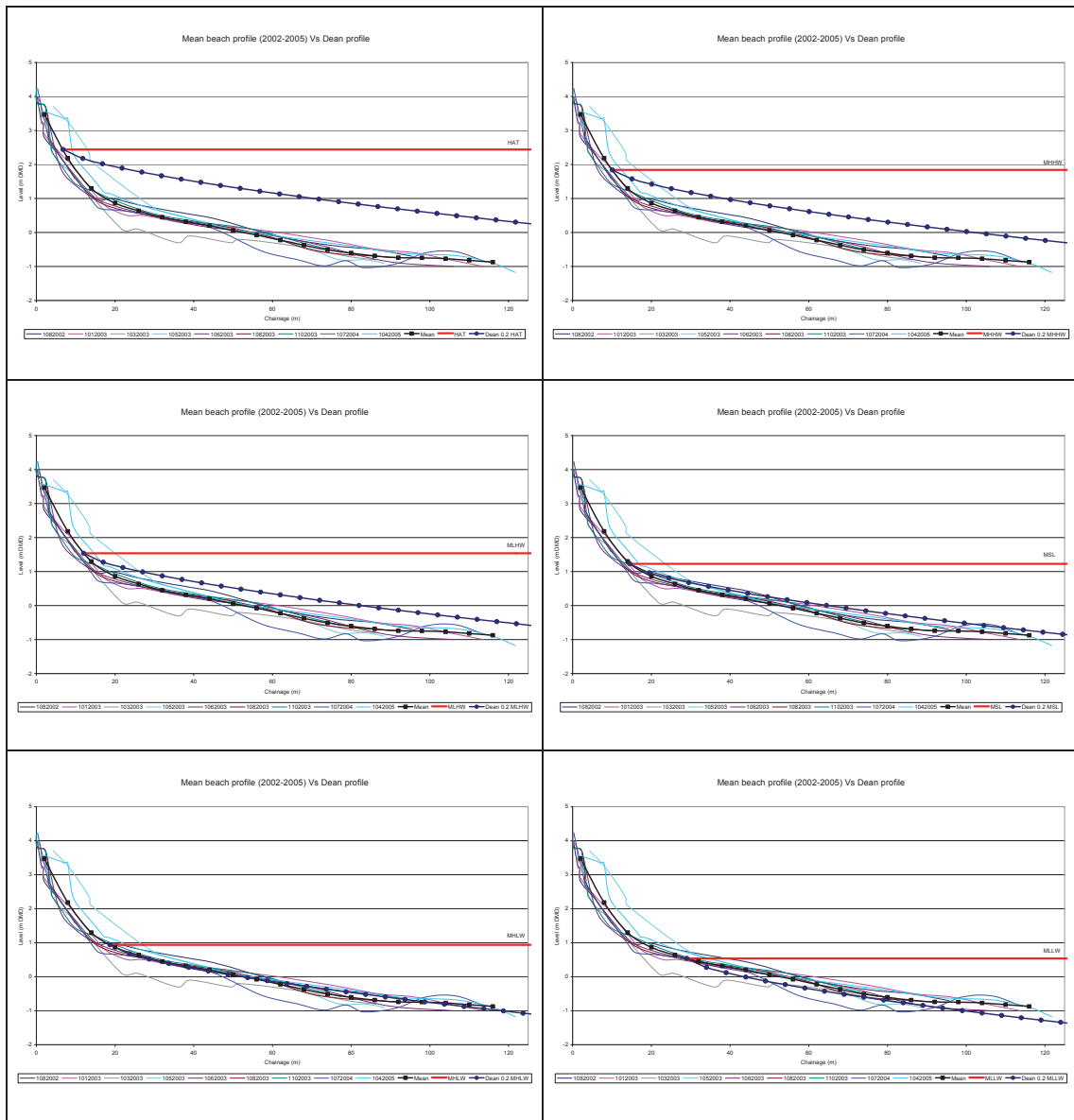


Figure 4: Comparison of the Dean profile at different water levels to measured beach profiles



Figure 5: Beach at Jumeirah showing steep upper profile and flatter lower profile

The resulting Dean profile at each water level was compared statistically (Root Mean Square Error) to the mean beach profile to determine the best fit. All of the mean profiles along the Gulf coast of Dubai fit the Dean profile best when using a shoreline datum below Mean Sea Level (MSL). Totalling the RMSE scores for each water level over all of the Dubai profiles gave Mean Higher Low Water (MHLW) as the best fitting datum. These results show that it is possible to predict the lower portion (MHLW to the closure depth) of Dubai beach profiles using the Dean profile to a degree of accuracy valuable for engineering use. However, the Dean profile did not fit the steeper upper portion of the beach, therefore to try and predict the portion of the profile not described, i.e. MHLW to HAT, two methods were investigated.

The first of the methods investigated was simply to plot the overall mean upper beach slope (1:8) of all the profiles along the Dubai coastline against the data. However, this simplified mean upper beach profile did not capture the concavity of the measured beach profiles. Therefore alternative EBP predictors were investigated.

There are a number of different EBP predictors available. Following research into the parameters for the various predictors and the requirement to maintain a "simple to apply engineering tool" it was found the EBP predictor prescribed by Turker and Kabdasli (2009) was best suited. Furthermore it is one of the few modifications to the original Dean profile that can be applied diagnostically. It was found that the Turker and Kabdasli predictor produced a steeper profile than that prescribed by Dean and provided, through RMSE analysis, a better fit for the upper portion of the beach profile.

To prescribe the whole beach profile a Hybrid profile predictor was created by combining the Turker and Kabdasli predictor for the upper beach (HAT to MHLW) with Dean's predictor for the lower beach (MHLW to the closure depth), as shown in Figure 6. The Hybrid profile predictor (Eq. 1) is valid for the following using the simple $Ax^{2/3}$ model:

$$h = Ax^{2/3} \tag{1}$$

Where [from HAT to MHLW]

$$A = 0.508w^{0.44} \quad (\text{Turker and Kabdasli, 2009})$$

And [from MHLW to closure depth]

$$A = 0.41D_{50}^{0.94} \rightarrow D_{50} < 0.4 \quad (\text{Hanson and Kraus, 1989})$$

$$A = 0.23D_{50}^{0.32} \rightarrow 0.4 \leq D_{50} < 10$$

- with
- h water depth [m]
 - A Scale parameter of the Dean equation [dimensionless]
 - w Ahrens (2000) sediment fall velocity [m/s]
 - D50 median grain size [mm]

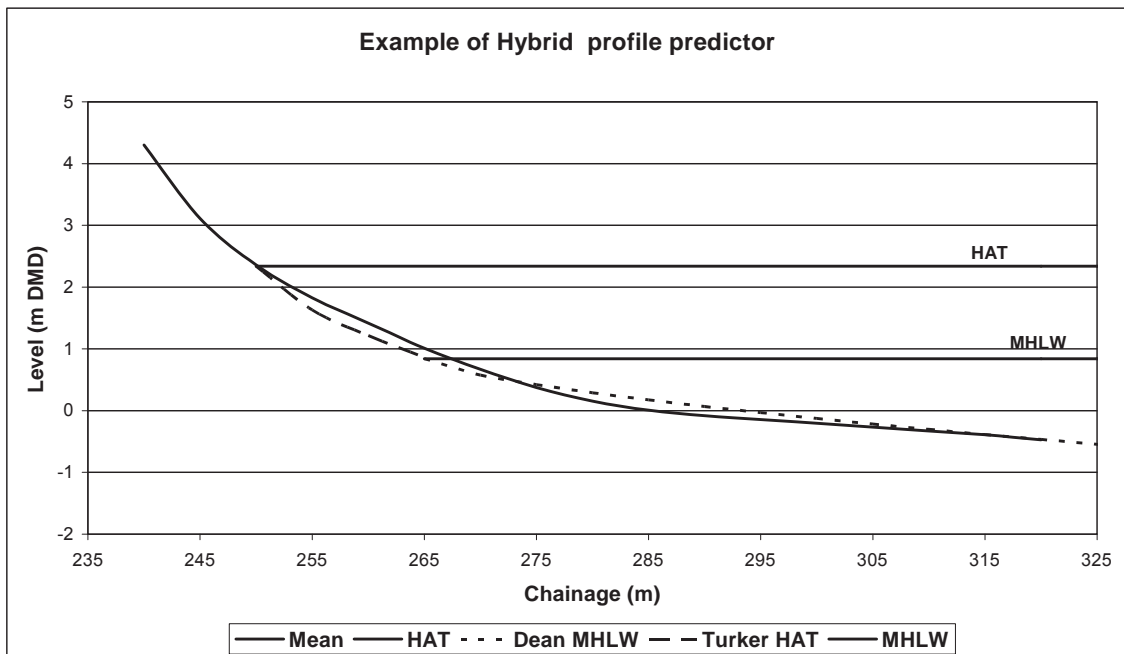


Figure 6: Example plot of the Hybrid profile predictor

4 Conclusion

The main conclusions are:

- Beach profile data from different beaches around the Gulf coast of Dubai have been analysed. It was found that the beaches along the Gulf coast of Dubai typically exhibit a steep upper beach slope from HAT to MHLW (around a 1:8 slope) and a gently sloping lower beach from MHLW to the closure depth (around a 1:45 slope); with a hinge point around the MHLW contour.
- When using the Dean profile to predict an equilibrium beach profile in Dubai it is recommended that MHLW be used as the shoreline datum. Results show that it is possible to predict the lower portion (MHLW to the closure depth) of Dubai beach profiles using the Dean profile to a degree of accuracy valuable for engineering use.

- Following an investigation of different methods for predicting the steeper upper section of the beaches in Dubai it was found, through RMSE analysis, that the Turker and Kabdasli method provided a better fit.
- To be able to predict the whole beach profile for the purpose of designing new artificial beaches in Dubai, a new Hybrid profile predictor has been proposed. The Hybrid consists of using the Turker and Kabdasli method for the upper beach (HAT to MHLW) and the Dean method for the lower beach (MHLW to the closure depth).

5 Acknowledgements

The authors are grateful for the support and guidance provided during the study by HR Wallingford, the University of Plymouth and Dubai Municipality, in particular Alan Brampton, Belen Blanco, Tim Chesher, David Finch, Katie Firman and Shunqi Pan.

6 References

- Bernabeu, AM (1999). Development, validation and application of a general model of equilibrium beach profile. Ph.D. thesis. University of Cantabria
- Bodge, KR (1992). Representing equilibrium beach profiles with an exponential expression. *Journal of Coastal Research* 8 (1) pp 47-55
- Bruun, P (1954). Coastal erosion and development of beach profiles. U.S. Army Beach Erosion Board Technical Memorandum 44 U.S. Army Corps of Engineers, Waterways Experiment Station, Vicksburg, Mississippi
- Dai, ZJ & Du, J & Li, CC & Chen, ZS (2007). The configuration of equilibrium beach profile in South China. *Geomorphology* 86 pp 441-454
- Dean, RG (1977). Equilibrium beach profiles: U.S Atlantic and Gulf coasts. Department of Civil Engineering, Technical Report 12, University of Delaware, Newark, Delaware
- Dean, RG & Dalrymple, RA (2002). Coastal processes with engineering applications. Cambridge University Press.
- Dean, RG (1991). Equilibrium beach profiles: Characteristics and applications. *Journal of Coastal Research* 7 (1) pp 53-84
- Hanson, H & Kraus, NC (1989) GENESIS: generalised model for simulating shoreline change; Report 1, technical reference. CERC-89-19 US Army Engineering Waterways Experimental Station. Coastal Engineering Centre, Vicksburg, MS
- Inman, DL & Elwany, MHS & Jenkins, SA (1993). Shoreline and bar-berm profiles on ocean beaches. *Journal of Geophysical Research* 98 (C10) pp 18-199
- Larson, M (1991). Equilibrium profile of a beach with varying grain size. *Coastal Sediments '91* pp 557-571
- Lee, PZ (1994). The submarine equilibrium profile: a physical model. *Journal of Coastal Research* 10 pp 1-7
- Komar, NC & McDougal, WG (1994). The analysis of exponential beach profiles. *Journal of Coastal Research* 10 pp 59-69
- Romanczyk, W & Boczar-Karakiewicz, B & Bona, JL (2005). Extended equilibrium beach profiles. *Coastal Engineering* 52 pp 727-744
- Turker, U & Kabdasli, MS (2009). The shape parameter and its modification for defining coastal profiles. *Environmental Geology* 57 pp 259-266

On wave transmission coefficient at low-crested structures

Giuseppe Roberto Tomasicchio¹, Felice D'Alessandro¹ and Gianluca Tundo¹

Abstract

The present paper faces the problem of the estimation of the wave transmission coefficient, K_t , at low-crested structures (LCS). As many formulae exist in literature, the aim of the study is not to come up with a new formula, but mainly to propose a re-calibrated version of the formulation by Goda and Ahrens (2008) with demonstration of its improved capability in predicting K_t against a valuable set of laboratory data. The adopted database considers 2D experiments on wave transmission at LCS; it consists of 3327 data from 33 datasets and includes various types of coastal structures in design conditions. Application of the new formulation after re-calibration shows a good agreement between measured and predicted values of K_t .

Keywords: low-crested structures (LCS), rubble-mound breakwaters, wave transmission, overtopping, laboratory data

1 Introduction

Wave transmission and overtopping are phenomena that allow a certain amount of wave energy to pass through and over a low-crested breakwater (Figure 1). The remaining part of the wave energy is dissipated by the wave breaking over the structure and seaward reflected. As the LCS is commonly adopted in coastal protection interventions, the prediction of the amount of energy transmitted behind the structure is a crucial point in design practice; in the past, the coastal research has led to various formulae for wave transmission that are widely used in engineering applications, but each with their own limitations.

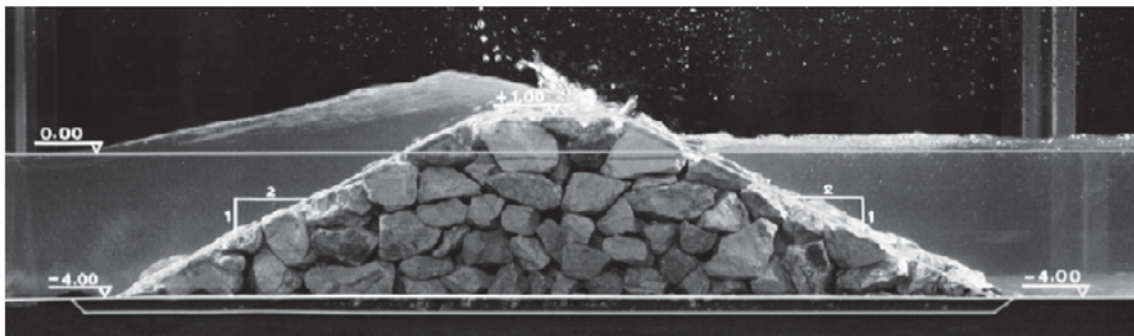


Figure 1: Wave transmission at LCS (Ruol et al. 2003)

Early studies on wave transmission coefficient were performed in Japan in 1960s (Iwasaki and Numata 1969, Goda and Ippen 1963) and in 1970s (Numata 1975, Tanaka 1976). Since the late 1980s, the number of papers/reports concerning the LCS performance greatly increased. Many studies have proposed empirical formulae for the wave transmission coefficient through regression analysis of the laboratory data from model tests conducted with irregular waves (d'Angremond et al. 1996, van der Meer et al. 2005, Buccino and Calabrese 2007).

More recently, based on 851 laboratory observations from 14 different physical model investigations, Goda and Ahrens (2008) provided a simple but consistent method to predict K_t , considering the wave energy transmitted over and through a LCS.

¹ University of Salento, Dept. of Engineering, via Monteroni 73100 Lecce, Italy – roberto.tomasicchio@unisalento.it; felice.dalessandro@unisalento.it; gianlucatumdo@libero.it

2 Formulation of the transmission coefficient in the original version (Goda and Ahrens 2008)

The formulation of wave transmission coefficient at LCS proposed by Goda and Ahrens (2008) is characterized with the following non-dimensional parameters:

$$K_t = \frac{H_t}{H_i} = f\left(\frac{R_c}{H_i}, \frac{H_i}{L}, \frac{B_{eff}}{L_o}, \frac{H_i}{D_{eff}}, \frac{B_{eff}}{D_{eff}}, \frac{h_c}{h + H_i}\right) \quad (1)$$

with the meaning of the symbols indicated in the notation. The wave period affects the transmission coefficient indirectly through the deepwater wavelength, L_o , and the local wavelength, L . The wave transmission coefficient at LCS is formulated as the summation of wave energy transmitted over and through LCS by referring to the approach by Wamsley and Ahrens (2003). The resultant formula becomes as follows:

$$(K_t)_{all} = \min\left\{1.0, \sqrt{(K_t)_{over}^2 + K_h^2 (K_t)_{thru}^2}\right\} : K_h = \min\{1.0, h_c / (h + H_i)\} \quad (2)$$

The factor K_h is introduced under the assumption that the runup height can be approximately equal to H_i and the contribution of waves passing through LCS to the energy of transmitted waves is proportional to the ratio of the LCS height to the height of wave runup above the sea bottom. The upper bound of $(K_t)_{all} = 1.0$ is imposed in Eq. 2, because there is a possibility that the sum of the energies of the waves passing over and through a LCS may exceed 1.0 when the waves incident to a porous and submerged LCS is very small in height. Eq. 2 is applied for both emerged and submerged LCS; for submerged structures, $(K_t)_{over}$ is usually much larger than $(K_t)_{thru}$ and thus the contribution of the latter to $(K_t)_{all}$ remains small. In particular, when the structure is submerged, the wave transmission is mainly governed by breaking and frictional dissipation over the crest and sloping surfaces of the structure. In this case, the transmission coefficient can be evaluated with the following equations:

$$(K_t)_{over} = \max\left\{0, \left(1 - \exp\left[a\left(R_c / H_i - R_{c,0}\right)\right]\right)\right\} : a = 0.248 \exp\left[-0.384 \ln\left(B_{eff} / L_o\right)\right] \quad (3)$$

$$R_{c,0} = \begin{cases} 1.0 & : D_{eff} = 0 \\ \max\left\{0.5, \min\left(1.0, H_i / D_{eff}\right)\right\} & : D_{eff} > 0 \end{cases} \quad (4)$$

$R_{c,0}$ represents an approximate limit of non-dimensional wave runup. When the relative freeboard R_c/H_i exceeds $R_{c,0}$, the exponential function takes a value larger than 1.0 and the term of $\left\{1 - \exp\left[a\left(R_c / H_i - R_{c,0}\right)\right]\right\}$ becomes negative. To prevent such an unrealistic outcome, the lower bound of $(K_t)_{over} = 0$ is provided in Eq. 3.

When the crest of the structure is high and little wave overtopping occurs, the wave transmission takes place through the voids among stones and units. In this case, K_t can be evaluated with the following equation:

$$(K_t)_{thru} = 1 / \left[1 + C\left(H_i / L\right)^{0.5}\right]^2 : C = 1.135\left(B_{eff} / D_{eff}\right)^{0.65} \quad (5)$$

which was originally proposed by Numata (1975) for the transmission coefficient of waves passing through a sloped mound made of tetrapods. The width B_{eff} is to be measured at the still water level for emerged breakwaters according to Numata (1975). The constant C was formulated with the data in the range of $B_{eff}/D_{eff} = 3$ to 10, but it appeared to be applicable for a wider range of B_{eff}/D_{eff} . Although Numata's data do not include impermeable structures, Eq. 5 yields $(K_t)_{thru} = 0$ for impermeable structures with $D_{eff} = 0$ because of the ratio of B_{eff}/D_{eff} approaching infinity. The interested reader is referred to Goda and Ahrens (2008) for a detailed description of the model formulation.

3 Laboratory datasets for re-calibration

Existing data on wave transmission have been collected to obtain an extensive database, the largest one in comparison with the other studies available in literature (Tomasicchio et al. 2011) The adopted database considers more than 3300 data of K_t from 33 datasets concerning experiments on wave transmission at LCS for various types of coastal structures in design conditions, such as rubble-mound structures with natural and concrete units, as well as impermeable slopes. The range of the parameters tested is shown in Table 1.

Table 1: Characteristics of laboratory datasets

Name	Nos	H_i (m)	T_p (s)	B_{eff} (m)	D_{eff} (m)	Remarks
Goda and Ahrens (2008) "adopted data"						
<i>Seelig (1980)</i>	69	0.08~0.18	0.91~3.46	0.60~1.26	0.11~0.16	RMn ¹ , P ² , E ³
<i>Ahrens (1987)</i>	201	0.01~0.18	1.33~3.64	0.25~0.67	0.02~0.03	Reef ¹ , P, E, S ³
<i>Allsop (1983)</i>	21	0.05~0.16	1.02~3.17	0.48~0.78	0.04~0.05	RMn, P, E
<i>Powell and Allsop (1985)</i>	42	0.09~0.22	1.39~2.30	0.16~0.49	0.08~0.09	RMn, P, S
<i>Van der Meer (1988)</i>	31	0.08~0.23	1.94~2.60	0.31~0.83	0.036	Reef, P, E, S
<i>Daemen (1991)</i>	53	0.03~0.15	0.98~2.88	0.37~0.88	0.04~0.06	Reef, P, E, S
<i>Daemrich and Kahle (1985)</i>						
<i>Crest B=0.2 m</i>	51	0.02~0.22	1.23~3.27	0.40~0.60	0.08	RMa ¹ , P, S
<i>Crest B=1.0 m</i>	45	0.02~0.28	1.23~3.27	1.20~1.40	0.08	RMa, P, S
<i>Delft H1872 (1994)</i>	39	0.06~0.17	1.02~2.22	0.47~0.71	0.04~0.05	RMa, P, E
<i>Delft M2090 (1985)</i>	31	0.05~0.20	1.07~2.26	0.35~0.95	0.044	RMn, P, E
<i>Delft H2061 (1994)</i>	32	0.09~0.25	1.24~2.89	0.35~0.80	0.04~0.05	RMn, P, E, S
<i>Kimura (2002)</i>	90	0.01~0.15	1.62~2.84	0.38~1.28	0.09	RMa, P, S
<i>Seelig (1980)</i>	13	0.13~0.17	1.33~3.32	0.52~0.75	none	SM, I ² , E
<i>Daemrich and Kahle (1985)</i>	45	0.02~0.21	1.23~3.27	0.40~0.60	none	SM, I, S
<i>Delft H2014 (1994)</i>	11	0.14~0.21	1.80~2.16	0.59~0.97	none	SM, I, S
Present paper "additional data"						
<i>Aquareef (2002)</i>	1063	0.03~0.14	1.07~2.39	0.12~2.38	0.04	AR ¹ , P, S
<i>UPC (2002)</i>	20	0.28~0.46	2.56~3.41	1.22~3.09	0.11	RMn, P, E, S
<i>Wang (2002)</i>	84	0.06~0.17	1.02~2.33	0.19~0.28	0.05	RMn, P, E, S
<i>Zanutigh (2000)</i>	56	0.02~0.15	0.74~1.97	0.28~0.71	0.05	RMn, P, E, S
<i>UCA (2001)</i>	53	0.03~0.09	1.60~3.20	0.37~1.24	0.04	RMn, P, E, S
<i>Seabrook and Hall (1998)</i>	633	0.05~0.19	1.16~2.13	0.38~3.65	0.06	RMn, P, S
<i>Melito and Melby (2002)</i>	122	0.03~0.23	1.07~3.36	0.36~1.14	0.05	RMa, P, E, S
<i>Calabrese and Buccino (2002)</i>	45	0.45~0.96	3.50~6.50	1.52~5.04	0.26	RMn, P, E, S
<i>Delft H4087 (2002)</i>	20	0.09~0.12	1.61~1.80	1.19~2.73	0.02~0.03	RMa, P, S
<i>Delft H1974 (1994)</i>	10	0.09~0.19	1.57~2.45	0.65~0.77	0.05	RMa, P, E
<i>TU Delft (1997)</i>	137	0.05~0.20	1.03~2.50	0.18~0.72	0.03~0.05	RMa, P, E
<i>Ruol and Faedo (2004)</i>	11	0.03~0.15	0.97~2.44	0.40	0.05	RMn, P, E, S
<i>Daemrich, Mai and Ohle (2001)</i>	100	0.02~0.15	1.00~1.75	0.20~0.60	0.04	RMn, P, S
<i>Delft H524 (1990)</i>	14	0.06~0.14	1.83~2.56	0.41~5.86	0.03	Reef, P, E, S
<i>Mori and Cappiotti (2005)</i>	57	0.07~0.01	1.50~1.80	0.12~0.33	0.03	RMn, P, E, S
<i>Delft H3374 (1998)</i>	28	0.04~0.15	1.03~1.75	0.19~2.01	none	SM, I, E, S
<i>Delft H4171 (2003)</i>	9	0.68~1.36	3.38~4.46	5.04	none	SM, I, S
<i>Delft M2090 (1985)</i>	7	0.07~0.21	1.30~2.28	0.45	none	SM, I, E
<i>Wang (2002)</i>	84	0.06~0.20	1.02~2.33	0.35~0.50	none	SM, I, E, S

Note: 1) AR = Artificial Reef; RMn = Rubble Mound with natural stones; RMa = Rubble Mound with artificial stones; SM = Smooth Structure; Reef = breakwater with same size stones. 2) P = Permeable; I = Impermeable. 3) E = Emerged; S = Submerged.

It is noticed that the effective B_{eff} has been calculated in accordance with Goda and Ahrens (2008). The effective diameter D_{eff} in Eq.s 4, 5 is the median diameter D_{n50} for rubble stone and $(M/\rho)^{1/3}$ for concrete blocks with M being the mass and ρ being the density (Goda and Ahrens 2008).

4 The new formulation: calibration and verification

In the present study, the performance of the formulation proposed by Goda and Ahrens (2008) has been verified against the full database. Figure 2 shows the comparison between K_t predicted and measured. The diagonal line represents the condition of complete agreement, $(K_t)_{pred} = (K_t)_{meas}$. It appears quite evident that for values of $K_t < 0.4$, Eq. 2 overestimates the transmission coefficient. This result confirms that if any practical formula is used outside the range in which it has been inferred, the accuracy of the estimate decreases (Van der Meer et al. 2005).

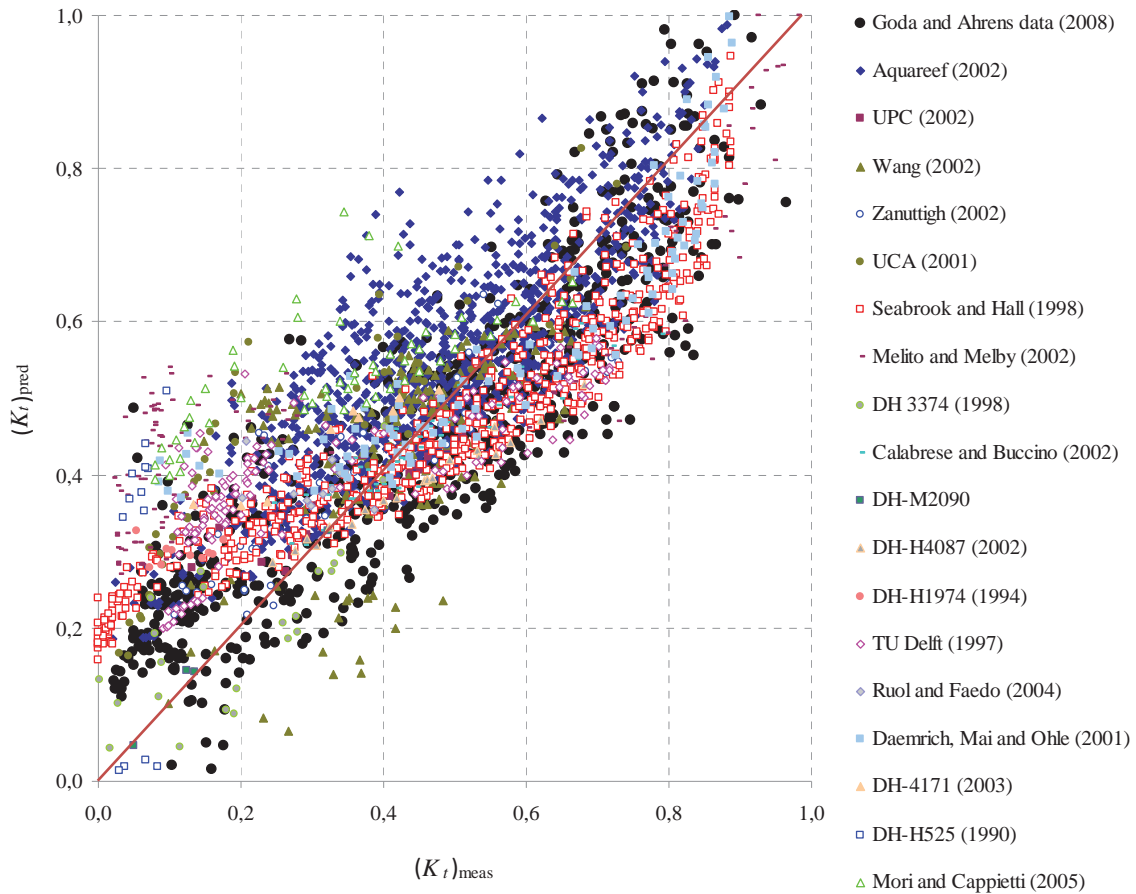


Figure 2: Performance of the Goda and Ahrens (2008) formulation against the extended database (correlation coefficient, $r = 0.831$; determination coefficient, $r^2 = 0.690$)

Accuracy of the Goda and Ahrens (2008) formulation is improved for $K_t < 0.4$ based on its modification and re-calibration. Re-calibration of the coefficients has been obtained by simply refitting Eq. 2 based on the full database. The results are:

$$K_h = \min\{0.8, h_c / (h + H_i)\} \quad (6)$$

$$C = 3.450(B_{eff} / D_{eff})^{0.65} \quad (7)$$

$$R_{c,o} = \begin{cases} 1.0 & : D_{eff} = 0 \\ \max\{0.6, \min(0.8, H_i / D_{eff})\} & : D_{eff} > 0 \end{cases} \quad (8)$$

Equation 8 somewhat intuitively sets the relative runup height as $R_{c,o}=1.0$ for impermeable LCS, and $R_{c,o}= 0.6$ to 0.8 for permeable LCS.

The adopted modifications determine a decrease of influence of $(K_t)_{thru}$ and, on the contrary, an increase of the effect induced by $(K_t)_{over}$ in the estimation of $(K_t)_{all}$. More precisely, respect to the Goda and Ahrens (2008) formulation, $(K_t)_{over}$ increases for $H_i/D_{eff} < 0.8$.

Figure 3 shows the comparison between the measured and predicted K_t from the full database by using the proposed formulation after re-calibration.

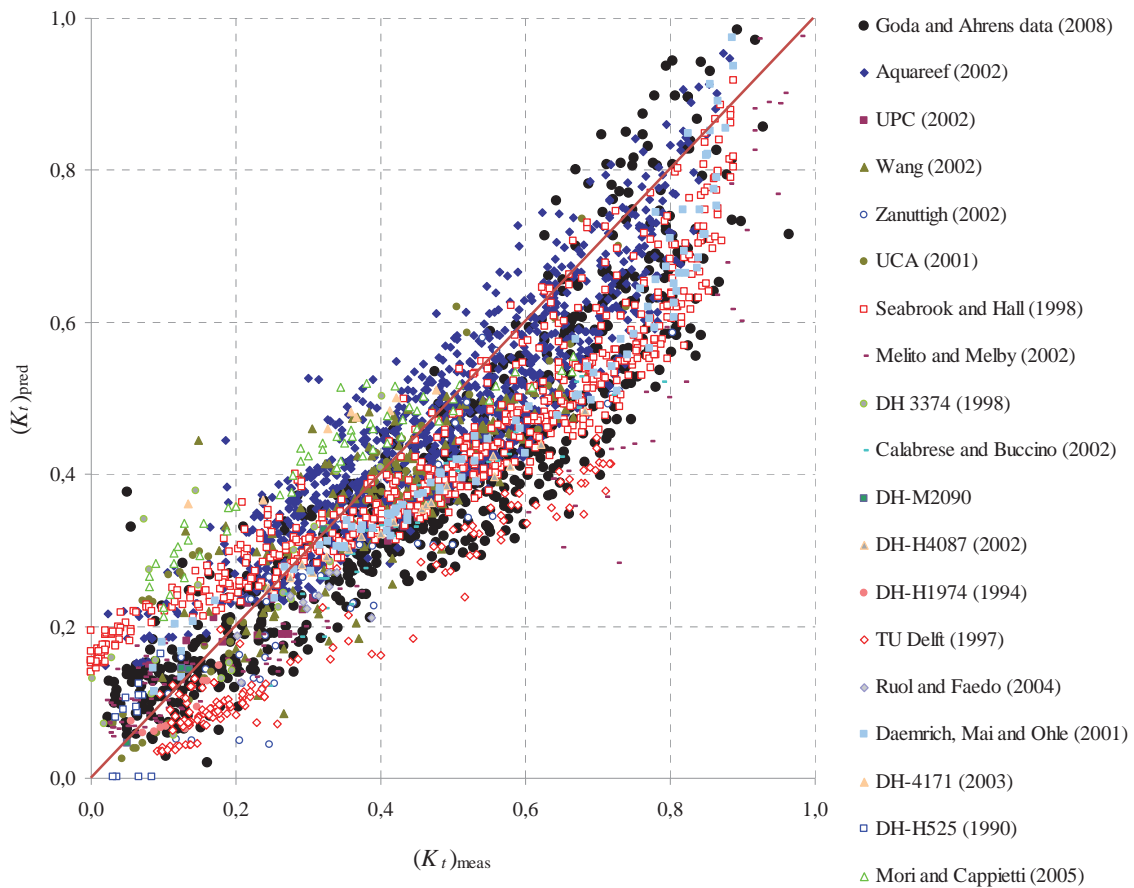


Figure 3: Comparison between measured and predicted transmission coefficient
 $(r = 0.902; r^2 = 0.814)$

Respect to Goda and Ahrens (2008), the application of the new formulation gives a better agreement between measured and predicted K_t in spite of a much larger number of data taken into account. An improvement in the accuracy of K_t prediction is evident for $K_t < 0.4$; this result overcomes the slight tendency of overestimation in the lower values of transmission coefficient derived by using the formulation by Goda and Ahrens (2008) in its original version.

Figure 4 shows the variation of K_t versus R_c/H_i for three groups of selected datasets ((a) Seelig (1980); (b) Van der Meer (1989) and Daemen (1991)). Both the observed and predicted transmission coefficients are plotted in the same diagrams with different symbols. As expected,

the transmission coefficient decreases as the relative freeboard increases. The trend of variation differs depending on dataset, because of the difference in the geometry and other conditions of the model. Although the scatter of data is large, the predicted values generally follow the trend of the observed values.

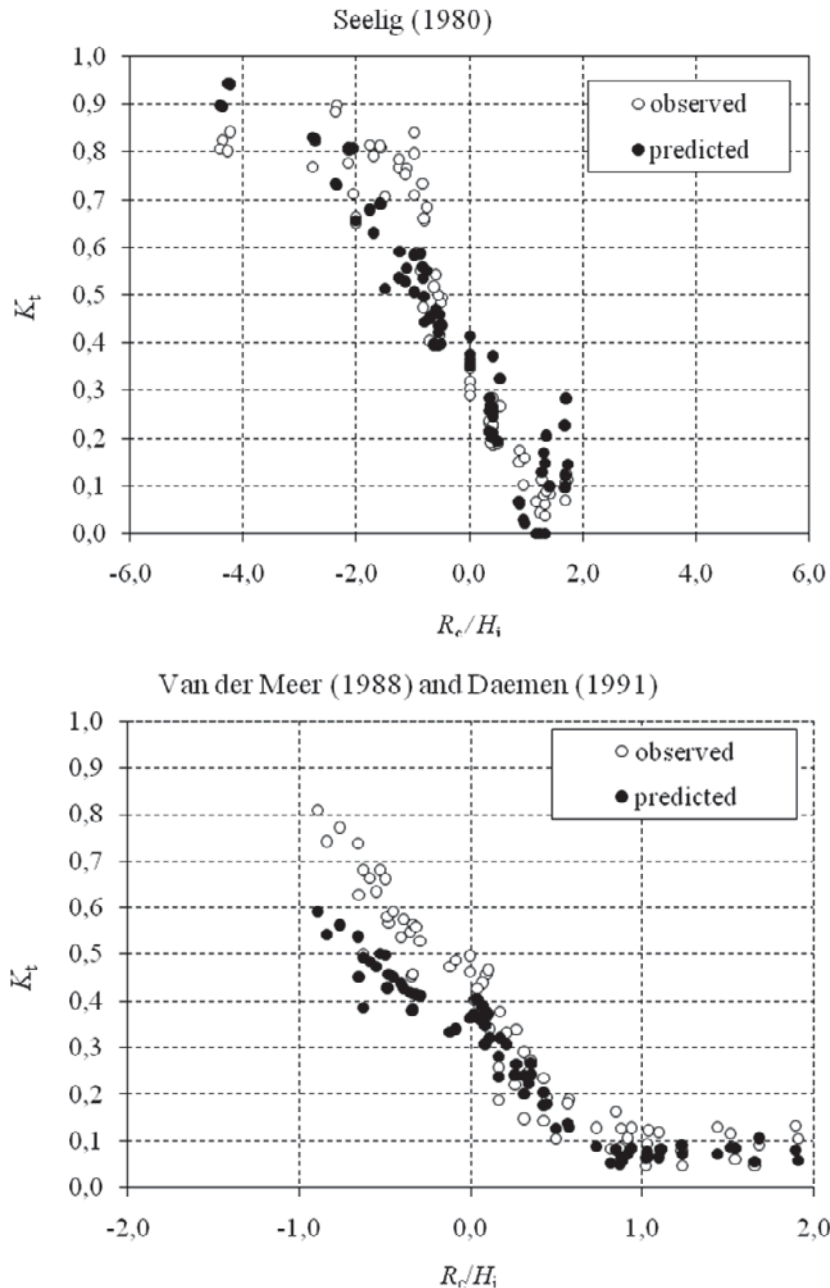


Figure 4: Comparison between observed (\circ) and predicted (\bullet) K_t for individual groups of datasets vs R_c/H_t

5 Conclusions

In the present study, an extensive database (Tomasicchio et al. 2011) has been analyzed and adopted to verify the performance of a new formulation (Goda and Ahrens 2008) for the prediction of the wave transmission coefficient. The comparisons between the results from the formulation by Goda and Ahrens (2008) with the experimental data showed an over-prediction for the smaller values of K_t . After re-calibration, even though the predicted K_t still varies around the laboratory data with a certain range of scatter, an improvement in the accuracy of the

estimation of the wave transmission coefficient appears evident for values of $K_t < 0.4$ respect to the original formulation by Goda and Ahrens (2008).

6 Notation

H_i	=	incident wave height, typically H_{m0i} , at the toe of the structure
H_t	=	transmitted wave height, typically H_{mot} , at the toe of the structure
T_p	=	peak wave period
L_o	=	deepwater wavelength
L	=	local wavelength
R_c	=	crest freeboard: positive upward, zero at still water level
h_c	=	structure height
h	=	water depth
D_{n50}	=	nominal diameter of armour units (in case of rubble mound structure)
K_t	=	transmission coefficient, H_t/H_i
B_{eff}	=	relative crest width
D_{eff}	=	effective diameter of materials composing LCS

7 Acknowledgements

The present work has been partly funded by the Italian Minister of University and Research (PRIN 2008 - "Strumenti operativi per la stima della vulnerabilità dei litorali sabbiosi anche in presenza di strutture costiere").

The authors gratefully acknowledge dr. J.W. Van der Meer for providing the data base from DELOS project.

8 References

- Buccino, M., and Calabrese, M. (2007): Conceptual approach for prediction of wave transmission at low-crested breakwaters. *Journal of Waterway, Port, Coastal and Ocean Engineering*, ASCE, 133(3), 213-224.
- d'Angremond, K., Van der Meer, J.W., and de Jong, R.J. (1996): Wave transmission at low-crested breakwaters. *Proc. of the 25th Int. Conference of Coastal Engineering*, Orlando, Florida, ASCE, 2418-2426.
- Goda, Y., and Ippen, A.T. (1963): Theoretical and experimental investigation of wave energy dissipators composed of wire mesh screens. M.I.T. Hydrodynamics Lab. Report n° 60, 66 pp.
- Goda, Y., and Ahrens, J.P. (2008): New formulation of wave transmission over and through low-crested structures. *Proc. of the 31st Int. Conf. of Coastal Engineering*, Hamburg, Germany, World Scientific, 3530-3541.

- Iwasaki, T., and Numata, A. (1969): A study on wave transmission coefficient of permeable breakwaters. Proceedings of 16th Japanese Conference of Coastal Engineering, JSCE, 329-334 (in japanese).
- Numata, A. (1975): Experimental study on wave attenuation by block mound breakwaters. Proceedings of 22nd Japanese Conference of Coastal Engineering, JSCE, 501-505 (in japanese).
- Ruol, P., Faedo, A., Paris, A. (2003): Prove sperimentali sul comportamento di una scogliera a cresta bassa e sul fenomeno del piling-up a tergo di essa. Studi Costieri, vol. 7, pp. 41-59, ISSN: 1129-8588 (in italian).
- Tanaka, N. (1976): Wave deformation and beach stabilization capacity of wide-crested submerged breakwaters. Proceedings of 23rd Japanese Conference of Coastal Engineering, JSCE, 152-157 (in japanese).
- Tomasicchio, G.R., D'Alessandro, F., Tundo, G. (2011): Further developments in a new formulation of wave transmission. Proc. Int. Conf. Coastal Structures 2011, Yokohama, Japan, in press.
- Van der Meer, J.W., Briganti, R., Zanuttigh, B., Wang, B. (2005): Wave transmission and reflection at low-crested structures: design formulae, oblique wave attack and spectral change. Coastal Engineering, (52) 915-929.
- Wamsley, T.V., and Ahrens, J.P. (2003): Computation of wave transmission coefficient at detached breakwaters for shoreline response modelling. Proc. Int. Conf. Coastal Structures 2003, Portland, Oregon, ASCE, pp. 593-695.

A numerical study for the stability analysis of articulated concrete mattress for submarine pipeline protection

Maria Gabriella Gaeta¹, Alberto Lamberti¹

Abstract

Submarine pipelines commonly operate along coastlines for wastewater draining or for fluid transportation from platforms at deep waters. Depending on the installation area, they are subject to waves and currents and the common solution to improve the pipe stability is to cover them with bitumen or articulated concrete block mattresses. The aim of the present study is the investigation of wave-induced forces on the articulated concrete block mattress covering a submarine pipe, laid on seabed, by using a RANS numerical model.

Keywords: articulated concrete mattress, pipeline protection, dynamic force, stability analysis, numerical modelling.

1 Introduction

Subsea pipelines are commonly used for wastewater draining along coastlines and for fluid transportation across seas or from platforms at deep waters to shore. For instance, the first and main pipeline crossing the Mediterranean Sea is the Transmed, transporting with the 156 km long submarine conduit 30.8% of the total gas imported by Italy from Algeria and Tunisia (IEA, 2011).

Depending on the where they are laid, pipelines are subject to breaker impact, to pulsating flow and currents, anchor drag and similar, inducing bed scour and potentially pipe free span (Sumer & Fredsøe, 2002). Table 1 summarizes most familiar hazards for submarine pipelines, induced by environmental factors and by human activities.

Table 1: Hazards for subsea pipeline stability.

Environmental Hazards	Human Hazards
Hydrodynamic forces (wave, currents)	Fishing operation
Sand waves, scour, pipe spanning	Dredging operation
Earthquakes, liquefaction, slope instability, submarine debris flows	Ship impact or anchor drag
	Construction works, platforms

In shallow waters, where current and waves are significant at seabed, where ships and swimmers are present, environmental and local restrictions usually force to bury the pipe.

At greater depth, a solution to improve submarine pipe stability is to cover them with a rubble mound or a mattress. In deep waters and for important pipelines bitumen mattresses are commonly installed (Figure 1, left); in some cases, the cheaper articulated concrete block mattresses are preferred (Figure 1, right). The last type of protection is the object of this study.

The mattress is usually assembled nearby the installation place and is laid down on the pipe suspended with steel cables and possibly with the help of a diver. When they are installed, they assume a particular shape, named "omega": this configuration gives a more hydrodynamic

¹ DICAM, University of Bologna, viale Risorgimento 2, 40136 Bologna (Italy), g.gaeta/alberto.lamberti@unibo.it

shape to the mattress-pipe system, eventually reducing the wave loads on it. At the same time, the added mass increases the inertia of the system.

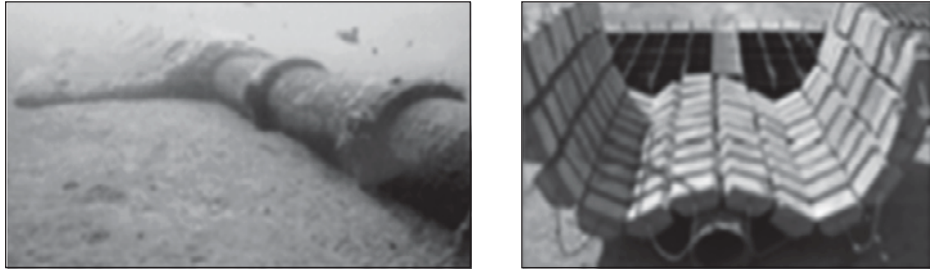


Figure 1: Mattress for the protection of pipes: bitumen mattress on site (left) and articulated concrete block mattress during lay down test (right).

Although experimental evidence shows that loads induced by regular sinusoidal wave are more irregular than Eq. 1 definition (especially for the lift force, that strongly depends on flow history effects, Sarpkaya & Rajabi, 1979), the hydrodynamic load acting on unprotected pipes is usually estimated using expressions proposed by Morison et al. (1950).

The drag force F_D and the lift force F_L , per unit length, are given by:

$$F_D(t) = \rho C_D D \cdot \frac{|u_x(t)|u_x(t)}{2} + \rho(1 + C_M)A \cdot a_x(t) \quad (1)$$

$$F_L(t) = \rho C_L D \cdot \frac{u_x^2(t)}{2} \quad (2)$$

where C_D , C_M and C_L are the drag, the added mass and the lift coefficients; D the pipe diameter, ρ is the water density, u_x the horizontal velocity component and a_x the horizontal acceleration component, both orthogonal to pipeline and evaluated for an undisturbed flow at pipe center position, A the pipe cross sectional area.

The choice of appropriate values for the coefficients C_D , C_M and C_L is essential for an accurate analysis of the global stability of the protected or unprotected pipeline.

These coefficients depend on the Reynolds number Re , the Keulegan-Carpenter number KC , the relative roughness and the relative trench depth (Sumer & Fredsøe, 1997).

For $Re > 10^6$, coefficients do not depend on flow regime and for a smooth pipe laid on the bed (neither trenched nor spanning), the relation given by Det Norske Veritas (DNV) recommendations (1988) and valid in the KC range 7-50 is commonly adopted:

$$C_{D0} = 2 + 3 \cdot 10^{-KC/30} \quad (3)$$

$$C_{L0} = 1.25 + 0.006 \cdot (9 - 0.1 \cdot KC)^3 \quad (4)$$

In case of trenching or soil penetration, a reduction coefficient is suggested. In any case, the recent recommendations by DNV (2009) only define requirements to concrete coating in terms of minimum thickness, minimum density and reinforcement.

Since neither flow velocity nor pipe diameter do influence the requirement, it is worth to define their influence and lack of scientific documentation on the hydrodynamic processes developing around these protected pipelines is found, motivating the present study, consisting into the investigation of wave-induced forces on the articulated concrete mattress using a 2DV numerical model.

2 Model set-up and validation

2.1 Numerical Model

The used numerical model, originally developed by Lin & Liu (1998) and recently implemented and validated by Lara et al. (2006), solves the 2DV Reynolds Average Navier-Stokes (RANS) equations.

The $k-\varepsilon$ closure (Launder et al., 1972) is adopted to model the Reynolds stress tensor. More details on the model can be found in Lin & Liu (1998), Lara et al. (2006) and Gaeta et al. (2009).

In the present study, the wave generation occurs at the left boundary of the numerical domain, imposing free surface elevation and velocity profile according to linear wave theory; the right boundary allows open flow; no-slip and Neumann conditions are imposed at the bottom and at the obstacle surface.

The model allows obtaining detailed information on velocity, pressure and turbulence field around the structure.

The hydrodynamic forces acting on mattress and pipe are calculated by integrating the pressure distribution around all the exposed parts of the obstacle cells.

2.2 Model validation

Wave-induced loads acting on an unprotected pipe laid over a horizontal bed are evaluated order to validate numerical results by comparison with a case that is well documented in literature. Regular waves are generated and 3 tests are performed with increasing KC number. Table 2 lists the wave height (H), wave period (T), water depth (d), pipe diameter (D) and corresponding KC and Re values for each test.

Table 2: Characteristics of validation tests.

Test	H (m)	T (s)	d (m)	D (m)	KC	Re
C01	2	6	10	0.9	4	$O(10^5)$
C02	2	6	10	0.5	7	$O(10^5)$
C03	4	6	8	0.5	12	$O(10^6)$

Observing the calculated streamlines during the wake development at the lee side of the pipe, the computed flow and vortex patterns qualitatively agree with experimental and numerical results shown in literature (among others, Zhao *et al.*, 2006).

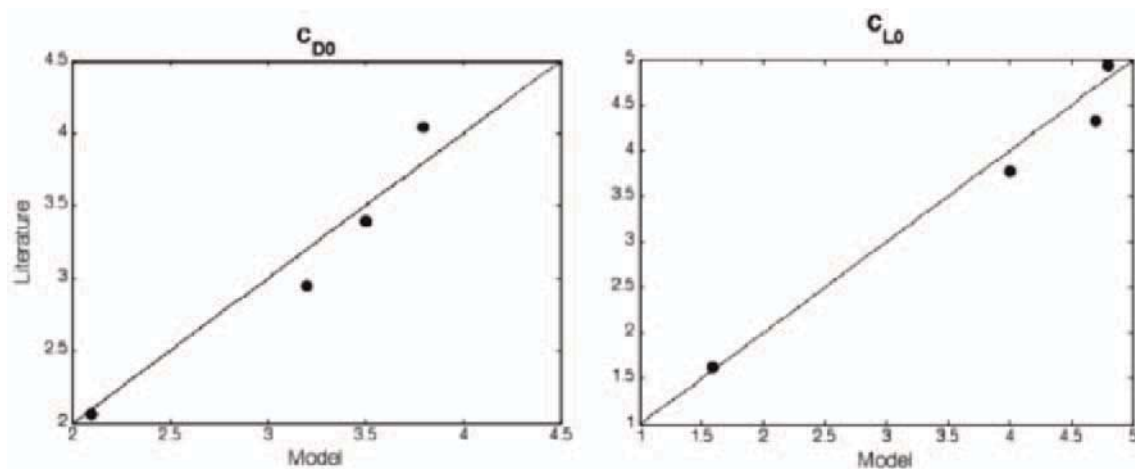


Figure 2: Model validation in terms of drag and lift coefficients: comparison between model and literature values.

In the first half period, a vortex develops on the leeside of the pipe; as the wave crest passes over the cylinder, the vortex size increases until velocity changes direction. Then, when the wave trough passes over the pipe, this vortex is partially dissipated while another smaller one develops in the seaside of the cylinder.

The computed drag and lift forces are compared to results by using the Morison's expression and using velocity and acceleration information by numerical results.

The drag, added mass and lift coefficients are estimated using the least mean square method and are found similar to the values proposed in literature by Sumer & Fredsøe (1997) for similar conditions.

It results also that the lift force signal shows two peaks in one wave period due to vortex shedding development at the leeside of the pipe.

Finally, achieving good agreement (Figure 2) in validation tests allows the following considerations on the protected pipeline configuration.

3 Articulated concrete block protection on pipe

3.1 Numerical set-up

The studied mattress is a concrete blanket composed by 12 hexagonal cross sectional blocks linked together (in the two directions) with a cable net (Figure 1, right), forming a flexible mattress, capable to form a highly resistant protection and stabilization system.

Mattresses with two different block thicknesses are simulated (20 cm -s20- and 30 cm -s30-), while a pipe with a constant 90 cm diameter is chosen.

After a grid accuracy analysis, a very fine resolution (grid size =5 cm) is chosen to discretize the area close to the pipeline in order to well determine velocity and pressure over each block and over the pipe, while wider cells define the generation and propagation zones of the numerical channel. Figure 3 shows the numerical discretization for the simulated mattress s20 (left) and s30 (right).

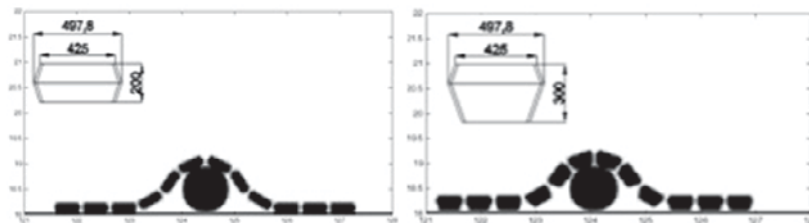


Figure 3: Numerical discretization of the studied articulated concrete block mattress: block thickness equal to 20 cm (left) and equal to 30 cm (right).

The analysis is carried out simulating:

- regular waves propagating in deep waters, with $H=8$ m, $T=12$ s, $d=24$ m, $KC= 25$ (*Test A*);
- solitary wave propagating in shallow waters, with $H=5$ m, $d=8$ m (*Test B*).

3.2 Hydrodynamics

Figure 4 shows the streamline evolution in 10 different temporal instants during the regular wave (*Test As20*) propagation over the mattress-pipe structure.

In the first half period ($t/T=0-0.5$), the wave crest passes over the cylinder and the previous generated vortex dissipates in upward direction while a clockwise vortex develops at the leeside of the protected pipe, grows and is convected upstream, until flow reverses at $t/T=0.5$.

This vortex is dissipated as the velocity is reduced. In the interval $t/T=0.5-1$, the wave trough passes over the pipe and another smaller counter-clockwise vortex is generated at the cylinder

seaside, potentially compromising the stability of the edge block. Two small recirculating cells are observed between the mattress and the pipe, generated by the flux through gaps between the blocks.

In case of solitary wave, the flow structure is slightly different due to the flow patterns generated by the positive water displacement above the mean water level.

The generation of clockwise vortex at the leeward side of the mattress is clearly observed in Figure 5: its size increases as the wave passes and the vortex is convected further shoreward than in the previous case.

The effects induced by turbulence field generated by previous pulsating waves are here not evident, and the vortex shedding effects induced on the mattress-pipe are eventually greater.

The analysis of hydrodynamics is also performed for the other block thickness (s30). A thicker concrete block does not substantially influence the flow pattern developing around the protected pipe, but a larger weight of the coat increases the pipe stability.

The analysis of the block edge stability is influenced by block shape and dimension and requires detailed and dedicated laboratory investigation, with a movable bed.

3.3 Force evaluation

The dynamic pressure field along each block contour and along the pipe diameter is evaluated: differences between the seaside and the leeside points of the pipe, probably due to turbulent fluxes through the block gaps, are observed.

The drag and the lift forces due to oscillatory flow on the mattress-pipe system are determined by integrating the computed dynamic pressure along each block contour and along the pipe diameter.

In order to evaluate the global stability, the force on each block is estimated, revealing that the inner and outer edge blocks as well as the suspended blocks (not laid on bed or pipe) are subject to the greater loads.

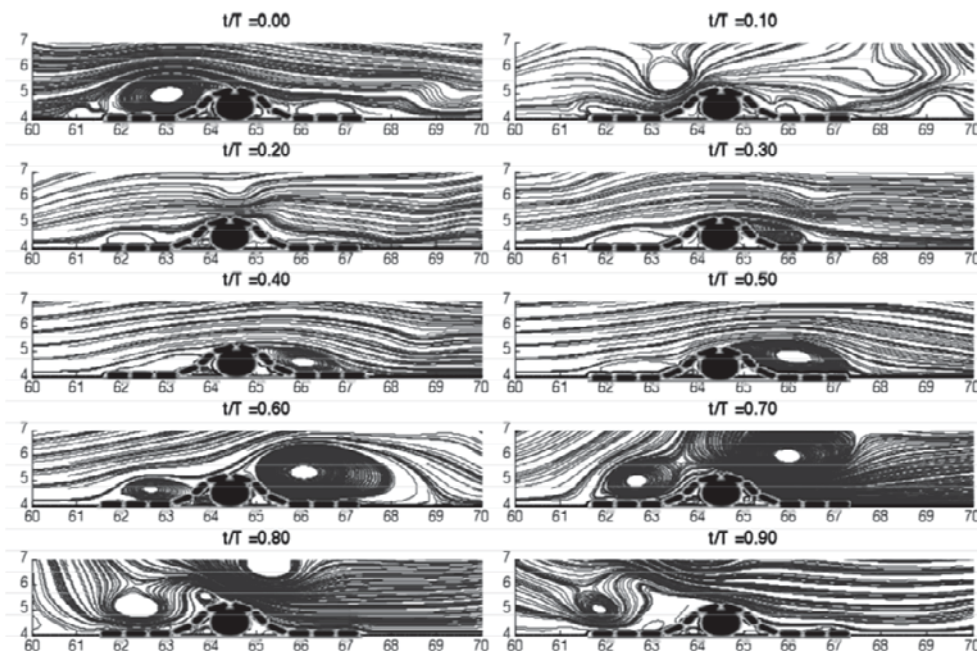


Figure 4: Evolution of streamlines around the mattress (Test As20): regular wave propagates in deep water from left to right.

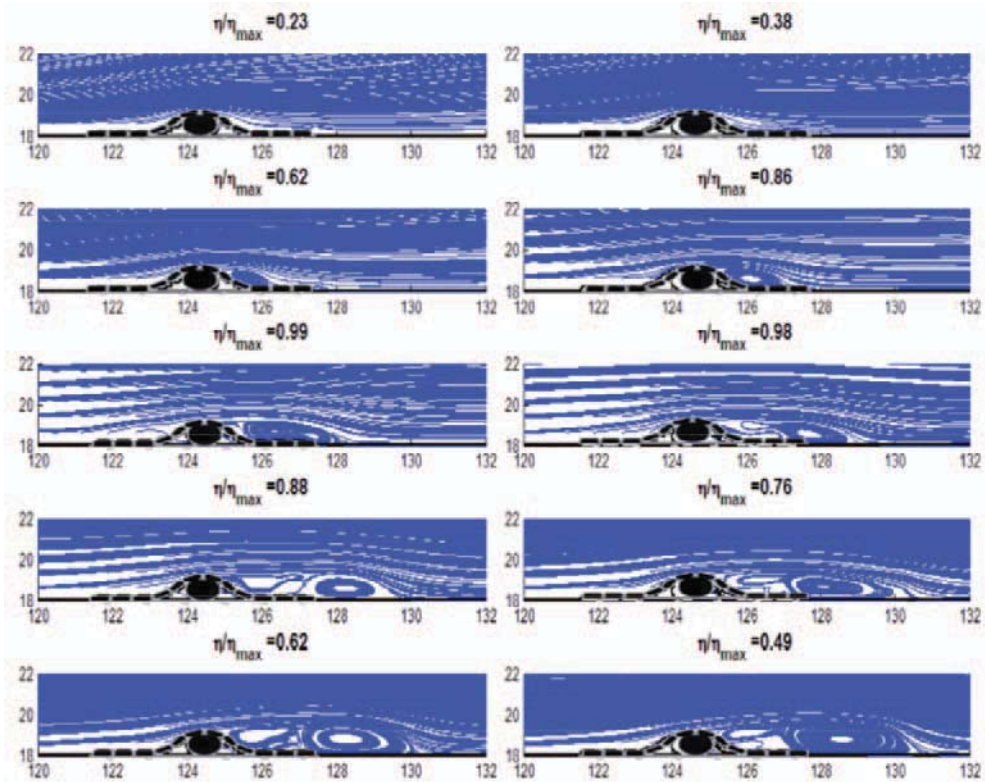


Figure 5: Streamlines around the mattress (Test Bs20): solitary wave propagates in shallow water from left to right.

Figures 6 and 7 show the evolution in time of the surface oscillation (η) and of the drag force on the mattress ($F_{D,M}$), induced by regular waves (Test As20) and by solitary wave (Test Bs20) respectively.

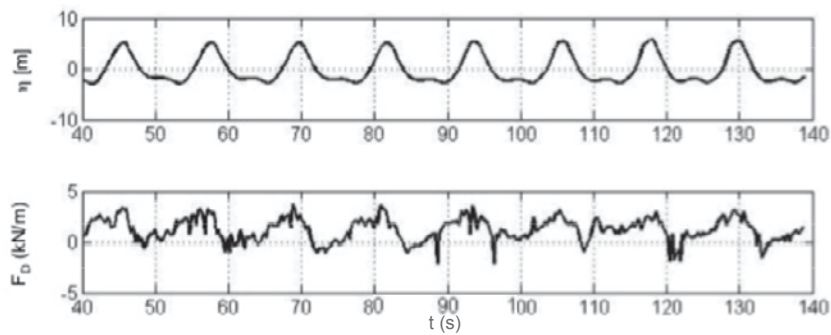


Figure 6: Numerical results for drag force $F_{D,M}$ on the mattress for Test As20.

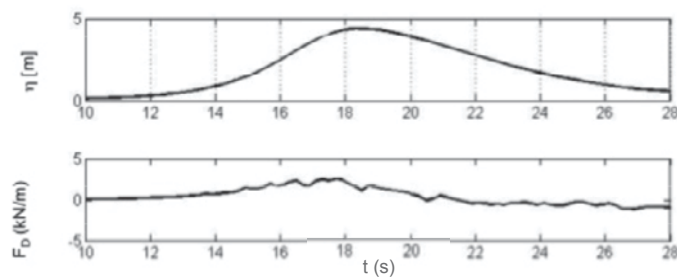


Figure 7: Numerical results for drag force $F_{D,M}$ on the mattress for Test Bs20.

The signal shape appears irregular, especially in case of regular wave train tests.

The computed global forces are compared to Morison's expressions (Eqs. 1 and 2), using numerical velocity and acceleration fields in an undisturbed position. A first estimation for the constant coefficients C_D , C_M and C_L are obtained by applying the least mean square method and, since no suggestions are found in case of protected pipeline, they are compared to the values C_{D0} , C_{M0} and C_{L0} , evaluated in case of a unprotected pipe over the seabed, in accordance with the DNV's recommendations (1988).

The results of the comparison are summarized in Table 3. The effect of the mattress installation over a submarine pipe is expressed in terms of reduction of the drag (C_D/C_{D0}), added mass (C_M/C_{M0}) and lift coefficients (C_L/C_{L0}) in comparison with unprotected pipes, that are found to be different for Tests A and Tests B.

Table 3: Drag CD, added mass CM and lift CL coefficients for protected pipe.

	C_D	C_M	C_L
Tests A	0.50 C_{D0}	0.25 C_{M0}	0.50 C_{L0}
Tests B	0.85 C_{D0}	0.25 C_{M0}	0.85 C_{L0}

In case of deep water and regular wave attack, turbulence induced by wave train propagation around mattress leads to disturbances on vortex development and in terms of loads on the structure, while in case of solitary wave propagating in shallow waters, this effect is less pronounced.

Finally, the total forces are calculated as summation of force on mattress and force acting on the pipe (i.e. $F_{-M} + F_{-P}$) and the global stability analysis is performed evaluating the safety factor f_s as:

$$f_s = \frac{k_g(P_{tot}' - F_L)}{F_D} \quad (5)$$

where P_{tot}' is the total (mattress and pipe) submerged weight, F_L and F_D are the total lift and drag forces, k_g is the seabed friction coefficient, chosen following DNV suggestions (i.e. 0.2 for sand and 0.4 for clay).

4 Conclusions and future works

In the present study, numerical simulations, solving 2DV RANS equations, have been carried out to investigate the interaction between waves and protected pipe laid on horizontal, smooth, impermeable and fixed seabed.

The model has been validated for unprotected pipes, showing a good agreement with literature in terms of force values.

The influence of the concrete block mattress on flow and vortex patterns and on the hydrodynamic forces on the pipe has been investigated for two hydraulic conditions (regular waves in deep waters and breaking wave in shallow waters), revealing the development of complex recirculating flow structure, also through the gaps between the mattress blocks and the pipe. The drag, the added mass and the lift coefficients are found to be smaller than the corresponding values computed for unprotected pipe.

Further analysis to evaluate the dependence of hydrodynamic force on wave and current characteristics are ongoing, extending the present results to a wider KC number range.

A laboratory investigation of wave-induced loads on protected pipelines is also suitable in order to extend numerical result validity and research sediment transport and 3D effects.

5 Acknowledgment

Officine Maccaferri spa is gratefully acknowledged for partially supporting the present study.

6 References

- Det Norske Veritas (1988): On bottom stability design for submarine pipelines, in: Recommended Practise DNV-E305, Oslo, pp. 42.
- Det Norske Veritas (2007): Rules for submarine pipeline system, On bottom stability design for submarine pipelines, in: Recommended practice DNV-RP-F109, Oslo, pp. 28.
- Gaeta, M.G.; Lamberti, A.; Liu, P. L.-F. (2009): A two-phase numerical model for incompressible fluids: air influence in wave propagation and applications, in: Proc. 31st Int. Conf. Coast. Eng., pp. 144-156.
- International Energy Agency (2011): Oil and Gas Emergency Policy - Italy 2010 update. In: Oil Supply Security: Emergency Response of IEA Countries, pp.16.
- Lara, J. L.; Garcia, N.; Losada, I. J. (2006): RANS modelling applied to random wave interaction with submerged permeable structures. In: Coastal Engineering, Vol. 53, pp. 395-417.
- Launder, B.E.; Morse, A.; Rodi, W.; Spalding, D.B. (1972): Prediction of free shear flows: a comparison of the performance of six turbulence models. In: Free Shear Flow, pp. 361-426.
- Lin, P.; Liu, P. L.-F. (1998) A numerical study of breaking waves in the surf zone. In: J. Fluid Mech., Vol. 359, pp. 239-264.
- Morison, J.R.; O'Brien, J.P. et al. (1950): The forces exerted by surface waves on piles. In: J. Petrol. Technology, AIME, Vol. 189, pp. 149-154.
- Sarpkaya, T.; Rajabi, F. (1979): Hydrodynamic drag on bottom-mounted smooth and rough cylinders in periodic flow, in: OTC 3761, Houston, Texas, pp. 219-226.
- Sumer, M.; Fredsøe, J. (1997): Hydrodynamics around Cylindrical Structures. In: Adv. Series on Ocean Eng., Vol. 12.
- Sumer, M.; Fredsøe J. (2002): The mechanics of scour in the marine environment. In: Adv. Series on Ocean Engineering, Vol. 17.
- Zhao, M.; Cheng, L.; Hongwei, A.H. (2006): A finite element solution of wave forces on a horizontal circular cylinder close to the sea-bed. In: J. of Hydrodynamics, Proc. of the Conference of Global Chinese Scholars on Hydrodynamics, Vol. 18, No. 3, pp. 139-145.

Geosynthetic tubes as construction element for coastal protection works – Fundamental design aspects; Application possibilities and practical experience

Markus Wilke¹, Hartmut Hangen²

Abstract

The scope of this paper is to give a short overview about the fundamental aspects of geosynthetic tubes regarding the design, application possibilities and the practical experience of projects already executed.

Keywords: geosynthetic tube, tube design, practical experience

1 Introduction

Geosynthetic tubes are oblong construction elements with an elliptical cross-sectional shape. The tubes are made out of special hydraulically engineered geosynthetic. This geotextile containment system is subsequently filled with a pumped sand-/water slurry mixture. The slurry is introduced into the tubes by multiple filling ports along the length of each tube.

Due to the retention characteristics of the tube shell fabric the sand deposited inside the tube remains in place whereas the water is able to drain out due to the fabric permeability.



Figure 1: Geosynthetic tubes as containment bund for land reclamation

The use of geosynthetic tubes as construction elements for coastal structures is increasing. As Heibaum pointed out in 2002 that geosynthetic containers are “a new field of application with nearly no limits” [Heibaum 2002], the system of geosynthetic tubes has become more common during the last decade. Although the use of formally so called “sand saugsages” has already been reported in 1982 [Bogossian, 1982] and the system has even been known before this time. Since these early days the experience and the understanding of these systems increased, filling methods as well as the materials have been modified fundamentally. However, there are still some uncertainties regarding the possible applications in the marine environment, the adequate design of such a structure and its successful installation.

To address these uncertainties, much research has been carried out [Van Steeg, 2008; Van Steeg, 2010; Aminiti, 2010] during recent years. In addition the CUR published a document

¹ HUESKER Synthetic GmbH, Fabrikstrasse 13-15, 48712 Gescher, Germany, wilke@huesker.de

² HUESKER Synthetic GmbH, Fabrikstrasse 13-15, 48712 Gescher, Germany, hangen@huesker.de

dealing with the design of geotextile sand elements [CUR 217, 2006]. Additionally, there are more works delivering further information regarding the design and performance of geosynthetic tubes (e.g. [Pilarczyk, 2000] or [Cantré, 2008]).

The intention of this paper is to briefly sum up the actual design approaches and to deliver a short insight into the application possibilities by means of executed projects in Latvia and Italy.

2 Design of geosynthetic tubes

Concerning the design of geosynthetic tubes external as well as internal failure mechanisms have to be taken into account. The external design focuses on the stability of the geotextile tube as an almost monolithic element e.g. exposed to wave loads whereas the internal stability analysis deals with the geotextile tube shell, the fill material and the interaction of these two elements. Another important design factor is the degree of filling, e.g. expressed as the ratio h/D of the filling height h and the nominal diameter (diameter of a perfectly shaped circle, D) of the geosynthetic tube. This ratio significantly influences the generated tensile forces in the geotextile tube shell.

2.1 Definition of the filling degree

The degree of filling limits the possibility of internal sand migration inside the tube. Moreover it is a good indicator for the overall performance of a geotextile tube. Normally it also acts as a first indicator for the determination of a first indicative permissible filling height. Two approaches exist for the formulation of the filling degree: the one based on the height and the other based on the cross-sectional area.

2.1.1 Filling degree according to the height

The definition of the filling percentage based on the height according to the definition of Deltares [van Steeg, 2010] is:

$$p_h = \frac{h}{h_{100\%}} \quad (1)$$

with p_h filling percentage based on the height [-]

h height of the tube after filling [m]

$h_{100\%}$ height of the maximum filled tube (equal to the diameter of the tube) [m]

As a very common and practical approach the filling degree can be re-written as the ratio between the tube height and the theoretical diameter of the tube:

$$\text{Filling Ratio} := \frac{h}{D} \quad (2)$$

with h height of the tube after filling [m]

D diameter of the 100% filled tube; cross-section is equal to a perfectly shaped circle [m]

2.1.1 Filling degree according to the cross-sectional area

The definition of the filling degree for geotextile container according to CUR [CUR 217, 2006] is:

$$f = \frac{4\pi A}{S^2} \quad (3)$$

with f filling degree [-]

A cross-sectional area of the filled tube [m²]

S Circumference of the tube [m]

f filling degree [-]

2.2 Internal stability analysis

2.2.1 Tensile strength

The determination of the required tensile strength of the tube fabric can be performed according to the "Leshchinsky method" [Leshchinsky, 1996]. The calculation program GeoCoPS 3.0 follows this design guideline. Figure 2 shows the development of the generated circumferential tensile forces in the tube shell (y-axis) depending on different tube diameters and the h/D ratio (x-axis). This graph is based on GeoCoPS calculations performed with only air surrounding the tube.

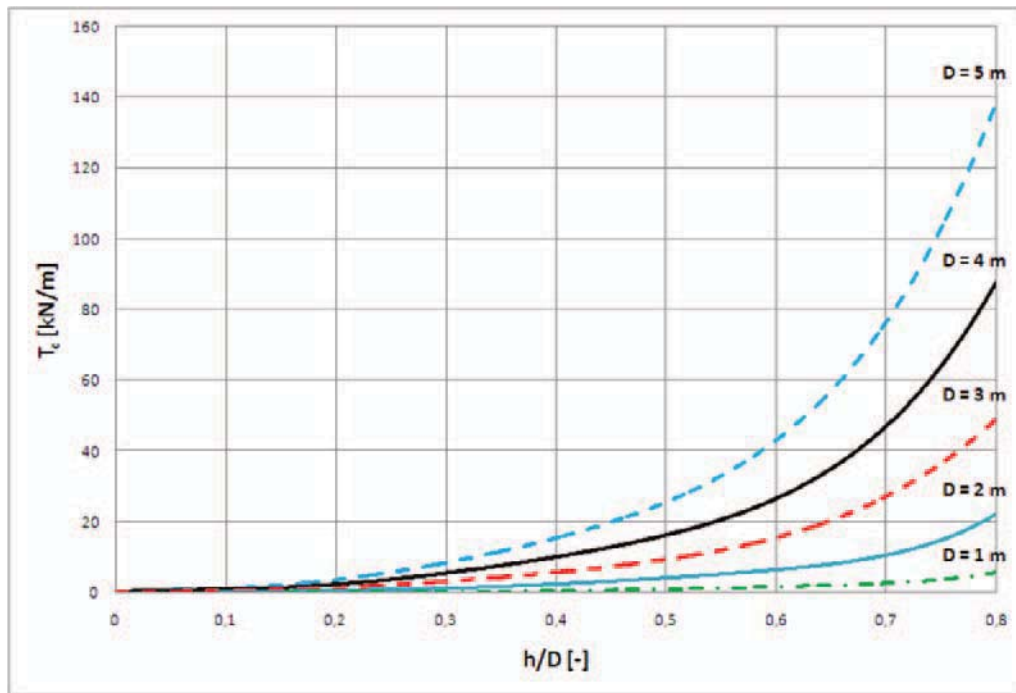


Figure 2: Theoretical circumferential tensile forces depending on filling ratio h/D for different tube diameters in the dry ($\gamma = 14 \text{ kN/m}^3$)

The above graph illustrates the almost exponentially increasing force with enlarged tube diameter in combination with greater filling heights.

2.2.2 Permissible opening size

The permissible opening size of the geotextile for the tube can be determined according to the CUR 217. The so called analysis of the "sand tightness" of the geotextile for "geometric tight geotextiles" has been developed for sands with $D_{40} > 60 \mu\text{m}$. In principle the recommendation for the filling material of geosynthetic tubes as coastal or riverine protection element is a sand with a maximal fraction of 15% fines [GRI, 1999]. Filling can be done with higher fine content, but this will cause an increased subsequent settlement, complicated filling procedure, etc. Therefore this cannot be generally recommended.

In reference to the CUR document, for current induced loads the permissible opening size can be determined with the following two formulas [CUR 217, 2006]:

$$O_{90} < 5 D_{10} C_u^{1/2} \quad (4)$$

- with
- O_{90} opening size which corresponds to the D_{90} of the soil passing the geotextile [mm]
 - D_x sieve size of the theoretical sieve with rectangular openings where x % of the grains of the sand passes through [mm]
 - C_u coefficient of uniformity [-]

and

$$O_{90} < 2 D_{90} \quad (5)$$

The uniformity coefficient C_u is defined as:

$$C_u < \frac{D_{60}}{D_{10}} \quad (6)$$

In case of wave loads the opening size O_{90} can be derived from following formulas:

$$O_{90} < 1,5 D_{10} C_u^{1/2} \quad (7)$$

and

$$O_{90} < D_{90} \quad (8)$$

2.3 External stability analysis

The external stability analysis of geosynthetic tubes includes failure modes caused by hydraulic forces (waves, currents) and typical geotechnical failure modes such as bearing capacity failures, sliding, etc. An overview of these modes can be found in the article of Chris Lawson [Lawson, 2008]. In this paper the focus is on the stability of geosynthetic tubes with regard to wave forces. Failure mechanisms that are related with the foundation (i.e. consolidation, seepage, and bearing capacity) and current induced loads were not considered in any detail.

2.3.1 Stability under wave loads according to CUR 217

Based on small-scale investigations and theoretical approaches [Pilarczyk, 2000] the following stability criteria for geotextile tubes under wave attack has been developed [CUR 217, 2006]:

$$\frac{H_s}{\Delta_t D_k} \leq 1,0 \quad (9)$$

with H_s significant wave height [m]

Δ_t relative density [-]

D_k characteristic thickness of the geotextile tube [m]

$D_k = h$ (height of the geotextile tube) for wave attack in perpendicular direction of the tube

$D_k = L$ (length of the geotextile tube) for wave attack in longitudinal direction of the tube;
max. $L = 2h$

The advantage of this formulae is it's simplicity. The disadvantage is, that the stability of a single tube is not only depending on the height but also on the width. Therefore some authors [Pilarczyk, 2000] also advise to check the stability with regard to the width of the tube instead of the height or length. Recent insights concerning the stability of geocontainers [van Steeg, 2008] suggest to substitute the characteristic thickness D_k by the product of the width B times the height h . This approach appears reasonable as both parameters are taken into account.

2.3.2 Stability under wave loads according to Deltares

During the large scale physical model tests in the Deltares wave flume the observed failure mechanism of a geosynthetic tube on a rigid foundation was sliding. Hence, a theoretical stability analysis based on the stability of rubble mound slopes against sliding led to the following stability formulae [van Steeg, 2010]:

$$\frac{H}{\Delta \sqrt{BD}} < \frac{\sqrt{\lambda}}{\varphi^2 (C_D + f C_L \lambda)} (f \cos \alpha \pm \sin \alpha) \quad (10)$$

with H wave height [m]

B	(max.) width of tube [m]
D	(max.) height of tube [m]
Δ	relative density [-]
λ	ratio between B and D ($\lambda = B/D$) [-]
φ	wave velocity coefficient (Pilarczyk (2000): $\varphi \sim 1 - 1,5$) [-]
C_D	drag coefficient [-]
C_L	lift coefficient [-]
f	friction coefficient [-]
α	slope angle [°]

This theoretically developed stability approach requires three large scale test derived input parameters (C_D , C_L and φ). Therefore the practical application is difficult. Moreover Recio [Recio, 2008] determined the drag and lift coefficients in wave flume tests for geotextile bags: The results were very wide spread. As a consequence of the Delateres tests the enhancement of the friction between the tube and the foundation is shown to be worthwhile.

3 Practical experience of executed projects

The following two described projects only give a short insight into the application possibilities. Additional information can be found e.g. in [Alexiew, 2008] or [Sobolewski, 2011].

3.1 Port Kuivizu, Baltic Sea, Latvia

This project is located close to another project at the Baltic Sea in Latvia where also geosynthetic tubes had been applied for harbour construction (land reclamation by use of geosynthetic tubes in Port Salacgriva).



Figure 3: Aerial photography of the project sites

In 2007/2008 the mole reconstruction at Port Kuivizu had been executed. The old fishing harbour had been closed almost 15 years. Since then no maintenance had been done to the pier constructions protecting the harbor entrance. Due to waves and ice loads especially the head of the structures had been massively damaged. As the former harbour area was to be re-opened for recreation the damaged piers had to be re-built.

An additional concern was the heavy sheet-piling equipment and the crane for placing the lighthouse which were not able to access the pier heads. A temporary construction road was therefore necessary.

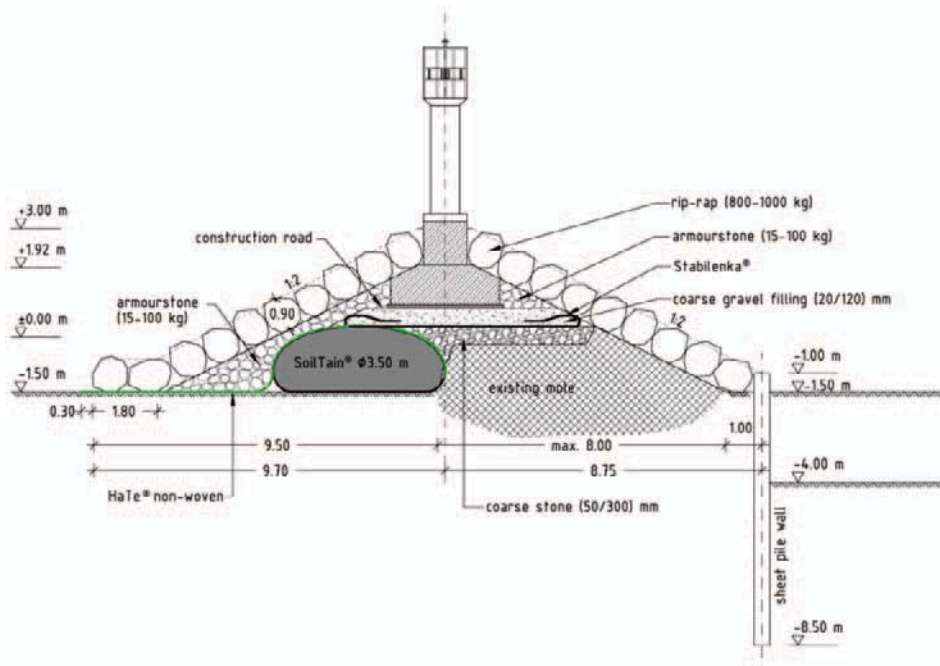


Figure 4: Cross-section of the reconstruction incorporating geosynthetic tubes at Port Kuivizu, Latvia, 2007/2008

The applied solution consisted of geosynthetic tubes, made out of a high strength Polyester woven, with a nominal diameter of 3,5 m and a final height of approximately 2,0 m as an outer bund. The corresponding maximum filling degree based on the height was therefore $f_{max} = 0,57$. The geosynthetic tubes would form a part of the pier core after the end of lighthouse construction. The space between the geosynthetic tube and the damaged pier was filled with stone fill. After installation and filling the tubes were protected with a heavy non-woven geotextile and subsequently covered with armour stone (2-4 t). This construction method offered two important advantages:

1. Directly after filling, the tubes formed a continuous containment bund for the subsequent construction process. The space between the tube and the damaged mole could be filled without any wave impact as the tubes were protecting the area.
2. Due to the geosynthetic tube system a great amount of the otherwise required stone fill could be substituted by locally available sand, locally sourced from the sea bed.

For filling of the tubes a dredger was used. The dredger was directly connected to the geosynthetic tubes by means of a floating flushing pipe system.

3.2 San Vincenzo, Tyrrhenian Sea, Italy

In order to reply to questions remaining unanswered regarding the long-term performance of geosynthetic tubes and the acceptance by the marine flora and fauna a still ongoing research project had been started in 2008 with building a submerged geotextile tube breakwater. The experimental section was constructed in front of the beach of San Vincenzo in preparation for the following definitive work. Scientific support and supervision is provided by the University of Florence. The structure consists of a main tube with a circumference of 9,4 m (nominal diameter of 3,0 m), a scour apron and two anchoring tubes attached to the apron keeping it in place. After filling the tube exhibits a height of 1,6 m. Therefore the corresponding filling ratio based on the height is $f = 0,53$. The cross-section of the breakwater is shown in Figure 5.

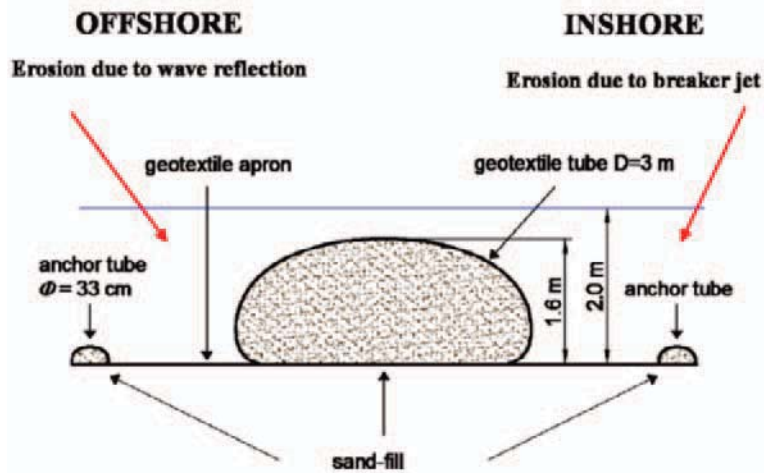


Figure 5: Cross-section of the tube installation in San Vincenzo [Aminti, 2010]

As material for the tube shell a sand coloured high strength Polyester geocomposite was used. For the scour apron different materials were applied (PP non-woven/woven geocomposite, PP woven, PET geocomposite). For comparing the tube performance with and without scour apron, in one section no apron was placed beneath the tube. During installation the negative buoyancy of Polyester made fabrics turned out to be beneficial.

In order to analyse the development of the surrounding area due to the construction of the submerged breakwater bathymetric surveys had been carried out. For documentation of the cross-sectional and longitudinal evolution of the sand filled tubes they had been furnished with a Differential Global Positioning System (DGPS).



Figure 6: Geotextile tube surface 13 months after installation [Mori]

Due to the applied measuring equipment and periodic diving inspections the performance and the colonization process of the submerged geotextile tube breakwater could be documented. The system exhibits a very good overall performance. After filling no subsequent settlement of the tubes could be observed and the structure remained in place. The acceptance by the marine flora and fauna is given [Figure 6].

For further results of the continuing research program see [Aminti, 2010].

4 References

- Alexiew, N. (2008): Temporary bund of geosynthetics and tubes for bridge piers in the river Daugava, Riga, in: Proceedings of the 31th International Conference Coastal Engineering, pp. 3818-3829. ISBN 13-978-981-4277-40-2. Hamburg, Germany.
- Aminti, P.; Mori, E.; Fantini, P. (2010): Submerged barrier for coastal protection application built in tubes with geosynthetics of big diameter in Tuscany - Italy, in: Proceedings of the 9th ICG: International Conference on Geosynthetics, pp. 1235-1240. ISBN 978-85-63456-00-7. Guarujá, Brazil.
- BAW (Bundesanstalt für Wasserbau; Federal Waterways Engineering and Research Institute) (1994): Guidelines for Testing Geotextiles for Navigable Waterways (RPG). Karlsruhe, Germany.
- Bogossian, F.; Smith R.T.; Vertematti, J.C.; Yazbek, O. (1982): Continuous Retaining Dikes by Means of Geotextiles, in: Proceedings of the Second International Conference on Geotextiles, pp. 211 – 216. Las Vegas, Nevada, USA.
- Cantré, S. (2008): Ein Beitrag zur Bemessung geotextiler Schläuche für die Entwässerung von Baggergut. Universität Rostock, Agrar- und Umweltwissenschaftliche Fakultät, Rostock, Germany. (In German). ISBN: 978-3-86009-032-9
- CUR Bouw & Infra, Rijkswaterstaat Bouwdienst en Dienst Weg- en Waterbouwkunde, NGO Nederlandse Geotextilorganisatie (2006). Ontwerpen met Geotextile Zandelementen. CUR-publicatie 217, Stichting CUR, Gouda, The Netherlands. (In Dutch). ISBN 90-3760-083-2
- Geosynthetic Confined Pressurized Slurry (GeoCoPS) Version 3.0, (1999-2007). ADAMA Engineering, Inc., The Horseshoe, Newark, Delaware, USA.
- Geosynthetic Research Institute (GRI), (1999): Installation of Geotextile Tubes used for Coastal or Riverine Structures. GRI Test Method GT 11, Folsom, PA 19033-1208, USA.
- Heibaum, M. (2002): Geosynthetic containers – a new field of application with nearly no limits, in: Proceedings of the 7th ICG: International Conference on Geosynthetics, pp. 1013-1016. ISBN 90-5809-523-1. Nice, France.
- Lawson, C.R. (2008): Geotextile containment for hydraulic and environmental engineering. In: Geosynthetics International, 15, No. 6, pp. 384-427.
- Leshchinsky, D.; Leshchinsky, O.; Ling, H.I.; Gilbert, P.A. (1996): Geosynthetic Tubes for Confining Pressurized Slurry: Some Design Aspects. In: Journal of Geotechnical Engineering, Vol. 122, No. 8, pp. 682-690. ISSN 0733-9410/96/0008-0682-0690
- Pilarczyk, K.W. (2000): Geosynthetics and Geosystems in Hydraulic and Coastal Engineering. A.A. Balkema/Rotterdam/Brookfield, Rotterdam, The Netherlands. ISBN: 90-5809-302-6
- Recio Molina, J. A. (2008): Hydraulic Stability of Geotextile Sand Containers for Coastal Structures – Effect of Deformation and Stability Formulae. Clausthal-Zellerfeld: Papierflieger, Germany. ISBN 978-3-89720-940-3
- Sobolewski, J.; Wilke, M.; Terauds, J. (2011): Geopipes filled with sand in marine and civil engineering. Dimensioning and practical examples. In: Inżynieria Morska i Geotechnika, Vol. 32, No. 1, pp. 34-43. (In Polish). PL ISSN 0867-4299
- Van Steeg, P.; Klein Breteler, M. (2008): Large Scale Physical Model Tests on the Stability of Geocontainer. Test report Deltares, Delft, The Netherlands.
- Van Steeg, P.; Vastenburg, E.W. (2010): Large Scale Physical Model Tests on the Stability of Geotextile Tubes. Test report Deltares, Delft, The Netherlands.

Wave overtopping resistance of grassed slopes in Viet Nam

Le Hai Trung¹, Henk Jan Verhagen² and Jentsje van der Meer³

Abstract

The Simulator was applied to test the resistance against wave overtopping of grass covered dike slopes in Viet Nam. Observation and measurement during destructive tests were performed to investigate the development process of damage induced by overtopping flow. Damages were likely to be initiated at transition of either geometry or materials, at eroded holes and around objects existing on the slope. Grass cover could withstand a certain overtopping rate that varies widely and in order of 10 l/s per m.

Keywords: wave overtopping, grass slope, damage, erosion, transition, grass root.

1 Introduction

Before 2009, the real quality of more than 800 km sea dikes in the north of Viet Nam could be only tested during storm season from May to September every year. It was almost impossible to estimate the resistance against wave overtopping and investigate the damage process of grass covered slope due to difficulties in performing observation or measurement in storm condition. Therefore in the present guidelines value of tolerable overtopping rate cannot be found. A series of destructive tests *in situ* using the Simulator has gradually revealed the potential capacity of the grass covered dike slope to withstand wave overtopping. Applied discharge causing failure of the grass slope was enormously different from section to section but not less than 10 l/s per m. It was specification of material and geometry that governed the failure mechanism of the grass slope.

2 Wave overtopping simulator

Already for many years that phenomenon of wave overtopping on sea dike has been studied on small to large scale physical models in wave flumes and formulae of overtopping volume, discharge and probability were established. However, the erosion and stability of dike crest and landward grass slope under attack of wave overtopping have been investigated intensively recently. The main reason is that these effects cannot be studied in a small wave flume as it is hardly possible to scale down properties of either soil or grass (root). Building up a section of real dike in a large wave flume is time consuming, very costly and grass needs about one or two years to get its mature condition, ready for testing. The Wave Overtopping Simulator was developed to simulate the overtopping waves on dike crest and then on landward dike slope and to study the behaviour of the stability of crest and landward slope in the Netherlands (Van der Meer et al., 2006). In 2008, the second simulator was designed and made for Viet Nam. The maximum volume is 5.5 m³ per 1 m wide (22 m³ for the simulator of 4 m in width). When working, the simulator is continuously filled by pump(s) with a constant discharge and is emptied at desired moments through two butterfly valves at the bottom in a way that simulates the overtopping tongues on dike crest and then on landward slope. The principle of the simulator is presented in van der Meer et al. (2006, 2007 and 2008) or Le et al. (2010).

3 Test set-up

Since 2006, a large number of destructive tests has been performed on different grass covered slopes in the Netherlands, Belgium and very recently in USA including river dikes, sea dikes

¹ Delft University of Technology, Faculty of Civil Engineering and Geosciences, Stevinweg 1, 2628 CN Delft, the Netherlands, H.T.Le@tudelft.nl

² Delft University of Technology, Faculty of Civil Engineering and Geosciences, Stevinweg 1, 2628 CN Delft, the Netherlands, H.J.Verhagen@tudelft.nl

³ Van der Meer Consulting BV, P.O. Box 423, 8440 AK, Heerenveen, the Netherlands, jm@vandermeerconsulting.nl

and artificial dike sections. In two years, 2009 and 2010, seven slope sections were tested with the simulator on three sea dike stretches in the north of Viet Nam.

3.1 Test sections

Destructive tests were performed on slope sections that were selected according to a set of criteria of operation and testing (Le et al., 2010). The pilot test was conducted in Do Son, Hai Phong where dike was reinforced with concrete on three sides: seaward slope, dike crest, upper part of landward slope and berm. The lower part of the landward slope was sandy soil covered with Vetiver grass (*Vetiveria Zizanioides*). Slope section DS_01 with inclination of 1:2 was tested and the Vetiver covered part was 5 m long, next to the dike toe was a water canal, Fig 1.

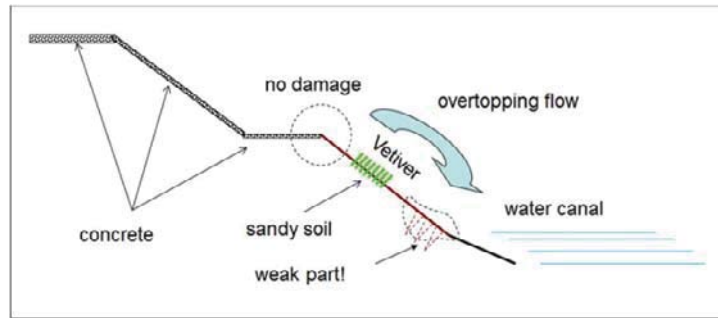


Figure 1: Do Son sea dike in Hai Phong, 2-year-old Vetiver grass on the low landward slope.

In Nam Dinh, Thinh Long sea dike with an inclination of 1:3 was tested and the slope was covered with Bermuda grass (*Cynodon Dactylon*) and sometimes Casuarina trees as well. The dike body was constructed by a sand core and a layer of clay with moderate quality, see Fig 2. The thickness of the clay layer was found to vary from 80 to 100 cm at 3 sections. On horizontal dike toe, it was Ray grass (*Hemarthria compressa*) that covered evenly toward a brackish water canal. Section TL_01: grass covered slope of 10 m long, relatively regular slope, no hole was found. TL_02: irregular slope, poorly covered with three different grass species (mainly Bermuda), 5 eroded holes and 7 Casuarina trees (amongst those, one with a trunk of 7 cm) were recognised. TL_03: relatively regular, covered with Bermuda grass and Crabgrass (*Eleusine indica*), 5 small Casuarina trees with diameter of 1 cm.

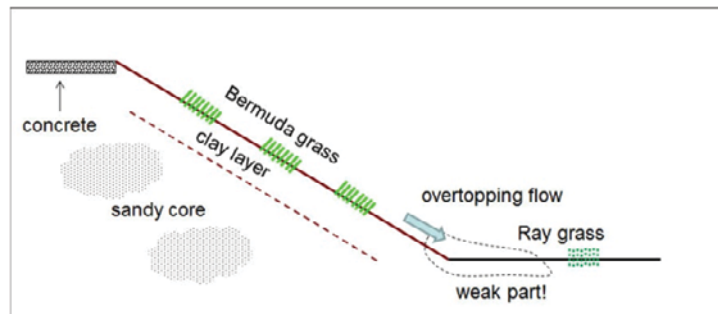


Figure 2: Thinh Long sea dike in Nam Dinh, 4-year-old Bermuda grass slope.

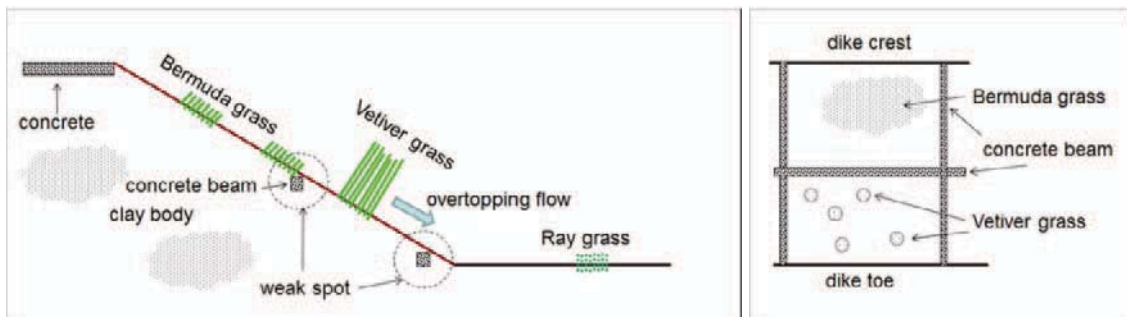


Figure 3: Thai Thuy sea dike in Thai Binh, a mixture of Bermuda and Vetiver grass on clay slope.

Within 50 m of the Thai Thuy dike stretch, 3 sections were tested. The slope inclination was 1:3. The dike body was constructed by good clay, a mixture of Vetiver and Bermuda grass was planted within concrete frames, see Fig 3. The horizontal berm was protected with a dense sward of Ray grass. Vetiver and Bermuda grass covered evenly section TT_01 and horizontal concrete beam was at the middle of the slope. TT_02: number of Vetiver clumps was few while Bermuda grass was dominant however with low density, concrete beams divided the slope section into 4 parts. TT_03: concrete beams divided the section into 4 parts, in which one was mainly covered with Vetiver while at the others both Vetiver and Bermuda grass could be found.

Local grass species like Bermuda grass, Crabgrass and Ray grass grow to knit a mat covering soil surface while Vetiver grass always grows in separate clumps, soil surface amongst these clumps are often bare or covered by mat grass.

3.2 Grass root quality

The resistance against erosion induced by wave overtopping of a grass covered slope is solely determined by the quality of grass turf. According to the Dutch guidelines for safety assessments of dikes (VTV 2006), quality of a grass cover can be estimated by the amount of roots in depth. 8 samples of 4 different grass species taken on Thai Thuy dike were analysed to derive the number of roots. In general, the quality of the tested grass slopes were far beyond “good” criterion of VTV, Fig 4. It should be noted that the growing condition of grass in Viet Nam and the Netherlands are obviously different and grass species are themselves different.

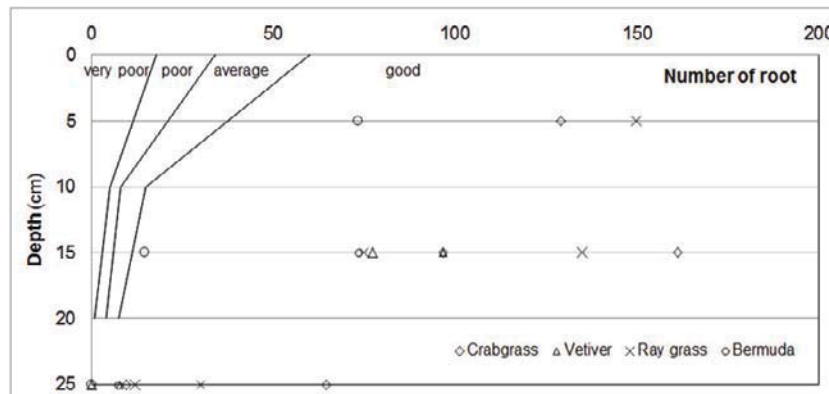


Figure 4: Classification of grass according to the Dutch guidelines VTV 2006.

3.3 Test set-up

The Simulator was always placed on dike crest that released water could flow over a short distance on the crest and then the grass covered slope. Two water pumps, capacity of 22 and 55 kW respectively, supplied a input discharge of more than 1000 m³/h to the Simulator. A 250 kVA diesel generator was applied to run all machines including the Simulator, water pumps, oil pump and other equipments on site. The two butterfly valves were operated manually according to control tables that were computed beforehand and dependent on the real input discharge and tested overtopping rate.

As wide as the out-put gate of the Simulator, each tested slope section was 4 m wide. On both sides of the section, a 50-cm-wall was erected to guide the water released from the Simulator. During destructive tests, grass slopes were captured with a digital camera in order to examine the development of damages induced by overtopping flows. Besides, dike slope profiles were also measured from crest to toe with a density of 1 point/ (0.5 – 1.0)m in either flow direction or transversely. In all tests, natural brackish or salt water was used.

The erosional resistance of grass covered slopes were tested with mean overtopping rate increasing from small to large: 10; 20; 40; 70; 80; 100 and 120 l/s per m. Each rate represented a real storm that was simulated (generated) by the Simulator lasting for 4 hours, a typical duration of storm attacking the north of Viet Nam. Each test condition is a distribution of overtopping volumes (see EurOtop, 2007) that is dependent on seaside wave boundary such as a wave height, wave period and a water depth. A significant wave height of 1.5 m and a peak

period of 6 s were applied to compute control tables in all tests. At some test sections, hydraulic measurements were carried out in order to determine the flow parameters on grass slope including flow depth, flow front velocity and flow duration.

4 Damages on grass slopes

Damage on a grass covered slope is defined as one or some aggregate(s) of soil including sward and root is (are) torn out of the slope surface and then moved away by overtopping flow. In other words, damage is initiated when at any point the grass cover is eroded, even within small area of some cm². Damage on a grass covered slope can be described by a limit state function of strength and load as follows:

$$Z = \text{Strength} - \text{Load} \quad (1)$$

In which, *Strength* is determined by the quality of grass cover that dependent on the combination of soil structure and root system. *Load* is mainly the effect of overtopping flow. Small overtopping discharge giving small overtopping volumes seemed to have little or no erosional effect (e.g. van der Meer et al., 2010 and Steendam et al., 2010). Depending on the specification of grass slope, there would be a certain rate of wave overtopping producing volumes that sufficiently energetic to initiate damage on the slope and later on enlarge it.

Damages were likely to be initiated at transition of either geometry or material. On slope, soil (bare or covered by mat grass, e.g. Bermuda grass) amongst Vetiver clumps was vulnerable spot which was often eroded first. Besides, damage could be also initiated around object like a big Casuarina tree and at an eroded hole existing on the slope. At dike toe, transition between steep part and horizontal part (berm in case of Thai Thuy) damage was found to take place as well but with relatively small probability. In general, at these position of transition or existing object, *Strength* was eliminated due to the discontinuity of grass cover. It was this discontinuity that caused flow blockage or/ and flow concentration, *Load* was hence enhanced.

4.1 Geometry transition

Section TL_01, slope surface was regular and covered with Bermuda grass, horizontal toe was covered with Ray grass. Around the transition between these two parts, grass cover was rather poor that clay was exposed directly to overtopping flow. Besides, at the transition acting force seemed larger than on the slope due to the rough guidance of overtopping flow, see left panel of Fig 5. Damages were therefore caused to take place at the dike toe, a geometry transition, right panel of Fig 5.



Figure 5: Rough guidance of overtopping flow (left) and damages (right) at dike toe, TL_01.

Section DS_01, bare soil was first eroded and subsequently Vetiver clumps were swept away at the transition between the low part of the slope and the canal bank as can be seen in Fig 6 right panel. It could be explained by the water flow with high energy flying into the air from the end of the concrete berm to attack the dike toe more or less vertically, Fig 6 left panel. Interestingly, the first row of Vetiver clumps next to the concrete berm was first hit by overtopping flow however these clumps remained intact till the end of the test, they were only forced to lie down.

Due to the long and straight root system, when Vetiver clumps were eroded and swept away hole with very steep wall was formed. The eroded hole was enlarged in upward direction under attack of overtopping flow. This is similar to the head-cut mechanism that is the last stage of an erosion process described by Valk (2009) consisting of: initial situation, scour hole due to surface erosion, transition and head-cut erosion. Scour hole due to surface erosion can be compared to the formation of trenches amongst separate Vetiver clumps and transition of surface erosion to head-cut erosion is like when these trenches get sufficient depth to split Vetiver clumps from the slope.



Figure 6: Overtopping flow flying from the berm attacks the dike toe.

Fig 7 left panel gives an impression of a damage at dike toe that expose the horizontal concrete beam, section TT_03. When the top layer of grass sod (about 10 cm) was eroded, a thin layer of mortar was found, Fig 7 right panel. The mortar layer prevented grass roots from penetrating deeply dike body underneath. As a result, the connection either between the top soil layer and the mortar layer or between the mortar layer and the soil body were weak. Therefore, either the top grass sod or the mortar layer were easily eroded to expose the underneath body of soil. The damage at geometry transition was facilitated by the transition of material.



Figure 7: Left: concrete beam was exposed. Right: mortar layer under a top grass sod.

Assuming parallel seepage condition, full saturation of fissured cover layer and soil cohesion is not taken into account, Young (2005) argued that a grass turf may slide at the turf base to create a large erosion on the slope surface. This turf sliding is partly comparable to the shallow slip of the grass turf lying on the mortar layer observed at section TT_03, the mechanism however is different. At two test sections at Boonweg, Friesland in the Netherlands, it was observed that spots of grass cover (0.5 and 1.0 m²) were lifted up 0.1 to 0.2 m and then washed away by large waves (Steendam et al., 2008). Location of these spots were below potential weak spots existing on the grass slope.

4.2 Material transition

On a slope that covered by a mixture of mat grass (e.g. Bermuda) and Vetiver grass in Thai Thuy, the development of these species were not proportional. It was observed that in April 2010, Bermuda grass was evenly covering the dike slope while Vetiver grass was short and

sparse. Bermuda grass predominantly protected the dike slope. More Vetiver clumps were planted on the riverside slope in May 2010, beginning of the rainy season and about 6 months before testing. In November, when destructive tests were carried out, Vetiver clumps were growing well and about 1 m high. As can be seen in Fig 8, left panel, Vetiver sward was cut off to expose the thin cover of Bermuda grass. It was Vetiver grass that overwhelmed the mat grass. Due to the high shape of Vetiver clumps, flow tended to concentrate amongst close clumps, as a result, trenches were formed. The more soil was eroded the deeper the trenches became. Sufficiently deep trenches split Vetiver clumps from the slope, the slope was therefore damaged. As described above, at section DS_01 damages were also first initiated amongst separate Vetiver clumps where soil directly exposed to overtopping flow. The existence of more than one species of grass caused discontinuity of the dike slope, weak spots were often found at these transitions of different grass species.



Figure 8: Left: damages amongst Vetiver clumps. Right: poor cover of Bermuda grass and settlement of soil around concrete beams,

Transition between grassed soil and concrete beam could be potential vulnerable spot where grass cover was often poor and soil surface was settled down, Fig 8 right panel. Poor cover of grass might be due to a low root density in top soil layer and uneven surface around the beam would introduce flow concentration. Combination of these two features caused higher chance of erosion around the concrete frames as illustrated in Fig 9 left panel.

Another example of using different materials on a grass covered slope was demonstrated at the Vecht dike, the Netherlands, where concrete blocks (40 x 40 x 12 cm) allowing grass to grow through were applied on the riverside berm. A deep track was presented above the berm to result in an initial damage at overtopping rate of 1 l/s per m. Blocks were moved away from original position at 50 l/s per m, see more Steendam et al. (2010).

4.3 Objects and existing damages

Casuarina trees and eroded holes that existing on a grass slope presented interruption to the continuity of the grass sod. These positions became weaker and more vulnerable under attack of overtopping flow. Therefore, damages were likely to be initiated around the Casuarina trees and at the existing eroded holes.

At section TL_02, damage was first started from an existing hole. Later on, it was rapidly extended to reach the Casuarina tree. Overtopping flow eroded and carried away soil aggregates hold by the root system that the connection between the Casuarina tree and the dike slope became increasingly weak. The anchoring forces were reduced smaller and no longer sufficient to retain the tree anymore, the Casuarina fell down. Due to the large trunk of about 7 cm wide, the Casuarina tree also caused flow blockage, force intensity was hence increased. Situation of the Casuarina tree before its collapse is shown in Fig 9, right panel.

Steendam et al. (2010) described a test at Vecht dike, in which there was a tree (trunk of 0.8 m wide) on the berm. Grass cover around the tree was already eroded under a discharge of 5 l/s per m, damage developed rapidly resulting a slope failure after about 5 hours of 50 l/s per m. Another similar example is a section at Afsluitdijk, where erosion easily started at both sides of a staircase on the grass covered slope with a discharge of 10 l/s per m.



Figure 9: Left: damage around concrete frames. Right: damage extension to the Casuarina tree.

4.4 Distribution of damages

Damage could be generated at weak spots due to the discontinuity of grass cover and flow concentration. The initial damage was likely to determine the final situation of the dike slope after testing with the Simulator. In Do Son, damage was first initiated at the transition between the dike slope and the canal bank and then extended upward. In Think Long and Thai Thuy, damages were always generated on the dike slopes, there was only one case in which erosion took place at the dike toe at the end of the test. It meant that if damage was initiated on the steep part, the toe would be hardly eroded later on, probability of 1/6. There were 2 tests (TT_02 and TT_03) where damages were found at the transition between steep part and horizontal berm, probability of 2/6. It is solely specification of the grass cover that determines position of the initial damage on the tested dike slope. The damage that is caused by the overtopping flow influences the hydraulic behaviour of the flow. The development process of damage is governed by the overtopping flow and the quality of the grass turf.

5 Maximum wave overtopping discharge on grass slopes

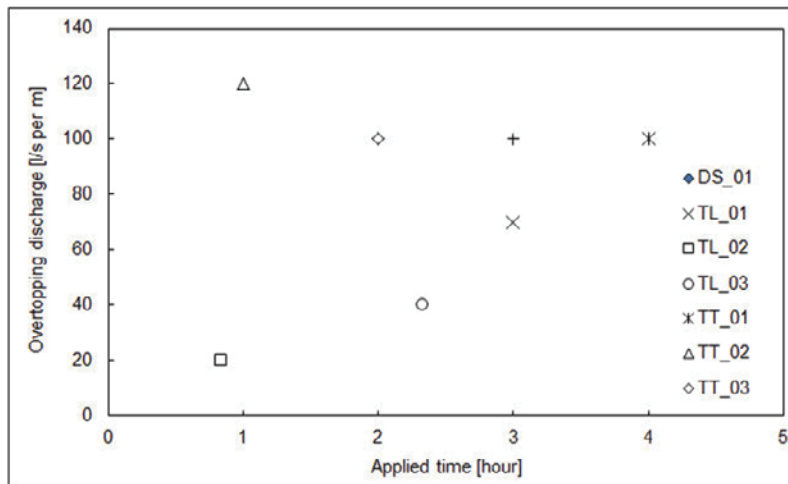


Figure 10: Maximum overtopping rate vs. applied time at 7 tested sections in Viet Nam.

A small number of destructive tests performed in Do Son, Think Long and Thai Thuy has given an impression of the resistance of different grass covered slopes against wave overtopping. At section DS_01, the low slope covered with 2-year-old Vetiver grass was severely damaged after 3 hours of 100 l/s per m. Test replications on a short dike stretch in Think Long, about 50 m long, revealed that strength of grass slope could vary considerably. At TL_01, the maximum applied discharge was up to 70 l/s per m lasting for 3 hours. TL_02 could withstand an overtopping rate of 20 l/s per m. Slope section TL_03 failed after more than 2 hours applying 40 l/s per m. Three tests performed within a 50 m dike stretch in Thai Thuy showed that the maximum applied discharge was likely to be consistent and not less than 100 l/s per m.

If the effect of smaller discharges that were applied before the maximum rate is not taken into account, the maximum rate and its applied time (time to failure) at each tested section are plotted in Fig 10. It can be seen that overtopping resistance of grass slope varies enormously from 20 to even more than 100 l/s per m. This high variability is due to the difference in geometry and soil/ grass characteristics of the tested sections and the length effect.

6 On-going research

By testing with the Simulator, the resistance against wave overtopping of several grass covered slopes were determined quantitatively. The formation and development of damages induced by wave overtopping flow were studied. Interacting relation between overtopping flow (*Load*) and resistance of grass cover (*Strength*) are under investigation.

7 Acknowledgements

The project “Technical Assistance for Sea Dike Research” financed by the Government of the Netherlands is acknowledged for funding to build the Wave Overtopping Simulator and to perform all the destructive tests in Viet Nam. Tests were performed by the Faculty of Marine and Coastal Engineering, Water Resources University, Ha Noi, Viet Nam.

8 References

- EurOtop, 2007. Wave Overtopping of Sea Defences and Related Structures: Assessment Manual. EA Environment Agency, UK; ENW Expertise Netwerk Waterkeren, NL; KFKI Karatorium für Forschung im Küsteningenieurwesen, DE.
- Le, H.T., van der Meer, J.W., Schiereck, G.J., Vu, M.C., van der Meer, G., 2010. Wave Overtopping Simulator tests in Viet Nam. ASCE, proc. ICCE 2010, Shanghai, China.
- Steendam, G.J., de Vries, W., van der Meer, J.W., van Hoven, A., de Raat, G., Frissel, J.Y., 2008. Influence of management and maintenance on erosive impact of wave overtopping on grass covered slopes of dikes; Tests. Proc. FloodRisk, Oxford, UK.
- Steendam, G.J., van der Meer, J.W., Hardeman, B. and van Hoven, A., 2010. Destructive wave overtopping tests on grass covered landward slopes of dikes and transitions to berms. ASCE, proc. ICCE 2010, Shanghai, China.
- Valk, A., 2009. Wave overtopping – Impact of water jets on grassed inner slope transitions. Master thesis, Delft University of Technology, Delft, the Netherlands.
- Van der Meer, J.W., Bernardini, P., Snijders, W. and Regeling, E., 2006. The Wave Overtopping Simulator. ASCE, proc. ICCE 2006, San Diego, US.
- Van der Meer, J.W., Bernardini, P., Steendam, G.J., Akkerman, G.J. and Hoffmans, G.J.C.M., 2007. The wave overtopping simulator in action. Proc. Coastal Structures, Venice, Italy.
- Van der Meer, J.W., Steendam, G.J., de Raat, G. and Bernardini, P., 2008. Further developments of the wave overtopping simulator. ASCE, proc. ICCE 2008, Hamburg, Germany.
- Van der Meer, J.W., Schrijver, R., Hardeman, B., van Hoven, A., Verheij, H. and Steendam, G.J., 2009. Guidance on erosion resistance of inner slopes of dikes from three years of testing with the Wave Overtopping Simulator. Proc. ICE, Coasts, Marine Structures and Breakwaters, Edinburgh, UK.
- VTV, 2006. Voorschrift Toetsen of Veiligheid Primaire Waterkeringen (in Dutch). Ministry of Transport, Public Works and Water Management. ISBN 978-90-369-5762-5.
- Young, M.J., 2005. Wave overtopping and grass cover layer failure on the inner slope of dikes. Master thesis, UNESCO – IHE Institute for Water Education, Delft, the Netherlands.

Technical Session 6: Modeling, Management

Chairman: Prof. Holger Schüttrumpf

Methods to detect change points in water level time series – Application to the German Bight

Sönke Dangendorf¹ and Jürgen Jensen¹

Abstract

Water level time series represent an important parameter for the assessment of coastal structures. The homogeneity of water level time series is of particular importance as only small inhomogeneities may impact the statistical analysis of the data. In this study a method for the detection of change points is evaluated. The adaptability is tested using a data set of 10.000 synthetic time series generated by Monte-Carlo-Simulations. Furthermore, the method is applied on observed sea level data of a tide gauge (Büsum) located in the German Bight. The results of this study show that anthropogenic interventions as building measures have significant influences on water level time series and can be reliably detected as change points in the water level observations.

Keywords: change points, Monte-Carlo-Simulations, inhomogeneities, coastal structures, building measures

1 Introduction

Water level time series are important for the assessment of coastal protection measures. They represent long term changes as a main loading factor for the dimensioning of buildings. For the issues of coastal engineering a large number of homogeneous water level time series is indispensable for the adequate selection of design parameters of coastal protection measures. Because of the extension of coastal areas and estuaries the homogeneity of time series is not always given. As shown in Mügge and Jensen (1991) local anthropogenic influences may impact or corrupt the statistical analysis of the data. To avoid inaccuracies when estimating design parameters it is important to detect and eliminate inhomogeneities.

Generally, discontinuities in time series result from different possible reasons. Abrupt change points can be caused by local short term vertical land movements at the gauge or building measures. Long term changes depend on long term vertical land movements of the coastline, morphological processes or climatic changes (Wahl et al. 2011). As shown in figure 1 the estimation of linear trends in time series is only feasible if the target series is homogeneous in time. If there is a change point the estimation of trend will be strongly affected. For this reason it is impossible to differentiate between local anthropogenic and large-scale natural changes of water level.

However, for the assessment of coastal protection measures undocumented anthropogenic change points may falsify the collection of data and finally affect the estimation of statistical parameters. This leads to misinterpretations of past developments and consequently in falsely dimensioned coastal structures. While oversizing indicates great monetary expenses, too small coastal structures may result in higher vulnerability of the hinterland.

In this study one of several detection techniques for abrupt changes is evaluated. Several methods have been established by different authors for detecting change points in climatic time series. Because of the high level of variance and natural variability in water level time series in the German Bight it is not possible to assign these methods without extensive analysis. Hence, the adaptability of the methods has been tested with Monte-Carlo-Simulations (MCS). For the consideration of different potential developments in water level time series different synthetic time series models have been built.

¹ Research Institute for Water and Environment, Department of Hydraulic Engineering, University of Siegen, Paul-Bonatz-Str. 9-11, 57076 Siegen, Germany, soenke.dangendorf@uni-siegen.de

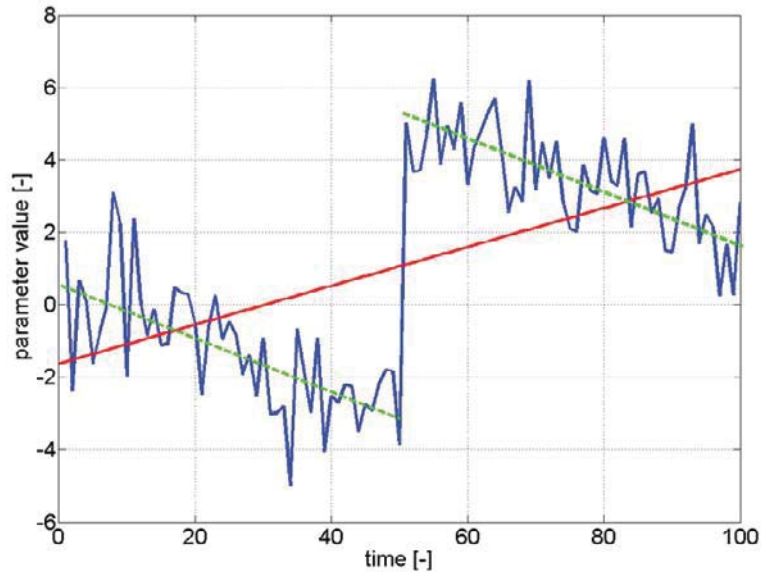


Figure 1: Consequences of anthropogenic induced change points for the estimation of linear trends

This paper is structured as follows. In Section 3 the used data and methods are described. The results are outlined and discussed in Section 4. An application for the German Bight is given in Section 5, while Section 6 includes the final conclusions.

2 Data and Methods

2.1 Data

This study contains investigations about the practical application of mathematical change point techniques to tidal water level time series in the German Bight. Because of this a representative group of tide gauges along the German North Sea coastline has been tested with respect to their statistical behaviour. Distributions and statistical parameters have been estimated by water level time series of annual resolution, recorded in the last 166 years. Figure 2 shows the investigation area with all selected tide gauges.

The adaptability of the method is tested with more than 50.000 synthetic water level time series. For the generation of synthetic water level time series MCS have been accomplished. In-depth information about the adaptability of MCS is given in von Storch and Zwiers (1999). With MCS it was possible to generate normally distributed water level time series with a sample size of $n = 100$ values. These time series have been combined with defined trends and change points (different sizes: 0.25σ , 0.5σ , 0.75σ , 1σ , 2σ) at selected positions to produce time series with statistical properties similar to those are observed in the annual mean water levels. In this way, two sets of data were generated. The first data set (Model a) indicates time series with a change point of varying sizes at selected positions of the sample. The change point splits the time series in two homogenous parts with different means. In the second group of time series (Model b) the second part of the time series after the change point is superimposed with an increasing trend. Hence, the second part of the time series is non-stationary. Both data sets – Model a and b – finally consists of 10.000 random samples per step size and selected position. Every single synthetic time series has been analysed. If a change point could be detected exactly, it was noted as a hit, if not, it was ignored. After the analysis of all synthetic time series at a single position, the number of hits has been computed and noted as a hit rate per 10.000 simulations:

$$\text{hit rate} = \frac{\text{sum of hits}}{\text{sum of simulations}} \quad [-] \quad (1)$$

As mentioned above, the variability of water level time series in the German Bight is very distinct. For the detection of change points this variability is problematic, as it leads to

chronological shifted detections. Hence, it was decided to define an interval of correct detection, the so called "hit rate window". This interval comprises ± 2 points around the real change point position. A single change point has been detected exactly, if it has been found in this interval.

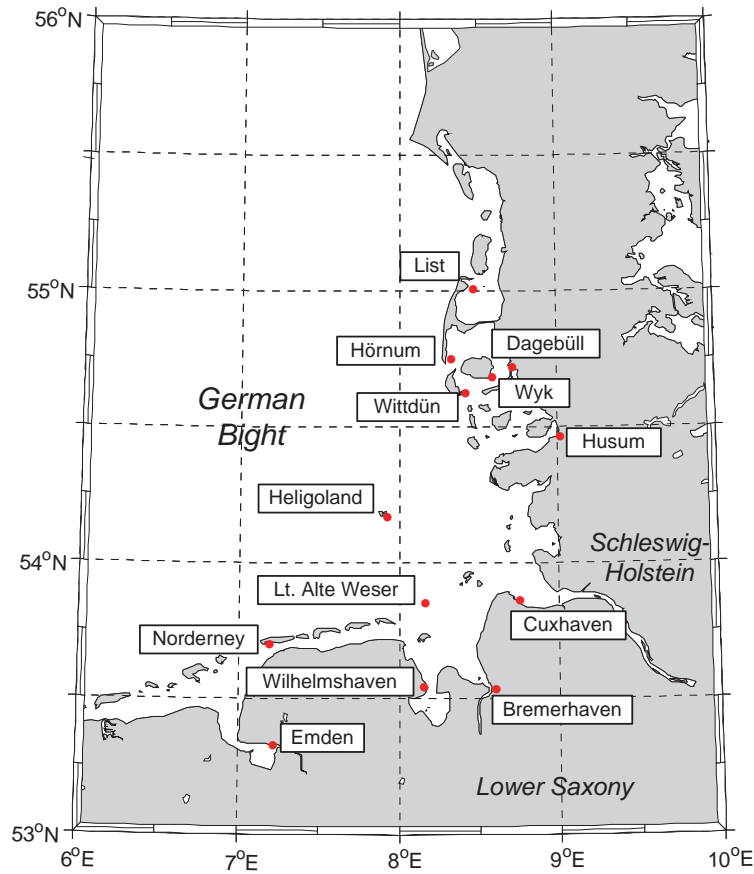


Figure 2: Investigation area with the location of different gauges in the German Bight, especially with the analyzed tide gauge of Büsum, located in the Meldorf Bight, Schleswig-Holstein

2.2 Methods

This study just includes one of several techniques, the Standard Normal Homogeneity Test (SNHT). For more approaches see Dangendorf (2010). Most of the existing change point techniques base on the comparison of mean or variance values of two different samples. The SNHT has been established first by Alexandersson (1986) for climatic time series. The test applies to a series of N elements with zero mean and unit variance. As the name suggests, it is a hypothesis test dealing with two cases:

$$H_0: Z \in N(0,1) \quad (2)$$

$$H_1: \begin{cases} \text{for some } 1 \leq t < n \text{ and } \mu_1 \neq \mu_2 \text{ we have} \\ Z \in N(\mu_1, 1), & \text{for } i \leq t \\ Z \in N(\mu_2, 1) & \text{for } i > t \end{cases} \quad (3)$$

In this equation Z is a standard normal distributed variable with a unit standard deviation of 1 and different means before and after the change point. To test the time series for a single shift, a simple ratio has been applied:

$$T_0 = \max_{1 \leq t < N} \{T_t\} = \max_{1 \leq t < N} \{t\bar{z}_1^2 + (n-t)\bar{z}_2^2\} \quad (4)$$

\bar{z}_1 and \bar{z}_2 are the arithmetic means of the two partial time series before and after the change point. A change point can be detected if T_1 gets maximal and overtops a defined critical limit. These limits can be taken from various literatures (Alexandersson 1986, Alexandersson and Moberg 1997, etc.) with respect to different significance levels.

3 Results

As described in Section 3.1 the adaptability of the SNHT has to be tested before applying the procedure on water level time series. In the following chapter the results for the two Models a and b are given.

3.1 Model a

In Model a 10.000 synthetic water level time series are combined with change points of varying sizes at selected positions. The two parts before and after the artificial change point are stationary in time. That means that the mean values before and after the change point does not underlie anymore gradual changes like trends. The results for this model are visualized in the left part of figure 3. All figures of hit rates just include the results for the first half of the analyzed samples because the hit rate distribution of the halves is symmetrically formed. The differently colored lines indicate linear linked hit rates of varying step sizes at different positions. It can be stated that the SNHT is able to detect change points larger or equal as 1σ very well. Unaffected of the position over 94% of all change points can be detected exactly. With diminishing step sizes the hit rates are getting smaller. Thus for steps in the order of 0.5σ the hit rate is dropping to approx. 25%. The smaller the step size is (compared to the variance of the analyzed sample), the lower the chance for a correct detection. In terms of the water level time series in the German Bight it can be interpreted that approx. 60% of all change points with a step size of 6-7 cm can be detected exactly.

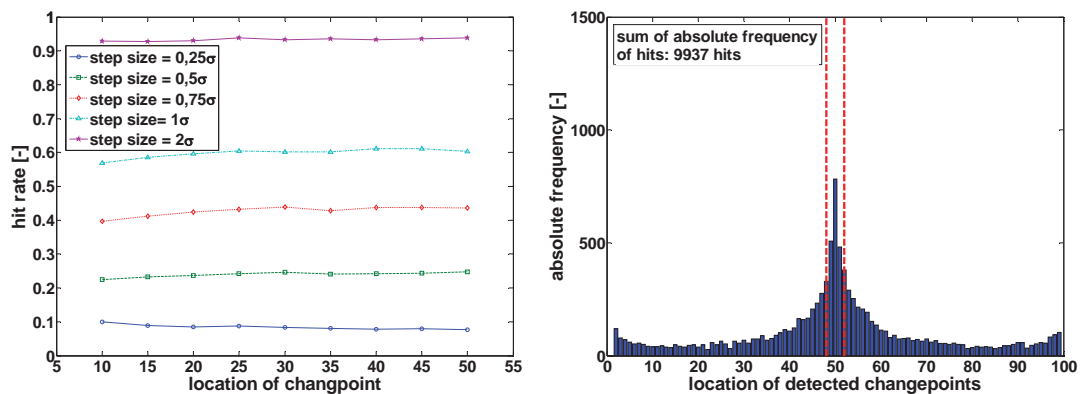


Figure 3: Hit rates for steps of varying sizes and positions in synthetic water level time series of model a (left side). Sum of absolute frequency of hits in model a for a step size of 0.5σ (right side)

As described above the exactly detection of change points is defined with a hit rate window of ± 2 points around the real position. Accordingly, potentially detected change points outside of this window are not noted as a hit. Hence, a final decision about detected change point outside of the hit rate window cannot be made. In order to get information about statistically significant detected change points, the right side of figure 3 provides an overview about the sum of absolute frequency of hits over the whole samples (exemplary for a step size of 0.5σ). The absolute frequencies at single positions are figured as blue bars. The red dotted vertical lines indicate the hit rate window. It can be noted, that in more than 99% of all analyzed samples a change point with a step size of 0.5σ could be detected. The positions of the detected change points are distributed over the whole sample. Only 24% of all detected change points have been found in the defined hit rate window. An enlargement of the hit rate window would cause a higher hit rate. If the step size increases compared to the variance of the analyzed sample, the SNHT is getting problems with the correct chronological classification of a change point. Water level time series are characterised by extreme events like extreme low or high water levels.

These extreme events may mask the real point of change. If a positive (negative) change point comes along with natural extreme low (high) values, the change point is not visible in the original time series as long as the water levels return to a normal level, as the extreme event and the step may mutually neutralise themselves.

3.2 Model b

In contrast to model a in model b the second segment after the change point is non-stationary in time because of a superimposed trend. This trend causes a gradual change in the mean of the second half of the time series. Figure 4 comprises the hit rates (left) and the absolute frequency of hits (right) for the model b. The hit rates are considerably lower as in model a. Thus the hit rates for step sizes of 2σ are reduced by approx. 30% for change points in the middle of the sample. While in model a the hit rates for this position are about approx. 94%, in model b they just cover 62%. Furthermore the hit rates decrease significantly to the sample boundaries for all step sizes. Consequently no change points can be detected at positions 1-10 of the samples. The nearer the change point approaches to the sample boundaries, the more complicated the exactly detection is. These small hit rates are mainly caused by the non-stationary behaviour of the second segment of the time series. As it has already been mentioned, gradual changes as trends cause changes in the mean of a sample. The SNHT is not able to differentiate between steps and trends. Hence, the gradual change in the second segment delays the temporal placement of the change points. This connection is also identified in the absolute frequency of hits. For a change point (step size 0.5σ), located in the middle of the sample, just approx. 5% of all steps can be exactly detected in the hit rate window. In this context it is noticeable that all change points can be detected referring to the whole sample and regardless of the hit rate window. Hence, approx. 95% of all change points have been detected outside of the hit rate window in an interval between position 53 and 87. The sensitivity of the SNHT strongly depends on the ratio between step size and intensity of trend. A higher step size (compared to the intensity of trend) improves the rate of exactly detected change points.

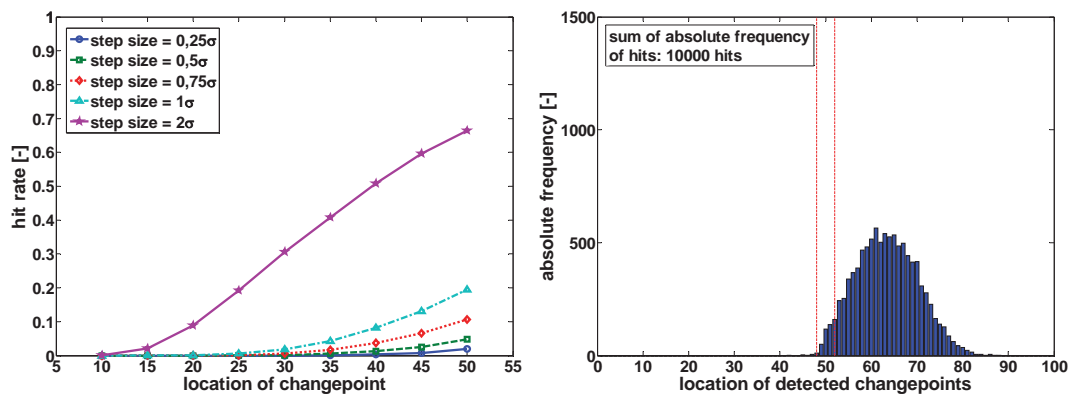


Figure 4: Hit rates for steps of varying sizes and positions in synthetic water level time series of model b (left side). Sum of absolute frequency of hits in model b for a step size of 0.5σ (right side)

It cannot be exactly pointed out here at which ratio of steps and trends a reliable detection of the change points is feasible, but the expected behaviour can be suspected by the absolute frequency of hits. By inserting the change point at different locations, it appears that the influence of the trends is increasing for changes to the sample boundaries. The intensity of the trend in the second segment has not been changing, but the sample size of the second segment after the change point increases with change points near the beginning of the time series. This is illustrated in figure 5. Considering a change in the middle of the sample (position 50), the step changes the mean around 1 unit, while the trend in the second segment changes the mean around 3 units. Moving the change point to position 10 of the sample, the influence of the trend on changes in the mean of the sample increases on 5.4:1. This example clarifies the impacts of trends on the detection of change points in non-stationary water level time series.

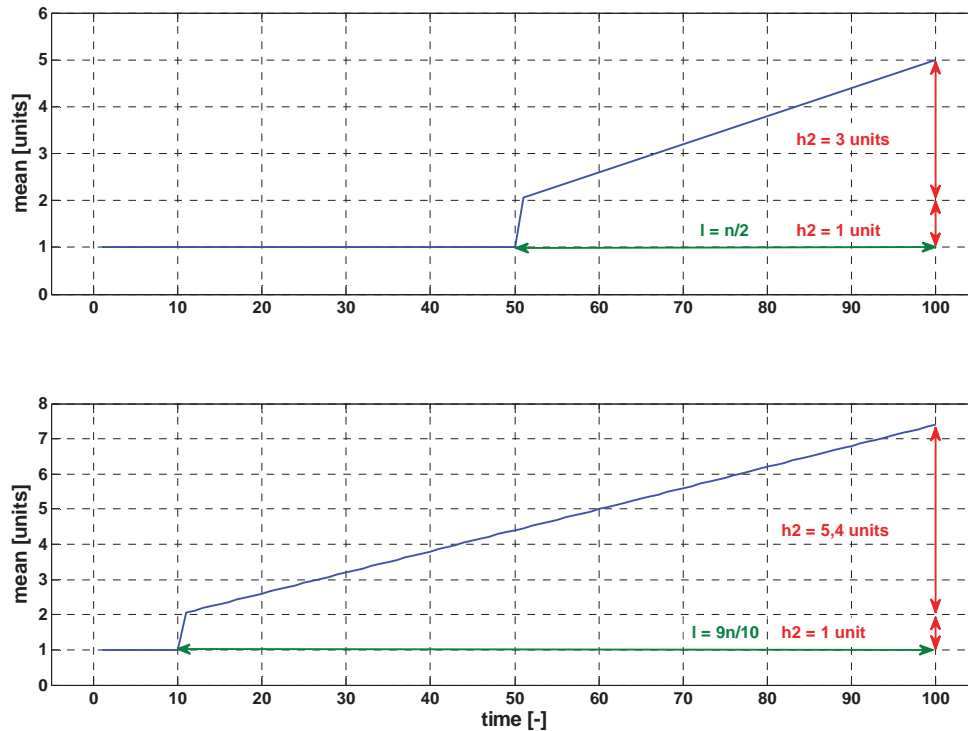


Figure 5: Comparative analysis of influence of steps and trends on changes in the mean. While the step size and trend intensity is constant, the size of the two segments before and after the change point is changing.

4 Application to the German Bight

After testing the principle behaviour of the SNHT the test has been applied to a data set of original water levels, recorded at the gauge of Büsum. Büsum is located on the outskirts of the Meldorf Bight at the north-eastern coastline of Schleswig Holstein (figure 2). Since the late 70's the tendency in the mean low water levels (MLW) differs significantly to those which has been observed at the neighbouring stations. Mügge and Jensen (1991) found, that this change has been caused by a big building measure in the Meldorf Bight. After the disastrous floods in the Netherlands (1953) and Germany (1962) the coastal protection has been basically changed. In this case the dike line along the Schleswig-Holstein coast has been shortened considerably. The coastal protection measure in the Meldorf Bight caused massive changes in the morphology and the tidal regime that has been observed especially in the MLW (Wieland, 1984 and Mügge and Jensen 1991).

Based on the findings gained in Mügge and Jensen (1991) the SNHT has been applied on the MLW for the period between 1937 and 2007. As mentioned in section 4 the SNHT has problems with the distinction between steps and trends. Furthermore, in section 2 has been outlined that changes in water level time series may not only be caused by anthropogenic influences, but rather as a result of climatic changes. In most cases climatic changes happens as large-scale changes including larger areas. Hence, climatic changes have to be detected at stations over a larger area. Anthropogenic changes as short-term vertical land movements may happen in a small area around a gauge. Thus, homogeneous reference series from neighbouring stations are useful to detect those changes (Aguilar et al. 2003) as climatic changes have to be detected in both series. In this study the record observed at the gauge of Cuxhaven is used as a reference series. Cuxhaven is the longest record in the German Bight with low and high water levels observed from 1843 until today. Many studies have been accomplished on the basis of this data (Jensen 1985, Jensen and Mudersbach 2007, Dangendorf et al. 2011, Mudersbach et al. 2011, Wahl et al. 2010, 2011). Cuxhaven gauge is located at the end of the Elbe estuary in Lower Saxony. The linear distance between the two gauges is about approx. 40km. It can be assumed that this distance is large enough in order to make sure that there is no influence of

the building measure in Cuxhaven. To separate the anthropogenic changes from changes due to climatic causes a new series D has been built from the differences between the reference Z_1 and candidate Z_2 series. This procedure is shown in figure 6. The two blue lines indicate the two original records observed at the stations. They show a similar development with slightly deviating tendencies at the end of the 70's. By computing the differences between both series, plotted in the middle of the figure, the different development is getting much clearer. The variance of the observed MLW and trends are reduced considerably and the change point becomes visible. At the bottom of the figure the result of the SNHT is presented. The red line represents the SNHT-ratio, detecting the change point in the year 1978 where the maximum of the ratio occurs. This maximum is statistically significant on the 99%-significance level and similar to the findings of Mügge and Jensen (1992). Hence, the example of Büsum clarifies that building measures have significant influences on water level time series and can be reliably detected as change points in the water level observations.

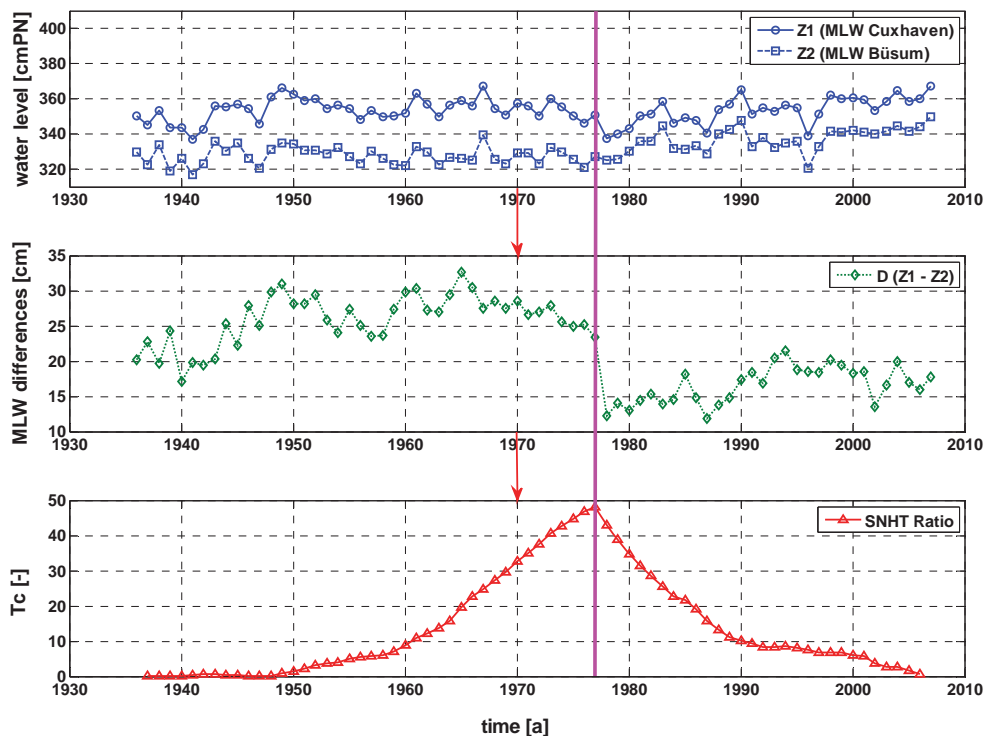


Figure 6: Comparative analysis of influence of steps and trends on changes in the mean. While the step size and trend intensity is constant, the size of the two segments before and after the change point is changing.

5 Summary and Conclusions

In the present study, the applicability of the SNHT to water level time series in the German Bight has been analysed using a large data set of synthetic time series from MCS. Moreover, the test has been applied to reconsider the homogeneity of MLW time series at the gauge of Büsum. The study of synthetic water level time series shows that the SNHT allows for the detection of change points in the mean of water level time series, even if there are a number of things to keep in mind when applying the test on tidal observations. Water level time series have a high level of variability, trends, autocorrelation and periodicity which influence the exact detection of change points. Especially the natural variability and periodicity may lead to chronologically shifted detections. Modifications such as building a new series by the use of the differences method applied in section 5 reduce the high level of variability, trends, autocorrelation and periodicity to a minimum. Simultaneously, the probability of false detection decreases significantly. However, every change point technique such as the SNHT has to be taken with caution. Without high quality metadata and homogeneous reference series the exact detection of change points in water level time series is rather crucial. Hence, for the future it will be

important to find homogeneous reference series that are representative for parts of the German Bight. Furthermore, an extensive literature research is necessary to bring changes into line with the historical events occurred at individual locations.

6 References

- Aguilar, E., Auer, I., Brunet, M., Peterson, T. and Wieringa, J. (2003): Guidelines on climate metadata and homogenization. World Meteorological Organization.
- Alexandersson, H. (1986): A homogeneity test applied to precipitation data, *Journal of Climatology*, Vol. 6, 661-675, ISSN 1097-0088
- Alexandersson, H. and Moberg, A. (1997): Homogenization of swedish temperature data. Part 1: Homogeneity test for linear trends, *International Journal of Climatology*, Vol. 17, 25-34, ISSN 0899-8418
- Dangendorf, S. (2010): Anwendung analytischer Verfahren zur Detektion von Instationaritäten in Wasserstandszeitreihen am Beispiel der Deutschen Bucht, diploma thesis, University of Siegen (unpublished)
- Dangendorf, S., Wahl, T., Jensen, J., Hein, H., Mai, S. and Mudersbach, C. (2011): Mean Sea Level variability and influence of the North Atlantic Oscillation on long-term trends in the German Bight (in prep.)
- Jensen and Mudersbach (2007): Zeitliche Änderungen in den Wasserstandszeitreihen an den Deutschen Buchten, in: Glaser R., Schenk, W., Vogt, J., Wießner, R., Zepp, H. und Wardenga, U. (Hrsg.), *Berichte zur Deutschen Landeskunde, Themenheft: Küstensenarien*, Vol. 81, No. 2, S. 99-112, Selbstverlag Deutsche Akademie für Landeskunde e.V., Leipzig, ISSN 0005-9099
- Mudersbach, C., Wahl, T., Haigh, I.D., Jensen, J.: Trends in extreme high sea levels along the German North Sea coastline compared to regional mean sea level changes, *Continental Shelf Research* (submitted)
- Mügge, H.E. and Jensen, J. (1991): Investigations of the Gauge Site of Büsum, *Deutsche Gewässerkundliche Mitteilungen*, Vol. 35, No. 1, pp. 13-21, ISSN 0012-0235
- von Storch, H. and Zwiers, F. W. (1999): *Statistical Analysis in Climate Research*, Cambridge University Press, Cambridge, ISBN 0 521 45071
- Wahl, T., Jensen, J., Frank, T. (2010): On analysing sea level rise in the German Bight since 1844, *Nat. Hazards Earth Syst. Sci.*, 10, 171-179, ISSN 1561-8633
- Wahl, T., Jensen, J., Frank, T. and Haigh, I.D. (2011): Improved estimates of mean sea level changes in the German Bight over the last 166 years, *Ocean Dynamics*, ISSN 1616-7341

The coastDat data set and its potential for coastal and offshore applications

Elke M. I. Meyer¹, Ralf Weisse¹, Janina Sothmann¹, Heinz Günther¹, Ulrich Callies¹, Hans von Storch¹, Frauke Feser¹, Katja Woth^{1,2} and Iris Grabemann¹

Abstract

CoastDat data-sets offer information about the past and possible future state for the North Sea and Baltic Sea. These data can be used for calculations of risk and application in coastal regions. The statistics of extreme wind, waves and storm surges are of central interest. Long and homogeneous data sets from numerical models are the backbones of coastDat. The methodology of these data-sets will be discussed and some examples for applications will be introduced, e.g. theoretical potential energy of wind and waves, respectively.

Keywords: coastal application and risk, sea state, numerical modelling

1 Introduction

Future coastal and offshore applications require appropriate planning and design. For most of them, statistics of extreme wind, waves and storm surges are of central importance. To obtain such statistics long and homogeneous time-series are needed. CoastDat is a data base of model results from regional numerical models for coastal regions. Numerical models can simulate the atmospheric and oceanic conditions for the recent past (hindcast) or for the future (scenarios). CoastDat offers a unique combination of consistent atmospheric (e.g. wind) and oceanic (sea state) variables at a high spatial and temporal resolution, even at places for which no measurements have been made.

The backbones of coastDat are regional wind, waves and storm surge hindcasts and scenarios mainly for the North Sea and the Baltic Sea. Furthermore, hindcast simulations are available for temperature, salinity, water level and currents for the North Sea for the last 60 years.

The hindcasts are validated with observations such as wind (Weisse et al. 2005, Winterfeldt and Weisse, 2009), tide surge simulations (Weisse and Pluess, 2006), wave model hindcast (Weisse and Günther, 2007) and sea temperature (Meyer et al. 2011). The validations show that multi-decadal hindcasts are perfectly suited to study statistics of events, their variability and their long-term changes, but single extreme events may or may not be reproduced (Weisse and Pluess, 2006).

2 Methodology

A regional atmosphere model with focus on Europe and adjacent seas is driven by the global NCEP/NCAR re-analysis (Kalnay et al. 1996) in combination with a simple data assimilation algorithm (Feser et al. 2001) in order to obtain a better representation of near-surface marine wind fields (von Storch et al. 2000). From this regional simulation, near-surface marine wind-fields and other parameters are stored hourly. Subsequently, the parameters are used to drive storm surge and wind wave models for the North Sea (Figure 1). In this way a high-resolution and consistent meteo-marine hindcast for the past 60 years has been generated. Here consistency refers to the fact that the output fields from the different models (wind, waves and storm surges) are in physical agreement, a fact that is frequently ignored e.g., when waves and surges from different sources are analysed jointly.

¹ Institute of Coastal Research, Helmholtz-Zentrum Geesthacht, Centre for Materials and Coastal Research GmbH, Max-Planck-Straße 1, 21502 Geesthacht, Germany, elke.meyer@hzg.de

² Max Planck Institute for Meteorology, Bundesstraße 53, 20146 Hamburg, Germany

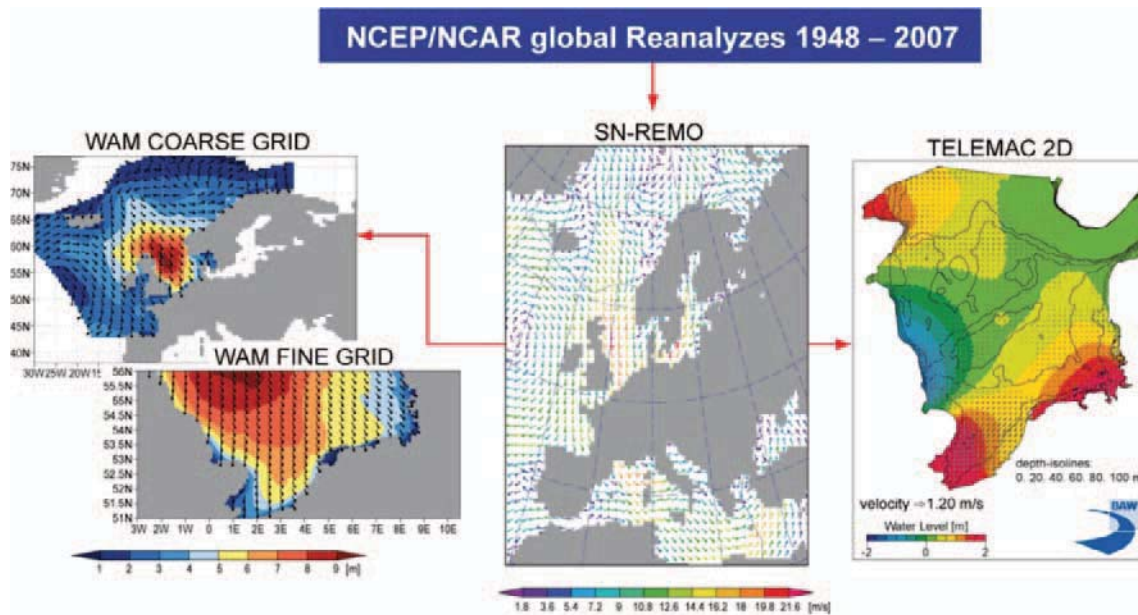


Figure 1: Layout of the consistent metocean hindcast 1948–2007 for the southern North Sea. From the (middle) regional atmosphere hindcast hourly wind fields were used to force a tide surge (right) and a wave model hindcast (left). The figure shows an example of consistent metocean conditions obtained from the hindcast for 1200 UTC 21 Feb 1993. Near-surface (10-m height) marine wind fields (m s⁻¹), and corresponding wind direction obtained from the regional atmospheric reconstruction (middle). Corresponding significant wave height fields (m) and mean wave direction from the coarse and the fine grid wave model hindcast (left). Tide surge levels (m) from the corresponding tide surge hindcast (right). After Weisse and Günther (2007).

3 Applications

The coastDat data are already used for a number of coastal and offshore applications for example in optimisation studies of ship design (Weisse et al. 2009), for the assessment of oil risk spreading or chronic oil pollution (Chrastansky et al. 2009, Chrastansky and Callies, 2009) and in studies of the future development of storm surge changes (Woth et al. 2006).

Another example for the application of coastDat data is the planning of offshore wind farms. The assessment of wind and sea state statistics supports the investigation of wind power availability. Also, the data are used to estimate the magnitude of rare events that may impact the fatigue life of wind turbines, such as the 50-year return value for near surface wind speed or significant wave heights. For the design process probability distributions such as a combination of wind speed, wind direction, significant wave height, wave periods and wave direction are frequently requested. The statistics of time slots for installation and maintenance (weather windows) of the wind turbines are important for an economic operation.

Another application is the requirement of energy capacity calculated for the onshore electricity network. Only at special locations the energy supplies in the electricity network, which has only limited feeding-in capacity. CoastDat enhances the planning of energy requirements from coal-burning power plants. Wiese (2008) calculated the realisable potential of full-load hours from wind turbine parks and coal-burning power plants (Fig. 2). Figure (2) shows the feasible potential of coal-burning power plants on the left side and that of wind parks on the right side (y-axis). The yellow area marks the excess supply of energy during the year (x-axis), due to the limited capacity of the electricity network. The white spacing displays the potential of energy supply. The German renewable energy law induces, that the available wind energy supplies in the electricity net. Wiese (2008) calculated for the four 800 MW coal-burning power plants full-load hours of 4111, 4411, 5243 and 6190 per year (8760h). Thus the coal-burning power plants have noticeable less base-load hours as planned. The frequent run-up and run-down of the coal-burning power plants decrease the efficiency of energy production and therefore cause a

rise in costs. Investigations shall be done to find possibilities to expand the base-load energy with different methods.

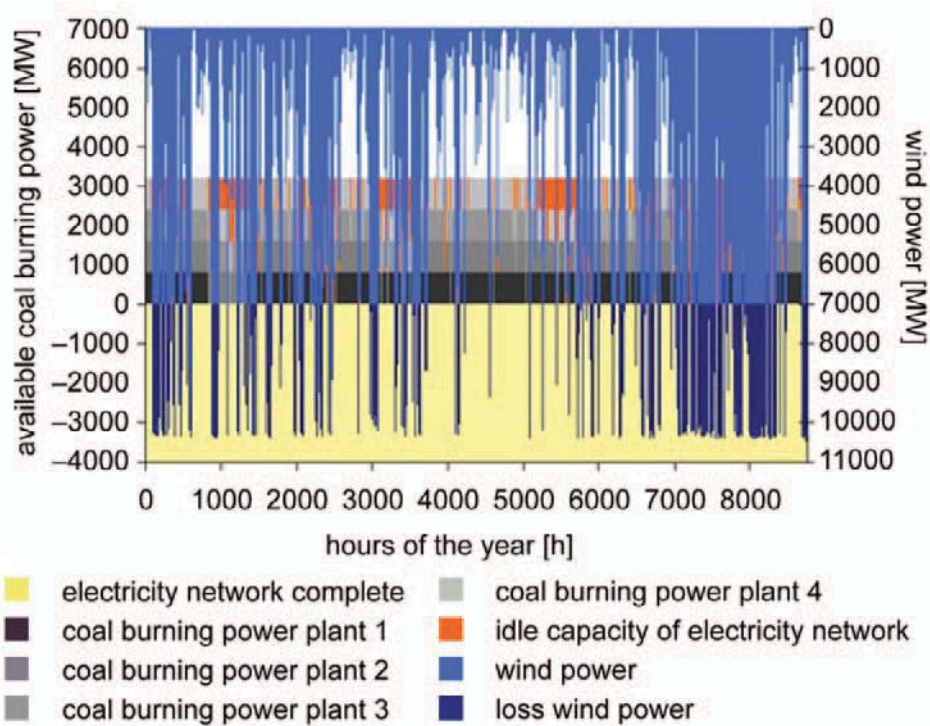


Figure 2: Annual supply of energy from offshore wind parks and coal burning power plants into an electricity network with a capacity of 7000MW (supply point Brunsbüttel; after Wiese, 2008).

Marx (2010) investigated the theoretical wave energy based on the coastDat data-set (Fig. 3). Wave energy depends on the significant wave height, wave period, wavelength and water depth. In Figure 3 the average 50-year (1958-2007) wave energy flux (kWm^{-1}) calculated for the south-eastern North Sea ($53\text{-}56^{\circ}\text{N}$; $3\text{-}9^{\circ}\text{E}$) is shown. Close to the coast only small wave energy fluxes are calculated. Offshore, the wave energy increases due to the higher significant wave height and water depth. The inter-annual variability of the wave energy flux is quite high. Highest fluxes are found for winter (December – February; $<4\text{-}40\text{kWm}^{-1}$) whereas small fluxes are found in summer (June-August; $<4\text{-}8\text{kWm}^{-1}$). In spring (March - May) and autumn (September - December) the energy fluxes are of similar magnitude with $<4\text{-}22\text{kWm}^{-1}$ and $<4\text{-}28\text{kWm}^{-1}$, respectively. Compared to other locations the annual potential of energy fluxes with $6\text{-}24\text{kWm}^{-1}$ in the German Bight is very low for commercial applications. For example west of Great Britain and west of South-India theoretical energy potentials of $\sim 30\text{-}90\text{kWm}^{-1}$ are expected (Graw, 1995). Marx (2010) investigated the theoretical potential of wind and wave energy depending on the potential of available wind power. Probably both can use the existing infrastructure to feed into the electricity net, but both energy extractions are subject to large temporal variability and thus are not suited for a constant energy input. The potential wave energy depending on the technical, ecological, economical and social potential and it can become much lower than the theoretical potential. The coastDat data-set is a suitable tool to calculate the feasible potential.

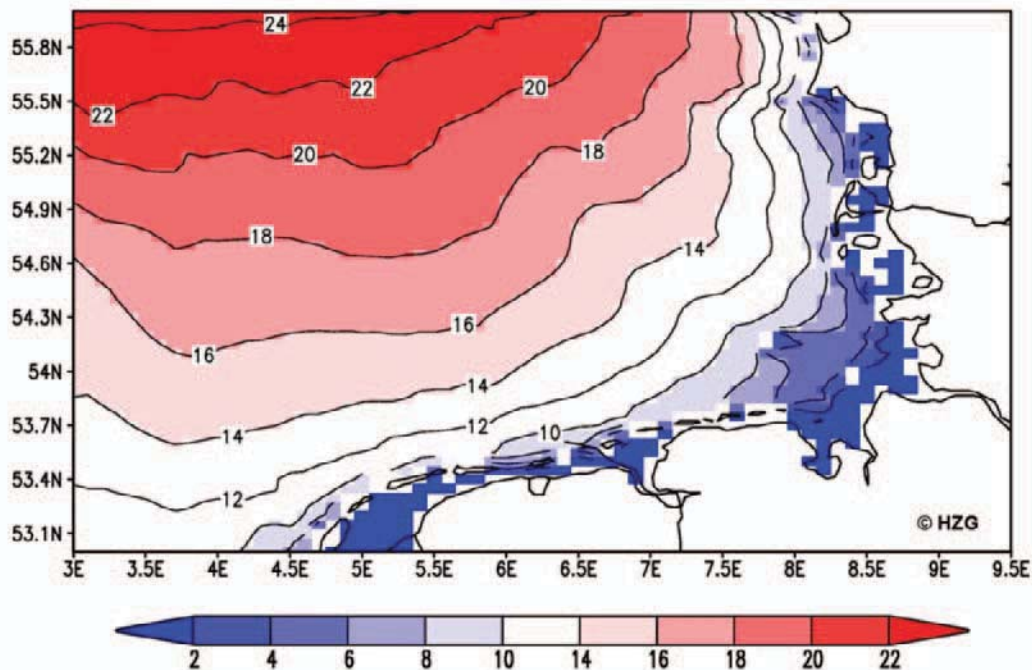


Figure 3: Average 50-year (1958-2007) theoretical wave energy flux (kWm^{-1}) for the south-eastern North Sea.

4 Summary and Outlook

The coastDat data-set is a compilation of coastal analyses and scenarios for the future from various sources. It contains no direct measurements but results from numerical models that have been driven either by observed data in order to achieve the best possible representation of observed past conditions or by climate change scenarios for the near future. Contrary to direct measurements which are often rare and incomplete, coastDat offers a unique combination of consistent atmospheric, oceanic, sea state and other parameters at high spatial and temporal detail, even for locations and variables for which no measurements have been made so far.

Currently, the coastDat data base will be enhanced with results from ensemble calculations of regional models. These results will allow an evaluation of the statistics and risks of future wind and wave characteristics in coastal regions. CoastDat can be applied amongst others as basis for decision making.

5 Acknowledgement

The authors thank Frauke Wiese for assignment of Figure 2 and Beate Gardeike for preparation of the figures.

6 References

- Chrastansky, A.; Callies, U.; Fleet, D.M. (2009): Estimation of the impact of prevailing weather conditions on the occurrence of oil-contaminated dead birds on the German North Sea coast. In: *Environmental Pollution* 157, pp. 194-198.
- Chrastansky, A.; Callies, U. (2009): Model-based long-term reconstruction of weather-driven variations in chronic oil pollution along the German North sea coast. In: *Marine Pollution Bulletin* 58, pp. 967-975.
- Feser, F.; Weisse, R.; von Storch H. (2001): Multi-decadal atmospheric modelling for Europe yields multi-purpose data. In: *Eos Transactions*, 82, pp. 305, 310.

- Graw, K.-U. (1995): Wellenenergie – eine hydromechanische Analyse. In: Bericht Nr. 8 des Lehr- und Forschungsgebietes Wasserbau und Wasserwirtschaft, Bergische Universität - GH Wuppertal
- Kalnay et al. (1996): The NCEP/NCAR 40-year reanalysis project, In: Bulletin of the American Meteorological Society, 77, pp. 437-470, 1996.
- Marx, J. (2010): Langzeitige Variabilität der Wellenenergiepotenziale in der Nordsee, Master-Thesis, University of Basel
- Meyer, E. M. I.; Pohlmann, T.; Weisse, R. (2011): Thermodynamic variability and change in the North Sea (1948-2007) derived from a multidecadal hindcast. In: Journal of Marine Systems. Vol. 86, pp. 35-44.
- von Storch, H.; Langenberg, H.; Feser, F. (2000): A spectral nudging technique for dynamical downscaling purposes. Monthly Weather Review, 128, pp. 3664-3673.
- Weisse, R.; von Storch, H.; Feser, F. (2005): Northeast Atlantic and North Sea storminess as simulated by a regional climate model 1958-2001 and comparison with observations. Journal of Climate, 18, pp. 465-479.
- Weisse, R.; Pluess, A. (2006): Storm-related sea level variations along the North Sea coast as simulated by a high-resolution model 1958-2002. In: Ocean Dynamics. TIERGARTENSTRASSE 17, D-69121 HEIDELBERG, GERMANY, MAY, 2006. Vol. 56(1), pp. 16-25. SPRINGER HEIDELBERG.
- Weisse, R.; Günther, H. (2007): Wave climate and long-term changes for the Southern North Sea obtained from a high-resolution hindcast 1958-2002. In: Ocean Dynamics. TIERGARTENSTRASSE 17, D-69121 HEIDELBERG, GERMANY, JUN, 2007. Vol. 57(3), pp. 161-172. SPRINGER HEIDELBERG.
- Weisse, R.; von Storch, H.; Callies, U.; Chrastansky, A.; Feser, F.; Grabemann, I.; Günther, H.; Pluess, A.; Stoye, T.; Tellkamp, J.; Winterfeldt, J.; Woth, K. (2009): Regional Meteorological-Marine Reanalyses and Climate Change Projections: Results for Northern Europe and Potential for Coastal and Offshore Applications. In: Bulletin of the American Meteorological Society. 45 BEACON ST, BOSTON, MA 02108-3693 USA, JUN, 2009. Vol. 90(6), pp. 849-860. AMER METEOROLOGICAL SOC.
- Wiese, Frauke (2008): Auswirkungen der Offshore-Windenergie auf den Betrieb von Kohlekraftwerken in Brunsbüttel, Diploma-Thesis, Universität und Fachhochschule Flensburg, Energie- und Umweltmanagement
- Winterfeldt, J.; Weisse, R. (2009): Assessment of Value Added for Surface Marine Wind Speed Obtained from Two Regional Climate Models. In: Monthly Weather Review. 45 BEACON ST, BOSTON, MA 02108-3693 USA, SEP 29, 2009. Vol. 137(9), pp. 2955-2965. AMER METEOROLOGICAL SOC.
- Woth, K.; Weisse, R.; von Storch, H. (2006): Climate change and North Sea storm surge extremes: an ensemble study of storm surge extremes expected in a changed climate projected by four different regional climate models. In: Ocean Dynamics. TIERGARTENSTRASSE 17, D-69121 HEIDELBERG, GERMANY, MAY, 2006. Vol. 56(1), pp. 3-15. SPRINGER HEIDELBERG.

Wave impact on a seawall with a deck and on a baffle in front of seawall

Nor Aida Zuraimi Md-Noar¹ and Martin Greenhow²

Abstract

Given the uncertainty in wave climate and water aeration (which dramatically affects the sound speed and hence acoustic pressure) in extreme conditions, and the sensitivity of maximum impact pressures on the exact alignment of the impacting wave surface with the seawall, results from measurements/calculations are highly variable. Thus Peregrine (2003) proposed using the pressure impulse $P(x,y)$ that is the time integral of the pressure over the duration of the impact. This results in a simplified, but much more stable, model of wave impact on the coastal structures. This paper continues the work of Greenhow (2006) who extended Cooker's (1990) model to breakwaters with a ditch or berm by using eigenfunction expansions of the pressure impulse. That paper will be reviewed and extended before considering the following simplified model for impact on a wall with: i) a deck extending from the top of vertical seawall, ii) a baffle in front of the vertical seawall.

1 Introduction

Cooker and Peregrine (1990, 1995) modified the theory of pressure impulse in order to investigate the problems of wave pressures on marine structures. The equation (12) below satisfies the boundary-value problem for impact on a vertical seawall, giving an analytical solutions for the pressure impulse using Fourier analysis. They also calculated the impulse (force impulse) and moment impulse on the wall and on the seabed. Cooker (1990) showed that his theoretical work was in good agreement with the experimental results, such as those of Bagnold (1939). He concluded that choosing a small value of impact parameter μ gives almost the same trends as those of the empirical rules used as engineering standards for which the maximum value of p_{peak} occurs below the free-surface level and decreases towards the bed.

2 Pressure-impulse theory

When a wave breaks against a rigid surface, such as seawall, large and short-lived pressures are generated. Bagnold (1939) pioneered investigation of this problem and suggested that a pressure which rises to a high peak value, p_{pk} , lasts for a very much shorter duration, Δt , which is normally from one to 10ms, than does a lower pressure. In his experiments, he discovered that the pressure impulse is approximately constant, even though the peak pressure changes unpredictably between apparently identical wave impacts. The pressure impulse, P is defined as

$$P(x, y) = \int_{t_b}^{t_a} p(x, y, t) dt \quad (1)$$

where t_b and t_a are characteristic times for the start and end of the pressure pulse or spike, x, y are spatial coordinates and p is measured relative to atmospheric pressure. The pressure impulse idea removes time from the equations, but p_{pk} can be estimated from a calculated value P by assuming the pressure during impact is approximately triangular:

¹ Brunel University, Department of Mathematical Sciences, John Crank Building, Uxbridge, Middlesex, UB8 3PH, United Kingdom, ¹ mapgnab@brunel.ac.uk and ² mastmmg@brunel.ac.uk

$$P \approx \frac{1}{2} p_{pk} \Delta t \quad (2)$$

so that

$$p_{pk} \approx \frac{2P}{\Delta t} \quad (3)$$

Since Δt is prone to uncertainty, any estimate of p_{pk} is also uncertain. For extreme impact p_{pk} may be very large and Δt very small, but the product given in (2) will remain finite and approximately constant for wave impacts from similar waves.

Cooker and Peregrine (1995) proposed a mathematical model for pressure-impulse theory for impact between a region of incompressible liquid and either a rigid surface or a second region of liquid. Boundary conditions are applied giving the peak pressure distribution and the normal velocity after impact as well. The hydrostatic reference pressure is $\rho g H$, where ρ is density of water, g is gravity and H is height of the top of the wave above the bed. The 'impact zone' refers to the rigid surface area which is impacted by the moving liquid. The mathematical formulation and boundary conditions proposed by Cooker and Peregrine (1995) are as follows:

The fluid is assumed to be incompressible, inviscid (no viscosity/internal friction) and irrotational:

1. The change in velocity during the impulsive event is supposed to take place over such a short time that the nonlinear convective terms in the Euler equations of motion are negligible compared to the time derivative, giving

$$\frac{\partial u}{\partial t} = -\frac{1}{\rho} \nabla p \quad (4)$$

2. Integrating equation (4) with respect to time through the impact interval $[t_b, t_a]$, and using definition (1) for the pressure impulse P , gives

$$u_a - u_b = -\frac{1}{\rho} \nabla P, \quad (5)$$

since $\nabla \cdot u_b$ and $\nabla \cdot u_a$ both vanish, taking the divergence of (5) shows that the pressure impulse satisfies Laplace's equation

$$\nabla^2 P = 0. \quad (6)$$

3. The boundary conditions to be applied are readily found:

- (a) At a free surface, the pressure is taken to be zero so (1) gives

$$P = 0 \text{ at } y = 0 \quad (7)$$

- (b) At a stationary (or even moving) rigid boundary, in contact with the liquid before and after the impulse, the normal velocity is unchanged so the equation (5) gives

$$\frac{\partial P}{\partial n} = 0. \quad (8)$$

- (c) Where liquid meets a solid boundary during impact, the change in normal velocity gives the normal derivative of pressure impulse. For the simplest case of a stationary rigid boundary

$$u_{nb} = \frac{1}{\rho} \frac{\partial P}{\partial n}, \quad (9)$$

where u_{nb} is the normal component of the approach velocity of the liquid.

- (d) When liquid meets liquid two boundary conditions are needed on the common interface. One is that the pressure impulse continuous:

$$P_1 = P_2. \quad (10)$$

Consideration of the change in velocity on each side of the interface gives

$$u_{1nb} - u_{2nb} = \frac{1}{\rho_1} \frac{\partial P_1}{\partial n} - \frac{1}{\rho_2} \frac{\partial P_2}{\partial n}, \quad (11)$$

where subscript n denotes the components normal to the boundary and subscript b denotes the liquid velocities immediately before the impact. In all the above cases, an inelastic impact assumed.

Cooker and Peregrine (1995) modified Cooker's model by introduced applying a distant vertical boundary on which $P = 0$, see figure 1. This introduces hyperbolic terms instead of exponential terms in the Fourier series. This still satisfies Laplace's equation (6). The mixed boundary value problem is illustrated in figure 1.

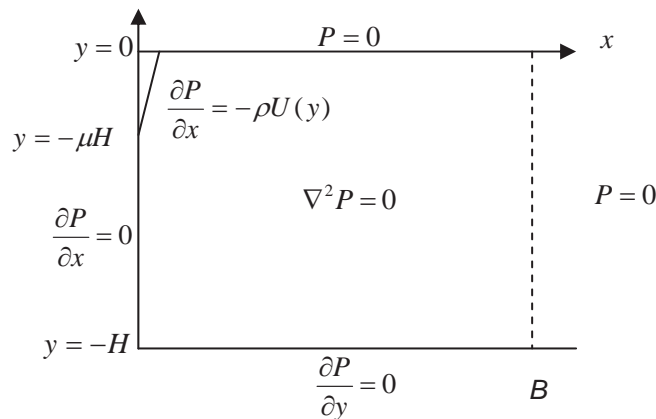


Figure 1: The boundary value problem for pressure impulse

The solution in the Fourier series form can be written as

$$P(x, y; \mu) = \sum_{n=0}^{\infty} a_n \sin\left(\frac{\lambda_n y}{H}\right) \frac{\sinh(\lambda_n(x-B)/H)}{\cosh(\lambda_n B/H)} \quad (12)$$

$$\text{with } a_n = \int_{-\mu H}^0 \frac{-2\rho U}{\lambda_n} \sin\left(\frac{\lambda_n y}{H}\right) dy \text{ where } \lambda_n = \left(n + \frac{1}{2}\right)\pi.$$

The results in figure 2 show the dimensionless pressure impulse ($P / \rho H U_0$).

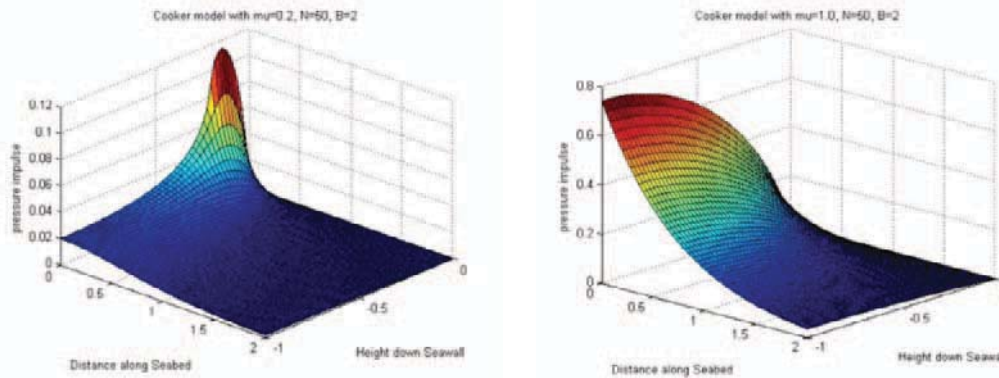


Figure 2: Non-dimensional pressure with distant boundary $B=2H$. The impact region defined by μ spans $0-0.2H$ (left figure, $\mu = 0.2$) and $0-1H$ (right figure, $\mu = 1.0$).

3 Pressure impulse on a seawall with a deck

We present the pressure-impulse calculations for a wave impact on a vertical seawall with a rigid horizontal deck of finite extension. The impacting wave is assumed to be vertical, with a constant horizontal velocity in the impact region $0 < x < \mu$. The problem is again non-dimensionalised using the water density, ρ and depth, $H=1$ and impact velocity, U_0 .

3.1 Mathematical Modelling

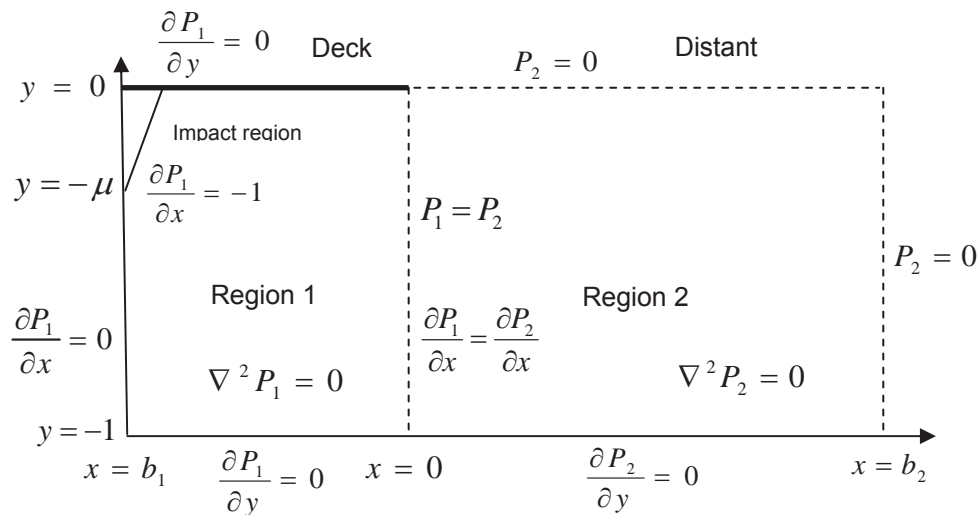


Figure 3: The boundary-value problem for deck problem.

Two regions, below the deck and below the free surface are written as appropriate eigenfunction expansions (including secular terms) and P and its x -derivative are matched by collocation at $x=0$ i.e. a vertical line at the end of the deck. This problem has a square root singularity where the end of the deck meets the free surface. To circumvent this, we use a collocation method with no collocation point at the singularity. Figure 4 shows the distribution of pressure impulse for different lengths of deck, the shorter deck being comparable to the no-deck solution of Cooke and Peregrine (1995) except near the deck where the pressure impulse is substantially higher. The solution in region 1 below the deck in Fourier series form can be written as

$$P_1(x, y) = \sum_{n=1}^{\infty} \cos(\gamma_n y) \left\{ \alpha_n \frac{\cosh(\gamma_n (x - B_1))}{\cosh(\gamma_n B_1)} + \beta_n \frac{\sinh(\gamma_n (x - B_1))}{\sinh(\gamma_n B_1)} \right\} + Ax + C$$

$$\text{where } \gamma_n = n\pi, n \in (1,2,3,\dots,N) \text{ for } -1 \leq y \leq 0, \text{ and } 0 \leq x \leq b_1 \quad (13)$$

The Fourier coefficients α_n, β_n and secular coefficients, A and C are found by applying equation 9 on the wall and matching with the outer region 2 (see figure 3), where the free surface, far field and bed boundary conditions are satisfied by a modified form of Cooker's eigenfunction expression:

$$P_2(x, y, \mu) = \sum_{n=1}^{\infty} c_n \sin(\lambda_n y) \frac{\sinh(\lambda_n(x - B_2))}{\cosh(\lambda_n B_2)}$$

$$\text{where } \lambda_n = \left(n - \frac{1}{2}\right)\pi, n = 1,2,3,\dots,N.$$

$$\text{for } -1 \leq y \leq 0, \text{ and } b_1 \leq x \leq b_2 \quad (14)$$

and c_n are Fourier coefficients to be found by matching. The series are truncated and a square matrix is found by using a Fourier method on the wall and choosing an appropriate number of collocation point at the matching line $x=0$. This is then solved using and plotted MATLAB.

3.2 Results

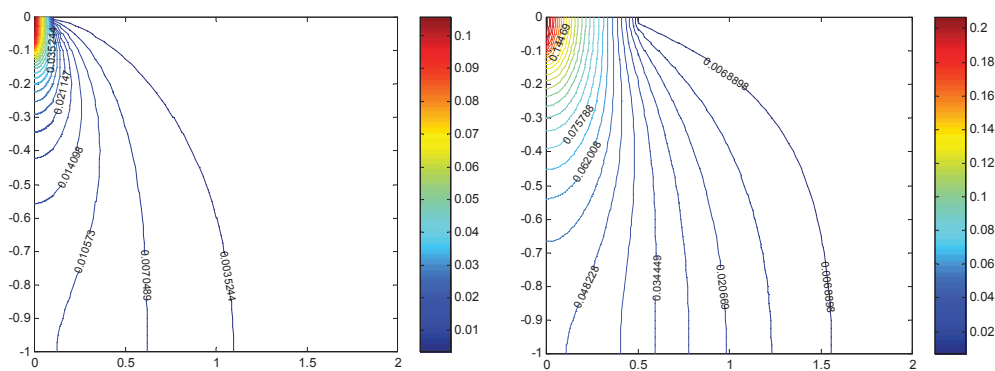


Figure 4: Pressure impulse down the wall for $\mu=0.1$. The maximum pressure impulse for deck lengths $b_1 = 0.1$ and $b_1 = 0.5$ are approximately $0.102 \rho U_0 H$ and $0.204 \rho U_0 H$ respectively.

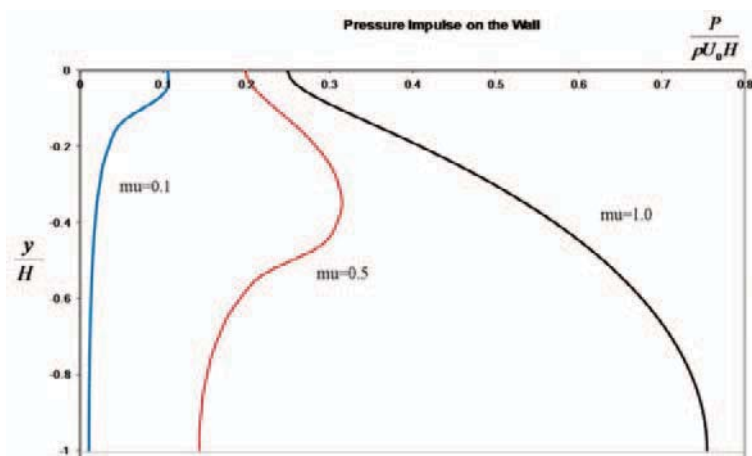


Figure 5: Pressure impulse on the wall for varying μ with deck $b_1 = 0.1$

To calculate the total impulse, I exerted by the fluid on the wall/deck, we need the expression for the pressure impulse at $x = 0$ and at $y = 0$ given in (13) respectively. Integrating over the wall/deck gives:

$$I = \int_a^b P_1(0, y) dy \quad (15)$$

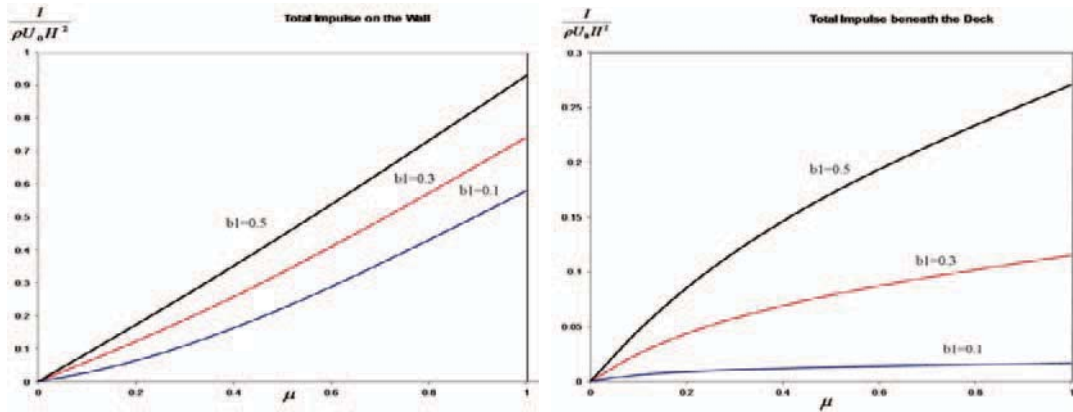


Figure 6: Total impulse on the wall and beneath the deck for varying length of deck, b_1 .

4 Pressure impulse on a baffle in front of seawall

Now we consider the pressure impulse acting on a vertical baffle in front of the seawall at $x=b_1$ with depth of penetration H_b . The formulation is similar to the deck problem, but the seawall and matching is again achieved by a combination of Fourier and collocation methods that have proved to be stable and converge. We consider two cases of problem: 1) a vertical baffle in front of the wall (the boundary conditions as in figure 7); 2) A vertical baffle at a deck in front of seawall (the boundary conditions as in figure 7 but equation $P_1 = 0$ is replaced by $\partial P_1 / \partial y = 0$ in the region 1).

4.1 Mathematical Modelling

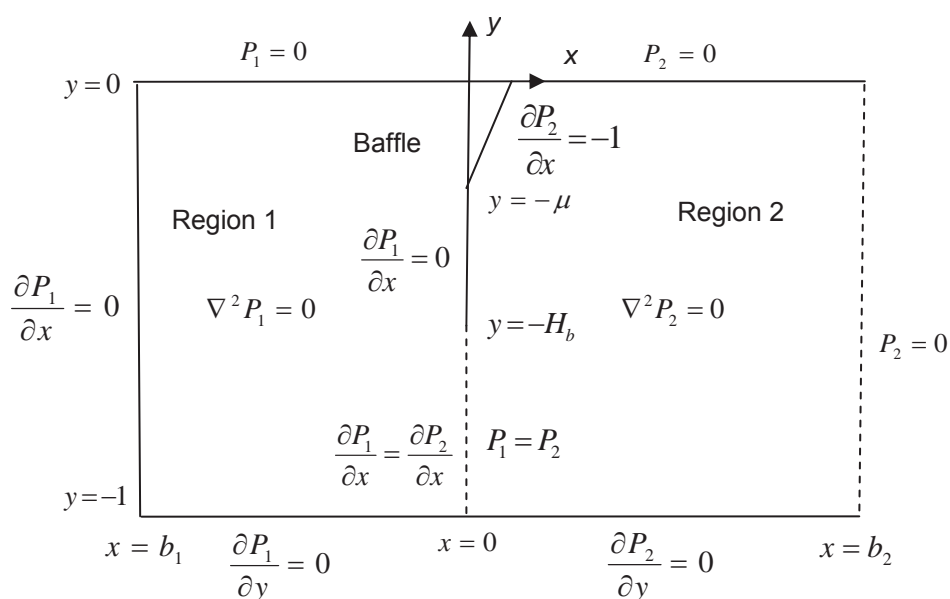


Figure 7: The boundary-value problem for baffle problem

The solution in the Fourier series form for case I and case II in region 1 can be written as

$$P_1(x, y) = \sum_{n=1}^{\infty} \alpha_n \sin(\lambda_n y) \frac{\cosh(\lambda_n(x - b_1))}{\cosh(\lambda_n b_1)}$$

where $\lambda_n = (n - 1/2)\pi$, $n \in (1, 2, 3, \dots, N)$ for $-1 \leq y \leq 0$, and $b_1 \leq x \leq 0$ (16)

or $P_1(x, y) = \sum_{n=1}^{\infty} \alpha_n \cos(\gamma_n y) \frac{\cosh(\gamma_n(x - b_1))}{\cosh(\gamma_n b_1)} + C$

where $\gamma_n = n\pi$, $n \in (1, 2, 3, \dots, N)$ for $-1 \leq y \leq 0$, and $b_1 \leq x \leq 0$ (17)

respectively. The solution which satisfies the boundary condition in the region 2 for both cases is as in equation (14).

4.2 Results

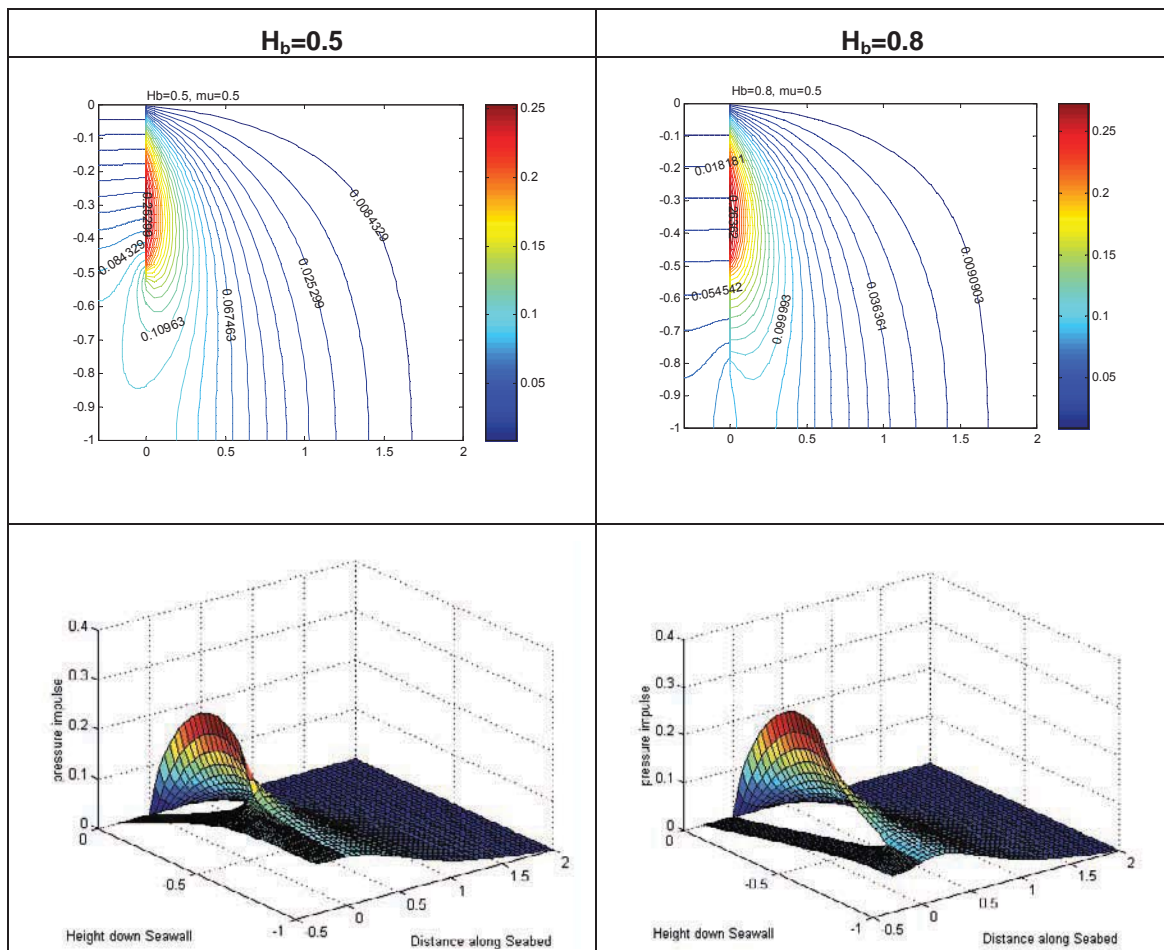


Figure 8: Pressure impulse contours and plots for $\mu=0.5$ for case I. The maximum pressure impulse for $H_b = 0.5$ and $H_b = 0.8$ are approximately $0.255 \rho U_0 H$ and $0.280 \rho U_0 H$ respectively.

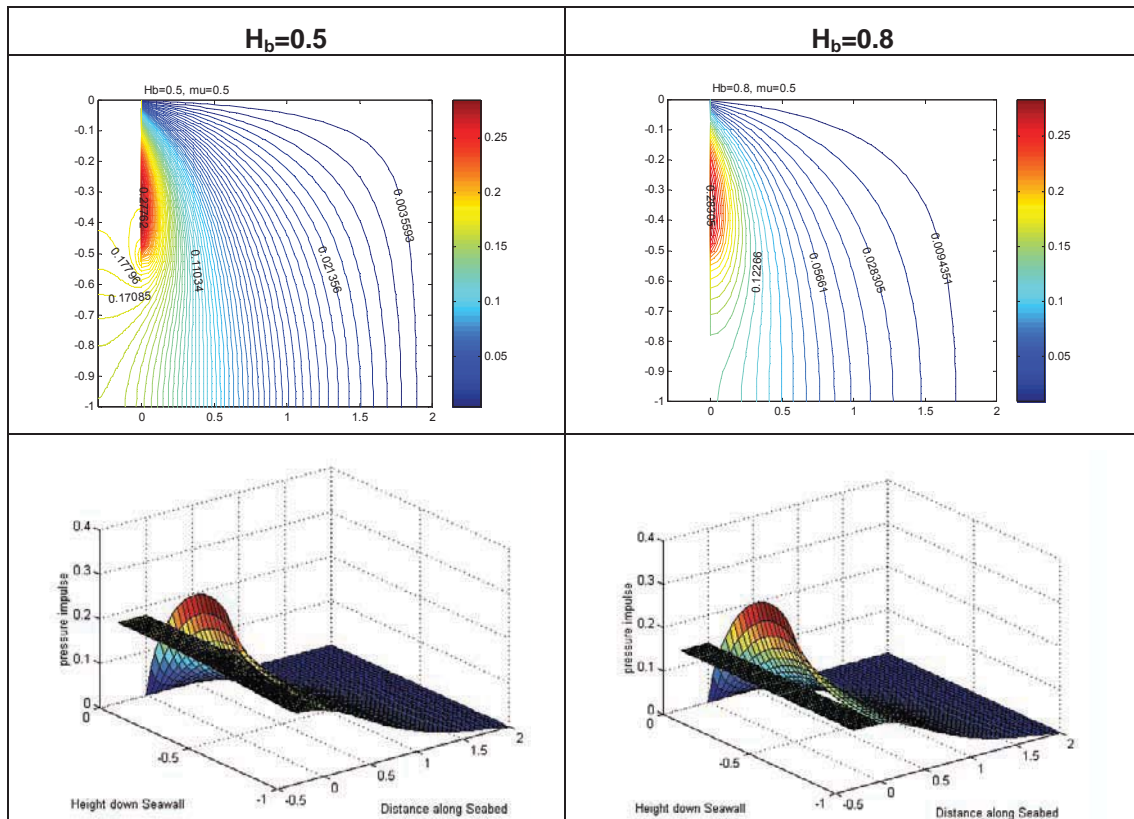


Figure 9: Pressure impulse contours and plots for $\mu=0.5$ for case II. The maximum pressure impulse for $H_b=0.5$ and $H_b=0.8$ respectively are approximately $0.280 \rho U_0 H$ and $0.290 \rho U_0 H$.

5 Conclusion

It is found that the pressure impulse increases with deck length, and with the size of the impact region μ (as in Cooker and Peregrine (1995) for the no-deck case). For the baffle, case I, the pressure impulse on the front/rear of the baffle increases/decreases with increasing baffle length. However in case II, there is a high pressure impulse behind the baffle for a deep baffle for large μ . This value is exceeded by the pressure impulse on the front of the baffle, but not over a very large region, so the resulting total impulse on the wall will be seaward, not landward.

6 References

- Greenhow, M. (2006) Wave impact on seawalls of various geometries. Proc. 1st Int. Conf. Coastlab, 517-524
- Peregrine, D.H. (2003) Water-wave impact on walls. Ann. Rev. Fluid Mech., 35:23-43
- Cooker, M.J., Peregrine, D.H (1995) Pressure-impulse theory for liquid impact problems. J. Fluid Mech. 297:193-214
- Cooker, M.J., Peregrine, D.H (1990) A model for breaking wave impact pressures. Proc. 22nd Intl. Conf. Coastal Eng. 1473-1486
- Bagnold, R.A. (1939) Interim report on wave-pressure research. J Inst. of Civil Engineers. 12: 202-206
- Cooker, M.J. (1990) The interaction between steep water waves and coastal structures. Ph.D Thesis University of Bristol

Mapping the temporal and spatial distribution of experimental impact induced pressures at vertical seawalls: a novel method

Dimitris Stagonas^{1*}, Gerald Müller¹, William Batten¹ and Davide Magagna¹

Abstract

Current knowledge on wave pressures at vertical walls mainly comes from 2D experimental studies. Nevertheless, maximum impact pressures are commonly assumed to occur in the middle of the structure and hence an array of pressure transducers is used to provide single point records of the vertical pressure distribution. Accordingly, it comes as no surprise that almost nothing is known regarding the horizontal, temporal and spatial, distribution of impact pressures on vertical seawalls and breakwaters. Through the transfer of technology from other fields of research, the simultaneous mapping of the horizontal and vertical distribution of impact induced pressures at the face of a vertical seawall is made possible here for the first time. Both the size of the mapping area (here, 100cm²) and the measuring resolution (here, 392 sensing points) cannot be achieved with traditional pressure transducers. Results presented reveal an uneven vertical and horizontal distribution with maximum pressures occurring in areas of the seawall where least expected. The cushioning effect of the entrapped air cavity and pressures induced at the lower part of the structure due to the large acceleration of the trough are documented here through the combination of the proposed technology with high speed video.

1 Introduction

The impact of waves on vertical seawalls has been the focus of numerous investigations over the past decades and it is by now a well-established fact that impulsive events create the most violent conditions at the vicinity of coastal structures. Important damages and failures attributed to wave impacts have been reported in the existing literature for vertical caisson and / or masonry breakwaters, e.g. see Oumeraci (1994) and Müller et al. (2002) respectively.

Within this context, a very large number of authors have provided field and mainly experimental measurements of impact pressure at vertical seawalls / breakwaters. Although large discrepancies have been observed for the pressure magnitudes between field and laboratory measurements a consensus has been long reached with regards to their vertical distribution at the wall, e.g. Miller et al. (1974) and Cuomo et al. (2010).

Nevertheless, previous measurements have been conducted using an array of, usually, 5 to 9 pressure transducers placed in few cm intervals and extending from the top of the structure all the way down to the sea bed. The area is located in the middle of the seawall, following the assumption that, for 2D studies, maximum impact pressures occur there. Although accurate, traditional pressure transducers provide only single point measurements entailing a very small and inconsistent measuring area. Accordingly it comes as no surprise that current knowledge regarding the horizontal, temporal and spatial, distribution of impact pressures on vertical seawalls is very limited.

Blackmore and Hewson (1984) and Hattori et al. (1994) amongst others, placed a pair of transducers a few cm away the main array, on either side or next to it, near or at SWL. These measurements were not particularly commented by the authors but they indicate a horizontal fluctuation of pressure magnitudes even for perpendicular wave attack angles.

Motivated by this gap in knowledge, the current work describes a novel technology capable to simultaneously map and measure the horizontal and vertical pressure distribution at vertical seawalls. A single measuring element of the proposed technology covers an area of 50cm² including 196 sensing points with a maximum sampling frequency of 4kHz. To the authors' best

¹ Sustainable Energy Research Group, Civil Engineering Department, University of Southampton, Highfield, Southampton, SO17 1BJ, UK, phone: +44(0)2380592442, fax: +44(0)2380677519, e-mail: ds3e10@soton.ac.uk, G.Muller@soton.ac.uk, W.Batten@soton.ac.uk, gm7@soton.ac.uk

knowledge, such a high spatial resolution has never before possible. Traditional pressure transducers provide only single point measurements and cover a small area, e.g. Hull and Müller (2002) used 5, 3.5mm in diameter, transducers for a model area larger than 60,000mm². If a small number of sensors are placed with a distance between them, the overall area increases in size but becomes inconsistent. In the same time the use of a very large number of transducers would be very expensive and time consuming; both in terms of setting up and data analysis.

Following, a brief literature review, the proposed technology is described along with the experimental arrangement used for its calibration and testing. Measurements of impulsive pressures at the face of a vertical seawall are reported in the results section and the work closes with the conclusions. Although strong reference is made to wave impacts the reader should keep in mind that the main focus of the present paper is to introduce this new technology to the coastal engineering community and not to analyse in depth the recorded impact events.

2 Literature review

Being, potentially, the most violent and impressive event in the coastal environment, wave impacts at coastal structures have been studied for more than a century. They are characterised by very short rise times, e.g. rise times as low as 1.2ms have been recorded, and are capable to exert highly localised and great in magnitude pressures. Bullock et al. (2007) and Bullock and Bredmose (2010) have reported values reaching up to 750kPa for field measurements and 3.5MPa for laboratory measurements respectively.

For all previous investigations, however, pressure measurements were acquired along the centreline of the structure using traditional pressure transducers. Final conclusions were based on the assumption that impulse pressures along the centreline are least affected by sidewall effects. Nevertheless it was, in most cases, acknowledged that irregularities on the wave crest kinematics, spatially shifted reflections, impacts and run-down occurring in 3D and 2D tests can have a direct effect on pressure magnitudes.

Overall, the review of existing literature suggests that the vertical distribution of wave impact pressures at seawalls and breakwaters is by now well understood but knowledge on their horizontal, spatial and temporal, distribution remains limited. However, the recent work of Bredmose et al. (2009) shows that large impact induced pressures can occur at areas of the seawall where least expected.

Although relatively few 3D investigations have been conducted in the past, e.g. Archetti et al (2000), our experimental capabilities are so far limited by the use of, single point measuring, pressure transducers. In the same time, deploying a large number of such sensors is expensive, laborious and time consuming. Nevertheless, within the current paper a newly developed technology is used to measure wave induced pressures at a vertical seawall. The proposed technology allows for the first time the instantaneous mapping of the spatial and temporal evolution of pressures at the face of coastal structures with a measuring resolution and over area sizes never seen before.

3 Experimental set up

3.1 The wave flume

All experiments reported here were conducted in the shallow water wave flume, 15×0.46×0.46m, of the University of Southampton hydraulics laboratory. The flume was equipped with a PC controlled, piston type wave maker and a series of resistant type wave gauges was employed to record the size of the regular waves generated. A 1:20, impermeable slope was placed at one end of the flume followed by a vertical seawall made out of Perspex (Fig. 1). A constant water depth of 20.5cm in front of the wave paddle and 5.7cm at the vicinity of the seawall was chosen for all measurements.

For most tests the impact of only the first incoming crest was recorded and analysed but records of subsequent waves breaking at the structure were also acquired. A Casio Exilim F1 camera was used to record impacts at 600 frames per second (fps) with 538×433pixels.

3.2 Pressure mapping system: the I-Scan system

A grid-based configuration of tactile sensors patented and provided by TekScan Inc. is used here to map wave impact pressures on vertical seawalls. This configuration is part of a PC controlled system referred to as Tekscan VersaTeck I-Scan High Speed System. The main components of I-Scan tactile sensor system include one or more pressure pads (the grid based configurations), one or more VersaTek Sensor handles and a purposely developed control and analysis software see TEKSCAN (2008). Each pad (pressure map) is connected to a single handle and a hub is used to link every handle to the PC; the pressure pads used for the current tests are illustrated in figure 2.

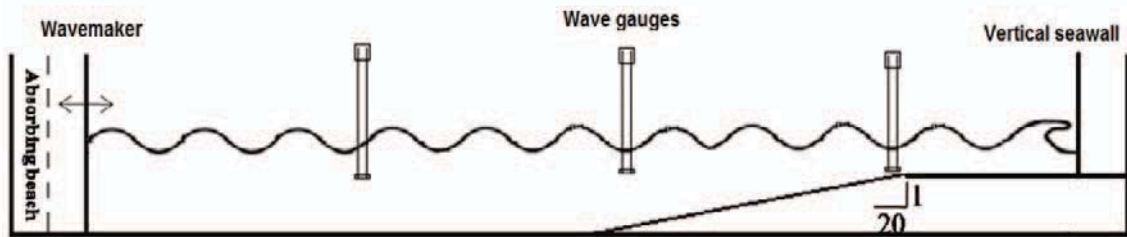


Figure 1: Schematic representation of the shallow water wave flume, 15×0.46×0.46m. Water depth in front of the wavemaker was 20.5cm and at the seawall 5.7cm.

3.3 Pressure mapping system: calibration

Particular attention was paid to the calibration of the system due the very short rise and duration times involved. Impact loads present a particular calibration challenge especially when a fluid-solid interaction is considered. Even if the non-uniform deformation of the fluid/water during impact is neglected, it still is very difficult to arrange a known calibration impact force with the same duration as a rapid event; wave impacts may affect the sensor as briefly as a few milliseconds.

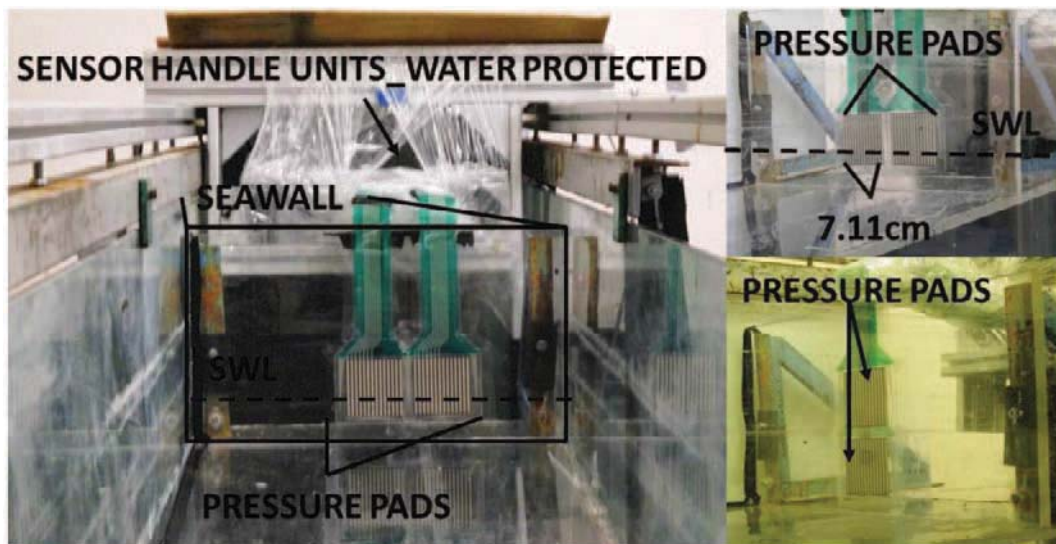


Figure 2: Pictures of the pressure pads used and placing at the seawall.

Hence, a drop test, calibration rig was especially designed and build based on the work of Müller et al. (2003). The apparatus consists of a drop tube, a cylindrical drop mass, and a pressure chamber linked to a smaller measuring / calibration chamber, referred to as the crack model in Müller et al. (2003).

The drop tube with an internal diameter of 6cm and a length of 36cm drives the cylindrical drop mass of 5cm diameter, 4 cm length and 0.94N (95.7gr) weight onto the circular opening of the water filled pressure chamber . The diameter of the drop mass was intentionally smaller than the guide tube in order to allow the escape of the air displaced during the free fall. The impact

induced pressure pulse travelled from the pressure chamber to the calibration chamber. Pressures at the upper part of the latter were measured using two ENDEVCO 8510B-5 transducers rated at 5PSI (35kPa). The pressure pad was fixed at the bed of the calibration chamber where by symmetry it was assumed that the pressure measured had to be the same as the one recorded by the transducers.

However, each sensor of the I-Scan system is somewhat unique in terms that during production slight variations may occur, which in turn may result in a non-uniform response of the system. Hence the manufacturer's instructions were followed and each pad was equilibrated using a known static force spreading equally at its surface; in this case a glass container filled with water and having the same base dimensions (7.1x7.1cm) as the sensing area (pad) was used.

3.4 Pressure mapping system: experimental expedition

The performance of the Tekscan VersaTeck I-Scan High Speed System against wave induced pressures was investigated in the wave flume and for the water conditions described in section 3.1. According to Hull and Müller (2002) plunging breakers are responsible for the most violent impacts and thus they were the only breaker type considered here. Results presented here refer to waves with periods between 3sec and 6sec and heights between 6cm and 10cm respectively.

4 Results

4.1 Pressure distribution at the seawall : Pressure pads horizontally placed

Figures 3, illustrates subsequent impacts at the vertical seawall for the same incoming wave conditions; $H = 6\text{cm}$ $T = 3.4\text{sec}$. Video frames (600 fps) of the impact are presented at the upper part of the image along with the corresponding records from the pressure pads; lower image part.

Impulsive pressures are originally recorded in the middle of the seawall and they are seen to propagate towards the flume's right side wall; from left to right in figures 3. Although an uneven longitudinal pressure distribution is not surprising, it is worth noticing that maximum impact pressures are recorded near the side wall and not at the middle of the seawall face. Apparently maximum pressures would have been ignored by an array of transducers placed along the centreline middle of the model structure.

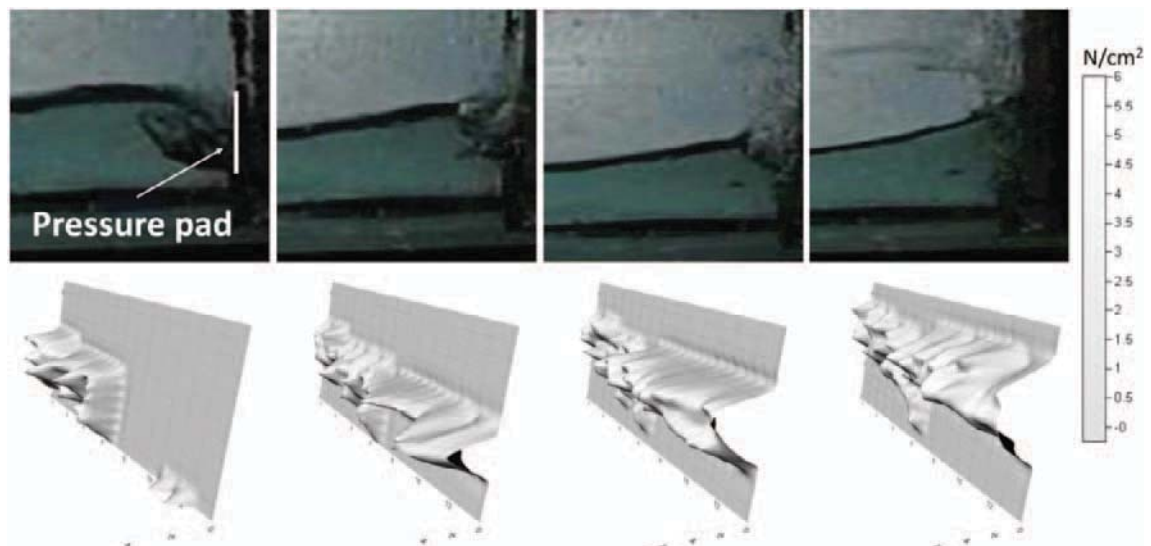


Figure 3: Above, video frames of a wave plunging at the seawall and below the corresponding pressure maps. Only the measuring area is represented in the maps and not the whole wall; $T = 3.4\text{sec}$ and $H = 6\text{cm}$.

4.2 Pressure distribution at the seawall: Pressure pads vertically placed

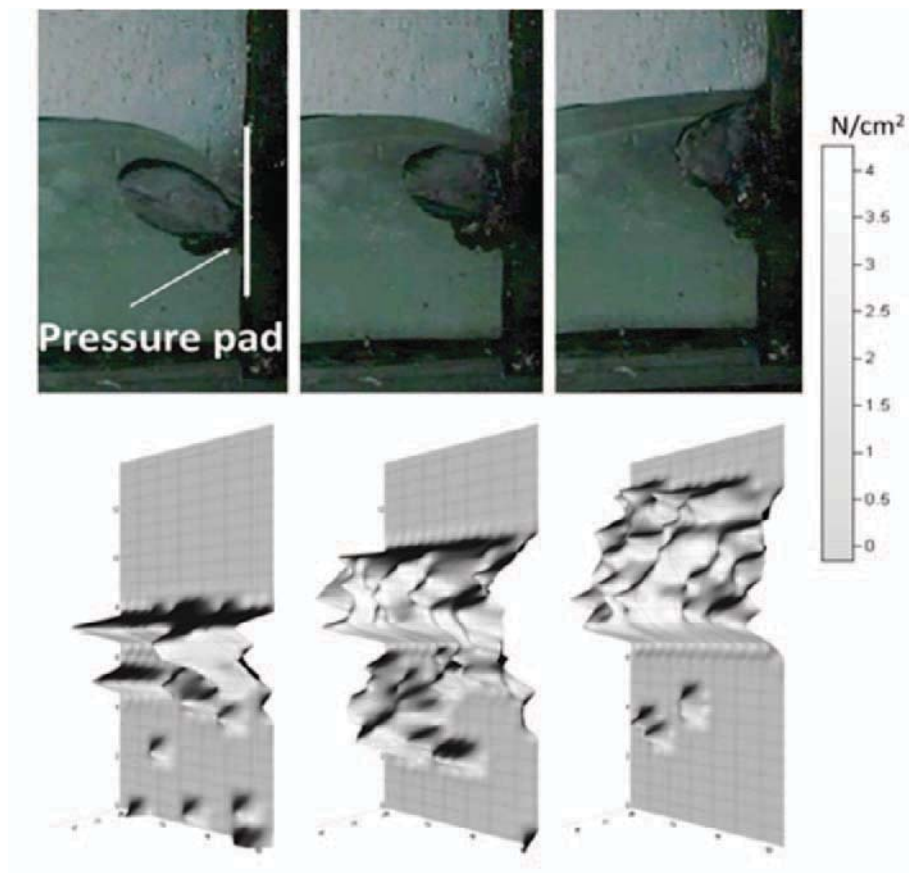


Figure 4: Above, video frames of a plunging wave forming a large air cavity and below, corresponding pressure maps.

Figure 4 presents the distribution of pressures induced by plunging waves forming an air cavity. As expected, the highest pressure zone is located at the point where the plunging jet interacts with the seawall. A longitudinal distribution of pressures was originally recorded followed by an upwards expansion and the creation of a 'pressure free' below the area of impingement. Although the overall horizontal pressure distribution agrees with the existing literature, the irregular spreading of high pressure peaks recorded constitutes an advantage of the proposed technology against traditional pressure transducers.

Finally, figure 5, depicts the time history of the normalised forces acting over the full area of both pads along with the 3D pressure frames for selected peaks. It is seen that large forces can be exerted not only from the impact but also due to high water accelerations (lower seawall part) and the subsequent quasi-static conditions (upper seawall part). The pressure maps corresponding to each force peak reveal a significant and uneven spread of pressures focusing near and slightly above the SWL prior to breaking and at the highest part of the seawall for post-breaking conditions.

Overall, a novel approach for the investigation of wave induced pressures is described here. The proposed technology can be combined with high speed videos allowing an optimized, compared with traditional transducers, overview of very interesting and important phenomena, like the cushioning effect of the air cavity formed between the plunging jet and the seawall.

5 Conclusions

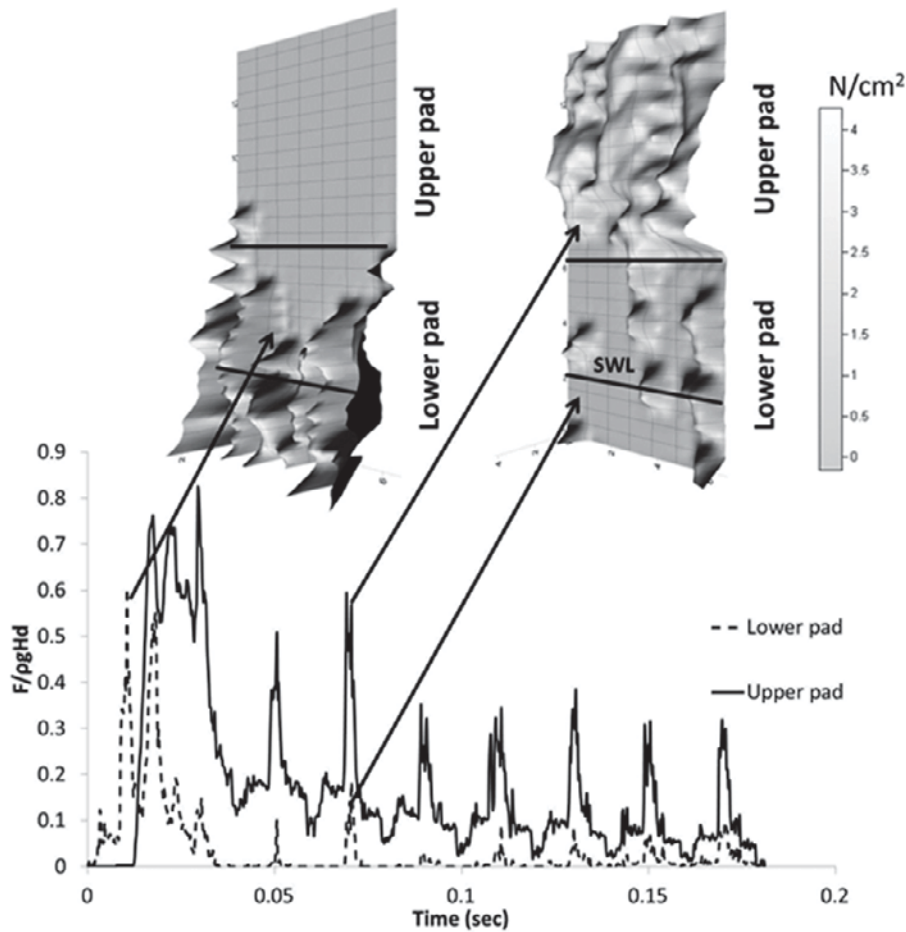


Figure 5: Time history of the normalised forces acting over the whole pressure pad and pressure maps corresponding to selected force peaks (dark arrows).

Through the transfer of technology from other fields of research, the simultaneous mapping of the horizontal and vertical distribution of impact induced pressures at the face of a vertical seawall has been achieved here. Both the size of the mapping area (here, 100cm^2) and the measuring resolution (here, 392 sensing points) cannot be achieved with traditional pressure transducers.

Accordingly, pressure maps were produced for waves breaking on a seawall. Results presented indicate the potential for maximum pressures to occur in areas of the seawall where least expected. The horizontal spreading resembles at first existing knowledge but an irregular distribution of peak pressures over time is also reported. Although further research is required in order to fully comprehend the capabilities and limitations of the pressure mapping technology used here, the use of such system with can provide views of a complex phenomenon never seen before by the coastal community.

6 References

- Archetti, R., Martinelli, L., Frigaard, P. and Lamberti, A., 2000. Horizontal coherence of wave forces on vertical wall breakwaters. Proc. of ICCE00, ASCE, Sydney, pp. 2058-2071.
- Blackmore, P.A. and Hewson, P.J., 1984. Experiments on full-scale wave impact pressures. Coastal Eng. 8, 331-346.
- Bredmose H. and Bullock G.N., 2010. Breaking wave impacts on coastal structures. Conf. of Adv. Computing and Technology, University of East London.

- Bredmose H., Peregrine D.H. and Bullock G.N., 2009. Violent breaking wave impacts. Part 2: modelling the effect of air. *J. Fluid Mech.* (2009), vol. 641, pp. 389–430.
- Bullock, G.N., Obhrai, C., Peregrine, D., Bredmose, H., 2007. Violent breaking wave impacts. Part 1: Results from the large-scale regular wave tests on vertical and sloping walls. *Coast. Eng.* 54, 602–617.
- Cuomo, G., Allsop, W., Bruce, T., Pearson, J., 2010. Breaking wave loads at vertical seawalls and breakwaters. *Coast. Eng.* 57, 424–439.
- Hattori M, Arami A, Yui T. 1994. Impact wave pressure on vertical walls under breaking waves of various types. *Coast. Eng.* 22:79– 114
- Hull, P. and Müller, G., 2002. An investigation of breaker heights, shapes and pressures. *Ocean Eng.* 29, 59–79.
- Miller, R.L., Leverette, S., Tochko, J. and Theriault, K., 1974. Field measurements of impact pressures in surf. In: *Proc. 14th Int. Conf. on Coastal Engineering*, Copenhagen. ASCE, New York, pp. 1762-1777.
- Muller G. U., Hull P., Allsop W., Bruce T, Cooker M, (2002). "Wave effects on blockwork structures: model tests." *IAHR Journal of Hydraulic Research*, 40, 117-124.
- Oumeraci, H., 1994. Review and analysis of vertical breakwater failures — lessons learned Special Issue on Vertical Breakwaters *Coastal Eng.* 22, 3–29.
- Tekscan, Inc., 2008. I-Scan and High Speed I-Scan User Manual. South Boston, MA 02127 pp. 223.

Experimental study on the stability of interlocking block placed revetments

Fabian Gier¹, Jens Mönnich², Hillel Rubin³, Holger Schüttrumpf¹ and Jentsje van der Meer⁴

Abstract

Revetments protect the shorelines of coasts, estuaries and rivers against wind waves, ship waves, currents and ice attacks. The resistance of revetments essentially depends on the properties of the cover layer. The resistance of interlocked pattern placed revetments depends on the weight of the individual stones and the block interlocking. In this study, extensive large scale model tests have been performed to assess the hydraulic stability of interlocked pattern placed revetments. The experimental results show a significant increase in the structural stability to wave attack of the revetment due to the block interlocking compared to traditional revetment elements.

1 General

Revetments are used to protect embankments against erosion at coastlines, estuaries and rivers. Concerning their construction, revetments are differentiated as rubble –, monolithic –, and block placed revetments. Furthermore, the group of block placed revetments can be subdivided into interlocked and loose block placed revetments. The following paragraphs primarily concern interlocked block placed revetments.

Regarding the interlocked block placed revetments (PIANC, 2011a) single blocks are force-locking connected over e.g. a horizontal, a vertical or a double bond structure (EAK, 1993). The application of interlocking systems produces an increase in stability against wave induced load compared with loose block revetments.

The Verkalit[®]-revetment block series of the Berding Beton GmbH belongs to the group of interlocked block placed revetments. The interlocking is ensured by an innovative key and slot system. The Verkalit[®]-revetment block series varies in material, block thickness and appearance of the key and slot system. In addition to other investigation, the stability against wave induced load of different types of Verkalit[®]-revetment blocks compared to loose revetment blocks with DIN EN 1338 was evaluated in this study by performing large scale model tests in the Large Wave Flume (LWF) Hannover.

2 Experimental setup and testing program

2.1 Experimental setup

Between November 2010 and March 2011, extensive large scale model tests were performed in the Large Wave Flume (LWF) in Hannover for the determination of the structural stability to wave attack of interlocked revetment blocks placed on a 1:3 sloped embankment in a scale of 1:1 (Figure 1).

¹ Institute of Hydraulic Engineering and Water Resources Management, RWTH Aachen University, Kreuzherrenstraße 7, 52056 Aachen, Germany, gier@iww.rwth-aachen.de, schuettrumpf@iww.rwth-aachen.de

² BERDING BETON GmbH, Industriestraße 6, 49439 Steinfeld, moennich@berdingbeton.de

³ Technion - Israel Institute of Technology, Faculty of Civil & Environmental Engineering, 32000 Haifa, Israel, hrubin@tx.technion.ec.il

⁴ Van der Meer Consulting BV, P.O. Box 423, 8440 AK, Heerenveen, The Netherlands, jm@vandermeerconsulting.nl



Figure 1: Reviewed Verkalit®-revetment blocks

The 1:3 sloped revetment was constructed on an embankment made of compressed sand core ($D_{50} = 0.35$ mm, $D_{10} = 0.19$ mm and $U = D_{60}/D_{10} = 38/19 = 2.0$) with an estimated hydraulic conductivity of $k_f = 1.0 \times 10^{-4}$ m/s. In order to investigate different revetment setups simultaneously, the slope was divided into two sections by a separation wall. The sequence of sublayers of the revetment was identical in all series of the experiments. On the profiled sand core, a geotextile layer ($k_f = 2.86 \times 10^{-3}$ m/s; $O_{90} = 0.1$ mm) was placed. The geotextile was covered with a 10 cm thick granular filter layer with a grain size from 2 to 16 mm. The cover layer consisted of the reviewed revetment blocks (Figure 1). The opening ratios of these revetment blocks were 3.3 % (loose revetment block with DIN EN 1338 180 mm), 3.0 % (Standard Verkalit®-revetment block 180 mm), 3.0 % (Open matrix Verkalit®-revetment block 180 mm), 5.8 % (Modified Verkalit®-revetment block 180 mm), 5.8 % (Modified Verkalit®-revetment block 250 mm). Structural details of the revetments in the 4 experimental periods are given in Table 1.

Table 1: Structure of the revetment in different experimental periods

Model-phase	Section	Revetment block				Grain filter					
		Description	length	Wide	height	weight	material	granulation	thickness	bulk density	porosity
		[-]	[mm]	[mm]	[mm]	[kg/m ²]	[-]	[mm]	[m]	[kg/m ³]	[%]
1	1	Standard Verkalit®- revetment block	300	300	180	412.76	Lime gritt	2 to 16	0.10	1731.00	17.65
1	2	Ordinary revetment block with DIN EN 1338	300	300	180	412.76	Lime gritt	2 to 16	0.10	1731.00	17.65
2	1	Standard Verkalit®- revetment block	300	300	180	412.76	Lime gritt	2 to 16	0.10	1731.00	17.65
2	2	Open matrix Verkalit®- revetment block	300	300	180	483.36	Lime gritt	2 to 16	0.10	1731.00	17.65
3	1	Standard-Verkalit®- revetment block	300	300	180	412.76	Lime gritt	2 to 16	0.10	1731.00	17.65
3	2	Modified Verkalit®- revetment block	300	300	180	401.84	Lime gritt	16to 32	0.10	1589.00	23.65
4	1	Modified Verkalit®- revetment block	280	280	250	518.76	-	-	-	-	-
4	2	Modified Verkalit®- revetment block	300	300	180	401.84	Lime gritt	16 to 32	0.12	1589.00	23.65

2.2 Test program

The model tests were performed with regular waves with a wave height H up to 1.90 m and wave spectra (JONSWAP-spectra) with a significant wave height H_s up to 1.40 m. All tests with wave spectra had a test duration of at least 1,000 waves. An overview of the test program with wave spectra is given in Table 1. To investigate the durability of the revetments, an additional long term test series were carried out with duration of up to 8 hours. The long-term tests consisted of the spectra JONSWAP D1, D2, D3 and D4 with a wave height H of 1.4 m, a wave period of 4.73 sec and duration of 2.0 hours each.

Table 2: Test program - wave spectra (Short term tests)

Test	Wave steepness s_0 [m]	Wave height H_s [m]	Wave period T_p [s]	Wave length L_0 [m]
JONSWAP 1	0.02	0.60	4.38	30.00
JONSWAP 2	0.02	0.80	5.06	40.00
JONSWAP 3	0.02	1.00	5.66	50.00
JONSWAP 4	0.02	1.20	6.20	60.00
JONSWAP 5	0.02	1.40	6.70	70.00
JONSWAP 6	0.04	0.60	3.10	15.00
JONSWAP 7	0.04	0.80	3.58	20.00
JONSWAP 8	0.04	1.00	4.00	25.00
JONSWAP 9	0.04	1.20	4.38	30.00
JONSWAP 10	0.04	1.40	4.73	35.00
JONSWAP Opt1	0.03	0.60	3.58	20.00
JONSWAP Opt2	0.03	1.00	4.62	33.33
JONSWAP Opt3	0.01	0.60	6.20	60.00
JONSWAP Opt4	0.01	1.00	8.00	100.00

3 Results of the experimental investigation

The assessment of the resistance of the revetment is performed by the dimensionless stability coefficient $H_s/(\Delta D_s)$ according to Pilarczyk (1992):

$$\frac{H_s}{\Delta D_s} \quad (1)$$

- with Δ = relative density of the placed block [-]
 D_s = thickness of the placed block, 20%-quantile [m]
 H_s = significant wave height at the foot of the embankment[m]

The relative density of the placed block Δ is calculated by:

$$\Delta = \frac{\rho_s - \rho_w}{\rho_w} \quad (2)$$

- with ρ_s = density of the placed block[kg/m³]
 ρ_w = density of water [kg/m³]

In connection with the dimensionless breaker parameter ξ_{op} , which contains the wave steepness and the slope angle, the stability coefficient gives information about the resistance of the tested revetment-layer. The breaker parameter ξ_{op} is defined as:

$$\xi_{op} = \frac{\tan \alpha}{\sqrt{\frac{H_s}{L_0}}} \quad (3)$$

with L_0 = wave length in deep water [m]
 α = slope angle, = 1:n [°]
 ξ_{op} = breaker parameter [-]

The wave length in deep water L_0 is defined as:

$$L_{0.0} = \frac{g}{2\pi} T_{m-1.0}^2 \quad (4)$$

with $T_{m-1.0}$ = wave period [s]

In Figure 2 and Figure 3, the stability coefficient for regular waves (Figure 3) and wave spectra (Figure 2) is plotted against the breaker parameter ξ_{op} . Each point in the diagram represents the maximum investigated load in the LWF for the different types of revetment blocks. If no failure occurred during the test phase, it could be concluded, that the revetment was able to resist wave load up to this stability coefficient $(H_s/(\Delta D_s))_{max}$. For the area above the stability coefficient $(H_s/(\Delta D_s))_{max}$, no statement concerning the resistance could be made.

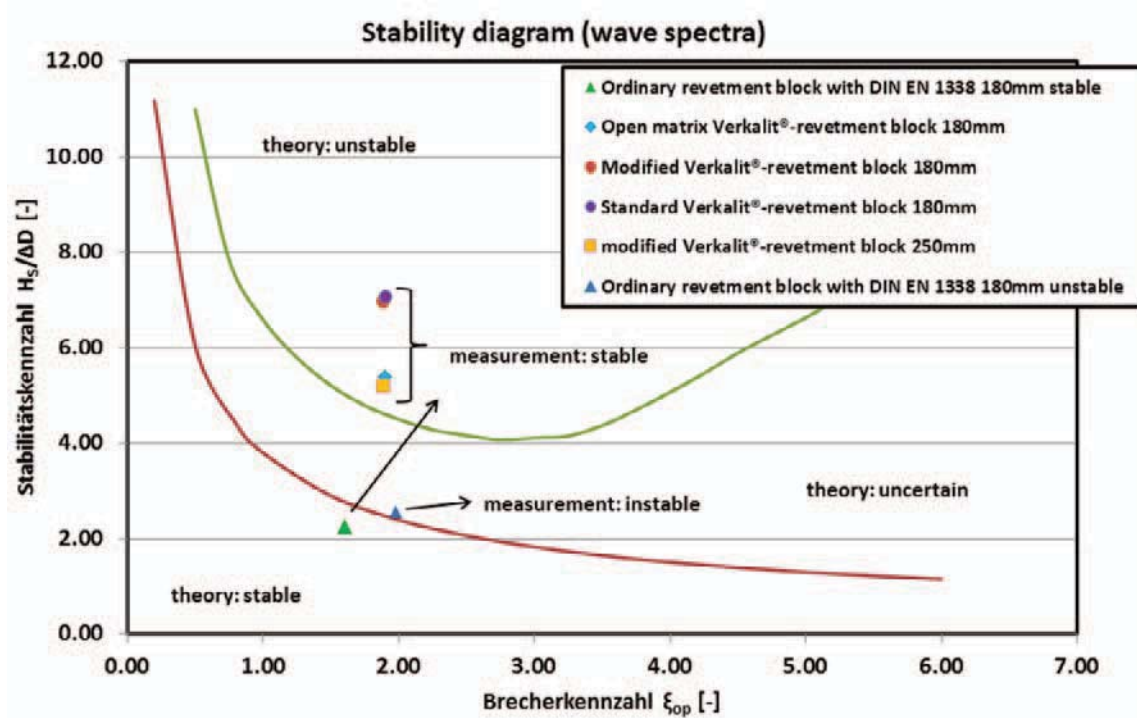


Figure 2: Stability chart of wave spectra (extended by Pilarczyk, 1992)

In the following paragraph information about values of maximum stability coefficients are provided obtained for regular waves and wave spectra, within which no significant deformations of the revetment structure during the model tests took place, namely no separation of single blocks out of the block layer could be identified, (results for regular waves are given in brackets):

1. Ordinary revetment block with DIN EN 1338 180 mm → $(H_s/(\Delta D_s))_{max} = 2.27$ (2.61)
2. Standard Verkalit®-revetment block 180 mm → $(H_s/(\Delta D_s))_{max} = 7.08$ (7.12)
3. Open matrix Verkalit®-revetment block 180°mm → $(H_s/(\Delta D_s))_{max} = 5.39$ (3.39)
4. Modified Verkalit®-revetment block 180°mm → $(H_s/(\Delta D_s))_{max} = 6.99$ (5.45)
5. Modified Verkalit®-revetment block 250 mm → $(H_s/(\Delta D_s))_{max} = 5.21$ (5.24)

For comparison the stability functions according to Pilarczyk (1992) were plotted in the charts (Figure 2 and Figure 3). They indicate that the ordinary revetment block with DIN EN 1338 followed exactly the theoretical calculation (Figure 2). (note: To protect the measuring instruments in the LWF, the extraction of single blocks out of the revetment was not tolerated! The model tests were stopped shortly before the ordinary revetment block failed. The data of this model test define the failure point). In spite of the operation of the wave generator at its power limit it was impossible to load up the different types of the Verkalit revetment block to the point of failure, although the theoretical stability coefficients indicate a failure of common ordinary revetments. This result implies the benefit on stability by using the key and slot locking system. The Standard-Verkalit®-revetment block as well as the modified Verkalit®-revetment block reached at least 2.3 times higher stability coefficient in comparison to the ordinary revetment block with DIN EN 1338 without failing.

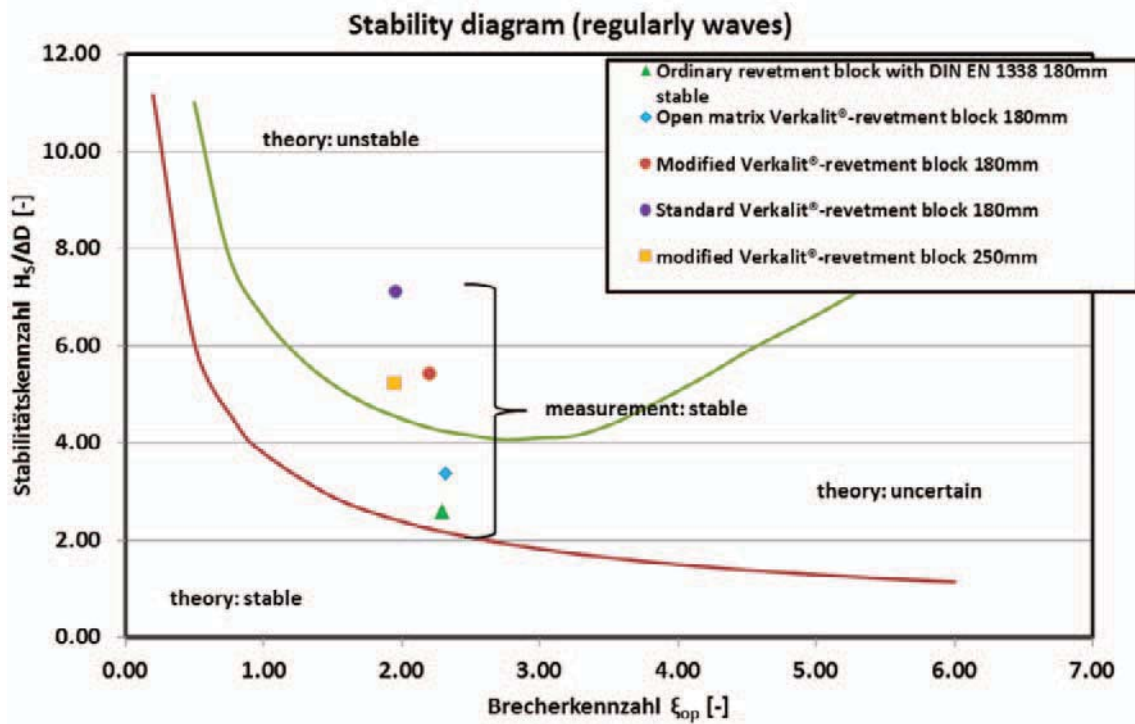


Figure 3: Stability chart of regular waves (extended by Pilarczyk, 1992)

4 Summary

A quantification of the stability of interlocked revetment blocks in comparison to traditional loose revetment blocks has not been possible until now. To quantify the benefit on stability of the Verkalit®-revetment blocks by using a key and slot locking system, extensive experimental investigations were performed in the LWF Hannover. The test results imply that the interlocked revetment blocks show at least a 2.3 higher stability coefficient compared to the ordinary revetment block with DIN EN 1338 under wave attack. In contrast to the ordinary revetment block with DIN EN 1338, it was impossible to load up the interlocked revetment blocks within the investigation and the maximum possible wave load to the point of failure.

5 References

- Bezuijen, A.; Klein Breteler, M.; Pilarczyk, K. W. (1986): Large-Scale Tests on a Block Revetment Placed on Sand with a Geotextile as Separation Layer. In: 3rd International Conference on Geotextiles, Vol. 2. Wien: Österr. Ingenieur- u. Architektenverein, (Proceedings / 3rd International Conference on Geotextiles / 7.-11.4.1986, Vienna/Austria ; Vol. 2; pp. 501-505.
- EAK (2003): Empfehlungen des Arbeitsausschusses Küstenschutzwerke der HTG und DGGT. Heide: Westholsteinische Verl.-Anst., Boye
- PIANC WG 57 (2011a): Stability of pattern placed revetment elements. Report of Expert Group 57 (expected release end of 2011)
- Pilarczyk, K. W. (1992): Dutch experience on design of dikes and revetments. In: Coastal Engineering Practice '92 : Proceedings of a Specialty Conference on the Planning, Design, Construction, and Performance of Coastal Engineering Projects, Long Beach, California, March 9 - 11, 1992 / Hughes, S. A. (ed.), New York, N.Y: ASCE, - ISBN 0-87262-866-3

Poster Presentations

Investigation of the effect of permeability on wave interaction with a barrier by application of PIV

Hany Ahmed¹, Andreas Schlenkhoff²

Abstract

Integrating a permeable part into a coastal barrier can substantially decrease its environmental impact. The application of PIV has become state-of-the-art in analyzing velocity fields. PIV can also be used for determination of the reflection and transmission coefficient, which will be shown in the study. The performance of such structures and their effect on permeability interacting with waves should be known. Therefore, wave interaction with a permeable wall has been investigated in a glassed-wall wave flume on a scale model modifying its permeability. The results gathered by PIV have been compared with the calculated wave particle velocities by the linear airy theory. The results of PIV are perfectly acceptable. Further, the velocity distribution of the incident, co-existing and transmitted wave are recorded and the reflection and transmission coefficients are calculated via PIV. The reflection and transmission coefficients calculated by the velocity distribution indicate an efficient performance of the permeable breakwater to reduce wave energy in shoreward.

Keywords: Coastal structures, Permeable breakwater, Velocity measurements, PIV application.

1 Introduction

Recently, permeable breakwaters, which have a smaller impact on the environment and provide a more economical protection from waves and currents, have been suggested to overcome the disadvantages of fully protection breakwaters.

Permeable barriers have the advantage of reducing wave reflection on the up wave side of the barrier. However, in many cases, vortexes and severe turbulent flow through the barriers near the seabed are generated. In order to increase the protection of harbours and beaches against waves and currents to an acceptable level as well as to reduce the side effect, it is proposed to use vertical barriers with impermeable structures in the lower and upper part and a permeable structure in the middle part. This type of breakwater is complex, where the lower part is considered as a submerged breakwater, the middle part as a slot barrier and the upper part as a semi-submerged vertical wall as shown in Fig. 1. The flow behaviour through this type is complex and demands further studies to find out the hydrodynamic characteristics and efficiency concerning the response to waves.

There are many commonly ways, which have been used to investigate the hydrodynamic characteristics and to assess the hydraulic performance of permeable breakwaters. Some of them are numerical and others are experimental. Numerical solutions have been developed on the basis of the boundary element method (Liu and Abbaspour, 1982), the Eigen function expansion method (Abul-Azm, 1993; Isaacson et al., 1998; Isaacson et al., 1999) and Green's Identity formula (Balaji and Sundar, 2004). The hydrodynamic characteristics of a permeable breakwater like reflection, transmission and energy dissipation coefficients can be measured in the laboratory by (Ultrasonic) wave gauges depending on a three point based approach of Mansard and Funke (1980).

In recent years, Particle Image Velocimetry (PIV) is one of the optical methods which have been increasingly applied to velocity measurements and also to find out the interaction of waves with structures. Some applications are the investigation of the interaction of wave induced flow fields with wave damping structures and semi-submerged breakwaters (Belorgey et al., 1986).

¹ Irrigation and Hydraulic Department, Al-Azhar University, Egypt. PhD. Student at Wuppertal University, Germany.
E-mail: hanygo3177@yahoo.com.

² Hydraulic Engineering Section (IGAW), Civil Engineering Department, Wuppertal University, Germany

Lengright et al. (2000) presented PIV for wave-structure interactions of monochromatic waves and a semi-submerged vertical wall. Cowen et al. (2003) used PIV to make vertically resolved two-dimensional measurements in swash zone flows, which are notoriously recalcitrant to quantitative measurement by PIV.

In the present study, laboratory tests have been performed to assess and optimize the accuracy of PIV due to adaption of the time increment between two frames. The results gathered by PIV have been compared with the wave particle velocities calculated by the linear airy theory. The velocity distribution of the incident, co-existing and transmitted wave are recorded via PIV to detect the reflection and transmission coefficients of the vertical slotted wall.

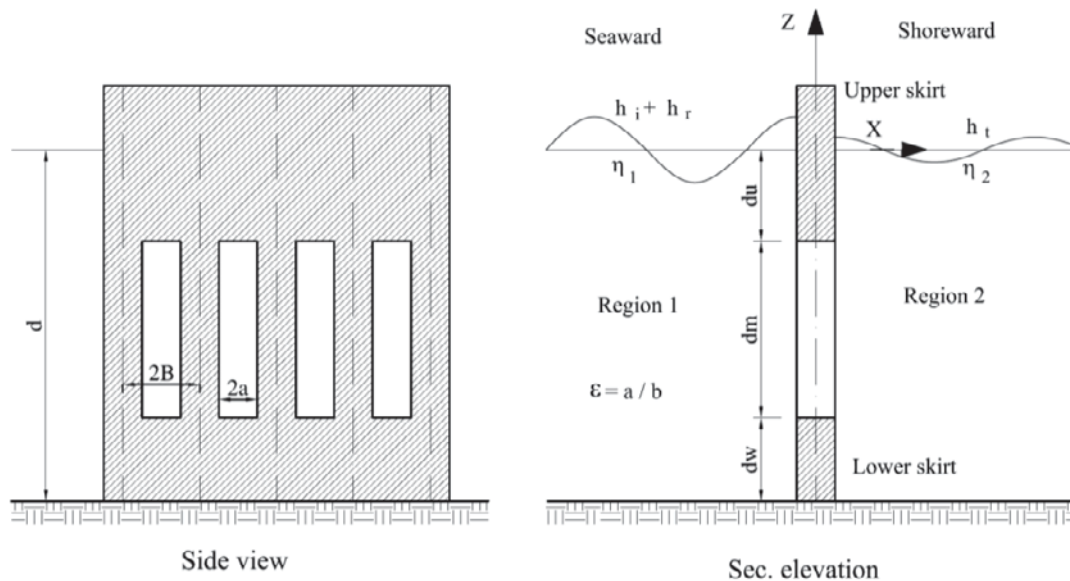


Figure 1: Definition sketch for a vertical slotted wall

2 Experimental set-up

The experiments have been conducted in the glassed wall wave flume of the University of Wuppertal as shown in photo 1. The flume is 24 m long, 0.30 m wide and 0.5 m deep. Tests were carried out with a constant water depth of $d = 0.3$ m. Waves are generated by a single paddle wave actuator located at the up-wave end and driven by a digital motor to which signals can be provided with high precision. An artificial parabolic beach is located at the down-wave end of the flume in order to minimize wave reflection. The proposed permeable breakwater model is a single vertical slotted wall and constructed of vertical panels with a width of 2.5 cm, and a thickness of 2.5 cm. The porosity of the slotted part of the barrier is 50 %. The draft of the permeable part is $dm = 0.2 d$. The upper and lower parts are impermeable with a draft of $0.4 d$. The model is tested under regular waves. The camera is placed at 1.5 m (focus) from the centre of the flume. Measurements of the velocity field are performed at a distance of 12.2 m from the wave maker using a high speed camera (Motion Scope M3), where the model, the light settings, and measurement devices are constructed as shown in photo 2. The wave-frequencies are 2 and 0.75 Hz, the corresponding wave heights are 1 and 4 cm. The resolution of the camera is 624x512 and 1200x704 (square pixels), the field of views are 22.5x18.5 and 42.5x24.5 cm², the sampling intervals are 0.001 and 0.002 s and the time between two selected frames are 0.008 and 0.014 s respectively. The model is situated in a distance of one wave length in front of the centre field of view (FOV) for transmission measurements and situated in a distance of one wave length behind the centre of FOV for reflection measurements. It is essential that the measurements must be terminated before any reflected wave is returning from both the flume end and the wave maker to the measurement position.

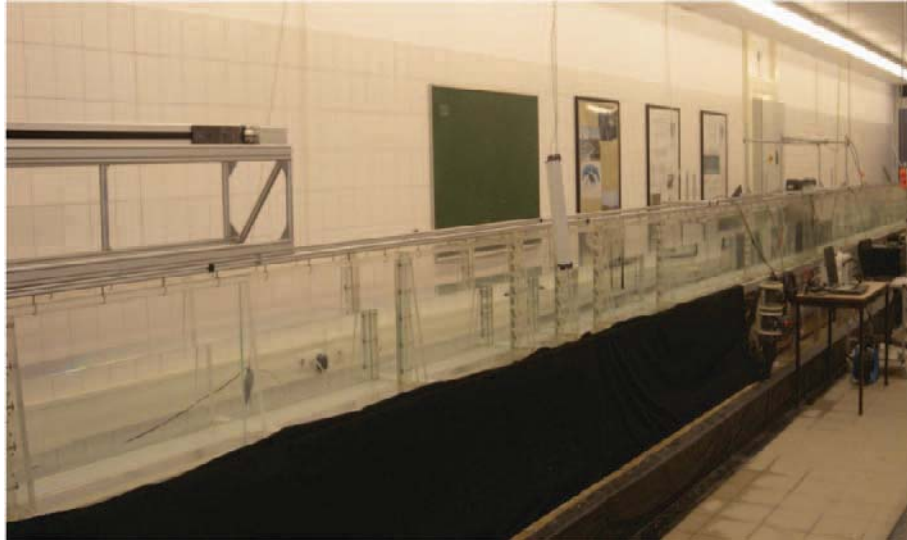


Figure 2: General view of the wave flume.

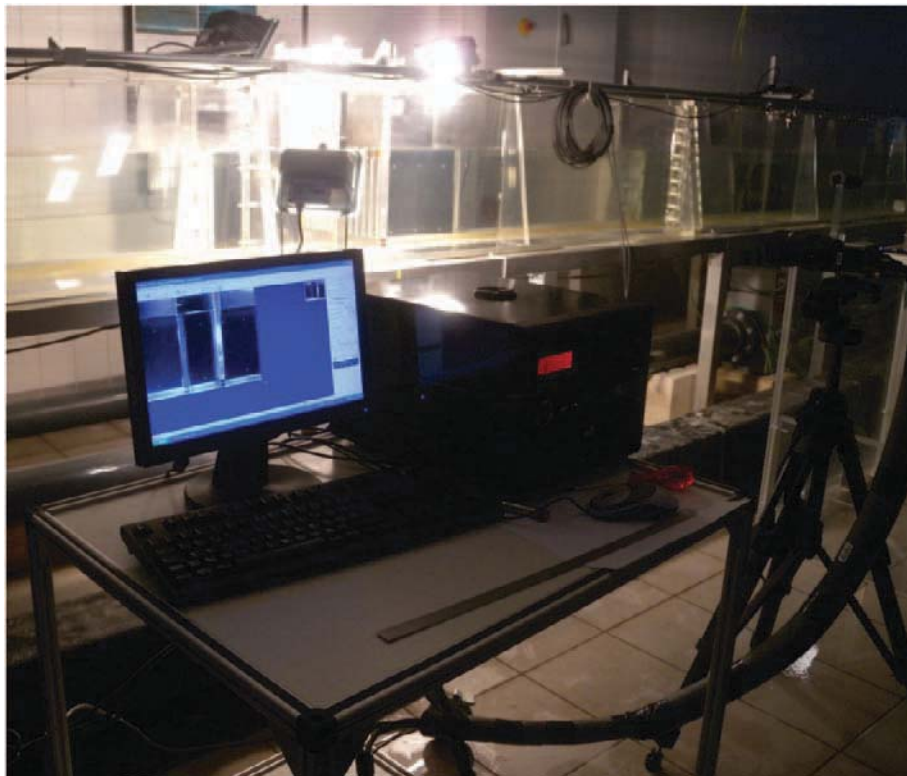


Figure 3: View of measuring devices, light settings and the model.

3 Results and discussion

3.1 Effect of the relative time increment $\delta t / T$

The accuracy of the velocity measurement by PIV can be optimized by tuning the time increment δt . The wave-frequencies are 2, 1.75, 1.5, 1.25, 1 and 0.75 Hz, and the corresponding wave heights are 1, 1, 2, 2, 3 and 4 cm respectively. The Field Of View (FOV), the sampling interval and the resolution of the camera are carefully taken to fit with the wave lengths.

Figure 2 shows the relation between the relative time increment $\delta t / T$ and the relative horizontal particle velocity U_{-ex} / U_{-th} where U_{-ex} is the measured horizontal particle velocity by PIV, U_{-th} is the calculated horizontal particle velocity by linear airy wave theory and T is the wave period. The accuracy of the measured wave-particle velocity is affected by the time increment δt . It is noted that the error is large for a small analysis time where the error is more than 30% at $\delta t / T < 0.01$ for short waves and the error is more than 20% at $\delta t / T < 0.0025$ for intermediate wave. The error for intermediate waves is reduced by increasing the relative time increment while the error for short waves is reduced only gradually. The relative time increment should be taken in a range of $0.01 T < \delta t < 0.015 T$, such that the error of the measurements will be less than $\pm 5\%$ within this study. The achievable accuracy of PIV measurement within this set-up is shown to be limited by the influence of the relative time increment $\delta t / T$.

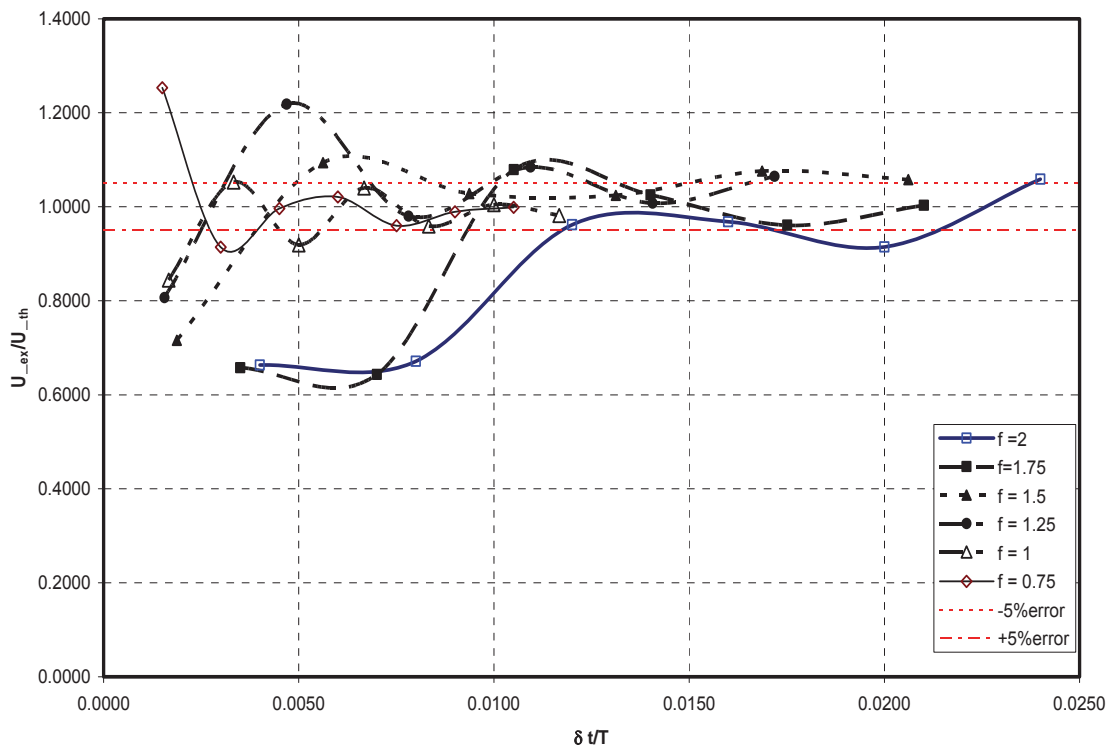


Figure 4: The relation between the relative horizontal particle velocity and the relative time increment.

3.2 Velocity measurement of the incident wave

Figure 3(a:f) shows the velocity magnitude for incident waves which are investigated during the experimental work. Properties of the waves, the samples and the field are shown in detail in table 1. The measurements illustrate the extent of compatibility between PIV and the linear airy theory where the high particle velocities are located at the surface. The particle velocity of intermediate waves diminish in amplitude with depth while the particle velocity of the short-wave vanishes after the mid-depth as shown in sub-figures 3a and 3b respectively.

Table 1: The details of the waves, camera and the Field Of View.

Frequency of waves (Hz)	Wave height h_i (m)	Frame rate of Camera (fps)	Time between selected frames (s)	Resolution (Square pixels)	FOV (cm ²)
2.00	0.01	1000	0.008	624*512	22.5*18.5
1.75	0.01	1000	0.008	624*512	22.5*18.5
1.50	0.02	800	0.009	800*576	28.5*20.5
1.25	0.02	800	0.011	800*576	28.5*20.5
1.00	0.03	600	0.010	1024*768	36.5*26.5
0.75	0.04	500	0.014	1200*704	42.5*24.5

3.3 Comparison between PIV and linear wave theory

The comparison between the water-particle velocity measured via PIV and the linear wave theory of incident waves can be carry out through a comparison of the velocity or one of its components (u or v). The comparison by one of the velocity components is adopted in this study where the maximum horizontal velocity at the crest of the wave is taken as a reference. The recorded velocities have been decomposed into horizontal and vertical components u and v in the x and z direction respectively. The comparison is conducted by the horizontal component u and the results are reported in table 2. The error percentage is higher for high frequencies where the error is more than 3% and lesser for lower frequencies where the error is less than 0.2%. The velocities of higher frequencies are small and the error increases with decreasing the velocities. The results of PIV are perfectly acceptable for high velocities and satisfactory to some extent in the case of low velocities.

Table 2: Comparison between PIV measurements and the theoretical horizontal water-particle velocities at the crest of the wave.

Frequency Hz	water depth (m)	Wave height h_i (m)	Maximum u (m/s) Linear theory	Maximum u (m/s) measurements	Error percent
2.00	0.3	0.01	0.063	0.0610	3.17 %
1.75	0.3	0.01	0.055	0.0564	-2.53 %
1.50	0.3	0.02	0.095	0.0973	-2.4 1%
1.25	0.3	0.02	0.082	0.0826	-0.77 %
1.00	0.3	0.03	0.107	0.1075	-0.47 %
0.75	0.3	0.04	0.129	0.1288	0.16%

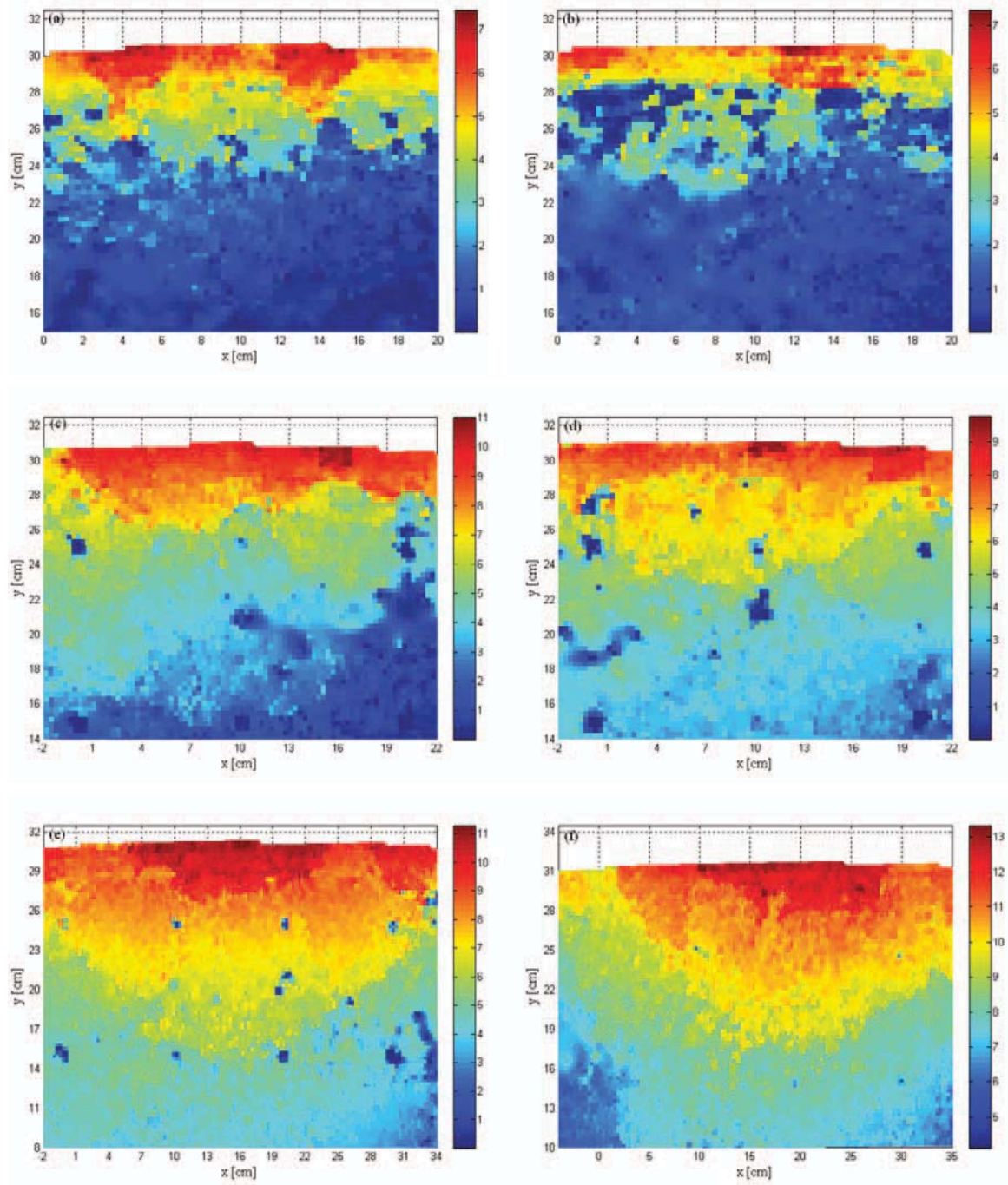


Figure 5: Velocity magnitude (cm/sec) of incident waves when the wave crest is within the VOF. a) for $f = 2$ Hz and $h_i = 1$ cm, b) for $f = 1.75$ Hz and $h_i = 1$ cm, c) for $f = 1.5$ Hz and $h_i = 2$ cm, d) for $f = 1.25$ Hz and $h_i = 2$ cm, e) for $f = 1$ Hz and $h_i = 3$ cm and f) for $f = 0.75$ Hz and $h_i = 4$ cm.

3.4 The effect of permeability on the transmitted wave

The effect of permeability can be investigated by the horizontal velocity distribution as shown in figures 4 and 5 which illustrate the horizontal velocity distribution at the crest of incident, co-existing and transmitted wave for both high frequency $f = 2$ Hz (short wave) and lower frequency $f = 0.75$ Hz (intermediate waves) respectively.

Generally, the amplitude of the horizontal velocity decreases with depth. Note that for short waves the orbits vanish after $0.5 d$ but for intermediate waves the orbits diminish in amplitude with depth and also become flatter. The orbit velocity of incident and transmitted waves agree with those of the linear airy theory. The co-existing wave is the arithmetic difference of the incident and the measured wave as defined in equation (1). The hydrodynamic performance of this model in reducing the wave energy can be investigated through the horizontal velocity distribution of the incident, co-existing and transmitted wave where the velocity is a measure of wave energy. The reflection and transmission coefficient (CR&CT) have been determined by measuring the maximum horizontal velocity of the co-existing u_{co-max} and the maximum horizontal velocity of the transmitted wave u_{t-max} at the crest of the wave as a reference point and comparing it with the maximum horizontal velocity of the incident wave u_{i-max} as follows

$$u_{r-max} = u_{i-max} - u_{co-max} \quad (1)$$

$$CR = \frac{h_r}{h_i} = \frac{u_{r-max}}{u_{i-max}} \quad (2)$$

$$CT = \frac{h_t}{h_i} = \frac{u_{t-max}}{u_{i-max}} \quad (3)$$

The results for the reflection and transmission coefficients are reported in table 3. It is noted that, the reflection and the transmission coefficient are 95 % and 4 % for waves of ($f = 2$ Hz) and 57 % and 48 % for intermediate waves ($f = 0.75$ Hz) respectively. These results are also compatible with results of a numerical model based on an Eigen function expansion method (Ahmed and Schlenkhoff, 2010). Finally, the reflection and transmission coefficients calculated by the velocity distribution indicate an efficient performance of the permeable breakwater to reduce the energy of waves in shoreward.

Table 3: Calculation of the reflection and transmission coefficients.

Frequency Hz	Water depth (m)	Wave height h_i (m)	Maximum u_{i-max} (m/s)	Maximum u_{co-max} (m/s)	Maximum u_{t-max} (m/s)	CR	CT
2	0.3	0.01	0.0636	0.0030	0.0027	0.95	0.04
0.75	0.3	0.04	0.1276	0.0546	0.0613	0.57	0.48

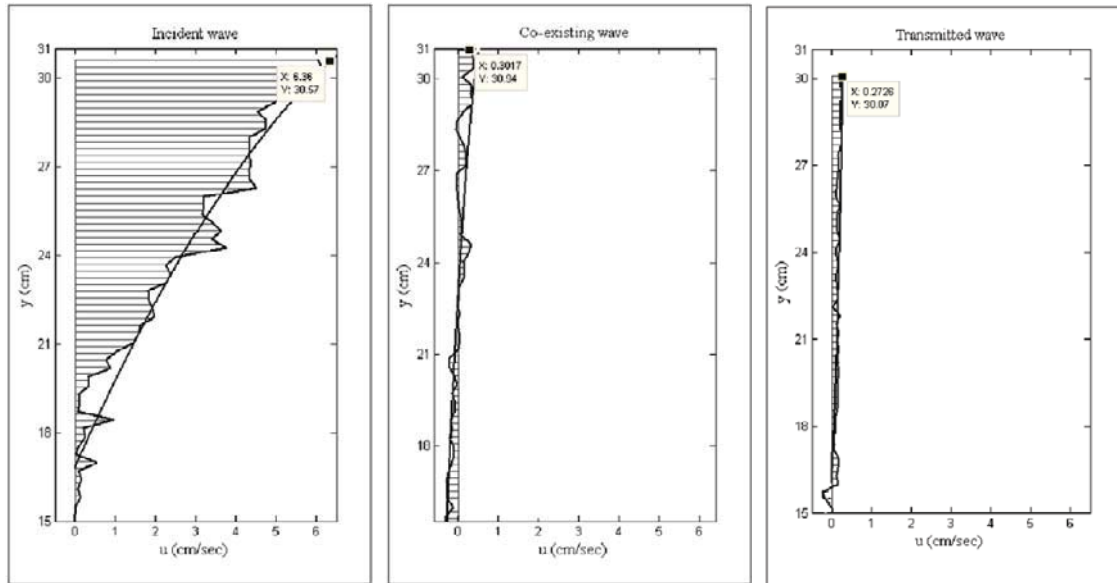


Figure 6: The distribution of the horizontal velocity of incident, co-existing and transmitted waves at the wave crest for the frequency of wave $f = 2$ Hz, and $h_i = 1$ cm

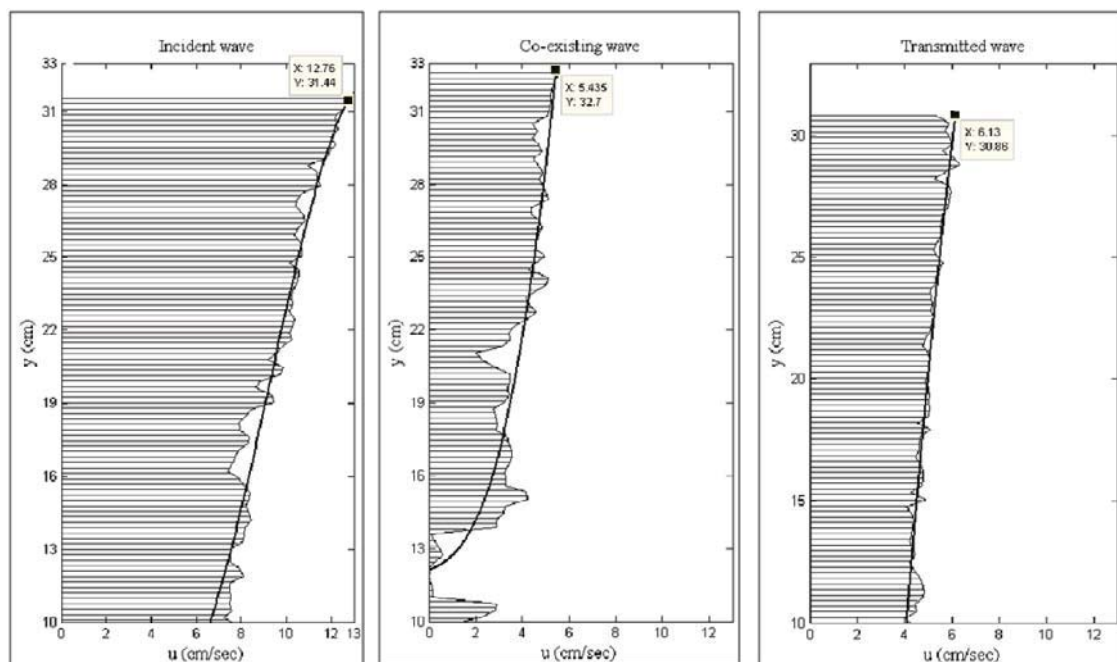


Figure 7: The distribution of the horizontal velocity of incident, co-existing and transmitted waves at the wave crest for the frequency of wave $f = 0.75$ Hz, and $h_i = 4$ cm.

4 Conclusions

This study describes the measurement of the velocity field induced by waves. The results gathered by PIV have been compared with wave particle velocities calculated by the linear airy theory. The measurements of PIV are perfectly acceptable for high velocities and satisfactory to some extent for low velocities.

The accuracy of PIV is depending on the selection of the time increment and the results indicate that, a high accuracy can be achieved within this study by fine tuning of the relative time increment $\delta t / T$.

In addition to that, PIV is employed for determining the reflection and transmission coefficients by investigating the velocity distribution in front of and behind a model of a slotted barrier and to present the influence of the permeability in reducing wave energy. The calculated reflection and transmission coefficients indicate an efficient performance of the permeable breakwater to reduce the energy of waves in shoreward. Therefore, the permeable structure shows an encouraging performance.

5 References

- Abul-Azm, R. G., 1993. "Wave diffraction through submerged breakwaters", *J. of Waterway, Port, Coastal and Ocean Eng.*, 119 (6), 587-605.
- Ahmed, H. & Schlenkhoff, A., 2010. "Wave interaction with vertical slotted wall" In Proc.1st International Conf. on Coastal Zone Management of River Deltas and Low Land Coastline, Egypt. Session 8, pp 33-48.
- Balaji, R., and Sundar, V., 2004. "Theoretical and experimental investigation on the wave transmission through slotted screens", *Oceanic Engineering International*, 8(2), 69-90.
- Belorgey, M., Bas, J. Le., J., & Grandjean, A., 1986. "Application of the Laser Doppler Velocimeter to the study of the turbulence generated by the swell in the vicinity of walls or obstacles." Proc. 3rd International Conf. on Application of laser Anemometry to Fluid Mechanics, Lisbon, Portugal.
- Cowen E. A., Sou I. M., Liu, p. L. F. & Raubenheimer, B., 2003. "Particle Image Velocimetry measurements within a laboratory-generated Swash zone." *J. of Eng. Mech. ASCE*, Vol. 129, No. 10, pp. 1119-1129.
- Isaacson, M., Premasiri, S., and Yang, G., 1998 "Wave interaction with vertical slotted barrier", *J. of Waterway, Port, Coastal and Ocean Engineering*, 124 (3), 118-125.
- Isaacson, M., Baldwin, J., Premasiri, S., and Yang, G., 1999. "Wave interaction with double slotted barrier", *Applied ocean research*, 21, 81-91.
- Lengright, J., Graw, K-U. & Kronewetter, H., 2000. "Stereoscopic PIV adapted to gravity wave analysis." Proc. 10th Int. Symp. Appl. of Laser Tech. to Fluid Mech., Paper 14.4. Lisbon, Portugal.
- Liu, P.L.-F, Abbaspour M., 1982. "Wave scattering by a rigid thin barrier". *J. of Waterway, Port, Coastal and Ocean Eng. Div. ASCE*, 108 (4), 479-491.
- Mansard, E .P. D. and Funke, E. R., 1980. "The measurement of incident and reflected spectra using a least squares method", In Proc. 17th Coastal Eng. Conf., Sydney, Australia, pp 159-174.
- Sveen, J. K., 2004. "An introduction to MatPIV v. 1.6.1." Department of Math. Mechanics and applied Mathematics, , No. 2, University of Oslo, Norwegian.

Monitoring phases of the re-naturalization process of the Torre del Porto beach

Corrado Altomare¹ and Girolamo Mauro Gentile²

Abstract

This shingle beach of Torre del Porto has been affected, during the last 30 years, by a huge erosive phenomenon. The causes which led to the erosion and the design lines through which to obtain the re-naturalization are identified. The lines of the project involved to entrust assorted rubble pebbly stones with a proper size. In this way the natural formation process could unfold again its effectiveness and the beach is get back. The monitoring of the sediment transport was essential to provide the information about the correct results of prediction and analysis of the nourishment. The monitoring phases are described in this paper.

Keywords: nourishment; re-naturalization; monitoring.

1 Introduction

The coast of the town of Mattinata runs along the north-east stretch of the Manfredonia Gulf, in the South of Italy. In its sections, from the boundary with the territory of Monte St. Angelo, is set the pebble beach called "Torre del Porto". This beach has always been a real asset to the promontory of Puglia Region, both for its size (about 2 km long, 35 meters wide on average) than for its capacity to accommodate a large number of bathers.

The beach of Torre del Porto showed, since 1980, a steady decrease in the total volume of sediment. The volume depletion, slow in its initial phase, led to a retreat of the beach dramatically highlighted as a result of storms occurring in December 2002. About 600m in length disappeared, concrete fences were torn down and the waves attacked also the walls of the private properties.

The innovative methodology adopted for the nourishment, implemented in the "Perfect Storm" software (G.M. Gentile), once discovered the natural process that led to the formation of the beach, identified the causes which led to the crisis and pointed out to the same process design lines through which obtaining the re-naturalization of the beach.

Once that the first reason of the crisis of the natural formation process of Mattinata beach was identified in the lack of contribution of sediment to the coast from hinterland, and verified the "energy closure" of the bend in which the beach is set, the project involved to entrust assorted rubble pebbly stones with dimensions calculated basing on the characteristics of the wave action. In this way the natural formation process of the beach was re-activated leading to the nourishment of the eroded stretch.

Three monitoring phases have been carried out, using different methodologies, in order to increase knowledge of the complex phenomena taking place and verify the hypothesis and results of the predictions done.

2 Brief history of the erosion leading to the disappearance of the beach at Torre del Porto

The beach, whose position and morphology are shown in fig. 1, underlies a fetch area identified by the wind directions from 60N to 160N degrees.

¹ PhD, Laboratori d'Enginyeria Marítima (LIM), Universitat Politècnica de Catalunya (UPC), Jordi Girona, 1-3, Edif. D1, Barcelona, 08034, Spain, corrado.altomare@upc.edu

² Civil and environmental engineering Department (DICA), Technical University of Bari, via E. Orabona, Bari, 70125, ITALY, gentilegirolamo@libero.it

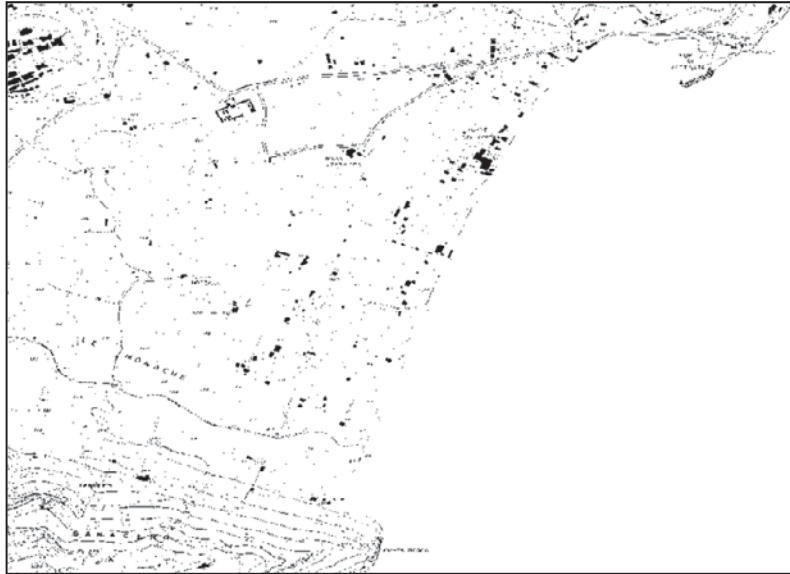


Figure 1: Map of the beach of Torre del Porto (Mattinata, FG) – Italy

In the 50s the beach of Torre del Porto, consisting of limestone pebbles, had an average width of 35 m for 2 km in length. The figures 2 and 3 show, respectively, from opposite points of view, the beach in the 50s and in the 80s. The consistency of beach at Torre del Porto, as the photos show, it was virtually unchanged at the beginning of the 80s.



Figure 2: The beach of Torre del Porto in the 50s.



Figure 3: The beach of Torre del Porto in the 80s. The arrows show the position of the walls of private properties, referred to the shoreline.

Since 1995, the beach showed a reduction in its cross section. At the beginning of December 2002, a storm caused the disappearance of the remaining beach and the walls of the private properties fell down, then another storm, between the 28th and the 30th of December 2002, eroded about 25 meters of private property that extended beyond the walls (fig. 4).

At the end of 2002, the beach of Torre del Porto was no more.



Figure 4: The waves of the storm of 28th and 29th of December 2002 completely eroded the beach and over the walls that border private property.

3 The re-naturalization of the beach: an innovative methodology

Perceived as a necessary requirement for bringing back the beach of Torre del Porto in its original extension, an innovative and tested methodology has been adopted (Gentile-Giasi 2000, 2001, 2003). It is based on the identification and subsequent reactivation of the natural formation processes of the coastal area. The used methodology designs interventions which, being inserted in the natural process of formation of the beach, reactivate the process itself and naturally lead to the nourishment of the beach.

3.1 The identification of the natural formation process

The identification of the nourishment process consists of:

- the creation of a database that merged the data obtained from historical research, the meteorological anemometry data, synoptic tables, finally allowing a cross comparison among these;
- the assessment of the wave energy pattern that characterizes the beach.

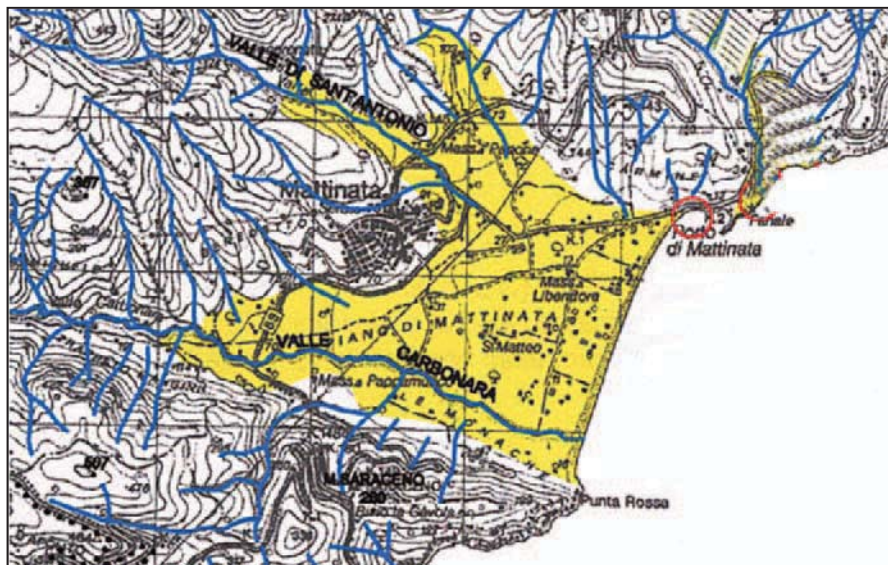


Figure 5: The beach of Torre del Porto and the Carbonara torrent.

The historical research has highlighted the role of the sediment transport of the Carbonara

torrent. More sources confirmed that this torrent, until 1970, had brought a lot of stones to the shoreline. The stone weight was between a few hundred grams and 5 kg. The data showed that since 1970, the decreased rainfall had not allowed the sediment to reach the shoreline. Therefore during the last 30 years, due to the climate changes, the Carbonara torrent no longer transported the sediments, in particular pebble stones, to the littoral stretch of Torre del Porto.

The energy pattern of the beach was identified by determining the resulting energy fluxes *FER* (SPM 1977, 1984), that, acting along each straight section in which it was sketched on the beach, move the sediment along the coast. The calculation of the wave energy applied to each section was performed by means of Perfect Storm, using the following input data: wind three-hour records, collected between 1951 and 2000; aerial photogrammetry of the shoreline; relief of the beach of Torre del Porto.

The steps of analysis were:

- the identification of anemometrical data that caused storm surges that can reach the coast near the town of Mattinata;
- the identification of wind data capable of determining a wave conditions likely to induce the transport of the sediments;
- the creation of a database of effective winds, using the results of the previous steps;
- the identification of the "wind events" that can provoke storms that reached the coastline. More than 1700 storms are identified, each of them in direction, significant wave height and period in deep water, and the duration of the event.

Once the energy flux, that each individual storm has applied to 12 sections individuated, has been evaluated, the balance of the energy fluxes, applied by all the 1700 identified storms, was calculated, by assessing the value of the resulting energy flows *FER* (see table 1 and fig. n. 6) that occurred during the entire analysed period (1951-2000).



Table 1: Resulting energy flows along the beach.

Stretch	FER
0-1	-2.015E+08
1-2	-1.820E+08
2-3	-1.822E+08
3-4	-1.262E+08
4-5	-1.474E+08
5-6	-8.814E+07
6-7	-1.270E+08
7-8	-1.041E+08
8-9	-5.749E+07
9-10	1.036E+07
10-11	1.006E+08
11-12	2.493E+08

Figure 6: Resulting energy pattern of the beach of Torre del Porto for the period 1951-2000.

The energy pattern derived suggests that the coast is energy – closed. In fact, the FERs, from the section 0 to the 9, point towards the North, and the FERs, from the section 9 to the 12, point toward the south: the sediments once reaching the shoreline cannot go out of its and their motion is confined along the coast between Punta Rossa, in the south, and the harbour, in the north.

The combined analysis of data from the first defined energy pattern and the historical information, that informs that the sediments have historically reached the shoreline by the river

Carbonara, has identified the natural formation process and evolution of the beach of Torre del Porto, as summarized in the following:

- the beach at Torre del Porto is made up of the sediments (pebbly stones) that have reached the shoreline from the Carbonara torrent;
- the sediments, deposited at the mouth of the river, were handled and distributed along the coastline by the FERs;
- the natural formation process was stopped, in the last thirty years, because the sediments have no longer reached the coastline.

3.2 The project "within the natural nourishment process" and its realization

In order to reactivate the natural formation process and then get back the beach, it was essential to supply the same sediments that the Carbonara torrent has no longer brought to the shoreline. The design, according to the principle of the methodology, has:

- provided for the supply of about 60,000 m³ of sharp edges stones (not rounded) of weight between 0.4 and 4 kg;
- detailed the rules for the deposition of material along the coast in order to enhance the handling of the same phenomena by the action of the incident waves so that the same action of the sea can perform a rapid rounding of the material;
- pre-figured for the execution of secondary works including those necessary to avoid the repetition of the beach near the new harbour.

3.3 The recreation of the beach in its original extension

Basing on the results of the analysis described, the works were executed in 2003. They have actually reactivated the natural process of formation and evolution of the beach of Torre del Porto, leading to its nourishment. The next figures show the beach of Torre del Porto respectively at the end of the works and three years later.



Figure 7: The beach of Torre del Porto in May 2004 Figure 8: The beach of Torre del Porto in 2007

4 The need of the monitoring. The phases carried out

The recreation of a natural process requires a monitoring campaign in order to check, on the basis of the available knowledge, the evolution of the unfolding process. Monitoring not only attempts to resolve the problems arising from differences of the variables considered in the model with the large number of prototype ones, or the uncertainties arising from the lack of field data, but also attempts to explain the knowledge about the "transition phases" that the beach will have to pass. The "transitional" phases are the stages of transition during which the natural process may start or not. The monitoring was divided into the following phases:

- Monitoring of energy data of the promoters of the coastal dynamic by the installation, in the middle of the bay of Torre del Porto, of an anemometer to record the wind speed and direction.
- Monitoring, by means of sample stones, of the coastal kinematics of its dynamic interpretation.

4.1 The monitoring by means of sample stone

Monitoring the kinematics of sediment, and ultimately monitoring the beach itself, was carried out by checking the actual development along the coast of the energy flows calculated starting from the registered wind data. The monitoring has been developed in three phases during which the sample stones were placed on the coast, trying to find that stones in the hours immediately following the storms. The stones were placed along sample control sections. During each phase the sample stones were placed at -3m, -2m, -1m, 0.00, +1 m and +2 m referred to SWL; so for each section have been provided 6 points of placement.

During the first phase of monitoring the sample stones were placed in different 10 sections (60 points totally), in each point was deposited a sample consisted of 7 stones, with weight of 4, 3, 2, 1, 0.8, 0.6, 0.4 kg; totally there were 840 sample stones.

In the first phase the sample stones were coded by means of paint colours that indicated the section of origin and the depth of the placement.



Figure 8: The sample stones coded by colours

In each of the other two monitoring phases the points of placement of the sample stones were 40, for a total of 280 sample stones. In each stone were done two holes: in the first one a metal bar was inserted necessary for the subsequent retrieval by means of a metal detector; in the second hole a "13.56 MHz radio frequency identification tag transponder smart label (RF-ID)" was inserted, that allows to identify the each stone.

After each storm, an inspection *in situ* was carried out to search for the stones. A total of 144 stones were found and for each of them has been identified both the starting position (using a colour code in the first phase and thanks to the microchip during the 2nd and 3rd phase) and the final position of discovery.

5 Monitoring results

The monitoring showed that the transport of the sediment along the shoreline is always according to the direction of the FERs as determined by the Perfect Storm software. This result is comforting, considering the importance that the FERs take in discovering the natural formation process of the coastline.

Furthermore the monitoring showed that the cross-shore transport of sediment occurs exclusively toward the inshore. The validity of this determination is confirmed by the findings, in the emerged area of the beach, of the stones placed up to 4m below the SWL and of the total absence of pebbles placed at depths greater than 5 m.

The displacements of the sample stones have shown that their "emergence" occurred with "limited" components longshore, i.e. the stones placed deeper than 1m below the SWL reaching the shore on the same section of their placement and only after the emersion large longshore displacements take place.

The found sample stones confirmed, as expected, that the transport characterizes the pebbly stones placed in a band of the beach (defined as *longshore energy band*) whose upper limit can be extended until the wave run-up line. The maximum emerged height reached by the *longshore energy band* varies with the characteristics of the breaking waves, therefore even during the same storm the size of that band varies over time. The width of the band generally increases until the maximum breaking wave characteristics are reached and decreases during the decay of the storm. Of course, more changes in the geometry of the band are possible during storms, characterized by the recovering of the waves due to the increase of generating wind speed. It's possible to consider the *longshore energy band* as an area where an action, that forces the sediment movement, is applied to the pebbly stones.

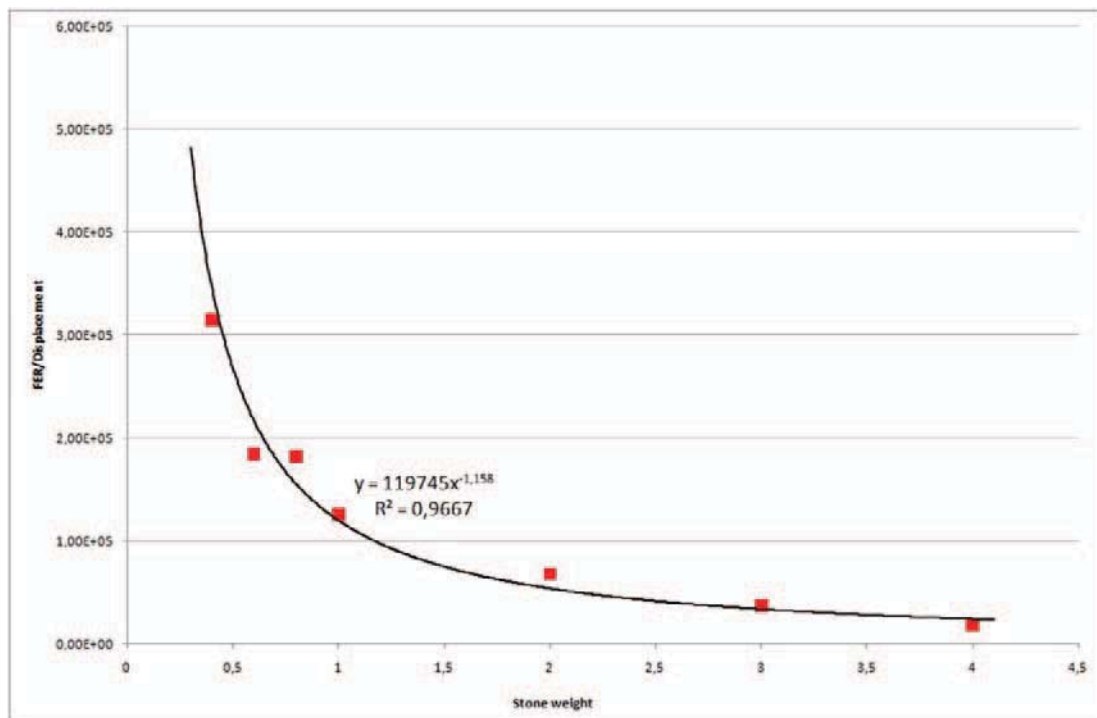


Figure 9: Relationship between stone weight and energy flux applied to obtain a displacement of 1 m

A consequence of the variability of the geometry of the energy band is a selective movement of the sediments along the coast. In fact, the *longshore energy band* reaches its maximum altitude and extension during the period of maximum characteristics of the breaking waves on the beach, while undergoes a gradual contraction (lowering of its upper limit) as the decay of the wave takes place. The result of the contraction of the band amplitude, amply demonstrated by the movements of sample stones detected during the three monitoring phases, is that the stones, driven during the maximum of the wave characteristics to regions no longer reachable from the upper limit of the band (for the subsequent decay of wave energy) present smaller displacements than the stones whose position is retained longer within the energy band.

Based on data provided by 144 stones found during the three monitoring phases, it has been possible to derive the relationship between:

- the wave energy that has caused a unit movement of the sample stones expressed as the ratio between the resulting energy flux and the their displacement (FER/Displacement);
- the stone weight.

6 Conclusions

A project for the re-naturalization of the beach of Torre del Porto was carried on in order to recreate the portion of the coastline eroded in the last 30 years.

The lack of sediments from the Carbonara torrent is identified as the main responsible of the erosion.

The project consisted in putting an appropriate sediment that the waves can move and handle to lead to the natural nourishment of the beach, according to the wave energy pattern that characterizes the area.

The monitoring has consistently shown that the heavier sample stones, that remain during the storm inside the *longshore energy band*, present displacements larger than the lighter ones. In fact, the lighter stones, brought by the waves over the upper limit of the energy band, are therefore excluded from the subsequent application of the forces that determine the movements along the coast and still remain on site.

It can be argued that the sediment transport is directly proportional to the residence time of the same stones in the energy band; for stones that remain the same time within the longshore energy band, there instead a relationship of inverse proportionality between displacement and the stone weight.

The relationship obtained is particularly interesting because, after calculating the FER value on a stretch of coastline, it allows to assess the most appropriate weight of sediment to provide to the coast in order to obtain the displacements necessary for the re-activation of the natural coastal dynamics.

7 References

- Army. Corps of Engineers of the United States. 1977, 1984. 'Shore Protection Manual'.
- Gentile, Giasi. 2000. 'I meccanismi dell'erosione costiera per il recupero della costa di Trani.' Atti del convegno GeoBen.
- Gentile, Giasi. 2001. 'Costruzione di una spiaggia con sterili di cava. Una metodologia di intervento ambientale ecocompatibile.' Published on the "rivista GEoingegneria AMbientale e Mineraria."
- Gentile, Selicato. 2002. 'Pianificazione e gestione dei sistemi costieri marini. Ipotesi di naturalizzazione e recupero di coste urbane in Puglia.' Proceedings of the International Conference Landscapes of Water.
- Gentile, Giasi. 2003. 'An example of eco-compatible methodology for coastal remodelling.' Proceedings of the European Conference on Application of Meteorology. Roma 2003

Numerical simulation on the motion of cubic armour block

Susumu Araki¹, Saki Fujii² and Ichiro Deguchi³

Abstract

The motions of armour blocks are simulated with DEM. In the DEM, the shape of each element is not a sphere but a cube. The motion of a cubic armour block before and after a simple collision between two cubic armour blocks is verified by measured data. The motion of a cubic armour block rolling down on a slope is also demonstrated.

Keywords: DEM, cube, armour block, numerical simulation

1 Introduction

The motions of armour blocks on coastal structures have been computed with Discrete Element Method (DEM). Araki et al. (2002) simulated the deformation of a rubble mound seawall with two-dimensional DEM. Itoh et al. (2002) simulated the motion of armour units on a submerged breakwater by a bore with two-dimensional DEM. In these studies, the shape of each element was a circle. Takayama et al. (2005) simulated the motions of caisson and rubble stones in composite breakwaters with two-dimensional DEM in which elliptical elements were used. Araki and Deguchi (2005) simulated the deformation of a submerged breakwater with three-dimensional DEM in which the shape of each element was a sphere. Latham et al. (2007) and Sakai et al. (2008) simulated the motions of wave dissipating blocks by using the model in which the position of each sphere-element was corrected after calculating the motions of the spheres in order to keep the shape of a wave dissipating block. However, the accuracy of the numerical model is expected to improve if the shape of each element itself is similar to that of an armour unit.

The final goal of this study is to simulate the motions of armour blocks with a complicated shape using the concept of DEM without using the position correction method. In this study, the motions of the cubic armour blocks were computed as a first step.

2 Numerical Procedure

2.1 Governing Equations

The DEM was proposed by Cundall (1979) in order to simulate the deformation of rock. The DEM is the method of simulating large deformation by calculating the motion of every element. The governing equations are the equations of motion for translation in the x-, y- and z-directions for the center of gravity of each cubic armour block and the rotational equations around the axes which go through the center of gravity of each armour block and are parallel to the x-, y- and z-axes, respectively. The equation of motion for translation for the cubic armour block i is as follows:

$$m_i \dot{u}_{iG} = F_{ix} \quad (1)$$

$$m_i \dot{v}_{iG} = F_{iy} \quad (2)$$

$$m_i \dot{w}_{iG} = F_{iz} - m_i g \quad (3)$$

¹ Dept. of Civil Engineering, Osaka University, 2-1 Yamada-oka, Suita, Osaka 565-0871 Japan, araki@civil.eng.osaka-u.ac.jp.

² Dept. of Civil Engineering, Osaka University, 2-1 Yamada-oka, Suita, Osaka 565-0871 Japan

³ Dept. of Civil Engineering, Osaka University, 2-1 Yamada-oka, Suita, Osaka 565-0871 Japan, deguchi@civil.eng.osaka-u.ac.jp

with	m_i	mass of the armour block i [kg]
	u_{iG}, v_{iG}, w_{iG}	velocities of the center of gravity of the armour block i in the x-, y- and z-directions, respectively [m/s]
	F_{ix}, F_{iy}, F_{iz}	forces acting on the armour block i in the x-, y- and z-directions, respectively [N]
	g	gravitational acceleration [m/s ²]

The rotational equation for the cubic armour block i is as follows:

$$I_i \dot{\xi}_{iG} = M_{ix} \quad (4)$$

$$I_i \dot{\psi}_{iG} = M_{iy} \quad (5)$$

$$I_i \dot{\zeta}_{iG} = M_{iz} \quad (6)$$

with	I_i	inertia moment of the armour block i [kg m ²]
	$\xi_{iG}, \psi_{iG}, \zeta_{iG}$	angular velocities around the axes which go through the center of gravity of the armour block i and are parallel to the x-, y- and z-axes, respectively [rad/s]
	M_{ix}, M_{iy}, M_{iz}	moments acting on the armour block i around the axes which go through the center of gravity of the armour block i and are parallel to the x-, y- and z-axes, respectively [Nm]

In the simulation, the positions of the vertices of cubic armour blocks need to be computed. The displacement of the vertex j of the cubic armour block i during Δt in the x-, y- and z-directions are calculated as follows:

$$\Delta x_{ij} = \Delta x_{iG} + r_{jyG} \cdot \psi_{iG} \cdot \Delta t \cdot \cos \theta_{jyGx} - r_{jzG} \cdot \zeta_{iG} \cdot \Delta t \cdot \sin \theta_{jzGy} \quad (7)$$

$$\Delta y_{ij} = \Delta y_{iG} + r_{jzG} \cdot \zeta_{iG} \cdot \Delta t \cdot \cos \theta_{jzGy} - r_{jxG} \cdot \xi_{iG} \cdot \Delta t \cdot \sin \theta_{jxGz} \quad (8)$$

$$\Delta z_{ij} = \Delta z_{iG} + r_{jxG} \cdot \xi_{iG} \cdot \Delta t \cdot \cos \theta_{jxGz} - r_{jyG} \cdot \psi_{iG} \cdot \Delta t \cdot \sin \theta_{jyGx} \quad (9)$$

with	$\Delta x_{iG}, \Delta y_{iG}, \Delta z_{iG}$	displacement for translation of the center of gravity of the armour block i during Δt in the x-, y- and z-directions, respectively [m]
	$r_{jxG}, r_{jyG}, r_{jzG}$	distances between the vertex j and the axes which go through the center of gravity of the armour block i and are parallel to the x-, y- and z-axes, respectively [m]
	$\theta_{jxGz}, \theta_{jyGx}, \theta_{jzGy}$	angles between the direction of the motion of the vertex j and the x-, y- and z-axes, respectively ($\xi_{iG} = d\theta_{jxGz}/dt$, $\psi_{iG} = d\theta_{jyGx}/dt$, $\zeta_{iG} = d\theta_{jzGy}/dt$) [rad]

2.2 Judgement of Collision

In the DEM, the collision between an element and other element is judged in every time step. If an element is judged to collide with other element, the collision force between the two elements is generated. In the DEM in this study where cubic elements are used, the collision between the cubic armour blocks was judged from finding the intersection between a square composing a cubic armour block and an edge (a line segment) composing a square in other cubic armour block.

2.3 Force Exerted by Collision

The exerted force between two cubic armour blocks by their collision was expressed by an elastic spring and a viscous dashpot shown in Figure 1. The collision force acts at the collision point between two cubic armour blocks. However, the collision forces were assumed to act in

the direction between the centers of gravity of the two cubic armour blocks and in the two perpendicular directions shown in Figure 2 in this study. Therefore, the effect of the eccentricity of the collision force on the rotational motion of the cubic armour block was not taken into account. The torsional moment was assumed to be neglected in this study. Table 1 shows the values of the spring constants and the damping coefficients used in this study. The values were determined in order that the computed motion of the cubic armour block would be similar to the measured one before and after a simple collision between two cubic armour blocks mentioned later.

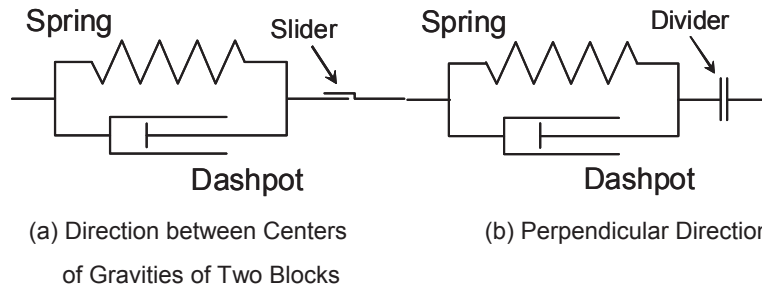


Figure 1: Expression of Collision Force

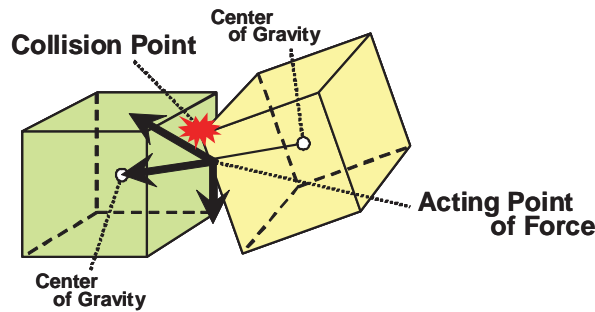


Figure 2: Direction of Collision Force

Table 1: Spring Constants and Damping Coefficients

	Direction between Centers of Gravity of Two Blocks	Two Perpendicular Directions
Spring Constant	5.8×10^7 [N/m]	2.4×10^7 [N/m]
Damping Coefficient	9.7×10^2 [Ns/m]	6.3×10^2 [Ns/m]

3 Computed Motions before and after Simple Collision

3.1 Outline

The motions of cubic armour blocks before and after a simple collision between the two cubic armour blocks were simulated. The one cubic armour block fell down to another cubic armour block fixed on the bottom. The edges of the falling cubic armour block were parallel or perpendicular to the bottom in the initial state. The collision was adjusted in order that the motion of the cubic armour block after the collision would be two-dimensional.

Figure 3 shows a rough sketch of the simple collision between the two cubic armour blocks. In the figure, the numbers of the vertices of the falling cubic armour block in the x-z plane are also shown. The origin of the x-z coordinates was set at the left lower vertex of the cubic armour block fixed on the bottom.

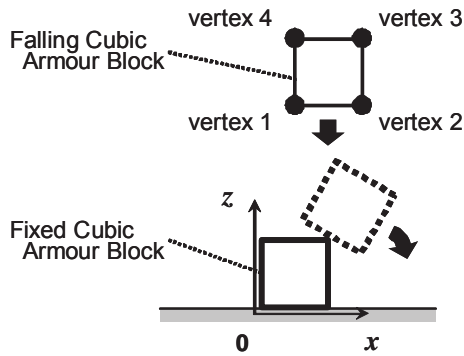


Figure 3: Simple Collision between Two Cubic Armour Blocks and Numbers of Vertices

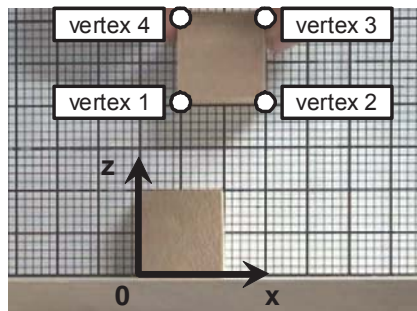


Figure 4: Initial State of Two Cubic Armour Blocks (Video Image)

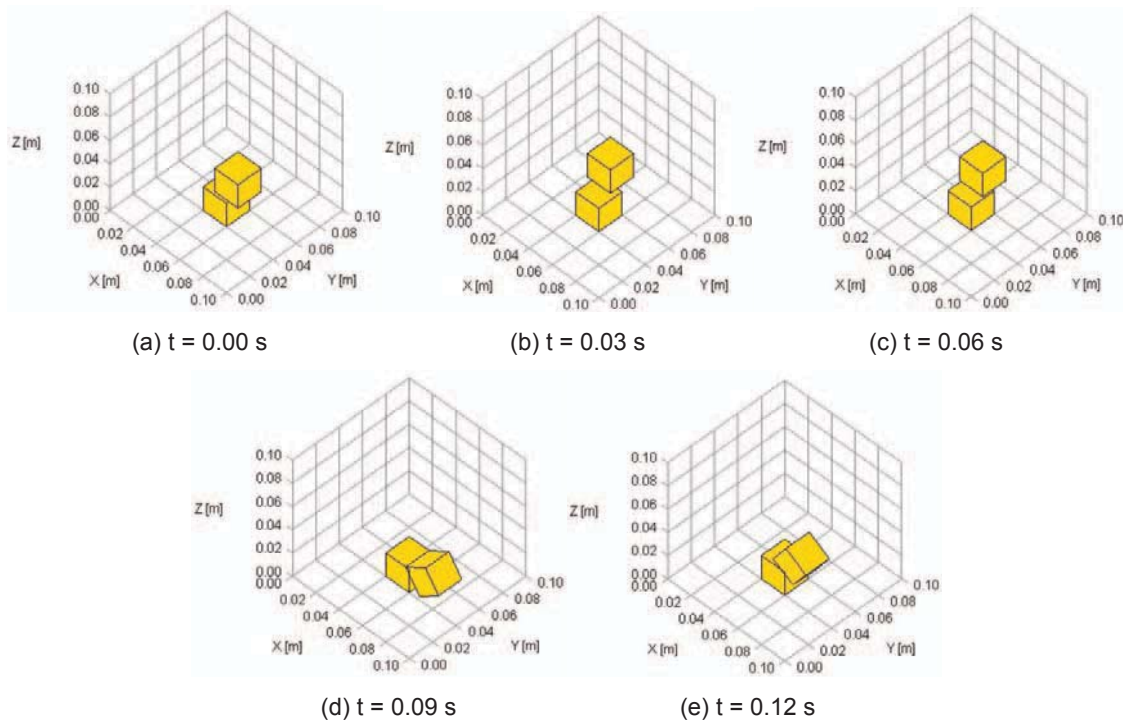


Figure 5: Snapshots of Simulated Simple Collision

3.2 Measurement

The falling motion of a wooden cube in the air and the collision with a wooden cube fixed on the bottom were taken by video. The size of the wooden cube was $0.02 \text{ m} \times 0.02 \text{ m} \times 0.02 \text{ m}$. A board with a grid was placed in the background. Figure 4 shows the initial state of the two

cubes. The positions of the vertices of the falling cube in the x-z plane were measured using the grid as a scale from the video image at every 1/30 s.

3.3 Comparison between Measured and Simulated Results

The motion of the falling wooden cube in the air was simulated with the model developed in this study. The time increment Δt was 5.0×10^{-6} s. The density of the wooden cube was 507.5 kg/m^3 . Figure 5 shows the snapshots of the simulated results at every 0.03 s. The origin shifted in the x-direction in this figure. The falling cube fell freely before $t = 0.06$ s. The falling cube collided with the cube fixed on the bottom between $t = 0.06$ s and $t = 0.07$ s. After $t = 0.07$ s, the falling cube rolled down clockwise on the right upper corner of the cube fixed on the bottom.

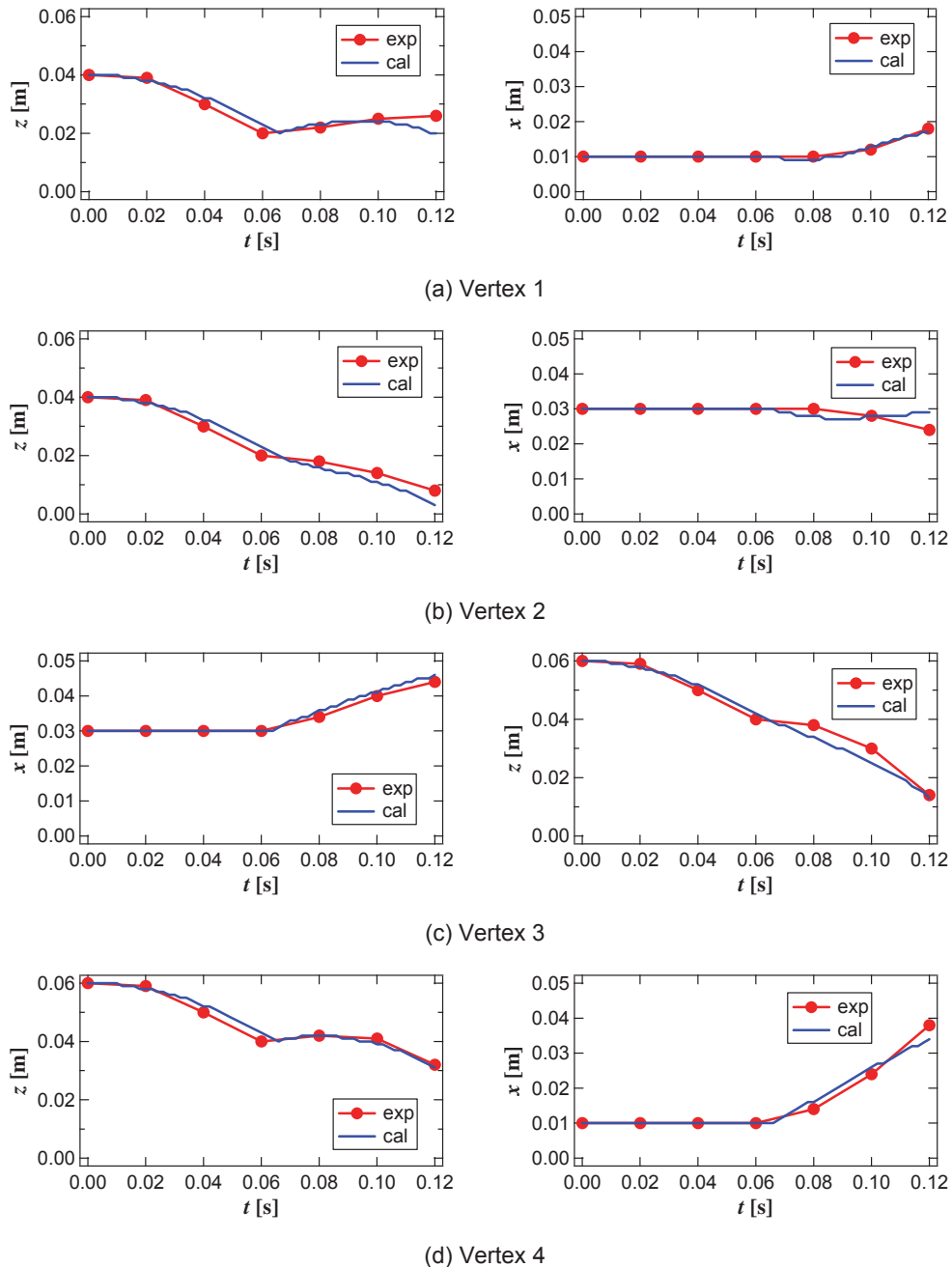


Figure 6: Measured and Simulated Positions of Each Vertex

Figure 6 shows the time series of the measured and the simulated positions of each vertex of the falling cube in the x- and z-directions. The solid circle shows the measured position of each vertex and the solid line shows the simulated position of each vertex.

On the whole, the simulated position of each vertex was almost in good agreement with the measured one. In Figure 6(b), the vertex 2 in the measured result moved toward the negative direction in the x-axis after the collision. On the other hand, the position of the vertex 2 in the simulated result in the x-direction almost remained at the initial position. In Figure 6(c), the numerical model underestimated the bound on the cube fixed on the bottom in the z-direction.

4 Trial Simulation

4.1 Outline

The numerical model developed in this study has been verified for the motion of a simple collision between two cubes. The numerical model has not been verified enough for the motions before and after the various kinds of collisions. For example, the motion before and after a collision shown in Figure 7 have not been computed enough yet. It seems that this results from taking no account of the effect of the eccentricity of the collision force on the rotational motion of the cube. However, a trial simulation was conducted in order to demonstrate the potential performance of the numerical model.



Figure 7: Example in Which Motion of Cube has not been Computed Enough (Video Images)

4.2 Simulated Results

Figure 8 shows a bird's-eye-view (x-y-z) and an elevation view (x-z) of the initial state in the trial simulation. A cube drawn in a bold line falls onto the cubes placed like steps in the air. The placed cubes drawn in a thin line are fixed. Figure 9 shows the snapshots of the simulated results at every 0.2 s. Figure 9(a) shows the snapshot just before the falling cube collided with the fixed cube. After the collision, the cube rolled down on the cubes placed like steps (Figures 9(b)-(d)). If the numerical model is verified for the various motions, such as the motion shown in Figure 7, the accuracy for the trial simulation shown in Figure 9 will be estimated. The accuracy of this numerical model is expected to be higher than the model based on DEM in which the position of each sphere-element is corrected after calculating the motion of the sphere in order to keep the shape of an armour block.

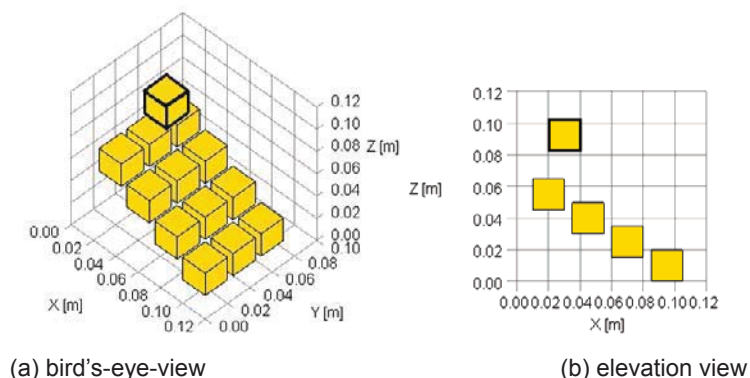


Figure 8: Initial State in Trial Simulation ($t = 0.00$ s)

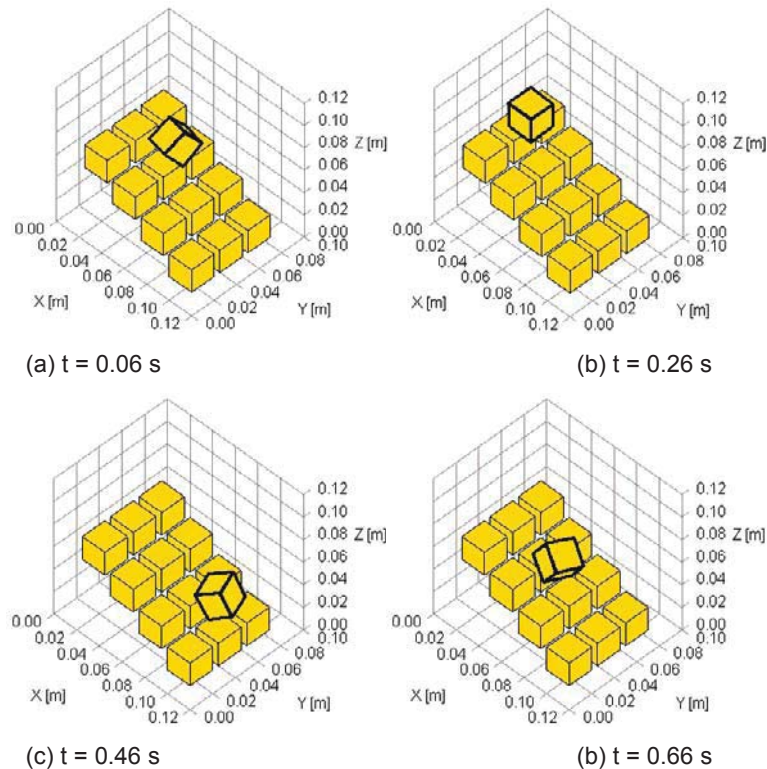


Figure 9: Snapshot of Trial Simulation

5 Summary

The numerical model based on DEM in which the shape of each element was a cube was developed in this study. The motion of a cube before and after a simple collision between two cubes and the motion of a cube on cubes placed like steps were simulated. The former was verified by the measured data. The simulated results were almost in good agreement with the measured results. In the numerical model developed in this study, the effect of the interlocking between armour blocks is expected to be simulated effectively. As a result, the accuracy of numerical simulation on the stability of wave-dissipating blocks and on the deformation in wave-dissipating-works will increase by this numerical model.

6 References

- Araki, S.; Kotake, Y.; Kanazawa, T.; Matsumura, A.; Deguchi, I. (2002): Development of numerical simulation method for predicting deformation of rubble mound seawall with VOF method and DEM, in: Proceedings of the 28th International Conference on Coastal Engineering, pp. 1485-1497, ISSN 2156-1028. Cardiff, Wales
- Araki, S.; Deguchi, I. (2005): Numerical simulation on 3-D deformation of submerged rubble mound structures with DEM, in: Proceedings of Second International Coastal Symposium (CD-ROM), Höfn, Iceland
- Cundall, P. A.; Strack, O. D. L. (1979): A discrete numerical model for granular assemblies, in: Géotechnique 29, No. 1, pp. 47-65, ISSN 0016-8505.
- Itoh, K.; Higuchi, Y.; Toue, T; Katsui, H. (2002): Numerical simulation of deformation of rubble structures by DEM and VOF, in: Proceedings of the 12th International Offshore and Polar Engineering Conference, Vol. III, pp. 714-721. ISSN 1098-6189. Kitakyusyu, Japan.

- Latham, J.-P.; Mindel, J.; Guises, R.; Gracia, X.; Xiang, J.; Pain, C.; Munjiza, A. (2007): Coupled FEM-DEM and CFD for coastal structures: application to armour stability and breakage, in: Proceedings of the 5th Coastal Structures International Conference, pp. 1453-1464. ISBN -13978-981-4280-99-0. Venice, Italy.
- Sakai, T.; Harada, E.; Gotoh, H. (2008): 3D Lagrangian simulation of compaction process of wave dissipating blocks due to high waves, in: Proceedings of the 31st International Conference on Coastal Engineering, pp. 3412-3422. ISSN 2156-1028
- Takayama, T.; Amamori, Y.; Higashira, K.; Kim, T. M. (2005): Computation of Composite Breakwater Deformation Modeled by Discrete Element Method, in: Proceedings of Second International Coastal Symposium (CD-ROM), Höfn, Iceland

Estimation and verification of long-shore sediment transport (LST) at Lecce coastline

Elvira Armenio¹, Felice D'Alessandro¹, Giuseppe Roberto Tomasicchio¹, Francesco Aristodemo²

Abstract

The purpose of the present study is to examine the accuracy of commonly used tools (USACE 1984, Kamphuis 1991) to estimate the longshore sediment transport (LST) rate for the case of the coastline of Lecce, Italy. The predictions of the mean annual LST, Q_m , obtained from CERC and Kamphuis (1991) formulae, have been compared with the value $Q_{m,e}$ derived from the analysis of the study area's aerophotogrammetries in terms of historical evolution of the shoreline in the reference period 1997-2004. The results indicate that the use of Kamphuis (1991) formula gives a better agreement between predictions and experimental observations.

Keywords: longshore sediment transport (LST), depth of closure, shoreline

1 Introduction

Accurate predictions of the LST rate and its cross-shore distribution pattern in the surf zone are central in coastal engineering studies. As an example, the design of coastal protection structures and beach nourishment projects relies on assessment of their impact on the shoreline that is often the result of gradients in the LST rate. Present understanding and methods for calculating the LST rate are largely developed based on field and laboratory studies (e.g. Dean 1989, Schoonees and Theron 1996, Wang et al. 1998). The most widely used formula for the estimation of LST is commonly known as CERC (USACE 1984); it has been calibrated by using field data from sandy beaches. The effects of the particle diameter and the bed slope, neglected in the CERC formula, have been considered by Kamphuis (1991), resulting in a more refined equation for LST prediction. In the present paper, the estimate of Q_m from the CERC and Kamphuis (1991) formulae have been compared and analyzed in a case study.

2 Methodology

The present study is organized as in the following:

- Determination of the wave climate by referring to the data of the National Sea Wave Measurement Network (RON) at the buoy of Monopoli;
- Evaluation of the effective wave climate at a "virtual" buoy located in front of the study coast by using the "geographical transposition" method to the directional wave records of the RON buoy of Monopoli;
- Wave Nearshore transformation analysis to calculate the propagated wave characteristics in terms of significant wave height, H_{sb} , and wave angle, θ_b , at breaking;
- Calculation of the potential LST, Q (m^3/s), by using CERC and Kamphuis (1991) formulae and estimation of its mean annual value, Q_m ($m^3/year$);
- Analysis of the study area's aerophotogrammetries for the years 1997 and 2004 and detection of the eroded areas, S ;

¹ Engineering Department, University of Salento, via Monteroni, 73100 Lecce, Italy. E-mail: elvira.armenio@unisalento.it; roberto.tomasicchio@unisalento.it; felice.dalessandro@unisalento.it

² Department for Soil Conservation, University of Calabria, via P. Bucci, 80136 Arcavacata di Rende (CS), Italy. E-mail: aristotool@gmail.com

- Estimation of the total eroded volume, V^* (m^3), in the reference period (1997-2004) by multiplying S for the depth of closure, D_c (Hallermeier 1978);
- Evaluation of the observed mean annual value of LST, $Q_{m,e}$ ($m^3/year$), by dividing V^* for 7 years (1997–2004);
- Comparison between Q_m predicted by CERC and Kamphuis (1991) formulae and $Q_{m,e}$ obtained from the historical observations of the shoreline in the reference period.

3 The study area

The study area is located on the southern Adriatic coast of the Apulia region, in Italy (Figure 1). It is oriented on east, 40° with respect to the geographic North and therefore it is affected by the waves from the 1° , 2° and 4° quadrant. This area, called Salento, presents a coastline with large variability of planshape and composition: sandy beaches are followed by rocky coast.

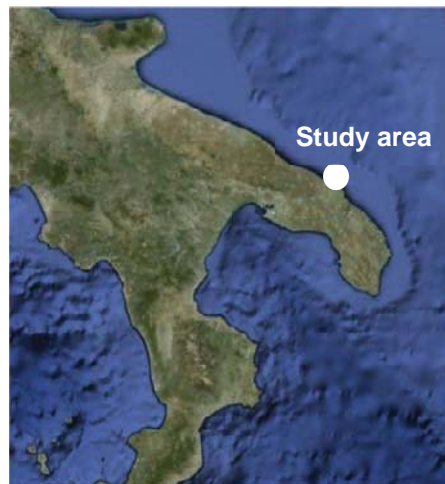


Figure 1: Aerial map of the study area

3.1 The wave climate

The wave climate is determined based on data from the National Sea Wave Measurement Network (RON) (available online at: <http://www.idromare.com>). Since 1989, RON provides measurements of the wave characteristics in Italian seas under deep water conditions with reliable results in terms of data acquisition rates and temporal coverage. The considered buoy is located offshore of Monopoli (70 m water depth), 100 km north of Lecce. The record length extends from 1 July 1989 to 5 April 2008 for a period of about 19 years.

Figure 2 shows the offshore wave rose representative of the wave climate. The most frequent and intense waves came from NNW (337.5°). The recorded mean annual offshore wave height is ≈ 2.0 m with typical wave periods of 4-6 s. However, during intense storms, offshore wave heights may exceed 5 m with peak spectral wave periods of 10-13 s.

The effective wave climate at a “virtual” buoy located in front of the study coast is derived by the application of the “geographical transposition” method to the directional wave records of the RON buoy of Monopoli. This method considers all the directional wave data recorded at the Monopoli’s buoy and transforms them into a new set, correcting the wave heights and periods through the comparison of the effective fetches.

In addition, based on the corrected set of wave heights and periods at a “virtual buoy”, a wave nearshore transformation analysis has been carried out in order to determine the propagated wave characteristics in terms of significant wave height, $H_{s,br}$, and wave angle, θ_{br} , at breaking.

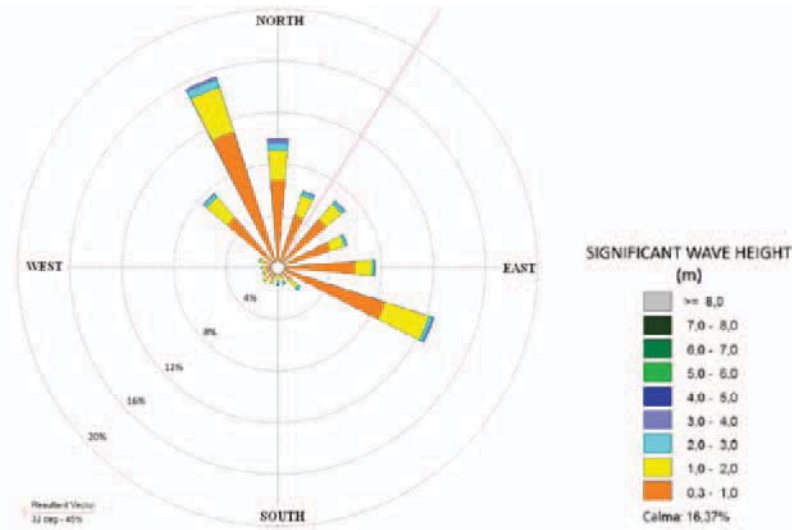


Figure 2: Offshore wave rose at buoy of Monopoli

3.2 The wave propagation model

The wave propagation simulations have been conducted by using a steady-state directional wave spectral transformation model (Rivero et al. 1993, 1997). The model is capable of simulating wave-structure and wave-current interactions. Moreover, it can compute wave diffraction, reflection and wave transmission through and over submerged structures. The model solves the spectral wave action conservation equation in the two spatial co-ordinates (x and y) and the wave direction, φ , taking into account wave energy dissipation rates due to bottom friction, D_b , and wave breaking, D_f :

$$\frac{\partial}{\partial x} \left((C_g \cos \varphi + U) \frac{E}{\sigma} \right) + \frac{\partial}{\partial y} \left((C_g \sin \varphi + V) \frac{E}{\sigma} \right) + \frac{\partial}{\partial \varphi} \left(C_\varphi \frac{E}{\sigma} \right) + \frac{D_b}{\sigma} + \frac{D_f}{\sigma} = 0 \quad (1)$$

where: $E(x,y,\varphi)/\sigma$ = wave action density with σ = angular frequency of the wave; U, V = current velocity components in x and y direction, respectively; C_g and C_φ = wave celerities. More details can be found in Rivero et al. (1993, 1997). For the current situation, Figure 3, representative of all cases, shows the wave propagation for $H_s = 0.75$ m, $T_p = 2$ s and waves from NNW.

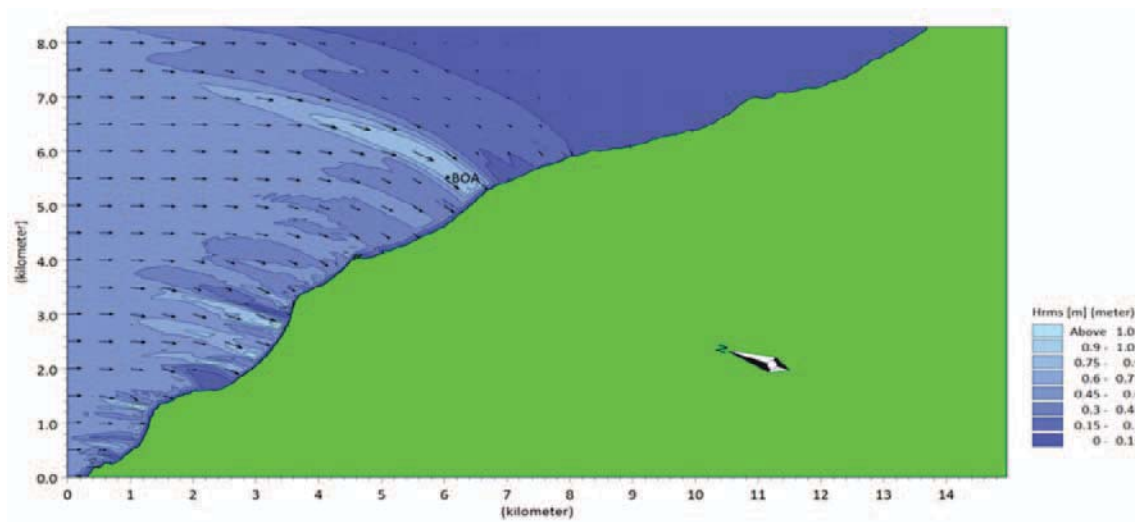


Figure 3: Example of calculation of wave propagation for $H_s=0.75$ m and $T_p=2$ s from NNW (337.5°)

4 The longshore sediment transport (LST)

The present paragraph shows the two formulae adopted in the calculations. The CERC formula (USACE 1984) gives:

$$Q = 0.023(1-p)\rho_s g^{0.5}(\gamma_{br})^{-0.52}(H_{s,br})^{2.5} \sin(2\theta_{br}) \quad (2)$$

where:

Q = potential longshore sediment transport (kg/s);

g = acceleration due to gravity (m/s^2);

$H_{s,br}$ = significant wave height at breaking (m);

γ_{br} = breaker index;

θ_{br} = wave angle at breaking (deg);

ρ_s = sediment density (kg/m^3);

p = porosity factor (≈ 0.4).

More recently, Kamphuis (1991) developed a relationship for estimating the longshore sediment transport rate:

$$Q = 2.33(T_p)^{1.5}(\tan \beta)^{0.75}(d_{50})^{-0.25}(H_{s,br})^2[\sin(2\theta_{br})]^{0.6} \quad (3)$$

where:

Q = potential longshore sediment transport (kg/s);

$H_{s,br}$ = significant wave height at breaking (m);

T_p = peak wave period (s);

θ_{br} = wave angle at breaking;

$\tan \beta$ = slope of the beach profile;

d_{50} = mean diameter of sediment (m).

The value 2.33 is a dimensional coefficient related to the SI system assuming salt water ($1030 kg/m^3$). In the present study, the value of d_{50} has been assumed equal to 0.050 mm and the value of $\tan \beta$ has been considered equal to 0.025 (= 1/40).

5 Results

In the present paper, for an assigned φ , the value of the annual "gross" LST, $Q_{m,G}$, induced by each wave characterized with H_s , T_p , and annual frequency of occurrence, f , has been calculated by multiplying Q resulting from equations (2) and (3) for the corresponding f . In particular, wave heights in the range 0.5-4.75 m, wave periods between 2-14 s and wave front directions from NW (315°) to ESE (112.5°) have been considered. As a consequence, the estimation of the annual "net" LST, $Q_{m,N} = Q_m$, has been derived from the sum, extended for all wave directions, of the calculated $Q_{m,G}$.

Table 1 summarizes the predicted values of $Q_{m,G}$ from NW to ESE by using CERC (USACE 1984) and Kamphuis (1991) formulae.

Table 1: $Q_{m,G}$, evaluated from NW (315°) to ESE (112.5°) by using CERC (USACE 1984) and Kamphuis (1991) formulae

Directions	$Q_{m,G}$ [m ³ /year]	
	CERC (USACE 1984)	Kamphuis (1991)
NW (315°)	47866	12208
NNW (337,5°)	114874	26187
N (360°)	108134	22364
NNE (22,5°)	79673	18983
NE (45°)	3128	-364
ENE (67,5°)	-54038	-14782
E (90°)	-118611	-25420
ESE (112,5°)	-105862	-22981

Taking into account the convention adopted, the positive values from calculation indicate a LST incoming from north.

With reference to the Table 1, Figure 4 shows the comparison between the calculated $Q_{m,G}$ by Kamphuis (1991) and CERC formula for wave front directions between NW (315°) and ESE (112.5°). The highest value of $Q_{m,G}$ corresponds to direction NNW (337,5°) which represents the dominant wave direction (Figure 2).

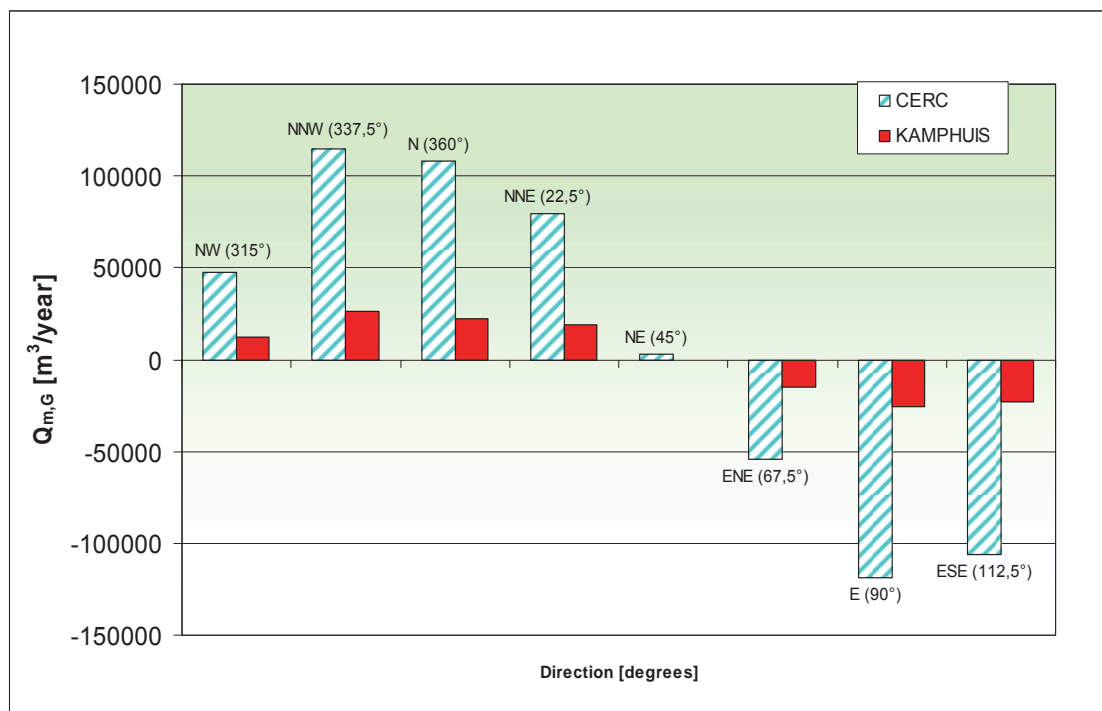


Figure 4: Evaluation of $Q_{m,G}$ for different wave front directions by using CERC (USACE 1984) and Kamphuis (1991) formulae

Table 2 shows the comparison between $Q_{m,N}$ evaluated by using CERC (USACE 1984) and Kamphuis (1991) formulae, respectively. In particular, the application of Kamphuis (1991)

formula gives, approximately, 16000 m³/year, whereas CERC equation results about 75000 m³/year.

Table 2: Comparison between $Q_{m,N}$ evaluated by using CERC (USACE 1984) and Kamphuis (1991) formulae

$Q_{m,N}$ [m ³ /year]	
CERC (USACE 1984)	Kamphuis (1991)
75165	16196

The analysis of the historical evolution of the shoreline has been carried out by using the aerophotogrammetries of the study area for the years 1997 and 2004.

With the scope to localize any possible coastal area subjected to erosion, the aerophotogrammetries have been georeferenced and overlapped. The comparison between the different shorelines in the reference period has allowed to mark the eroded surface area, S (m²), where it has been observed a retreat of the coastline. As shown in Figure 5, it has been detected three main coastal surface areas with evident erosion conditions.

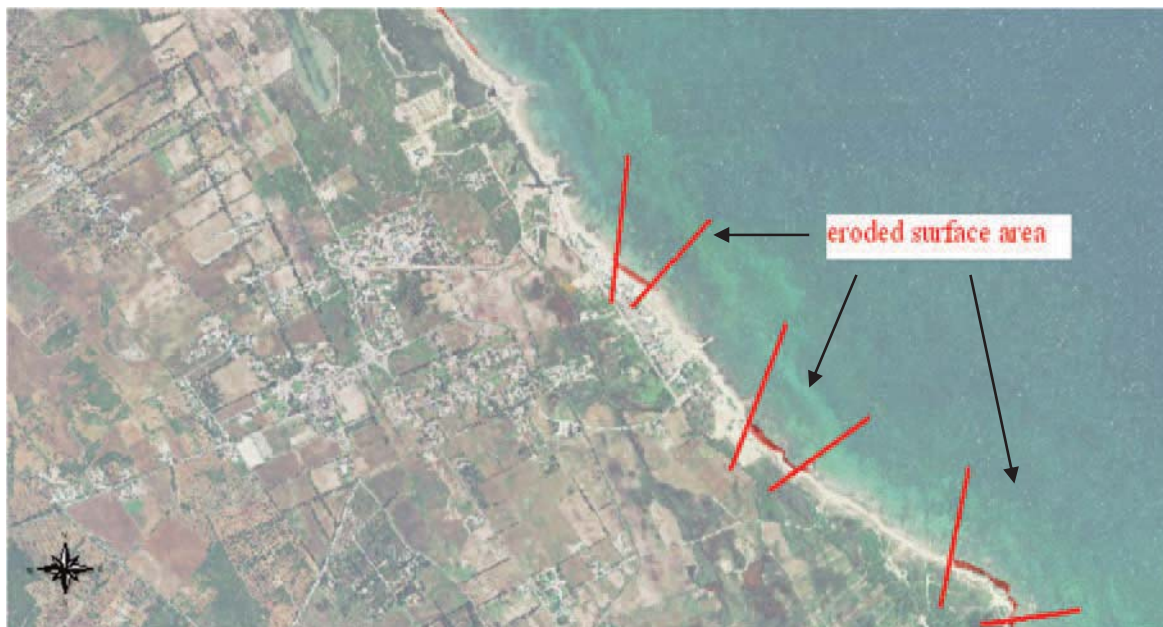


Figure 5: Aerophotogrammetry of Salento coastline. The marked areas along the coastline indicate the coastal erosion in the reference period 1997-2004

In order to obtain the total eroded volume, V^* (m³), in the reference period (1997-2004), the detected S have been multiplied by the depth of closure, D_c (m) (Hallermeier 1978):

$$V^* = S * D_c \quad (4)$$

The D_c is an important concept in coastal engineering and a fundamental variable in modelling coastal evolution due to sea-level change and longshore sediment transport (Dean, 1989). It represents the most landward depth seaward of which there is no significant change in bottom elevation and no significant net sediment transport between the nearshore and the offshore (Kraus et al. 1998).

By using linear wave theory, Hallermeier (1978) derived the following equation for the calculation of D_c :

$$D_c = 2.28H_{0.136\%} - 68.5 \left(\frac{H_{0.136\%}^2}{gT_{0.136\%}^2} \right) \quad (5)$$

where:

$H_{0.136\%}$ = significant wave height exceeded 12 hours per year (m);

$T_{0.136\%}$ = period associated with $H_{0.136\%}$ (s).

In the present case study, in eq.(4), V^* has been evaluated assuming D_c equal to 6.5 m. As a consequence, the value of V^* resulted equal about to 271200 m³; the corresponding mean annual value of coastal erosion, $Q_{m,e}$, was about 38700 m³/year; it has been estimated by dividing V^* for 7 years (2004-1997).

The comparison of the results shown in Table 3 indicates that Eq. (4) gives an intermediate value between the CERC and Kamphuis (1991) evaluations.

Table 3: Comparison between $Q_{m,N}$ evaluated by using CERC (USACE 1984), Kamphuis (1991) formulae and Eq. (4)

$Q_{m,N}$ [m ³ /year]		$Q_{m,e}$ [m ³ /year]
CERC (USACE 1984)	Kamphuis (1991)	Eq. (4)
75165	16196	38700

6 Conclusions

In the present study, the estimation of the mean annual LST, $Q_{m,N} = Q_m$ has been evaluated by using CERC (USACE 1984) and Kamphuis (1991) formulae for the case of the coastline of Lecce; then, the predicted Q_m have been compared with the value of $Q_{m,e}$ derived from the analysis of the available historical observations of the shoreline in the reference period 1997-2004.

The mean annual LST obtained from the analysis of the historical observations of the shoreline was found to be an intermediate value in comparison with the CERC (USACE 1984) and Kamphuis (1991) evaluations. In particular, CERC formula (USACE 1984) overestimates the observations, whereas Kamphuis (1991) formula gives an underestimation.

7 References

- Dean, R.G. (1989): Measuring longshore sediment transport with traps. In: Nearshore sediment transport. R.J. Seymour, ed., Plenum Press, New York, 313-337.
- Hallermeier, R.J. (1978): Uses for a calculated limit depth to beach erosion. In: Proc. 16th Coastal Engineering Conf. ASCE, New York, pp.1493 – 1512.
- Kamphuis, J.W. (1991): Alongshore sediment transport rate. In: Journal of Waterway, Port, Coastal and Ocean Engineering, ASCE, 117(6), 624-641.
- Rivero, F.J., Sanchez-Arcilla, A. (1993): Propagation of linear gravity waves over slowly varying depth and currents. In: Proc. Waves '93 Symposium, ASCE, New Orleans, pp. 518–532.
- Rivero, F.J., Sanchez-Arcilla, A., Carci, E. (1997): Analysis of diffraction effects in spectral wave models. In: Proc. Waves '97 Symposium, Virginia, USA.
- Schoonees, J.S., and Theron, A.K. (1996): Review of the field database for longshore sediment transport. In: Coastal Engineering, Elsevier, (19) 1-25.
- USACE (1984): Shore Protection Manual. Department of the Army, U.S. Corps of Engineers, Washington, DC 20314.
- Wang, P., Kraus, N.C., and Davis Jr., R.A. (1998): Total rate of longshore sediment transport in the surf zone: field measurements and empirical predictions. In: Journal of Coastal Research 14(1), 269-283.

Developing sustainable coastal protection- and management strategies for Schleswig-Holstein's Halligen considering climate changes (ZukunftHallig)

Arne Arns¹, Doris Blutner³, Hilmar von Eynatten², Roger Häußling³, Frerk Jensen⁴, Volker Karius², Christoph Mudersbach¹, Dirk van Riesen⁴, Malte Schindler², Holger Schüttrumpf⁵, Henrike Strack⁴, Theide Wöffler⁵ and Jürgen Jensen¹

Abstract

Within the joint research project "ZukunftHallig", a team of researchers are investigating the future development of the Halligen considering climate change. The project is a joint research project which brings together scientists from different areas to derive holistic and sustainable coastal protection- and management strategies, focusing on the protection and preservation of the Halligen. Due to their location, the Halligen and their residents have always been exposed to extreme conditions. Through the centuries, the number and the overall size of the Halligen have been reduced. As time passed by, people invented measures to adapt to these changing conditions. Since the fixture of the Hallig edges in the 19th century e.g., the quantity of land losses has been considerably reduced. The Halligen seem to have a certain capacity of compensating changes in the Mean Sea Level (MSL) by accumulating washed up sediments. In times of rapid sea level changes, it seems there are limits in this adaptability. In "ZukunftHallig", the system dependent behaviour of the Halligen focusing on the hydraulics and sedimentation as well as the existing protection measures and the acceptance of new strategies in the area of the Halligen will be analysed.

1 Scope

With an area of approximately 9.000 km², the depositional coastline of the Wadden Sea is one of the world's largest intertidal wetlands. In 2009, the Wadden Sea was added to UNESCO's World Heritage List. Besides its ecological and historico-cultural relevancy, the Wadden Sea itself is an important element of coastal protection. Surrounded by the North Sea, the Wadden Sea includes 10 marsh islands called Halligen. These small islands are a natural phenomenon, which is unique worldwide. Although the Halligen are inhabited by around 350 residents, the Halligen have no dikes. Consequently, the Halligen are inundated up to 50 times a year. In order to protect themselves from these inundations, houses are built on dwelling mounds. Residents learned to cope with these extreme conditions, but as time goes by, the Halligens' shapes and conditions are gradually negatively affected, especially in consequence of rising sea levels.

According to Katsman et al. (2008), sea level is predicted to rise by 40 cm to 80 cm by 2100 for the northeast Atlantic (see also Wahl et al. 2011). Among others, these changes are directly affecting the ability of disturbance regulation of the Wadden Sea while ocean currents and sediment fluxes are influenced and the Halligens' flooding frequency increases. Coastal ecosystems are known to be dynamic with a certain capacity of compensating changes in Mean Sea Level (MSL) by non-linear feedback mechanisms. However, observations are indicating limits in this adaptability (Kirwan et al. 2010). The intention of the research project is to gain insight into the processes involved in the evolution of the Halligen, which is the basis for an

¹ Research Institute for Water and Environment (fwu), University of Siegen, email: arne.arns@uni-siegen.de

² Geoscience Center, University of Göttingen

³ Institute of Sociology, Aachen University

⁴ Schleswig-Holstein Agency for Coastal Defence, National Park and Marine Conservation, Husum

⁵ Institute of Hydraulic Engineering and Water Resources Management, Aachen University

effective and sustainable protection strategy. Simultaneously the demands but also the worries of the Halligen residents have to be considered.

2 Study area

The study area is located at Schleswig-Holsteins coastline, the most northern part of Germany (see Figure 1). Due to the comprehensive work schedule, the study will only be conducted for three of the overall ten existing Halligen exemplarily. These are Langeneß, Nordstrandischmoor and Hooge. Because the Halligen have no proper dikes, the investigations will include two diked Islands in Lower Saxony, further west of Schleswig-Holstein. Hence the system-dependent behaviour shall be derived.

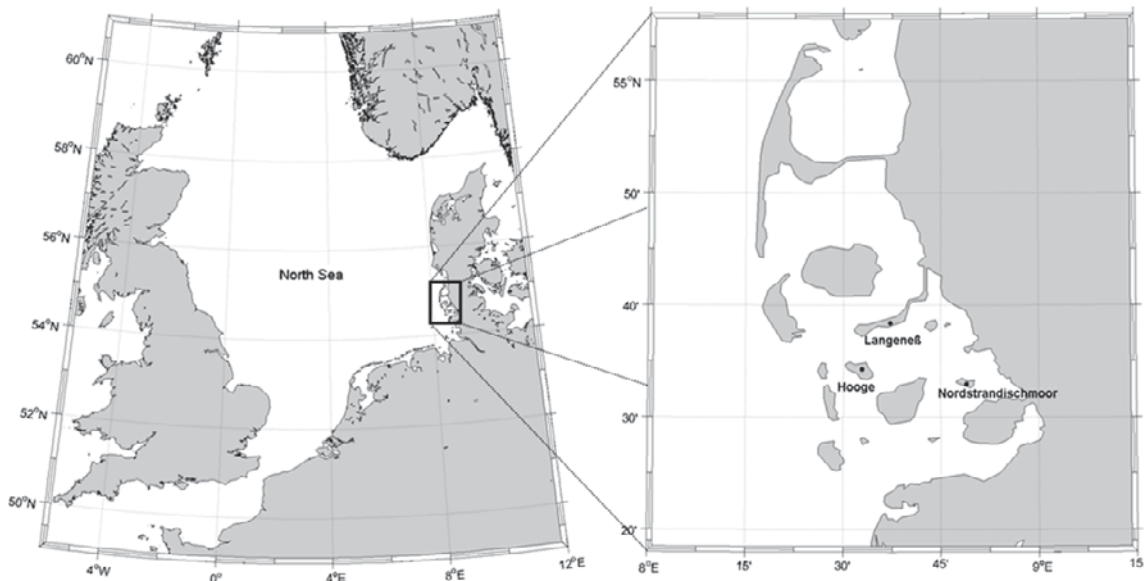


Figure 1: Primary investigation area of the research project „ZukunftHallig“. The analyses will be conducted for the Halligen Langeneß, Hooge and Nordstrandischmoor.

3 Extent of work

Within the joint research project “ZukunftHallig”, an interdisciplinary team of researchers is investigating the future development of the Halligen considering climate changes. The project aims for the development of new impulses to sustainable coastal protection- and management strategies, focusing on the protection and preservation of the Halligen. Therefore the research project is divided into five subprojects. A short description of these subprojects is presented below.

3.1 ZukunftHallig A (fwu): The hydrodynamic forcing of today and future conditions

The research project “ZukunftHallig” is a joint research project which is coordinated by the Research Institute for Water and Environment (fwu) of the University of Siegen. In subproject A, the hydrodynamic forcing of today and under future conditions will be investigated. Therefore, local sea levels, extreme water levels but also general tidal characteristics are going to be analysed.

The research is based on a huge number of tide gauges located all over the study area. At first, all data were tested for homogeneity. As stated in Aguilar et al. (2003), in a homogeneous climate time series all variability and changes are caused by variations in climate. Actually, tide gauge data sets are affected by a number of non-climatic factors as i.e. changes in instruments, locations and observation techniques but also erroneous recordings and data management techniques. In consequence these data sets are technically speaking unrepresentative of climate variations and can bias a time series. It is therefore desirable to remove or at least to detect inhomogeneities for quantifying possible errors they may cause. Because climate data

contains a large variability, it is a difficult task to detect inhomogeneities, especially if their magnitude is small compared to climate related variations. In "ZukunftHallig", the "candidate-reference" method, which is widely used in other disciplines of climatology, was adapted to tide gauge data. With this method possible errors in data were detected and eliminated. Despite using this method, the detection and eliminating of erroneous data is still a very time-consuming task. For more information see e.g. Arns & Jensen (2010) and Aguilar et al. (2003).

Once the data has been homogenised, data analyses will be conducted. As in most international MSL studies, the MSL analyses in "ZukunftHallig" will be accomplished according to the definition of the Permanent Service for Mean Sea Level (PSMSL, <http://www.psmsl.org>). Following this definition at least 11 months each with a minimum of 15 days of data are required. Many gauges surrounding the Halligen are operational in the summer months. In consequence up to 40% of the tide gauge data is missing. To fulfil the PSMSL criteria, it is therefore important to fill these gaps with proper methods or to quantify errors that can occur in consequence of missing data. Filling longer gaps in time series is a difficult task in coastal engineering and has been subject to many investigations. Most prominent approaches are based on neural networks, spectral analyses and regression models or combinations of the previously mentioned. While none of these methods are able to exactly reproduce missing data, it is therefore important to be able to quantify the error of the reproduction. In "ZukunftHallig" multiple regression based models will be applied to make the tide gauge data fulfil the PSMSL requirements.

In the next step, the filled up tide gauge data will be included in analyses focussing on tidal high and low waters as well as the tidal range and other tidal characteristics. Hereafter analyses concerning the evolution of the flooding frequency as well as the occurrence of extreme water levels will be elicited. Within the subproject, we are trying to derive knowledge about the application of different statistical methods for the assessment of extreme water levels considering limited high resolution data. The outcome of all analyses shall serve as input parameters for inundation models. These models will be designed to gain knowledge about processes affecting the erosion and sedimentation on the Halligen.

3.2 ZukunftHallig B (part I, IWW): Risk analysis

At the Institute of Hydraulic Engineering and Water Resources Management (IWW) of the RWTH Aachen University a hazard-analysis is to be employed using a risk based approach. This analysis is a suitable instrument in order to evaluate existing coastal protection techniques and to design new coastal protection- and management strategies. The hazard-analysis will be based on determined present and future scenarios and has the aim to ensure life for further generations on the Halligen under sustainable ecological and economic conditions. Because of the well-defined delimitation of areas and damage potentials the analysis will be performed on microscale level.

To perform this analysis it is necessary to have a complete system description of the Halligen and the surrounding Wadden Sea, as the results will serve as input parameters for all later investigations. These results include hydrological parameters as extreme water levels, tides, currents, windfields, waves and morphological parameters such as ground elevation, bathymetry, relief, sedimentation and morphological dynamics. Furthermore cartographical data of land use as well as statistical data of tourism, agricultural structure and existing building stock will be collected and evaluated.

Due to the lack of data for some input parameters and the different temporal horizons that will be analysed in this project, numerical simulations have to be performed. In preparation for the hazard-analysis the software package Delft3D, including the numerical wave model SWAN (Simulating Waves Nearshore) by Deltares systems, will be used to perform a numerical wave-simulation for the Northfrisian Wadden Sea. The boundary conditions for the simulation of the present situation are taken from local windstations and wave buoy measurements of the Schleswig-Holstein Agency for Coastal Defence, National Park and Marine Conservation (LKN-SH). To simulate the sea state of future conditions wind fields of the Climate Local Model (CLM) based on the IPCC-Scenario A1B will be statistically analysed and used as respective boundary conditions. Also changes in the dynamic bathymetry of the Wadden Sea and future water levels

will be considered in order to estimate the development of the natural height increase of the Halligen conditioned by sedimentation.

The knowledge of these investigated future scenarios and storms that threaten the ten Halligen under changing climate conditions are the main basis for the evaluation of their development. Additionally it can be used for the design of new coastal protection techniques and the artificial improvement of sedimentation rates. The strategies, whether it is an increase of revetments, dwelling mounds or greater object protection, have to be developed in cooperation with the inhabitants.

3.3 ZukunftHallig B (part II, IfS): The Joint Development of Coastal Protection as a Sociotechnical Innovation

Technical innovations are always also social innovations because they – no matter whether novelties or optimizations – have to be embedded in social contexts for them to be able to achieve their goals effectively. Even though today we manage to do so better and better, it should not be overlooked that we take a path which en passant generates risks (Perrow 1987; Japp 2000). And as we position ourselves as creators of innovations, it is catastrophes which we humans are responsible for which we take even more seriously than those caused by nature (Abels & Bora, 2004: 5). Not only nuclear energy, but also information and communication technologies have to be viewed under this aspect.

The Sociology of Technology constitutes the scientific discipline which is concerned with exactly these interactions (Simmel 1908) between man and technology in processes of innovation and implementation. We take into account that innovation processes do not always run in a straight line. Quite the opposite, innovation processes are usually marked by zigzag movements, loops, recursion and changing constellations of actors (Ortmann 1995; Rammert 1997; Weyer 2008). That is why we understand innovation processes as an “interplay between dynamics at multiple levels” (Geels 2005), is characterized by four innovation phases. “In the first phase, novelties emerge in niches in the context of existing regime and landscape developments. [...] In the second phase the novelty is used in small market niches, which provide resources for technical specialisation.” (Geels 2005). The successful conclusion of the second phase presupposes collective action as an off-the-path option between producers and users (Blutner 2005). “This second phase results in a stabilisation of rules. [...] The third phase is characterised by a breakthrough of the new technology, wide diffusion and competition with the established regime. [...] In the fourth phase the new technology replaces the old regime, which is accompanied by changes on wider dimensions of the sociotechnical regime.” (ibid.).

The Halligen have always been a special place to live because of their recurring storm tides and flooding, constant sea-level fluctuations and the changes of the currents. The forces of nature have produced very specific living and working conditions, which the inhabitants of the Halligen experience as part of their daily lives. This is not only reflected by well-established everyday cultures of shopping, garbage disposal, etc., but also in the way that storm tides are dealt with before and after their occurrences - also with the help of technology. As a result, a unique culture has arisen: it relies on far-reaching traditions on the one hand and on the knowledge from the experiences of the inhabitants of the Halligen on the other hand.

Our sociological accompanying research comprises the following three stages:

- a) For preparing participatory technology design we have set ourselves the goal to lend an ear to the traditions and knowledge of the inhabitants of the Halligen and document our findings.
- b) The second stage involves problem-oriented workshops concerning coastal protection (for every Islet under scrutiny) and a future-oriented sustainability workshop for the inhabitants of the Halligen. Both measures are meant to integrate the inhabitants' ideas and doubts into the (engineering) process of optimizing coastal protection (s. a. Jungk 1981). This process makes two high demands on all persons involved. First it constitutes a meeting of the “interest groups as fully entitled participants” (Abels & Bora 2004). This means that none of the participants can be dismissed as mere “suppliers” (ibid.). Secondly, the mutual discourse is not limited to votes. Instead, groups are formed in order to facilitate mutual understanding and to come to an agreed way of

dealing with coastal protection. Therefore one of the goals of this stage is to develop coastal protection measures which on the one hand build upon the culture of the inhabitants of the Halligen and on the other take account of the changed climatic conditions.

c) In the third stage the processes of participatory technology development are evaluated.

The methods used include the utilization of network cards, qualitative interviews (documentation), workshops and standardized surveys (documentation and evaluation).

Within the framework of the documentation (first stage), sociology functions as a mediator between the inhabitants of the Halligen and the engineers. In the second stage, it establishes the conditions for participatory technology development. In the third stage, sociology serves as an instrument for evaluating this process.

3.4 ZukunftHallig C (LKN): Evaluation of existing coastal protection systems, hydrological monitoring and data supply

One task of Schleswig-Holstein's federal state government is to protect and to preserve the Halligen. Therefore the Halligen have to be adjusted to the rising hydrodynamic loads caused by the North Sea. Previous methods of coastal protection of the Halligen were based on building and adjusting coastal protection facilities (e.g. revetments, groynes) and flood protection facilities (summer dikes, dams/walls, dwelling mounds). The implementation of these coastal safety facilities prevent erosion and therefore minimize the surface loss, while coastal flood protection facilities protect humans and their property against floods.

The preservation of the Halligen depends considerably on its functional coastal protection systems. That is why these systems always have to be controlled and adjusted. One part of the project is to point out, where deficits in the existing coastal protection systems are and how the Halligen can be protected against the rising loads due to the climate change by innovative strategies and concepts. Therefore, the Schleswig-Holstein Agency for Coastal Defence, National Park and Marine Conservation (LKN-SH) supplies the basic data. Apart from the information about the coastal protection structures, hydrologic, morphologic and meteorological data will also be prepared and delivered to the other project members. Furthermore the LKN-SH evaluates the existing coastal protection systems regarding their function and effect.

At first an inventory of all existing coastal protection structures have been done in order to evaluate the effectiveness of the structures. The result was that due to setting processes, trampling of livestock or wrong dimensioning of the structures some of these facilities are no longer functional. Because of that new approaches of dimensioning of the revetment's geometry are in execution. Furthermore the development of new construction methods of revetments led to a success. Thus revetments with following rough blocks protect the border of the Hallig more effectively from erosion. Currently the LKN-SH accomplishes measures to enhance existing revetments, so that they become functional again. These measures take account of the climate change and are to be realized until 2013.

For this project the existing hydrological monitoring program of the LKN-SH is developed further, the existing facilities are maintained, collected data are verified and prepared. An optimization of the measuring is to improve the quality of the data, so that inhomogeneities and gaps in the time series can be avoided in future. Therefore a screening of the existing gauges is in progress at present in order to determine the complex hydrologic processes of the Halligen. The data of the gauges are examined and verified before delivery.

The basic data provided for the project essentially results from the hydrologic monitoring program and the coastal preservation information system (KIS) of the LKN-SH. In addition, data from other agencies are ordered, prepared and delivered.

3.5 ZukunftHallig D (LKN): Sedimentological analyses on the Halligen

The Halligen are relicts of former mainland that was flooded and disrupted during catastrophic storm surges in 1362 and 1634. Characteristic for the region are very low land surface elevations of only a few decimetre above mean high water, frequent storm surges, as well as changes in sea level and land surface elevation. Frequent inundations (up to 50 times a year)

are the consequence of the flat topography and the absence of high dykes. A worldwide unique lifestyle and architecture has developed in order to cope with these harsh conditions. Besides the cultural and historic relevancy the Halligen are of high ecological value and importance for coastal protection of the hinterland. Observation of the processes during flooding, investigations on the upper most sediment layers and dating of percussion cores revealed an increase of land surface elevation due to sediments that are deposited during inundations of the Halligen (Deicke et al., 2007, Karius et al., 2009, Karius et al., 2011). Sea level changes and land surface increase seemed to be in a dynamic balance at least for the past centuries. Today, the inhabitants have to deal with climatic changes and a further increasing mean sea level.

The IPCC (2007) predicts a mean sea level (MSL) rise of 18 to 59 cm until the end of the century. Coastal ecosystems like salt marshes are highly dynamic systems, which can compensate for MSL changes. However, this capability depends on tidal ranges and concentration of suspended sediment in the flooding water (Kirwan et al. 2010). The Halligen will be preserved if marsh levels rise at the same rate as the MSL changes. Therefore changes in inundation frequency, intensity and related changes in sediment deposition rates are of critical interest. In addition, local land subsidence has to be considered. Ongoing glacial fore bulge subsidence caused by melting of the former Fennoscandinavian icesheet increases the effective MSL rise by 0 to 1 mm per year (CPSL 2010). The ongoing process of Holocene peat layer compaction could also contribute to the effective sea level rise.

Subproject D within the interdisciplinary research group "ZukunftHallig" will focus on current and historical sedimentation dynamics on the Halligen Hooge, Langeness and Nordstrandischmoor. Additionally, dyked and undyked marshlands on selected East Frisian islands (Norderney and Juist) will be investigated.

- The annual sediment amount deposited during inundations will be quantified.
- A mean rate of surface elevation increase will be measured for the last 40-120 years based on sediment datings.
- Processes of sediment transport and distribution during inundation of the Halligen will be investigated in the context of coastal protection measures.
- Changes of land surface elevation due to isostatic processes and compaction will be estimated based on a compilation of literature data and models.

In order to quantify the recent sedimentation rates two different types of sediment traps as well as Sedimentation-Erosion-Bars (SEBs) will be used at all investigated locations. The methods for quantification of recent sedimentation rates are developed and tested since 2007 on several Halligen (Karius & Machunze, 2011, Sander et al., 2011, Vogt et al., 2011). In order to assess sedimentation dynamics of the past century, samples will be taken by vibration coring and will be analysed by ²¹⁰Pb and ¹³⁷CS dating.

In order to detect changes in topography over time aerial photographs and LIDAR data (Light detection and ranging) will be used together with GIS-based simulations of flooding. Finally, subproject D aims to predict future morphological and sedimentological changes on the Halligen by correlating the sedimentological record with hydrological parameters including concentration of suspended matter, current velocity and direction (Cooperation with Senckenberg institute, Wilhelmshaven). Subproject D is highly interlinked with subproject A, that is dealing with hydrodynamics.

4 Acknowledgements

This is a German Coastal Engineering Research Council (KFKI) project, funded by the German Federal Ministry of Education and Research (BMBF) (Project No. 03KIS093, No. 03KIS094, No. 03KIS095 and No. 03KIS096). We would like to thank these funding bodies for making this project possible.

5 References

- Abels, G., Bora, A. (2004): Demokratische Technikbewertung. Bielefeld: Transkript.
- Aguilar, E., Auer, I., Brunet, M., Peterson, T., Wieringa, J. (2003): Guidelines on climate metadata and homogenization. World Meteorological Organization.
- Arns, A., Jensen, J. (2010): Developing sustainable coastal protection- and management strategies for Schleswig-Holstein's Halligen considering climate change (ZukunftHallig) - Subproject A: Hydrodynamic analyses in the region of the Halligen. Tagungsband des 1. CoastDoc-Seminars, In: Mitteilungen des Forschungsinstituts Wasser und Umwelt, Heft 2, ISSN 1868-6613 (in press).
- Blutner, D. (2005): Kontrafakt Innovation. Eine kontrafaktische und sozialwissenschaftliche Analyse innovativen Handelns im Vertrieb. Berlin.
- CPSL (2010): Trilateral working group on coastal protection and sea level rise: Third Report: The role of spatial planning and sediment in coastal risk management, Common Wadden Sea Secretariat, Wadden Sea Ecosystems, No. 28.
- Deicke, M., Karius, V., Jahnke, W., Kallweit, W., Rebens, M., Reyer, D. (2007): Charakterisierung von Sturmflutablagerungen auf Hallig Hooge - Quantifizierung des Sedimentwachstums seit 1914. In: Gönnert, G., Pflüger, B., Bremer, J.-A. (eds.). Von der Geoarchäologie über die Küstendynamik zum Küstenzonenmanagement. Coastline Reports (9), pp. 93-102. EUCC - The Coastal Union, Leiden.
- Geels, F. W. (2005): Processes and patterns in transitions and system innovations: Refining the co-evolutionary multi-level perspective/Technological Forecasting & Social Change 72, pp. 681-696.
- IPCC (2007): Intergovernmental Panel on climate change: Fourth Assessment Report: Climate Change.
- Jungk, R. (1981): Zukunftswerkstätten. Hamburg: Hoffmann und Campe.
- Karius, V., Deicke, M., von Eynatten, H. (2009): Über das Oberflächenwachstum der Nordfriesischen Halligen. In: Ratter, B.M.W. (Hrsg.) Hamburger Symposium Geographie, Band 1: Küste und Klima, S. 35-38, Hamburg (ISBN: 978-3-9806865-8-7).
- Karius, V. Deicke, M., Michler, A., Hilgers, A., von Eynatten, H. (2011): Sediment accumulation at Northern Germany's marsh islands - An evaluation of a natural adaptation mechanism to Holocene sea level rise. Geophysical Research Abstracts Vol. 13, EGU2011-3646, 2011. EGU General Assembly 2011
- Karius, V., Machunze C. (2011): Bestimmung des Feststoffanteils in Brackwassersuspensionen. In: Karius V., Hadler H., Deicke M., von Eynatten H., Brückner H. & Vött A.. Dynamische Küsten - Grundlagen, Zusammenhänge und Auswirkungen im Spiegel angewandter Küstenforschung. Coastline Reports (17), pp. 5-18. EUCC-D - Die Küsten Union Deutschland e.V., Rostock.
- Kirwan, M., Gunterspergen, G., D'Alpaos, A., Morris, J., Mudd, S., Temmerman, S. (2010): Limits on the adaptability of coastal marshes to rising sea level, Geophysical Research Letters, Vol. 32., 1-5, 2010.
- Meehl, G. A., et al. (2007): Global climate projections, in Climate Change Fourth Assessment Report of the Intergovernmental Panel on Climate Change, edited by S. Solomon et al., pp. 747- 845, Cambridge Univ. Press, Cambridge, U. K.
- Ortmann, G. (1995): Formen der Produktion. Opladen, Wiesbaden: Westdeutscher Verlag.
- Rammert, W. (1997): Innovation im Netz. Neue Zeiten für technische Innovationen: heterogen verteilt und interaktiv vernetzt. In: Soziale Welt, Jg. 48, H. 4, pp. 397-416.
- Sander A., Deicke M., Karius V. (2011): Bestimmung der Sedimentakkumulation auf Hallig Hooge im Winter 2009/10. In: Karius V., Hadler H., Deicke M., von Eynatten H., Brückner H. & Vött A.. Dynamische Küsten - Grundlagen, Zusammenhänge und

Auswirkungen im Spiegel angewandter Küstenforschung. Coastline Reports (17), pp. 19-32. EUCC-D - Die Küsten Union Deutschland e.V., Rostock.

Simmel, G. (1908): Soziologie. Untersuchungen über die Formen der Vergesellschaftung, Duncker & Humblot Verlag, Berlin.

Vogt M., Deicke M., Karius V. (2011). Bestimmung der Sedimentakkumulation auf Hallig Langeness im Winter 2009/10. In: Karius V., Hadler H., Deicke M., von Eynatten H., Brückner H. & Vött A.. Dynamische Küsten - Grundlagen, Zusammenhänge und Auswirkungen im Spiegel angewandter Küstenforschung. Coastline Reports (17), pp. 49-58. EUCC-D - Die Küsten Union Deutschland e.V., Rostock.

Weyer, J. (2008): Techniksoziologie. Genese, Gestaltung und Steuerung sozio-technischer Systeme. Weinheim: Juventa.

Artificial surfing reefs – An option for the German Baltic Sea coast?

M. Behrendt¹

Abstract

The possibility of building artificial surfing reefs to improve the local surfing conditions have been shown at several locations all over the world. To design such a reef, a detailed knowledge about shallow water effects and the local sea state conditions is needed. A short introduction to the sport of surfing is given, followed by an explanation of the basic functioning principles of a surfing reef. Three different locations at the German Baltic Sea coast are analyzed from a statistical point of view, using a 20 years wind data set. The possible usability of a surfing reef for the purpose of coastal protection is discussed. Finally, a new reef layout for the special requirements of the German Baltic Sea coast with its wind wave dominated sea state is presented.

Keywords: surfing; artificial reef; breakwater; Baltic Sea.

1 Introduction

Surfing is the process of riding on a wave with a board. The sport of surfing is a traditional sport with more than 200 years of documented history and today, it is a billion dollar industry with millions of surfers all over the world. To catch a wave, a surfer moves with his surfboard to the seaward site of the breaker zone. When a surfable wave reaches the surfer in the water, the surfer increases his velocity by paddling and then “takes off” to ride the wave. The main purpose is to surf parallel to the wave crest and meanwhile to perform maneuvers and to surf at specific regions of the wave, for example underneath a plunging breaker (tubertide).

The numbers of waves in the ocean is endless, but there are not endless surf spots in the world. This is due to the fact that only specific bathymetries cause breaking waves that are good for surfing purposes. These bathymetries, for example natural reefs and sandbanks, are characterized by two main components:

- I) Components that make the wave starting to break at one point and peel along the crest and thereby give the surfer the possibility to perform maneuvers at the front (face) of the wave.
- II) Components that focus the wave energy to a specific point in the nearshore region and thereby increases the wave height.

2 Artificial surfing reefs

Additional to natural surfing locations it is possible to build artificial surfing reefs that offer the same kind of quality waves. The first artificial surfing reef was built at the Gold Coast of Australia in 1999, with the purpose of coastal protection and improving surfing conditions. Today there are several surfing reefs in the world. Most of them are made of geotextile megacontainers filled with sand.

The main purpose of an artificial surfing reef is to influence the shallow water effects which are modifying the incoming waves. The shallow water effects are influenced in the following way:

- I) Refraction – on the first part of the reef, which is shaped like a ramp with a small slope angle, the incoming waves are refracted towards the favoured orthogonal direction.

¹ Scientific employee, Chair of Geotechnic and Coastal Engineering, University of Rostock, 18059 Rostock, Germany,
Email: marcus.behrendt@uni-rostock.de

- II) Shoaling – when the slope angle increases, the process of shoaling becomes significant and the waves are getting higher before they start to break.
- III) Wave breaking – waves with a defined size or bigger will break at the end of the reef along the crest of the reef.

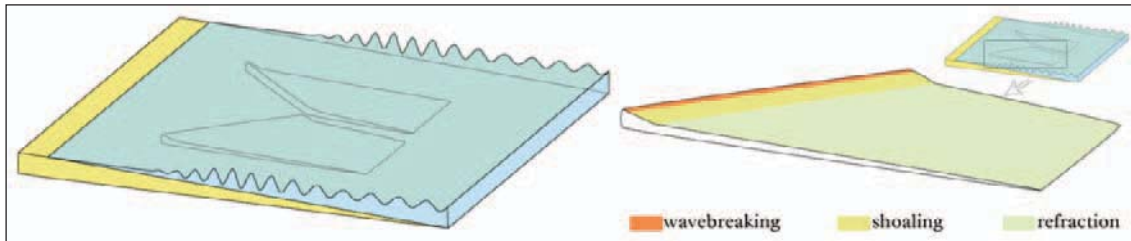


Figure 1: aerial view of an artificial surfing reef (left), functional parts of an artificial surfing reef (right)

The main improvement that is caused by the reef is the controlled breaking of the waves along the crest of the reef. Depending on the angle between the reef crest and the incoming waves, the level of difficulty of surfing this wave can be influenced. The smaller the so called peel angle is, the more difficult it is to surf the wave. The reef can have several parts with different peel angles, so the reef can be surfed by beginners and advanced surfers. Furthermore it is possible to create local features by including for example a pinnacle or a ridge in the crest of the reef. With these tools it is possible to design the characteristics of the breaking waves.

Refraction and shoaling do not occur at one specific point, but over a long distance. The beginning of these processes starts at intermediate depth ($1/20 < d/L < 1/2$). Refraction depends very much on the directional spreading of the incoming waves. Wind waves with a great directional spreading are less refracted than long travelled swell. This is of great significance for building a reef at the German Baltic Sea Coast and will be discussed later on. Shoaling depends mostly on the wavelength. Similar to refraction, shoaling is more significant in long travelled swell than in wind waves, because the wavelength of windwaves can be relatively small.

Even though it is possible to surf on the face of a wave that is not breaking, surfing on a breaking wave (especially plunging breakers) is the favoured way of surfing. Waves are breaking along the reef crest, if one of the breaking criteria is fulfilled. There are two existing breaking criteria, the critical wave steepness and the minimum water depth. The minimum water depth varies according to the used theory.

Critical wave steepness:
$$\frac{H_0}{L_0} \approx 0.10 \quad (1)$$

Minimum water depth: from
$$\frac{H_b}{d_b} \approx 0.73 \quad (2) \quad \text{to} \quad \frac{H_b}{d_b} \approx 1.03 \quad (3)$$

H_0 is the wave height and L_0 the wave length in deep water, H_b is the wave height and d_b the water depth at the breaking point. In the nearshore region the minimum water depth is the governing parameter for wave breaking and this has to be included in the reef design process. The water depth at the crest of the reef is one very important parameter for the reef design. Only waves that fulfill the breaking criteria will break along the reef crest. Thereby a minimum wave height is needed for the reef to cause breaking waves. Waves that do not fulfill the breaking criteria will pass the reef without breaking.

3 Statistical analysis of the German Baltic Sea wave climate

When reefs are designed one very important fact is often neglected by the public. A reef can influence and thereby improve waves at a specific location, but it cannot create waves. A minimum wave height is needed for the interaction of wave and reef to take place.

To design a reef and to calculate the amount of time of possible interaction of the waves with the reef, it is necessary to define a minimum wave height that fulfills the breaking criteria at the reef crest. In the following example, the minimum wave height was defined with $H_s = 1.0$ m. Three different locations for the statistical analysis were chosen along the German Baltic Sea Coast (see Fig. 2). They are oriented northwest (315°), north (0°) and northeast (45°).

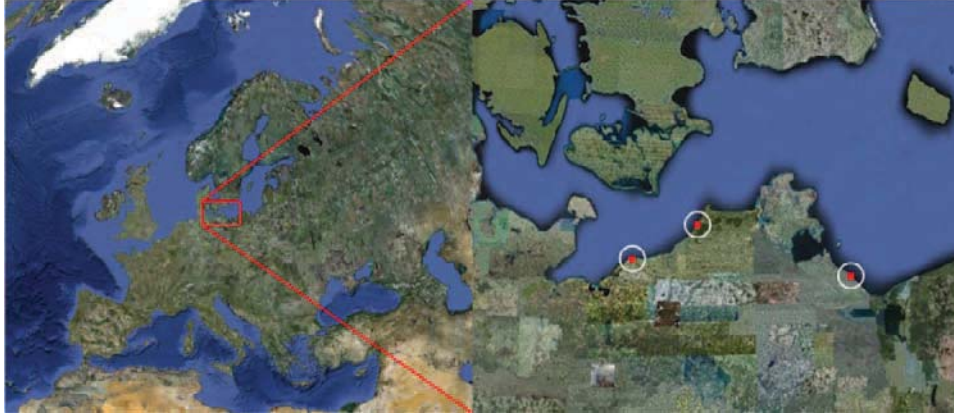


Figure 2: situation of the survey area (left), investigated shorelines with different orientations (right)

Averaged sea state distributions depending on the incident wave angle are available for these locations. The sea state distribution was calculated by the use of wind measurements over 20 years. They have been filtered with the minimum wave height $H_s = 1.0$ m and the relevant incident wave angles for the specific location. Thereby the annual occurrence for the fulfillment of the breaking criteria at each location could be calculated. In the following text, this value will be named performance. The calculated performances can be seen in figure 3a (Rostock, orientation 0°), 3b (peninsula Fischland, orientation 315°), and figure 3c (Island of Usedom, orientation 45°).

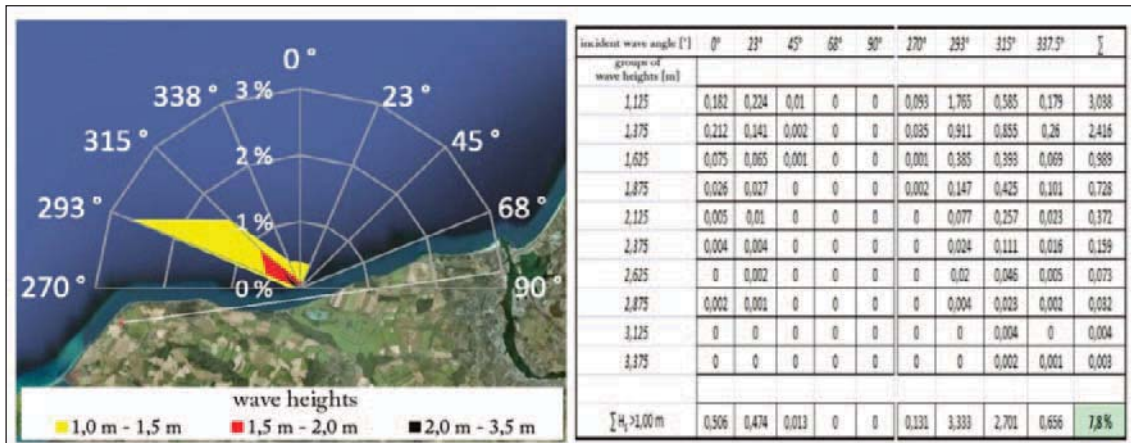


Figure 3a: visualization of the significant wave heights and their incident wave angle near Rostock (left), sea state distribution for the specific location (right)

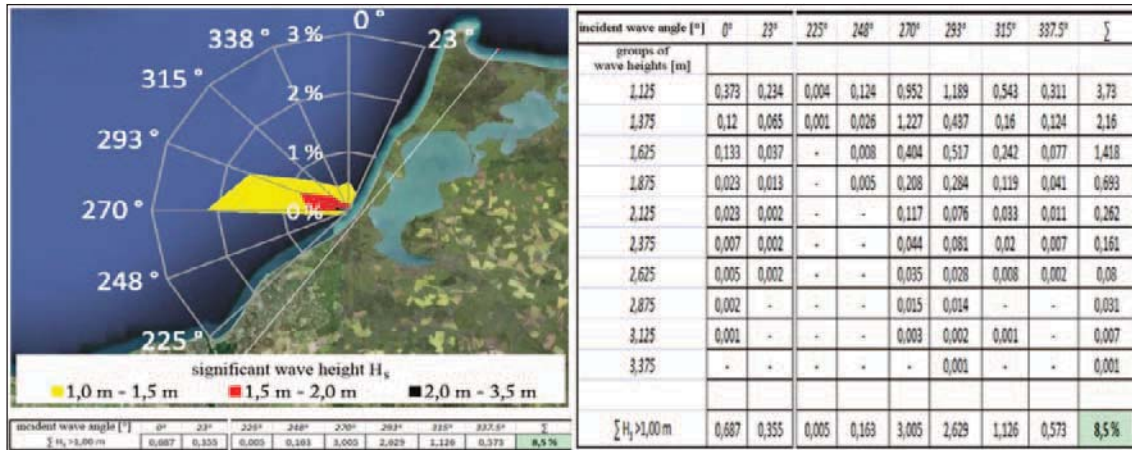


Figure 3b: visualization of the significant wave heights and their incident wave angle at the peninsula Fischland (left), sea state distribution for the specific location (right)

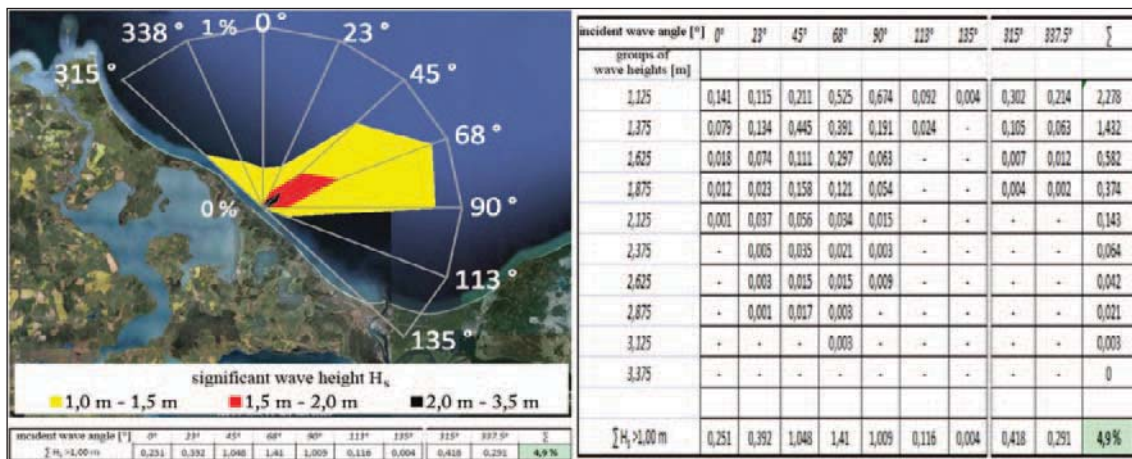


Figure 3c: visualization of the significant wave heights and their incident wave angle at the island of Usedom (left), sea state distribution for the specific location (right)

The performance for the region around Rostock is about 7.8%, for the peninsula Fishland the performance is about 8.5% and for the island of Usedom about 4.9%. This is due to the fact that westerly winds are dominating in the north of Germany. The performance of a surfing reef at the German Baltic Sea coast designed for a minimum significant wave height of $H_s = 1.0 \text{ m}$ is below 10% for all orientations of the coastline. With building costs of round about two million Euros, such a project with the single purpose of improving the surfing conditions is hard to finance. Thereby additional benefits of the artificial reef have to be identified.

4 Coastal protection possibilities

Even though the reef is designed for the improvement of the surfing conditions, it can be seen as a submerged breakwater. The effect of a submerged breakwater on the evolution of a salient at the coastline depends on the transmission coefficient K_t . This coefficient is calculated by dividing the incident wave height H_i by the transmitted wave height behind the breakwater H_t .

The higher the breakwater is, the smaller is the transmission coefficient and the bigger is the influence of the breakwater on the coastline and its development. For calculating the transmission coefficient it is necessary, to know the height of the freeboard R_c . By using equation (2) and an incident wave height of $H_s = 1.0 \text{ m}$ the freeboard is calculated with $R_c = -1.37 \text{ m}$. The sea state distribution used for the calculation of the performance was also used for the calculation of the transmission coefficient. Thereby a weighted transmission coefficient for a defined freeboard and varying incident wave heights could be calculated. For an artificial surfing

reef with the described parameters the transmission coefficient is $K_t = 0.75$. In comparison to non submerged breakwaters this transmission coefficient is relative high and the effect on the coastline will be not very intense. Nevertheless it can be enough to protect the coast from erosion by a certain amount.

5 Alternative reef layout for German Baltic Sea wave climate

Two out of three shallow water effects, namely refraction and shoaling are strongly influenced by the velocity of the wave. Waves with a small period and a small wavelength have a small velocity. The chosen locations are characterized by wind waves with small wave periods and great directional spreading. Until now, no artificial reefs in the world have been built at locations where wind waves are the dominating sea state. There is a danger, that the described shallow water effects are not taking place at the expected intensity and the improvement of the surfing conditions through the reef will be insignificant.

Even though shoaling and refraction are depending strongly on the same parameter, the velocity, the effect on the improvement of surfing conditions is different for each of them. If the dimension of shoaling would be small, the performance of the reef would still be as calculated in figure 3 a, b and c, because the design wave height H_s is the wave height in deep water and is independent from shoaling. So if shoaling would take place, the performance of the reef would increase but if shoaling would not take place the performance of the reef would not decrease. For refraction this is a different thing, if the amount of refraction is too small, the wave is not breaking along the crest of the reef because the wave is orientated in a wrong direction. The performance of the reef stays the same because the waves are still breaking at the reef, but they are not breaking in the way they are supposed to. Without a significant amount of refraction at the reef, it would not improve the surfing conditions at all. An alternative reef concept is needed for the German Baltic Sea wave climate to ensure that there is a significant improvement of the surfing conditions through the reef.

One possibility would be to build a non submerged breakwater with a very small transmission coefficient at the seaward site of the artificial reef with a specific distance to this (see Fig. 4). As a result of this breakwater, there would be no direct wave approach (according to the most frequent incident wave angle) to the artificial reef, but only diffracted waves. The choppy and unsorted wind waves would be blocked by the breakwater and only the diffracted (and thereby sorted) waves would reach the artificial reef.

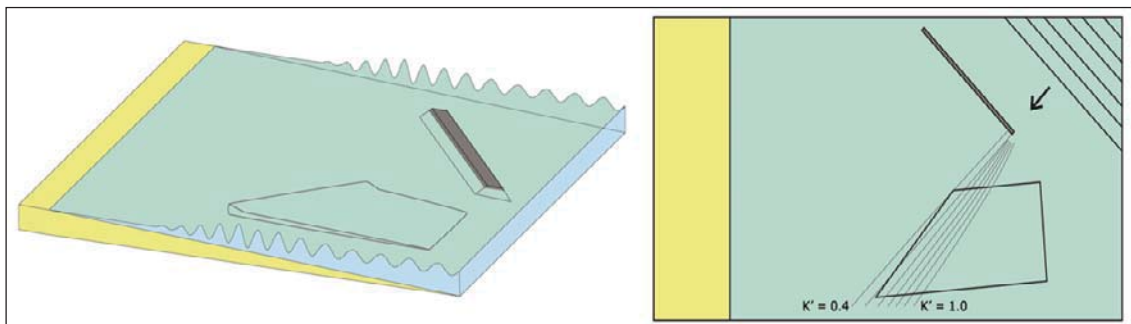


Figure 4: aerial view of the new reef layout (left), diffraction pattern behind the breakwater at the artificial reef for incident waves with $T = 4$ s and $L = 22$ m in 5 meters water depth (right)

It is obvious, that the diffracted wave will be smaller than the incident wave, this will decrease the performance of the reef, but that does not necessarily means a worsening of the surfing conditions. There is a proven correlation of H_s and H_{max} , which means a sea state situation with $H_s = 1.0$ m also includes waves with $H_{max} \approx 1.8$ m. If H_{max} is multiplied with the diffraction coefficient, for example $K' = 0.5$ the height of the diffracted wave will be $H_{max}' = 0.9$ m. To fulfill the breaking criteria at the crest of the reef, the incident wave height has to be $H_s = 1.1$ m. The number of waves within one storm that will break at the reef will decrease, but the quality of the waves that break at the reef will improve significantly. As a result, there will be a good surfable wave not every four or five seconds (mean wave period for Baltic Sea waves), but every 60 or

every 90 seconds. From a surfers point of view, this are still good surfing conditions, especially for surfers in the Baltic Sea who surf in choppy conditions most ocean surfers would not even think about to surf in. Next to the improvement of the surfing conditions, the non submerged breakwater would decrease the transmission coefficient for the whole construction and thereby the usability for coastal protection becomes more realistic.

6 Conclusions

An artificial surfing reef at the German Baltic Sea Coast is a possible option. By combining a submerged breakwater (to influence the shallow water effects refraction, shoaling and wave breaking) with a non submerged breakwater (blocking of choppy wind waves and diffracting clean waves) it is possible to create a setup that offers everything that is needed for a high quality surfing experience at the German Baltic Sea coast. Even though the performance of a reef, designed for a minimum wave height of $H_s = 1.0$ m, is below 10 % and the costs for building two independent constructions are not insignificant, the creation of such a building could be realized, if the aspects of coastal protection are taken into consideration. The positive effects for the maritime tourism and the local sport and youth culture could also influence the decision makers to build an artificial surfing reef at the German Baltic coast. By using the proposed set up, a high quality surf spot could be created.

7 References

- DAEMRICH, K.F.; KOHLHASE, S. 1978. Diffraktion an halbbunendlichen Wellenbrechern. Mitteilungen des Franzius-Institut für Wasserbau und Küsteningenieurwesen.
- FRÖHLE, P.; HORLACHER, H.B. 2006. Bemessungsseegang Außenküste Mecklenburg-Vorpommern – Abschlussbericht.
- KURATORIUM FÜR FORSCHUNG IM KÜSTENINGENIEURWESEN 2007: Die Küste Heft 65. Empfehlungen für die Ausführungen von Küstenschutzwerken. Die Küste.
- MEAD, S.; BLACK, K. 2001. Field Studies Leading to the Bathymetric Classification of World – Class Surfing Breaks. Journal of Coastal Research Special Issue No. 29,
- VAN DER MEER, J. W.; BRIGANTI, R.; ZANUTTIGH, B.; WANG, B. 2005. Wave transmission and reflection at low crested structures: Design formulae, oblique wave attack and spectral change. Coastal Engineering Volume 52.
- WALKER, J. 1974, Recreational Surf Parameters. LOOK Laboratory TR-30, University of Hawaii.

Abrasion rates of coarse sediments on two artificial pebble beaches at Marina di Pisa (Italy)

Duccio Bertoni¹, Giovanni Sarti², Giuliano Benelli³ and Alessandro Pozzebon⁴

Abstract

In this paper pebbles marked by passive integrated transponders from two artificial coarse-grained beaches at Marina di Pisa (Tuscany, Italy) were analyzed in order to measure the in situ abrasion rate. The beaches (Cella 7 and Barbarossa) were set up in 2006 as a form of coastal protection and differ in length (250 m and 110 m respectively) and in the presence of a submerged breakwater 50 m off the coastline at Cella 7. The aim of the study is to reckon the abrasion rate of individual pebbles and evaluate abrasion differences of pebbles released on Cella 7 and on Barbarossa. The RFID technology (Radio Frequency Identification) was used to track the pebbles. The tracers were released on the beaches in March 2009 along closely-spaced cross-shore transects. The recovery campaign was carried out in May 2009. A total of 127 pebbles was detected, 83 of which were recovered. The pebbles that were recovered showed a significant increase in roundness, in particular the tracers that were released on Barbarossa. The average pebble weight loss measured at Cella 7 was slightly lower, which means higher mobilization rate at this site rather than at Barbarossa. The resulting values are significant considering the short time frame of the research (two months) and the limited energy of the storms occurred during the experiment.

Keywords: abrasion, coarse-clastic beach, pebble

1 Introduction

Tagging individual pebbles with devices that enable an easy detection is a methodology that has been often used recently (Allan et al., 2006; Bertoni et al., 2010). A useful application of this method concerns the measurement of sediment in situ abrasion, which makes up for a more complete dataset rather than laboratory tests. First laboratory experiments about sediment abrasion involved measurements under conditions that only simulate the physical processes acting on a beach (Kuenen, 1964; Latham et al., 1998; Nordstrom et al., 2008). Matthews (1983) measured beach pebble attrition on pebbles of significantly different lithology relative to the native sediments using statistical methods, then compared the results to laboratory tests performed with the same lithology. Preliminary attempts on individual pebbles were performed by Zhdanov (1958), but the technique implied the breakage of the pebbles to identify them once recovered. Dornbusch et al. (2002) provided a remarkable impulse to this topic, measuring the in situ abrasion of individual pebbles without the need to break them. To allow both recognition and recovery of the marked samples, the rock types that were used in the experiment were different from the lithology of the study site, which constitutes the limit of the method. Recently the recognition of the pebbles was attained by means of the Radio Frequency Identification (RFID) technology, which enables to detect items that have been coupled to small devices (Allan et al., 2006; Curtiss et al., 2009). A later work by Bertoni et al. (2010) allowed to extend this technique to the underwater environment. The aim of the study is to measure the abrasion rate of individual pebbles of different grain-size and shape, highlighting the differential weight loss on two artificial coarse-clastic beaches at Marina di Pisa (Tuscany, Italy).

¹ Department of Earth Sciences, University of Pisa, Via S. Maria 53, 56126 Pisa, Italy, bertoni@dst.unipi.it

² Department of Earth Sciences, University of Pisa, Via S. Maria 53, 56126 Pisa, Italy, sarti@dst.unipi.it

³ Department of Information Engineering, University of Siena, Via Roma 56, 53100 Siena, Italy, benelli@unisi.it

⁴ Department of Information Engineering, University of Siena, Via Roma 56, 53100 Siena, Italy, alessandro.pozzebon@unisi.it

2 Study area

The artificial pebble beaches at Marina di Pisa (Tuscany, Italy) were chosen as the study site because they match several of the needed requirements, such as the limited length and the defined boundaries. Marina di Pisa is located towards the southern edge of the Ligurian Sea, on the left side of the River Arno mouth, just 11 km southwest of the city of Pisa (Fig. 1). The two beaches where the experiment was carried out, Cella 7 and Barbarossa, are similar except for the length and for the different protection scheme (Fig. 1). The former is 250 m long and 30 to 40 m wide; it is bounded by two large groins composed of marble boulders and it is confined seaward by a submerged breakwater, about 50 m off the coastline. The latter, located just 1 km to the south of Cella 7, is 110 m long and 20 m wide, but its width is reduced to less than 10 m in a couple of sectors due to manmade structures that were built on the backshore of the beach; two groynes define the cell, but no longshore protection structure is present seaward.

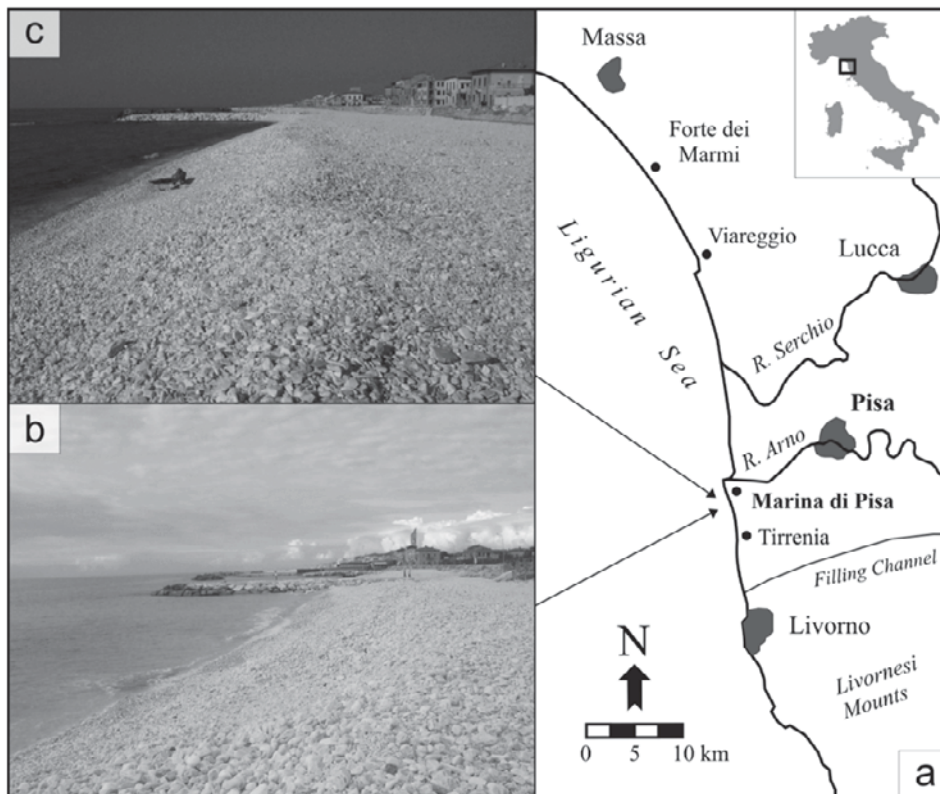


Figure 1: Map of the study site (a); southern view of the beaches where the experiment took place: Barbarossa (b) and Cella 7 (c).

Both beaches present a seawall made of large, angular boulders that separates the backshore from the littoral promenade. The sediments used to replenish the beaches are waste material (pebbles of about 40 to 90 mm of mean diameter) at marble quarries, which are not distant from Marina di Pisa. Both Barbarossa and Cella 7 are characterized by a steep beachface and a pronounced step, which is the break in slope at the transition between the foreshore and the upper shoreface. The step can reach 60 cm of height, and is usually more prominent at Barbarossa. The step base is still composed by a predominance of pebbles, but here lies the transition to the typical grain size of the area, that is medium-to-fine sand. The sea floor is flat and its slope value (1%) is similar to that of this region (Cipriani et al., 2001). The tides are not particularly significant in this sector of the Tuscan coast: the tidal range hardly exceeds 30 cm (Nordstrom et al., 2008). The littoral drift (Fig. 1, site map) is southward-trending throughout this region (Gandolfi and Paganelli, 1975; Pranzini, 2004).

3 Methods

Coarse sediments were traced by means of the RFID (Radio Frequency Identification) technology, which proved a reliable method to track particles on the subaerial portion of a beach (Allan et al., 2006; Curtiss et al., 2009) and even underwater (Bertoni et al., 2010). About 200 marble pebbles were sampled randomly on the beaches where the experiments would have been undergone and coupled to a 30 mm diameter transponder. These small devices made the tracers unequivocally identifiable. Each pebble was drilled to carve a 27 mm deep and 32 mm diameter hole to fit the transponders in. The transponders were then fixed with a strong epoxy adhesive. The hole was filled with a small marble core and a synthetic resin to seal everything up (Fig. 2). This procedure should minimize undesired effects on the textural properties of the tracers. Once ready, the wet weight of the pebbles was measured by means of an accurate scale (instrument error of 0.1 g). The pebbles were then carefully dried and weighed again. In March 2009, the samples were injected on the beaches along cross-shore transects, placing three tracers per transect (on the fair-weather berm, on the swash zone, and on the step crest). Recovered pebbles were analyzed again in laboratory, measuring the wet and dry weight. A mobile antenna, transmitting a low-frequency radio signal (125 kHz), was used to allow the recovery of the marked pebbles. The detection range of the antenna reached 40 cm, and it was often difficult to dig up those pebbles that were transported toward the step and then buried.



Figure 2: Picture of a marked pebble during the preparation procedures.

4 Results

The recovery campaign took place after two months (May 2009). Three storms occurred during this span of time. A total of 81 pebbles were retrieved, which is a good feature considering that another 46 samples were detected by the instrument, but not recovered because they were deeply buried (the actual detection range was about 45 cm). Five of these tracers were found back broken, but they were still working (the transponder was exposed, but avoided contact with the water thanks to the envelope of resin and glue). Weight loss due to breakage would have affected the abrasion rate, so the broken pebbles were not taken into account when calculating the average abrasion rate.

Fifty-two marked pebbles were recovered at Cella 7, four of which were found back broken. Thirty-six pebbles have been covered by a thin layer of algae, which was accurately removed prior to the weighing procedure. The results showed a slight weight decrease for every pebble: the weight decrease was on average about 2.4% (Fig. 3). Table 1 highlights that a lower abrasion rate was measured on pebbles that were recovered close to their injection position. Pebbles that moved further away from their starting position experienced a higher abrasion rate.

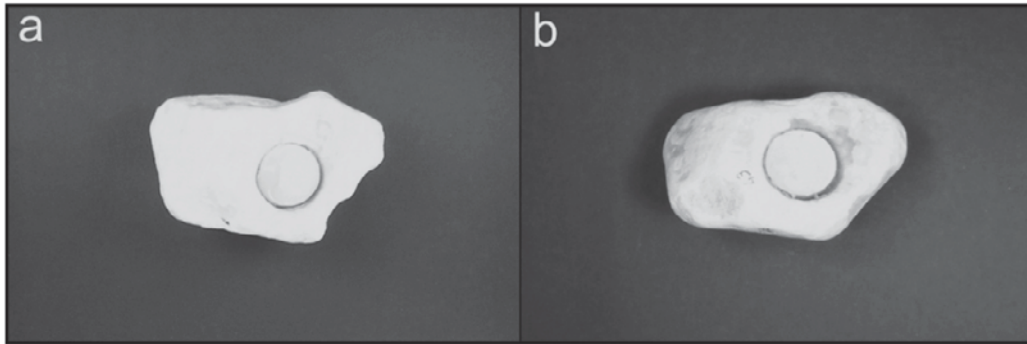


Figure 3: Pictures of a marked pebble recovered at Cella 7 before (a) and after (b) the experiment.

Pebbles that were placed on the fair-weather berm showed a higher abrasion rate than any other starting positions.

Table 1: Measurements of the pebbles that were recovered at Cella 7. Keys: WT. BEF.: weight of the pebbles before the release (g); WT. AFT.: weight of the pebbles after the recovery (g); % DIFF.: weight loss percentage; DISPL.: length of displacement of the pebbles (m); REL. POS.: release position of the pebbles.

#	WT. BEF.	WT. AFT.	% DIFF.	DISPL.	REL. POS.
1	951.1	297.3	68.7	12.2	Step Crest
6	902	883.2	2.1	16.2	Step Crest
7	425.1	256	39.8	13.8	F-W Berm
10	492.5	484.7	1.6	23.4	F-W Berm
15	589.8	580.8	1.5	22.2	Swash Zone
16	470.4	428.1	9.0	18.3	F-W Berm
18	541.2	525.5	2.9	7.4	F-W Berm
19	841.2	819	2.6	19.3	Step Crest
20	329.6	286.5	13.1	33.1	F-W Berm
24	586.5	578.5	1.4	10.0	Swash Zone
26	766.3	754.2	1.6	19.5	Swash Zone
27	938.7	898.4	4.3	21.3	Step Crest
31	660.6	655.1	0.8	108.9	Swash Zone
34	492.7	490.5	0.4	5.2	F-W Berm
38	573.4	567	1.1	10.0	Step Crest
49	530.8	525.2	1.1	10.9	Swash Zone
54	569.2	553.8	2.7	9.8	Swash Zone
58	675.2	648.8	3.9	43.6	Swash Zone
59	599.7	595.9	0.6	4.6	Swash Zone
60	793.8	792	0.2	7.5	Swash Zone
64	981.8	961	2.1	13.2	Swash Zone
83	516.9	479.5	7.2	22.1	F-W Berm
86	623.2	601	3.6	9.4	F-W Berm
87	390.9	376.5	3.7	37.4	F-W Berm
88	604.5	578.4	4.3	50.0	F-W Berm
90	655.3	654.8	0.1	4.3	F-W Berm
91	1102.2	1098.8	0.3	1.4	Step Crest
96	534	291.2	45.5	26.3	F-W Berm

101	908.5	879.3	3.2	14.4	Swash Zone
102	887.8	882.4	0.6	13.6	Swash Zone
109	637	633.1	0.6	3.8	Swash Zone
111	686.3	680	0.9	18.7	Swash Zone
113	413.7	181.4	56.2	1.9	F-W Berm
114	323.2	305.6	5.4	5.5	F-W Berm
116	1557.1	1556.3	0.1	2.0	Step Crest
119	616.2	611.8	0.7	2.4	Swash Zone
122	590.3	579.5	1.8	5.2	F-W Berm
123	561.3	552.1	1.6	9.2	F-W Berm
152	1377.7	1359.3	1.3	12.9	Step Crest
153	771.2	754.7	2.1	18.6	Step Crest
154	755.2	742.9	1.6	15.2	Swash Zone
162	1496.8	1492.1	0.3	11.6	Step Crest
164	791.6	785.8	0.7	4.8	Step Crest
168	778.6	776.5	0.3	0.2	Swash Zone
179	923.9	889.3	3.7	24.8	Step Crest
181	631.8	576.6	8.7	21.5	F-W Berm
186	585.6	573.9	2.0	2.0	Step Crest
187	784.4	750.8	4.3	5.4	Swash Zone
192	415.5	409.3	1.5	21.0	F-W Berm
193	568.9	567.5	0.2	1.8	Swash Zone
195	485.3	476.1	1.9	10.6	F-W Berm
202	734.5	731.3	0.4	4.8	Step Crest
		AVERAGE	2.4		

Thirty-one pebbles were recovered at Barbarossa, only one was found back broken. In two cases, only the transponder still pasted to the small marble core was recovered, bringing the total count to 29 pebbles. Algae covered no pebble during the two-months-long experiment. The results remarked a significant weight decrease for every pebble: the weight decrease was on average about 8.5% (Fig. 4).

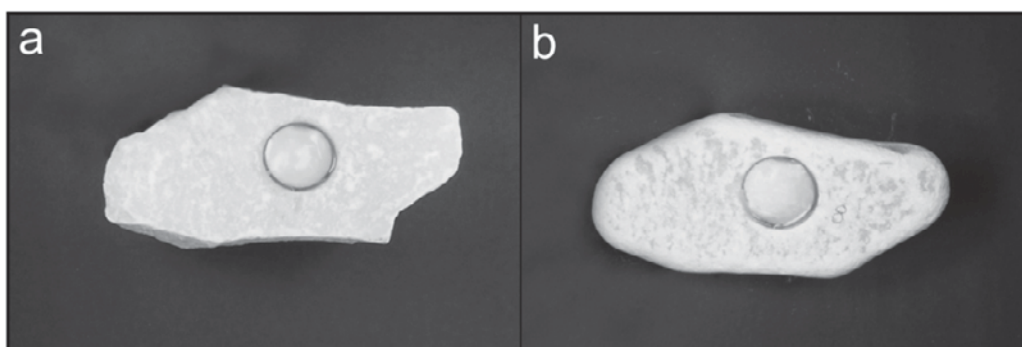


Figure 4: Pictures of a marked pebble recovered at Barbarossa beach before (a) and after (b) the experiment.

Table 2 shows an apparent lack of correlation between the displacement length of the pebbles and their abrasion rate. In addition, tracers that moved slightly eastwards (less than 10 m on average) were abraded more than those that experienced long movement (either northwards or southwards). Pebbles that were placed on the fair-weather berm showed a higher abrasion rate than any other starting positions.

Table 2: Measurements of the pebbles that were recovered at Barbarossa. Keys: WT. BEF.: weight of the pebbles before the release (g); WT. AFT.: weight of the pebbles after the recovery (g); % DIFF.: weight loss percentage; DISPL.: length of displacement of the pebbles (m); REL. POS.: release position of the pebbles.

#	WT. BEF.	WT. AFT.	% DIFF.	DISPL.	REL. POS.
13	992.3	927.4	6.5	69.5	F-W Berm
40	1338.5	1285.7	3.9	21.7	Step Crest
41	1000.6	774	22.6	58.4	Beachface
52	789.4	777.2	1.5	29.5	F-W Berm
53	743.1	486.1	34.6	13.9	F-W Berm
67	987.4	927.2	6.1	82.4	Beachface
82	991.4	939.8	5.2	29.7	Beachface
93	990	895.8	9.5	79.9	Beachface
103	1088.6	1030.6	5.3	54.0	Beachface
105	772.6	688.6	10.9	18.1	F-W Berm
106	660.2	606.7	8.1	23.3	F-W Berm
108	941.3	912.1	3.1	8.1	Beachface
115	931.3	848.8	8.9	59.9	Beachface
124	881.9	809.3	8.2	77.3	F-W Berm
127	1094.8	991.4	9.4	23.8	Beachface
138	1132.8	1011.1	10.7	48.4	Beachface
142	1010	994.3	1.6	7.1	Beachface
146	1881.6	1855	1.4	27.6	Step Crest
150	1341.9	1152.9	14.1	22.1	Step Crest
155	792.3	719.1	9.2	41.8	F-W Berm
156	782.9	331.7	57.6	99.0	F-W Berm
161	1343.6	1224.6	8.9	27.3	Beachface
171	1018	998.8	1.9	23.4	Beachface
174	1599.5	1398.6	12.6	18.4	Step Crest
182	954.6	795.5	16.7	8.2	F-W Berm
184	1299.2	1288.3	0.8	24.6	Step Crest
188	1205.3	1113.8	7.6	29.4	Beachface
190	874.8	851.3	2.7	36.0	F-W Berm
200	1447.1	1363.2	5.8	60.2	Step Crest
		AVERAGE	8.5		

5 Discussion

The two-months-long experiment provided significant results in terms of abrasion rate of coarse-grained sediments. Considering the short time period of the research and the occurrence of only three storms, the average abrasion rate that was reckoned on the recovered pebbles has been noteworthy. The considerable difference in weight loss attained on the two study sites (2.4% at Cella 7 and 8.5% at Barbarossa) stems from the configuration of the beaches themselves. While Cella 7 is well protected by the submerged breakwater, Barbarossa is devoid of any offshore protection structures, which means higher energy of the incoming waves. The lack of wave dissipation in the nearshore generates higher mobilization of the sediments and higher abrasion rate thereof. Intuitively, pebbles that moved further away from their injection point were abraded more than those that were detected close to their starting position. Although somewhat expected, it did not happen at Barbarossa: here, the tracers that moved the less showed higher

abrasion rate on average. However, this feature is largely skewed by a couple of pebbles that lost 34.6% and 16.7% in weight respectively. Without those two samples, the average abrasion rate of shortly-displaced pebbles would be just 2.3%, which is consistent with the values measured at Cella 7. The only thing that those highly-abraded pebbles have in common is the injection point, that is the fair-weather berm. Considering the sector (northern, central and southern) of the beach where the pebbles were originally injected, again the abrasion rate would be directly proportional to the displacement length barring the fair-weather berm-released pebbles. The higher abrasion rate of the tracers that were injected on the fair-weather berm is probably related to the higher mobilization of that portion of the beach even during fair-weather periods. Sediments on the storm berm are only moved during high-energy events, while sediments on the step are not reworked by the wave motion typical of fair-weather periods. That leaves sediments on the upper limit of the swash zone those that are subjected to slight abrasion processes even under low-energy waves. While this trend is easily recognizable at Barbarossa, it is less appreciable at Cella 7. Due to the higher wave energy dissipation, the resulting abrasion rates are lower than at Barbarossa. Anyhow, the difference between the abrasion rate measured on fair-weather-placed pebbles and pebbles injected elsewhere is remarkable (4.2% and 1.6% respectively).

6 Conclusions

This research highlighted once again the efficiency of the RFID technology as a mean to trace and detect coarse-grained sediments, which is paramount to assess and evaluate the modification of sediment textural properties such as the abrasion directly on site and not only in laboratory. Measuring in situ abrasion rates of pebbles might be useful to improve and optimize future coarse-clastic beach fills, which are more consistently used as a form of protection from coastal erosion. The measured abrasion of almost 10% on pebbles sampled on the beach is significant considering the short span of time of the experiment and the limited energy of the storms. The higher weight loss recorded on the pebbles that were released on Barbarossa (8.5% in contrast to 2.4% at Cella 7) is related to the protection level of the two beaches: Barbarossa does not have any offshore breakwater, resulting in less wave dissipation and in more energy unloaded on the nearshore. At last, the results remarked a strong abrasion of the pebbles released on the fair-weather berm, which might imply that this is the area that is subjected to most intense reworking even during fair-weather periods.

7 References

- Allan, J. C.; Hart, R.; Tranquilli, V. (2006): The use of Passive Integrated Transponder (PIT) tags to trace cobble transport in a mixed sand-and-gravel beach on the high-energy Oregon coast, USA. In: *Marine Geology*, Vol. 232, pp. 63-86.
- Bertoni, D.; Sarti, G.; Benelli, G.; Pozzebon, A.; Raguseo, G. (2010): Radio Frequency Identification (RFID) technology applied to the definition of underwater and subaerial coarse sediment movement. In: *Sedimentary Geology*, Vol. 228, pp. 140-150.
- Cipriani, L. E.; Ferri, S.; Iannotta, P.; Paolieri, F.; Pranzini, E. (2001): Morfologia e dinamica dei sedimenti del litorale della Toscana settentrionale. In: *Studi Costieri*, Vol. 4, pp. 119-156.
- Curtiss, G. M.; Osborne, P. D.; Horner-Devine, A. R. (2009): Seasonal patterns of coarse sediment transport on a mixed sand and gravel beach due to vessel wakes, wind waves, and tidal currents. In: *Marine Geology*, Vol. 259, pp. 73-85.
- Dornbusch, U.; Williams, R. B. G.; Moses, C.; Robinson, D. A. (2002): Life expectancy of shingle beaches: measuring in situ abrasion. In: *Journal of Coastal Research*, Vol. SI 36, pp. 249-255.
- Gandolfi, G.; Paganelli, L. (1975): Il litorale pisano-versiliese (Area campione Alto Tirreno). In: *Bollettino della Società Geologica Italiana*, Vol. 94, pp. 1273-1295.
- Kuenen, P. H. (1964): Experimental abrasion: 6 surf action. In: *Sedimentology*, Vol. 3, pp. 29-43.

- Latham, J. P.; Hoad, J. P.; Newton, M. (1998): Abrasion of a series of tracer materials on a gravel beach, Slapton Sands, Devon, UK. In: Latham, J. P. (ed.) *Advances in Aggregates and Armourstone Evaluation*. Geological Society, London, Engineering Geology Special Publications, Vol. 13, pp. 121-135.
- Matthews, E. R. (1983): Measurements of beach pebble attrition in Palliser Bay, southern North Island, New Zealand. In: *Sedimentology*, Vol. 30, pp. 787-799.
- Nordstrom, K. F.; Pranzini, E.; Jackson, N. L.; Coli, M. (2008): The marble beaches of Tuscany. In: *The Geographical Review*, Vol. 98, pp. 280-300.
- Pranzini, E. (2004): Caratteristiche morfologiche e sedimentologiche di una zona di convergenza del trasporto litoraneo (Versilia, Toscana). In: *Studi Costieri*, Vol. 8, pp. 135-149.
- Zhdanov, A. M. (1958): Attrition of pebbles under the wave action. In: *Bulletin of the Oceanographic committee of the USSR Academy of Sciences*, Vol. 1, pp. 81-88.

The risk assessment for North Sea coastal lowlands

Holger Blum¹, Frank Thorenz² and Hans-Jörg Lambrecht³

Abstract

The coastal lowlands located in Lower Saxony and Schleswig-Holstein are flood prone by storm surges. The BMBF-KFKI research project HoRisk focuses within the subproject lead by the Lower Saxony Water Management, Coastal Defence and Nature Conservation Agency NLWKN one the different coastal defence systems that are typical for the North Sea lowlands and their influence on the extension of flooding in case of failure. Further the influence of the hinterland topography is investigated. First results of the inventory of the existing coastal defence systems situated at the Lower Saxony mainland are the classification of coastal defence systems at the mainland coast and the ratios of these categories. The category "foreland and main dike" is prevalent with 49% of the mainland coast length; excluding estuary dikes. Preliminary results of hydrodynamic 1d/2d coupled simulations of flood propagation for different failure scenarios and various topographic situations yield a significant influence of the dike foreland on the inundation of the protected hinterland. The reduction is found regarding the inflow volume as well as the extension of flooded area.

Keywords: coastal defence, risk-analysis, flooding, foreland

1 Introduction

On its northern side the German Federal State Lower Saxony borders the North Sea. The coastal lowlands of Lower Saxony represent an important economical, agricultural, cultural and ecological area. Due to height levels ranging from below to a few meters above mean sea level, about 6,600 km², 1/7th of the total state area, is flood prone by storm surges. The main coastal defence elements on the mainland coast are main dikes and storm surge barriers. In case of main dikes, on significant stretches of the coastline additional protection elements such as dike forelands and secondary dike lines are present. These elements in combination with the main dike form a coastal defence system of varying shape depending on the particular local situation (fig. 1). The coastal defence system provides flood protection for 1.2 million inhabitants. By these elements a flood protection line with a total length of 610 km is formed.

The present coastal defence strategy for the flood prone areas and a legal safety level are defined in the Master Plan Coastal Defence - Mainland Coast Lower Saxony-Bremen (NLWKN 2007) and the Lower Saxony Dike Law (NDG, 2010) as a legal basis. According to the EU Flood Risk Management Directive, for areas with potential significant flood risks, flood hazard maps and flood risk maps as well as flood risk management plans have to be prepared. Aspects of flooding due to failure of coastal defences and the consequences are investigated by the Lower Saxony Water Management, Coastal Defence and Nature Conservation Agency (NLWKN) within two research projects SAFECOAST (Safecoast, 2008) and HoRisk (Flooding Risk Management for Coastal Areas) in order to facilitate technical aspects of the directives implementation.

The project HoRisk is conducted by cooperation of the three lead partners:

- RWTH Aachen - Institute of Hydraulic Engineering and Water Resources Management,
- University Rostock – Geotechnics and Coastal Engineering Group,

¹ Lower Saxony Water Management, Coastal Defence and Nature Conservation Agency (NLWKN), Jahnstrasse 1, 26506 Norden, Germany, holger.blum@nlwkn-nor.niedersachsen.de

² Lower Saxony Water Management, Coastal Defence and Nature Conservation Agency (NLWKN), Jahnstrasse 1, 26506 Norden, Germany, frank.thorenz@nlwkn-nor.niedersachsen.de

³ Lower Saxony Water Management, Coastal Defence and Nature Conservation Agency (NLWKN), Jahnstrasse 1, 26506 Norden, Germany, hans-joerg.lambrecht@nlwkn-nor.niedersachsen.de

- Lower Saxony Water Management, Coastal Defence and Nature Conservation Agency NLWKN Division Norden-Norderney,

who are leading separate subproject, HoRisk - A (Failure of coastal defence systems and damages), HoRisk - B (Loads on coastal defence systems and consequences of failure for the Baltic Sea coastal area) and HoRisk - C (Consequences of failure for the North Sea coastal area and damage minimization), respectively. Each of these subprojects integrates contributions of additional institutions and experts.

2 Objectives and Methods

With in subproject HoRisk - C led by NLWKN consequences of flooding at the North Sea Coast, hydrodynamic flooding simulations for selected boundary conditions in case of failure of the coastal defence system, damage and risk assessment und methods to reduce damages and risks are investigated. The concept used is the Source-Pathway-Receptor approach. The subproject HoRisk - C focuses mainly on the last aspects. For this purpose a model chain consisting of a numerical hydrodynamic simulation software and a geographical information system (GIS) is used to determine flood propagation and water depth. For dike failure scenarios these results, damage potentials and appropriated flood-damage-functions yield the spatial distribution of estimated damages that can be used to calculate the flood risk. The results of the investigations conducted in SAFECOAST by NLWKN delivered significant influences of topographical elements such as drainage systems, positive break lines and small variations of elevation on the simulated inundation (Burg et al., 2008; Thorenz & Burg, 2008).

Taking these findings into account, main objectives of HoRisk - C are investigations regarding the consequences of failure for coastal lowlands protected by different coastal defence systems. Therein included are the influence of specific defence elements, topography and utilisation of the hinterland on flood propagation and extension. In a further phase of the project the findings will be integrated in options to reduce exposure of receptors and risks in flood prone coastal areas.

2.1 Inventory and categorization of coastal defence system

The coastal defence system of Lower Saxony mainland coast is categorized using the Masterplan Coastal Defence combined with remote sensing data and official cadastral data. A schematic cross section of a typical coastal defence system is given in fig. 1. The situation shown also illustrates the shoreward area including the wadden sea and a barrier island facing the North Sea.



Figure 1: Schematic cross section of coastal defence system "foreland and main dike"

A comprehensive digital terrain model (DTM) covering the German North Sea Coast is generated using data of Schleswig-Holstein and Lower Saxony state survey agencies (fig. 2).

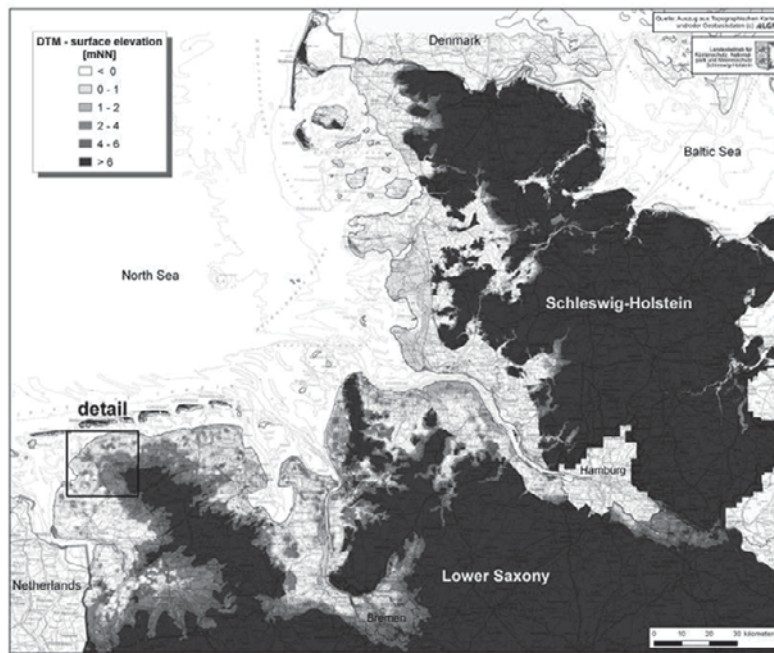


Figure 2: Digital terrain model of Lower Saxony and Schleswig-Holstein, detail see fig. 6

The preliminary evaluation of coastal defence systems yields 7 categories located at the Lower Saxony mainland coast. For each category the percentage of the total coastal defence line is calculated. Figure 3 shows the proportions of each. With 49% the category main dike in combination with a foreland (see fig. 1) is the dominating coastal defence system, followed by the categories main dike without foreland (19%) and main dike with foreland combined with a secondary dike (15%).

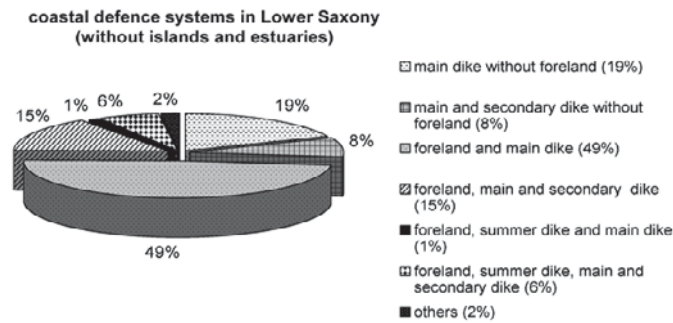


Figure 3: Proportions of coastal defence systems related to total length of coastal defence line at the Lower Saxony mainland excluding defence systems in estuaries

Additionally, a geostatistical analysis was conducted, delivering height distributions for flood prone areas legally defined by Lower Saxony Dike Law (fig. 4).

Figure 4 shows exemplary the situation for the area in responsibility of the Dike Board Norden located in the north-west of Lower Saxony. Significant parts of the analysed area show a terrain level below mean high tide. In case of a failure of the coastal defences even regular tides affect the hinterland if a breach cannot be closed rapidly.

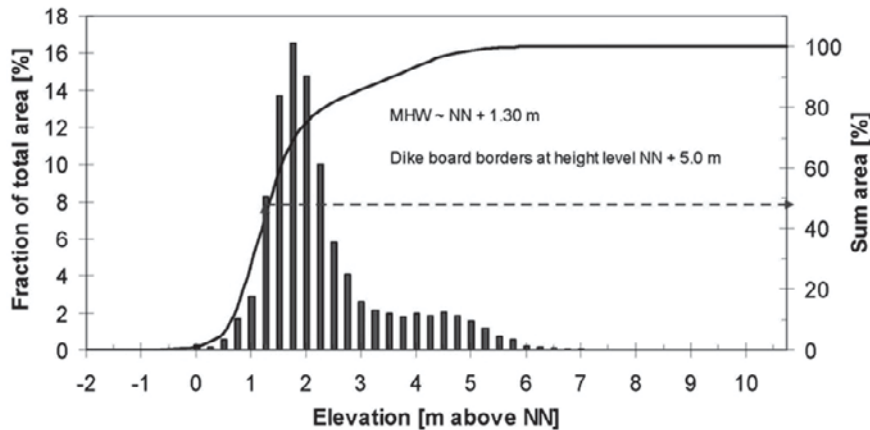


Figure 4: Terrain level distribution related to mean high tide

The results of categorization are used to support the choice of pilot areas to be investigated in more detail within the project.

2.2 Hydrodynamic simulation

The software package used for hydrodynamic simulation is SOBEK Rural using 1D-Flow in combination with Overland Flow (2D). The software allows two dimensional (2D) simulations as well as combined simulations of one dimensional network (1D) and 2D-overlandflow. The necessary boundary conditions especially water level and failure mode of the coastal defence system, will be investigated and delivered by the other subprojects. During the first project phase a scenario based approach is chosen to set-up the numeric model and to conduct a parameter study. The parameter study using both, synthetic and real topographies, facilitate the assessment of particular parameters regarding the influence on the areas affected by flooding and damages. The synthetic topography idealizes the coastal lowlands characteristics and enables a systematic investigation with a focus on specific parameters like the topographic situation in front of the coastal defence system, i.e. foreland height and width.

3 Preliminary results

The hydrodynamic simulations of a dike failure scenario using an idealized synthetic topography that consists of a horizontal landscape with a constant roughness in front of the dike and different width of a dike foreland yield time series of water level behind the dike as well as time series of stored water volume. The height of the foreland was chosen by 1 meter above mean high water level as a typical level of a well developed foreland. Figure 5 illustrates the differences of stored volume for four different width of foreland compared to the idealized topography without a foreland. Additionally, the hydraulic boundary condition and the beginning of the breaching are given in the upper part of figure 5.

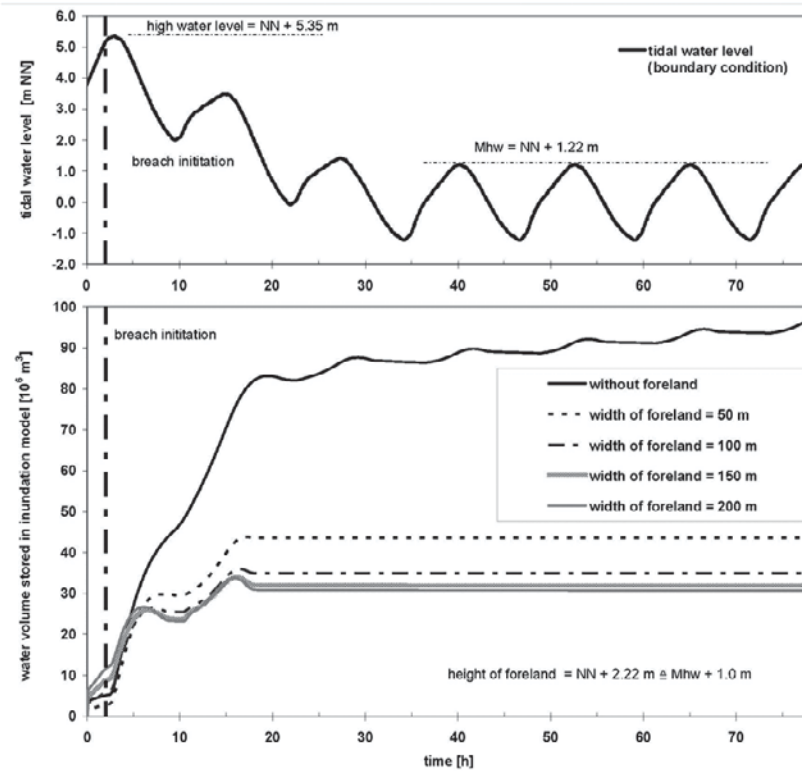


Figure 5: Simulated flood volume for different foreland widths and idealized topography

For the idealized topography the influence of the foreland width on the inflow volume is increasing with the width. For width of 150 m and 200 m the simulations yield only a small reduction of inflow volume (fig. 5).

In a further phase an existing coastal defence system consisting only of a main dike was investigated (fig. 6). This system has been modified with a theoretical foreland. Applying the same hydraulic boundary conditions and failure scenario for both cases and an identical topographical situation yields the calculated resulting maximum water depths shown in figure 7 and figure 8.

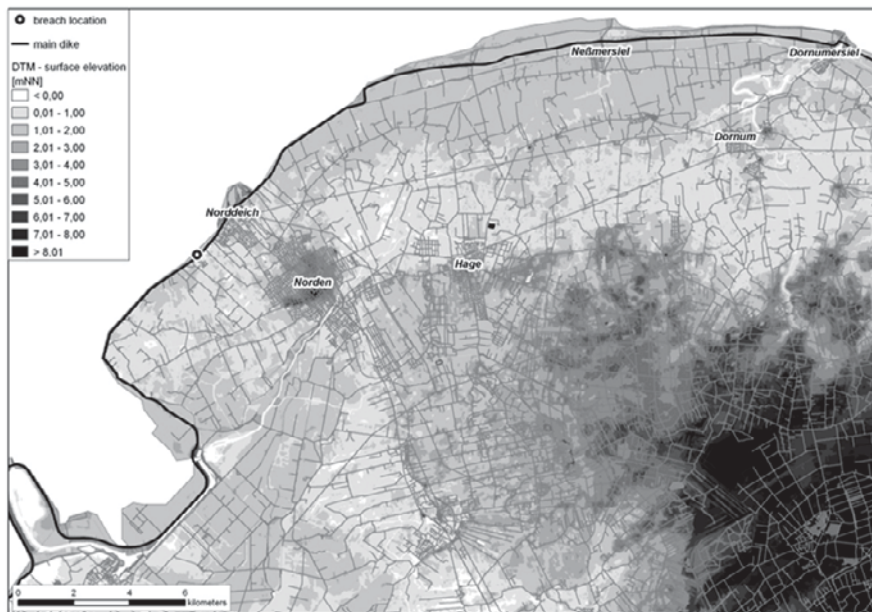


Figure 6: Digital terrain model overlaid with a road map

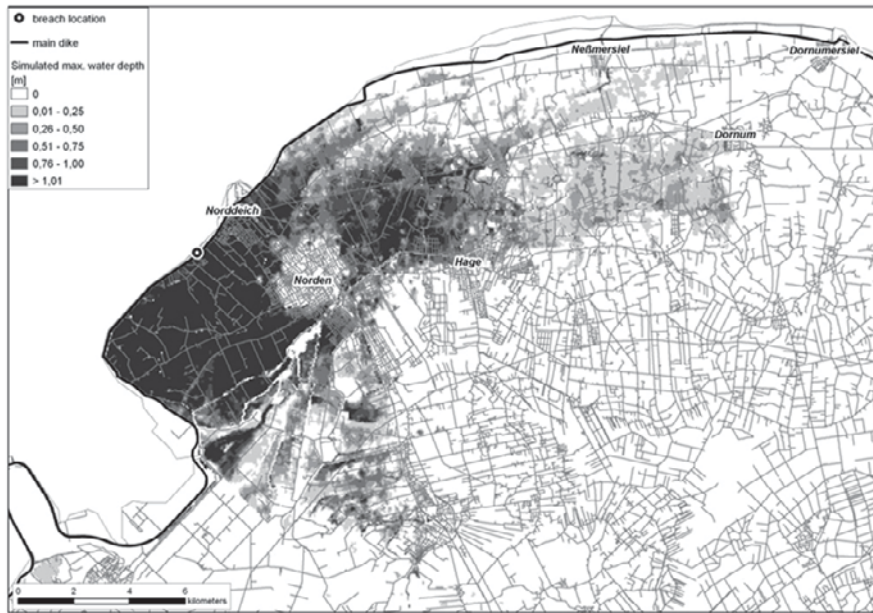


Figure 7: Max. water depth for dike failure scenario without foreland



Figure 8: Max. water depth for dike failure scenario with foreland (width = 100 m)

For the topography and the failure scenarios investigated the amount of inflow volume in case of a failure of a system “dike with foreland” was approximately 1/3 of the volume simulated for a comparable situation without foreland. With respect to the simulated inundated area the rate of reduction in case of an existing foreland was smaller than 2/3, but for large areas accompanied by a reduced maximum water depth (fig. 7 and fig.8).

4 Preliminary conclusions

The hydrodynamic simulations for dike breach scenarios with variations of topography in front of a dike show, that in comparison of a coastal defence system ‘main dike without foreland’ a system with a foreland will reduce the inflow volume as well as the flooded area, significantly.

The foreland in front of dikes is subject of the Lower Saxony Dike Law (NDG, 2010) and the Lower Saxony Master Plan Coastal Defence (NLWKN, 2007). There its functionality to protect

the dike by reduction of the loads, e.g. currents, is addressed. The effect of reducing the inflow volume through a breach in case of a failure of the coastal defence system was shown for selected synthetic and real cases. As a consequence a foreland of sufficient height and width can reduce the consequences for the hinterland and should be taken into account for flooding calculations.

During the projects time frame further investigations, including additional coastal defence elements, are planned to be conducted.

1 Acknowledgements

HoRisk is founded as a research project of the German Coastal Engineering Research Council (KFKI) by Federal Ministry of Research (BMBF) under project number 03KIS080. SAFECOAST was found by the EU INTERREG IIIb North Sea Region programme.

5 References

- Blum, H.; Thorenz, F. (2006): Risk Assessment for the Island of Langeoog. Die Küste Heft 70. Boyens Verlag, Heide in Holstein, Germany.
- Burg, S.; Thorenz, F.; Blum, H. (2008): Coastal Flood Inundation Modelling for North Sea Lowlands. Proc. Floodsite conference, Oxford.
- NDG (2010): Niedersächsisches Deichgesetz i.d.F. vom 23. Februar 2004 (Nds. GVBl. S. 83) zuletzt geändert durch Artikel 2 des Gesetzes vom 19. Februar 2010.
- NLWKN (2007): Niedersächsischer Landesbetrieb für Wasserwirtschaft, Küsten- und Naturschutz. Generalplan Küstenschutz Niedersachsen/Bremen – Festland. Norden, Germany.
- Safecoast (2008): Coastal Flood Risk and Trends for the Future in the North Sea Region. Synthesis report. Safecoast project team, pp. 136. The Hague, The Netherlands.
- Thorenz, F.; Burg, S. (2008): Risk Assessment for Coastal Lowlands in Lower Saxony. Proc. Fourth Chinese-German Joint Symposium on Coastal and Ocean Engineering. Darmstadt, Germany.

The use of integrated wave-current-sediment numerical tools to model coastal dynamics: an application in the North Adriatic Sea

Sandro Carniel¹, Mauro Sclavo¹ and Renata Archetti²

Abstract

The paper presents a preliminary implementation of a 3-D integrated, wave-current-sediment numerical model in a shallow water area of the NW Adriatic Sea, with the aim of assessing the erosion patterns and bottom morphology modifications that may be induced by severe marine conditions. The numerical modeling results show how complex, integrated numerical tools are becoming suitable both for preliminary investigations and for effective littoral management activities as well.

Keywords: integrated wave-current-sediment models; sediment transport; Adriatic Sea

1 Introduction

Complex, integrated wave-current-sediment numerical models that simulate near-shore processes need to account for several processes, such as wave-current interactions, turbulent mixing, wetting and drying processes, bottom-boundary layer interactions and sediment re-suspension and transport (Warner et al., 2008; Warner et al., 2010). Nevertheless, in the last years it has become possible for these integrated numerical tools to increasingly support decision makers in the field of coastal erosion and vulnerability (e.g. beach protection, support to maritime engineering operations such as groins or rocks deployment, usually followed to protect littoral regions; see also Carniel et al., 2007).

Several national and international projects have been dealing with the issue of coastal areas protection in the Mediterranean sea (e.g. BEACHMED-e, Strategic management of beach protection for sustainable development of Mediterranean coastal zones, see <http://www.beachmed.it/>) or more specifically in the Adriatic basin (e.g. VECTOR, VulnErability of the Italian coastal area and marine Ecosystems to Climatic changes and Their rOlE in the Mediterranean caRbon cycles, see <http://vector.conismamibi.it/>), also following recent EU regulations, especially in the perspective of the effects induced by severe storms. The complexity of these applications is generally increased by the fact that very often coastal areas constitute also a relevant economic resource to be exploited in terms of aquaculture activities and tourist attraction, which requires for instance indications for periodic beach nourishment.

With the final aim to describe the geo-morphological and hydrodynamic conditions in a shallow region induced by an intense Bora storm (see also Boldrin et al., 2009), we present here a very high resolution numerical application focused on the NW Adriatic coast close by the city of Ravenna (see Figure 1). A state-of-the-art, fully 3-D, integrated, coupled wave-currents-sediment model was adopted (see Warner et al., 2008 and Warner et al., 2010).

The paper is organized as follows: after a short Introduction, the study area is described and the numerical tests performed to simulate the nearshore dynamics are presented. Numerical results are then discussed and, eventually, a summary of the lessons learnt and some suggestions for future activities are drawn.

¹ CNR-ISMAR, Castello 2737, I-30122 Venice, Italy, sandro.carniel@cnr.it

² DICAM, University of Bologna, Italy. renata.archetti@unibo.it

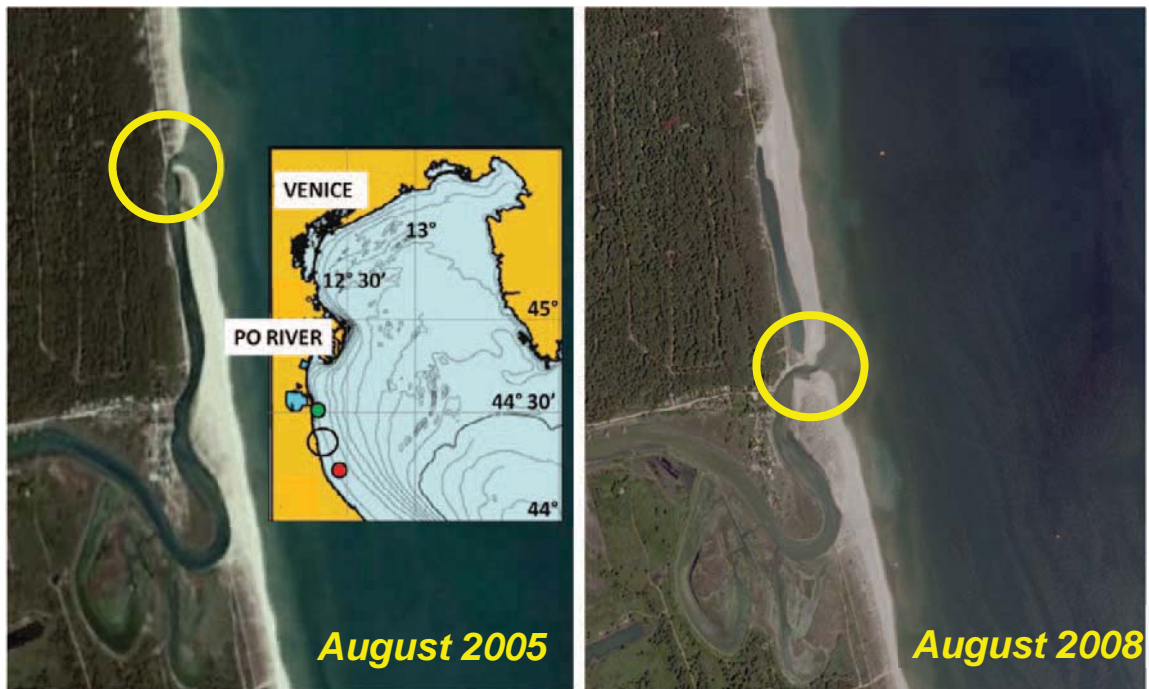


Figure 1: Satellite view of the Bevano river region (Google Earth™) before (left panel) and after (right panel) the dredging of the new river mouth (both mouths are shown by the large circles). In the inset, the area of the Bevano river is shown in the black circle; the dot to its south indicated the position of the ARPA-SIMC Cesenatico wave rider, the dot to its north the location of the Ravenna tide gauge (approx. Lat 44°30' N).

2 The case study

The study area is focused on the NW Adriatic coast south of the river Po, along the coast of Emilia-Romagna region, more specifically in the proximity of the Bevano river inlet, located just few km south of Ravenna (see the small circle in the inset in Figure 1).

The open sea coastline of the Emilia-Romagna region is subjected to erosion processes, mainly resulting from the combined action of waves and marine currents impacting the shoreline. Dominant waves in the region of interest are impacting from the NE and SE sectors (Bora and Sirocco, respectively; see Signell et al., 2005; Dorman et al., 2006); the former, driven by largest winds in terms of magnitude, can result in producing significant wave heights higher than 3 meters, while the latter are characterized by less energy but by a longer fetch.

Despite significant recent efforts devoted to a better understanding and a more efficient management of these shallow coastal areas, including initiatives undertaken to protect the shoreline with groins and submerged barriers as in Lamberti et al. (2005), the combined waves-currents interaction may generate significant erosion/deposition patterns (Harris et al., 2008; Martucci et al., 2010).

The frequency and intensity of storms measured in the last decade has indicated that specific dynamic parameters play an essential role in the equilibrium of the coastal region; namely, the influence of coastal and bottom currents, which are able to transport eroded material, re-suspend sediments and rebuild the bottom topography, appeared to be of primary importance (Harris et al., 2008; Bever et al., 2009).

Until 2005 (Figure 1, left panel) the Bevano inlet region was left free to evolve naturally and was showing a progressive migration to the north. At the beginning of 2006 (see again Figure 1, right panel), the existing northern river mouth was closed, and a new inlet dredged about 500-600 m to its south. Immediately to the south of this new opening, a new floodway connected the river system to the open sea, allowing the water to exit directly to the sea in case of river flood. The new river mouth was then armoured with a timber structure in order to limit the typical northward

migration of the river mouth, mostly due to the action of SE waves and spring tides (Gardelli et al., 2007).

3 Materials and methods

The numerical model adopted is ROMS (www.myroms.org) in its two-way coupled version with the wave model SWAN (www.wdelft.nl/soft/swan) and a dedicated sediment transport module. It is a state-of-the-art, fully 3-D integrated wave-currents-sediment numerical model capable of describing the morphological evolution of the new river mouth region as a consequence of ordinary (tidal) or extreme (river flood, wave storms) events.

Part of the numerical domain adopted for this study is shown in Figure 2; emerged areas are represented by negative depth values, and consists of 145x105 points (15 “sigma” levels along the vertical) arranged on a curvilinear grid having mean resolution in the order of 15 meters along X-axis, and 40 meters along the Y-axis.

The coupled model was running adopting a wetting/drying option able to flood progressively the grids in case of rising sea surface elevation, and with the capability of reproducing nearshore currents via radiation stresses as described in Warner et al. (2008) and following. Vertical mixing was modeled using a two-equation second order moment closure ($k-\epsilon$) via the GLS approach as in Carniel et al. (2009).

Hydrodynamical and morphological conditions of the river mouth under forcings such as a purely tidal cycle, river flooding and severe wind storms have been implemented. In this paper we will focus our discussion on a “river flooding case” (a 24-hour triangular river flow curve, discharging $110 \text{ m}^3/\text{s}$ after 12 hours at its peak, was added to the purely tidal case) and on a severe “Bora storm case”, occurred during 2008 March 5-6 and characterized by several hours of significant wave heights around 3 m peak, period of 8 s, incoming direction $60-65^\circ$. Figure 3 shows the measured storm event as registered by the wave rider buoy owned by ARPA-SIMC near Cesenatico (www.arpa.emr.it/sim/?mare/boa), approx. 10 km off the Bevano river mouth, deployed at 10 meters depth. These values were used as boundary to the wave model (SWAN) coupled to the hydrodynamic one.

Sediment characteristics were chosen following previous studies of the area (Gardelli et al., 2007); a median grain size of 0.190 mm has been used, together with corresponding typical sinking velocities, critical shear for erosion and deposition. The sediment transport and resuspension strategy adopted are thoroughly discussed in Warner et al. (2008).

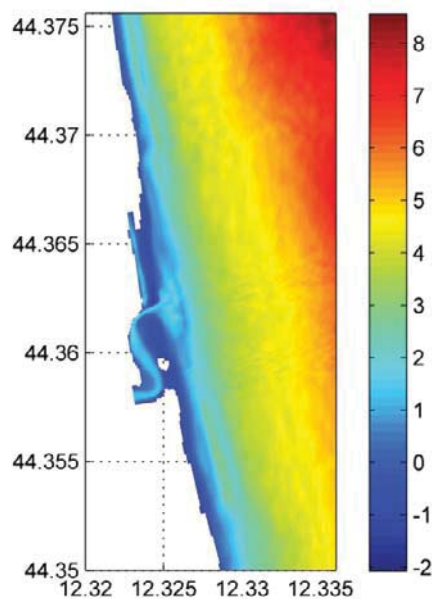


Figure 2: Numerical domain and bathymetry of the simulated region. Both emerged regions (indicated by negative depths, e.g. in the proximity of the river mouth) and permanently wet areas (positive depths) are shown.

Since the focus of the modeling was on a relative short periods, the model started from a sea level situation at rest, with a stable density profile. The values of sea surface elevation at the sea boundary were imposed from the measurements registered by the tide gauge at Punta Corsini (Ravenna) and the wind fields from a local-area meteo model (Signell et al., 2005).

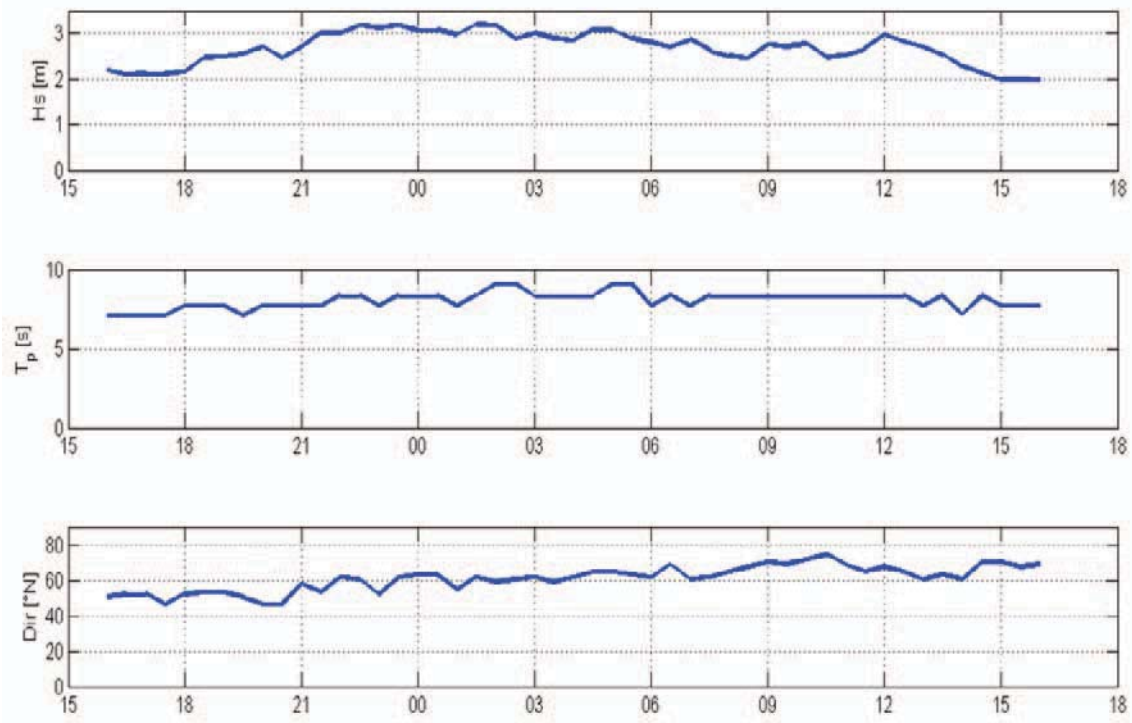


Figure 3: significant wave height (top panel, m), period (central panel, seconds) and direction (bottom panel, °N) of the Bora storm on March 5-6, 2008, as registered by the ARPA-SIMC Cesenatico wave rider buoy.

4 Preliminary results

For clarity of presentation, results are shown for a portion of the domain near the inlet mouth. Figure 4a shows the sediment transport (kg/m/s) at the peak of the river flood, with superimposed integrated velocities (max value 1.4 m/s). Note how the flow, besides flowing through the new mouth at north, also breaks through the shallow, wettable region in the southern area. Figure 4b shows the bottom modification (as erosion/deposition areas, dimensionless) with respect to the initial sea bottom status. Erosion or deepening of the inlet channel and deposition of the sediment outside the inlet during the large flood event are also evident. The contour shown in the Figure shows the zero-level change.

Results for the Bora storm simulation present larger velocities up to ~1 m/s, a larger amount of sediments (Figure 5a) and an increased erosion tendency on the southern side of the inlet mouth compared to the northern side (Figure 5b).

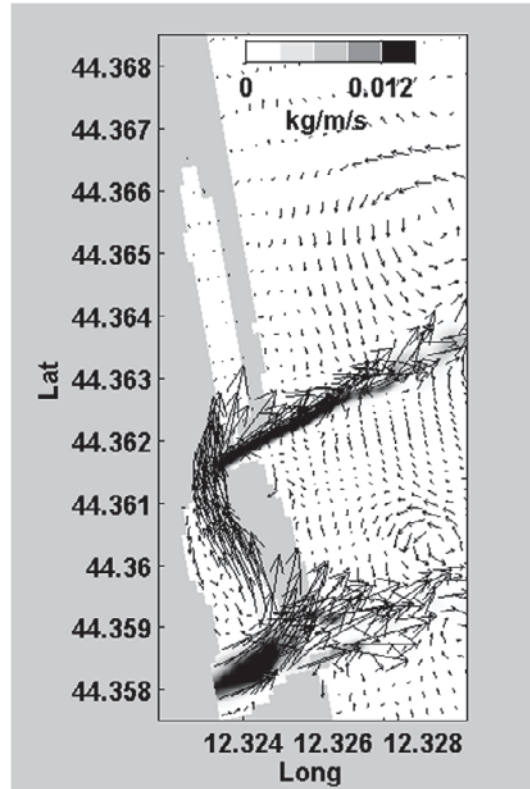


Figure 4a: total transport and integrated velocities (maximum value 1.4 m/s) at the peak of the river flood event.

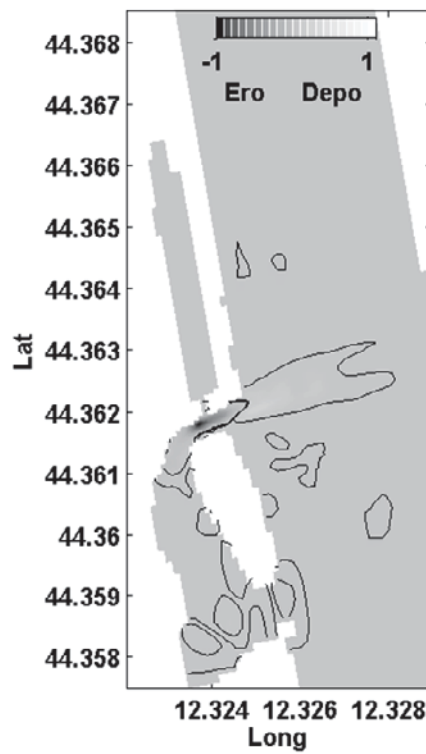


Figure 4b: bottom modification at the peak of the river flood event. The contour line represents the zero-level.

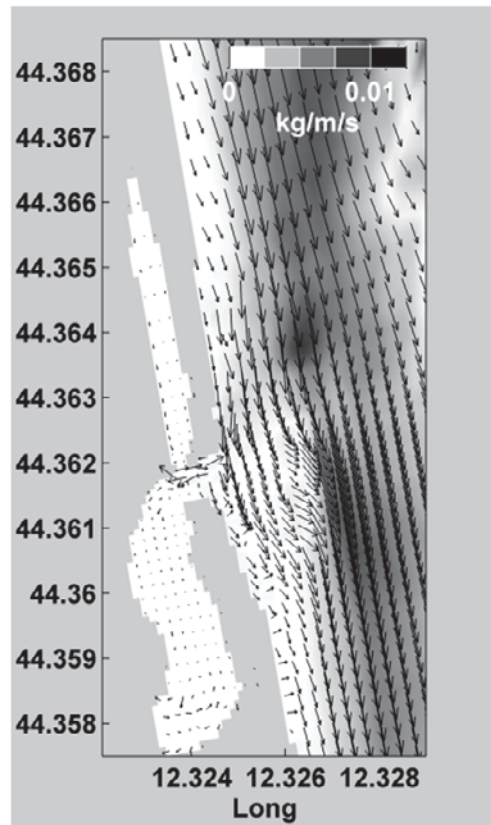


Figure 5a: total transport (kg/m/s) and integrated velocities at the peak of the Bora storm case

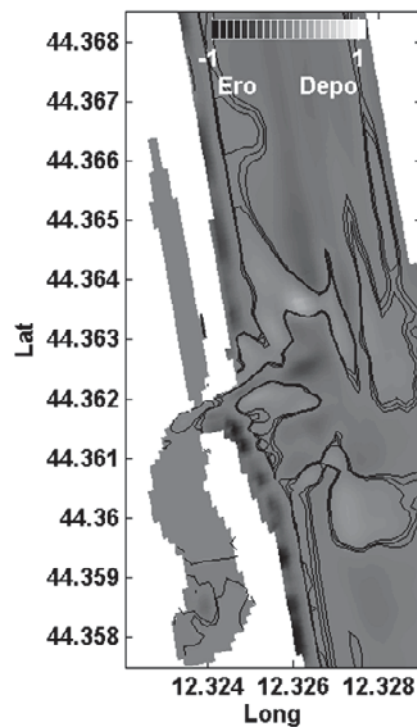


Figure 5b: bottom modification (adimensional) at the peak of the Bora storm case. The contour line represents the zero-level.

Resulting bottom variations induced by the Bora storm (after one day of simulation), and again expressed in terms of erosion/deposition, are shown in Figure 5b. Values are dimensionless, i.e. divided by the maximum erosion value, and represent the integrated effect of the whole simulated sediment classes.

As a general consideration, almost the totality of the littoral region nearby the coastline has been subject to an erosional process with respect to the initial status; the most affected areas are located southern of the current river mouth. There is also a tendency to deposition in front of the river mouth, that could be likely be due to the combined effect of the reduced tidal flow and the wave action. Figure 5b clearly shows the tendency of an offshore migration of the previously mentioned bar, estimated in the range of 30-40 meters. The seaward bar migration is a typical morphological response due to intensive storm events (see also Quartel et al., 2007; Aagard et al. 1998; Aagard et al., 2005; Parlagreco et al., 2011), and has also been estimated using an approach based on video images.

5 Final considerations

A state-of-the-art, 3-D, fully coupled integrated wave-current-sediment numerical tool has been implemented in a shallow area of the NW Adriatic Sea, Italy.

Clearly, more tuning and data acquisitions are needed to bring integrated numerical models applications into a more operational phase (e.g., evaluation of critical shear stress velocities based on the grain-size of sediments, more in situ data to map sediment dynamics, more accurate determination of nearshore currents, verification under non-extreme situations, etc.).

Nevertheless, these preliminary results, suggest that integrated numerical tools can be applied at high resolution in coastal environments, and are becoming suitable to be employed in shallow and complex regions. They could indeed provide useful support both during the phase of preliminary investigations and for planning effective littoral management activities as well, ranging from designing scenarios such as dredging a new river mouth, defining nourishment strategies or modifying the beach geometry to assessing sediment transport figures and resulting morphodynamic evolution. The validation of such numerical tools will be the focus of a successive paper.

6 Acknowledgements

SC and RA acknowledge the PRIN 2008YNPNT9_005. SC and MS also acknowledge the FIRB Project RBFR08D825 ("DECALOGO") and the partial support from the EC FP7/2007-2013 under grant agreement n° 242284 (Project "FIELD_AC").

7 References

- Aagard T., Nielsen J. and B. Greenwood, 1998. Suspended sediment transport and nearshore bar formation on a shallow intermediate state beach. *Marine Geology*, 148, 203-225
- Aagard T., Kroon A., Andersen S., Moller Sorensen R., Quartel S. and N. Vinther, 2005. Intertidal beach change during storm conditions: Egmond, The Netherlands. *Marine Geology*, 218, 65-80
- Bever A.J., Harris C.K., Sherwood C.R. and R.P. Signell, 2009. Deposition and flux of sediment from the Po River, Italy: An idealized and wintertime numerical modeling study. *Marine Geology*, 260 (1-4), 69-80. DOI:10.1016/j.margeo.2009.01.007
- Boldrin A., Carniel S., Giani M., Marini M., Bernardi Aubry F., Campanelli A., Grilli F. and A. Russo, 2009. The effect of Bora wind on physical and bio-chemical properties of stratified waters in the Northern Adriatic. *Journal of Geophysical Research – Ocean*, 114, C08S92. DOI:10.1029/2008JC004837
- Carniel S., Sclavo M., Warner J.C. and M. Tondello, 2007. Predicting sediment transport at coastal structures: an integrated model approach. In: *Proceedings of the 5th Coastal Structures Intern. Conf., CSt 2007, 2-4 July, Venice, Vol. II, pp. 1047-1057* (Franco, Tomasicchio and Lamberti Eds.). DOI 10.1142/9789814282024_0092

- Carniel S., Warner J.C., Chiggiato J. and M. Sclavo, 2009. Investigating the impact of surface wave breaking on modelling the trajectories of drifters in the Northern Adriatic Sea during a wind-storm event. *Ocean Modeling*, 30, 225-239. DOI:10.1016/j.ocemod.2009.07.001
- Dorman C.E., Carniel S., Cavaleri, L., Sclavo, M., Chiggiato J. and others, 2006. February 2003 marine atmospheric conditions and the Bora over the Northern Adriatic. *J. Geophys. Res.-Ocean*, 111, C03S03. DOI: 10.1029/2005JC003134
- Gardelli M., Caleffi S. and P. Ciavola, 2007. Evoluzione morfodinamica della foce del Torrente Bevano. *Studi Costieri*, 13, 53-74 (in Italian)
- Harris C.K., Sherwood C.R., Signell R.P., Bever A. and J.C. Warner, 2008. Sediment dispersal in the northwestern Adriatic Sea. *J. Geophys. Res.-Ocean*, 113, C11S03, DOI:10.1029/2006JC003868
- Lamberti A., Archetti R., Kramer M., Paphitis D., Mosso C. and M. Di Risio, 2005. European experience of low crested structures for coastal management. *Coastal Engineering*, 52 (1011), 841–866, ISSN: 0378-3839
- Martucci G., Carniel S., Chiggiato J., Sclavo M., Lionello P. and M.B. Galati, 2010. Statistical trend analysis and extreme distribution of significant wave height from 1958 to 1999. An application to the Italian seas. *Ocean Science*, 6, 525-538. DOI: 10.5194/os-6-525-2010
- Parlagreco L. Archetti R., Simeoni U. and S. Devoti, 2011, Video-monitoring of a barred nourished beach (Iatium, central Italy). *Journal of Coastal Research*, 64, 110–114
- Quartel S., Ruessink B.G. and A. Kroon, 2007. Daily to seasonal cross-shore behavior of quasi-persistent intertidal beach morphology. *Earth Surf. Process. Landforms* 32, 1293–1307. DOI: 10.1002/esp.1477
- Signell R.P., Carniel S., Cavaleri L., Chiggiato J., Doyle J., Pullen J. and M. Sclavo, 2005. Assessment of wind quality for oceanographic modeling in semi-enclosed basins. *Journal of Marine System*, 53(1-4), 217-233. DOI: 10.1016/j.marsys.2004.03.006
- Warner J.C., Sherwood C.R., Signell R.P., Harris C. and H. Arango, 2008. Development of a three-dimensional, regional, coupled wave, current, and sediment-transport model. *Computers and Geosciences*, 34, 1284-1306
- Warner J.C., Armstrong B., He R. and J.B. Zambon, 2010. Development of a Coupled Ocean-Atmosphere-Wave-Sediment Transport (COAWST) Modeling System. *Ocean Modelling*, 35, 230-244

Estimate of cross-shore coastal erosion induced by extreme waves and by effects of sea level rise through ETS model

Carla Faraci¹, Enrico Foti² and Rosaria E. Musumeci³

Abstract

In the present paper the Equivalent Triangular Storm (ETS) model has been applied along with the SBEACH morphological model to describe the beach erosion caused by a severe storm attack of the littorals of Ragusa (Italy) in order to develop an easy-to-use tool for the evaluation of the shoreline recession. By using the proposed methodology, the next step forward could be the estimate of the return period of cross-shore beach erosion associated to severe storms.

The simulations have been performed considering two different scenarios, i.e. the present s.w.l., and the s.w.l projection over the next twenty years, in order to take into account the effects of climate changes by means of sea level rise. Results showed that the sea level rise induces a strong retreat due to wave attack, to be added to the land loss that has to be attributed to the static sea level rise.

Keywords: Equivalent Triangular Storm (ETS), morphological modelling, beach erosion, sea level rise.

1 Introduction

Severe storms impacting on sandy beaches may cause strong shoreline recessions, thus increasing the vulnerability of buildings and infrastructures located in the proximity of coastal areas. For coastal zone management the vulnerability of exposed areas has to be determined in a reliable manner, by considering the variety of factors which plays a role in the risk evaluation. It follows that many technical, social and economical skills should be involved in the solution of such a multidisciplinary problem. Unfortunately, due to the complexity of the problem itself and also to the shortage of resources, regional government and local authorities may not be able to properly carry out risk-based management of coastal areas. Therefore a simplification of the overall procedure for risk assessment as much as reasonably applicable could help decision makers for improving their present level of judgment. In the present work, also taking into account the recent suggestions of *Goda (2007)* about the efforts that researchers should make in order to strengthen the sense of their engineering research, the possibility to use the Equivalent Triangular Storm (ETS) model, introduced by *Boccotti (2000)*, has been investigated in order to develop an easy-to-use tool for the evaluation of the risk of beach erosion.

During an actual sea storm the significant wave height changes in a very irregular manner. Due to such a randomness, it is quite difficult to deal with natural storms and in turn to determine their actual effects on the beach, especially when future predictions are concerned. In the present work, the ETS model has been adopted in order to evaluate the shoreline recession. This latter information could be adopted also for estimating return period of cross-shore beach erosion associated to severe storms. The effects of climate changes, which may induce substantial modifications in the nearshore wave climate and in turn in the effects of wave attacks on the coast (*Olabarrieta et al. 2007*), have been also taken into account by considering the sea level rise forecast for the next twenty years, according to the IPCC predictions (*Bindoff et al, 2007*). The procedure has been applied to the littorals of Ragusa (Italy), on the South coast of Sicily, where field measurements of cross-shore profiles have been acquired.

¹ Department of Civil Engineering, University of Messina, C.da di Dio, 98166, S.Agata (ME), Italy, faraci@ingegneria.unime.it

² Department of Civil and Environmental Engineering, University of Catania, v.le A. Doria, 6, 95125 Catania, Italy, efoti@dica.unict.it

³ Department of Civil and Environmental Engineering, University of Catania, v.le A. Doria, 6, 95125 Catania, Italy, rmusume@dica.unict.it

2 Hydrodynamic model

To the aim of estimating the return period of extreme waves, and in turn to derive the design significant wave height, Boccotti (2000) proposed the Equivalent Triangular Storm (ETS) model, in which the actual storm (see Figure 1a) is described by means of a triangle, i.e. by means of just two parameters: (i) the storm intensity a , which is equal to the maximum significant wave height of the actual storm and (ii) the storm duration b , which is determined in such a way that the maximum expected wave height is the same both for the actual and the triangular storm. In particular, the latter parameter may be calculated by considering that the maximum expected wave height of a storm is defined by the following relation:

$$\bar{H}_{\max} = \int_0^{\infty} 1 - e^{-\left\{ \int_0^b \frac{1}{\bar{T}[h(t)]} \ln[1 - P(H; H_s = h(t))] dt \right\}} dH \quad (1)$$

where \bar{H}_{\max} represents the maximum expected wave height, H and H_s are respectively the wave height and its significant value, h indicates the threshold of wave height, and \bar{T} is the averaged period, provided by:

$$\bar{T} = 6.6\pi \sqrt{\frac{H_s}{4g}} \quad (2)$$

One of the most interesting properties of such a model is that the triangular storm and the actual storm have the same statistical properties (see Boccotti, 2000; Arena, 2004), since the probability $P(H_{\max} > H)$ that the maximum wave height H_{\max} exceeds a given value H , is the same for the actual storm and for the ETS (see Figures 1b).

Moreover, once all the properties of the ETSS are known, the return period R of a sea storm in which the maximum significant wave height H_s exceeds a fixed threshold h can be evaluated by using the analytical solutions described in Boccotti (2000) and in Arena et al. (2006), for the all wave direction analysis $R(H_s > h)$ and the directional analysis $R(H_s > h; \Delta\sigma)$ respectively, where $\Delta\sigma$ is the angular sector of the dominant wave directions.

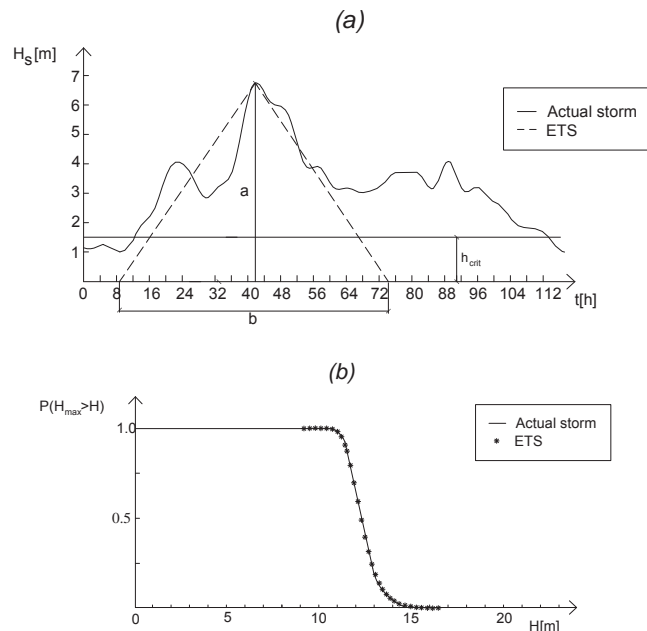


Figure 1: (a) Example of a time series of the significant wave height of an actual sea storm and the corresponding ETS; (b) Probability distribution $P(H_{\max} > H)$ of the actual storm and of the corresponding ETS (adapted from Boccotti, 2000).

Arena (2004) demonstrated that, when dealing with ETS for estimating of the return period of extreme sea waves, the significant parameter is the storm intensity, while the storm duration can be assumed to be equal to 60 hours without significant errors. This simplifying assumption however may not mean that the equivalent storm duration does not influence coastal erosion and shoreline retreat.

3 Morphodynamic model

In the present work the morphological model originally developed by Larson and Kraus (1989) known as SBEACH has been applied. It is a two-dimensional model where obliquely incident waves, longshore currents, and sediment transport processes are omitted. Therefore, it should only be applied if longshore gradients in transport processes can be neglected. SBEACH simulates beach profile change, including the formation and movement of major morphologic features such as longshore bars, troughs, and berms, under varying storm waves and water levels.

The model is suitable for many applications in the coastal environment and it has been used to determine the response of proposed beach fill alternatives under storm conditions and to compare the performance of different beach fill cross-sectional designs (Neilans, 1994). The model is sufficiently accurate to be of engineering use, provided that the sediment must be in the sand range of grain size (particle diameters between 0.062 and 2.00 mm) and that beach profile change is mainly governed by breaking of short-period waves (periods in the approximate range of 3-20 s). SBEACH requires as input data: initial beach profile, median grain size representative of the active profile; water elevation, wave height and period (time series or constant value). Moreover, additional data may be input to represent the beach configuration and forcing conditions, such as shoreward boundary condition (e.g. seawall) time series of wave directions, of wind speed and direction. In addition, a beach fill options allows the fill cross section to be defined. The model output concerns simulated profiles at intermediate time steps and the final calculated profile, the cross shore variation of some physical parameters, such as wave height, water elevation and setup, along with the beach response, i.e. accretion/erosion, runup, etc.

4 Preliminary tests on the role of the storm duration

Preliminary tests have been carried out on the proposed model. In particular, such tests have been aimed at verifying the possibility to apply to the analysis of the beach modification due to a storm attack the simplifying assumption proposed by Arena (2004) on the storm duration, i.e. the fact that the storm duration can be considered constant and always equal to 60 hours.

In order to verify such a consideration, the effects on the coasts of a single storm event have been considered, by varying its duration within the ETS model.

To check the sensitivity of shoreline retreat to the storm duration, the model has been run exposing a planar beach profile with a slope of 1:10 to ETSs' attacks characterized by the same wave height and period (i.e. $H_s=4\text{m}$ and $T_p=8.5\text{ s}$) and different triangle bases. The results are shown in Figure 2. It is here remarkable that, as expected, the longer the ETS, the stronger the shoreline recession, thus implying that the real ETS duration must be taken into account when morphological effects of storms are observed. As regards the maximum estimated runup, a slight decrease is shown when the ETS is longer that can be related to the change in the ETS shape.

5 Application to a case study

The effects on the coast of a severe storm attack have been investigated with reference to a real case study, i.e. the beach of Ragusa, located on the South coast of Sicily (Italy), between Santa Maria del Focallo and Scoglitti (see Figure 3). For a smaller span of littoral, i.e. that between Spinasanta resort and the Dirillo river mouth, the Ragusa Local Authority charged the University of Messina to perform a monitoring program during the years 2002-2003, with the aim to collect a detailed data set concerning bathymetry and sedimentology, functional to plan a

renourishment intervention. Cross-shore beach profiles have thus been recovered starting from such campaign.

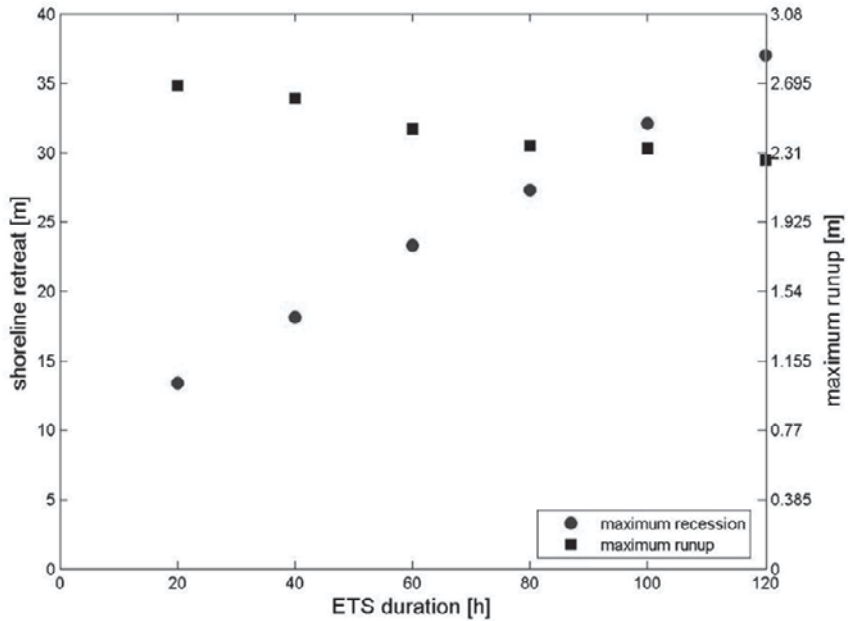


Figure 2: Shoreline retreat and maximum runup trend versus ETS duration

The wave climate, namely the significant wave height, the peak and mean period and the direction, has been provided through elaboration of wind fields calibrated with direct measurements of the wave field, by the United Kingdom Meteorological Office (UKMO) data.



Figure 3: Geographic location of case study

The available dataset cover the period from October the 1st 1986 to March the 31st 2002 and is relative to a point located offshore the harbor of Pozzallo. In order to identify the storms within the wave height time series a Peak Over Threshold method has been applied to the entire dataset.

In Figure 4 an example that shows the 1999 data as provided by the UKMO, is reported, along with the adopted threshold, taken equal to 3 m.

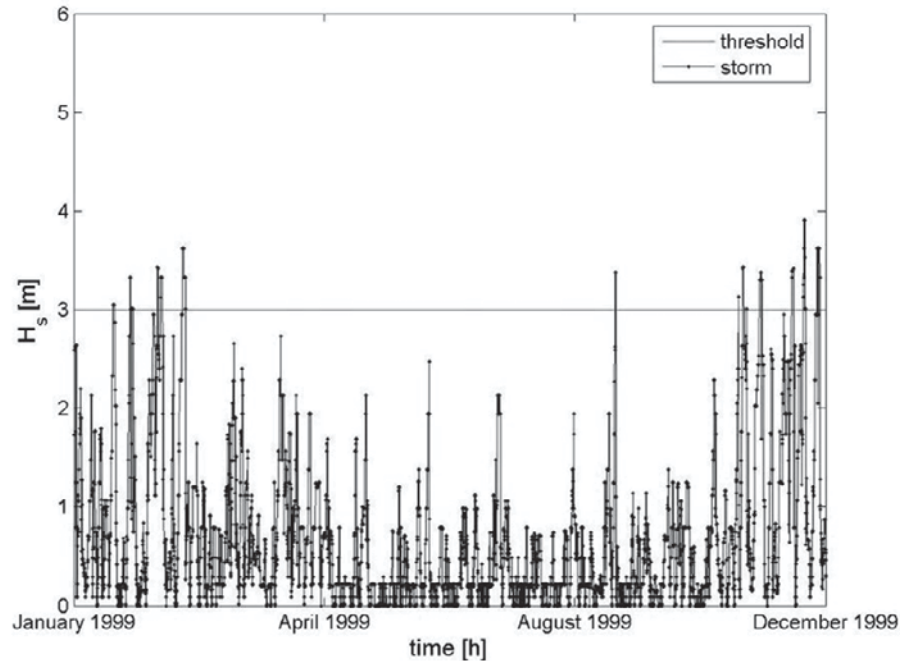


Figure 4: Significant wave height during 1999 (UKMO data)

The storm data as obtained by the peak over threshold method have been interpreted in the light of ETS model, deriving the equivalent duration and the maximum wave height for each single storm, i.e. the base and the height of the triangle. The yearly sequence of ETS has been then propagated by means of the SBEACH model in order to determine the shoreline retreat for the significant cross-sections indicated in Figure 5.

These simulations have been performed considering two different scenarios, i.e. the present s.w.l., which reference has been assumed to be equal to zero, and the s.w.l projection over the next twenty years, in order to take into account the effects of climate changes in terms of sea level rise. The rate of sea level has been estimated in the framework of the Intergovernmental Panel on Climate Change (IPCC), which provided a projection for the next hundred years over the Mediterranean area of about 4 mm/y, with regional variations (Bindoff et al., 2007).

In Figure 6 the initial and final cross-shore profiles, obtained after the propagation of 1999 storms, i.e. a time period of about 15 years and a half, with the present s.w.l. and the projected one are shown at the section in the correspondence of the Scoglitti resort. The morphological model provides a recession caused by the wave attack at the 0 reference level equal to 24 m, with the present s.w.l and 28.5 m with a 0.08 m risen s.w.l. In this latter situation moreover the total retreat should be obtained summing also the land loss deriving from the increased s.w.l, which considering the fact that the mean beach slope is about 0.013 can be estimated to be about equal to about 6 m. Moreover the model realistically predicts in both situations the appearance of a berm in the swash zone, and the sand deposit just outside the surf zone.



Figure 5: Location of the cross-sections of the beach profile which have been investigated by means of the SBEACH models, by using ETS storm data.

Finally in Figure 7 the estimated shoreline retreat at all the considered locations, in terms of the yearly averaged shoreline retreat at the 0 reference level, are summarized in the two above mentioned scenarios. A stronger recession is evident for the steeper beaches). The sea level rise produces at the investigated cross-sections a stronger retreat due to wave attack which ranges between 2 and 18%, to be summed to the land loss that has to be imputed to the static sea level rise, which in this case ranges from 1.5 to 8 m.

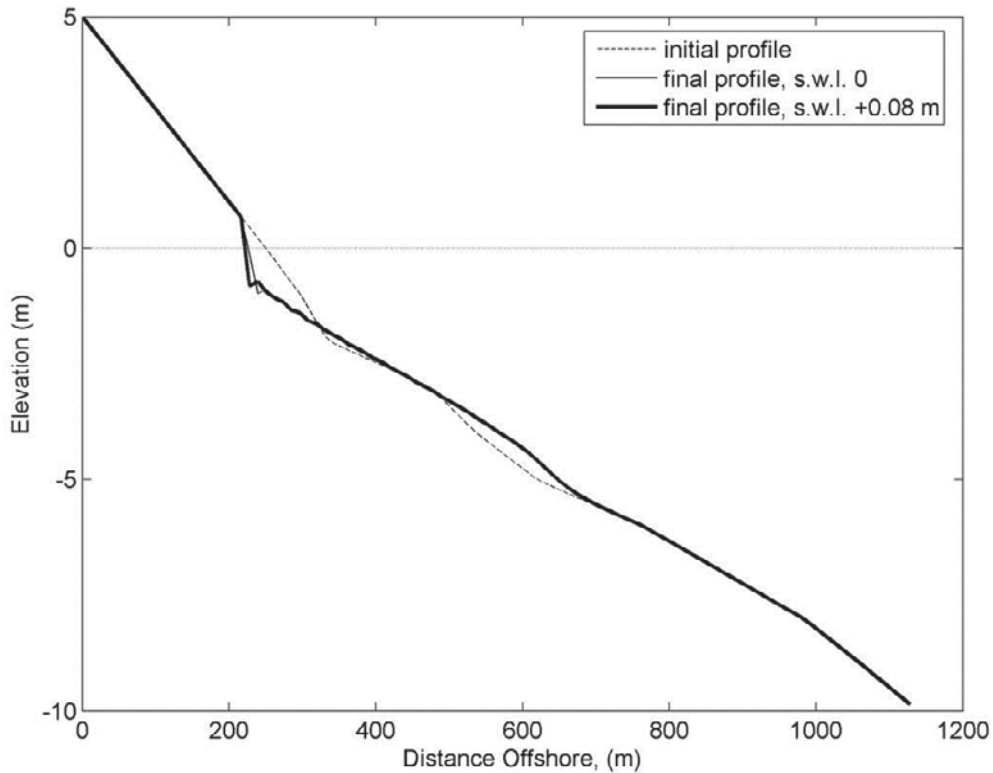


Figure 6: Cross-shore initial and final profiles at Scoglitti after the 1999 storms, with present s.w.l and projection of s.w.l in 20 years.

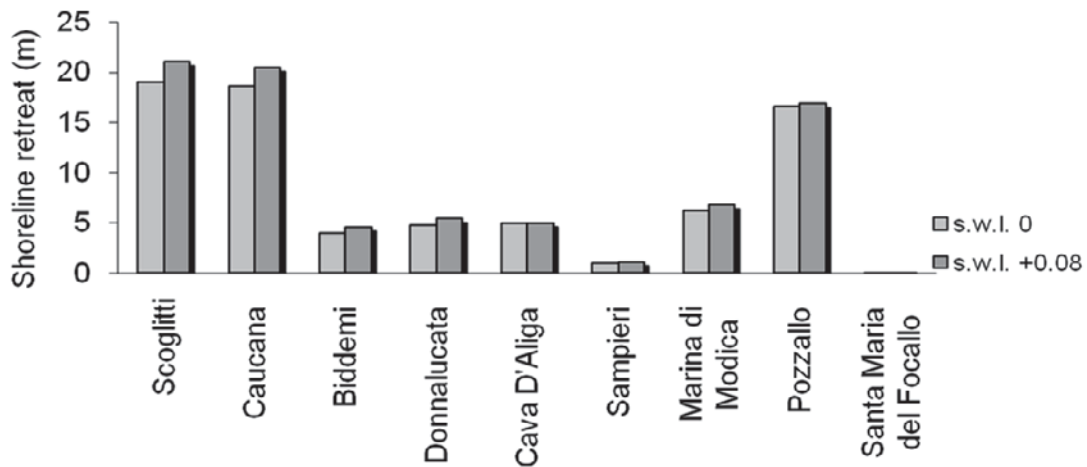


Figure 7: Significant wave height during 1999 (UKMO data)

6 Conclusions

In the present study the Equivalent Triangular Storm (ETS) approach along with the SBEACH morphological model have been applied to the littorals of Ragusa (Italy) in order to develop an easy-to-use tool for the evaluation of the shoreline recession, also in the light of estimating return period of cross-shore beach erosion associated to severe storms. The effects of climate changes have been also taken into account by considering the sea level rise in the next twenty years according to the IPCC predictions, i.e. considering a sea level rise of 0.08 m at the location of interest.

Results obtained by propagating the ETS derived by the UKMO data for the period 1986 - 2002 showed that the cross-shore profiles are reliable and the yearly averaged shoreline recession

reaches maximum values of about 18 m where the beaches are steeper. The sea level rise induces a stronger retreat due to wave attack ranging between 2% and 18%, to be summed to the land loss that has to be attributed to the static sea level rise. These results can be of practical interest for Local Authorities dealing with coastal zone management to establish a schedule of planned interventions.

7 Acknowledgements

The UKMO data has been provided by the Ragusa Local Authority. The work has been partially funded by the Italian Minister of University and Research (PRIN 2008- "Strumenti operativi per la stima della vulnerabilità dei litorali sabbiosi anche in presenza di strutture costiere")

8 References

- Arena, F. (2004). On the prediction of extreme sea waves, *Environmental Sciences and Environmental Computing*, Vol II, Ch. 10 (EnviroComp Inst., Fremont, CA, USA) pp. 1-50.
- Arena, F., Meduri, S., Pavone, D., Romolo, A., (2006). Directional return period of severe storms off Italian coasts. Proc. 25th OMAE, Hamburg.
- Bindoff, N.L., J. Willebrand, V. Artale, A. Cazenave, J. Gregory, S. Gulev, K. Hanawa, C. Le Quéré, S. Levitus, Y. Nojiri, C.K. Shum, L.D. Talley and A. Unnikrishnan, (2007): Observations: Oceanic Climate Change and Sea Level. In: *Climate Change 2007: The Physical Science Basis. Contribution of Working Group I to the IV Assessment Report of the IPCC*. Cambridge University Press.
- Boccotti, P., (2000). *Waves mechanics for ocean engineering*. Elsevier Science.
- Goda, Y., (2007). Call for enhanced engineering judgement in coastal engineering research, *Proceedings of Coastal Structure 2007, Venice (Italy), July 2-4*.
- Larson, M., Kraus, N., (1989). SBEACH: Numerical model fo simulating storm-induced beach changes. Tech. Rep. CERC-89-9, USACE
- Neilans, P. J. 1994, "Storm-induced beach erosion, Glynn County, Georgia, " U.S. Army Engineer Waterways Experiment Station, Coastal Engineering Research Center, Vicksburg, MS.
- Olabarrieta M., Medina, R., Losada, I. J., Méndez, F.J. (2007). Potential effects of climate change on coastal structures: application to the Spanish littoral, *Proc. of Coastal Structure 2007, Venice (Italy), July 2-4*.

Risk management in coastal engineering – A case study in northern Germany

Christian Grimm¹, Daniel Bachmann² and Holger Schüttrumpf³

Abstract

In the last decades storm surges and river floods had a major impact on the life of the people and the economy in Europe. As a consequence the European Union adopted in 2007 a Directive on the assessment and management of flood risks. The practical realisation of the legal standards is a major task for the flood protection agencies. The development of methods and computer based tools to support this process is one of the major challenges for the scientific research. Therefore, the Institute of Hydraulic Engineering and Water Resources Management of RWTH Aachen University developed the software package PROMAIDES. It integrates modules for reliability analysis, hydrodynamic analysis, analysis of consequences as well as the combining risk analysis. This paper focuses on the adaption of the PROMAIDES system for an application to coastal regions. The development process and the verification on selected study sites is part of the HoRisk-project.

Keywords: Flood risk analysis, Coastal protection, Decision support system

1 Introduction

In October 2007 the European Parliament and the Council of the European Union have adopted the Directive 2007/60/EC (EU, 2007) on the assessment and management of flood risks. The objective of the Directive is to reduce and manage the risk that floods pose to human health, the environment, cultural heritage and economic activity. According to the directive the Member States of the European Union have to carry out a preliminary risk assessment by December 2011 to identify river basins and coastal areas which are threatened by floods. For the appointed areas flood risk maps have to be drawn up by December 2013. Flood risk management plans focused on prevention, protection and preparedness have to be established until December 2015. The Directive applies to river basins as well as to coastal areas.

The practical realisation of the legal standards is a major task for the flood protection agencies. The identification of flood prone areas, the flood risk mapping as well as the conception of flood mitigation measures are complex problems, which have to be solved. Methods and computer based tools to support the practical realisation of the legal standards are required. The development of these methods and tools are the major challenges for research.

The joint research project HoRisk (Flood Risk Management of Coastal Areas) focuses on the development of an application-oriented flood risk analysis approach for coastal regions (see Section 2). Approaches concerning the flood risk assessment and the required base analyses are theoretically adapted, developed and applied. The transfer of the theoretical developed approaches within the project is performed by an extension of the software package PROMAIDES, a computer-based decision support system (DSS) for the evaluation of flood risk and the selection of flood protection measures (see Section 3). An application for selected study sites at the German coast (see Section 4 and 5) is performed. Thus, the approaches and their implementation in PROMAIDES can be verified.

¹ Institute of Hydraulic Engineering and Water Resources Management, RWTH Aachen, Mies-van-der-Rohe-Strasse 1, 52056 Aachen, Germany, grimm@iww.rwth-aachen.de

² Institute of Hydraulic Engineering and Water Resources Management, RWTH Aachen, Mies-van-der-Rohe-Strasse 1, 52056 Aachen, Germany, bachmann@iww.rwth-aachen.de

³ Institute of Hydraulic Engineering and Water Resources Management, RWTH Aachen, Mies-van-der-Rohe-Strasse 1, 52056 Aachen, Germany, schuettrumpf@iww.rwth-aachen.de

2 The HoRisk-project – Flood Risk Management of Coastal Areas

The objective of the HoRisk-project is to develop an approach for an application-oriented flood risk analysis for coastal regions supporting the federal coastal agencies on the implementation of the Directive 2007/60/EC in Germany. The joint research project “HoRisk – Flood Risk Management for Coastal Areas” is funded by the German Coastal Engineering Research Council (KFKI) and the Federal Ministry of Education and Research (BMBF). It started in April 2010 and will run until April 2013.

The three main project partners are the Coastal Engineering Group of the University of Rostock, the Lower Saxony Water Management, Coastal Defence and Nature Conservation Agency (NLWKN) and the Institute of Hydraulic Engineering and Water Resources Management of RWTH Aachen University. In addition Schleswig-Holstein’s Government-Owned Company for Coastal Protection, National Parks and Ocean Protection (LKN-SH) and the State Agency for Agriculture and the Environment (StALU-MM) join the project as consultants. For the analysis of salt water influence on agriculture industry and tourist economy the Lower Saxony Chamber of Agriculture and HKV Hydrokontor are involved in the project.

The HoRisk project is divided into nine work packages. These nine work packages are all part of the flood risk analysis itself (see Figure 1). The work packages (WP) focus on the following topics:

1. WP 0: Definition of terms
2. WP 1: Comparison of flood risk analyses approaches
3. WP 2: Loadings
4. WP 3: Failure mechanisms
5. WP 4: Inundation
6. WP 5: Damages
7. WP 6: Risk analysis
8. WP 7: Risk mitigation measures
9. WP 8: Application

A sustainable information exchange between the project partners is achieved by regular internal workshops, where the state of each work package is presented and discussed. Moreover, the steering committee of the German Coastal Engineering Research Council (KFKI) inspects every six month the outcome of the results.

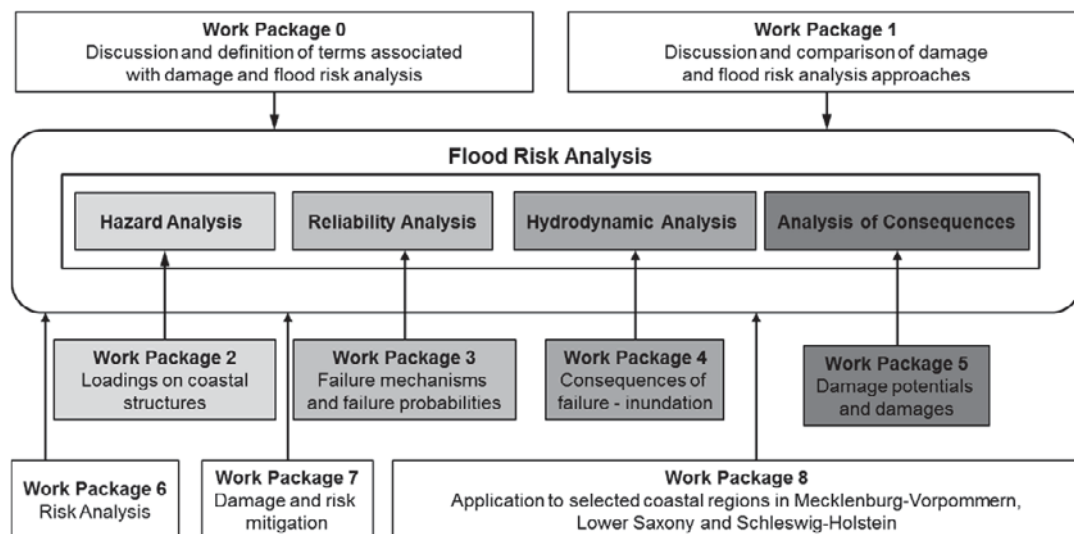


Figure 1: Outline of the HoRisk-project

3 The decision support system PROMAIDES

The modular designed software package PROMAIDES (**P**rotection **M**easure **a**gainst **I**nundation **D**ecision **S**upport), developed at the Institute of Hydraulic Engineering and Water Resources Management of the RWTH Aachen University is a computer-based decision support system (DSS) for the selection of flood protection measures (Bachmann, 2012). The protective efficiency of a measure is evaluated using risk-based criteria. Approaches for an integral flood risk assessment are implemented. The probability and the consequences of risk relevant system states are combined in the risk analysis. Therefore, approaches for the base analyses as the reliability analysis, the hydrodynamic analysis and the analysis of consequences are part of the decision support system PROMAIDES. In order to support effectively the design and selection of flood protection measures, the PROMAIDES software package is supplemented by a graphical user interface, a data base interface as well as mathematical algorithms to prioritize flood protection measures.

The main advantages of the developed software tool PROMAIDES are:

- The integral aspects of flood risk analysis (reliability analysis, hydrodynamic analysis and analysis of consequences) in one software package,
- the identification of possible risk mitigation measures and
- the estimation of construction and maintenance costs for risk mitigation measures.

Detailed information on the PROMAIDES decision support system and the theoretical fundamentals of the implemented procedures are provided in Bachmann (2012).

The development of PROMAIDES started within the REISE-project, funded by the BMBF (Schüttrumpf et al., 2009; Huber et. al., 2009). This project focused on the risk-based evaluation of flood protection measures for riverine areas. In the HoRisK-project (see Section 5) PROMAIDES is currently adapted, extended and verified for an application to coastal regions. In principle, the applied methods for the risk analysis and the base analyses are identical for coastal and riverine regions. In detail, extensions and adaptations are required.

In the following the three base analyses are presented (see Figure 2). The main coastal specific aspects are mentioned:

- The Reliability Analysis (FPL): The aim of the reliability analysis is to quantify the failure probability of a coastal defence structure within the coastline. The input variables of the reliability analysis are geometrical characteristics and material specific values of a structure, like crest height and friction angles. These values are modelled by probabilistic distributed variables. With the help of a fault tree analysis the failure specific events for a given structure type is defined. The reliability is calculated by a Monte Carlo analysis applied to the structure specific fault tree. The fragility curve as a result of reliability analysis summarizes the performance of a structure. It shows the failure probability of a structure conditional to the applied stress, like the water level (Bachmann et. al., 2009). Coastal specific structure types are sea dikes, storm surge gates, flood protection walls and natural grown dunes. For these types of coastal defence structures failure models will be developed and integrated in the flood risk assessment tool PROMAIDES.
- The Hydrodynamic Analysis (HYD): The numerically based hydrodynamic analysis determines the water level and flow velocity of the inundated area for a given storm surge hydrograph under consideration of the site specific topography. Main input data are the storm surge hydrograph as a boundary condition of the hydrodynamic model and digital terrain models to represent the topography. The hydrodynamic analysis implemented in PROMAIDES is based on a finite difference approach discretising the diffusive wave formula (Tsai, 2003). The hinterland is represented by a 2d grid in the model.
- The Analysis of Consequences (DAM): The determined hydraulic variables are transformed into consequences for people and economic values. Therefore, land use information, e. g. based on the official topographic cartographic information system data

(ATKIS), and damage functions for the transformation of the hydraulic variables are required (Kutschera, 2008). Coastal specific aspects are the impact of salt water to the agriculture, the industry and housing as well as the impact of flooding on the tourist economy.

The three base analyses, their input data and their results are summarised in Figure 2.

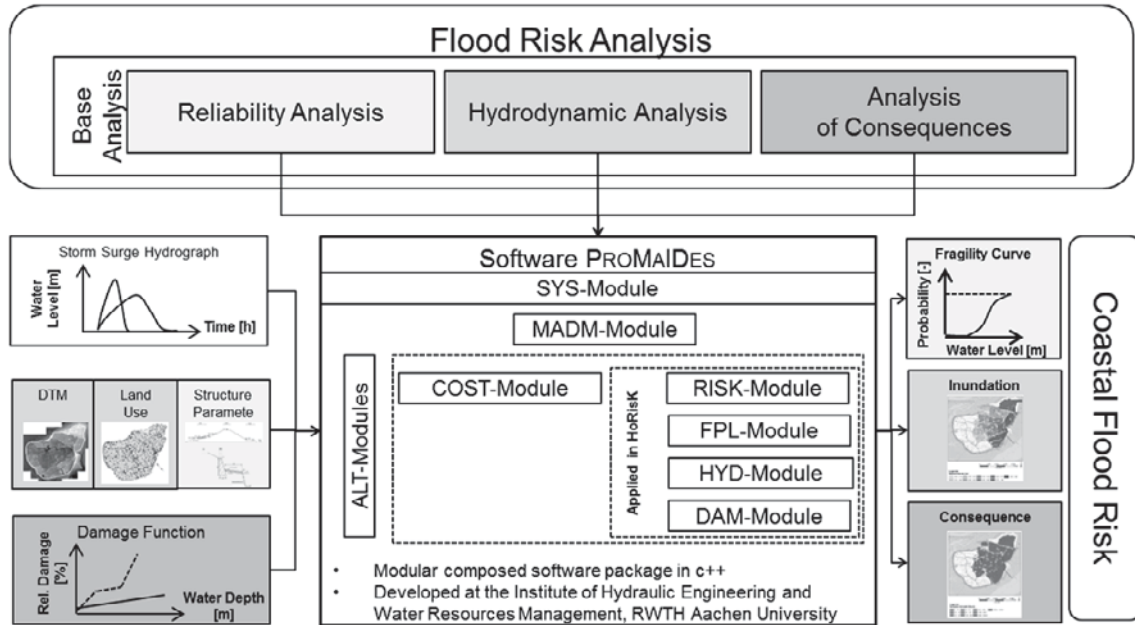


Figure 2: Flood risk analysis and base analyses as implemented in PROMAIDES

The risk analysis (RISK) is a system analysis, where the system is defined as a coastal region. The risk analysis manages the named base analyses and combines the results of these into a total risk for the system. In general, the risk is quantified mathematically using the risk definition (Merz, 2006):

$$R = P(D) \cdot K(D). \quad (1)$$

In Equation (1) R defines the risk, P the probability of an event D and K is the consequences resulting from this event D . Finally, the risk is depending on the state of the analysed system.

In the context of flood risk, one system state i includes a storm surge event j , failure or non-failure events in the coastal defence line resulting in an inundation event and finally in the consequences for goods and people in the affected area. The sum over the system states i and the storm surge events j results in the total risk R_t for the analysed system:

$$R_t = \sum_j \sum_i P(D_{i,j}) \cdot K(D_{i,j}). \quad (2)$$

The automatic selection and the calculation of the risk relevant system states are the main challenges within a risk analysis. The risk approach implemented in PROMAIDES is tested and verified for a riverine catchment area (Bachmann, 2012) and will be adopted to coastal regions within the HoRisk-project.

4 Application to selected study sites

The selection of the four study sites was carried out in close collaboration with the Schleswig-Holstein's Government-Owned Company for Coastal Protection, National Parks and Ocean Protection (LKN-SH) and the State Agency for Agriculture and the Environment (StALU-MM). The four study sites are located in the northern part of Germany. Two study sites, Büsum and the island Pellworm, have their coasts at the North Sea. The study sites, Bay of Lübeck and Markgrafenheide, are located at the Baltic Sea (see Figure 3).

The North Sea and the Baltic Sea have different hydraulic conditions. The German North Sea coast is threatened by storm tides, which are caused by changes in barometric pressure combined with strong wind creating high significant wave heights. In the Baltic Sea, the tidal influence on storm surges is less significant. Also the significant wave height is in general considerably lower than for North Sea conditions.

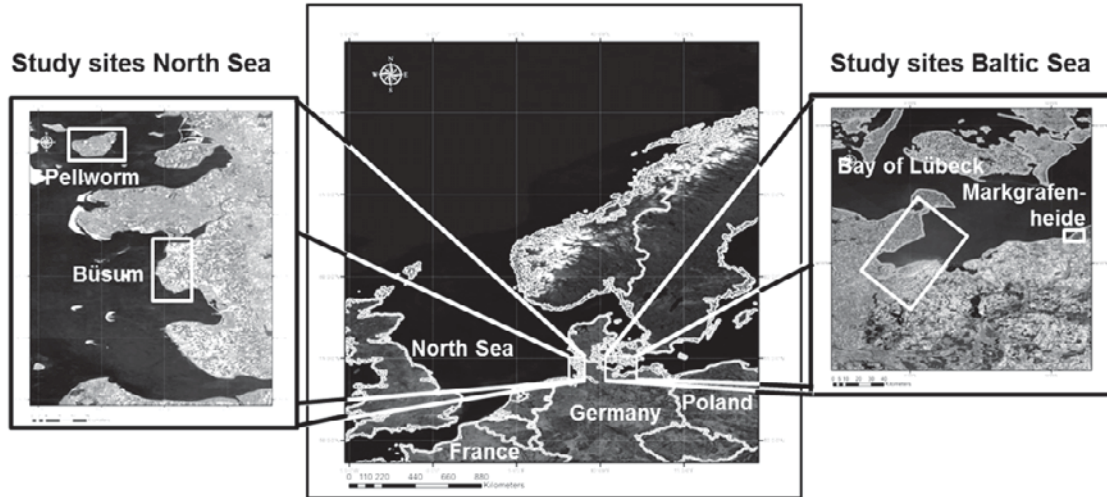


Figure 3: Study sites for flood risk assessment with PROMAIDES

Each study site represents typical characteristics of the German North Sea and Baltic Sea coast. An overview of the characteristics of the study sites is presented in Table 1.

Table 1: Characteristics of the study sites

Study Site	Hydraulic Conditions	Area [km ²]	Coast Line [km]	Population	Predominated Land Use
Pellworm	North Sea	37	25	1,100	Agriculture
Büsum	North Sea	85	48	7,500	Agriculture / Tourism
Bay of Lübeck	Baltic Sea	1,250	100	250,000	Industry and Tourism
Markgrafenheide	Baltic Sea	2	1.8	700	Tourism

The study sites Büsum and Pellworm have similar coastal defence structures. The predominant coastal defence structure is the sea dike. At several locations the dike line is interrupted by storm surge gates for the drainage of the area as well as for purpose of transportation infrastructure. The coastline of the study site Büsum is approximately 48 km, the coastline of Pellworm is 25 km. A second flood defence line forming polder exists in both regions. The land use in both hinterlands is affected by the agriculture industry. Over 85 percent of the land use is agricultural area. Both study sites are also popular vacation destinations in Germany.

The study sites at the German Baltic Sea (Markgrafenheide and Bay of Lübeck) have mainly natural grown dunes as protection against storm surges. The coastal protection system of Markgrafenheide consists of dikes, natural grown dunes and flood protection walls. In contrast to the study sites along the North Sea, the study sites at the Baltic Sea Coast are not predominantly affected by agriculture land use. These study sites are generally influenced by the tourist economy as well as the heavy industry. The Bay of Lübeck is the largest study site with an investigation area of about 1,250 km² and a 100 km long coast line. Markgrafenheide is an inhabited polder and the smallest study site with a 1.8 km long coast line and an area of 1.75 km².

5 Preliminary results for a flood risk assessment of the North Sea Island Pellworm

5.1 The island Pellworm

Pellworm is a North Frisian Island in the North Sea situated near the German mainland. It is part of the northernmost state of Germany Schleswig-Holstein. The island Pellworm has an area of 37.44 km². About 1,100 people live permanently on Pellworm. It is primarily covered by meadows and grassed areas. Agricultural land use is dominant. The 25 km long coastline consists mainly of sea dikes. In the eastern part of the defence line two storm surge gates are integrated to achieve a connection between the harbour and the open sea. The second flood defence line, consisting also of dikes, divides the island into 13 polders.

5.2 Data processing for the hydrodynamic analysis

The hydrodynamic analysis determines the water level and flow velocity of the inundated area for a given storm surge hydrograph under consideration of the site specific topography. Main input data are the storm surge hydrograph as a boundary condition of the hydrodynamic model and digital terrain models for representing the topography.

The storm surge hydrograph used for the preliminary calculation is based on a storm surge event which occurred on the 3rd/4th of January 1976. This "Century Flood" still has the highest peak water level along the German North Sea Coast. For preliminary calculations, the original storm surge hydrograph of the "Century Flood" at the water level gauge Büsum (Stadelmann, 2008) was increased by 50 percent (see Figure 4). The virtual storm surge hydrograph has a peak water level at 7.74 meter above mean sea level (AMSL). The modeled storm surge duration is 21 h.

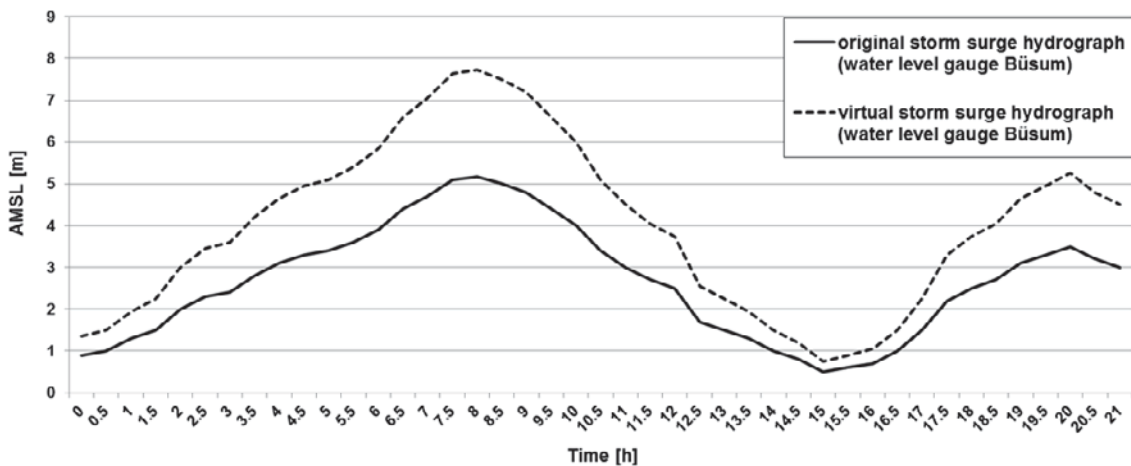


Figure 4: Original and applied, virtual storm surge hydrograph

The second input parameter for the hydrodynamic analysis is the topography. The topography of Pellworm has an average height of zero meters above mean sea level (see Figure 5). A digital terrain model (DTM) for Pellworm in 1x1 m grid size is available.

For the numerical calculation the 1x1 m digital terrain model is aggregated into a 100x100 m grid. The topographical height of the 1x1 m grid is averaged within the aggregation process. The resulting mean height was used for hydrodynamic analysis. The final grid consists of 6622 elements. The hydraulic effective second dike lines as well as the coastal defence line are modelled by linear objects, to which the relevant crest height is assigned.

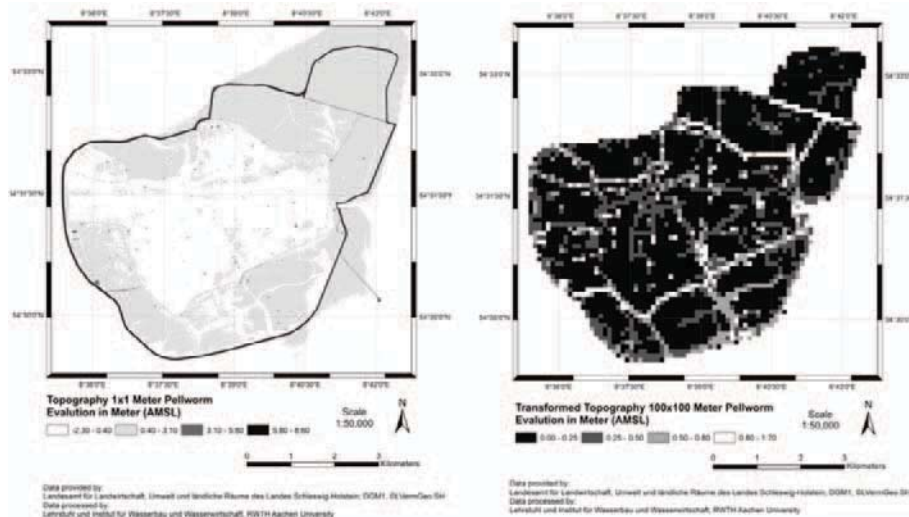


Figure 5: Topography (left) and aggregated topography of Pellworm (right)

5.3 Results of the test run

The maximum water levels for the described virtual storm surge hydrograph are presented in Figure 6. For this test run only overflowing of the coastal dike line is taken into account. Dike breaching is not considered at this stage of work.

The sea dikes at the southern and western coast of Pellworm have a minimum height of 8 m. Therefore, no overflow occurs. The main overflow emerges at the northern and eastern part of the island resulting in maximum water levels to 1.5 m. The effect of the poldering, depicted by the white lines in Figure 6, gets obvious. Some parts of the island are not affected by inundations.

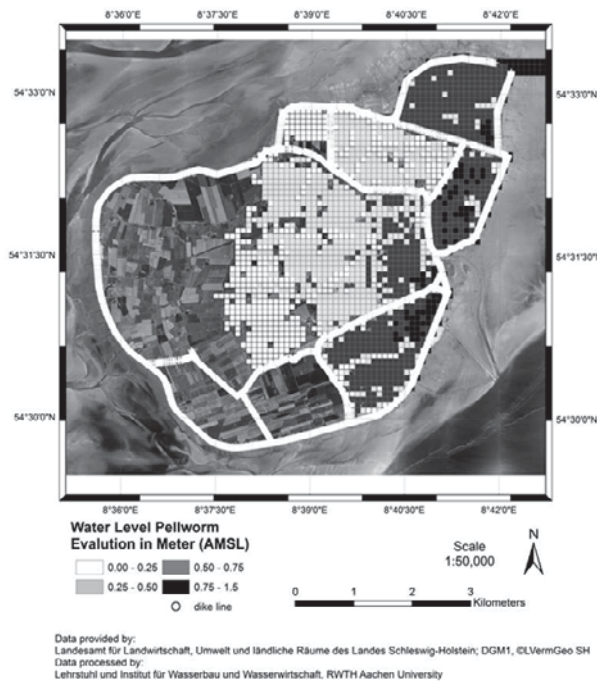


Figure 6: Maximum water level in Pellworm for the virtual storm surge hydrograph

6 Conclusion

The joint research project HoRisK (Flood Risk Management of Coastal Areas) focuses on the development of an application-oriented flood risk analysis approach for coastal regions. In this

paper the outline of the HoRisK-project is presented. Within the project the decision support system PROMAIDES will be adapted and further developed for an application to coastal regions. The basic principles of the PROMAIDES system and coastal specific aspects are described including the base analyses and the risk analysis itself. For a verification of the developed software package four study sites at the German coast are selected. The data processing and the preliminary results of a test run for the North Sea island Pellworm are presented.

At this stage of the project the data processing for the test sites and the computational development of the software package are the predominant tasks. In the next steps the data processing for the other base analyses as the analysis of consequences and the reliability analysis will be performed.

7 Acknowledgement

The joint research project "HoRisK – Flood Risk Management for Coastal Areas" is funded by the German Coastal Engineering Research Council (KFKI) and the Federal Ministry of Education and Research (BMBF).

8 References

- Bachmann, D. (2012): Beitrag zur Entwicklung eines Entscheidungsunterstützungssystems zur Bewertung und Planung von Hochwasserschutzmaßnahmen. Dissertation. Aachen: Institut für Wasserbau und Wasserwirtschaft, RWTH Aachen; (submitted); [Last access: 13.01.2012].
- Bachmann, D.; Huber, N. P.; Schüttrumpf, H. (2009): Fragility Curve Calculation for Technical Flood Protection Measures by the Monte Carlo Analysis. In: Flood Risk Management: Research and Practice / Samuels et al. London (GB): Taylor & Francis Group, - ISBN 978-0-415-48507-4.
- EU (2007): Directive on the assessment and management of flood risks (2007/60/EC); Brüssel: Commission of the European Community; <http://eur-lex.europa.eu/LexUriServ/LexUriServ.do?uri=OJ:L:2007:288:0027:0034:EN:PDF>; [Last access: 05.03.2012].
- Huber, N. P.; Bachmann, D.; Petry, U.; Bless, J.; Arránz-Becker, O.; Altepost, A.; Kufeld, M.; Pahlow, M.; Lennartz, G.; Romich, M.; Fries, J.; Schumann, A. H.; Hill, P. B.; Schüttrumpf, H.; Köngeter, J. (2009): Ein Konzept für eine risikobasierte Entscheidungshilfe im Zuge der Identifikation von Schutzmaßnahmen bei extremen Hochwasserereignissen. In: Hydrologie und Wasserbewirtschaftung, Vol. 53, No. 3, pp. 154-159. - ISSN 1439-1783.
- Kutschera, G. (2008): Analyse der Unsicherheiten bei der Ermittlung der Schadenspotentiale infolge Überschwemmung. Dissertation. Aachen: Institut für Wasserbau und Wasserwirtschaft, RWTH Aachen; <http://darwin.bth.rwth-aachen.de/opus3/volltexte/2009/2664/>; [Last access: 14.09.2010].
- Merz, B. (2006): Hochwasserrisiken - Grenzen und Möglichkeiten der Risikoabschätzung, Stuttgart: Schweizerbart'sche Verlagsbuchhandlung - ISBN 3-510-65220-7.
- Schüttrumpf, H.; Lennartz, G.; Hill, P. B.; Schumann, A. (2009): Entwicklung eines risikobasierten Entscheidungshilfesystems zur Identifikation von Schutzmaßnahmen bei extremen Hochwasserereignissen -REISE- (Abschlussbericht). Aachen: Institut für Wasserbau und Wasserwirtschaft (RWTH Aachen).
- Stadelmann, R. (2008): Den Fluten Grenzen setzen (Bd. 1: Nordfriesland). (S.-H. H. SHHB, Hrsg.) Husum Druck- und Verlagsgesellschaft mbH u. Co. KG. ISBN 978-3-89876-312-7.
- Tsai, C. W. (2003): Applicability of Kinematic, Noninertia and Quasi-Steady Dynamic Wave Models to Unsteady Flow Routing. In: Journal of Hydraulic Engineering, Vol. 129, No. 8, pp. 613-627. - ISSN 0733-9429.

On failure mechanisms and failure probabilities of flood protection dunes at the German Baltic Sea Coast

– first results of a research project –

Angelika Gruhn¹, Peter Fröhle¹, Dörte Salecker¹ and Christian Schlamkow¹

Abstract

For the assessment of risk caused by extreme storm surges, predictions need to be made about failure probabilities of flood protection measures protecting low lying coastal areas. The present paper describes a method to calculate the probability of failure of flood protection dunes. At first, dunes as flood protection measures are characterized. Following, possible failure mechanisms and the dune erosion processes are described. The dune erosion model of Van Gent et al. (2008) is explained, being the basis for the calculation of the failure probability. Further, the input parameters for the model as well as the initial dune profile are described. Subsequently, a description of the calculation method for the probability of failure by means of reliability analysis and Monte Carlo simulation is given.

Keywords: flood protection dunes, dune erosion model, probability of failure, Monte Carlo simulation

1 Introduction

Coastal areas have always been preferred residential, trading and industrial areas. So these areas are densely populated with huge property assets. Unfortunately, those areas are in many cases low lying areas, which are threatened by extreme storm surge events. In the past, these extreme events became more frequent and it is quite likely that this will not change in the future. So, there is the necessity to protect life and limb of the human beings as well as trading and industry against adverse consequences of extreme storm surges. One way is the realization of flood protection structures like flood protection dunes. These structures are, due to reasons of economy, constructed for certain design conditions. If these design conditions are exceeded, there is the danger and a certain probability that this structure fails. But also if the loading on the structure during a storm surge are lower than the design conditions, there is a certain probability of failure of the flood protection structure. Every flood protection structure may fail in different failure modes respectively failure mechanisms. That means before failure probability can be determined the relevant failure mechanisms for every component of the flood protection structure need to be defined. Afterwards, an appropriate calculation model is needed describing the specific failure mechanism. The actual calculation method of the failure probability depends on the required level of complexity. Uncertainties can be taken into account using a calculation model with the corresponding input parameters. Failure probabilities are then calculated using Monte Carlo Simulations. Determination of the failure probability of a flood protection structure is an essential part of a risk analysis.

The paper describes an approach for the calculation of failure probability of flood protection dunes. First of all dunes will be characterized as a measure for flood protection. Afterwards the paper will give a closer look on the possible failure mechanisms of flood protection dunes. For the failure mechanism "dune erosion due to wave attack" a calculation model is described, which will be the basis for the calculation of the failure probability via Monte Carlo Simulation. The following chapter address the input parameters needed for the calculations. The results of the calculations will be presented and conclusions are given.

¹ University of Rostock, Institute of Environmental Engineering, Coastal Engineering Group; Justus-von-Liebig-Weg 6, D18059 Rostock; Email: angelika.gruhn@..., peter.froehle@..., doerte.salecker@... christian.schlamkow@uni-rostock.de

2 Flood protection dunes and dune erosion process

2.1 Flood protection dunes

Flood protection dunes are an essential part element of flood protection at the German Baltic Sea Coast. Low lying coastal areas of the outer coast of Mecklenburg-Western Pomerania are protected by flood protection dunes over a length of 106 km (StALU 2009).

Flood protection dunes can be either realized in a system with other flood protection structures like groins, dikes or flood protection walls or as single structures. As single structure dunes have to withstand occurring storm surges and need to be designed in an adequate way.

Dunes as single flood protection structures comprise: a seaward lying i) wear part, followed by the effective ii) flood protection part and the iii) safety part, lying most landward (Figure 1).

The wear part of the dune is exposed to and eroded by natural erosion processes and minor storm surges and provides sediment for natural sediment transport processes along the coast. Following, the effective flood protection part supply the amount of sediment which is needed for transformation processes during a design storm surge. If the wear and the effective flood protection part are eroded, the safety part as the most landward part of the flood protection dune has to ensure the protective function of the dune. In Mecklenburg-Western Pomerania this part has, in general, a width of 5m (StALU 2009).

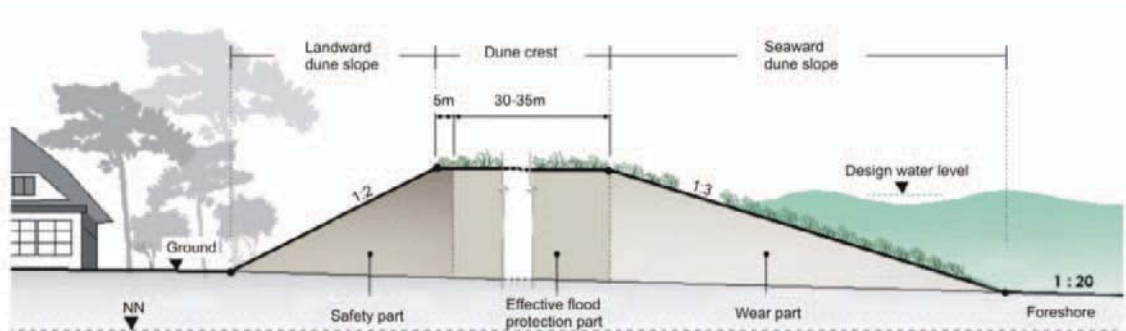


Figure 1: Cross section of a flood protection dune (after StALU 2009)

2.2 Dune erosion processes

Within the scope of the FloodSite-project Allsop et.al. (2007) compiled failure mechanisms and the corresponding calculation model for different flood protection structures. For the structure type "flood protection dune" the failure mechanisms:

- Erosion of the seaward slope by waves
- Erosion of the landward slope by overflow
- Erosion of the landward slope by overtopping

have been determined to be significant.

In the literature available on dune erosion, the focus is on the failure of dunes due to erosion of the seaward slope by waves.

Van Gent et.al. (2008) describe the dune erosion process due to wave attack as a temporal varying process, where different processes alternate. In the beginning, the dune foot is under the water level. So a high number of waves reach the dune face. Consequently, the dune face gets steeper until it is almost vertical. Further wave impact leads to an episodically sliding of limbs of sediment. Deposited sediment is stirred up by incoming wave and transported in seaward direction. By this the foreshore is broaden and further dune erosion in temporally obstructed. With ongoing erosion dune foot is moving landward and upward. In consequence fewer waves reach the dune and the erosion rate decreases.

3 Dune erosion models

As the basis for the calculation of the failure probability it is the necessity to find an appropriate calculation model. Calculation models range, depending on the complexity of the models, from simple empirical models to more complex process-based models. Concerning application-oriented methods and approaches for risk and damage analysis, a calculation model should be simple. Simple empirical models describing dune erosion due to wave impact mainly based on an equilibrium profile approach. Following this approach it is assumed that the dune profile, which is exposed to wave attack and high water levels during a storm surge, is adjusting itself to these hydrodynamic loads. Hence, after a sufficient long period, the equilibrium profile is reached and no additional erosion of the dune profile occurs. It is further assumed, that the amount of sediment eroded from the dune is completely deposited on the foreshore.

Van Gent et al. (2008) introduce such a model. It is an extension of the dune erosion model of Vellinga (1986).

With the basic model of Vellinga (1986), the shape and the length of the subaqueous erosion profile is calculated in dependence of the wave height (H_{0s}) and the fall velocity (w) of the sediment. The storm surge water level which has an essential influence on the dune erosion is taken into account in an implicit way. The beginning of the subaqueous erosion profile is located on the storm surge water level. For the morphological development of the landward part of the dune is assumed that the dune face has a slope of 1:1 after the erosion. The erosion profile of the dune results from a combination of the subaqueous erosion profile and the profile of the eroded dune. The duration of the storm is not taken into account for the calculation of the dune erosion profile. The model is valid for both, a storm duration of 5 hours with a constant load and a natural storm with a storm duration of 45 hours (Brandenburg 2010).

Van Gent et.al. (2008) extended the Vellinga (1986) model to take into account the influence of the wave period on the development of the erosion Profile. In large scale hydraulic test the authors investigated the influence of the wave period and the wave spectrum. In conclusion, it can be said that both the period $T_{m-1,0}$ and the peak period T_p can be used to determine the erosion profile of the dune. Here the peak period T_p is used. A definition sketch is given in Figure 2

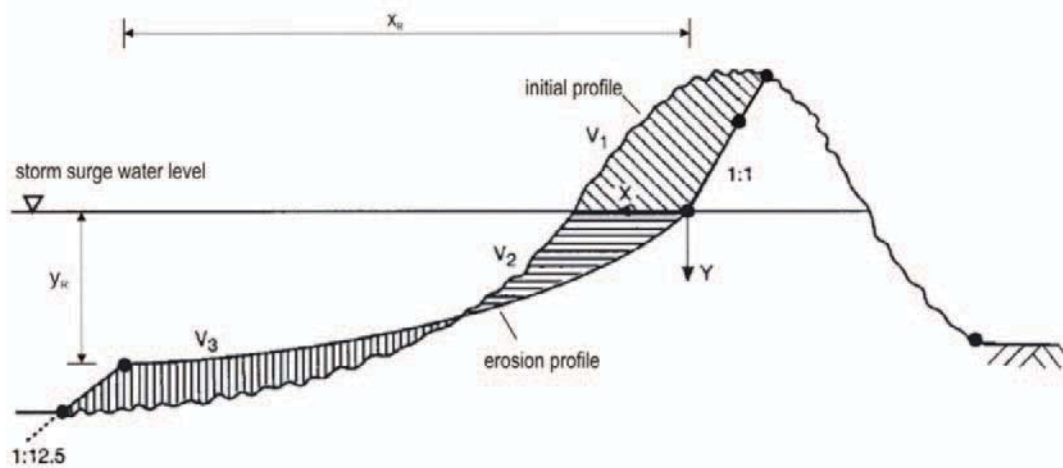


Figure 2: Definitions sketch for the dune erosion model of Van Gent et.al. (2008)

Following the equations for the calculation of the dune erosion profile are given:

$$\frac{7,6}{H_{0s}} = 0,4714 * \left[\left(\frac{7,6}{H_{0s}} \right)^{1,28} * \left(\frac{12}{T_p} \right)^{0,45} * \left(\frac{w}{0,0268} \right)^{0,56} * x + 18 \right]^{0,5} - 2 \quad (1)$$

$$x_R = 250 * \left(\frac{H_{0s}}{7,6} \right)^{1,28} * \left(\frac{0,0268}{w} \right)^{0,56} \quad (2)$$

$$y_R = \left(\frac{H_{0s}}{7,6} \right) * \left[0,4714 * \left(250 * \left(\frac{12}{T_p} \right)^{0,45} + 18 \right)^{0,5} - 2 \right] \quad (3)$$

- where
- H_{0s} wave height [m]
 - T_p peak wave period [sec]
 - w fall velocity [m/sec]
 - x_R seaward end of erosion profile [m]
 - y_R seaward end depth of erosion profile [m]
 - D_{50} grain diameter [m]

4 Input parameters

4.1 Dune profile

For the application of the dune erosion model of Van Gent et al. (2008), the initial profile of the dune and the foreshore need to be characterized. As single structures, flood protection dunes typically have an outer slope of 1:3 and an inner slope of 1:2 (see Figure 1 & 3). The foreshore is divided into an upper part (dry beach) with a slope of 1:100 and a lower part (wet beach) which has a slope of 1:200. The dune crest can be of variable height and width (Figure 3). Within the investigations carried out the dune crest height is set to 5m above NN.

The grain diameter needed for the fall velocity w (see eq. (1) & (2)) is defined to be $d_{50}=0,3$ mm which corresponds to medium sand.

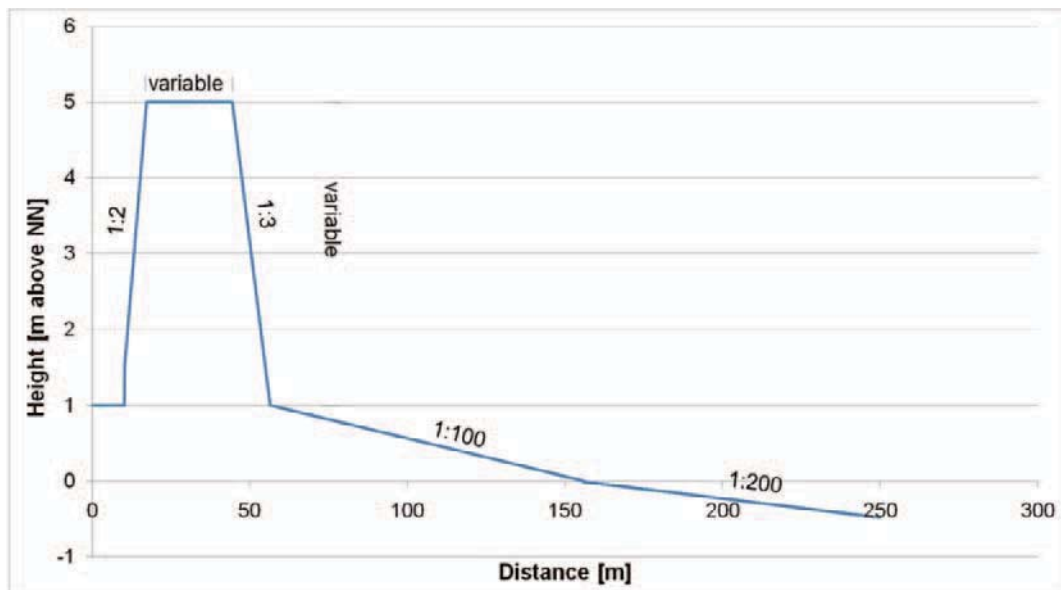


Figure 3: Shape of the initial dune profile

4.2 Hydrodynamic input parameters

Failure probability shall be calculated in a probabilistic way via Monte Carlo Simulations. Therefore it is necessary to generate large number of wave heights, as input for the calculations. For this purpose statistical analysis are applied on measured wave heights. In order to find the distribution function which describe the measured wave heights best different distribution functions were fitted to the measurements. In conclusion it can be said that the Generalized Extreme Value Distribution (GEV, see eq. 4) describes the wave heights best.

$$H(x) = \exp\left(-\left(1 + \zeta \cdot \left(\frac{x - \mu}{\beta}\right)\right)^{-1/\zeta}\right) \quad (4)$$

where ζ Shape parameter, $\zeta = 0,01528$
 μ Location parameter, $\mu = 1,58829$
 β Scale parameter, $\beta = 0,58894$

With the help of random number generator and the fitted GEV realizations of the wave heights were generated as input parameters for the Monte Carlo Simulations.

4.3 Selection of input parameters

As a first step, the parameters storm surge water level (Swl), peak period (T_p) and crest width of the initial dune are varied in a deterministic way. Furthermore, the uncertainty model factor (m, see section 5) was varied as well, in order to investigate the influence of this parameter on the results of the calculations. The crest height of the initial dune is defined to be 5m NN in all simulations. Table 1 gives an overview of all sets of input parameters for the calculations. Wave heights are simulated by means of Monte Carlo Simulation (sec. 4.2)

Table 1: Set of input parameters for the Monte Carlo Simulations

Set	Simulation	H_{0s} [m]	T_p [s]	Swl [m NN]	crest width [m]	m [-]	Pf [%]
1	1	0,1 -3	6,05	3	30	0,4	0
	2	0,1 -3	6,05	3	25	0,4	57
	3	0,1 -3	6,05	3	20	0,4	98
	4	0,1 -3	6,05	3	15	0,4	100
2	5	0,1 -3	6,05	3	30	0,5	0
	6	0,1 -3	6,05	3	25	0,5	19
	7	0,1 -3	6,05	3	20	0,5	81
	8	0,1 - 3	6,05	3	15	0,5	100
3	9	0,1 -3	5	2	14	0,5	0
	10	0,1 -3	5	2	13	0,5	45
	11	0,1 -3	5	2	12	0,5	80
	12	0,1 -3	5	2	11	0,5	95
	13	0,1 - 3	5	2	10	0,5	100

5 Reliability analysis and failure probability

Once the failure mechanisms are detected and an appropriate calculation model is chosen, the corresponding failure probability must be calculated by means of reliability analysis. Within reliability analysis the strength of the flood protection structure, here flood protection dunes, is compared with the loadings impacting on the structure. Both parameters are combined in a limit state equation. The structure fails if the loadings exceed the strength of the structure. Means failure probability can be regarded as the probability of negative limit state equation.

Regarding flood protection dunes, limit state equation result from the comparison of the dune crest width after the storm surge event with a minimum allowable dune crest width (see eq. (5)).

$$Z = m * d_{cr_act} - d_{cr_crit} \quad (5)$$

where m model factor [-]

d_{cr_act} dune crest width after storm surge event

d_{cr_crit} minimum allowable dune crest width

The factor m takes into account uncertainties corresponding to the adopted calculation model. Since there is little literature concerning model uncertainties of dune erosion models, this factor was deterministically set to 40% respectively 50%.

The minimum allowable dune crest width is set to 5m, which corresponds to the crest width of the landward safety part of the flood protection dune applied for design in the north eastern part of Germany.

On the basis of the selected limit state equation failure probability is calculated. There a different methods depending on the level of complexity and accuracy of the calculations. Here, Monte Carlo Simulations are used to calculate the failure probability. For a sufficient number of simulations failure probability can be regarded as the relative frequency of simulations with a failing of the flood protection dune (see eq. (6)).

$$P_f \approx \frac{n_{fai}}{n} \quad (6)$$

where P_f failure probability [-]

n_{fai} number of simulations with failing of the flood protection dune [-]

n number of carried out simulations [-]

6 Results and discussion

Via the dune erosion model of Van Gent et al. (2008) and Monte Carlo Simulations failure probabilities are calculated for different sets of input parameters. Within the simulations the parameters i) crest width of the initial dune, ii) storm surge water level, iii) peak period and the iv) uncertainty model factor are varied in order to gain the failure probabilities.

Figure 4 shows the calculated failure probabilities in dependence of the crest width of the initial dune for all three sets of input parameters. As expected, an increase of the crest width of the initial dune leads to a decrease of the failure probability (Figure 4 & Table. 1). That means, the wider the crest width, the more resistant the flood protection dune. This can be concluded for every simulation carried out.

Furthermore, the choice of the uncertainty model factor has an influence on the results which cannot be neglected (see Table 1 & Figure 4, Set 1 & Set 2). It can be concluded that for a higher uncertainty model factor a failure of the flood protection dune is more probable than for a smaller uncertainty model factor. That means, for further investigations the uncertainty model

factor has to be determined in an appropriate way in order to gain reliable information about the failure probabilities of flood protection dunes.

Figure 5 exemplarily shows the cumulative frequency of the remaining crest widths for one set of input parameters (Set 1 simulation 2). The graph shows the distribution of the remaining crest widths within the results of the simulation. The dashed line represents the threshold (critical crest width of the dune, $d_{cr_crit} = 5\text{m}$) by which the failure of the flood protection dune occurs. It can be seen from Figure 4 that more than 50% of the simulations lead to a failure of the flood protection dune.

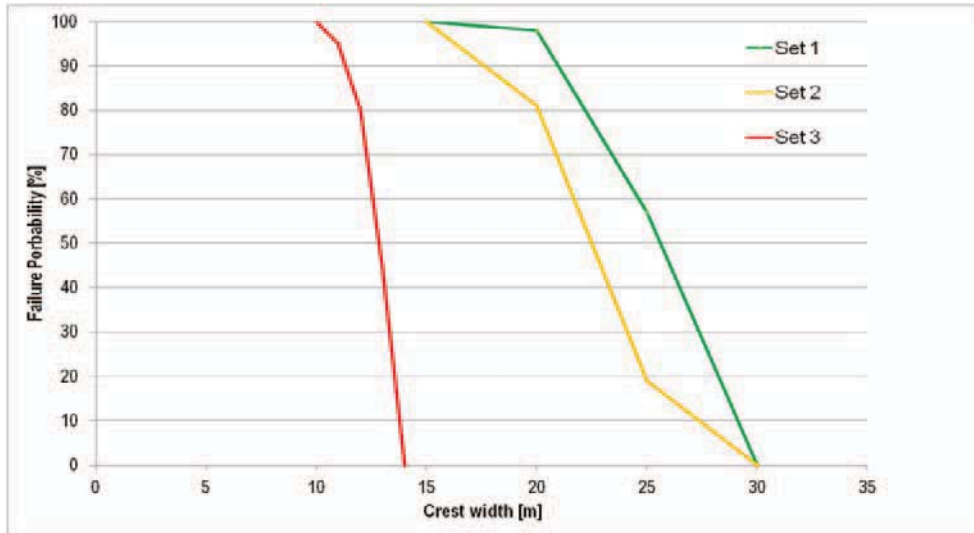


Figure 4: Resulting failure probabilities for different sets of simulations

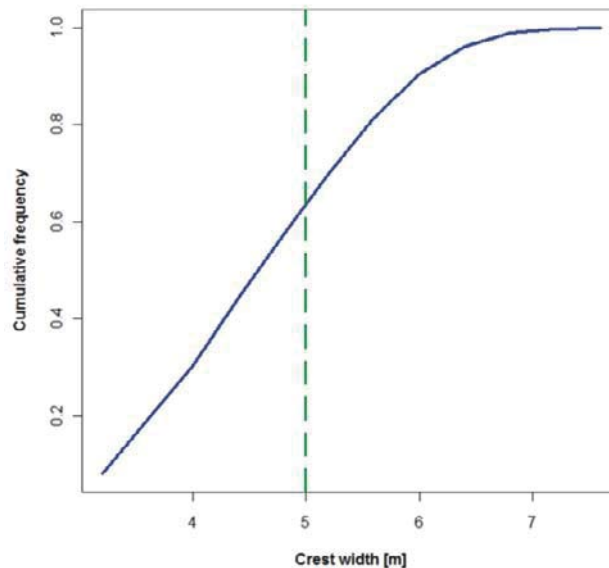


Figure 5: Cumulative frequency of the remaining crest width (Set 1 simulation 2)

7 Conclusion and Outlook

The present paper describes a method for the calculation of failure probability of flood protection dunes by means of Monte Carlo Simulations. From the first results, described in the paper, it can be concluded that that the methods is capable to give reasonable results for the calculation of the failure probabilities of flood protection dunes.

Nevertheless, for further improvement of the described method adaptations have to be made. This means to gain the input parameters wave height and storm surge water level with a joint probability of occurrence to investigate the failure probability of flood protection dunes for storm surges with a certain recurrence period. The parameters wave height and peak period need to be correlated as well.

The determination of the uncertainty model factor needs to be adapted as well. Methods for the determination of this factor are mainly based on the comparison of the calculated erosion profile of the dune and field measurements of an eroded dune. Another possibility is the comparison between the calculated erosion profile and results of proven numerical models (CEM 2001, Slijkhuis 1998 in Kortenhaus 2003).

In addition, more complex process-based dune erosion models, e.g. XBeach, will be applied for the calculation of the failure probabilities of flood protection dunes.

8 Acknowledgment

The work described in this paper is part of the HoRisk project which is funded by the Federal Ministry for Education and Research and supported by KFKI (German Coastal Engineering Research Council).

9 References

- Allsop, W. et.al. (2007): Failure Mechanisms for Flood Defence Structures, FloodSite Report Nr. T04-06-01, www.floodsite.net/html/publications2.asp?ALLdocs=on&Submit=View
- Brandenburg, P. (2010): Scale dependency of dune erosion models - Performance assessment of the DUROS and XBeach model for various experiment scales, Master Thesis, Deltares, Rotterdam
- CUR/TAW (1990): Guide to the assessment of the safety of dunes as a sea defence, TAW Report 140
- Kortenhaus, A. (2003): Probabilistische Methoden für Nordseedeiche, PhD Thesis, Technical University Carolo-Wilhelmina zu Braunschweig, Department of Civil Engineering, 242 pages, Braunschweig
- Roelvink, D. et.al. (2009): Modelling storm impacts on beaches, dunes and barrier islands, Coastal Engineering, Vol. 56, S. 1133 - 1152, doi:10.1016/j.coastaleng.2009.08.006
- Schlamkow, C; Fröhle, P. (2009): Final report: Joint project - MUSTOK, Project - SEBOK-B: Development of methods for the determination of relevant hydrodynamic design parameter for coastal protection structures at the Baltic Sea, University of Rostock, Institute of Environmental Engineering, Coastal Engineering Group
- StALU (2009): Regelwerk Küstenschutz Mecklenburg-Vorpommern Übersichtsheft: Grundlagen, Grundsätze, Standortbestimmung und Ausblick, Editor: Ministry for Agriculture, Environment and Consumer Protection Mecklenburg-Vorpommern
- University of Rostock (2011): 1. Zwischenbericht: Project HoRisk, University of Rostock, Coastal Engineering Group, Rostock 2011
- Van Gent, M.R.A. et.al. (2008): Large-scale dune erosion tests to study the influence of wave periods, Coastal Engineering, Vol. 55, S. 1041 – 1051
doi:10.1016/j.coastaleng.2008.04.003
- Vellinga, P. (1986): Beach and dune erosion during storm surges, Dissertation, Technical University Delft, 200 pages

Opportunities and threats along Iranian coastlines

Bahareh Majdi¹, Freydoon Vafai², S. Mohammad Hossein Jazayeri Shoushtari³ and Alireza Kebriaee⁴

Abstract

In Iranian integrated coastal zone management plan, the strengths, weaknesses, opportunities, and threats (SWOT) framework was used to categorize and evaluate significant marine physical parameters (or internal factors) and human and development activities (or external factors) to achieve a shoreline management plan for future coastal zone developments. In the SWOT framework, internal factors consist of strengths and weaknesses and external factors consist of opportunities and threats. In this approach an analysis of internal factors is first completed through consideration of environmental quality (strengths) and vulnerability (weaknesses) among marine physical indicators. Then, an external analysis is made considering the relation between human activities and natural environment to determine threats and opportunities which may vary depending on the activity under consideration.

Keywords: Opportunities, Threats,

1 Opportunities and Threats

Internal factors considered in this study are beach/bottom material, storm surge levels, extreme wave height, hazard zone (flooding + erosion) extent, tsunamis, rip currents, water level fluctuations, ground water level, river flood, erosion, accretion, seismic fault, landform and vegetation or plant coverage. These factors are shown in Table 1. However, it was decided not to divide them into strengths and weaknesses as these definitions may differ from one human activity to other. In other words, a factor may be considered as weakness in one application but as strength in another application or even in the same application but from a different aspect. Instead, a score was allocated to each factor ranging between 0 and 1 to show the intensity of that factor. The range was divided into 4 or 6 levels depending on the factor. If quantified data was not available for a factor, it was scored as either 1 or 0 to show its existence or non-existence, respectively. For rip current and ground water level factors, the available information was not sufficient and therefore, these factors were not included in the calculations.

Five types of human activity (development) were considered: 1) recreational and tourism, 2) commercial and industrial, 3) fishery and aquaculture, 4) agricultural, and 5) residential. For each human activity, an internal factor may represent a threat, an opportunity or sometimes both. The factors were weighted from 1 to 4 depending on their level of risk or advantageousness to each activity. A color scheme is used in Table 1 to show the weight of each factor for individual human activities. For each activity, weight is multiplied by score and summed up over relevant internal factors and then averaged to arrive at the total score:

$$\text{Total Score} = \sum_{i=1}^N \frac{A_i B_i}{N} \quad (1)$$

¹ Energy Industries Engineering & Design (EIED), No.4, Second Koohestan St., Passdaran Ave, Tehran, Iran, majdi-b@eied.com

² Civil Engineering Department K.N.Toosi University of Technology, No. 1346, Vali-Asr St., P.C. 19697, Tehran, Iran, fvafai@kntu.ac.ir

³ Formerly, Graduate Student K. N. Toosi Univ. of Tech., No. 1346, Vali-Asr St., P.C. 19697, Tehran, Iran, mh_jazayeri@sina.kntu.ac.ir

⁴ General Directorate of Coast and Port Engineering, Ports and Maritime Organization, Tehran, Iran, kebriaee@pmo.ir

Where A_i is the intensity of internal factor i , B_i is the weight of that factor and N is the number of internal factors relevant to that human activity. The range between zero and total possible scores for each activity was then equally divided into 4 levels of neutral, low, moderate and high to classify opportunity and threat levels. Based on the above calculations, opportunities and threats maps were prepared for each type of development and individual maps were provided for each littoral cell. A littoral cell is a coastal compartment that contains a complete cycle of sedimentation including sources, transport paths, and sinks. The cell boundaries delineate the geographical area within which the sediment budget is balanced, providing the framework (or study unit) for the quantitative analysis of coastal erosion and accretion. The entire Iranian coastline on the Caspian Sea was determined as one littoral cell, as no distinct cell boundary could be identified within this coastline. Of the remaining 13 littoral cells, 7 cells were defined along the Persian Gulf coastlines and 6 cells along the Oman Sea coastlines. Figures 1 to 5 show distributions of opportunities and threats in Cell #12 as an example.

Table 1: Marine physical parameters and their relation to opportunities and threats

Human Activity		Real Values	Intensity Score	Threats					Opportunities												
				Recreational/ Tourism	Commercial/ Industrial	Fishery/ Aquaculture	Agriculture	Residential	Recreational/ Tourism	Commercial/ Industrial	Fishery/ Aquaculture	Agriculture	Residential								
Hydrodynamic Characteristics	Storm & Surge	<0.5m	0																		
		1.0	0.2																		
		1.5	0.4		Human Life Loss	Human Life Loss															
		2.0	0.6																		
		2.5	0.8																		
	> 2.5	1																			
	Hazard Line Extent	< 100m	0																		
		100-300	0.33	Human Life Loss				Damage	Human Life Loss												
		300-1000	0.66						Damage												
		> 1000	1																		
	Extreme Waves	<2.5m	0	Human Life Loss	Human Life Loss	Human Life Loss															
		3.5	0.2																		
		4.5	0.4																		
		5.5	0.6																		
		6.5	0.8	Damage	Damage	Damage															
	7.5	1																			
	Tsunami	Yes	1	Human Life Loss	Human Life Loss	Human Life Loss			Damage	Human Life Loss											
		No	0	Damage						Damage											
	Rip Current	Information not available		Human Life Loss												Water Quality Improve	Water Quality Improve	Water Quality Improve	Water Quality Improve		
	Short Term Water Level Fluctuation	<1.5m	0																		
2.0		0.2																			
2.5		0.4																			
3.0		0.6	Damage	Cost Increase	Cost Increase			Damage	Damage												
3.5		0.8																			
>3.5m	1																				
Long Term Water Level Fluctuation	Yes	1		Damage	Damage																
	No	0	Damage	Cost Increase	Cost Increase			Damage	Damage												

Human Activity	Real Values	Intensity Score	Threats					Opportunities						
			Recreational /Tourism	Commercial /Industrial	Fishery/ Aquaculture	Agriculture	Residential	Recreational/ Tourism	Commercial/ Industrial	Fishery/ Aquaculture	Agriculture	Residential		
Marine Physical Factors	High Ground Water Level	Information not available		Damage	Damage Cost Increase	Damage Cost Increase	Damage	Damage						
	River Flood	Yes	1	Human Life Loss	Human Life Loss	Human Life Loss	Damage	Human Life Loss						
		No	0	Damage	Damage	Damage	Damage	Damage						
Beach / Bottom Material	Sand	Yes	1						Natural Protection	Natural Protection	Natural Protection	Natural Protection	Natural Protection	
		No	0						Water Quality Improve	Water Quality Improve	Water Quality Improve			
	Cobbles	Yes	1						Water Quality Improve	Water Quality Improve		Natural Protection	Natural Protection	
		No	0						Water Quality Improve	Water Quality Improve		Natural Protection	Natural Protection	
	Bedrock	Yes	1		Cost Increase	Cost Increase			Natural Protection	Natural Protection	Natural Protection	Natural Protection	Natural Protection	
		No	0						Water Quality Improve	Water Quality Improve	Water Quality Improve			
Fine	Yes	1		Cost Increase	Cost Increase			Natural Protection	Natural Protection	Natural Protection	Natural Protection	Natural Protection		
	No	0												
Geomorphology	Erosion	<0.5m/y	0											
		>0.5m/y	1	Damage	Damage	Damage	Damage	Damage						
	Accretion	<0.5m/y	0		Cost Increase	Cost Increase			Increase of Shore lands	Increase of Shore lands	Increase of Shore lands	Increase of Shore lands	Increase of Shore lands	
		>0.5m/y	1											
	Seismicity (Faults)	1	0.0											
		2	0.33	Human Life Loss	Human Life Loss	Human Life Loss	Damage	Human Life Loss						
3		0.66												
4		1.0	Damage	Damage	Damage	Damage	Damage							
Landform (estuary, bay, etc)	Yes	1						Natural Protection	Natural Protection	Natural Protection	Natural Protection	Natural Protection		
	No	0												
Environmental	Mangrove or Marsh	Yes	1						Natural Protection					
		No	0						Promotion of Tourism	Natural Protection	Natural Protection	Natural Protection	Natural Protection	

Weight Coefficients for Threats

1	2	3	4
---	---	---	---

Weight Coefficients for Opportunities

1	2	3	4
---	---	---	---

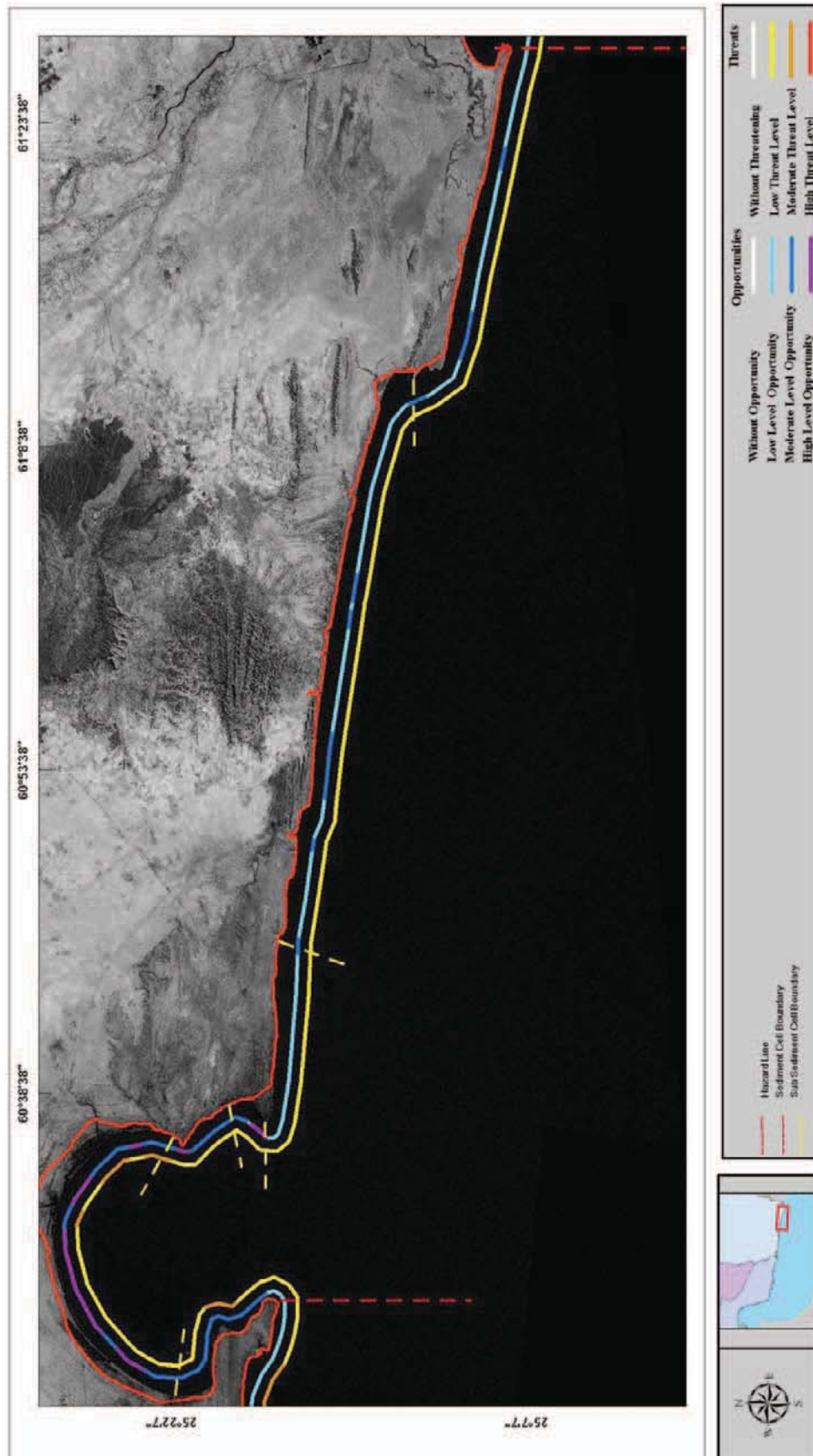


Figure 1: Opportunities and threats for residential development in Cell 12

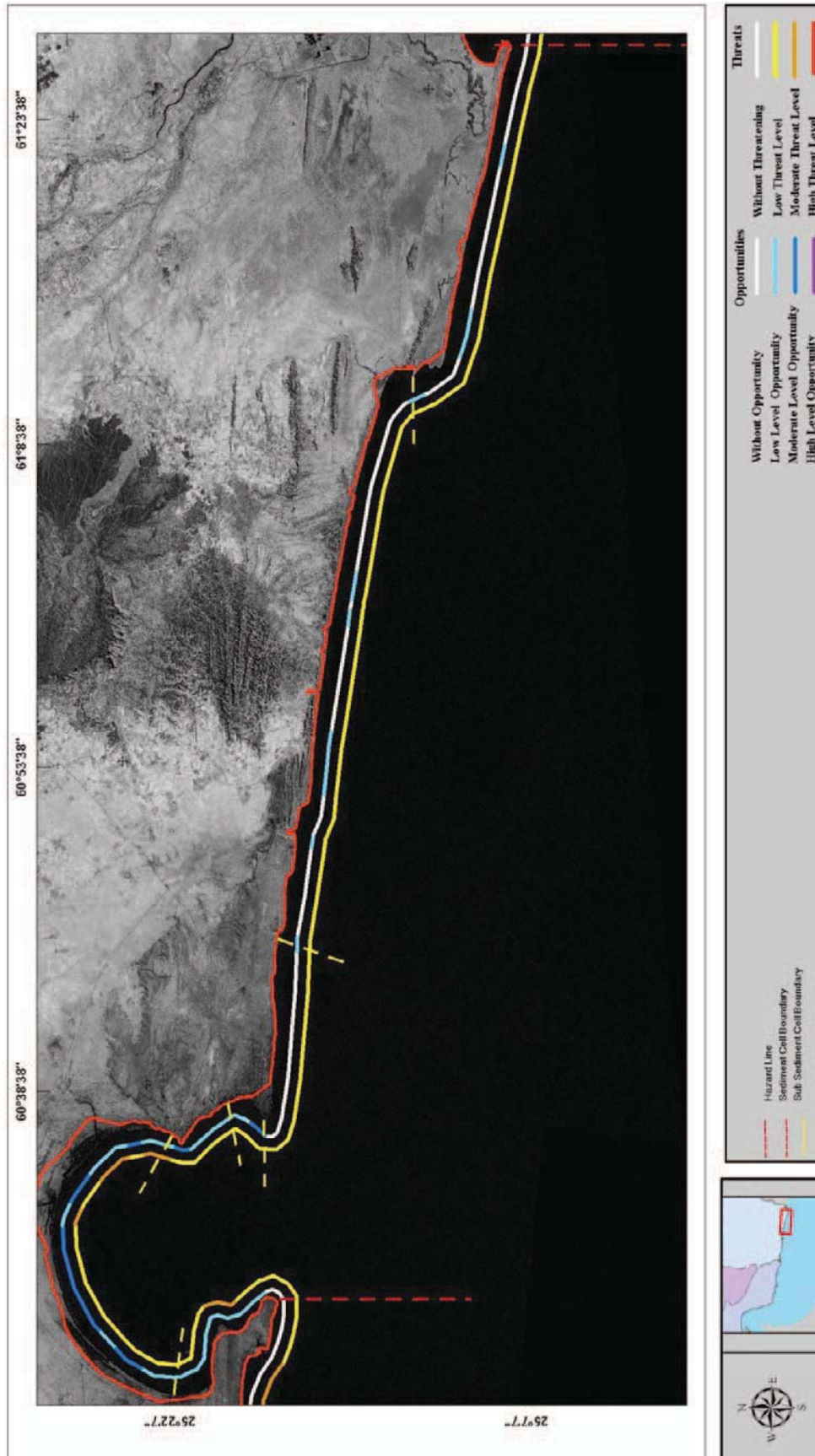


Figure 2: Opportunities and threats for agricultural development in Cell 12

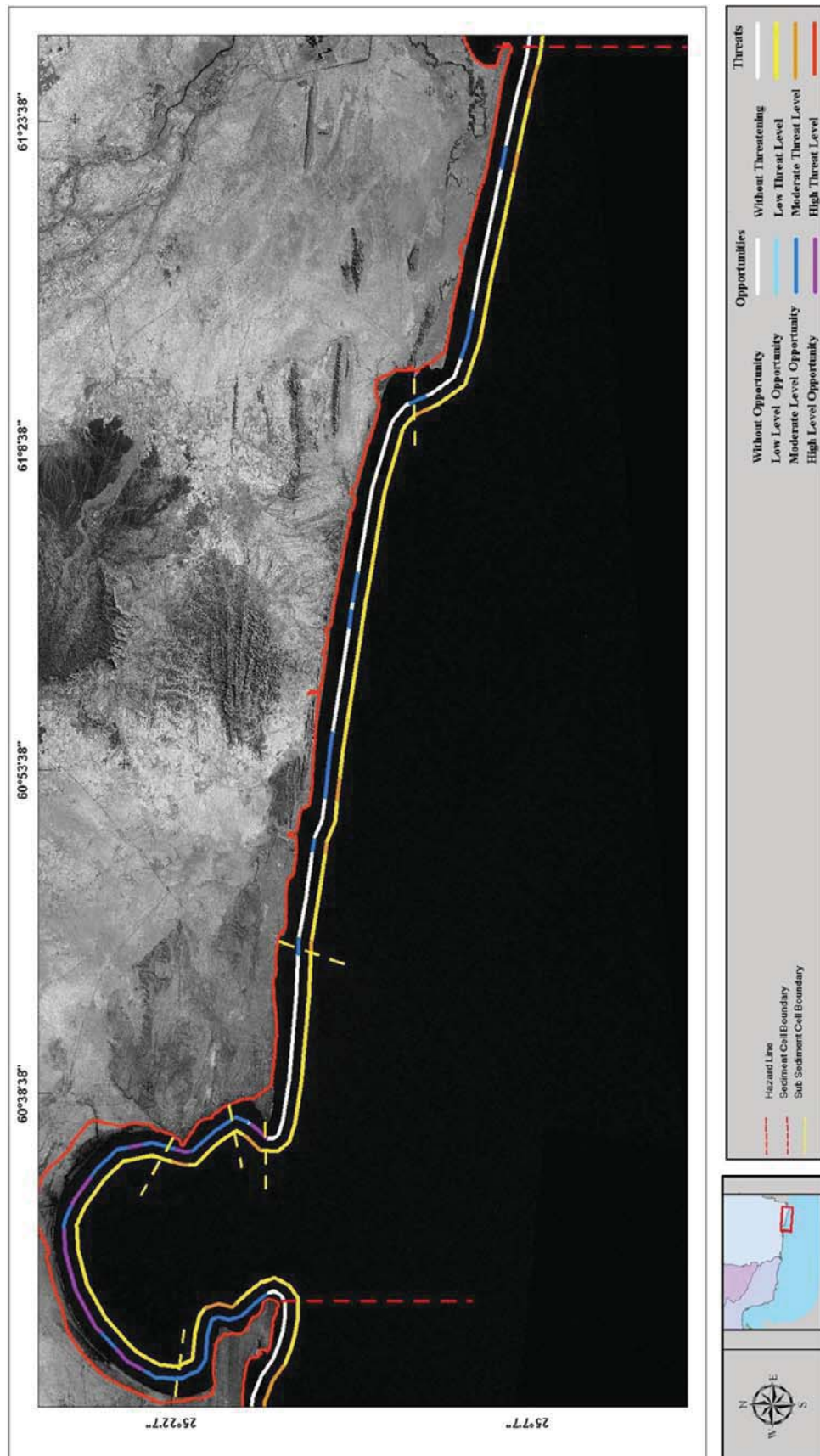


Figure 3: Opportunities and threats for industrial development in Cell 12

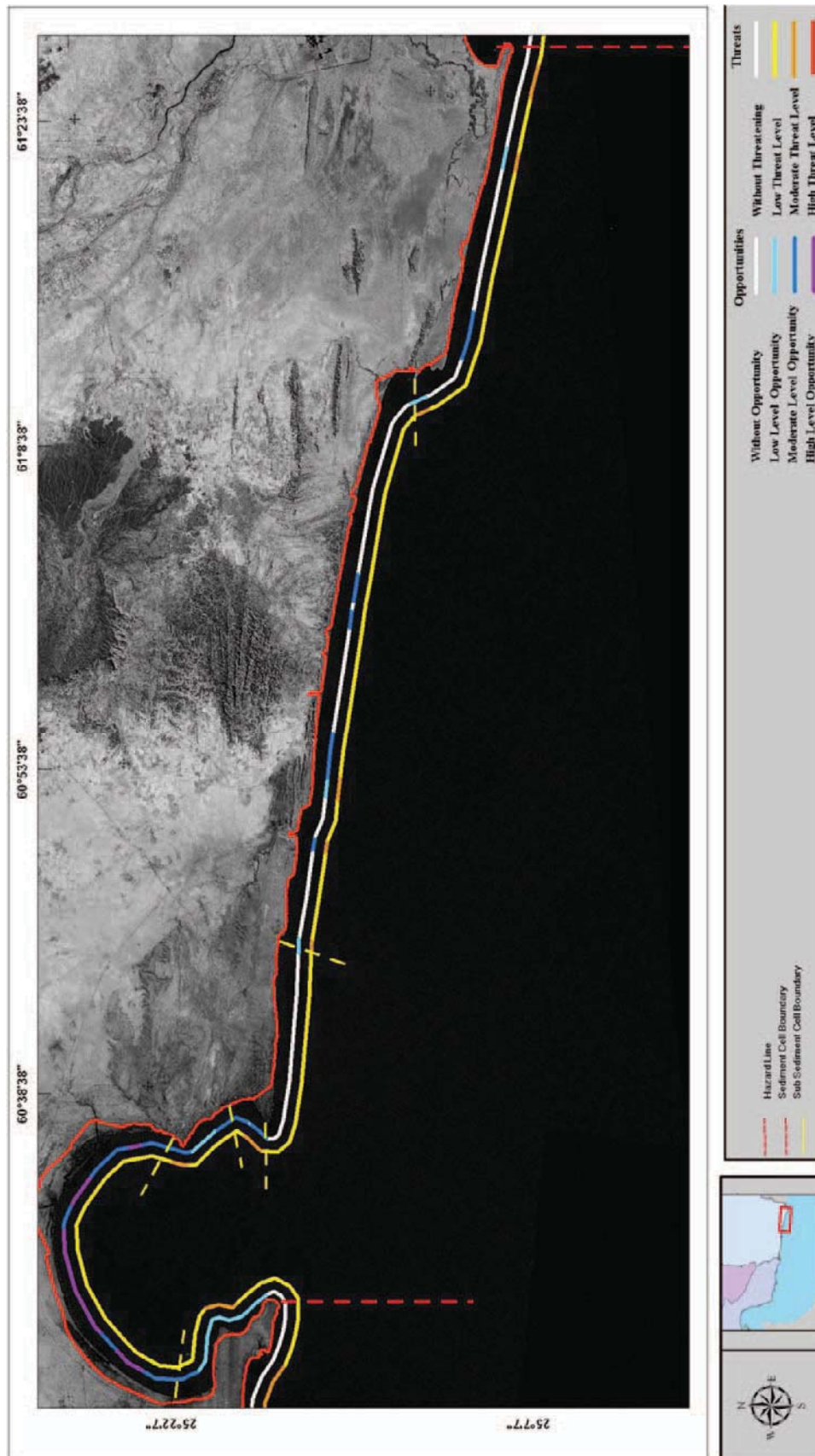


Figure 4: Opportunities and threats for commercial development in Cell 12

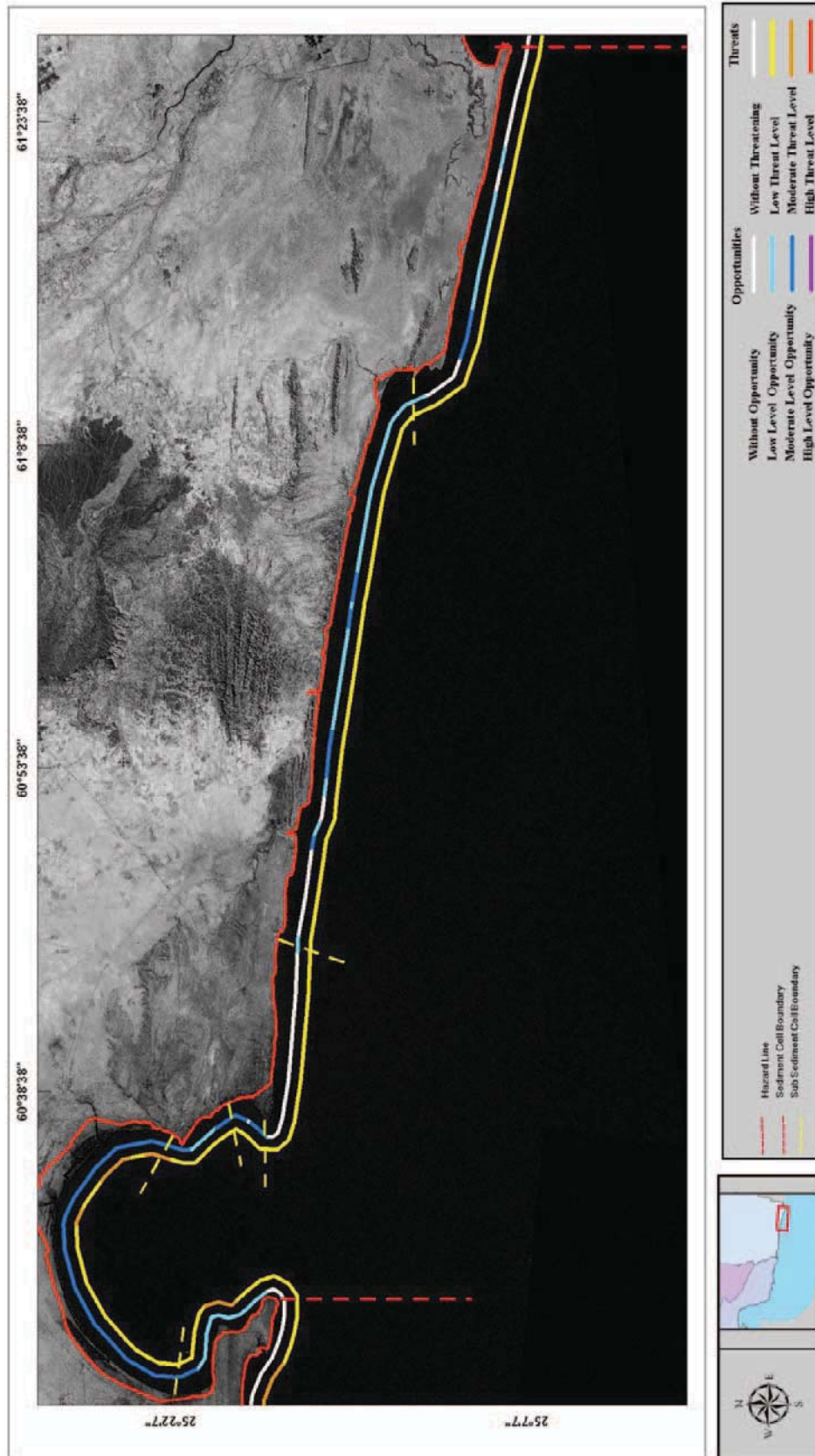


Figure 5: Opportunities and threats for tourism development in Cell 12

2 Conclusion

It can be seen that the level of threats along Cell 12 is generally low with occasional medium threat areas. The main threat in the area is from tsunamis. The threat seen on the northeast corner of Chabahar Bay is from erosion as this part of the bay has been suffering from natural beach erosion.

The Oman Sea coast of cell 12 is featured with high coastal cliffs. Opportunities along this part of Cell 12 are low to moderate mostly in areas where there is a sandy shoreline particularly for tourism. Moderate to high opportunities exist inside the Chabahar Bay because it is a rather sheltered embayment protected from the Oman Sea waves. The southeast corner of Chabahar Bay is sheltered and deep, providing a good opportunity for various port development projects.

Regarding residential development threats maps it is recommended that any residential development should be limited to beyond (landward side) of the Hazard Line. In this case, some of the threats such as storm surge will no longer be applicable.

3 References

Jahad Water and Energy Research Co. (JWERC): (2008) - Report of Second Part of Integrated Coastal Zone Management Studies (ICZM), Shoreline Management Plan (SMP) Studies, Criteria for Shoreline Management Plan Report.

Modelling of breaking wave dynamics, surf zone turbulence and wave-induced mean flows with the SPH numerical method

Christos Makris¹, Constantine Memos² and Yannis Krestenitis³

Abstract

Continuing our previously published work, plunging wave breaking over relatively mild sloping beach-type formations is investigated in this paper. Numerical modeling aspects on the matter are discussed, by pursuing comparisons against experimental data. The modern robust method Smoothed Particle Hydrodynamics is used and the recently enhanced version of the academic 'open source' code SPHysics v.2 is being validated. Spatial resolution is discerned as the most crucial factor in forming plausible results. Exquisite visual representation of the violent free-surface deformations is further upheld by coincidence of numerical and experimental results of classic and sophisticated flow characteristics, in terms of wave heights, ensemble-averaged values of hydrodynamic features, Fourier spectral analysis of turbulent velocities, vorticity patterns and wave-induced mean flows. Further need to verify the model's ability to capture the near-shore wave breaking dynamics and surf/swash zone turbulence sets the path of future research, based on extremely refined simulations with a new 'parallel' version of SPHysics.

Keywords: SPH, numerical modelling, wave breaking, plunging, spatial discretization, Smagorinsky, wave height, ensemble-average, surf zone, turbulence, Fourier spectra, vorticity, undertow, Stokes drift

1 Introduction

The evolution of near-shore waves and the consequent shaping of the surrounding hydrodynamic field have traditionally been of major concern for coastal engineers and scientists. Particularly the wave breaking, with its extremely complicated mechanisms, distinguishes among other relevant coastal processes for lack of exhaustive elucidation. The detailed description of the surf zone wave pattern, the consequent turbulent flow characteristics and the wave-induced near-shore currents demand nowadays the use of enhanced computational approaches. Following our previously published research work (Makris et al., 2009; 2010a; 2010b) on the subject, we pursue in the present paper the improvement of our investigations by incorporating newer, more elaborate versions of computational models.

The precise numerical simulation of the solely nonlinear process of plunging wave breaking on plane and relatively mild impermeable slopes, in terms of wave height, free-surface elevation and velocity field persists as the primary aim of our research effort. In addition we focus on the simulation of the wave-induced mean flows in the surf zone, namely the cross-shore return-type flow called the undertow and the shoreward mass transport flow called the Stokes drift. Several other surf and swash zone features such as the mean free-surface elevation (wave setup) and run-up on a mildly sloping beach-type profile are derived as well. Moreover a detailed description of the difficult to obtain turbulent features such as the coherent turbulent structures, the vortical recurring patterns and the power spectra of the fluctuating components of the Eulerian velocity field inside the surf and swash zones is pursued. Finally a wide range of computational simulation results, describing thoroughly the turbulent surf and swash zone features not yet approachable by classic wave models, is presently introduced. All of the above

¹ Aristotle University of Thessaloniki, Laboratory of Maritime Engineering and Maritime Works, Division of Hydraulics and Environmental Engineering, Department of Civil Engineering, Faculty of Engineering, GR-54124, Thessaloniki, Greece, cmakris@civil.auth.gr

² National Technical University of Athens, School of Civil Engineering, Laboratory of Harbour Works, Heron Polytechniou 5, GR-15780, Zografos, Athens, Greece, memos@hydro.ntua.gr

³ Aristotle University of Thessaloniki, Laboratory of Maritime Engineering and Maritime Works, Division of Hydraulics and Environmental Engineering, Department of Civil Engineering, Faculty of Engineering, GR-54124, Thessaloniki, Greece, ynkrest@civil.auth.gr

are attempted by means of one of the most ingenious modern CFD methods for the simulation of hydrodynamic free-surface flows, called Smoothed Particle Hydrodynamics (SPH), as described in detail by Monaghan (2005). Results of SPH simulations in the recent literature, albeit visually impressive, demand urgently creditable verification against circumstantial experimental data (Gómez-Gesteira et al., 2010b). Thus the calibration and the overall capability of a state-of-the-art implementation of the SPH method to predict the details of the entire wave breaking process ensues as the major goal of our research.

2 Methodology

SPH is a mesh-free particle method, implementing Lagrange-type approximation for the Navier-Stokes equations, through integral interpolation smoothing functions. Its Lagrangian particle nature allows the unhindered simulation of free-surface flows with strong deformations, such as plunging wave breaking in coastal areas, as thoroughly described by Dalrymple & Rogers (2006). The method's foundational aspect is based on the integral interpolation of any given function $A(\mathbf{r})$ (scalar or vectorial) in the computational domain and its derivatives that finally leads in discrete notation to:

$$A(\mathbf{r}) = \int A(\mathbf{r}')W(\mathbf{r}-\mathbf{r}',h)d\mathbf{r}' \Rightarrow A(\mathbf{r}) = \sum_j A_j (m_j/\rho_j)W_{ij} \quad (1)$$

with h smoothing length [m]

\mathbf{r}, \mathbf{r}' arbitrary particle point location, distance between particles respectively [m]

$W(\mathbf{r},h)$ distance varied weighting (bell-shaped) function called kernel (W_{ij} in particle notation)

m_j, ρ_j mass, density of particle j respectively [kgr, kgr/m³]

In-depth analysis of the SPH method can be found in Monaghan (2005) and crucial assumptions of the present implementation of the method can be traced in our previously published work (Makris et al., 2009) as well as in Gómez-Gesteira et al. (2010b).

2.1 SPHysics model

Proceeding further, in the ongoing framework of our former research analysis (Makris et al., 2009; 2010a;b), the recent series (launched in sectional work packages in 2010) of the academic 'open source' numerical code SPHysics v.2 (Gómez-Gesteira et al., 2010a) is used. Basic theoretical assumptions remain unmodified, yet several computational code bugs are corrected and new features are inserted in our analysis as far as numerical schemes and kernel manipulation are concerned. Particularly we hereby use a symplectic time integration algorithm and a cubic-spline kernel, presented thoroughly in Gómez-Gesteira et al. (2010a), instead of a predictor-corrector numerical scheme and a quadratic weighting function implemented previously (Makris et al., 2009). In the latter, thorough calibration of all of the model's significant parameters, namely weighting functions $W(\mathbf{r},h)$, smoothing length h , numerical schemes, time-step Δt , viscosity treatment etc, was attempted separately (see also Makris et al., 2010b). It was found that the spatial resolution Δx and the smoothing length h are most important in shaping the results. Acceptable agreement was thereby succeeded in terms of wave heights H and bore front velocities U_b , for one optimum dimensionless smoothing ratio $\Delta x/h$. Nonetheless extended refinement of the SPH particle resolution was not formerly attempted due to high computational cost and lack of robustness for solid boundary treatment in older versions of our simulation efforts. The new version of the SPHysics code and new efficient computer equipment in our laboratory allow us to simulate finer flow scales within reasonable computation times.

As far as treatment of viscosity effects is concerned, we persevere in the use of a Sub-Particle Scale (SPS) Smagorinsky type turbulence closure model incorporating a compressible fluid Favre-type averaging technique for the calculated density (Gómez-Gesteira et al., 2010a), in the likes of Large Eddy Simulation Sub-Grid Scale models used in traditional mesh-based methods. The eddy viscosity assumption (Boussinesq hypothesis) is employed, in the framework of a standard non-dynamic Smagorinsky-type model for the derivation of turbulent eddy viscosity, where the Smagorinsky coefficient C_s is kept constant throughout the computational domain.

The model is also supported by a Shepard density averaging filter to ensure smoothness of free surface depiction and physically plausible results for the description of the highly nonlinear processes of wave breaking, like plunging, overturning, splash-up and wave impact (Makris et al., 2009). Based on Fourier spectral analysis of the fluctuating turbulent component of the velocity field derived from our simulations, it was previously suggested that the aforementioned SPS model performs plausibly in simulating the effects of isotropic (inertial sub-range) turbulence, up to a frequency of $f=10\text{Hz}$ (Makris et al., 2010b). On the contrary the model behaved poorly for high power spectrum frequencies. Therefore no scaling law was evident for the small unresolved scale eddies, whose effects are supposed to be simulated by the SPS model. This was relevant to areas inside the surf zone near the free surface, where thick layers of vorticity and strong vorticity gradients are present. Throughout the rest of the water column the aforementioned model's attributes become questionable for even broader frequency band widths, namely for larger scale eddies in the flow field. In spite of that, the use of a previously proposed (Makris et al., 2010a;b) quite arduous dynamic Smagorisky-type turbulence closure model was postponed for future research, until correct calibration of the spatial resolution of the particles in the SPHysics v.2 model is completed firstly. For the latter to be fulfilled, past experience has shown that the size of the particle discretization Δx should be at least equal or smaller than the integral turbulence length scales of a real flow, whose values are extracted from experimental data.

2.2 Experimental and numerical data for comparisons

Following Makris et al. (2009), SPHysics numerical results are being compared against the experimental output data of Stansby & Feng (2005) [SF05 hereafter], which describe near-shore wave breaking and consequent turbulence transport. The geometric, hydraulic and gauge measurement attributes of the experimental setup used as input data to our numerical wave tank simulations undertaken for validation of SPHysics v.2 have been previously presented in Makris et al. (2009; 2010a,b). Further detailed descriptions can be found in SF05.

Table 1: Discrete simulation test cases based on spatial resolution Δx and other calibration factors

Test	Case	Δx (m)	Caibrated Factor	Test	Case	Δx (m)	Caibrated Factor
1	17_a	0.02	$\Delta x/h = 0.77$	7	17_xxx	0.005	$\Delta x/h = 0.77$
2	17_b7	0.02	$\Delta x/h = 0.58$	8	17_xxx2	0.006	$\Delta x/h = 0.77$
3	17_xx	0.015	$\Delta x/h = 0.77$	9	17_xxx3	0.00592	$\Delta x/h = 0.77$
4	17_x	0.01	$\Delta x/h = 0.77$	10	17_xxx3b	0.00632	$\Delta x/h = 0.77$
5	17_xb7	0.01	$\Delta x/h = 0.58$	11	17_xxx3c	0.0061	$\Delta x/h = 0.77$
6	17_xt	0.01	$t_0 = 121 \text{ sec}$ $\Delta x/h = 0.77$	12	17_xxx4	0.004	$\Delta x/h = 0.77$
				13	17_xxx5	0.003	$\Delta x/h = 0.77$

In Table 1 the Test cases employed, based on spatial/particle resolution, are shown. Numerical results according to the progressively refined discretization factors are used in convergence and sensitivity analysis presented below, in terms of inter-comparisons of wave height distributions throughout the whole computational domain including wave propagation, surf and swash zones. The dimensionless smoothing ratio $\Delta x/h$ is set to default as in our older simulations except two cases (2, 5) where a previously demonstrated optimum value is implemented (Makris et al., 2010b). In Test case 6 a large simulation recording time, involving 50 wave periods, is inserted, in order to trace stability issues about derived output data, especially for turbulent features. The values of Test cases 9-11 hinge upon our analysis above, i.e. about the SPS model's ability to represent reasonably the shear effects for unresolved scales. In SF05 the authors state that the integral turbulence length scales should be estimated to vary from 0.04 to 0.18 of the water depth from the outer to the inner surf zone respectively. Thus their values range from 5.92 to 6.32 mm and from 1.35 to 1.71 cm for the outer to the inner surf zone respectively. In Test cases 9-11 we focus on the former values, for the reason that inner surf zone integral

turbulence length scales have been resolved in past simulations. Predicted wave height and mean free-surface elevation values in that region were satisfactory in our past endeavors (Makris et al., 2010a).

3 Results and discussion

Following Makris et al. (2009; 2010a;b), various SPHysics v.2 numerical results, ranging from simple depictions of wave characteristics to more sophisticated representations of turbulent features, are compared below against the respective experimental ones of SF05.

3.1 Depiction of near-shore plunging wave breaking

In Fig.1 a streaming sequence of the instantaneous portrayals for Test 13 numerical results (fine particle resolution) is presented. The weak plunging incident reported in SF05 is astonishingly reproduced permitting fine qualitative agreement between numerical and experimental output. The plunging jet formation is initiated and afterwards overturning and impinging of the sharp water tongue upon the forward trough takes place. Consequently a rebound splash-up follows creating an accompanying free-surface bulge shoreward of the breaking surface roller. The latter constitutes the main mechanism of vorticity generation and enhancement due to turbulent production in wave breaking. Finally a turbulent bore formation is shaped and propagation of it is visually traceable up to the swash region. Colour scale refers to velocity magnitudes, whose maximum values at the propagating crest of the breaking wave are roughly 1.5 times the theoretical value of celerity in shallow water, $c_t=(g \cdot d)^{1/2}$. It is slightly higher than the experimental ones, which oddly enough correspond to those for spilling and not for plunging breakers. Referring to spatial discretization calibration, we can observe that the finer analysis certainly invokes higher quality representation of the plunging event.

In Fig.2 graphs are given of the bore front propagation and its transformation to a swashing run-up tongue near the shoreline margin. The unaccounted for discrepancy at the bottom and the coastline due to exaggerated repulsion in solid boundary conditions, depicted in Makris et al. (2009; 2010a), is now vanished. Fine particle resolution, combined with the use of the enhanced SPHysics model version, has addressed the matter, although modelling of friction effects at solid boundaries remain an open issue in SPH simulations.

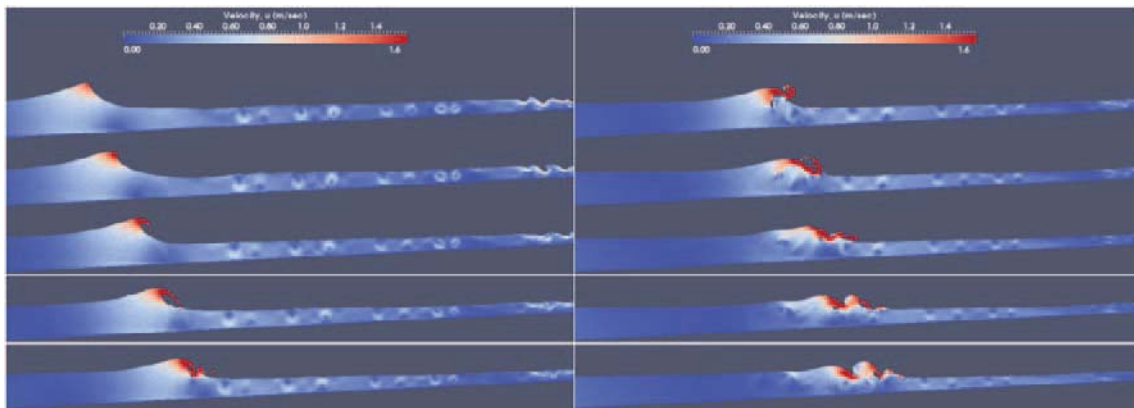


Figure 1: Consecutive captured SPHysics-Paraview output depictions of plunging wave breaking and turbulent bore formation for fine particle resolution

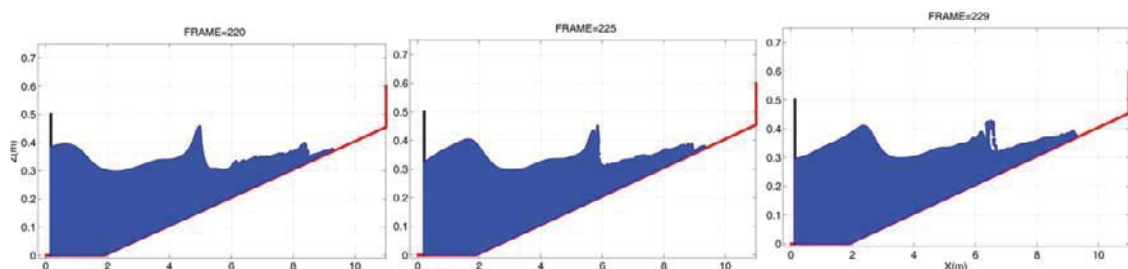


Figure 2: SPHysics-Matlab output frames for plunging wave breaking

3.2 Free-surface elevation patterns, wave height and setup

Characteristic free-surface elevation patterns for simulation Test case 13 are presented in Fig.3. Snapshots of the newly refined simulations' free-surface elevation throughout the whole computational domain appear in the upper part. They portray a sensible and stable undular form of the free surface, which appears to be smoother than the respective published in the past. Time-series of free-surface elevation at specific gauge points in crucial regions throughout the examined domain are shown in the lower part of Fig.3. For all of them the oscillation amplitude reaches a steady magnitude within 10 wave periods and that is also the case for the Test case 6, where a larger simulation recording time of 50 periods is taken into account. In Fig.4 (left) comparison of wave height and mean free-surface elevation (wave setup) for Test case 13 is shown. Agreement is reinforced compared to formerly published results, for all cases with spatial discretization equal to $\Delta x=0.01\text{m}$ and lower. This is valid for both the pre-breaking region and the whole surf/swash zone. Especially in Test case 13 the wave height in the incipient breaking region, where shear effects are intense and the SPS model used to perform poorly, is now closer to the experimental values than any other case. In other regions different resolution may excel more, based on optimum $\Delta x/h$ values. Moreover, the wave setup continues to be very well predicted by the SPPhysics v.2 model everywhere (Makris et al. 2009). Correlation coefficients, portrayed in Fig.4 (right), are of the order of 0.9 and higher, in most test cases.

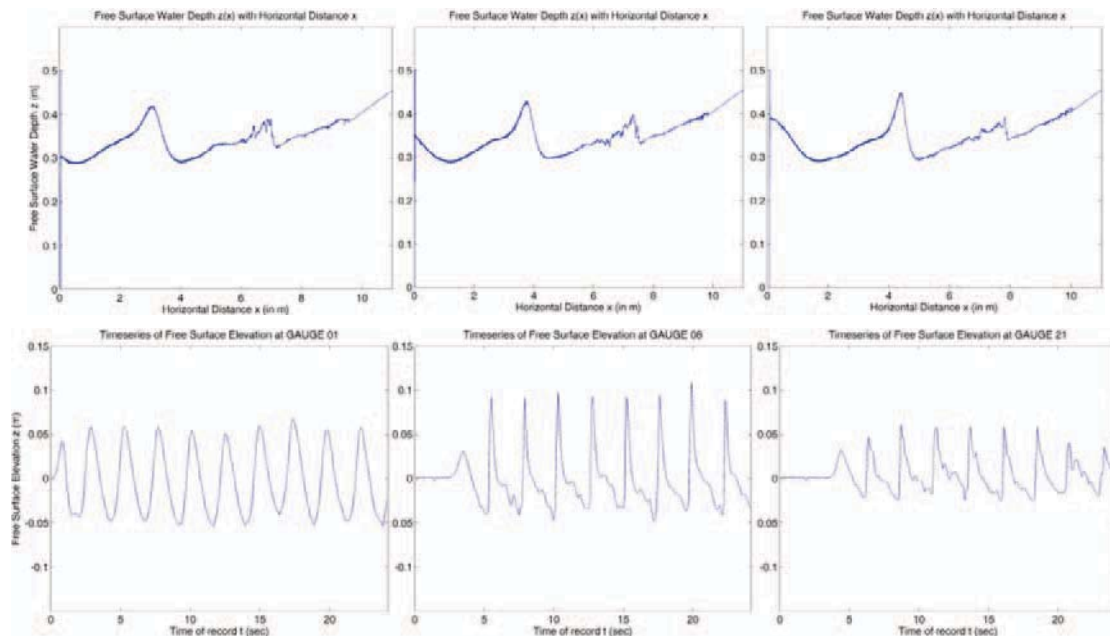


Figure 3: [Upper] SPPhysics free-surface elevation snapshots for simulation test case 13; [Lower] SPPhysics free-surface elevation time-series portrayal at specific gauges out of the surf zone [left], in the incipient breaking region [middle] and inner surf zone [right]

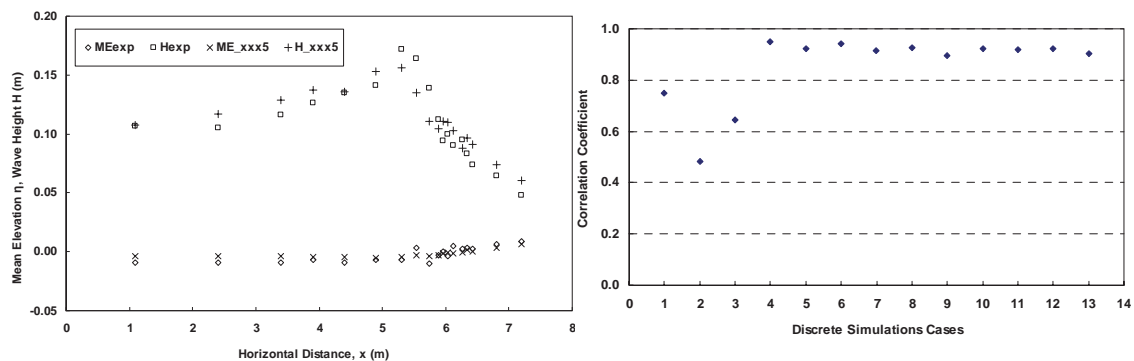


Figure 4: Wave height H and mean free-surface elevation ME distribution comparison between experiments (exp) and characteristic simulation test case 13 [left] - Correlation coefficients between experimental and simulation output for wave heights [right]

3.3 Free-surface elevation and depth-averaged velocities elaborate versions

In Fig.5 the root mean square (r.m.s.) values of the fluctuating free-surface elevation (left) and depth-averaged velocities (right) are given for Test case 12. Comparisons with the experimental respective values reveal striking coincidence (correlation coefficient 0.96) for the first and somewhat discrediting results for the second (correlation coefficient ~ 0.5). This has probably something to do with the SPH model's inherent incapability to simulate correctly boundary layer effects, due to lack of water-solid friction modelling. That produces spuriously effects for the velocity field values near the solid boundaries. This is also discussed further below, concerning undertow simulation. The ensemble-averaged (Nadaoka et al., 1989) free-surface elevation (left) and depth-averaged velocities (right), in the outer (upper) and the inner (lower) surf zone, are presented in Fig.6. Very well agreement is pursued against SF05 results even in terms of raw values of our simulations, for all Test cases. Depth-averaged velocities, in deep or shear intensified regions like the breaking point, are a mild exception, likely due to the aforementioned reasons. In shallower regions accordance criteria are met, no matter the calibration.

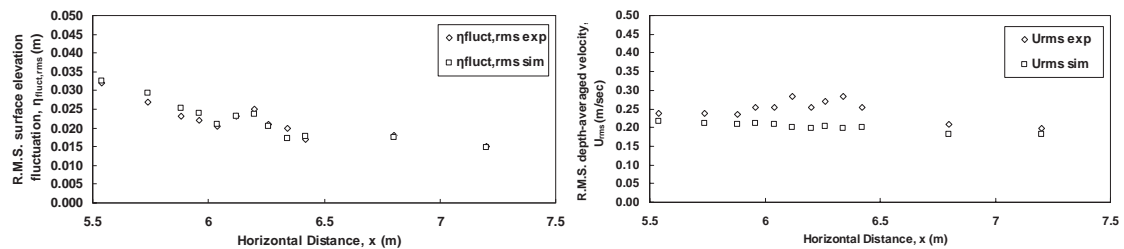


Figure 5: Comparison of experimental (square) and simulated (rhombus) r.m.s. values of free-surface elevation fluctuation [left] and depth-averaged velocities [right]

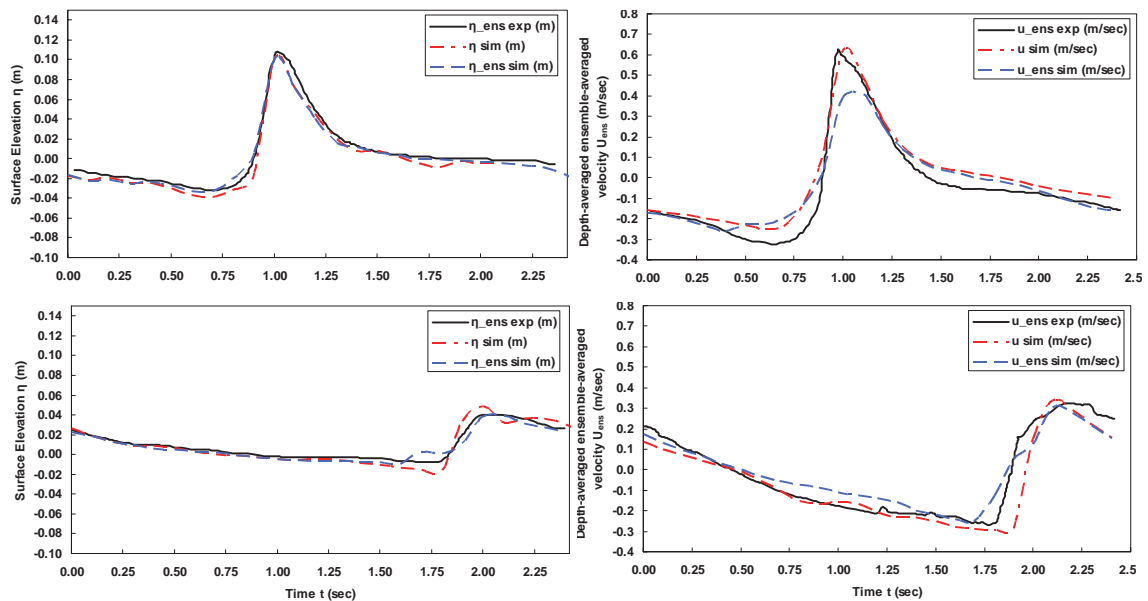


Figure 6: Comparisons of SF05 derived output data (full line) against simulation ones for ensemble-averaged (dashed line) and real-time (dash-dotted line) values of free-surface elevation [left] and depth-averaged velocities [right] at specific gauges in the incipient breaking region [upper] and the inner surf zone [lower]

3.4 Turbulent flow features (velocity Fourier power spectra - vorticity patterns)

The horizontal and vertical turbulent (fluctuating component) velocity Fourier spectra, derived by the simulated velocity field of Test case 6, at the incipient breaking region and still surface level are presented in Fig.7. Gradients of approximately $-5/3$ (on the log/log scale), typical of isotropic (inertial sub-range) turbulence, and -3 , typical of two-dimensional frozen turbulence, are sketched on the graphs (SF05). Improvement of results is evident, compared to Makris et al. (2010b), since the computed velocity power spectrum trend tails closely the $-5/3$ gradient up to high frequencies, that correspond to SPS-treated small scale eddies. Refined resolution and

sufficient recording times contribute to this improvement. Despite that, the background gradient close to -3 still eludes even from our present analysis of enhanced resolution. The above only occur at still water level throughout the entire surf zone region. At mid-depth the statistically isotropic turbulence defining scaling law is concealed for nearly all frequency bands. In Fig.8 vortical periodic flow structures are shown in a two-dimensional vertical plane, from large-scale down to small-scale eddies. Coherent multiple vortical structures were evident during breaking, becoming elongated along the surface during bore propagation just as reported in SF05. A thick layer of positive vorticity from the free surface to trough level is apparent while a thin layer of counter-rotative vorticity prevails near the bed just as in SF05. At the end of the plunging region and following the bore, there were also concentrated regions of mean-valued vorticity. Simultaneously, persisting elongated structures of negative vorticity are observed at the toe of the roller, initially similar to a mixing layer. These coherent turbulent structures generated there together with multiple horizontal vortices shoreward of the crest were also clearly reported by SF05. The intense obliquely descending eddies (Nadaoka et al., 1989) seaward of the plunging wave crest cannot be identified yet, due to lack of three-dimensional effects. Preliminary respective results seem promising in future depicting of this kind of structures.

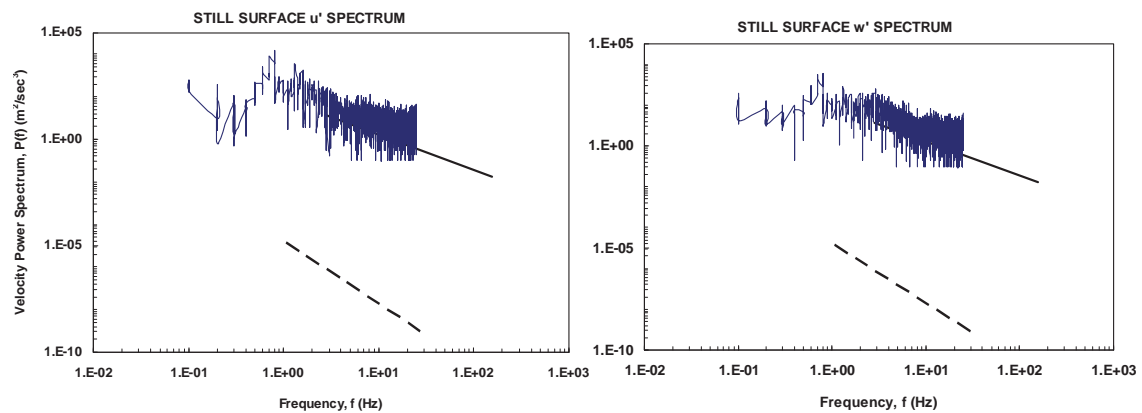


Figure 7: Fourier spectra of simulated horizontal [left] and vertical [right] turbulent velocity components for the incipient wave breaking region (Gauge 8) and large recording time (Test 6) at still-surface level. The $-5/3$ (full line) and -3 (dashed line) log-log gradients are also shown. Ensemble-averaging Nyquist filter is set to 25 Hz.

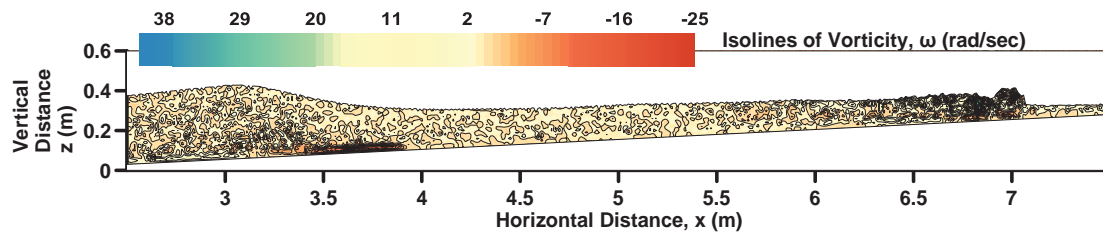


Figure 8: Simulated SPHysics vorticity field under plunging breaking waves and respective coherent structures and patterns of large-scale eddies

3.5 Wave-induced mean flows (Undertow and Stokes drift)

Period-averaged kinematics for the whole computational domain was also obtained (Test case 12 in Fig.9) showing shoreward mass transport above trough level (Stokes drift) and undertow below. Even the shoreward inversion of the undertow near the bed is well predicted. In general the vertically distributed time-averaged velocity follows a somewhat plausible trend, yet its depth-averaged value shows a questionable overall net shoreward propensity, where naught balance should exist. Non-linearity of propagating and breaking waves is also plausibly depicted, if the positioning of the setup level compared to the crest and trough envelopes is carefully observed (Fig.9), yet the undertow, although predicted, seems underestimated, as noted above. On the other hand, the Stokes drift is intensified in the breaking region causing considerable increase in momentum and mass transport and thus dramatic degradation of the crest envelope and consequent decrease in wave height, as deduced firstly by Nadaoka et al. (1989) and SF05.

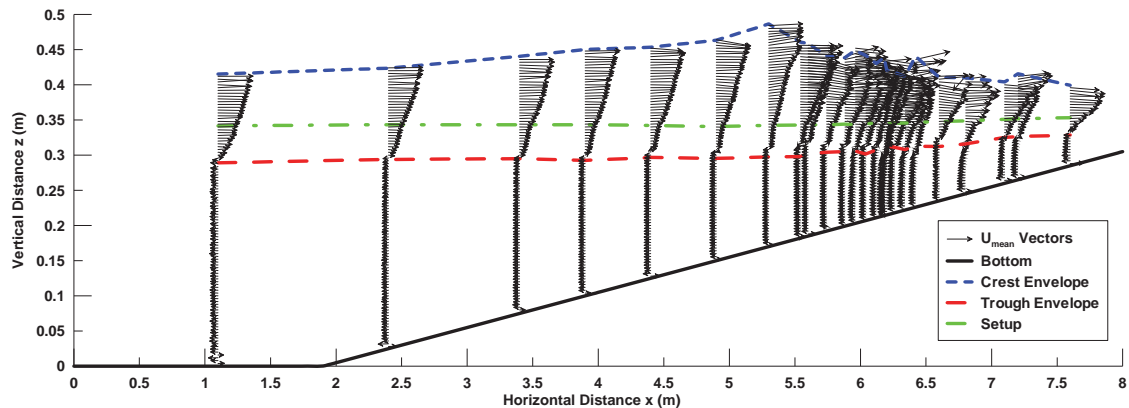


Figure 9: Time-averaged vertical distribution of velocity vectors at various gauges covering the whole computational field, clearly discriminating the lower (undertow) and upper (Stokes's drift) wave-induced mean flow regions defined by wave crest (small dashed line), trough (large dashed line) and wave setup (dash-dotted line) envelopes

4 Conclusions

The recently brought out SPHysics v.2 model combined with refined resolution calibration is put to the test against the experimental data of SF05. Following several past efforts with lean results, very good agreement was finally achieved for various simple and more sophisticated features concerning the hydrodynamics of plunging wave breaking, consequent surf zone turbulence and wave-induced mean flows. Spatial resolution turns out to be the most significant factor in forming plausible results for SPH simulations. An effort to bend the extremely time-consuming computations, moving towards 1~2 million particles, with the use of a new 'parallel' version of the SPHysics code is set as a future research goal.

5 References

- Dalrymple R. A.; Rogers B. D. (2006): Numerical modeling of water waves with the SPH method. In: Coastal Engineering, Vol. 53, pp. 141-147. ISSN 0378-3839.
- Gómez-Gesteira M.; Rogers B. D.; Dalrymple R. A.; Crespo A. J. C.; Narayanaswamy M. (2010a): User Guide for the SPHysics Code v2.0. <http://wiki.manchester.ac.uk/sphysics>.
- Gómez-Gesteira M.; Rogers B. D.; Dalrymple R. A.; Crespo A. J. C. (2010b): State-of-the-art of classical SPH for free-surface flows. In: Journal of Hydraulic Research, Vol. 48, Extra Issue, pp. 6–27. doi:10.3826/jhr.2010.0012.
- Makris C. V.; Memos C. D.; Krestenitis Y. N. (2009): Numerical simulation of near-shore wave breaking using SPH method, in: Proceedings of the 4th SCACR, – Int. Short Conference on Applied Coastal Research. ISBN 978-3-00-030141-4. Barcelona, Spain.
- Makris C. V.; Krestenitis Y. N.; Memos C. D. (2010a): SPH Numerical Simulation of Surf Zone Characteristics, in: Proceedings of 6th ISEH - International Symposium on Environmental Hydraulics, Vol. 1, pp. 445-450. ISBN 978-0-415-59545-2. Athens, Greece.
- Makris C. V.; Krestenitis Y. N.; Memos C. D. (2010b): SPHysics code validation against a near-shore wave breaking experiment, in: Proceedings of 5th SPHERIC - International SPH European Research Interest Community Workshop, pp. 245-252. Manchester, UK.
- Monaghan, J. J. (2005): Smoothed particle hydrodynamics. In: Rep. Prog. Phys., Vol. 68, pp. 1703-1759. ISSN 0034-4885.
- Nadaoka K.; Hino M.; Koyano Y. (1989): Structure of the turbulent flow field under breaking waves in the surf zone. In: J. Fluid Mech., 204, pp. 359-387.
- Stansby P. K.; Feng T. (2005): Kinematics and depth-integrated terms in surf zone waves from laboratory measurement. In: J. Fluid Mech., Vol. 529, pp. 279-310. doi: 10.1017/S0022112005003599

Impact of the dredging process on the granulometry of a shelly sand. Case study of TAPARURA project, Sfax, Tunisia

Samir Medhioub¹, Abir Baklouti² and Chokri Yaich³

Abstract

This article aims to shed some light on the particular aspect of the change of the mean size distribution of a shelly sand after undergoing a dredging process. We are concerned with the particular sand extracted from a marine borrow site and used to fill the 420 ha reclaimed area along the northern coast of the city of Sfax, Tunisia. The sand grains are in fact shell fragments of very different sizes and have therefore a carbon content higher than 99%. The use of this type of sand for land reclamation is uncommon and its behavior with respect to dredging is yet little known.

Our results show an overall increase of the mean grain size after the dredging and the hydraulic fill operations. It is also found out that the length of the inland pumping pipeline has an impact on the mean sand size.

Keywords: Shelly sand, mean sand size distribution, borrow site, dredging, hopper, hydraulic fill

1 Context of the study

The northern coastline of the Sfax, Tunisia's second city, starting from the commercial harbor up to the "oued Ezzit" (Fig. 1.), is one of the most industrialized coastal zones in Tunisia. This coastline was substantially hit by pollution which led to a serious degradation of its marine ecosystem. During the last decade, decision makers and developers were interested to reconcile this important area with its natural environment. Their efforts were rewarded by the launching of TAPARURA project with the main objective to remove the accumulated pollution over a distance of 6 km along the coastline and the reclamation of a new area of 420 ha.

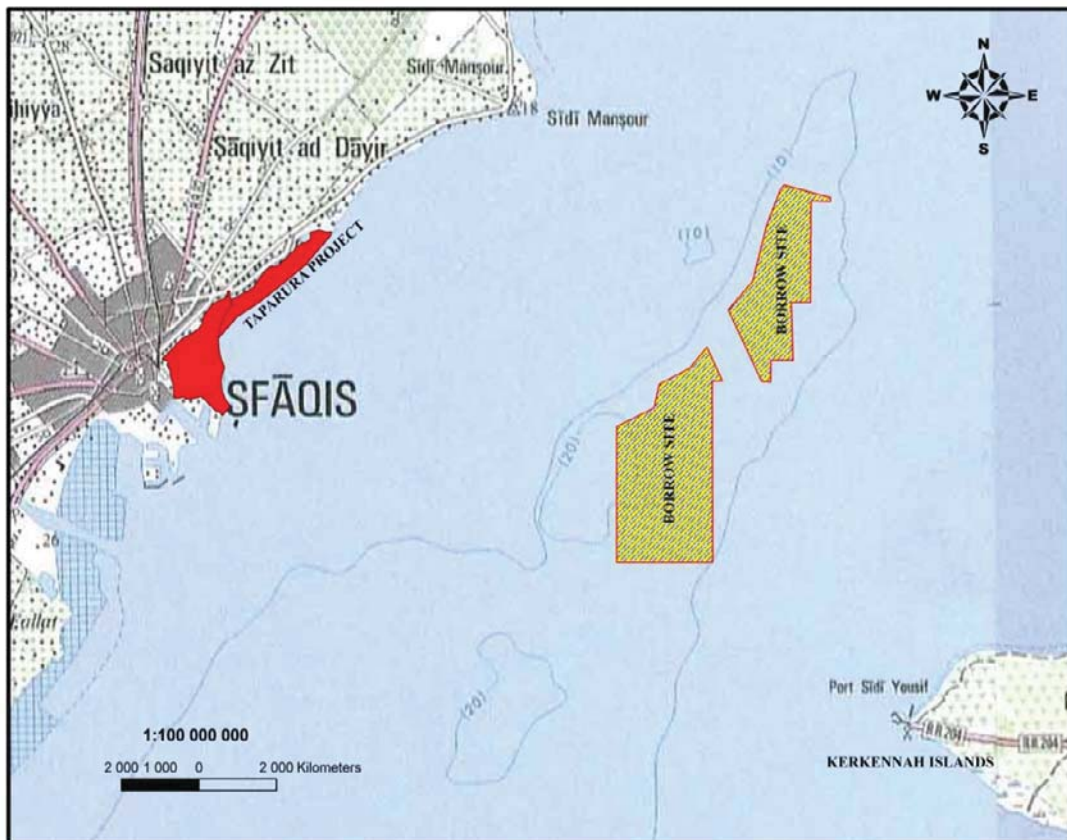
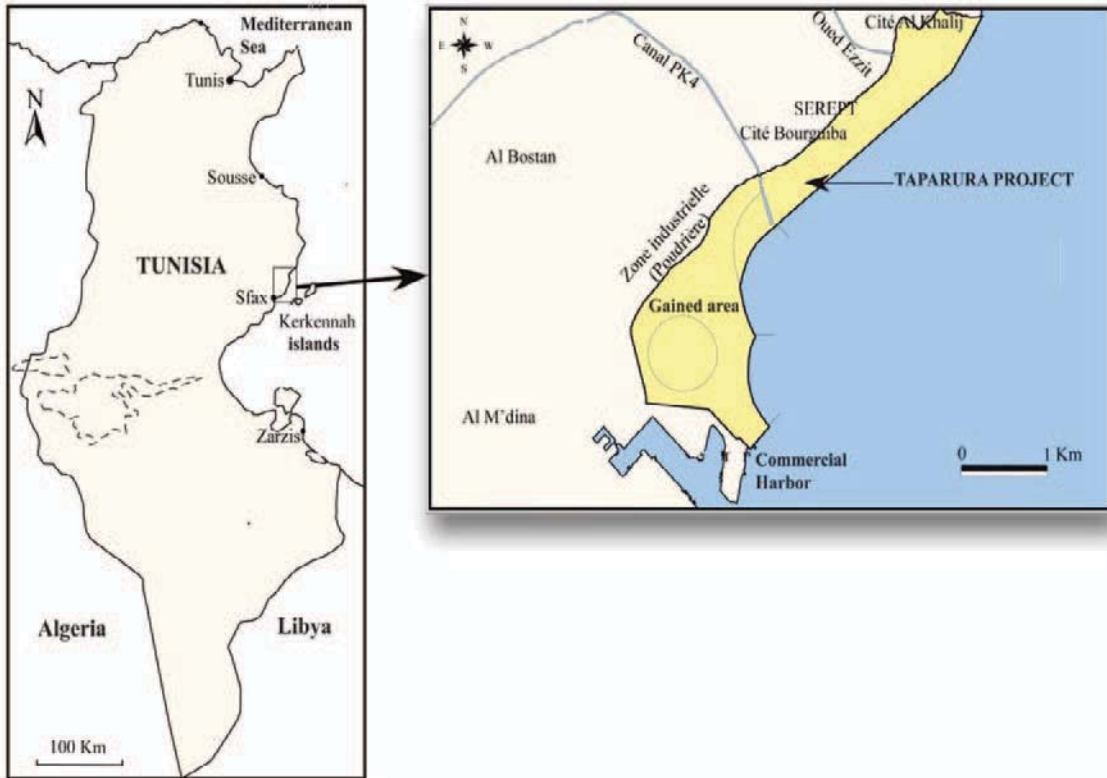
The material used for the land reclamation is a shelly sand material dredged from an offshore borrow site located at Kerkennah channel shown on the map in Fig. 2. This sand was tested by the engineering firms SCET-Tunisie and NEDECO in 1994 in the laboratories of Delft Hydraulics in The Netherlands in order to determine the change of the grain size characteristics after passing through a pumping system. In fact, it was necessary to know to which extent the shelly sand grains break up after undergoing the whole dredging process. This would allow the prediction of the actual grain size (D50) of the final fill material which in turn is used to compute the long-shore sediment transport of the northern coastline.

At that time, the conducted tests confirmed the influence of the pumping operations and a clear wear of the particles was noticed. The global particles reduction was then estimated at around 35%. This value was considered by SCET-Tunisie and NEDECO to be overestimated and the final adopted value for the grain size reduction was assumed to be 10% only. Our present study takes the opportunity of the ongoing project and the possibility to collect some realistic data at the different stages of the dredging process in order to check the consistency of this assumption.

¹ High institute of technological studies of Sfax, PTT Chihia, BP46, 3041 Sfax, Tunisia, samir.medhioub@gnet.tn

² National Engineering School of Sfax, Route de la Soukra km 4, 3038 Sfax, Tunisia, abboura.baklouti@gmail.com

³ National Engineering School of Sfax, Route de la Soukra km 4, 3038 Sfax, Tunisia, chokri.yaich@enis.rnu.tn



2 Description of the shelly sand, the dredging method and the sediment sampling campaigns

2.1 Shelly sand characterization

The shelly sand has grayish color and often contains some entire shells as shown in the photographs of Fig. 3. It has a flattened texture and is composed essentially by calcified seaweeds. Our microscopic investigation of some sand samples led to the following composition: Ulvophyceae 58%, shell pieces 23%, Bryosoa 8%, Rhodophyceae 5%, Foraminifera 3%, Echinidae 2% and Ostracoda 1%.



Figure 3: Photographs illustrating the shelly sand composition and the variety of entire shells pumped with the sand

The mechanical and other characteristics of the sand grains are shown in table 1. All these characteristics are measured according to the AFNOR standard tests. The mean sand size distribution is determined using the granular spindle method (André, 1977).

Table 1: Photographs illustrating the shelly sand composition and the variety of entire shells pumped with the sand.

Sand equivalent	Organic matter	Dry density	Relative density	Carbon content (CaCO ₃)
90%	0.48%	2.71	1.20	99%

2.2 Sediment sampling campaigns

We carried out three sediment sampling campaigns on the 6th, 11th and 13th March 2008. Table 2 shows for each campaign the number of sediment samples taken together with the corresponding depths. In the hopper of the dredger, samples were taken at the moment where the dredger comes alongside and starts pumping sand. Samples were generally taken according to the systematic grid sketched in Fig. 4. using a simple perch every meter and over a depth of 3 m, which corresponds to approximately the half of the hopper. In the fill area, sediments samples were also taken according to a regular grid at the surface and at a depth of 50 cm as shown in Fig. 5.

Table 2: Details of the sediment sampling campaigns

Campaign	Date	Location	Number of samples	Depth of sampling (m)	Represented area (m ²)
Campaign 1	06/03/2008	Dredger	20	0 ; 1 ; 2 ; 3	-
		On site	10	0	2600
Campaign 2	11/03/2008	Dredger	10	0 ; 1 ; 2 ; 3	-
		On site	20	0 ; 0.50	1200
Campaign 3	13/03/2008	Dredger	20	0 ; 1 ; 2 ; 3	-
		On site	20	0 ; 0.50	1300

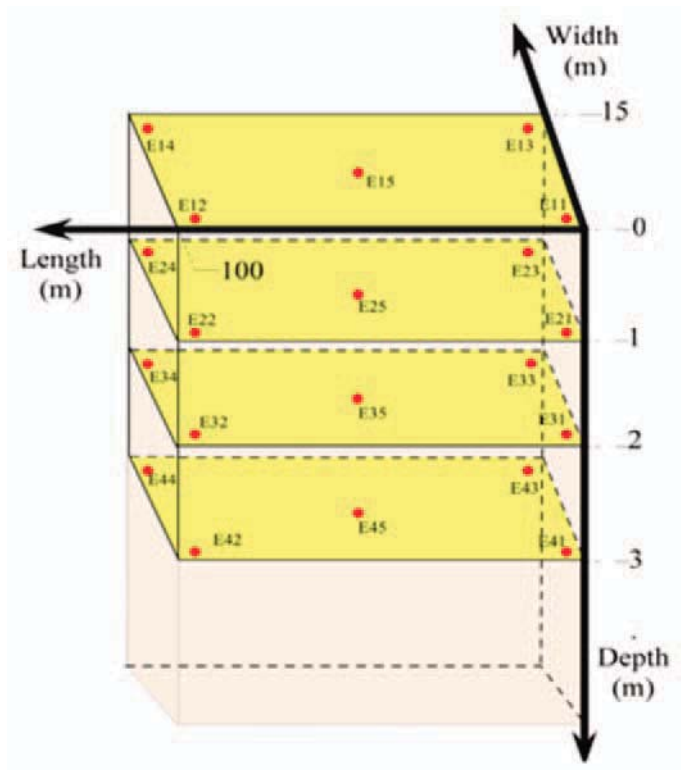


Figure 4: Systematic sediment sampling in the hopper of the dredger

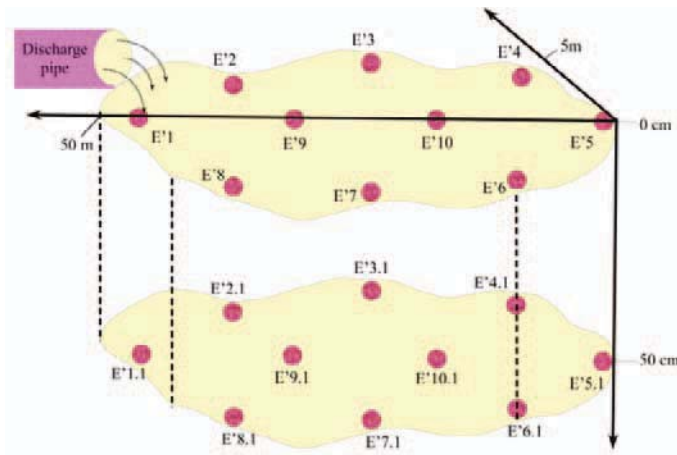


Figure 5: Systematic sediment sampling at the reclamation site

At the marine borrow site of Canal Kerkennah, an investigation was carried out by the consortium of contractors JES in charge of the execution of the Taparura project (2006-2009). One hundred cores were taken by a diver over a depth of 2.50 m. The cores were taken by piston sampling which is a modified vibrocore system. The ERC (Environment Research Center) in Belgium carried out the particle size distribution (PSD) analysis on samples taken at every 50 cm of each core. In total 485 sieve analysis were made available. In order to fulfill the contract specifications with respect to the quality of sediments (less than 15% by weight is smaller than 0.064mm), an optimal exploitation scheme of the borrow site was determined. One of the conditions imposed by the environmental local authorities was to limit the dredging to the 1.5 m thick layer (JES, 2006).

Among the whole set of the available sieve analysis, only 41 were considered in our study. These were chosen in such a way that the location of the corresponding samples coincides with the dredger tracks of the three campaigns shown in Fig. 6.

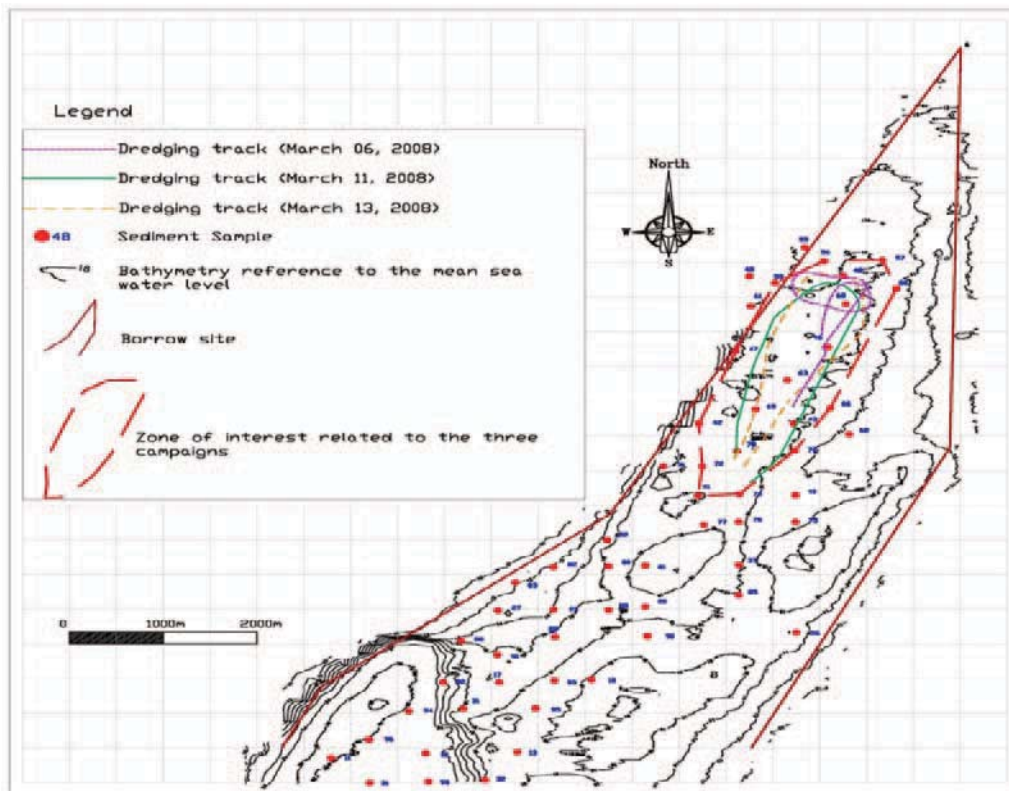


Figure 6: Dredging tracks at the borrow site

2.3 Short description of the adopted dredging method

The dredging operation consists of repeated elementary cycles (CUR,1987). The cycle starts with the dredger heading towards to the borrow site. The navigated distance will be different for each cycle but generally is in the order of 11 to 14 miles. Once approaching the dredging zone, the dredger reduces its speed and begins the trailed suction operation at the seabed using his drag head. The mixture of around 40% sand and 60% water is pumped into the dredger well. According to the dredger operators, this relatively high ratio is due to the shelly nature of the sand. The dredged material settles down in the hopper due to gravity forces and the excess of cloudy water is returned back to sea through an adjustable overflow. This operation continues until reaching the full 9000 m³ capacity of the hopper.

Once the hopper filled, the dredger navigates towards to the commercial harbor of Sfax. As soon as the coupling with floating pipe was done, the unloading operation starts. Sea water is pumped into the hopper and gradually mixed by the sand stored therein. The created mixture is then pumped with a rate flow of around 20 000 m³/h towards its final destination in the open fill area through a combination of floating and onshore 800 mm diameter pipes. The final reshape of the fill is achieved using the proper equipments (see Fig. 7.).



Figure 7: Photos of the dredger and the ongoing hydraulic fill

3 Behavior of the shelly sand: Results and discussion

3.1 Mean sand size distribution in the borrow site, in the dredger and on site

The Standard according to which the PSD analyses was carried out is the AFNOR NF P94-041 related to dry sieving. For each campaign, the mean sand size distribution is determined by the granular spindle (GS) method. It is limited by curves of the maximum and minimum percent passing of a several samples called respectively the fine limit and the coarse limit of the spindle (André, 1967). The curve of the mean sand size distribution passes by the average of the finest value and the coarsest value of each sieve size.

Table 3, gives the computed statistical parameters (CEM, 2003) characterizing the mean sand size distribution in the borrow site, in the hopper dredger and in the reclamation site. A few remarkable conclusions can be drawn from the obtained results. In the three locations (borrow

site, the hopper dredger and on site), the material appears to be a coarse sand, very well sorted and very coarse skewed. The superposition of the curves of the mean sand size distribution from the granular spindle method for the three campaign's (see Fig. 8 to Fig.10.) shows an overall increase of the sand grain size during its journey from the borrow site to reclamation site through the dredger. At the same time, it shows a reduction of the finer particles percentage against an increase of the coarser particles percentage. In particular and as shown in table 4, the mean sand size D50 at the site reclamation went up to around 86% against 262% for the D90 compared to their initial values at the borrow site.

Table 3: Statistical parameters of the shelly sand resulting from the mean sand size distribution of sediment samples in the borrow site, the hopper and the reclamation site

Location	Campaign	Mean D50 (mm)	Std. deviation	Skew-ness	% finer	% coarser
Borrow site	JES	0.55	-2.12	-1.23	4.0	79
Dredger	1	0.75	-0.99	-1.81	1.0	95
	2	0.57	-0.95	-1.65	0.5	90
	3	0.96	-1.17	-1.82	0.3	92
On site	1	0.81	-0.97	-1.99	0.2	95
	2	1.27	-1.04	-2.28	0.1	97
	3	1	-1.02	-2.07	0.4	93

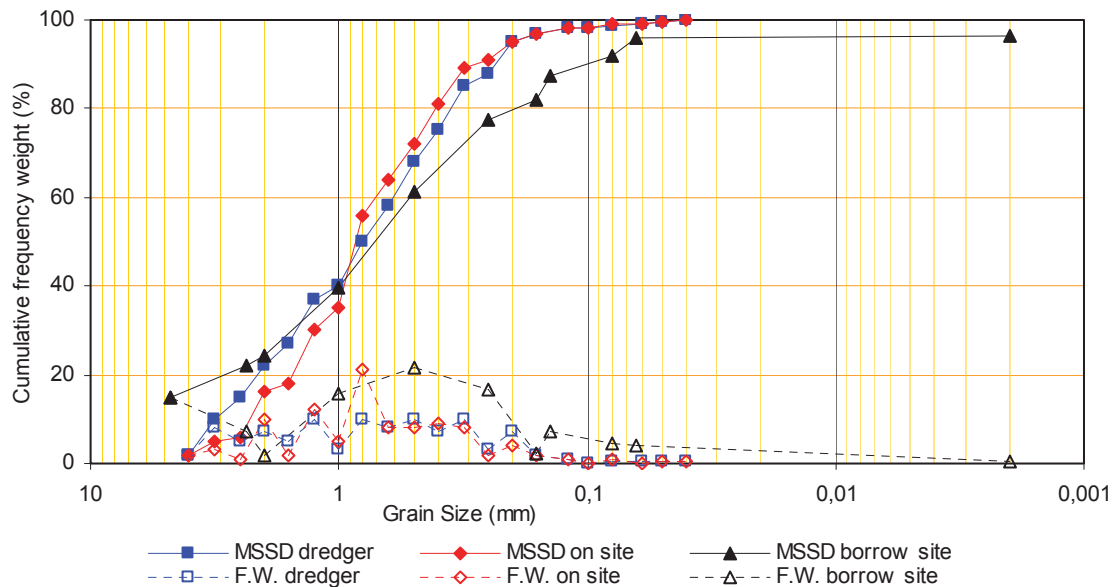


Figure 8: Mean Sand Size Distribution of campaign 1

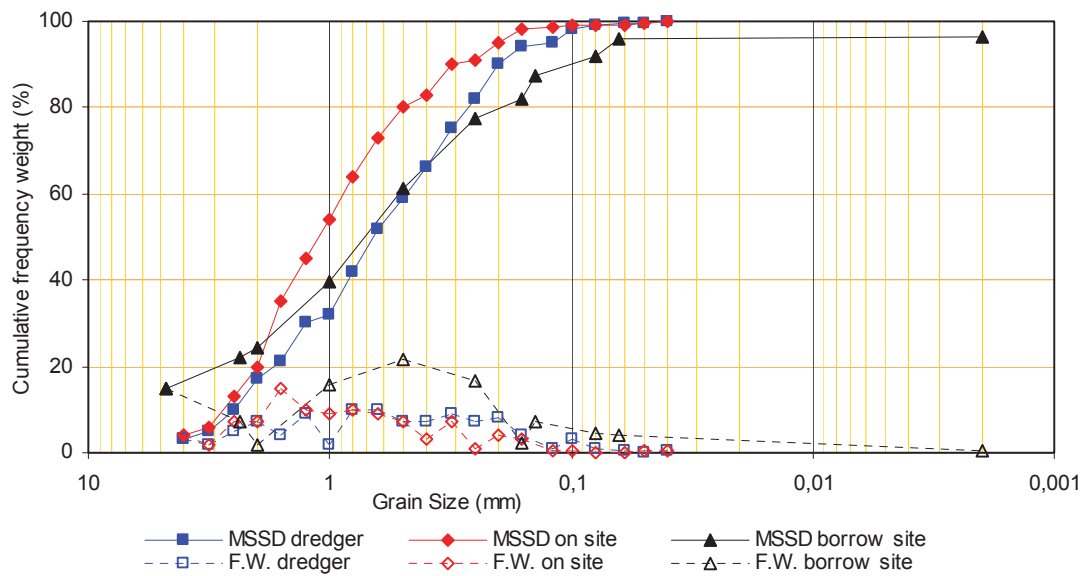


Figure 9: Mean Sand Size Distribution of campaign 2

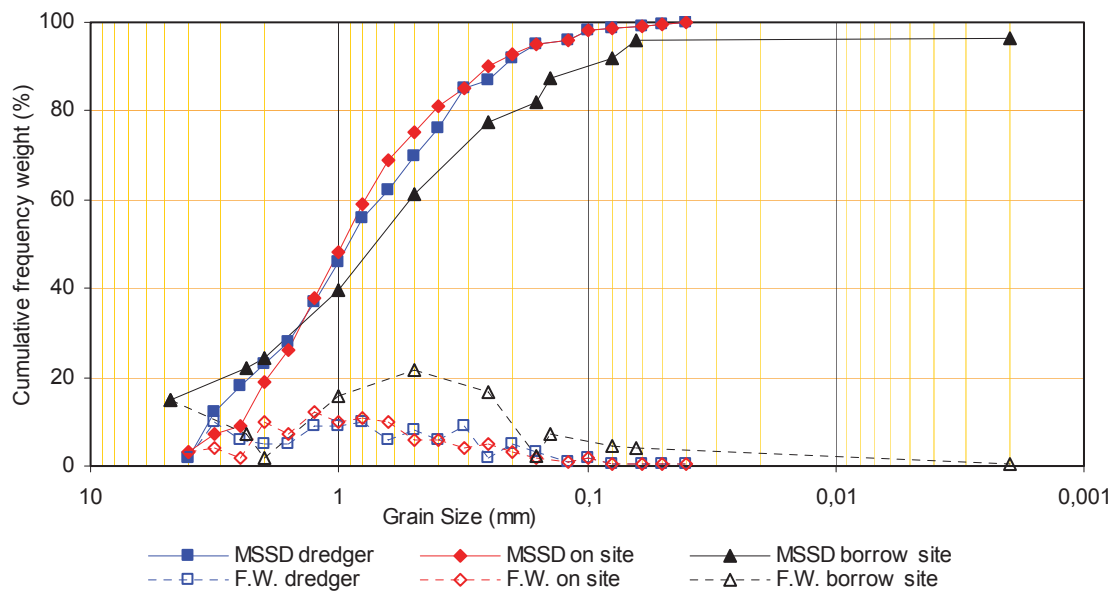


Figure 10: Mean Sand Size Distribution of campaign 3

These figures can be explained by the loss of fine particles which returned to sea through the dredger overflow and during pumping the water-sand mixture at the reclamation site. The reduction of around 40% of the finer sand size D10 can be explained by the effect of turbulent journey of the sand particles through the powerful pumps and other equipments of the dredger.

Table 4: For each of the three campaigns and for each of the three grain sizes, this table shows the ratios between cumulative frequency weights for each two different locations. Locations are taken two by two (Hopper/Borrow site, Reclamation site/Hopper and Reclamation site/Borrow site)

Ratio	Hopper / Borrow site			Reclamation site / Hopper			Reclamation site / Borrow site			Pumping distance (m)
	D10	D50	D90	D10	D50	D90	D10	D50	D90	
Campaign 1	0.63	1.36	2.50	0.63	1.08	1.55	0.40	1.48	3.87	1500
Campaign 2	0.50	1.04	2.50	1.00	2.22	1.55	0.50	2.30	3.87	500
Campaign 3	0.62	1.75	2.50	0.77	1.03	1.25	0.48	1.81	3.12	700
Average ratio	0.58	1.38	2.50	0.80	1.44	1.45	0.46	1.86	3.62	-

3.2 Influence of the length of the pumping pipeline on the evolution of the mean sand size D50

The result of our study shows that the pumping distance affects the mean sand size of the shelly sand. In fact, the superposition of the mean sand size distribution of the sand samples taken at the reclamation site during the three campaigns shows that compared to their homogenous behaviour in the hopper shown in Fig. 11, the mean sand size decreases when the pumping distance is increased as shown in Fig. 12. This can be simply explained by the fact that sand particles are subject to the breaking up process during a longer period of time in longer pipes.

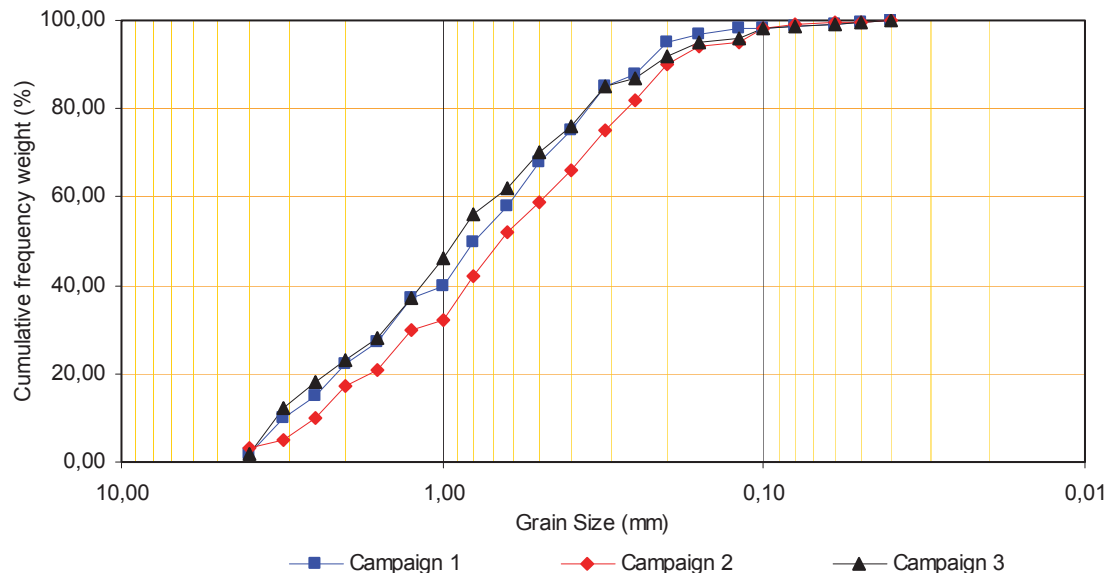


Figure 11: Mean sand size distribution of the three campaigns in the hopper

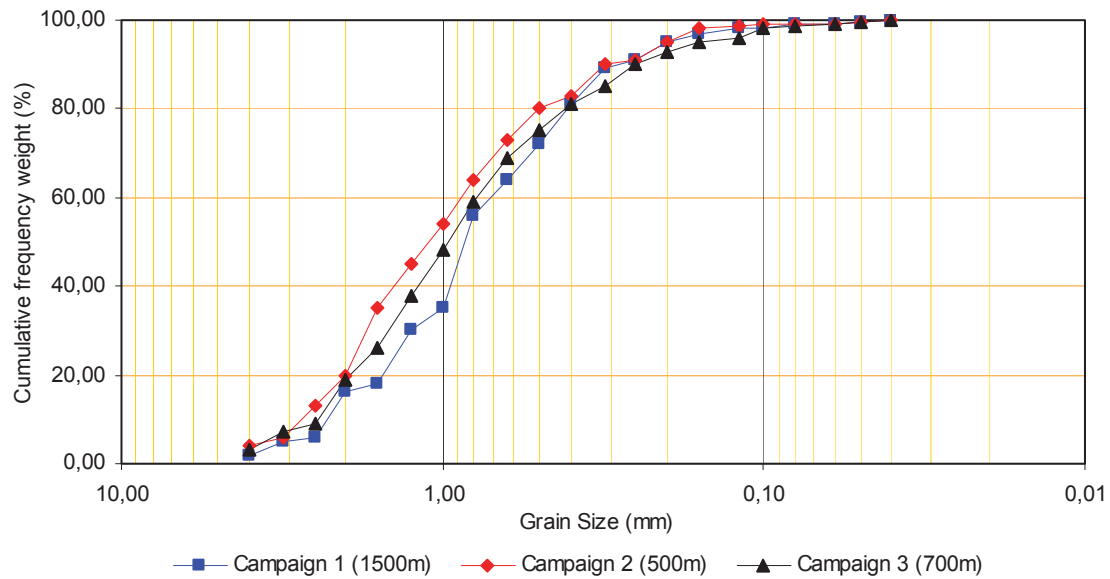


Figure 12: Mean sand size distribution of the three campaigns on site

4 Conclusion

In the present work we show that the mean sand size distribution has tendency to increase after undergoing the successive dredging processes in the dredger and at the discharging point. This is due to the fact that some quantities of the fine sand particles are released back in the sea. The release of fines takes place either in the borrow site through the overflow of the dredger or in the reclamation site carried by the pumped water along its way back to the sea.

It is also highlighted in this study that when the pumping distance on-site gets longer, the mean shelly sand size gets less coarse.

5 Acknowledgements

This work is undertaken as part of a research project funded by the SEACNVS (Société des Etudes et de l'Aménagement des Côtes Nord de la Ville de Sfax) in cooperation with ENIS (National Engineering School of Sfax). Helpful contributions have been supplied by the TAPARURA project works contractor JDN, the researchers of the DSE laboratory and the executive team of the SEACNVS. Their help is gratefully acknowledged.

The authors would also like to acknowledge the review of Prof. Enzo Pranzini and his valuable comments..

6 References

6.1 Book

- André, V. (1967). Manuel de sédimentologie. Edition Technip,- Paris.
- André, R.(1977). Méthodes granulométriques ; techniques et interprétations. Masson.
- AFNOR (Norme française sol: reconnaissance et essais), 2000. NFP 94- 041: Sols: reconnaissance et essais - Identification granulométrique - Méthode de tamisage par voie humide, AFNOR, Vol.1.
- CEM, (2003). Coastal Engineering Manual, U.S. Army Engineer Research and Development Centre, Coastal and Hydraulics Laboratory, Vicksburg, MS.
- CUR (Centre of civil Engineering Research , codes and specifications) (1987). Report 130: Manual on Artificial Beach Nourishment., Rijkswaterstaat & Delft Hydraulics, The Netherlands.

6.2 Document Not Published

JES (Consortium Jan De Nul & Envisan & Somatra) (2006). Report « Recherches géotechniques additionnelles dans la zone d'emprunt du Canal Kerkennah »,

SCET-Tunisie & NEDECO (1994),. 'Etudes d'avant-projet détaillé et élaboration du DAO pour l'exécution des travaux de dragage et de remblaiement nécessaires au projet Taparura à Sfax. Volume III : étude morphologique'

Physical modelling of wave propagation and wave breaking in a wave channel

Diogo R.C.B. Neves¹, Luiz A. M. Endres², Conceição J.E.M. Fortes³ and Takashi Okamoto⁴

Abstract

The presented work describes a wide range of wave channel tests performed at the National Laboratory of Civil Engineering (LNEC), considering different incident wave conditions, with the objective of studying the wave breaking hydrodynamics. Special attention was made to the end of the wave breaking process. The experimental setup, the incident wave conditions, the equipment and the performed measurements (free surface elevation and particle velocity) are herein described. Time, spectral and statistical analysis based upon the measured data are also performed and presented. Moreover, a more deepen analysis related: (i) the relative wave height (H/d); (ii) the wave celerity; (iii) the two-dimensional distribution of the particle velocities components in the xy , xz and yz planes and; (iv) the average wave direction and spreading angle is carried out and presented. Vertical velocity profiles are also presented.

Keywords: wave breaking, wave propagation, physical modelling, wave channel

1 Introduction

The determination of the wave breaking zone is an important matter for studies referring coastal hydrodynamics and sediment transport. More accurately, the location and extension of the wave breaking section are two of the main factors for the coastal structures foundation and stability or for the nearshore sediment dynamics.

Many studies aimed to analyze the initial process of the wave breaking (Goda, 1970; Weggel, 1972; Tsai et al., 2004; Camenen and Larson, 2007) however the processes after the initial point until the end of the wave breaking are still object of a broad discussion in the scientific community (Svendsen et al., 1978 and 2003; Tsai et al., 2004). The traditional wave breaking indexes are usually related with the initial location of the wave breaking, leaving in background the end section of the process, which is, as mentioned above, especially important in coastal dynamics studies and for the set up of maritime structures.

Following this reasoning, an extensive set of experimental tests was carried out to study the wave breaking characteristics and hydrodynamics, considering different incident conditions. Special attention is given to data from the wave breaking section and especially at the end of it. The experimental tests were performed in a wave channel with a 32.4 m length, at the National Laboratory of Civil Engineering (LNEC), Lisbon, Portugal. The bottom profile of the wave channel consisted essentially in different bottom slopes. The tested wave conditions represented a combination of regular waves with wave periods of 1.1, 1.5, 2.0 and 2.5 s and wave heights of 12, 14, 16 and 18 cm.

This paper presents the experimental conditions, the incident wave conditions and the experimental procedures (section 2). Data and results from time, spectral and statistical analysis are presented (section 3). Moreover, a more in-depth data analysis was carried out for the calculation of several parameters, such as: (i) the definition of the wave breaking zone; (ii) the relative wave height (H/d); (iii) the wave celerity; (iv) the two-dimensional distributions of the

¹ National Laboratory of Civil Engineering, Av. do Brasil 101, Lisbon, 1700-066, Portugal, dneves@lnec.pt

² Universidade Federal do Rio Grande do Sul, Av. Bento Gonçalves 9500, Porto Alegre, 91501-970, Brazil, endres@ufrgs.br

³ National Laboratory of Civil Engineering, Av. do Brasil 101, Lisbon, 1700-066, Portugal, jfortes@lnec.pt

⁴ Hiroshima University, 1-5-1 Kagamiyama, Higashi-Hiroshima, Hiroshima, 739-8529, Japan, tokamoto@hiroshima-u.ac.jp

velocity components in the xy , xz and yz planes; (v) and the directional analysis with the evaluation of the spreading angle. Vertical velocity profiles are also presented. Finally, the conclusions are drawn in section 4.

2 Experimental Settings

Wave tank experiments were conducted at the National Laboratory of Civil Engineering (LNEC) in Lisbon, Portugal. The wave flume is 32.4 m long from the wave maker (Figure 2(a)). A beach profile, with different bottom slopes, was constructed as shown in Figure 1. The slope angle of the front face of the bar and the beach section was fixed with 1:20 and the slope of the lee side of the bar was of 1:80. Water depth was measured to be 10 cm at the crest of the 1:20 bar.

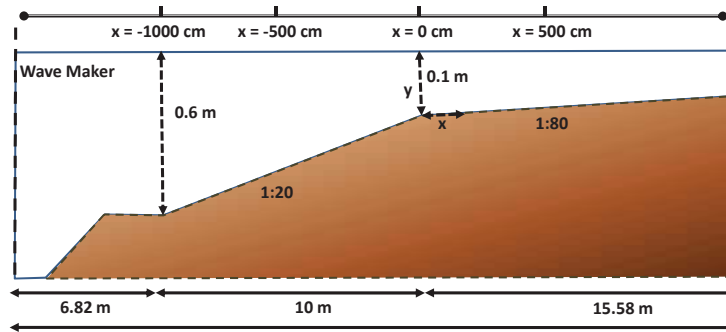


Figure 1: Wave Channel profile and positions along the longitudinal (x) axis

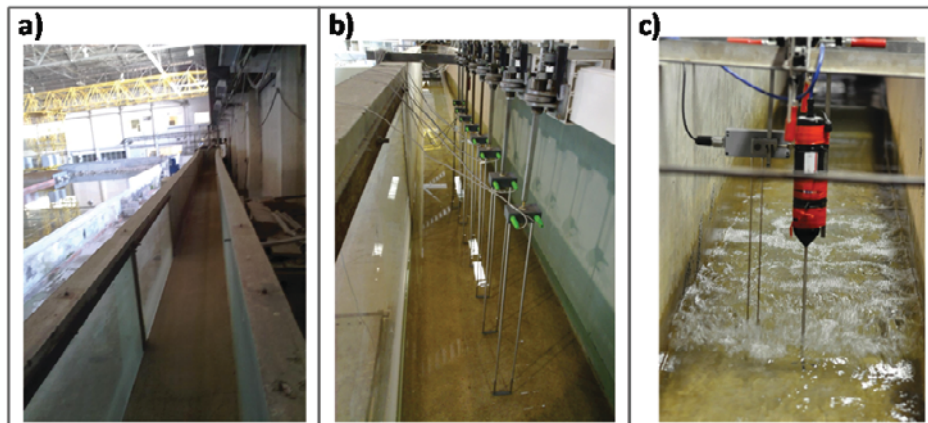


Figure 2: (a) Wave Channel; (b) the 8 gauge mobile structure; (c) The ADV and the resistive gauge

2.1 Incident wave characteristics and experimental tests

A piston-type wave maker generated a combination of regular waves with four wave periods ($T=1.1, 1.5, 2.0$ and 2.5 sec) and four wave heights ($H=12, 14, 16$, and 18 cm). The case of $T=1.1$ sec, and $H=18$ cm presented a very steep wave that broke in front of the wave maker, therefore, this incident wave condition was excluded from the experimental tests. Thus, in total, for each position along the canal, fifteen combinations of waves were tested.

The total set of experiments was divided in three phases: (i) Phase I - Free surface elevations measurements along the channel with an 8 gauge mobile structure; (ii) Phase II - Particle velocity measurements along the channel in the middle of the water column, using an Acoustic Doppler Velocimeter (ADV) sensor; (iii) Phase III - Vertical velocity profiles using the same ADV sensor. In phases II and III, together with the particle velocity measurements, free surface elevations were measured simultaneously in the same transverse section of the channel.

2.2 Equipment and experimental procedures

At Phase I, free surface elevations were measured using an eight gauge mobile structure, Figure 2(b). This structure moved along the channel, and measurements were taken from the beginning of the first ramp ($x = -1000$ cm) till $x = 560$ cm when the wave breaking is showed to be completely over for every incident wave condition. In order to calibrate the input wave height, a wave gauge was installed at the toe of the front face of the first slope ($x = -1080$ cm). Each gauge in the mobile structure was separated by a fixed distance (20 cm), and measurements separated by 10 cm were taken along the covered area.

For Phases II and III, the particle velocity was measured by an ADV with a down-looking probe, enabling the three orthogonal components of the suspended particle velocities (volume measurements), Figure 2(c). Together with the ADV, a resistive gauge was placed for simultaneous measurements of the free surface elevation (Figure 2(c)). In Phase II, the ADV probe was located in the middle of the water column. Measurements were obtained between $x = -200$ cm and $x = 560$ cm, at every 10 cm, while between $x = -1000$ cm and $x = -200$ cm the interval was of 100 cm.

For the phase III, vertical velocity profiles were measured (separated by 5 cm in the vertical axis (z)) for selected (x) locations ($x = -1000$; -500 ; -100 ; 0 ; 50 ; and 150 cm).

The sampling frequency of all the measurements was of 25 Hz and each experimental test (incident wave) had the duration of 490 s.

The wave breaking section (from the beginning till the end of the wave breaking zone) was defined by visual observation. The beginning and the end of the wave breaking zone was considered when the air bubbles started tipping over the crest and vanished from the water, respectively. Considering the nature of these observations, about 50 samples were collected and an average value was determined.

3 Results

For each of the 15 incident wave conditions, time series of the free surface elevation and the particle velocity along the wave channel (and especially from $x = -1000$ cm to $x = 560$ cm) were obtained. Based on the data, different types of data analysis were considered:

Phase I – Time, spectral, and statistical analysis of the free surface elevation measurements. Also, the wave celerity and the relative wave height (H/d) along the wave channel were calculated for each wave condition.

Phase II – Time, spectral, and statistical analysis of the particle velocity measurements. Moreover, the ADV measurements allowed the calculation of the particle velocities main characteristics, the two-dimensional distributions of velocity components at the (xy), (xz) and (yz) planes and the average wave direction as well as the directional dispersion (spreading).

Phase III – Time analysis of the vertical velocity profiles in the selected locations of the wave channel.

In the next sections, beyond the beginning and ending of the wave breaking zone, for each phase, some samples are presented from the calculated results. The incident wave condition of $T = 1.5$ s and $H = 18$ cm was chosen as an example of results for the majority of the presented samples.

3.1 Wave breaking zone

As referred in section 2, the wave breaking section was defined for each one of the 15 incident waves. About 50 samples were obtained and an average value was determined for the initial and terminal location of the wave breaking. Both locations were defined by eye observation (Table 1).

Table 1: Initial and terminal location of the wave breaking section

T (s) H (cm)	Initial location of the wave breaking section				Terminal location of the wave breaking section			
	1.1	1.5	2.0	2.5	1.1	1.5	2.0	2.5
12	-267	-212	-203	-220	205	265	330	445
14	-332	-276	-289	-270	200	245	330	445
16	-427	-340	-361	-295	200	245	305	428
18		-395	-410	-367		245	293	415

3.2 Phase I results

3.2.1 Relative Wave Height

The relative wave height (H/d) is often used as an index for the wave breaking section in shallow water conditions. Dally et al. (1985) considers this index as reference for a stabilized wave condition.

Figure 3 shows, for all the 15 incident wave conditions, the relative wave height evolution from the top of the bar until the end of the surf section. The x-axis was normalized by the wave breaking section, $x = 0$ indicates the beginning and $x = 1$ the terminal location of wave breaking (see 3.1). From the figure it can be concluded that the curve of H/d has two phases. Before the wave breaking zone the curve is steeper, increasing rapidly, while after the wave breaking the slope presents a smoother curve. Between $x = 0.0$ and 0.6 , H/d decreases until $H/d = 0.35 \approx 0.65$ depending on the incident wave condition, this value remains constant until $x = 1$. The average rate of H/d at the end of the wave breaking section is of 0.45 , for an incident wave of $T = 1.5$ s and $H = 18$ cm (see the "Poly. ($T=15s$ & $H=18cm$)" that represents the trendline for the $T = 1.5$ s and $H = 18$ cm incident wave condition).

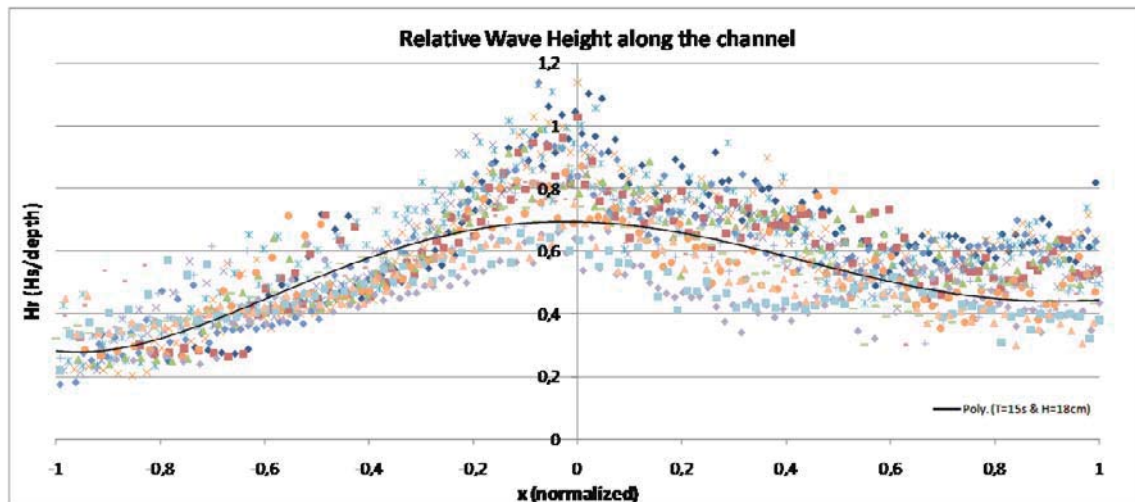


Figure 3: Relative wave height evolution ($x = 0$ is the beginning and $x = 1$ is the end of the wave breaking) using a normalized scale for all the wave conditions.

3.2.2 Wave Celerity

To calculate the wave celerity it is necessary to estimate the average time required for the passing waves between each two consecutive gauges. The wave passing time was calculated

as the one corresponding to the largest cross-correlation value between the full records of each pair of gauges. This method was applied by Okamoto et al. 2010.

Figure 3 shows the wave celerity along the channel for the incident wave conditions of $H = 18$ cm, and wave periods of $T = 1.5, 2.0$ and 2.5 s. In the figure, the "theoretical curve" is the curve of the values of \sqrt{gh} and the fit curves "Poly. (H(18cm)T15(s))", "Poly (H(18cm)T20(s))" and "Poly (H(18cm)T25(s))" correspond to the "H(18cm)T15(s)", "H(18cm)T20(s)" and "H(18cm)T25(s)" incident wave conditions.

For the three periods: (i) at the initial section there is a slightly increase of the celerity; (ii) then, the wave celerity is almost constant; (iii) after $x = -400$ cm, where the wave breaking occurs, the celerity decreases, following the depth reduction of the channel, starting first in the minor periods. This behavior agrees with the occurrence of earlier wave breaking for shorter periods (see 3.1); (iv) in the final section of the channel the large reduction of the slope and the end of the wave breaking section motivates the curve smoothing and the tendency to collapse in one curve.

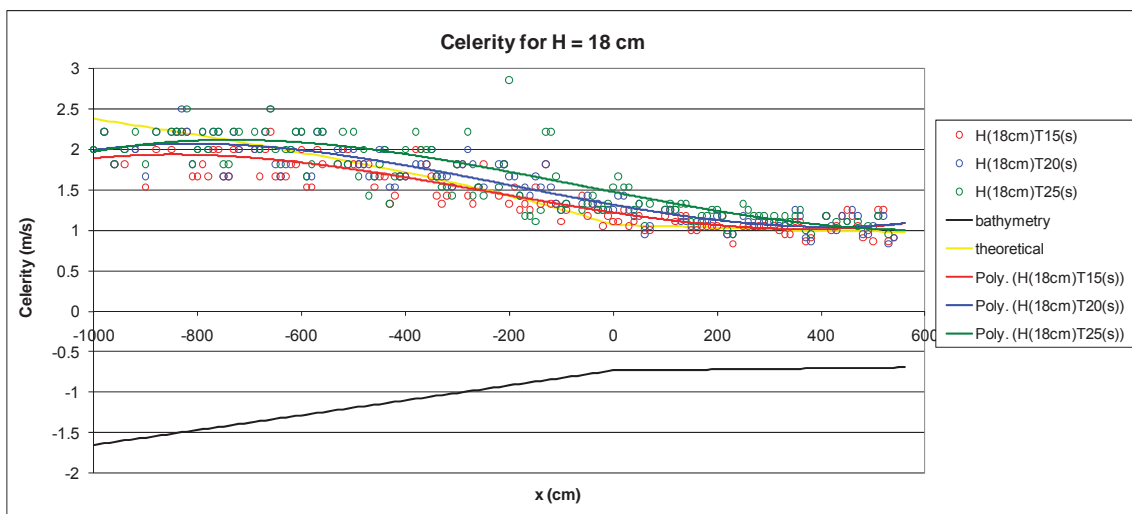


Figure 3: Wave celerity results along the channel for incident waves of $H = 18$ cm and $T = 1.5, 2.0$ and 2.5 s.

3.3 Phase II results

3.3.1 Time, spectral, and statistical analysis of the velocity data

The statistical analysis consisted in determining the average, standard deviation, skewness (distortion) and kurtosis of the particle velocity values (V_x) recorded for each incident wave condition along the x -axis position (positive V_x values are toward the wave maker) (Sancho et al., 2001), Figure 4. The average of the velocity values at each record was calculated through the average of all measured values in the record. The averages of the maximum and minimum velocities were calculated by the identification of each "wave" using the criterion of the downward zero crossing, each intersection was considered effective when there were at least two points before and after the zero reference.

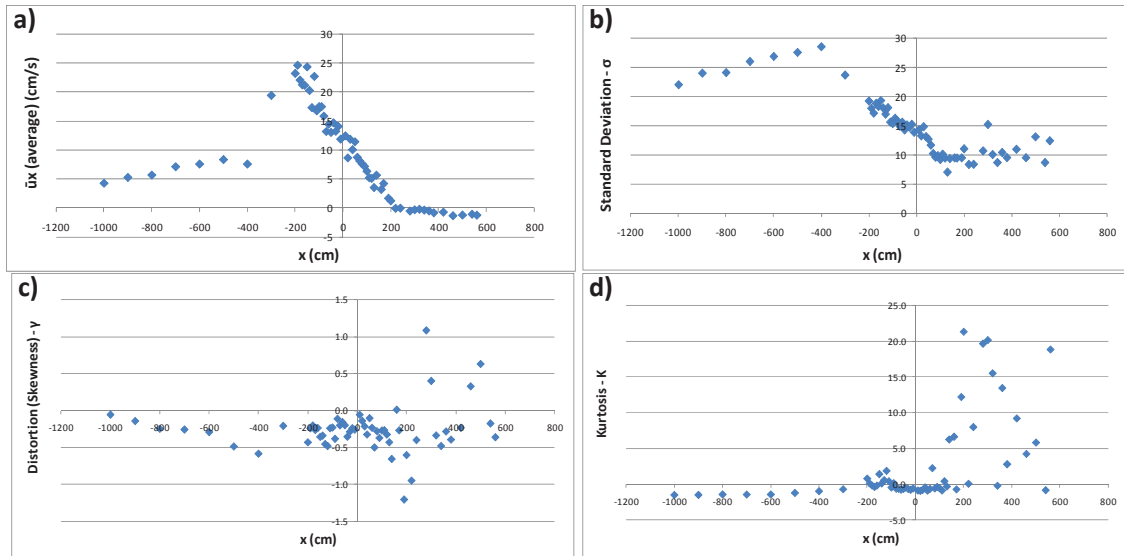


Figure 4: (a) Average, (b) the standard deviation, (c) skewness and (d) kurtosis of the velocity (V_x) values along the channel, for $T = 1.5$ s and $H = 18$ cm

Figure 4(a) shows that after the breaking point (near $x = -400$ cm), the average values increase abruptly and when the wave collapses (around $x = -200$ cm) those values start to decrease till they become almost constant by the end of the wave breaking, after $x = 200$ cm. The standard deviation (Figure 4(b)) depicts values that are similar to the average of the velocities, first an increment till the breaking point followed by a decrease till the end of the surf section, after that, some scattered values show some inconsistency probably due to the harmonics generation created by the bottom slope or by the wave breaking effect. For the skewness and the kurtosis (Figure 4(c)(d)), a general trend can be observed indicating huge differences at the end of the wave breaking (after $x = 100$ cm) possibly due to the appearance of some waves generated by the bottom slope and by the wave breaking effect.

3.3.2 Two-dimensional distribution of the three orthogonal components of the velocity

In this section the analysis of the two-dimensional distributions of the velocity components in the xy , xz and yz planes is performed. The procedure followed, firstly, the evaluation of the parameters (E_x , E_y , E_z , Figure 5). E_x , E_y and E_z are the differences between the averages of the positive and negative velocities for each orthogonal component (x , y , z) measured by the ADV. In Figure 6, the E_z/E_x , E_y/E_x and E_y/E_z ratios are represented for an incident wave condition of $T = 1.5$ s and $H = 18$ cm.

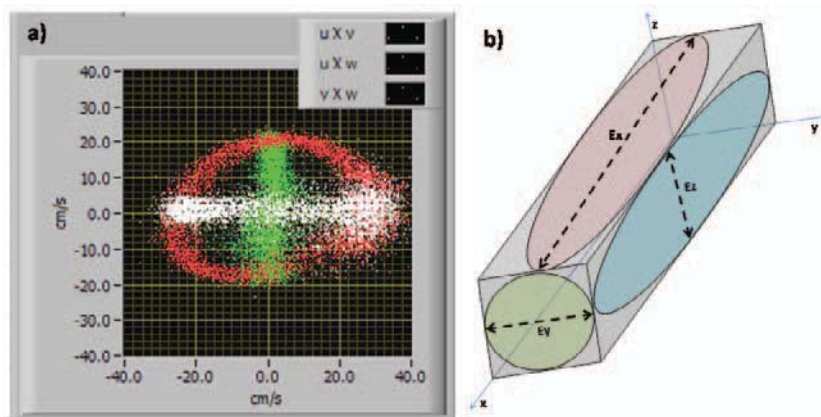


Figure 5: Typical two-dimensional distributions of the velocity components (a) the recorded data cloud ($u = V_x$, $v = V_y$, $w = V_z$) and (b) parameters lengths schematically represented

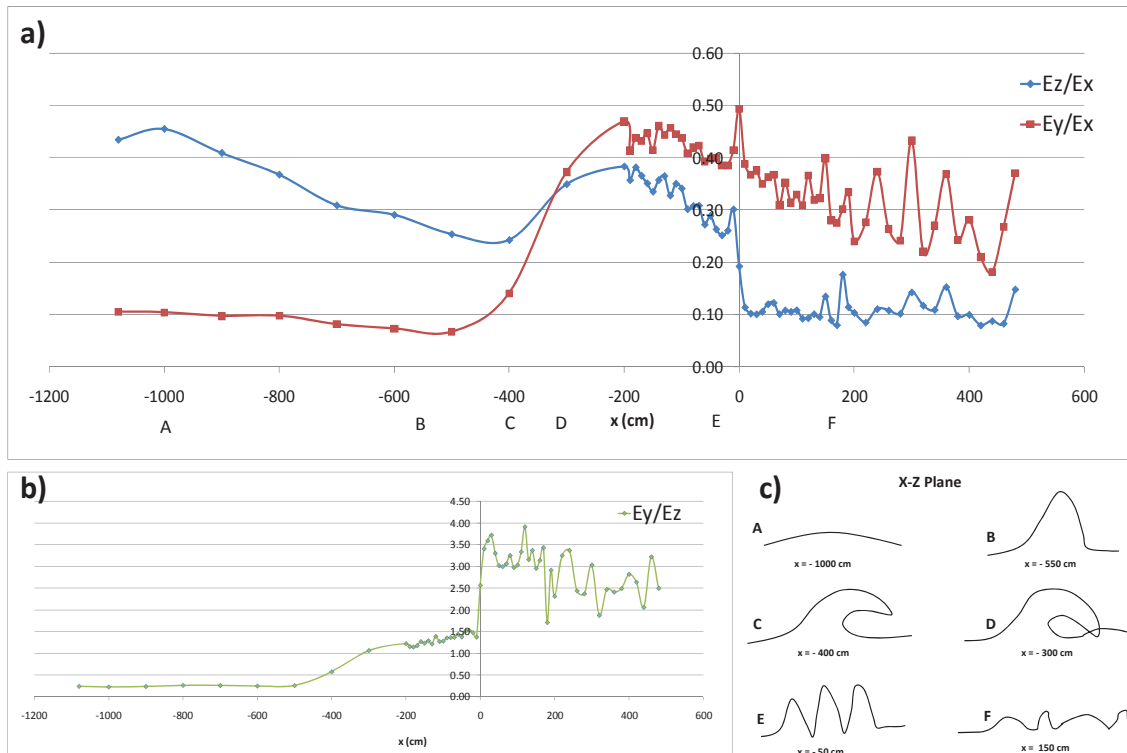


Figure 6: (a) E_z/E_x and E_y/E_x ; (b) E_y/E_z ratios along the x axis of the channel $T = 1.5$ s and $H = 18$ cm; (c) wave shape in the xz plane for positions along the channel (A-F)

From Figure 6, one can conclude that the beginning of the channel and approaching the wave breaking zone, the ratios are $E_y/E_x < 0.1$ and $E_z/E_x < 0.4$, not far from the ideal, $E_y/E_x = E_z/E_x = 0$.

Later, though with an increase in the ratios values involving the parameter E_y , the results remain fairly unchanged until the position near $x = -500$ cm, when a new change is felt, particularly considering the ratio E_y/E_z .

The position $x \cong -400$ cm represents the beginning of the wave breaking section, from this point an abrupt increase of the E_z/E_x ratio occurs till $x = -200$ cm. For $x > -200$ cm, the values decrease, forcing a stretch of the waveform in the longitudinal direction of the channel.

Interesting is to observe that the wave breaking affects differently the three ratios (E_z/E_x ; E_y/E_x ; E_y/E_z). Following E_z/E_x the response to the wave breaking is felt 100 cm later than both E_y/E_x and E_y/E_z . Around $x = -400$ cm the E_z/E_x starts to increase, meanwhile the curves of the ratios E_y/E_x and E_y/E_z had already begun to increase around $x = -500$ cm. Figure 6 shows clearly the transformation of the E_x component into the E_z and E_y components. This is mainly due to the rolling effect of the wave that obliges the water spreading during the wave breaking phenomena. The transverse component (E_y) is due to the turbulent mixture from the roller effect of the breaking wave, which starts around $x = -500$ cm.

3.3.3 Average wave direction and dispersion

One highlight of this work was the directional analysis (based on the simultaneous measurements of the particle velocities and the free surface values), that at first approach would not make sense in a 2D wave channel. Nevertheless, due to the generated turbulence in the wave breaking process, the directional spreading is observed along the wave propagation on the wave channel. Thus, the directional analysis of the experimental data may constitute a framework for the turbulence quantification associated with the wave breaking phenomena.

To obtain the directional wave spectrum the method developed by Longuet-Higgins (Dean & Dalrymple, 1993) can be used. This method, in addition to the free surface elevation records, considers also the simultaneous records of the velocities in the horizontal plane distribution. In this method, the directional spectrum is expressed by a Fourier series. According to Trageser

and Elwany (1990), the estimation of the mean wave direction as a function of frequency $\theta(f)$ is accurate. However, the estimation of the directional dispersion value can be coarse for a limited number of coefficients.

The average wave direction and dispersion were calculated by using the simultaneous measurements of the particle velocity and the free surface elevation made along the x axis of the channel. The obtained results for the spreading angle and wave direction are shown through the Figure 7 below.

According to Figure 7, the main direction angles remain around the original generation value (270°). The breaking wave still propagates into the same direction and keeps the wave train unchanged. However, the growth of the spreading angle during the wave breaking process is remarkable. In fact this analysis presents very low spreading values before the wave breaking, increasing during the wave breaking, specially just before $x = 0$, in order to decrease considerably after the end of the wave breaking section. This might also indicate that after the wave breaking, the residual frequency changes into more waves with different frequencies that propagate independently (Okamoto *et al.*, 2010).

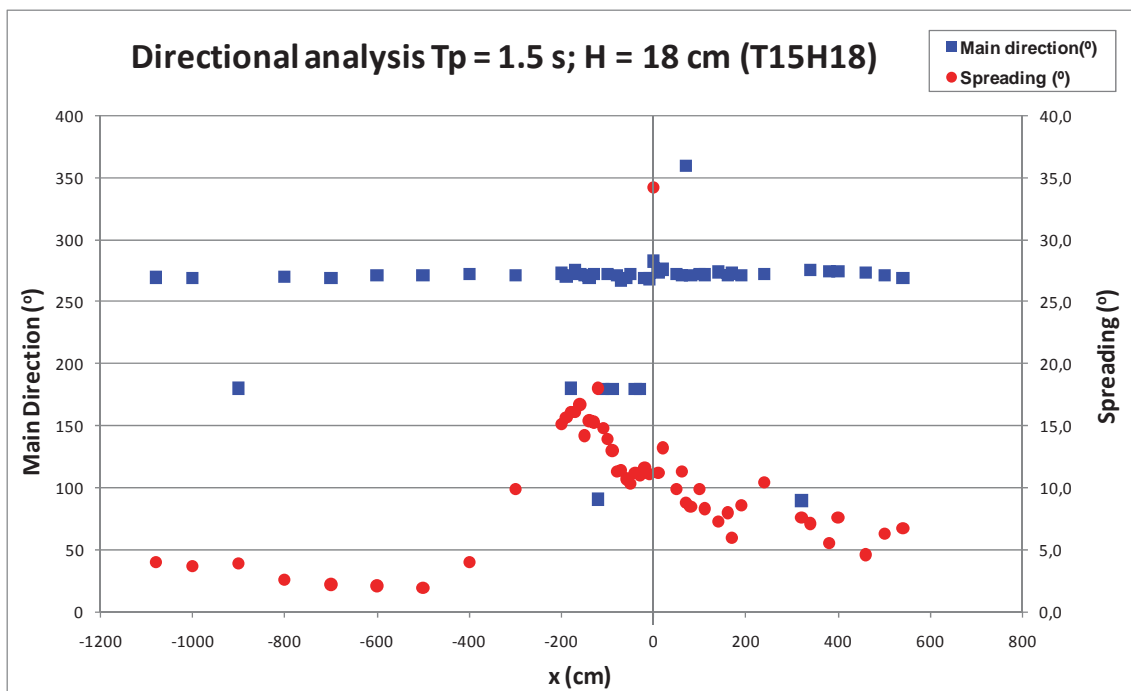


Figure 7: Main direction ($^\circ$) and spreading angle for $T = 1.5$ s and $H = 18$ cm

3.4 Phase III - results

3.4.1 Vertical Velocity profiles

To analyse the vertical profiles of the velocity, the maximum, minimum and average values of the velocities were calculated (V_x) (Figure 8). The maximum, minimum and average values represent, respectively, the maximum, minimum and average of the complete record. It is important to note that the positive values of the velocities are towards the paddle, in the opposite direction of the wave propagation.

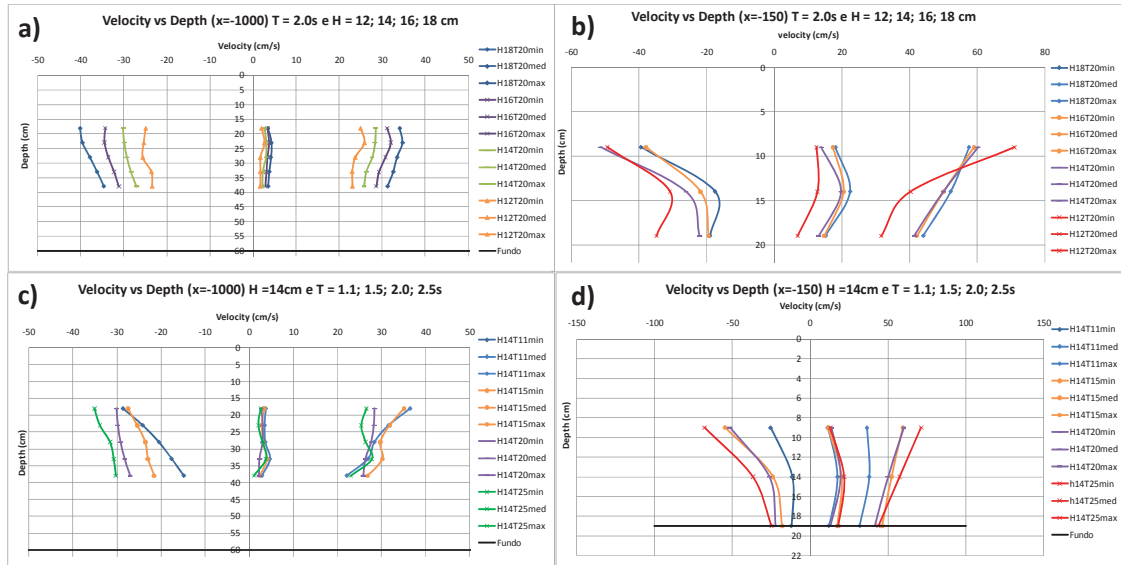


Figure 8: Vertical velocity profiles in (a) $x = -1000$ cm and (b) $x = -150$ cm for $T = 2.0$ s and $H = 12, 14, 16$ and 18 cm; (c) $x = -1000$ cm and (d) $x = -150$ cm for a incident wave of $H = 14$ cm and $T = 1.1, 1.5, 2.0$ and 2.5 s

Figure 8 shows that the greater velocities happen to be in occasions of bigger wave heights and periods. For $x = -1000$ cm, the values do not vary significantly along the vertical axis (about 5 cm/s). For the position $x = -150$ cm (Figure 8(b)(d)), the bottom effect produces a 20 cm/s velocity differences for the maximum and minimum values.

4 Conclusions

In this paper, recent physical modelling tests on a wave channel from the National Laboratory of Civil Engineering (LNEC) in Lisbon were presented. The tests aimed to study the wave breaking hydrodynamics on a beach profile with variable bottom slopes since its beginning till the very end.

The physical modelling was performed on a wave channel, built for the regular wave propagation studies, with a bottom characterized by a flat section followed by two ramps with 1:20 and 1:80 slopes respectively, forming a characteristic beach profile. The tested waves resulted from a combination of 1.1, 1.5, 2.0 and 2.5 s periods with wave heights of 12, 14, 16 and 18 cm. The measured data from the resistive gauges (free surface) and the Acoustic Doppler Velocimeter (ADV) enabled the calculation of several parameters, such as the wave celerity, the relative wave heights, the two-dimensional distributions of the velocity components in the xy , xz and yz planes, the main wave direction and the spreading angle of the wave propagation, the initial and final location of the wave breaking section was observed and the temporal analysis of the vertical velocity profiles in selected locations of the wave channel are presented.

From the tests with the physical model, a wide set of wave data (free surface elevation and particle velocity) along the channel and especially in the wave breaking section is available. This constitutes an important output of this work since it can be used to understand more deeply the wave breaking process but also for the establishment/improvement of the wave breaking numerical models and its validation.

5 Acknowledgements

This study is funded by the FCT under the contracts of SFRH/BPD/20508/2004, PTDC/ECM/73145/2006 and PTDC/ECM/67411/2006 and FCT/CAPES (Brazil) – “Building a Base for Research and Knowledge in Coastal Engineering”.

6 References

- Camenen, B., M. Larson (2007). Predictive Formulas for Breaker Depth Index and Breaker Type. *Journal of Coastal Research: Volume 23, Issue 4*: pp. 1028 – 1041, West Palm Beach (Florida), ISSN 0749-0208.
- Dally, W. R., R. G. Dean, R. A. Dalrymple (1985). Wave height variation across beaches of arbitrary profile. *Journal of Geophysical Research*, Vol. 90, No. C6, Nov. 20, 11917-11927.
- Dean, R. G., R. A. Dalrymple (1993). *Water Wave Mechanics for Engineers and Scientists*. World Scientific, Singapore.
- Goda, Y. (1970). A Synthesis of Breaking Indices. *Transactions of JSCE*, Vol.2, Part 2, 39-49.
- Okamoto, T., C. J. Fortes, D.R. Basco (2010). Bore propagation speed at the termination of wave breaking. ICCE, Proceedings of 32nd Conference on Coastal Engineering, Shanghai, China.
- Sancho, F., P.A. Mendes, J.A. Carmo, M.G. Neves, G.R. Tomasicchio, R. Archetti, L. Damiani, M. Mossa, A. Rinaldi, X. Gironella, A.S. Arcilla (2001) Wave hydrodynamics over a barred beach. Proc. Int. Symp. on Ocean Wave Measurement and Analysis, "Waves 2001", S. Francisco, ASCE.
- Svendsen, I.A., P.A. Madsen, J.B. Hansen (1978). Wave characteristics in the surf zone. Proc. of 16th ICCE, ASCE, 520-539
- Svendsen, I.A., W. Qin, B.A. Ebersole (2003). Modelling waves and currents at the LSTF and other laboratory facilities. *Coastal Engineering*, 50, Issues 1-2, 19-45, ISSN 0378-3839, DOI: 10.1016/S0378-3839(03)00077-2
- Trageser, J.H., H. Elwany (1990). The S4DW, an integrated solution to directional wave measurements. Proc. IEEE Working Conf. on Current Measurement, 154-168, DOI: 10.1109/CURM.1990.110902
- Tsai C.P., H. B. Chenb, H. H. Hwungc, M. J. Huang (2004). Examination of empirical formulas for wave shoaling and breaking on steep slopes. *Ocean Engineering*, Volume 32, Issues 3-4, Pages 469-483, ISSN 0029-8018, DOI: 10.1016/j.oceaneng.2004.05.010
- Weggel, J. R. (1972). Maximum Breaker Height. *Journal of Waterways, Harbors, and Coastal Engineering Division*, ASCE, vol. 98,529-54

Methodology for overtopping risk assessment in port areas. Application to the Port of Praia da Vitória (Azores, Portugal)

Paulo Duarte Raposeiro¹, Maria Teresa Reis², Diogo Neves², Conceição Juana Fortes², João Alfredo Santos², Adriana Vieira², Javier Ramalheira², Anabela Simões³, Eduardo Brito de Azevedo³, M. Conceição Rodrigues⁴

Abstract

In this paper, a methodology to assess the risk associated with wave overtopping in port areas is presented. The methodology is implemented in the GUIOMAR system, which is an integrated system for port and coastal engineering modelling, developed in a GIS commercial software. The overtopping determination is performed by using empirical tools. To assess the risk of overtopping, the combination of the probability of occurrence of an event of wave overtopping and of the consequences of that occurrence is considered. The paper illustrates the application of this methodology to the Port of Praia da Vitória, at the Terceira Island, Azores Archipelago, considering the sea-wave conditions between 2009 and 2010.

Keywords: Wave overtopping, Risk assessment, Geographic information systems, Numerical models, Port of Praia da Vitória

1 Introduction

The length of the Portuguese coast, the severity of the sea conditions and the importance of the coastal zone regarding the socio-economic activities, justify the relevance of studying wave-induced risks, and in particular, overtopping due to wave action. Indeed, emergency situations caused by adverse sea conditions are frequent and put in danger the safety of people and goods, with negative impacts for society, the economy and the environment. Therefore, a methodology to assess the overtopping risk in port or coastal areas is essential for a proper planning and management of these areas. A detailed characterization of tide levels, currents and sea waves is essential to improve the risk assessment methodologies, increasing the reliability of the results, enabling the issue of warnings and supporting the preparation of mitigation plans.

In this context, the National Laboratory for Civil Engineering (LNEC) has been developing two integrated decision support tools for port and coastal management, whose focus is to prevent and support the management of emergency situations (MOIA system) and the long-term planning of interventions in the study area (GUIOMAR system).

The MOIA system (Santos *et al.*, 2008, 2011) is a real-time tool to evaluate sea-wave action and its effects on port and coastal activities and to issue warning messages whenever the safety of such activities are deemed to be at risk. In this system, the wave regime characteristics are determined 1 or 2 days in advance, using numerical models that forecast the wind generated sea waves at a regional scale. The corresponding consequences for port and coastal activities (e.g. for navigation) are defined using empirical formulae or numerical models. This *a priori* knowledge of the characteristics of the waves and their consequences allows timely issues of warnings to the relevant authority members when there is a possibility of occurrence of emergency situations (short-term management).

¹ Universidade Nova de Lisboa – FCT/DCEA, Campus de Caparica, 2829-516, Caparica; praposeiro@fct.unl.pt

² LNEC, Av. do Brasil, 101, 1700-066 Lisboa, Portugal; treis, jfortes, dneves, jasantos@lnec.pt, javier.ramalheira@gmail.com, adriana.ilha@gmail.com

³ Universidade dos Açores, Campus da Terra Chã, 9701-851, Angra do Heroísmo, Portugal; anabela, edubrito@uac.pt

⁴ Administração dos Portos da Terceira e Graciosa, S.A., Zona Portuária - Cabo da Praia, 9760-571 Praia da Vitória, Portugal; mcrodrigues@aptg.pt

The GUIOMAR system (Zózimo *et al.*, 2008; Neves *et al.*, 2009, 2010) is an integrated system based on a geographic information system (GIS) for the management of numerical wave propagation models in port and coastal areas that enables the user to calculate the risk for various port and coastal activities, based on the sea-wave characterization. This system is intended as a tool for long-term planning. Therefore, using long term (years) time series for the sea wave characteristics, the system evaluates the sea-wave consequences for the activities, allowing the construction of GIS based risk maps. These maps aim to support decision-making of the responsible entities regarding long-term management.

These systems have already been tested for the navigation risk in two Portuguese ports: the GUIOMAR system has been used to create risk maps in the Port of Sines (Neves *et al.*, 2010) and the MOIA warning system has been tested for the Port of Praia da Vitória (Santos *et al.*, 2011).

The GUIOMAR system has also been tested for flood risk assessment in Vale do Lobo beach, in the Algarve, Portugal. A methodology is implemented for the run-up calculation on beaches and coastal defence structures, for the estimation of the corresponding flood levels and for the creation of flood risk maps. This methodology applies empirical formulations based on experimental or field data (Raposeiro *et al.*, 2010).

This paper focus on the prediction of wave overtopping of maritime structures for risk assessment purposes using the GUIOMAR system. Section 2 describes the case study and section 3 presents the three main steps of the methodology for overtopping risk assessment: the sea wave characterization, the prediction of overtopping and the risk assessment, including the preparation of risk maps. The paper closes with some conclusions and directions for future work (section 4).

2 Study Area

The Port of Praia da Vitória, Figure 1, is located at the Terceira Island, the second largest of the Azores archipelago.

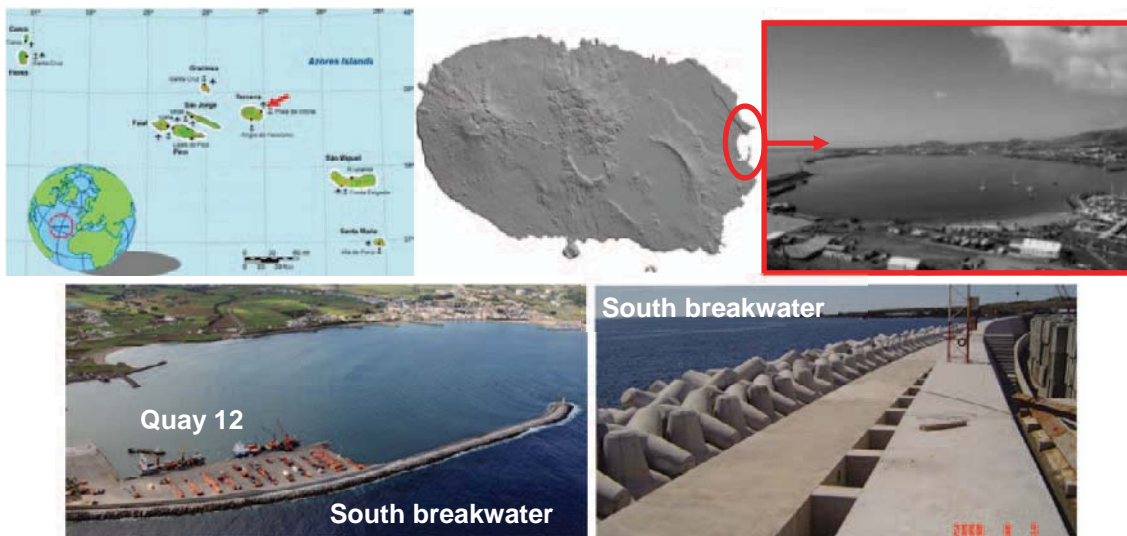


Figure 1: Azores, Terceira Island, Port of Praia da Vitória, south breakwater and quay 12

The port basin, which is approximately 1 km x 2 km, is protected by two breakwaters: the north and the south breakwaters. The south breakwater directly protects quay 12 (Figure 1).

In the port area, there are now several measuring devices that can characterize the sea wave regime within the port. In fact, within the scope of the CLIMAAT project, a directional wave-buoy was installed 4 km northeast from the port, in a region 100 m deep, which was used to validate the methodology for wave propagation applied in this study.

3 Methodology

The methodology implemented in the GUIOMAR system to assess the risk of overtopping of the south breakwater of the Port of Praia da Vitória, and especially at quay 12, follows three main steps (Figure 2):

1. Sea wave characterization at the breakwater;
2. Determination of wave overtopping over the breakwater;
3. Overtopping risk assessment.

The next sections describe in more detail each of these three steps and the GUIOMAR system.

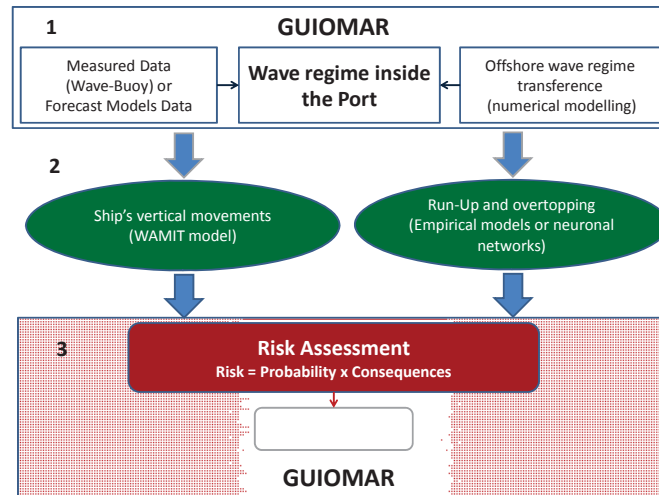


Figure 2: Methodology for risk assessment implemented in the GUIOMAR system

3.1 Sea wave characterization (GUIOMAR)

For the sea wave characterization at the studied port, two years of sea wave characteristics predicted offshore by WAVEWATCH III (WWIII), a third generation wave model developed at NOAA/NCEP (Tolman, 1999), were propagated onshore, first with the spectral wave model SWAN (Booij *et al.*, 1999) up to the port entrance (point P1) and from there into the port with the mild slope wave model DREAMS (Fortes, 2002) (Figure 3). Point P19, located in front of the south breakwater, was pre-defined as an output point for the DREAMS model to determine the wave characteristics at the breakwater section that directly protects quay 12. Figure 3 presents the time series of significant wave height (HS) for point P19 in the study period (January 2009 to December 2010). The reason for coupling two wave propagation models was the lack of a single model that can simulate, in a computationally efficient way, the spread of the wave climate in this vast region, taking into account all the relevant phenomena.

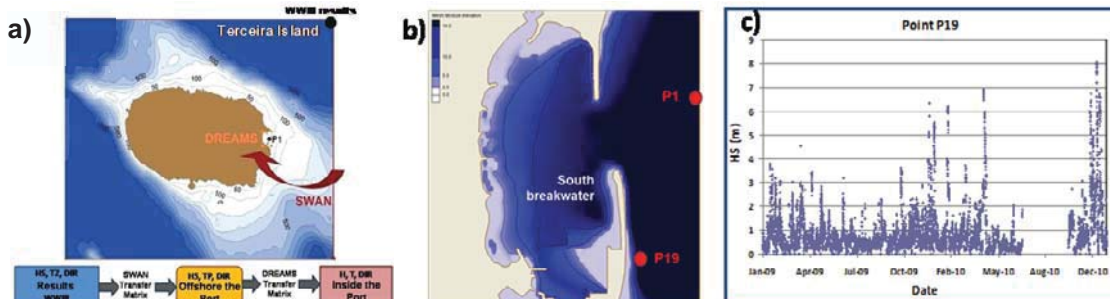


Figure 3: (a) Coupling scheme for the numerical models; (b) point P1 (SWAN) and studied point P19 in front of the south breakwater; (c) Hs (m) for the two-years at P19

The numerical simulations were made for a constant water level of +1.4 m (ZH), which is the sum of a mean water level of +1.0 m (ZH) and a storm surge of 0.4 m.

The sea wave characterization was carried out using the GUIOMAR system (Neves *et al.*, 2009, 2010), which is an integrated system for port and coastal engineering modelling, developed in VBA programming language (Visual Basic for Applications), in a GIS commercial software ArcGis™. It has three main components (Figure 4): the GIS software; a set of 6 modules corresponding to different wave propagation and deformation models with different domains of application; and a Graphical User Interface (GUI), developed in VBA, that enables the liaison between the GIS software and the numerical wave models, that is, it enables: i) the execution of the models; ii) the pre- and post-processing of the data and of the model results; and iii) the use of the capabilities inherent to the GIS software, for instance to analyse and visualise data and results in both 2D and 3D.

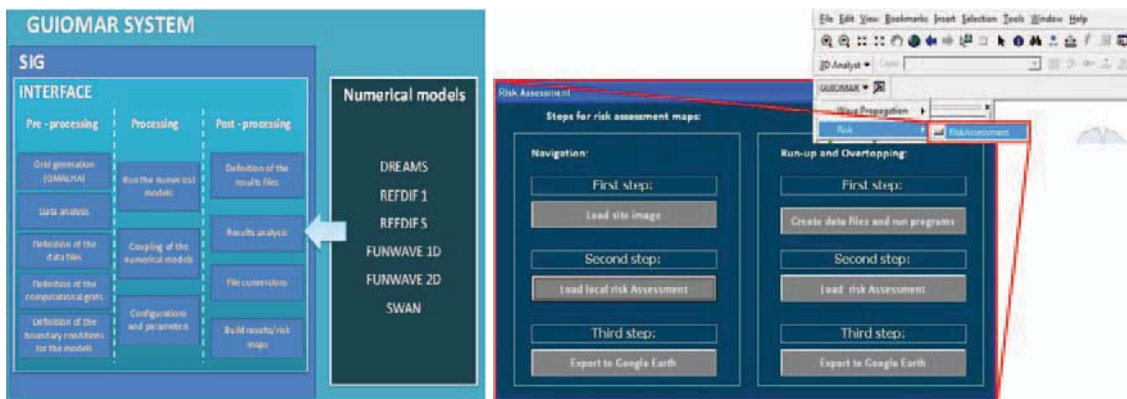


Figure 4: The GUIOMAR system and its toolbar for risk assessment

The modular nature of the system enables its easy expansion and upgrade, such as including more advanced models that may tackle different physical processes. The GUIOMAR system is also characterized by the implementation of several automated procedures to reduce human errors and to speed up the user's familiarity with the procedures for operating the numerical models.

The latest development to GUIOMAR includes a module to automatically produce risk maps based on the methodology presented in section 3.3. Figure 4 shows the GUIOMAR toolbar used to access the risk maps production area.

3.2 Overtopping Determination

In this study, the overtopping determination was performed by using the tool NN_OVERTOPPING2, which is a prediction tool based on neural network (NN) modelling, developed as part of the CLASH European project (Coeveld *et al.*, 2005) to predict Froude-scaled mean wave overtopping discharges, q , and the associated confidence intervals for a wide range of coastal structure types (such as dikes, rubble mound breakwaters, and caisson structures). In addition, prototype mean overtopping estimations, allowing for scale and model effects, are provided.

The results from this tool are built on a database of about 8400 tested conditions from small-scale physical model tests at many different laboratories. The method uses fifteen input parameters, which include three about the wave conditions (the spectral significant wave height at the toe of the structure, H_{m0} ; the mean spectral wave period at the toe of the structure, $T_{m-1,0}$; and the direction of wave attack, β) and twelve on the geometry of the structure (the water depth in front of the structure, h ; the water depth on the toe of the structure, h_t ; the width of the toe, B_t ; the roughness / permeability of the armor layer, γ_f ; the slope of the structure downward of the berm, $\cot\alpha_d$; the slope of the structure upward of the berm, $\cot\alpha_u$; the width of the berm, B ; the water depth on the berm, h_b ; the slope of the berm, $\tan\alpha_b$; the crest freeboard of the structure, R_c ; the armor crest freeboard of the structure, A_c ; and the crest width of the structure, G_c).

In this work, the mean overtopping discharge per unit length of structure, q , of the breakwater section that directly protects quay 12 (Figure 5) was calculated using the two years of wave data obtained at point P19 (Figure 3c). For this section of the breakwater and for a water level of +1.4 m (ZH), $h=h_t=19.4\text{m}$, $B_t=0.0\text{m}$, $\cot\alpha_d=4.3$, $h_b=10.15\text{m}$, $B=0.0\text{m}$, $\tan\alpha_b=0$, $\cot\alpha_u=1.5$,

$A_c=7.2\text{m}$, $R_c=9.6\text{m}$ and $\gamma_f=0.35$ (tetrapod armour layer with a wave return wall - Coeveld *et al.*, 2005). Since the crest berm does not have the same configuration throughout its width, the value of q considered for the cross-section of the breakwater for each sea-state condition (H_{m0} , $T_{m-1,0}$, β) was obtained from the average of two values of q calculated with the NN_OVERTOPPING2 for $G_c=8\text{m}$ and $G_c=16\text{m}$.

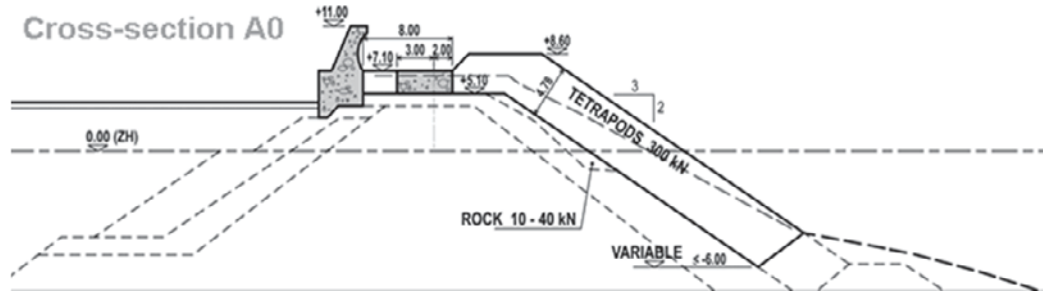


Figure 5: Cross-section of the south breakwater that directly protects quay 12

Figure 6 shows the calculated values of q for the two years of wave data obtained at point P19. The figure also shows $gHST_{m-1,0}$ (with $HS=H_{m0}$), a parameter commonly used to non-dimensionalise q (Reis, 1998).

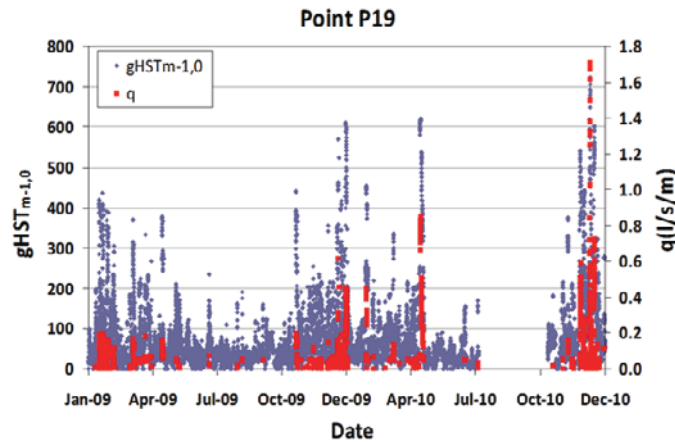


Figure 6: Overtopping calculation for the breakwater section that directly protects quay 12 using NN_OVERTOPPING2 and the two years of wave data obtained at point P19

3.3 Risk assessment

After determining the mean overtopping discharges, q , of the breakwater section that directly protects quay 12 for the two years of wave data obtained at point P19, a qualitative assessment of the risk of overtopping was carried out by applying the following methodology, which is based on five main steps:

- Definition of acceptable thresholds for the values of q based on the Pullen *et al.* (2007) guidance;
- Development of a table of probability of exceedance of the pre-set thresholds of q (Table 1) and establishment of the level of probability for the different thresholds;
- Development of a table of consequences of exceedance of the pre-set thresholds of q (Table 2) and establishment of the level of consequences for the different thresholds;
- Combination of the values of the levels of probability and of consequences to obtain the risk level associated with the different pre-set thresholds, considering that the level of risk is the product of the two other levels (Table 3);
- Production of risk maps and analysis of risk acceptability (Figure 7).

The probability of exceedance was evaluated by using a frequency approach, i.e. by dividing the number of sea states for which overtopping exceeded a pre-set threshold by the total number of sea states in the 2-years wave regime for which the overtopping was computed.

Table 1: Probability of exceedance of overtopping pre-set thresholds

Description	Probability (Guidelines)	Level
Improbable	0 – 1%	1
Remote	1 – 10%	2
Occasional	10 – 25%	3
Probable	25 – 50%	4
Frequent	>50%	5

The table of consequences was developed in straight collaboration with the port authority and has taken into account the consequences for human lives, the environment, the port management and the property. The levels of consequences were assigned in order to take into account the importance of the risk, in relation to its treatment and prioritization, in the assessment of the risk level. For example, it is important to distinguish between an event with high probability of occurrence but with low consequences and an event with a low probability of occurrence but with very high consequences, which is typically more important to manage.

Table 2: Table of consequences (guidelines)

Description	CONSEQUENCES (Guidelines)						Level
	People	Environment	Port Management	Property			
				Buildings	Equipment ¹	Maritime Structure	
Insignificant	Almost no injuries (bruises at most)	Almost no environmental impact	Small changes to port activities	Almost no exterior damage	Almost no damage	Damage in the active area of the structure requiring no intervention	1
Marginal	Single slight injury	Small cargo spills (e.g. oil)	Some changes to port activities; bad local publicity for the port	Minor exterior and interior damage	Minor damage requiring no stopping; almost immediate problem resolution	Occurrence of block movements and falls without filter exposure; immediate intervention not required	2
Relevant	Multiple slight injuries or single major injury	Some areas are restricted due to pollution caused by cargo spills	Restrictions on loading and unloading; possible partial shutdown; bad widespread publicity	Moderate interior damage	Damage requiring temporary equipment downtime for repair	Occurrence of block movements and falls with filter exposure; superstructure affected but with no significant movements	5
Serious	Multiple major injuries or single fatality	Pollution episodes in and out of port zone with potential irrecoverable losses to the environment	Loading and unloading are impossible for several days; bad national publicity	Major interior damage; building structure affected	Major damage; prolonged equipment downtime	Filter layer affected; substantial movements of the superstructure	10
Catastrophic	Multiple fatalities	Widespread cargo spills; serious contamination; irrecoverable losses to the environment; international aid needed	Very serious constraints to loading and unloading over a long period; very serious and long term loss of trade; bad international publicity	Very serious interior damage; building structure seriously damaged; imminent danger of collapse	Equipment loss (no recovery possibility)	Collapse of the structure	25

¹ "Equipment" is intended to include machinery, containers and vessels.

Table 3: The risk level

Risk Level		Consequences				
		1	2	5	10	25
Probability	1	1	2	5	10	25
	2	2	4	10	20	50
	3	3	6	15	30	75
	4	4	8	20	40	100
	5	5	10	25	50	125

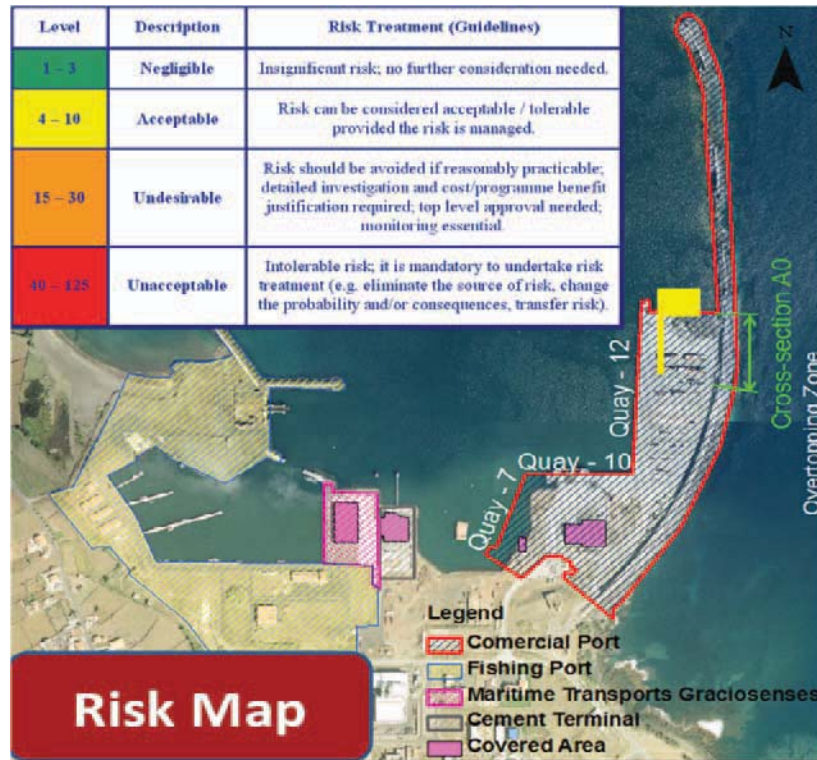


Figure 7: Risk map for wave overtopping in the south breakwater of the Port of Praia da Vitória

4 Conclusions

This paper presents recent developments to GUIOMAR, an integrated system for port and coastal engineering modelling. A set of automatic procedures was developed to implement a methodology for overtopping risk assessment in port areas. To illustrate and test the new procedures, offshore wave predictions from 2009 and 2010 of the WAVEWATCH III third generation wave model were transferred into several points inside the Port of Praia da Vitória, Azores, Portugal, using two numerical models for sea wave propagation and deformation (SWAN and DREAMS), included in the GUIOMAR system. The tool NN_OVERTOPPING2, based on neural network analysis, was used to study the mean wave overtopping for the south breakwater section that directly protects quay 12. Finally, the risk level was established, based on the combination of the probability of exceedance of pre-set thresholds for wave overtopping and of its consequences, and risk maps were generated.

The recent developments in the GUIOMAR system are a step forward in the implementation of a methodology for the overtopping risk assessment in port and coastal areas using the numerical simulation of scenarios based upon historical sea wave data.

A test of the new functionality of GUIOMAR, using the case study of the Port of Praia da Vitória, confirmed that this integrated system is a valuable tool for port and coastal engineering studies and an important tool for supporting decision-making processes in port and coastal management. However, the comparison of forecast results to prototype measurements is essential to improve the reliability of the integrated tool.

5 Acknowledgements

The authors gratefully acknowledge the financial support by the Portuguese Foundation for Science and Technology (FCT) through contracts PTDC/AMB/67450/2006, PTDC/ECM/67411/2006 and PTDC/ECM/73145/2006.

6 References

- Booij, N.; Ris, R.C.; Holthuijsen L.H. (1999): A third-generation wave model for coastal regions, Part I, Model description and validation. In *Journal of Geophysical Research*, 104(C4), pp. 7649-7666.
- Coeveld, E.M.; Van Gent, M.R.A.; Pozueta, B. (2005): *Neural Network. Manual NN_OVERTOPPING 2. CLASH WP8, WL | Delft Hydraulics, Delft, The Netherlands* June.
- Fortes, C.J.E.M. (2002): *Nonlinear wave transformations in harbours. A Finite element analysis. PhD thesis, Mechanical Engineering, IST (in Portuguese).*
- Neves, D.R.; Rodrigues, S.; Reis, M.T.; Fortes, C.J.E.M.; Santos, J.A. (2010): Application to the Port of Sines (Portugal) of a new methodology for risk assessment for harbour navigation based upon the GUIOMAR system. In *Journal of Integrated Coastal Zone Management*, 10, 4, pp. 483-504. ISSN 1646-8872 (In Portuguese)
- Neves, D.R.C.B.; Zózimo, A.C.; Pinheiro, L.V.; Fortes, C.J.E.M. (2009): GUIOMAR: Geo(graphical) User Interface for cOastal and MARine Modeling. Supported Decision System. In *Journal of Coastal Research*, SI 56, pp. 1542-1546.
- Pullen, T.; Allsop, N.W.H.; Bruce, T.; Kortenhaus, A.; Schuttrumpf, H.; Van Der Meer, J.W. (2007): *EurOtop: Wave Overtopping of Sea Defences and Related Structures: Assessment Manua, Environment Agency, UK, Expertise Netwerk Waterkeren, NL, and Kuratorium fur Forschung im Kusteningenieurwesen, DE, August.*
- Raposeiro, P.D.; Fortes, C.J.E.M.; Reis, M.T.; Ferreira, J.C. (2010): Development of a methodology to evaluate the flood risk at the coastal zone. In *Geographic Technologies Applied to Marine Spatial Planning and Integrated Coastal Zone Management*, Calado, H. e Gil, A. (Eds.), Universidade dos Açores – Centro de Informação Geográfica e Planeamento Territorial, August, pp. 129-137. ISBN: 978-972-8612-64-1.
- Reis, M.T. (1998): *Probabilistic Assessment of the Safety of Coastal Structures. PhD thesis, Department of Civil Engineering, University of Liverpool, UK, January.*
- Santos, J.A.; Guilherme, L.; Fortes, C.J.E.M.; Palha, A.; Simões, A. (2008): Methodology for wave forecast in the MOIA package. In *O Sector Marítimo Português, Edições Salamandra, Lda., Lisbon. (In Portuguese)*
- Santos, J.A.; Rodrigues, S.; Neves, D.R.; Vieira, A.; Fortes, C.J.E.M.; Reis, M.T.; Simões, A.; Azevedo, E.B. (2011): MOIA: an integrated decision support tool for port management, in *Proc. ISCRAM 2011, 8th International Conference on Information Systems for Crisis Response and Management: From early-warning systems to preparedness and training, 8-11 May, LNEC, Lisbon.*
- Tolman, H.L. (1999): *User manual and system documentation of WAVEWATCH-III version 1.18. NOAA / NWS / NCEP / OMB technical note 166, 110 pp.*
- Zózimo, A.C.; Fortes, C.J.E.M.; Neves, D.R.C.B. (2008): GUIOMAR: Geographical User Interface for cOastal and MARine modeling. Recent developments and assessment of potential geographical errors, in *Proc. Med Days of Coastal and Port Eng., Palermo, 7-9 October.*

Rapid evolution of shoreline after a beach nourishment downdrift of a groin and at an embayed beach: theory vs. observation

Renata Archetti¹, Sandro Carniel², Claudia Romagnoli³ and Mauro Sclavo²

Abstract

This paper describes the evolving shoreline over a 3,5 years period after an important nourishment, approx. 100 m³/m, made by submarine sand carried out in Lido di Dante beach, Italy. The focus is made on the evolution of an embayed beach of Lido di Dante and of the rapid evolution of the shoreline located down drift a groin.

Different behaviors were observed downdrift the groin and in the embayed beach: in the unprotected zone, downdrift the groin system, a seasonal variation is evident. The shoreline retreated very fast after the nourishment and the evolution has been modeled by the classic Pelnard Consideré equation. At the embayed beach no evident seasonal variation was observed. Main changes are due to beach rotation, dependent on the wave direction.

Keywords: nourishments, video-monitoring, one line model, beach evolution, groin.

1 Introduction

Information about the post-nourishment evolution of replenished beaches from direct observation is scarce in literature (Browder and Dean, 2000; Van Duin et al., 2004; Grunnet and Ruessink, 2005; Elko et al., 2005) and commonly based on relatively sparse (in time) and expensive in-situ surveys. Recently, video-imaging techniques (Holman and Stanley, 2007) are becoming a common tool in coastal monitoring and management, also due to their low-cost and high spatial-temporal resolution (Kroon et al., 2007; Jimenez et al., 2007; Archetti et al., 2008; Nieto et al., 2010). These techniques are proving to be a worthy complement to traditional beach profiles in post-nourishment monitoring (Elko et al., 2005; Ojeda et al., 2008). The lifetime of nourishments can be predicted in various ways, among which the use of empirical methods and one-line models (Dean, 1977, 1983; Hanson and Kraus, 1989, Larson et al., 1997).

Beach nourishments are frequently carried out along the Italian coasts, being very often associated to other beach defence interventions, so that the combined use of breakwaters and nourishment represents a new beach defence strategy. In the last decades, the Emilia-Romagna region carried out a number of safety intervention on some critical littoral stretches subject to erosion and flooding by means of beach nourishment (Preti, 2002). Since 2000, submarine sands from offshore deposits are used in nourishment interventions, which follow a multi-annual frequency (ARPA, 2009); the largest nourishments were realized in 2007, including Lido di Dante (Ravenna). In the following years, monitoring activities were periodically carried out by ARPA (Preti et al., in press).

In 2003 an Argus video monitoring station was installed in Lido di Dante (Davidson et al., 2007), in the framework of the 5th European Funded Project CoastView. Time series of video-images span now over 7 years (from January 2004) and allowed observation on the medium- and short-term evolution of the beach (Archetti and Lamberti, 2009; Archetti, 2009; Archetti and

¹ Dipartimento di Ingegneria Civile, Ambientale e dei Materiali, Università di Bologna, Viale Risorgimento, 2 . 40136 Bologna Italy. renata.archetti@unibo.it

² CNR-ISMAR, Castello 2737, I-30122 Venice, Italy, sandro.carniel@cnr.it

³ Dipartimento di Scienze della Terra e Geologico-Ambientali, Piazza di Porta S. Donato 1, 40127 Bologna, Italy, claudia.romagnoli@unibo.it

Romagnoli, 2011; Armaroli and Ciavola, 2011). Images from the ARGUS video station also witness the different stages of nourishment interventions (Fig. 1) as well as the following beach readjustment.



Figure 1: Snapshot images of the 2007 nourishment intervention at Lido di Dante taken from the ARGUS video station.

The aim of the paper is twofold, to give a description of shoreface behaviour after the nourishment, to compare the shoreline behaviour of the embayed beach with the adjacent unprotected beach and to compare the observation with the most common one-line evolution models results.

2 The study site

Lido di Dante is a small tourist area in the Emilia Romagna region on the Adriatic Sea, 7 km south of Ravenna (Fig. 2a). The area is affected by serious subsidence and erosion problems (ARPA, 2009); starting from the 1980's, part of it has been defended by a system of shore-parallel low-crested structures (LCS in Fig. 2b), i.e. a parallel semi-submerged barrier and three groynes (see also Lamberti et al., 2005), while the southern part is not protected at all and extends between Lido di Dante and the river Bevano mouth (Carniel et al., 2011). The system of groins and barrier forms two cells, which are referred to here as the Northern cell and the Southern cell (Fig. 2b). The submerged detached breakwater, 770 m long and interrupted by a 30-m-wide gap, is placed 180 m from the coast at a 3.5-m depth and is emergent during low tide and submerged during high tide. Lido di Dante is a microtidal beach; tidal excursion is commonly about ± 0.4 m at the spring tide and ± 0.15 m at neap tide (Lamberti et al., 2005). The unprotected beach extends from the southernmost groyne and is still in natural conditions (Fig. 2b); in particular, the tract close to the groyne has a single submerged bar next to the shoreline.

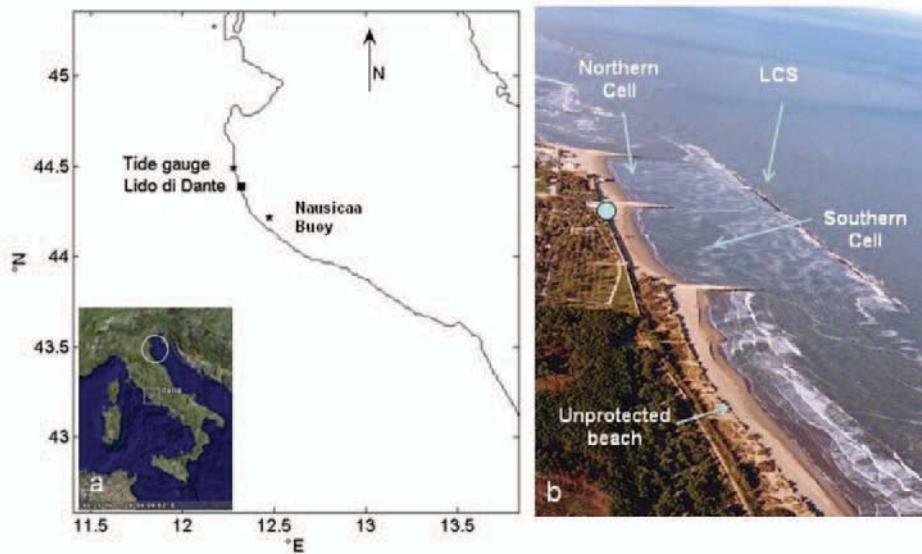


Figure 2: a) Location of Lido di Dante in the Northern Adriatic and of the wave buoy and tide gauge; b) Aerial view of Lido di Dante, including the beach protected by the Low Crested Structures (LCS), with indication of the Northern and Southern cell, and the unprotected beach to the south of it. The ARGUS station position is indicated as a bullet.

The erosive tendency of this coastal tract (evident in the area since the 1970s) is associated with the limited fluvial sediment contribution at the coast and has been particularly enhanced by marked local subsidence due to water and gas extraction (an extended gas extraction field is located close to the site; Teatini et al., 1997). The latest field measurements (high-precision leveling campaigns) indicate a subsidence rate of approximately 19 mm/year in the interval 2000-2006 (ARPA, 2009), which is the greatest value measured in the whole Emilia Romagna region in that time frame. The beach is thus artificially maintained by nourishment, periodically carried out over the last few years: in the time frame 1996-2006, repeated minor nourishment interventions at Lido di Dante placed on the whole about 187,000 m³ of sediment that has been lost at a rate of 25-30 m³/m every year (ARPA, 2009). In order to maintain the Lido di Dante beach it has been estimated the need of approx. 20,000 m³/y for the protected area and of 30,000-40,000 m³/y for the unprotected beach to the south of it (ARPA, 2009). In the nourishment intervention of spring 2007, 107,000 m³ of sand, corresponding to about 97 m³/m, were placed both inside the protected beach and on the northern tract of the unprotected beach, along a distance of about 500 m from the breakwater (Fig. 3). The mean grain size of the nourished sediment in 2007 was approximately 0.177 mm (M. Preti, pers. comm.), similar to the native average grain size (Lamberti et al., 2005). Despite these interventions the erosion is still undergoing and the beach is narrowing, mainly in the natural area next to structures.

The wave climate in this coastal tract is characterized by 0.5 m significant wave height (H_s) and 3.5-4.0 s peak period (T_p) for semi-permanent wave conditions, coming either from the NE and generated by the Bora wind or from the SE and generated by the Scirocco wind. Typical annual storm conditions, generated by the Bora wind, consist of waves up to 3.5 m in H_s and 7 seconds in T_p; while the strongest waves may reach a height of 6.0 m (Archetti and Lamberti, 2009). Simulations of typical Northern and Southern storms at Lido di Dante, where a hydrodynamic field in presence of low-crested structures is modeled, are discussed in Archetti and Romagnoli (2011). The results of the numerical simulations in the protected area are in agreement with the recent observations on the short-term shoreline variability in the “artificially embayed” beach of Lido di Dante, where shoreline rotation in counterclockwise and clockwise direction are related to Bora and Scirocco storms, respectively, due to the occurrence of longshore currents in opposite direction in the nearshore (Archetti and Lamberti, 2009; Archetti and Romagnoli, 2011).

Edge effects, generated at the southern end of the low crested-groynes system, on wave propagation are felt as far as 900 m far from the structure in the unprotected beach (Armaroli et

al., 2005). Here, the beach experienced in the 2000-2006 time frame a shoreface lowering corresponding to a volume loss of about 645,000 m³ on a 600 m-wide area of the emerged-submerged beach (extended to the -8 m isobath; ARPA, 2009). Moreover, despite the prevalent longshore drift along the Emilia-Romagna coast is from the south to the north, an opposite direction (from north to the south) is locally assumed for drift in the southern tract of Lido di Dante (ARPA, 2009).

3 Results

A selection of shoreline positions at the 0 sea water level was made for the January 2007-December 2010 time frame, i.e just before and 3.5 years after the nourishment intervention. The time intervals between video-based surveys are not regularly distributed, because surveys were performed only during days with a very calm sea and a relatively wide tidal excursion. The wave and swl measurements, and the video-survey times are plotted in Fig. 3.

The characteristics of the ARGUS station at Lido di Dante are described in Davidson et al. (2007) and Archetti (2009) and the methodology to extract the shoreline and the assessment of its accuracy are presented in Archetti (2009) and discussed in Archetti and Romagnoli, (2011). The shorelines and the intertidal bathymetric surfaces are given in a defined reference system (Fig. 4) for the Lido di Dante beach, where the Argus station is located in the origin, the y-axis represents the longshore direction (positive values to the north of the Argus site and negative values to the south) and the x-axis runs across the shore (values increasing seaward). The Argus reference is rotated -9.3° from N in this geographical reference system in order to keep the detached barrier parallel to the y-axis (Fig. 4).

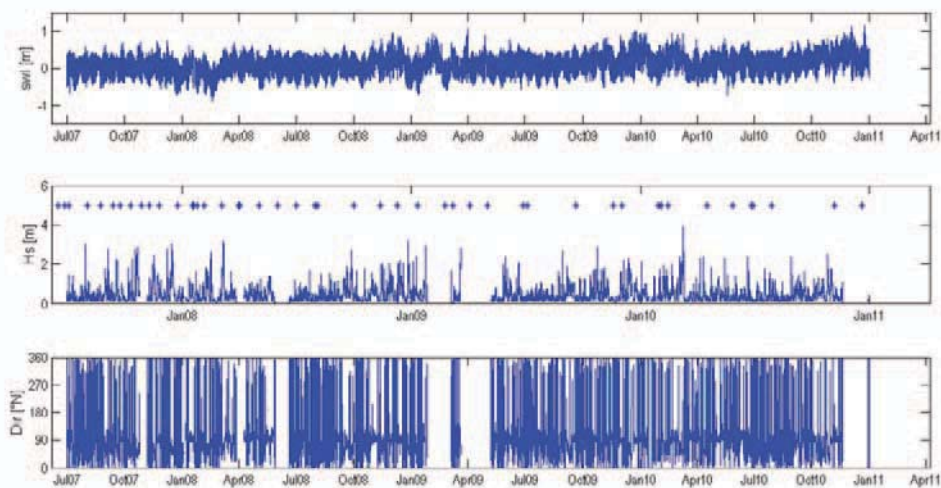


Figure 3: Time series of sea water level measured at the Porto Corsini tide gauge (top panel, data from ISPRA) and of significant wave height (middle panel) and direction (bottom panel) from the NAUSICAA Buoy by ARPA SIMC. Argus surveys are indicated by * at the top of the middle plot.

Figure 4 shows a selection of shoreline positions for the protected beach and part of the unprotected beach (to the south of the groins system, 1200 m from the Argus site), respectively. We can observe that in the protected zone the beach keeps its dimension in the time, while in the southern zone it decreases rapidly.

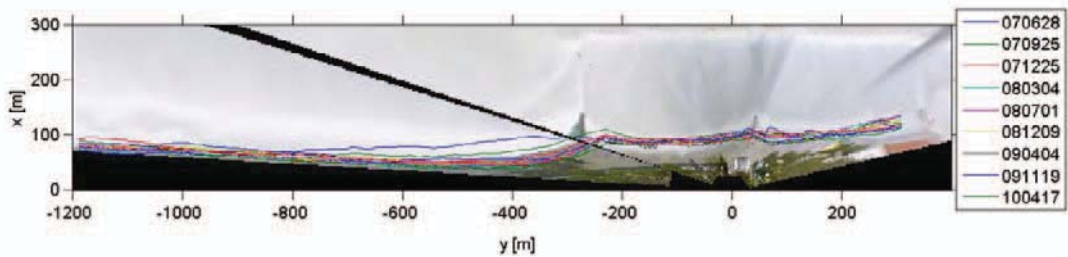


Figure 4: Local reference system adopted at Lido di Dante protected and unprotected beach (merged and rectified image). The ARGUS station is located at the origin of the local reference system. A selection of shorelines is plotted on the figure. Corresponding dates are in legend in format yymmdd.

A quantification of the erosion and accretion of the beach is deeply described in Romagnoli and Archetti, (2011). Main results are here reported.

Time series of the alongshore-averaged shoreline displacement of each survey with respect to the 19 January 2007 shoreline, relevant to the protected beach (N and S cells) and the unprotected beach (where N and S means to the north and the south of the $x=-800$ m transect) are shown in Fig. 5. Positive values indicate shoreline advance with respect to the “reference” position (19/01/07), while negative value are associated with shoreline retreat.

Major shoreline advancements occur among pre-nourishment (before mid-May 2007) and post-nourishment surveys, but with different behaviour in the observed beach sectors (Fig. 5). The most relevant and immediate shoreline advance is recorded in the northern sector of the unprotected beach, where the nourishment was placed: here, an average shoreline advance >30 m (with respect to the Jan, 19th 2007 survey) is observed in the surveys from mid-May to June (Fig. 5). Then, the shoreline gradually (but constantly) retreats to positions close to the pre-nourishment ones within the end of the year. In the southern sector of the unprotected beach, where the shoreline is still retreating in May and June 2007, the average beach advance (within 10 m, Fig. 5) is observed since the end of June, i.e. with a time delay of a few months with respect to the northern sector, and lasts until the end of 2007. In the following years (2008, 2009, 2010) the shoreline in the unprotected beach (both the northern and the southern sectors) fluctuates in the range $-5/+11$ m with respect to the pre-nourishment condition (survey 17/01/07), showing a seasonal ciclicity with winter erosion and small summer recovery.

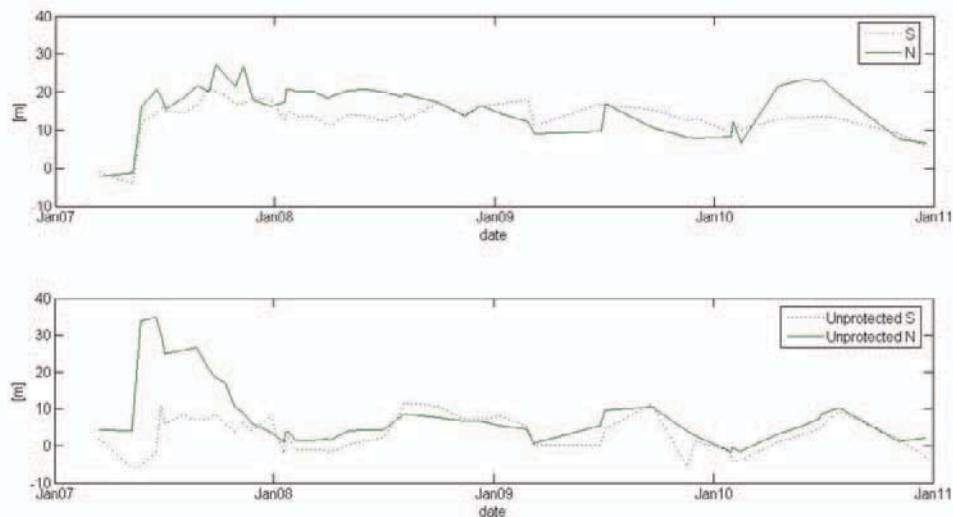


Figure 5: Time series of the alongshore-averaged shoreline positions for the protected beach (above, N and S cells) and the unprotected beach (below, N and S of the $x=-800$ m transect) in the period January 2007-December 2010.

No seasonal variation is observed in the protected beach, as also noted for the time frame 2004-2009 by Archetti and Romagnoli (2011), which pointed out that the sand redistribution frequently occurs here through beach rotation processes, particularly in the southern cell.

The nourishment lifetime and its evolution can be predicted in various ways, among which the use of empirical methods and one-line models (Dean, 1977, 1983, 1996; Hanson and Kraus, 1989) developed from the Pelnard-Considère (1956) diffusion equation.

In an idealized case of an initially rectangular planform, on an infinitely long shoreline at one side, and limited by a groin at the other, the shoreline evolution is modelled by the Pelnard Considère diffusivity equation: the beach fill gradually diffuses from a rectangular planform to a bell-shaped curve that spreads out to a straight shoreline eventually over time .

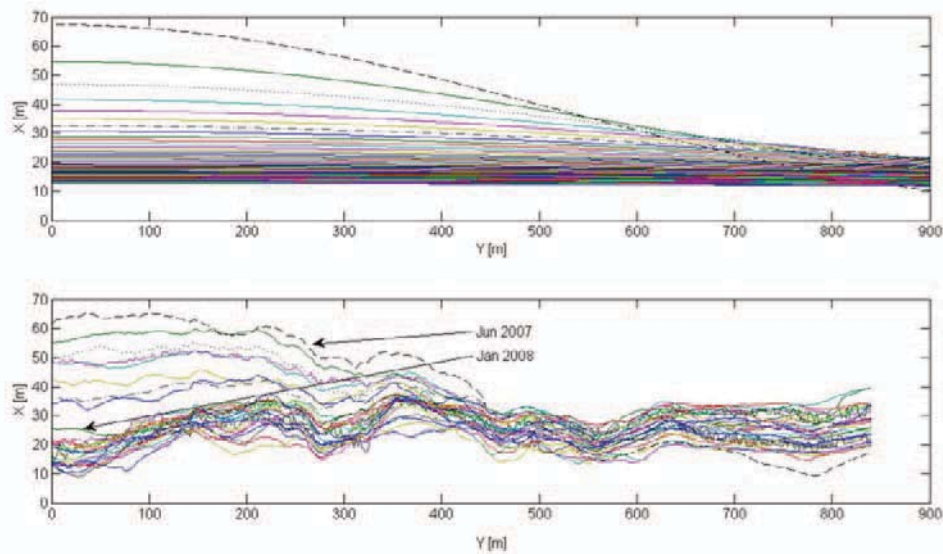


Figure 6: Beach shoreline evolution in time: analytical model (top) and measured shorelines referred to the pre nourishment shoreline (bottom). Each line represents an increasing time.

The longshore diffusivity, is dependent on wave height and sediment characteristics, during the diffusion process, the post-nourishment shoreline perturbation is smoothed by incoming wave energy that drives longshore transport.

Figure 6 shows in the upper panel the theoretical shoreline evolution based on the already mentioned Pelnard Considère diffusive equation and in the lower panel the video surveyed shoreline evolution. The shorelines are stretched by subtracting the pre-nourishment (Jan, 19th, 2007) shoreline, in order to reduce the original curvilinear shape of the coastline and to meet the theoretical model initial shoreline position.

The theoretical beach evolution model seems to well represent the beach evolution the Lido di Dante beach downdrift the southern groin. More analysis will be carried out in the calibration of the model.

4 Discussion and Conclusion

A very rapid evolution characterizes the shoreline in the unprotected area: starting from the sector where the nourishment was mainly placed, just to the south of the groins system, the effects of nourishment were gradually felt southward. Over the first months after the nourishment, in fact, the sediment was gradually redistributed downdrift of the nourished area. This behavior is in agreement with the assumed southward longshore drift for this coastal tract that experienced severe erosion in the last years (ARPA, 2009) and was likely enhanced by the occurrence of a number of storms events from Bora in the July-December 2007 time frame, two

of which having major impacts on the Emilia-Romagna coast. The evolution seems to be well represented by theoretical diffusion model proposed by Pelnard Considère.

Different behavior was observed in the embayed beach, where no evident seasonal variation was observed. Main changes are described by beach rotation, dependent on the wave direction.

5 Acknowledgements

The research was supported by the project PRIN 2008 YNPNT9_005 "Tools for the assessment of coastal zone vulnerability related to the foreseen climate change" financed by the Italian Ministry of University and Research (MIUR).

6 References

- Archetti R., 2009. Quantifying the evolution of a beach protected by low crested structures using video monitoring. *Journal of Coastal Research* 25 (4), 884-899.
- Archetti R., Schiaffino C.F., Ferrari M., Brignone M. and Rihouey D., 2008. Video systems for the coastal monitoring. In: Pranzini E. and Wetzel L. (eds.) *Beach Erosion monitoring*. Nuova Grafica Fiorentina, Italy, 101 – 109.
- Archetti R. and Lamberti A., 2009. Storm-driven shore changes of a beach protected by a low crested structure. In: McKee Smith J. (ed.) *Proceedings International Conference on Coastal Engineering*, 30 August- 5 September 2008, Hamburg, Germany, 2: 1977 - 1989. ISBN-13 978-981-4277-38-9.
- Archetti R. and Romagnoli C., 2011. Analysis of the effects of different storm events on shoreline dynamics of an artificially embayed beach. *Earth Surface Processes and Landforms*, doi: 10.1002/esp.2162.
- Amaroli C. and Ciavola P., 2011. Dynamics of a nearshore bar system in the northern Adriatic: A video-based morphological classification. *Geomorphology* 126, 201-216.
- ARPA, 2009. Stato del litorale emiliano-romagnolo all'anno 2007 e piano decennale di gestione. In: Preti M. (ed). *I quaderni di ARPA*, Regione Emilia-Romagna, Bologna, Italy.
- Browder A.E. and Dean R.G., 2000. Monitoring and comparison to predictive models of the Perdido Key beach nourishment project, Florida, USA. *Coastal Engineering* 39 (2-4), 173-191.
- Carniel S., Sclavo M. and Archetti R., 2011. The use of integrated wave-current-sediment numerical tools to model coastal dynamics: applications in the North Adriatic Sea. In *Proc. 5th International Short Conference on Applied Coastal Research*.
- Davidson M., Van Koningsveld M., De Kruif A., Rawson J., Holman R., Lamberti A., Medina R., Kroon A. And Aarninkhof S., 2007. The CoastView project: Developing video-derived Coastal State Indicators in support of coastal zone management. *Coastal Engineering* 54: 463-475.
- Dean R.G., 1977. Equilibrium beach profiles: U.S. Atlantic and Gulf coasts. In: *Ocean Engineering Technical Report*, vol. 12. Department of Civil Engineering and College of Marine Studies, University of Delaware, USA.
- Dean R.G., 1983. Principles of beach nourishment. In: Komar P.D. (ed.), *CRC Handbook of Coastal Processes and Erosion*. CRC Press, Boca Raton, USA, 217-232.
- Elko N.A., Holman R.A. and Gelfenbaum G., 2005. Quantifying the rapid evolution of a nourishment project with video imagery. *Journal of Coastal Research* 21(4), 633-645.
- Grunnet N.M. and Ruessink B.G., 2005. Morphodynamic response of nearshore bars to a shoreface nourishment. *Coastal Engineering* 52, 119-137.

- Hanson H. and Kraus N.C., 1989. GENESIS, A Generalized Model for Simulating Shoreline Change. In: Technical Report CERC-89-19, Coastal Engineering Research Center. U.S. Army Corps of Engineer Waterways Experiment Station, Vicksburg, MS, USA.
- Holman R.A. And Stanley J., 2007. The history, capabilities and future of Argus. *Coastal Engineering* 54 (6-7), 477-491.
- Jimenez A., Osorio A., Marino-Tapia I., Davidson M., Medina R., Kroon A., Archetti R., Ciavola P. and Aarnikhof S., 2007. Beach recreation planning using video-derived coastal state indicators. *Coastal Engineering* 54 (6-7), 504 – 522.
- Kroon A., Aarninkhof S.G.J., Archetti R., Armaroli C., Gonzalez M., Medri S., Osorio A., Aagaard T., Davidson M.A., Holman R.A. and Spanhoff R., 2007. Application of remote sensing video systems for coastline management problems. *Coastal Engineering* 54(6-7), 493-505.
- Lamberti A., Archetti R., Kramer M., Paphitis D., Mosso C. and Di Risio M., 2005. European experience of low crested structures for coastal management. *Coastal Engineering* 52 (1011), 841-866, ISSN: 0378-3839.
- Larson M., Hanson H. and Kraus N. C. 1997. Analytical solutions of one-line model for shoreline change near coastal structures. *Journal of Waterway, Port, Coastal, and Ocean Engineering*, Vol. 123, (4). 180 – 191.
- Nieto M. A., Garau B., Balle S., Simarro G., Zarruk G.A., Ortiz A., Tintoré J., Álvarez-Ellacuría A., Gómez-Pujol L. and Orfila A., 2010. An open source, low cost video-based coastal monitoring system. *Earth Surface Processes and Landforms* 35 (14), 1712-1719.
- Pelnard-Considere R., 1956. Essai de Theorie de l'Evolution des Formes de Rivage en Plages de sable et de Galets. In: 4th Journees de l'Hydraulique. Les Energies de la Mer, Question III. Rapport 1.
- Preti M., 2002. Ripascimento di spiagge con sabbie sottomarine in Emilia-Romagna. *Studi Costieri* 5, 107-134.
- Preti M., Aguzzi M., Costantino R., De Nigris N. and Morelli M., 2011. Monitoraggio delle spiagge nel periodo 2007-2009. *Studi costieri*, in press.
- Romagnoli C., and Archetti R. 2011. post-nourishment shoreline evolution of a partially protected beach. *Geoacta*. In press.
- Teatini P., Gambolati G., Tomasi L. and Putti M., 1997. Simulation of land subsidence due to gas production at Ravenna coastline. In: Gambolati G. (ed.) CENAS project, University of Padova (Italy), 135-152.
- Van Duin M.J.P., Wiersma N.R., Walstra D.J.R., Van Rijn L.C. and Stive M.J.F., 2004. Nourishing the shoreface: observations and hintcasting of the Egmond case, The Netherlands. *Coastal Engineering* 51, 813-837.

Dune erosion regimes observed in large-scale experiments

Felice D'Alessandro¹ and Giuseppe Roberto Tomasicchio¹

Abstract

Different regimes of wave attacks on a sandy beach/dune system have been observed during a recent large-scale experiment in a flume. The physical model tests have been performed at the LIM/UPC in Barcelona, within the EU-Hydralab III Integrated Infrastructure Initiative (Tomasicchio et al. 2011a). An innovative 'composite' numerical modelling approach has been adopted to reach a model test set-up valid to observe dune erosion, overwash and breaching induced by a combination of water levels and wave conditions (Kamphuis 1996, 2010; Tomasicchio et al. 2011b). The study provides a unique set of physical data concerning hydrodynamics, sediment concentrations and beach-dune profile evolution. In the present paper, profile measurements have been adopted to analyze the retreat of the dune face and calculate the eroded volume at specific time intervals. Furthermore, profile measurements have been also used to calibrate and verify the numerical model C-SHORE (Kobayashi et al. 2007, Figlus et al. 2010) to predict beach-dune profile modifications over the near-shore region.

Keywords: dune erosion, large-scale experiments, numerical model

1 Introduction

Dunes and beaches are effective natural coastal defences, due to their ability to adapt to the forcing agents (waves, tides, currents, wind). However, in sediment-starved coastal sectors, they often become out of balance with the forcing agents, and erosion takes place, pushing the coastline inland and causing dune destruction. Particularly, under storm-driven surges, wind and waves can cause severe dune erosion with rapid large-scale morphological changes, and possibly damage to hinterland infrastructure and loss of human lives (Tomasicchio et al. 2011a, Sancho et al. 2011). It is thus crucial to better understand the hydrodynamics and sediment dynamics of such systems (beaches and coastal dunes) and under such conditions, in order to better establish efficient coastal protection schemes. It is common to define four regimes of storm attack on a beach/dune system (Sallenger et al. 2003): (1) swash regime with wave run-up confined to the foreshore; (2) collision regime with swash and run-up to the dune face; (3) overwash regime with wave run-up overtopping the dune crest; (4) breaching and inundation regime. Coastal engineers are often faced with estimation of the impact on the beach-dune system of severe storms in terms of recession distance, eroded volume and overwash rate. In the recent years several numerical models have been developed for these purposes (e.g. C-SHORE, Kobayashi et al. 2007; Figlus et al. 2010). As an alternative to a numerical approach, analytical models typically require marked simplifications in the description of the governing processes, forcing, and initial and boundary conditions, whereas numerical models can deal with these aspects with less restrictions. However, analytical models still have their use since the simplicity make them easy to apply, which is valuable in the preliminary stage of a project when approximate estimates are required (Larson et al. 2004).

The present paper provides further insight in the knowledge of the different mechanisms of dune erosion induced by wave action. The following sections give a brief description of the adopted composite modelling approach which has successfully used to individuate the set-up of the physical model tests; the wave conditions and the observations of the investigated dune erosion regimes are then described. Furthermore, the beach-dune profile evolution due to the impact of different wave attacks has been analyzed and discussed.

¹ University of Salento, Department of Engineering, via Monteroni 73100 Lecce, Italy – felice.dalessandro@unisalento.it; roberto.tomasicchio@unisalento.it

2 Set-up of physical model

A carefully designed set of experiments has been conducted at the CIEM wave flume of the *Laboratori d'Enginyeria Marítima* (LIM) at the *Universitat Politècnica de Catalunya* (UPC), from October to December 2009 (Tomasicchio et al. 2011a). The dimensions of the CIEM wave flume (100 m long, 3 m wide and 5 m deep) allowed to perform large-scale tests with a movable bed beach. The initial cross-shore beach and dune profile is shown in Figure 1.

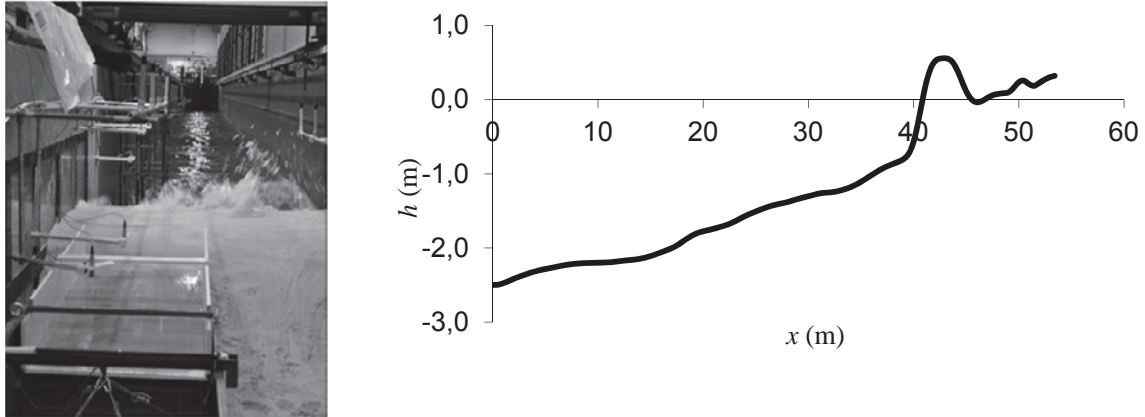


Figure 1: The considered cross-shore profile

The dune front and back faces had equal slopes (0.445). The beach was formed of a quite homogeneous sand, with median diameter, d_{50} , equal to 0.246 mm, and fall velocity, w_f , of 34 mm/s. A wedge-type wave paddle was capable to generate irregular waves based on a Jonswap spectrum with peak enhancement factor, γ , equal to 3.3.

The study of the interaction of a sandy beach-dune system with waves is complex since the beach response is governed by a combination of geometric, hydrodynamic and sediment variables which are very difficult to manage. Although the experience and knowledge of the investigator can help to get an idea about the beach response, a number of uncertainties persist, indicating that a single tool cannot adequately reproduce all processes involved in such coastal problems. Recent trends in designing physical model experiments have included the concept of 'composite modelling' (Kamphuis 1996, 2010; Tomasicchio et al. 2011b) integrating the benefits of both physical (experience) and numerical models (predictable capability), using them together in a balanced approach. In this path, in order to obtain more insight into the effect of the design wave characteristics on dune reshaping, a numerical study has been carried out by varying the off-shore water depth, h_o , and incident wave conditions for given initial bottom profile and dune geometry. The interested reader is referred to Tomasicchio et al. (2011b) for a detailed description of the composite modelling approach. The numerical study gave useful directions concerning the most suitable wave conditions and h_o to be reproduced in the wave flume. After this process was completed, the actual physical tests programme to be run in the CIEM flume was defined with the scope to investigate the influence on the dune erosion rate exerted by different load parameters (significant wave height, $H_{s,o}$, peak wave period, T_p , wave steepness, s_p , and h_o). Two different values of h_o have been considered in the flume. The lower value, $h_o = 2.35$ m, has been increased to 2.50 m to simulate the storm surge in three out of a total of nine tests. As a consequence, two different freeboards, F , have been considered. The hydrodynamic boundary conditions for each test varied and are summarized in Table 1. The initial beach geometry was rebuilt at the end of each test. Wave conditions have been selected in order to investigate the influence of the considered factors ($H_{s,o}$, T_p , s_p and h_o) on the dune erosion rate. The duration of a single test was divided into different wave attacks composed by 250, 250, 250, 500, 1000 and 1000 waves, respectively. Wave attacks for each test have been conducted until total dune collapse.

Table 1: Tests programme with wave conditions at the wave paddle

h_o (m)	F (m)	Test	$H_{s,0}$ (m)	T_p (s)	s_p	Duration (s)	Key findings
2.35	0.65	A	0.25	2.5	0.026	4500	Collision regime
		B	0.30	2.5	0.031	4500	Collision regime
		C	0.30	3.0	0.021	5400	Minor overwash – Collision regime
		D	0.33	2.5	0.034	4500	Collision regime
		E	0.33	3.0	0.024	5400	Minor overwash – Collision regime
		F	0.33	3.5	0.017	6300	Major overwash – Collision regime
2.50	0.50	G	0.25	2.5	0.026	4500	Collision regime
		H	0.30	2.5	0.031	4500	Minor overwash – Collision regime
		I	0.33	3.0	0.024	600	Major overwash and breaching

Measurements of water surface elevation, flow velocities and sediment concentration along the flume were carried out during each test with several instruments. Bed profile measurements were conducted using a mechanical profiler, together with detailed photogrammetric surveys at the emerged part of the dune. The profiles were measured at the beginning/ending of each time series. Overtopping and overwashing fluxes over the dune crest were measured by means of acoustic wave gauges, pressure sensors and an overtopping/overwashing collection tank. More details on the experimental setting is given in Tomasicchio et al. (2011a).

3 Observations on dune erosion regimes

During the model tests, three different regimes of dune erosion have been observed (Sallenger et al. 2003): collision, overwash and breaching regimes.

In the following, observations from two model tests, selected among the others as representative of collision with minor overwash regime (Test E) and major overwash and breaching regime (Test I), respectively, are shown.

Figure 2 shows an example of minor overwash with collision regime occurred during Test E.

At the beginning of the wave attack, the incident waves reach the dune face and run over it. Sediment eroded from the dune was predominantly transported in the offshore direction. Only limited wave overtopping and sediment overwash occurred (Figure 2 (a)). As a result, the dune front becomes steeper with the formation of scarping at the toe of the dune (Figure 2 (b)). The incoming breaking waves impacting with the outgoing reflected broken waves (wave collision) generate a large amount of turbulence (Figure 2 (c and d)). As a consequence, the dune face retreats under waves impacting it. Episodically, part of the dune face collapses and big lumps of sediment fall or slide downwards. This sand is picked up by swash and surf zone processes that move the sediment seaward to form a bar/step (Figure 2 (e and f)) (Tomasicchio et al. 2011a).

A rapid increase of wave overtopping and sediment overwash was observed in conjunction with rapid dune crest lowering during Test I (Figures 3 (a), (b) and (c)). The evolution of the eroded area corresponded with the increment of the collected sand volume in the sediment trap, confirming dune erosion mostly due to overwash (Tomasicchio et al. 2011a). The wave action was stopped after 250 waves ($t = 600$ s) when the dune was breached. The dune breach appeared at the left side of the flume, clearly influenced by side wall effects highly limiting the lateral diffusion of incoming and reflected wave energy. A similar behaviour has been observed during small-scale flume experiments conducted by Kobayashi et al. (2007). In these experiments, however, differently respect the LIM model tests, the dune breaching was caused by a few overtopping waves at the alongshore location where the dune crest was lowered earlier by minor wave overwash. As reported by the authors, the dune breaching appeared to be sensitive to the slight alongshore non-uniformity (Kobayashi et al. 2009).

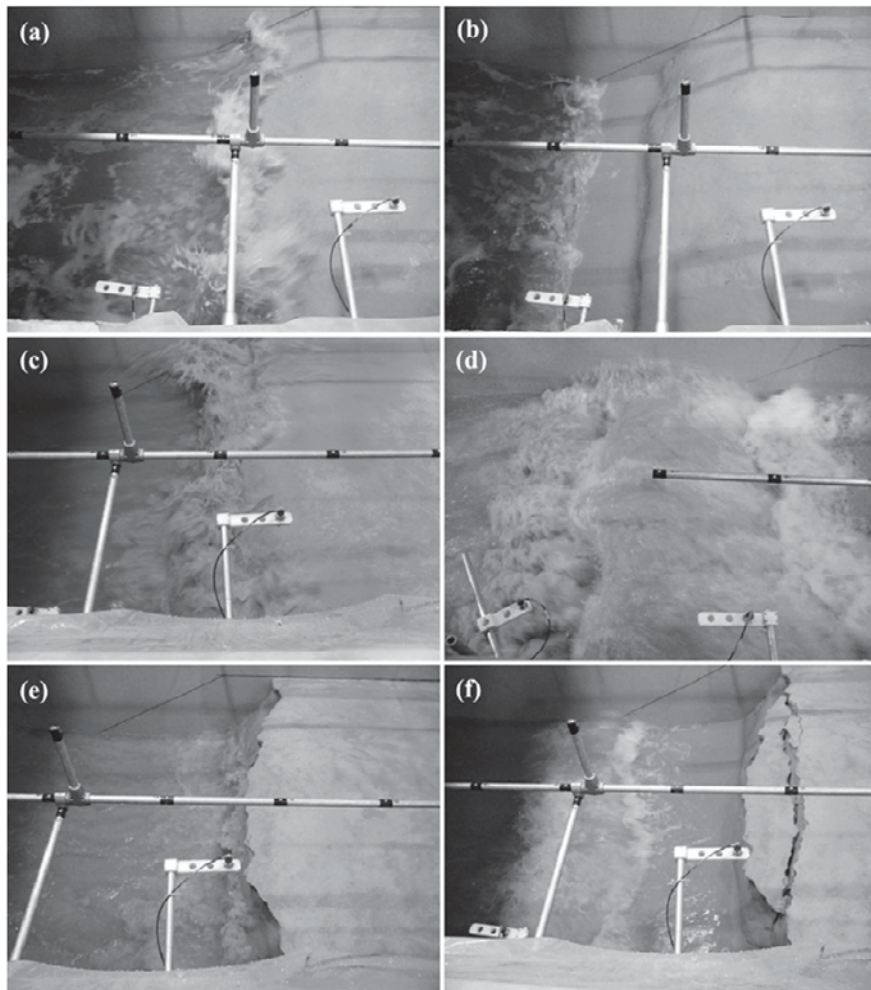


Figure 2: The observed collision regime. Test E

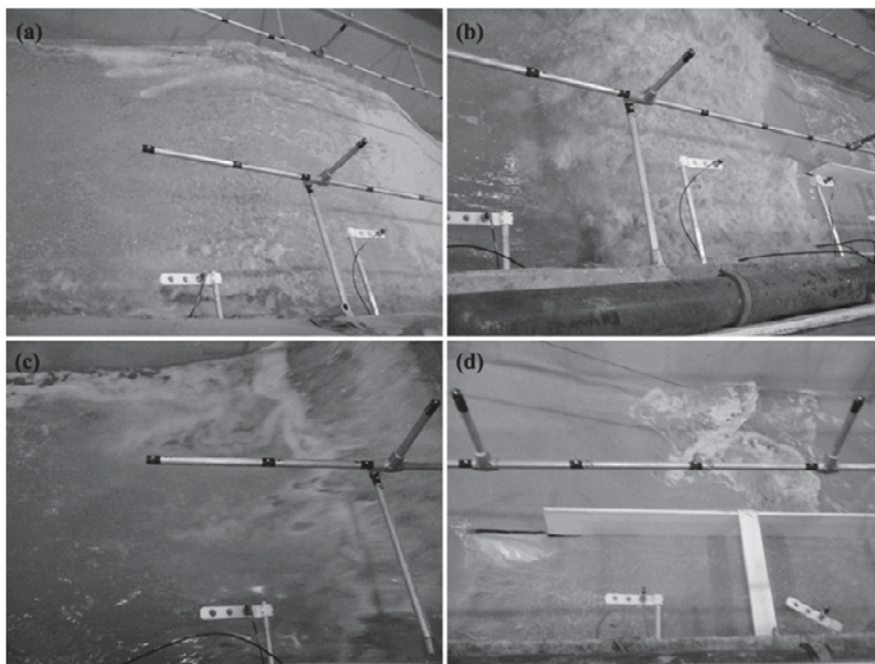


Figure 3: The observed overwash regime. Test I

The beach profile surveys for each test (A to H) have been adopted to determine the retreat of the dune face, Δx , and to obtain the eroded volume, ΔV_E , at specific time intervals (after 250, 500, 750, 1250 and 2250 waves). Figures 4 and 5 show, for each test, the variation of the dune recession rates in terms of $\Delta x/\Delta t$ and $\Delta V_E/\Delta t$, respectively, during the wave attacks.

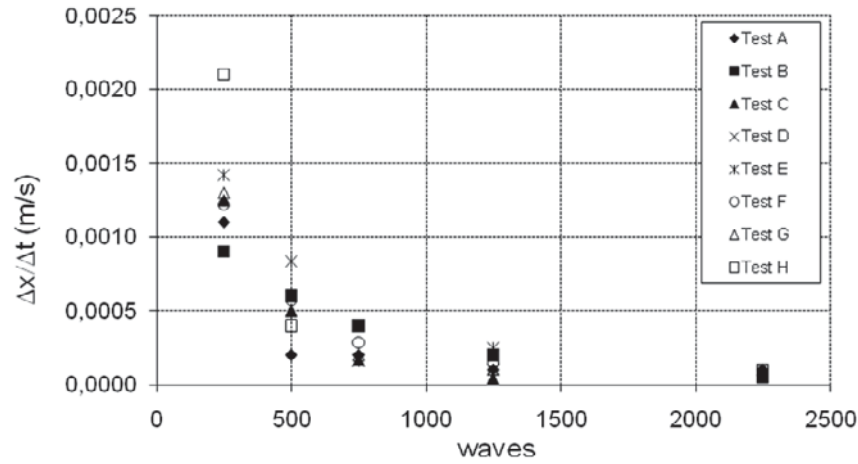


Figure 4 : $\Delta x/\Delta t$ vs number of waves (tests A to H)

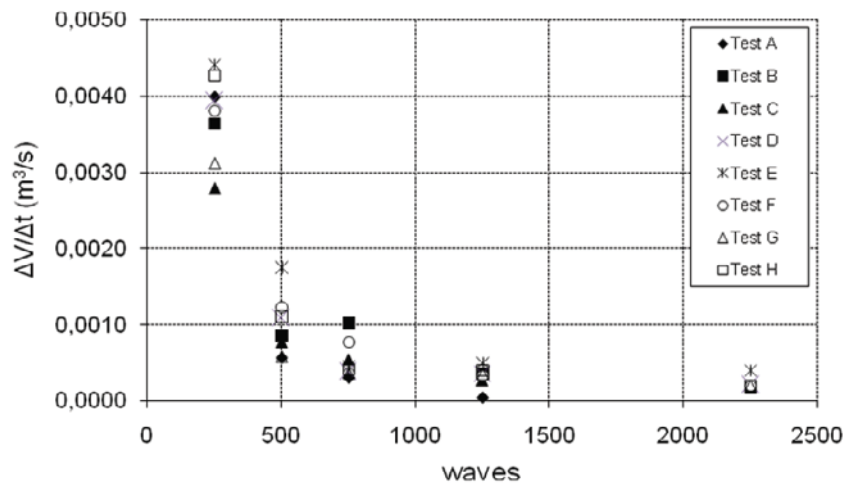


Figure 5 : $\Delta V_E/\Delta t$ vs number of waves (tests A to H)

The observed behaviour is similar for each test. The initial survey ($t = 0$ min) was taken prior to wave action on the beach. Subsequent surveys showed that the dune face retreated rapidly during the first 250 waves, losing a large amount of its original sand volume. The dune face continued to decrease as the test progressed, but the rate of changes were smaller.

4 Numerical model calibration and verification

The adopted time-averaged numerical model was C-SHORE (Kobayashi et al. 2007) predicting beach-dune profile evolution over the near-shore region in response to waves, currents and water levels. The model considers wave and current interaction and wave-related sediment transport. Data on the beach profile evolution were used to calibrate and validate C-SHORE (Kobayashi et al. 2007). A selection of 6 representative tests was considered. The measured initial profile at time $t = 0$ was adopted as input bathymetry. C-SHORE was implemented with the values of parameters reported in Tomasicchio et al. (2011a). Figure 6 shows the C-SHORE predictions along with initial and final measured profiles at the end of the wave attacks.

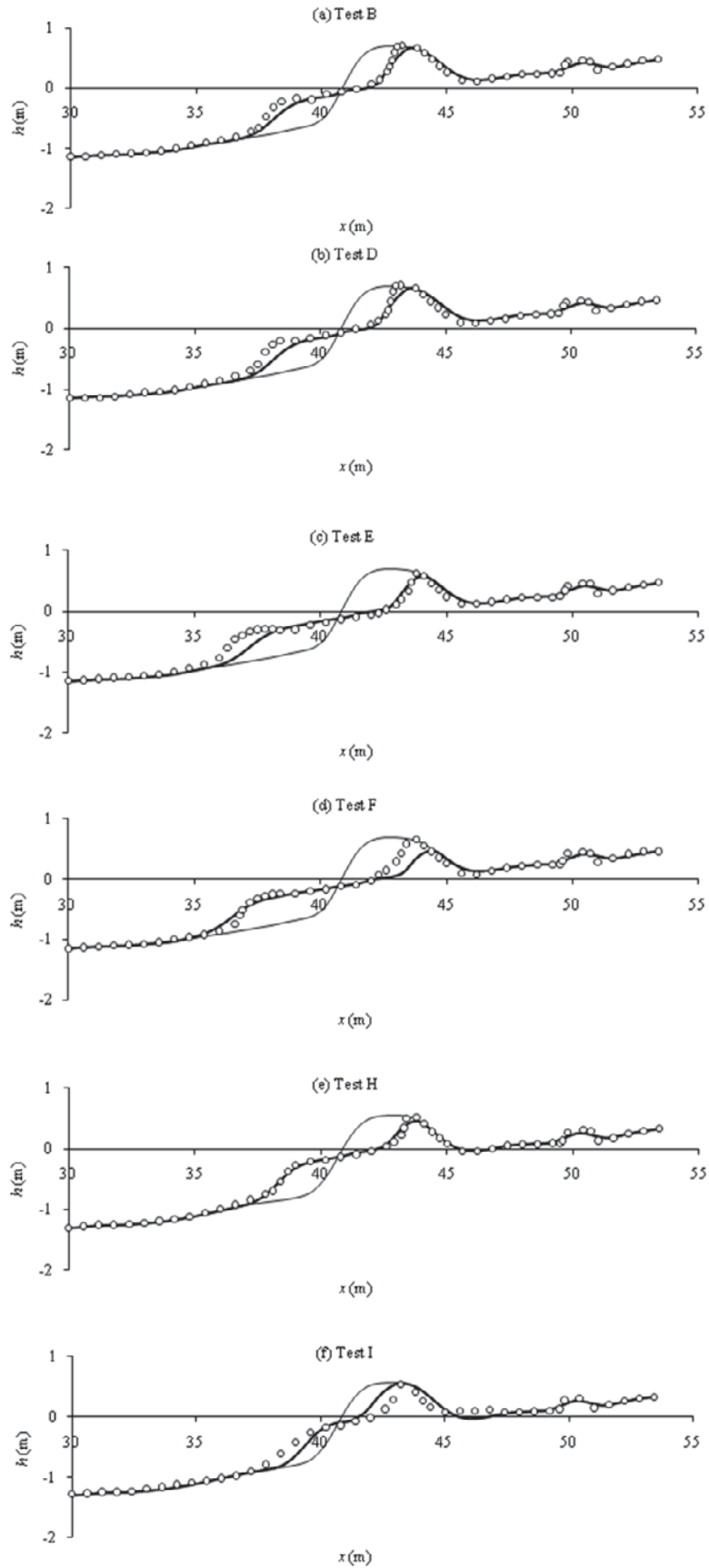


Figure 6: Comparisons between (○) measured, (—) computed and (---) initial beach profiles

The numerical model is shown to be generally in agreement with the experimental data. Test F and Test I have more evident scatter between physical observations and numerical results. In Test I overtopping waves already started to significantly erode the backdune during the first waves (Fig. 6f). Dune erosion and overwash lowered and destroyed the entire dune quickly until dune breaching occurred. During overwash, the increased backdune erosion due to increased wave overtopping resulted in apparent onshore migration of the lowered dune crest until the formation of an horizontal platform in substituting the concave beach. Note that the adopted numerical model C-SHORE was developed to predict berm and dune erosion in the absence of overtopping and in this form cannot predict accurately the sediment accretion landward of the dune crest around the cross-shore location at $x = 46$ m due to the major overwash event.

5 Conclusions

Large-scale physical model tests were performed to observe the occurrence of 3 different dune erosion regimes (Sallenger et al. 2003): collision, overwash and breaching under different water levels and wave conditions. A composite modeling procedure was considered to define the wave characteristics and the offshore water depth to be reproduced in the flume for the given beach-dune profile. It is shown that the propaedeutic use of a numerical model reduces a not negligible waste of time and cost during the selection of the physical model among different scenarios depending mostly on the number of the available technicians and tools in the laboratory (Tomasicchio et al. 2001b). Experimental data on beach profile evolution were used to calibrate and validate the numerical model C-SHORE (Kobayashi et al. 2007). The model is shown to predict the foreshore and dune profile evolution with reasonable accuracy in case of collision regime with minor overwash. In one case, the measured and computed profiles, landward of the dune crest, appear to compare poor under a combination of strong overtopping-overwash conditions. To improve the capability in capturing the morphological processes during the transition from minor to major overwash, the C-SHORE model was recently improved. Data from experiments with major overwash represent a useful source for the calibration and verification of the recently extended C-SHORE code (Figlus et al. 2010).

6 Acknowledgements

The present research has been supported by the European Community's Sixth Framework Programme through the grant to the budget of the Integrated Infrastructure Initiative HYDRALAB III within the Transnational Access Activities, Contract no. 022441. It also was partly funded by the Italian Ministry of University and Research (PRIN 2008 – '*Strumenti operativi per la stima della vulnerabilità dei litorali sabbiosi anche in presenza di strutture costiere*').

7 References

- Figlus, J., Kobayashi, N., Gralher, C., Iranzo, V. (2010): Wave overtopping and overwash of dunes. *J. Wway., Port, Coastal and Ocean Eng.* 137(1), 26-33.
- Kamphuis, J.W. (1996): Coastal hydraulic models. 25th Int. Conf. *Coastal Eng.*, Physical Modeling Workshop, Orlando FL. ASCE.
- Kamphuis, J.W. (2010): Coastal modeling: Indispensable design tool, but how? Proc. *Coastlab '10*, 29-30. IAHR.
- Kobayashi, N., Agarwal, A., Johnson, B.D. (2007): Longshore current and sediment transport on beaches. *J. Wway., Port, Coastal and Ocean Eng.* 133(4), 296-306.
- Kobayashi, N., Buck, M., Payo, A., Johnson, B.D. (2009): Berm and dune erosion during a storm. *J. Wway., Port, Coastal and Ocean Eng.* 135(1), 1–10.
- Larson, M., Erikson, L., Hanson, H. (2004): An analytical model to predict dune erosion due to wave impact. *Coastal Eng.* 51(8–9), 675–696.

- Sallenger, A.H., Howd, P., Stockdon, H., Guy, K., Morgan, K.L.M. (2003): On predicting storm induced coastal change. Proc. *Coastal Sediments*, Clearwater Beach FL, World Scientific [CD-ROM].
- Sancho, F., Abreu, T., D'Alessandro, F., Tomasicchio, G.R., Silva P.A. (2011): Surf hydrodynamics in front of collapsing coastal dunes. *Journal of Coastal Research*, SI 64, ISSN 0749-0208.
- Tomasicchio, G.R., Sanchez Arcilla, A., D'Alessandro, F., Ilic, S., James, M., Fortes, C.J.E.M., Sancho, F., Schüttrumpf, H. (2011): Large-scale flume experiments on dune erosion processes. *Journal of Hydraulic Research*, ISSN 0022-1686 print/ISSN 1814-2079 online, Vol. 49, No. S1, pp. 20-30.
- Tomasicchio, G.R., D'Alessandro, F., Barbaro, G. (2011): Composite modelling for large-scale experiments on wave-dune interactions. *Journal of Hydraulic Research*, ISSN 0022-1686 print/ISSN 1814-2079 online, Vol. 49, No. S1, pp. 15-19.

Tsunamis in the Gulf of Kyparissia (western Peloponnese, Greece) – risk assessment based on numeric simulation and field evidence

Björn R. Röbke¹, Holger Schüttrumpf², Theide Wöffler², Hanna Hadler³, Timo Willershäuser³ and Andreas Vött³

Abstract

This paper provides an assessment of the tsunami hazard in the Gulf of Kyparissia (western Peloponnese, Greece) derived from numeric simulations of tsunami waves and geo-scientific field evidence of tsunami-impact during the Holocene. Located in the close vicinity to the seismically highly active Hellenic Trench and showing a distinct submarine relief prone to submarine mass movements, the Gulf of Kyparissia exhibits a high tsunamigenic potential. This is reflected by the large number of tsunamis listed in tsunami and earthquake catalogues for this region as for the whole west coast of Greece. The analysis of selected vibrocores and earth resistivity transects obtained from the coast between Katakolo and Kato Samiko, showed that the coast was affected by severe tsunami impacts both during historic and prehistoric times. In order to gain insight into the dynamics of tsunami inundation at the northern gulf coast, six tsunami scenarios were simulated, namely with tsunami waves approaching from the west, southwest and south and with two different intensities (moderate and extreme). In all scenarios, the gulf coast was seriously affected by the simulated tsunami waves. Especially in the extreme scenarios, dramatic flooding of the whole coast was observed with considerable inland penetration and inundation depth. The greatest inland penetration of nearly 15 km was recorded in the valley of the Alpheios, showing a substantial funnel effect. Taking into consideration the high vulnerability of the area, especially the numerous villages, tourist centers and cities along the coast, for example the city of Pyrgos with almost 24,000 inhabitants, the damage potential by tsunami inundation is high.

Keywords: Gulf of Kyparissia, tsunami, tsunamite, numeric simulations, palaeotsunami, Olympia Tsunami Hypothesis

1 Introduction

The Gulf of Kyparissia is an elongated bay in the eastern Ionian Sea at the western Peloponnese in Greece (Fig. 1). The gulf coast extends from the village of Katakolo in the northwest to the city of Filiatra in the southeast. The coastline's length amounts to circa 80 km and shows a crescentic course. The entire coast is dominated by sandy beaches showing a width of 20-70 m in the northern part and of 10-30 m in the southern part (Poulos et al. 2002: 256ff.). At the northern gulf coast, the beaches partly merge into dunes showing a width of up to 600 m and a maximum altitude of 15 m a. s. l. (above present sea level) (Poulos 2002: 256 ff.). The dunes separate two drained lagoons from the gulf, the former Mouria and Agoulenitsa Lagoon, now lying a few meters below sea level. Further inland, the former lagoons are bordered by hills out of Lower Pleistocene marine mud-, silt- and sandstones, marl and sandy conglomerates of the Vounargo-Formation (Lekkas et al. 2000: 23; Papanikolaou et al. 2007: 16 f.) reaching elevations up to 200 m a. s. l. To the south of the former Agoulenitsa Lagoon as far as the city of Filiatra, extensive coastal lowlands are missing in favour of more elevated areas between 10 and 100 m a. s. l. appear close to the present coastline.

¹ Institute for Geography, Universität zu Köln, Albertus-Magnus-Platz, 50923 Köln, Germany, broebke@smail.uni-koeln.de

² Institute of Hydraulic Engineering and Water Resources Management, RWTH Aachen, Mies-van-der-Rohe-Straße 1, 52056 Aachen, Germany, schuettrumpf@iww.rwth-aachen.de

³ Institute for Geography, Johannes Gutenberg-Universität, Johann-Joachim-Becher-Weg 21, 55099 Mainz, Germany, voett@uni-mainz.de

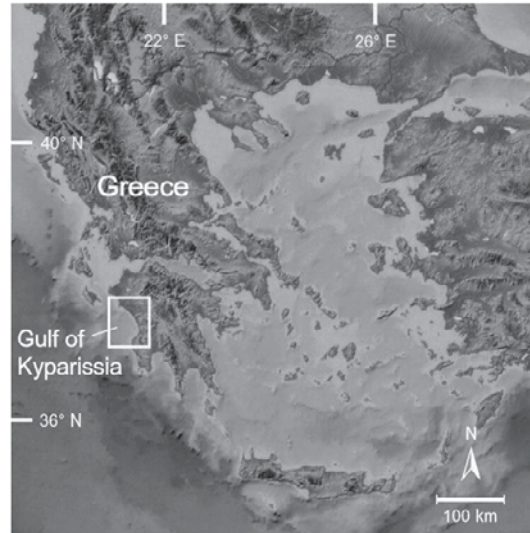


Figure 1: Geographical location of the Gulf of Kyparissia (Peloponnese, Greece)

In the northern part of the gulf, the perennial Alpheios River, the largest river of the Peloponnese, flows into the Ionian Sea. Due to strong littoral currents in the Gulf of Kyparissia, the Alpheios River formed a cusped delta of about 110 km² (Poulos et al. 2002: 252ff.). The entire coastal area is used for agricultural purpose, especially the area of the former lagoons as well as the Alpheios valley, where irrigation farming is prevalent. Besides the agriculture the landscape of the gulf coast is shaped by several villages and cities, the city of Pyrgos being the largest one, located in the northern part and counting almost 24,000 inhabitants (General Secretariat of the NSSG 2001). The total population of all communities situated at the coast between Katakolo and Filiatra together with those located in the Alpheios valley up to the ancient Olympia accounts to circa 130,000. Additionally, about 300,000 tourists visit the region (between May and September every year (General Secretariat of the NSSG 2010a; 2010b) which makes the Gulf of Kyparissia to one of the most vulnerable areas in coastal Greece.

As tsunami and earthquake catalogues demonstrate, the Gulf of Kyparissa is located in the most tsunamigenic area of the entire Mediterranean, namely the west coast of Greece. According to Schielein et al. (2007: 164ff.) and Soloviev et al. (2000: 14) there are 47 and 44 tsunami reports for this coastal area since 373 BC, respectively. The average recurrence interval for tsunamis that have occurred along the coasts of the Ionian Sea since 1622 AD (without the Gulf of Corinth) – irrespective of their magnitude – is 14 years only (Soloviev et al. 2000: 14).

The considerable number of tsunamis at the west coast of Greece is chiefly a consequence of the high seismicity in this region due to the vicinity to the Hellenic Trench, located less than 100 km west of the Peloponnese, where the African Plate is subducted by the Aegean Microplate, a part of the Eurasian Plate, by a rate of roughly 35 mm/a (Shaw & Jackson 2010: 966). The subduction of the African Plate is associated with strong earthquakes in the area between the Hellenic Trench and the western Peloponnese. This becomes obvious regarding the mean repetition rate of earthquakes with $M_s \geq 6.5$ in this region between 1801 and 2011 with a value of 15 years only (Papazachos 1996: 893; Benetatos et al. 2004: 257ff.; USGS 2012). Almost all of these earthquakes are shallow focus earthquakes with focal depths of less than 40 km originating at shallow dipping thrust faults as long as 300 km (Papazachos 1996: 894ff.; Papoulia et al. 2008: 1ff.; Tsambas et al. 2009: 48ff.). Consequently, their focal mechanisms can be attended with substantial vertical shifts of the earth crust, not uncommonly reaching values of 1 m over a large area (Ferentinos 1991: 274) – a setting prone to generate tsunamis (Bryant 2008: 135 f.). Besides the high seismicity of the Gulf of Kyparissia also the distinct submarine relief of this region, which is vulnerable to submarine mass movements (Ferentinos 1991: 266ff., Ferentinos 1992: 93ff.; Poulos 2002: 254ff.), involves a remarkable tsunamigenic potential. Finally the west coast of Greece in general may be hit by teletsunamis generated further away in other tsunamigenic zones of the Mediterranean such as the eastern part of the

Hellenic Trench, the Calabrian Arc, the east coast of Sicily (Mount Etna) or the volcanic arc in the southern Aegean (cf. Schielein et al. 2007: 161ff.).

The main objectives of our study were (1) to search for high-energy sediments as field evidence of severe palaeotsunami impact during the Holocene, (2) to generate numeric simulation calculations of tsunami waves in order to better understand tsunami inundation, and (3) to compare field evidence with modelling results in terms of tsunami risk assessment for the Gulf of Kyparissia.

2 Methods

During several field campaigns between March 2009 and March 2011 numerous vibracores with diameters of 60 and 50 mm were retrieved from the coastal lowlands in the northern part of the Gulf of Kyparissia using a hand-operated engine driven Atlas Copco coring device (type Cobra mk1) as well as a Nordmeyer drilling rig (type RS 0/2.3). Maximum coring depth was 12 m. X-ray fluorescence analyses were conducted for each core by means of a handheld instrument (type Niton XI3t 900S GOLDD) in order to obtain the chemical composition of the sediment. Furthermore, earth resistivity tomography (ERT), using a multi-electrode geo-electrical instrument (type Syscal R1 Plus) and the RES2DINV inversion model, was applied for spatial interpolation and extrapolation of vibracore data. A Topcon DGPS-device (type HiPer Pro) served for determining the position and elevation of coring sites and ERT transects.

The digital terrain model used for the numeric simulations is based on terrain models of ASTER GDEM and bathymetric data of several map sheets of the Soviet Ordnance Map (1:50,000, 1:200,000 and 1:500,000) and has a resolution of 30 x 30 m². Numeric simulations of tsunami waves in the Gulf of Kyparissia were implemented using the simulation software Delft3D 4.0 developed by the Dutch Institute Deltares. Simulation calculations were conducted using the program module Delft3D-FLOW and a two-dimensional, depth-averaged calculation approach (Deltares 2010: 187ff.). The computational grid used had a resolution of 60 x 60 m² in the area of interest (cf. Fig. 4) and of 900 x 900 m² in the remaining parts of the simulation area, which had an overall extent of about 166 x 148 km². In total, six tsunami scenarios were simulated arising from three different propagation directions (tsunamis from west, southwest and south) and two different magnitudes (moderate and extreme). A tripartite tsunami wave train was simulated with increasing wave heights, namely 0.5 m, 1.0 m and 2.0 m for the moderate scenarios and 2.5 m, 5.0 m and 10.0 m for the extreme scenarios. The boundary conditions for the simulation calculations were generated according to the solitary wave theory (cf. Lehfeltdt et al. 2007: 112f.). Solitary waves with the above-mentioned wave heights were calculated using the following formula by Dean & Dalrymple (1991: 314ff.) based on the shallow water wave theory by Korteweg & DeVries (1895):

$$\eta = H \cdot \operatorname{sech}^2 \left(\sqrt{\frac{3-H}{4-d^3}} \cdot c \cdot t \right)$$

with η elevation above water surface [m]

H wave height [m]

d water depth [m]

t time [s]

c wave's phase velocity [s]

A Manning coefficient of 0.03 was chosen in order to consider the increased friction on the coast's mainland, showing woodless, partly developed and cultivated land (Bryant 2008: 45f.). The time step was set to 3 s in order to satisfy the CFL stability condition (Deltares 2010: 39 f.). Simulations were implemented for timeframes of 4 h 45 min in the extreme scenarios and of 5 h 30 min in the moderate scenarios.

3 Geo-scientific evidence of multiple tsunami impact

In the following, detailed stratigraphic information for two vibracores recovered from the northern coastal lowlands of the Gulf of Kyparissia is presented. Besides the sedimentological composition of the cores also the Ca-Ti ratios are regarded in order to differentiate between marine and terrestrial influences. As calcium carbonate production by organisms in marine environments is high and the occurrence of titanium predominantly reflects terrigenous input by subaerial weathering, marine sediments are characterized by high Ca-Ti ratios, terrestrial deposits by low Ca-Ti ratios on the contrary (cf. Vött et al. 2011a: 14f.; Vött et al. 2011b: 260ff.).

Vibracore AGI 5 (37.674483° N/21.387230° E, ground surface at 0.28 m a. s. l.) was retrieved at the northern margin of the former Mouria Lagoon about 500 m to the south of the village of Aghios Ioannis on a ploughed tomato field, nearly 2 km away from the present coastline. The lower part of the core is made up of clayey silt deposited in a limnic environment showing low Ca-Ti ratios (Fig. 2). At 8.95 m below ground surface (b. s.) the core shows a clear erosional unconformity which is followed by several fining-upward sequences consisting of medium sand to silt and exhibiting a slightly increased Ca-Ti ratio as an indicator of marine conditions. The abrupt change of the sedimentological environment documented by the erosional unconformity, fining-upward sequences as a typical feature of high-energy event deposits as well as the relative coarseness and the sediment's marine character suggest a sudden input of marine deposits by tsunami influence from the seaside. Subsequently, a long existing limnic environment developed, which is reflected by thick clayey silt to silty clay (8.23 - 2.11 m b. s.). Between 4.93 and 4.68 m b. s. the limnic sediments are interrupted by allochthonous, coarse-grained material showing fining-upward tendencies and topped by a mud cap. Although the Ca-Ti ratio of this layer is not increased, it may represent a second marine high-energy event because of its typical tsunamigenic features (cf. Morton et al. 2007). Above 2.11 m b. s. the limnic silt and clay is covered by a range of fining-upward sequences composed of gravel, sand and silt as well as numerous fragments of marine molluscs. This setting, in combination with the distinctly increased Ca-Ti ratio, indicates a third tsunami impact on the coast. Earth resistivity transect AGI ERT 5, running in a SSW-NNE direction close to coring site AGI 5, shows that the coarse-grained high-energy event layer continues in both directions but pinches out quite suddenly about 15 m inland from the coring site, which is another feature typical of tsunami influence. Finally, on top of this event layer, an anthropogenic soil consisting of clayey silty fine sand was found.

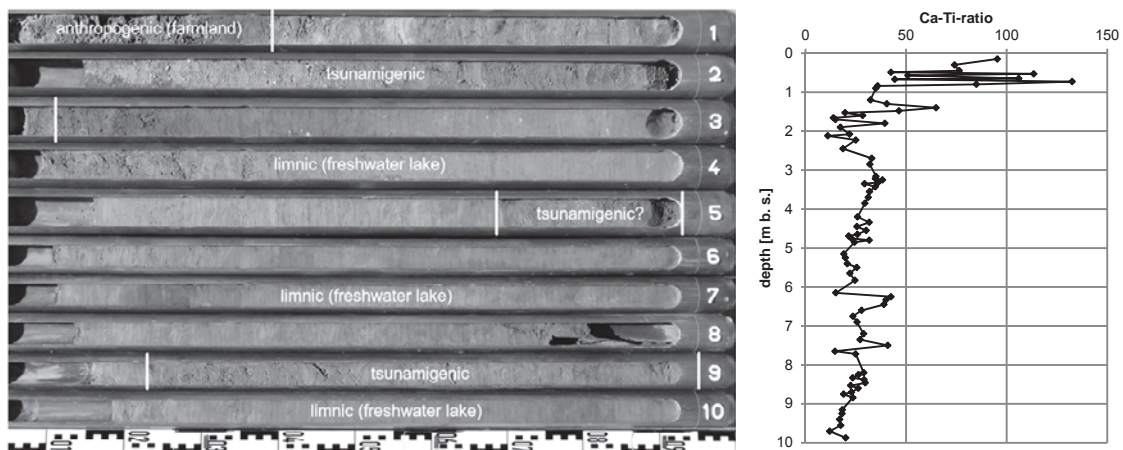


Figure 2: Facies profile of vibracore AGI 5 (left) and appropriate vertical profile of the Ca-Ti ratio (right). For location of vibracoring site see Fig. 4. Photo taken by T. Willershäuser, 2010.

Vibracore SAM 1 (37.542104° N/21.598991° E, ground surface at 11.18 m a. s. l.) was drilled almost 500 m to the south-southeast of the village of Kato Samiko on grassland at the foot of the Lapithas Mountains at the entrance of a small valley. The distance to the coastline is almost 2.5 km. The base of vibracore SAM 1 consists of silty fine sand probably deposited in a marine environment. The basal unit is covered by clayey silt with a comparatively low Ca-Ti ratio accumulated in a limnic environment. The following profile section (10.14 - 8.22 m b. s.) shows

layers of littoral, marine fine to coarse sand and abundant marine shell with an increased Ca-Ti ratio as well as limnic to fluvial clayey, fine sandy silt with a reduced Ca-Ti ratio. Subsequently, a limnic environment developed reflected by clayey silt low-energy deposits with a low Ca-Ti ratio (8.22 - 7.60 m b. s.). The limnic environment then changed into a fluvial milieu, lasting for a long time period. These conditions are reflected by a thick layer of fine sandy silt with a still low Ca-Ti ratio (7.60 - 2.79 m b. s.). The fluvial sediments are shortly interrupted between 7.00 and 6.75 m b. s. by allochthonous silty fine to coarse sand, showing a fining-upward tendency and a slightly increased Ca-Ti ratio. On the one hand, these deposits may arise from tsunami landfall, the other hand, they could also represent a fluvial high-energy flood event. In the latter case the slightly increased Ca-Ti ratio could be explained by the input of eroded material rich in calcium of the nearby Lapithas Mountains. Above 2.79 m b. s. vibracore SAM 1 shows a thick layer of fine to coarse sand also including silt and grus. Partly, the degree of sorting is distinctly low, however, there are several fining-upward sequences. A marine origin of these sediments is documented by numerous fragments of marine molluscs as well as by an abruptly increasing Ca-Ti ratio. Earth resistivity transect SAM ERT 4, which runs from WSW to ENE across coring site SAM 1, suggests that this high-energy event layer abruptly pinches out about 14 m further inland but continues seaward with an unchanged thickness. All in all, the layer between 2.79 and 0.85 m b. s., due to its characteristic sedimentary features, gives evidence of tsunami impact on the coast near Kato Samiko. Finally, this event layer is covered by fluvial deposits composed of fine sandy silt showing again a low Ca-Ti ratio.

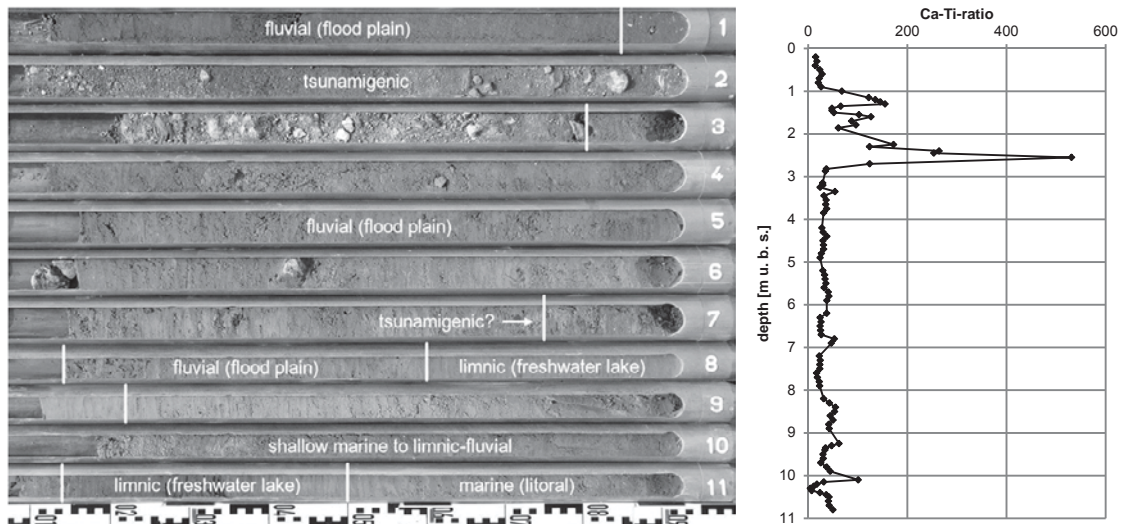


Figure 3: Facies profile of vibracore SAM 1 (left) and appropriate vertical profile of the Ca-Ti ratio (right). For location of vibracoring site see Fig. 4. Photo taken by T. Willershäuser, 2010).

4 Results of the simulated tsunami scenarios

In this paper, we present the results of a moderate scenario with a tsunami from a southwestern direction and wave heights of 0.5 m, 1.0 m and 2.0 m and the results of an extreme scenario with a tsunami from a western direction and wave heights of 2.5 m, 5.0 m and 10.0 m. These modeled tsunamis caused the most dramatic inundation in the northern gulf for the moderate and the extreme setting, respectively.

The first wave of the moderate scenario having an initial wave height of 0.5 m at the western margin of the simulation area arrives at the northern coast of the Gulf of Kyparissia after 1 h or so and causes water levels of about 1 m a. s. l. along the shoreline as a consequence of shoaling effects (Fig. 4, left column). This merely leads to an inundation of the beaches whereas the inland area is well protected especially by the dune belts. The second wave, arriving nearly one and a half hour afterwards, shows a slightly greater inundation most notably in the area of the Alpheios River delta as well as in the Bay of Katakolo. The third tsunami wave, hitting the northern gulf after a simulation time of about 4 h, causes water levels up to 6 m a. s. l. at the shoreline. Consequently, the entire area of the drained lagoons as well as the lowlands to the

west of the former Mouria Lagoon are flooded. To the south of the Kaiafa Lagoon waves reach an inland penetration of only a few 100 m due to higher elevations along the coast. In the Neda Valley, however, water masses penetrated up to 2 km inland. Biggest run-up heights of about 6 m are reached by the third tsunami wave, namely to the east of Cape Katakolo as well as along the entire coast to the south of the former Agoulenitsa Lagoon. Maximum inundation depths amount to more than 3 m, maximum flow velocity up to 4 m/s (= 14.4 km/h), namely in the area of the former Mouria Lagoon. Residential areas threatened by a moderate tsunami coming from the southwest are especially the village of Katakolo, the coast between Katakolo and the mouth of the Alpheios River as well as nearshore villages to the south of the Kaiafa Lagoon.

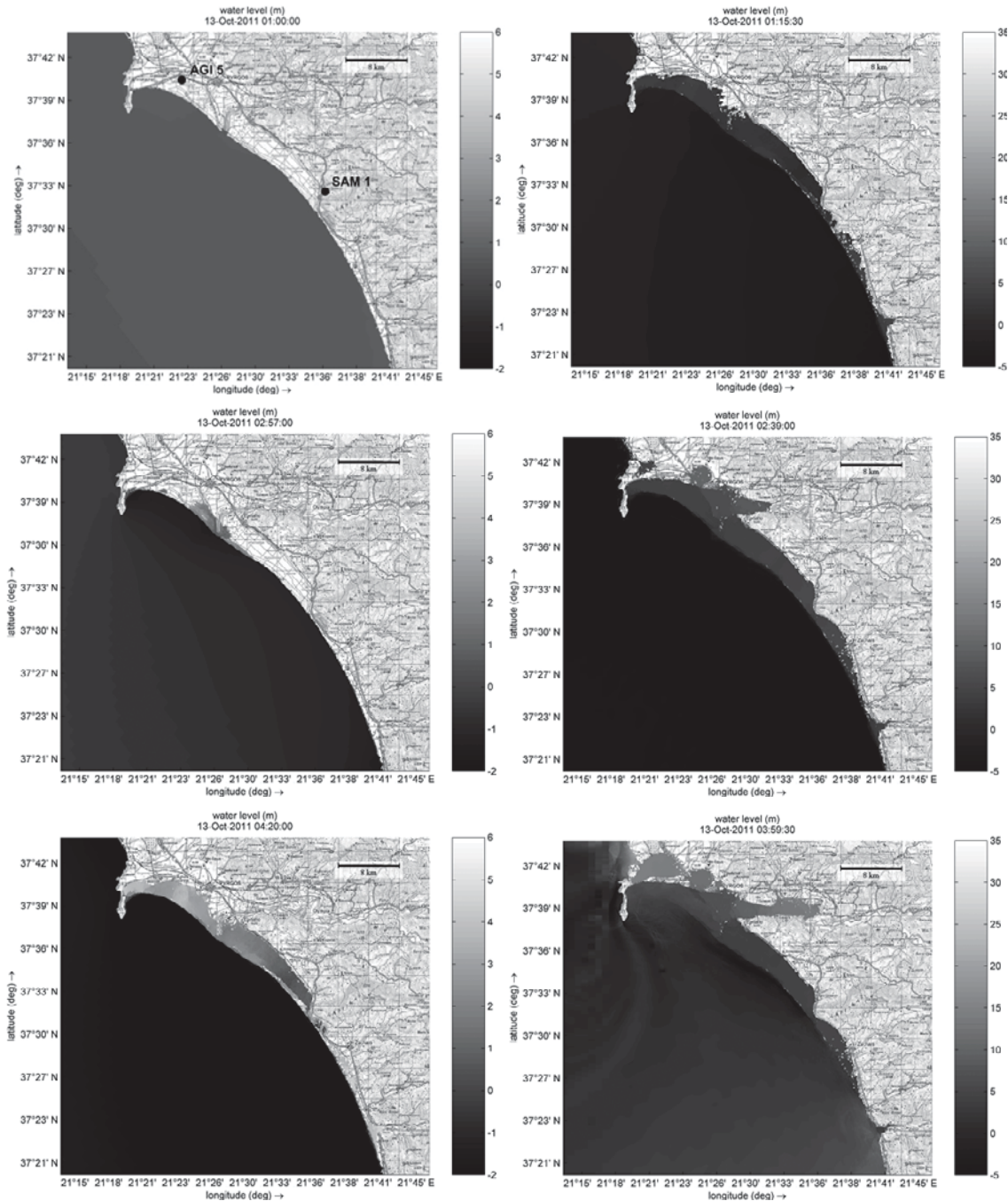


Figure 4: Waterlevels (in m a. s. l.) at the northern coast of the Gulf of Kyparissia after arrival of the first (top), second (middle) and third tsunami wave (below) in a moderate scenario from southwest (left right column) and an extreme scenario from west (right column). Black dots in the upper left figure show locations of coring sites AGI 5 and SAM 1.

In the extreme scenario, already the first tsunami wave, having an initial wave height of 2.5 m, results in a similar inundation of the northern gulf (Fig. 4, right column) as did the third wave in the moderate scenario described above. Only to the south of the former Agoulenitsa Lagoon the water masses penetrate considerably deeper inland. The second tsunami wave arrives 1 h 15 min after the first wave, causing water levels in excess of 10 m a. s. l. at the shoreline. The wave inundates an area much wider as the first one, especially to the northwest and to the east of the city of Pyrgos as well as at the entrance of the Alpheios River valley. As expected, the third tsunami wave with an initial height of 10.0 m engenders the greatest inundation in the northern gulf. The wave arrives at a simulation time of about 3 h; due to shoaling effects it reaches a height of more than 20 m at the shoreline. Widespread areas to the northwest and to the northeast of the former Mouria Lagoon, the entire city of Pyrgos as well as the Alpheios River valley almost up to ancient Olympia are now flooded. The great inland penetration in the Alpheios River valley of about 15 km is due to substantial considerable local funnel effect. Furthermore, the third also causes dramatic inundation along the coastal strip to the south of the Agoulenitsa Lagoon, especially in the Neda Valley, where water masses penetrate almost 8 km inland. The biggest run-up heights of 30 to 35 m are reached by the third wave between the mouths of the Alpheios River and the Neda River as well as to the northeast of Pyrgos. Maximum inundation depths amount to about 30 m in the whole area of the former lagoons where flow velocities exceed 9 m/s (= 32.4 km/h). Remarkable flow velocities are also calculated for the Alpheios River valley showing values of almost 10 m/s (= 36 km/h). Nearly all residential areas along the shores of the northern gulf are inundated by an extreme tsunami coming from the west. Also, Pyrgos is completely flooded with maximum inundation depths up to 10 m. Further villages completely inundated in this tsunami scenario are Epitalio at the entrance of the Alpheios River valley, counting approximately 2,000 inhabitants, as well as to the south of the Kaiafa Lagoon, with approximately 6,700 inhabitants.

5 Discussion

The two vibracores presented in this paper document that autochthonous sedimentary conditions in the northern part of the Gulf of Kyparissia were repeatedly interrupted by high-energy flood events from the seaside during the Holocene leading to the deposition of corresponding sediments. As the coring sites are located way inland (up to 2 km) on higher ground (up to 11.18 m a.s.l.) and are well protected from storm surges and as the deposits show numerous features of tsunamites, the event layers are interpreted as tsunami deposits. This fits well to the fact that the Gulf of Kyparissia and its vicinity was affected by multiple tsunami events in historic times. The thickness of the tsunami deposits (up to 1.94 m for SAM 1) and the maximum elevation above present sea level where they were found (up to 10.33 m a. s. l. for SAM 1) further suggest that the responsible tsunami events were quite severe. This is also indicated when regarding the simulation results; here, it has to be considered that the scenarios were generated on the base of the recent shoreline position and the present sea level. During any point of time in the past, the shoreline lay further inland and the relative sea level was lower compared to the present situation. Whereas coring site AGI 5 is affected by both the moderate and extreme tsunami scenario presented in this paper, coring site SAM 1 is only reached by the tsunami waters of the extreme scenario.

The most serious threat to the northern part of the Gulf of Kyparissia is related to tsunamis from the west or southwest, since they hit the coast more or less perpendicularly and therefore with the largest momentum. But also the ostensibly sheltered Bay of Katakolo is seriously affected by tsunamis from a western and southwestern direction due to refraction and diffraction processes around Cape Katakolo. The dramatic inundation in the northern part of the gulf caused by moderate and especially by extreme tsunamis is mainly due to two circumstances: On the one hand, the coast exhibits extensive lowlands, particularly in terms of former lagoons, and except for the dune belts does not show any natural protection against major tsunami waves. On the other hand, the great water depths in the Gulf of Kyparissia (more than 1,000 m only 20 km offshore) guarantee small losses of energy of incoming tsunami waves. Moreover, the steeply ascending continental slope causes strong shoaling effects. Consequently, even low amplitude tsunami waves on the open sea may transform into devastating tsunamis by approaching the coast of the Gulf of Kyparissia. Tselentis et al. (2010) who calculated tsunami inundation scenarios for the same area based on four assumed seismic sources, also pointed

out to the high tsunami hazard of the area. These authors end up with a maximum calculated inundation of 4 m. Our study, for the first time, brings together field evidence and simulation results for the Gulf of Kyparissia showing that these two data sets are in good accordance. Finally, in the light of inundation depths of minimum 10 to 18 m as documented by field data near Kato Samiko and Aghios Andreas near Cape Katakolo (Vött et al. 2011a), our study documents that the regional tsunami hazard in western Greece is highly underestimated.

Considering the recently published Olympia Tsunami Hypothesis (OTH) – saying that ancient Olympia was repeatedly flooded by tsunami waters intruding the Alpheios River valley as suggested by numerous sedimentological, geochemical and geomorphological observations (Vött et al. 2011b) – the extreme scenario presented in this paper impressively documents that the local topographies of the steep continental shelf, the crescentic configuration of the bay and the narrow lower Alpheios River valley play a major role in amplifying tsunami signals towards inland by shoaling and funnelling effects. Taking into consideration that the presented extreme scenario is calculated on the base of the present shoreline configuration and the present sea level, it has to be assumed that extreme tsunami landfall in former times, when the coastline lay further inland and the relative sea level was lower (Vött et al. 2011b), had reached even further inland. So, the results of the numeric simulations presented in this paper are not suited to falsify the OTH. On the contrary, they emphasize the exceptional susceptibility of the area between Olympia and the present coast to tsunami inundation.

6 Conclusions

The Gulf of Kyparissia and its vicinity exhibit a high tsunami risk. This arises particularly from the high seismicity of the region as well as from the distinct submarine relief which is prone to submarine mass movements and is in accordance with numerous reports on tsunami landfall during history recorded by tsunami and earthquake catalogues. As shown by two vibracores retrieved from the northern part of the gulf, especially regarding the thickness of the tsunami deposits, their elevation above present sea level and their distance to the present shoreline, the related palaeotsunami events must have been quite severe. Numeric simulations of tripartite tsunami wave trains are in good accordance with field observations. Moreover, they show that the northern gulf is distinctly vulnerable to tsunami landfall due to its extensive lowlands and the deep waters of the Gulf of Kyparissia, allowing an undisturbed propagation of tsunami waves close to the coast. The simulation results for an extreme scenario further document that the lower Alpheios River valley, due to funnelling effects, constitutes an exceptional setting with an extraordinarily high susceptibility to tsunami flooding that supports the Olympia Tsunami Hypothesis (Vött et al. 2011b). By virtue of the high tsunamigenic potential of the nearby Hellenic Trench and the steep continental slope, prone to underwater mass movements, the tsunami risk for the coasts along the Gulf of Kyparissia has to be considered as high.

7 Acknowledgements

We thank G. Chatzi-Spiliopoulou (7th Ephorate of Prehistoric and Classical Antiquities, Hellenic Ministry of Culture, Olympia), H.-J. Gehrke (German Archaeological Institute, DAI, Berlin) and R. Senff (German Archaeological Institute, DAI, Athens) for valuable support during field work and intense discussion. Work permits were kindly issued by the Greek Institute of Geology and Mineral Exploration (IGME, Athens). Funding of the project by the DFG (German Research Foundation, Bonn, VO 938/3-1) is gratefully acknowledged.

8 References

- Benetatos, C., Kiratzi, A., Papazachos, C. & Karakaisis, G. (2004): Focal mechanisms of shallow and intermediate depth earthquakes along the Hellenic Arc. - *Journal of Geodynamics*, **37** (2): 253 - 296.
- Bryant, E. (2008): *Tsunami. The Underrated Hazard*. - Berlin².
- Dean, R. G. & Dalrymple, R. A. (1991): *Water Wave Mechanics for Engineers and Scientists*. - *Advanced Series on Ocean Engineering*, **2**, Singapur.

- Deltares (2010): Delft3D-FLOW. Simulation of multi-dimensional hydrodynamic flows and transport phenomena, including sediments. User Manual. - Rotterdam. (called at the homepage http://delftsoftware.wldelft.nl/index.php?option=com_docman&task=cat_view&gid=39&Itemid=61. 2011-09-05)
- Ferentinos, G. (1991): Offshore Geological Hazards in the Hellenic Arc. - *Marine Geotechnology*, **9** (4): 261 - 277.
- Ferentinos, G. (1992): Recent gravitative mass movements in a highly tectonically active arc system: The Hellenic Arc. - *Marine Geology*, **104** (1 - 4): 93 - 107.
- General Secretariat of the National Statistical Service of Greece (2001): Table 18: De facto population by sex and age groups Greece total, geographic areas (NUTS I), regions (NUTS II), departments, municipalities/communities and municipal/communal departments (Year 2001). http://www.statistics.gr/porta_l/page/portal/ESYE/PAGE-themes?p_param=A1604&r_param=SAP01&y_param=2001_00&mytabs=0. 2011-07-17.
- General Secretariat of the National Statistical Service of Greece (2010a): Table 3: Arrivals in hotels, similar establishments and camping, by region and prefecture (Cumulative 2009). http://www.statistics.gr/portal/page/portal/ESYE/PAGE-themes?p_param=A2001&r_param=STO12&y_param=2009_00&mytabs=0. 2011-07-17.
- General Secretariat of the National Statistical Service of Greece (2010b): Table 8: Arrivals in hotels, similar establishments and camping, by month (Cumulative 2009). http://www.statistics.gr/portal/page/portal/ESYE/PAGE-themes?p_param=A2001&r_param=STO12&y_param=2009_00&mytabs=0. 2011-07-17.
- Korteweg, D. J. & DeVries, G. (1895): On the Change of Form of Long Waves advancing in Rectangular Channel, and on a New Type of Long Stationary Waves. - *Philosophical Magazine*, 5. Folge, **39**: 422 - 433.
- Lehfeldt, R., Milbradt, P., Plüss, A. & Schüttrumpf, H. (2007): Propagation of a Tsunami-wave in the North Sea. - In: *Die Küste. Archiv für Forschung und Technik an der Nord- und Ostsee*, **72**: 105 - 123, Heide.
- Lekkas, E., Fountoulis, I. & Papanikolaou, D. (2000): Intensity Distribution and Neotectonic Macro-structure Pyrgos Earthquake Data (26 March 1993, Greece). - *Natural Hazards*, **21**: 19 - 33.
- Morton, R. A., Gelfenbaum, G. & Jaffe, B. E. (2007): Physical criteria for distinguishing sandy tsunami and storm deposits using modern examples. - *Sedimentary Geology*, **200** (3 - 4): 184 - 207.
- Papanikolaou, D., Fountoulis, I. & Metaxas, C. (2007): Active faults, deformation rates and Quaternary paleogeography at Kyparissiakos Gulf (SW Greece) deduced from onshore and offshore data. - *Quaternary International*, **171 & 172**: 14 - 30.
- Papazachos, B. C. (1996): Large seismic faults in the Hellenic arc. - *Annali di Geofisica*, **39** (5): 891 - 903.
- Papoulia, J., Makris, J., Tsambas, A. & Fasoulaka, Ch. (2008): Seismic Deformation In The South Western Hellenic Arc: Preliminary Results From Active And Passive Seismic Observations. - *Bulletin of the Geological Society of Greece*: 1 - 12 (accepted).
- Schielein, P., Zschau, J., Woith, H. & Schellmann, G. (2007): Tsunamigefährdung im Mittelmeer – Eine Analyse geomorphologischer und historischer Zeugnisse. - In: *Bamberger Geographische Schriften*, **22**: 153 - 199, Bamberg.
- Shaw, B. & Jackson, J. (2010): Earthquake mechanisms and active tectonics of the Hellenic subduction zone. - *Geophysical Journal International*, **181** (2): 966 - 984.
- Soloviev, S. L., Solovieva, O. N., Go, C. N., Kim, K. S. & Shchetnikov, N. A. (2000): Tsunamis in the Mediterranean Sea 2000 B.C. – 2000 A.D. - Dordrecht.

- Tsambas, A., Fasoulaka, C., Papoulia, J., Makris, J. & Karastathis, V. (2009): Application Of Passive Tomography Method And Correlation With Active Seismic Observations In The Kyparissiakos Gulf, Southwestern Hellenic Arc. - In: 9th Symposium on Oceanography & Fisheries - Proceedings, Volume 1. Patra: 48 - 52.
- Tselentis, G-A., Stavrakakis, G., Sokos, E., Gkika, F., Serpetsidaki, A. (2010): Tsunami hazard assessment in the Ionian Sea due to potential tsunamigenic sources – results from numerical simulations. - *Natural Hazards and Earth System Sciences* **10**: 1021-1030.
- United States Geological Survey's (USGS) Earthquake Hazards Program (2012): Significant Earthquakes of the World. <http://earthquake.usgs.gov/earthquakes/eqarchives/significant/>. 2012-01-06.
- Vött, A., Bareth, G., Brückner, H., Lang, F., Sakellariou, D., Hadler, H., Ntageretzis, K. & Willershäuser, T. (2011a): Olympia's harbour site Pheia (Elis, western Peloponnese, Greece) destroyed by tsunami impact. - *Die Erde*, **142** (3): 259-288 (in press).
- Vött, A., Fischer, P., Hadler, H., Handl, M., Lang, F., Ntageretzis, K., Willershäuser, T. (2011b): Sedimentary burial of ancient Olympia (Peloponnese, Greece) by high-energy flood deposits – the Olympia Tsunami Hypothesis. - In: Grützner, C., Pérez-Lopez, R., Fernández-Steege, T., Papanikolaou, I., Reicherter, K., Silva, P. G., Vött, A. (Hrsg.): *Earthquake Geology and Archaeology: Science, Society and Critical facilities. Proceedings of the 2nd INQUA-IGCP-567 International Workshop on Active Tectonics, Earthquake Geology, Archaeology and Engineering*, 19.-24. September 2011. Corinth: 259 - 262.

Seasonal changing sand waves and the effect of surface waves

Fenneke Sterlini¹, Thaiënne A.G.P. van Dijk^{1,2}, Steven IJzer³ and Suzanne J.M.H. Hulscher¹

Abstract

Sand waves are wavelike subaqueous sediment structures that exist in large areas in shelf seas. Due to their characteristics sand waves can severely affect human offshore activities, such as navigation. This makes it important to understand the physical processes that shape and change sand waves. In field data, temporal variation in the migration and the shape of sand waves are found. Besides other factors, surface wave action might cause this variation.

In this study, a morphodynamic model and field data were used to investigate the importance of the surface waves on sand wave migration and shape. The field observations show that periods with surface waves can significantly affect the sand waves.

Model results indicate that the surface waves explain these changes partly. Possibly surface waves in combination with a variation in the tidal current will explain the effects in a larger extent.

Keywords: sand wave, surface wave, field data, numerical modelling

1 Introduction

The seabed of shallow shelf seas is rarely flat. When sediment is in good supply and tidal flows are sufficiently strong, wavelike subaqueous sediment structures, called sand waves, may occur. With a migration rate up to several tens of meters per year, a wave length of several hundreds of metres and a height up to 1/3 of the local water depth, sand waves can severely affect human offshore activities, such as navigation. This makes it important to understand the physical processes that shape and change sand waves, in order to improve management strategies of expensive operations such as e.g. the dredging of shipping lanes.

Empirical data showed that both temporal changes in currents and surface waves can affect the sand wave shape and migration. Van Dijk & Egberts (2008) describe a seasonal back and forth migration of sand waves that are located 50 km off the Dutch Coast. An example of asymmetry change due to current is given by Harris (1989), who found that Monsoon driven currents reversed the asymmetry and direction of migration of bed forms in the Adolphus Channel.

Van Dijk & Kleinhans (2005) find that the variability in dynamics between offshore and coastal sand wave sites may be explained by the relative contribution of current and wave action. Houthuys et al. (1994) find an average lowering of the sand wave height of 1.2 metres in a pre- and post storm study of the Middelkerke Bank in the southern North Sea near Belgium. The effect increased with decreasing water depth on the flank of the sand bank where the sand waves were superimposed upon.

Using an idealized sand wave model, Sterlini *et al.* (2009) showed that the relative rate of the M2 and the unidirectional tidal current has an influence on the bed form height and shape. Sterlini (2009) predicted lower bed forms for increasingly higher surface waves. Also, the surface waves were found to cause a higher migration rate for higher surface waves.

In the previous study by Sterlini (2009), surface waves were included, but their direction was always kept collinear with respect to the current. In reality, wave directions are variable. In this paper we present the model, including the free surface wave direction.

¹ University of Twente, Faculty of Engineering Technology, Water Engineering and Management, PO box 217, 7500 AE Enschede, the Netherlands, F.M.Sterlini@utwente.nl.

² Deltares, Dept. Of Applied Geology and Geophysics, PO box 85467, 3508AL Utrecht, the Netherlands.

³ Rijkswaterstaat, the Netherlands

The hypothesis is that variations in both currents as well as surface wave activity have a significant role in the sand wave shape and direction of migration. This research aims to quantify the role of surface waves, including both height and direction and which part must be attributed to other processes, such as variations in tidal currents. We use bathymetric and surface wave field data at two sites, the Varne (UK) and near Alkmaar (Netherlands Continental Shelf), together with an idealized model to investigate the effect of surface waves in more detail.

2 Methods

2.1 Bathymetry

The bathymetry data is interpolated from spatially distributed points to regular grids, using a kriging algorithm, using inhouse software that was especially designed to deal with large amounts of data (Van Dijk *et al.*, 2008). Resampled transects were used to determine shape characteristics by means of the Fast Fourier Transform (FFT). The FFT fits a discrete function through the points of the transect in order to separate the signal of sand waves, from large and small scale morphology (E.g. mega ripples and sand banks). For details on the separation method, see Van Dijk *et al.* (2008).

2.2 Sand Wave Model

The model used in this study is based on the model developed by Németh *et al.* (2006), further developed by Van den Berg & Van Damme (2006). Their work is based on analytical models such as made by Hulscher (1996) and Komarova & Hulscher (2000).

The model is a 2DV, non-linear, idealized, process-based model, named the Sand Wave Code (SWC). The latest refinement of this model was done by Sterlini (2009). In separate studies, she added surface waves and suspended sediment to the code.

This research focuses on the action of surface waves, using the version of the code that only described bed load transport with waves. A combination of waves and suspended sediment will be worked on later. This is justified to some extent, as bed load transport is considered the dominant mode of transport in offshore sandy tidal regimes where sand waves occur (Németh *et al.* 2002).

The initial model set up is as described in Sterlini *et al.* 2009. The flow of the model is calculated using the hydrostatic shallow water equation for 2DV flow. The domain setup is shown in Figure 1. The model uses periodic boundary conditions. Physically this represents the sand wave in between identical sand waves. The tidal flow is modelled as a sinusoidal current prescribed by means of a forcing. Boundary conditions at the bed disallow flow perpendicular to the bottom.

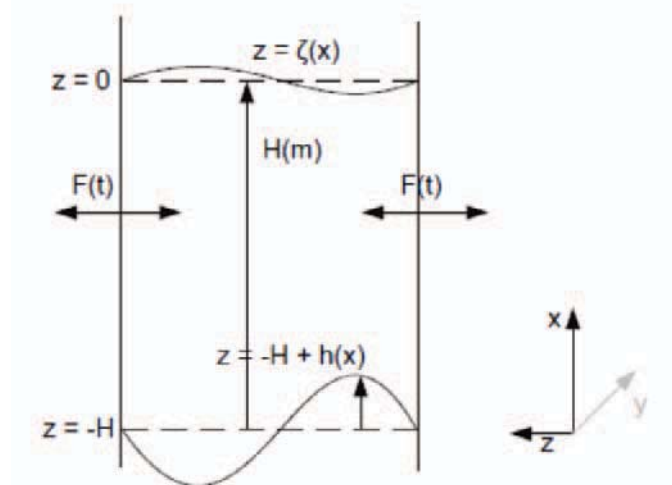


Figure 1: SWC domain set up

Further, a partial slip condition compensates for the constant eddy viscosity, which is known to overestimate the eddy viscosity near the bed. At the water surface there is no friction and no

flow through the surface. Since the flow changes over a timescale of hours and the morphology over a timescale of years, the bathymetry is assumed to be invariant within a single tidal cycle. The flow and the sea bed are coupled through the continuity of sediment. Only bed load transport is taken into account, for equations we refer to Van den Berg and Van Damme (2006) and Sterlini *et al.* (2009).

As sand waves occur in relatively deep water with respect to wind waves, the wind waves are expected not to break. To implement the effect of surface waves we use the linear wave theory, i.e. monochromatic waves for which the linear approximation holds ($ak \ll 1$, $a/h \ll 1$ and $a/k^2 h^3 \ll 1$, where a is wind wave amplitude, k wavenumber and h local water depth). We assume that the currents will influence the wave characteristics, while the waves do not influence the currents (Mei 1999). With a given incoming wave period and direction, the wave number k and the wave energy per location over the sand wave are calculated by

$$\begin{aligned} \omega &= Uk + \sqrt{gk \tanh(kh)}, & \frac{d}{dx} \left((U + C_g) \frac{E}{\sigma} \right) &= 0 \\ C_g &= \frac{\omega}{2k} \left(1 + \frac{2kh}{\sinh(2kh)} \right), & \omega &= \frac{2\pi}{T} \end{aligned} \quad (1)$$

Here U is the depth averaged current velocity, g the gravitational acceleration, E the wave energy, σ the intrinsic wave frequency, C_g and T represent the group velocity and the wave period of the surface waves respectively, and φ represents the angle between the waves and the tidal current. Via the surface wave height H_w and wave orbital velocity u_w , we finally determine the bed shear stress due to the wind waves, τ_w , by

$$E = \frac{1}{8} \rho g H_w^2, \quad u_w = \frac{\omega H_w}{2 \sinh(kh)}, \quad \tau_w = \frac{1}{2} f_w u_w^2, \quad f_w = 0.237 \left(\frac{a}{2.5D} \right)^{-0.52} \quad (2)$$

Here f_w is the bed friction factor according to Soulsby (1997), and D is the grain size. Note that we use the volumetric bed shear stress. To combine both the current and the wave shear stress, we extend the sediment transport equation with an extra term, for the wind wave bed shear stress. This causes an extra transport by the tidal flow and affects the slope adjustment, both due to the stirring effect of the wind waves:

$$q_b = \alpha \left| \tau_{bf} \right|^{\frac{1}{2}} \left(\left| \tau_{bf} \right| + \gamma \left| \tau_{bw} \right| \right) \left(\frac{\tau_{bf}}{\left| \tau_{bf} \right|} - \lambda \frac{dh}{dx} \right) \quad (3)$$

In this we follow Roos *et al.* (2004) and Calvete *et al.* (2001), here rewritten for a z-coordinate dependent situation, i.e. for the bed shear stress τ instead of depth averaged velocity u . The bed load sediment transport and the bed shear stress due to the current are represented by q_b and τ_{bf} respectively and γ equals $(\frac{1}{2} + \cos^2(\varphi))$ and represents the angle between the waves and the current.

3 Data from the Varne area

3.1 Bathymetry

The studied sand wave field in the Varne area is located in the Dover Strait, just north of a sand bank. The sand wave crests are perpendicular to the main direction of the asymmetric tidal flow. The sand waves have been recorded 3 times, and from the recordings two transects could be used for tracking changes in time, see Figure 2 (data supplied by the UK Hydrographic office).

The most northern transect has a length of 956m; the southern transect is 1091m long. The recording in October shows short and tall crested sand waves, the later recordings show broader and flatter crests (Figure 3). The time difference between the recordings of the northern transect was 66 days. The mean sand wave length in the area changed from 92 to 96m, the sand wave height was lowered with one metre from a mean value of 4.1m tot 3.1m. This is mainly due to a lowering of the sand wave crest, but also the troughs were lowered. Another interesting fact is that the horizontal asymmetry (L_{lee}/L_{stoss}) reversed, from 2.7 to 0.5.

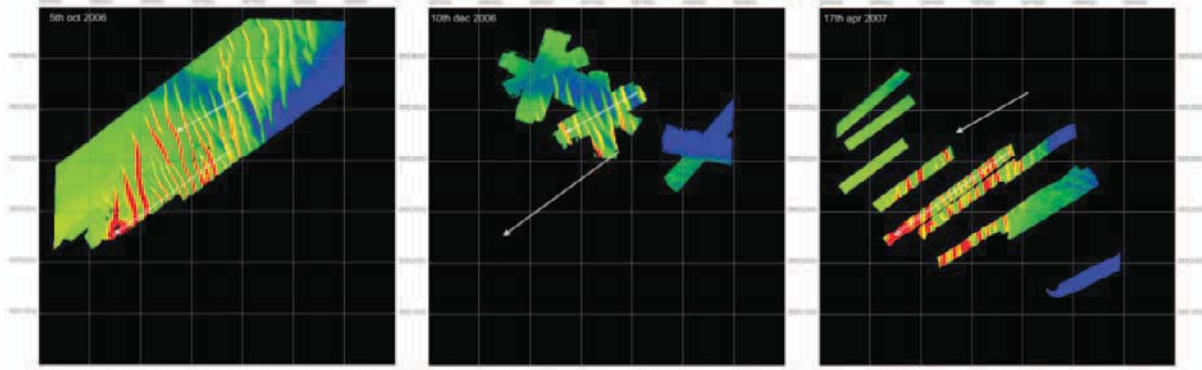


Figure 2: Bathymetry measurements in the Varne area. The white arrows indicate the used profiles.

Due to the shape change of the sand wave field, the migration of the troughs and crests is in different directions. The crests moved on average 25m to the North East (a speed of 139 m/y), while the troughs moved 12m to the South West (66 m/y). Note that the high migration rate values are mainly due to the shape change of the sand waves and not due to the migration of the total bed form.

For the southern transect, the average sand wave length remained 86m. The average sand wave height was also reduced by 1m, from 4.9m to 3.9m. The crest height was again reduced, while here the troughs were elevated suggesting a decay of the bedform. The sand waves show less horizontal asymmetry, which changed from 1.2 to 1.9. Both crests and troughs migrated to the North East with a rate of 22 and 32m/y respectively.

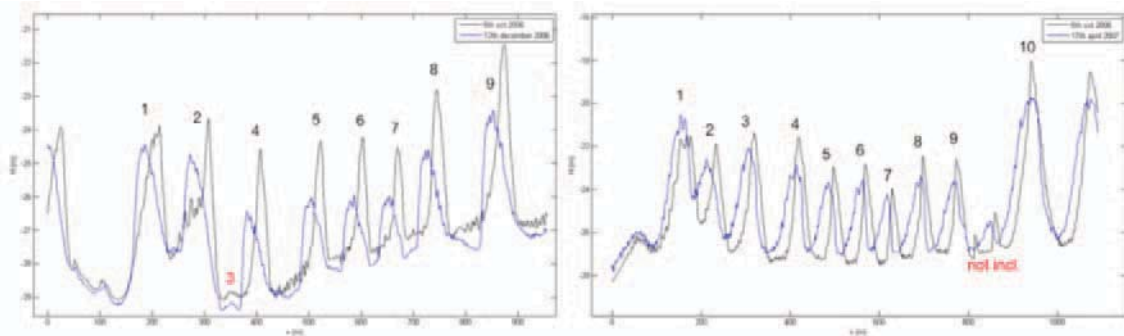


Figure 3: transects in the Varne area from the NE to the SW, corresponding to the white arrows in Figure 2.

3.2 Wave and weather data

We investigated the weather and wave climate before the three recordings. Periods of 66 days are used, equal to the shortest period between the different recordings. Wave characteristics were supplied by the UK Hydrographic office. Before the first recording (October 2006), the investigated 8 weeks before were weeks of calm weather, there was one short 2 day storm with waves higher than 2 meters. The wind direction was mainly from the south west. We assume this as a long period of calm weather. The recorded short crested and tall sand waves are therefore assumed to be fair weather sand waves.

In the period between the first and second recording, multiple storms with waves higher than 2m occurred. Most storm periods came from the south west (70% of the wind/waves), but approximately 20% of the wind/waves came from the north/north west. Mega ripples on the sand waves in the second recording (December 2006) suggest that the last migration direction of the sand waves was in the North Eastern direction.

Finally, the period before the recording in April 2007, contained of several stormy periods. In January-March waves came mainly from the South West, while just before the recording a North Eastern storm period took place. The migration of transect 2 over the period October 2006 to April 2007 was less then the migration of transect 1 over the shorter period (October – December), but significantly in the North Eastern direction.

3.3 Sand wave model results

Table 1 shows the parameter settings for the model runs. Values of the eddy viscosity A_v , the slip parameter S and the slope parameter λ are chosen according to Németh *et al.* (2002) as typical parameters for the Southern North Sea. It also summarizes the results of the model runs without surface waves.

Table 1: Parameter values and results for the model runs of the Varne area.

Parameter	Value	Unit	Results	no waves	with waves
Eddy viscosity	1.0e-2	m ² /s	FGM	210m	210m
Slip parameter	8.0e-3	m/s	Sand wave height	6m	6m
Slope parameter	1.7	-	migration	15m/y	22-45m/y
Tidal flow	1.0	m/s	L_{crest}/L_{trough}	0.78	0.94
Residual flow	0.05	m/s	L_{stoss}/L_{lee}	1.5	2.3
Water depth	30	m			

When waves are introduced in the model, waves of 1.4m/s have no significant effect on the sand wave shape. Waves of 2.8m/s have a significant effect. The sand wave crest reduces with approximately 0.5m in 40-50 weeks, while the trough depth is deepened by 0.4m in 30-40weeks. The result is a lower sand wave, but the total sand wave height remains more or less unchanged. The length of the crest increases due to the waves, from 92 to 102m. This results in a smaller horizontal asymmetry, the L_{crest}/L_{trough} goes from 0.78 to 0.94 when waves are included. When looking at the L_{stoss}/L_{lee} ratio, we see that the length of the stoss side of the sand wave is instantly affected by waves. The ratio goes from 1.5 to 2.3, and changes back when the wave height is reduced again.

Note that even without the waves, the sand wave crest and trough already vary in height in time.

When investigating the migration of the sand waves, smaller wind waves (1.4m/s) already affect the sand wave migration. Due to the asymmetric current there is already a background migration of 15m/y. When waves of 1.4m/s or 2.8m/s respectively are introduced, the migration increases to approximately 22m/y and 45m/y respectively. These values hold for waves that are collinear with the residual current. When waves were opposing the tidal migration direction, the migration was slowed down, but never reversed.

3.4 Discussion Varne area

When the results of the recordings and the model are compared we see that the wave length predicted by the model is a factor 2 to 2.5 larger than the observed length (210m vs. 86-96m), the sand wave height is overestimated by 1-3m (6m vs. 3.0-4.9m), and although the crest lowered in the model, this was counteracted by the lowering of the trough. The total sand wave height was therefore not affected in the model, while the recordings show a lowering of 1m. Finally the migration was estimated by the model between 20 and 45m/y, while the recordings showed migration rates of 66-139m/y and 22-32m/y depending on the transects. Note however,

that the high values of Transect 1 (66-139m/y) were mainly caused by the change in shape and not by the migration of the bedforms.

4 Data from the Alkmaar area

4.1 Bathymetry

The Alkmaar area is located about 50km out of the Dutch coast near Alkmaar. The sea floor ranges between 25 and 30m below mean sea level. The recorded area is 2x2.5km and was recorded 5 times between March 2001 and September 2002 (Figure 4). There was no systematic change of the sand wave shape in the area over the whole period, but sand waves migrated back and forth in time. The average values of the area are a sand wave length of 222m, a height of 1.79m and a $L_{\text{stoss}}/L_{\text{lee}}$ of 3.6. The average migration rate over the whole period was 1.6m/y, but varies over the year with maxima migration of the pattern of 4.5m/y and of 12.2m/y for individual sand waves. In general the crest and trough of sand waves show the same migration rate and direction.

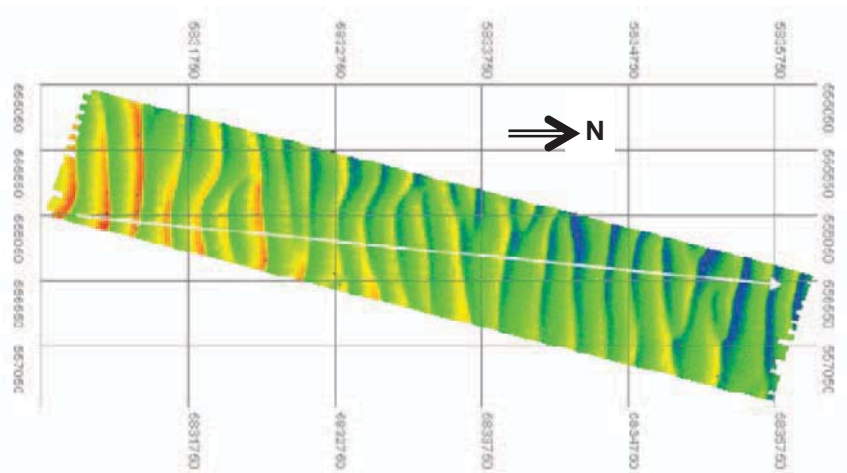


Figure 4: Area overview of the Alkmaar area

4.2 Wave and weather data

Wave data from www.waterbase.nl show that waves in general are directed towards the north east and the south east. In the four periods between the recordings the wave energy was primarily towards the south east between July 2001 and April 2002. From March 2001 to July 2001 and from April to September 2002 the wave energy was more equally distributed between the north east and the south east.

Investigating the conditions in this area showed a strong correlation between the wave energy and the residual current in the flow. The asymmetric tide has a symmetric part of 0.5m/s and a residual current of 0.05m/s. Investigating the flow data however showed that in case of high wave energy, the residual current could be up to 4 times larger. Most likely this combination of wave energy and higher flow conditions cause the migration of the sand waves in various directions.

4.3 Sand wave model results

Unfortunately we are currently unable to include this correlation between the waves and the current in the SWC. Runs have therefore been carried out with a constant residual current on top of the symmetric tidal current and waves. Waves were used comparable to measured waves near IJmuiden (De Leeuw, 2005). Different wave heights and periods were used, corresponding to different chances of occurrence. Table 2 shows the parameter settings and the results.

Although the preferred wave length that was found was 280m, simulations were carried out with a wave length of 220m to represent the data better. This, because the length also influences the sand wave height due to a maximum possible angle. Still the sand wave height is largely

overpredicted both with and without waves and residual currents. When a symmetric tide is simulated (residual current of 0m/s) the sand waves grow to 12 m high and waves reduce the height to 10 and 9m for small and large waves respectively. When the residual current is included, leading to an asymmetric tide, we see that wave inclusion leads to higher sand waves (8.5 and 9.5m, respectively without and with waves).

Table 2: Parameter values and results for the model runs of the Alkmaar area.

Parameter	Value	Unit	Results	no waves	with waves
Tidal flow	0.5	m/s	FGM	280m (used 220m)	280m (used 220m)
Residual flow	0.00 / 0.05	m/s	Sand wave height	12-8.5m	9,10 – 9.5m
Water depth	28	m	migration	0-2m/y	4-11m/y

Migration under low waves is 0-2m/y under a symmetric tide. The direction depends on the wave direction and can be in both directions. Under an asymmetric tide, waves cause a migration of 4-11m/y when in the same direction of the residual current. Opposing waves will slow down the migration but no longer cause migration in the opposite direction. Migration under high waves is larger, but due to their low frequency of occurrence, they are not incorporated here.

With an asymmetric tide and waves, the sand wave crests become wider and lower. With a symmetric tide the effect of waves was not significantly changing the shape. The L_{lee}/L_{stoss} value was 1.0 under an symmetric tide and could be changed to slightly smaller than 1.0 when opposing waves were introduced. With the residual current and low waves the L_{lee}/L_{stoss} value was 3.5.

4.4 Discussion Ecomorf 3 area

Although the sand wave height is nearly overpredicted by a factor 6, other characteristics are well described by the model. The predicted sand wave length (280m) is relatively close to the observed (214m) and the same holds for the migration rate (4-11m/y and 4.5-12.2m/y) and horizontal asymmetry (3.5 and 3.6).

5 Discussion

In the Varne area, the SWC shows a lowering of the sand wave crests due to surface waves. However, this lowering needs about 30weeks of storm conditions, while in the data the lowering of the crests resulted from a much shorter periods with storm conditions in the order of days. One possible explanation might be that the combination with suspended sediment load is not included in the model. For example Tonnon *et al.* (2007) suggest that this is a key process that causes flattening (and lowering) of the sand wave.

The two areas studied in this paper differ mainly in the tidal strength. Still the sand waves show very different characteristics (wave length and height) and also show a different reaction to storm conditions. The Varne area mainly reacts by a change in the sand wave profile, while the Alkmaar area only shows a back and forth migration. The reasons for this are not yet clear, one option might be the saturation of the sand waves. As Van Dijk & Kleinhans (2005) noted the Ecomorph3 sand waves are fairly saturated, their shape is not affected as much as the possible less saturated sand waves in the Varne area. Another option might still be the flow velocity, due to which changes are induced on the sand wave shape quicker and stronger. Neither theories are confirmed by the model results. Predictions suggested much higher sand waves in the Alkmaar area and a change in the sand wave height up to 3m, while the lowering in the Varne area was less than 1m, and the predicted sand wave height was much closer to the observed value.

As shown by e.g. Bowden (1956) surface waves can also cause an extra current to flow. In the used SWC it is not possible to include a fluctuating residual current coupled to the surface waves. However as shown by Sterlini et al. (2009) this might have a large effect on the sand wave characteristics. Further research to this effect will be carried out.

6 Conclusion

In this study, a morphodynamic model and field data were used to investigate the importance of surface waves for sand wave migration and shape. The field observations show that periods with surface waves can significantly affect the sand waves. In the case of the Varne area the effect was both a change in the sand wave shape and (local) migration. In the case of the Alkmaar area the effect was only found in a seasonal variation in migration.

Model results indicate that the surface waves explain these changes partly. Waves in the direction of the residual tidal current add to migration. Waves opposing the residual current reduce the migration. Sand waves can be lowered up to half a metre. Possibly surface waves in combination with a variation in the tidal current will explain the effects in a larger extent.

7 Acknowledgement

This work originates from S. IJzers master's thesis Civil Engineering & Management, University of Twente. The authors would like to acknowledge Andrew Winterbottom (UK Hydrographic Office) for supplying the Varne data.

8 References

- Bowden, K.F., "The Flow of Water through the Straits of Dover, Related to Wind and Differences in Sea Level", Royal Society Publishing, 1956
- Calvete, D., Falqués, A., de Swart, H.E., Walgreen, M., 2001. Modelling the formation of shoreface-connected ridges on storm-dominated inner shelves. *Journal of Fluid Mechanics* 441, 169–193.
- De Leeuw, C.J., 2005. Model predictions of wave-induced sediment transport on the shoreface. Msc thesis, University of Twente.
- Harris, P.T., 1989. Sand wave movement under tidal and wind-driven currents in a shallow marine environment: Adolphus Channel, northeastern Australia. *Continental Shelf Research* 9 (11), 981–1002.
- Houthuys, R., Trentesaux, A. and De Wolf, P., 1994. Storm influence on a tidal sandbank's surface (Middelkerke Bank, southern North Sea), *Marine Geology*, p. 23–41, 1994
- Hulscher, S.J.M.H., 1996. Tidal-induced large-scale regular bed form patterns in a three-dimensional shallow water model. *Journal of Geophysical Research* 101, 727–744.
- Komarova, N.L., and S.J.M.H. Hulscher, 2000. Linear instability mechanisms for sand wave formation, *Journal of Fluid Mechanics*, 413, 219–246.
- Mei, C.C., 1999. The applied dynamics of ocean surface waves. Vol. 1 of *Advanced Series on Ocean Engineering*. World Scientific Publishing Co Pte Ltd.
- Németh, A.A., Hulscher, S.J.M.H. and De Vriend, H.J., 2002. Modelling sand wave migration in shallow shelf seas, *Continental Shelf Research*, 22 (18), 2795–2806.
- Németh, A.A., Hulscher, S.J.M.H. and Van Damme, R.M.J., 2006. Simulating offshore sand waves. *Coastal Engineering* 53, 265–275.
- Roos, P.C., Hulscher, S.J.M.H., Knaapen, M.A.F., 2004. The cross-sectional shape of tidal sandbanks: Modeling and observations. *Journal of Geophysical Research* 109 (F02003, doi:10.1029/2003JF000070).
- Soulsby, R., 1997. *Dynamics of marine sands, a manual for practical application*, Thomas Telford.

- Sterlini, F., 2009. Modelling sand waves variation, Ph.D.thesis, University of Twente, The Netherlands.
- Sterlini, F., Hulscher, S.J.H.M., and Hanes, D.M. (2009). Simulating and understanding sand wave variation: A case study of the Golden Gate sand waves. *Journal of Geophysical Research*, 114 (F02007,doi:10.1029/2008JF000999).
- Tonnon, P.K.,L.C. Van Rijn, and D.J.R. Walstra, 2007. The morphodynamic modelling of tidal sand waves on the shoreface, *Coastal Engineering*, 54,279–296.
- Van den Berg, J., Van Damme, D., 2006. Sand wave simulations on large domains. In: Parker, Garcia (Eds.), *River, Coastal and Estuarine Morphodynamics: RCEM2005*.
- Van Dijk, T.A.G.P. and Kleinhans, M.G. (2005). Processes controlling the dynamics of compound sand waves in the North Sea, Netherlands. *Journal of Geophysical Research - Earth Surface*, 110 (F04S10,doi:10.1029/2004JF000173).
- Van Dijk, T.A.G.P. and P.J.P. Egberts, 2008. The variability of sand wave migration in the North Sea, in *Marine Sandwave and River Dune Dynamics III: MARID2008*, edited by D. R. Parsons, T. Garlan, and J. L. Best, pp. 63-67, 2008.
- Van Dijk, T.A.G.P., Lindenbergh, R.C. and Egberts, P.J.P., 2008. Separating bathymetric data representing multiscale rhythmic bed forms: A geostatistical and spectral method compared. *Journal of Geophysical Research*, 113 (F04017,doi:10.1029/2007JF000950).

Analysis of tide measurements in a Sicilian harbour

Pietro Danilo Tomaselli¹, Carlo Lo Re² and Giovanni Battista Ferreri³

Abstract

Designing of ports and coastal protection works and planning of coastal human activities require knowledge of tidal oscillations. The latter vary noticeably from site to site and present an “astronomic” component, which is roughly periodic, and a “meteorological” component, which is usually considered as random. In this paper, the tidal oscillations observed in a Sicilian harbour in the period 1999-2009 are analysed statistically, in order to recognize a probability distribution which allows one to predict the highest tidal levels. First, the measurements are used to obtain, for each year, the *astronomic tide* through harmonic analysis using the software package *T_TIDE*. The difference between the observed tide and the astronomic tide, indicated as “noise”, is imputed to meteorological factors and treated with a statistical approach. The noise imputable to sea storms moving onshore is divided from that imputable to storms moving offshore. Several probability distributions are then considered for each noise and it is established that each noise closely follows the Weibull extreme value distribution better than other distributions.

Keywords: Tide analysis, coastal protection, probability distribution, extreme value distribution, storm surges.

1 Introduction

Sea level oscillations, usually indicated as tides, are produced by superposition of many contributions, the main ones being *astronomic* and *meteorological* (Coastal Engineering Manual, 2002). The former (which produce the “astronomic tide”), are *persistent*, although not exactly periodic (Kamphuis, 2010), and can be predicted with adequate precision. Several models based on harmonic analysis are available for simulation of the astronomic tide (e.g., Pashova and Popova, 2011). Each model takes into account a different number of tidal harmonic constituents, each related to an astronomic, geographic or geophysical factor (Pawlowicz *et al.*, 2002). The meteorological contributions (“meteorological tide”) are *contingent*, depending on many factors, like changes in the atmospheric pressure, wind, storms, etc., related to the passing of atmospheric disturbances, whose duration varies between a few hours and several days. Such phenomena are roughly foreseeable within a few hours but not at all in the medium and the long term, so that a statistical approach proves to be necessary to forecast the meteorological tide.

In this paper, early results of analysis of tidal measurements taken in a harbour in the Mediterranean Sea are reported. The measurements are first processed to recognize in the total oscillations the meteorological part. The latter is then analysed statistically aiming at recognizing a probability distribution allowing one to predict tidal oscillations in the medium as well as in the long term.

¹ Dipartimento di Ingegneria Civile, Ambientale e Aerospaziale, Università degli Studi di Palermo (Dept. of Civil, Environmental and Aerospace Engineering, University of Palermo), Italy; Viale delle Scienze, Ed. 8, I-90128 Palermo, Italy; kobelak@libero.it.

² Dipartimento di Ingegneria Civile, Ambientale e Aerospaziale, Università degli Studi di Palermo (Dept. of Civil, Environmental and Aerospace Engineering, University of Palermo), Italy; Viale delle Scienze, Ed. 8, I-90128 Palermo, Italy; lore@idra.unipa.it.

³ Dipartimento di Ingegneria Civile, Ambientale e Aerospaziale, Università degli Studi di Palermo (Dept. of Civil, Environmental and Aerospace Engineering, University of Palermo), Italy; Viale delle Scienze, Ed. 8, I-90128 Palermo, Italy; giofer@idra.unipa.it.

2 Data set and meteorological contribution

The harbour selected for the analysis is that of *Porto Empedocle* (lat 37° 17' 08.72" N; long 13° 31' 36.64' E) which is located on the South coast of Sicily (Italy). The harbour is about 100 km from the wave buoy of *Mazara del Vallo* (lat 37° 38' 43.19" N; long 12° 34' 57.0" E); both are located along the same almost rectilinear coast (Fig. 1). The presence of the wave buoy close to the harbour makes it possible to investigate the connection between the tide measurements outside the usual astronomic oscillation range and the wave data recorded by the buoy. The study on this connection will be carried out in further papers. Both the tide gauge and the wave buoy record data every hour. The tide gauge of *Porto Empedocle* has operated since several decades ago, with different instrumentation, but continuous data recorded with the late gauge are available only for the period 1999-2009, which was adopted for the present study.

In order to recognize the *meteorological* tide, for each year the tide measurements were used to draw the *astronomic* tide by means of a harmonic analysis made by T_TIDE, which is a package of MATLAB routines (Pawlowicz *et al.*, 2002). By varying some input options, T_TIDE makes it possible to select up to 145 tide components. We chose to use four different configurations of the model, which were the following: *10comp* with the 10 basic components (SA, O₁, P₁, K₁, N₂, M₂, S₂, K₂, M₄, MS₄); *Default* with the components chosen automatically by T_TIDE between 68 components with a period smaller than or equal to one year, including 44 astronomic and 24 shallow-water ones; *allcomp-sw* with all the 68 components with a period smaller than or equal to one year; *allcomp* with the 44 astronomic components. Therefore, for each year we obtained four different tide simulations. Fig. 2 shows, as an example, the four one-year tide simulations relating to the year 2005.

Comparative examination of all the simulated one-year tides with the corresponding ones observed in the period 1999-2009 led us to choose, for the subsequent processing, the one-year simulations obtained using the 44 components that Pawlowicz *et al.* (2002) refer to as astronomic. Each of these simulations was assumed as the *astronomic tide* of the related year. Fig. 3 shows, as an example, the astronomic tide and the observed tide relating to the year 2005. The window in the figure allows one to observe that, generally, the astronomic oscillations follow the observed ones but they prove to range in a noticeably narrower band. The difference between the observed and the simulated tide, considerably varying from one cycle to another, is likely due to meteorological factors and its prediction then presents uncertainties at least analogous to those of the meteorological factors themselves. Indeed, such uncertainties are even higher, because of those proper to the models for transformation of meteorological factors into sea level oscillations. Therefore, a statistical approach based on the observed oscillations seems to be the best way for prediction of the sea level oscillations in the site of interest.



Figure 1: The wave buoy of Mazara del Vallo and the tide gauge of *Porto Empedocle* are located along the same almost rectilinear coast (source <http://maps.google.com>).

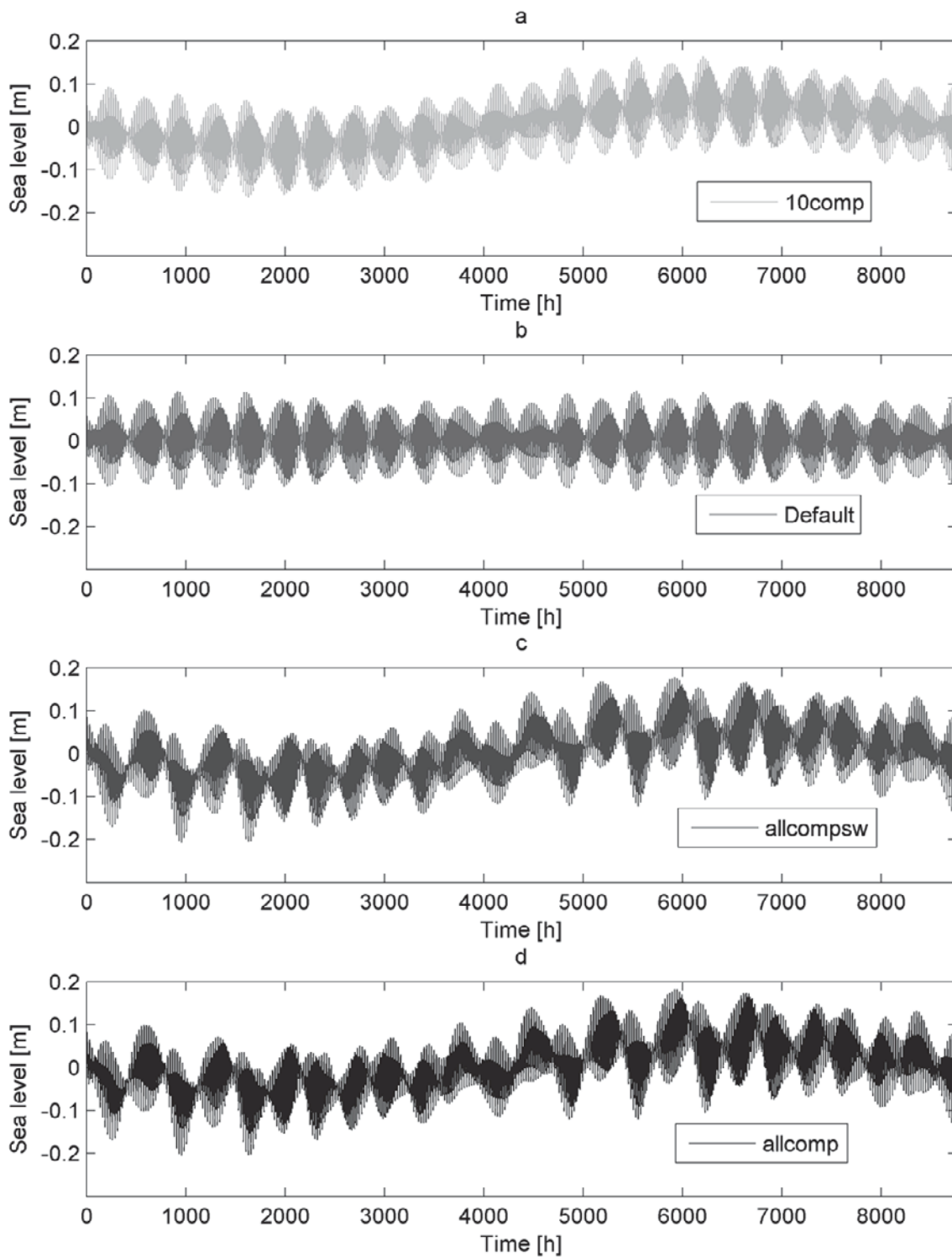


Figure 2: Comparison between the astronomic tides of the year 2005 simulated with the four different configurations of T_TIDE: a) the 10 basic components; b) components chosen automatically by T_TIDE between 68 components having a period smaller than or equal to one year; c) all the 68 components with a period smaller than or equal to one year; d) all the 44 astronomic components.

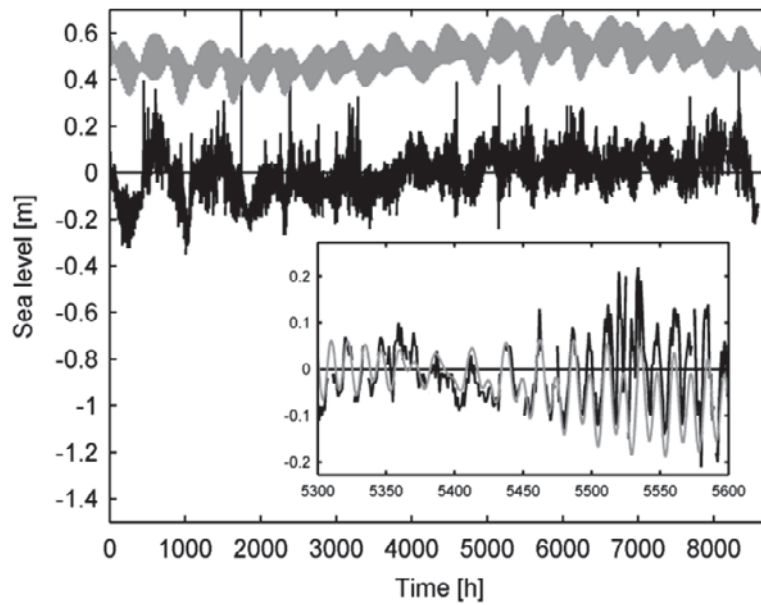


Figure 3: Comparison between the observed tide (black line) and the simulated tide (grey line) relating to the year 2005; the simulated tide is shifted to allow clear observation; the window shows a comparison between the two tides in a time-interval of 300 hours.

To this aim, the difference between the observed and the astronomic tide was then calculated for each year. From now on this difference will be indicated as "noise." The noise proved to be both positive and negative: it is likely that positive noise is imputable to sea storms moving onshore and negative noise to storms moving offshore. Fig. 4 shows, as an example, the noise relating to the year 2005; the same figure reports the time intervals during which the buoy recorded sea storms with a 1.5 m threshold. Note that intense noise may have occurred even for sea storms slightly less than 1.5 m which, however, are not reported in the figure; moreover, the occurrence of high sea levels also depends on storm duration. Anyway, as mentioned above, the noise-storm connection will be stressed in further papers. It is to be noted that the magnitude of noise often prevails over that of the astronomic oscillation (see also Fig. 3).

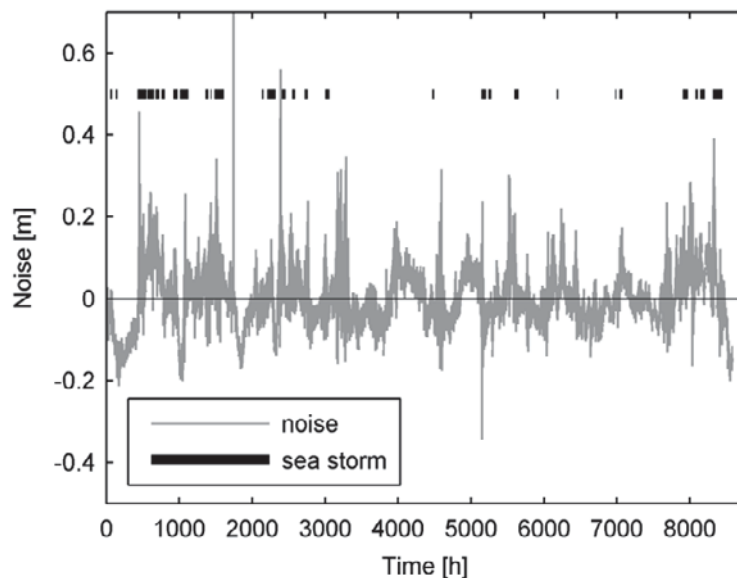


Figure 4: Comparison, relating to the year 2005, between the noise fluctuations (grey line) and the occurrence of sea storms equal to or higher than 1.5 m (bold black line).

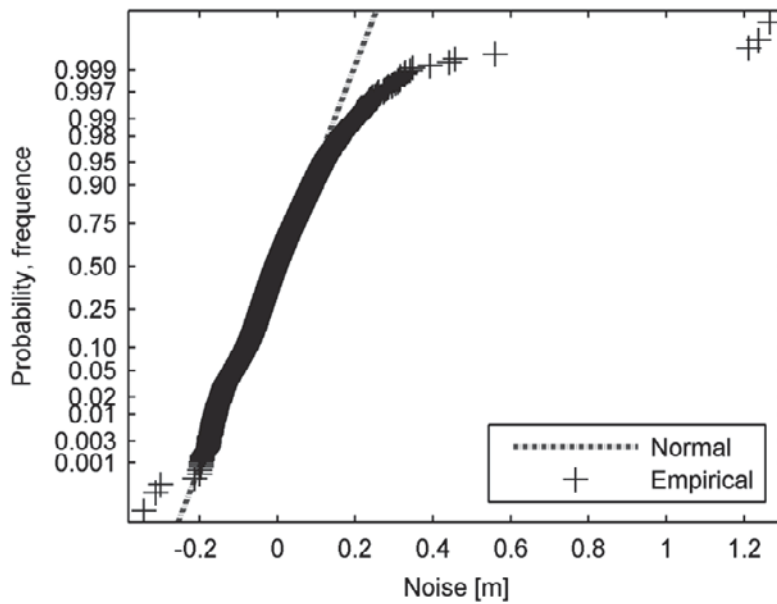


Figure 5: Normal probability plot of noise relating to the year 2005.

3 Statistical analysis of the meteorological contribution

By reporting the points of each year on the probability plot, it was first established that the noise values do not follow the normal distribution (Fig. 5). This is an expected result, since the noise, if really due to meteorological factors, should rather follow an extreme value distribution, as the crosses on the NE corner of the figure confirm.

Therefore, the Gumbel, GEV (Generalized Extreme Value) and Weibull distributions were considered (Kotz and Nadarajah, 2001). To this aim, the positive noise (onshore storms) was separated from the negative noise (offshore storms) and the latter considered in its *absolute value*, because, actually, what is connected with the contingent meteorological situation is the noise *intensity*. The two data sets were then treated separately, as belonging to different populations.

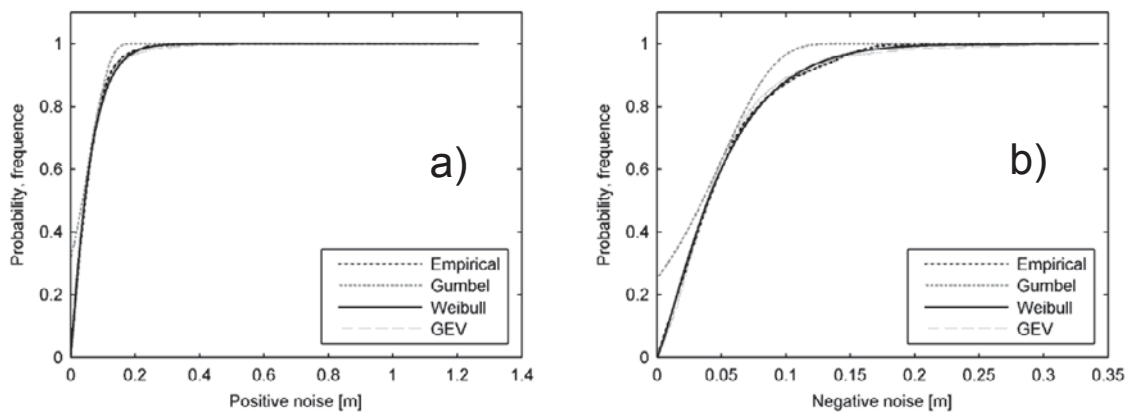


Figure 6: Comparison, for the noise relating to the year 2005, of the empirical cumulative distribution with GEV, Gumbel and Weibull distributions: a) positive noise; b) negative noise.

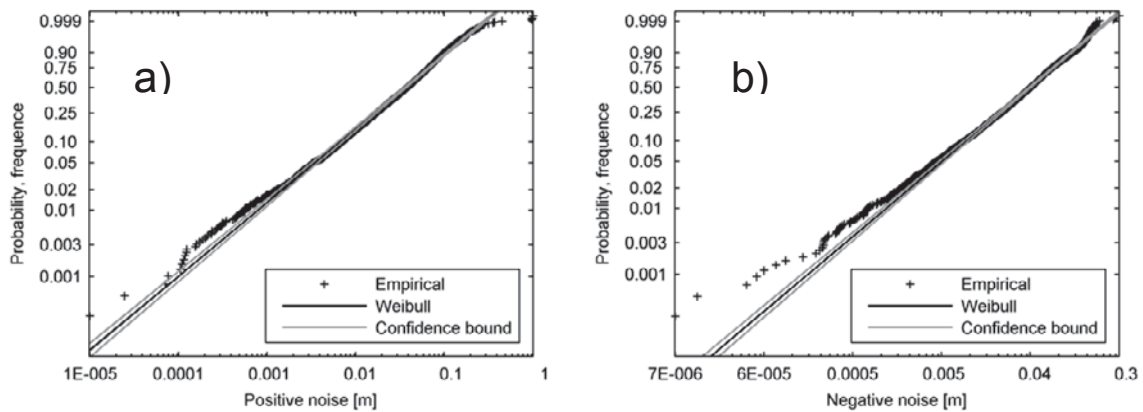


Figure 7: Weibull probability plot, with 95% confidence bounds, relating to the noise of the year 2005: a) positive noise; b) negative noise

For each data set of each year, the empiric frequency curve was compared with the curves of the three laws considered. Fig. 6 shows, as an example, the comparison relating to the year 2005. On the whole, both the positive (Fig. 6a) and negative noises (Fig. 6b) follow the Weibull distribution more closely than the other two. The same result was obtained for the other years.

Fig. 7, shows, as an example, the Weibull probability plot relating to the positive noise (Fig. 7a) and the negative noise (Fig. 7b) of the year 2005. This figure too shows an overall good fit, for the practical purposes, of the Weibull distribution with the experimental points, both for the positive and the negative noise, even though more than half of the points fall outside the confidence bounds. It has to be noted that the deviations of the lowest points seem appreciable because of the logarithmic scale. Similar results were obtained for the other years examined. However, in order for reliable predictions in the medium and long term to be carried out a multi-year distribution has to be recognized.

Therefore, the noise data of the whole observation period 1999-2009 (the positive values being separated from the negative values) were processed *altogether*, considering the same extreme value distributions as above. Once again the Weibull distribution proved to be the best and, therefore, it was assumed by us as the *noise distribution*. Figs. 8a and 8b show the probability plots with 95% confidence bounds of the Weibull distribution for the positive and negative noise respectively. Both panels show a good fit of the Weibull distribution with the points. Once again, the apparent noticeable detachment of the lower points of the negative noise from the line, due to the logarithmic scale, is actually less than 1 cm.

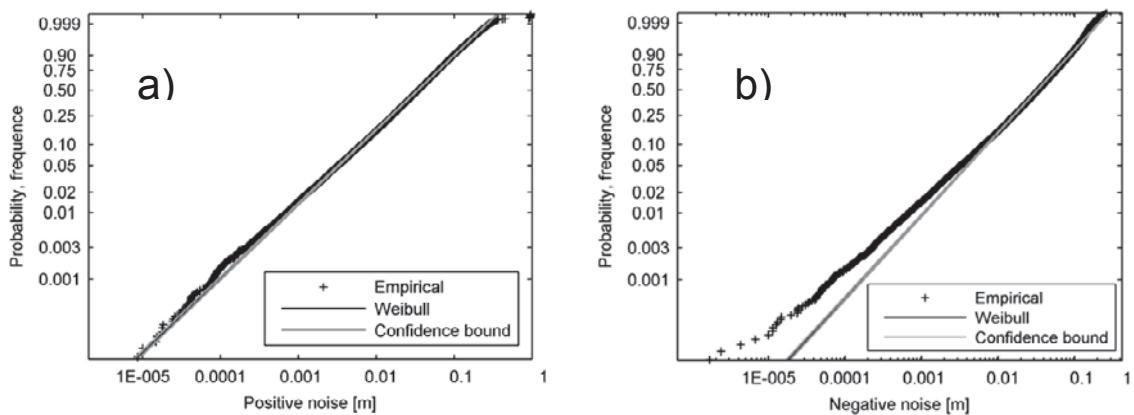


Figure 8: Weibull Probability plot, with 95% confidence bounds, relating to the whole period 1999-2009: a) positive noise; b) negative noise

4 Discussion of results

The result that the Weibull distribution fits both the points of each year and the points of all the years together, on the one hand, gives robustness to the assumption that the noise is produced by “extreme” meteorological factors, and, on the other hand, makes likely the supposition that this law can be used to forecast extreme sea levels even in the long term, as is required in many practical applications. To the latter aim, obviously, the measurement data set in the site of interest should concern an observation period longer enough than the 11-year period considered in the case study on *Porto Empedocle*. Of course, in order for the Weibull distribution to be recognized as a “general” law for tide noise, further investigations have to be performed in many different sites, in the Mediterranean Sea as well as in other seas and oceans.

As for the practical applicability of these results, it has to be noted that in the practical applications a probability expressed in terms of a return period *in years* is required, which is not the same probability as expressed by the Weibull distribution we obtained processing *hourly* data. Actually, the connection between these two probabilities is not immediate, because in each year we find positive and negative noise values which differ in numerosness and magnitude: usually, in our data set the positive values are less numerous than the negative ones, but on average they are higher; numerosness and magnitude vary from year to year. Therefore, when calculating the empirical frequency of a noise value, belonging to the one-year observations either of positive or negative noise, the allocation of the noise values between positive and negative *in that year* has to be taken into account. The calculation becomes more complicated when we have to process altogether the data collected in a multi-year period. This basic topic will be developed in further papers.

Another major question to be developed, in the perspective of a more organic view, is the relationship between storm surges and tides, or the compound probability that a storm surge of fixed intensity (and consequent probability) will effect a tide of given amplitude (and consequent probability). In this respect, it is interesting to observe that the Weibull distribution is that usually adopted for the wave heights (Coastal Engineering Manual, 2002). The storm-tide connection, as already mentioned, will be developed in further papers, using the tide measurements of the present paper together with the wave measurements of the nearby buoy.

5 Conclusions

Analysis of tide measurements taken in a harbour located in the middle of the Mediterranean Sea was carried out in order for a robust law able to predict sea level oscillations to be recognized. The harbour chosen as a case study is located on the south coast of Sicily (Italy) and is relatively close to a wave buoy located along the same almost straight coast, which will allow us to study the connection between tides and storms in this site.

It was first recognized that sea level oscillations are a result of so-called astronomic factors, persistent and quasi-periodic, and meteorological factors, by contrast contingent and not predictable for certain in the medium and the long term. As a consequence, the extreme tides, mainly produced by extreme meteorological situations, are not predictable by a deterministic way, so that a statistical approach proves to be necessary.

For each year of the period 1999-2009, during which data were continuously recorded, the measurements were used to draw the astronomic tide through the harmonic analysis carried out by means of the software package T_TIDE. Then, the tide part imputable to meteorological factors, that we called the “noise”, was estimated as the difference between the observed tide and the astronomic tide. The positive noise was imputed to sea storms onshore and the negative noise to sea storms offshore: consequently, statistical analysis was carried out separately for the positive noise and negative noise, considered as distinct populations.

Having discarded the Gaussian distribution, which of course proved to be unfit for a variable like noise, the Gumbel, GEV and Weibull distributions were tested, which in contrast with the former are expressly conceived for extreme values, as the higher and the lower sea levels have to be considered. The tests showed that the Weibull distribution fits the points better than the other two, both for the data of each year and for the data of the whole observation period altogether.

This result shows that the Weibull distribution can be adopted for predicting exceptional sea levels in the study site. Of course, in order for a robust prediction in the long term to be carried out a measurement data set related to an observation period rather longer than the 11-year period considered in the present study is necessary.

Further tests in different sites, both in the Mediterranean Sea and in other seas and oceans, are necessary to confirm whether the Weibull distribution can be assumed as a "general" probability law for sea level oscillations.

The next steps of this research will concern attainment of a probability expressed as a return period in years on the basis of hourly recordings and the connection between the storm surges observed by the buoys and the tides gauged onshore.

6 References

- Faggioni, O.; Arena, G.; Bencivenga, M.; Bianco, G.; Bozzano, R.; Canepa, G.; Lusiani, P.; Nardone, G.; Piangiamore, G. L.; Soldani, M.; Surace, L.; Venzano, G. (2006): The Newtonian approach in meteorological tide waves forecasting: preliminary observations in the East Ligurian harbours. In: *Annals Of Geophysics*, Vol. 49, No 6, pp. 1177-1187, ISSN 1593-5213.
- Kamphuis, J. (2010): *Introduction to coastal engineering and management*. World Scientific Pub Co Inc, Singapore. ISBN 13 978-981-283-484-3.
- Kim, S.Y.; Terrill, E.J.; Cornuelle, B.D.; Jones, B.; Washburn, L.; Moline, M.A.; Paduan, J.D.; Garfield, N.; Largier, J.L.; Crawford, G.; Kosro, P.M. (2011): Mapping the U.S. West Coast surface circulation: a multiyear analysis of high-frequency radar observations. In: *Journal Of Geophysical Research-Oceans*, Vol. 116, No 3, ISSN 0148-0227.
- Kotz, S.; and Nadarajah, S. (2001): *Extreme Value Distributions: Theory and Applications*, World Scientific Publishing Company. ISBN 1860942245.
- Manzano-Agugliaro, F.; Corchete, V.; Lastra, X. B. (2011): Spectral analysis of tide waves in the Strait of Gibraltar. In: *Scientific Research And Essays*, Vol. 6, No 2 pp. 453-462, ISSN 1992-2248.
- Pashova, L.; Popova, S. (2011): Daily sea level forecast at tide gauge Burgas, Bulgaria using artificial neural networks. In: *Journal of Sea Research*, Vol. 66, No 2, pp. 154-161, ISSN 1385-1101.
- Pawlowicz, R.; Beardsley, B.; Lentz, S. (2002): Classical tidal harmonic analysis including error estimates in MATLAB using T_TIDE. In: *Computer & Geosciences*, Vol. 28, No 8, pp. 929-937, ISSN 0098-3004.
- U.S. Army Corps of Engineers. (2002): *Coastal Engineering Manual*. Engineer Manual 1110-2-1100, U.S. Army Corps of Engineers, Washington, D.C. (in 6 volumes).

Estimation of the wave energy potential of the northern Mediterranean Sea

Valentina Vannucchi¹ and Lorenzo Cappietti²

Abstract

This paper presents some preliminary analyses of a wave data set arising from a numerical simulation model carried out to obtain distribution maps of the wave energy potential in the northern Mediterranean sea. The most energetic areas are highlighted, as well as the values of the monthly mean power in front of several existing harbours in the studied domain with the aim of providing supporting evidence for further studies on the localization and assessment of wave energy pilot plant.

1 Introduction

At present, the energy sector is obliged to use a renovating process directed towards environment friendly renewable energy. This process has seen the emergence of the use of wave energy. The EU Commission publications "WERATLAS—Atlas of Wave Energy Resource in Europe" by Pontes et al. (1996) and "Ocean Energy Conversion in Europe, Recent Advancements and Prospects, (2006), OEC2006 indicate a basis of the potential for extracting energy from sea waves (see also Nielsen, 2005), however, the idea of converting the energy of ocean surface waves into useful energy forms is not new (Salter 1974). There are techniques that were first patented as early as 1799 (Girard & Son, France). Indeed, the amount of research and development work on Wave Energy Converters (WEC) is quite large and extensive reviews have been provided, among others Salter (1989), Thorpe (1992), Thorpe (1999), Ross 1995, Petroncini (2000), Clément et al. (2002), Falnes 2007 and Falcao, 2010.

In order to assess the feasibility of constructing an energy production plant based on WECs, a proper characterization of the local wave climate as well as the estimation of the available wave energy potentials must be effected. In this perspective, the Mediterranean sea has received less attention since it is much less energetic than the oceans. However, the utilization of the wave energy available in the Mediterranean sea could be of some interest, for example, in a circumstance such as WECs embodied into harbour breakwaters. In this case, the harbour breakwater becomes a multifunctional structure where the cost of the infrastructures required by both functionalities are shared (harbour tranquillity and energy production) thus enhancing the value of the use of the WECs.

In this work, a preliminary set of analyses concerning the wave energy potential of the Northern Mediterranean Sea has been carried out.

2 Used wave data set

The analyses of this paper are based on wave data arising from numerical simulation models for wave generation coupled with atmospheric models. The data was provided by IFREMER that has developed a pre-operational system, called PREVIMER, aiming to provide short-term forecasts concerning the coastal environment along the French coastlines bordering the English Channel, the Atlantic Ocean and the Mediterranean Sea.

¹ Università di Firenze-Dipartimento di Ingegneria Civile e Ambientale, Via S.Marta 3, 50139 Firenze, Italy, valentina.vannucchi@dicea.unifi.it

² Università di Firenze-Dipartimento di Ingegneria Civile e Ambientale, Via S.Marta 3, 50139 Firenze, Italy, cappietti@dicea.unifi.it

The numerical simulation model used is the WaveWatch III, with a third-order accuracy propagation scheme in space and time (the model used in the present paper is Menor4000M). The weather forecast conditions were provided by Météo-France and covered the twelve hours' duration and the following six days. The results are provided in the NetCDF format at 3 hour intervals and the variables are, for example, wave height, period, direction.

The data available, at the time of this writing, covers a period of 1 year and 10 months, from July 2009 to April 2011, so the only complete year, up to now, is 2010.

3 Methodology

It is well known that in case of regular waves the specific wave power is equal to eq. (1)

$$P = \frac{1}{8} \gamma H^2 C_g \quad (1)$$

with γ specific weight [N/m³]
 H wave height [m]
 C_g group celerity [m/s]

Irregular waves can be considered a superposition of an infinity number of regular components and the total power is calculated as the sum of the power associated to any component, according the eq. (2).

$$P = \sum_{i=1}^{\infty} \frac{1}{8} \gamma H^2(f_i) C_g(f_i) \quad (2)$$

In terms of frequency spectrum, $S(f_i)$, the wave height squared is expressed as in eq. (3)

$$H^2(f_i) = 8 \cdot S(f_i) \Delta f \quad (3)$$

In case of deep water the group celerity is computed as in eq. (4)

$$C_g(f_i) = \frac{1}{4} \frac{g}{\pi f_i} \quad (4)$$

with g acceleration of gravity [m/s²]
 π Pi constant [-]
 f frequency [1/s]

Substituting eq. (3) and eq. (4) into eq. (2), the eq. (5) is obtained:

$$P = \frac{g\gamma}{4\pi} m_{-1} \cdot \frac{m_0}{m_0} \quad (5)$$

where

$$m_k = \sum_{i=1}^{\infty} S(f_i) f_i^k \Delta f \quad (6)$$

Finally, in case of irregular waves, wave power per unit length of wave front is calculated as in eq. (7)

$$P = \frac{1}{64} \frac{g^2}{\pi} \rho H_{m0}^2 T_{m-1,0} \quad (7)$$

with ρ water density and providing that $H_{m0}=4m_0^{1/2}$ is the significant wave height wave height and $T_{m-1,0}=m_1/m_0$ is the mean wave period.

4 Results

The spatial distribution of the monthly mean power has been computed and reported in the form of contour maps for each month of a given year (not shown in this paper for brevity). The maximum values of the monthly mean power that resulted in the studied spatial domain have been highlighted in figure 1 and the localization of the related points is depicted in figure 2. Moreover, the spatial distribution of the mean power for the year 2010 has been computed as the mean of the monthly mean powers, see figure 3.

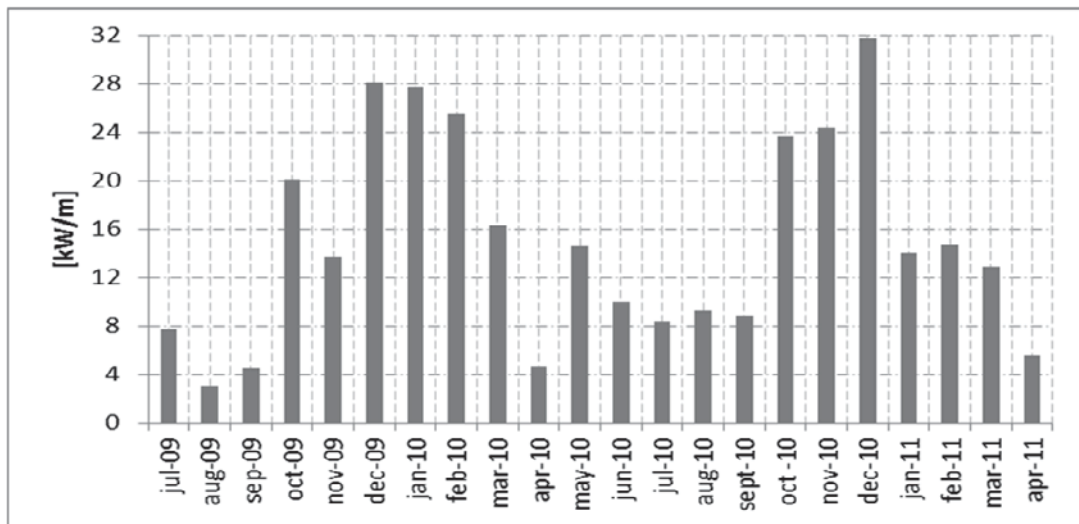


Figure 1: Maximum values of the monthly mean power and its spatial localization as reported in figure 2.

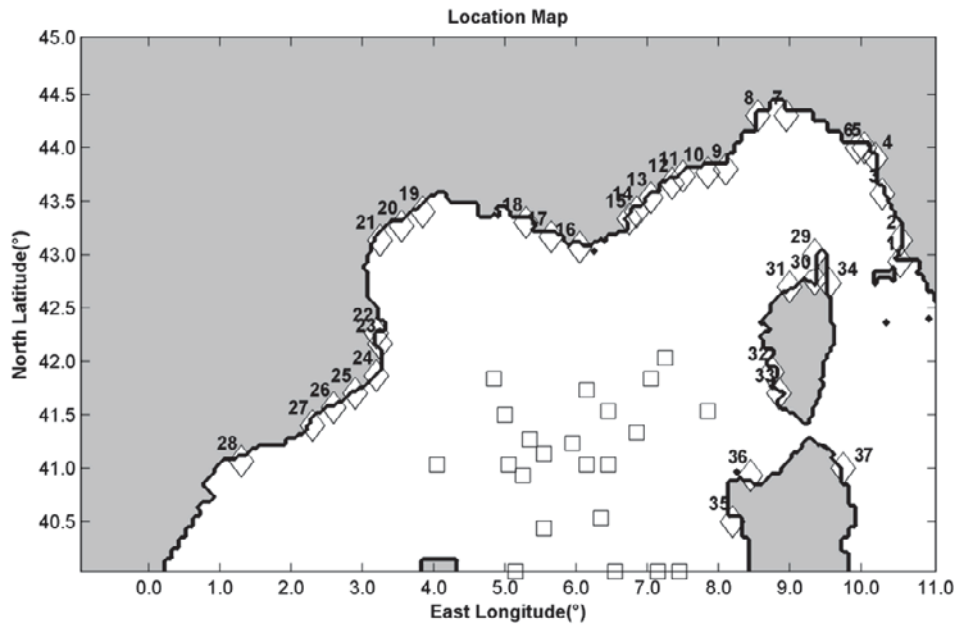


Figure 2: Location map of sea sites characterized by the maximum monthly mean power (□) and of harbours in front of which the values of monthly mean power were extracted, see figure 4, 5 and 6 (◇ and the corresponding number).

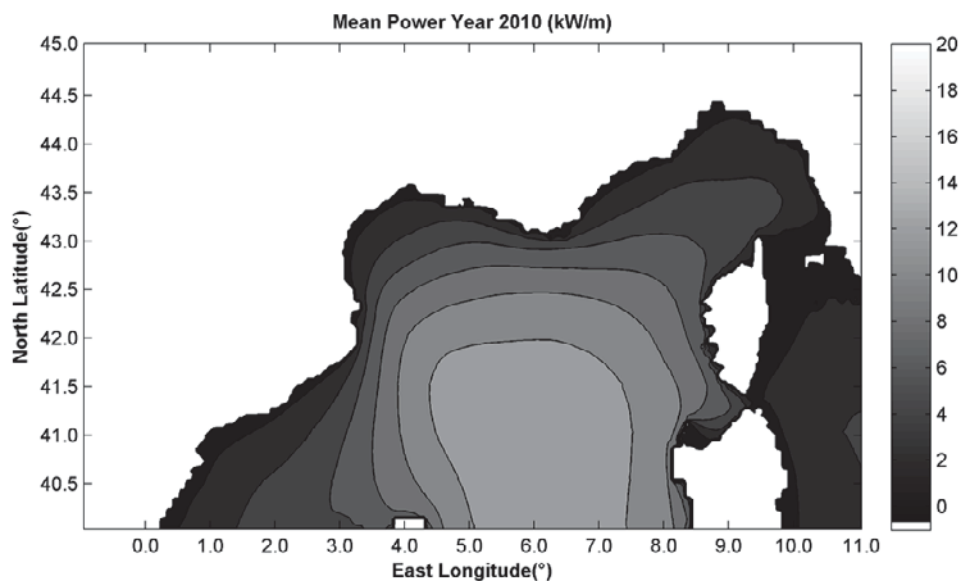


Figure 3: Spatial distribution of the Yearly Mean Power computed by using the data for the Year 2010 [kW/m]

In addition to the above analysis, it was also considered important to analyse the monthly mean power in 37 different points located in front of the main harbours present in the Northern Mediterranean, see figure 2. In fact we extracted the values computed at the points of the numerical domain that are close to the harbours locations. These values are reported in the following figures: i) figure 4 for the Italian harbours, ii) figure 5 for the French harbours; iii) figure 6 for the Spanish harbours.

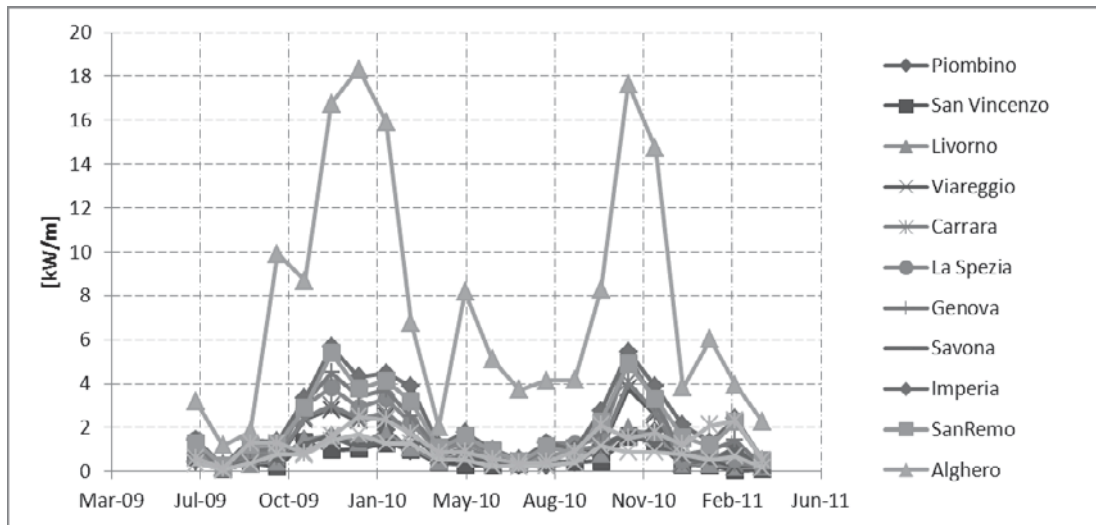


Figure 4: Mean Power Italian Harbours [kW/m]

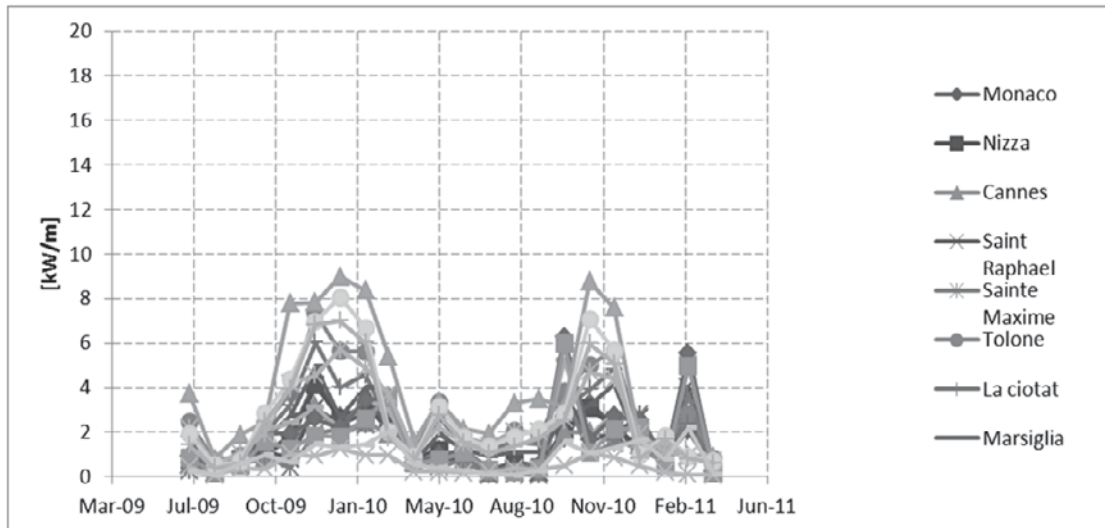


Figure 5: Mean Power French Harbours [kW/m]

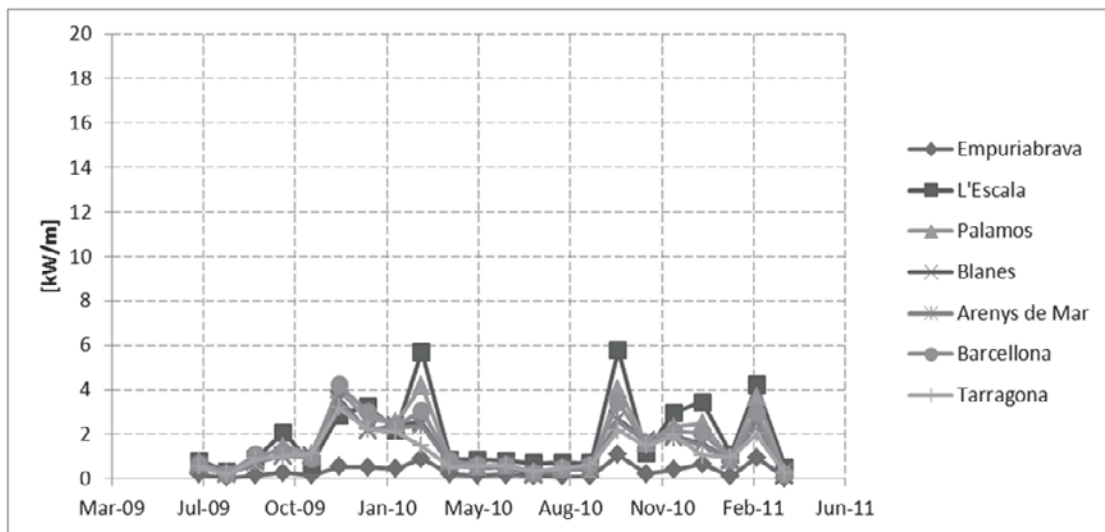


Figure 6: Mean Power Spanish Harbours [kW/m]

Table 1: Yearly mean power computed by using the wave data for the Year 2010 [kW/m] at the 37 harbours analyzed, see figure 2.

			Mean Power Year 2010 [kW/m]			Port	Cap	Mean Power Year 2010 [kW/m]
1	Italy	Piombino	0.90	20	France	Port d'Adge		2.00
2		San Vincenzo	0.74	21		Gruissan		1.71
3		Livorno	1.01	22	Spain	Empuriabrava		<u>0.36</u>
4		Viareggio	1.56	23		L'Escala		2.13
5		Carrara	1.63	24		Palamos		1.71
6		La Spezia	2.02	25		Blanes		1.34
7		Genoa	2.15	26		Arenys de Mar		1.31
8		Savona	0.86	27		Barcellona		1.58
9		Imperia	2.63	28		Tarragona		1.21
10		SanRemo	2.30	29		Port de Cent.		4.84
11	France	Monaco	1.63	30	France (Corsica)	San Fiorenzo		0.59
12		Nice	1.63	31		Isola Rossa		3.01
13		Cannes	1.24	32		Ajaccio		3.61
14		Saint Raphael	1.62	33		Propriano		3.12
15		Sainte Maxime	1.39	34		Bastia		0.87
16		Toulon	3.37	35	Italy (Sardinia)	Alghero		<u>9.08</u>
17		La ciotat	2.66	36		Porto Torres		0.78
18		Marseille	2.14	37		Golfo Aranci		1.33
19		Sete	1.88					

5 Discussions

It is evident that the most energetic parts of the northern Mediterranean are those on the Western coasts of the islands of Corsica and Sardinia, see figure 3. It is worth noting that during the months of October, November and December, the maximum monthly mean power in the studied domain is always greater than 20 kW/m (except Nov 09). It is interesting to notice that the monthly mean power values in front of all harbours analysed: i) do not exceed the value of 8 kW/m during the autumn-winter months (except Alghero that reaches the considerable value of 18 kW/m) and ii) do not exceed the value of 4 kW/m, during the spring-summer months. Between the Italian (figure 4), French (figure 5) and Spanish (figure 6) harbours it seems that those located on the French coast are characterized by slightly higher values of monthly mean power in their waterfronsts, at least considering the studied spatial domain, see also Table 1.

Previous analysis carried out by Vicinanza et al. 2011, using wave buoys located at Alghero (Sardinia) and La Spezia have indicated a yearly mean power equal to 9.05 kW/m and 3.46 kW/m. Their results, that are based on wave time series of about 18 years in length, are quite close to the values presented here (see table 1).

6 Concluding remarks

The yearly mean wave power, calculated by using the wave data registered in the year 2010, in the different points located in front of the main harbours present in the Northern Mediterranean, are usually below 3.0 kW/m, and the only values close or over 5 kW/m are in front of the

harbours at Alghero (9.08 kW/m,) and Port de Centauri (4.84 kW/m). These values are considerably lower than the potential energy in the oceans (approximately 20-80 kW/m), and it would seem that the construction of power plants based on WECs, in the studied area, would not be a viable option if merely for economic reasons. The Northern Mediterranean, however, may be of some interest for the testing of scale models in order to assess their effectiveness and to achieve an optimization before the installation of the final prototype. Moreover, the sustainability of the construction of multifunctional structures devoted to harbours/shore defence and energy production could be studied considering the added value which would arise from the sharing of construction costs.

7 Acknowledgements

This work has been conducted as partial fulfilment of the PhD student-program of the author V. Vannucchi, PhD course on Civil and Environmental Engineering, DICeA, University of Florence.

The authors wish to thank the IFREMER centre for data delivery and Doct. Fabrice Lecornu for his help regarding the understanding of data structure.

8 References

- Falnes J. (2007): Review - A review of wave-energy extraction. In: *Marine Structures*, Vol. 20, pp. 185-201.
- Falcao A. (2010): Wave energy utilization: a review of the technologies. In: *Renewable and Sustainable Energy Reviews*, Vol. 14, pp. 899-918.
- Vicinanza, D., Cappietti, L., Ferrante, V., and Contestabile, P. (2011): Estimation of the wave energy in the Italian offshore. In *Journal of Coastal Research*, SI 64, pp. 613-617.
- Clément A.H., McCullen, P., Falcão A., Fiorentino, A., Gardner, F., Hammarlund, K., Lemonis, G., Lewis, T., Nielsen, K., Petroncini, S., Pontes, M.-T., Schild, P., Sjöström, B.O., Sørensen H. C., Thorpe, T. (2002) "Wave Energy in Europe - Current Status and Perspectives", *Renewable and Sustainable Energy Reviews* 6, pp. 405-431.
- Nielsen K., (2005): Coordination Action on Ocean Energy, CA-OE. IEA- OES Newsletter, February 2005. <http://www.iea-oceans.org>.
- OEC2006, Ocean Energy Conversion in Europe, Recent Advancements and Prospects (2006), European Commission, Centre for Renewable Energy Sources Ocean Energy Conversion in Europe - Recent Advancements and Prospects 2006 -36 pp.
- Petroncini, S., (2000), "Introducing Wave Energy into the Renewable Energy Marketplace", Msc Thesis, University of Edinburgh, UK
- Ross, D., (1995), "Power from the Waves", Oxford University Press
- Salter S.H. "Wave power. Solar energy is one form of income on which we can afford to live. Here is another proposal: the use of power from the waves at sea" *Nature* 249, 720 - 724, 1974
- Salter, S.H. (1989). "World progress in wave energy - 1988". *The international Journal of Ambient Energy*. Vol. 10 (1).
- Pontes, M.T., Athanassoulis, G.A., Barstow, S., Cavaleri, L., Holmes, B., Mollison, D., and Oliveira Pires, H., 1996, "WERATLAS—Atlas of Wave Energy Resource in Europe," Technical Report, DGXII Contract No. JOU2-CT93-0390, INETI, Lisbon (URL: <http://www.ineti.pt/proj/weratlas>).
- Thorpe, T.W., (1992), "A Review of Wave Energy", ETSU-R-72
- Thorpe, T.W., (1999), "An Overview of Wave Energy Technologies: Status, Performance and Costs", "Wave Power - Moving Towards Commercial Viability", IMECHE Seminar, London, UK.

Comparative analysis of wind generated waves on the Ilha Solteira lake, by using numerical models OndisaCAD and SWAN

Adriana S. Vieira¹, Conceição J.E.M. Fortes², Geraldo de Freitas Maciel³ and Carlos Roberto Minussi⁴

Abstract

This paper describes the in-situ measurements and the application of two wind wave generated numerical models (SWAN and OndisaCaD) to the reservoir of Ilha Solteira dam in order to simulate the wind waves generation and propagation in that reservoir. A comparison between numerical results for selected wind conditions (highest average wind speed and the highest wind speed) is made and discussed. SWAN is also applied to the wind conditions observed during a six month period. This work permits to evaluate the performance of the numerical models and its adequacy to characterize the wind generated waves at that region.

Keywords: Wind waves, Numerical modeling, in-situ measurements, SWAN, OndisaCAD, Ilha Solteira

1 Introduction

The dam reservoirs of São Paulo State have multiple uses and are part of the country waterways where important commercial navigation routes are established. In this way those reservoirs have an important role in the economy of the regions around them.

Due their huge dimensions, the wind effects on the water surface can cause problems to the navigation security, to the stability of the river banks, to the infrastructures around the reservoir or even to public safety. Accidents which have already occurred in the Tietê-Paraná waterway show the need to have studies/methodologies to forecast and to monitor wind waves in those huge artificial lakes.

One of these studies is the ongoing project ONDISA (*Ondas no lago de Ilha Solteira*), UNESP (1997, 2008), which aims to improve the understanding of hydrodynamics and morphodynamics inside Ilha Solteira dam reservoir. This reservoir is located in the northwest of São Paulo state, Brazil, with an extension of 100 km. The project goal is being achieved through the implementation of an interdisciplinary study that integrates three distinct methodologies: field data acquisition, laboratory investigation and numerical modelling.

In particular, one important aspect of this study is the evaluation of the effects of wind generated waves on the lake margins and/or on the navigability security. For that, field-data acquisition and processing and numerical modelling of wind-generated waves have being used to characterize the local wave climate.

An extensive field data campaign has been undertaken since January, 2008. Several instruments were deployed in different locations on the Ilha Solteira reservoir and on its margins to measure waves, currents and winds.

These measurements, in spite of being very useful to describe local wave characteristics, are of too short duration to characterize the long-term wave climate. Besides, they also suffer from a restricted spatial representation of the wave conditions in addition to the high cost of equipment deployment, maintenance and monitoring.

¹ UNESP, Av. Brasil, 54, Ilha Solteira- S.P – Brasil, adriana.ilha@gmail.com

² National Laboratory of Civil Engineering, Av. do Brasil 101, Lisbon, 1700-066, Portugal, jfortes@lnec.pt

³ UNESP, Av. Brasil, 54, Ilha Solteira- S.P – Brasil, maciel@dec.feis.unesp.br

⁴ UNESP, Av. Brasil, 54, Ilha Solteira- S.P – Brasil, minussi@dee.feis.unesp.br

The use of numerical wind-wave models can overcome this aspect. Since 2009, OndisaCAD model, developed at the São Paulo State University (UNESP), has been used to calculate the wave heights and periods inside the dam reservoir. This model is based upon empirical formulation like JONSWAP, SMB, Wolf, Creager and SGM. Using the fetch and climatology of the winds, the model determines the largest wave heights, periods and identifies critical points for both the safety of navigation and the stability of the banks of the reservoir (Maciel et al., 2009, Morais et al. 2009). However, this model is based in simpler formulations which do not take into account the variability and non-stationary of the winds and waves as well as the nonlinear characteristics of the wind-generated waves.

In order to consider these effects, the use of the nonlinear spectral numerical model SWAN, Booij et al. (1999), is a good alternative and constitutes the main objective of the present work.

Spectral nonlinear model SWAN is a numerical model that takes into account the wave generation, propagation, attenuation phenomena and non linear interactions between waves and currents. One big advantage of the SWAN model is its versatility: it can be applied to large open coastal areas or it can be applied in confined areas (such as estuaries or lakes) and in both cases the forcing of the model can be carried out by winds, waves and/or currents. In both situations, the model performs the generation and/or propagation of these waves on the coastal area or inside the estuary until the waves are dissipated at their boundaries (beaches, cliffs).

Anyway, the application of SWAN involves the establishment of a set of parameters, which must be calibrated for each case study. Therefore, it is interesting to apply the model to situations where data exists (or where results from another numerical model already calibrated are available) and to evaluate its performance.

The present work, which is a contribution to the ONDISA project, deals with the application of both SWAN and OndisaCad models to Ilha Solteira dam reservoir, in order to simulate the wind waves generation and propagation inside the dam. The behavior of these two models is analyzed and their results are compared for several wind conditions selected from the period between 2007 and 2009. From this comparative analysis, it is possible to assess the performance of SWAN model. Finally, the numerical model is applied to a small period of that study period, between July and December 2009.

This paper begins with a short description of the study area (section 2) and of the data acquisition. Then the description of the numerical models used (section 3) and its application to the study area (section 4) is presented. A discussion of the results obtained with both models is presented in section 5. Finally, the conclusions are drawn in section 6.

2 Study area

The system under study is the Ilha Solteira dam reservoir which is located near the Ilha Solteira city, one of the Brazilian city councils at the northwest of São Paulo state, Brazil, Figure 1, 699 km far away from São Paulo capital. The artificial lake has an extension of 100km and its dam is located at: latitude 20°25'58" S, longitude 51°20'33" W, and an altitude of 335 m, approximately. This dam is one of the most important in the Tietê-Paraná waterway. It is located where the rivers Tietê and Paraná meet and it is near the border of the Mato Grosso do Sul State.

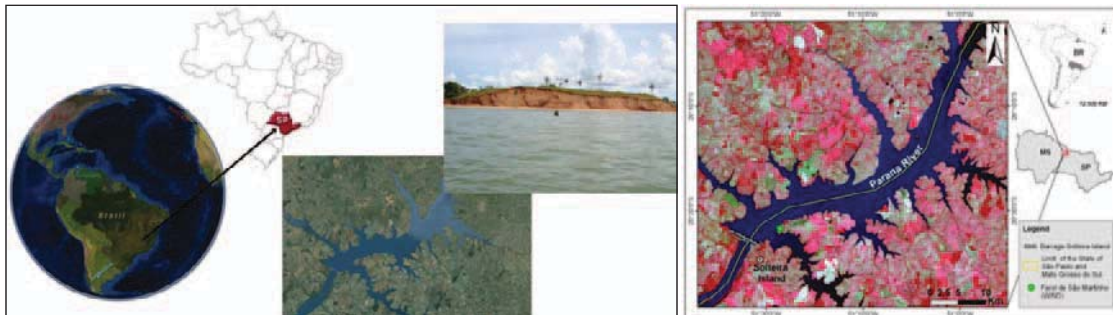


Figure 1: Dam reservoir of Ilha Solteira, São Paulo, Brazil. General views.

2.1 Data Collection

An extensive monitoring plan in this region is being carried out as well the definition of an alert system within the framework of the research project FINESP - ONDISA5. The objective is to develop predictive models for wind wave generation to be included in a warning system for navigation. Several wind and wave measuring campaigns have been undertaken.

The data acquisition system for wind velocity and its direction comprises 2D anemometers distributed around the lake and positioned 30 meters high on lighthouses. Once these field data are collected they are sent by radio telemetry to be processed and stored in the laboratory of Hydrology and Hydrometric of UNESP at Ilha Solteira. For the analysis and processing of wind data, the software OndisaCsat3 is used. This software automatically displays the results on a chosen interval, as follows: the number of samples taken, the wind average intensity, its frequency of occurrence, the wind direction and the highest winds. It has also the option of saving the original data to be able to analyze the raw data, to check it and compare results (Maciel et al., 2009).

Moreover, there is also a vertical structure 6 m tall implemented inside the lake, attached to a tree, where shell-type anemometers positioned at 0.3, 0.6, 1.2 m were attached, Figure 2. The objective is to profile the wind data at this site. On top of this tower, it is installed a 2D anemometer, Figure 3a, whose wind data is used in the present work. The wind data have been recorded in a CR1000 data-logger from Campbell Scientific. The shell-type anemometers are used to measure the wind speed only, while the 2D sonic anemometer measures wind speed and direction.

For wave measurements, a wave rider buoy and ADCP wave system, located at the bottom of the lake, are used. This last system is still under implementation and its data will be transmitted online to the central receiving data. An example of wave processing is shown on Figure 3b.

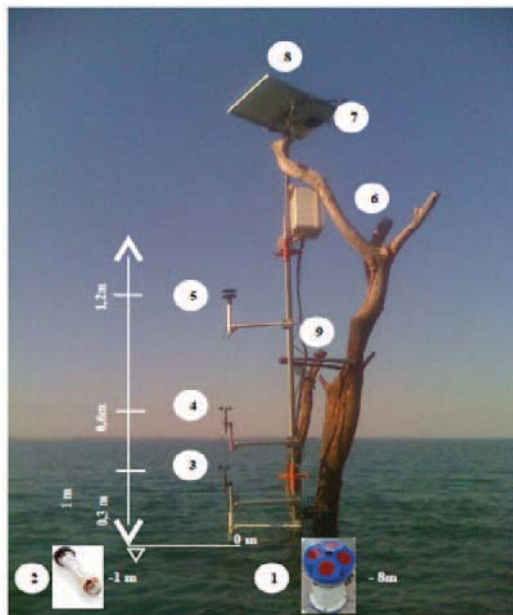


Figure 2: Instrumentation and telemetry.

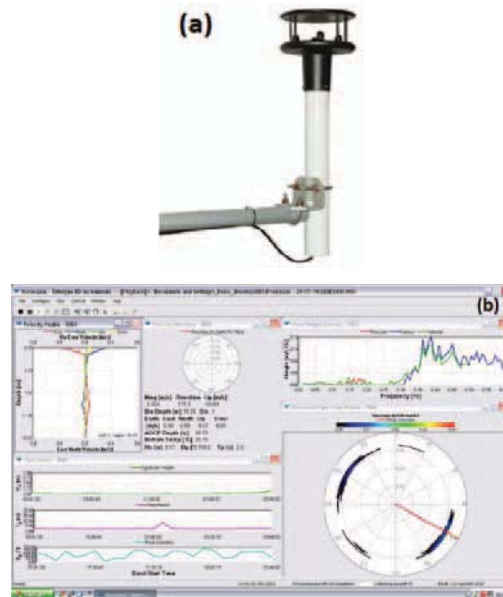


Figure 3: (a) 2D sonic anemometer,
(b) Wave processing software
WAVESMON.

In detail, the equipment deployed inside the lake and near the tree consist on (Figure 2 and Figure 3a): (1) an ADCP-WAVES, which was deployed at 8 m depth, 20 m away from the tree basis and connected via cable to the radio located in the instrumentation box; (2) a pressure transducer (Druck), which was deployed at 1 m depth and connected to the data-logger set / radio located in the box instrumentation; (3 and 4). Conventional shell-type anemometers, which are located at 0.3, 0.6, 1.2 m high on the structure tied to the tree; (5) a 2D Ultrasonic

Anemometer, which was located at the top of the structure; (6) Box instrumentation, which contains radio, data loggers, batteries, etc; (7) Antennas for data transmission; (8) a solar panel power system, 80w; (9) a camera camcorder with high resolution and low power, for real time wave visualization.

2.2 Wind conditions at the São Martinho station

As an example, Figure 4 shows the directional distribution of the tri-hourly wind speed values measured at the 2D anemometer in the period from July to December 2009, at the São Martinho station, near the dam. Based on that data, it appears that the most frequent directions are from the NE-SE quadrant or from S-W.

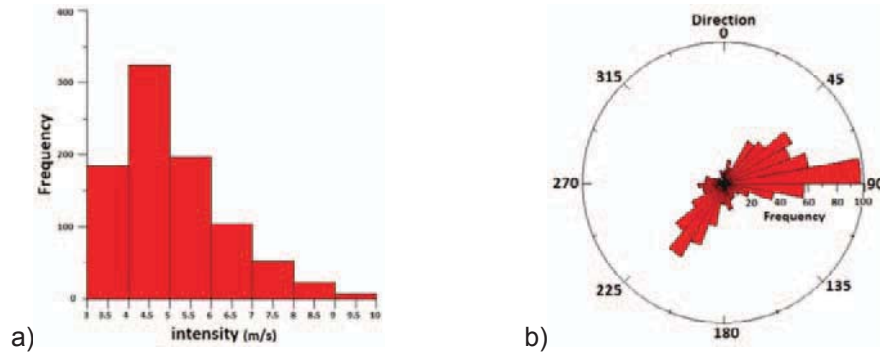


Figure 4: Characteristics of the wind in the period July to December 2009:
a) intensity, b) direction.

3 Numerical models

3.1 SWAN model

The numerical model SWAN (Simulating WAVes Nearshore) computes sea-wave generation, propagation and dissipation based on the wave action balance equation, Booij et al. (1999). This freeware wave model is being continuously upgraded by Delft University of Technology (The Netherlands).

The SWAN model is able to propagate sea waves from offshore up to the shoreline and takes into account the major physical processes of wave refraction, diffraction and shoaling due to bottom depth variation and to the presence of currents. It also includes wind induced wave growth, wave breaking due to bottom variation and to whitecapping, energy dissipation by bottom friction, wave blocking and reflection by opposing currents as well as wave transmission.

The wave field at the study region is characterized by a 2D wave action spectrum which enables the model to represent the wave growth caused by wind or the presence of swell. In this paper, it was used wave propagation at stationary modes over a rectangular grid with Cartesian coordinates.

The required data to run the SWAN model are the bathymetry of the study region and the boundary conditions at the domain entrance, in addition to a set of computation parameters. Among the several results produced by SWAN it is worth mentioning the significant wave height, the average and the peak periods, directional spreading, the bandwidth parameter and the mean water level at any point of the defined computational domain.

For a systematic application of SWAN model to different incident wave conditions, a software package named SOPRO-SWAN, Fortes et al. (2006), was developed. It is made of a user interface and the numerical model SWAN itself. The user interface facilitates data storage and manipulation and the execution of the SWAN model, as well as the post-processing of its output, namely their graphical visualization. The package was built using both Microsoft Access database and Visual Basic for Applications programming language.

3.2 ONDISACad model

The OndisaCAD model is a wind wave forecast model. It was developed in the FEIS/UNESP from the earlier work of Marques (2007), and it has been improved since then.

Motivated by historical events involving accidents with boats in the Tietê-Paraná, the team's work of UNESP Ilha Solteira, has been developing since 1997 a project to set a warning system to support navigation. As a result of this work, the software was developed and named OndisaCAD based on CADs and Autodesk AutoCAD. It is a numerical model for estimating the wave height, from the knowledge of fetch and the wind climatology. It determines the largest wave heights and it identifies the critical points for both the safety of navigation and the stability of the reservoir banks (Maciel et al., 2009).

The software is basically composed of four major computational structures: a routine that generates maps of fetches, a routine that generates maps of wave heights and a final routine that prepares diagrams of runway length or maximum heights of waves.

The software performs the calculation of the fetch using the classic method of Saville (1954), whose input variables are the contour of the lake and the wind direction. The contour of the lake can be extracted from a digitized map using an appropriate model. Then, the software provides the calculation of wave heights and periods through the JONSWAP, SMB, Wolf, Creager and SGM methods. Their input variables are the wind intensity and direction and the fetch.

The software allows the prediction of waves in real time from a database of winds. The winds are measured at the different anemometers placed around the lake. Data are sent to the laboratory of Hydrology and Hydrometric of the FEIS / UNESP where they are processed. For the analysis and processing of the data acquired, the OndisaCsat3 software is used.

The developed routines are easy to use and the graphical output is automatic. The fetch and wave characteristics maps can be generated almost instantly.

OndisaCAD program does not work fully automatically. It always requires some user interaction in all processes. The Figure 5 illustrates the flowchart of processes performed by the user:

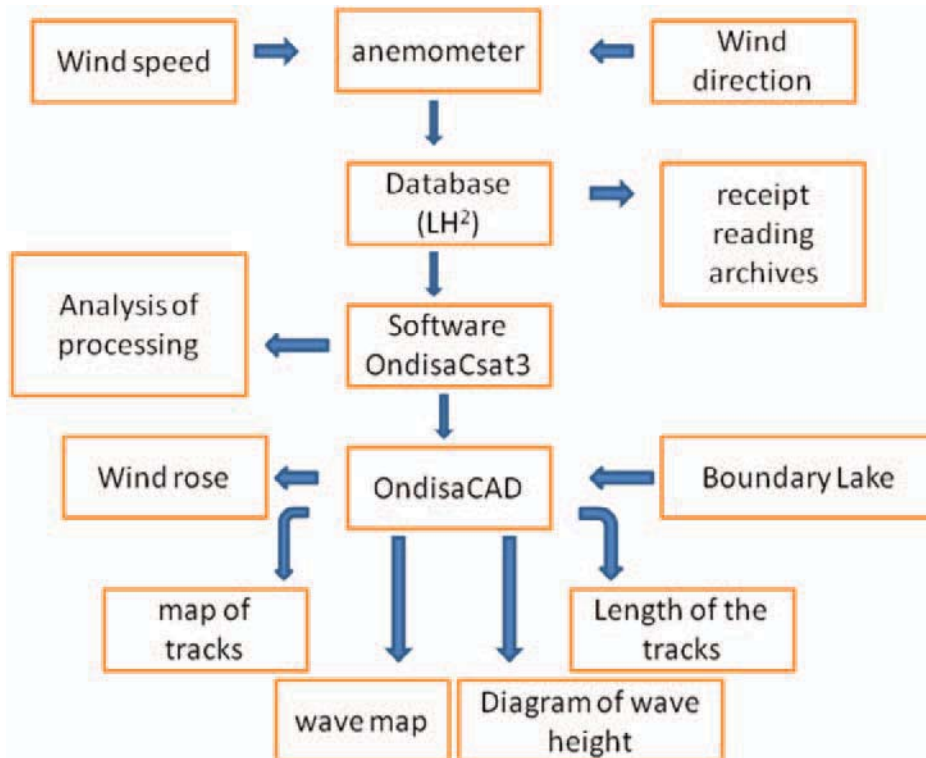


Figure 5: Flowchart.

4 Application of models

The application of SWAN and OndisaCAD models to the study area of Ilha Solteira dam reservoir in order to characterize the wind-generated waves is herein described. In the following sections, we present the input conditions of the models and compare their numerical results considering some wind conditions observed during 2007 until 2009. Finally, we present the results obtained with SWAN model for a small time period between July to December 2009.

4.1 Input conditions

4.1.1 SWAN conditions

The domain calculation of the SWAN model was discretized with 3 grids, Figure 6. The largest grid is 54 km by 33 km, the node spacing is 1000 m and it covers the whole Ilha Solteira dam reservoir. The following grid is 26.6 km by 28.4 km and with a 500 m distance between nodes. The third grid is 14.8 km by 14.3 km and has 250 m between nodes. Progressively more refined bathymetry files are used for each finer mesh, Figure 6. Several points (P1 to P5) were defined in order to obtain the SWAN results.

The use of multiple grids is needed to achieve better numerical performance. With the three grids mentioned above, the simulation typically takes 120 s, whereas with only one mesh, with the size of the first and with the resolution of the third, the simulation takes more than 10 min. If we had adopted only one grid, the realization of half year simulations (708 calculations) would be unfeasible.

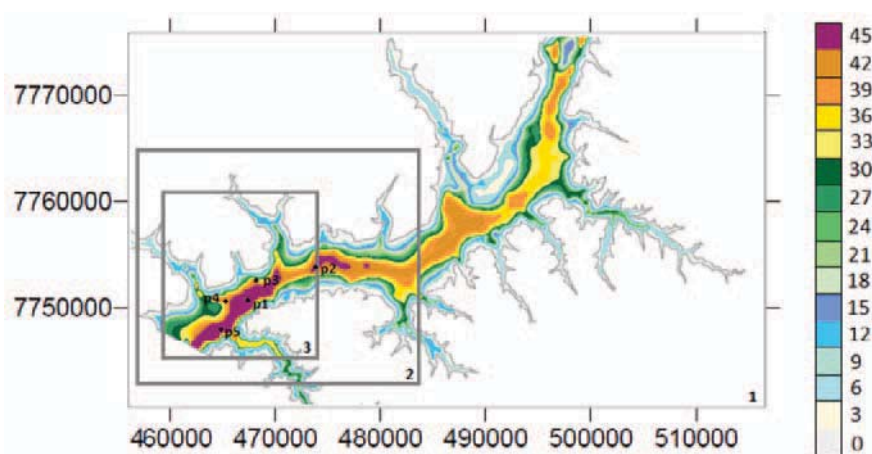


Figure 6: Grids and bathymetry. Vertical and horizontal scale in UTM.

Table 1: SWAN model. Grid characteristics.

Grid	X initial	Y initial	Nº. DX	Nº. DY	DX (m)	DY (m)
1	456680	7741700	58	33	1000	1000
2	457220	7744520	53	34	500	500
3	459329	7745690	58	57	250	250

The directional spectrum in SWAN computations was defined with a frequency discretization of 21 intervals of 0.070 to 2.0 Hz with a logarithmic distribution and a directional discretization of 2.5° covering the whole 360° range (which gives 144 direction intervals). All the SWAN version 40.72 runs were carried out in stationary mode, without the presence of currents. The physical phenomena included were at the three grids: refraction, diffraction, shoaling and wave breaking due to bottom influence and whitecapping. All the relevant parameters were introduced in the SOPRO-SWAN (Fortes et al. 2009) package.

For the input conditions indicated above, two calculations were made with the SWAN model considering: a) selected wind conditions (NNE and NNW) observed from 2007 to 2009, namely those corresponding to the highest average wind speed and the other to the highest wind speed. These wind conditions are based on measurements obtained at the vertical structure deployed inside the lake; b) all the wind conditions measured in that period.

4.1.2 OndisaCAD conditions

Considering the same wind conditions used in SWAN calculations and the JONSWAP method, the OndisaCAD model provides the wave heights all over Ilha Solteira reservoir. It was decided to adopt the JONSWAP method due to its extensive use in previous studies. It should be noted that all available methods are designed for use in deep water conditions, yet the bibliography also suggests its application to inland water bodies.

For each wave conditions, the software OndisaCAD produces the winds rose, fetch maps and diagrams of wave heights, all in real time, requiring only the introduction of the previous lake contour.

4.2 Results, analysis and discussion

4.2.1 Comparison between SWAN and OndisaCad results

Figure 7 and Figure 8 illustrate the wave-height maps for input wind conditions of NNE directions (higher average wind speed - 5.92 m/s) and NNW (maximum wind speed - 24.62 m/s) for OndisaCAD and SWAN models, respectively.

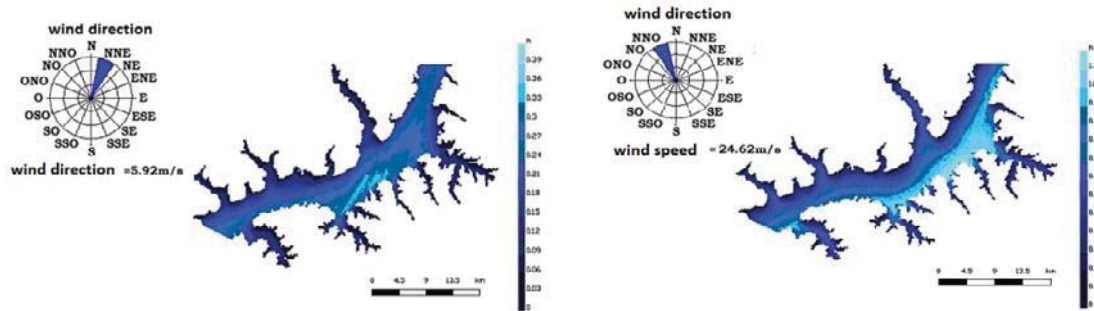


Figure 7: OndisaCAD model - wave height values: a) NNE direction, higher average wind speed (5.92 m/s); b) NNW direction, maximum wind speed (24.62 m/s).

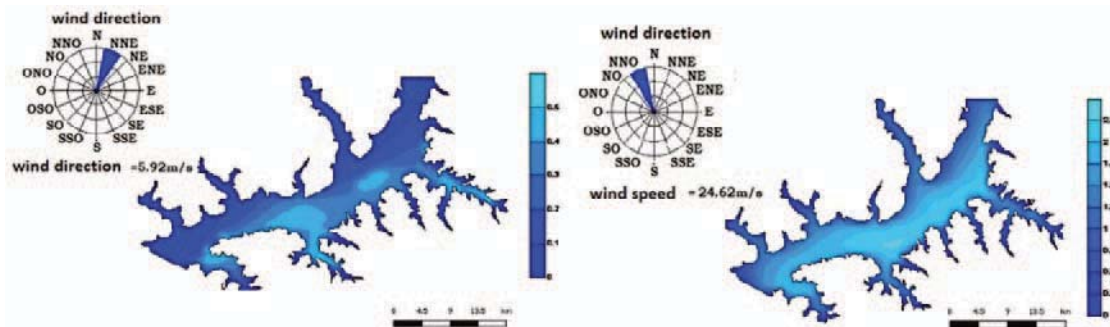


Figure 8: SWAN model – wave height values: a) NNE direction, the highest average wind speed (5.92 m/s); b) NNW direction, maximum wind speed (24.62 m / s).

From figures one can say that for both models, the wave height contours show a similar behaviour, whatever the input wind direction. Moreover, the largest waves are located on the same points that have the longest fetches for each wind direction: a) the biggest waves in the NNE direction are at southeast of Ilha Solteira reservoir, about 0.4 m in height using the model Ondisa and 0.5 m height using the model SWAN; b) for NNW direction, the biggest waves are also of the lake to the southeast of Ilha Solteira, but with about 1.20 m height using the model Ondisa and 2m using the SWAN model, since the intensity of wind in this case was 24.62 m/s.

There are some differences between the results of both models. SWAN gives in general higher values than OndisaCAD – NNE: 0.4 m for OndisaCAD and 0.8 for SWAN while NNW: 1.2 m for OndisaCAD and 2.25 for SWAN. The distribution of the wind wave contours in SWAN is smoother than in OndisaCAD. Note that SWAN model is a nonlinear spectral model while OndisaCAD uses an empirical formulation that depends only on the lake contour, wind characteristics and fetches.

4.2.2 SWAN simulations from July to December 2010

From Figure 9 to Figure 11, the time series of the significant wave height, mean wave period and wave direction in the period from July to December 2010 (a very recent period) are presented. Those results were obtained with SWAN at point P2.

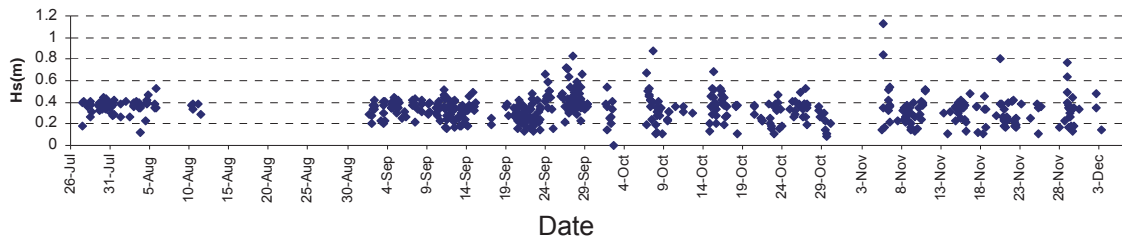


Figure 9: Significant wave height obtained with SWAN for the period July to December 2010.

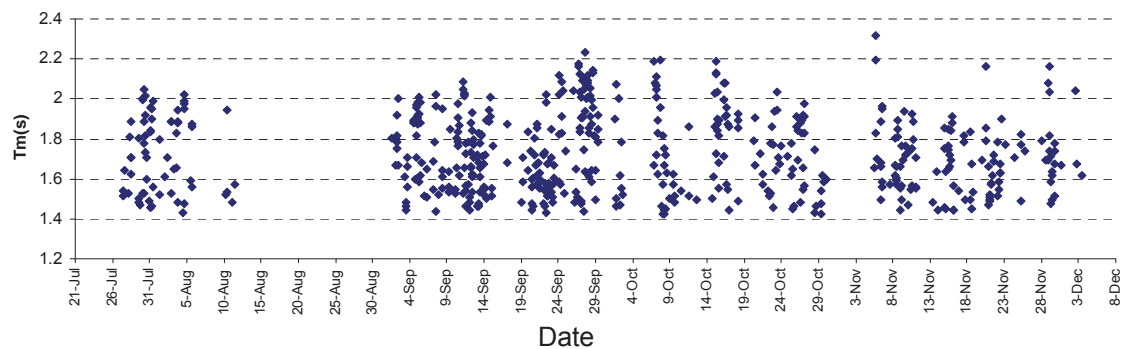


Figure 10: Average times obtained with SWAN for the period July to December 2010.

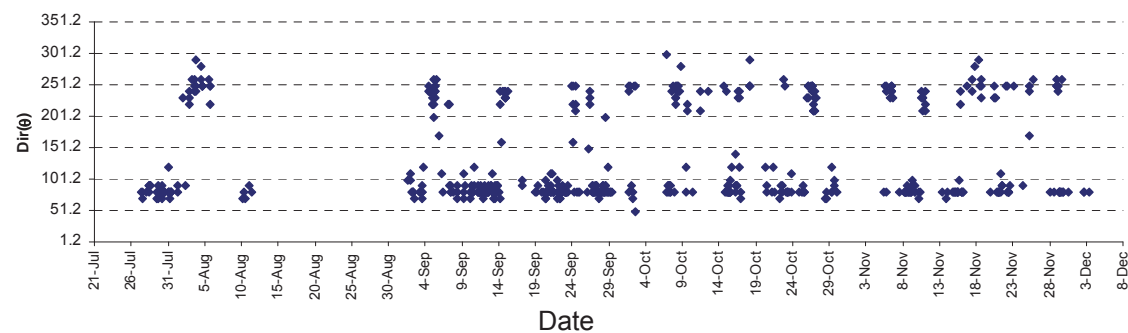


Figure 11: Wave directions obtained with SWAN for the period July to December 2010.

Table 2 presents a statistical analysis of the results in terms of average, maximum, minimum, that characterize the time series.

Table 2: Statistical analysis of SWAN model results for Ilha Solteira reservoir.

	Hs (m)	Tm (s)	Dir_peak (°)
Average	0.340	2.563	129.7
Standard Error	0.005	0.011	3.0
Median	0.350	2.448	80
Mode	0.367	2.448	80
Standard deviation	0.119	0.269	72.8
Variance	0.014	0.073	5293.7
Kurtosis	5.296	2.733	-1.03
Asymmetry	1.116	1.310	0.92
Range	1.125	1.844	250
Minimum	0.000	2.213	50
Maximum	1.125	4.057	300
Score	561	561	561

From the results presented it appears that the average significant wave heights and mean periods are 0:34 m and 2.6 s, low values, which are in agreement with the simulated wind speeds. The range of wave heights is between 0.0 and 1.1 m, while for average periods are between 2.2 and 4.2. Regarding the peak directions, the average value is around 130° with a range between 50° and 300°.

5 Conclusions

This paper presented the application of OndisaCAD and SWAN models to the study region of the dam reservoir of Ilha Solteira, São Paulo, Brazil. The models were used to simulate the wind-generated waves at the reservoir, considering some selected wind conditions from the period between 2007 until 2009. Results of both models were compared and discussed. Finally, SWAN is applied to a six month wind conditions in order to confirm its capability to perform long simulations.

It was found that the general behaviour of both models was quite similar. In fact, both models show at the same place the highest waves, and the same distribution of the wave height contours. Differences do occur especially in what concerns the values of the wave heights obtained. SWAN shows always higher waves than OndisaCAD. Notice that SWAN is a spectral nonlinear wave propagation model whereas OndisaCAD is based in empirical formulations.

Future work consists on the validation of both models with measurements which are being taken.

6 Acknowledgements

This study is funded by the FCT under the contracts of PTDC/ECM/73145/2006 and PTDC/ECM/67411/2006 and FCT/CAPES (Brazil) – “Building a Base for Research and Knowledge in Coastal Engineering”. The authors acknowledge the support made possible by the projects financed by CAPES – *Conselho Nacional de Desenvolvimento Científico e Tecnológico* contracts of refs. 0022101 and PPGE/FEIS-UNESP – *Programa de Pós Graduação em Engenharia Elétrica- Faculdade de Engenharia de Ilha Solteira-Brazil*. The authors acknowledge also the revision of Dr. João Alfredo Santos.

7 References

- BOUIJ, N., RIS, R. C. and HOLTHUIJSEN, L. H. (1999). A Third-generation Wave Model for Coastal Regions, Part I, Model Description and Validation. *Journal Geophysical Research*, 104 (C4), pp. 7649-7666.
- FORTES, C. J.; PINHEIRO, L.; SANTOS, J. A.; NEVES, M.G.; CAPITÃO, R. (2006). SOPRO – Pacote integrado de modelos de avaliação dos efeitos das ondas em portos. *Tecnologias da Água*, Edição I, Março 2006, pp. 51-61

- MACIEL, G.F; et al. (2009) Alerta de ventos e ondas para a segurança da navegação. 6º Seminário de Transporte e Desenvolvimento Hidroviário Interior. Rio de Janeiro, 21 and 22 October.
- MARQUES, M (2007) - Estimativa das máximas pistas de vento no reservatório da barragem de Ilha Solteira, Estado de São Paulo - DOI: 10.4025/actascitechnol.v29i1.112; Acta Scientiarum. Technology, Vol. 29, No 1 (2007).
- MORAIS, V. S.; CUNHA, E. F., MACIEL, G. F. (2009). "Medição, Previsão e Análise Numérica dos Mecanismos de Geração de Ondas a Partir da Cinética de Ventos e Dissipação de Ondas na Presença de Fundos com Vegetação, em Lagos de Barragens", In XVIII Simpósio Brasileiro de Recursos Hídricos. Campo Grande - Mato Grosso do Sul - Brasil: Anais do XVIII Simpósio Brasileiro de Recursos Hídricos.
- SAVILLE, T. et al. (1954). "The effect of fetch width on wave generation", Journal Technical Memorandum, n. 70.
- UNESP (1997, 2008) - ONDISA Project. Project support by FAPESP and FINESP Brazilian agencies.